CODEN: JASMAN

The Journal of the Acoustical Society of America

ISSN: 0001-4966

Vol. 110, No. 4 October 2001

(Continued)

THE JOURNAL OF THE ACOUSTICAL SOCIETY OF AMERICA VOL. 110, NO. 4, OCTOBER 2001

CONTENTS—*Continued from preceding page*

(Continued)

THE JOURNAL OF THE ACOUSTICAL SOCIETY OF AMERICA VOL. 110, NO. 4, OCTOBER 2001

CONTENTS—*Continued from preceding page*

(Continued)

THE JOURNAL OF THE ACOUSTICAL SOCIETY OF AMERICA VOL. 110, NO. 4, OCTOBER 2001

CONTENTS—*Continued from preceding page*

SPEECH PERCEPTION [71]

BIOACOUSTICS [80]

ACOUSTICAL NEWS—USA

Elaine Moran
Acoustical Society of America, Suite 1NO1, 2 Huntington Quadrangle, Melville, NY 11747-4502

Editor's Note: *Readers of this Journal are encouraged to submit news items on awards, appointments, and other activities about themselves or their colleagues. Deadline dates for news items and notices are 2 months prior to publication.*

New Fellows of the Acoustical Society of America

Shira Broschat—For contributions to scattering and biomedical acoustics.

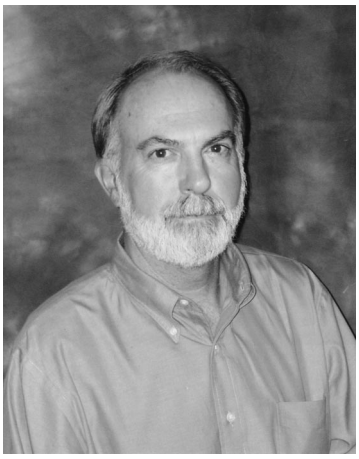

Michael F. Dorman—For contributions to the understanding of speech perception.

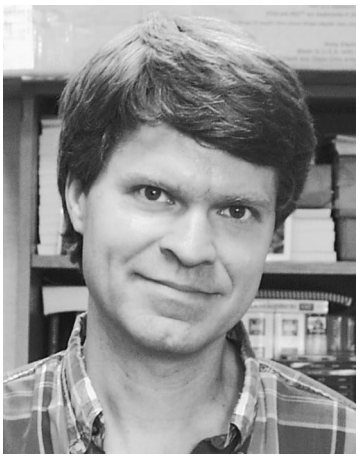

E. Carr Everbach—For contributions to biomedical ultrasound and education in acoustics.

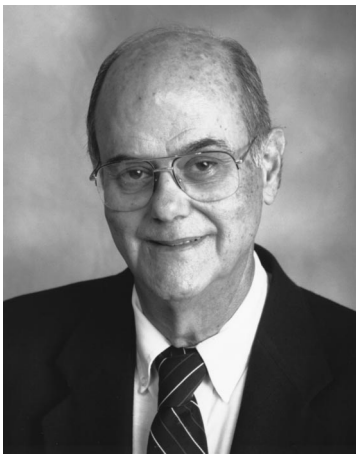

Allan G. Piersol—For application of random process theory in acoustics and vibration.

 0001-4966/2001/110(4)/1699/6/$18.00

The 141st meeting of the Acoustical Society of America held in Chicago, Illinois

The 141st meeting of the Acoustical Society of America was held 4–8 June 2001 at the Palmer House Hilton Hotel in Chicago, Illinois. This was the eighth time the Society has met in this city.

The meeting drew a total of 1303 registrants. There were 164 nonmembers and 341 students in attendance.

Attesting to the international ties of our organization, 195 of the registrants (that is, about 15%) were from outside North America, the United States, Canada, and Mexico, which accounted for 1022, 26, and 2, respectively. There were 36 registrants from the United Kingdom, 31 from Japan, 18 from France, 11 from Korea, 10 from Germany, 6 each from China, Denmark, and Sweden, 5 each from the Netherlands and Norway, 4 from Italy, 3 each from Australia, Brazil, and Ireland, 2 each from Finland, Hong Kong, India, Spain, and Turkey, and 1 each from Austria, Chile, Israel, New Zealand, Russia, Singapore, and the Ukraine.

A total of 1026 papers organized into 110 sessions covered the areas of interest of all 13 Technical Committees. The meeting also included six different meetings dealing with standards.

The local meeting committee arranged the following technical tours: Riverbank Acoustical Laboratories, the world's first independent laboratory dedicated to the science of architectural acoustics; Orchestra Hall, home to the Chicago Symphony Orchestra with a presentation from members of the firm who were involved in the renovation of the hall, and a walking tour of three Chicago theaters.

The tutorial lecture series was continued at the Chicago meeting. Thomas D. Rossing of Northern Illinois University and Uwe J. Hansen of Indiana State University presented ''Demonstration Experiments: Videos and Audios for Teaching Acoustics'' to an audience of about 120. A team of Chicago-area physics teachers assisted in the presentations.

Other special events included a Student Design Competition cosponsored by the Technical Committee on Architectural Acoustics and the National Council of Acoustical Consultants and receptions for students in various areas of acoustics. The Fellows Luncheon included a presentation by Dr. Emily A. Tobey of the University of Texas at Dallas on the subject of cochlear implants.

FIG. 2. ASA President Katherine Harris (l) presents the Helmholtz–Rayleigh Interdisciplinary Silver Medal to William M. Hartmann.

The plenary session included the presentation of awards, announcement of newly elected Fellows of the Society, recognition of the meeting organizers, and presentation of the ASA President's tuning fork to outgoing President Katherine S. Harris. The President presented three Society awards (see Figs. 1–3) and announced the election of 24 new Fellows.

The R. Bruce Lindsay Award was presented to Andrew J. Oxenham ''for contributions to the measurement of peripheral auditory nonlinearity, and to understanding its effects in normal and hearing-impaired listeners.'' The Helmholtz–Rayleigh Interdisciplinary Silver Medal was presented to William M. Hartmann ''for research and education in psychological and physiological acoustics, architectural acoustics, musical acoustics, and signal processing.'' The Gold Medal was presented to Herman Medwin ''for innovative research in ocean acoustics and leadership and service to the Society.''

FIG. 1. Andrew J. Oxenham (l), recipient of the R. Bruce Lindsay Award, with ASA President Katherine Harris (r).

FIG. 3. ASA President Katherine Harris (l) with Herman Medwin, recipient of the Gold Medal.

FIG. 4. Newly elected Fellows of the Acoustical Society of America receive their certificates from ASA Vice President Gilles Daigle and ASA President Katherine Harris.

Election of the following persons to Fellow grade was announced: Paul J. Abbas, Shira L. Broschat, Søren Bech, Angelo J. Campanella, Rene Causse, Michael F. Dorman, Stan E. Dosso, E. Carr Everbach, Brian G. Ferguson, Michael P. Gorga, John H. Grose, Takayuki Hidaka, Paul C. Hines, Christy K. Holland, Jun-ichi Kushibiki, Nathan C. Martin, Cynthia F. Moss, Virginia M. Richards, Mario A. Ruggero, Christian Soize, Thomas L. Szabo, Bernhard R. Tittmann, Emily A. Tobey, and William A. Watkins (see Fig. 4).

The President expressed the Society's thanks to the Local Committee for the excellent execution of the meeting, which clearly required meticulous planning. She introduced the Chair of the Meeting, Scott D. Pfeiffer, who acknowledged the contributions of the members of his committee including: Paul T. Calamia and John W. Kopec, Technical Program Cochairs; David Moyer, Audio-Visual; David Larson, Hotel/Facilities; Stephen Kiss, Registration; Martha Larson, Signs; Edward Dugger, Dawn Schuette, Technical Tours/Accompanying Persons Program and Social Programs; Ian Hoffmann, Plenary Session/Fellows Luncheon; Brian Homans, Al Shiner, Food & Beverage; and Brian Homans, Publicity.

The President also extended thanks to the members of the Technical Program Organizing Committee: Paul T. Calamia and John W. Kopec, Technical Program Cochairs; Mohsen Badiey and William L. Siegmann, Acoustical Oceanography; Larry L. Pater, Animal Bioacoustics; Robin S. Glosemeyer and Brandon D. Tinianov, Architectural Acoustics; J. Brian Fowlkes, Biomedical Ultrasound/Bioresponse to Vibration; Uwe J. Hansen, Education in Acoustics; Stephen C. Thompson, Engineering Acoustics; James A. Beauchamp, Musical Acoustics; Bennett M. Brooks and Angelo J. Campanella, Noise; Anthony A. Atchley and Larry A. Wilen, Physical Acoustics; William P. Shofner, Psychological and Physiological Acoustics; Ning Xiang and Charles H. Gaumond, Signal Processing in Acoustics; Gary H. Weismer, Speech Communication; Richard L. Weaver, Structural Acoustics and Vibration; and Stewart A. L. Glegg and Joseph F. Lingevitch, Underwater Acoustics.

KATHERINE S. HARRIS
President 2000–2001

ASA presents special awards to young scientists at the 52nd annual International Science and Engineering Fair (ISEF)

The Acoustical Society of America (ASA) presented four special awards at the 52nd International Science and Engineering Fair (ISEF), held 6 to 12 May 2001, at the San Jose, CA, Convention Center. The ISEF began in 1950 as a means of encouraging precollege students to conduct scientific research. Today, it is the only international science project competition for students in grades 9 to 12. This year's ISEF attracted more than 1200 high school students from 38 countries around the world to compete for more than $3 million in prizes and scholarships. ISEF 2001 also brought together almost 1200 professionals, representing university faculty, industrial scientists and engineers, representatives of private and federal research centers and agencies, and medical researchers. Over 70 professional organizations, including the ASA, representing a wide variety of scientific disciplines, affiliate with the ISEF as Special Awards sponsors. The ASA's First Prize Award of $500 went to Naveen Sinha, 16, from Los Alamos High School, Los Alamos, New Mexico, for his project, entitled, ''Interaction Between Sound and Liquid Crystals.'' Naveen designed and built an apparatus to investigate the use of light transmission through liquid crystals to visualize sound fields (He even built the liquid crystals himself!). It is noteworthy that Naveen was an ASA Honorable Mention awardee at last year's ISEF. In addition to the first prize, the ASA also presented three Honorable Mention Awards, to Josh Borts, 16, and Josep Lallouz, 16, from Saint Georges School Montreal, Montreal, QC, Canada, for their project, entitled ''Stop, Look, and Listen,'' an interesting psychoacoustics project in which the effect of an auditory cue on the reaction time for a three-dimensional visual search was investigated; to Roman Eskue, 16, from Wilcox High School, Wilcox, Arizona, for his project, entitled ''Star in a Jar,'' a very ambitious physical acoustics project in which sonoluminescence was demonstrated; and to Surey Santini, 16, and Sheila Gonzalez, 16, from Bonifacio Sanchez Jimenez High School, Aiboito, Puerto Rico, for their project, entitled ''Noise: Destructor Sound in School,'' an environmental acoustics project in which the students demonstrated that the noise exposure at certain locations at their school exceeds legal limits. It is interesting to note that two of the four ASA awardee projects are from outside the U.S., and that, coincidentally, all of this year's awardees are 16 years of age!

Each winner also received a one-year student membership in ASA. These winners were selected from some 30 projects determined by the ASA judges to be relevant to acoustics among the 1000 projects entered in the ISEF 2001. The ASA judges were Dr. Doug Corl (PharmaSonics, Inc., Sunnyvale, CA), Dr. Larry Crosby (Symphonix Devices, Inc., San Jose, CA), and Dr. Steve Baker (Department of Physics, U.S. Naval Postgraduate School, Monterey, CA). Dr. Corl represented the ASA at the awards ceremony. I would like to add what a rewarding experience it was to serve as an ASA Special Awards judge, and encourage all ASA members to consent to serve at a future ISEF if asked.

STEVE BAKER

Student Design Competition Awards presented at Chicago meeting

The Acoustical Society of America (ASA) Technical Committee on Architectural Acoustics (TCAA) and the National Council of Acoustical Consultants (NCAC) sponsored a student design competition, judged at the 141st ASA meeting in Chicago, June 2001. The project involved the preparation of a schematic design for a college performing arts center with emphasis on room acoustics and noise control. There were 17 posters submitted from 10 different schools. This year's panel of judges included: Mark

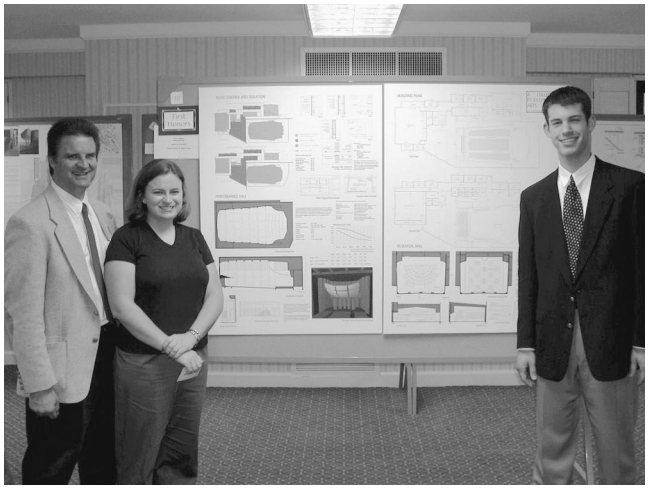

FIG. 5. Bob Celmer (l) with First Honors Award recipients Jessica Newton and Byron Harrison.

Holden (Jaffe Holden Acoustics), Gary Madaras (The Talaske Group), Ron McKay (McKay Conant Brook), Dawn Schuette (Kirkegaard Associates), and Leslie Ventsch (Skidmore Owings & Merrill).

First Honors with a cash prize of $1000 was awarded to Jessica Newton and Byron Harrison from the University of Hartford (faculty advisor: Bob Celmer) (see Fig. 5). Four Commendations with cash prizes of $500 were given to the following groups: Mona Tamari and Jorge Carbonell from the Massachusetts Institute of Technology (faculty advisor: Carl Rosenberg); Lance Hayes and Derrick Knight from Rensselaer Polytechnic Institute (faculty advisor: Rendell Torres); Brian Corry and Lucy Williams from the University of Kansas (faculty advisor: Bob Coffeen); and Greg Hughes, Ryan O'Halloran, and Jon Peterson from the University of Kansas (faculty advisor: Bob Coffeen).

The following organizations generously sponsored this year's competition: Wenger Corporation, the Newman Student Award Fund, Telex/Electro-Voice and Auralex Acoustics, Inc. Additional pictures from the competition may be viewed at the following website: http://www.ae.unomaha.edu/lwang/asa2001.htm

USA Meetings Calendar

Listed below is a summary of meetings related to acoustics to be held in the U.S. in the near future. The month/year notation refers to the issue in which a complete meeting announcement appeared.

2001

7–10 October	2001 IEEE International Ultrasonics Symposium Joint with World Congress on Ultrasonics, Atlanta, GA [W. O'Brien, Electrical and Computer Engineering, Univ. of Illinois, 405 N. Mathews, Urbana, IL 61801; Fax: 217-244-0105; WWW: www.ieee-uffc.org/2001].
29–31 October	NOISE-CON 01, The 2001 National Conference and Exposition on Noise Control Engineering, Portland, ME [Institute of Noise Control Engineering, P.O. Box 3206 Arlington Branch, Poughkeepsie, NY 12603; Tel: +1 914 462-4006; Fax: +1 914 462 4006; E-mail: omd@ince.org; WWW: users.aol.com/inceusa/ince.html].
15–18 November	American Speech Language Hearing Association Convention, New Orleans, LA [American Speech-Language-Hearing Association, 10801 Rockville Pike, Rockville, MD 20852; Tel: 888-321-ASHA; E-mail: convention@asha.org; WWW: professional.asha.org/convention/abstracts/welcome.asp].
3–7 December	142nd Meeting of the Acoustical Society of America, Ft. Lauderdale, FL [Acoustical Society of America, Suite 1NO1, 2 Huntington Quadrangle, Melville, NY 11747-4502; Tel.: 516-576-2360; Fax: 516-576-2377; E-mail: asa@aip.org; WWW: asa.aip.org].

2002

21–23 February	National Hearing Conservation Association Annual Conference, Dallas, TX [NHCA, 9101 E. Kenyon Ave., Ste. 3000, Denver, CO 80237; Tel.: 303-224-9022; Fax: 303-770-1812; E-mail: nhca@gwami.com; WWW: www.hearingconservation.org/index.html].
10–13 March	Annual Meeting of American Institute for Ultrasound in Medicine, Nashville, TN [American Institute of Ultrasound In Medicine, 14750 Sweitzer Lane, Suite 100, Laurel, MD 20707-5906; Tel.: 301-498-4100 or 800-638-5352; Fax: 301-498-4450; E-mail: conv_edu@aium.org; WWW: www.aium.org].
3–7 June	143rd Meeting of the Acoustical Society of America, Pittsburgh, PA [Acoustical Society of America, Suite 1NO1, 2 Huntington Quadrangle, Melville, NY 11747-4502; Tel.: 516-576-2360; Fax: 516-576-2377; E-mail: asa@aip.org; WWW: asa.aip.org].
2–6 December	Joint Meeting: 144th Meeting of the Acoustical Society of America, 3rd Iberoamerican Congress of Acoustics and 9th Mexican Congress on Acoustics, Cancun, Mexico [Acoustical Society of America, Suite 1NO1, 2 Huntington Quadrangle, Melville, NY 11747-4502; Tel.: 516-576-2360; Fax: 516-576-2377; E-mail: asa@aip.org; WWW: asa.aip.org/cancun.html].

Cumulative Indexes to the *Journal of the Acoustical Society of America*

Ordering information: Orders must be paid by check or money order in U.S. funds drawn on a U.S. bank or by Mastercard, Visa, or American Express credit cards. Send orders to Circulation and Fulfillment Division, American Institute of Physics, Suite 1NO1, 2 Huntington Quadrangle, Melville, NY 11747-4502; Tel.: 516-576-2270. Non-U.S. orders add $11 per index.

Some indexes are out of print as noted below.

Volumes 1–10, 1929–1938: JASA, and Contemporary Literature, 1937–1939. Classified by subject and indexed by author. Pp. 131. Price: ASA members $5; Nonmembers $10.

Volumes 11–20, 1939–1948: JASA, Contemporary Literature and Patents. Classified by subject and indexed by author and inventor. Pp. 395. Out of print.

Volumes 21–30, 1949–1958: JASA, Contemporary Literature and Patents. Classified by subject and indexed by author and inventor. Pp. 952. Price: ASA members $20; Nonmembers $75.

Volumes 31–35, 1959–1963: JASA, Contemporary Literature and Patents. Classified by subject and indexed by author and inventor. Pp. 1140. Price: ASA members $20; Nonmembers $90.

Volumes 36–44, 1964–1968: JASA and Patents. Classified by subject and indexed by author and inventor. Pp. 485. Out of print.

Volumes 36–44, 1964–1968: Contemporary Literature. Classified by subject and indexed by author. Pp. 1060. Out of print.

Volumes 45–54, 1969–1973: JASA and Patents. Classified by subject and indexed by author and inventor. Pp. 540. Price: $20 (paperbound); ASA members $25 (clothbound); Nonmembers $60 (clothbound).

Volumes 55–64, 1974–1978: JASA and Patents. Classified by subject and indexed by author and inventor. Pp. 816. Price: $20 (paperbound); ASA members $25 (clothbound); Nonmembers $60 (clothbound).

Volumes 65–74, 1979–1983: JASA and Patents. Classified by subject and indexed by author and inventor. Pp. 624. Price: ASA members $25 (paperbound); Nonmembers $75 (clothbound).

Volumes 75–84, 1984–1988: JASA and Patents. Classified by subject and indexed by author and inventor. Pp. 625. Price: ASA members $30 (paperbound); Nonmembers $80 (clothbound).

Volumes 85–94, 1989–1993: JASA and Patents. Classified by subject and indexed by author and inventor. Pp. 736. Price: ASA members $30 (paperbound); Nonmembers $80 (clothbound).

Volumes 95–104, 1994–1998: JASA and Patents. Classified by subject and indexed by author and inventor. Pp. Price: ASA members $40 (paperbound); Nonmembers $90 (clothbound).

Revision List

New Associates

Arata, Jonathan J., Foster-Miller, Inc., DSI, 350 Second Ave., Bldg. 4, Waltham, MA 02451

Asch, Mark, Engineering Mechanics, Inst. des Sciences de I'Ingenieur de Toulon et du Var, Ave. G. Pompidou BP 56, La Valette du Var 83162, France

Barros, Alessio T., Rue Apriglio Veloso, 882 Bodocongo, Campina Grande, Paraiba 10031, Brazil

Bonaventura, Patrizia, Conversay, Core Technology, 15375 NE 90th St., Redmond, WA 98052

Collier, Sandra L., P.O. Box 1624, Beltsville, MD 20704

Connelly, Terence, 619 N. Center St., Northville, MI 48167-1225

Crosswhite, Katherine M., Center for Language Sciences, Dept. of Linguistics, Univ. of Rochester, Lattimor Hall, Rochester, NY 14627

Dain, Yefim, Mechanical Engineering, Northwestern Univ., 2145 Sheridan Rd., Evanston, IL 60208-3111

Davidson, Steve, Davidson & Associes Inc., 392 Principale St., St. Sauveur, QC J0R 1R0, Canada

DiMassa, Diane E., Mechanical Eng. Dept., II-116A, Univ. of Massachusetts, 285 Old Westport Rd., North Dartmouth, MA 02747
Esquivel, Adolfo, National Center of Metrology, Vibrations and Acoustics, Km. 4.5 Conr. o los Cues, Mpio del Marques, Queretaro, Mexico
Eswaran, Hari, Dept. of Applied Science, Univ. of Arkansas at Little Rock, ETAS575, 2801 S. University Ave., Little Rock, AR 72204
Fitz, Kelly R., Electrical Engineering and Computer Science, Washington State Univ., P.O. Box 642752, Pullman, WA 99164-2752
Golick, Alexander V., Materials and Chemical Tech. Res. Inst., Marmara Research Center, Tubitak, Gebze, Kocaeli 41470, Turkey
Goody, Michael C., NSWC Carderock Div., Signatures Directorate, Code 7250, 9500 MacArthur Boulevard, West Bethesda, MD 20817-5700
Gottlieb, Hans P., School of Science, Griffith Univ., Kessles Rd., Nathan, QLS 411, Australia
Gray, Lincoln C., Otolaryngology, Univ. of Texas Houston Medical School, 6431 Fannin, Ste. 5.003, Houston, TX 77030
Harma, Aki J., Bell Labs., Lucent Technologies, Media Signal Processing Research, Room 2D-544, 600 Mountain Ave., Murray Hill, NJ 07974
Harper, V. P., Biomedical Engineering, Purdue Univ., 1285 Electrical Engineering, West Lafayette, IN 47906
Hernandez-Canedo, Pedro, VoCAL Technologies Europa, Placa Gran 13, Peralada, Girona, 17491 Spain
Houston, Derek M., Dept. of Otolaryngology, Head and Neck Surgery, Indiana Univ. School of Medicine, 699 W. Drive, RR044, Indianapolis, IN 46202
Ibisi, Michael I., 6832 SW 11th St., Pembroke Pines, FL 33023
Jensen, Troy B., ALTEL Systems, Inc., 601 N. Main St., Brewster, NY 10509
Joiner, David P., Shen Milsom Wilke + Joiner, 100 E. San Antonio, Ste. 201, San Marcos, TX 78666
Kapur, Ajay, Lernout & Hauspie, 320 Nevada St., Newton, MA 02460
Kim, Sang-Myeong, Mechatronics Dept., Kwang-ju Inst. of Sci. and Tech., 1 Oryong-dong, Puk-gu, Kwang-ju, Keon-Nam, 500-712 South Korea
Kimura, Miwako, 4-18-3 Hongo, Bunkyo-ku, 113-0033 Tokyo, Japan
Larson, Charles R., Northwestern Univ., CSD, 2299 N. Campus Dr., Evanston, IL 60208
Lee, Heewon, Dept. of Mechanical Design, Seoul National Univ. of Tech., 172 Gongnung-dong, Nowon-gu, Seoul 139-743, Korea
Lesser, Martin, Royal Inst. of Technology, Osquarsbacke 18, Stockholm SE100-44, Sweden
Lewis, James W., Medical College of Wisconsin, Cell Biology, Neurobiology & Anatomy, 8701 Watertown Plank Rd., Milwaukee, WI 53226
Li, Ming-xuan, Inst. of Acoustics, Chinese Academy of Sciences, Dept. of Acoustical Micro-Transducer & Testing, No. 17, Zhongguancun St., Beijing 100080, China
Liu, Donald, Siemens Medical Systems Ultrasound Group, Advanced Ultrasound Engineering, 22010 SE 51st St., Issaquah, WA 98029
Mizumachi, Mitsunori, ATR Spoken Language Translation Research Labs., Dept. 1, 2-2-2 Hikaridai, Seika-chou, Souraku-gun, Kyoto 619-0288, Japan
Morishita, Tatsuya, Electrical Engineering Dept., Tokyo National College of Technology, 1220-2 Kunugida-machi, Hachioji-shi, Tokyo 193-097, Japan
Mukai, Tohru, Graduate School of Fisheries Sciences, Hokkaido Univ., 3-1-1 Minato-cho, Hakodate, Hokkaido 041-8611, Japan
Nagahata, Koji, Faculty of Administration & Social Sci., Fukushima Univ., Kanayagawa 1, Fukushima 960-1296, Japan
Ozawa, Kenji, Dept. of Computer Sci. and Media Eng., Yamanashi Univ., 4-3-11 Takeda, Kofu, Yamanashi 400-8511, Japan
Pappas, Richard A., Battelle, Pacific Northwest Div., Engineering Physics, 902 Battelle Boulevard, Richland, WA 99352
Parastates, Elias, Swedish Defence Research Agency, Div. of Systems Tech, Dept. of Underwater Acoustics, Enkopingsvageu 126, Stockholm SE-17290, Sweden
Penrod, Clark S., Applied Research Labs., Univ. of Texas, Austin, TX 78713
Perry, Matthew R., 7913 High Hollow Dr., Austin, TX 78750
Plemons, Terry D., Applied Research Labs., Univ. of Texas, P.O. Box 8029, Austin, TX 78713
Popolo, Peter S., Denver Center for the Performing Arts, W. J. Gould Voice Center, 1245 Champa St., Denver, CO 80204
Saenz, Daniel W., Pelton Marsh Kinsella, 1420 W. Mockingbird Ln., #400, Dallas, TX 75247
Sansone, Stan A., 6206 Sampras Ace Ct., Spring, TX 77379
Schedl, Hans P., AUDI AG, I/EG−1A, Ingolstadt 85045, Germany
Simons, Dick G., TNO Physics and Electronics Lab., Underwater Acoustics Group, Oude Waalsdorperweg 63, The Hague 2509JG, The Netherlands
Snyder, Barbara A., Dept. of Justice−FBI, Federal Government, Engineering Research Facility, Bldg. 27958A, Quantico, VA 22135
Stecenko, Tatjana B., Polyfab/MTI, Aerospace, 7391 Pacific Cir., Mississauga, ON L5T 2A4, Canada
Sydorenko, Mark R., BrainMedia, 150 E. 23rd St., New York, NY 10010
Talavage, Thomas M., Electrical and Computer Eng., Purdue Univ., 1285 EE Bldg., West Lafayette, IN 47907
Tangonan, Stacey L. E., Group 70 International, 925 Bethel St., 5th Floor, Honolulu, HI 96813-4398
Tavakkoli, Jahangir, Focus Surgery, Inc., 3940 Pendleton Way, Indianapolis, IN 46226
Tayama, Niro, Higashihorikiri 2-26-5, #201, Katsusika-ku, Tokyo 124-0004, Japan
Teklu, Alem A., NCPA, Coliseum Dr., University, MS 38677
Tiemann, Christopher O., SAIC, Ocean Sciences Div., 888 Prospect St., Ste. 201, La Jolla, CA 92037
Tisato, Graziano G., Via Bachelet 5, Vigonza PD-35010, Italy
Veidt, Martin, Mechanical Engineering, Univ. of Queensland, Brisbane QLD 4072, Australia
Zurek, Robert A., 1055 Autumn Dr., Antioch, IL 60002

New Students

Aoki, Takuya, Dept. of Electrical Engineering, Tokyo Metropolitan Univ., 1-1 Minami-Osawa, Hachioji, 192-0397 Tokyo, Japan
Badri, Rohima, 208-1 1915 Maple Ave., Evanston, IL 60201
Bajwa, Manjit S., 460 W. Forest, #903, Detroit, MI 48201
Barrera, Leandro M., San Juan 197, Torre B2, Dept. 1A, Neuquen 8300, Argentina
Blacklock, Oliver S., ISIS, Univ. of Southampton, Bldg. 1, University Rd., Southampton SO17 1BJ, UK
Bravo, Luis A., Palmeras 1410 y Madronos, Quito, Pichingha, Ecuador
Bray, Jodi P., 1130 SW 16th Ave., #46, Gainesville, FL 32601
Brennan, Marc A., 140 W. Gorham, Apt. 103, Madison, WI 53703
Carpendale, Lucy M., Brunel Univ., Mechanical Engineering, Howell Bldg., Uxbridge, Middlesex UB8 3PH, UK
Carron, Henry, LAMI Univ. Paul Sabatier, 118 Rte. De Narbonne, 31062 Toulouse, Cedex 4, France
Carter, Barton P., 2913 Prairie Flower Cir., No. C, Bryan, TX 77802-3006
Chan, Arthur H., 13626 26th Ave., SE, Mill Creek, WA 98012
Choy, Yat-Sze, Flat D 9/F Block 82, Mei Foo Sun Chuen, KLN, Hong Kong
Corry, Brian P., 1217 Berquist Ct., Ballwin, MO 63011
Declercq, Nico F., Interdisciplinary Research Center, KULAK, E. Sabbelaan 53 (A112), Kortrijk, West Flanders, 8500, Belgium
de Silva, Sharin R., Dept. of Mechanical and Materials Eng., Univ. of Western Australia, Nedlands WA 6009, Australia
Devlin, Adam T., 2948 River Meadow Cir., Canton, MI 48188
Dick, Elliott B., 1176 Lincoln Ave., St. Paul, MN 55105
Dunn, Camille C., Barkely Memorial Speech & Hearing Clinic, 253 BKC, Lincoln, NE 68583
El-Khateeb, Ahmed Ali, 8B-Shakh Olish St., Cairo, El-Ziton 1131, Egypt
Epstein, Michael J., P.O. Box 230338, Boston, MA 02123-0338
Fishbeck, Kristen M., 707 W. Martin Luther King, Apt. 608E, Cincinnati, OH 45220
Fouts, Bruce E., 2120 Saint James Ave., Cincinnati, OH 45206
Hakim, Souheil, Chouran, Cleopatra St., Hakim Motors Bldg., Beirut, Lebanon
Haldipur, Pranaam, Material Science Dept., Iowa State Univ., ASC II, #124, 1915 Scholl Rd., Ames, IA 50011
Harvey, Ryan, 603 Willowdale Rd., Luling, LA 70070
Holt, Marla M., Univ. of California, Santa Cruz, Long Marine Lab., 100 Shaffer Rd., Santa Cruz, CA 95060
Horan, Daniel M., 1630 W. Lunt Ave., #1B, Chicago, IL 60626-2757
Hughes, Gregory M., 1908 New Hampshire St., Lawrence, KS 66044
Ikram, Muhammad Z., 338028 Georgia Tech Station, Atlanta, GA 30332
Jaouen, Luc, Groupe d'acoustique et vibrations, Univ. de Sherbrooke, Faculte de genie, 2500 Boul. Universite, Sherbrooke, QC J1K 2R1, Canada
Lance, Tara R., 7427 W. 84th Way, #2122, Arvada, CO 80003
Lee, Matthew E., 1201 Noble Creek Dr., Atlanta, GA 30327

Liehr, April M., 5725 Abilene Trail, Austin, TX 78749
Madison, Jeffrey S., RPG Diffusor Systems, Inc., 651-C Commerce Dr., Upper Marlboro, MD 20774
Marozeau, Jeremy P., UC Berkeley, CNMAT, 1750 Arch St., Berkeley, CA 94709
Mast-Finn, John, Dept. of Linguistics, Ohio State Univ., 1712 Neil Ave., Oxkley Hall Room 222, Columbus, OH 43210
McDermott, Brian J., 127 Ryckmon Ave., Apt. 2L, Albany, NY 12208
McLennan, Conor T., Language Perception Lab., Univ. at Buffalo, 245 Park Hall, Buffalo, NY 14260
Meltzner, Geoffrey S., Voice and Speech Lab., Massachusetts Eye and Ear Infirmary, 243 Charles St., Boston, MA 02114
Mou, Xiaomin, 305 Memorial Dr., #406A, Cambridge, MA 02139
Nagi, Ashnapreet S., 460 W. Forest, Apt. 903, Detroit, MI 48201
Neil, Coffey, Language and Linguistic Sci., Univ. of York, Heslington, York YO10 5DD, UK
Obando, Miguel A., J. M. Infante 2007, Santiago 684-1362, Chile
Osmanski, Michael S., Dept. of Psychology, Univ. of Maryland, Biology-Psychology Bldg., College Park, MD 20742
Park, Eun-Joo, Aerospace and Mechanical Eng., Boston Univ., 110 Cummington St., Boston, MA 02215
Pfau, Kenneth J., Pfau Audio Productions, 2641 1/2 N. Spaulding Ave., #2N, Chicago, IL 60647
Quarles, William M., 800 S. Main St., Harrisonburg, VA 22807
Salomon, Ariel, EECS, Massachusetts Inst. of Technology, 77 Massachusetts Ave., 36-511, Cambridge, MA 02142
Schneider, Terri L., 4631 Dakeman Rd., Lakeland, FL 33813
Schneider, Wendy E., Medical College of Wisconsin, Cell Biology, Neurobiology and Anatomy, 8701 Watertown Plank Rd., Milwaukee, WI 53226
Senova, Melis, Defence Science and Technology Organization, Air Operations Division, 506 Lorimer St., Fishermens Bend, Melbourne VIC 3101, Australia
Sirovic, Ana, Scripps Inst. of Oceanography, Univ. of California, San Diego, 9500 Gilman Dr., MC 0205, La Jolla, CA 92093-0205
Smet, Kevin, Centre for Marine Geology, Ghent Univ., Krijgslaan 281 (S8), Ghent OV B9000, Belgium
Tallon, Andrew J., 521 W. 112th St., Apt. 72B, New York, NY 10025
Tiwari, Vikrant, Mechanical Eng. and Applied Mechanics, 110 Wales Hall, 92 Upper College Rd., Kingston, RI 02881
Walton, Martin A., Inst. Univ. de Technologie, Univ. de Pau et des Pays de l'Adour, Informatique, Tech. de. Co. G.E.A. et FORCO, 3 Ave. Jean Darrigrand, Bayonne, 64100, France
Wayand, Joseph F., Psychology Dept., Kent State Univ., P.O. Box 5190, Kent, OH 44242
Wheatley, Joseph S., P.O. Box 1102, Picayune, MS 39466
White, Ross A., 1902 N. Laurence St., Tacoma, WA 98406
Wilks, Carsten, Neuroinformatics, Univ. of Bonn, Roemerstrasse 164, Bonn NRW 53117, Germany
Windels, Filip W., Interdisciplinary Research Center, KULAK, E. Sabbelaan 53, Kortrijk 8500, Belgium
Yazicioglu, Yigit, Mechanical Engineering, Univ. of Illinois, 842 W. Taylor St., ERF 1072, Chicago, IL 60607
Yin, Xiangtao, Bioacoustics Research Lab., Electrical and Computer Eng., Univ. of Illinois at Urbana-Champaign, 405 N. Mathews, Urbana, IL 61801

Associates Elected Members

K. Adachi, D. E. Ballesty, J. Bassett, A. Bayon, A. R. Bradlow, K. E. Bunton, P. Chiu, G. Clement, T. H. Dat, S. Dugelay, M. Ermann, X-F. Gong, H. M. Hanson, D. Hunsaker, II, J. Y. Jeon, B. H. Juang, H. Kato, T. L. Lago, D. R. Moore, T. F. Noonan, Y. Simard, S. O. Ternstrom, H. K. Vorperian, M. Zampolli, J. Zhang

Students to Associates

E. C. Odgaard, Y. Shibuya

Member to Student

A. D. Munro

Reinstated

K. A. Gillis—*Associate*

Resigned

A. B. Brenig—*Fellow*

P. A. Chinnery, J. F. Guess, K. Ikegaya, P. J. Kolston, H. V. L. Patrick, D. van Dord—*Members*

C. M. Bissonnette, A. Ratle—*Students*

Deceased

J. N. Decarpigny, L. L. Foldy, D. E. Weston—*Fellows*

E. F. Murphy—*Member*

Fellows	978
Members	2716
Associates	2451
Students	843
	6988

OBITUARIES

Antares M. Parvulescu • 1923–1998

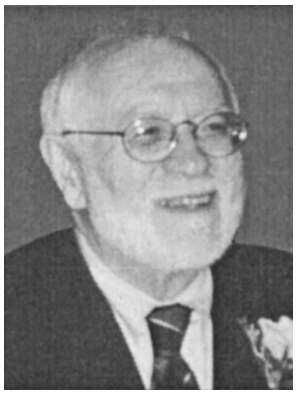

Antares Parvulescu, a Fellow of the Acoustical Society of America and a leading figure in underwater acoustics and the inventor of the Matched Field Processing technique, now widely used in underwater acoustics, died on July 15, 1998 from complications of a stroke.

Antares was born in Romania, and his father, an astronomer, named him after a super-giant star: first magnitude Antares in Scorpio; 300 times the diameter of our sun; and 3000 times as luminous. Antares, who became a super star in his own right, was exceptionally gifted and received his doctoral degree in mathematics in 1943 from the University of Bucharest at the early age of 19. He learned to fly at 14, and at age 20 flew his own plane, escaping from Romania to Turkey on an anti-Nazi mission. He spent the remainder of the war at the Romanian mission in Egypt. After the Communist take-over of Romania, he moved to South Africa, where he taught at the University of Witwatersrand (1947–1950), and then in 1950 moved to the United States, where he continued to progress in an academic career at Berkeley (1950–1951), Bard (1951–1954), Villanova (1954–1955), and Gallaudet (1955–1960), serving the latter as Head of the Physics Department. In 1960, he joined Columbia University's Hudson Laboratories and concentrated on research in oceanography and underwater acoustics. Many of the ideas for which he is now well known trace back to this period at Hudson Laboratories. Perhaps his greatest one is what we now call Matched Field Processing, which can alternately be termed Phase Conjugation or Time Reversal. He called this invention MESS, because sound propagation is indeed a mess, and he had various explanatory names for the acronym (for example, Matched Environment Sonar Signal). Although the technique of matched filtering had been published earlier for radar, he grasped the concept perfectly, and used the ocean as its own matched filter. His seminal publication was a terse abstract in *The Journal of the Acoustical Society of America* in 1961. He was granted a patent for the technique in 1962, and many years later, in 1996, published (with the help of his good friend Ray Fitzgerald) the historical perspective in *The Journal of the Acoustical Society of America*. Other research in the 1960s anticipated Synthetic Aperture Sonar.

When Hudson Laboratories closed in 1968 he moved to the University of Hawaii, with an appointment as Professor of Ocean Engineering and continued to work there, doing teaching and research, supervising graduate student work, until the nominal retirement age. During this period, he served in 1983 on an Intergovernmental Personnel Agreement (IPA) at the Naval Research Laboratory (NRL) in Washington, DC. After retirement from the University of Hawaii he joined NRL as a permanent employee and resumed a full-time research involvement. At NRL, Antares applied a broad knowledge of all aspects of ocean acoustics on a variety of projects, and was a major advisor to several Navy organizations. After his retirement from NRL, less than a year before his passing away, he had considerable success as an independent consultant, with a number of projects that had attracted the interest of Navy research program officers and which he intended to pursue in the years to come. He was especially interested in active noise cancellation, and a project in near field noise cancellation was scheduled to be funded by the Office of Naval Research at the time of his death.

Dr. Parvulescu is survived by his wife Elaine and by his son Constantin.

THEO KOOIJ

William Mott Hall • 1906–2000

William Mott Hall, a Fellow of the Acoustical Society of America, died of natural causes in Lexington, Massachusetts, on 3 August 2000. Dr. Hall was born on 10 July 1906 in Burlington, Vermont, and began his undergraduate studies at the University of Vermont in 1923. He transferred to the Massachusetts Institute of Technology (MIT) in 1925 and received his BSEE in 1928, his MS in 1932, and his Sc.D. in 1935; all of his degrees were in Electrical Engineering. He joined the Acoustical Society of America in 1930 and his name appears in the membership listing published in the April 1931 issue of JASA. Both of his dissertations were written under the direction of Professor Richard D. Fay, a charter member of the Acoustical Society and a long-term distinguished contributor to this journal. Hall's MS thesis was titled ''An investigation of sound fields within regions restricted by finite boundaries,'' and this formed the basis for his first paper in the Journal, ''Comments on the theory of horns'' [J. Acoust. Soc. Am. **3**, No. 4, 552–561 (1932)].

During the latter phase of his graduate work, Hall worked with Fay on problems of electroacoustic measurements and public address systems. A paper published in the July 1933 issue of JASA [J. Acoust. Soc. Am. **5**, 46–56 (1933)] with Fay was titled ''Determination of the acoustical output of a telephone receiver from input measurements.'' At the 14th meeting of the ASA, held at Harvard in December 1935, Fay and Hall both gave talks reporting the discovery of what was later to become known as the Haas effect or the precedence effect, whereby (as expressed in a letter to the editor published in January 1956) ''in a sound-enforcing system, a suitable time delay in the amplified sound produces a desirable illusion in that the enforced sound, as well as the direct, appears to originate at the mouth of the listener.''

Following the completion of his doctorate, Hall remained at MIT and held appointments as Instructor and Assistant Professor of Electrical Communications. It was during this period that he wrote what was destined to become one of the best-cited papers in the history of acoustics, this being titled ''An acoustic transmission line for impedance measurement'' [J. Acoust. Soc. Am. **11**, No. 1, Pt. 1, 140–146 (1939)]. This paper contains the theory of the impedance tube which is typically discussed in every textbook on acoustics—''The measurement consists of a simple determination of the location and relative magnitude of the maximum and minimum sound pressures along the tube.'' Hall was made a Fellow of the Acoustical Society of America in 1940.

Hall's research in acoustics was largely curtailed with a call to help in the US research and development work related to World War II. During 1940 and 1941 he was head of the Indicator Group of the MIT Radiation Laboratory. In 1941, when his expertise in microwaves was needed for Raytheon's activities in the war effort, he joined the Raytheon Company, at which he worked for the remainder of his professional career. While a graduate student at MIT, Hall had done some work with Vannevar Bush, who was then Dean of the School of Engineering. In 1940, Dr. Bush, then Chairman of the National Defense Research Committee (NDRC), appointed Hall a consultant to the Microwave Section of the NDRC. During World War II, Hall was responsible for the design, development, and installation of the first radar aboard ships in the United States Navy. He received a certificate of commendation from the United States Government for this effort. During the Cold War, he served on the Gaither Committee, a group appointed by President Eisenhower in 1957 to survey national security problems. In 1962, he became the first person to be awarded Raytheon's distinguished title of Consulting Scientist, and in 1966 he was made a Fellow of the Institute of Electrical and Electronics Engineers.

He held 37 patents covering infrared, acoustics, instrument landing systems, radar devices, and the microwave oven. At the time of his retirement in 1971 he was the Raytheon Company's Director of Developmental Engineering. He continued to consult for the company until he was 84 years old.

He leaves three sons, 12 grandchildren, and 12 great-grandchildren.

JOSEPH L. HALL

 0001-4966/2001/110(4)/1707/2/$18.00

Dan Jerry Ramsdale • 1942–2000

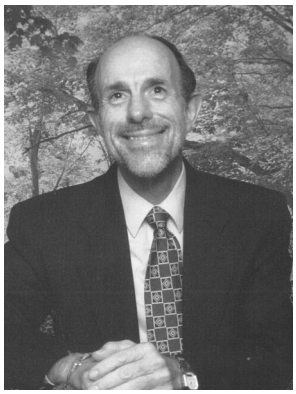

Dan Jerry Ramsdale, a member of the Acoustical Society of America and an authority on Arctic Ocean acoustics and atmospheric acoustics, died in New Orleans on September 12, 2000 after a three-year battle with cancer. Ramsdale was born in El Paso, Texas, on December 12, 1942 and did his undergraduate work at the University of Texas at El Paso, where he received a BS in Physics with highest honors. He subsequently carried out graduate work in nuclear physics at Kansas State University, receiving his doctorate in 1969.

Dr. Ramsdale returned to El Paso in 1969 and began research in atmospheric acoustics at Globe Universal Science and Manufacturing, eventually becoming the Director of Acoustic Research for that organization. A principal problem addressed during the Globe years was the use of acoustics to extract data on temperature and wind structure in the upper atmosphere. In 1974 Dr. Ramsdale left Globe and became a research physicist at the Naval Research Laboratory in Washington DC and began a career in underwater acoustics, with the study of low-frequency fluctuations within the deep ocean. A principal achievement was a model that predicted the statistical fluctuations that were observed in long-range propagation due to source motion and medium variability.

In 1977, Dr. Ramsdale transferred to the newly established Naval Ocean Research and Development Activity [NORDA, which later became the Naval Oceanographic and Atmospheric Research Laboratory (NOARL), and which is presently the Naval Research Laboratory]—Stennis Space Center (NRL–SSC) in Mississippi, where he carried out research in the acoustics of arrays and in signal processing, with a major activity involving the use of vertical arrays for the understanding of different propagation paths. In the 1980s, he became extensively involved in the acoustic problems of the Arctic Ocean, and in 1985, he undertook technical management of the Arctic Undersea Warfare Environmental Technology Program, with subsequent appointments (1988) as Assistant Director of the Ocean Acoustics and Technology Directorate and Head of the Ocean Acoustics Branch (1992). The work in the acoustics of the Arctic led to two Distinguished Unit Citations from the Chief of Naval Research.

Following his retirement from NRL–SSC in 1998, Dan became an independent consultant to NRL–SSC and to the Los Alamos National Laboratory, with services in support of the Comprehensive Nuclear Test Ban Treaty, embracing infrasonic monitoring, ambient noise, and high-frequency atmospheric acoustics. At the time of his death he was working with the National Center for Physical Acoustics at the University of Mississippi on atmospheric acoustic problems associated with cruise missile defense.

Throughout his career, Dr. Ramsdale was active in both the ASA's Technical Committee on Underwater Acoustics and in the IEEE Oceanic Engineering Society, serving the latter as Chairman of the Committee on Underwater Acoustic Technology. He is survived by his wife Portia, his son Stuart, and his daughter, Jerry Elizabeth Novak.

ROBERT W. FARWELL

BOOK REVIEWS

P. L. Marston
Physics Department, Washington State University, Pullman, Washington 99164

These reviews of books and other forms of information express the opinions of the individual reviewers and are not necessarily endorsed by the Editorial Board of this Journal.

Editorial Policy: *If there is a negative review, the author of the book will be given a chance to respond to the review in this section of the Journal and the reviewer will be allowed to respond to the author's comments. [See "Book Reviews Editor's Note," J. Acoust. Soc. Am.* ***81****, 1651 (May 1987).]*

Fundamentals of Hearing: An Introduction (4th edition)

William A. Yost

Academic, San Diego, 2000.
349 pp. Price: $44.95.

Fundamentals of Hearing: An Introduction (4th edition) is a self-contained introductory textbook that covers basic acoustics as well as a wide range of topics in the fields of auditory anatomy, physiological acoustics and psychological acoustics. The organization of the text is nearly identical to the 3rd edition. The first 20% of the book is a primer on acoustics. Roughly 30% of the book is devoted to peripheral auditory anatomy and physiology, 20% to auditory perception of simple sounds, 20% to complex sounds, central auditory nervous system and auditory disorders, and the remaining 10% to the appendixes.

This 4th edition of the book is similar to the previous edition. This is not surprising given the previous edition's success as an introductory text, and that no scientific advances that would change the fundamental knowledge base for an introductory course in hearing occurred in the 6 years since the publication of the previous edition. Appropriately, references were updated to include a number of recently published books addressing special topics in hearing science. Many of these monographs and advanced textbooks are cited in a section at the end of each chapter titled ''Supplement.'' These supplements are a significant contribution to the text. Each chapter is written at a very basic level and the supplements are used in a variety of ways to complement the content of chapters. These include the discussion of historical notes, the introduction of controversies, the discussion of topics at a higher level than found in the chapter, math proofs, and references for further study.

Another change to the text is the replacement of a chapter titled ''Noise'' with one called ''Auditory Disorders.'' ''Noise'' described the deleterious effects of high-level sounds on hearing, including the physiological and perceptual consequences. ''Auditory Disorders'' covers this topic as well as ototoxicity, aging, diseases, infections, heredity, and the relationship between inner ear damage and hearing loss. This is an important change to the book given the large number of persons who are interested in hearing science who are also interested in impaired auditory systems. This chapter also includes a spectacular photograph of the basilar papilla from a bird shortly after damage to hair cells and 90 days later after the hair cells regenerated. This photo from a study by Ryals *et al.* (1999) is a nice complement to the spectacular photos representing damage to hair cells by intense sounds shown in earlier sections of the same chapter.

The most significant change since the publication of the 3rd edition is the simultaneous publication with the 4th edition of an instructor's workbook and compact disk (CD). The workbook has problem sets and tips for instructors. Examples of problems include the derivation of neural histograms from tabled data and the plotting of psychometric functions. The workbook also suggests examples of appropriate auditory demonstrations on CD (Houstma *et al.*, 1987) that might be helpful for conveying concepts discussed in the book. The CD included with the workbook does not contain these auditory demonstrations, but it does contain executable programs for a signal generator, a two-alternative forced-choice (2AFC) task, and neural firing rate simulations. Also included are software functions (a ''toolbox'') for use with the program MatLab, a signal processing program, and all of the figures in the book in two formats: files of each figure and PowerPoint presentations, organized by chapter, of the figures in each chapter. The signal generator and 2-AFC program work with Windows 95, 98 or NT operating systems. In less than 10 minutes, I was able to download the files for these programs, generate the sound files for a tone in noise, and set up a 2-AFC task for the detection of a tone in noise (fixed level). The neural firing rate simulator was just as easy to implement, and it simulated the synchronous firing of a single nerve fiber to tones of different frequencies and levels. This software would provide useful demonstrations for laboratory sections. Further, the files of the figures from the text on CD would aid in the development of lectures. The quality of the figures is outstanding for the most part and the use of this material would eliminate the time required to scan each figure from the book for the development of lectures presented using PowerPoint or similar presentation software. The MatLab ''toolbox'' provides a powerful tool for setting up auditory demonstrations/laboratory sections for a course, but the CD does not include the MatLab program that is required to run this software. Over the past few years MatLab has become a defacto standard for signal processing in auditory laboratories so this should not be a concern.

For those not familiar with this book (or its 3rd edition), the following is a summary and critical review of the major sections of the book.

Part I of the book titled ''The auditory stimulus'' introduces students to basic physics of sound. This section assumes knowledge of algebra and trigonometry (and not calculus). The four chapters in this section define terms used in the study of hearing such as modulation, envelope, fine structure, filters, and linear systems to name a few. In order to include all of the background material on acoustics necessary for understanding the rest of the text without having this section become an even larger proportion of the book, the presentation is quite dense. That is, there are not many examples to support newly learned knowledge in this area. This is not a problem though if instructors supplement the material in the book with some additional readings or exercises, such as those cited in the text or found in the recently released *Fundamentals of Hearing: An Instructors Workbook*. My only suggestion for improving this already excellent introduction to ''The Auditory Stimulus'' would be to follow the discussion of linear systems with a discussion of transfer functions. Given the importance of transfer functions to the study of hearing, their discussion here would be more effective than in the section of the text describing head-related transfer functions where this concept is currently introduced.

Part II and Part III represent the peripheral auditory system anatomy and physiology and the auditory perception of simple sounds. These eight chapters are logically presented in a clear manner, and there are many figures to support the text. In the chapters on physiology, there are many spectacular photos of the middle and inner ear. All of these chapters include figures representing data that are adapted from actual studies. Some of these adaptations aid the presentation of a particular idea more than the original figure would. For example, Fig. 9.13 was adapted from a study by Sachs and Young (1979) to show how neural firing rate represents adequately the peaks in the spectrum of a steady-state vowel for low presentation levels but not for moderate presentation levels. The adapted textbook figure combines two figures from Sachs and Young's original study to allow a direct comparison of the vowel stimulus with the neural firing pattern to that stimulus. Adaptations such as this one make the presentation of complex material easier for beginning students. The only disappointment with these sections was several significant errors in the figures or their legends that eluded the proofreaders. In one case, an erroneous figure in the book is presented correctly on the CD

 0001-4966/2001/110(4)/1713/3/$18.00

that accompanies the workbook. The errors are relatively minor given all of the positive aspects of these chapters.

Part IV describes complex sounds processing, the central nervous system (CNS), and auditory disorders. Less is known about the processing of complex sounds and the CNS than is known about the auditory periphery and the processing of simple sounds, but the author's description of these areas is clear yet still able to represent the complexity of these topics. This section describes the possible link between the CNS and perception just as earlier chapters were able to show the link between the auditory periphery and the processing of simple sounds.

The appendixes are an intrinsic part of the book. It is here where among other things ''techniques and tools used to study hearing (Appendix F)'' and ''Psychophysics (Appendix D)'' are discussed. Appendix F contains a brief introduction to microscopy, neural stains and markers, imaging, and genetics to provide the student with an appreciation of the difficulty with which measurements are obtained in physiological studies. Similarly, Appendix D provides a description of classical psychophysical procedures, direct scaling and matching procedures, and a brief introduction to the theory of signal detection (TSD), including receiver operating characteristic curves. The description of TSD is accurate but no references are cited. These appendixes do not have supplements, as do the chapters of the book, so additional readings are not suggested as was done so well in the earlier chapters. Given the importance of TSD to hearing science and other fields, a reference to the classic book by Green and Swets (1974) or to the more recent book by MacMillan and Creelman (1991) about this topic would be nice as a supplemental reading for interested students.

Finally, the author points out in the preface that the massive amount of literature and vast number of topics in hearing science make it difficult for an author to write a textbook that represents a general survey of this field. Professor Yost meets this challenge by covering the important points and major controversies of prior research in a manner that inspires rather than intimidates. He avoids the more subtle controversies and as a consequence, does not get bogged down citing the entire history of publications about a particular topic. Although this is contrary to the approach often taken in scholarly journals, it is good fortune for the beginning student of hearing science who needs to master basic concepts and to understand how these concepts relate to each other and to the entire field of study. This approach also gives the instructor flexibility in emphasizing his or her specialty with supplemental readings or more detailed lectures.

Green, D. M., and Swets, J. A. (**1974**). *Signal Detection Theory and Psychophysics* (Krieger, New York).

Houtsma, A. J. A., Rossing, T. D., and Wagenaars, W. M. (**1987**). *Auditory Demonstrations* (Institute for Perception Research, Eindoven, The Netherlands).

McMillan, N. A., and Creelman, C. D. (**1991**). *Detection Theory: A User's Guide* (Cambridge University Press, Cambridge, England).

Ryals, B. M., Dooling, R. J., Westbrook, E., Dent, M. L., MacKenzie, A., and Larsen, O. N. (**1999**). ''Avian species differences in susceptibility to noise exposure,'' Hear. Res. **131**, 71–88.

Sachs, M. B., and Young, E. D. (**1979**). ''Encoding of steady-state vowels in the auditory nerve: Representation in terms of discharge rate,'' J. Acoust. Soc. Am. **66**, 1381–1403.

ROBERT S. SCHLAUCH
Department of Communication Disorders
University of Minnesota
Minneapolis, Minnesota 55455

Master Handbook of Acoustics, Fourth Edition

F. Alton Everest

McGraw-Hill, New York, 2001.
xix+615 pp. Price: $34.95 paperback.

The application of science in the practice of acoustics can be a lifelong endeavor. Mathematical analysis is necessary for a more complete understanding of what happens and most people do not have the technical and/or academic training to undertake a quantitative analysis of the physical principles involved with architectural room acoustics. There is a yearning on the part of many people, who would describe themselves as audiophiles, as well as for people involved in audio production and post-production and for people for which sound is an avocation, for a nontechnical presentation of many of the aspects involved in acoustic room design. This book is a good introduction to acoustics for the layman. This lay guide provides an overview of and to the *lingua franca* of acoustics. The treatment is not rigorous—it provides the basic concepts involved in a qualitative descriptive way.

The fourth edition of F. Alton Everest's *Master Handbook of Acoustics* covers a lot of material in the 28 chapters, appendix, and glossary in the book. The review of the material is easy going with not much mathematics beyond logarithms and the physics is light and prosaic. The book appears to have grown since the first edition by the bulking up of some chapters, the revision of other chapters and the addition of some new chapters. The fourth edition has three new chapters.

While the book can provide a good introduction to many of the major concepts involved with studio and listening space design, a reader is left with the feeling that some areas are beaten to death while others are perfunctory in their coverage. A brief review of the contents follows.

The first portion of the book deals with the basics. Fundamentals of Sound, Chapter 1 (21 pages), talks about sinusoids, propagation of sound, wavelength and frequency and complex waves (harmonics, phase, partials, octaves, and the concept of spectrum) as well as the use of analogs (mechanical, electrical, and acoustical) for analysis. In Chapter 2, Sound Levels and the Decibel are covered in 17 pages while Chapter 3 (42 pages) deals with The Ear and the Perception of Sound (sensitivity, anatomy, loudness, audibility, pitch, timbre, localization, the ear as both analyzer and measurement instrument, perceptions of reflections, and occupational and recreational deafness). Sound Waves in the Free Field are described in a 6 page Chapter 4. Speech, Music and Noise, Chapter 5, deals with the voice system, music, speech and music power and frequency ranges, ''future'' dynamic range requirements, noise, signal distortion, harmonic distortion in 30 pages. The reviewer found that some chapters were overdone (in length) and some were a little too concise.

The next chapter delves into the realm of Analog and Digital Signal Processing where concepts such as filters, DSP and application of DSP to room equalization are developed. The placement of this chapter here is perplexing as some of the concepts discussed are not introduced until later in the book.

The next 11 chapters (7 to 17) present architectural acoustics issues. Reverberation, Control of Interfering Noise, Absorption of Sound, Reflection of Sound, Diffraction of Sound, Refraction of Sound, Diffusion of Sound, the Schroeder Diffuser, Modal Resonances in Enclosed Spaces, Reflections in Enclosed Spaces and Comb-Filter Effects are the Chapter titles. The coverage of these topics is uneven, with some areas receiving more attention and others, less. Some of the chapters here appear to remain unchanged from earlier editions with newer material presented in another area (e.g., number theory based diffusers). The author covers a lot of material, but the presentation is uneven from chapter to chapter—one travels from 1960s design to the present between chapters and sometimes within one.

Chapter 18, Quiet Air for the Studio, emphasizes the role of proper design in keeping an expensive proposition from becoming more so. Basic requirements and guidelines are described in a prosaic manner.

The next five chapters deal with Acoustics of the Listening Room, the Small Recording Studio, the Control Room, for Multitrack Recording and for Audio/Video Tech Room and Voice-Over Recording. Items such as small room acoustics, low frequency phenomena for rooms, echoes, flutters, modes, specular and other reflections, and others are described here. Some readers may wonder why there are separate chapters here—the answer may be due to the changing popularity of room design philosophies, separate chapters were developed to deal with these changes in fashion. However, one could also see that this is a good thing—as we get more proficient in the understanding of the phenomena involved for these facilities, and develop more and varied solutions, the art and science of room design benefits.

Chapter 24, Adjustable Acoustics, describes some commercially available products in more detail than in the previous chapters. Among these are products based upon number theory and limp mass (antinode mitigation).

Some of the nonlinear mechanisms of sound are covered in the next chapter, Acoustical Distortion. The descriptions are basic and cover well-known phenomena—comb filtering, resonances, and speaker boundaries.

Some are more theological in nature—and are dependent on your belief in a particular theory of room design.

Computer software for use in measurement and design of listening spaces are covered in the next two chapters. Chapter 26, reviews two of the commercially available software programs that are used to measure room acoustic metrics. Time domain spectroscopy and maximum length sequences are the two techniques used. The types and kinds of measurements that can be done are described.

Chapter 27 describes another commercially based program which is also the title of the chapter—Room Optimizer. This program is used to investigate modal properties of rooms under design and it then optimizes the room in regard to the placement of sound sources, such as loudspeakers, and the type and location of acoustic treatment of surfaces within the same.

The final chapter, Desktop Auralization, introduces what auralization is and how it can be used in the design phase of a room. Heretofore, the only way to get an idea of how a room sounded before it was built was to use physical scale models of the room. Now, there are several programs that run on personal computers.

The appendix contains selected absorption coefficients in octave bands as well as reference to where the coefficients were found. A glossary of terms follows. A subject index is at the end of the book.

Master Handbook of Acoustics is a book that many in the Society may find uneven with some chapters containing many references and some none, some subjects detailed in lengthy prose and some in a very short manner, some photographs that are almost historic in nature while some graphics are modern. It is a comprehensive introductory guide for people who need to understand what designers and technicians are talking about.

NEIL A. SHAW
Menlo Scientific Acoustics, Inc.,
Topanga, California

REVIEWS OF ACOUSTICAL PATENTS

Lloyd Rice
11222 Flatiron Drive, Lafayette, Colorado 80026

The purpose of these acoustical patent reviews is to provide enough information for a Journal reader to decide whether to seek more information from the patent itself. Any opinions expressed here are those of reviewers as individuals and are not legal opinions. Printed copies of United States Patents may be ordered at $3.00 each from the Commissioner of Patents and Trademarks, Washington, DC 20231. Patents are available via the Internet at http://www.uspto.gov.

Reviewers for this issue:

KEVIN P. SHEPHERD, *M.S. 463, NASA Langley Research Center, Hampton, Virginia 23681*
WILLIAM THOMPSON, JR., *601 Glenn Road, State College, Pennsylvania 16803*
ERIC E. UNGAR, *Acentech, Incorporated, 33 Moulton Street, Cambridge, Massachusetts 02138*

6,185,153

43.28.We SYSTEM FOR DETECTING GUNSHOTS

Mark William Hynes and James Lee Cole, assignors to the United States of America as represented by the Secretary of the Navy
6 February 2001 (Class 367/124); filed 19 February 1999

This audio analysis system is designed to detect a gunshot sound within some reasonable distance of the microphone. The analog circuitry includes at least one threshold detector, a pulse width detector, and a pulse counter. If a small number of pulses are detected which exceed a threshold

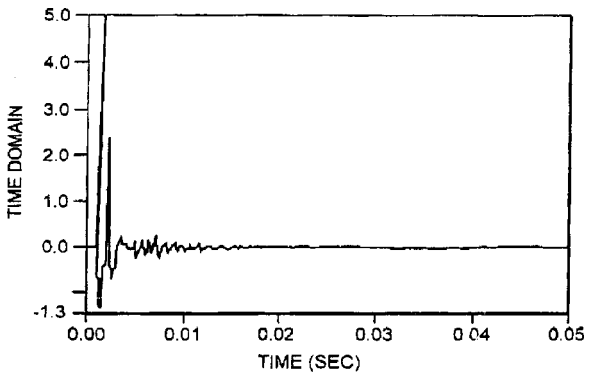

setting and those pulses have a certain maximum duration and a certain minimum peak amplitude, then a gunshot event is noted. The output indication may be a light or alarm, or the unit may be connected to a transmitter to signal events at a remote location.—DLR

5,943,293

43.30.Yj SEISMIC STREAMER

John Luscombe, Sugarland, Texas *et al.*
24 August 1999 (Class 367/20); filed 24 May 1996

A seismic underwater streamer consists of conventional hydrophone units housed in an oil-filled flexible tube of polyurethane. Novelty seems to reside in the method for adjusting the buoyancy of the unit, in improved tensile load bearing rope elements within the tube, and in the design of the interconnecting end fittings at each end of the tube.—WT

6,173,613

43.35.Le MEASURING CRACK GROWTH BY ACOUSTIC EMISSION

Harold L. Dunegan, Laguna Niguel, California
16 January 2001 (Class 73/587); filed 31 October 1995

A false-aperture transducer, consisting of a piezoelectric crystal that is partially mass-loaded by a concentrated mass, is attached to a platelike test item in which acoustic emissions are to be monitored. The transducer is constructed and calibrated to be equally sensitive to lower-frequency out-of-plane waves and to higher-frequency in-plane waves, and its output is separated into a lower-frequency and a higher-frequency component via analog filters. The peak amplitudes of the two components are measured and their ratio is calculated. This ratio is used to determine crack depth on the basis of a calibration against a fracture specimen in which crack growth is simulated.—EEU

6,164,073

43.35.Ud METHOD AND APPARATUS FOR ADAPTING STEADY FLOW WITH CYCLIC THERMODYNAMICS

Gregory W. Swift *et al.*, assignors to The Regents of the University of California
26 December 2000 (Class 60/721); filed 18 December 1998

This heat transfer apparatus makes use of standing acoustic waves in a fluid-filled chamber to enhance the transfer of energy between the fluid and solid heat exchangers. Fluid passes through the chamber, entering and leaving at pressure nodes, so that no acoustic power is lost at these points. The heat exchangers and the sound generators are placed near the pressure antinodes for maximum efficiency. The apparatus is claimed to combine the advantages of both steady flow and oscillatory flow equipment.—EEU

6,182,499

43.35.Zc SYSTEMS AND METHODS FOR CHARACTERIZATION OF MATERIALS AND COMBINATORIAL LIBRARIES WITH MECHANICAL OSCILLATORS

Eric W. McFarland and Leonid Matsiev, assignors to Symyx Technologies
6 February 2001 (Class 73/24.06); filed 9 October 1996

In the context of this patent, a ''library'' is a large collection of molecules, typically located in separate regions arrayed on a substrate. These

 0001-4966/2001/110(4)/1717/7/$18.00

molecules, for example, might be semiconductors of many different compositions. The methods discussed in this patent are intended for the rapid, automated screening of the molecules, in order to identify those with certain desired properties. In one embodiment, an ultrasonic detector scans the library in a raster pattern and provides information on the elastic properties of the molecules. In another embodiment, the library is placed in a liquid-filled tank in which acoustic waves are generated, and the library is scanned with a laser beam. For evaluation of liquid elements, these are placed in contact with a resonator, whose response is calibrated against standard liquids.—EEU

6,176,132

43.38.Dv METHOD FOR DETERMINING LIQUID LEVEL IN A CONTAINER USING AN ELECTROMAGNETIC ACOUSTIC TRANSDUCER (EMAT)

Daniel T. MacLauchlan, assignor to BWX Technologies, Incorporated
23 January 2001 (Class 73/290 V); filed 27 July 1995

An electromagnetic transducer is placed near a thin metal wall or thin metal foil seal at the base of a liquid-filled container. The transducer actuates the wall or foil so as to launch ultrasonic compressional waves into the liquid. These waves are reflected from the liquid surface, causing the wall or foil to vibrate in the magnetic field produced by the transducer. The resulting voltage induced in the transducer's eddy current coil is used to determine the time of flight of the waves in the fluid, and the liquid level is determined from that time and from the known wave speed in the liquid.—EEU

5,949,741

43.38.Fx DUAL-SECTION PUSH-PULL UNDERWATER PROJECTOR

Jean C. Piquette, assignor to the United States of America as represented by the Secretary of the Navy
7 September 1999 (Class 367/161); filed 21 December 1998

A rigid cylindrical housing, typically fashioned from stainless steel, has aperture openings **14** and **16** on opposite ends. Items **18**, **20**, **22**, and **24** are electrostrictive annular rings, preferably of lead magnesium niobate or lead magnesium niobate-lead titanate. Faces **40** and **42** of the top- and bottom-most rings are bounded to the housing to prevent motion of these two surfaces. The cylindrical faces **44** of all four rings are not bonded to the inner face of the housing but faces **46** and **48** of the inner two rings are bonded to rigid disc **26** which is anchored on the housing. Discs **28** and **30** are, however, free to move. The two internal cavities between plates **28, 26**, and **30** are oil filled. The discs of electrostrictive material are electrically

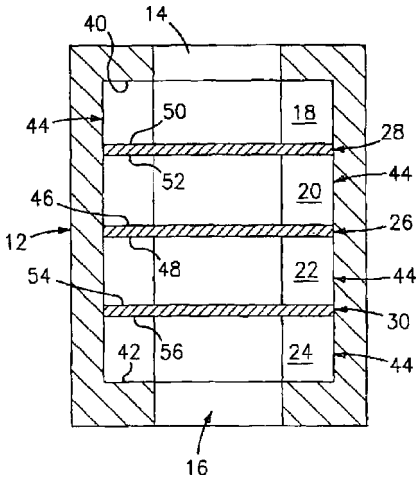

driven in a push-pull mode of operation such that when **18** and **24** contract, for example, **20** and **22** expand so that discs **28** and **30**, which are the actual radiating faces, flex in opposite vertical directions relative to the position of the fixed disc **26** and thus the net radiation from the two orifices **14** and **16** is monopolelike. Because the displacement response of these particular electrostrictive materials displays quadratic nonlinearity as a function of charge (but not voltage) excitation, the projector is to be excited by a constant current (i.e., charge) source so that the nonlinear responses of the two pairs of rings will cancel because of the push-pull mode of operation.—WT

6,178,820

43.38.Hz SENSOR FOR MEASURING ACCELERATION AND SOUND PRESSURE

Kari Kirjavainen *et al.*, assignors to VTT
30 January 2001 (Class 73/647); filed in Finland 20 November 1996

This sensor is intended for measuring sound pressure and acceleration at essentially the same location, as may be useful for active control applications. The sensor consists of a platelike base, on which is mounted an annulus of pressure-sensitive film and a second pressure-sensitive film in the center of the annulus. Each film comprises flat gas bubbles, has a metal

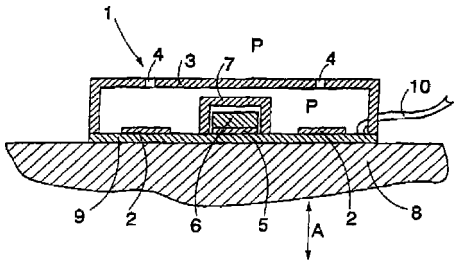

coating on at least one side, and a permanent electric charge. A mass is attached atop the film in the center of the annulus, and this entire central arrangement is enclosed by a cover, so that sound pressure will not affect it. Thus, the annular film serves as an acoustic pressure sensor, and the central arrangement serves as an accelerometer.—EEU

6,175,637

43.38.Ja ACOUSTIC TRANSDUCER

Masao Fujihira *et al.*, assignors to Sony Corporation
16 January 2001 (Class 381/412); filed in Japan 1 April 1997

This patent relates to an acoustic transducer of the electromagnetic induction type, such as may be used for loudspeakers or headphones or for microphones. As in classical loudspeaker designs, two coils are located in a magnetic gap: one is fastened to a diaphragm, and the other to the structure that contains the magnetic gap. The novel feature of the configurations described in this patent consists of the latter coil being of a flat annular shape. This is claimed to result in a more sensitive, more compact, and cheaper design that is capable of handling low frequencies better.—EEU

6,164,137

43.40.Le ELECTROMAGNETIC ACOUSTIC TRANSDUCER (EMAT) INSPECTION OF TUBES FOR SURFACE DEFECTS

Jimmy W. Hancock and Daniel T. MacLauchlan, assignors to McDermott Technology, Incorporated
26 December 2000 (Class 73/643); filed 3 February 1999

The EMAT of this patent consists of a housing with a single transmitter and a pair of receivers arranged to fit around part of the circumference of a tube that is to be inspected. The two receivers are on the same side of the transmitter, which generates a surface-wave acoustic signal that propagates

around the circumference in both directions. The signals detected by the two receivers are different if a surface defect is present under one of the receivers, but otherwise are substantially the same. Observation of the electrical signals obtained as the transducer is moved around the tube's circumference thus permits one to determine the presence and locations of defects.—EEU

6,170,336

43.40.Yq ELECTROMAGNETIC ACOUSTIC TRANSDUCER AND METHODS OF DETERMINING PHYSICAL PROPERTIES OF CYLINDRICAL BODIES USING AN ELECTROMAGNETIC ACOUSTIC TRANSDUCER

Ward L. Johnson *et al.*, assignors to the United States of America, as represented by the Secretary of Commerce
9 January 2001 (Class 73/643); filed 2 August 1994

A number of magnets are mounted at evenly spaced intervals around a circular opening in a housing. Wire coils are mounted in the housing adjacent to this opening and near the polar ends of the magnets. Depending on the orientation of the coils relative to the magnets, introduction of current into these coils at a given frequency can induce axial, shear, radial, or plane strain vibrations in a cylindrical test object placed in the opening. Comparison of resonance frequencies of the test object, which may be a solid circular cylinder or in the shape of a tube, to those of a similar standard object can provide information on its various physical properties, as can observation of the vibration decay rates.—EEU

6,178,821

43.40.Yq VIBRATION SENSING DEVICE

Sudhir Dattatraya Savkar and Walter Whipple, assignors to General Electric Company
30 January 2001 (Class 73/650); filed 25 January 1999

A strip with a pattern of markings, such as a series of parallel lines, is made to pass back and forth in front of a sensor. This arrangement is used to evaluate the relative motion between the object on which the sensor is mounted and the object to which the strip is attached. The sensors may be of various types, including those using the Hall effect or optical means, and the patterns on the strip may be magnetic, optical, etc., compatible with the sensor. The device described in this patent is applicable to sensing out-of-balance motions of a piece of equipment such as a washing machine, motor, or engine.—EEU

6,173,808

43.50.Gf AUTOMOBILE EXHAUST NOISE SILENCER

Kazushige Maeda *et al.*, assignors to Nissan Motor Company, Limited
16 January 2001 (Class 181/254); filed in Japan 16 May 1996

An automobile muffler consists of inlet **7** and exhaust **10**. There are two flow paths. At low engine speeds, exhaust gases flow from porous section **8** into porous section **11** and exit. At higher speeds the spring-controlled valve **16** opens, thus creating an additional flow path. The valve serves to reduce pressure losses and also changes exhaust resonance frequencies in response to increasing engine speeds. Numerous geometrical variations are described.—KPS

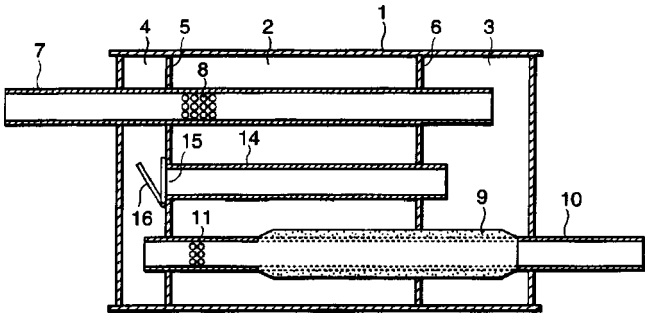

6,188,961

43.60.Rw ACOUSTIC LOGGING APPARATUS AND METHOD

Batakrishna Mandal, assignor to Hilliburton Energy Services, Incorporated
13 February 2001 (Class 702/6); filed 31 March 1999

The apparatus for well logging described in this patent consists of a downhole tool that includes a single dipole source (capable of generating an acoustic signal in a borehole) and receivers at multiple levels. At each level there are provided four receivers, which may be conventional pressure transducers, to sense the shear/flexural wave signals that propagate along the borehole earth formation. A computer interpolates the pressure fields between receivers and performs cross-component decomposition on these fields to determine the shear wave orientation and velocity, from which information one may determine transit time anisotropy, energy anisotropy, and slowness anisotropy.—EEU

6,193,751

43.70.Aj TRACHEOSTOMA VALVE WITH SPRING-LOADED PISTON

Mark I. Singer, Tiburon, California
27 February 2001 (Class 623/9); filed 2 November 1998

This cylindrical valve attaches to the outside of the stoma, or hole, cut into the patient's airway to allow breathing. The valve normally rests in a central opened position under a light spring pressure. The valve remains open during normal breathing, but is pushed against the outer end, closing

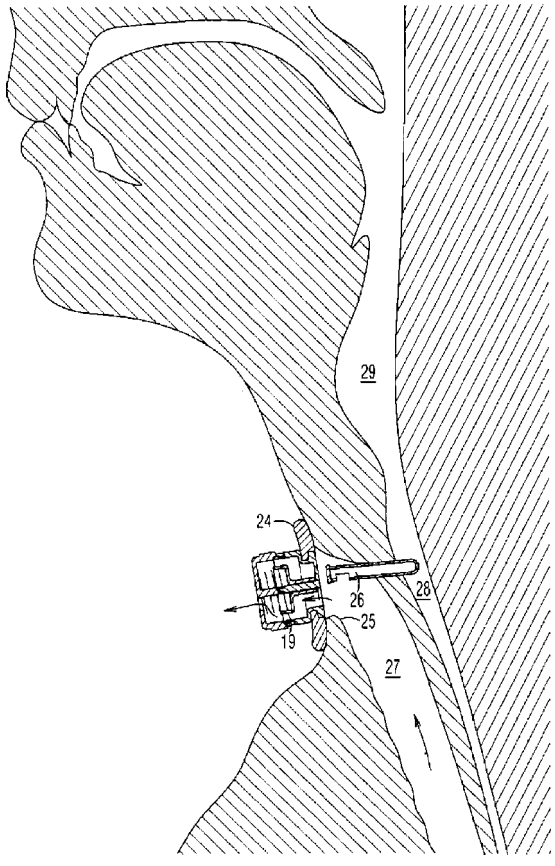

off the air passage, when the patient exhales strongly as when speaking. This allows lung air to be used to produce speech, perhaps using an esophageal passage if necessary. Item **26** in the figure is a typical prosthesis which lets lung air pass into the pharynx, allowing a more normal way of speaking than that produced by esophageal air.—DLR

6,192,135

43.70.Dn DEARTICULATOR

Donald S. Monopoli, Melbourne, Florida
20 February 2001 (Class 381/95); filed 18 November 1997

It is well known that listening to a delayed version of one's own speech causes severe disruption in speaking ability. This device makes that effect available to general audiences, such as in the home, at a party, or in a bar. Ideally, a group of users would be seated around a table, at least one of whom wears a headset with a microphone boom. Others hear the speaker's

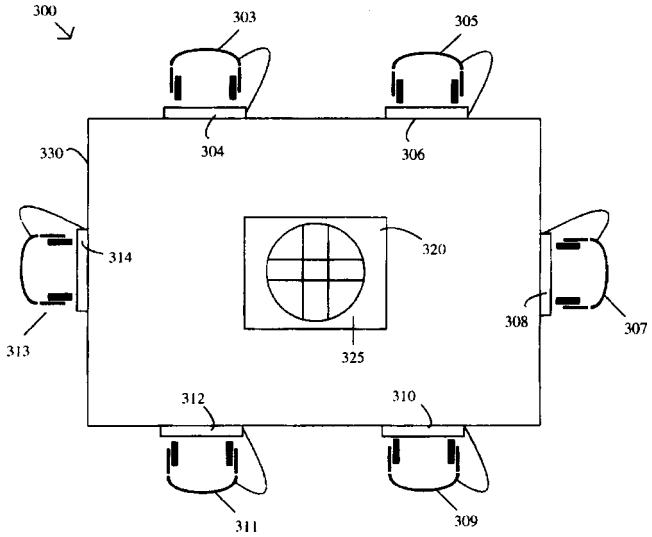

voice, either on headphones or on a loudspeaker. The device incorporates a delay of 0.5 s from the speaker's microphone to the audio output. Alternate arrangements include a video camera to record the speaker's stumbling speech, public presentations of the effect, and coin-operated booths featuring the device.—DLR

6,190,173

43.71.Ky METHOD AND APPARATUS FOR TRAINING OF AUDITORY/VISUAL DISCRIMINATION USING TARGET AND DISTRACTOR PHONEMES/GRAPHICS

William M. Jenkins *et al.*, assignors to Scientific Learning Corporation
20 February 2001 (Class 434/169); filed 17 December 1997

This speech perception training device is intended for persons who suffer from a deficiency in the auditory transition detection capability known as specific language impairment. A target sound is first presented, along with appropriate graphical displays, such as a picture involving the sound in a prominent way. A randomized sequence of sounds is then presented and the subject must identify the target sound as it occurs in the randomized se-

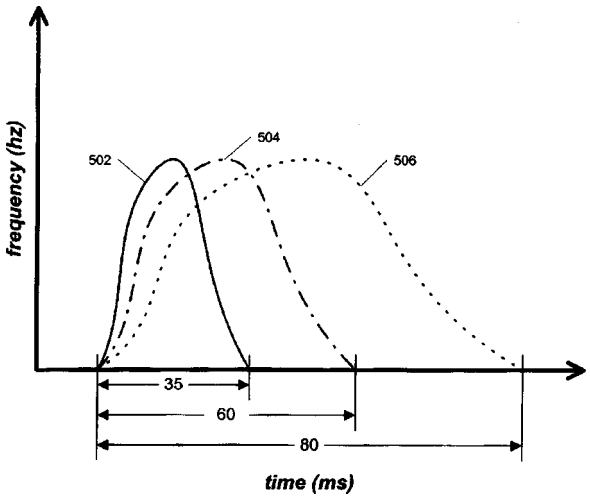

quence of distractor sounds. Initially, the speech waveforms are processed in a way which slows the rate of transition of critical frequency shifts. As the subject improves in the ability to identify the target sound, the degree of rate slowing is reduced until, eventually, the phonetic output will match that of normal speech as seen in curve **502**.—DLR

6,188,979

43.72.Ar METHOD AND APPARATUS FOR ESTIMATING THE FUNDAMENTAL FREQUENCY OF A SIGNAL

James Patrick Ashley, assignor to Motorola, Incorporated
13 February 2001 (Class 704/205); filed 28 May 1998

This speech pitch analyzer forms an initial integer-sample-period pitch estimate based on an autocorrelation of the linear prediction residual. This so-called ''lag estimate'' is used to drive a number of harmonic analyzers. These analyzers take the form of second-order filters tuned to frequencies close to the pitch estimate. Analyzing the phase of the filter outputs provides a sensitive measure of whether each filter tuning is above or below the actual fundamental period.—DLR

6,188,981

43.72.Ar METHOD AND APPARATUS FOR DETECTING VOICE ACTIVITY IN A SPEECH SIGNAL

Adil Benyassine and Eyal Shlomot, assignors to Conexant Systems, Incorporated
13 February 2001 (Class 704/233); filed 18 September 1998

This speech presence detector, designed to discriminate between speech and silence, is referred to here as either a ''voice activity detector'' or a ''voicing detector,'' both clearly inappropriate choices of terms. The system performs a linear prediction analysis followed by line spectral frequency extraction and also measures energy, pitch gain, and pitch lag. All of these parameters are exponentially smoothed and a decision tree then extracts an initial speech-presence decision. The frame-by-frame value of that decision is then itself smoothed and several time interval counts are consulted to determine the final speech-presence result.—DLR

6,185,528

43.72.Bs METHOD OF AND A DEVICE FOR SPEECH RECOGNITION EMPLOYING NEURAL NETWORK AND MARKOV MODEL RECOGNITION TECHNIQUES

Luciano Fissore *et al.*, assignors to CSELT—Centro Studi e Laboratori Telecomunicazioni S.p.A.
6 February 2001 (Class 704/232); filed in Italy 7 May 1998

This speech recognition system uses a combination of Markov models (HMMs) and neural networks (ANNs) to recognize isolated words from a large vocabulary. An initial pass with the ANN identifies a list of possible candidate words. These portions of the input speech are then further analyzed by the HMM recognizer to obtain more accurate best likelihood scores for the candidate items. The list of candidates is then sorted according to the combined ANN and HMM scores to produce a final list of recognized words. No specific acoustic analysis method is identified for use with the patented system.—DLR

6,192,342

43.72.Fx AUTOMATED CAMERA AIMING FOR IDENTIFIED TALKERS

Adam Akst, assignor to VTEL Corporation
20 February 2001 (Class 704/275); filed 17 November 1998

A continuing problem during video conferences is how to point the cameras, that is, which video images should be transmitted. The patent states that camera settings, such as aiming, focus, etc., are typically adjusted during a conference setup period, reducing the on-line decision to one of camera selection. As described here, that task would be done by a speaker recognition system. Several issues not addressed here include the time required to switch camera pointing, what happens when one speaker interrupts another, and why direct acoustic clues, perhaps which mic line is active, would not be a better source of the needed information.—DLR

6,192,335

43.72.Gy ADAPTIVE COMBINING OF MULTI-MODE CODING FOR VOICED SPEECH AND NOISE-LIKE SIGNALS

Erik Ekudden and Roar Hagen, assignors to Telefonaktiebolaget LM Ericsson (publ)
20 February 2001 (Class 704/223); filed 1 September 1998

This patent presents a modification to the standardized CELP vocoder intended to improve performance for nonspeech sounds while maintaining high-quality, low-bit-rate coding for speech signals. The basic change is the use of spectral and waveform matching to replace the standard perceptually weighted linear prediction spectrum matching. A waveform match distortion figure and a corresponding energy match distortion figure are combined into a single, weighted distortion measure. The relative weighting of the two factors can thus be adjusted gradually to create a smooth transition between the different match criteria.—DLR

6,192,344

43.72.Ja MESSAGING SERVER LANGUAGE CONFIGURATION METHOD AND APPARATUS

Scott Lee *et al.*, assignors to Altigen Communications, Incorporated
20 February 2001 (Class 704/277); filed 16 December 1998

A multi-language speech or text synthesis system is described in which tables of language-specific structure are processed to generate output in the language of choice. The language tables include syntactic structure, passage tables, and property tables. Although not entirely clear, it appears that any application software which used the system would need to produce all of its output in the form of codes for language table access. A separate setup instruction would specify which set of tables to use. The program's output would then be generated in the selected language. Some very brief examples are given as to how the tables might be structured for some specific languages.—DLR

6,185,527

43.72.Ne SYSTEM AND METHOD FOR AUTOMATIC AUDIO CONTENT ANALYSIS FOR WORD SPOTTING, INDEXING, CLASSIFICATION AND RETRIEVAL

Dragutin Petkovic *et al.*, assignors to International Business Machines Corporation
6 February 2001 (Class 704/231); filed 19 January 1999

This audio analysis system is intended as a sort of preprocessor for a word-spotting application. The audio signal is scanned for silence intervals and, on that basis, divided into segments which include at least one audio event. Selected band zero crossing and energy measures are collected from the segment. Based on these and various derived measures, such as spectral energy concentration, the audio activity is classified as speech, music, or a combination of those. Speech activity is further characterized by the patterns of spectral changes to determine ''interesting events,'' such as emphasis, hesitations, conclusions, and regions of interest for further recognition analysis.—DLR

6,185,529

43.72.Ne SPEECH RECOGNITION AIDED BY LATERAL PROFILE IMAGE

Chengjun Julian Chen *et al.*, assignors to International Business Machines Corporation
6 February 2001 (Class 704/251); filed 14 September 1998

This head-mounted device contains a video camera **105** and a mirror **103**, which provide a real-time side view of the lips as additional input to improve the performance of a speech recognition system, particularly in a high-noise environment. Depending on the lighting situation, the camera may detect visible or infra-red light from a light source. The lateral profile

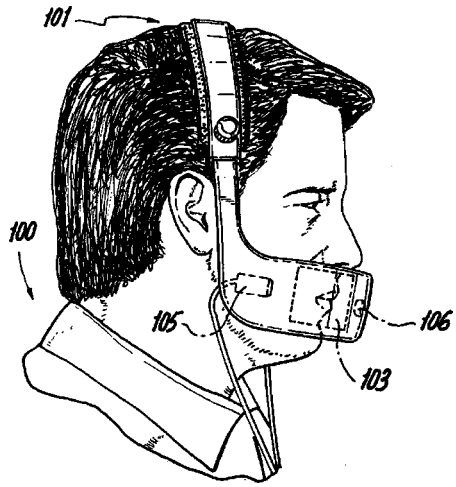

image is analyzed to determine lip shape, separation, protrusion, and possible appearances of the tongue tip or the lower teeth. The patent describes the extraction of several such image features. These features are used along with the normal acoustic features to train the speech recognition system.—DLR

6,185,530

43.72.Ne APPARATUS AND METHODS FOR IDENTIFYING POTENTIAL ACOUSTIC CONFUSIBILITY AMONG WORDS IN A SPEECH RECOGNITION SYSTEM

Abraham Ittycheriah and Stephane H. Maes, assignors to International Business Machines Corporation
6 February 2001 (Class 704/255); filed 14 August 1998

Even though this patent lists 17 other speech patents as references, the background and summary sections are written as if the idea was new to these authors. The problem of detecting similarity between new words to be added and existing vocabulary items is as old as isolated word recognition. The method covered here seems to be based on comparisons of the HMM probability distributions corresponding to the phonetic symbols of the new and existing items.—DLR

6,185,535

43.72.Ne VOICE CONTROL OF A USER INTERFACE TO SERVICE APPLICATIONS

Jan Hedin and Bernhard Meier, assignors to Telefonaktiebolaget LM Ericsson (publ)
6 February 2001 (Class 704/270); filed 16 October 1998

This two-part speech recognition system is organized for use in a wireless device, which typically has less available processing power than a base station. A low-power part of the recognizer, running in the wireless device is able to recognize terminal functions and predefined markup language (WML) phrases. The latter may be forwarded to the remote server in the form of text. Other portions of the audio input are encoded and forwarded to the server, where they are processed by a more powerful part of the recognition system. This applies particularly to application-specific phrases. The server computer may also be used to generate speech output, which is passed to the wireless device in encoded form, where it may be played over the loudspeaker.—DLR

6,185,537

43.72.Ne HANDS-FREE AUDIO MEMO SYSTEM AND METHOD

Stephen S. Oh and Stephen Ira Popik, assignors to Texas Instruments Incorporated
6 February 2001 (Class 704/275); filed 3 December 1996

This speech recording device uses voice controls to start and stop recording. A voice-activated controller unit is connected as needed to start and stop collection of compressed speech, to activate voice feedback to the user, and optionally to operate voice mail or telephone functions. Intended applications include use in an automobile, allowing completely hands-free operation.—DLR

6,188,976

43.72.Ne APPARATUS AND METHOD FOR BUILDING DOMAIN-SPECIFIC LANGUAGE MODELS

Ganesh N. Ramaswamy *et al.*, assignors to International Business Machines Corporation
13 February 2001 (Class 704/9); filed 23 October 1998

This patent can reasonably be paraphrased by saying that the recognition system language model builder begins with a small domain-specific seed model and a larger corpus of items from the language and from these, constructs a larger domain-specific model. The new model is evaluated and, if it is found to be inadequate, the process repeats. The details of how it all works are omitted, making reference to various public domain materials.—DLR

6,188,982

43.72.Ne ON-LINE BACKGROUND NOISE ADAPTATION OF PARALLEL MODEL COMBINATION HMM WITH DISCRIMINATIVE LEARNING USING WEIGHTED HMM FOR NOISY SPEECH RECOGNITION

Tung-Hui Chiang, assignor to Industrial Technology Research Institute
13 February 2001 (Class 704/256); filed 1 December 1997

This two-stage speech recognition model builder adapts a clean-speech model for better performance in a noisy environment. In the first stage, as each training item is processed, the clean-speech HMM parameters are adapted by estimating the noise component in the cepstral domain. This is done by subtracting the clean-model cepstral data for frames of the training item from the actual training item cepstral data. The noise adapted model is passed to the second stage, where a risk function is computed based on the differences between HMM parameters for the most confusable pairs of training items. Final HMM parameters are obtained by adjusting the adapted HMM models so as to decrease the confusability risk.—DLR

6,188,986

43.72.Ne VOICE ACTIVATED SWITCH METHOD AND APPARATUS

Richard Matulich and Allan Ligi, assignors to VOS Systems, Incorporated
13 February 2001 (Class 704/275); filed 2 January 1998

This device-embedded speech recognition system includes both speaker-dependent and speaker-independent recognition modes. The device will recognize a vocabulary of three or four words, either in preprogrammed (factory) independent mode or in user-programmable dependent mode. Designed in the form of a wall plate to replace either a wall switch or a power receptacle, the device includes a microphone jack and a rf receiver for a remote microphone. Device controls, such as user vocabulary training, are entered by touching a pad on the unit and speaking, while watching a front-panel LED and receiving voice feedback from the device.—DLR

6,192,337

43.72.Ne APPARATUS AND METHODS FOR REJECTING CONFUSIBLE WORDS DURING TRAINING ASSOCIATED WITH A SPEECH RECOGNITION SYSTEM

Abraham Ittycheriah and Stephane H. Maes, assignors to International Business Machines Corporation
20 February 2001 (Class 704/231); filed 14 August 1998

This patent is a minor variation of United States Patent 6,185,530 by the same authors and reviewed above. Referring to one of the oldest problems in speech recognition, that of detecting when a new item would be confused with an existing item, the patent text states that conventional training approaches were unable to identify items from the existing vocabulary that were acoustically similar to the uttered word. The methods described are the same as those in the related patent.—DLR

6,192,338

43.72.Ne NATURAL LANGUAGE KNOWLEDGE SERVERS AS NETWORK RESOURCES

Edward Dennis Haszto *et al.*, assignors to AT&T Corporation
20 February 2001 (Class 704/257); filed 12 August 1997

This patent describes a voice interface to a network database system, such as an on-line airline reservation system. The primary server performs speech recognition of the user's speech input. Access to information provided by a database server allows more accurate recognition. The most likely text form of the input is sent to the database server, which contains the

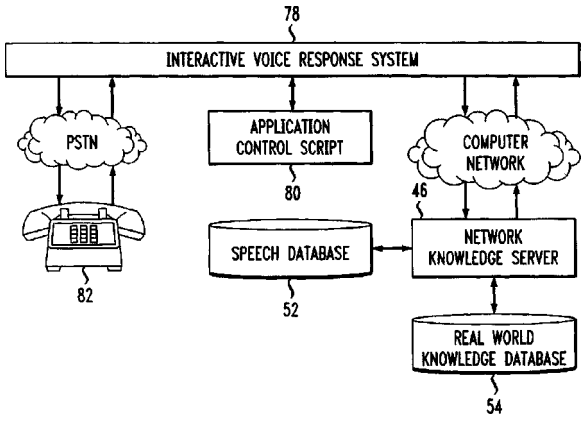

information system as well as software for query semantics analysis and translation. Query responses in text form are sent back to the primary server where they are converted to speech and sent on to the user. The arrangement allows user access to the system from an ordinary telephone.—DLR

6,192,339

43.72.Ne MECHANISM FOR MANAGING MULTIPLE SPEECH APPLICATIONS

Cory W. Cox, assignor to Intel Corporation
20 February 2001 (Class 704/270); filed 4 November 1998

What is patented here is the idea that a common set of user and software developer interface standards would result in a more efficient, user-friendly voice controlled computer system. Of course, the software developers would have to agree that this particular set of standards was worth their effort to build applications which conformed to the standard. Assuming that happened, then the end user would presumably benefit by the ability to control many applications in a uniform manner. The patent offers a few examples of what the user and developer interactions might be like using such a set of standards.—DLR

6,192,343

43.72.Ne SPEECH COMMAND INPUT RECOGNITION SYSTEM FOR INTERACTIVE COMPUTER DISPLAY WITH TERM WEIGHTING MEANS USED IN INTERPRETING POTENTIAL COMMANDS FROM RELEVANT SPEECH TERMS

Scott Anthony Morgan *et al.*, assignors to International Business Machines Corporation
20 February 2001 (Class 704/275); filed 17 December 1998

This interactive voice-operated computer control system maintains lists of possible user utterances and their probability of being spoken at any moment as determined by the current state of the computer. The speech recognition system goes beyond this, however, by producing visual displays which guide the user and, almost as a side effect, inform the user of the current set of most probable items. The latter information is not explicit in the form of lists and such, but rather in the form of useful cues to the functions available for the presumed user's task as predicted by the computer state analysis. Such cues indirectly inform the user of the current state of the speech recognition system, making the system and the user more aware of each other.—DLR

6,012,779

43.80.Vj THIN FILM ACOUSTIC ARRAY

Richard F. Morris, assignor to Lunar Corporation
11 January 2000 (Class 300/459); filed 4 February 1997

An acoustic transducer array for assessing, in particular, the bone density of a human heel consists of a planar sheet of PVDF with multiple small square electrodes arranged in a grid format thereby establishing a large rectangular set of transducers. Polarization is presumably accomplished after the electrode pattern is established so that the interstitial areas are not polarized. Since time of flight from a source to each transducer is proportional to the density of the intervening material, a density profile can be made of an insonified foot placed between the source and this array.—WT

Remarks about the depth resolution of heterodyne interferometers in cochlear investigations[a)]

Ernst Dalhoff,[b)] Ralf Gärtner, Hans-Peter Zenner, Hans J. Tiziani, and Anthony W. Gummer

University of Tübingen, Department of Otolaryngology, Section for Physiological Acoustics and Communication, Silcherstrasse 5, 72076 Tübingen, Germany

(Received 26 April 2001; revised 19 July 2001; accepted 27 July 2001)

Criteria of depth resolution of interferometric vibration measurements in the cochlea are discussed. Depending on the aim of the measurement, attention should be directed to the outer flank of the interference visibility curve, in contrast to the usual criterion of full width at half maximum. The depth at 30 dB suppression is proposed as a more appropriate criterion, when the measurement site is to be viewed through tissue. © *2001 Acoustical Society of America.* [DOI: 10.1121/1.1404975]

PACS numbers: 43.64.Kc [LHC]

Growing understanding of cochlear mechanics has drawn attention to vibration modes belonging to sections of the cochlear partition that lie at different distances from the focal plane of the imaging microscope. The possibility of the occurrence of such modes, different with respect to amplitude and phase, poses a problem for the interpretation of interferometric vibration measurements performed without introducing reflective targets, such as microbeads. Several authors have used a criterion of depth resolution as an indicator of the quality of the optical sectioning (Khanna and Koester, 1989; Cooper, 1999), in a similar fashion as that commonly used in describing image formation. Recently, Ren and Nuttall (2001) questioned the meaning of the criterion when interpreting cochlear vibration measurements. They showed that an object far out of the focus depth of the microscope objective could produce a processable signal. This letter evaluates common criteria of depth resolution of interferometeric vibration measurements and discusses their implications for applications in the cochlea.

One of the first definitions of resolution is due to Lord Rayleigh (1879). Two point images of equal intensity are said to be just spatially resolved if the principal maximum of the intensity distribution of the one image coincides with the first minimum of the other. The diffraction (or so-called ''Airy'') pattern of the incoherently, uniformly illuminated imaging apertures that he considered, is given by $(J_1(x)/x)^2$, where J_1 is the first-order Bessel function of the first kind. The pattern shows a first minimum at $x=1.22\pi$. The total intensity midway between the two point images falls to 0.74 of the maximum value [Fig. 1(A)]. Another criterion is the full width at half maximum (FWHM). Obviously, one can give a relation between FWHM of the Airy function and the Rayleigh resolution. Moreover, other criteria for spatial resolution are possible and in many applications the exact criterion chosen is irrelevant. However, in some applications it can be critical, particularly when the intensities of the two objects are considerably different. For example, the question whether two stars are resolvable is known to depend not only on the intensity ratio but also on the signal-to-noise ratio (SNR) of the measurement and on *a priori* knowledge of the objects. If one assumes, for example, that a star is generally an ideal point source, a weak star can be resolved as a faint bulge on the intensity profile of the bright one, provided the SNR is sufficient [Fig. 1(B)].

For heterodyne interferometry, it is known that the beat signal power, as well as the SNR, are directly proportional to the reflected object light power (omitting for the moment the mixing efficiency). Therefore, to a first approximation the depth resolution of the heterodyne interferometer is the same as the depth of focus of the image. If the FWHM of the carrier power[1] is used as the criterion for depth resolution, then one would conclude that an ''unwanted'' reflection of a surface spaced half of the FWHM from the image plane produces an unwanted signal of $1/\sqrt{2}$ relative amplitude, and unknown phase difference, adding vectorially to the image plane signal, provided the reflected light power of the two surfaces is identical. Therefore, the unwanted contribution yields a maximum amplitude error of -10.7 dB and a maximum phase error of $\pm 35.3°$. This is certainly not acceptable, and since the shape of the function of carrier voltage amplitude versus defocusing depends on the exact arrangement of the interferometer, a more detailed analysis is required. The unwanted contribution here is analogous to the second Airy distribution in the case of imaging. The fact that, in the case of only one object surface, the interferometrically measured vibration is recordable at depths far beyond the FWHM without major change of amplitude and phase indicates nothing else than high dynamic range of the apparatus (Ren and Nuttall, 2001). However, contrary to the assertion in Ren and Nuttall (2001), this finding does not detract from the validity of the usual definitions of depth resolution, provided they are applied in the context of the underlying assumptions.

The heterodyne signal voltage, u, of the photodetector is

$$u \propto m\sqrt{P_o P_r \cos(2\pi(f_h t-\varphi))}, \tag{1}$$

where P_o, P_r is the optical power at the detector of object and reference light, respectively, m the mixing efficiency (a measure of wavefront match, also called relative interference

[a)]Published as Letter to the Editor.

[b)]Author to whom correspondence should be addressed; electronic mail: ernst.dalhoff@uni-tuebingen.de

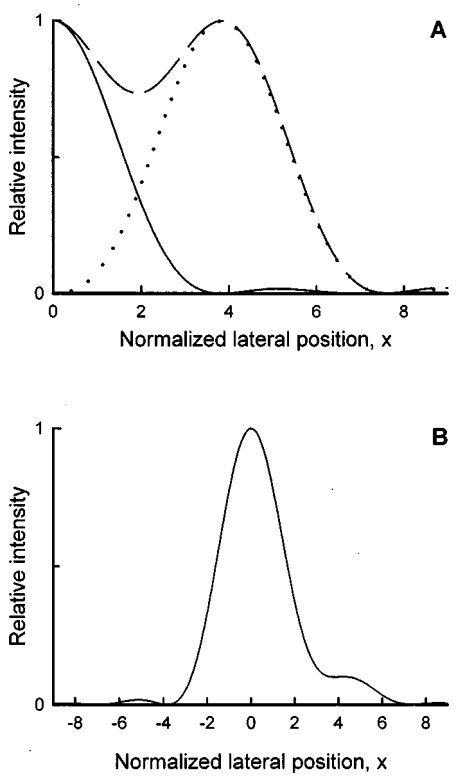

FIG. 1. Resolution criterion of Rayleigh. (A) Normalized intensity distribution of an Airy pattern (solid line), Airy intensity distribution shifted by 1.22π (dotted line), and superposition of the two Airy distributions placed according to the Rayleigh criterion (dashed line). (B) Superposition of two Airy distributions according to the Rayleigh criterion, but the right-hand one reduced in intensity to 1/10.

amplitude), f_h the heterodyne frequency, and φ the difference phase of the two interfering fields. P_o, m, and φ depend on the object distance, z.

The object light power depends on the nominal intensity reflection coefficient of the object, its roughness, the absorption of the traversed tissues, and the confocal suppression at a distance, z, from the focal plane, denoted as $V(z)$. For further discussion, all of these parameters except the confocal suppression $V(z)$ can be collectively given as the effective reflectivity r. Here, we present two alternative approaches to obtain an estimate of the depth response. The depth response for a confocal microscope with moderate numerical aperture can be written as (cf. Wilson, 1990)

$$V(z)=\left(\frac{\sin(Z)}{Z}\right)^2, \quad \text{with} \quad Z=\pi(N.A.)^2 z/n\lambda \tag{2}$$

where n is the refractive index of the intervening medium and λ is the wavelength in air.[2] The numerical aperture is defined as $N.A.=n\sin\alpha$, where α is the angular aperture of the imaging lens, or the $1/e^2$-divergence of a Gaussian beam, if it does not fill the aperture of the lens completely. A different approach is required if the focus is imaged onto the core of a monomode fiber, as in the interferometer developed by our own group. In this case, the monomode fiber acts as the confocal pinhole, and the coupling efficiency and hence the confocal depth response take the form (cf. Marcuse, 1977)

$$V(z)=\frac{4(4Z^2+1)}{(4Z^2+2)^2+4Z^2}, \quad \text{with} \quad Z=\pi(N.A.)^2 z/n_2 n\lambda, \tag{3}$$

where n_2 is the refractive index of the fiber cladding.[3]

Consider now the situation at the basilar membrane (BM). Two major concerns arise: (i) is a measurement made on the BM affected by reflections from tissue located behind the object plane? and (ii) could vibration measurements be made from such remote sites, if it were possible to focus on them? In the absence of any experimental data, assume that the reflectivity of the BM seen from the scala tympani side is similar to that of the cuticular plate from the scala vestibuli side. Let us for the moment assume that as the wavefront is being distorted when transversing the structures of the cochlea, the effective reflectivity of the second reflecting plane is reduced by a factor of 20. Then, in case (i), we obtain a maximum phase error of $\pm 9.0°$ at a distance corresponding to half of the FWHM, and a maximum amplitude error of -1.5 dB. On the other hand, to focus through the tissues on more remote structures, which corresponds to case (ii), using the same factor of 20 a confocal suppression of 29 dB is required to achieve the same maximum phase error. Consequently, in this case defocus values at large depth suppression ($\geqslant 30$ dB) should be considered. Of course, the assumption of a factor of 20 seems acceptable only in case (ii), where we obtain 30-dB distances of some 50 μm (Fig. 2), where scattering, wavefront distortion, and absorption for the double passage of the light could sum to such a value. This rather arbitrary example serves to illustrate the importance of the sequence of object and second reflecting plane, when there is a considerable attenuation between them.

As a first example, consider the heterodyne interferometer reported by Cooper (1999). It shows the general behavior of an on-axis confocal arrangement, even without pinholes, because only if the object is in the focal plane does the wavefront of the reflected signal, as well as its extent, match the reference wave. Using Eqs. (2) and (3), we find that the theoretical depth responses coincide with the experimental result of Cooper [Fig. 2(A)], provided $N.A.=0.25$ and $n=1.0$. The experimental curve suggests that structures more than about 20 μm behind the focal plane are not likely to introduce large phase errors ($<\pm 13°$, if effective reflectivity is the same for both planes). On the other hand, the 30-dB confocal suppression appears about 100 μm away from the focal plane, so that focusing through the cochlear partition might be impossible to achieve.

As a second example, consider the low-coherence fiber heterodyne interferometer developed by Dalhoff *et al.* (1998). The $N.A.$ of the Gaussian beam ($1/e^2$-definition) is 0.14. Figure 2(B) shows the square root of the reflected object light together with the heterodyne signal amplitude as a function of defocus. Measurements were made from a mirror under water. For this interferometer the interference signal is additionally suppressed due to the short coherence length of the multimode laser diode as the plane comes out of focus. We see that on the outer flank the depth response declines much steeper than in Fig. 2(A) (30 dB at $-60\,\mu$m defocus, corresponding to the case of reflections in the foreground

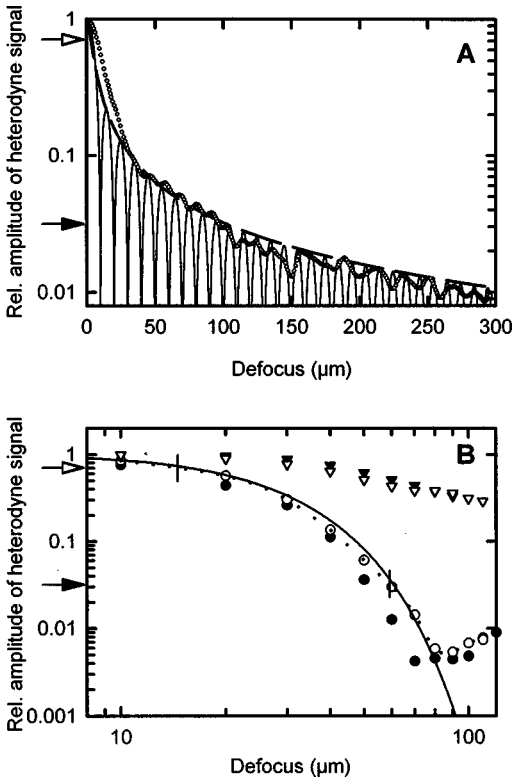

FIG. 2. (A) Theoretical depth response for the interferometer used by Cooper (1999) with $N.A.=0.25$, $\lambda=633$ nm, $n=1$, $n_2=1$, using Eqs. (2) (solid line) and (3) (dashed line), compared with his experimental data (open circles). Note the close correspondence between the two theoretical curves. (B) Theoretical and experimental depth response for the low-coherence fiber heterodyne interferometer developed by Dalhoff *et al.* (1998). Experimental value of the square root of the object light power coupled into the fiber (triangles). Theoretical value of the detector voltage signal (solid line) compared with measured values (circles). The detector voltage depends predominantly on the coherence properties of the laser diode. Open circles and triangles: object out of focus toward shorter distances; full circles and triangles: out of focus toward longer distances. Note that when comparing data and figures with the original publications, our definition of FWHM refers to heterodyne carrier signal power rather than to its voltage. Arrows indicate relative amplitudes at half of the full width at half maximum (open arrow) and at 30-dB suppression (closed arrow).

when focusing through tissues to a more remote site), although the FWHM (27 μm) is considerably broader than in Cooper (1999) (16 μm with respect to carrier power) or than in Khanna and Koester (1989) (9–22 μm, depending on slight tilt of the mirror). The suppression due to the coherence properties of the laser is given by the squared magnitude of the autocorrelation function of the electromagnetic field which is related to the spectral distribution (Born and Wolf, 1975)

$$V(z)=\exp\left(-\frac{z^2}{1.44z_{\mathrm{HWHM}}^2}\right)$$

$$\text{with}\quad z_{\mathrm{HWHM}}=\frac{\lambda^2}{1.44n\pi\Delta\lambda_{\mathrm{HWHM}}}, \tag{4}$$

where $\Delta\lambda_{\mathrm{HWHM}}=2.3$ nm is half width at half maximum of the emission spectrum of the laser diode (Dalhoff *et al.*, 1998). Here, only the envelope of the emission spectrum is considered, neglecting effects due to multiple longitudinal modes. The confocal arrangement chosen by Khanna and Koester (1989), with geometrically separated transmission and receiving optics, yields a suppression on a plane mirror of 30 dB at $z=-68$ to -92 μm with $N.A.=0.35$, depending on the tilt of the mirror ($\pm 2°$).[4]

The foregoing applies to other interferometric arrangements (homodyne phase modulation), where interference signal power is proportional to object light power. It applies as well to the case of self-mixing interferometry as used by Kössl and Russell (1995) and Bearden *et al.* (1993), where weak feedback is used, so that the relationship between laser intensity and effective object reflectivity is linear [cf. Eq. (3) in Wang *et al.*, 1993]. In these cases, only those unwanted reflections that are in quadrature will introduce an error; the error can also be estimated with the confocal equations (2) and (3).

In conclusion, there is too little quantitative *a priori* optical information to substantiate the assessment of possible measurement errors of interferometric methods applied to the cochlea. Nevertheless, it is seen that with some guesswork it is instructive to assess which properties of the interferometric setups deserve special attention. Moreover, it would be worthwhile investigating the optical properties of the cochlea, for example, surface microshape and multiple scattering.

ACKNOWLEDGMENTS

We gratefully thank Dr. N. Cooper for providing us with the data of his Fig. 7. This work was supported by the Deutsche Forschungsgemeinschaft, Grant Number Gu 194/3-3. We also appreciate the constructive suggestions of the reviewers.

[1]We prefer here a FWHM definition with respect to carrier power rather than detector voltage amplitude, since this is consistent with a 3-dB drop of the carrier as well as of the reflected object light power reaching the detector.

[2]This equation was developed originally for the incoherently illuminated confocal microscope. It is also an approximation for the case of the heterodyne interferometer, provided the focal plane of the microscope/interferometer is conjugated to the detector plane; this requires that the reference light be focused onto the detector. In this case, only object light coming from the plane mirror lying in the focal plane will contribute maximally to the interference signal. In the case of defocus, the object light spot blurs on the detector, and part of the light not matching the reference light spot is shed. (Although this increases the noise level, it can be neglected because the object light level in cochlear measurements is always much less than the reference light level.) The reference light spot is said to "act like a synthetic pinhole" (cf. Wilson, 1990, p. 399). Since we define the depth suppression using the heterodyne carrier signal power rather than its voltage, the depth suppression is proportional to the amount of object light overlapping the reference light and Eq. (2), which characterizes the amount of incoherent light passing through a confocal pinhole, applies without change. Note that Eq. (2) is a rough estimate even in the case of incoherent illumination because the details of the depth response depend on several factors, one of them being the aberrations of the microscope optics. For the case of coherent illumination for interferometric measurements, an additional suppression appears due to the changing curvature of the phase front of the object light. However, it can be shown that this effect does not change the depth response considerably.

[3]Provided the *N.A.* is moderate ($\leqslant 0.25$), the mode field diameter of the fiber in the original equation (Marcuse, 1977) can be substituted by $\lambda/(\pi N.A.)$. Since a beam coupled into a monomode fiber matches perfectly to the reference light field coupled into the same fiber, this formula takes the changing curvature of the defocused object light field into account. Note that in the limit of large defocus, the envelope of Eq. (2) equals Eq. (1).

[4]This divided aperture confocal arrangement is a very interesting setup, which can achieve even higher depth suppression, when numerical apertures around 0.5 are used (Khanna *et al.*, 1996). The principal difference to the in-line arrangement is that when considering only geometrical optics the illuminating cone of light separates completely from the receiving cone behind a certain, relatively small amount of defocus. Thus, it is claimed by Koester *et al.* (1989) that for larger defocus values, reflected object light can not directly enter the receiving aperture, so that the difference between the theoretically predicted and the experimentally measured depth responses is due to stray light. This is not strictly true because diffraction prevents the illuminated area at any possible object plane from having sharp boundaries. Nevertheless, using a coarse estimate with a rectangular aperture model, we have come to the conclusion that indeed stray light must dominate in all experimentally obtained depth responses known to us. Apart from such considerations, this arrangement is very effective, and a combination with a low-coherence light source appears to give the highest suppression.

Bearden, A., O'Neill, M. P., Osborne, L. C., and Wong, T. L. (**1993**). ''Imaging and vibrational analysis with laser-feedback interferometry,'' Opt. Lett. **18**, 238–240.

Born, M., and Wolf, E. (**1975**). *Principles of Optics*, 5th ed. (Pergamon, Oxford), pp. 503–504.

Cooper, N. P. (**1999**). ''An improved heterodyne laser interferometer for use in studies of cochlear mechanics,'' J. Neurosci. Methods **88**, 93–102.

Dalhoff, E., Gärtner, R., Hofbauer, U., Tiziani, H., Zenne, H. P., and Gummer, A. W. (**1998**). ''Low-coherence fiber heterodyne interferometer for both dc and high-frequency vibration measurements in the inner ear,'' J. Mod. Opt. **45**, 765–775.

Khanna, S. M., and Koester, C. J. (**1989**). ''Optical sectioning characteristics of the heterodyne interferometer,'' Acta Oto-Laryngol., Suppl. **467**, 61–67.

Khanna, S. M., Koester, C. J., Willemin, J. F., Dändliker, R., and Rosskothen, H. (**1996**). ''A noninvasive optical system for the study of the function of the inner ear in living animals.'' SPIE **2732**, 64–81.

Koester, C. J., Khanna, S. M., Rosskothen, H., and Tackaberry, R. B. (**1989**). ''Incident light optical sectioning microscope for visualization of cellular structures in the inner ear,'' Acta Oto-Laryngol., Suppl. **467**, 27–33.

Kössl, M., and Russell, I. J. (**1995**). ''Basilar membrane resonance in the cochlea of the mustached bat,'' Proc. Natl. Acad. Sci. U.S.A. **92**, 276–279.

Lord Rayleigh (**1879**). ''Investigations in optics, with special reference to the spectroscope,'' Philos. Mag. **5**, Ser. 8, 261–274.

Marcuse, D. (**1977**). ''Loss analysis of single-mode fiber splices,'' Bell Syst. Tech. J. **56**, 703–718.

Ren, T. Y., and Nuttall, A. L. (**2001**). ''Recording depth of the heterodyne laser interferometer for cochlear vibration measurement,'' J. Acoust. Soc. Am. **109**, 826–829.

Wang, W. M., Boyle, W. J. O., Grattan, K. T. V., and Palmer, A. W. (**1993**). ''Self-mixing interference in a diode laser: Experimental observations and theoretical analysis,'' Appl. Opt. **32**, 1551–1558.

Wilson, T. (Ed.) (**1990**). *Confocal Microscopy* (Academic, London).

A comparative assessment of speech sound discrimination in the Mongolian gerbil[a)]

Joan M. Sinnott[b)] and Kelly W. Mosteller
Comparative Hearing Laboratory, Psychology Department, University of South Alabama, Mobile, Alabama 36688

(Received 30 March 2001; revised 5 July 2001; accepted 6 July 2001)

The Mongolian gerbil is a small rodent with human-like absolute auditory sensitivity in the speech range below 4 kHz. Here, gerbil ''speech DLs'' (difference limens) are measured along several synthetic speech continua and compared with human data. Results show that gerbils are similar to humans in that they discriminate ''within-category'' information more easily for vowels than for consonants. However, gerbils are less sensitive to all the speech stimuli, with DLs about 2–3 times higher. Interestingly, gerbil speech DLs are not accurately predicted by their pure-tone frequency DL, which is 36 times that of the human at 1 kHz. Thus, gerbils are actually much more similar to humans in speech sound discrimination than in pure-tone discrimination. It is concluded that the gerbil offers a promising ''small-mammal'' model for the processing of spectral cues in human speech sounds. © *2001 Acoustical Society of America.* [DOI: 10.1121/1.1398055]

PACS numbers: 43.66.Fe, 43.66.Gf, 43.71.Es [MRL]

I. INTRODUCTION

The Mongolian gerbil (*Meriones unguiculatus*) is a small rodent with human-like absolute auditory sensitivity in the speech range below 4 kHz (Ryan, 1976; Sinnott *et al.*, 1997). Thus, gerbil hearing is quite distinct from that of other small rodents such as mice and rats, which hear mainly high frequencies (Fay, 1988). Largely because of this low-frequency specialization, gerbils have become favorite ''small-mammal'' models for auditory anatomy and physiology research and have produced a wealth of data too numerous to reference here. However, gerbil *psychoacoustic capacities* are relatively unknown. Gerbils have been systematically studied only for absolute auditory thresholds (Ryan, 1976; Sinnott *et al.*, 1997), sound localization (Heffner and Heffner, 1988), and pure-tone frequency and intensity discrimination (Sinnott *et al.*, 1992). The goal of the present study is to help correct this imbalance between the vast amount of gerbil auditory anatomical and physiological data, on the one hand, and the relative scarcity of gerbil psychoacoustic data, on the other.

An important question in exploring a potential animal model for human hearing is: What stimuli are most relevant to investigate? Beginning in the late 1970's, many prominent auditory physiologists began to use complex human speech sounds, rather than simple tones and noises (e.g., Sachs and Young, 1979; Young and Sachs, 1979). Following this ever-growing trend, we also choose to use speech sounds to explore gerbil psychoacoustic sensitivity. As many data already exist for human and monkey speech sound discrimination (Sinnott, 1994), the gerbil can easily be put into a comparative perspective using speech stimuli.

How does the processing of speech sounds relate to simple pure-tone resolution? A superficial examination of gerbil pure-tone frequency DLs (difference limens) might lead one to infer that the gerbil has a very poor capacity to discriminate the spectral cues in human speech. For example, the gerbil DL at 1 kHz is 108 Hz, or 36 times that of the human (Sinnott *et al.*, 1992). However, evidence is emerging from comparative psychoacoustics that animal pure-tone frequency DLs do not reflect their true resolution for speech sounds: The monkey, for example, is much closer to the human in discrimination of speech sounds compared to pure tones (Sinnott, 1994). This striking mismatch between the monkey's ability to discriminate frequency differences in pure tones versus speech sounds leads us to ask if the gerbil will also perform relatively better on speech sounds compared to simple pure tones. In this study we measure gerbil ''speech DLs'' along several synthetic continua differentiating vowel, liquid-, and stop-consonant contrasts, and compare them with human data, in order to assess both qualitative and quantitative differences in sensitivity.

II. METHOD

Twenty-five gerbils (10 females and 15 males aged 1–2 years old) participated in either vowel ($n=9$), liquid ($n=8$), or stop-consonant ($n=8$) conditions (see below). All gerbils were third- or fourth-generation offspring of three ''wild'' gerbil pairs obtained from the Tuva Research Institute in Russia, via the University of California at Davis in 1990. This wild strain is distinct from the more widely used domestic ''Tumblebrook Farms'' strain that originates from six gerbil pairs imported to the USA from Japan in 1950 (Thiessen and Yahr, 1977). According to McGinn and Faddis (1998), the wild strain is not marked with serious cochlear nucleus degeneration compared to the domestic strain. During testing, our gerbils were typically maintained at 90% of their free-feeding weights (about 60–80 g for females, 70–90 g for males). All animal care and experimental procedures were approved by the Animal Care and Use Committee of the University of South Alabama.

[a)]Published as Letter to the Editor.
[b)]Author to whom correspondence should be addressed; electronic mail: jsinnott@jaguar1.usouthal.edu

Testing was conducted inside a double-walled IAC booth lined with acoustic foam (see Sinnott, 1995; Sinnott *et al.*, 1997). Briefly, gerbils were tested in wire cage (20 $\times 20 \times 20$ cm) containing a cue light, a food cup, a platform with an embedded photobeam emitter, and a sensor mounted above the platform that sensed when the gerbil was on and off the platform. The stimulus system consisted of a 16-bit D/A converter, a low-pass filter (8 kHz), a programmable attenuator (all made by Tucker-Davis Technologies), and an amplifier (NAD). A loudspeaker (Genesis) was located in the corner of the booth, 84 cm from the cage.

Stimuli were synthesized using the Computerized Speech Research Environment (AVAAZ Innovations, Ontario, Canada). All stimuli were 300-ms long, with an $F0$ that began at 125 Hz and decreased linearly to 100 Hz at the end of the stimulus. All stimuli used the default bandwidths ($F1=50$, $F2=70$, and $F3=110$ Hz) and the cascade branch to automatically set the formant amplitudes. Three speech continua, each consisting of 8 stimuli (S1–S8), were constructed. *Vowels*: The /I–i/ continuum (Sinnott and Kreiter, 1991) was constructed by changing the steady-state values $F1$, $F2$, and $F3$. $F1$ ranged from 390–270 Hz (-17-Hz steps); $F2$ ranged from 1990–2290 Hz ($+45$-Hz steps), and $F3$ ranged from 2550–3000 Hz ($+64$-Hz steps). *Liquids*: The /ra–la/ continuum (Sinnott and Brown, 1997) was constructed using the steady-state vowel /a/ ($F1=700$ Hz, $F2=1200$ Hz, and $F3=2500$ Hz). $F1$ was similar for all eight stimuli: It began at 350 Hz, stayed flat for 35 ms, and then began a 35-ms transition to 700 Hz. $F2$ remained flat for all stimuli at 1200 Hz. The continuum was generated by increasing the $F3$ onset frequency in 200-Hz steps from 1600–3000 Hz. For /ra/, $F3$ began at 1600 Hz, remained flat for 35 ms, and then began an 85-ms transition to 2500 Hz. For /la/, $F3$ began at 3000 Hz, and then followed the same temporal pattern as /ra/. *Stops*: The /ba–da/ continuum (Sinnott *et al.*, 1976) also used the steady-state vowel /a/ as described above. $F1$, $F2$, and $F3$ all contained initial 30-ms transitions. The $F1$ onset frequency (400 Hz) was similar for all stimuli. The $F2$ onset frequency ranged from 900 Hz for /ba/ to 1700 Hz for /da/, and the $F3$ onset frequency ranged from 2000 Hz for /ba/ to 2800 Hz for /da/, both formants using approximate 115-Hz steps.

Note that the acoustic cues are shorter and more complex progressing from vowels to liquids to stop consonants. For vowels, the differentiating cues are steady-state changes in all three formants (total duration $=300$ ms). For liquids, the cues are both a 35-ms steady state and an 85-ms transition (total duration$=120$ ms) in $F3$. For stops, the cues are brief transitions in both $F2$ and $F3$ (total duration$=30$ ms). Despite these different cues, all the continua were synthesized such that the human phoneme boundary occurred in the center of each continuum between stimuli 4 and 5 (see Fig. 1). This method of construction allowed us to equate these three types of multidimensional speech stimuli in terms of the human phoneme boundary.

At the age of 6 months, gerbils were trained on a procedure to measure their absolute auditory thresholds (Sinnott *et al.*, 1997). By about 9 months, all gerbils produced normal human-like thresholds for the vowel /a/ (5-15 dB SPLC). At about 12 months, they were introduced to the ''repeating background'' discrimination procedure (Sinnott, 1995), which trained the gerbil to report when a ''background'' stimulus (e.g., ''BA'') changed to a ''target'' stimulus (e.g., ''DA''). Each trial began with the flashing cue light, which signaled the gerbil to mount the platform inside the testing cage. When the gerbil mounted, the light steadied and the background started pulsing (1 per 750 ms). After 2–8 pulses, a ''target'' was pulsed twice, for a total response time of 1.5 s. If the gerbil reported the target by jumping off the platform during this interval, a *hit* was scored and the gerbil was rewarded with a food pellet and a brief 100-ms, 2-kHz tone as a secondary reinforcer. If the gerbil *missed* the target, a 3-s time-out occurred, during which the light extinguished and a 300-Hz tone was presented. Control trials occurred on 25% of the trials. A *false alarm* to a control trial as well as any other report response in the absence of a target resulted in a 4-s time-out. A *correct rejection* to a control trial was immediately followed by a superthreshold ''probe'' target at $+10$ dB, which was normally 100% discriminable and thus always led to a reward.

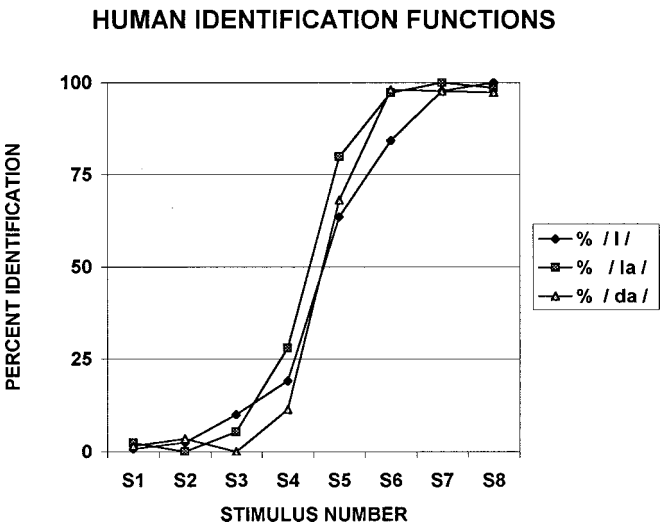

FIG. 1. Human identification functions for the vowel, liquid-, and stop-consonant continua showing the location of the phoneme boundary in the center of each continuum. Data were based on the mean boundaries from authors JMS and KWM and two other human listeners.

To measure speech DLs, continuum stimuli were presented at 60-dB SPL using the method of constant stimuli. The DL was defined as a d' of 2.0, which approximates the 50%-level of detection with a false-alarm rate of 5%. Data were discarded for test sessions in which a gerbil responded to $>25\%$ control trials, or $<15\%$ probe trials, since such events indicated that the gerbil was not attentive during testing. Gerbils worked in 15-m daily sessions to earn a total of 60 rewards, which resulted in about 8 presentations of each test stimulus. Gerbils were tested for at least 30 consecutive days (about 1 month) to obtain a stable DL. If their lowest DL occurred in the last three sessions tested, then additional sessions were run until the lowest DL did not occur in the last three sessions. The ''final DL'' was obtained by averaging the three lowest DLs obtained during the monthly run.

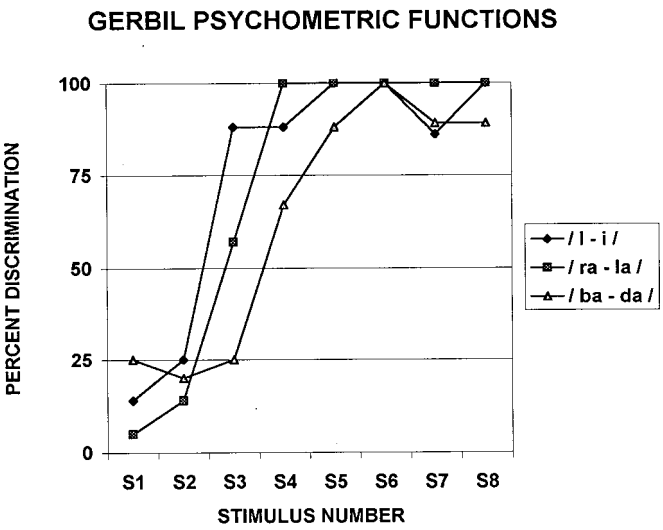

FIG. 2. Individual psychometric functions from three different gerbils discriminating along the /I–i/, /ra–la/, and /ba–da/ continua. On the *x* axis, S1 denotes the repeating background stimulus /I/, /ra/, or /ba/. Responses to S1 indicate each gerbil's false-alarm rate to the catch trial. The gerbils are rewarded for correctly discriminating the target stimuli (S2–S8).

III. RESULTS AND DISCUSSION

Examples of daily psychometric functions from three gerbils discriminating along the vowel, liquid-, and stop-consonant continua are shown in Fig. 2. Note that they all show normal monotonic psychometric functions as the target stimulus difference (S2–S8) increases from the background (S1). These functions can be compared with Fig. 1 to assess gerbil sensitivity in relation to the human phoneme boundary.

To more easily quantify gerbil sensitivity, the concept of a ''speech DL'' is introduced here. There are several ways to calculate a speech DL for these multidimensional stimuli. One way that would be of most interest to speech-oriented researchers is in terms of ''steps along the continuum.'' Since the background stimulus was always S1, a DL could range from <S2 through >S8. For example, a DL of S4.5 would place the DL at the center of the continuum, which was the approximate location of the human phoneme boundary (see Fig. 1). This DL will be referred to as the ''continuum DL'' or DLC. Mean gerbil DLCs summarized in this way are shown in Table I (column A). If the human phoneme boundary at S4–S5 is taken as a reference, then gerbil DLCs were clearly lowest for the vowel continuum, occurring well within the /I/ phoneme category at S2.8. The next lowest DLCs were for the liquid continuum, occurring slightly within the /ra/ category at S3.7. The highest gerbil DLCs occurred for the stop continuum at S4.7, coinciding almost exactly with the location of the human /ba–da/ phoneme boundary at S4–S5.

A second way to calculate the DL is in terms of absolute formant frequency changes, e.g., the formant frequency DL or ''DLFF.'' DLFFs for each of the relevant formants in the vowel, liquid-, and stop continua are shown in Table I (column B). According to this analysis, gerbil DLFFs are also clearly lower for the vowel continuum (31–115 Hz) than for either of the consonant continua (540 Hz for liquids; 422 Hz for stops). A third way to calculate the DL is in terms of formant frequency changes relative to the background stimulus (S1), e.g., the relative formant frequency DL or ''DLFF/FF,'' as shown in Table I (column C). According to this analysis, gerbil DLFF/FFs are also clearly lower for the vowel continuum (0.04–0.08) than for either of the consonant continua (0.30 for liquids, 0.19–0.37 for stops).

TABLE I. Mean gerbil ''speech DLs'' measured in different ways for the three types of speech continua (Vowel, Liquid, Stop): Column A shows the means (SDs) of DLs calculated in terms of continuum steps (DLC). Column B shows DLs in terms of absolute formant frequency changes for each formant (DLFF). Column C shows DLs in terms of formant frequency changes relative to S1, the background stimulus (DLFF/FF).

	A DLC	B DLFF	C DLFF/FF
Vowel	S2.8 (0.70)		
*F*1		31	0.08
*F*2		77	0.04
*F*3		115	0.05
Liquid	S3.7 (1.00)		
*F*3		540	0.30
Stop	S4.7 (1.10)		
*F*2		422	0.37
*F*3		422	0.19

The present results show that gerbils can easily discriminate the spectral cues used in human speech with DLs that are close to the phoneme boundary (liquids or stop consonants) or within the phoneme category (vowels). In addition, the DLs analyzed in three different ways indicate that gerbils are more sensitive to changes in steady-state vowels than in liquids or stop consonants. This result appears to be qualitatively the same effect as shown in human ''categorical perception'' studies using more memory-loaded procedures such as the ABX (Liberman *et al.*, 1967).

Table II compares the present gerbil DLFFs with previous human and monkey DLFFs using similar stimuli and procedures. For vowels and stops, DLFFs are based on *F*2, which is traditionally considered to be the single most important formant in human speech perception (Liberman *et al.*, 1967). For liquids, DLFFs are based on *F*3, which is the only formant that changes. Note the general trend for all species to have lower DLFFs for the simpler vowel stimuli compared to the more complex liquids and stops. However, the most interesting trend emerges by comparing the gerbil

TABLE II. Comparison of human and animal frequency DLs for four types of stimuli. The gerbil speech DLs are from the present study. The gerbil 1-kHz tone DL is from Sinnott *et al.* (1992). The human and monkey data are from Sinnott *et al.* (1985; 1-kHz tone), Sinnott and Kreiter (1991; /I–i/), Sinnott *et al.* (1976; /ba–da/) and Sinnott and Brown (1997; /ra–la/). All studies used stimuli presented at 50–60-dB SPL. The G:H ratio denotes the ratio between the gerbil and human DL for each type of stimulus.

	Stop /ba–da/	Liquid /ra–la/	Vowel /I–i/	Pure tone 1–kHz
Gerbil	387	540	75	108
Monkey	320	80	48	33
Human	160	180	21	3
G:H ratio	2.4	3.0	3.6	36.0

and human DLFFs *with each other*, specifically by calculating the gerbil DLFF: human DLFF ratios for the three types of speech stimuli. Note that the ratio is smallest for the stops (2.4), next smallest for the liquids (3.0), and largest for the vowels (3.6). Thus, the gerbil is closest to the human in sensitivity to the 30-ms-transition-based stop-consonant continuum. A fourth stimulus comparison is also shown in Table II: The simple pure-tone DL (DLF). It is with this comparison that the most intriguing difference between gerbils and humans emerges, for here gerbil sensitivity is 36 times that of the human. This is quite a change from the ratio of 2.4 for the stop-consonant /ba–da/ continuum!

It is beyond the scope of this paper to go into a detailed discussion of the possible significance of the extremely divergent (relative to animal) human pure-tone frequency DL (but see Sinnott *et al.*, 1985, for a discussion of this issue). Suffice it to say that, if human data are taken as a reference, then the gerbil pure-tone frequency DL does not accurately predict sensitivity to spectral speech sound continua. *Gerbils are much closer to humans in spectral sensitivity for speech sounds than for pure-tone stimuli*. Thus, if we are interested in assessing and developing the gerbil as a model for human speech sound perception, it appears almost irrelevant to study its pure-tone frequency DL.

IV. CONCLUSION

Psychoacoustic data are a necessary adjunct to anatomical and physiological data to uncover the best potential animal models of the human auditory system. There are many obvious advantages to working with gerbils in auditory anatomical, physiological, and behavioral research. First and foremost, their acute low-frequency hearing makes them excellent models for human hearing. Second, being small, they are relatively cheap to maintain in the laboratory and easy to handle. Third, their altricial birth process and short life span renders them useful models for auditory development and aging. The present study indicates that Mongolian gerbils are qualitatively similar to humans in their spectral sensitivity to speech sounds, although they are quantitatively less sensitive. We propose that they offer promising small-mammal models for the study of higher-level aspects of speech perception involving categorical perception, trading relations, and perceptual constancy for phoneme categories.

ACKNOWLEDGMENTS

This research was supported by the NIDCD, the Fidelity Investments Charitable Gift Fund, the University of South Alabama Foundation, and Pfizer Corporation. These data were presented at the February 2001 Meeting of the Association for Research in Otolaryngology in Tampa, FL. We thank Jazmin Camchong, Jaquese James, and Kelly Tyler for assistance in testing gerbils.

Fay, R. (**1988**). *Hearing in Vertebrates: A Psychophysics Databook* (Hill-Fay, Winnetka, IL).

Heffner, R., and Heffner, H. (**1988**). ''Sound localization and the use of binaural cues in the gerbil,'' Behav. Neurosci. **102**, 422–428.

Liberman, A., Cooper, F., Shankweiler, D., and Studdert-Kennedy, M. (**1967**). ''Perception of the speech code,'' Psychol. Rev. **74**, 431–461.

McGinn, M., and Faddis, B. (**1998**). ''Neuronal degeneration in the gerbil brainstem is associated with spongiform lesions,'' Microsc. Res. Tech. **41**, 187–204.

Ryan, A. (**1976**). ''Hearing sensitivity of the Mongolian gerbil,'' J. Acoust. Soc. Am. **59**, 1222–1226.

Sachs, M., and Young, E. (**1979**). ''Encoding of steady-state vowels in the auditory nerve: Representation in terms of discharge rate,'' J. Acoust. Soc. Am. **66**, 470–479.

Sinnott, J. (**1994**). ''Comparisons of human and monkey differential sensitivity to speech, non-speech and monkey speech sounds,'' Curr. Top. Acous. Res. **1**, 355–364.

Sinnott, J. (**1995**). ''Methods to assess the processing of speech sounds by animals,'' in *Methods in Comparative Psychoacoustics*, edited by G. Klump, R. Dooling, R. Fay, and W. Stebbins (Birkhauser, Basel, Switzerland).

Sinnott, J., Beecher, M., Moody, D., and Stebbins, W. (**1976**). ''Speech sound discrimination by monkeys and humans,'' J. Acoust. Soc. Am. **60**, 687–695.

Sinnott, J., and Brown, C. (**1997**). ''Perception of the American-English liquid /ra–la/ contrast by humans and monkeys,'' J. Acoust. Soc. Am. **102**, 588–602.

Sinnott, J., Brown, C., and Brown, F. (**1992**). ''Frequency and intensity discrimination in Mongolian gerbils, African monkeys and humans,'' Hear. Res. **59**, 205–212.

Sinnott, J., and Kreiter, N. (**1991**). ''Differential sensitivity to vowel continua in Old World monkeys and humans,'' J. Acoust. Soc. Am. **89**, 2421–2429.

Sinnott, J., Petersen, M., and Hopp, S. (**1985**). ''Frequency and intensity discrimination in humans and monkeys,'' J. Acoust. Soc. Am. **78**, 1977–1985.

Sinnott, J., Street, S., Mosteller, K., and Williamson, T. (**1997**). ''Behavioral measures of vowel sensitivity in gerbils: Effects of age and genetic origin,'' Hear. Res. **112**, 235–246.

Thiessen, D., and Yahr, P. (**1977**). *The Gerbil in Behavioral Investigations* (University of Texas Press, Austin).

Young, E., and Sachs, M. (**1979**). ''Encoding of steady-state vowels in the temporal aspects of the discharge patterns of populations of auditory nerve fibers,'' J. Acoust. Soc. Am. **66**, 1381–1403.

Time-lapse nondestructive assessment of shock wave damage to kidney stones *in vitro* using micro-computed tomography[a)]

Robin O. Cleveland[b)]
Department of Aerospace and Mechanical Engineering, Boston University, 110 Cummington Street, Boston, Massachusetts 02215

James A. McAteer
Department of Anatomy and Cell Biology, Indiana University School of Medicine, 635 Barnhill Drive, Indianapolis, Indiana 46202

Ralph Müller[c)]
Orthopedic Biomechanics Laboratory, Beth Israel Deaconess Medical Center and Harvard Medical School, 330 Brookline Avenue, Boston, Massachusetts 02215

(Received 27 March 2001; accepted for publication 14 July 2001)

To better understand how lithotripter shock waves break kidney stones, we treated human calcium oxalate monohydrate (COM) kidney stones with shock waves from an electrohydraulic lithotripter and tracked the fragmentation of the stones using micro-computed tomography (μCT). A desktop μCT scanning system, with a nominal resolution of 17 μm, was used to record scans of stones at 50-shock wave intervals. Each μCT scan yielded a complete three-dimensional map of the internal structure of the kidney stone. The data were processed to produce either two- or three-dimensional time-lapse images that showed the progression of damage inside the stone and at the surface of the stone. The high quality and excellent resolution of these images made it possible to detect separate patterns of damage suggestive of failure by cavitation and by spall. Nondestructive assessment by μCT holds promise as a means to determine the mechanisms of stone fragmentation in SWL *in vitro*.
 [DOI: 10.1121/1.1401742]

PACS numbers: 43.80.Gx [FD]

I. INTRODUCTION

Shock wave lithotripsy (SWL) was first introduced in 1980[1] and has subsequently revolutionized the treatment of kidney stones. Despite its predominance in the treatment of urinary calculi there is a growing recognition that shock waves (SWs) cause trauma to the kidney[2–4] that can result in acute problems[5] and can lead to long-term complications in some patient groups.[6–8] We present an imaging technique that provides new information on the fragmentation of kidney stones *in vitro*, information that may lead to advances in SWL that reduce side-effects.

A number of mechanisms have been proposed by which lithotripsy shock waves may destroy kidney stones. These include: *Spall*: the compressive component of the shock wave reflects off the distal surface and the stone fails in tension.[1,9,10] *Cavitation*: the tensile component of the shock wave makes small bubbles grow in the fluid surrounding the stone; the violent collapse of the bubbles acts principally on the proximal surface of the stone.[9,11,12] *Squeezing*: as the shock wave propagates through the stone a differential stress between the stone and the fluid develops which leads to a bulging and splitting along the SW axis.[13] *Superfocusing*: reflections from curved surfaces or corners of the stone can interfere constructively to produce localized regions of high stress.[14] *Fatigue*: microscopic flaws in the stone grow due to the tensile stress[15] or shear stress[16] induced by successive SWs until macroscopic cracks develop and the stone breaks. These mechanisms are dependent to variable extent on different components of the lithotripter pressure pulse[17] and the material properties of kidney stones.[18]

There is limited agreement in the literature as to the role of the mechanisms discussed above in the fragmentation process of kidney stones. We suggest that examination of a kidney stone at frequent intervals during its exposure to SWs will reveal the role of the various mechanisms. To test this idea we used an emerging imaging technique, x-ray micro-computed tomography (μCT), which allows for the nondestructive assessment of x-ray attenuating materials. In μCT, focused beams of x-rays are passed through an object and the absorption measured by a detector on the opposite side. The object is rotated about an axis and computed tomography (CT) is used to determine a 2D absorption map through thin slices. Stacks of 2D slices are then used to provide a 3D reconstruction of the object. The principal advantage of μCT is that it is nondestructive and therefore allows time-lapse measurements. We demonstrate that with μCT it is possible to track the early progression of SW damage in human kidney stones and that the pattern of damage is dependent on experimental manipulation of the environment surrounding the stone.

[a)]Published as Letter to the Editor
[b)]Author to whom correspondence should be addressed; electronic mail: robinc@bu.edu
[c)]Now at: Institute for Biomedical Engineering, ETH and University of Zürich, Moussonstrasse 18, 8044 Zürich, Switzerland.

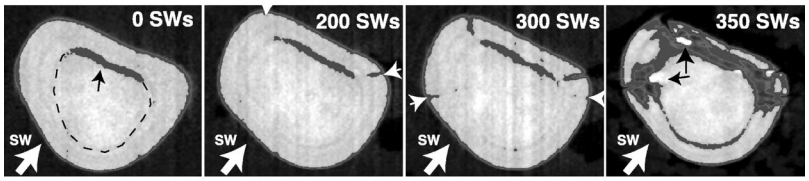

FIG. 1. Serial μCT images of a COM stone "A1" at 0, 200, 300, and 350 SWs. Shock waves were incident from the lower left as indicated by the arrow. The black arrow in the baseline image denotes a region of low absorption that was in-line with a prominent lamella (dashed line). The gray color indicates regions of very low x-ray absorption. The small white arrows at 200 and 300 SWs denote the locations of new crack formation. By 300 SWs small gaps are visible along the lamellae and by 350 SWs the stone has separated into an outer shell and central core. The black arrows at 350 SWs indicate regions of high x-ray absorption.

II. MATERIALS AND METHODS

A. Kidney stones

Calcium oxalate mono-hydrate kidney stones (~4 mm diameter) were harvested from patients by percutaneous nephrostolithotomy (PCNL); COM is the most common stone formed in the body. At PCNL the stones were transferred directly into vials of sterile water for storage. Stone composition was determined by Beck Analytical Services (Indianapolis, IN) using microscopic visual inspection, qualitative chemical analysis, and infrared spectroscopy.

The stones were packaged so that they could be transported back and forth between the lithotripter (Indianapolis) and the μCT facility (Boston) and could be re-positioned to their original spatial orientation within the lithotripter and the μCT scanner. The stones were placed in polypropylene screw-cap cryovials (2 ml, 12×48 mm, Dot Scientific, Burton, MI) that were packed with water-saturated cotton gauze sponges (Johnson and Johnson, New Brunswick, NJ). In order to minimize transfer of air into the vial the gauze was soaked for 3 h in deionized water and kneaded by hand to displace bubbles. Gauze was inserted into the vials under water and packed tightly so that when a stone was put in and the cap secured, all under water, it would be held securely near the cap. One stone (stone A1) was packed entirely surrounded by gauze. This was done to reduce the opportunity for cavitation to take place at the surface of the stone. A second stone (stone A2) was loaded into a vial that had an optically clear, 0.1 μm thick, mylar window in the cap and was packed without gauze at its proximal surface. That is, the leading face of this stone was open to the surrounding water and was visible through the mylar window. Stone A1 was scanned by μCT prior to treatment, and then scanned at 50 SW intervals until 350 SWs had been administered (8 μCT scans performed). Stone A2 was treated until damage was visible through the mylar window (10 SWs). This stone was then scanned by μCT.

B. Micro-computed tomography

A desktop μCT imaging system (μCT 20, Scanco Medical AG, Basserdorf, Switzerland) was used to image the stones. The system used a microfocus x-ray tube with a focal spot of 10 μm as an x-ray source. The filtered 40 kVp x-ray spectrum was peaked at 25 keV, allowing excellent stone-water contrast due to the pronounced photoelectric effect. The source produced a fan beam that was detected by a charge coupled device (CCD) array with 1024 elements. Measurements were obtained by mounting the unprocessed specimen on a turntable that could be shifted automatically in the axial direction. Six hundred projections were taken over 216° (180° plus half the fan angle on either side). A standard convolution-back-projection procedure with a Shepp–Logan filter was used to reconstruct the CT images in 1024×1024 pixel matrices. The spatial resolution of the system was defined by the 10% contrast level in the modulation transfer function (MTF) resulting in a spatial resolution of 28 μm.[19]

The vial that was used for shock wave treatment of the stone was placed directly inside the μCT imaging device, that is, without disturbing the kidney stone. At each scan a total of 250 to 300 micro-tomographic slices, using a slice increment of 17 μm, were acquired depending on the height of the sample (4.3–5.1 mm). The typical imaging time for a single scan of 300 slices was 8 h. Measurements were stored in three-dimensional image arrays with an isotropic voxel size of 17 μm. A constrained three-dimensional Gaussian filter was used to partly suppress the noise in the volumes. Stone samples were segmented from background using a global thresholding procedure.[20] Because of the amount of data collected (of the order 1 GByte per 3D image of a stone) special visualization software was used that addresses the demands of rendering large triangulated objects including real-time functional animations.[21]

C. Shock wave lithotripsy

Shock wave exposures were performed using a research electrohydraulic lithotripter in which the acoustic output is equivalent to the Dornier HM3 lithotripter.[22] The HM3 is the most widely used lithotripter in the US.[23] Vials were positioned with the stone at the focus of the lithotripter and the cap facing the SW source. The orientation of the vial ensured that SWs entered through the flat surface of the vial, which reduces artifacts associated with the interaction of the SW and the vial.[24] SWs were delivered at 20 kV and pulse rate of 1 Hz.

III. RESULTS

Figure 1 shows time-lapse μCT images of a slice through the center of the stone A1 (gauze surrounded stone). Dark gray coloring was added during post-processing to regions of low absorption which we interpret to be associated with fractures or voids. The pre-SWL scan showed an internal region of low absorption in the form of a narrow band

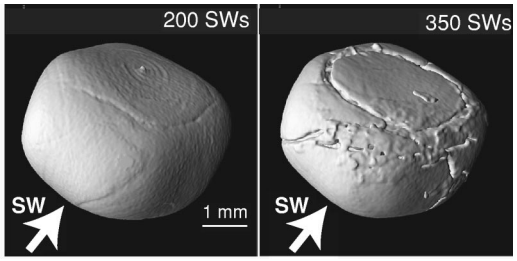

FIG. 2. Serial 3D surface rendered images of kidney stone A1 at 200 and 350 SWs. The formation of a circular chip at the distal side of the stone is consistent with failure by a spall mechanism.

near the distal side (relative to the SW source) of the stone. This region appeared to be in line with a prominent lamella that circumscribed the core of the stone. At 200 SWs and 300 SWs precursors of cracks were evident at both ends of this region, appearing to grow in from the surface of the stone. Also at 300 SWs small cracks had formed at midline on the right and the left. This is the location where squeezing and stress concentrations associated with curvature would be expected. In addition, at 300 SWs minute defects could be seen along the lamella previously observed in frame 0-SW. At 350 SWs growth of fractures along this lamella had separated the stone into an inner core and an outer shell. The growth of the cracks observed in these images consistent with a fatigue type of process. A broad chip had separated from the distal side of the stone. Loss of this piece is consistent with failure by spall. At 350 SWs there were also localized regions of very high x-ray absorption, as indicated by the presence of bright white spots.

Figure 2 shows two images formed using 3D surface rendering from the same measurement series. The 3D images clearly show the formation and separation of a cap at the distal surface. Figure 3 shows the 350 SW frame of Fig. 2 rotated approximately 180 deg and demonstrates that the SW-entry side of this stone (stone A1, surrounded by gauze) suffered no loss of material. After 350 SWs the stone was removed from the vial and was observed to have broken into *seven* main pieces which corresponded with the 3D μCT image. These included the distal cap, a central core, and five pieces that made up the remainder of the outer shell.

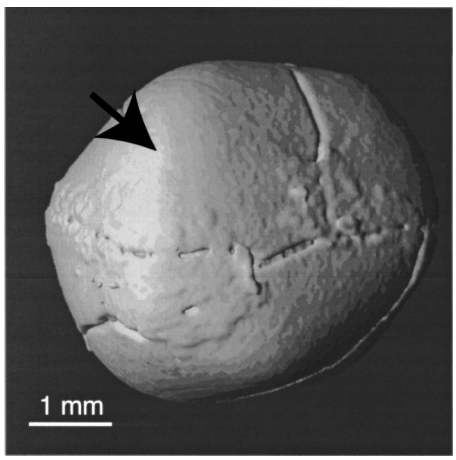

FIG. 3. Opposite side of stone A1 (Fig. 2, 350 SW). This image shows that the location of the SW entry, indicated by the arrow, has no sign of damage.

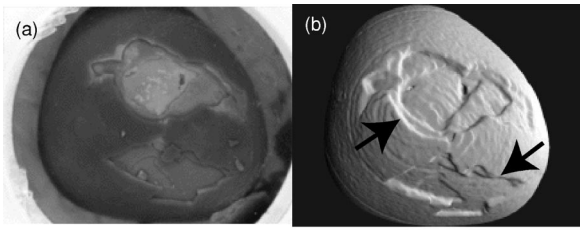

FIG. 4. Proximal surface of COM stone "A2" after 10 SWs. The upper frame is a surface rendering from μCT data and shows that this surface has been chipped away, in contrast to Fig. 3. The lower frame shows an optical micrograph for comparison. The damage on this surface is consistent with a cavitation mechanism.

Figure 4 shows correlative μCT and optical images of the proximal surface of stone A2 after 10 SWs. This face of the stone was open to the surrounding water, thus creating an environment that should allow cavitation to occur. Damage at this surface showed loss of broad, thin chips that revealed the lamellar substructure of the stone, in contrast to stone A1 which had no damage (Fig. 3). The μCT scans (data not shown) indicated no other noticeable damage to the stone. Surface damage of this type is consistent with damage caused by cavitation in the surrounding fluid.

IV. DISCUSSION AND CONCLUSIONS

Our findings show for the first time that with μCT it is possible to detect the initiation of micro-fractures within kidney stones treated by SWL. The resolution of the images was sufficient to reveal intrinsic structural features within the stones, such as concentric lamellae, and to nondestructively monitor the propagation of SW-induced cracks in relation to these landmarks. The long scan time (8 h/image) restricts the use of the technique to *in vitro* systems.

This demonstration involved only two stones. Thus it is premature to make any firm conclusions about the mechanisms that were involved in fragmentation. In this first test we chose to manipulate the environment surrounding the stones in order to alter cavitation. One stone (stone A2) was positioned with its proximal face open to the surrounding water, giving conditions that should be conducive to cavitation. This stone showed damage at its leading surface after only 10 SWs. Such damage *in vitro* seems comparable to the damage that occurs to target foils due to cavitation bubble collapse.[25]

We packed the other stone (stone A1) tightly in water-saturated gauze in order to reduce the potential for cavitation to occur. This may not have eliminated cavitation altogether, but it is likely that gauze would interfere with bubble expansion, therefore, reducing the opportunity for effective bubble collapse.[10] This stone showed essentially no damage at its proximal face, rather it suffered the loss of a large chip from its distal side. This is consistent with failure by spall. The μCT images showed that cracks in this stone required hundreds of SWs to grow consistent with the idea that fatigue contributed to the failure. This stone also exhibited localized regions of high absorption and we speculate that the stone material may have been compacted in these regions, although the mechanism for the compaction is not clear.

In conclusion, we have demonstrated that μCT imaging can reveal the internal structure of kidney stones and can be used to track the propagation of micro-fractures within the stone interior and at the stone surface. This preliminary test suggests that μCT can detect patterns of SW-induced damage that are consistent with mechanisms of stone failure predicted by theory.

ACKNOWLEDGMENTS

The authors thank James Williams, Jr. for his suggestions during the preparation of this manuscript. This study has been partially supported by the National Institutes of Health through P01-DK-43881 (RC and JM) and the Maurice E. Müller Professorship in Bioengineering at Harvard Medical School (RM).

[1] C. Chaussy, W. Brendel, and W. Schmiedt, ''Extracorporeally induced destruction of kidney stones by shock waves,'' Lancet **2**, 1265–1268 (1980).
[2] J. V. Kaude, C. M. Williams, M. R. Millner, K. N. Scott, and B. Finlayson, ''Renal morphology and function immediately after extracorporeal shock-wave lithotripsy,'' Am. J. Roentgenol. **145**, 305–313 (1985).
[3] J. E. Lingeman, J. Woods, P. D. Toth, A. P. Evan, and J. A. McAteer, ''The role of lithotripsy and its side effects,'' J. Urol. (Baltimore) **141**, 793–797 (1989).
[4] A. P. Evan and J. A. McAteer, ''Q-Effects of shock wave lithotripsy,'' in *Kidney Stones: Medical and Surgical Management*, edited by F. Coe, C. Pak, and G. M. Preminger (Raven, New York, 1996), pp. 549–570.
[5] A. P. Evan, L. R. Willis, J. E. Lingeman, and J. A. McAteer, ''Renal trauma and the risk of long-term complications in shock wave lithotripsy,'' Nephron **78**, 1–8 (1998).
[6] A. K. Tuteja, J. P. Pulliam, T. H. Lehman, and L. W. Elzinga, ''Anuric renal failure from massive bilateral renal hematoma following extracorporeal shock wave lithotripsy,'' Urology **50**, 606–608 (1997).
[7] D. A. Lifshitz, J. E. Lingeman, F. S. Zafar, D. H. Hollensbe, A. W. Nyhuis, and A. P. Evan, ''Alterations in predicted growth rates of pediatric kidneys treated with extracorporeal shock wave lithotripsy,'' J. Endourol **12**, 469–475 (1998).
[8] G. Janetschek, F. Frauscher, R. Knapp, G. Hofle, R. Peschel, and G. Bartsch, ''New onset hypertension after extracorporeal shock wave lithotripsy: Age related incidence and prediction by intrarenal resistive index,'' J. Urol. (Baltimore) **158**, 346—351 (1997).
[9] W. Sass, M. Braunlich, H. P. Dreyer, E. Matura, W. Folberth, H. G. Preismeyer, J. Seifert, ''The mechanisms of stone disintegration by shock waves,'' Ultrasound Med. Biol. **17**, 239–243 (1991).
[10] Z. Ding and S. M. Gracewski, ''Response of constrained and unconstrained bubbles to lithotripter shock wave pulses,'' J. Acoust. Soc. Am. **96**, 3636–3644 (1994).
[11] L. A. Crum, ''Cavitation microjets as a contributory mechanism for renal calculi disintegration in ESWL,'' J. Urol. (Baltimore) **140**, 1587–1590 (1988).
[12] M. Delius, W. Brendel, and G. Heine, ''A mechanism of gallstone destruction by extracorporeal shock waves,'' Naturwissenschaften **75**, 200–201 (1988).
[13] W. Eisenmenger, ''The mechanisms of stone fragmentation in ESWL,'' Ultrasound Med. Biol. **27**, 683–693 (2001).
[14] S. M. Gracewski, G. Dahake, Z. Ding, S. J. Burns, and E. C. Everbach, ''Internal stress wave measurements in solids subjected to lithotripter pulses,'' J. Acoust. Soc. Am. **94**, 652–661 (1993).
[15] M. Lokhandwalla and B. Sturtevant, ''Fracture mechanics model of stone comminution in ESWL and implications for tissue damage,'' Phys. Med. Biol. **45**, 1923–1940 (2000).
[16] X. Xi and P. Zhong, ''Dynamic photoelastic study of the transient stress field in solids during shock wave lithotripsy,'' J. Acoust. Soc. Am. **109**, 1226–1239 (2001).
[17] A. J. Coleman and J. E. Saunders, ''A survey of the acoustic output of commercial extracorporeal shock wave lithotripters,'' Ultrasound Med. Biol. **15**, 213–227 (1989).
[18] P. Zhong and G. M. Preminger, ''Mechanisms of differing stone fragility in extracorporeal shock wave lithotripsy,'' J. Endourology **4**, 263–268 (1994).
[19] P. Rüegsegger, B. Koller, and R. Müller, ''A microtomographic system for the nondestructive evaluation of bone architecture,'' Calcif. Tissue Int. **58**, 24–29 (1996).
[20] R. Müller and P. Rüegsegger, ''Micro-tomographic imaging for the nondestructive evaluation of trabecular bone architecture,'' Studies in Health Technology and Informatics **40**, 61–79 (1997).
[21] R. Müller, T. Hildebrand, and P. Rüegsegger, ''Noninvasive bone biopsy: A new method to analyze and display the three-dimensional structure of trabecular bone,'' Phys. Med. Biol. **39**, 145–164 (1994).
[22] R. O. Cleveland, M. R. Bailey, N. Fineberg, B. Hartenbaum, M. Lokhandwalla, J. A. McAteer, and B. Sturtevant, ''Design and characterization of a research electrohydraulic lithotripter patterned after the Dornier HM3,'' Rev. Sci. Instrum. **71**, 2514–2525 (2000).
[23] J. E. Lingeman, ''Extracorporeal shock wave lithotripsy devices: Are we making progress,'' in *New Developments in the Management of Urolithiasis*, edited by J. E. Lingeman and G. M. Preminger (Igaku-Shoin, New York, 1996), pp. 79–96.
[24] R. O. Cleveland, J. A. McAteer, S. P. Andreoli, and L. A. Crum, ''Effect of polypropylene vials on lithotripsy shock waves,'' Ultrasound Med. Biol. **23**, 939–952 (1997).
[25] M. R. Bailey, D. T. Blackstock, R. O. Cleveland, and L. A. Crum, ''Comparison of electrohydraulic lithotripters with rigid and pressure-release ellipsoidal reflectors: II. Cavitation fields,'' J. Acoust. Soc. Am. **106**, 1149–1160 (1999).

Comment on "Ultrasound-induced lung hemorrhage is not caused by inertial cavitation" [J. Acoust. Soc. Am. 108, 1290–1297 (2000)]

Robert E. Apfel[a)]
Yale University, 9 Hillhouse Avenue, New Haven, Connecticut 06520-8286

(Received 21 April 2001; accepted for publication 13 July 2001)

This contribution summarizes the reasons for disagreeing with a conclusion by O'Brien *et al.* [J. Acoust. Soc. Am. **108**, 1290–1297 (2000)] that ultrasound-induced lung hemorrhage is not caused by inertial cavitation. An argument is provided that illustrates how cavitation inception conditions in the lungs of animals are not altered significantly if the hydrostatic pressure is increased by increasing the pressure of air that is being breathed by the animal. © *2001 Acoustical Society of America.* [DOI: 10.1121/1.1401758]

PACS numbers: 43.80.Gx [FD]

The authors of an otherwise excellent paper by O'Brien *et al.*,[1] which reports on comprehensive tests of lung hemorrhage in adult rats exposed to ultrasound, have misinterpreted their own data. They report on the effects of hydrostatic pressure on lung hemorrhage and find that ''No effect of hydrostatic pressure on the probability of hemorrhage was observed.'' It then goes on to conclude that ''If inertial cavitation were responsible for lung hemorrhage, then elevated hydrostatic pressure should have resulted in less rather than more tissue damage at each ultrasonic pressure level.''

The problem stems from a clear understanding of the conditions for the onset of cavitation. An unstable mechanical equilibrium of a bubble is achieved when the following equation holds:

$$P_0 + 2\sigma/R + P_A \sin \omega t = P_g + P_v ,$$

where P_0 is the externally applied static pressure, the second term is the inward stress due to surface tension for a bubble of radius, R, the third term is the time-varying acoustic pressure (which is a tension in the negative part of the acoustical cycle), P_g is the equilibrium gas tension, and P_v is the constant vapor pressure.

When an animal is exposed to an increased ambient pressure due to an increase in the gas pressure that the animal is breathing, two things happen. P_0 increases immediately, and P_g increases more slowly. The very first tissues to equilibrate with the applied increased gas pressure are the lung tissues, and this occurs on a time scale of seconds to minutes. That is, the increase of P_0 is eventually just balanced by the increase in P_g. Thus if one were to measure the acoustic cavitation threshold amplitude P_A for producing cavitation in the lungs before increasing the hydrostatic pressure, and then were to apply gas pressure and repeat that measurement, it would be surprising to see much of a difference in the threshold (as shown in the paper's Fig. 1).

This equilibration effect on thresholds for cavitation is well known for decompression sickness (''the bends''), but in small animals (and especially mice that have a much higher respiration and perfusion rate) the equilibration rate can be very rapid not only for lung tissues but other tissues in proximity to the circulation system.[2]

The authors comment that for increased hydrostatic pressure, the severity of the lesions increased. This too is not unexpected. If the same acoustic threshold pressures produce lesions of about the same size while the animal is under pressure, then it is expected that once the chamber is decompressed and the mice are removed, the bubbles in the hydrostatically compressed group will grow.

The only information given about time scales for compression and decompression are given on p. 1292 of the article. The 6 min allocated for compression is certainly adequate for saturating the lung tissues even for the reduced respiration rates of the anesthetized animals. The 4 min for decompression to atmospheric pressure will be sufficient for much of the gas to diffuse out, especially that which is in immediate contact with the capillary circulation system. Gas trapped in bubbles may take longer to give up their extra gas.

The comments made herein point to a conclusion that is the opposite to that inferred by the title of the paper and its conclusions. By no means, therefore, does the paper prove in any conclusive way that ''Ultrasound-induced lung hemorrhage is not caused by inertial cavitation.'' To the contrary, the results remain consistent with inertial cavitation, if by this term it is meant bubble motion driven primarily by the inertia of the material surrounding the bubble induced by the tension phase of the acoustic cycle.

It should be noted that quite often ''inertial cavitation'' refers to the effects of the collapse of nearly spherical bubbles. In situations where *in vivo* cavitation is possible, it will often be likely that the bubble motions will not be symmetrical. Rather, the inward imploding motion of bubbles near free interfaces will produce asymmetric collapse and high shear velocities in the immediate vicinity of the bubble. Such motions may be responsible for lesions and are properly called inertial cavitation, because it is the growth and collapse of the bubble in relatively few cycles that has produced the high shear effects.

[a)]Electronic mail: robert.apfel@yale.edu

[1] William D. O'Brien, Jr., Leon A. Frizzell, Ronald M. Weigel, and James F. Zachary, ''Ultrasound-induced lung hemorrhage is not caused by inertial cavitation,'' J. Acoust. Soc. Am. **108**, 1290–1297 (2000).

[2] Robert E. Forster, ''Exchange of gas between alveolar air and pulmonary capillary blood,'' Physiol. Rev. **37**, 391–452 (1957), and conversation with the author, a physiologist, Dr. Robert E. Forster (Cell Biology and Physiology Faculty, University of Pennsylvania Health System).

Response to "Comment on 'Ultrasound-induced lung hemorrhage is not caused by inertial cavitation'" [J. Acoust. Soc. Am. 110, 1737 (2001)]

Leon A. Frizzell[a)]
Bioacoustics Research Laboratory, Department of Electrical and Computer Engineering, University of Illinois, 405 North Mathews, Urbana, Illinois 61801

Jeffery M. Kramer
Department of Molecular and Integrative Physiology, University of Illinois, Urbana, Illinois 61801

James F. Zachary
Department of Veterinary Pathobiology, University of Illinois, Urbana, Illinois 61801

William D. O'Brien, Jr.
Department of Electrical and Computer Engineering, University of Illinois, Urbana, Illinois 61801

(Received 21 April 2001; accepted for publication 13 July 2001)

We reply to the preceding letter [R. E. Apfel, J. Acoust. Soc. Am. **110**, 1737 (2001)].
 [DOI: 10.1121/1.1401759]

PACS numbers: 43.80.Gx [FD]

The comments presented in the letter from Robert Apfel[1] raise an important issue. If there is a difference in the behavior of inertial cavitation nuclei in lung versus other tissues such that overpressure does not affect the inertial cavitation threshold in lung, then there would be an impact on the conclusion in our publication.[2] To examine this question, let us first be clear as to what we believe would and would not constitute inertial cavitation nuclei. We do not believe that inertial cavitation nuclei are the relatively large gas bodies in the adult mouse's lung called alveoli (mean alveolar diameter:[3–5] 38–49 μm). The alveolar spaces essentially fill the lung and are separated by thin layers of tissue called alveolar septa, like the air pockets in bubble wrap. Each alveolus is surrounded by other air-filled alveoli connected to each other by Pores of Kohn, and thus would not exhibit the behavior of a bubble surrounded by liquid. Instead, we believe that any existing inertial cavitation nuclei would be much smaller stabilized gas pockets (with diameters likely less than 1 μm) within the blood in the vascular system or possibly in other tissues or liquid layers within the lung.

If cavitation nuclei were to be present in and/or around the lung, and we know of no support for this premise, three anatomic locations could be hypothesized, viz., the monolayer of surfactant within alveoli, the capillary beds within the septa and visceral pleura, and within the tissue layers forming the visceral pleura. Molecular gases found in the surfactant, such as oxygen, carbon dioxide, and nitrogen, do not exist as micron size bubbles but as diffuse gas molecules. In fact, the blood-gas barrier that exists between the alveolar space and the alveolar capillaries is less than 1 μm thick. Physiologically, micron size bubbles in the surfactant and surrounding tissue would impede the very rapid transport of these gases across the surfactant layer, alveolar wall, and red blood cells (all of which occurs in less than 1 s), thereby severely affecting respiration.

We would expect the gas pressures within the alveolar spaces to closely follow the increases in the ambient air pressure within the pressure chamber. We also agree with Dr. Apfel that it is likely that there would be equilibration, in a short period of time, of gas pressure within the tissues immediately surrounding the alveoli and "other tissues in proximity to the circulation system."[1] In fact, given that most gas exchange and equilibration processes take place in the capillary bed of the lung and other tissues throughout the body, we would expect the same equilibration to take place fairly rapidly within other tissues in the body. That is, equilibration in the lung would raise the partial gas pressures in the blood. These partial gas pressures would be relatively unaffected during transport in the large vessels until reaching the capillary beds of other tissues where equilibration again takes place raising the partial gas pressure in the surrounding tissues. Thus the state of blood-born nuclei would be similar in all tissues of the body. Also, it should be noted that very little oxygen or carbon dioxide is dissolved in plasma which is why we have red blood cells for transport of these gases and that nitrogen equilibration takes much longer.

The central question is "what is the influence of the overpressure on inertial cavitation thresholds in the lung if there has been sufficient time for increases in the partial gas pressures in the blood and other tissues of the lung?" Some insight can be gained from first considering an *in vitro* study that showed that overpressure increased the threshold for inertial cavitation.[6] These *in vitro* results also showed that there was no significant cavitation threshold change under overpressure regardless of the time period between when the overpressure was applied and when the ultrasound was applied (between 5 min and 3 h), suggesting that equilibration of partial pressures of dissolved gases in the liquid sample had no effect.[6]

[a)]Author to whom correspondence should be addressed; electronic mail: frizz@uiuc.edu

Clearly overpressure has also had a mitigating effect on the severity of damage in other body tissues *in vivo*.[7–9] Further, these *in vivo* results have been accepted as providing the levels at which cavitation is involved in the resultant bioeffect, hind limb paralysis. If the nuclei in that case are blood-born, and we have no proof that is the case, then the argument could be made that we would expect the same effect on blood-born and tissue-born nuclei in the lung. Of course, if the nuclei are not blood-born in one or the other of these tissues, then the comparison becomes much more complex and we cannot rule out the scenario suggested by Dr. Apfel. However, we believe this scenario is unlikely.

Regarding the increased volume of the lesions for animals exposed under overpressure conditions, we do not agree that this lesion would be a result of the bubbles expanding after decompression. The nature of the lesions is that they start to develop at the lung surface and progress into lung, perhaps associated with increased ultrasound penetration as the alveoli fill with blood. If this suggestion by Dr. Apfel were applicable, then the lung damage would not necessarily be as localized as it is. Rather, it is likely that bleeding into alveolar spaces is caused by small injuries to tissues in the pathway of the ultrasound beam originating at the air-blood barrier immediately beneath the visceral pleura. Because we and others have observed no tissue or cellular damage in lung using light microscopy, it is likely that the lesion initiating the hemorrhage is extremely small and not visible with routine histologic assessment of lung lesions induced by ultrasound. Because the lesions and the volume of hemorrhage have a finite limit, it appears that the punctate lesions heal or close rapidly following initial injury. These punctate lesions would allow hemorrhage from capillaries forming the air-blood barrier into contiguous alveolar spaces. It is unlikely that bubbles are formed within the walls of the septa that have no effect until they expand upon decompression to cause hemorrhage into adjacent alveoli.

Finally, even though it does not directly address the issue raised by Dr. Apfel, we think it is important to point out that other pieces of evidence continue to develop showing that lung hemorrhage is not caused by inertial cavitation.[10,11]

[1] R. E. Apfel, Comment on ''Ultrasound-induced lung hemorrhage is not caused by inertial cavitation,'' J. Acoust. Soc. Am. **110**, 1737 (2001).

[2] W. D. O'Brien, Jr., L. A. Frizzell, R. M. Weigel, and J. F. Zachary, ''Ultrasound-induced lung hemorrhage is not caused by inertial cavitation,'' J. Acoust. Soc. Am. **108**, 1290–1297 (2000).

[3] E. R. Weibel, ''Dimensions of the tracheobronchial tree and alveoli'' in Biological Handbooks: Respiration and Circulation, edited by P. L. Altman and D. S. Dittmer (Federation of American Societies for Experimental Biology, Bethedsa, MD, 1971), Chap. 5.

[4] S. M. Tenney and J. E. Remmers, ''Comparative quantitative morphology of the mammalian Lung: diffusing area,'' Nature (London) **197**, 54–56 (1963).

[5] M. L. Crosfill and J. G. Widdicombe, ''Physical characteristics of the chest and lungs and the work of breathing in different mammalian species,'' J. Physiol. (London) **158**, 1–14 (1961).

[6] C. R. Hill, ''Ultrasound exposure thresholds for changes in cells and tissues,'' J. Acoust. Soc. Am. **52**, 667–672 (1972).

[7] L. A. Frizzell, C. S. Lee, P. D. Aschenbach, M. J. Borrelli, R. S. Morimoto, and F. Dunn, ''Involvement of ultrasonically induced cavitation in the production of hind limb paralysis of the mouse neonate,'' J. Acoust. Soc. Am. **74**, 1062–1065 (1983).

[8] C. S. Lee and L. A. Frizzell, ''Exposure levels for Ultrasonic cavitation in the mouse neonate,'' Ultrasound Med. Biol. **14**, 735–742 (1988).

[9] L. A. Frizzell, E. Chen, and C. Lee, ''Effects of pulsed ultrasound on the mouse neonate: Hind limb paralysis and lung hemorrhage,'' Ultrasound Med. Biol. **20**, 53–63 (1994).

[10] C. H. Raeman, D. Dalecki, S. Z. Child, R. S. Meltzer, and E. L. Carstensen, ''Albunex does not increase the sensitivity of the lung to pulsed ultrasound,'' Echocardiogr. **14**, 553–557 (1997).

[11] E. L. Carstensen, S. Gracewski, and D. Dalecki, ''The search for cavitation *in vivo*,'' Ultrasound Med. Biol. **26**, 1377–1385 (2000).

Reply to Frizzell *et al.*'s comment to our comment

Robert E. Apfel[a)]
Yale University, 9 Hillhouse Avenue, New Haven, Connecticut 06520-8286

(Received 10 June 2001; accepted for publication 13 July 2001)

This is a reply to the preceding letter [Frizzell *et al.*, J. Acoust. Soc. Am. **110**, 1738–1739 (2001)].
 [DOI: 10.1121/1.1401760]

PACS numbers: 43.80.Gx [FD]

I agree with O'Brien *et al.*'s comment to our comment[1] of their paper that in order for there to be inertial cavitation, the nuclei must be smaller than resonant size, and therefore less than 2 μm in diameter, much smaller than the mean alveolar diameter. Yet it seems entirely unreasonable to suggest that *not a single* such small nuclei exist in the immediate vicinity of the alveoli sacs, which are saturated with gas. It only takes a single such site to act as a nuclei. Furthermore, it is well known that once a site undergoes inertial cavitation, it will produce other small bubble fragments that can themselves act as inertial cavitation nucleation sites. Recent studies support the contention that small nuclei do occur in lung tissue.[2]

It is true that gas equilibration will take place fairly rapidly in the circulation system of the animal. In unpublished tests of decompression in mice that I ran with Dr. Karl Schaefer many years ago, the nominal time for saturation of the animals in a decompression chamber was about 20 min. The slowest tissues, of course, are the fatty tissues, which, in our decompression studies, often were the site of hind limb paralysis of the mice. If overpressure is to produce a strengthening of the animal to cavitation, it must compress the existing sites such that the internal gas in the bubbles has time to dissolve into the surrounding tissue. That dissolution time must be shorter than the saturation time, which depends both on perfusion and diffusion. So it may well be that where the perfusion is slower, as in fatty tissues, overpressure may be successful in reducing bubble nuclei size, whereas where the perfusion and diffusion are faster, as in the lung, this does not take place.

Finally, in their paper, O'Brien *et al.* choose to adopt a negative approach in saying that a particular model does *not* explain their experimental results. They give no convincing model of what *is* responsible for the effects they have observed. When such a negative approach is adopted (and is actually emphasized in the title of their paper), it puts a very high standard on the proof of the contention, a standard they do not reach. Saying that it is unlikely that cavitation nuclei of the appropriate size exist in the lung is, once again, another negative statement that is unverified by any direct evidence, and furthermore is contradicted by the work of others. If any such nuclei exist, then the explanation I have given in my comment (which is *not* contradicted in the paper or in the present comments by O'Brien *et al.*) offers a reasonable explanation for much of the data from their careful experiments.

To illustrate why the standard on the proof of a contention is greater, consider two of the references given in their comment to my comment that they say support their argument. In both, a raised hydrostatic pressure leads to raised cavitation thresholds. In the paper by Hill,[3] a polystyrene tube with the sample under consideration is in an aqueous bath. The pressure of the entire environmental chamber is increased by up to 0.75 atmospheres for anywhere between 5 min and 3 h, and in all cases the cavitation threshold goes up, suggesting that nuclei are removed or at least reduced in size. In this situation one must rely on diffusion through the outer bath and then to the tube opening in order for gas to diffuse into the tube. Diffusion is a very slow process, and so it is not surprising that before gas could diffuse into the tube, many of the small gas nuclei could have dissolved entirely into solution. Furthermore, in this situation, given the distance that gas would have to diffuse and given the relatively small pressure increment of 0.75 atmospheres, even 3 h might not be sufficient for total saturation of the gas in the tube.

In a second quoted paper of Frizzell *et al.*,[4] the hind limb paralysis of neonatal mice was observed. Increased hydrostatic pressure reduced this paralysis leading the authors to conclude that cavitation was involved in causing the paralysis (because it could be suppressed by raising the hydrostatic pressure). An important detail of this experiment was that the mice were kept at 10 °C. I have performed tests with liquid breathing mice kept at 18 °C, and in those circumstances the respiration rate and heart rate are enormously reduced. Working at 10 °C permitted Frizzell *et al.* to avoid chemical anesthesia. The neonatal mice were virtually in suspended animation, a conclusion echoed by Dalecki *et al.*[5] In this case it is certain that the perfusion of blood is negligible compared to the present paper where adult mice are held at 30 °C. (Dalecki *et al.* also find that for adult mice, the lesion area in the lung is very much smaller in the case of mice at 37 °C as compared to those for which the blood flow is significant reduced at 10 °C.[6]) Also, the hind limb paralysis in the neonatal mice study is likely caused by bubbles that are not carried by the blood but rather that are situated stably in other tissue, such as fat, putting pressure on the nervous system. This tissue will not saturate with the speed of lung tissue.

These two studies illustrate an essential message: When discussing cavitation mechanisms, the devil is often in the

a)Electronic mail: robert.apfel@yale.edu

details. In some cases hydrostatic pressure will inhibit cavitation and in other it will not. It is very hard to make generalizations. And the generalization about inertial cavitation not being a mechanism in lung hemorrhage in the paper under contention is simply not supported by the data or the arguments given in the paper or in the authors' comments to my comment. In fact, a mechanism of inertial cavitation is consistent with the arguments given in my comment.

[1] R. E. Apfel, "Comment on 'Ultrasound-induced lung hemorrhage is not caused by inertial cavitation' " [J. Acoust. Soc. Am. **108**, 1290–1297 (2000)], J. Acoust. Soc. Am. **110**, 1737 (2001).

[2] See, for example, C. K. Holland, R. A. Roy, R. W. Biddinger, C. J. Dimile, and C. Cawood, "Cavitation mediated rat lung bioeffects from diagnostic ultrasound," J. Acoust. Soc. Am. **109**, 2433(A) (2001).

[3] R. Hill, "Ultrasound exposure threshold changes in cells and tissues," J. Acoust. Soc. Am. **52**, 667–672 (1972).

[4] L. A. Frizzell, S. S. Lee, P. D. Aschenbach, M. J. Borrelli, R. S. Morimoto, and F. Dunn, "Involvement of ultrasonically induced cavitation in the production of hind limb paralysis of the mouse neonate," J. Acoust. Soc. Am. **74**, 1062–1065 (1983).

[5] D. Dalecki, S. Z. Child, C. H. Raeman, C. Cox, and E. L. Carstensen, "Age dependence of ultrasonically induced lung hemorrhage in mice," Ultrasound Med. Biol. **23**, 767–776 (1997), p. 775.

[6] *ibid.*

Comment on Apfel's second comment

Leon A. Frizzell[a)]
Bioacoustics Research Laboratory, Department of Electrical and Computer Engineering, University of Illinois, 405 North Mathews, Urbana, Illinois 61801

Jeffery M. Kramer
Department of Molecular and Integrative Physiology, and Veterinary Pathobiology, University of Illinois, Urbana, Illinois 61801

James F. Zachary
Department of Veterinary Pathobiology, University of Illinois, Urbana, Illinois 61801

William D. O'Brien, Jr.
Department of Electrical and Computer Engineering, University of Illinois, Urbana, Illinois 61801

(Received 9 July 2001; accepted for publication 13 July 2001)

This is a comment to the preceding letter [R. E. Apfel, J. Acoust. Soc. Am. **110**, 1740 (2001)].
 [DOI: 10.1121/1.1401775]

PACS numbers: 43.80.Gx [FD]

We agree that it is incumbent on the authors of an article to prove their case, whether the result is ''negative'' or ''positive.'' It is also true that it is harder to prove a ''negative.'' It is clear that Dr. Apfel and we are going to continue to disagree on whether we met that burden of proof in our article.[1]

Three other points are as follows. (1) Although the authors of a very recent oral presentation[2] showed, using an active cavitation detection system, evidence of echoes characteristic of bubbles when lung hemorrhage occurs at 1-atmosphere hydrostatic pressure, this would not be surprising as the hemorrhage itself will produce mixing of blood and air in the alveoli which could be expected to produce large scattered signals. (2) In the Hill paper,[3] referenced in our first response and again by Dr. Apfel in his second letter, the liquid in the vessel was exposed directly to the air and the vessel was rotated. Under these conditions we would expect that the time for equilibration of gas partial pressures in the liquid after application of overpressure would be short compared to the three hours that Hill applied the overpressure. (3) The neonatal mouse studies using overpressure showed similar effects of overpressure at both 10 °C and 37 °C, as reported by Lee and Frizzell[4] in one of the studies that we cited in our response to Apfel's first letter.

a)Author to whom correspondence should be addressed; electronic mail: frizz@uiuc.edu

[1] W. D. O'Brien, Jr., L. A. Frizzell, R. M. Weigel, and J. F. Zachary, ''Ultrasound-induced lung hemorrhage is not caused by inertial cavitation,'' J. Acoust. Soc. Am. **108**, 1290–1297 (2000).
[2] C. K. Holland, R. A. Roy, R. W. Biddinger, C. J. Disimile, and C. Cawood, ''Cavitation mediated rat lung bioeffects from diagnostic ultrasound,'' J. Acoust. Soc. Am. **109**, 2433(A) (2001).
[3] C. R. Hill, ''Ultrasound exposure thresholds for changes in cells and tissues,'' J. Acoust. Soc. Am. **52**, 667–672 (1972).
[4] C. S. Lee and L. A. Frizzell, ''Exposure levels for ultrasonic cavitation in the mouse neonate,'' Ultrasound Med. Biol. **14**, 735–742 (1988).

Treatment of frequency-dependent admittance boundary conditions in transient acoustic finite/infinite-element models

Benoît Van den Nieuwenhof[a)]
Civil Engineering Department, Université catholique de Louvain, 1 Place du Levant, B1348 Louvain-la-Neuve, Belgium

Jean-Pierre Coyette[b)]
Civil Engineering Department, Université catholique de Louvain, 1 Place du Levant, B1348 Louvain-la-Neuve, Belgium and Free Field Technologies S.A., 16 Place de l'Université, B1348 Louvain-la-Neuve, Belgium

(Received 13 October 2000; revised 19 July 2001; accepted 20 July 2001)

The paper addresses the handling of frequency-dependent, local admittance boundary conditions in acoustic transient finite/infinite-element models. The proposed approach avoids the evaluation of a convolution integral along the related boundary. Based on a similar technique developed in an aeroacoustic/finite difference context, the spatially local boundary condition is rewritten in a discrete form that involves normal accelerations and pressure time derivatives at the current time step and few steps before. The incorporation of such a discrete (in time) boundary condition in a finite/infinite-element context is addressed. The infinite-element scheme selected for that purpose relies on the conjugated Astley–Leis formulation. Implementation aspects cover the handling of frequency-dependent boundary conditions along both finite- and infinite-element edges. Numerical examples (waveguide, single source in a half-space bounded by an impedance plane, diffraction by an acoustically treated screen) are presented in order to demonstrate the efficiency of the proposed approach. [DOI: 10.1121/1.1404436]

PACS numbers: 43.20.El, 43.20.Fn, 43.20.Px, 43.28.Js, 43.50.Gf [ANN]

I. INTRODUCTION

Domain-based methods[1] are more and more widely used for modeling either interior or exterior acoustic problems. In this context, hybrid finite/infinite-element methods[2–8] exhibit interesting features[9] versus boundary element methods,[10] traditionally considered as reference methods in this field. A major advantage of finite/infinite-element methods relies on the fact that they preserve the natural structure of FE programs, have attractive convergence properties, and prove to be efficient at a computational point of view.

Acoustic finite/infinite-element schemes are primarily used for time-harmonic analyses. The discrete problem is reduced to a (complex-valued) algebraic system whose solution gives the complex steady-state nodal pressures. Although this approach formally enables the investigation of broadband excitations (using Fourier and inverse Fourier transforms), it loses some efficiency in this case and suffers from a strong restriction to linear problems. A direct transient scheme is expected to be more competitive in such a generalized context.

A key factor in acoustic simulations is, however, the capability to model accurately damping mechanisms. One such dissipative mechanism is provided by absorbent materials. In the present context, these materials are described by local normal admittance conditions that can be obtained either by tests[11] or numerical studies using appropriate models.[12] The related admittance coefficient usually exhibits some frequency dependence[11] that can easily be accounted for in time-harmonic analysis. The handling of such frequency dependence in a transient model requires more caution. The convolution integral induced by a formal inverse Fourier transform of the admittance condition leads to various penalties (evaluation of inverse Fourier transforms, storage of long-time histories) that could adversely affect the performances of the transient solver. For these reasons, a more suitable[13–15] approach originating from the aeroacoustic community (and originally applied in a finite difference context) is applied in order to recast the admittance boundary condition in a more suitable form. The related condition is incorporated in an hybrid finite/(conjugated) infinite-element model[6,16] in such a way that frequency-dependent admittance boundary conditions can be handled along both finite- and infinite-element edges. Numerical applications are presented in order to demonstrate the efficiency of the proposed approach.

II. PROBLEM STATEMENT

A. Interior problems

The usual linear acoustic approximations lead to the derivation of the scalar wave equation for the acoustic pressure within an acoustic domain Ω (Fig. 1)

$$\nabla^2 p(\mathbf{x},t) - \frac{1}{c^2}\frac{\partial^2 p(\mathbf{x},t)}{\partial t^2} = 0 \quad \text{in } \Omega, \tag{1}$$

where $p(\mathbf{x},t)$ is the transient acoustic pressure at point $\mathbf{x}$ and time t, while c is the speed of sound. This equation is com-

a)Author to whom correspondence should be addressed; electronic mail: vandennieuwenhof@gce.ucl.ac.be
b)Electronic mail: jean-pierre-coyette@fft.be

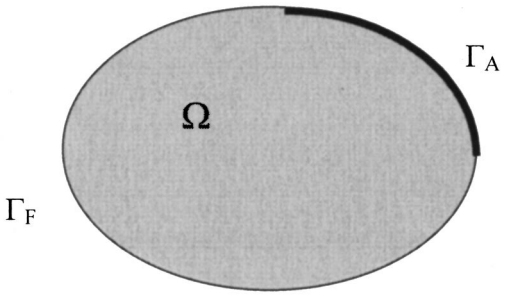

FIG. 1. Interior problem configuration.

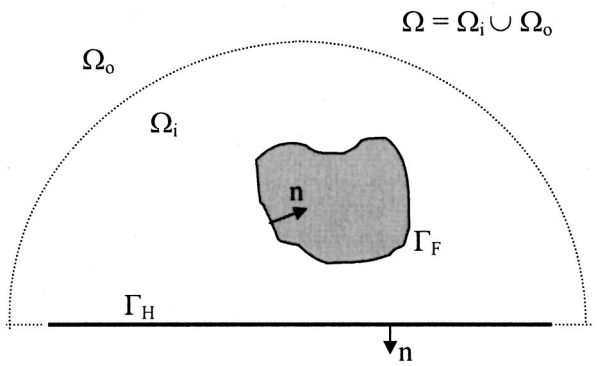

FIG. 2. Acoustic radiation problem in a half-space.

pleted by suitable boundary conditions (that are usually related to normal acceleration or normal admittance constraints) and initial conditions (related to pressure and pressure time derivative at $t=0$). In the sequel, it will be assumed that the boundary surface Γ can be partitioned into two parts, Γ_F and Γ_A. Along Γ_F, a prescribed normal acceleration $\overline{a_n}(\mathbf{x},t)$ is considered while boundary Γ_A supports a frequency-dependent admittance boundary condition. For simplicity, the system is supposed to be initially at rest (zero initial conditions). The boundary conditions can therefore be expressed as

$$\frac{\partial p(\mathbf{x},t)}{\partial n} = -\rho \overline{a_n}(\mathbf{x},t) \quad \text{along } \Gamma_F, \tag{2}$$

$$\frac{\partial p(\mathbf{x},\omega)}{\partial n} = -\frac{i\omega\beta(\omega)p(\mathbf{x},\omega)}{c} \quad \text{along } \Gamma_A, \tag{3}$$

where n is the unit outward normal along $\Gamma=\Gamma_A\cup\Gamma_F$, ρ is the fluid density, and $\beta(\omega)$ is the specific normal admittance ($\beta\equiv A_n\rho c$) along Γ_A. Note that the boundary condition along Γ_A presents a frequency dependence and thus has to be stated in the frequency domain. A direct transformation of this boundary condition to the time domain is obtained using an inverse Fourier transform, and leads to the following convolution integral [assuming that $\beta(t)$, the inverse transform of $\beta(\omega)$, exists]:

$$\frac{\partial p(\mathbf{x},t)}{\partial n} = -\frac{1}{c}\int_{t_0}^{t} \beta(t-\tau)\dot{p}(\mathbf{x},t)\,d\tau. \tag{4}$$

B. Exterior problems

The transient exterior problem can be set up in a similar way. Since a main concern of this paper is the handling of frequency-dependent admittance conditions along semi-infinite edges, a half-space acoustic domain Ω is considered (Fig. 2). The finite boundary surface Γ_F supports a prescribed normal acceleration $\overline{a_n}(\mathbf{x},t)$ while a frequency-dependent admittance boundary condition is considered along the infinite plane Γ_H. The system is supposed to be at rest initially.

The problem is again to solve the wave equation [Eq. (1)] in the unbounded domain Ω with the acceleration boundary condition along Γ_F [Eq. (2)] and the admittance condition along the half-plane, stated in the frequency domain

$$\frac{\partial p(\mathbf{x},\omega)}{\partial n} = -\frac{i\omega\beta(\omega)p(\mathbf{x},\omega)}{c} \quad \text{along } \Gamma_H. \tag{5}$$

These boundary conditions have to be supplemented by the so-called ''Sommerfeld'' radiation condition, hereafter written in a 3D context in order to allow only outgoing waves at infinity

$$r\left(\frac{\partial p(\mathbf{x},t)}{\partial r} + \frac{1}{c}\frac{\partial p(\mathbf{x},t)}{\partial t}\right) \to 0, \quad \text{as } r\to\infty. \tag{6}$$

C. Scattering problems

The above relations for exterior radiation problems can easily be extended to scattering problems. In such a context, the ''total'' acoustic pressure field is decomposed into a known incident field $p_i(\mathbf{x},t)$ [which satisfies the wave equation in free field (i.e., in an unbounded space)] and an unknown scattered field $p_s(\mathbf{x},t)$

$$p(\mathbf{x},t) = p_i(\mathbf{x},t) + p_s(\mathbf{x},t). \tag{7}$$

This scattered pressure field is obtained by solving the wave equation subjected to the radiation condition [Eq. (6)] and the above boundary conditions [Eqs. (2) and (5)] rewritten in terms of p_s using Eq. (7)

$$\frac{\partial p_s(\mathbf{x},\omega)}{\partial n} = -\frac{i\omega\beta(\omega)p_s(\mathbf{x},\omega)}{c} - \frac{i\omega\beta(\omega)p_i(\mathbf{x},\omega)}{c} - \frac{\partial p_i(\mathbf{x},\omega)}{\partial n} \quad \text{along } \Gamma_H, \tag{8}$$

$$\frac{\partial p_s(\mathbf{x},t)}{\partial n} = -\rho\overline{a_n}(\mathbf{x},t) - \frac{\partial p_i(\mathbf{x},t)}{\partial n} \quad \text{along } \Gamma_F. \tag{9}$$

III. TIME-DOMAIN TRANSFORMATION

The treatment of a frequency-dependent boundary condition in a transient context requires to transform Eqs. (3), (5), and (8) from the frequency domain to the time domain. Using Euler's law, Eq. (5) can be written in the usual impedance form

$$p(\omega) = \rho c Z_s(\omega) v_n(\omega), \tag{10}$$

where $Z_s(\omega)=\beta(\omega)^{-1}$ denotes the specific impedance and $v_n(\omega)$ is the fluid normal velocity.

Assuming that $Z_s(\omega)$ has an inverse Fourier transform, the time-domain transform of Eq. (10) leads to the convolution integral

$$p(t)=\int_{t_0}^{t}\rho c Z_s(t-\tau)v_n(\tau)d\tau, \tag{11}$$

the use of which in a transient scheme leads to various penalties (computation of inverse Fourier transforms, storage of long-time histories, recurrent evaluation of integrals).

As shown in Refs. 13–15, the time-domain transformation can be achieved more efficiently using a rational, complex valued, representation of $Z_s(\omega)$

$$Z_s(\omega)=R(\omega)+iI(\omega),$$

$$\text{with } R(\omega)=\frac{a_1+a_3\omega^2+a_5\omega^4+\cdots}{1+a_2\omega^2+a_4\omega^4+\cdots}$$

$$\text{and } I(\omega)=\frac{b_1\omega+b_3\omega^3+b_5\omega^5+\cdots}{1+b_2\omega^2+b_4\omega^4+\cdots}. \tag{12}$$

With such a representation and using a time discretization (with a time step Δt), a discrete transient model equivalent to the continuous frequency model $Z_s(\omega)$ can be written

$$p(m\,\Delta t)=\sum_{i=1}^{K}\alpha_i v_n((m-i+1)\Delta t)+\sum_{i=1}^{L}\beta_i p((m-i)\Delta t). \tag{13}$$

Equation (13) may be seen as a local approximation of the convolution integral from Eq. (11).

Two steps are thus needed before writing this time relation: (a) fitting a rational continuous model to the available specific impedance data, and (b) transformation of Eq. (12) into Eq. (13).

A. Continuous frequency-domain model

Stability requirements related to Eq. (13) are restricting the choice for the rational continuous model of Eq. (12). The following form[14,15] has been used in this work

$$Z_s(\omega)=r_1+\frac{r_2-r_1}{1+i\omega r_3}+\frac{i\omega r_4}{1+i\omega r_5-\dfrac{\omega^2}{r_6^2}}+i\omega r_7. \tag{14}$$

The fitting of Eq. (14) to the specific impedance data reduces to a nonlinear problem. In a least-square sense, the problem can be solved by simultaneous minimization of model errors for real (χ_r) and imaginary (χ_i) parts related to the N sampled data values

$$\chi_r^2=\sum_{j=1}^{N}\frac{(\mathrm{Re}(Z_s(\omega_j))-R_j)^2}{\sigma_j^2}$$

and (15)

$$\chi_i^2=\sum_{j=1}^{N}\frac{(\mathrm{Im}(Z_s(\omega_j))-I_j)^2}{\sigma_j^2},$$

where $Z_j=R_j+iI_j$ is the input value of the specific impedance at frequency ω_j and σ_j^2 is a conventional value of variance of the experimental data. Now, it is obvious that the parameters $r_1,\ldots,r_7$ that minimize one of the two functions are unlikely to be the ones that minimize the second function. A way of bypassing this problem and of finding a less rigorous solution is to find the parameters $r_1,\ldots,r_7$ that minimize, for example, the cumulated error $\chi_r^2+\chi_i^2$. Two methods of minimization[17] have been used (Levenberg–Marquardt algorithm, simplex method), but none of them proved to be really efficient for the particular function to be minimized. In fact, results are strongly dependent on initial guesses of the parameters used in the minimization algorithm. A more efficient way for solving this problem is to use a minimization of the model error related to the modulus and to neglect the phase. A sensitivity analysis of the model also showed that the parameter r_6 is related to the circular frequency corresponding to a maximum impedance value, which should thus be used as an initial guess for r_6.

Practically, we have used the experimental data and parameter values extracted from[14,15] as listed in Table I.

TABLE I. Measured and fitted specific resistance and reactance values for the constant depth ceramic tubular liner (CT 73)—Parameters of the fitted model (Refs. 14, 15).

Frequency (kHz)	$R/\rho c$ (expt.) (−)	$R(\omega)/\rho c$ (fit) (−)	$I/\rho c$ (expt.) (−)	$I(\omega)/\rho c$ (fit) (−)
0.5	0.41	0.406	−1.56	−1.587
1.0	0.46	0.476	0.03	0.113
1.5	1.08	1.078	1.38	1.638
2.0	4.99	5.009	0.25	−0.276
2.5	1.26	1.263	−1.53	−1.237
3.0	0.69	0.673	−0.24	−0.286

Parameters of the fitted model

$r_1=0.346\,888\,140\,876\,44$	$r_5=1.899\,634\,895\,912\,6\times10^{-5}$
$r_2=109.947\,719\,535\,85$	$r_6=12\,379.898\,172\,461$
$r_3=1.662\times10^{-2}$	$r_7=6.694\,928\,001\,321\,7\times10^{-5}$
$r_4=8.994\,618\,670\,346\,4\times10^{-5}$	

B. *z*-Transform and discrete transient representation

In this section, use is made of the z transform to set up the discrete transient representation in Eq. (13) and to get the stability properties of the resulting recurrence.

1. Definition

The z-transform[18,19] $X(z)$ of a discrete-time signal $x(m)$ is defined as the series

$$X(z)=\sum_{m=-\infty}^{+\infty}x(m)\cdot z^{-m}=Z[x(m)]. \tag{16}$$

Its mathematical definition implies that it only converges within a ring of the complex plane.

2. Main properties

The discrete z transform, which is by definition analytic and linear, shares some properties with well-known transformations like the continuous Fourier (or Laplace) transform and the discrete Fourier transform. One particular property that proves to be very useful in the present context is the shifting property: if $X(z)$ is the z transform of the discrete time signal $x(m)$, then the z transform of the signal shifted

of k time steps $[y(m)=x(m-k)]$ is given by $Y(z)=z^{-k}X(z)$. The convergence domains of $X(z)$ and $Y(z)$ are obviously identical.

Another useful property of the z transform in this context is related to the transformation of the time-derivative operator. Since the z transform is only defined on discrete time signals, the time-derivative operator has to be approximated by a finite difference. This can be done using, for example, a backward first-order finite difference approximation

$$\dot{x}(t)\cong\frac{1}{\Delta t}(x(m)-x(m-1)). \tag{17}$$

The shifting property then allows us to write the time-derivative operator in the z domain as $(1-z^{-1})/\Delta t$. This last property leads to a transformation key between the frequency domain and the z domain: $\partial/\partial t$ operator in the time-domain, $i\omega$ operator in the frequency domain, and $(1-z^{-1})/\Delta t$ operator in the z domain. Substitution in the rational continuous model $Z_s(\omega)$ [Eq. (14)] gives a rational function in the z domain

$$Z_s(z)=\frac{\Sigma_{i=1}^{K}\alpha_i\cdot z^{-i+1}}{1-\Sigma_{i=1}^{L}\beta_i\cdot z^{-i}}. \tag{18}$$

Using an inverse z transform and the shifting property, the impedance relation in the z domain $p(z)=\rho c Z_s(z)v_n(z)$ can be written in the time domain in the form provided by Eq. (13). This difference equation relates the pressure $p(m\Delta t)$ to previous pressures $p((m-1)\Delta t),\ldots,p((m-L)\Delta t)$ and current and previous normal velocities $v_n(m\Delta t),\ldots,v_n((m-K+1)\Delta t)$.

It is interesting to note that, in the continuous model $Z_s(\omega)$ of Eq. (14), the real part $R(\omega)$ must necessarily be an even function and the imaginary part $I(\omega)$ an odd function. This can be shown easily using the fact that the coefficients α_i and β_i in Eq. (13) have to be real.

3. Stability and causality

Two conditions have to be examined at this stage: the system represented by Eq. (18) has to be stable (no algorithmic amplification of the system's response, whatever the excitation is) and causal (the system's response should not precede the system's excitation). It can be shown[19] that all the poles of the rational function $Z_s(z)$ have to be strictly confined within a unit circle centered at the origin of the complex plane in order to ensure both causality and stability requirements.

A way of satisfying these two conditions is to choose a *stable* continuous specific impedance model $Z_s(\omega)$ and to use the transformation key $i\omega\leftrightarrow(1-z^{-1})/\Delta t$. The stability condition in the Laplace domain $(s=i\omega)$ requires that all the poles of $Z_s(s)$ are strictly located in the half-left Laplace complex plane. The transformation key $s\leftrightarrow(1-z^{-1})/\Delta t$ projects the half-left Laplace complex plane into a disk of radius $\frac{1}{2}$ centered at the point $(\frac{1}{2},0)$ in the z domain that is located within the convergence region required for $Z_s(z)$. It is clear therefore, that, if one imposes the stability condition on the continuous model $Z_s(\omega)$, the stability of the integration scheme based on Eq. (13) will be ensured independently of the time step selected for the sampling.

Practically, with the frequency-dependence model of Eq. (14), the stability conditions can be written

$$r_3>0 \quad \text{and} \quad \mathrm{Re}\left(\frac{-r_5\pm\sqrt{r_5^2-\frac{4}{r_6^2}}}{2/r_6^2}\right)<0. \tag{19}$$

Note that alternative transformation keys, based on other approximations of derivation/integration operators, are possible. In such a context, the key based on the approximation of the time-derivative operator by a central difference $[i\omega\leftrightarrow(z-z^{-1})/(2\cdot\Delta t)]$ doesn't allow for the use of the above stability verification procedure. The key $i\omega\leftrightarrow(z-z^{-1})/(\Delta t(1+z^{-1}))$ related to the time-integration operator projects the half-left Laplace complex plane into a unit disk centered at the origin of the z domain. This transformation has, however, not been used because it was leading to a rational function $Z_s(z)$ of higher order.

IV. FINITE/INFINITE-ELEMENT MODEL

This section shows how frequency-dependent admittance boundary conditions can be incorporated in a mixed finite/infinite-element model. A conventional pressure formulation is selected for that purpose. The derivation of the final transient model relies on several ingredients. First, a frequency-domain solution scheme is selected based on the conjugated Astley–Leis infinite-element method.[2–5] The weak variational form related to this model is formulated. The boundary integral in this variational form involves the normal pressure gradient or, using Euler's law, the normal particle acceleration which is kept as an unknown field at this stage. Selection of appropriate test and trial functions leads to a set of algebraic equations where matrix coefficients exhibit a simple quadratic dependence versus the frequency. A formal inverse Fourier transform allows us to convert this set of algebraic equations into a set of second-order differential equations. The related right-hand-side vector now involves transient normal accelerations along the boundary surface. If frequency-dependent admittance boundary conditions are considered, the use of Eq. (13) allows us to rewrite these instantaneous normal accelerations in terms of current pressure time derivatives and normal accelerations/pressure time derivatives at a few previous time steps. This substitution allows for the incorporation of frequency-dependent admittance boundary conditions in the discrete model.

A. Frequency-domain model

The weak variational form for either interior or exterior acoustic problems can be easily expressed using the divergence theorem and appropriate functional settings. The solution of the original problem can therefore be rewritten as: Find $p\in H_w^1(\Omega)$ such that

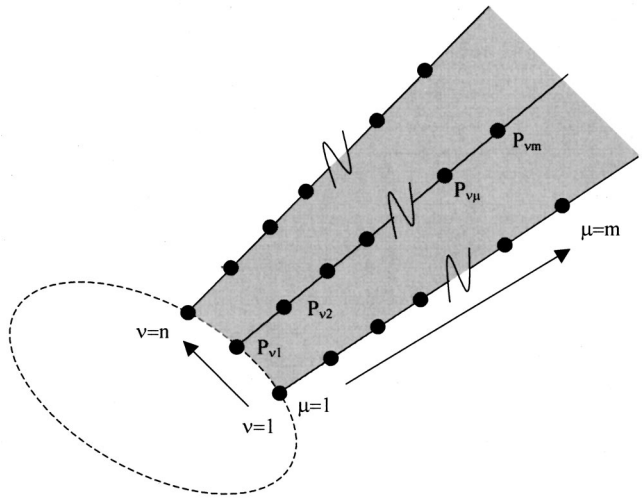

FIG. 3. Numbering of pressure dofs within an infinite element.

$$\int_\Omega \nabla p(\mathbf{x},k)\cdot\nabla\overline{q}(\mathbf{x},k)d\Omega-\omega^2\int_\Omega\frac{p(\mathbf{x},k)\overline{q}(\mathbf{x},k)}{c^2}d\Omega$$

$$=\int_\Gamma\frac{\partial p(\mathbf{x},k)}{\partial n}\overline{q}(\mathbf{x},k)d\Gamma,\quad \forall q\in H^1_{w*}(\Omega), \tag{20}$$

where $H^1_w(\Omega)$ and $H^1_{w*}(\Omega)$ denote appropriate weighted Sobolev spaces that allow for a direct incorporation of the Sommerfeld radiation condition (see Refs. 7 and 8 for more details).

The discrete finite/infinite-element model relies on the selection of appropriate test and trial functions. Within finite elements, conventional (Serendipity or Lagrange) interpolation functions are selected

$$p(\mathbf{x},\omega)=\sum_j N_j^{\mathrm{FE}}(\xi,\eta,\zeta)P_j(\omega), \tag{21}$$

where $N_j^{\mathrm{FE}}(\xi,\eta,\zeta)$ are polynomial functions in parent coordinates while $P_j(\omega)$ are nodal pressures. Infinite elements refer to particular interpolation functions closely related to a truncated multipole expansion[20]

$$p(\mathbf{x},\omega)=\sum_j N_j^{\mathrm{IE}}(\xi,\eta,r;\omega)P_j(\omega), \tag{22}$$

where interpolation functions $N_j^{\mathrm{IE}}(\xi,\eta,r;\omega)$ are obtained by a suitable combination of polynomial functions $N_\nu^a(\xi,\eta)$ along angular directions (ξ,η) and polynomial functions $N_\mu^r(r)$ in $1/r$ along the radial direction

$$N_j^{\mathrm{IE}}(\xi,\eta,r;\omega)=N_\nu^a(\xi,\eta)N_\mu^r(r)e^{-ik(r-r_\mu)}. \tag{23}$$

Here, r is the radial coordinate and r_μ is the radial distance between a node and the finite/infinite-element interface. The numbering of pressure degrees of freedom within an infinite element (Fig. 3) is given by $j=(\nu-1)m+\mu$, $\mu=1,2,3,...,m$, $\nu=1,2,3,...,n$.

Test functions reduce to trial functions for finite elements

$$Q_j^{\mathrm{FE}}(\xi,\eta,\zeta)=N_j^{\mathrm{FE}}(\xi,\eta,\zeta), \tag{24}$$

while a scale factor $(1/r^2)$ is applied to infinite-element test functions

$$Q_j^{\mathrm{IE}}(\xi,\eta,r;\omega)=\frac{N_j^{\mathrm{IE}}(\xi,\eta,r;\omega)}{r^2}. \tag{25}$$

The discrete model (in the frequency domain) reduces to the following set of algebraic equations:

$$(\mathbf{A}_0+i\omega\mathbf{A}_1-\omega^2\mathbf{A}_2)\mathbf{P}(\omega)=\mathbf{B}(\omega). \tag{26}$$

The explicit form of matrices $\mathbf{A}_0$, $\mathbf{A}_1$, and $\mathbf{A}_2$ can be found in Ref. 16.

An appropriate expression for vector component B_j results from substitution of Euler's law $(\partial p(\mathbf{x},\omega)/\partial n=-\rho a_n(\mathbf{x},\omega))$ and the test function Q_j into the boundary integral

$$B_j(\omega)=-\int_\Gamma\rho a_n(\mathbf{x},\omega)\overline{Q}_j(\mathbf{x},\omega)d\Gamma, \tag{27}$$

which takes the following two forms along finite and infinite boundaries:

Finite boundary:

$$B_j(\omega)=-\int_\Gamma\rho a_n(\mathbf{x},\omega)N_j^{\mathrm{FE}}(\xi,\eta,\zeta)d\Gamma, \tag{28}$$

Infinite boundary:

$$B_j(\omega)=-\int_\Gamma\rho a_n(\mathbf{x},\omega)N_\nu^a(\xi,\eta)N_\mu^r(r)e^{+ik(r-r_\mu)}(1/r^2)d\Gamma. \tag{29}$$

B. Time-domain model

A transient model can be easily obtained by a formal application of the inverse Fourier transform to Eq. (26). The resulting system of second-order differential equations can be written as

$$\mathbf{A}_0\mathbf{P}(t)+\mathbf{A}_1\dot{\mathbf{P}}(t)+\mathbf{A}_2\ddot{\mathbf{P}}(t)=\mathbf{B}(t), \tag{30}$$

where $\mathbf{B}(t)$ is the inverse Fourier transform of $\mathbf{B}(\omega)$ [as given by Eqs. (28) and (29) along finite and infinite boundaries, respectively]

$$F^{-1}\left\{-\int_\Gamma\rho a_n(\mathbf{x},\omega)N_j^{\mathrm{FE}}(\xi,\eta,\zeta)d\Gamma\right\}$$

$$=-\int_\Gamma\rho a_n(\mathbf{x},t)N_j^{\mathrm{FE}}(\xi,\eta,\zeta)d\Gamma, \tag{31}$$

$$F^{-1}\left\{-\int_\Gamma\rho a_n(\mathbf{x},\omega)\overline{N}_j^{\mathrm{IE}}(\xi,\eta,\zeta)(1/r^2)d\Gamma\right\}$$

$$=-\int_\Gamma\rho a_n\left(\mathbf{x},t+\frac{r-r_\mu}{c}\right)N_\nu^a(\xi,\eta)N_\mu^r(r)(1/r^2)d\Gamma. \tag{32}$$

If the boundary Γ supports a prescribed frequency-dependent boundary condition, the time derivative of Eq. (13) can be injected into Eqs. (31) and (32) so that the right-hand-side vector can be rewritten as

$$\mathbf{B}(t)=C\dot{\mathbf{P}}(t)+\mathbf{D}(t), \tag{33}$$

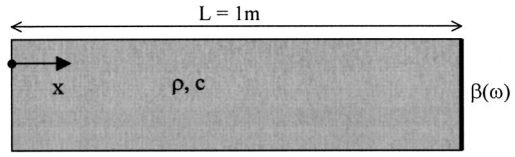

FIG. 4. Waveguide with frequency-dependent admittance at one end.

where the vector D includes contributions related to previous time steps.

As it appears in Eq. (32), the phase factor $e^{+ik(r-r_\mu)}$ induces a time shift for sampled normal accelerations along infinite boundaries. In the same way,[5] the nodal degrees of freedom P_j along infinite elements are related to nodal pressures at retarded times $t+[(r_j-r_\mu)/c]$.

A direct time integration procedure is selected in order to solve Eq. (30). An implicit Newmark scheme has been used here. At each intermediate step, current accelerations along admittance boundaries are evaluated using the approximate (discrete) boundary condition. Pressure time derivatives (as involved in this expression) are also computed at each time step. In this way, all discrete contributions related to the handling of frequency-dependent boundary conditions can be generated efficiently.

V. NUMERICAL SIMULATIONS

The proposed approach has been validated through comparisons with available steady-state reference solutions that can be easily produced using a frequency-domain approach (numerical[21] or analytical) and the inverse Fourier transform. The frequency-dependence model presented above (see Table I for parameter values) is used in all examples below.

Three examples are considered hereafter. The first example is concerned with the study of the transient pressure field in a waveguide. A finite-element model is used for that purpose. The second example (source radiating above an impedance plane) and the third example (source radiating near a spherical-shaped screen) involve axisymmetric finite/infinite-element models.

A. Pressure field in a waveguide

This first example involves a waveguide of length a (=1 m) (Fig. 4) with a prescribed pressure at one end ($x=0$) and a frequency-dependent admittance boundary condition at the other end ($x=a$). The tube is filled with air (usual properties $\rho=1.225\,\mathrm{kg\,m^{-3}}$ and $c=340\,\mathrm{m\,s^{-1}}$ are assumed). The prescribed pressure at $x=0$ is given by the following tonal description:

$$\overline{p}(x=0,t)=\sum_{m=1}^{6} m\omega_0 \sin(m\omega_0 t) \quad [10^{-9}\mathrm{Pa}], \tag{34}$$

with $\omega_0=2\pi\ 500\,\mathrm{rad\,s^{-1}}$. Zero initial conditions are selected. Three finite-element meshes M_1, M_2, and M_3 have been used (element sizes are equal to $a/200$, $a/400$, and $a/800$, respectively). Three different time steps have also been investigated: $5\cdot10^{-5}$ s, 10^{-5} s, and $5\cdot10^{-6}$ s.

Figure 5 shows the acoustic pressure at the mid-distance ($x=a/2$). It can be observed that a steady-state response is obtained after $\approx$12 periods and that the transient solution is

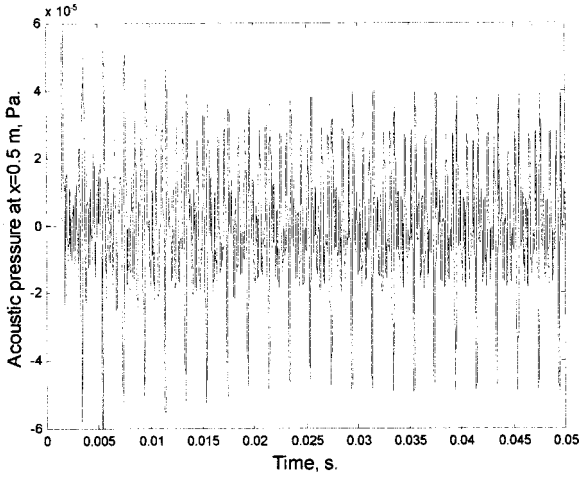

FIG. 5. Acoustic pressure at the mid-waveguide: transient numerical solution.

stable. The reference solution for this problem can easily be found from an analytical treatment in the frequency domain. The transfer function for the pressure is given by

$$H(x,\omega)\equiv\frac{p(x,\omega)}{p(0,\omega)}=\frac{e^{-ikx}}{1+A_1A_2}+\frac{e^{+ikx}}{1+(A_1A_2)^{-1}}, \tag{35}$$

with

$$A_1=\frac{1/\rho c-A(\omega)}{1/\rho c+A(\omega)}, \quad A_2=e^{-2ika}. \tag{36}$$

Figure 6 shows the comparison of the transient solution with the reference solution for the three selected time steps (using mesh M_2). A stable solution is obtained in each case and the transient solution is shown to converge to the steady-state response as the time step is refined. Figure 7 compares transient solutions obtained with meshes M_1, M_2, and M_3 (using a time step$=10^{-5}$ s). The spatial convergence is effectively ensured. The steady-state pressure field is represented in Fig. 8 for the following admittance values: (a) frequency-dependent admittance; (b) constant admittance value $A=2.5/\rho c$, and (c) constant admittance value $A=0.2/\rho c$. The

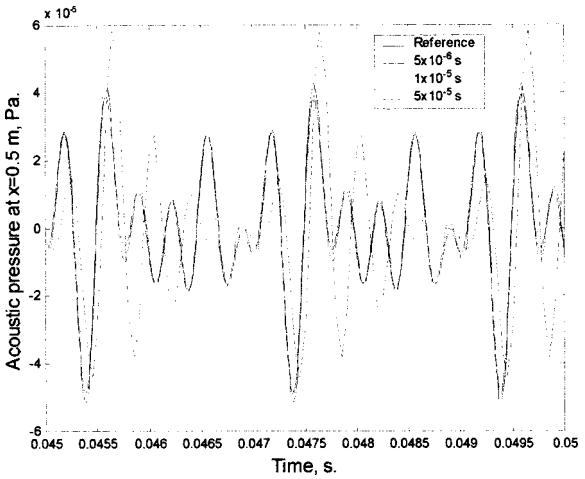

FIG. 6. Acoustic pressure at the mid-waveguide: comparison of the numerical simulations to the reference steady-state solution as a function of the time step.

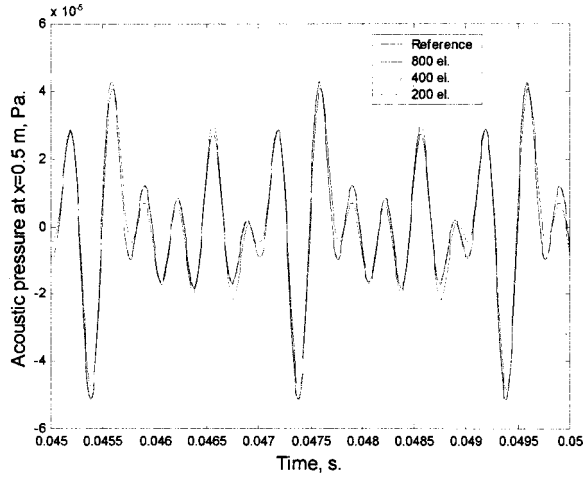

FIG. 7. Acoustic pressure at the mid-waveguide: comparison of the numerical simulations to the reference steady-state solution as a function of the resolution of the mesh.

last two values are upper and lower bounds of the actual frequency-dependent admittance coefficient. Figure 8 clearly demonstrates the need to handle the frequency-dependent admittance in order to get an accurate transient solution.

B. Source radiating above an impedance plane

This example involves a spherical source located at a distance a (=0.5 m) above an impedance plane [Fig. 9(a)]. The impedance along the boundary plane is assumed to be frequency dependent as before. An axisymmetric model has been used. The finite-element mesh of radial extension $2a$ contains 354 nodes and 637 TRIA03 elements. The average resolution of the mesh is about $a/10$. Infinite elements of radial interpolation order equal to 7 are added to the finite-element mesh in order to provide a reflection-free boundary [Fig. 9 (b)]. The source amplitude is given by the following tonal description:

$$S(t)=\sum_{m=1,1.2,\ldots,1.8,2}^{6} m\omega_0 \sin(m\omega_0 t) \quad [10^{-9}\ \text{Pa}], \qquad (37)$$

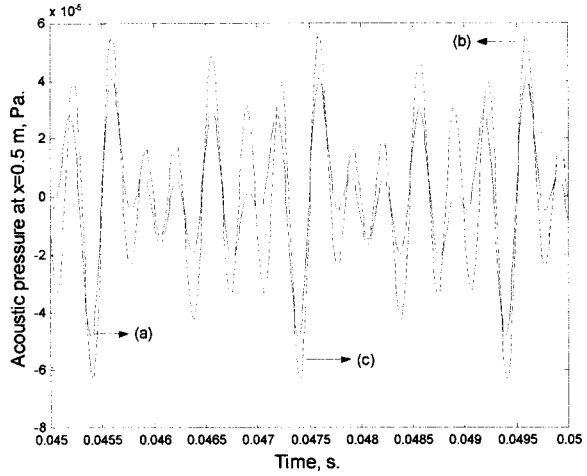

FIG. 8. Acoustic pressure at the mid-waveguide: comparison of the reference solutions for different values of $\beta(\omega)$.

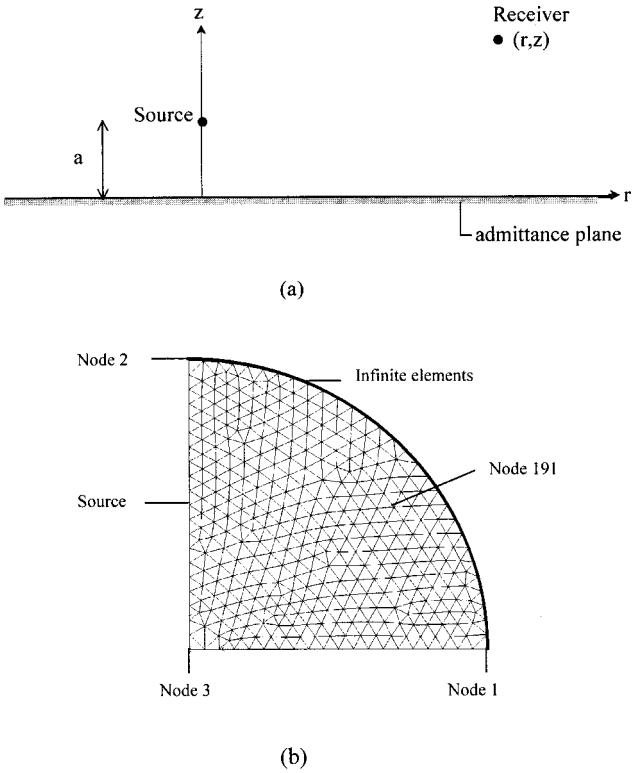

FIG. 9. Source radiating above an impedance plane: (a) spherical source and receiver positions; (b) finite-element mesh.

with $\omega_0=2\pi\ 500\,\text{rad}\,\text{s}^{-1}$. Initial rest conditions are supposed. Three time steps for the transient analysis have been investigated: 10^{-4} s, $5\cdot10^{-5}$ s, and 10^{-5} s.

The transient acoustic pressure at node 1 quickly converges to the steady-state solution (Fig. 10). Again, the integration scheme proves to be stable for each case studied.

A reference solution based on a frequency-domain formulation is presented in Refs. 16 and 22. Comparison of transient and steady-state reference solutions for the acoustic pressure at nodes 1 and 191 are presented in Figs. 11 and 12 for the three time steps selected. As expected, the best accuracy is obtained with the smallest time step but, even for the largest time step, numerical stability is ensured.

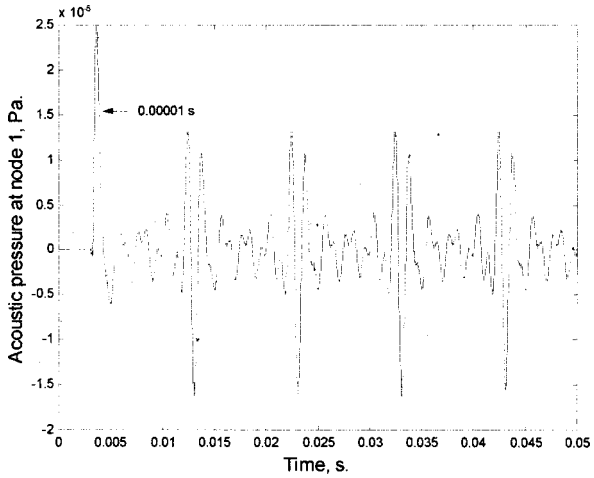

FIG. 10. Acoustic pressure at node 1: transient numerical solution.

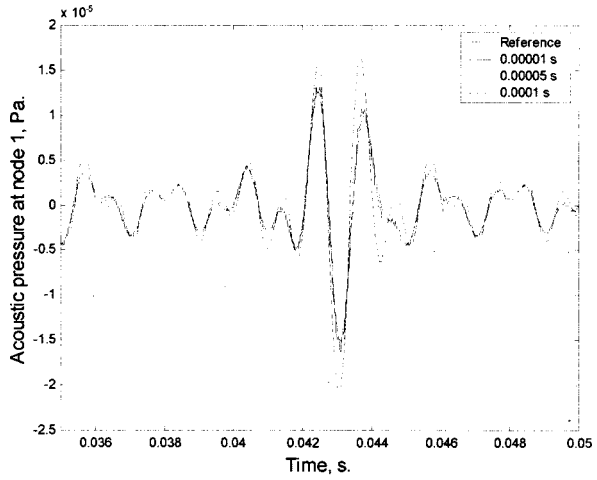

FIG. 11. Acoustic pressure at node 1: comparison of the numerical simulations to the reference steady-state solution as a function of the time step.

C. Source radiating near a screen

In this last example [Fig. 13(a)], the efficiency of the method is demonstrated for another 2D axisymmetric configuration involving a point source radiating near a spherical screen. The screen appears as a spherical cap (radius $a=0.5\,\mathrm{m}$, thickness $t=a/25$). A frequency-dependent admittance condition is considered along inner and outer screen faces. Figure 13(b) shows the finite-element mesh which has been used. This mesh contains 4606 nodes and 8913 TRIA03 elements. Infinite elements of radial interpolation order equal to 7 are again added to the finite-element mesh in order to handle the Sommerfeld radiation condition. The source amplitude is given by Eq. (37). Zero initial conditions are assumed. Three time steps for the transient analysis have been investigated: $5\cdot10^{-5}\,\mathrm{s}$, $10^{-5}\,\mathrm{s}$, and $5\cdot10^{-6}\,\mathrm{s}$.

For this example, the reference (steady-state) solution has been obtained by performing frequency-domain calculations with the same mesh. Figure 14 compares the three transient solutions with this numerically produced reference solution. Again, a good agreement can be observed.

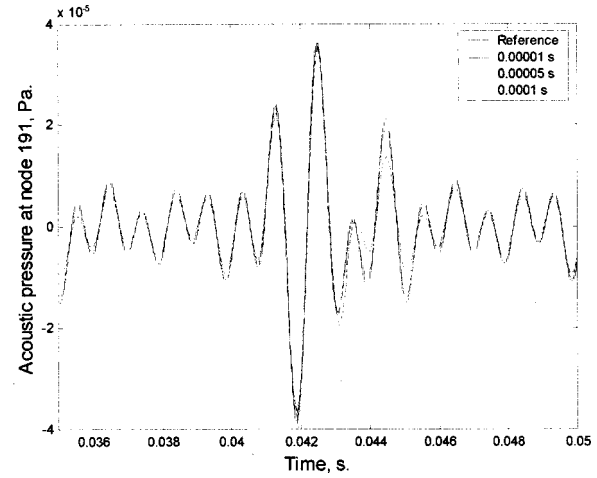

FIG. 12. Acoustic pressure at node 191: comparison of the numerical simulations to the reference steady-state solution as a function of the time step.

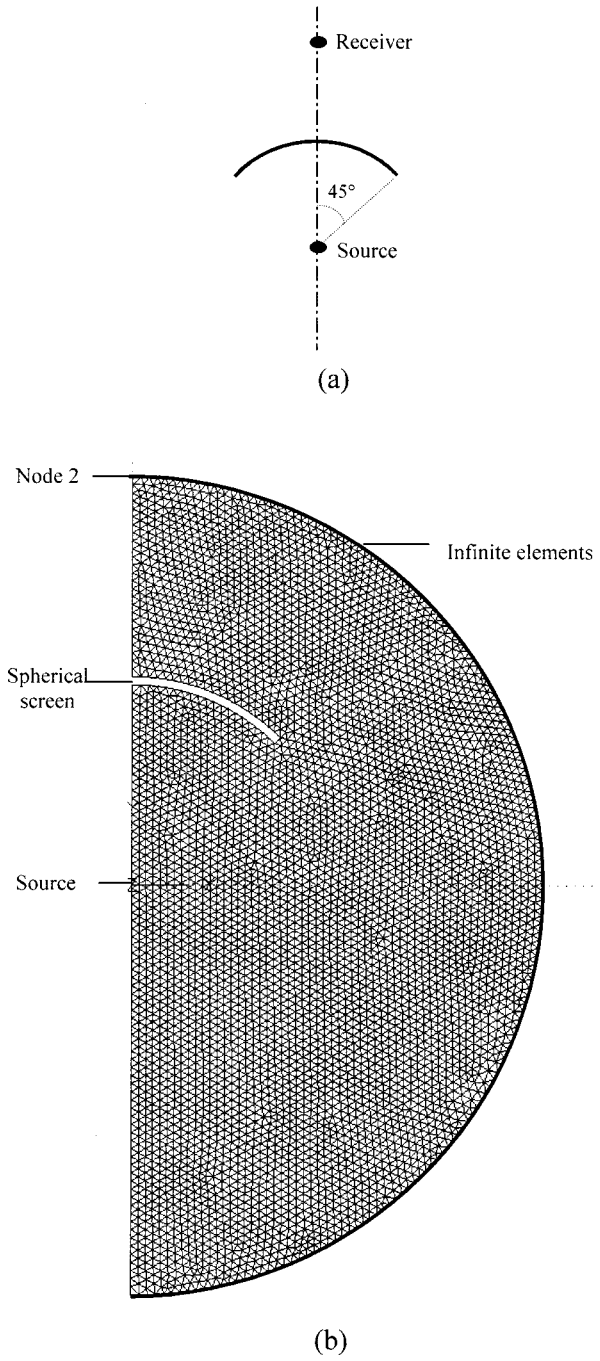

FIG. 13. Diffraction of sound by a screen: (a) spherical source and receiver positions; (b) finite-element mesh.

VI. CONCLUSIONS

Transient solution schemes are known to offer attractive computational performances and have the capability to handle broadband excitations. The introduction of frequency-dependent damping mechanisms in transient models give rise to some difficulties. The handling of frequency-dependent admittance boundary conditions in a transient finite/conjugated infinite-element scheme has been addressed. Instead of using a formal inverse Fourier transform of the frequency-domain boundary condition, which leads to a computationally expensive convolution integral, a discrete representation more local in time is selected. It relies on a

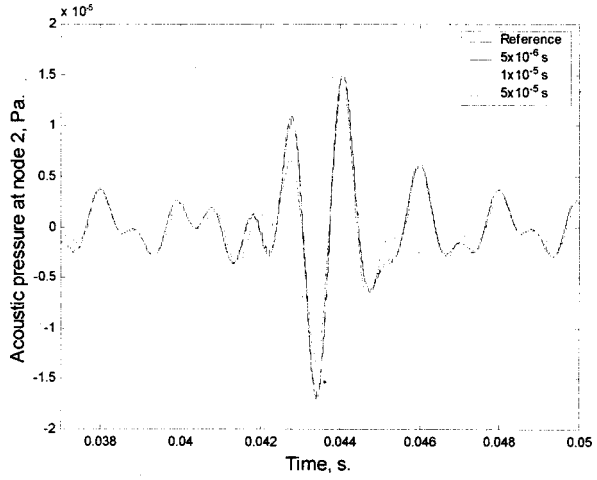

FIG. 14. Acoustic pressure at node 2: comparison of the numerical simulations to the steady-state solution as a function of the time step.

rational approximation of the frequency-dependent admittance. Stability and causality requirements related to this representation have been studied using the *z* transform properties. In the particular finite/infinite-element context, the approximate boundary condition involves current local (normal) acceleration and pressure time derivative and similar quantities evaluated at a few previous time steps. Numerical results involving interior and exterior problems show the efficiency of the method.

ACKNOWLEDGMENTS

The support of this work by the Belgian National Fund for Scientific Research (F.N.R.S.) is gratefully acknowledged.

[1] D. Givoli, *Numerical Methods for Problems in Infinite Domains* (Elsevier, New York, 1992).
[2] R. J. Astley, J. P. Coyette, and G. J. Macaulay, ''Mapped wave envelope elements for acoustical radiation and scattering,'' J. Sound Vib. **170**, 97–118 (1994).
[3] L. Cremers, K. R. Fyfe, and J. P. Coyette, ''A variable order infinite acoustic wave envelope element,'' J. Sound Vib. **171**, 483–508 (1994).
[4] R. J. Astley, J. P. Coyette, and L. Cremers, ''Three-dimensional wave-envelope elements of variable order for acoustic radiation and scattering. I. Formulation in the frequency domain,'' J. Acoust. Soc. Am. **103**, 49–63 (1998).
[5] R. J. Astley, J. P. Coyette, and L. Cremers, ''Three-dimensional wave-envelope elements of variable order for acoustic radiation and scattering. II. Formulation in the time domain,'' J. Acoust. Soc. Am. **103**, 64–72 (1998).
[6] R. J. Astley, ''Infinite elements for acoustics,'' Proceedings of the Sixth International Congress on Sound and Vibration, 5–8 July, 1999, Copenhagen, (1999), pp. 523–538.
[7] K. Gerdes, ''A summary of infinite element formulations for exterior Helmholtz problems,'' Comput. Methods Appl. Mech. Eng. **164**, 95–105 (1998).
[8] K. Gerdes, ''The conjugated vs the unconjugated infinite element method for the Helmholtz equation in exterior domain,'' Comput. Methods Appl. Mech. Eng. **152**, 125–145 (1998).
[9] J. J. Shiron and I. Babuska, ''A comparison of approximate boundary conditions and infinite element methods for exterior Helmholtz problems,'' Comput. Methods Appl. Mech. Eng. **164**, 121–139 (1998).
[10] I. Harari and T. J. R. Hughes, ''A cost comparison of boundary element and finite element methods for problems of time-harmonic acoustics,'' Comput. Methods Appl. Mech. Eng. **97**, 77–102 (1992).
[11] M. E. Delany and E. N. Bazley, ''Acoustical properties of fibrous absorbent materials,'' Appl. Acoust. **3**, 105–116 (1970).
[12] K. Attenborough, ''Acoustical properties of rigid fibrous absorbents and granular materials,'' J. Acoust. Soc. Am. **73**, 785–799 (1983).
[13] Y. Özyörük and L. N. Long, ''A time-domain implementation of surface acoustic impedance condition with and without flow,'' 2nd AIAA/CEAS Aeroacoustics Conference (1996).
[14] Y. Özyörük and L. N. Long, ''Impedance boundary conditions for time-domain computational aeroacoustics methods,'' 35th Aerospace Sciences Meeting & Exhibit (1997).
[15] Y. Özyörük, L. N. Long, and M. G. Jones, ''Time-domain simulation of a flow-impedance tube,'' J. Comput. Phys. **146**, 29–57 (1998).
[16] J.-P. Coyette and B. Van den Nieuwenhof, ''A conjugated infinite element method for half-space acoustic problems,'' J. Acoust. Soc. Am. **108**, 1464–1473 (2000).
[17] W. H. Press, B. P. Flannery, S. A. Teukolsky, and W. T., Vetterling, *Numerical Recipes—The Art of Scientific Computing* (Cambridge University Press, Cambridge, England, 1986).
[18] E. I. Jury, *Theory and Application of the z-transform Method* (Wiley, New York, 1964).
[19] A. V. Oppenheim and R. W. Schaffer, *Discrete-time Signal Processing* (Prentice-Hall, 1989).
[20] D. S. Burnett, ''A three-dimensional acoustic infinite element based on a prolate spheroidal multipole expansion,'' J. Acoust. Soc. Am. **96**, 2798–2816 (1994).
[21] J. P. Coyette, J. L. Migeot, G. Lielens, and T. Leclercq, ACTRAN *User's Manual* (Free Field Technologies S.A., Louvain-la-Neuve, 2000).
[22] S. I. Thomasson, ''Reflection of waves from a point source by an impedance boundary,'' J. Acoust. Soc. Am. **59**, 780–785 (1976).

Scattering of Lamb waves by a circular cylinder

Xiao-Min Wang[a] and C. F. Ying
Institute of Acoustics, Academia Sinica, P.O. Box 2712, Beijing 100080, People's Republic of China

(Received 15 January 2001; revised 1 June 2001; accepted 28 June 2001)

Following our previous attempt at the scattering from a cylinder in a slab to the incidence of a guided shear wave, we hereby discuss the scattering by an elastic cylinder embedded in an isotropic plate for a variety of bonding states to incidence of the fundamental Lamb wave modes S_0 and A_0 at the low-frequency regime. The plate is divided up into three regions by introducing two imaginary planes located symmetrically some distance from the cylinder and perpendicular to surfaces of the plate. The wave fields in various regions are expanded either into cylinder wave modes or into Lamb wave modes. A system of equations determining the coefficients of expansion is obtained according to the traction-free boundary conditions on the plate walls and the displacement and stress continuity conditions across the virtual planes. By taking an appropriate finite number of terms of the infinite expansion series and some selected points on the two properly chosen imaginary planes and the surfaces of the plate through convergence and precision tests, a matrix equation to numerically evaluate the expansion coefficients is found. Coefficients of the reflection and transmission versus the normalized radius of the cylinder in welded, slip, and cracked interfacial conditions are numerically computed. In the low-frequency range, the relative errors are found to be less than 1%. Contrast curves of the reflection coefficient for the cylinder of nearly all permissible size in perfect and imperfect interfacial bonding are shown and prominent differences are noted. [DOI: 10.1121/1.1396330]

PACS numbers: 43.20.Fn [DEC]

I. INTRODUCTION

Much work has been done on the study of wave scattering from cylindrical objects embedded in an infinite elastic medium since the 1950s.[1–10] The increasing prominence of fibrous composite materials has excited a new interest in these acoustic studies.[11–18] In general, the fiber-reinforced materials are composed of a matrix and cylindrical fibers. The mechanical performance of the fibrous composites is determined by the quality of the interface bonding of the fibers with the matrix. Ultrasonic scattering from such interfaces carries important information about the bonding state of the fibers, thus having potential application for fiber-matrix interface characterization.

Guided waves that travel along a rod, tube or plate could be much more efficient than the traditional technique of point-by-point examination in defects detection and material evaluation. With the help of mode and frequency selection, one may improve inspection sensitivity to various discontinuities.

Therefore, the scattering of guided waves has been vigorously studied. Tan and Auld have analyzed the scattering of Lamb waves from a crack normal to the surface of the plate using a variational method.[19] Rokhlin has studied the diffraction of Lamb waves by a finite crack parallel to the plate surfaces by the modified Winer–Hopf method.[20] Scattering of a fundamental symmetric Lamb wave from an internal crack and a surface crack has been investigated by Koshiba *et al.* using a combination of the finite-element and the analytical method.[21]

Not long ago, Cho *et al.* employed the boundary element method to analyze the Lamb wave interaction with various defects having different sharpness and depth.[22] The reflection and transmission coefficients were numerically calculated to evaluate mode sensitivity and extract physical information for defect characterization. Experimental results of measurement of transmission factor for a particular incident mode had been presented to verify the theoretical predictions.

Recently, Pavlacovic *et al.* have used the propagation and reflection properties of the guided waves in a solid rod embedded in an infinitely thick layer to detect defects in the grouted steel tendons and evaluate their condition.[23] For the purpose of guided wave mode selection, numerical modeling work has been undertaken to get the phase velocity and attenuation dispersion curves for the axisymmetric modes of a steel bar surrounded by infinite medium of grout. The behavior of the guided wave modes has been validated experimentally.

In Ref. 18, we considered the scattering from an infinite elastic cylinder in a two-dimensional traction-free slab to the incidence of a guided SH wave. An approach termed mode matching technique used by Nilsen[24] and Lakhtakia *et al.*[25,26] to the scattering of electromagnetic and elastic waves was applied in that article for the scattering of a SH wave for several conditions of physical contacts between the cylinder and the slab.

Extending our previous work, we use the mode matching technique to examine the scattering by an infinite elastic cylinder in a two-dimensional isotropic plate for a variety of interfacial conditions to a Lamb wave mode incidence, of which we are unaware of any attempt before. An analytic solution is obtained and is approximately plotted. This search turns out to be more complicated than that of the guided SH

[a]Electronic mail: lab8@sina.com

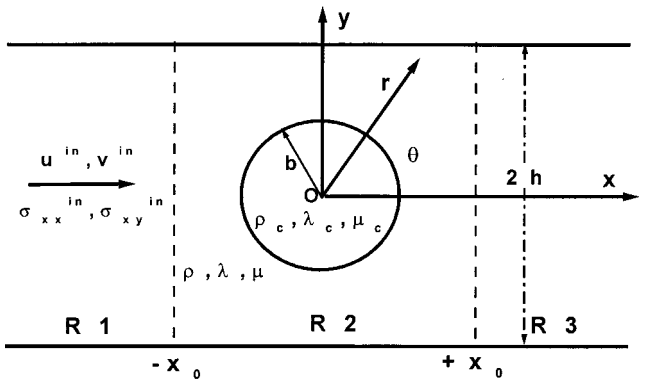

FIG. 1. Incidence of Lamb wave on an elastic cylinder in a plate.

wave incidence, and therefore only two special cases of incidence of the fundamental Lamb modes S_0 and A_0 are examined in the low-frequency regime.

The theory developed here is based, as in Ref. 18, on the method of expanding the field into a sum of wave modes and on the method of mode matching. Ideally, exact results may be obtained for any cylinder of diameter no larger than the plate thickness if an infinite number of terms in the field expansion are retained. In practice, however, for numerical computation, truncation of the field expansion is needed. The cutoff errors from the finite term approximation will inevitably affect the precision of the numerical results. We accordingly adopt a convergence criterion for the choice of the number of retained terms as well as formulated an expression to estimate the precision of the numerical results so obtained.

II. THEORY

The plate considered is assumed to be two-dimensional, of uniform thickness $2h$ with traction-free surfaces, and of density ρ and Lame constants λ and μ. A Cartesian coordinate system is shown in Fig. 1, the origin of which is in the middle plane of the plate. An elastic circular cylinder of radius b is centered in the plate with its axis coinciding with the z axis of the coordinate system. The material of the cylinder is taken to be of density ρ_c and Lame constants λ_c and μ_c.

The waves are assumed to be time harmonic, but the complex time factor $e^{-j\omega t}$ (where ω is the angular frequency, t is the time, and $j=\sqrt{-1}$) will be omitted in all the following expressions. Let a single Lamb mode of order m traveling in the direction of positive x-axis impinge on the interface of the cylinder. For clearness, the incident Lamb wave mode will be assumed to be symmetric. Antisymmetric Lamb mode incidence can be similarly formulated.

An incident Lamb wave of mode m can be expressed as[27,28] (see Appendix A)

$$u^{in}=A_m\overline{U}_m(y)\exp(jk_mx), \tag{1a}$$

$$v^{in}=A_m\overline{V}_m(y)\exp(jk_mx), \tag{1b}$$

$$\sigma_{xx}^{in}=A_m\overline{S}_m(y)\exp(jk_mx), \tag{1c}$$

$$\sigma_{xy}^{in}=A_m\overline{T}_m(y)\exp(jk_mx), \tag{1d}$$

where A_m is the amplitude of the given incident wave, k_m is the wave number of the incident mode, and $\overline{U}_m$, $\overline{V}_m$, $\overline{S}_m$ and $\overline{T}_m$ are the normalized modal functions of the incident Lamb mode. By virtue of the problem's symmetry, for a symmetric Lamb mode incidence the antisymmetric Lamb waves are not exited.

On dividing the plate up into three regions R1, R2 and R3 by two imaginary planes at $x=\pm x_0$ $(x_0>b)$, the respective fields in the two half infinite outer regions R1 and R3 can be expanded into the sum of all propagating and nonpropagating Lamb wave modes[27,28]

$$u^I=u^{in}+\sum_{n=0}^{\infty}B_n\overline{U}_n(y)\exp(-jk_nx), \quad (x,y)\in \mathrm{R1}, \tag{2a}$$

$$v^I=v^{in}+\sum_{n=0}^{\infty}B_n\overline{V}_n(y)\exp(-jk_nx), \quad (x,y)\in \mathrm{R1}, \tag{2b}$$

$$\sigma_{xx}^I=\sigma_{xx}^{in}+\sum_{n=0}^{\infty}B_n\overline{S}_n(y)\exp(-jk_nx), \quad (x,y)\in \mathrm{R1}, \tag{2c}$$

$$\sigma_{xy}^I=\sigma_{xy}^{in}+\sum_{n=0}^{\infty}B_n\overline{T}_n(y)\exp(-jk_nx), \quad (x,y)\in \mathrm{R1}, \tag{2d}$$

$$u^{III}=\sum_{n=0}^{\infty}C_n\overline{U}_n(y)\exp(jk_nx), \quad (x,y)\in \mathrm{R3}, \tag{3a}$$

$$v^{III}=\sum_{n=0}^{\infty}C_n\overline{V}_n(y)\exp(jk_nx), \quad (x,y)\in \mathrm{R3}, \tag{3b}$$

$$\sigma_{xx}^{III}=\sum_{n=0}^{\infty}C_n\overline{S}_n(y)\exp(jk_nx), \quad (x,y)\in \mathrm{R3}, \tag{3c}$$

$$\sigma_{xy}^{III}=\sum_{n=0}^{\infty}C_n\overline{T}_n(y)\exp(jk_nx), \quad (x,y)\in \mathrm{R3}, \tag{3d}$$

where B_n and C_n are the amplitudes of the reflected and transmitted waves, respectively. The fields in the finite central region R2 outside the cylinder can be expanded into the sum of cylindrical wave modes[4] (see Appendix B):

$$u^{II}(x,y)=\sum_{l=0}^{\infty}D_lU_l^D(r,\theta)+\sum_{l=1}^{\infty}E_lU_l^E(r,\theta), \quad r>b, \quad (x,y)\in \mathrm{R2}, \tag{4a}$$

$$v^{II}(x,y)=\sum_{l=0}^{\infty}D_lV_l^D(r,\theta)+\sum_{l=1}^{\infty}E_lV_l^E(r,\theta), \quad r>b, \quad (x,y)\in \mathrm{R2}, \tag{4b}$$

$$\sigma_{xx}^{II}(x,y)=\sum_{l=0}^{\infty}D_lS_l^D(r,\theta)+\sum_{l=1}^{\infty}E_lS_l^E(r,\theta), \quad r>b, \quad (x,y)\in \mathrm{R2} \tag{4c}$$

$$\sigma_{xy}^{II}(x,y)=\sum_{l=0}^{\infty} D_l T_l^D(r,\theta)+\sum_{l=1}^{\infty} E_l T_l^E(r,\theta),$$

$$r>b,\quad (x,y)\in \mathrm{R2}, \tag{4d}$$

$$\sigma_{yy}^{II}(x,y)=\sum_{l=0}^{\infty} D_l \Gamma_l^D(r,\theta)+\sum_{l=1}^{\infty} E_l \Gamma_l^E(r,\theta),$$

$$r>b,\quad (x,y)s\in \mathrm{R2}, \tag{4e}$$

where D_l and E_l are complex expansion coefficients, and U_l^D, U_l^E, V_l^D, V_l^E, S_l^D, S_l^E, T_l^D, T_l^E, Γ_l^D and Γ_l^E are functions pertinent with the displacement and stress components of the cylinder wave modes containing the Bessel and Neumann functions of the lth order and the trigonometric functions. In the arguments (r,θ) of these functions, r is the distance from the cylinder axis to the field point, and θ is the polar angle. Interfacial contact conditions for the welded, the slip or the completely cracked state between the cylinder and the matrix are considered in terms of the spring model[15] discussed in Appendix B.

From the equations (2)–(4), it is found that the fields in all three regions R1, R3, and R2 outside the cylinder are expressed in terms of the unknown complex expansion constants B_n, C_n, D_l and E_l. These unknown coefficients can be evaluated by using the continuity conditions of the displacement and stress on the virtual planes and the traction-free boundary conditions on the top and bottom of the plate. These boundary conditions are given by

$$u^{III}=u^{II}(x,y),\quad v^{III}=v^{II}(x,y),\quad \sigma_{xx}^{III}=\sigma_{xx}^{II}(x,y),$$
$$\sigma_{xy}^{III}=\sigma_{xy}^{II}(x,y),\quad x=+x_0, \tag{5a}$$

$$\sigma_{xy}^{II}(x,y)=0,\quad \sigma_{yy}^{II}(x,y)=0,\quad y=\pm h, \tag{5b}$$

$$u^{I}=u^{II}(x,y),\quad v^{I}=v^{II}(x,y),\quad \sigma_{xx}^{I}=\sigma_{xx}^{II}(x,y),$$
$$\sigma_{xy}^{I}=\sigma_{xy}^{II}(x,y),\quad x=-x_0. \tag{5c}$$

Since the fields are all symmetrical about the xOz plane, only half of the plate corresponding to, say, $y>0$, has to be taken into account. Equation (5b) then will be evaluated only for $y=+h$. The set of linear equations determining B_n, C_n, D_l and E_l can now be shown to be, corresponding respectively to Eqs. (5a), (5b), and (5c),

$$\sum_{n=0}^{\infty} C_n \overline{U}_n(y_a)\exp(jk_n x_0)-\sum_{l=0}^{\infty} D_l U_l^D(r_a,\theta_a)$$
$$-\sum_{l=1}^{\infty} E_l U_l^E(r_a,\theta_a)=0, \tag{6a}$$

$$\sum_{n=0}^{\infty} C_n \overline{V}_n(y_a)\exp(jk_n x_0)-\sum_{l=0}^{\infty} D_l V_l^D(r_a,\theta_a)$$
$$-\sum_{l=1}^{\infty} E_l V_l^E(r_a,\theta_a)=0, \tag{6b}$$

$$\sum_{n=0}^{\infty} C_n \overline{S}_n(y_a)\exp(jk_n x_0)-\sum_{l=0}^{\infty} D_l S_l^D(r_a,\theta_a)$$
$$-\sum_{l=1}^{\infty} E_l S_l^E(r_a,\theta_a)=0, \tag{6c}$$

$$\sum_{n=0}^{\infty} C_n \overline{T}_n(y_a)\exp(jk_n x_0)-\sum_{l=0}^{\infty} D_l T_l^D(r_a,\theta_a)$$
$$-\sum_{l=1}^{\infty} E_l T_l^E(r_a,\theta_a)=0, \tag{6d}$$

$$y_a=x_0\tan\theta_a,\quad r_a=\frac{x_0}{\cos\theta_a},\quad 0<\theta_a\leqslant\tan^{-1}\left(\frac{h}{x_0}\right),$$

$$\sum_{l=0}^{\infty} D_l T_l^D(r_b,\theta_b)+\sum_{l=1}^{\infty} E_l T_l^E(r_b,\theta_b)=0, \tag{7a}$$

$$\sum_{l=0}^{\infty} D_l \Gamma_l^D(r_b,\theta_b)+\sum_{l=1}^{\infty} E_l \Gamma_l^E(r_b,\theta_b)=0, \tag{7b}$$

$$r_b=\frac{h}{\sin\theta_b},\quad \tan^{-1}\left(\frac{h}{x_0}\right)\leqslant\theta_b\leqslant\pi-\tan^{-1}\left(\frac{h}{x_0}\right),$$

$$\sum_{n=0}^{\infty} B_n \overline{U}_n(y_c)\exp(jk_n x_0)-\sum_{l=0}^{\infty} D_l U_l^D(r_c,\theta_c)$$
$$-\sum_{l=1}^{\infty} E_l U_l^E(r_c,\theta_c)=-A_m \overline{U}_m(y_c)\exp(-jk_m x_0), \tag{8a}$$

$$\sum_{n=0}^{\infty} B_n \overline{V}_n(y_c)\exp(jk_n x_0)-\sum_{l=0}^{\infty} D_l V_l^D(r_c,\theta_c)$$
$$-\sum_{l=1}^{\infty} E_l V_l^E(r_c,\theta_c)=-A_m \overline{V}_m(y_c)\exp(-jk_m x_0), \tag{8b}$$

$$\sum_{n=0}^{\infty} B_n \overline{S}_n(y_c)\exp(jk_n x_0)-\sum_{l=0}^{\infty} D_l S_l^D(r_c,\theta_c)$$
$$-\sum_{l=1}^{\infty} E_l S_l^E(r_c,\theta_c)=-A_m \overline{S}_m(y_c)\exp(-jk_m x_0), \tag{8c}$$

$$\sum_{n=0}^{\infty} B_n \overline{T}_n(y_c)\exp(jk_n x_0)-\sum_{l=0}^{\infty} D_l T_l^D(r_c,\theta_c)$$
$$-\sum_{l=1}^{\infty} E_l T_l^E(r_c,\theta_c)=-A_m \overline{T}_m(y_c)\exp(-jk_m x_0), \tag{8d}$$

$$y_c=-x_0\tan\theta_c,\quad r_c=\frac{-x_0}{\cos\theta_c},\quad \pi-\tan^{-1}\left(\frac{h}{x_0}\right)<\theta_c\leqslant\pi.$$

The unknown complex expansion constants B_n, C_n, D_l and E_l depend on the known amplitude A_m of the incident mode as is evident from the combined equations (6a)–(6d), (7a)–(7b) and (8a)–(8d). Therefore, we have now apparently solved our problem by finding out the wave functions in all regions of the plate: R1, R2 and R3. From the expansion coefficients B_n and C_n, two field quantities of practical in-

terest may be defined and emphasized because they are more easily measurable. They are

$$R_{mn} = \text{reflection coefficient of the } n\text{th scattered mode for the } m\text{th incident mode} = B_n/A_m, \quad (34)$$

$$T_{mn} = \text{transmission coefficient of the same} = C_n/A_m, \quad (35)$$

both holding in the region $|x| \geqslant x_0$. These two field quantities will later be numerically illustrated.

III. APPROXIMATE EVALUATION OF THE EXPANSION COEFFICIENTS

The expansion coefficients B_n, C_n, D_l and E_l are determined by Eqs. (6a)–(6d), (7a)–(7b), and (8a)–(8d). Their practical evaluation is yet difficult because the Lamb wave modes and the cylinder wave modes are infinite in number, that is, n, $l \in [0,+\infty)$. For the infinite expansion series, one may truncate them somewhere such that $n \in [0,N]$, $l \in [0,L]$, N and L being some finite positive integers. In addition, the locations of the virtual planes at $x = \pm x_0$ in Fig. 1 need to be settled. Then, a system of linear equations to obtain the expansion coefficients of the truncated series has to be formed in someway with proper parameters N, L and x_0. The question is, how to choose values of N, L and x_0 such that relatively small errors in the evaluation of the expansion coefficients will be assured.

It turns out, however, that before the demand on precision, a demand on convergence has to be satisfied first in choosing N, L and x_0. During our numerical computation we find that certain choices of these three crucial parameters will induce divergence and hence evidently should be avoided. The details of how to choose N, L and x_0, the way to form the system of linear equations, were given in Ref. 18.

One of the possible schemes to make the optimized selection of these three parameters N, L and x_0 is first to set a reasonable initial value for $x_0 > b$ approximately and then to search for the appropriate values of N and L such that all the boundary conditions implied in Eqs. (6a)–(6d), (7a)–(7b), and (8a)–(8d) be satisfied in a certain precision. Once the values of N and L are found, the initial choice of x_0 has to be modified so as to improve the precision of the results in the case of the precision being unsatisfactory, especially when the diameter of the cylinder is close to the thickness of the plate. On account of the finite thickness of the plate and the symmetry of the geometrical configuration, a reasonable initial value for x_0 is approximately equal of the half thickness of the plate.

It should be noted that the placement of the matching plane $x = \pm x_0$ in mode matching techniques is always difficult. There is no restriction on the specific choice that x_0 has to be equal to the half thickness of the plate. One should choose an appropriate matching surface or zone according to a specific problem. For instance, Lakhtakia *et al.* select the tangent plane of the periodically spaced cylinders to be the matching plane to study the reflection characteristics of an elastic slab containing a periodic array of cylinders.[25,26] On the contrary, Lakhtakia *et al.* choose the overlapping zones of subregions as the matching zones where the continuity of the internal magnetic field is enforced when they calculate the power absorption in biological models exposed to incident electromagnetic plane waves.[29]

To determine a suitable value of N in the plate wave mode expansion, all the propagating modes and an appropriate number of nonpropagating modes have to be included.[27] Thus, $N = N_p + N_E$, where N_p is the number of the propagating modes and N_E represents a finite number of the nonpropagating modes. The nonpropagating modes always exist in pairs since the squared k_n of the complex Lamb wave number appears in the dispersion equation.[27] So, appropriate pairs of the nonpropagating modes are to be taken into account in the selection of N_E.

To determine the suitable number of L in the cylinder wave mode expansion, it is necessary to work out a small auxiliary program so as to examine the variations of the cylindrical functions with increase of order l for different argument values. In this way, the appropriate number of $l = L$ can be found through the convergence test with the selected values of N, L and x_0. This procedure has the characteristics of trial and error.

For chosen values of N, L and x_0, there are to be determined $2(N+L+1)$ unknown coefficients B_n, C_n, D_l and E_l, $n \in [0,N]$, $l \in [0,L]$. A system of linear equations needed to obtain these unknown coefficients may be formed by the inner-product method or the point-mate method. On account of the fact that the Bessel and Neuman functions involved in cylinder wave mode expansion are highly oscillatory functions, we prefer the point-mate technique. Based on the fact that any arbitrary point on the top surface of the plate has to satisfy Eqs. (7a) and (7b), any arbitrary point on the upper half part of the right virtual plane has to satisfy Eqs. (6a)–(6d), and any arbitrary point on the upper half part of the left virtual plane has to satisfy Eqs. (8a)–(8d), a set of equations, $2(N+L+1)$ in number, needed for solving the problem can be found from Eqs. (6a)–(6d), (7a)–(7b) and (8a)–(8d) by taking the advantage of the arbitrariness of θ_a, θ_b, and θ_c. For example, if one takes a single point on each partition, ten equations can be selected from Eqs. (6a)–(6d), (7a)–(7b) and (8a)–(8d) by giving θ_a, θ_b, and θ_c a specific value, respectively; if two points are taken on each partition, 20 equations can be selected, and so on. For the problem at hand, the number of the points needed on each partition is $\mathrm{Mp} = 2(N+L+1)/10$. On letting the chosen geometric points spread with equal angular spacing on each respective partition, the corresponding values of θ_a, θ_b, and θ_c can subsequently be calculated. Substituting these values of N, L, Mp, x_0, θ_a, θ_b, and θ_c, as well as the values of the material parameters, the dimensionless quantity $k_T h$ and the ratio b/h, into Eqs. (6a)–(6d), (7a)–(7b) and (8a)–(8d), a matrix equation necessary to solve the problem can be constructed.

The method to select a few specific points, Mp in number, on each involved boundaries when x_0/h, N, L, and hence Mp are known, can be found in Ref. 18. The selected points are dispersed in the whole range of each partition. Their coordinates (r_a, θ_a), (r_b, θ_b) and (r_c, θ_c) in the polar coordinate system can easily be obtained from trigonometry. One may choose these points in a different way as long as

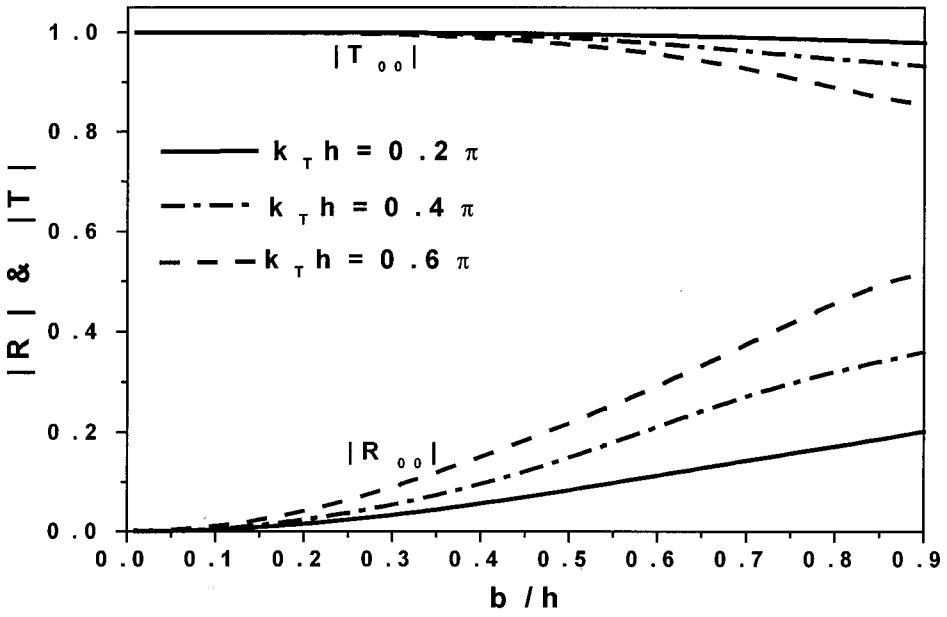

FIG. 2. Reflection and transmission coefficients versus normalized cylinder radius b/h for $k_T h = 0.2\pi$, 0.4π and 0.6π (S_0 mode incidence).

the relative errors calculated by Eq. (11) in the final results are satisfactory.

Finally, to check the accuracy of the numerical technique, the principle of conservation of energy is used. This states that

$$P^{\text{in}} = \sum_{n=0}^{N_p} (P_n^r + P_n^t), \tag{9}$$

where P^{in} is the energy flux transported by the incident mode through the imaginary planes, P_n^r and P_n^t represent the energy fluxes transported by the reflected and transmitted nth mode through the imaginary planes, and N_p, as before, is the number of propagating modes. Now, the error involved in the numerical calculation can be estimated by the deviation from Eq. (9). Thus[28] the relative error of the reflected and transmitted energies from the input energy flux P^{in} is

$$\varepsilon = 1 - \frac{\Sigma_{n=0}^{N_p}(P_n^r + P_n^t)}{P^{\text{in}}}. \tag{10}$$

Because the wave structure of each mode has been normalized by the factor $\sqrt{Q_n}$ related closely to the energy flux[27] (see Appendix A), the relative error can finally be expressed as[28]

$$\varepsilon = 1 - \sum_{n=0}^{N_P} (|R_{mn}|^2 + |T_{mn}|^2), \tag{11}$$

whose absolute value in percentage is used to evaluate the consistency of the numerically computed results.

IV. NUMERICAL IMPLEMENTATION

In this section, some numerical results are presented showing the coefficients of reflection and transmission against the ratio of the radius b/h of the cylinder to the half thickness of the plate for given value of $k_T h$. The relative errors are estimated for each case.

The material constants used for numerical calculations are chosen to be $c_P = 5.6$ km/s, $c_T = 3.5$ km/s, $\rho = 2.4$ g/cm^3 for the plate, and $c_L = 7.8$ km/s, $c_s = 4.5$ km/s, $\rho_c = 3.2$ g/cm^3 for the cylinder. The cylinder is hard compared to its matrix, so waves propagate faster in the cylinder. The welded, the slip and the completely cracked interface boundary conditions are considered. We set the half thickness of the plate to $h = 1.0$ mm, and let the radius b of the cylinder vary from 0.01 to less than 0.9 mm. The incoming Lamb wave is the fundamental symmetric or antisymmetric single propagating mode of order $m = 0$ with unit amplitude in the low-frequency domain.

A. S_0 mode incidence

Figure 2 shows the numerically calculated reflection and transmission coefficients $|R_{00}|$ and $|T_{00}|$ versus the normalized radius b/h for the incidence of S_0 mode at the values of $k_T h = 0.2\pi$, 0.4π and 0.6π, in the welded boundary conditions, where $k_T = \omega\sqrt{\rho/\mu}$. All the Lamb wave modes higher than S_0 are nonpropagating ones. In these cases of low frequency, the results are satisfactory since the relative errors ε estimated by Eq. (11) are found to be less than 1% even for b/h as large as 0.9. The number of the Lamb modes N and that of the cylinder wave modes L used in the numerical evaluations are 7 and 8, respectively, the number of the geometric points Mp on each partition of the plate are 3 and the location of the virtual planes are selected at $x_0 = \pm h$.

From Fig. 2 it may be seen that when the normalized radius b/h is very small or the nondimensional frequency value $k_T h$ is very low, little energy of the incident mode is scattered such that $|T_{00}| \approx 1$ and $|R_{00}| \approx 0$, as expected. As the diameter of the cylinder or the frequency of the incident wave increases, $|T_{00}|$ descends and $|R_{00}|$ ascends due to the reflection from the scattering of cylinder to the incident mode.

Figures 3 and 4 show the R's and T's when $k_T h$ takes the values of 0.8π and 1.0π, respectively. At these frequencies, the cylinder generates stronger reflections such that $|T_{00}|$ decreases, while $|R_{00}|$ and the new propagating modes

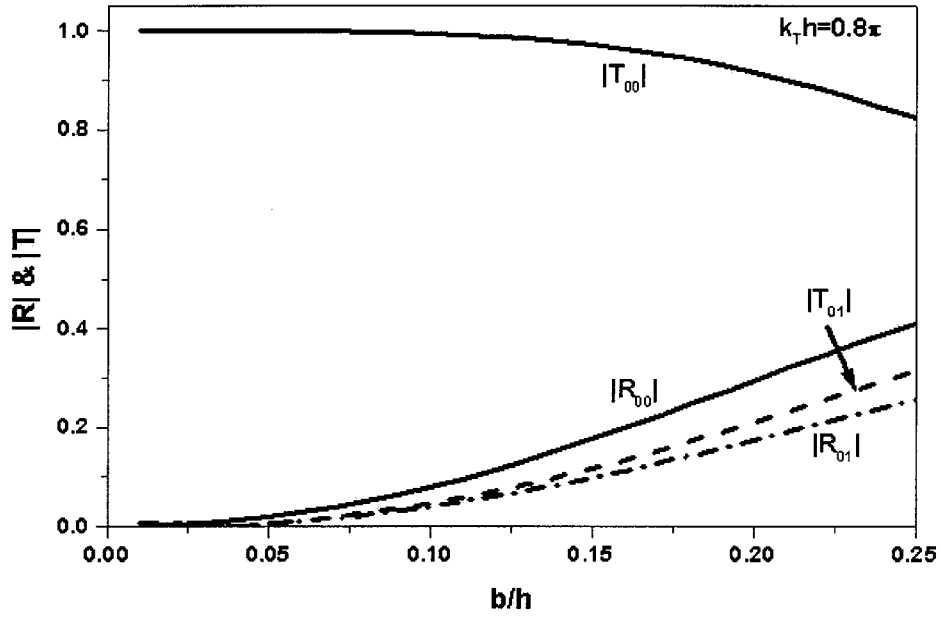

FIG. 3. Reflection and transmission coefficients versus normalized cylinder radius b/h for $k_T h = 0.8\pi$ (S_0 mode incidence).

$|R_{01}|$ and $|T_{01}|$ creep up rapidly, $|R_{01}|$ and $|T_{01}|$ being respectively the reflection and transmission coefficients of mode S_1 for the S_0 mode incidence. The cut-off frequency of the S_1 mode is $k_T h = 0.77\pi$ for the studied solid plate. Thus, this S_1 mode becomes propagating when $k_T h > 0.77\pi$ and mode conversion from S_0 to S_1 occurs due to the scattering of the cylindrical post to the incident S_0 mode.

Yet, the numerical results given in Figs. 3 and 4 only have those parts for which the principle of conservation of energy has been satisfied to within 1% error, for we find that the relative errors ascend drastically when the normalized radius $b/h > \frac{1}{4}$ for $k_T h = 0.8\pi$ and $b/h > \frac{1}{3}$ for $k_T h = 1.0\pi$. This therefore restricts the applicability of the present approach to only the low-frequency regime unless the cylinder radius is very small relative to the plate thickness. It may be mentioned that in the numerical calculations for $k_T h = 0.8\pi$ and 1.0π in Figs. 3 and 4, two propagating modes plus two pairs of nonpropagating modes of the Lamb wave and 12 cylindrical wave modes are taken into account while the positions of the two imaginary planes are chosen to be at $x_0 = \pm 1.4h$.

Contrasts among the reflection coefficients versus the normalized radius of the cylinder at the frequency $k_T h = 0.5\pi$ are given in Fig. 5 for the welded, the slip and the cracked bonding states between the cylinder and the matrix. The relative errors ε for all these results are found to be less than 1%. In Fig. 5, it is seen that the reflection coefficient $|R_{00}|$ in the perfect bonding condition varies smoothly with b/h, in consistence with Fig. 2. However, the reflection coefficients in the imperfect bonding condition (slip and cracked) have rather different appearances. Remarkable differences in the reflection coefficients can also be found between the slip and the cracked bonding states.

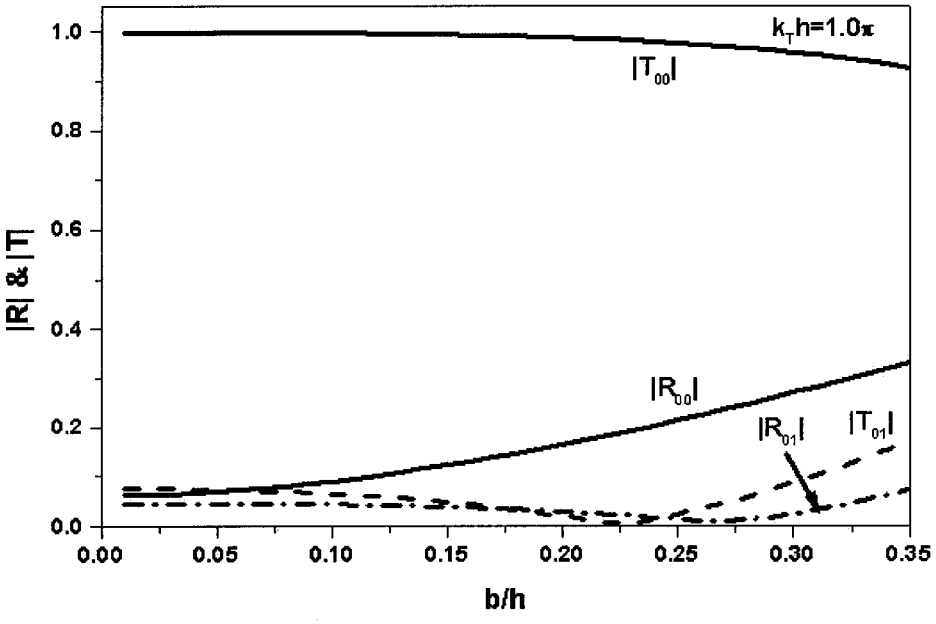

FIG. 4. Reflection and transmission coefficients versus normalized cylinder radius b/h for $k_T h = 1.0\pi$ (S_0 mode incidence).

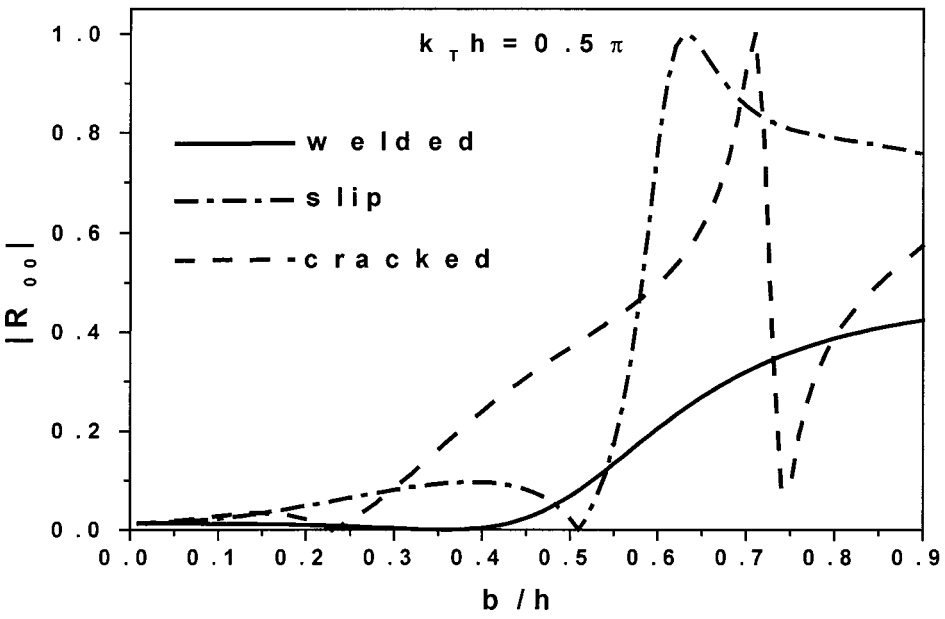

FIG. 5. Reflection coefficients $|R_{00}|$ versus normalized cylinder radius b/h for $k_T h = 0.5\pi$ in the welded, slip and cracked bonding conditions (S_0 mode incidence).

B. A_0 mode incidence

The reflection and transmission coefficients $|R_{00}|$ and $|T_{00}|$ versus the normalized radius b/h for incidence of the A_0 mode are shown in Fig. 6 at the values of $k_T h = 0.1\pi$, 0.3π and 0.5π respectively in the welded boundary conditions. These results are satisfactory since the relative errors ε estimated according to Eq. (11) are less than 1%. The parameters N, L, Mp and x_0 chosen in the numerical evaluations are the same as those for S_0 mode incidence.

From Fig. 6, one finds that the transmission coefficient $|T_{00}|$ is almost always equal to 1.0 while the reflection coefficient $|R_{00}|$ is always smaller than 0.25, indicating that the incident mode is transmitted without being much disturbed at these low frequencies. Further numerical studies reveal that, similar to the case of S_0 mode incidence, large relative error appears when the frequency is higher than $k_T h = 0.52\pi$ where the A_1 mode starts to propagate.

Similar to Fig. 5, Fig. 7 gives the contrasts among the reflection coefficients versus the normalized radius of the cylinder at the frequency $k_T h = 0.4\pi$ in the welded, the slip and the cracked bonding states. The relative errors ε for these results are found to be still less than 1%. In Fig. 7, it is found that, contrary to the welded contact condition, the reflection coefficients in the imperfect bonding condition (slip and cracked) ascend steeply up to nearly 1 with the increase of b/h. The reflection coefficient for the cracked bonding state is always larger than that for the welded and the slip conditions and its increasing rate is also much larger. Sufficient contrast of the reflection coefficients for the perfect and imperfect bonding situations can be found from Fig. 7. This will be useful for the testing of disbonds.

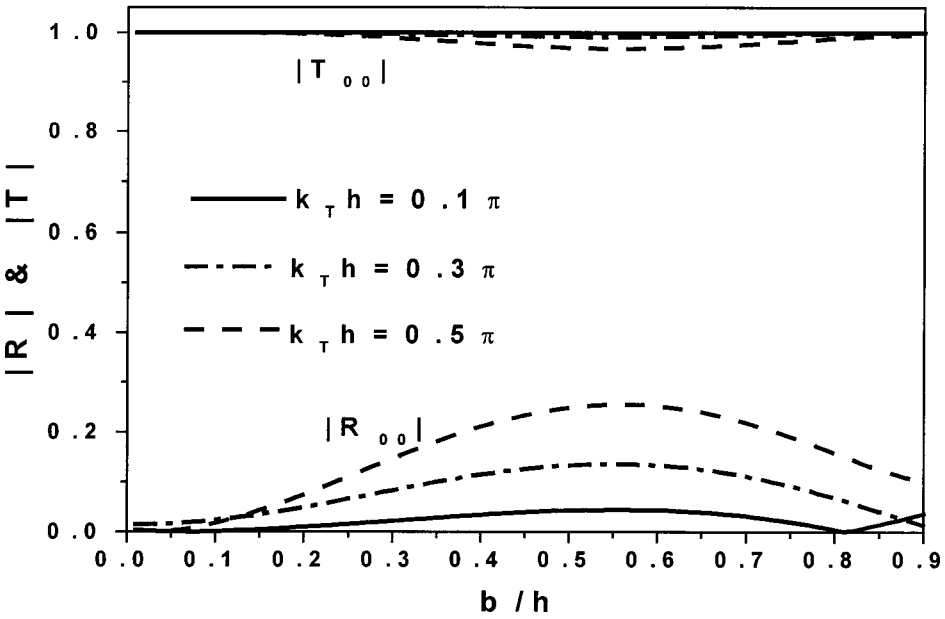

FIG. 6. Reflection and transmission coefficients versus normalized cylinder radius b/h for $k_T h = 0.1\pi$, 0.3π and 0.5π (A_0 mode incidence).

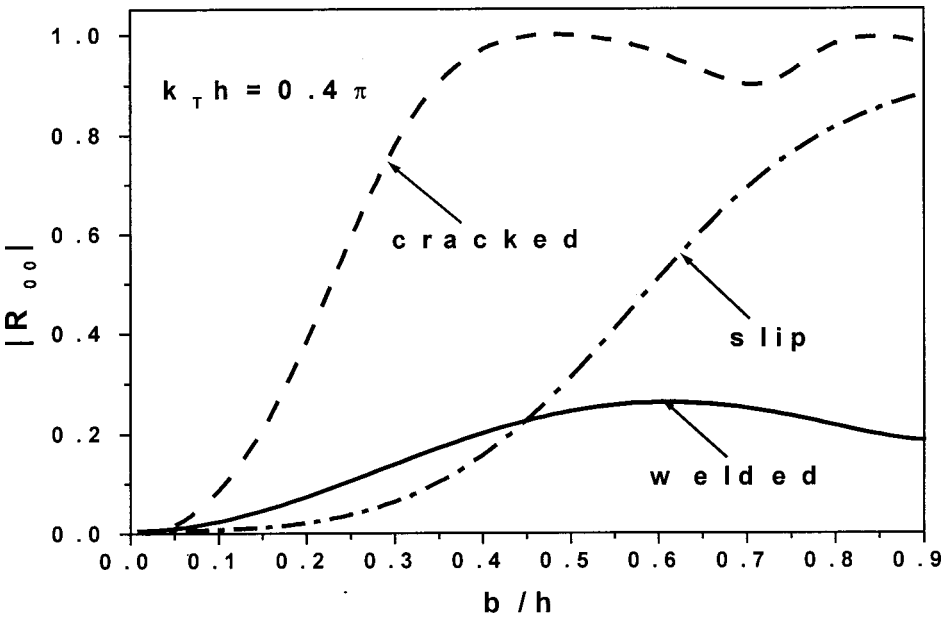

FIG. 7. Reflection coefficients $|R_{00}|$ versus normalized cylinder radius b/h for $k_T h = 0.4\pi$ in the welded, slip and cracked bonding conditions (A_0 mode incidence).

V. CONCLUSIONS

Solutions are obtained for the scattering of a Lamb wave propagating in a traction-free two-dimensional plate by an infinite cylinder centered therein, bonded perfectly or imperfectly, by the use of the method of wave expansion and the method of mode matching. The expressions for the reflection and transmission coefficients can be numerically evaluated by truncating the infinite expansion series. The numerical results for S_0 and A_0 mode incidence are found to be sufficiently accurate in the low-frequency range for cylinder diameter as large as $\frac{9}{10}$ of the plate thickness with the relative errors being smaller than 1%. By the low frequency, it is presently understood to be that lower than the frequency of generation of the scattering S_1 or A_1 mode, respectively.

According to the theoretical predictions, detection of disbonds between the cylinder and the matrix is possible by choosing a suitable incident Lamb wave mode and examining the amplitude of a suitable scattered mode as illustrated in the present article.

ACKNOWLEDGMENT

The work reported here is supported by a grant (No. 19774065) from the National Natural Science Foundation of China.

APPENDIX A: CONSTRUCTION OF THE NORMALIZED MODAL FUNCTIONS FOR LAMB WAVES

Consider the propagation of the time-harmonic Lamb wave in a traction-free plate of thickness $2h$, with material parameters ρ, λ, and μ. Denote the **P** and **SV** wave numbers by $k_p = \omega/\sqrt{(\lambda+2\mu)/\rho}$ and $k_T = \omega/\sqrt{\mu/\rho}$, respectively. Choose the two-dimensional Cartesian coordinate system xOy with the positive x axis in the propagation direction of the Lamb wave, the y axis perpendicular to the surfaces of the plate and the origin O lies in the middle plane of the plate, the Lamb wave displacement components u^m, v^m and the stress components σ^m_{xx}, σ^m_{xy} for the mth order are given by[27]

$$u^m(x,y,t) = U_m(y)\exp[j(k_m x - \omega t)], \tag{A1}$$

$$v^m(x,y,t) = V_m(y)\exp[j(k_m x - \omega t)], \tag{A2}$$

$$\sigma^m_{xx}(x,y,t) = S_m(y)\exp[j(k_m x - \omega t)], \tag{A3}$$

$$\sigma^m_{xy}(x,y,t) = T_m(y)\exp[j(k_m x - \omega t)], \tag{A4}$$

where ω is the angular frequency, $j=\sqrt{-1}$, m is an integer, $U_m(y)$, $V_m(y)$, $S_m(y)$ and $T_m(y)$ are termed as the modal functions, k_m is the Lamb wave number which can be obtained by the dispersion relations

$$\frac{\tan(\alpha_m h)}{\tan(\beta_m h)} = -\frac{(k_m^2-\beta_m^2)^2}{4k_m^2\alpha_m\beta_m} \tag{A5}$$

for the symmetric mode, and

$$\frac{\tan(\alpha_m h)}{\tan(\beta_m h)} = -\frac{4k_m^2\alpha_m\beta_m}{(k_m^2-\beta_m^2)^2} \tag{A6}$$

for the antisymmetric mode, respectively, where $\alpha_m = \sqrt{k_p^2-k_m^2}$ and $\beta_m = \sqrt{k_T^2-k_m^2}$.

The modal functions for the symmetric or antisymmetric mode are:

$$U_m(y) = (jk_m)\left[\cos(\alpha_m y) - \frac{(k_m^2-\beta_m^2)}{2k_m^2} \cdot \frac{\cos(\alpha_m h)}{\cos(\beta_m h)}\cos(\beta_m y)\right]A, \tag{A7}$$

$$V_m(y) = -\alpha_m\left[\sin(\alpha_m y) - \frac{2k_m^2}{(k_m^2-\beta_m^2)} \cdot \frac{\sin(\alpha_m h)}{\sin(\beta_m h)}\sin(\beta_m y)\right]A, \tag{A8}$$

$$S_m(y)=\mu\left\{[(2\nu^2-1)k_T^2-2k_m^2]\cos(\alpha_m y)+(k_m^2-\beta_m^2)\cdot\frac{\cos(\alpha_m h)}{\cos(\beta_m h)}\cos(\beta_m y)\right\}A, \tag{A9}$$

$$T_m(y)=-\mu\cdot j2k_m\alpha_m\left[\sin(\alpha_m y)-\frac{\sin(\alpha_m h)}{\sin(\beta_m h)}\sin(\beta_m y)\right]A \tag{A10}$$

for the symmetric mode, and

$$U_m(y)=(jk_m)\left[\sin(\alpha_m y)-\frac{(k_m^2-\beta_m^2)}{2k_m^2}\cdot\frac{\sin(\alpha_m h)}{\sin(\beta_m h)}\sin(\beta_m y)\right]B, \tag{A11}$$

$$V_m(y)=\alpha_m\left[\cos(\alpha_m y)-\frac{2k_m^2}{(k_m^2-\beta_m^2)}\cdot\frac{\cos(\alpha_m h)}{\cos(\beta_m h)}\cos(\beta_m y)\right]B, \tag{A12}$$

$$S_m(y)=\mu\left\{[(2\nu^2-1)k_T^2-2k_m^2]\sin(\alpha_m y)+(k_m^2-\beta_m^2)\cdot\frac{\sin(\alpha_m h)}{\sin(\beta_m h)}\sin(\beta_m y)\right\}B, \tag{A13}$$

$$T_m(y)=\mu\cdot j2k_m\alpha_m\left[\cos(\alpha_m y)-\frac{\cos(\alpha_m h)}{\cos(\beta_m h)}\cos(\beta_m y)\right]B \tag{A14}$$

for the antisymmetric mode, respectively, where ν denotes the velocity ratio of **SV** to **P** waves, and A and B are constants.

It is seen that the Lamb wave modal functions are expressed in terms of the unknown constants A in Eqs. (A7)–(A10) for the symmetric mode and B in Eqs. (A11)–(A14) for the antisymmetric mode. Hence, it is necessary to normalize the Lamb wave modal functions for direct comparisons of the reflection and transmission coefficients of arbitrary modes with that of the incident mode. The orthogonality relations of the Lamb wave modal functions are used to obtain the normalized modal functions. We choose the normalization factor $\sqrt{Q_m}$ for the mth mode of Lamb wave such that

$$\overline{U}_m(y)=U_m(y)/\sqrt{Q_m}, \tag{A15}$$

$$\overline{V}_m(y)=V_m(y)/\sqrt{Q_m}, \tag{A16}$$

$$\overline{S}_m(y)=S_m(y)/\sqrt{Q_m}, \tag{A17}$$

$$\overline{T}_m(y)=T_m(y)/\sqrt{Q_m}, \tag{A18}$$

where Q_m is defined by[27]

$$Q_m=\int_{-h}^{h}\{[U_m(y)S_n^*(y)+V_m(y)T_n^*(y)]-[S_m(y)U_n^*(y)+T_m(y)V_n^*(y)]\}\,dy, \tag{A19}$$

where $k_n=k_m^*$, the superscript asterisk denotes a complex conjugate, and the subscripts m and n stand for the mth and nth Lamb modes, respectively.

Positive m refers to the wave of mode m propagating (for real values of k_m) or decaying exponentially (for complex values of k_m) in the $+x$ direction, while negative m refers to the mode m propagating or decaying in the opposite direction. That is,

$$k_{-m}=-k_m. \tag{A20}$$

It will be noted that u^m and σ_{xx}^m are even functions but v^m and σ_{xy}^m are odd functions about the $y=0$ plane for the symmetric mode, and vise versa for the antisymmetric mode. This phenomenon occurs also in the construction of cylindrical waves (see Appendix B).

APPENDIX B: DISPLACEMENT AND STRESS COMPONENTS OUTSIDE AN ELASTIC CYLINDER

Consider an elastic cylinder (ρ_c, λ_c and μ_c) of radius b embedded in a bounded region ($|x|<x_0$, $|y|<h$) of a plate having the density ρ, and the Lame constants λ and μ as shown in the middle part R2 of Fig. 1. Denote the **P** and **SV** wave numbers outside the cylinder to be $k_p=\omega/\sqrt{(\lambda+2\mu)/\rho}$ and $k_T=\omega/\sqrt{\mu/\rho}$, respectively, and let the respective **P** and **SV** wave numbers in the cylinder be $k_L=\omega/\sqrt{(\lambda_c+2\mu_c)/\rho_c}$ and $k_s=\omega/\sqrt{\mu_c/\rho_c}$.

Assume that the time-harmonic waves are polarized in the plane perpendicular to the cylinder's axis and choose the cylindrical coordinate system such that the origin is located at the center of the cylinder's cross-section and the z-axis is directed along the cylinder axis. With the time-harmonic factor $e^{-j\omega t}$ being suppressed throughout, the displacement components u_r, u_θ and the stress components σ_{rr}, $\sigma_{\theta\theta}$ and $\sigma_{r\theta}$ in the bounded region but outside the cylinder are given by[4]

$$ru_r(r,\theta)=\sum_{l=0}^{+\infty}D_l^s U_{1l}(r)\cos(l\theta)+\sum_{l=1}^{+\infty}E_l^s U_{2l}(r)\cos(l\theta), \tag{B1}$$

$$ru_\theta(r,\theta)=-\sum_{l=0}^{+\infty}D_l^s U_{3l}(r)\sin(l\theta)-\sum_{l=1}^{+\infty}E_l^s U_{4l}(r)\sin(l\theta), \tag{B2}$$

$$\frac{r^2\sigma_{rr}(r,\theta)}{2\mu}=\sum_{l=0}^{+\infty}D_l^s T_{1l}(r)\cos(l\theta)+\sum_{l=1}^{+\infty}E_l^s T_{2l}(r)\cos(l\theta), \tag{B3}$$

$$\frac{r^2\sigma_{\theta\theta}(r,\theta)}{2\mu}=\sum_{l=0}^{+\infty}D_l^s T_{3l}(r)\cos(l\theta)-\sum_{l=1}^{+\infty}E_l^s T_{4l}(r)\cos(l\theta), \tag{B4}$$

$$\frac{r^2\sigma_{r\theta}}{2\mu}=-\sum_{l=0}^{+\infty}D_l^s T_{5l}(r)\sin(l\theta)-\sum_{l=1}^{+\infty}E_l^s T_{6l}(r)\sin(l\theta) \tag{B5}$$

for the symmetric waves, and

$$ru_r(r,\theta)=\sum_{l=1}^{+\infty} D_l^a U_{1l}(r)\sin(l\theta)-\sum_{l=0}^{+\infty} E_l^a U_{2l}(r)\sin(l\theta), \tag{B6}$$

$$ru_\theta(r,\theta)=\sum_{l=1}^{+\infty} D_l^a U_{3l}(r)\cos(l\theta)-\sum_{l=0}^{+\infty} E_l^a U_{4l}(r)\cos(l\theta), \tag{B7}$$

$$\frac{r^2\sigma_{rr}(r,\theta)}{2\mu}=\sum_{l=1}^{+\infty} D_l^a T_{1l}(r)\sin(l\theta)-\sum_{l=0}^{+\infty} E_l^a T_{2l}(r)\sin(l\theta), \tag{B8}$$

$$\frac{r^2\sigma_{\theta\theta}(r,\theta)}{2\mu}=\sum_{l=1}^{+\infty} D_l^a T_{3l}(r)\sin(l\theta)+\sum_{l=0}^{+\infty} E_l^a T_{4l}(r)\sin(l\theta), \tag{B9}$$

$$\frac{r^2\sigma_{r\theta}}{2\mu}=\sum_{l=1}^{+\infty} D_l^a T_{5l}(r)\cos(l\theta)-\sum_{l=0}^{+\infty} E_l^a T_{6l}(r)\cos(l\theta) \tag{B10}$$

for the antisymmetric waves, respectively. In these equations,

$$U_{1l}(r)=k_p rJ_l'(k_p r)-\varepsilon_l^{PT} lY_l(k_T r)-\varepsilon_l^{PP} k_p rY_l'(k_p r), \tag{B11}$$

$$U_{2l}(r)=lJ_l(k_T r)-\varepsilon_l^{TP} k_p rY_l'(k_p r)-\varepsilon_l^{TT} lY_l(k_T r), \tag{B12}$$

$$U_{3l}(r)=lJ_l(k_p r)-\varepsilon_l^{PT} k_T rY_l'(k_T r)-\varepsilon_l^{PP} lY_l(k_p r), \tag{B13}$$

$$U_{4l}(r)=k_T rJ_l'(k_T r)-\varepsilon_l^{TP} lY_l(k_p r)-\varepsilon_l^{TT} k_T rY_l'(k_T r), \tag{B14}$$

$$T_{1l}(r)=\xi_l^J(k_p r)-\varepsilon_l^{PT} f_l^Y(k_T r)-\varepsilon_l^{PP}\xi_l^Y(k_p r), \tag{B15}$$

$$T_{2l}(r)=f_l^J(k_T r)-\varepsilon_l^{TP}\xi_l^Y(k_p r)-\varepsilon_l^{TT} f_l^Y(k_T r), \tag{B16}$$

$$T_{3l}(r)=g_l^J(k_p r)+\varepsilon_l^{PT} f_l^Y(k_T r)-\varepsilon_l^{PP} g_l^Y(k_p r), \tag{B17}$$

$$T_{4l}(r)=f_l^J(k_T r)+\varepsilon_l^{TP} g_l^Y(k_p r)-\varepsilon_l^{TT} f_l^Y(k_T r), \tag{B18}$$

$$T_{5l}(r)=f_l^J(k_p r)-\varepsilon_l^{PT}\eta_l^Y(k_T r)-\varepsilon_l^{PP} f_l^Y(k_p r), \tag{B19}$$

$$T_{6l}(r)=\eta_l^J(k_T r)-\varepsilon_l^{TP} f_l^Y(k_p r)-\varepsilon_l^{TT}\eta_l^Y(k_T r). \tag{B20}$$

In Eqs. (B11)–(B20), $J_l(.)$ and $Y_l(.)$ are the Bessel and Neumann functions of the lth order, while the functions f_l^Z, g_l^Z, ξ_l^Z and η_l^Z are defined as follows:

$$f_l^Z(kr)=l[(kr)Z_l'(kr)-Z_l(kr)], \tag{B21}$$

$$g_l^Z(kr)=krZ_l'(kr)+\left[\left(1-\frac{1}{2\nu^2}\right)(kr)^2-l^2\right]Z_l(kr), \tag{B22}$$

$$\xi_l^Z(kr)=\left[l^2-\frac{1}{2\nu^2}(kr)^2\right]Z_l(kr)-krZ_l'(kr), \tag{B23}$$

$$\eta_l^Z(kr)=\left[l^2-\frac{1}{2}(kr)^2\right]Z_l(kr)-krZ_l'(kr), \tag{B24}$$

where Z_l may be the Bessel function J_l or the Neumann function Y_l, and Z_l' is the derivative of Z_l, and ν is the velocity ratio of **SV** wave to **P** wave. The constants ε_l^{PP}, ε_l^{PT}, ε_l^{TP} and ε_l^{TT} are determined by the boundary conditions on the circle $r=b$. The boundary conditions on the surface of the cylinder $r=b$ are here expressed in terms of the spring model described in Ref. 15:

$$\begin{aligned} &u_r-u_r^c=s_N\sigma_{rr}^c, \quad u_\theta-u_\theta^c=s_T\sigma_{r\theta}^c,\\ &\sigma_{rr}-\sigma_{rr}^c=0, \quad \sigma_{r\theta}-\sigma_{r\theta}^c=0, \end{aligned} \tag{B25}$$

where s_N and s_T are the normal and transverse compliances of the spring, the superscript c denotes the wave fields in the cylinder at $r=b$, and the corresponding fields outside the cylinder are represented by the letters without the superscripts. As $s_N\to 0$ and $s_T\to 0$, the welded boundary condition can be obtained, when $s_N\to 0$ and $s_T\to\infty$, the slip boundary condition results, while for $s_N\to\infty$ and $s_T\to\infty$, the cracked boundary condition occurs.

Also in Eqs. (B11)–(B20),

$$\varepsilon_l^{PP}=\frac{\Delta_l^{PP}}{\Delta_l}, \quad \varepsilon_l^{PT}=\frac{\Delta_l^{PT}}{\Delta_l}, \quad \varepsilon_l^{TP}=\frac{\Delta_l^{TP}}{\Delta_l}, \quad \varepsilon_l^{TT}=\frac{\Delta_l^{TT}}{\Delta_l}, \tag{B26}$$

where

$$\Delta_l=\begin{vmatrix} k_pbY_l'(k_pb) & lY_l(k_Tb) & k_Lbf_l'(k_Lb)+s_N\xi_l^J(k_Lb) & lJ_l(k_sb)+s_Nf_l^J(k_sb)\\ lY_l(k_pb) & k_TbY_l'(k_Tb) & lJ_l(k_Lb)+s_Tf_l^J(k_Lb) & k_sbJ_l'(k_sb)+s_T\eta_l^J(k_sb)\\ \xi_l^Y(k_pb) & f_l^Y(k_Tb) & \tilde{\mu}\xi_l^J(k_Lb) & \tilde{\mu}f_l^J(k_sb)\\ f_l^Y(k_pb) & \eta_l^Y(k_Tb) & \tilde{\mu}f_l^J(k_Lb) & \tilde{\mu}\eta_l^J(k_sb) \end{vmatrix},$$

$$\Delta_l^{PP}=\begin{vmatrix} k_pbJ_l'(k_pb) & lY_l(k_Tb) & k_Lbf_l'(k_Lb)+s_N\xi_l^J(k_Lb) & lJ_l(k_sb)+s_Nf_l^J(k_sb)\\ lJ_l(k_pb) & k_TbY_l'(k_Tb) & lJ_l(k_Lb)+s_Tf_l^J(k_Lb) & k_sbJ_l'(k_sb)+s_T\eta_l^J(k_sb)\\ \xi_l^J(k_pb) & f_l^Y(k_Tb) & \tilde{\mu}\xi_l^J(k_Lb) & \tilde{\mu}f_l^J(k_sb)\\ f_l^J(k_pb) & \eta_l^Y(k_Tb) & \tilde{\mu}f_l^J(k_Lb) & \tilde{\mu}\eta_l^J(k_sb) \end{vmatrix},$$

$$\Delta_l^{PT}=\begin{vmatrix} k_pbY_l'(k_pb) & k_pbJ_l'(k_pb) & k_Lb J_l'(k_Lb)+s_N\xi_l^J(k_Lb) & lJ_l(k_sb)+s_Nf_l^J(k_sb) \\ lY_l(k_pb) & lJ_l(k_pb) & lJ_l(k_Lb)+s_Tf_l^J(k_Lb) & k_sbJ_l'(k_sb)+s_T\eta_l^J(k_sb) \\ \xi_l^Y(k_pb) & \xi_l^J(k_pb) & \tilde{\mu}\xi_l^J(k_Lb) & \tilde{\mu}f_l^J(k_sb) \\ f_l^Y(k_pb) & f_l^J(k_pb) & \tilde{\mu}f_l^J(k_Lb) & \tilde{\mu}\eta_l^J(k_sb) \end{vmatrix},$$

$$\Delta_l^{TP}=\begin{vmatrix} lJ_l(k_Tb) & lY_l(k_Tb) & k_Lb J_l'(k_Lb)+s_N\xi_l^J(k_Lb) & lJ_l(k_sb)+s_Nf_l^J(k_sb) \\ k_TbJ_l'(k_Tb) & k_TbY_l'(k_Tb) & lJ_l(k_Lb)+s_Tf_l^J(k_Lb) & k_sbJ_l'(k_sb)+s_T\eta_l^J(k_sb) \\ f_l^J(k_Tb) & f_l^Y(k_Tb) & \tilde{\mu}\xi_l^J(k_Lb) & \tilde{\mu}f_l^J(k_sb) \\ \eta_l^J(k_Tb) & \eta_l^Y(k_Tb) & \tilde{\mu}f_l^J(k_Lb) & \tilde{\mu}\eta_l^J(k_sb) \end{vmatrix},$$

$$\Delta_l^{TT}=\begin{vmatrix} k_pbY_l'(k_pb) & lJ_l(k_Tb) & k_Lb J_l'(k_Lb)+s_N\xi_l^J(k_Lb) & lJ_l(k_sb)+s_Nf_l^J(k_sb) \\ lY_l(k_pb) & k_TbJ_l'(k_Tb) & lJ_l(k_Lb)+s_Tf_l^J(k_Lb) & k_sbJ_l'(k_sb)+s_T\eta_l^J(k_sb) \\ \xi_l^Y(k_pb) & f_l^J(k_Tb) & \tilde{\mu}\xi_l^J(k_Lb) & \tilde{\mu}f_l^J(k_sb) \\ f_l^Y(k_pb) & \eta_l^J(k_Tb) & \tilde{\mu}f_l^J(k_Lb) & \tilde{\mu}\eta_l^J(k_sb) \end{vmatrix},$$

in which $\tilde{\mu}=\mu_c/\mu$.

The wave fields in Eqs. (B1)–(B10) involve cosines and sines of the argument $l\theta$ which are even and odd functions, respectively, about $y=0$. Hence, displacement and stress components have already been decomposed into two sets of waves termed symmetric and antisymmetric modes, which are denoted by the superscripts s in Eqs. (B1)–(B5) and a in Eqs. (B6)–(B10) in the expansion constants, respectively.

For the purpose of solving the scattering of the Lamb wave by a cylinder in a traction-free plate, we have to obtain the displacement and stress components in the Cartesian coordinate system xOy from that of the cylindrical coordinate system. With the coordinate transform relations

$$x=r\cos\theta, \quad y=r\sin\theta, \tag{B27}$$

and the following relations,[21]

$$u=u_r\cos\theta-u_\theta\sin\theta, \quad v=u_r\sin\theta+u_\theta\cos\theta \tag{B28}$$

$$\begin{aligned} \sigma_{xx}&=\sigma_{rr}\cos^2\theta+\sigma_{\theta\theta}\sin^2\theta-\sigma_{r\theta}\sin 2\theta, \\ \sigma_{yy}&=\sigma_{rr}\sin^2\theta+\sigma_{\theta\theta}\cos^2\theta+\sigma_{r\theta}\sin 2\theta, \\ \sigma_{xy}&=(\sigma_{rr}-\sigma_{\theta\theta})\sin\theta\cos\theta+\sigma_{r\theta}\cos 2\theta, \end{aligned} \tag{B29}$$

the displacement components and stress components outside the cylinder in the Cartesian coordinate system xOy for the symmetric and antisymmetric waves can be obtained.

As in Appendix A, from Eqs. (B28) and (B29) one finds that u and σ_{xx} are even functions but v and σ_{xy} are odd functions about the $y=0$ plane for the symmetric waves, and vise versa for the antisymmetric waves.

[1] J. J. Faran Jr., "Sound scattering by solid cylinders and spheres," J. Acoust. Soc. Am. **23**, 405–418 (1951).
[2] C. F. Ying and R. Truell, "Scattering of plane longitudinal wave by a spherical obstacle in an isotropically elastic solid," J. Appl. Phys. **27**, 1086–1097 (1956).
[3] R. M. White, "Elastic wave scattering at a cylindrical discontinuity in a solid," J. Acoust. Soc. Am. **30**, 771–785 (1958).
[4] Y. H. Pao and C. C. Mow, *Diffraction of Elastic Waves and Dynamic Stress Concentrations* (Crane Russak, New York, 1973).
[5] J. Miklowitz, *Theory of Elastic Waves and Waveguides* (North-Holland, New York, 1978).
[6] D. J. Jain and R. P. Kanwal, "Scattering of elastic waves by circular cylindrical flaws and inclusions," J. Appl. Phys. **50**, 4067–4109 (1979).
[7] J. D. Achenbach, Y. Lu, and M. Kitahara, "3-D reflection and transmission of sound by an array of rods," J. Sound Vib. **125**(3), 463–467 (1988).
[8] B. Y. Liu, and R. S. Wu, "Scattering and attenuation of a visco-elastic cylinder: I. P-wave incidence," J. Acoust. Soc. Am. **95**, 2803(A) (1994).
[9] Y. Lu, "Three-dimensional reflection and transmission of elastic waves by an array of cylinders," J. Sound Vib. **175**(1), 1–15 (1994).
[10] Y. B. Liu and C. F. Ying, "Scattering and attenuation of a visco-elastic cylinder: II. SV-wave incidence," J. Acoust. Soc. Am. **101**, 3153(A) (1997).
[11] Y. C. Chu and S. I. Rokhlin, "Determination of macro- and micro- mechanical and interfacial elastic properties of composites from ultrasonic data," J. Acoust. Soc. Am. **92**, 920–931 (1992).
[12] P. Beattie, R. C. Chivers, and L. W. Andson, "Ultrasonic backscattering from solid cylindrical inclusions in solid elastic matrices: A comparison of theory and experiment," J. Acoust. Soc. Am. **94**, 3421–3427 (1993).
[13] A. N. Sinclair and R. C. Anddison, "Acoustic diffraction spectrum of a SiC fiber in a solid elastic medium," J. Acoust. Soc. Am. **94**, 1126–1135 (1993).
[14] Y. C. Chu and S. I. Rokhlin, "Fiber-matrix interphase characterization in composites using ultrasonic velocity data," J. Appl. Phys. **76**, 4121–4129 (1994).
[15] W. Huang and S. Brisuda, S. I. Rokhlin, "Ultrasonic wave scattering from fiber-matrix interphases" J. Acoust. Soc. Am. **97**, 807–817 (1995).
[16] W. Huang, J. Y. Wang, I. S. Rokhlin, "Oblique scattering of an elastic wave from a mutilayered cylinder in a solid: Transfer-matrix approach," J. Acoust. Soc. Am. **99**, 2742–2754 (1996).
[17] Y. Lu, "Guided antiplane shear wave propagation in layers reinforced by periodically spaced cylinders," J. Acoust. Soc. Am. **99**, 1937–1943 (1996).
[18] X. M. Wang, C. F. Ying, and M. X. Li, "Scattering of antiplane shear wave by a circular cylinder in a traction free plate," J. Acoust. Soc. Am. **108**, 913–923 (2000).
[19] M. Tan, and B. A. Auld, "Normal mode variational method for two- and three-dimensional acoustic scattering in an isotropic plate," in 1980 Ultrason. Symp. Proc. 857–861 (1980).
[20] S. I. Rokhlin, "Diffraction of Lamb waves by a finite crack in an elastic layer," J. Acoust. Soc. Am. **67**, 1157–1165 (1980).
[21] M. Koshiba, and H. Morita, M. Suzuki, "Finite-element analysis of Lamb wave scattering in an elastic plate waveguide," IEEE Trans. Sonics Ultrason. **SU-31**, 18–25 (1984).
[22] Y. Cho, D. D. Hongerholt, and J. L. Rose, "Lamb wave scattering analysis for reflector characterization," IEEE Trans. Ultrason. Ferroelectr. Freq. Control **44**(1), 44–52 (1997).
[23] B. Pavlakovic, M. J. S. Lowe, and P. Cawley, "The inspection of tendons

in post-tensioned concrete using guided ultrasonic waves,'' Insight **41**(7), 446–452 (1999).
[24] E. D. Nielsen, ''Scattering by a cylindrical post of complex permittivity in a waveguide,'' IEEE Trans. Microwave Theory Tech. **MTT-17**(3), 148–153 (1969).
[25] A. Lakhtakia, V. V. Varadan, and V. K. Varadan, ''Reflection characteristics of an elastic slab containing a periodic array of cylinders: SH wave analysis,'' J. Acoust. Soc. Am. **80**(1), 311–316 (1986).
[26] A. Lakhtakia, V. V. Varadan, and V. K. Varadan, ''Reflection characteristics of an elastic slab containing a periodic array of cylinders: P and SV wave analysis,'' J. Acoust. Soc. Am. **83**, 1267–1275 (1988).
[27] B. A. Auld, *Acoustic Fields and Waves in Solids, Vol. II* (Wiley, New York, 1973).
[28] J. L. Rose, *Ultrasonic Waves in Solid Media* (Cambridge U. P., Cambridge, 1999), pp. 318–319.
[29] A. Lakhtakia, M. F. Iskander, and C. H. Durney, ''An iterative extended boundary condition method for solving the absorption characteristics of lossy dielectric objects of large aspect ratios,'' IEEE Trans. Microwave Theory Tech. **MTT-31**(8), 640–647 (1983).

Leaky helical flexural wave scattering contributions from tilted cylindrical shells: Ray theory and wave-vector anisotropy

Florian J. Blonigen and Philip L. Marston
Department of Physics, Washington State University, Pullman, Washington 99164-2814

(Received 27 February 2001; revised 3 July 2001; accepted 5 July 2001)

At sufficiently high frequencies, cylindrical shells support a wave whose properties are analogous to those of the lowest antisymmetric Lamb wave on plates. When the shell is in water and the frequency exceeds the coincidence frequency, the flexural wave is a leaky wave that can be a major contributor to the scattering by tilted shells [G. Kaduchak, C. M. Wassmuth, and C. M. Loeffler, J. Acoust. Soc. Am. **100**, 64–71 (1996)]. While the meridional ray-scattering contributions for such leaky flexural waves were previously modeled, the helical contribution can also be significant. A ray theory for those contributions is compared with the exact partial wave series (PWS) solution for infinitely long empty shells. The agreement between the ray theory and the PWS is only possible when a weak anisotropy of the flexural wave parameters is included in the evaluation of the ray theory. The anisotropy is determined numerically from the roots of a denominator in the PWS because approximations for the anisotropy from thin-shell mechanics are not applicable significantly above the coincidence frequency.
[DOI: 10.1121/1.1398049]

PACS numbers: 43.20.Fn, 43.40.Fz, 43.30.Ft [ANN]

I. INTRODUCTION

Investigations into the scattering of high-frequency sound by submerged cylindrical shells have shown that leaky antisymmetric (flexural) Lamb waves can be important at large tilt angles.[1–3] Ray theories were previously employed to describe meridional leaky ray-scattering contributions.[1] Ray calculations of scattering contributions are extended here to include helical rays. The emphasis here is on situations where formulations based on thin-shell mechanics[4] are not directly applicable. The emphasis of most other studies concerns coupling mechanisms that are important for tilts relatively close to broadside illumination.[4–6] The class of moderately damped scattering contributions considered here is important for wide-bandwidth high-frequency sonar.[2,3] The subtleties associated with the previously unexplored aspects of ray theory make certain computational tests described here for infinitely long tilted shells a prerequisite for the quantitative understanding of antisymmetric Lamb wave contributions to the scattering by truncated cylindrical shells.

Relevant ray paths are shown in Fig. 1. Rays are launched at those points on the cylinder where the angle between the incident wave vector and the local shell normal is equal to the leaky wave coupling angle, $\theta_l = \sin^{-1}(c/c_l)$, for the lth class of leaky wave under consideration. Here, c_l is the phase velocity ($c_l > c$) of the leaky wave of type l, and c is the speed of sound in the surrounding fluid. The outgoing rays leave the cylinder at the same coupling angle relative to the shell normal at the detachment points. When the tilt angle of the cylinder, γ, measured from broadside incidence, is equal to the coupling angle θ_l, an incident ray A can launch a meridional leaky ray that runs strictly in the axial direction on the cylinder (ray B) and leaks radiation in the specular direction (ray C). For tilt angles less than the coupling angle, $\gamma < \theta_l$, an incident ray D launches a leaky ray on the shell at a nonzero azimuthal angle ϕ, measured from the meridian as shown in Fig. 1. The resulting leaky ray E travels along a helical path on the cylinder with helix angle, ψ.

Helical rays and meridional rays[1,7,8] radiate wavefronts into the surrounding fluid with a vanishing principal curvature. Helical rays typically have longer ray paths on the shell, which tends to decrease their scattering contributions because of radiation damping. Nevertheless, helical waves of the lowest-order antisymmetric (a_0) leaky Lamb mode make appreciable scattering contributions and are important for understanding the high-frequency response from shells at tilt angles smaller than the coupling angle, $\gamma < \theta_l$, where the meridional contribution is diminished. Our ray formulation is compared with the partial wave series solution (PWS) for scattering by infinitely long empty cylindrical shells in water. Amplitudes are calculated for scattering in the specular direction, so that both helical and meridional rays are included in the analysis. By allowing the meridional and helical ray contributions to interfere, the important scattering features of the shell are described over a wide tilt-angle range. The range of relevant γ increases as the frequency is decreased to near the coincidence frequency since θ_l approaches 90°.

The agreement between the ray model and the PWS solution was facilitated by allowing the a_0 leaky wave speed (c_l with $l = a_0$) and also the radiation damping to vary with helix angle ψ. The calculation of the dependence of c_l and the attenuation rate on ψ is summarized in Sec. IV, since relevant results above the coincidence frequency appeared to be unavailable. It was not necessary to include this weak anisotropy in the derivation of the expressions, Eqs. (5) and (6), for the ray amplitude. The anisotropy of the ray parameters was included in the numerical evaluation of Eq. (5) for the helical wave contribution.

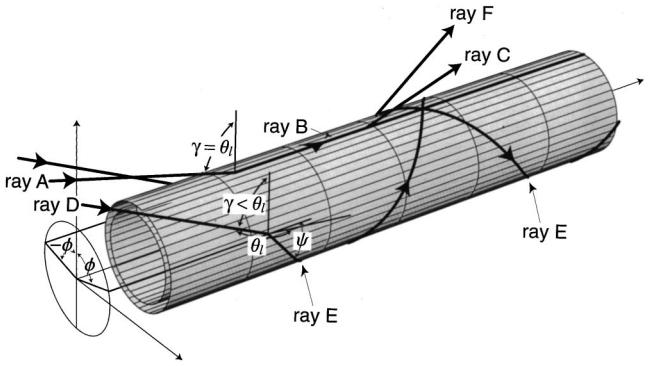

FIG. 1. Typical leaky ray paths on a cylinder. Leaky rays are launched at those points on the cylinder where the angle between the incident wave vector and the local shell normal is equal to the leaky wave coupling angle θ_l. When the tilt angle is equal to the coupling angle, $\gamma=\theta_l$, an incident ray (ray A) can launch a meridional leaky ray which runs along the meridian of the cylinder (ray B). This reradiates in the specular direction at the same coupling angle (ray C). For $\gamma<\theta_l$, an incident ray (ray D) may launch a helical leaky ray (ray E) at a point off the meridian at azimuthal angle, ϕ, measured from the meridian. It travels along a helical path with helix angle ψ. It reradiates in the specular direction at the azimuthal angle $-\phi$ (ray F).

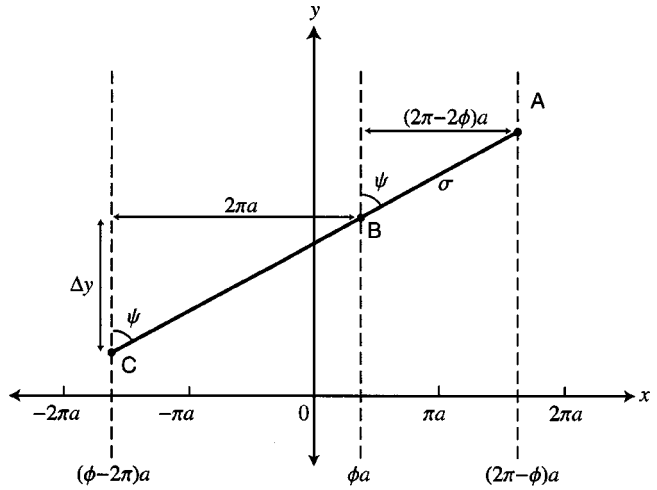

FIG. 2. Diagram of helical rays on the unwrapped plane surface of the cylinder. The y axis is parallel to the cylinder's axis. A helical ray is launched along $x=\phi a$ at some point B, where ϕ satisfies the condition given by Eq. (1). It travels on the cylinder with helix angle ψ, where ψ satisfies the condition given by Eq. (2). The ray reradiates in the specular direction at point A where $x=(2\pi-\phi)a$. A family of other helical rays launched further to the left at $x=(\phi-2\pi n)a$ will also contribute to the leaky wave pressure at point A. One such ray is launched at point C, where $x=(\phi-2\pi)a$. This ray also travels with helix angle ψ. It makes one full circumnavigation of the cylinder before reaching point A. A similar family of helical rays is launched at $x=-\phi a$ which travels with helix angle $-\psi$.

II. EXTENSION OF RAY THEORY TO INCLUDE HELICAL FLEXURAL WAVES

Consider a plane wave of wave number $k=\omega/c$ and tilt angle γ incident on an infinitely long cylindrical shell of radius a and inner radius b (Fig. 1). Let the phase of the plane wave be referenced to the cylinder's axis. Reference 8 (referred to hereafter as Paper M) gives an approximation for the pressure at an interface radiated by leaky waves, expressed as a convolution integral of the incident acoustic pressure over the object's surface [Eq. (2a), Paper M]. This formulation is applied to smooth surfaces, such as a cylinder, as explained in Paper M.

In Sec. V of Paper M, the convolution approach is applied to helical waves on cylinders. The results, summarized below, are extended in the present application to allow for the summation of repeated circumnavigations and for the interference with the meridional ray contributions. In the high-frequency limit, the convolution integral is evaluated using the stationary phase approximation, with the stationary phase points corresponding to the launch points of leaky rays on the cylinder. Figure 2 shows the plane of the unwrapped cylinder surface parametrized by the Cartesian coordinates x and y. The y axis is parallel to the cylinder's axis and the x axis runs in the circumferential direction perpendicular to the cylinder's axis. One set of stationary phase points is given by the central dashed line in Fig. 2 parallel to the y axis at $x=\phi a$. Here, ϕ satisfies the stationary phase condition

$$\cos\,\phi=\cos\,\theta_l/\cos\,\gamma. \tag{1}$$

By symmetry, there is also a set of stationary points at $x=-\phi a$ which satisfies the condition of Eq. (1). Another stationary phase condition, given by Eq. (29b) of Paper M

$$\cos\,\psi=\sin\,\gamma/\sin\,\theta_l, \tag{2}$$

uniquely determines the helix angle ψ, which indicates the direction of propagation of the leaky ray on the cylinder surface. Equations (1) and (2) can alternatively be derived using the trace velocity matching condition.

Consider the specularly directed helical wave contributions. By symmetry arguments, leaky rays launched at $x=\phi a$ will reradiate in the specular direction at detachment points along $x=-\phi a$ (ray F in Fig. 1). The leaky wave pressure p_l is needed at $x=(2\pi-\phi)a$ (the right-most dashed line in Fig. 2), which is physically equivalent to the line $x=-\phi a$. This may be found using the method of Paper M, Sec. V, which gives

$$p_1^{(0)}\approx\kappa(2/\pi k_p)^{1/2}p_i e^{i\varphi_{\mathrm{BA}}+i\pi/4}e^{-ika\,\cos\,\theta_l}e^{iky_0\,\sin\,\gamma}\times A_f\sigma^{-1/2}/\pi. \tag{3}$$

The superscript (0) on the left-hand side of Eq. (3) indicates that this is only the lowest-order contribution to the leaky wave pressure at $x=(2\pi-\phi)a$. This contribution is due to the ray that travels once around the backside of the cylinder from $x=\phi a$ to $x=(2\pi-\phi)a$, such as ray BA in Fig. 2. On the right-hand side of Eq. (3), $k_p=k_l+i\alpha$ is the complex leaky wave number for the lth class of leaky wave where $k_l=\omega/c_l$ and α is the leaky wave attenuation, p_i is the magnitude of the incident pressure, $\kappa\approx-\alpha k_l\exp(i\varphi_{bl})$ is a leaky wave-coupling parameter whose coupling background phase φ_{bl} is discussed in Appendix A of Paper M and in Ref. 7, and $\varphi_{\mathrm{BA}}=(k_l+i\alpha)\sigma$, where $\sigma=(2\pi-2\phi)a/\sin\,\psi$ is the path length of ray BA. The Fresnel area A_f is that area around the helical ray launch point (point B) containing the launch points of all leaky paths that arrive at the detachment point (point A) with a phase defect $\leqslant\pi$ with respect to the phase along the Fermat path (ray BA). The Fresnel zone is elliptical in shape. The expression for A_f is given by Eq. (30a) of Paper M, where in that equation θ' corresponds to

the azimuthal angle denoted by ϕ here. The other phase factors in Eq. (3), not analyzed in Paper M, are essential for the numerical tests given in Sec. III. These account for the phase of the illumination at the helical ray launch point, where y_0 is the coordinate of the launch point.

In general, a family of leaky rays will make contributions $p_l^{(n)}$ to the radiated leaky wave pressure at point A. They are launched at azimuthal angles $\phi - 2\pi n$ ($n = 0,1,2,\ldots$), each of which satisfies the stationary phase condition of Eq. (1) and propagates with the same helix angle ψ. These rays correspond to higher-order helical rays which make n complete circumnavigations of the cylinder. An example of one such ray is ray CA shown in Fig. 2. It is launched at point C on the line $x=(\phi-2\pi)a$ (the left-most dashed line in Fig. 2) and completes one full circumnavigation of the cylinder ($n=1$). Because of its longer ray path, the pressure contribution of ray CA takes on a slightly different form from the expression of $p_l^{(0)}$ in Eq. (3). In the expression of φ_{BA}, the length of path BA, σ, must be replaced by the length of path CA, $\sigma + 2\pi a/\sin\psi$, where $2\pi a/\sin\psi$ is the distance from C to B. [A similar substitution is not necessary for σ in the factor $\sigma^{-1/2}$ of Eq. (3) since this cancels with a factor of $\sigma^{1/2}$ embedded in the expression for A_f.] There is also a phase advance due to the fact that ray CA is launched at a smaller value of y: $y_0=\Delta y$, where $\Delta y = 2\pi a/\tan\psi$ (see Fig. 2). Replacing y_0 with $y_0-\Delta y$ in Eq. (3) gives a phase advance of $(k\sin\gamma)\Delta y = 2\pi ka\sin\gamma/\tan\psi$, where $k\sin\gamma$ is the projection of the incident wave vector along the y axis. Thus, $p_l^{(1)}$, the pressure contribution of ray CA, is given by the expression on the right-hand side of Eq. (3) with an additional factor of $\exp(i\Gamma_1)$, where $\Gamma_1=[2\pi(k_l+i\alpha)a/\sin\psi] - [2\pi ka\sin\gamma/\tan\psi] = 2\pi k_l a[(\sin\psi)^{-1} - (\sin\gamma/\sin\theta_l)/\tan\psi] + i2\pi\alpha a/\sin\psi$. Here, we have used $\sin\theta_l = k_l/k$, an alternative form for the definition of the leaky wave-coupling angle. Using Eq. (2), this result can be written as $\Gamma_1 = 2\pi k_l a\sin\psi + i(2\pi\alpha a/\sin\psi)$.

It follows from similar arguments that the contribution to the leaky wave pressure at point A by the nth leaky ray in the family, $p_l^{(n)}$, is given by Eq. (3) with an additional factor of $\exp(in\Gamma_1)$. Summing all contributions $p_l^{(n)}$ gives the total helical leaky wave pressure p_l at point A due to the lth class of leaky wave, with the resulting sum being proportional to a geometric series. An analogous result is obtained in summing the backscattering contributions from repeated circumnavigations of leaky Lamb waves on cylindrical shells under broadside illumination.[4,9]

Construction of a relevant ray tube allows one to propagate the leaky wave pressure p_l from the surface of the cylinder at $x=(2\pi-\phi)a$ to the far field in the specular direction. This far-field pressure will be denoted by p_{lff}. Figure 6 of Paper M shows the projection of helical ray paths onto a plane perpendicular to the cylinder axis (a plane of constant y), where the angle labeled as the leaky wave-coupling angle θ_l in that figure is replaced here by the azimuthal launching angle ϕ for oblique incidence. In this plane, the outgoing wave appears to diverge from a point at a distance $a\cos\phi$ behind the detachment point of the helical ray on the cylinder surface (point B' in Paper M, Fig. 6). This results in a far-field pressure of magnitude $|p_{lff}| = (a\cos\phi/r)^{1/2}|p_l|$, where r is the distance from the cylinder's axis to the observation point. The phase of p_{lff} corresponds to the phase of $p_l\exp(ikq\cos\gamma + iky\sin\gamma)$, where $q = r - a\cos\phi$ and y is the axial coordinate of the observation point. Here, q is the length of the propagation distance of the outgoing ray from the detachment point B' to the far-field point as projected onto a plane of constant y and $k\cos\gamma$ gives the magnitude of the projection of the outgoing wave vector in that plane. Part of the phase can also be written $kq\cos\gamma = kr\cos\gamma - ka\cos\theta_l$ using the identity $\cos\theta_l = \cos\gamma\cos\phi$ which follows from Eq. (1). Thus, the far-field pressure in the specular direction is

$$p_{lff} = (a\cos\phi/r)^{1/2} p_l e^{ikr\cos\gamma - ika\cos\theta_l} e^{iky\sin\gamma}. \tag{4}$$

It is convenient to express the far-field pressure in terms of a dimensionless form function f defined by the equation $p_{lff} = p_i(a/2r)^{1/2} f\exp(ikr\cos\gamma + iky\sin\gamma)$ as in Eq. (1) of Ref. 7. Here, y is the axial coordinate of the far-field point. The coordinate y_0 is determined in Eq. (3) from the required phase dependence on y and geometric construction. Comparing the form function definition with Eq. (4) and using the expression for the total leaky wave pressure p_l, we find that

$$f_{lh} = -\frac{8\alpha a}{\sin\psi}\sqrt{\frac{\pi}{ka\cos\gamma}}\, e^{i\varphi_{bl} + i\pi/2} e^{-i2ka\cos\theta_l} \times \frac{e^{ik_l\sigma\sin^2\psi} e^{-\alpha\sigma}}{(1 - e^{i2\pi k_l a\sin\psi - 2\pi\alpha a/\sin\psi})}, \tag{5}$$

where, to obtain this expression, the approximation $k_p \approx k_l$ is used for the factor $(k_p)^{-1/2}$ in Eq. (3). This is the form function due to helical wave contributions in the specular direction. Note that a factor of 2 is included in the final expression for f_{lh} to account for an identical scattering contribution due to rays that circumnavigate the cylinder with the opposite helicity (helix angle $-\psi$). In the broadside limit, $\gamma\to 0$, this expression agrees with Eq. (3) of Ref. 9 (modified to allow for $\varphi_{bl}\neq 0$), which gives the backscattering form function for leaky wave contributions from an infinite cylindrical shell under broadside illumination.

The form-function symbol has the subscript lh to indicate that this result only accounts for the contributions due to leaky helical rays. The form-function modulus for meridional ray contributions, $|f_{lm}|$, is given by Eq. (26) of Ref. 7 for a tilted infinite cylinder. Upon combining this with the correct phase of f_{lm}, as discussed in Appendix A of Ref. 7, the meridional ray form function may be added to the helical ray form function of Eq. (5), giving

$$f_{lt} = f_{lh} + f_{lm}. \tag{6}$$

Equation (6) gives the total leaky ray contribution for leaky waves of class l to the far-field scattering form function in the specular direction. It should be kept in mind with regard to Eq. (6) that meridional ray contributions require a different ray analysis from the one used here (see Ref. 7). One cannot recover the meridional ray enhancement from the helical ray analysis by simply setting the tilt angle equal to the meridional condition, $\gamma=\theta_l$, in the helical ray form function. In fact, f_{lh} vanishes in the limit $\gamma\to\theta_l$ according to Eq.

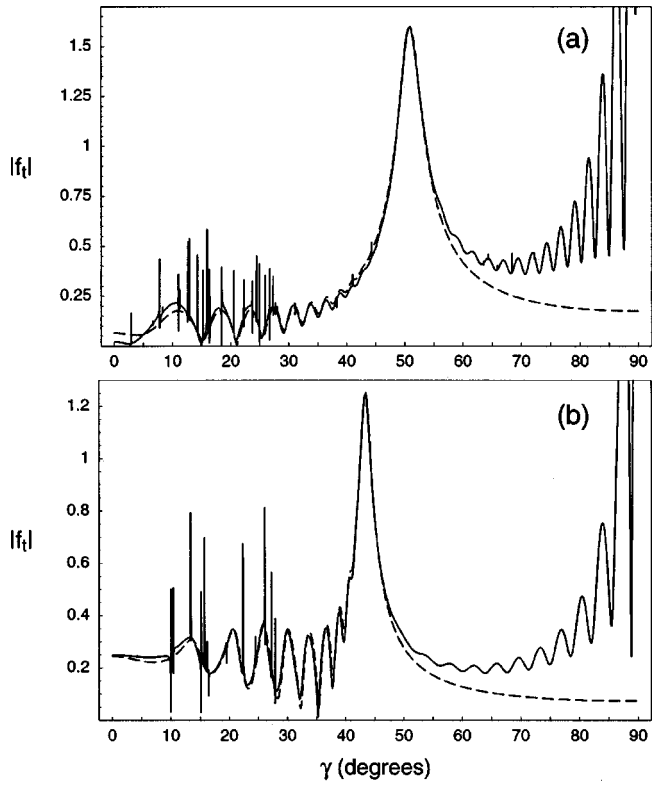

FIG. 3. Far-field scattering form function in the specular direction as a function of tilt angle at fixed frequency for plane-wave scattering by an infinitely long, empty steel cylindrical shell (SS304). (a) Corresponds to a shell 7.6% thick (shell A) at $ka=30$ and (b) corresponds to a shell 16.25% thick (shell B) at $ka=20$. The solid curve is the partial wave series solution with a rigid background subtraction. The dashed curve is the ray theory given by Eq. (6) which has no free parameters. The ray theory combines the helical and meridional ray contributions of leaky flexural waves. The large peak in both plots is the meridional ray enhancement and the smaller peaks at smaller tilt angles are due to helical waves. It is important to allow the meridional and helical ray contributions to interfere with each other to recover the correct shape of the form function out to the position of the meridional peak.

(5). This can be interpreted physically as the damping out of the helical ray contributions due to the elongation of their ray paths as the helix angle ψ goes to zero.

III. COMPARISON OF RAY THEORY WITH PARTIAL WAVE SERIES

The ray prediction for the total leaky ray contribution to the form function f_{lt} was compared against an exact PWS solution for the case of an infinitely long evacuated stainless-steel shell of type 304 (SS304). The material parameters for SS304 and those used for water are given in Sec. I of Ref. 1. Two shells of differing thicknesses, labeled A and B, were used in the comparison, as was done in Ref. 1. Shells A and B have thickness-to-radius ratios of $h/a=0.076$ and $h/a=0.1625$, respectively, where $h=a-b$ is the thickness of the shell. From the dispersion curves for these shells, the coincidence frequencies correspond to $ka\sim16$ and 7, respectively.[1] There is evidence that flexural helical wave contributions to the scattering are significant for these shells.[1,3]

Figure 3 shows both the ray theoretic and PWS solutions for the form-function magnitude in the specular direction plotted as a function of tilt angle γ. Figure 3(a) is the plot for the thinner of the two shells, shell A, at $ka=30$, and Fig. 3(b) is the corresponding plot for shell B at $ka=20$. In both figures, the dashed curve is the form-function magnitude for the ray solution given by Eq. (6) and the solid curve is the PWS solution. As in Ref. 1, a rigid background was subtracted from the PWS solution in order to eliminate the contribution of the specular reflection which was not included in the ray analysis.

A large peak in the scattering at $\gamma\approx51°$ in Fig. 3(a) and $\gamma\approx43°$ in Fig. 3(b) corresponds to the a_0 meridional ray enhancement. The broad oscillations at smaller tilt angles are due to contributions of a_0 helical rays. The ray theory is in good agreement with the PWS solution from near broadside, $\gamma\approx0°$, to the meridional condition, $\gamma\approx\theta_l$, although the agreement seems to be better for those helical wave peaks that are not too close to the meridional peak. This is because near the meridional condition helical ray paths lengthen, which increases the sensitivity of the errors in the calculation of leaky wave attenuations. This discrepancy is more pronounced at higher frequencies where the complex leaky wave numbers k_p are larger, thus yielding larger percent errors. The peaks in the PWS result near γ of 90° (corresponding to axial illumination) are also evident in Ref. 1. These peaks are unrelated to the leaky helical and meridional ray contributions under investigation. It should also be mentioned that the dashed curves in Fig. 3 are not meant to reproduce the sharp peaks in the PWS solution that appear in the tilt-angle range $0°\leqslant\gamma\leqslant30°$. These are meridional or helical wave contributions from weakly damped compressional waves on the shell (analogous to s_0 leaky Lamb waves) or contributions from weakly damped torsional waves. In Fig. 3, the ray theory only attempts to model the flexural wave contributions, since it is those contributions that are likely to be the most important in wide-bandwidth sonar.

IV. ANISOTROPY OF HELICAL FLEXURAL LEAKY WAVE PARAMETERS

The general agreement of the ray synthesis of the helical flexural leaky wave contributions with the PWS result was only possible by including the weak anisotropy of the parameters c_l and α in the evaluation of Eq. (5). This anisotropy appears to be a more significant difficulty than in previous studies of helical leaky wave-scattering contributions associated with compressional waves on thin shells.[4,5]

Leaky wave numbers k_p on the shell were calculated by extending the method of Kargl[10] to the case of a cylindrical target. They are, in essence, the roots of the determinant $D_n(ka,k_ya)$ in the denominators of the exact PWS,[11] where n is the partial wave index and $k_y=k\sin\gamma$ is the projection of the incident wave vector along the cylinder's axis. The expression for D_n is simplified here by taking the interior of the shell to be a vacuum. Morse[1] previously found the leaky wave numbers for meridional rays by setting $n=0$ and calculating the k_y roots of the equation $D_n(ka,k_ya)=0$ for fixed ka. The partial wave index corresponds to the circumferential component of the leaky wave vector (in units of $1/a$), which is zero for the meridional ray. The calculated

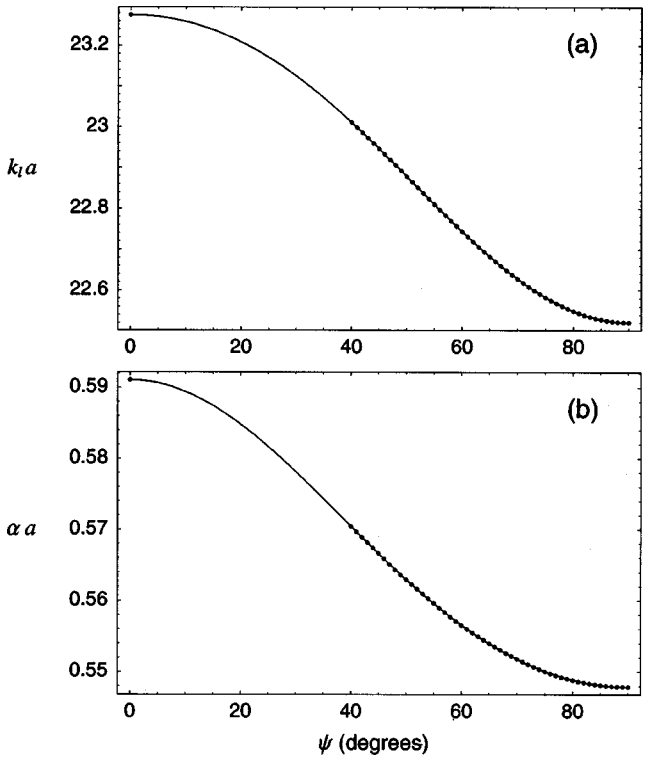

FIG. 4. Helical flexural leaky ray wave numbers for shell A at $ka=30$ as a function of helix angle. (a) Is a plot of the real part and (b) the imaginary part of the wave number. The solid points are wave numbers calculated by finding complex roots of Eq. (7). The solid curve is the least-squares fit of those points to a Fourier series of period π [Eq. (8)]. The shell medium is noticeably anisotropic. Both the real and imaginary parts of the wave number are greater in the axial direction ($\psi=0°$) than in the circumferential direction ($\psi=90°$).

roots were used for k_p in the expression for f_{lm}, the meridional ray contribution to the total form function of Eq. (6). The helical wave roots were calculated in a different manner since their corresponding wave vectors do have circumferential components. If k_p is the leaky wave number for a helical ray which travels on the cylinder with helix angle ψ, then the x component of the leaky wave vector is $k_x=k_p \sin \psi$, as can be inferred from the diagram in Fig. 2. The y component is then $k_y=k_p \cos \psi$. The leaky wave numbers k_p for helical rays are then found from the complex k_p roots of the equation

$$D_\nu(ka,k_y a)=0, \tag{7}$$

where $k_y a=k_p a \cos \psi$ and $\nu=k_p a \sin \psi$ for fixed ka and ψ. Thus, the helical ray wave numbers depend not only on the frequency ka but also on propagation direction ψ, so that the shell appears to the helical rays to be an anisotropic medium. This procedure for finding the roots was tested by replacing $D_\nu(ka,k_y a)$ by the simpler determinant given in Ref. 7 for a solid rod.

Figure 4 shows a plot of helical ray leaky wave numbers as a function of ψ. These were calculated for shell A at $ka=30$, corresponding to the form function plot in Fig. 3(a). The real part of the leaky wave number, $k_l a$, is plotted in Fig. 4(a) and the imaginary part, αa, in Fig. 4(b). The leaky wave numbers were calculated starting at $\psi=90°$, corresponding to leaky waves that propagate strictly in a circumferential direction, and continuing downward in helix angle in 1-degree steps until $\psi \approx 40°$. The meridional ray root, as calculated by Morse (Table I of Ref. 1), is plotted at $\psi=0$. Except at $\psi=0$, the root-finding algorithm fails for $\psi<40°$ for reasons that are not easily determined. The relevant parameters may be interpolated between the available roots by fitting those roots to the first five terms of a Fourier series using the method of least squares

$$k_l(\psi)=k_{0l}+\sum_{j=1}^{4} k_{jl} \cos(2j\psi), \tag{8}$$

with an analogous series for the damping parameter α. The fitted curves are given by the solid lines in Fig. 4. The fundamental period is required to be π. This ensures that the fitted curves are symmetric about the points $\psi=0$ and $\psi=90°$, which must be true for physical reasons. Five terms were sufficient to provide an adequate fit. The interpolation functions $k_l(\psi)$ and $\alpha(\psi)$ can be converted to functions of tilt angle γ using Eq. (2), giving k_p as a function of ka and γ. This is then inserted into the helical ray form-function expression f_{lh} of Eq. (5) and used to construct the plots of Eq. (6) in Fig. 3. The interpolation for $0<\psi<40°$ affects only the helical contribution close to the meridional ray peak, which is where the helical contribution is generally weak as explained below Eq. (6). For example, in Fig. 3(a), $\gamma=36.4°$ corresponds to $\psi=40°$.

Inspection of Fig. 4(a) shows that k_l increases for propagation along the cylinder's axis ($\psi=0$) when compared with propagation perpendicular to the cylinder's axis ($\psi=90°$). The sign and magnitude of the anisotropy are similar at other frequencies for the ka range examined (30 to 40 for shell A and 20 to 30 for shell B). Pierce and Kil[12] discuss an approximation for the anisotropy of k_l for flexural waves on thin shells [their Eq. (19a)] which makes use of an assumption that the frequency ω greatly exceeds the ring frequency $\omega_{\text{ring}}=[E/\rho_e(1-\nu^2)]^{1/2}$, where E is Young's modulus, ρ_e is the density of the shell, and ν is Poisson's ratio. Expressed using the wave number in water k, the ring frequency is $(ka)_{\text{ring}}=c_p/c=3.52$ (for stainless steel), where c_p denotes the compressional plate wave speed. Consequently the ka values considered by us greatly exceed the $(ka)_{\text{ring}}$ and, as reviewed by Pierce and Kil, it is appropriate to classify one of the shell waves as a flexural wave. The anisotropy predicted by Pierce and Kil gives a decrease in k_l for $\psi=0$ and the anisotropy is smaller in magnitude. Evidently, their approximation breaks down above the coincidence frequency because the assumptions of thin-shell mechanics are not applicable at such high frequencies for steel shells in water. Their result that k_l is predicted to decrease for propagation with $\psi=0$ remains when fluid loading is included in the analysis for thin shells.[13]

V. DISCUSSION

Ray methods are important tools used to describe and interpret the scattering responses from shell structures. These theories are not limited to extremely high frequency, as Fig. 3 clearly shows that there is agreement between ray and wave solutions at frequencies as low as $ka=20$. Compari-

sons at larger *ka* values not presented here show similar agreement except for the discrepancies at tilt angles slightly less than the meridional tilt ($\gamma = \theta_l$) discussed in Sec. III. The ray theory was applied to the infinite cylinder to facilitate a good computational test since an exact PWS solution is available. One objective of ray theories is to understand and model the scattering from structures more complicated than infinite cylindrical shells, where exact wave solutions may not be available. The verification given here of the combined meridional and helical ray models is important for the ray analysis of more realistic targets. The meridional ray enhancement is an important scattering mechanism to model because the path does not involve the backside of the cylinder. Helical waves, by contrast, propagate around the backside of the shell and tend to give weaker contributions. Figure 3 shows, however, that helical flexural waves give significant contributions to the scattering. The helical wave scattering amplitudes appear to be relatively large for the thicker of the shells (compare the form function of shell B to shell A).

ACKNOWLEDGMENT

This work was supported by the Office of Naval Research.

[1] S. F. Morse and P. L. Marston, ''Meridional ray contributions to scattering by tilted cylindrical shells above the coincidence frequency: Ray theory and computations,'' J. Acoust. Soc. Am. **106**, 2595–2600 (1999).

[2] G. Kaduchak, C. M. Wassmuth, and C. M. Loeffler, ''Elastic wave contributions in high-resolution acoustic images of fluid-filled, finite cylindrical shells in water,'' J. Acoust. Soc. Am. **100**, 64–71 (1996).

[3] S. F. Morse, P. L. Marston, and G. Kaduchak, ''High-frequency backscattering enhancements by thick finite cylindrical shells in water at oblique incidence: Experiments, interpretation, and calculations,'' J. Acoust. Soc. Am. **103**, 785–794 (1998); S. F. Morse, ''High frequency acoustic backscattering enhancements for finite cylindrical shells in water at oblique incidence,'' Ph.D. dissertation, Washington State University, Department of Physics, 1998; S. F. Morse and P. L. Marston, ''Degradation of meridional ray backscattering enhancements for tilted cylinders by mode conversion: Wide-band observations using a chirped PVDF sheet source, IEEE J. Oceanic Eng. **26**, 152-155 (2001).

[4] L. B. Felsen, J. M. Ho, and I. T. Lu, ''Three dimensional Green's function for fluid-loaded thin elastic cylindrical shell: Alternative representations and ray acoustic forms,'' J. Acoust. Soc. Am. **87**, 554–569 (1990); A. N. Norris and D. A. Rebinsky, ''Acoustic coupling to membrane waves on elastic shells,'' *ibid*. **95**, 1809–1829 (1994); D. A. Rebinsky and A. N. Norris, ''Benchmarking an acoustic coupling theory for elastic shells of arbitrary shape,'' *ibid*. **98**, 2368–2371 (1995).

[5] M. L. Rumerman, ''Contribution of membrane wave reradiation to scattering from finite cylindrical steel shells in water,'' J. Acoust. Soc. Am. **93**, 55–65 (1993).

[6] L. Haumesser, A. Baillard, D. Décultot, and G. Maze, ''Behavior of first guided wave on finite cylindrical shells of various lengths: Experimental investigation,'' J. Acoust. Soc. Am. **109**, 583–590 (2001); N. Touraine, L. Haumesser, D. Décultot, G. Maze, A. Klauson, and J. Metsaveer, ''Analysis of the acoustic scattering at variable incidences from an extra thin cylindrical shell bounded by hemispherical endcaps,'' *ibid*. **108**, 2187–2196 (2000).

[7] P. L. Marston, ''Approximate meridional leaky ray amplitudes for tilted cylinders: End-backscattering enhancements and comparisons with exact theory for infinite solid cylinders,'' J. Acoust. Soc. Am. **102**, 358–369 (1997); **103**, 2236 (1998).

[8] P. L. Marston, ''Spatial approximation of leaky wave surface amplitudes for three-dimensional high-frequency scattering: Fresnel patches and application to edge-excited and regular helical waves on cylinders,'' J. Acoust. Soc. Am. **102**, 1628–1638 (1997).

[9] N. H. Sun and P. L. Marston, ''Ray synthesis of leaky Lamb wave contributions to backscattering from thick cylindrical shells,'' J. Acoust. Soc. Am. **91**, 1398–1402 (1992).

[10] S. G. Kargl and P. L. Marston, ''Observations and modeling of the backscattering of short tone bursts from a spherical shell: Lamb wave echoes, glory, and axial reverberations,'' J. Acoust. Soc. Am. **85**, 1014–1028 (1989); **89**, 2462 (1991).

[11] F. Léon, F. Lecroq, D. Décultot, and G. Maze, ''Scattering of an obliquely incident acoustic wave by an infinite hollow cylindrical shell,'' J. Acoust. Soc. Am. **91**, 1388–1397 (1992).

[12] A. D. Pierce and H.-G. Kil, ''Elastic wave propagation from point excitations on thin-walled cylindrical shells,'' Trans. ASME, J. Vib. Acoust. **112**, 399–406 (1990).

[13] A. D. Pierce, ''Waves on fluid-loaded inhomogeneous elastic shells of arbitrary shape,'' Trans. ASME, J. Vib. Acoust. **115**, 384–390 (1993).

Application of three-dimensional resonant acoustic spectroscopy method to rock and building materials

Lev Ostrovsky
Zel Technologies/NOAA Environmental Technology Laboratory, 325 Broadway, Boulder, Colorado 80305 and Institute of Applied Physics, Russian Academy of Sciences, Nizhny Novgorod, Russia

Andrey Lebedev, Alexander Matveyev, Andrey Potapov, Alexander Sutin, and Irina Soustova
Institute of Applied Physics, Russian Academy of Sciences, Nizhny Novgorod, Russia

Paul Johnson
Los Alamos National Laboratory, Los Alamos, New Mexico 87501

(Received 12 December 2000; accepted for publication 16 July 2001)

This paper presents the experimental and theoretical results of applying resonant acoustic spectroscopy (RAS) to determine elastic parameters and losses in such consolidated granular materials as rock and building bricks. First, the theoretical aspects of the RAS method are outlined. A computer code for the rectangular and cylindrical samples was developed and tested. The results of experiments on specimens of rock and ceramic brick are then described. Finally, a modification of the previously published RUS algorithm is presented which permits a significant reduction in computing time for elongated samples. © *2001 Acoustical Society of America.*
[DOI: 10.1121/1.1402255]

PACS numbers: 43.20.Ks, 43.60.Pt, 91.60.Lj [ANN]

I. INTRODUCTION

Among the fundamental characteristics of crystalline and noncrystalline materials are their elastic constants. Knowledge of the elasticity tensor is very important, in particular, for geophysical applications, where elastic constants obtained from seismic data provide information about Earth's interior structure.[1] Elastic constants are determined as derivatives of the free elastic energy with respect to the components of strain tensor. In the linear approximation, when the elastic energy is quadratic in strain, the number of independent elements of elastic tensor C_{ijkl} is, in the general case, 21. Symmetries of a specific crystal group (or crack/pore distribution) further reduce the number of independent constants (e.g., 2 for an isotropic medium, 3 for a cubic symmetry, 5 for hexagonal, and 6 for tetragonal).

There exist various methods for measuring elastic constants. They are considered in detail, for example, in Refs. 2 and 3. Until recently, most often used have been the methods based on pulse propagation. However, along with an obvious simplicity, they have shortcomings associated with a relatively low preciseness. In particular, errors are associated with high-frequency sound scattering by grains in rock samples.[4] Another group is resonance methods based on the measurement of resonance frequencies of a sample and an inversion for its elastic parameters. Introduced as early as the 1960s–70s, they have attracted a broad interest relatively recently, with the development of computer data processing. These methods are known as resonant ultrasound spectroscopy, RUS. The method was designed first for samples of spherical geometry.[4] Later, with the advent of the numerical solutions to inverse problems, it became possible to analyze resonant frequencies of a sample of arbitrary geometry. In Ref. 3 it is stated that the RUS technique provides the highest accuracy for elastic moduli determination.

A typical algorithm of RUS is based on the Lagrangian approach: a basis of eigenfunctions is substituted into Lagrangian equations which leads to an eigenvalue problem. Since the infinite-dimensional eigenvalue problem cannot be solved in general, approximate variational methods such as the Rayleigh–Ritz algorithm are used which involve a finite set of basis functions. Then, some M approximate eigenvalues and the corresponding eigenfunctions are obtained. If the series of basis functions is chosen properly, the lower eigenvalues can be calculated quite accurately. For rectangular samples, products of Legendre polynomials are typically used as basis functions for displacement.

In later works, products of power functions were suggested as a basis. Visscher *et al.*[5] have pointed out that using basis functions of the form $x^l y^m z^n$ allows for a solution for samples of several different shapes (shells, bells, cylinders, eggs, potatoes, etc.). This approach is known as the "algorithm of Ming/Migliori/Visscher."

The RUS analysis algorithm requires that RUS measurements determine the natural frequencies of a sample with stress-free boundary conditions. Resonance oscillations are excited by one transducer. The second transducer measures the amplitude and phase of the sample's response. To obtain the desired accuracy, one must minimize sample loading by the transducers. Ohno[6] proposed a method to control such a loading: a rectangular sample was supported by transducers at its opposite corners. The corners were used for contact because the displacements have a maximum in these points. Unlike conventional ultrasonic pulse measurements where strong coupling between the transducer and the sample is needed, the RUS method is attractive in that the sample acts as a natural amplifier due to resonance with a gain equal to the quality factor, so that strong coupling with the source is not necessary.

In our study we used the RUS technique modified for

 0001-4966/2001/110(4)/1770/8/$18.00

finding the complex elasticity tensor of large samples of structured materials such as rocks and ceramics. Because of the relatively low frequency range, this method is free of the shortcomings of impulse measurements such as local scattering from local inhomogeneities, at least when the macroscopic sample parameters are of interest, or the nondestructive testing is being performed. We also suggest a modification of the RUS algorithm to significantly reduce the computing time for prolate cylindrical bars often used in experiments. Due to the large size of the rock samples in contrast to most of RUS measurement in crystals, the frequency range for our measurements was between 1 and 40 kHz. Thus, instead of RUS (resonant ultrasound spectroscopy) we suggest the name RAS (resonant acoustic spectroscopy).

A first application of resonant spectroscopy to rock (granites) is described in the early work by Birch[4] who used a spherical sample and derived its elastic parameters. Hence, the present paper can be somewhat considered a development of Birch's work with the use of more recent RUS algorithms, different materials and specimen shapes. The code developed here is applicable for both rectangular and cylindrical sample geometries. Experimental verification of the code, including its modification for elongated samples, was performed for rectangular parallelepipeds. Workability of the modified code for thin cylindrical bars was tested by using asymptotic analytical solutions.

II. BASIC RELATIONS FOR THE RAS METHOD

A. General consideration

As mentioned above, RAS analysis is based on the use of the variational principle and the Rayleigh–Ritz method, i.e., an approximation of eigenvectors of variational equations by a proper set of basis functions.[3] We begin with outlining the direct problem: finding the resonance frequencies. Since the RUS algorithm is thoroughly described in, e.g., Ref. 3, here we omit all intermediate equations and concentrate on main results on which our program has been based and then on the specifics of long samples (subsection E). The most usable sets of basis functions for a cylindrical sample are products of exponents:[5]

$$\Psi_\nu(x_1,x_2,x_3)=\left(\frac{x_1}{R}\right)^{n_1}\left(\frac{x_2}{R}\right)^{n_2}\left(\frac{2x_3}{H}\right)^{n_3},$$
$$\nu=\{n_1,n_2,n_3\}, \tag{1}$$

where R and H are the radius and the length of the cylinder, respectively. The basis Eq. (1) can also be used for the rectangular parallelepiped shape (for the sake of brevity, we shall occasionally refer to the latter as rectangular shape). For the analysis of our experiments with rectangular samples we shall use Legendre polynomials.[3] [However, in the last section we shall use the representation Eq. (1) as well]:

$$\Psi_\nu(x_1,x_2,x_3)=P_{n_1}\left(\frac{2x_1}{L_1}\right)P_{n_2}\left(\frac{2x_2}{L_2}\right)P_{n_3}\left(\frac{2x_3}{L_3}\right),$$
$$\nu=\{n_1,n_2,n_3\}, \tag{2}$$

where L_j are sides of the parallelepiped.

The displacement vector **u** can be represented as a series:

$$u_i(x_1,x_2,x_3)=a_{i\nu}\Psi_\nu(x_1,x_2,x_3). \tag{3}$$

The indexes n_1, n_2 and n_3 in Eq. (1) are chosen to provide integration inside the sphere

$$|k|\leqslant K \tag{4}$$

in the wave number space. The value of K can be evaluated using a simple idea: $K=\max(\omega)/\min(V)$, where $\max(\omega)$ is maximal frequency to be determined and $\min(V)$ is minimal phase velocity in the considered frequency range, $\min(\omega)\leqslant\omega\leqslant\max(\omega)$. On the other side, the absolute value of wave vector can be evaluated as ($|k|\leqslant K$)

$$|k|\simeq\pi\sqrt{\left(\frac{n_1}{L_1}\right)^2+\left(\frac{n_2}{L_2}\right)^2+\left(\frac{n_3}{L_3}\right)^2}, \tag{5}$$

where L_j are characteristic dimensions of the sample. If the number of frequencies which have wave vectors inside the sphere Eq. (4) is large enough and all sizes L are of the same order, this coincides with the rule

$$n_1+n_2+n_3\leqslant N, \tag{6}$$

proposed in Refs. 7 and 5 for a nearly cubic shape. Here N is related to the number of resonance frequencies to be determined: $(N+1)(N+2)(N+3)/6$.

As mentioned, the Lagrangian approach is typically used for such problems. As the Lagrangian $L(a_\gamma)$ is stationary at natural frequencies (a_γ are the complex amplitudes of eigenmodes), all derivatives $\partial L/\partial a_\gamma$ must be zero. As a result, resonance frequencies ω_γ can be determined as a solution for the eigenvalue problem (the notation of Ref. 5 is used):

$$\omega^2\hat{E}_{ik\nu\gamma}a_{k\gamma}=\hat{\Gamma}_{ik\nu\gamma}a_{k\gamma}. \tag{7}$$

Here the "mass" matrix $\hat{E}$ for a homogeneous sample is defined as follows:

$$\hat{E}_{ik\nu\gamma}=\rho\omega^2\langle\Psi_\nu|\Psi_\gamma\rangle\delta_{ik}. \tag{8}$$

For a homogeneous sample, the "rigidity" matrix $\hat{\Gamma}$ can be written in the following form:

$$\hat{\Gamma}_{ik\nu\gamma}=\sum_{j,l}^{3}C_{ijkl}b_{jl}(n_1,n_2,n_3|\tilde{n}_1,\tilde{n}_2,\tilde{n}_3). \tag{9}$$

The values of $\langle\Psi_\nu|\Psi_\gamma\rangle$ and b_{jl} related to the basis functions Ψ_γ are defined in the Appendix for both rectangular and cylindrical geometries of a specimen.

As the tensor C_{ijkl} is symmetrical,[8] the matrix $\hat{\Gamma}$ is symmetrical too. Because the matrix $\hat{E}$ is positive definite, the corresponding eigenvalues of Eq. (7) are real. Then, we can use one of the standard methods to solve the problem in Eq. (7) (see, e.g., Ref. 9).

In what follows we shall use this standard approach for our experiments with RAS of rectangular specimens.

B. Calculation of dissipative parameters

For the materials considered here, due to their complex grainy structure, losses are a very important characteristic

which can, in particular, prevent using high-frequency impulse methods of testing. Usually losses in solids are described by small imaginary parts of elastic moduli. Such a description is valid for a wide range of frequencies[10] and can be invalid only for specific conditions, for example, when grain sizes are compatible with the length of the elastic waves. Therefore, the elastic moduli can be written as follows (the standard double-subscript notation is used below[8]):

$$C_{kl} - i\tilde{C}_{kl} = C_{kl}(1 - i\,\eta_{kl}), \tag{10}$$

where η_{kl} are small dimensionless parameters representing the internal friction normalized by the elastic constants C_{kl}.

In the paper in Ref. 11, a possible way to determine dissipation parameters was proposed. The main idea of this paper is, in fact, the perturbation method: i.e., to use a RAS solution for a medium without losses as a basic solution and then make corresponding adjustments. The resonance frequency of each mode is a function of the elastic moduli C_{kl}, the size of the sample L_j, and the material density ρ:

$$\omega_n = \omega_n(C_{kl}, L_j, \rho). \tag{11}$$

It is assumed that the functions ω_n of all their arguments in Eq. (11) are regular. Using the Cauchy–Riemann conditions for the complex functions Eq. (11), written separately for each variable, one immediately obtains (all derivatives correspond to $C_{kl}^{(0)}$ that are the solutions of RUS problem without losses):[12]

$$\begin{aligned} \Delta\omega_n &= \sum_{k,l} \left(\frac{\partial \omega_n}{\partial C_{kl}} \Delta C_{kl} - \frac{\partial \tilde{\omega}_n}{\partial C_{kl}} C_{kl}^{(0)} \eta_{kl} \right), \\ \tilde{\omega}_n &= \sum_{k,l} \left(\frac{\partial \omega_n}{\partial C_{kl}} C_{kl}^{(0)} \eta_{kl} + \frac{\partial \tilde{\omega}_n}{\partial C_{kl}} \Delta C_{kl} \right), \end{aligned} \tag{12}$$

where ΔC_{kl} are the adjustments of the real parts of elastic moduli due to losses, $\Delta\omega_n$ is the perturbation of an nth resonance frequency, $\tilde{\omega}_n = \omega_n / 2\mathcal{Q}_n$, and $\mathcal{Q}_n$ is the Q-factor for the frequency ω_n. If $\mathcal{Q}_n \gg 1$, all terms in the first equation of Eqs. (12) and, consequently, $\Delta\omega_n$ are of the second order with respect to $\tilde{\omega}_n$. Hence, the change of resonance frequencies due to losses can be neglected. Similarly, the last term in the expression for $\tilde{\omega}_n$ can also be omitted. As a result, the loss factors η_{kl} for the elastic moduli can be determined as a solution of a linear set of equations:

$$\sum_{k,l} \frac{\partial \omega_n}{\partial C_{kl}} C_{kl}^{(0)} \eta_{kl} = \frac{\omega_n}{2\mathcal{Q}_n}. \tag{13}$$

For the overdetermined set of equations in Eq. (13), η_{kl} are the medium parameters to be found. The measured values in Eq. (13) are resonance frequencies ω_n and quality factors $\mathcal{Q}_n$. From Eq. (13) one can also predict Q_n using the tensor η_{kl}.

C. Inverse problem

Equations (7) and (13) allow one to solve a general direct problem of resonant acoustic spectroscopy for samples with dissipation. To solve the inverse problem, one should start with a guessed set of elastic constants in the direct problem and then use an iteration procedure to find the set of constants in question. Random errors can be reduced by using a larger number of measured frequencies and solving a least squares problem. In general, numerous iteration algorithms and fitting criteria can be used to find the best approach for obtaining the values of the elastic constants with the needed accuracy.[13]

The problem is commonly formulated as one of minimization of the mean-square-root difference between the measured and calculated resonance frequencies or, more exactly, of the corresponding functional. The latter can be defined as

$$\varepsilon = \sqrt{\sum_{n=1}^{N} (f_n - \check{f}_n)^2 \Big/ \sum_{n=1}^{N} (\check{f}_n)^2}, \tag{14}$$

where f_n are calculated frequencies depending on current values of C_{ijkl}; subscript "n" denotes the number in the list of frequencies (in ascending order); $\check{f}_n$ are the corresponding measured values of the frequencies. Experimental mode identification can be successfully used to eliminate ambiguity and regular errors in the evaluation of C_{ijkl}.[14] However, such identification is a very complicated problem, and we did not use it here. In this paper we restricted ourselves to the use of Eq. (14) to define fit error in the inverse RAS problem.

The problem of finding medium parameters which minimize the difference between experimental data and calculations can be represented by a system of equations

$$d_l(\mathbf{p}) = 0, \quad l = 1,2,\ldots,n, \tag{15}$$

where $\mathbf{p} = p_1, \ldots p_n$ is the vector of parameters to be determined. In our case, functions d_l in Eq. (15) are the differences $f_j^{(i)} - \check{f}_j^{(i)}$. In terms of the extremal problem, the system Eq. (15) is equivalent to the problem of minimization of the function:[15]

$$\mathcal{D}(p_1, p_2, \ldots, p_n) \equiv \sum_{l=1}^{n} |d_l(p_1, p_2, \ldots, p_n)|^2, \tag{16}$$

or of any other monotonically increasing function of $|d_l|$. In particular, the value of ε defined above can also be used as the function $\mathcal{D}$.

To solve the problem Eq. (16) by an iteration method, one should start with some arbitrary values $p_l^{[0]}$. Then sequential approximations are created:

$$p_l^{[k+1]} = p_l^{[k]} + \delta p_l^{[k]}, \tag{17}$$

which should converge to the "exact" values $\mathbf{p}$ when $k \to \infty$.

To reduce the time of calculations, gradient schemes are usually used. In what follows we use Newton's gradient method. Namely, one finds sequential approximations for $p_l^{[k]}$ as the solution of a set of linear equations:

$$d_l(\mathbf{p}^{[k]}) + \sum_{j=1}^{n} \left. \frac{\partial d_l}{\partial p_j} \right|_{\mathbf{p}=\mathbf{p}^{[k]}} \delta p_j^{[k]} = 0. \tag{18}$$

The convergence conditions for procedure Eq. (18) are defined by the Kantorovich theorem.[15]

The number of measured and predicted (from the direct problem) resonance frequencies is typically greater than the

number of parameters to be determined. In this case the solution of Eq. (18) can be obtained as that of the corresponding least squares problem:

$$\delta\mathbf{p} = -(\hat{\mathcal{A}}^T\hat{\mathcal{A}})^{-1}\hat{\mathcal{A}}^T\mathbf{d}, \tag{19}$$

where $\delta\mathbf{p} = \mathbf{p}^{[k+1]} - \mathbf{p}^{[k]}$, $\hat{\mathcal{A}} = (\partial d_l / \partial p_j)$, $\mathbf{d}$ is the vector of functions d_l, and $\hat{\mathcal{A}}^T$ is a transposed matrix. We shall use this scheme in calculations presented below.

D. Test of the code

To verify the workability of our code we applied it to the data given in the book[3] (page 112, data for steel sample 5120). The corresponding parameters are: elastic moduli $C_{11} = 2.7372 \cdot 10^{11}$ Pa, $C_{44} = 8.9190 \cdot 10^{10}$ Pa, density $\rho = 7790$ kg/m^3 and sample size $3.045 \times 2.665 \times 2.645$ mm^3. Data presented in Ref. 3 were obtained for $N = 10$ and the inequality (6) was used. We used the same conditions in our calculations too. The difference in calculated frequencies appears only in sixth digit. Thus our code works as well as that of Ref. 3 for rectangular geometry.

To evaluate this code for cylindrical geometry, we compared its results with analytical models such as Pochgammer-Chree equation[16] for compression modes and Timoshenko's equations for flexural modes.[17] As is well known, these models give a good approximation for long cylindrical bars. Indeed, as a cylinder becomes longer/thinner, the difference between the corresponding asymptotic solutions and numerical calculations becomes negligible (see Ref. 18). Both inequalities (6) and (20) (see the next subsection for the latter) were tested to verify the code for the cylindrical geometry.

E. Modification of RAS method for prolate specimens

To conclude the theoretical part, we suggest a useful modification of RAS that may enable one to significantly save computer time when prolate objects with $L_1 \gg L_{2,3}$ (such as many borehole specimens) are tested. In this case, the use of the condition Eq. (6) that actually supposes that the same-order amount of modal numbers is used for all sides of the sample is excessive, and it is natural to accept the same order of *spatial scale* of the modes for each side to keep the same preciseness. For prolate samples we use the following natural restriction on numbers n_j:

$$\frac{n_1}{L_1} + \frac{n_2}{L_2} + \frac{n_3}{L_3} \leqslant \frac{N}{\max(L_j)}. \tag{20}$$

To obtain the same resolution in all directions, we keep all three terms in the left-hand part of Eq. (20) comparable in order [this is actually the reason for using $\max(L_j)$ in the right-hand side of that inequality]. As a result, $n_{1,2} \ll n_3$, and instead of a sphere in the n-space it suffices to consider a prolate spheroid of a much smaller volume, practically without an increase in error in comparison with the sphere Eq. (6).

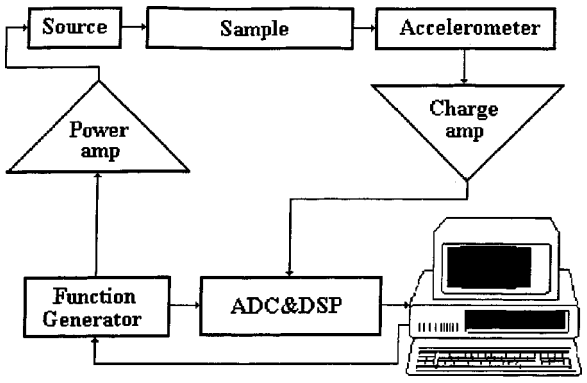

FIG. 1. Block-diagram of experimental setup for measuring the amplitude-frequency response of tested samples. DSP—digital signal processor; ADC—analog-to-digit converter.

III. EXPERIMENTAL SETUP, DATA PROCESSING, AND RESULTS OF MEASUREMENTS

A. Experimental design

The first tested specimen was a black rock of rectangular shape (from Zhitomir, Ukraine). The sizes of the parallelepiped sides were $L_1 = 150.5$ mm, $L_2 = 114.2$ mm, and $L_3 = 102.8$ mm; its mass was $M = 5.435$ kg. The sample had a fine granular structure with no visible flaws.

The block-diagram of the experimental setup for measuring the amplitude-frequency response of tested samples is shown in Fig. 1. A function generator produced a frequency-modulated signal with the frequency swept linearly in time under computer control. After passing a power amplifier, the signal was applied to the transmitting acoustical transducer which excited vibrations in the specimen. The receiving sensor (accelerometer) transformed the specimen vibrations into an electrical signal which was then amplified by a charge amplifier and forwarded to the first input channel of the data acquisition board (ADC&DSP). The transmitting and receiving sensors were thin piezoelectric plates 16 mm in diameter and 2.5 g made of lead zirconate titanate. Epoxy glue was used to attach them to the sample. The electrical signal produced by a function generator was sent to the second channel. Both signals were used for signal processing by a DSP. The signal from the receiving acoustical sensor (accelerometer), after frequency conversion by a function generator and subsequent narrow-band filtering, was recoded into real–imaginary form and sent to the hard disk together with the corresponding frequencies. The total sweep time was chosen according to the Q-factor values to record all peaks with high accuracy. The Q-factors were about 10^3 for measured modes so that all resonant peaks were resolved quite well. In this case the positions of maximums coincide well with resonance frequencies, and the Q-factor for each peak could be defined from the peak width. In Fig. 2 the amplitude-frequency response of the rock is shown on a log-lin scale. To reduce the influence of supports, the sample was hung on thin threads. Simple evaluation of the resonances of the threads gives resonance frequencies of about 0.04 Hz for transverse (''pendulumlike'') motions and about 4 Hz for vertical oscillations (due to thread elasticity). Also the effect of transducer masses on resonance frequencies was estimated

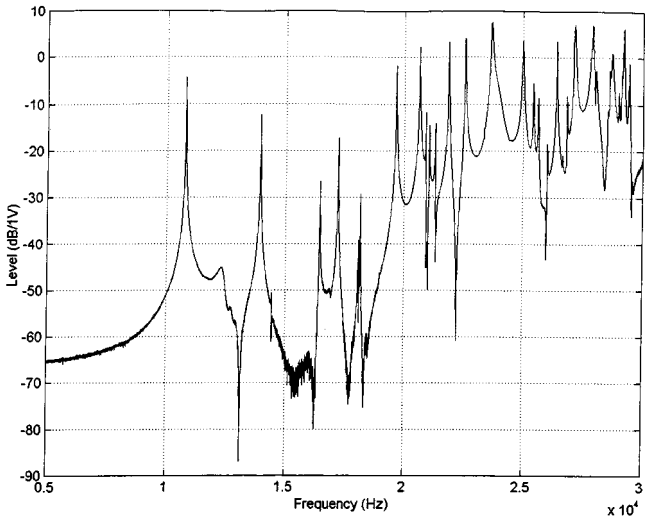

FIG. 2. Amplitude-frequency response of the rock sample.

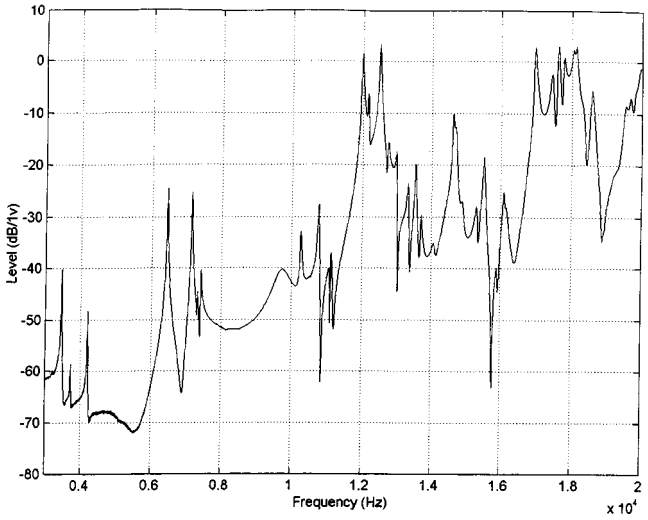

FIG. 4. Amplitude-frequency response of the brick obtained for transmitter in position 5 and receiver in position 2.

to not exceed a fraction of a percent. Therefore, at the frequencies of 3 to 20 kHz used in the experiments, free boundary conditions can be considered as a good approximation.

The second sample tested as an example of a building material was a standard ceramic brick of rectangular shape, having a lower Q-factor (that is closer to that of some sandstone-type rocks). The sizes of the parallelepiped were $L_1=250$ mm, $L_2=125$ mm and $L_3=85$ mm; the mass was $M=5$ kg. This sample had larger grains than the first one, also with no visible flaws.

To excite and measure all oscillation modes in the brick, we put five small sensors to positions shown in Fig. 3. Because of lower values of the Q-factor, several positions of the emitter and receiver were used to resolve all resonant frequencies within the frequency band of interest. The third and the fifth of the sensors were used to excite acoustic vibrations in the brick and the others to receive them. The transmitting and receiving sensors are piezoelectric plates (20 mm in diameter and 1 mm thick) made of lead zirconate titanate. Epoxy glue was used to attach them to the sample. Similarly to the first sample, the brick was hung on thin threads. For example, in Fig. 4 we show the amplitude-frequency response of the brick excited by the transmitter in position 5 and measured by the receiver in position 2 (see Fig. 3).

Resonant frequencies and corresponding Q-factors were associated with local maxima in the amplitude-frequency response. We picked all local maxima in the amplitude-frequency response which exceeded the background level by 2–3 dB and more (as seen from Figs. 2 and 4, in most cases this ratio was much larger). To measure the Q-factors, we used the vicinity of a resonance maximum and represented this vicinity by a standard Lorentz shape. Taking advantage of several transmitters and receivers, for each resonance the amplitude-frequency response was chosen which gives the largest signal/background ratio.

The corresponding frequencies and Q-factors of the vibrations in the samples were calculated according to the scheme described above. Tables I and II demonstrate the results for the rock sample. Tables III and IV demonstrate the results for the ceramic brick.

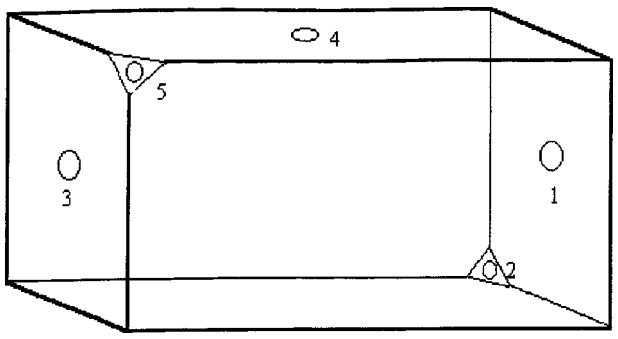

FIG. 3. Sensor positions for experiments with the brick.

B. Elasticity and loss parameters of the tested samples

A comparison of measured and calculated frequencies and Q-factors for the rock sample is given in Table I. The mean-square-root difference between measured and calculated frequencies is 0.17%. Such a small error can, at least partly, be caused by the small lumped impedance of the piezo-ceramics transmitters. Indeed, their total mass was approximately 5 g, while the specimen mass was slightly over 5 kg. According to the estimate, the maximal frequency shift due to the lumped impedance can reach 0.1%. We considered this fit error as small enough, and no special procedures were undertaken to reduce this effect.

The results of inverse RAS problem solution are shown in Table II. To start the iterations for the elastic modulus, we performed special pulse-delay measurements for the compressional wave (the result is $C_l \approx 6380$ m/s), whereas the initial value of the Poisson ratio ($\nu \simeq 0.1$) was taken from standard tables[19] to define the shear modulus.

The sample has parameters which are rather close to a basalt from the mantle top:[20] $C_{11}=0.81$ to 1.04×10^{11} N/m^2, $C_{44}=3\times 10^{10}$, Poisson ratio $\nu=0.23$ and density $\rho=3300$ kg/m^3. This seems to agree with the fact that

TABLE I. Calculated and measured frequencies and Q-factors for a rectangular rock specimen of $150.5\times114.2\times102.8\ \mathrm{mm}^3$ having a 5.435 kg mass and considered isotropic. The number of polynomials is limited by $N=13$ with the constraint Eq. (6). Q-factors were calculated from Eq. (13) after finding the η's.

#	Frequencies (kHz)		Error	Q-factors		Error
	Calc.	Meas.	%	Calc.	Meas.	%
1	10.8051	10.8020	+0.03	1304	1441	−9.48
2	13.9212	13.9510	−0.21	1221	1601	−23.8
3	14.4560	14.4570	−0.01	1215	1415	−14.1
4	16.5271	16.4760	+0.31	1303	1546	−15.7
5	17.1951	17.2460	−0.29	1292	1360	−5.02
6	18.1429	18.1350	+0.04	1261	1128	+11.8
7	18.1692	18.1820	−0.07	1291	1256	+2.76
8	19.7260	19.6780	+0.24	1265	1513	−16.4
9	20.5777	20.6520	−0.36	1162	1311	−11.4
10	20.8999	20.9100	−0.05	1270	1016	+25.0
11	21.0045	21.0200	−0.07	1265	1335	−5.28
12	21.2718	21.2630	+0.04	1281	1291	−0.81
13	21.9518	21.8910	+0.28	1285	1255	+2.40
14	22.5604	22.5800	−0.09	1218	1280	−4.84
15	23.3352	23.3670	−0.14	1292	1461	−11.6
16	23.6955	23.7150	−0.08	1193	1444	−17.4
17	25.0200	25.0050	+0.06	1226	1064	+15.2
18	25.4484	25.4000	+0.19	1149	934	+23.0
19	25.6512	25.6350	+0.06	1110	1188	−6.53
20	26.0721	26.0650	+0.03	1260	1145	+10.0
21	26.4261	26.4430	−0.06	1298	1243	+4.42

the corresponding site lies on the Ukraine's shield known to have reached a very shallow area.

For comparison we performed the same procedure supposing that the specimen's material is anisotropic with cubic symmetry. As there were no *a priori* data regarding symmetry axes, we aligned them along the specimen axes. From Table II it is seen that error remains of the same order as for an isotropic sample model. As there is no evident physical reason for any systematic anisotropy, it can be concluded that the sample is isotropic.

The values of the Q-factor have greater dispersion than those of resonance frequencies. This seems natural because the measured Q is found from the widths of the corresponding resonance curves that are ''contaminated'' by neighboring resonances. Factors such as sound radiation into air may also be significant. A simple estimate shows that at the frequency of 10 KHz, the radiation alone limits the Q-factor by a maximum of about 10^4. The corresponding error is comparable with the values given in Table II.

TABLE II. The results of an inverse problem solution for the rock specimen. Values of δF and $\delta\mathcal{Q}$ were obtained as relative rms errors of the fits. ΔC_{ij} are errors which correspond to obtained δF.

	Isotropic specimen	Cubic anisotropy
C_l (m/s)	6366	6363
C_t (m/s)	3592	3590[a]
ν	0.27	—
C_{11} GPa	$124.6\cdot(1-0.0011i)$	$124.5\cdot(1-0.0011i)$
C_{12} GPa	$45.25\cdot(1-0.0016i)$	$45.06\cdot(1-0.0017i)$
C_{44} GPa	$39.70\cdot(1-0.0008i)$	$39.66\cdot(1-0.0008i)$
δF (%)	0.17	0.17
$\delta\mathcal{Q}$ (%)	13.3	13.3
ΔC_{11} GPa	2.10	0.39
ΔC_{12} GPa	2.39	0.44
ΔC_{44} GPa	0.14	0.23

[a]Along the main crystal axis ''100.''

TABLE III. The results of an inverse problem solution for a ceramic brick of $250\times125\times85\ \mathrm{mm}^3$ size and 5 kg mass considered isotropic. Values δF and $\delta\mathcal{Q}$ were obtained as relative rms errors of the fits. ΔC_{ij} are errors corresponding to obtained δF.

C_l (m/s)	3305.4
C_t (m/s)	2155.1
ν	0.13
C_{11} GPa	$21.4\cdot(1-0.0040i)$
C_{44} GPa	$9.11\cdot(1-0.0036i)$
δF (%)	0.59
$\delta\mathcal{Q}$ (%)	21.3
ΔC_{11} GPa	1.08
ΔC_{44} GPa	0.17

The results of inverse RAS problem solution for the brick are shown in Tables III and IV. One can see a good correspondence between measured and calculated resonance frequencies. The errors in Q are larger in comparison with the first sample. As the values of the Q-factor are typically 3–4 times less than those for the rock sample, these errors can be due to interference of neighboring resonances. Some ways to better resolve interferring resonances is the subject of our present research.

Data in parentheses in Table IV correspond to the results

TABLE IV. Calculated and measured frequencies and Q-factors for a ceramic brick considered isotropic. The order of the polynomials was limited by $N=17$ with the constraint Eqs. (6) and, for data in parentheses, (20).

#	Frequencies (kHz)		Error
	Calc.	Meas.	%
1	3.466 60(3.466 54)	3.466 30	+0.01(+0.01)
2	3.717 01(3.717 02)	3.732 80	−0.42(−0.42)
3	4.187 72(4.187 65)	4.209 40	−0.51(−0.52)
4	6.460 20(6.460 09)	6.439 70	+0.32(+0.32)
5	7.165 39(7.165 32)	7.138 00	+0.38(+0.38)
6	7.291 85(7.291 93)	7.309 40	−0.24(−0.24)
7	7.428 62(7.428 54)	7.409 80	+0.25(+0.25)
8	10.2172(10.2174)	10.2780	−0.59(−0.59)
9	10.4107(10.4108)	10.5400	−1.23(−1.23)
10	10.8838(10.8837)	10.7870	+0.90(+0.90)
11	10.9152(10.9151)	10.8540	+0.56(+0.56)

#	Q-factor		Error
	Calc.	Meas.	%
1	+262.52(+262.53)	227.70	+15.29(+15.30)
2	+279.56(+279.55)	267.20	+4.62(+4.62)
3	+263.08(+263.09)	271.80	−3.21(−3.21)
4	+262.28(+262.29)	387.20	−32.26(−32.26)
5	+266.64(+266.64)	358.70	−25.67(−25.66)
6	+278.38(+278.37)	314.60	−11.51(−11.51)
7	+270.85(+270.85)	336.40	−19.49(−19.49)
8	+264.01(+264.02)	231.00	+14.29(+14.30)
9	+276.06(+276.06)	309.00	−10.66(−10.66)
10	+274.90(+274.89)	316.00	−13.01(−13.01)
11	+272.74(+272.74)	188.00	+45.07(+45.07)

of calculations according to the code modified for prolate samples. It is noteworthy that the use of the constraint Eq. (20) instead of Eq. (6) enables us to reduce the time of calculations by a factor of 10 with practically the same accuracy, even for the brick in which the ratio of different sides does not exceed 3.

IV. CONCLUSIONS

This paper demonstrates that the method of resonant acoustic spectroscopy can be effectively applied to large specimens of structurally inhomogeneous materials such as rocks and ceramics. After Birch who also worked with large specimens, we utilized the more recently developed RUS algorithms and applied them to large rectangular specimens. Note that the numerical program created and used here can be applied to anisotropic samples as was demonstrated above on a simple example of cubic symmetry. Also, a modification of the method significantly reducing the numerical time for prolate samples has been suggested and verified. We suppose that a further development will result in creating practical tools for testing borehole samples and industrial materials, including those with defects.

ACKNOWLEDGMENT

This work was partially supported by the Russian Foundation for Basic Research (Grants 00-05-64252 and 00-15-96741).

APPENDIX: MASS AND RIGIDITY MATRIX ELEMENTS

As both cylindrical bars and rectangular parallelepipeds are important from the point of view of their practical application, both these cases are considered here.

Cylindrical shape:

$$\langle \Psi_\nu | \Psi_\gamma \rangle = \mathcal{P}(n_1+\tilde{n}_1, n_2+\tilde{n}_2, n_3+\tilde{n}_3), \tag{A1}$$

where the functions $\mathcal{P}(\cdots)$ are defined as

$$\mathcal{P}(\alpha_1,\alpha_2,\alpha_3) = \begin{cases} \dfrac{2R^2H}{(\alpha_2+1)(\alpha_3+1)} \cdot \dfrac{\Gamma\left(\dfrac{\alpha_1+1}{2}\right)\Gamma\left(\dfrac{\alpha_2+3}{2}\right)}{\Gamma\left(\dfrac{\alpha_1+\alpha_2}{2}+2\right)} \\ \quad \alpha_1,\alpha_2 \text{ are even} \\ 0 \quad \text{otherwise,} \end{cases} \tag{A2}$$

and $\Gamma(\ldots)$ is the gamma function, R is the radius of a cylinder and H is its length.

Values of $b_{ij}(\cdots|\cdots)$ are defined as follows:

$$\begin{aligned} b_{11} &= n_1\tilde{n}_1\mathcal{P}(n_1+\tilde{n}_1-2, \quad n_2+\tilde{n}_2, \quad n_3+\tilde{n}_3), \\ b_{12} &= n_1\tilde{n}_2\mathcal{P}(n_1+\tilde{n}_1-1, \quad n_2+\tilde{n}_2-1, \quad n_3+\tilde{n}_3), \\ b_{13} &= n_1\tilde{n}_3\mathcal{P}(n_1+\tilde{n}_1-1, \quad n_2+\tilde{n}_2, \quad n_3+\tilde{n}_3-1), \\ b_{21} &= n_2\tilde{n}_1\mathcal{P}(n_1+\tilde{n}_1-1, \quad n_2+\tilde{n}_2-1, \quad n_3+\tilde{n}_3), \\ b_{22} &= n_2\tilde{n}_2\mathcal{P}(n_1+\tilde{n}_1, \quad n_2+\tilde{n}_2-2, \quad n_3+\tilde{n}_3), \\ b_{23} &= n_2\tilde{n}_3\mathcal{P}(n_1+\tilde{n}_1, \quad n_2+\tilde{n}_2-1, \quad n_3+\tilde{n}_3-1), \\ b_{31} &= n_3\tilde{n}_1\mathcal{P}(n_1+\tilde{n}_1-1, \quad n_2+\tilde{n}_2, \quad n_3+\tilde{n}_3-1), \\ b_{32} &= n_3\tilde{n}_2\mathcal{P}(n_1+\tilde{n}_1-1, \quad n_2+\tilde{n}_2-1, \quad n_3+\tilde{n}_3), \\ b_{33} &= n_3\tilde{n}_3\mathcal{P}(n_1+\tilde{n}_1, \quad n_2+\tilde{n}_2, \quad n_3+\tilde{n}_3-2). \end{aligned} \tag{A3}$$

In the case of *rectangular shape* it is better to use a Legendre polynomial expansion in the Ritz representation Eq. (3). In this case the values of interest are written as follows (L_1, L_2, L_3 are sizes of a rectangular specimen):

$$\langle \Psi_\nu | \Psi_\gamma \rangle = \frac{L_1L_2L_3\delta_{\nu\gamma}}{(2n_1+1)(2n_2+1)(2n_3+1)}, \tag{A4}$$

and

$$\begin{aligned} b_{11} &= \frac{2\delta_{n_2\tilde{n}_2}\delta_{n_3\tilde{n}_3}}{(2n_2+1)(2n_3+1)}\frac{L_2L_3}{L_1}G_{n_1\tilde{n}_1}, \\ b_{12} &= \frac{\delta_{n_3\tilde{n}_3}}{2n_3+1}L_3F_{\tilde{n}_1n_1}F_{n_2\tilde{n}_2}, \\ b_{13} &= \frac{\delta_{n_2\tilde{n}_2}}{2n_2+1}L_2F_{\tilde{n}_1n_1}F_{n_3\tilde{n}_3}, \\ b_{21} &= \frac{\delta_{n_3\tilde{n}_3}}{2n_3+1}L_3F_{n_1\tilde{n}_1}F_{\tilde{n}_2n_2}, \\ b_{22} &= \frac{2\delta_{n_1\tilde{n}_1}\delta_{n_3\tilde{n}_3}}{(2n_1+1)(2n_3+1)}\frac{L_1L_3}{L_2}G_{n_2\tilde{n}_2}, \\ b_{23} &= \frac{\delta_{n_1\tilde{n}_1}}{2n_1+1}L_1F_{\tilde{n}_2n_2}F_{n_3\tilde{n}_3}, \\ b_{31} &= \frac{\delta_{n_2\tilde{n}_2}}{2n_2+1}L_2F_{n_1\tilde{n}_1}F_{\tilde{n}_3n_3}, \\ b_{32} &= \frac{\delta_{n_1\tilde{n}_1}}{2n_1+1}L_1F_{n_2\tilde{n}_2}F_{\tilde{n}_3n_3}, \\ b_{33} &= \frac{2\delta_{n_1\tilde{n}_1}\delta_{n_2\tilde{n}_2}}{(2n_1+1)(2n_2+1)}\frac{L_1L_2}{L_3}G_{n_3\tilde{n}_3}, \end{aligned} \tag{A5}$$

with

$$F_{mn} = \begin{cases} 2, & n>m \text{ and } n+m \text{ is odd,} \\ 0, & \text{otherwise,} \end{cases}$$

$$G_{mn} = \begin{cases} (\min(m,n))\cdot(\min(m,n)+1), & n+m \text{ is even,} \\ 0 \quad \text{otherwise.} \end{cases} \tag{A6}$$

[1] G. Mavko, T. Mukeji, and J. Dvorkin, *The Rock Physics Handbook. Tools For Seismic Analysis in Porous Media* (Cambridge University Press, Cambridge, MA, 1998).

[2] J. E. White, *Underground Sound, Application of Seismic Waves* (Elsevier, New York, 1983).

[3] A. Migliori and J. L. Sarrao, *Resonant Ultrasound Spectroscopy* (Wiley, New York, 1998).

[4] F. Birch, "Velocity and attenuation from resonant vibrations of spheres of rock, glass, and steel," J. Geophys. Res. **80**, 756–764 (1975).

[5] W. Visscher, A. Migliori, T. Bell, and R. Reinert, "On the normal modes of free vibrations of inhomogeneous and anisotropic elastic objects," J. Acoust. Soc. Am. **90**, 2154–2162 (1991).

[6] I. Ohno, "Free vibration of a rectangular parallelepiped crystal and its

application to determination of elastic constants of orthorhombic crystals,'' J. Phys. Earth **24**, 355–379 (1976).
[7] H. Demarest, ''Cube-resonance method to determine the elastic constants of solids,'' J. Acoust. Soc. Am. **49**, 768–775 (1971).
[8] L. D. Landau, E. M. Lifshitz, A. M. Kosevich, and L. P. Pitaevskii, *Theory of Elasticity* (Pergamon, New York, 1986).
[9] J. H. Wilkinson and C. Reinsch, *Handbook for Automatic Computation, Vol. 2, Linear Algebra* (Springer-Verlag, New York, 1971).
[10] A. D. Nashif, D. I. G. Johnes, and J. P. Henderson, *Vibration Damping* (Wiley, New York, 1985).
[11] Y. Sumino, I. Ohno, and M. Kumazawa, ''Measurement of elastic constants and internal frictions on single-crystal MgO by rectangular parallelepiped resonance,'' J. Phys. Earth **24**, 263–273 (1976).
[12] B. V. Shabat, *Introduction in Complex Analysis, Vol. 2, Functions of Several Variables*, 3rd edition [in Russian] (Nauka, Moscow, 1985).
[13] R. W. Hamming, *Numerical Methods for Scientists and Engineers* (Bell Telephone Laboratories, McGraw-Hill, New York, 1962).
[14] J. Maynard, ''Resonant ultrasound spectroscopy,'' Phys. Today **27**, 26–32 (1996).
[15] G. A. Korn and T. M. Korn, *Mathematical Handbook for Scientists and Engineers*, 2nd ed. (McGraw-Hill, New York, 1968).
[16] J. N. Sneddon and D. S. Berry, *The Classical Theory of Elasticity* (Springer-Verlag, New York, 1958).
[17] M. C. Junger and D. Feit, *Sound, Structures and Their Interactions*, 2nd ed. (MIT Press, Cambridge, MA, 1986).
[18] A. V. Lebedev, L. A. Ostrovsky, I. A. Soustova, Calculation of natural frequencies for a solid cylinder, Project No. F37750018-35, Technical report 2.6.6, Institute of Applied Physics (Russia)—LANL (USA), 1998.
[19] *Handbook of Physical Values*, edited by acad. I. K. Kikoin (Atomizdat, Moscow, 1976).
[20] *Encyclopedia Britannica*, CD-version 1997, Tables 35, 36.

Near-field scanning in the time domain on a spherical surface—A formulation using the free-space Green's function

Sencer Koc, O. Aydin Civi, and O. Merih Buyukdura
Department of Electrical and Electronics Engineering, Middle East Technical University, 06531 Ankara, Turkey

(Received 9 June 2000; revised 19 July 2001; accepted 20 July 2001)

Two formulations for determining the characteristics of an unknown source of acoustic waves using the measurement of its field at its near zone are presented. The measurement in both cases is to be performed on a spherical scan surface which encapsulates the source. The first is for an ideal probe which measures the field at its location. The knowledge of the field is sufficient; its normal derivative is not required. In the second formulation a realistic probe is considered. This time it is required only that the probe has an axially symmetric receiving characteristic. With this formulation, the time functions which characterize the source are found using only the signal at the output of the probe. Both formulations are such that they are not specific to the scan surface radius. Furthermore, they are entirely in the time domain, requiring no inverse Fourier transformations left to be performed. © *2001 Acoustical Society of America.* [DOI: 10.1121/1.1403698]

PACS numbers: 43.20.Px [ANN]

I. INTRODUCTION

The problem of characterizing a source using data obtained from the measurement of its field at its near zone is well known to be important. This has relatively recently found application also in the time domain. Performing the characterization in the time domain has the advantage that if the radiator is fed by a narrow, therefore wide-band pulse, the performance of the source can be found over a large range of frequencies simultaneously.

Here, we report a scheme by which a test source is characterized using the measurement of its field, in the time domain, on a spherical surface. This surface may be in the near zone of the source; it is sufficient that the source be enclosed by the surface. Two formulations are presented. In the first it is assumed that the probe used to measure the field is ideal: that is, its output is exactly the field at the point where the measurement is made. The formulation is such that the measurement of the field is sufficient; its normal directional derivative, as might be expected of a consideration of the field equivalence principle, is not required. Another formulation is presented in which a realistic probe is considered: one which is a reciprocal electroacoustic device with an axially symmetrical receiving characteristic.

The work presented here is very closely related to that reported in two previous articles: Buyukdura *et al.*[1] and Hansen.[2] The time domain free-space Green's function expansion in terms of spherical wave functions reported in the former is extensively used in the following sections. In particular, the fact that the Green's function has been expressed in terms of time domain outgoing wave functions as well as orthogonal spherical harmonics is seen to prove very useful. The way in which the orthogonality of these harmonics is used is very similar to that reported in the latter article. As opposed to previous work however, we start at the outset with a *time domain* expansion for the field outside the scan surface. Furthermore this expansion is in terms of universal outgoing time domain wave functions which are independent of the scan sphere radius. This leads to two features of the formulation which are both novel and superior to those given earlier in the literature:

(i) Once the time dependent expansion coefficients are determined, the expressions for the field both in the near and the far zones are much simpler as compared to those given earlier which involve complex zeros of the Hankel functions and are relatively complicated.
(ii) The present probe corrected formulation, in addition to the above feature, has the further advantage that it leaves no inverse Fourier integrals to be evaluated.

In summary, the present approach is that of stating, formulating, and solving the problem entirely in the time domain. This is in contrast to earlier work, the essence of which is to solve the problem in the frequency domain and suggest that the result be inverse Fourier transformed to the time domain.

The formulation for the ideal probe is given in Sec. II, and that for the realistic probe in Sec. III. Some practical aspects of sampling positions on the scan sphere and discretization in time are discussed in Sec. IV. A numerical example is presented in Sec. V, followed by concluding remarks in Sec. VI.

Throughout the article the velocity of waves in free space is taken to be $c=1$, so that in any frequency domain expression which appears the wave number, k, is equal to the angular frequency, ω.

II. FORMULATION—WITHOUT PROBE CORRECTION

For the problem of interest, the reader is referred to Fig. 1 in which it is seen that a source of acoustical waves is totally enclosed within a spherical surface S of radius a. We wish to characterize the source from a measurement of the

 0001-4966/2001/110(4)/1778/5/$18.00

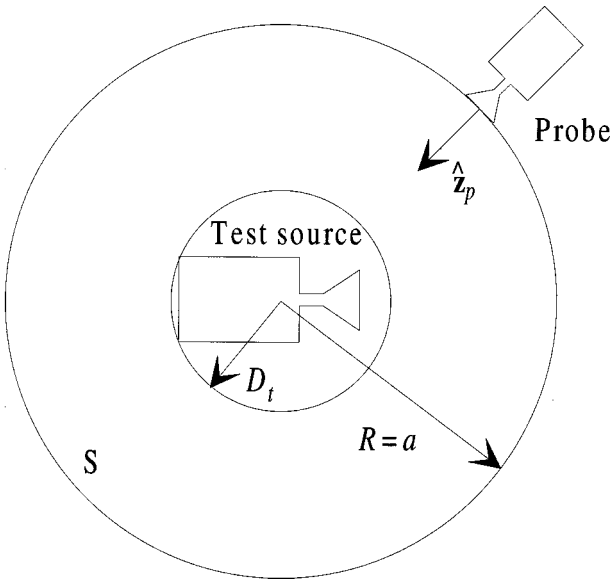

FIG. 1. The spherical scan geometry.

pressure field on S. In this section it is assumed that an ideal probe, i.e., the output of which is exactly the unperturbed pressure field at its location, is available.

From Buyukdura *et al.*[1] it is seen that the field outside the smallest spherical surface which encloses the test source can be expressed in terms of the spherical harmonics as

$$\varphi(\mathbf{R},t)=\sum_{n=0}^{\infty} O_n(R,t)*\sum_{p=e,o}\sum_{m=0}^{n} c_{pnm}(t)Y_{pnm}(\theta,\phi), \tag{1}$$

where the parity index p takes on the "values" either e or o (standing for "even" and "odd," respectively), $*$ stands for the convolution operation and the time functions $c_{pnm}(t)$ are, as yet, unknown. (R,θ,ϕ) are the familiar spherical coordinate variables. The spherical harmonics are given by

$$Y_{\substack{e\\o}nm}(\theta,\phi)=P_n^m(\cos\theta)\begin{matrix}\cos m\phi\\ \sin m\phi\end{matrix}, \tag{2}$$

in which P_n^m are the associated Legendre functions of the first kind as defined in Abramowitz *et al.*;[3] $\cos m\phi$ goes with parity e and $\sin m\phi$ goes with parity o. The radial dependence of the outgoing wave functions is given by

$$O_n(R,t)=\frac{1}{R}U_n(R,t-R), \tag{3}$$

in which the functions $U_n(R,t-R)$ are defined in Buyukdura *et al.*[1] A few of these are as follows:

$$O_0(R,t)=\frac{\delta(t-R)}{R}, \tag{4a}$$

$$O_1(R,t)=\frac{\delta(t-R)}{R}+\frac{u(t-R)}{R^2}, \tag{4b}$$

$$O_2(R,t)=\frac{\delta(t-R)}{R}+3\frac{u(t-R)}{R^2}+3\frac{(t-R)u(t-R)}{R^3}, \tag{4c}$$

where δ and u are the unit impulse and unit step functions, respectively. These functions can also be generated by using the recursion relation:

$$O_n(R,t)=\frac{2n-1}{n-1}\frac{t}{R}O_{n-1}(R,t)-\frac{n}{n-1}O_{n-2}(R,t). \tag{5}$$

Note that the determination of $c_{pnm}(t)$ completely specifies the test source. In particular, the far zone field is given by

$$\varphi(\mathbf{R},t)=\frac{1}{R}\sum_{n=0}^{\infty}\sum_{p=e,o}\sum_{m=0}^{n} c_{pnm}(t-R)Y_{pnm}(\theta,\phi), \tag{6}$$

since, as seen from Eqs. (4), only the first (the impulsive) term of each O_n contributes in the far zone.

To find $c_{pnm}(t)$, we evaluate Eq. (1) at $R=a$, multiply both sides by $Y_{p'n'm'}(\theta,\phi)$ and integrate over S. Exploiting the orthogonality property of the spherical harmonics:

$$\int_0^{2\pi}\int_0^{\pi} Y_{pnm}(\theta,\phi)Y_{p'n'm'}(\theta,\phi)\sin\theta\,d\theta\,d\phi$$

$$=\frac{4\pi(n+m)!}{\epsilon_m(2n+1)(n-m)!}\delta_{pp'}\delta_{nn'}\delta_{mm'}$$

yields (δ is the Kronecker delta),

$$c_{pnm}(t)*O_n(a,t)=f_{pnm}(t). \tag{7}$$

The right-hand side of Eq. (7) is given by

$$f_{pnm}(t)=\frac{\epsilon_m(2n+1)(n-m)!}{4\pi(n+m)!}\times\int_0^{2\pi}\int_0^{\pi}\varphi(\hat{\mathbf{R}}a,t)Y_{pnm}(\theta,\phi)\sin\theta\,d\theta\,d\phi, \tag{8}$$

where $\epsilon_0=1$, $\epsilon_m=2$ for $m\neq 0$ and $\hat{\mathbf{R}}$ is the unit vector in the radial direction such that $\hat{\mathbf{R}}a$ denotes a position on the surface S. The function $\varphi(\hat{\mathbf{R}}a,t)$ which appears on the right-hand side is the field measured by the ideal probe. Possible methods of solution of Eq. (7) are discussed in the Appendix. Note that with this formulation, the measurement of the pressure field on the scan sphere is sufficient (in that the normal derivative of φ is not needed). Furthermore, the analysis is not restricted to any particular value of the scan sphere radius; nothing needs to be changed for a larger or smaller scan surface.

III. FORMULATION—WITH PROBE CORRECTION

The problem in this section is similar to that in the preceding section except that the probe in question is not ideal. However, the analysis is valid only for an electroacoustic transducer whose receiving characteristic is axially symmetric. In other words, the probe receiving characteristic is independent of the probe-local coordinate variable ϕ_p, where the probe-local coordinate unit vector $\hat{\mathbf{z}}_p$ is such that it always points towards the center of the scan sphere as shown in Fig. 1. It is also assumed that any multiple interactions between the probe and the test source are negligible. Then as in Hansen *et al.*,[4] Yaghjian,[5] Yaghjian *et al.*,[6] and Wittmann,[7]

the probe can be characterized as a differential operator acting on the pressure field as expressed by the *frequency-domain* equation:

$$b(\hat{\mathbf{R}}a,k)=\sum_{l=0}^{\infty} a_l(k)P_l\left(\frac{-1}{jk}\frac{\partial}{\partial R}\right)\varphi(\hat{\mathbf{R}}R,k)\Big|_{R=a}, \tag{9}$$

where b is the signal at the output of the probe and k is the angular frequency. Considering the inverse Fourier transform of Eq. (9) and substituting for $\varphi(\mathbf{R},t)$ from Eq. (1), one obtains

$$b(\hat{\mathbf{R}}a,t)=\sum_{n=0}^{\infty}\sum_{p=e,o}\sum_{m=0}^{n} Y_{pnm}(\theta,\phi)c_{pnm}(t) * \sum_{l=0}^{\infty} a_l(t)*\Lambda_{ln}(a,t). \tag{10}$$

Here, $a_l(t)$ are the inverse Fourier transforms of $a_l(k)$. If the probe is reciprocal, they can also be determined from the far field pattern of the probe.[2] The time-domain Green's function expression given in Buyukdura *et al.*[1] suggests that they should be time limited. For a known probe, these time functions are, naturally, known. The time functions $\Lambda_{ln}(a,t)$ are given by

$$\Lambda_{ln}(a,t)=\mathcal{F}^{-1}\left\{P_l\left(\frac{-1}{jk}\frac{\partial}{\partial R}\right)\right\}*O_n(R,t)\Big|_{R=a}. \tag{11}$$

Again, these functions are given for a few values of their indices:

$$\Lambda_{00}(a,t)=O_0(a,t), \tag{12a}$$

$$\Lambda_{0n}(a,t)=O_n(a,t), \tag{12b}$$

$$\Lambda_{10}(a,t)=O_1(a,t), \tag{12c}$$

$$\Lambda_{11}(a,t)=H_0(a,t)+2H_1(a,t)+2H_2(a,t), \tag{12d}$$

$$\Lambda_{12}(a,t)=H_0(a,t)+4H_1(a,t)+9H_2(a,t)+\tfrac{9}{2}H_3(a,t), \tag{12e}$$

$$\Lambda_{20}(a,t)=H_0(a,t)+3H_1(a,t)+3H_2(a,t), \tag{12f}$$

$$\Lambda_{21}(a,t)=H_0(a,t)+4H_1(a,t)+9H_2(a,t)+\tfrac{9}{2}H_3(a,t), \tag{12g}$$

$$\Lambda_{22}(a,t)=H_0(a,t)+6H_1(a,t)+24H_2(a,t)+27H_3(a,t)+9H_4(a,t), \tag{12h}$$

in which the generic functions H are given by

$$H_0(a,t)=\frac{\delta(t-a)}{a}, \tag{13a}$$

$$H_1(a,t)=\frac{1}{a^2}u(t-a), \tag{13b}$$

and

$$H_m(a,t)=\frac{(t-a)^{m-1}}{a^{m+1}}u(t-a). \tag{13c}$$

A recursive relation which can be used to generate the functions Λ is

$$\Lambda_{l,n}(a,t)=\frac{2l-1}{l}\mathcal{L}\{\Lambda_{l-1,n}(a,t)\}-\frac{l-1}{l}\Lambda_{l-2,n}(a,t), \tag{14a}$$

$$\Lambda_{0,n}(a,t)=O_n(a,t), \tag{14b}$$

$$\Lambda_{1,n}(a,t)=\mathcal{L}\{O_n(a,t)\}, \tag{14c}$$

in which the operator $\mathcal{L}\{\cdot\}$ is given by

$$\mathcal{L}\{f(a,t)\}=\left[-\int_{-\infty}^{t}\frac{\partial}{\partial R}f(R,\tau)d\tau\right]_{R=a}. \tag{15}$$

Since the functions Λ and O can be expressed as linear combinations of the generic functions H, the result of $\mathcal{L}\{H\}$ suffices to use the recursion given in Eqs. (14). This is given as

$$\mathcal{L}\{H_0\}=H_0+H_1, \tag{16a}$$

$$\mathcal{L}\{H_m\}=H_m+\frac{m+1}{m}H_{m+1}, \quad m\neq 0. \tag{16b}$$

The rest of the analysis is as in the preceding section. Again, the orthogonality of the spherical harmonics is used to obtain

$$c_{pnm}(t)*L_n(t)=g_{pnm}(t), \tag{17}$$

using which $c_{pnm}(t)$ are found as discussed in the Appendix. Here,

$$L_n(t)=\sum_{l=0}^{\infty} a_l(t)*\Lambda_{ln}(a,t), \tag{18}$$

and this time, the right-hand side is

$$g_{pnm}(t)=\frac{\epsilon_m(2n+1)(n-m)!}{4\pi(n+m)!}\times\int_0^{2\pi}\int_0^{\pi} b(\hat{\mathbf{R}}a,t)Y_{pnm}(\theta,\phi)\sin\theta\,d\theta\,d\phi. \tag{19}$$

IV. PRACTICAL ASPECTS

Some practical aspects which will arise in the application of the above are discussed in this section.

The first aspect to be addressed involves the choice of the number and the positions of the points on the scan sphere at which the probe output signals are to be measured. The determination of the time domain expansion coefficients of the test source requires the evaluation of a surface integral over the measurement sphere as seen in, for instance, Eq. (19). In practice, the measurements can be done only at certain points of the measurement surface, and the integral must be evaluated by a numerical technique. A straightforward method for this purpose is to use the product formula

$$\oint f(x,y,z)d\Omega=\int_0^{2\pi}\int_0^{\pi} f(\theta,\phi)\sin\theta\,d\theta\,d\phi=\sum_{i=1}^{N_\theta}\sum_{j=1}^{2N_\theta} w_i^g w_j^c f(\theta_i,\phi_j), \tag{20}$$

which is exact[8] for polynomials $x^\alpha y^\beta z^\gamma$ if $\alpha+\beta+\gamma<2N_\theta$ where θ_i are chosen as the Gauss–Legendre points, ϕ_j are

$2N_\theta$ equally spaced points over the interval $[-\pi, \pi]$, w_i^g are the Gauss–Legendre weights and $w_j^c = \pi/N_\theta$. The upper limit N_θ of the summation given in Eq. (20) should be chosen according to how rapidly the integrand varies. For this purpose the spherical series expansion of the test source is considered. This series can be truncated at N_t where $N_t \approx C\omega_m D_t$ and C is a factor that determines the accuracy. Similarly, the probe expansion coefficients can be disregarded beyond $N_p \approx C\omega_m D_p$. In these expressions, D_t and D_p are the maximum dimensions of the test source and the probe, respectively, and ω_m is the bandwidth of the wave form of interest. Thus, the probe output $b(\hat{\mathbf{R}}a,t)$ can be expanded in a series with highest order

$$N = N_t + N_p \approx C\omega_m(D_t + D_p) \tag{21}$$

which also implies that $2(N+N_t)^2$ measurement points on the scan sphere will suffice. However, this method is quite inefficient in that the measurements points are clustered near the poles ($\theta = 0, \pi$) of the measurement sphere. A more efficient method is described in McLaren.[9] This method uses sampling points that are determined using the symmetry properties of regular polyhedra and are more uniformly distributed over the sphere.

The second aspect to be considered in this section is the discretization in time. If the time wave forms of interest are band limited functions, the sampling period is given by the Nyquist rate as

$$\Delta t = \frac{\pi}{\omega_m}. \tag{22}$$

The reconstruction of the time wave forms can be achieved by using the Shannon sampling theorem,[10] or if an oversampling rate of δ is used, the following more general reconstruction formula[11,12]

$$f(t) = \sum_{k=-\infty}^{\infty} f(k\Delta t) \frac{\sin \frac{\omega_m}{1-\delta}(t-k\Delta t)}{\frac{\omega_m}{1-\delta}(t-k\Delta t)} \psi(t-k\Delta t) \tag{23}$$

should be used where $\psi(t-k\Delta t)$ can be chosen to reduce the error bound when the reconstruction expression, Eq. (23), is truncated.

V. A NUMERICAL EXAMPLE

Following Hansen,[2] we choose a point source located at $\mathbf{R}_s = 0.1\hat{\mathbf{x}} - 0.4\hat{\mathbf{y}} + 0.2\hat{\mathbf{z}}$. The excitation is such that the pressure field due to this source is given by

$$\varphi(\mathbf{R},t) = \frac{e^{-4(t-|\mathbf{R}-\mathbf{R}_s|)^2}}{4\pi|\mathbf{R}-\mathbf{R}_s|}. \tag{24}$$

The scan sphere is centered at the origin with a radius of 0.6. We assume that the probe used is such that its characterizing time functions $a_l(t)$ are given by

$$a_0(t) = \delta(t), \quad a_1(t) = \delta(t), \quad a_l(t) = 0, \quad l > 1. \tag{25}$$

With this choice, the output signal of the probe would be

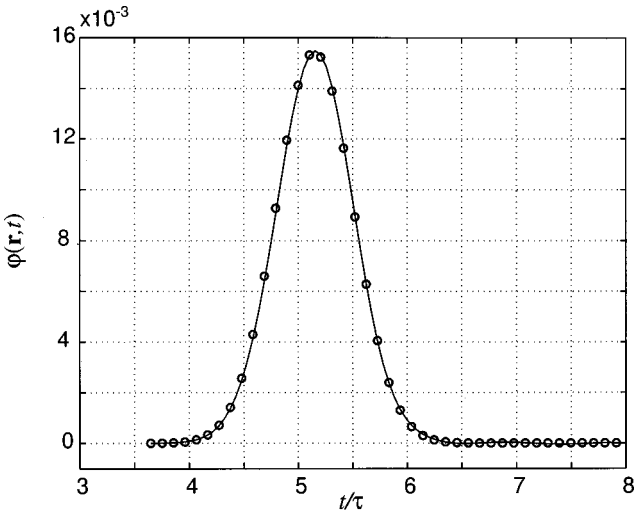

FIG. 2. The calculated and the exact field vs. time. The solid curve is obtained using the present formulation, and the circles are from the exact solution.

$$b(\hat{\mathbf{R}}a,t) = \varphi(\hat{\mathbf{R}}a,t) - \int_{-\infty}^{t} \frac{\partial}{\partial R}\varphi(\hat{\mathbf{R}}R,\tau)\bigg|_{R=a} d\tau, \tag{26}$$

which is used in Eq. (19). Once the time functions $c_{pnm}(t)$ are determined as described in Sec. III, they are used in Eq. (1) to find the field at the location $\mathbf{R} = 3\hat{\mathbf{x}} - 2.1\hat{\mathbf{y}} + 4.1\hat{\mathbf{z}}$. The result is shown in Fig. 2. The solid curve is obtained using the present formulation, while the circles are from the exact solution given by Eq. (24). As in Hansen,[2] eight terms from the expansion Eq. (1) have been found to be sufficient. Note the excellent agreement between the calculated and the exact fields.

It should be noted that although we have chosen the same source and scan surface as in Hansen,[2] this example is substantially different in that we consider a probe which is *not* ideal and that we have used our probe corrected formulation. To the best of our knowledge, this is the first such numerical solution in the time domain given in the literature. Since the formulation is given entirely in the time domain, we have found it attractive to perform the numerical solution of Eq. (17) also in the time domain using direct deconvolution (see the Appendix).

VI. CONCLUSION

Two formulations which are useful in characterizing a test source via the measurement of its near field in the time domain on a spherical surface have been presented. In one of these an ideal probe is assumed. The other formulation is based on the output of a realistic probe. The probe in this formulation is assumed to be a reciprocal device with a receiving characteristic which is axially symmetric.

Both formulations are developed using the spherical wave expansion of the free-space time domain Green's function in which the functional form of the outgoing wave functions is known explicitly. It is seen that both are such that the expressions used are not specific to the scan sphere radius. Furthermore the analysis is entirely in the time domain

where the unknown quantities of interest are solved using deconvolution.

A numerical example has also been given which demonstrates the validity of the analysis.

APPENDIX: DECONVOLUTION

In this appendix we discuss the solution of an equation of the form

$$h(t)*x(t)=y(t), \tag{A1}$$

in which $x(t)$ and $y(t)$ are known functions of time and we want to determine $h(t)$. In fact, the functions $x(t)$ and $y(t)$ are available only at sampling points $t_n=nT$ where T is the sampling period. We will denote the nth sample of a function $x(t)$ by $x_n=x(nT)$. All the functions that appear in Eq. (A1) are bandlimited and we will assume that the sampling is fast enough to determine these functions at any time. There are several possible approaches to this problem.

One method could be to Fourier transform Eq. (A1) after which the Fourier transform of $h(t)$ can be readily determined and transformed back into the time domain. Actually, DFT (in particular the FFT algorithm) should be used since only samples of the functions are available.

Another approach could be to consider $h(t)$ as the impulse response of an unknown linear time invariant system. Thus, the deconvolution problem is equivalent to the task of the identification of a dynamical system from its known response, $y(t)$, to a known input, $x(t)$. The general approach in the system identification problem is to fit an approximate parametric model and the most commonly used model is the autoregressive moving average (ARMA) model; many texts[13] can be found on this subject.

We have chosen however, to deconvolve Eq. (A1) directly in the time domain. In discrete time Eq. (A1) can be approximated by a convolution sum as

$$y_n \approx h_n \circledast x_n = T\sum_{k=0}^{n} x_{n-k}h_k \tag{A2}$$

which is equivalent to evaluating the convolution integral as a Riemann sum.

The first few terms of y_n can be written as

$$y_0=(h_0x_0)T, \tag{A3a}$$

$$y_1=(h_1x_0+h_0x_1)T, \tag{A3b}$$

$$y_2=(h_2x_0+h_1x_1+h_0x_2)T, \tag{A3c}$$

which shows that at each step one sample of the unknown function can be determined as

$$h_0=\frac{1}{x_0}\frac{y_0}{T}, \tag{A4a}$$

$$h_1=\frac{1}{x_0}\left(\frac{y_1}{T}-h_0x_1\right), \tag{A4b}$$

$$h_2=\frac{1}{x_0}\left(\frac{y_2}{T}-h_1x_1-h_0x_2\right), \tag{A4c}$$

$$\vdots$$

$$h_n=\frac{1}{x_0}\left(\frac{y_n}{T}-\sum_{k=0}^{n} h_kx_{n-k}\right). \tag{A4d}$$

It must be noted that this formulation is valid only if $x_0\neq 0$. However, since the function $x(t)$ cannot be identically zero, we can shift our time origin so that the first sample is nonzero, i.e., $x_0\neq 0$.

A complication that may arise (and indeed does in the numerical example given) is that the function $x(t)$ contains a term proportional to the unit impulse function $\delta(t)$. In this case we can decompose the function $x(t)$ as

$$x(t)=\xi(t)+\alpha\delta(t) \tag{A5}$$

where α is a constant and $\xi(t)$ is a smooth function. Then Eq. (A1) becomes

$$h(t)*x(t)=h(t)*(\xi(t)+\alpha\delta(t))=h(t)*\xi(t)+\alpha h(t) =y(t). \tag{A6}$$

Again, approximating the continuous convolution by a convolution sum, we can solve for the samples of the unknown function as

$$h_0=\frac{1}{\xi_0+\alpha}\frac{y_0}{T}, \tag{A7a}$$

$$h_1=\frac{1}{\xi_0+\alpha}\left(\frac{y_1}{T}-h_0x_1\right), \tag{A7b}$$

$$h_2=\frac{1}{\xi_0+\alpha}\left(\frac{y_2}{T}-h_1x_1-h_0x_2\right), \tag{A7c}$$

$$\vdots$$

$$h_n=\frac{1}{\xi_0+\alpha}\left(\frac{y_n}{T}-\sum_{k=0}^{n} h_kx_{n-k}\right). \tag{A7d}$$

[1] O. M. Buyukdura and S. Koc, "Two alternative expressions for the spherical wave expansion of the time domain scalar free-space Green's function and an application: Scattering by a soft-sphere" J. Acoust. Soc. Am. **101**, 87–91 (1997).

[2] T. B. Hansen, "Spherical expansions of time-domain acoustic fields: Application to near-field scanning" J. Acoust. Soc. Am. **98**, 1204–1215 (1995).

[3] M. Abramowitz and I. A. Stegun, *Handbook of Mathematical Functions* (Dover, NY, 1972).

[4] T. B. Hansen and A. D. Yaghjian, "Formulation of probe-corrected planar near-field scanning in the time-domain" IEEE Trans. Antennas Propag. **AP-43**, 569–584 (1995).

[5] A. D. Yaghjian, "Simplified approach to probe-corrected spherical near-field scanning" Electron. Lett. **20**, 195–196 (1984).

[6] A. D. Yaghjian and R. C. Wittmann, "The receiving antenna as a linear-differential operator—application to spherical near-field scanning" IEEE Trans. Antennas Propag. **33**, 1175–1185 (1985).

[7] R. C. Wittmann, "Probe-corrected spherical near-field scanning theory in acoustics" IEEE Trans. Instrum. Meas. **41**, 17–21 (1992).

[8] A. H. Stroud and D. Secrest, *Gaussian Quadrature Formulas* (Prentice-Hall, Englewood Cliffs, NJ, 1966).

[9] A. D. McLaren, "Optimal numerical integration on a sphere" Math. Comput. **17**, 361–383 (1963).

[10] C. E. Shannon, "Communication in the presence of noise" Proc. IRE **37**, 10–21 (1949).

[11] J. J. Knab, "Interpolation of band-limited functions using the approximate prolate series" IEEE Trans. Inf. Theory **IT-25**, 717–720 (1979).

[12] J. J. Knab, "The sampling window" IEEE Trans. Inf. Theory **IT-29**, 157–159 (1983).

[13] G. C. Goodwin and K. S. Sin, *Adaptive Filtering, Prediction and Control* (Prentice-Hall, Englewood Cliffs, NJ, 1984).

Acoustic radiation of cylindrical elastic shells subjected to a point source: Investigation in terms of helical acoustic rays

Christophe Lecable, Jean-Marc Conoir, and Olivier Lenoir
Laboratoire d'Acoustique Ultrasonore et d'Electronique, UMR CNRS 6068, Université du Havre, Place R. Schuman, Le Havre 76610, France

(Received 4 April 2001; accepted for publication 26 July 2001)

The paper deals with the acoustic radiation of a cylindrical elastic shell with no internal loading surrounded by a fluid medium when its external surface is subjected to a point source. The problem is addressed via the use of the spatial Fourier transform. An expression is obtained for the radiated pressure that is evaluated for the far field using both the stationary phase method and the fast Fourier transform (FFT). The acoustic field calculated from the FFT is much more complicated than that obtained by using only the stationary phase method. In agreement with the geometrical theory of diffraction (GTD), alternative interpretations of the radiated field in terms of helical acoustic rays allows one to understand the reason for this result. The outstanding phenomenon underlined by the use of the FFT is the emergence of an infinite number of spatial dispersion curves associated with each leaky wave propagating in shells when excited by a point source. © *2001 Acoustical Society of America.* [DOI: 10.1121/1.1404437]

PACS numbers: 43.20.Tb, 43.20.Dk, 43.20.Ks [JGM]

I. INTRODUCTION

The interaction of an incident wave with elastic cylindrical and spherical shells has long been a problem of constant interest.[1–12] There are many reasons to explain this fact. At first, cylindrical and spherical geometries permit an analytical separation of the linear elasticity equations leading to solutions based upon normal-mode series. Contrary to numerical methods used to calculate the sound interaction with more complicated objects (finite-element method, T-matrix approach, Fredholm integral equation method, etc.), the fast computation of these series is easy today even at very high frequencies. Therefore, it becomes possible to analyze specific high-frequency phenomena as the bifurcation of Lamb wave dispersion curves for elastic spheres,[9,10] the overlapping of resonances associated with leaky waves,[13,14] and the coupling between leaky waves and Whispering Gallery waves propagating around cylindrical shells filled with fluid,[15] for example. Then, the Sommerfeld–Watson transform of the normal-mode series led to a better physical understanding of the leaky wave propagation.[16–20] In particular, it showed that resonances are closely linked to stationary states of leaky waves.[4,21–23] The first developments of the Sommerfeld–Watson transform have been discussed by Derem.[19] The generalizations based on the geometrical theory of diffraction (GTD) have been used to study the acoustic scattering by more complicated objects at higher frequencies.[24–28] The elastic GTD is fundamentally based on the knowledge of the leaky wave propagation on cylinders and spheres but its progress is still rather limited compared to the electromagnetic GTD.[29] Alternative descriptions based on the resonant scattering theory (RST) adapted from classical nuclear-scattering theory have also been developed.[30–32] A large amount of literature is given by Veksler *et al.*[32] on this subject. Finally, many other physical problems deal with cylindrical and spherical geometries, as those found in the wide field of the multiple scattering theory.[33,34] It is essential for a complete study of multiple scattering that the one-body scattering be considered as solved. Exact solutions are known only for simple geometries in a large frequency range.

Although a large body of literature exists for the acoustic scattering problem, the forced vibration and radiation problems have received relatively less attention.[35–37] In the present case, one deals with the acoustic radiation of a cylindrical elastic shell surrounded by a fluid medium when its external surface is subjected to a point source. Our aim is to understand how leaky waves (Lamb-type waves), which are excited by a local impact (laser impact, for example), propagate.

Felsen *et al.*[38,39] have derived the Green's function for a harmonic source located inside or outside a thin elastic cylindrical shell immersed in different interior and exterior fluid media. Alternative interpretations of the wave field in terms of acoustic rays and leaky waves are also discussed. Our study is different because the point source is located directly on the surface, contrary to Felsen *et al.*, who consider the point source without contact with the shell. In that case, there is one dimension more and another difficulty that consists of determining the reflected wave and the leaky wave points of excitation. In our case, leaky waves are merely excited from the point source. Our analysis in terms of acoustic rays is less sophisticated than that of Felsen *et al.* but, on the other hand, the influence of leaky waves on the acoustic radiation is displayed from computations, and an analysis in terms of resonances is discussed.

The analytical formulation of the problem leading to the normal-mode series is based straightforwardly on that of Pathak and Stepanishen.[36] The problem of harmonically excited cylindrical shells surrounded by a fluid medium is addressed via the use of the spatial Fourier transform. The normal-mode series for the field variables of interest is developed using the linear theory of elasticity (Felsen *et al.*

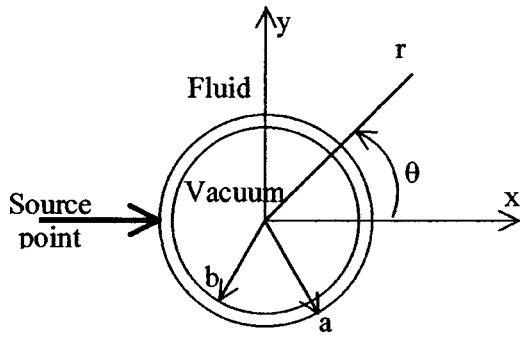

FIG. 1. Fluid-loaded cylindrical elastic shell subjected to a point force.

deal with the equations governing the thin-walled shell dynamics[40]). Consequently, results are applicable over a wide range of excitation frequencies and shell thicknesses. An expression is obtained for the radiated pressure in the fluid, which is evaluated for the far field, using first the standard stationary phase method (as Pathak and Stepanishen[36,37]) and then a fast Fourier transform. Results are compared and interpreted from an analysis in terms of acoustic rays. Clearly, the standard stationary phase method used by Pathak and Stepanishen is an approximation taking into account the direct field only. The direct field is associated with the acoustic ray coming from the point source which circumnavigates around the external surface of the shell before reaching the observation point, the ray travel on the external surface being limited to less than a full turn around the shell. Computations using the fast Fourier transform show additional contributions due to several trips around the shell that cannot be neglected. Numerical calculations are performed for values of the normalized frequency kh going up to 4, where k is the wave number in the fluid medium and h the shell thickness. This maximum reduced frequency value is higher than the value considered by Pathak and Stepanishen in their paper, which is $kh=0.1$. This can explain why contibutions due to several trips do not appear in their results; it is a phenomenon occurring rather at higher frequency.

The presentation begins in Sec. II with the normal mode series using the FFT and is followed in Sec. III with numerical calculations and discussions. The Sommerfeld–Watson transformation of the normal mode series is made in Sec. IV.

II. MODAL THEORY

Consider an evacuated elastic cylindrical shell of inner radius b and outer radius a surrounded by a fluid medium (cf. Fig. 1). Both the shell and the fluid are assumed to be homogeneous. A time-harmonic point source located at $(r=a, \theta=\pi, z=0)$ is assumed to be acting normally on the outer surface of the shell, and is modeled by

$$p_S(r=a,\theta,z)=ap_0\delta(\pi-\theta)\,\delta(z)e^{-i\omega t}, \tag{1}$$

where δ denotes the Delta function, ω the excitation frequency, and p_0 a constant with the dimension of a pressure. In the following development, the $e^{-i\omega t}$ factor will be suppressed in all cases. The irrotational ϕ and rotational $\boldsymbol{\psi}=(\psi_r,\psi_\theta,\psi_z)$ elastic displacement potentials for the shell are governed by two Helmholtz equations, Eq. (2a) for the scalar potential ϕ and Eq. (2b) for the vector potential $\boldsymbol{\psi}$

$$\nabla^2\phi+k_L^2\phi=0, \tag{2a}$$

$$\boldsymbol{\nabla}^2\boldsymbol{\psi}+k_T^2\boldsymbol{\psi}=\mathbf{0}, \tag{2b}$$

where $k_L=\omega/c_L$, $k_T=\omega/c_T$, c_L is the dilatational wave speed, and c_T is the shear wave speed. The shell displacement is written as

$$\mathbf{u}^{(s)}=\boldsymbol{\nabla}\phi+\boldsymbol{\nabla}\times\boldsymbol{\psi}, \tag{3}$$

according to the Helmholtz's decomposition. The radiated pressure p obeys the Helmholtz equation

$$\nabla^2 p+k^2 p=0, \tag{4}$$

where $k=\omega/c$ and c is the sound wave in the surrounding fluid. The fluid displacement is given by

$$\mathbf{u}^{(f)}=\frac{1}{\rho_f\omega^2}\boldsymbol{\nabla}p, \tag{5}$$

where ρ_f is the fluid density.

The solution of the problem is obtained via the introduction of the following Fourier transform:

$$\hat{f}(r,\theta,\xi)=\int_{-\infty}^{+\infty} f(r,\theta,z)e^{-i\xi z}\,dz, \tag{6}$$

$$f(r,\theta,z)=\frac{1}{2\pi}\int_{-\infty}^{+\infty}\hat{f}(r,\theta,\xi)e^{+i\xi z}\,d\xi. \tag{7}$$

After transforming Eqs. (2) and (4) with respect to z, the resulting partial differential equations can be solved by the standard method of variable separation.[13] The pressure and the potentials in the transformed domain can then be expressed as follows:

$$\hat{p}=\sum_{n=0}^{+\infty} A_n H_n^{(1)}(\eta r)\cos(n\theta), \tag{8a}$$

$$\hat{\phi}=\frac{1}{\rho_s\omega^2}\sum_{n=0}^{+\infty}(B_nJ_n(\eta_L r)+C_nN_n(\eta_L r))\cos(n\theta), \tag{8b}$$

$$\hat{\psi}_r=\frac{1}{\rho_s\omega^2}\sum_{n=0}^{+\infty}(D_nJ_{n+1}(\eta_T r)+E_nN_{n+1}(\eta_T r))\sin(n\theta), \tag{8c}$$

$$\hat{\psi}_\theta=-\frac{1}{\rho_s\omega^2}\sum_{n=0}^{+\infty}(D_nJ_{n+1}(\eta_T r)+E_nN_{n+1}(\eta_T r))\cos(n\theta), \tag{8d}$$

$$\hat{\psi}_z=\frac{1}{\rho_s\omega^2}\sum_{n=0}^{+\infty}(F_nJ_n(\eta_T r)+G_nN_n(\eta_T r))\sin(n\theta), \tag{8e}$$

where

$$\eta=(k^2-\xi^2)^{1/2},\quad \eta_L=(k_L^2-\xi^2)^{1/2},\quad \eta_T=(k_T^2-\xi^2)^{1/2}, \tag{9}$$

ρ_s is the shell density, J_n and N_n are the Bessel and the Neumann functions, respectively, and $H_n^{(1)}$ is the Hankel function of the first kind. Of course, the Fourier transform of

the radiated pressure in the fluid satisfies the radiation condition of Sommerfeld.[13,38] As indicated by Pathak and Stepanishen, only the values of the Bessel functions $(J_n, N_n, H_n^{(1)})$ with complex arguments are used, eliminating the need to switch between the Bessel functions for real arguments and the modified Bessel functions (I_n, K_n) for purely imaginary arguments. The constants $A_n, \ldots, G_n$ are determined from the boundary conditions on the inner and outer surfaces of the shell. The boundary conditions are

(a) on the inner surface $r=b$:

$$\hat{u}_r^{(s)}=0, \quad \hat{\sigma}_{rr}=0, \quad \hat{\sigma}_{r\theta}=0, \quad \text{and} \quad \hat{\sigma}_{rz}=0, \tag{10a}$$

(b) on the outer surface $r=a$:

$$\hat{u}_r^{(s)}=\hat{u}_r^{(f)}, \quad \hat{\sigma}_{rr}=-(\hat{p}+\hat{p}_S), \quad \hat{\sigma}_{r\theta}=0, \quad \text{and} \quad \hat{\sigma}_{rz}=0. \tag{10b}$$

The components of the stress tensor of interest are given by

$$\sigma_{rr}=\rho_s(c_L^2-2c_T^2)k_L^2\phi+2\rho_s c_T^2\left[-\frac{\partial^2\phi}{\partial r^2}+\frac{1}{r}\frac{\partial^2\psi_z}{\partial r\,\partial\theta}-\frac{1}{r^2}\frac{\partial\psi_z}{\partial\theta}-\frac{\partial^2\psi_\theta}{\partial r\,\partial z}\right],$$

$$\sigma_{r\theta}=\rho_s c_T^2\left[\frac{2}{r}\left(-\frac{\partial^2\phi}{\partial r\,\partial\theta}+\frac{1}{r}\frac{\partial\phi}{\partial\theta}\right)+\frac{\partial^2\psi_r}{\partial r\,\partial z}-\frac{1}{r}\frac{\partial\psi_r}{\partial z}-\frac{1}{r}\frac{\partial^2\psi_\theta}{\partial\theta\,\partial z}-\frac{\partial^2\psi_z}{\partial r^2}+\frac{1}{r}\frac{\partial\psi_z}{\partial r}+\frac{1}{r^2}\frac{\partial^2\psi_z}{\partial\theta^2}\right],$$

$$\sigma_{rz}=\rho_s c_T^2\left[-2\frac{\partial^2\phi}{\partial r\,\partial z}-\frac{1}{r}\frac{\partial^2\psi_r}{\partial r\,\partial\theta}+\frac{1}{r^2}\frac{\partial\psi_r}{\partial\theta}+\frac{1}{r}\frac{\partial\psi_\theta}{\partial r}-\frac{1}{r^2}\psi_\theta+\frac{\partial^2\psi_\theta}{\partial r^2}-\frac{\partial^2\psi_\theta}{\partial z^2}+\frac{1}{r}\frac{\partial^2\psi_z}{\partial\theta\,\partial z}\right],$$

and the Fourier transform of the point source can be expressed as

$$\hat{p}_S=ap_0\delta(\pi-\theta)=\frac{ap_0}{2\pi}\sum_{n=0}^{+\infty}\varepsilon_n(-1)^n\cos n\theta, \tag{11}$$

because of the periodicity with regard to θ (ε_n is the Neumann's factor; $\varepsilon_0=1$ and $\varepsilon_n=2$ for $n\geqslant 1$). Finally, one obtains a system of equations for the unknowns $(A_n, \ldots, G_n)$ in a matrix form as

$$[D_n]\begin{Bmatrix} A_n \\ \cdot \\ \cdot \\ \cdot \\ G_n \end{Bmatrix}=\begin{Bmatrix} (k_T a)^2\dfrac{ap_0}{2\pi}(-1)^n\varepsilon_n \\ 0 \\ \cdot \\ \cdot \\ 0 \end{Bmatrix}, \tag{12}$$

where the elements of the matrix $[D_n]$ are those given by Veksler.[13]

It is of interest to note that the previous equations permit us to calculate the acoustic scattering of an obliquely incident plane wave by the shell. To achieve this goal, the variable ξ is rewritten as

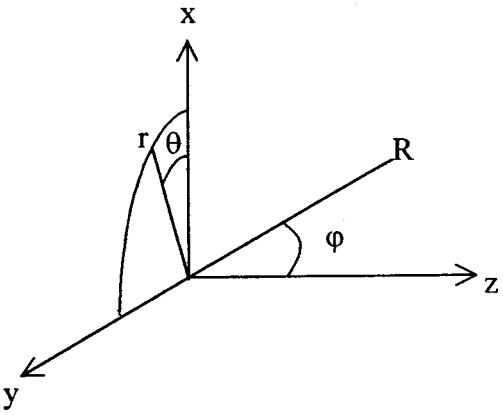

FIG. 2. Polar coordinate system.

$$\xi=k\sin\alpha, \tag{13}$$

where α is the angle of incidence and the right-hand side of Eq. (12) is replaced by the vector[13]

$$\left(-(k_T a)^2 J_n(\eta a)\varepsilon_n i^n, \frac{\rho_s}{\rho_f}(\eta a)J_n'(\eta a)\varepsilon_n i^n, 0, \ldots, 0\right), \tag{14}$$

where $\eta=(k^2-(k\sin\alpha)^2)^{1/2}=k\cos\alpha$. At normal incidence $(\alpha=0)$, the incident wave is propagating in the direction defined by $\theta=0$. After carrying out the indicated operations, the acoustic scattering at oblique incidence is then given by

$$p_{\text{oblique}}=\hat{p}e^{i(\xi=k\sin\alpha)z}=\sum_{n=0}^{+\infty}A_n H_n^{(1)}(kr\cos\alpha)\cos(n\theta)e^{ikz\sin\alpha}. \tag{15}$$

The radiated pressure of the shell excited by a point source can be expressed using Eqs. (7), (8a), (9), and (12) as follows:

$$p(r,\theta,z)=\frac{1}{2\pi}\int_{-\infty}^{+\infty}\hat{p}(r,\theta,\xi)e^{i\xi z}\,d\xi=\frac{1}{2\pi}\int_{-\infty}^{+\infty}\sum_{n=0}^{+\infty}A_n(\xi)H_n^{(1)}(\eta r)\cos(n\theta)e^{i\xi z}\,d\xi. \tag{16}$$

According to Pathak and Stepanishen,[36,37] the far-field pressure can be derived from the stationary phase integration method.[41] For this purpose, the coordinate system is changed to the spherical polar coordinate system (R,φ,θ) where R is the distance from the origin to the observation point (cf. Fig. 2). With this transformation and the use of the stationary phase integration method, the saddle point is located at $\xi=k\cos\varphi$ and the radiated pressure can be written as

$$p(r,\theta,z)=\frac{1}{\pi\sqrt{k\sin\varphi}}\left[\sum_{n=0}^{+\infty}i^{-(n+1)}A_n(k\cos\varphi)\cos(n\theta)\right]\frac{e^{ikR}}{R}. \tag{17}$$

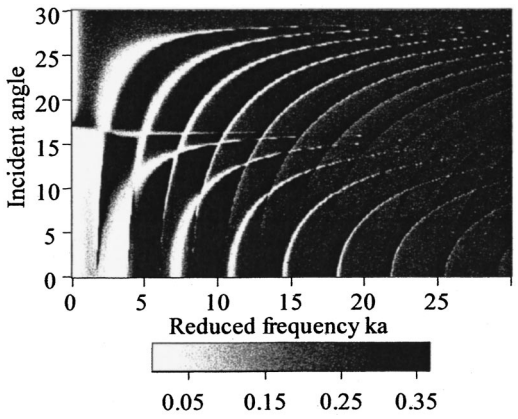

FIG. 3. Modulus of the backscattering at oblique incidence: Excitation by a plane wave (steel shell).

III. NUMERICAL RESULTS AND DISCUSSIONS

We have first compared the radiated pressure evaluated from the stationary phase method with the acoustic scattering at oblique incidence for a steel shell in water. The parameters used in the calculations are $\rho_f = 1000\,\mathrm{kg/m^3}$, $\rho_s = 7900\,\mathrm{kg/m^3}$, $c = 1470\,\mathrm{m/s}$, $c_L = 5790\,\mathrm{m/s}$, $c_T = 3100\,\mathrm{m/s}$, and $b/a = 0.98$. Figure 3 shows the modulus of the acoustic scattering at oblique incidence in the plane (ka, α) for $\theta = \pi$ (backscattering) and Fig. 4 shows the modulus of the radiated pressure in the plane $(ka, z/a)$ for $\theta = 0$ (forward scattering). This choice has been made in view of obtaining figures with as much contrast as possible. Both figures reveal a predominant phenomenon which is the evolution of the shell resonances with regard to the reduced frequency *ka*. Shell resonances appear as troughs and peaks in backscattering and as peaks in forward scattering. These figures can also be interpreted as spatial dispersion curves associated with leaky waves propagating around the shell.[21–23] It results from this comparison that information about shell resonances and leaky waves is the same in both cases. Moreover, the resonant wave numbers associated with leaky waves are solutions of the characteristic equation $D_n(\xi) = 0$, where D_n is the determinant of the linear system of equations coming from the boundary conditions [cf. Eq. (12)]. Numerical calculations show that ξ varies in the same way when α and z/a run over the ranges $[0°, 30°]$ and $[0, 6]$, which explains the coincidence of dispersion curves in Figs. 3 and 4. In order to complete this first point, one can note that the radiated pressure evaluated with the use of the stationary phase method can be interpreted as the radiation of a point source in three dimensions [in relation to the Green's function $\exp(ikR)/R$] with a modulated frequency amplitude. One can observe in Fig. 5 that $\xi = k \sin\alpha = kz/R_0$ for oblique incidence and $\xi = k\cos\varphi = kz/R$ for the point source with $R \approx R_0$ in the far field $(r \to +\infty)$. Therefore, it seems rather natural to observe comparable results in both cases.

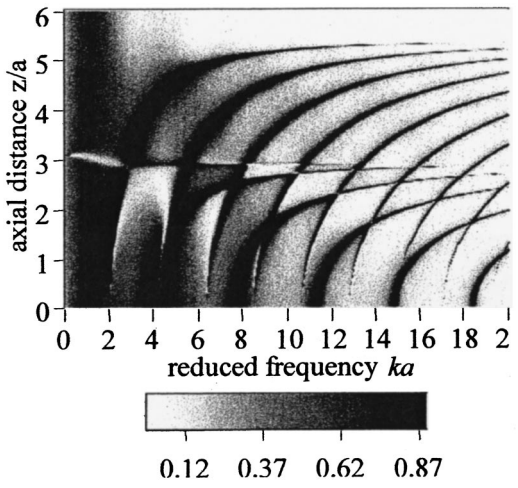

FIG. 4. Modulus of the radiated pressure calculated with the use of the stationary phase method (steel shell).

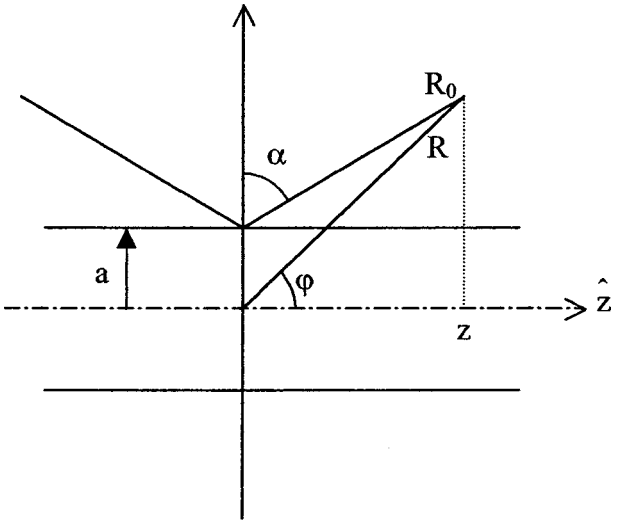

FIG. 5. Acoustic paths for the backscattering at oblique incidence and for the radiated pressure calculated with the use of the stationary phase method (steel shell).

The computation of the radiated pressure by the use of the Fourier transform needs some care. In order to ensure a good resolution in frequency and a well-defined delta function with negligible oscillations, the fast Fourier transform (FFT) is performed over 2^{17} points with $\Delta\xi = 0.005$ as sampling. In fact, $\hat{p}$ exponentially vanishes outside the range $[-k, k]$ and a series of zeros is added at the end of the signal according to the zero padding procedure. One must note that the exponential vanishing of $\hat{p}$ is reinforced far from the shell $(r \to +\infty)$ and that it is not possible to calculate the acoustic field on the shell surface because $\hat{p}$ dramatically increases outside the range $[-k, k]$ close to the shell surface. The radiated pressure obtained by using the FFT is shown in Fig. 6. When compared to the results of Fig. 4 obtained with the use of the stationary phase method, the behavior of the radiated pressure appears to be much more complicated. Obviously, the radiated field seems to be influenced by multiple interferences. The two vertical lines at low frequency are merely due to subsampling. They can be explained by the presence of the so-called *A* wave.[7,9,13] This wave radiates very weakly at low frequency. Therefore, the sampling $\Delta\xi$ is too large compared to the damping coefficient of the *A* wave, which is very small in that case. Of course, the smaller the damping coefficient is, the smaller the sampling has to be in order to describe the behavior of leaky waves accurately.

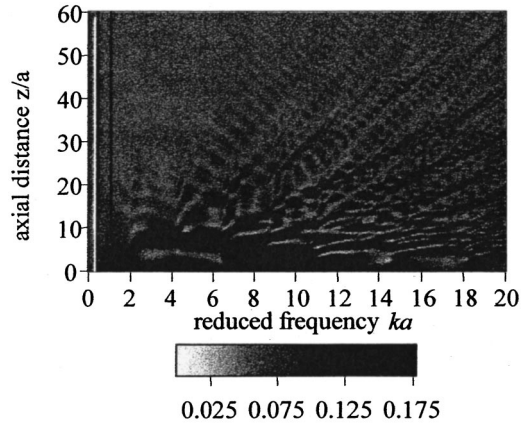

FIG. 6. Modulus of the radiated pressure calculated with the use of the FFT (steel shell), $r=10a$.

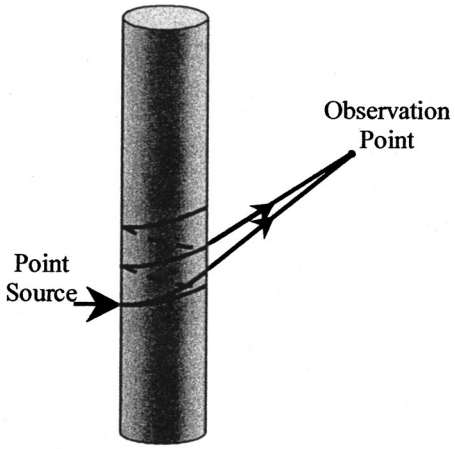

FIG. 8. The two first helical acoustic rays associated with the propagation of helical leaky waves from the point source to the point of observation.

Instead of analyzing the radiated pressure from a modal series, it is better to investigate the radiated pressure mode by mode. From a physical point of view, all modes bring the same phenomenon to light. Therefore, we shall focus only on the mode $n=2$ as an example (the first ten modes have been analyzed). Results are depicted in Fig. 7, where two phenomena are observed. The first, starting at the cutoff frequency $ka=4.23$, is related to the first leaky guided wave and the second one, starting at the cutoff frequency $ka=7.7$, is associated with the leaky circumferential wave, named the S_0 wave.[13] The first leaky guided wave has a polarization which is both perpendicular to its direction of propagation and parallel to the shell axis. It is a predominantly shear wave of torsional type.[42] Because of its polarization, it radiates weakly in the fluid and can propagate far from the point source. Contrary to the first leaky guided wave, the leaky circumferential wave S_0 does not have a particular polarization (except that it is a symmetric wave). It can propagate far or not, depending on the value of its damping coefficient, which varies with frequency.

The outstanding phenomenon is the emergence of an infinite number of spatial dispersion curves associated with each leaky wave. By comparison, the radiated pressure calculated with the use of the stationary phase method shows the first spatial dispersion curves only, those of lower order

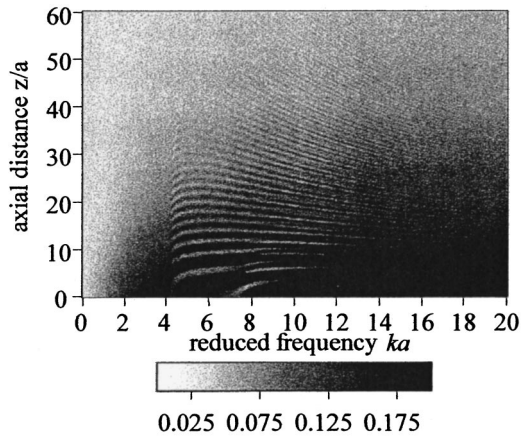

FIG. 7. Modulus of the partial radiated pressure, mode $n=2$, calculated with the use of the FFT (steel shell).

(cf. Fig. 4). The understanding of this phenomenon comes from an alternative interpretation of the radiated pressure in terms of acoustic rays associated with leaky waves.[39] From now on, one considers the wave propagation from the point source adopting a local point of view instead of the propagation of leaky waves along the shell axis according to a global point of view. The point source generates wavefronts which are circular close to the point of excitation and then deformed as the wave fronts propagate. The deformation is due to the fact that all the points of the wavefronts do not propagate with the same velocity. As shown in Fig. 8, an infinite numbers of acoustic rays starting from the point source and going to the point of observation can be associated with each leaky wave when excited by a point source. From the geometrical theory of diffraction point of view, each acoustic ray can be considered as a helical leaky wave when propagating on the shell surface. As a result, one can associate an infinity of helical leaky waves with each leaky guided wave and to each circumferential wave, as much as rays. This is the local point of view. As previously indicated, the helical leaky waves do not propagate with the same velocity, and in addition, their damping coefficients are different. As established by Conoir *et al.* for oblique incidence,[23] resonances occur because of the phase matching of circumnavigating helical leaky waves. Resonance frequency values depending on the nth mode of vibration are obtained by stating that n wavelengths take place on the distance $d=\delta\cos\gamma$ where δ is the pitch of the helix and γ the angle between the helical leaky wave direction of propagation and the shell axis. As the phase matching depends on the pitch of the helix, which itself depends on the number of times the helical leaky wave associated with the acoustic ray travels around the shell before reaching the observation point, there are as many resonances associated with the nth mode of vibration as rays drawn on the shell surface. This is why one can observe an infinite number of spatial dispersion curves which are associated to the infinite number of helical acoustic rays.

The phenomenon associated with the emergence of an infinite number of spatial dispersion curves is more pronounced for the first leaky guided wave than for the S_0 wave

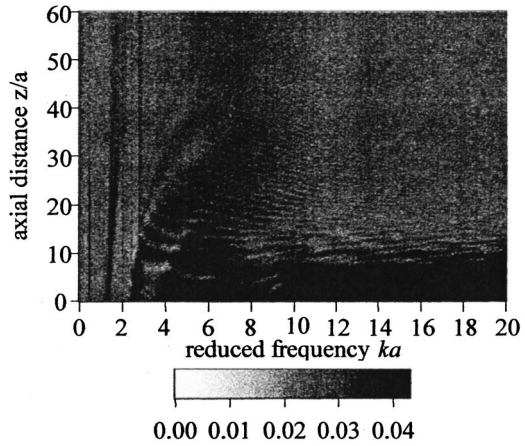

FIG. 9. Modulus of the radiated pressure calculated with the use of the FFT (aluminum shell), $r=10a$.

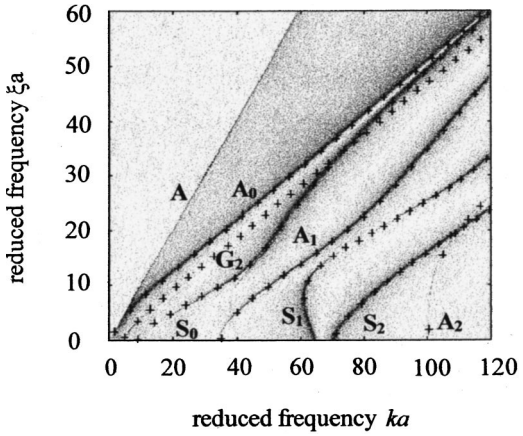

FIG. 10. Modulus of $\hat{p}(r,\phi,\xi)$ for the mode $n=2$ and roots of the characteristic equation associated with leaky waves propagating along evacuated shell in vacuum (aluminum shell).

because the damping coefficient of the first one is much weaker than that of the second one. Helical leaky waves associated with the first leaky guided wave can then propagate very far following the helical path and travel a long time around the shell before vanishing. In this case, the phase matching is reinforced and the phenomenon associated with the emergence of an infinite number of spatial dispersion curves is greatly advantaged.

The maximum value of the reduced frequency kh previously considered was $kh=1$ (k is the wave number in fluid and h the shell thickness). In order to investigate this phenomenon for higher values of the reduced frequency, we have considered a thicker shell. The parameters used in the calculations are those of an aluminum shell: $\rho_s=2800$ kg/m^3, $c_L=6355$ m/s, $c_T=3140$ m/s, and $b/a=0.8$. With this shell thickness the maximum value of the reduced frequency is $kh=4$. Figure 9 shows the modulus of the radiated pressure in the plane $(ka,z/a)$ for $\theta=0$. Results are very comparable to those of the steel shell. Once more the sampling $\Delta\xi$ is too large compared to the damping coefficient of the A wave which makes vertical lines with no physical meaning appear.

The investigation has been enlarged, for this shell, by studying the leaky waves which can propagate. For this purpose the Fourier transform of the radiated pressure is analyzed in the plane of the reduced wave numbers (ka,ξ). Our aim is to determine the leaky waves which govern the resonant behavior of the radiated pressure. The modulus of $\hat{p}$ is plotted in Fig. 10 and compared to the roots of the characteristic equation associated with leaky waves propagating along an evacuated shell in vacuum. As before, it is the mode $n=2$ that is investigated. The coincidence is noteworthy. From the RST point of view, it means that no background has to be taken into consideration, in this case its influence is negligible.[30–32] Of course, there are no roots corresponding to the A wave since the characteristic equation giving them is associated with the shell in vacuum. In this case, the A wave does not exist. In the frequency range of interest ($0\leqslant ka\leqslant 20$), four leaky waves are propagating. The influence of the A wave has already been discussed; it gives rise to vertical lines with no physical meaning because of the subsampling. The A_0 wave is obviously too damped to radiate efficiently as soon as the axial distance z increases. The only waves still appearing are: the first leaky guided wave, labeled G_2 in order to refer to the mode $n=2$, and the S_0 wave. This is a justification *a posteriori* of the fact that one has only considered the first leaky guided wave and the S_0 wave to analyze the results of the steel shell. It is relevant because the results on the steel and aluminum shells are comparable.

IV. SOMMERFELD–WATSON TRANSFORMATION AND HELICAL ACOUSTIC RAYS

The aim of this section is to obtain the analytical expressions corresponding to helical leaky waves introduced in the previous section, by using the Sommerfeld–Watson transform (SWT). The SWT has been introduced in acoustics in order to interpret the scattering by cylinders and spheres in terms of acoustic rays.[16–28] In contrast, the use of the SWT is not classical for radiation problems. However, there are no great modifications when using the SWT in this case. This is why it is developed rather briefly in this paper, up to the point where analytical expressions can be interpreted in terms of acoustic rays. Interpretations in terms of acoustic rays are given in the work of Felsen *et al.*[39] and not reproduced herein.

In order to separate phase terms from amplitude ones when carrying out the SWT, the radiated pressure is rewritten as

$$p=\frac{1}{2\pi}\int_{-\infty}^{+\infty}\sum_{n=0}^{+\infty}(-1)^n\varepsilon_n a_n\frac{H_n^{(1)}(\eta r)}{H_n^{(1)}(\eta a)}\cos(n\theta)e^{i\xi z}\,d\xi, \tag{18}$$

where

$$a_n=\frac{H_n^{(1)}(\eta a)}{(-1)^n\varepsilon_n}A_n. \tag{19}$$

The SWT begins with the transformation of the modal series into an integral. In order to perform this transformation, an analytical extension is made on the vibration mode numbers, which are replaced by the complex variable ν, and the following relation is used:

$$\sum_{n=0}^{+\infty}(-1)^n F_n(\xi)=\frac{i}{2}P\int_C \frac{F_\nu(\xi)}{\sin \pi\nu}d\nu, \tag{20}$$

where the C contour encloses the positive real axis. The integral is calculated with the use of the principal value because of the Neumann's factor.[20] The C contour being as close as we want to the axis, the only singularities enclosed by C are those coming from the equation $\sin \pi\nu=0$; the evaluation of the integral, thanks to the residue method, leads to Eq. (20). The aim of the SWT is then to perform a deformation of C in order to take into account the physical singularities in the complex ν-plane, singularities located in the first quadrant [$\mathrm{Re}(\nu)>0$ and $\mathrm{Im}(\nu)>0$] because of the principle of causality. In our case, the singularities are solutions of the characteristic equation

$$D_\nu(\xi)=0, \tag{21}$$

where D_ν is the complex extension of D_n [in Eq. (21), ξ plays the role of a parameter]. This operation is described by Doolittle *et al.*[2] and the discussion is the same for radiation problems. So, the modal series in Eq. (18) is transformed into an integral on a contour that encloses physical singularities, and this integral is evaluated by the residue method. It follows that

$$p=\sum_m p_m, \tag{22}$$

with

$$p_m=\frac{1}{2\pi}\int_{-\infty}^{+\infty}(-2\pi)\beta_m(\xi)\frac{H_{\nu_m}^{(1)}(\eta r)}{H_{\nu_m}^{(1)}(\eta a)}\frac{\cos(\nu_m\theta)}{\sin(\pi\nu_m)}e^{i\xi z}\,d\xi, \tag{23}$$

where

$$\beta_m(\xi)=\mathrm{Res}(a_\nu,\nu_m(\xi)) \tag{24}$$

is the residue of a_ν associated to the mth root $\nu_m=\nu_m(\xi)$ of the characteristic equation Eq. (21).

At this point of the SWT, the high-frequency hypothesis is introduced. This hypothesis is rather natural since the SWT leads in fact to a ray theory. Therefore, we have to introduce the adapted asymptotic expansions of the Bessel functions. Many asymptotic expansions can be used, but the ray theory which is analyzed herein only requires the use of the asymptotic expansions of Debye. In the case of leaky waves, the asymptotic expansion to be used is

$$H_\nu^{(1)}(x)\approx\sqrt{\frac{2}{\pi}}\frac{1}{(x^2-\nu^2)^{1/4}}e^{-i[\nu\cos^{-1}(\nu/x)-(x^2-\nu^2)^{1/2}+(\pi/4)]}. \tag{25}$$

Using Eq. (25) and performing the standard following decomposition:

$$\frac{\cos(\nu_m\theta)}{\sin(\pi\nu_m)}=-i\left[\sum_{q=0}^{+\infty}e^{i\nu_m(\pi-\theta+2q\pi)}+\sum_{q=0}^{+\infty}e^{i\nu_m(\pi+\theta+2q\pi)}\right], \tag{26}$$

the mth contribution of the radiated pressure takes the form

$$p_m=\sum_{q=0}^{+\infty}\left[\frac{1}{2\pi}\int_{-\infty}^{+\infty}A_{mq}^{+}(\xi)e^{i\eta\phi_{mq}^{+}(\xi)}\,d\xi\right]+\sum_{q=0}^{+\infty}\left[\frac{1}{2\pi}\int_{-\infty}^{+\infty}A_{mq}^{-}(\xi)e^{i\eta\phi_{mq}^{-}(\xi)}\,d\xi\right], \tag{27}$$

with

$$A_{mq}^{\pm}(\xi)=2\pi\frac{[(\eta a)^2-\nu_m^2]^{1/4}}{[(\eta r)^2-\nu_m^2]^{1/4}}\beta_m(\xi)e^{i\pi/2}e^{-\mathrm{Im}(\nu_m)\psi_{mq}^{\pm}(\xi)}, \tag{28}$$

and

$$\phi_{mq}^{\pm}(\xi)=\eta\left[\sqrt{r^2-r_{cm}^2}-\sqrt{a^2-r_{cm}^2}+\frac{\xi}{\eta}z\right]+\mathrm{Re}(\nu_m)\psi_{mq}^{\pm}(\xi), \tag{29}$$

where

$$r_{cm}=\frac{\mathrm{Re}(\nu_m)}{\eta}, \tag{30}$$

and

$$\psi_{mq}^{\pm}(\xi)=\pi\pm\theta+2q\pi-\cos^{-1}\left(\frac{r_{cm}}{r}\right)+\cos^{-1}\left(\frac{r_{cm}}{a}\right). \tag{31}$$

In the previous relations, the signs $\pm$ indicate either an anticlockwise $(+)$ or a clockwise $(-)$ propagation of acoustic rays around the shell. The phase term $\psi_{mq}^{\pm}$ in Eq. (31) is introduced by making the hypothesis $\mathrm{Im}(\nu_m)\ll\mathrm{Re}(\nu_m)$, which is always verified at high frequencies. The quantity r_{cm} introduced by Felsen *et al.*[39] denotes the radius of the caustic that generates the relevant system of rays. The quantity $\mathrm{Re}(\nu_m)/a$ represents the projected propagation coefficient for waves propagating in the θ-direction. The attenuation coefficient associated with $\mathrm{Im}(\nu_m)$ accounts for the damping of leaky waves during their propagation. The integer q indicates the number of full circumnavigation of acoustic rays around the shell. Finally, $[\beta_m(\xi)]^{1/2}$ appearing in the terms $A_{mq}^{\pm}$ may be interpreted as a launching or detachment coefficient (they are identical because of the reciprocity).

Using the stationary phase method, it follows that

$$\frac{1}{2\pi}\int_{-\infty}^{+\infty}A_{mq}^{\pm}(\xi)e^{i\eta\phi_{mq}^{\pm}(\xi)}\,d\xi \approx\frac{1}{2\pi}\sqrt{\frac{2\pi}{\eta|\phi_{mq}^{\pm}(\xi_s)''|}}e^{[i\pi\,\mathrm{sgn}(\phi_{mq}^{\pm}(\xi_s)'')/4]}\times A_{mq}^{\pm}(\xi_s)e^{i\eta\phi_{mq}^{\pm}(\xi_s)}, \tag{32}$$

where the stationary phase point ξ_s is solution of the equation

$$\phi_{mq}^{\pm}(\xi)'=0, \tag{33}$$

with $\mathrm{sgn}(x)=1$ if $x>0$ and $\mathrm{sgn}(x)=-1$ if $x<0$.

Equation (32) can be interpreted in terms of propagating helical acoustic rays as those depicted in Fig. 8. The trajectories of helical acoustic rays depend directly on the phase terms $\phi_{mq}^{\pm}(\xi_s)$. For this geometrical interpretation, we refer

to the work of Felsen *et al.*[39] Of course, it requires effort to adapt because the point source is not in contact with the shell surface in the case of the three-dimensional Green's function investigated in this reference. A discussion about this problem is presented in the Appendix.

V. CONCLUDING REMARKS

We have shown that the acoustic radiation of a cylindrical elastic shell subjected to a point force can be analyzed from the emergence of an infinite number of spatial dispersion curves which are related to helical acoustic rays. This phenomenon has been established by calculating the radiated pressure with the help of the FFT. The reason why the standard stationary phase method does not exhibit this phenomenon has been explained from the interpretation of the radiated field in terms of helical acoustic rays. In fact, the stationary phase method neglects the helical acoustic rays which travel more than one time around the shell. A numerical calculation of the three-dimensional Green's function of Felsen *et al.*[39] could be performed in order to bring a similar phenomenon to light.

APPENDIX

In the following, the correspondence between our notations and those of Felsen *et al.*[39] is given. For the geometry, we have

$$\theta \equiv \phi. \tag{A1}$$

The point source of the three-dimensional Green's function tends towards the point source acting on the shell surface (in agreement with our geometry) when choosing

$$r' = a, \quad \phi' = \pi, \quad \text{and} \quad z' = 0. \tag{A2}$$

For the wave numbers, we have

$$k = k_2, \quad \xi = \beta, \quad \text{and} \quad \eta = \kappa_2, \tag{A3}$$

and from Eq. (18) of Felsen *et al.* it follows that

$$\frac{\xi}{k} = \sin\omega \quad \text{and} \quad \frac{\eta}{k} = \cos\omega. \tag{A4}$$

It is important to note that Eq. (27) is very similar to Eq. (23) of Felsen *et al.*, but is different since the term

$$[(\eta a)^2 - \nu_m^2]^{1/4} \approx \eta^{1/2}[a^2 - r_{cm}^2]^{1/4}$$

is in the nominator in Eq. (28) and at the denominator in Eq. (23) of Felsen *et al.* As a consequence, the solution of the radiated problem cannot be deduced from the three-dimensional Green's function merely using the limiting values of Eq. (A2). Despite this fact, the phase terms related to propagation of helical acoustic rays are the same in both cases. This is why it is possible to refer to the work of Felsen *et al.*, in order to interpret the radiated pressure in terms of helical acoustic rays. So, the problem is to show that phase terms of Eq. (29)

$$\phi_{mq}^{\pm}(\xi) = \eta\left[\sqrt{r^2 - r_{cm}^2} - \sqrt{a^2 - r_{cm}^2} + \frac{\xi}{\eta} z\right] + \mathrm{Re}(\nu_m) \times \left\{ \pi \pm \theta + 2q\pi - \cos^{-1}\left(\frac{r_{cm}}{r}\right) + \cos^{-1}\left(\frac{r_{cm}}{a}\right)\right\}, \tag{A5}$$

are equal to those of Felsen *et al.* [cf. their Eq. (23a)] defined by

$$\hat{\phi}_m^{(a)} = k_2[(z - z')\sin\omega + (l_m^{(a)} + l_m^{(a)'} + r_{cm}\overline{\psi}_m^{(a)})\cos\omega], \tag{A6}$$

with

$$l_m^{(a)} = \sqrt{r^2 - r_{cm}^2} - \sqrt{a^2 - r_{cm}^2}, \tag{A7}$$

$$l_m^{(a)'} = \sqrt{r'^2 - r_{cm}^2} - \sqrt{a^2 - r_{cm}^2}, \tag{A8}$$

$$\overline{\psi}_m^{(a)} = |\phi - (\phi' + 2q\pi)| - \psi_m^{(a)} - \psi_m^{(a)'}, \tag{A9}$$

$$\psi_m^{(a)} = \cos^{-1}\left(\frac{r_{cm}}{r}\right) - \cos^{-1}\left(\frac{r_{cm}}{a}\right), \tag{A10}$$

$$\psi_m^{(a)'} = \cos^{-1}\left(\frac{r_{cm}}{r'}\right) - \cos^{-1}\left(\frac{r_{cm}}{a}\right). \tag{A11}$$

We have $l_m^{(a)'} = 0$ and $\psi_m^{(a)'} = 0$ because of Eq. (A2). Then, from Eqs. (A1)–(A4) and Eq. (30) it follows that

$$\hat{\phi}_m^{(a)} = \eta\left[\frac{\xi}{\eta} z + \sqrt{r^2 - r_{cm}^2} - \sqrt{a^2 - r_{cm}^2}\right] + \mathrm{Re}(\nu_m) \times \left\{ |\theta - (\pi + 2q\pi)| - \cos^{-1}\left(\frac{r_{cm}}{r}\right) + \cos^{-1}\left(\frac{r_{cm}}{a}\right)\right\}. \tag{A12}$$

It is easy to verify that Eq. (A12) is equal to Eq. (A5) in agreement with the discussion given in Fig. 3 of Felsen *et al.* (in our case q is always a positive integer, contrary to q in Felsen *et al.*, which can take negative values).

[1] J. J. Faran, "Sound scattering by solid cylinders and spheres," J. Acoust. Soc. Am. **23**, 405–418 (1951).
[2] R. D. Doolittle, H. Überall, and P. Ugincius, "Sound scattering by elastic cylinders," J. Acoust. Soc. Am. **43**, 1–14 (1968).
[3] Y. H. Pao and C. C. Mow, "Theory of normal modes and ultrasonic spectral analysis of the scattering of waves in solids," J. Acoust. Soc. Am. **59**, 1046–1056 (1976).
[4] A. Derem, "Relation entre la formation des ondes de surface et l'apparition des résonances dans la diffusion acoustique" (Relation between surface waves and resonances in acoustic scattering), Rev. Cethedec **58**, 43–79 (1979).
[5] G. Maze and J. Ripoche, "Méthode d'isolement et d'identification des résonances (MIIR) de cylindres et de tubes soumis à une onde acoustique plane dans l'eau" [Method of isolation and identification of resonances (MIIR) applied to cylinders excited by an acoustic plane wave in water], Rev. Phys. Appl. **18**, 319–326 (1983).
[6] G. C. Gaunaurd and D. Brill, "Acoustic spectrogram and complex-frequency poles of a resonantly excited elastic tube," J. Acoust. Soc. Am. **75**, 1680–1693 (1984).
[7] G. Maze, J. Ripoche, A. Derem, and J. L. Rousselot, "Diffusion d'une onde ultrasonore par des tubes remplis d'air immergés dans l'eau" (Scat-

tering of ultrasonic waves by air filled cylindrical shells in water), Acustica **55**, 69–85 (1984).
[8] G. C. Gaunaurd and M. F. Werby, ''Resonance response of submerged acoustically excited thick and thin shells,'' J. Acoust. Soc. Am. **77**, 2081–2093 (1985).
[9] G. S. Sammelmann, D. H. Trivet, and R. H. Hackmann, ''Acoustic scattering by a submerged spherical shell. I. The bifurcation of the dispersion curve for the spherical antisymmetric Lamb wave,'' J. Acoust. Soc. Am. **85**, 114–124 (1989).
[10] R. H. Hackmann and G. S. Sammelmann, ''Acoustic scattering by a submerged spherical shell. III. Pole trajectories in the complex-ka plane,'' J. Acoust. Soc. Am. **90**, 2705–2717 (1991).
[11] Y. P. Guo, ''Approximate solutions of the dispersion equation for fluid-loaded cylindrical shells,'' J. Acoust. Soc. Am. **95**, 1435–1440 (1994).
[12] P. L. Marston and N. H. Sun, ''Backscattering near the coincidence frequency of thin cylindrical shells: Surface wave properties from elasticity theory and an approximate ray synthesis,'' J. Acoust. Soc. Am. **97**, 777–783 (1995).
[13] N. D. Veksler, *Resonance Acoustic Spectroscopy* (Springer, Berlin, 1993).
[14] H. Peine and D. Guicking, ''Acoustical resonance scattering theory for strongly overlapping resonances,'' Acustica **3**, 233–241 (1995).
[15] N. D. Veksler, J. L. Izbicki, and J. M. Conoir, ''Flexural waves in the acoustic wave scattering by a liquid-filled shell,'' Akust. Zh. **45**(3), 279–288 (1999).
[16] G. V. Frisk, J. W. Dickey, and H. Überall, ''Surface wave modes on elastic cylinders,'' J. Acoust. Soc. Am. **58**, 996–1008 (1975).
[17] G. V. Frisk and H. Überall, ''Creeping waves and lateral waves in acoustic scattering by large elastic cylinders,'' J. Acoust. Soc. Am. **59**, 46–54 (1976).
[18] K. L. Williams and P. L. Marston, ''Backscattering from an elastic sphere using the Sommerfeld–Watson transformation and giving a Fabry–Perot analysis of resonances,'' J. Acoust. Soc. Am. **78**, 1093–1102 (1985).
[19] A. Derem, ''Théorie de la matice S et transformation de Sommerfeld–Watson dans la diffusion acoustique'' (S-matrix theory and Sommerfeld–Watson transform in acoustic scattering), in *La Diffusion Acoustique*, edited by N. Gespa (CEDOCARE, 1987).
[20] J. M. Conoir, J. L. Izbicki, and P. Rembert, ''Scattering by cylindrical objects at oblique incidence,'' in *Acoustic Interaction With Submerged Elastic Structures*, Series on Stability, Vibration and Control of Systems, Series B, Vol. 5, edited by A. Guran, J. Ripoche, and F. Ziegler (World Scientific, Singapore, 1996).
[21] H. Überall, L. R. Dragonette, and L. Flax, ''Relation between creeping waves and normal modes of vibration of a curved body,'' J. Acoust. Soc. Am. **61**, 711–715 (1977).
[22] G. C. Gaunaurd and H. Überall, ''Relation between creeping wave acoustic transient and the complex frequency poles of the singularity expansion method,'' J. Acoust. Soc. Am. **78**, 234–243 (1985).
[23] J. M. Conoir, P. Rembert, O. Lenoir, and J. L. Izbicki, ''Relation between helical surface waves and elastic cylinder resonances. Resonances shift and guided waves polarization study,'' J. Acoust. Soc. Am. **93**, 1300–1307 (1993).
[24] P. L. Marston, ''GTD for backscattering fom elastic spheres and cylinders in water and the coupling of surface elastic waves with the acoustic field,'' J. Acoust. Soc. Am. **83**, 25–37 (1988).
[25] N. H. Sun and P. L. Marston, ''Variable phase coupling coefficient for leaky waves on spheres and cylinders from thick cylindrical shells,'' J. Acoust. Soc. Am. **91**, 1398–1402 (1992).
[26] J. M. Ho, ''Acoustic scattering by submerged elastic cylindrical shells: Uniform ray asymptotics,'' J. Acoust. Soc. Am. **94**, 2936–2946 (1993).
[27] P. L. Marston, ''Variable phase coupling coefficient for leaky waves on spheres from resonance scattering theory,'' Wave Motion **22**, 65–74 (1995).
[28] J. M. Conoir and P. Millerat, ''Relation between coupling and damping coefficients of surface elastic waves propagating around cylindrical targets. Study of coupling coefficient phases,'' Acust. Acta Acust. **84**, 448–454 (1998).
[29] D. Bouche, and F. Molinet, *Méthodes Asymptotiques en Électromagnétisme*, Mathématiques & Applications 16 (Springer, Berlin-Heidelberg, 1994).
[30] L. Flax, L. R. Dragonette, and H. Überall, ''Theory of elastic resonance excitation by sound scattering,'' J. Acoust. Soc. Am. **63**, 723–731 (1978).
[31] G. C. Gaunaurd and H. Überall, ''Theory of resonant scattering from spherical cavities in elastic and viscoelastic media,'' J. Acoust. Soc. Am. **63**, 1699–1712 (1978).
[32] N. D. Veksler, J. L. Izbicki, J. M. Conoir, and P. Rembert, ''Methods of isolation of modal resonances (a review),'' Appl. Mech. Rev. **51**, 449–474 (1998).
[33] V. K. Varadan and V. V. Varadan, *Acoustic, Electromagnetic and Elastic Wave Scattering–Focus on the T-Matrix Approach* (Pergamon, New York, 1980).
[34] P. Sheng, *Introduction to Wave Scattering, Localisation, and Mesoscopic Phenomena* (Academic, New York, 1995).
[35] M. C. Junger and D. Feit, *Sound, Structures, and Their Interaction*, 2nd ed. (MIT, Cambridge, MA, 1986).
[36] A. G. Pathak and P. R. Stepanishen, ''Acoustic harmonic radiation from fluid-loaded infinite cylindrical elastic shells using elasticity theory,'' J. Acoust. Soc. Am. **96**, 573–582 (1994).
[37] A. G. Pathak and P. R. Stepanishen, ''Acoustic harmonic radiation from fluid-loaded spherical shells using elasticity theory,'' J. Acoust. Soc. Am. **96**, 2564–2575 (1994).
[38] L. B. Felsen, J. M. Ho, and I. T. Lu, ''Three-dimensional Green's function for fluid-loaded thin elastic cylindrical shells: Formulation and solution,'' J. Acoust. Soc. Am. **87**, 543–553 (1990).
[39] L. B. Felsen, J. M. Ho, and I. T. Lu, ''Three-dimensional Green's function for fluid-loaded thin elastic cylindrical shells: Alternative representations and ray acoustic forms,'' J. Acoust. Soc. Am. **87**, 554–570 (1990).
[40] A. D. Pierce, ''Wave Propagation on Thin-Walled Elastic Cylindrical Shells,'' in *Elastic Wave Propagation*, edited by M. F. McCarthy and M. A. Hayes (Elsevier, New York, 1989), pp. 205–210.
[41] L. B. Felsen and N. Marcuvitz, *Radiation and Scattering of Waves*, edited by D. G. Dudley, IEE Series on Electromagnetic Waves (1994).
[42] J. Zemanek, Jr., ''An experimental and theoretical investigation of elastic wave propagation in a cylinder,'' J. Acoust. Soc. Am. **51**, 265–283 (1972).

Lagrangian effective material constants for the modeling of thermal behavior of acoustic waves in piezoelectric crystals. I. Theory

Bernard Dulmet[a] and Roger Bourquin
Laboratoire de Chronométrie Electronique et Piézoélectricité, École Nationale Supérieure d'Ingénieurs de Micromécanique et des Microtechniques, 26 Chemin de l'Epitaphe, 25000 Besançon, France

(Received 5 June 2000; accepted for publication 18 June 2001)

After some necessary recalls on the nonlinear theory of thermoelectroelasticity in piezoelectric crystals, asserting the need of constitutive equations which derive from a rotationally invariant energy function, this paper presents the governing equations for a small vibration superimposed on a bias originated by a slow and homogeneous temperature variation from a well-defined reference state. Thereafter, the authors define the effective coefficients appearing in the linearized incremental dynamic balance equations for linear momentum and electrical charge in Lagrange configuration, not omitting associated boundary conditions. The main features of these coefficients are discussed and explicit relations with more conventionally defined coefficients are given. Determination of numerical values of the proposed effective coefficients and examples of their use in the higher order modeling of static frequency–temperature characteristics of either bulk acoustic wave or surface acoustic wave devices are given in a companion paper. © *2001 Acoustical Society of America.*
[DOI: 10.1121/1.1391250]

PACS numbers: 43.25.Dc [MFH]

I. INTRODUCTION

The subject of this paper is to present the analysis of infinitesimal vibrations in a piezoelectric crystal which can freely expand in all space directions upon submission to slow and homogeneous temperature variations. The classical treatment[1] implicitly uses the coordinates of a material point of the crystal in the slowly varying state at the current temperature prior to any vibration. In this description, the dimensions, mass density, and orientation of the solid as well as the properties of the material vary with temperature. This leads to tedious computations to rigorously fit the frequency–temperature characteristic of a piezoelectric resonator by a high order expansion while correctly considering the effect of temperature on its size and crystalline orientation. This can be avoided by using the Lagrangian description in which the field variables are the coordinates of a material point in a reference state defined at a fixed temperature. Since those coordinates are fixed and known, the boundary conditions are expressed on surfaces which do not depend on temperature. Similarly, since the equations of motion are mapped onto the fixed volume of the body in its reference state, the mass density appearing in these equations is constant and the coefficients which describe the material are the only parameters which may vary with temperature. As a consequence, useful simplifications occur for the treatment of frequency–temperature characteristics of resonators with rather complicated shapes, such as radius of contour, gratings, and so on.

This introductory presentation of the use of the Lagrangian description for a particular purpose is indeed somewhat practical. Nevertheless, this treatment also has more theoretical justifications, since it derives from the rotationally invariant and general nonlinear theory established in the case of piezoelectric solids submitted to finite deformations.[2,3] The acceptance of this theory is quite general for the study of force–frequency effects as well as for the study of frequency shifts arising from thermal transient biasing states or from applying static electric fields,[4] but is not so widespread for the study of simple biasing states such as the one arising from an homogeneous temperature variation. More specifically, the presented work defines and makes use of *effective material constants* which are the expansion coefficients of the dynamic part of the Piola–Kirchhoff stress tensor versus the dynamic part of the total strain and of the rotationally invariant electric vector expressed in a Lagragian description. The present paper (paper I) is devoted to the definition of the coefficients while the companion paper (paper II) is devoted to the calculation of their numerical values and their use in predicting the frequency–temperature dependence of commonly encountered kinds of resonators (bulk and surface acoustic waves).

As usual in this kind of problem, we shall consider three states of a solid described by three sets of respective coordinates, as illustrated in Fig. 1:

(1) a *natural* (or *reference*) state, at a fixed temperature Θ_0, in which the coordinates of a material point of the solid are X_M,
(2) an *intermediate* state prior to vibration at a current homogeneous temperature Θ, the coordinates of the material points being ξ_α,
(3) a *final* state when an adiabatic vibration is superimposed on the initial state, the associated coordinates being y_j.

This convention leads to a straightforward writing of equations provided the derivatives with respect to space co-

[a]Electronic mail: bernard.dulmet@ens2m.fr

 0001-4966/2001/110(4)/1792/8/$18.00

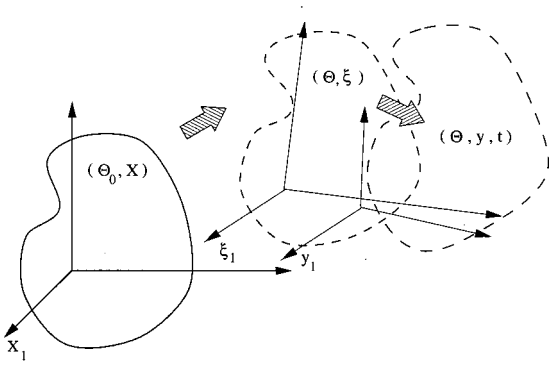

FIG. 1. A solid in successive states.

ordinates are denoted in the following manner:

$$y_{k,L} \equiv \frac{\partial y_k}{\partial X_L}, \quad \xi_{\alpha,L} \equiv \frac{\partial \xi_\alpha}{\partial X_L}, \quad X_{M,j} \equiv \frac{\partial X_M}{\partial y_j}. \tag{1}$$

In this paper we only use Cartesian coordinates and automatic summation over repeated indices is implicitly admitted. The position at time t of a material point referred to by its material coordinates X_L in the natural state is

$$y_j = (\xi_\alpha(X_L) + u_\alpha(X_L,t))\,\delta_{j\alpha}, \tag{2}$$

where u_α is the dynamic displacement and the Kronecker symbol $\delta_{j\alpha}$ is introduced to handle index correspondences from the intermediate state to final state.

II. BASIC EQUATIONS

Although most of the material presented in this section conforms to the general theory of thermoelectroelasticity of Ref. 2, the subsequent treatment involves precise definitions of notations and terms requiring a proper understanding, which makes the recall of this information necessary for our purpose.

We temporarily postpone any use of the intermediate coordinates to address the issue of Lagrange vs Euler representation. The well-known classical field equations expressing the conservation of linear momentum and electric charge are written in the final state:

$$(T^M_{ij} + T^E_{ij})_{,i} = \rho \frac{d^2 y_j}{dt^2}, \quad D_{i,i} = 0, \tag{3}$$

where $\mathbf{D}$ denotes the electric displacement and ρ the mass density. $\mathbf{T}^M$ is the pure mechanical stress tensor which refers to the traction exerted onto a surface element taken in its *final* (deformed) state and $\mathbf{T}^E$ is Maxwell's electrostatic tensor:

$$T^E_{ij} = D_i E_j - \tfrac{1}{2}\varepsilon_0 E_k E_k \delta_{ij}, \tag{4}$$

where $\mathbf{E}$ is the macroscopic electric field. All quantities in Eq. (3) are functions of the final coordinates y_k and the boundary conditions are expressed on the external surface taken in its final state S:

$$\begin{aligned} &n_i[T^M_{ij} + T^E_{ij}] = 0 \\ &n_i[D_i] = \sigma \end{aligned} \quad \text{on } S. \tag{5}$$

σ is the electric charge density and [ ] refers to the discontinuity of an enclosed quantity across the surface the orientation of which is given by the outward unit normal $\mathbf{n}$.

The balance equation for the angular momentum is fulfilled by

$$e_{kij}(P_i E_j + T^M_{ij}) = 0, \quad k = 1,...,3, \tag{6}$$

where $\mathbf{P}$ denotes the polarization related to the field and electric displacement by the classical relation:

$$D_i = \varepsilon_0 E_i + P_i, \quad i = 1,...,3, \tag{7}$$

and e_{kij} denotes Levi-Civita's tensor which takes the value $+1$ if (k, i, j) form a circular permutation of (1, 2, 3), and the value -1 if (k, i, j) form a circular permutation of (3, 2, 1). e_{kij} vanishes in all other cases. Then, Eq. (6) is equivalent to

$$T^{AM}_{ij} = \tfrac{1}{2}(E_i P_i - P_i E_j), \tag{8}$$

where T^{AM}_{ij} denotes the antisymmetric part of the mechanical stress tensor $T^M_{ij} - T^M_{ji}$. It should be observed that all the above-mentioned equations use actual coordinates y_i as field variables. At this point, since the number of equations in (3), (4), (6), and (7) is far smaller than the number of unknowns, it is required to introduce the so-called constitutive equations. In accordance with the pertinent choice of complementary sets of dependent and independent variables for the considered problem, they express the intrinsic properties of matter as relations between those sets. More precisely, all material constants appear as partial derivatives of a thermodynamic potential with respect to the independent variables of the considered problem. A natural way of introducing an energy function consists in writing the balance between the storage of kinetic, internal, and electric field induced energies in the volume of the body, and the work performed on its boundaries:

$$\frac{d}{dt}\int_V \rho\left(\frac{1}{2} v_i v_i + \mathcal{E}\right) dV = \int_S (t^M_i v_i - n_i q_i)\, dS + \int_V \zeta\, dV, \tag{9}$$

where $\mathcal{E}$ is the internal energy per unit mass, $\mathbf{t}^M$ is the local mechanical traction applied to the boundary, $\mathbf{v} \equiv d\mathbf{y}/dt, \mathbf{q}$ is the outwardly orientated heat flow, and ζ is the rate of energy production under the action of applied electric field $\mathbf{E}$. This expression of the first principle of thermodynamics leads to the following differential form:

$$\rho \frac{d\mathcal{E}}{dt} = T^M_{ij} v_{j,i} + \rho E_i \frac{d\Pi_i}{dt} - q_{i,i}, \tag{10}$$

where $\mathbf{\Pi}$ indicates the polarization per mass unit, which is related to the polarization appearing in Eq. (7) in the following manner:

$$P_i = \rho \Pi_i. \tag{11}$$

It can be shown that in the restricted case of nondissipative behavior, the second principle of thermodynamics reduces to

$$\rho\Theta \frac{d\eta}{dt} = -q_{i,i}, \tag{12}$$

where Θ denotes absolute temperature and η is the entropy per mass unit. This result allows for easy substitution of the entropy instead of heat flow into Eq. (10), which can thus be written in two mathematically equivalent differential forms:

$$\rho\frac{d\mathcal{E}}{dt}=X_{L,i}T_{ij}^{M}\frac{dy_{i,L}}{dt}+\rho E_i\frac{d\Pi_i}{dt}+\rho\Theta\frac{d\eta}{dt},$$
$$\rho_0\frac{d\mathcal{E}}{dt}=K_{Li}^{M}\frac{dy_{i,L}}{dt}+\rho_0 E_i\frac{d\Pi_i}{dt}+\rho_0\Theta\frac{d\eta}{dt}. \tag{13}$$

Equivalence between both forms comes from the conservation of mass and the expression of Piola Kirchhoff's asymmetric mechanical tensor $\mathbf{K}^M$:[5]

$$\rho_0=\rho J,\quad J=|y_{i,L}|,\quad K_{Lj}^{M}=JX_{L,i}T_{ij}^{M}. \tag{14}$$

The above-given formula for $\mathbf{K}^M$ derives from its definition expressing the conservation of a surface traction force $\mathbf{t}^M$ along the surface representation:

$$t_j^M=T_{ij}^{M}n_i\,dS=K_{Lj}^{M}n_L^0\,dS_0, \tag{15}$$

where we denote by dS_0 the elementary surface consisting in the whole set of material points in the natural state which become the actual elementary surface dS in the deformed state. n_L^0 denotes a component of the unit normal $\mathbf{n}^0$ in the natural state, corresponding to the actual normal $\mathbf{n}$ (component n_i with notations of this paper). Equation (13b) establishes the internal energy as a function of a well-defined set of independent variables:

$$\mathcal{E}\equiv\mathcal{E}(y_{i,L};\Pi_i;\eta), \tag{16}$$

whereas the corresponding dependent variables are defined by

$$T_{ij}^{M}=\rho y_{i,L}\frac{\partial\mathcal{E}}{\partial y_{j,L}}\bigg)_{\Pi_k,\eta},\quad E_k=\frac{\partial\mathcal{E}}{\partial\Pi_k}\bigg)_{y_{i,j},\eta},\quad \theta=\frac{\partial\mathcal{E}}{\partial\eta}\bigg)_{y_{i,j},\Pi_i}. \tag{17}$$

Nevertheless, a consistent derivation of the constitutive equations requires the proper energy function for the class of considered problems to be an invariant quantity with respect to an arbitrary rotation of either the body itself or the frame used to refer the y_i coordinates.[2,3] This property is not ensured by the above-mentioned writing of internal energy. A mathematical theorem due to Cauchy[6] on the invariance of scalar functions of vectors shows that this property will be granted if $\mathcal{E}$ can be reduced to some combination of scalar products of the four vectors Π, $\partial\mathbf{y}/\partial X_1,\partial\mathbf{y}/\partial X_2,\partial\mathbf{y}/\partial X_3$ and of their determinants. Two alternative forms of $\mathcal{E}$ granting the rotational invariance are given in the following:

$$\mathcal{E}\equiv\mathcal{E}(C_{LM};\mathcal{P}_L;\eta),$$
$$C_{LM}=y_{i,L}y_{i,M},$$
$$\mathcal{P}_L=y_{i,L}\Pi_i, \tag{18}$$

and

$$\mathcal{E}\equiv\mathcal{E}(E_{LM};p_I;\eta),$$
$$E_{LM}=y_{i,L}y_{i,M}-\delta_{LM},$$
$$p_K=JX_{K,i}P_i\equiv\rho_0X_{K,i}\Pi_i. \tag{19}$$

In this paper, we follow the approach previously suggested by Tiersten,[2] implying the choice of the latter set (19). Thus, the differential form of internal energy per mass unit becomes

$$\rho_0\frac{d\mathcal{E}}{dt}=\tau_{LM}\frac{dE_{LM}}{dt}+W_L\frac{dp_L}{dt}+\rho_0\Theta\frac{d\eta}{dt} \tag{20}$$

instead of Eq. (13b) and the dependent variables of the problem are then defined by

$$\tau_{LM}=\rho_0\frac{\partial\mathcal{E}}{\partial E_{Lm}}\bigg)_{p_K,\eta},\quad W_K=\rho_0\frac{\partial\mathcal{E}}{\partial p_K}\bigg)_{E_{LM},\eta},$$
$$\Theta=\frac{\partial\mathcal{E}}{\partial\eta}\bigg)_{E_{LM},p_K}. \tag{21}$$

One can show, with help of rules for chain derivatives and related identities, that the above-mentioned formulas imply

$$T_{ij}^{M}=\frac{1}{J}y_{i,L}\tau_{LM}y_{j,M}-P_iE_j,$$
$$W_L=y_{k,L}E_k^{M}\equiv-\varphi_{,L}, \tag{22}$$

where φ denotes the electrostatic potential. Equation (22a) shows that the balance of kinetic momentum is identically satisfied:

$$T_{ij}^{AM}\equiv T_{ij}^{M}-T_{ji}^{M}=E_iP_j-E_jP_i \tag{23}$$

since the symmetry of τ_{LM} derives from relation (21a) and the symmetry of elastic deformations E_{KL}. It can readily be observed that, from Eqs. (4) and (7), the antisymmetric part of the Maxwell electostatic tensor is exactly the opposite of the antisymmetric part of the purely mechanical stress tensor:

$$T_{ij}^{AE}\equiv T_{ij}^{E}-T_{ji}^{E}=E_jP_i-E_iP_j\equiv-T_{ij}^{AM}. \tag{24}$$

Since it is known that the internal energy is not the most pertinent thermodynamic potential to formulate resonator problems, we conform to Tiersten's approach and we take Gibbs' electric enthalpy χ as the preferred thermodynamic potential for the considered class of problems, according to

$$\rho_0\chi=\rho_0\mathcal{E}-W_Lp_L-\rho_0\Theta\eta, \tag{25}$$

which establishes χ as a function of the tensor of deformation E_{LM}, the rotationally invariant electric vector W_L, and the absolute temperature Θ:

$$\chi\equiv\chi(E_{LM};W_L;\Theta). \tag{26}$$

If the variation of the independent variables of the considered problem from the given reference state to the actual state of the crystal remain finite, the corresponding variation of the thermodynamic potential χ can be represented by a generalized Taylor's expansion in terms of the independent variables $(E_{LM};W_L;\Theta)$. The coefficients of this development define the material constants characterizing the crystal, and using χ energy function defines the following quantities as ''thermodynamic'' dependent variables:

$$t_{KL}=\rho_0\frac{\partial\chi}{\partial E_{KL}}\Big)_{W,\Theta},\quad p_K=-\rho_0\frac{\partial\chi}{\partial W_K}\Big)_{E,\Theta},$$
$$\eta=-\frac{\partial\chi}{\partial\Theta}\Big)_{E,W}. \tag{27}$$

Although the thermodynamic stress t_{KL} and the polarization p_K differ from the usual mechanical stress and the electric induction, they are clearly connected with them. Abovementioned relations (7), (21)–(22), and (25) are consistent with the following simple relations between the mechanical stress tensor, the electric displacement, i.e., the dependent variables of the fundamental balance equations (3), and partial derivatives of Gibbs' function:[2]

$$T^M_{ij}=\rho y_{i,M}\frac{\partial\chi}{\partial E_{MN}}\Big)_{W,\Theta}\quad y_{j,N}+\rho y_{i,M}\frac{\partial\chi}{\partial W_M}\Big)_{E,\Theta}X_{L,j}W_L,$$
$$D_i=\rho\varepsilon_0 X_{M,i}W_M-y_{i,M}\frac{\partial\chi}{\partial W_M}\Big)_{E,\Theta}. \tag{28}$$

The fundamental elastic constants defined as coefficients of Taylor's expansion of $\chi(E_{LM};W_l;\Theta)$ are isothermal elastic constants. Thus, for the sake of simplicity, we shall systematically omit the notation $)_{W,\Theta}$ and $)_{E,\Theta}$ for partial derivatives of any energy function appearing in the followings.

Although conservation equations (3) and boundary conditions (5) are absolutely correct by themselves, they are not well matched with the fundamental constitutive equations which can be established by the above-mentioned expansion of χ in terms of material constants and independent variables, mainly because E_{LM} and W_L are mapped onto the coordinates of the natural state. Furthermore, recalling our introductory argument about the boundary conditions, it is also more convenient to map the balance equations onto the coordinates of the natural state because the dimensions and the orientation of the finite body in crystallographic axes are well known in this state. Thus we reformulate the problem by using new quantities, which are the *total* asymmetric Piola–Kirchhoff stress tensor **K** and the material electric displacement **Δ**:[7]

$$K_{Lj}=JX_{L,i}(T^M_{ij}+T^E_{ij})=K^M_{Lj}+K^E_{Lj},$$
$$\Delta_L=JX_{L,i}D_i. \tag{29}$$

They are related to the usual stress and electric displacement by expressing the conservation of the polarization-induced surface force $\mathbf{t}^E$ and electric charge σ per unit surface:

$$t^E_j=T^E_{ij}n_i\,dS=K^E_{Lj}n^0_L\,dS_0,$$
$$\sigma=D_in_i\,dS=\Delta_Ln^0_L\,dS_0. \tag{30}$$

Substitution of Eq. (28) into Eq. (29), together with the mutual cancellation of antisymmetric parts of $\mathbf{T}^E$ and $\mathbf{T}^M$ gives the following expression for K_{Lj} and Δ_L:

$$K_{Lj}=\rho_0y_{i,M}\frac{\partial\chi}{\partial E_{LM}}+\varepsilon_0J(X_{L,i}X_{M,i}X_{Nj}-\tfrac{1}{2}X_{L,j}X_{M,k}X_{N,k})W_MW_N,$$
$$\Delta_L=\varepsilon_0JX_{L,i}X_{M,i}W_M-\rho_0\frac{\partial\chi}{\partial W_L}. \tag{31}$$

One must note that the partial derivatives of χ in these relations are evaluated in the *final* state. The stress equation of motion and charge equation become

$$K_{Lj,L}(X_M;\Theta;t)=\rho_0\frac{d^2y_j(X_M;\Theta;t)}{dt^2},$$
$$\Delta_{L,L}(X_M;\Theta;t)=0. \tag{32}$$

The associated boundary conditions at the interface between the crystal and a perfect conductor are the following when mapped in the *natural* state:

$$N_L[K_{Lj}]=0\quad N_L[\Delta_L]=\sigma\quad\text{on } S_0. \tag{33}$$

III. SMALL VIBRATION SUPERIMPOSED ON A HOMOGENEOUS THERMAL BIAS

We consider the propagation of an elastic wave in a piezoelectric medium subject to the static deformation arising from a slow and uniform temperature change. Since both static and dynamic problems are superimposed in the above-given formulation, tractable equations can readily be obtained by separating the static and the dynamic parts of the problem. Thus, the approach in this section exhibits similarities to the one of Ref. 4, which considers a quite different biasing state (static electric field). Here, since we restrict our interest to quasistatic and homogeneous temperature variation, explicitly solving the static problem is not expected to generate many difficulties.

The infinitesimal dynamic increment u_α of the mechanical displacement is defined by Eq (2). Since the transformation $X_L\to\xi_\alpha$ only depends on thermal expansion, we can arbitrarily map the dynamic displacement either as $u_\alpha(\xi_\gamma;t)$ or as $u_\alpha(X_L;\Theta-\Theta_0;t)$. The first choice corresponds to the approach followed by Bechmann, Ballato, and Lukaszek[1] and later by James,[8] for the practical determination of thermal derivatives of elastic constants of quartz. Temperature is then considered as a simple parameter acting on all material constants and on the dimensions of crystal through thermal expansion. Thus, it is also necessary to properly appreciate the small temperature-dependent change of crystalline orientation of an arbitrarily oriented device, which appears in the intermediate description due to the anisotropy of thermal expansion.[9] This effect is rather small, but is not negligible when the velocity of acoustic wave varies quickly with the direction of propagation. It is omitted in Refs. 1 and 8, but it is automatically taken into account in the present analysis which conforms to the second choice of mapping. Now, substituting Eq. (2) in Eq. (19b) with help of the chain rules for derivatives:

$$y_{j,M}=y_{j,\alpha}\xi_{\alpha,M}=\xi_{\alpha,M}\delta_{j,\alpha}+u_{\alpha,M}\delta_{j,\alpha}. \tag{34}$$

One can split the total deformation in two parts, the static one and a small dynamic increment:

$$E_{LM}=\overline{E}_{LM}+\tilde{E}_{LM},$$
$$\overline{E}_{LM}=\tfrac{1}{2}(\xi_{\alpha,L}\xi_{\alpha,M}-\delta_{LM}),\tag{35}$$
$$\tilde{E}_{LM}=\tfrac{1}{2}(\xi_{\alpha,L}u_{\alpha,M}+\xi_{\alpha,M}u_{\alpha,L}+u_{\alpha,L}u_{\alpha,M}).$$

Dynamic increments of stress tensor $\tilde{K}_{Lj}$, material electric induction $\tilde{\Delta}_L$, and electric vector $\tilde{W}_L$ are defined in the same way:

$$K_{Lj}=\overline{K}_{Lj}(\Theta)+\tilde{K}_{Lj}(u_\alpha;\tilde{W}_M),$$
$$\Delta_L=\overline{\Delta}_L(\Theta)+\tilde{\Delta}_L(u_\alpha;\tilde{W}_M),\tag{36}$$
$$W_L=\overline{W}_L(\Theta)+\tilde{W}_L(t).$$

Assuming a null electric field and a uniform temperature distribution in the intermediate state, and considering a nonpyroelectric material free to expand without external constraint, we have

$$\overline{K}_{Lj}=0,\quad \overline{W}_L=0,\quad \overline{\Delta}_L=0.\tag{37}$$

Since we are only interested in infinitesimal dynamic fields, we may use the following Taylor's expansions of partial derivatives of χ:

$$\frac{\partial\chi}{\partial E_{LM}}=\frac{\partial\chi}{\partial E_{LM}}\Big)_1+\frac{\partial^2\chi}{\partial E_{LM}\partial E_{NP}}\Big)_1\tilde{E}_{NP}+\frac{\partial^2\chi}{\partial E_{LM}\partial W_K}\Big)_1\tilde{W}_K+\frac{\partial^2\chi}{\partial E_{LM}\partial\Theta}\Big)_1\Delta\tilde{\Theta}+\cdots,$$
$$\frac{\partial\chi}{\partial W_K}=\frac{\partial\chi}{\partial W_K}\Big)_1+\frac{\partial^2\chi}{\partial W_K\partial E_{LM}}\Big)_1\tilde{E}_{LM}+\frac{\partial^2\chi}{\partial W_K\partial W_L}\Big)_1\tilde{W}_L+\frac{\partial^2\chi}{\partial W_K\partial\Theta}\Big)_1\Delta\tilde{\Theta}+\cdots,\tag{38}$$

where the notation $)_1$ indicates that the partial derivatives are evaluated in the intermediate state. Since the thermal exchanges are much slower than the variation of dynamic mechanical field, the high-frequency vibration can be assumed isentropic, and Eq. (27c) can be used to determine the small dynamic temperature shift created by the vibration:

$$\Delta\tilde{\Theta}=-\frac{\dfrac{\partial^2\chi}{\partial\Theta\,\partial E_{KL}}\Big)_1\tilde{E}_{KL}+\dfrac{\partial^2\chi}{\partial\Theta\,\partial\tilde{W}_L}\Big)_1\tilde{W}_L}{\dfrac{\partial^2\chi}{\partial\Theta^2}\Big)_1}.\tag{39}$$

With help of the following notations:

$$\chi_{KLMN})_1=\frac{\partial^2\chi}{\partial E_{KL}\partial E_{MN}}\Big)_1-\frac{\dfrac{\partial^2\chi}{\partial E_{KL}\partial\Theta}\Big)_1\dfrac{\partial^2\chi}{\partial E_{MN}\partial\Theta}\Big)_1}{\dfrac{\partial^2\chi}{\partial\theta^2}\Big)_1},$$
$$\chi_{K.LM})_1=\frac{\partial^2\chi}{\partial W_K\partial E_{LM}}\Big)_1-\frac{\dfrac{\partial^2\chi}{\partial W_K\partial\Theta}\Big)_1\dfrac{\partial^2\chi}{\partial E_{MN}\partial\Theta}\Big)_1}{\dfrac{\partial^2\chi}{\partial\Theta^2}\Big)_1},\tag{40}$$
$$\chi_{KL})_1=\frac{\partial^2\chi}{\partial W_K\partial W_L}\Big)_1-\frac{\dfrac{\partial^2\chi}{\partial W_K\partial\Theta}\Big)_1\dfrac{\partial^2\chi}{\partial W_L\partial\Theta}\Big)_1}{\dfrac{\partial^2\chi}{\partial\Theta^2}\Big)_1}$$

and taking advantage of the possibility to exchange the order of derivation in mixed derivatives, we use Eq. (39) to eliminate $\Delta\tilde{\Theta}$ from Eq. (38), thereby obtaining

$$\frac{\partial\chi}{\partial E_{LM}}=\frac{\partial\chi}{\partial E_{LM}}\Big)_1+\chi_{LMNP})_1\tilde{E}_{NP}+\chi_{K.LM})_1\tilde{W}_K+\cdots,$$
$$\frac{\partial\chi}{\partial W_K}=\frac{\partial\chi}{\partial W_K}\Big)_1+\chi_{K.LM})_1\tilde{E}_{LM}+\chi_{KL})_1\tilde{W}_L+\cdots.\tag{41}$$

Substituting Eqs. (34)–(36) and (41) into Eq. (31), using the chain rules of differentation in the reverse way:

$$X_{M,i}=X_{M,\alpha}\xi_{\alpha,i}=X_{M,\alpha}(\delta_{i\alpha}-u_{\alpha,\varepsilon}\xi_{\varepsilon,i}+\cdots),\tag{42}$$

and taking into account the fact that the partial derivatives $\partial\chi/\partial E_{LM})_1$ and $\partial\chi/\partial W_K)_1$ identically vanish for the stress-free unpolarized bias of interest, we obtain the following linearized expression for $\tilde{K}_{Lj}$ and $\tilde{\Delta}_L$:

$$\tilde{K}_{Lj}=\delta_{j\alpha}\xi_{\alpha,M}\xi_{\beta,N}\rho_0\chi_{LMNP})_1u_{\beta,P}+\delta_{j\alpha}\xi_{\alpha,M}\rho_0\chi_{K.LM})_1\tilde{W}_K+\cdots,$$
$$\tilde{\Delta}_L=[\varepsilon_0\overline{J}X_{L,\alpha}X_{M,\alpha}-\rho_0\chi_{LM})_1]\tilde{W}_M-\rho_0\chi_{L.MN})_1\xi_{\alpha,M}u_{\alpha,N}+\cdots,\tag{43}$$

where $\overline{J}=\rho_0/\rho_1$ is the Jacobian of the transformation $X_L\rightarrow\xi_\alpha$. Thus, the incremental constitutive equations can be rewritten in the following form:

$$\tilde{K}_{Lj}=(G_{L\gamma M\varepsilon}u_{\varepsilon,M}-R_{M\gamma L}\tilde{W}_M)\delta_{j\gamma},$$
$$\tilde{\Delta}_L=N_{LM}\tilde{W}_M+R_{L\alpha N}u_{\alpha,N},\tag{44}$$

which define new *effective* elastic material coefficients $G_{L\gamma M\varepsilon}$, piezoelectric coefficients $R_{M\gamma L}$, and dielectric coefficients N_{LM} which govern an adiabatic vibration superposed on the bias resulting from an homogeneous temperature change accompanied by stress-free thermal expansion:

$$G_{L\gamma M\varepsilon}=\xi_{\gamma,K}\xi_{\varepsilon,N}\rho_0\chi_{LK.MN})_1,$$
$$R_{M\gamma L}=-\xi_{\gamma,K}\rho_0\chi_{M.LK})_1,\tag{45}$$
$$N_{LM}=\varepsilon_0\overline{J}X_{L,\alpha}X_{M,\alpha}-\rho_0\chi_{LM})_1.$$

These coefficients have tensorial properties and their values in a new rotated frame can be obtained by the classical rule of frame change of tensors. The associated stress equation of motion and charge equation of electrostatics take the form:

$$\tilde{K}_{Lj,L}=\rho_0\frac{\partial^2 u_\alpha}{\partial t^2}\delta_{j\alpha},$$
$$\tilde{\Delta}_{L,L}=0, \tag{46}$$

and the corresponding boundaries conditions are

$$\begin{matrix} N_L[\tilde{K}_{Lj}]=0 \\ N_L[\tilde{\Delta}_L]=\tilde{\sigma}_0 \end{matrix} \quad \text{on } S_0, \tag{47}$$

where $\tilde{\sigma}_0$ is the dynamic increment of surface charge density mapped on S_0. Equations (44)–(47) constitute the basic relations for the problem of a small vibration superimposed on a thermal bias, mapped in the *natural* state.

IV. PROPERTIES OF EFFECTIVE COEFFICIENTS

The effective coefficients defined by Eqs. (44) and (45) are related to the fundamental derivatives of energy function in a rather cumbersome though perfectly well defined way. They only depend on temperature provided that it is homogeneous and no thermally induced stress is present. All these sets of *G*, *R*, and *N* coefficients can be expanded up to any power of the temperature shift from Θ_0 to Θ, according to the following formula, given here for elastic coefficients:

$$G_{L\gamma M\varepsilon}(\Theta)=G_{L\gamma M\varepsilon}(\Theta_0)\times\left[1+\sum_{k=1}^{n}T^{(k)}G_{L\gamma M\varepsilon}(\Theta-\Theta_0)^k\right], \tag{48}$$

where

$$T^{(k)}G=\frac{1}{k!}\frac{\partial^k G}{\partial\Theta^k} \tag{49}$$

is the temperature coefficient of order *k* of the *G* coefficient. Similar expressions occur for piezoelectric and dielectric coefficients. When $\Theta_0=\Theta$, the intermediate and natural states are identical and the effective coefficients reduce to $\rho_0\chi_{KL})_1$, $\rho_0\chi_{K.LM})_1$, $\rho_0\chi_{KLMN})_1$. Fundamental elastic constants and their first-order temperature derivatives were previously defined from those quantities, which actually are the partial derivatives of energy under adiabatic conditions for the vibration, and were evaluated for quartz in Ref. 10. The fundamental constants must be used in case of any inhomogeneous bias inducing a field of nonzero static stresses, but no evaluation of their higher order thermal derivatives is available at this moment. In the special case when the intermediate state degenerates to the natural one, effective and fundamental constants have the same values and symmetry properties as the classical linear coefficients. But when the temperature Θ differs from the reference temperature Θ_0:

$$\xi_{\alpha,L}=\delta_{\alpha L}+\sum_n \alpha^{(n)}_{LM}\delta_{\alpha M}(\Theta-\Theta_0)^n, \tag{50}$$

and the effective coefficients have different values and lower symmetries than the classical coefficients which will be outlined in Sec. V. This holds for the *G* and *R* coefficients (but not *N* which exhibits the usual symmetries):

$$\begin{aligned} &G_{L\gamma M\varepsilon}(\Theta)\neq G_{P\alpha M\varepsilon}(\Theta)\delta_{P\gamma}\delta_{\alpha L}, \\ &G_{L\gamma M\varepsilon}(\Theta)\neq G_{L\gamma Q\beta}(\Theta)\delta_{Q\varepsilon}\delta_{\beta M}, \\ &G_{L\gamma M\varepsilon}(\Theta)\equiv G_{M\varepsilon L\gamma}(\Theta), \\ &R_{LM\varepsilon}\neq R_{LP\alpha}(\Theta)\delta_{P\varepsilon}\delta_{\alpha M}, \end{aligned} \tag{51}$$

where the Kronecker translators $\delta_{P\alpha}$ are necessary for consistency of Greek–Latin convention of indices. As a consequence, the $(L\alpha)$ couples can take nine different values. We adopt the same rule as Tiersten[4] for index compression:

$$\begin{aligned} &11\leftrightarrow1 \quad 22\leftrightarrow2 \quad 33\leftrightarrow3 \\ &23\leftrightarrow4 \quad 31\leftrightarrow5 \quad 12\leftrightarrow6 \\ &32\leftrightarrow7 \quad 13\leftrightarrow8 \quad 21\leftrightarrow9. \end{aligned} \tag{52}$$

Care must be taken of index order of the deformation gradients in Eq. (44). At the temperature Θ, the structures of the matrices of the *G* and *R* coefficients for the crystallographic class 32 are the following:

$$\begin{bmatrix} G_{11} & G_{12} & G_{13} & G_{14} & 0 & 0 & G_{17} & 0 & 0 \\ G_{12} & G_{11} & G_{13} & -G_{14} & 0 & 0 & -G_{17} & 0 & 0 \\ G_{13} & G_{13} & G_{33} & 0 & 0 & 0 & 0 & 0 & 0 \\ G_{14} & -G_{14} & 0 & G_{44} & 0 & 0 & G_{47} & 0 & 0 \\ 0 & 0 & 0 & 0 & G_{55} & G_{17} & 0 & G_{47} & G_{17} \\ 0 & 0 & 0 & 0 & G_{17} & G_{66} & 0 & G_{14} & G_{66} \\ G_{17} & -G_{17} & 0 & G_{47} & 0 & 0 & G_{55} & 0 & 0 \\ 0 & 0 & 0 & 0 & G_{47} & G_{14} & 0 & G_{44} & G_{14} \\ 0 & 0 & 0 & 0 & G_{17} & G_{66} & 0 & G_{14} & G_{66} \end{bmatrix} \tag{53}$$

$$\begin{bmatrix} R_{11} & -R_{11} & 0 & R_{14} & 0 & 0 & R_{17} & 0 & 0 \\ 0 & 0 & 0 & 0 & -R_{14} & -R_{11} & 0 & -R_{17} & -R_{11} \\ 0 & 0 & 0 & 0 & 0 & 0 & 0 & 0 & 0 \end{bmatrix}. \tag{54}$$

These coefficients are not independent. At first, from Eq. (50) and remarking that, for the crystalline class of interest, only $\alpha_{11}^{(n)}$, $\alpha_{22}^{(n)}=\alpha_{11}^{(n)}$ and $\alpha_{33}^{(n)}$ are nonzero, it is easy to show that $G_{12}\equiv G_{11}-2G_{66}, \forall\Theta$. Thus, G_{12} is eliminated, and one can choose $G_{11}, G_{13}, G_{14}, G_{33}, G_{44}$, and G_{66} as independent coefficients, considering that G_{17} depends on G_{14} while G_{47} and G_{55} depend on G_{44}. From the definition (45) with the help of (50) we find

$$
\begin{aligned}
T^{(1)}G_{17} &= T^{(1)}G_{14}+\alpha_{11}^{(1)}-\alpha_{33}^{(1)},\\
T^{(1)}G_{47} &= T^{(1)}G_{44}+\alpha_{11}^{(1)}-\alpha_{33}^{(1)},\\
T^{(1)}G_{55} &= T^{(1)}G_{44}+2(\alpha_{11}^{(1)}-\alpha_{33}^{(1)}),
\end{aligned}
\tag{55}
$$

$$
\begin{aligned}
T^{(2)}G_{17} &= T^{(2)}G_{14}+\alpha_{11}^{(1)}T^{(1)}G_{14}-\alpha_{33}^{(1)}T^{(1)}G_{17}\\
&\quad +\alpha_{11}^{(2)}-\alpha_{33}^{(2)},\\
T^{(2)}G_{47} &= T^{(2)}G_{44}+\alpha_{11}^{(1)}T^{(1)}G_{44}-\alpha_{33}^{(1)}T^{(1)}G_{47}\\
&\quad +\alpha_{11}^{(2)}-\alpha_{33}^{(2)},\\
T^{(2)}G_{55} &= T^{(2)}G_{44}+2\alpha_{11}^{(1)}T^{(1)}G_{44}-2\alpha_{33}^{(1)}T^{(1)}G_{55}\\
&\quad +2(\alpha_{11}^{(2)}-\alpha_{33}^{(2)})+(\alpha_{11}^{(1)})^2-(\alpha_{33}^{(1)})^2,
\end{aligned}
\tag{56}
$$

$$
\begin{aligned}
T^{(3)}G_{17} &= T^{(3)}G_{14}+\alpha_{11}^{(1)}T^{(2)}G_{14}-\alpha_{33}^{(1)}T^{(2)}G_{17}\\
&\quad +\alpha_{11}^{(2)}T^{(1)}G_{14}-\alpha_{33}^{(2)}T^{(1)}G_{1}+\alpha_{11}^{(3)}-\alpha_{33}^{(3)},\\
T^{(3)}G_{47} &= T^{(3)}G_{44}+\alpha_{11}^{(1)}T^{(2)}G_{44}-\alpha_{33}^{(1)}T^{(2)}G_{17}\\
&\quad +\alpha_{11}^{(2)}T^{(1)}G_{14}-\alpha_{33}^{(2)}T^{(1)}G_{17}+\alpha_{11}^{(3)}-\alpha_{33}^{(3)},
\end{aligned}
\tag{57}
$$

$$
\begin{aligned}
T^{(3)}G_{55} &= T^{(3)}G_{44}+2\alpha_{11}^{(1)}T^{(2)}G_{44}-2\alpha_{33}^{(1)}T^{(2)}G_{55}\\
&\quad +2[\alpha_{11}^{(2)}+(\alpha_{11}^{(1)})^2]T^{(1)}G_{44}\\
&\quad -2[\alpha_{33}^{(2)}+(\alpha_{33}^{(1)})^2]T^{(1)}G_{55}\\
&\quad +2[\alpha_{11}^{(3)}-\alpha_{33}^{(3)}+\alpha_{11}^{(1)}\alpha_{11}^{(2)}-\alpha_{33}^{(1)}\alpha_{33}^{(2)}].
\end{aligned}
$$

V. CONNECTION WITH THE CLASSICAL TREATMENT

In this section, we briefly give the relation between here-defined effective coefficients and the ones used in the classical treatment[1] of the problem. The latter implicitly use the coordinates in the intermediate state as independent variables. In this state, the dynamic parts of the stress $\tilde{L}$ tensor and electric displacement vector $\tilde{D}$ can be obtained by the transformation laws:

$$
\tilde{L}_{\alpha j}=\frac{1}{J}\xi_{\alpha,L}\tilde{K}_{Lj}, \quad \tilde{D}_{\alpha}=\frac{1}{J}\xi_{\alpha,L}\tilde{\Delta}_{L}. \tag{58}
$$

By substituting Eq. (44) into Eq. (58), with help of the chain rules of differentiation, we obtain

$$
\begin{aligned}
\tilde{L}_{\alpha j} &= \delta_{j\gamma}(H^4_{\alpha\gamma\beta\delta}u_{\delta,\beta}+H^3_{\varepsilon\gamma\alpha}\tilde{\varphi}_{,\varepsilon}),\\
\tilde{D}_{\alpha} &= H^3_{\alpha\delta\beta}u_{\delta,\beta}-H^2_{\alpha\beta}\tilde{\varphi}_{,\beta},
\end{aligned}
\tag{59}
$$

where H^4 are the elastic coefficients of which temperature derivatives are most commonly determined,[1,8] and the following relations exist between both kinds of effective coefficients:

$$
\begin{aligned}
H^4_{\alpha\gamma\beta\delta} &= \frac{1}{J}\frac{\partial\xi_\alpha}{\partial X_L}\frac{\partial\xi_\beta}{\partial X_M}G_{L\gamma M\delta},\\
H^3_{\alpha\delta\beta} &= \frac{1}{J}\frac{\partial\xi_\alpha}{\partial X_M}\frac{\partial\xi_\beta}{\partial X_L}R_{M\delta L},\\
H^2_{\alpha\beta} &= \frac{1}{J}\frac{\partial\xi_\alpha}{X_M}\frac{\partial\xi_\beta}{\partial X_N}N_{MN},
\end{aligned}
\tag{60}
$$

or, conversely:

$$
\begin{aligned}
G_{L\gamma M\varepsilon} &= J\frac{\partial X_L}{\partial\xi_\alpha}\frac{\partial X_M}{\partial\xi_\delta}H^4_{\alpha\gamma\delta\varepsilon},\\
R_{L\gamma M} &= J\frac{\partial X_L}{\partial\xi_\varepsilon}\frac{\partial X_M}{\partial\xi_\alpha}H^3_{\varepsilon\gamma\alpha},\\
N_{MN} &= J\frac{\partial X_M}{\partial\xi_\alpha}\frac{\partial X_N}{\partial\xi_\beta}H^2_{\alpha\beta}.
\end{aligned}
\tag{61}
$$

These relations and (50) allow one to readily obtain the expressions between the thermal derivatives of the classical coefficients and the thermal derivatives of the effective material constants in Lagrange's formulation. Obviously, the quantities appearing in (59) are associated with the equilibrium equations:

$$
\begin{aligned}
\tilde{L}_{\alpha j,\alpha} &= \rho_1\frac{\partial^2 u_\beta}{\partial t^2}\delta_{j\beta},\\
\tilde{D}_{\alpha,\alpha} &= 0,
\end{aligned}
\tag{62}
$$

and the boundary conditions:

$$
\begin{aligned}
n_\alpha[\tilde{L}_{\alpha j}] &= 0\\
n_\alpha[\tilde{D}_\alpha] &= \tilde{\sigma}_1
\end{aligned}
\quad \text{on } S_1, \tag{63}
$$

where $\tilde{\sigma}_1$ is the dynamic increment of charge mapped onto the boundary surface S_1 in the intermediate state.

VI. CONCLUSION

The formalism presented here allows one to rigorously treat the problem of acoustic wave propagation in a piezoelectric medium submitted to an homogeneous temperature variation. The effect of temperature on the actual crystalline orientation and shape of the device is automatically taken into account by using effective material constants referred to the fixed coordinates of the natural state. Although we detailed the main properties of these constants as well as their relations with other possibly defined material constants for the description of vibrations superposed on a bias, they are essentially suited for the special kind of bias considered here, thereby allowing for a consistent description of higher order static frequency–temperature characteristics of vibrating devices, which will be outlined in the companion paper, along with the obtention of numerical values of the thermal derivatives of effective constants.

[1] R. Bechmann, A. Ballato, and K. Lukaszek, ''High order temperature coefficients of the elastic stiffnesses and compliances of quartz,'' Proc. IRE **50**, 1812–1822 (1962).
[2] H. F. Tiersten, ''On the nonlinear equations of thermoelectroelasticity,'' Int. J. Eng. Sci. **9**, 587–604 (1971).
[3] R. A. Toupin, ''The elastic dielectric,'' J. Rat. Mech. Anal. **5**, 849–916 (1956).
[4] J. C. Baumhauer and H. F. Tiersten, ''Nonlinear electroelastic equations for small fields superposed on a bias,'' J. Acoust. Soc. Am. **54**, 1017–1034 (1973).
[5] C. Truesdell and R. A. Toupin, ''The classical field theories,'' vol. in *Handbuch der Physik* (Springer, Berlin, 1960), Vol. III/I, pp. 226–793.
[6] A. L. Cauchy, Mem. Acad. Sci. **XXII**, 615 (1850).
[7] R. N. Thurston, ''Waves in solids,'' in *Mechanics of Solids IV* (Springer, Berlin, 1974), pp. 109–132, Vol. VIa/4 of Encyclopedia of Physics.
[8] B. James, ''A new measurement of the basic elastic and dielectric constants of quartz,'' Proceedings of the 42nd Annual Freq. Cont. Symp., 1988, pp. 146–154.
[9] B. Dulmet and R. Bourquin, ''Méthodes de détermination des courbes fréquence-température d'un résonateur à quartz vibrant en mode d'épaisseur,'' Rev. Phys. Appl. **18**, 619–624 (1983).
[10] B. K. Sinha and H. F. Tiersten, ''First temperature derivatives of the fundamental elastic constants of quartz,'' J. Appl. Phys. **50**, 2732–2739 (1979).

Lagrangian effective material constants for the modeling of thermal behavior of acoustic waves in piezoelectric crystals. II. Applications and numerical values for quartz

B. Dulmet[a] and R. Bourquin
Laboratoire de Chronométrie Électronique et Piézoélectricité, École Nationale Supérieure d'Ingénieurs de Micromécanique et des Microtechniques, 26 Chemin de l'Épitaphe, 25000 Besançon, France

E. Bigler and S. Ballandras
Laboratoire de Physique et Métrologie des Oscillateurs, CNRS Avenue de l'Observatoire, 25000 Besançon, France

(Received 5 June 2000; accepted for publication 18 June 2001)

This paper presents a set of numerical values of temperature derivatives of Lagrangian effective elastic coefficients suitable for the modeling of small vibrations in quartz devices submitted to slow and homogeneous temperature variations. After a short description of the proper writing of vibration problems in practical applications with the help of this kind of coefficient, we determine the proposed set of numerical values from the frequency–temperature characteristics of an heterogeneous set of bulk and surface acoustic wave devices. © *2001 Acoustical Society of America.* [DOI: 10.1121/1.1391251]

PACS numbers: 43.25.Dc [MFH]

I. INTRODUCTION

In the preceding paper[1] we have defined effective elastic, piezoelectric, and dielectric coefficients suitable for the thermal study of vibrating piezoelectric devices. Since Lagrangian effective coefficients have different symmetries than effective constants of the more conventional method, where the equations of motion are mapped onto the coordinates of the intermediate state, their practical use requires one to rewrite the problems from the very beginning, although the actual changes in the achievement of computer programs and/or analytical derivations remain in fact rather slight. In this paper, paper II, we present the use of Lagrangian effective coefficients in widely used models for BAW resonators and SAW propagation, we discuss the various ways to determine the numerical values of their thermal derivatives and we show how, with help of a proper least-squares treatment, a set of heterogeneous experimental results obtained from bulk acoustic resonators and surface acoustic wave delay lines can be used to establish numerical values suitable for either kind of device of practical interest. At the difference of fundamental constants and their temperature derivatives previously proposed by Sinha and Tiersten,[2] Lagrangian effective constants are restricted to dynamic problems involving stress-free biasing states but their temperature derivatives can be straightforwardly obtained up to third order, thereby allowing their use in a rigorous modeling of frequency temperature characteristics of a wide variety of BAW and SAW devices. The connection with the fundamental constants is emphasized in Appendix A. In the absence of specific indication, all notations of the companion paper, paper I, are conserved in the present paper.

[a]Electronic mail: bernard.dulmet@ens2m.fr

II. VIBRATION MODELS IN LAGRANGIAN FORMULATION

Thermal derivatives of elastic coefficients are most suitably determined from frequency–temperature characteristics of resonant devices.[3] Conversely, their numerical values are needed for the modeling of bulk and surface acoustic devices. As a consequence, it is required to describe the proper writing of both classes of problems with the help of the Lagrangian effective coefficients defined in the companion paper to determine their numerical values as well as to properly use them in practice. In the present section, we briefly reformulate, first, the modeling of trapped energy modes in a doubly rotated (contoured) bulk acoustic wave resonator, and second, the calculus of Rayleigh wave velocity in the framework of the Lagrangian formulation of small vibrations arising in a crystal submitted to slow and homogeneous temperature variations.

A. Bulk acoustic wave resonators

At the very beginning, let us consider an infinite plate of arbitrary orientation. We can always choose the rotated coordinate axes such that X_2' lies along the thickness of the plate. Assuming that the mechanical displacement and the electric potential depend only on X_2', and evaluating all quantities in the rotated axes, from the effective constitutive equations (44) of the companion paper, we can write:

$$G'_{2\alpha 2\beta}\frac{\partial^2 u_\beta}{(\partial X_2')^2}+R'_{2\alpha 2}\frac{\partial^2 \tilde{\varphi}}{(\partial X_2')^2}=\rho_0\frac{d^2 u_\alpha}{dt^2},$$
$$R'_{2\alpha 2}\frac{\partial^2 u_\beta}{(\partial X_2')^2}-N'_{22}\frac{\partial^2 \tilde{\varphi}}{(\partial X_2')^2}=0. \tag{1}$$

To avoid any confusion, we use prime indices to denote material constants evaluated in the rotated frame associated with the plate, whereas unprimed constants appearing in the

 0001-4966/2001/110(4)/1800/8/$18.00

following will always be expressed in crystallographic axes. Taking plane waves traveling along the thickness as solutions of the above-mentioned system:

$$u_\alpha = u_\alpha^\mu \exp\left[j\left(\omega t - \frac{X_2'}{V^\mu} \right) \right],$$
$$\tilde{\varphi} = \tilde{\varphi}^\mu \exp\left[j\left(\omega t - \frac{X_2'}{V^\mu} \right) \right], \tag{2}$$

where the superscript μ labels a particular mode of propagation (classically denoted A, B, or C, in decreasing order of velocity), and combining the second equation in Eq. (1) with the first one, we obtain Christoffel's secular determinant in terms of the Lagrangian effective coefficients:

$$\begin{bmatrix} G_{99}' + \frac{(R_{26}')^2}{N_{22}'} & G_{29}' + \frac{R_{22}'R_{26}'}{N_{22}'} & G_{49}' + \frac{R_{26}'R_{27}'}{N_{22}'} \\ G_{29}' + \frac{R_{22}'R_{26}'}{N_{22}'} & G_{22}' + \frac{(R_{22}')^2}{N_{22}'} & G_{24}' + \frac{R_{22}'R_{27}'}{N_{22}'} \\ G_{49}' + \frac{R_{26}'R_{27}'}{N_{22}'} & G_{24}' + \frac{R_{22}'R_{27}'}{N_{22}'} & G_{44}' + \frac{(R_{27}')^2}{N_{22}'} \end{bmatrix} \begin{bmatrix} u_1^\mu \\ u_2^\mu \\ u_3^\mu \end{bmatrix}$$
$$= \rho_0 (V^\mu)^2 \begin{bmatrix} u_1^\mu \\ u_2^\mu \\ u_3^\mu \end{bmatrix}. \tag{3}$$

When the plate abuts a perfectly conductive film of sufficiently small thickness h^f, the propagation of acoustic waves in the film can be neglected, and the incremental boundary conditions, Eq. (47) of paper I, take the form:

$$\tilde{K}_{2j} = \rho^f \omega^2 h^f u_\alpha \delta_{j\alpha},$$
$$\tilde{\Delta}_2 = \tilde{\sigma}_0, \quad \tilde{\varphi} = \tilde{\varphi}^f, \tag{4}$$

where the superscript *f* indicates quantities for the film. Thus, in matrix notation, the first two equations of Eq. (4) are rewritten as

$$G_{99}'\frac{\partial u_1}{\partial X_2'} + G_{92}'\frac{\partial u_2}{\partial X_2'} + G_{94}'\frac{\partial u_3}{\partial X_2'} + R_{26}'\frac{\partial \tilde{\varphi}'}{\partial X_2'} = \rho^f \omega^2 h^f u_1,$$
$$G_{29}'\frac{\partial u_1}{\partial X_2'} + G_{22}'\frac{\partial u_2}{\partial X_2'} + G_{24}'\frac{\partial u_3}{\partial X_2'} + R_{22}'\frac{\partial \tilde{\varphi}}{\partial X_2'} = \rho^f \omega^2 h^f u_2,$$
$$G_{49}'\frac{\partial u_1}{\partial X_2'} + G_{24}'\frac{\partial u_2}{\partial X_2'} + G_{44}'\frac{\partial u_3}{\partial X_2'} + R_{27}'\frac{\partial \tilde{\varphi}}{\partial X_2'} = \rho^f \omega^2 h^f u_3, \tag{5}$$
$$i = -R_{26}'\frac{\partial^2 u_1}{\partial X_2' \partial t} - R_{22}'\frac{\partial^2 u_2}{\partial X_2' \partial t} - R_{27}'\frac{\partial^2 u_1}{\partial X_3' \partial t} + N_{22}'\frac{\partial^2 \tilde{\varphi}}{\partial X_2' \partial t}.$$

i is the current density in the electrodes. From the above equations, the resonant frequency of the *n*th overtone of pure thickness mode in an infinite piezoelectric plate of total thickness $2h_0$ in the reference state is easily obtained with the usual treatment of such problem:[4]

$$\omega_n^2 \simeq \frac{n^2\pi^2}{4h_0^2} V_\alpha^2 \left(1 - 8\frac{k_\alpha^2}{n^2\pi^2} - 2\frac{\rho^f h^f}{\rho_0 h_0} \right), \tag{6}$$

where *n* is the overtone number and k^α the coupling factor of the α mode:

$$(k^\alpha)^2 = \frac{(u_1^\alpha R_{26}' + u_2^\alpha R_{22}' + u_3^\alpha R_{27}')^2}{\rho_0 V_\alpha^2 N_{22}'}. \tag{7}$$

As a consequence of the Lagrangian formulation, which maps actual problems onto the fixed geometry of the solid in the reference state, we must note that in the preceding expressions, all quantities, except **G** coefficients, are independent of the temperature Θ. In particular, the velocity of acoustic waves V^μ in the direction defined in the natural coordinate system depends on Θ *only* through the **G** coefficients (see Sec. IV).

Contoured resonator

The Lagrangian formulation is particularly useful when the shape of the resonator varies along temperature changes, which happens in contoured resonators. Such device is shown in Fig. 1. Trapped modes in contoured resonators have been previously described in an asymptotic model due to Tiersten and Stevens.[5] From Eqs. (1) and (4) this model leads to the following expression of resonant frequencies for essentially thickness modes in contoured resonators:

$$\omega_{nmp}^2 = \omega_n^2 \left[1 + \frac{1}{n\pi}\sqrt{\frac{2h_0}{R_0}} \left(\sqrt{\frac{M_n'}{G_\mu}}(2m+1) + \sqrt{\frac{P_n'}{G_\mu}}(2p+1) \right) \right]. \tag{8}$$

G_μ is the μth eigenvalue $\rho_0 (V^\mu)^2$ of Christoffel's problem (3) multiplied by the factor $(1 - 8(k_\alpha^2/n^2\pi^2) - 2(\rho^f h^f/\rho_0 h_0))$. R_0 is the radius of curvature of the resonator at the reference temperature, while *m* and *p* are integers which characterize the mode pattern along rotated in-plane axes. The angle shift from doubly rotated axes is equal to $\frac{1}{2}$ arctan $(-Q_n/(M_n - P_n))$, where M_n, P_n, and Q_n are primary dispersion constants provided in Ref. 5. This angle shift depends on plate orientation, overtone number, and thickness mode group (A, B or C), but not on the radius of curvature R_0. Rotated dispersion constants are simply deduced from M_n, P_n, and Q_n. *m* and *p* are equal to zero for the so-called metrological mode. The dispersion constants have cumbersome expressions in terms of special elastic constants c_{ijkl}^T through Eqs. (74) and (100) of Ref. 5. The latter constants c_{ijkl}^T are themselves obtained from standard elastic constants by means of a linear transformation, which can be understood as expressing a projection of the unknown mechanical displacement onto the basis of solutions of Christ-

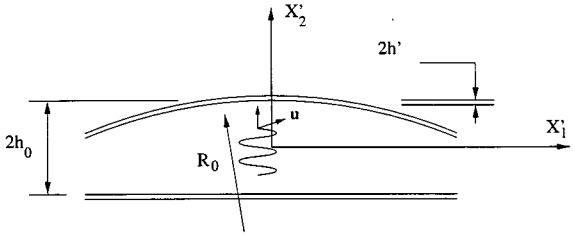

FIG. 1. Cross section of a spherically contoured resonator.

offel's problem. This is an efficient technique to alleviate the search for essentially thickness-dependent modes in thin plates. Using Lagrangian formulation does not imply any change in using analytical formulas provided in Ref. 5, if the transformed constants c^T_{ijkl} are expressed in terms of $G'_{L\gamma M\varepsilon}$ rotated coefficients, instead of the classical ones, in the following manner:

$$c^T_{lprm} = Q_{p\gamma} Q_{r\varepsilon} G'_{L\gamma M\varepsilon} \delta_{lL} \delta_{mM}, \tag{9}$$

where the matrix Q is defined from the normalized eigenvectors of the 3×3 matrix in Eq. (3):

$$Q_{i\alpha} = \delta_{i\mu} u^{\mu}_{\alpha}. \tag{10}$$

This approach allows a convenient extension of the model suggested in Ref. 5 to account for high order temperature sensitivities of trapped modes in contoured resonators. Due to the use of Lagrangian configuration, only M'_n, P'_n, and G_μ are affected by temperature variations and there is no need to evaluate the effect of temperature on the radius of curvature, which would be a problem in the conventional approach since a spherical surface does not remain spherical along temperature variations, according to the anisotropy of thermal expansion.

B. Rayleigh waves

Let us now consider a surface wave traveling along an arbitrary direction on the free surface of a semi-infinite piezoelectric crystal. We assume the coordinate system being such that the X'_2 axis is outwardly oriented perpendicular to the surface of the plate and X'_1 denotes the direction of propagation, shifted by an angle ψ from the standard in-plane axis for the doubly rotated plate. Then, a partial surface wave is characterized by the following dynamic field:

$$\begin{aligned} u_\alpha &= A_\alpha \exp[ik(X'_1 + rX'_2 - V_R t)] \quad (\alpha = 1,...,3), \\ \varphi &= A_4 \exp[ik(X'_1 + rX'_2 - V_R t)], \end{aligned} \tag{11}$$

k being the propagation wave number, V_R the velocity of the partial wave, and r a factor governing its behavior along the depth of the substrate. Since we restrict our attention to straight-crested waves, all the derivatives with respect to X'_3 are zero and the partial derivatives equations simply reduce to

$$\begin{aligned} &\frac{\partial \tilde{K}_{1\alpha}}{\partial X'_1} + \frac{\partial \tilde{K}_{2\alpha}}{\partial X'_2} = \rho_0 (kV_R)^2 u_\alpha, \\ &\frac{\partial \tilde{\Delta}_1}{\partial X'_1} + \frac{\partial \tilde{\Delta}_2}{\partial X'_2} = 0. \end{aligned} \tag{12}$$

After substituting Eq. (11) into Eq. (12) and using the effective constitutive equations (44) of the companion paper, we get a 4×4 system:

$$[L][A] = 0, \tag{13}$$

where each element of the symmetric matrix $\mathbf{L}$ is a quadratic polynomial in terms of r:

$$\begin{aligned} L_{\alpha\beta} &= L_{\beta\alpha} = G'_{L\alpha M\beta} f_{LM}, \\ L_{\alpha 4} &= L_{4\alpha} = R'_{M\alpha L} f_{LM}, \\ L_{44} &= -N'_{LM} f_{LM}, \\ f_{LM} &= r^2 \delta_{2M}\delta_{2L} + r(\delta_{2M} + \delta_{2L})(1-\delta_{LM}) \\ &\quad + (1-\delta_{2L})(1-\delta_{2M}) \end{aligned} \tag{14}$$

with $\alpha,\beta \in \{1,2,3\}$ and $L,M \in \{1,2\}$. For instance, using the symmetries and rules for index compression equations (51) and (52) of paper I, we obtain

$$\begin{aligned} L_{23} &= r^2 G'_{24} + r(G'_{28} + G'_{46}) + G'_{68}, \\ L_{24} &= r^2 R'_{22} + r(R'_{12} + R'_{29}) + R'_{19}. \end{aligned} \tag{15}$$

In accordance with the classical approach,[6] we use the following boundary conditions:

$$\begin{aligned} &\tilde{K}_{2\alpha} = 0 \quad \alpha = 1,...,3 \\ &\varphi - i\frac{ZV^2}{\omega}\tilde{\Delta}_2 = 0 \quad \text{at } X'_2 = 0, \end{aligned} \tag{16}$$

where Z is the surface impedance. $Z=0$ if the surface is coated with a perfect conductive film at null potential, and $Z = i/\varepsilon_0 V$ for a free surface abutted to vacuum. Rayleigh waves in piezoelectric material are expressed[7] as a sum of four partial waves $\{u^{(n)}, \varphi^{(n)}\}$, each one corresponding to a root $r^{(n)}$ of the determinantal equation $|L| = 0$ for a given value of V_R and only the four roots such that $\Im(r) < 0$ are retained:

$$u = \sum_{n=1}^{4} C_n u^{(n)}, \quad \varphi = \sum_{n=1}^{4} C_n \varphi^{(n)}. \tag{17}$$

In the case of a free surface abutted to vacuum, Rayleigh wave velocity is determined from the boundary conditions (16):

$$\begin{aligned} &\sum_{n=1}^{4} K^{(n)}_\lambda C_n = 0, \quad \lambda = 2,4,9, \\ &\sum_{n=1}^{4} \left[\varphi^{(n)} + \frac{i}{\varepsilon_0}\tilde{\Delta}^{(n)}_2 \right] C_n = 0. \end{aligned} \tag{18}$$

Piola–Kirchhoff's stress components of the partial waves $K^{(n)}_\lambda$, appearing in the above-mentioned system, have a simple expression in terms of effective coefficients:

$$\begin{aligned} K^{(n)}_\lambda &= (G'_{\lambda 1} + r^{(n)} G'_{\lambda 9}) A^{(n)}_1 + (G'_{\lambda 6} + r^{(n)} G'_{\lambda 2}) A^{(n)}_2 \\ &\quad + (G'_{\lambda 8} + r^{(n)} G'_{\lambda 4}) A^{(n)}_3 \\ &\quad + (R'_{1\mu(\lambda)} + r^{(n)} R'_{2\mu(\lambda)}) A^{(n)}_4, \quad \lambda = 2,4,9, \end{aligned} \tag{19}$$

where the amplitudes set $\mathbf{A}^{(n)}$ for a given root $r^{(n)}$ is obtained as a solution of the linear system (13) and has been normalized. In this expression, the compressed index $\mu \in \{2,6,7\}$ is obtained upon reverting the order of primary indexes $i,j \in \{1,2,3\}$ which from λ itself is obtained, i.e., $\mu = 2,6,7$ when $\lambda = 2,9,4$, respectively. The material electric displacement $\tilde{\Delta}^{(n)}_2$ also appearing in Eq. (18) is equal to

$$\tilde{\Delta}_2^{(n)} = (R'_{21} + r^{(n)} R'_{26}) A_1^{(n)} + (R'_{29} + r^{(n)} R'_{22}) A_2^{(n)} + (R'_{25} + r^{(n)} R'_{27}) A_3^{(n)} - (N'_{12} + r^{(n)} N'_{22}) A_4^{(n)} . \quad (20)$$

Let us recall that, in the case of a metallized surface, $\tilde{\Delta}_2^{(n)}$ simply disappears from the last equation of the system (18). The velocity of Rayleigh waves is numerically obtained as the value zeroing the determinant of this system.

III. NUMERICAL VALUES

Numerical values of temperature derivatives of effective coefficients can be obtained in three different ways.

(a) In principle they can be computed through their definitions [Eq. (45) of paper I] from existing values of temperature derivatives of fundamental ''thermodynamic'' constants. Relations between effective and thermodynamic constants are outlined at Appendix A.

(b) They can be deduced from currently existing values of temperature derivatives of effective coefficients referred to the intermediate state[3,8] through the relations previously given by Eq. (59) of Paper I. This approach was previously used in Ref. 9. Explicit relations between temperature derivatives of elastic constants referred to the reference state and to the intermediate one are given in Appendix B.

(c) They can be directly determined from measurements of the temperature sensitivity of vibrations in piezoelectric devices, for instance coefficients of frequency of BAW resonators and coefficients of delay of SAW delay lines.

Although the first approach is very enlightening from a theoretical point of view, it is not suitable for the modeling of frequency–temperature characteristics of resonant devices, since only the first-order temperature derivatives of fundamental elastic constants can be determined in practice. The second approach is easy but has the drawback of ignoring the recent advances in the analytic modeling of resonators to determine the numerical values of material coefficients from dynamic measurements. As a matter of fact, since asymptotic models such as Ref. 5 allow one to consistently take into account the dispersion of guided waves in thin plates, they are much more accurate than the unidimensional model of the infinite plate used in Refs. 3 and 8 to describe the thermal sensitivity of actual BAW resonators. This is why we have adopted the last choice. We made a program to compute the values of $T^{(n)}G_{IJ}$ by a least-squares method, from the temperature coefficients of resonant frequency $T^{(n)}f$ of thickness modes in both parallel plates and contoured resonators, and from the temperature coefficients of Rayleigh waves $T^{(n)}V_R$. Data for parallel plates are still taken from Ref. 3, greatly reinforced by confirmed measurement data for contoured resonators made at LCEP, and data for SAW delay lines provided by LPMO.

If, for a given order of expansion n, the six unknown independent coefficients $T^{(n)}G_{IJ}$ ($IJ = 11,13,14,33,44,66$) in crystallographic axes are stored in a vector $\mathbf{G}^{(n)}$ and the experimental data $T^{(n)}f$ and $T^{(n)}V_R$ in a vector $\mathbf{Y}^{(n)}$, the following relations are observed:

TABLE I. Selected data from BBL.

ϕ	θ	Mode	$T^1 f(10^{-6})$	$T^2 f(10^{-9})$	$T^3 f(10^{-12})$
30.0	20.00	A	−42.00	−86.00	−92.70
05.0	−47.00	B	−0.90	−41.10	−118.0
05.0	−48.00	B	−1.50	−43.10	−122.6
10.0	−38.00	B	1.10	−39.00	−91.30
10.0	−40.00	B	−2.40	−41.90	−115.4
15.0	−34.50	B	−7.40	−28.10	−39.70
15.0	−35.00	B	−7.45	−33.50	−58.80
30.0	20.00	B	−9.30	−21.80	−34.40
30.0	30.00	B	−19.10	−24.50	−28.90
00.0	00.00	C	92.50	57.50	5.80

$$Y_I^{(1)} = M_{IJ}^{(1)} G_J^{(1)},$$
$$Y_I^{(2)} = M_{IJ}^{(1)} G_J^{(2)} + \tfrac{1}{2} M_{IJK}^{(2)} G_J^{(1)} G_K^{(1)}, \quad (21)$$
$$Y_I^{(3)} = M_{IJ}^{(1)} G_J^{(3)} + M_{IJK}^{(2)} G_J^{(2)} G_K^{(1)} + \tfrac{1}{6} M_{IJKL}^{(3)} G_J^{(1)} G_K^{(1)} G_L^{(1)},$$

where the coefficients $\mathbf{M}^{(n)}$ are the partial derivatives of successive order n, up to 3, of the temperature coefficients of frequency or celerity with respect to independent elastic constants. Thus, they are numerically computed for a given type of input data and geometry (infinite plate, contoured resonator of known radius of curvature and given overtone, SAW delay line) including cut angles, by successive small increments of each independent coefficient, followed by the proper rebuilding of the G_{IJ} matrix for the required symmetries in class 32. In the least-squares treatment of Eq. (21), the vector $\mathbf{Y}^{(n)}$ holding the experimental data must be much larger than the vector $\mathbf{G}^{(n)}$ of the independent unknowns. The first-order coefficients are directly obtained from the linear system:

$$([\mathbf{M}^{(1)}]^T \cdot [\mathbf{M}^{(1)}]) \cdot \mathbf{G}^{(1)} = [\mathbf{M}^{(1)}]^T \cdot \mathbf{Y}^{(1)}. \quad (22)$$

Higher order coefficients are then recursively determined by the same least-squares treatment after substituting already known lower order terms into the right-hand members of Eq. (21).

Data retained in our treatment are summarized in Tables I–III, which give the temperature coefficients of retained data at orders up to three. Orientation angles of considered plates, ϕ, θ, ψ conform to conventions of Ref. 10.

Table I is a much restricted subset of $T^{(n)}f$ coefficients provided in Ref. 3 for parallel plates. Retaining such data was useful to asses the cut angles on a larger basis than measurements available at the moment for contoured resonators and SAW devices. This subset was selected by considering the ability of cuts to be correctly trapped in the sense of the theory of Tiersten and Stevens.[5] For instance, since M'_n and P'_n for A modes in X cuts are negative for the first three odd overtone numbers, we did not make use of any corresponding data $T^{(n)}f$ for X cut provided in Ref. 3, since, in such a case, the dispersion properties of a finite plate will actually result in a frequency–temperature behavior of resonant modes significantly different from the theoretical temperature behavior expected for an infinite plate. The infinite plate model should also be considered as inaccurate when M'_n and P'_n appearing in Eq. (8) are positive and extremely large.

TABLE II. Data from contoured BAW resonators.

ϕ	θ	$\mu(n,m,p)$	h (mm)	R_0 (mm)	$T^1f(10^{-6})$	$T^2f(10^{-9})$	$T^3f(10^{-12})$
0.00	35.45	C(5,0,0)	0.835	150	−0.635	−2.690	110.0
22.417	34.025	C(3,0,0)	0.6656	230	0.956 06	−12.754	59.359
22.70	34.00	C(3,0,0)	0.6656	230	1.053 53	−14.041	65.522
22.75	34.00	C(3,0,0)	0.6656	230	0.997 63	−12.906	57.281
22.633	34.00	C(3,0,0)	0.6656	230	1.023 21	−12.714	55.332
22.633	34.00	C(3,0,0)	0.6656	230	0.991 10	−11.443	45.393
22.771	34.038	C(3,0,0)	0.5456	230	0.896 98	−12.231	50.681
22.432	34.104	C(3,0,0)	1.089	300	0.654 9	−12.44	53.91
0	−45.25	B(3,0,0)	1.53	150	3.590	−40.70	−54.0
0	−46.00	B(3,0,0)	0.5126	132.5	0.00	−48.91	−99.24
22.75	34.025	B(3,0,0)	0.555	250	−26.65	−25.70	5.00
16.00	−34.50	C(5,0,0)	1.275	200	−2.463	−5.586	−27.80
16.167	−34.50	C(5,0,0)	1.275	200	−2.453	−6.00	−22.90
16.30	−35.50	C(5,0,0)	1.230	150	−2.52	−9.30	11.0
19.10	34.50	C(3,0,0)	1.068	120	0.609 8	−11.132	75.08
19.10	34.50	C(3,0,0)	1.068	120	0.629 0	−11.573	76.52
22.75	34.025	C(3,0,0)	0.555	250	0.867	−12.90	59.0
22.75	34.025	C(3,0,0)	0.555	250	0.903	−13.50	61.0
29.967	34.675	C(3,0,0)	1.200	200	−0.807	−15.394	30.19
29.967	34.675	C(5,0,0)	1.200	200	−1.353	−18.677	43.95

Table II presents data from contoured resonators measured at LCEP, mainly C modes of SC cut, plus a few data for AT, BT, and IT cuts and one B-mode SC cut. Retained SAW data are given in Table III and consist of $T^{(n)}V_R$ measured from delay lines made at LPMO: three doubly rotated cuts, LSP1, LSP2, and LSP3, four simply rotated cuts in the range $\theta \in [-2.5,-10]$ and two STC cuts.[11] We found that adding the data for SAW increased the standard deviation, especially for the $T^{(3)}G_{IJ}$. Due to that and since most temperature compensated cuts used in SAW technology exhibit a parabolic behavior of frequency–temperature characteristic, we decided to retain input data of Table III for the determination of $T^{(1)}G_{IJ}$ and $T^{(2)}G_{IJ}$ only.

Our purpose was to determine a set of $\mathbf{G}^{(n)}$ derivatives preserving a reasonable accuracy for widely used practical devices of either kind, BAW or SAW, rather than performing a new and extensive measurement campaign. To achieve this goal, contradictory requirements must be met, thereby implying some compromise:

Available SAW data available at LPMO were not numerous enough to allow by itself a reliable determination of $\mathbf{G}^{(n)}$. The same remark also holds for data from contoured BAW resonators available at LCEP. But, adding new data from SAW devices to existing data from BAW resonators results in an increase of the standard error, which is not surprising since reliabilities of the models suitable for each kind of device is not expected to be identical. Thus, we found pertinent to constraint the computed $\mathbf{G}^{(n)}$ coefficients to accurately fit some particular measurements of well-known and technologically stable devices. The lines which correspond to such selected input data are thus isolated in system (21) and treated as external constraints that must be exactly satisfied by the least-squares treatment. This is achieved by the well-known technique of Lagrange multipliers, in a way quite similar to the approach extensively described in Ref. 12 for the determination of third-order elastic coefficients of quartz. It should be observed that such external constraints can be imposed independently for $\mathbf{Y}^{(1)}$, $\mathbf{Y}^{(2)}$, and $\mathbf{Y}^{(3)}$. Also, beside its flexibility, this method is also more refined than the method used in Ref. 3, where $T^{(n)}H_{11}$ and $T^{(n)}H_{66}$ are first obtained separately from X cut and Y cut, $T^{(n)}H_{14}$ and $T^{(n)}H_{44}$ come from the knowledge of AT and BT cuts, the least-squares treatment concerning only $T^{(n)}H_{13}$ and $T^{(n)}H_{33}$. Thus, in the approach of Refs. 3 and 8, the standard error on $T^{(n)}H_{11}$, $T^{(n)}H_{66}$, $T^{(n)}H_{14}$, and $T^{(n)}H_{44}$ is assumed to be zero, thereby fully transferring the whole error on $T^{(n)}H_{13}$ and $T^{(n)}H_{33}$, whereas with Lagrange multiplier, the standard error is more widely distributed over the whole set of independent $\mathbf{G}^{(n)}$.

Obtained values of $\mathbf{G}^{(n)}$ vary significantly, according to the choice of data to be ''overweighted'' by a Lagrange multiplier. First, since SC-cut data are well represented in the presented tables, we decided to use the Lagrange multiplier for the AT cut only, with $n=1,2,3$. In this way, we obtain a set of $\mathbf{G}^{(n)}$ which leads to a better agreement for the temperature characteristics of Rayleigh waves on singly rotated substrates than for STC and LSP orientations, whereas accuracy for the temperature behavior of BAW resonators remains similar to the one provided by results of Ref. 8. Obtained values of nonzero $T^{(n)}G_{IJ}$ in crystallographic axes are presented in Table IV. Note that standard errors are given only for the independent coefficients. Other treatments can

TABLE III. Data from SAW delay lines.

Type	ϕ	θ	ψ	$T^1V_R(10^{-6})$	$T^2V_R(10^{-9})$	$T^3V_R(10^{-12})$
LSP1	−10.0	40.0	51.0	3.892	−29.09	−14.17
LSP2	−20.0	−35.0	16.5	0.103	−38.58	−35.71
LSP3	−30.0	−45.0	62.0	2.337	−18.96	−58.99
TG0	0.0	−10.0	30.0	0.137	−29.57	−165.74
TG1	0.0	−7.0	31.0	0.091	−26.20	234.16
TG2	0.0	−5.0	31.5	0.100	−38.48	−232.95
TG3	0.0	−2.5	32.5	−0.323	−23.03	−009.12
STC	0.0	41.8	46.9	4.912	−06.63	59.78
STC	0.0	41.8	48.2	−0.070	−23.38	58.21

TABLE IV. Numerical values obtained with the presented treatment.

$T^{(n)}G_{IJ}$ IJ	10^{-6} $n=1$	10^{-9} $n=2$	10^{-12} $n=3$
11	−33.7±3.2	−113±9	−103±30
13	−680±40	−1043±107	−67±390
14	95.7±3.0	−43.9±8.1	−537±24
17	102	−40.3	−546
33	−204±12	−151±32	132±108
44	−171.6±3.6	−224±9	−173±31
47	−165.5	−222	−184
55	−159.3	−220	−195
66	181.2±3.2	131.3±8.5	41.4±2.6

be made: For instance, we found that using the Lagrange multiplier for LSP data improved accuracy for the predicted temperature behavior of doubly rotated SAW data, at the expense of a limited loss of accuracy for BAW resonators.

IV. CONCLUSION

It should be observed that we assumed $T^{(n)}\mathbf{R}$ and $T^{(n)}\mathbf{N}$ to be zero in the treatment presented here, according to the difficulty of establishing reliable data for those constants in quartz, as a consequence of its rather low piezoelectric coupling. Such restriction should and can easily be avoided when applying the presented analysis to emerging new materials retaining the same kind of crystalline symmetry but exhibiting larger piezoelectric constants, for instance langasite and similar materials, or $GaPO_4$. About quartz, the accuracy of $T^{(n)}G_{IJ}$ obtained from dynamic measurements with the help of least-squares analysis would benefit from an enlargement of the set of experimental data, but we leave this improvement for further developments, since the main point we wished to stress in this paper was the suitability of the formalism presented here to properly describe the static high order temperature behavior of both BAW and SAW devices. In addition to the clear relationship of the formalism with the consistent theory of thermoelectroelasticity, more detailed in the companion paper, this suitability appears more obvious also from a practical point of view, if one considers that the Lagrangian formalism matches well with the use of elaborate dispersive analytical models and numerical models. For instance, when performing frequency–temperature analyses with finite element method, the use of Lagrangian coefficients avoids the need of successive computations of the shape of the device prior to vibration along temperature variations.

APPENDIX A: DIFFERENCE BETWEEN EFFECTIVE AND FUNDAMENTAL CONSTANTS

According to discussions presented in Paper I, fundamental constants are partial derivatives of the pertinent energy function for the class of problem considered. More precisely, they are the coefficients of multivariate Taylor's expansion of this energy function around the reference state. For instance, using $\chi(E_{KL};E_{MN};\Theta)$ defines $\rho_0\partial^2\chi/\partial E_{KL}\partial E_{MN})_0$ as a fundamental isothermal elastic coefficient at constant electric field c^0_{KLMN}, and $\rho_0\partial^3\chi/\partial E_{KL}\partial E_{MN}\partial\Theta)_0$ as its first-order temperature derivative c^1_{KLMN}. Here, the notation $)_0$ stands for the calculation of partial derivatives in the reference state. A Taylor's expansion up to third order in terms of all independent variables, sufficient for any purpose regarding the first-order temperature derivatives of elastic, electrostatic, and piezoelectric constants, is given in the following:

$$
\begin{aligned}
&\rho_0\chi(\mathbf{E},\mathbf{W},\Theta_0+\Delta\Theta)-\rho_0\chi(0,0,\Theta_0)\\
&=\tfrac{1}{2}\,c^0_{KLMN}E_{KL}E_{MN}-e^0_{K\cdot LM}W_KE_{LM}-\tfrac{1}{2}\,\kappa^0_{KL}W_KW_L+\tfrac{1}{6}\,c^0_{KLMNPQ}E_{KL}E_{MN}E_{PQ}-\tfrac{1}{2}\,e^0_{K\cdot LMNP}W_KE_{LM}E_{NP}\\
&-\frac{1}{2}e^0_{KL\cdot MN}W_KW_LE_{MN}-\frac{1}{6}\,\kappa_{KLM}W_AW_MW_N+\frac{1}{2}\,\frac{\rho_0C^0}{\Theta_0}\Delta\Theta^2+\frac{1}{6}\,\frac{\rho_0C^1}{\Theta^0}\Delta\Theta^3-\Lambda^1_{KL}E_{KL}\Delta\Theta-\frac{1}{2}\,\Lambda^2_{KL}E_{KL}\Delta\Theta^2\\
&-p^0_KW_K\Delta\Theta-\tfrac{1}{2}\,p^1_KW_K\Delta\Theta^2+\tfrac{1}{2}\,c^1_{KLMN}E_{KL}E_{MN}\Delta\Theta-e^1_{K\cdot LM}W_KE_{LM}\Delta\Theta-\tfrac{1}{2}\kappa^1_{KL}W_KW_L\Delta\Theta+h.o.t.\cdots,
\end{aligned}
\tag{A1}
$$

where the superscript 1 indicates the first-order temperature derivative of a material coefficient otherwise denoted by the superscript 0. With rather standard notations, $\mathbf{c}^n$ relates to elastic constants, linear or not, and their temperature derivatives of nth order, $\mathbf{e}^n$ generically relates to piezoelectric and electrostrictive constants and their temperature derivatives, $\boldsymbol{\kappa}^n$ indicates electric susceptibilities and their temperature derivatives, while C^n stays for calorific capacity and its temperature derivatives, $\boldsymbol{\Lambda}^n$ stays for thermoelastic coupling of order n under constant field. The terms containing $\mathbf{p}^0$ and $\mathbf{p}^1$ identically vanish since quartz is not pyroelectric. In this manner, all partial derivatives involved in the expressions of $\chi_{KLMN})_1$, $\chi_{K\cdot LM})_1$, $\chi_{KL})_1$ defined by Eq. (40) of Paper I, which in turn appear in the definition of Lagrangian effective constants, Eq. (44) of Paper I, can be expressed in terms of fundamental constants. In particular, we obtain:

$$\rho_0\frac{\partial^2\chi}{\partial E_{KL}\partial E_{MN}}\Big)_1 = c^0_{KLMN} + c^1_{KLMN}\Delta\overline{\Theta} + c^0_{KLMNPQ}\overline{E}_{PQ} - e^0_{P\cdot KLMN}\overline{W}_P$$

$$\rho_0\frac{\partial^2\chi}{\partial W_K\partial E_{LM}}\Big)_1 = -e^0_{K\cdot LM} - e^1_{K\cdot LM}\Delta\overline{\Theta} - e^0_{K\cdot LMNP}\overline{E}_{NP} - e^0_{KP\cdot LM}\overline{W}_P \tag{A2}$$

$$\rho_0\frac{\partial^2\chi}{\partial W_K\partial W_L}\Big)_1 = -\kappa^0_{KL} - \kappa^1_{KL}\Delta\overline{\Theta} - \kappa^0_{KLM}\overline{W}_M - e^0_{KL\cdot MN}\overline{E}_{MN}$$

together with similar expressions for other quantities appearing in $\chi_{KLMN)_1}$ and $\chi_{K\cdot LM)_1}$:

$$\rho_0\frac{\partial^2\chi}{\partial E_{KL}\partial\Theta}\Big)_1 = -\Lambda^1_{KL} + c^1_{KLMN}\overline{E}_{MN} - \Lambda^2_{KL}\Delta\overline{\Theta} - e^1_{M\cdot KL}\overline{W}_M$$

$$\rho_0\frac{\partial^2\chi}{\partial W_K\partial\Theta}\Big)_1 = -e^1_{K\cdot LM}\overline{E}_{LM} - \kappa^1_{KL}\overline{W}_L \tag{A3}$$

$$\rho_0\frac{\partial^2\chi}{\partial\Theta^2}\Big)_1 = \frac{\rho_0 C^0}{\Theta^0}\left(1 - \frac{\Theta^0}{\rho_0 C^0}\Lambda^2_{KL}\overline{E}_{KL} + \frac{C^1}{C^0}\Delta\overline{\Theta}\right).$$

Taking into account the nullity of $\overline{\mathbf{W}}$ and substituting into Eq. (40) of Paper I yields the following relations:

$$\begin{aligned}
\rho_0\chi_{KLMN)_1} &= c^{0,\eta}_{KLMN} + c^{1,\eta}_{KLMN}\Delta\overline{\Theta} + c^{0,\eta}_{KLMNPQ}\overline{E}_{PQ}\\
\rho_0\chi_{K\cdot LM)_1} &= -e^0_{K.LM} - e^1_{K\cdot LM}\Delta\overline{\Theta} - e^{0,\eta}_{K\cdot LMNP}\overline{E}_{NP}\\
\rho_0\chi_{KL)_1} &= -\kappa^0_{KL} - \kappa^1_{KL}\Delta\overline{\Theta} - e^0_{KL\cdot MN}\overline{E}_{MN},
\end{aligned} \tag{A4}$$

where some new constants need to be introduced:

$$\begin{aligned}
c^{0,\eta}_{KLMN} &= c^0_{KLMN} - \frac{\Theta^0}{\rho_0 C^0}\Lambda^1_{KL}\Lambda^1_{MN},\\
c^{0,\eta}_{KLMNPQ} &= c^0_{KLMNPQ} + \frac{\Theta^0}{\rho_0 C^0}\left(+\Lambda^1_{KL}c^1_{MNPQ} + \Lambda^1_{MN}c^1_{KLPQ} - \frac{\Theta^0}{\rho_0 C^0}\Lambda^1_{KL}\Lambda^1_{MN}\Lambda^2_{PQ}\right),\\
c^{1,\eta}_{KLMN} &= c^0_{KLMN} + \frac{\Theta^2}{\rho C^0}\left(-\Lambda^1_{KL}\Lambda^2_{MN} - \Lambda^1_{MN}\Lambda^2_{KL} + \frac{C^1}{C^0}\Lambda^1_{KL}\Lambda^1_{MN}\right),\\
e^{0,\eta}_{K\cdot LMNP} &= e^0_{K\cdot LM} + \frac{\Theta^0}{\rho_0 C^0}e^1_{K\cdot NP}\Lambda^1_{LM}.
\end{aligned} \tag{A5}$$

The superscript η indicates a constraint of null entropy. Although they appear as independent coefficients in Taylor's expansion of χ, it should be observed that thermoelastic coupling constants $\mathbf{\Lambda}^n$ can be expressed in terms of thermal expansion coefficients and elastic constants (and their temperature derivatives). This can be done remarking that thermal expansion coefficients α^n_{KL} appear in Taylor's expansion of the thermodynamic potential $\mathcal{G}(\mathbf{t};\mathbf{W};\Theta) = \chi - t_{KL}S_{KL}$ which uses the thermodynamic stress as independent variable instead of strain:

$$\alpha^n_{KL} = \frac{1}{n!}\frac{\partial^n E_{KL}}{\partial\Theta^n} = \frac{\rho_0}{n!}\frac{\partial^{1+n}\mathcal{G}}{\partial t_{KL}\partial\Theta^n} = -\frac{\rho_0}{n!}\frac{\partial^n\eta}{\partial t_{KL}\partial\Theta^{n-1}}\,. \tag{A6}$$

Hence, using the following identity

$$\frac{\partial\eta}{\partial E_{KL}}\Big)_{\Theta,\mathbf{W}} \equiv \frac{\partial\eta}{\partial t_{MN}}\Big)_{\Theta,\mathbf{W}}\frac{\partial t_{MN}}{\partial E_{KL}}\Big)_{\Theta,\mathbf{W}} \tag{A7}$$

and deriving it with respect to temperature provides with expressions of Λ^1 and Λ^2 in terms of α^1_{KL}, α^2_{KL}, c^0_{KLMN}, and c^1_{KLMN}:

$$\begin{aligned}
\Lambda^1_{KL} &= c^0_{LKMN}\alpha^1_{MN},\\
\Lambda^2_{KL} &= c^0_{LKMN}\alpha^2_{MN} + c^1_{KLMN}\alpha^1_{MN}.
\end{aligned} \tag{A8}$$

Substituting (A4) into Eq. (45) of Paper I, using Eq. (50) of Paper I and retaining the first-order terms with respect to $\Delta\overline{\Theta}$ gives access to the relations between effective and fundamental constants, up to the first order in terms of temperature:

$$\begin{aligned}
G_{L\gamma M\beta} &= c^{0,\eta}_{L\gamma M\beta} + (c^{1,\eta}_{L\gamma M\beta} + c^{0,\eta}_{L\gamma M\beta NP}\alpha^1_{NP} + c^{0,\eta}_{LJM\beta}\alpha^1_{\gamma J} + c^{0,\eta}_{L\gamma MN}\alpha^1_{\gamma N})\Delta\overline{\Theta},\\
R_{K\cdot L\gamma} &= e^0_{K\cdot L\gamma} + (e^1_{K\cdot L\gamma} + e^0_{K\cdot LM}\alpha^1_{\beta M} + e^{0,\eta}_{K\cdot L\gamma NP}\alpha^1_{NP})\Delta\overline{\Theta},\\
N_{KL} &= \varepsilon_0\delta_{KL}(1+\overline{J^1}) + [(\overline{J^1}\delta_{KL} - 2\alpha_{KL})\varepsilon_0 + \kappa^1_{KL} + e^0_{KL\cdot MN}\alpha^1_{MN}],
\end{aligned} \tag{A9}$$

where $\overline{J^1}$ is the first-order temperature derivative of $\overline{J}$. For quartz, $\overline{J^1} = 2\alpha^{(1)}_{11} + \alpha^{(1)}_{33}$. At this moment only the first-order temperature derivatives of the adiabatic fundamental elastic coefficients at constant electric field $c^{1,\eta}_{KLMN}$ have been determined,[2] due to the complexity of explicit writing of dynamic problems in terms of fundamental constants. Also, explicit relations at orders higher than one in terms of temperature involve nonlinear constants whose numerical values are not yet determined, even for a rather well known material such as quartz. Remaining with the first-order case, we may now remark that, from the above-mentioned relations and Sec. V of Paper I, numerical values of first-order thermal derivatives of fundamental elastic constants given in Ref. 2 could as well be calculated from the values of T^1G_{IJ} proposed here or from numerical values of first-order temperature derivatives of constants used in the so-called usual treatment.[3]

APPENDIX B: RELATIONS BETWEEN $T^{(n)}G_{IJ}$ AND $T^{(n)}H_{IJ}$

They derive immediately from Eqs. (50), (53), (55)–(57), (61) of the companion paper, Paper I. Since we deter-

mined first a set of data for $T^{(n)}G_{IJ}$ for quartz, we provide in the following $T^{(n)}H_{IJ}$ in terms of independent $T^{(n)}G_{IJ}$, with $(IJ)\in\{13,14,33,44,66\}$,

$$
\begin{aligned}
&T^{(1)}H_{11}=T^{(1)}G_{11}-\alpha_{33}^{(1)},\\
&T^{(1)}H_{13}=T^{(1)}G_{13}-\alpha_{11}^{(1)},\\
&T^{(1)}H_{14}=T^{(1)}G_{14}-\alpha_{33}^{(1)},\\
&T^{(1)}H_{33}=T^{(1)}G_{33}+\alpha_{33}^{(1)}-2\alpha_{11}^{(1)},\\
&T^{(1)}H_{44}=T^{(1)}G_{44}-\alpha_{44}^{(1)},\\
&T^{(1)}H_{66}=T^{(1)}G_{66}-\alpha_{66}^{(1)},
\end{aligned}
\tag{B1}
$$

$$
\begin{aligned}
&T^{(2)}H_{11}=T^{(2)}G_{11}-(T^{(1)}G_{11}-\alpha_{33}^{(1)})\alpha_{33}^{(1)}-\alpha_{33}^{(2)},\\
&T^{(2)}H_{13}=T^{(2)}G_{13}-(T^{(1)}G_{13}-\alpha_{11}^{(1)})\alpha_{11}^{(1)}-\alpha_{11}^{(2)},\\
&T^{(2)}H_{14}=T^{(2)}G_{14}-(T^{(1)}G_{14}-\alpha_{33}^{(1)})\alpha_{33}^{(1)}-\alpha_{33}^{(2)},\\
&T^{(2)}H_{33}=T^{(2)}G_{33}-T^{(1)}G_{33}(2\alpha_{11}^{(1)}-\alpha_{33}^{(1)})\\
&\qquad+\alpha_{11}^{(1)}(3\alpha_{11}^{(1)}-2\alpha_{33}^{(1)})-2\alpha_{11}^{(2)}+\alpha_{33}^{(2)},\\
&T^{(2)}H_{44}=T^{(2)}G_{44}-(T^{(1)}G_{44}-\alpha_{33}^{(1)})\alpha_{33}^{(1)}-\alpha_{33}^{(2)},\\
&T^{(2)}H_{66}=T^{(2)}G_{66}-(T^{(1)}G_{66}-\alpha_{33}^{(1)})\alpha_{33}^{(1)}-\alpha_{33}^{(2)},
\end{aligned}
\tag{B2}
$$

$$
\begin{aligned}
&T^{(3)}H_{11}=T^{(3)}G_{11}-T^{(2)}G_{11}\alpha_{33}^{(1)}-((\alpha_{33}^{(1)})^2-\alpha_{33}^{(2)})\\
&\qquad\times(T^{(1)}G_{11}-\alpha_{33}^{(1)})+\alpha_{33}^{(1)}\alpha_{33}^{(2)}-\alpha_{33}^{(3)},\\
&T^{(3)}H_{13}=T^{(3)}G_{13}-T^{(2)}G_{13}\alpha_{11}^{(1)}-((\alpha_{11}^{(1)})^2-\alpha_{11}^{(2)})\\
&\qquad\times(T^{(1)}G_{13}-\alpha_{11}^{(1)})+\alpha_{11}^{(1)}\alpha_{11}^{(2)}-\alpha_{11}^{(3)},\\
&T^{(3)}H_{14}=T^{(3)}G_{14}-T^{(2)}G_{14}\alpha_{33}^{(1)}-((\alpha_{33}^{(1)})^2-\alpha_{33}^{(2)})\\
&\qquad\times(T^{(1)}G_{14}-\alpha_{33}^{(1)})+\alpha_{33}^{(1)}\alpha_{33}^{(2)}-\alpha_{33}^{(3)},\\
&T^{(3)}H_{33}=T^{(3)}G_{33}-(2\alpha_{11}^{(1)}-\alpha_{33}^{(1)})T^{(2)}G_{33}\\
&\qquad+[\alpha_{11}^{(1)}(3\alpha_{11}^{(1)}-2\alpha_{33}^{(1)})-2\alpha_{11}^{(2)}+\alpha_{33}^{(2)}]T^{(1)}G_{33}\\
&\qquad+2(\alpha_{33}^{(1)}-3\alpha_{11}^{(1)})\alpha_{11}^{(2)}-2\alpha_{11}^{(1)}\alpha_{33}^{(2)}\\
&\qquad+(\alpha_{11}^{(1)})^2(3\alpha_{33}^{(1)}-4\alpha_{11}^{(1)})-2\alpha_{11}^{(3)}+\alpha_{33}^{(3)},\\
&T^{(3)}H_{44}=T^{(3)}G_{44}-T^{(2)}G_{44}\alpha_{33}^{(1)}-((\alpha_{33}^{(1)})^2-\alpha_{33}^{(2)})\\
&\qquad\times(T^{(1)}G_{44}-\alpha_{33}^{(1)})+\alpha_{33}^{(1)}\alpha_{33}^{(2)}-\alpha_{33}^{(3)},\\
&T^{(3)}H_{66}=T^{(3)}G_{66}-T^{(2)}G_{66}\alpha_{33}^{(1)}-((\alpha_{33}^{(1)})^2-\alpha_{33}^{(2)})\\
&\qquad\times(T^{(1)}G_{66}-\alpha_{33}^{(1)})+\alpha_{33}^{(1)}\alpha_{33}^{(2)}-\alpha_{33}^{(3)}.
\end{aligned}
\tag{B3}
$$

[1] B. Dulmet and R. Bourquin, "Lagrangian effective material constants for the modeling of thermal behavior of acoustic waves in piezoelectric crystal. I. Theory," J. Acoust. Soc. Am. **110**, 1792 (2001).

[2] B. K. Sinha and H. F. Tiersten, "First temperature derivatives of the fundamental elastic constants of quartz," J. Appl. Phys. **50**, 2732–2739 (1979).

[3] R. Bechmann, A. Ballato, and K. Lukaszek, "High order temperature coefficients of the elastic stiffnesses and compliances of quartz," Proc. IRE **50**, 1812–1822 (1962).

[4] H. F. Tiersten, *Linear Piezoelectric Plate Vibrations* (Plenum, New York, 1969).

[5] D. S. Stevens, and H. F. Tiersten, "An analysis of doubly rotated quartz resonators utilizing essentially thickness modes with transverse variations," J. Acoust. Soc. Am. **79**, 1811–1826 (1986).

[6] K. A. Ingebrigtsen, "Surface waves in piezoelectrics," J. Appl. Phys. **40**, 2681–2686 (1986).

[7] G. W. Farnell, "Properties of elastic surfaces waves," in *Physical Acoustics*, edited by W. P. Mason and R. N. Thurston (Academic, New York, 1970), Vol. 6, pp. 109–166.

[8] B. James, "A new measurement of the basic elastic and dielectric constants of quartz," Proc. 42nd Ann. Freq. Cont. Symp., 1988, pp. 146–154.

[9] B. Dulmet and R. Bourquin, "Influence de l'état de référence sur les coefficients de température des modules lastiques du quartz α," C. R. Acad. Sci. Paris **294**, 361–364 (1982).

[10] "IRE standards on piezoelectric crystals," Proc. IRE **37**, 1378–1395 (1949).

[11] S. Ballandras and E. Bigler, "Surface acoustic wave devices with low sensitivity to mechanical and thermoelastic stresses," J. Appl. Phys. **72**, 3272–3281 (1992).

[12] R. N. Thurston, "Waves in solids," in *Mechanics of Solids IV* (Springer, Berlin, 1974), pp. 109–132, Vol. VIa/4 of Encyclopedia of Physics.

Acoustic streaming in closed thermoacoustic devices

Hélène Bailliet[a)]
National Center for Physical Acoustics and Department of Physics and Astronomy, University of Mississippi, University, Mississippi 38677

Vitalyi Gusev
Laboratoire de l'Etat Condensé de la Faculté des Sciences, UPRESA-CNRS 6087, av. O. Messiaen, 72085 Le Mans Cedex 9, France

Richard Raspet and Robert A. Hiller
National Center for Physical Acoustics and Department of Physics and Astronomy, University of Mississippi, University, Mississippi 38677

(Received 3 November 2000; accepted for publication 21 June 2001)

A derivation of acoustic streaming in a steady-state thermoacoustic device is presented in the case of zero second-order time-averaged mass flux across the resonator section (nonlooped device). This yields analytical expressions for the time-independent second-order velocity, pressure gradient, and time-averaged mass flux in a fluid supporting a temperature gradient and confined between widely to closely separated solid boundaries, both in the parallel plate and in the cylindrical tube geometries (two-dimensional problem). From this, streaming can be evaluated in a thermoacoustic stack, regenerator, pulse tube, main resonator of a thermoacoustic device, or in any closed tube that supports a mean temperature gradient, providing only that the acoustic pressure, the longitudinal derivative of the pressure, and the mean temperature variation are known. © *2001 Acoustical Society of America.* [DOI: 10.1121/1.1394739]

PACS numbers: 43.25.Nm, 43.35.Ud [MFH]

I. INTRODUCTION

Thermoacoustics involves the generation of a second-order hydrodynamic heat flux across a stack by an acoustic field in a fluid filled cavity, or the contrary.[1] In the stack region, thermal boundary layer effects yield a heat flux and the fluid supports a temperature gradient. Heat exchangers at each end of the stack communicate this heat with external reservoirs. Physical principles of thermoacoustic processes are nowadays fairly well understood[2,3] and linear thermoacoustic theory[2,4] provides efficient tools for predicting the behavior of the engines (e.g., the simulation code DeltaE).[5] But, progress towards a theoretical description of this behavior has been mainly restricted to the linear theory and the development of practical devices has required numerical simulations and trial and error. The well-established foundations of thermoacoustics, based on the acoustic approximation, reach their limits when used to describe the behavior of high-amplitude thermoacoustic devices. A deeper understanding of the high-amplitude phenomena, important for optimization of the performance of thermoacoustic devices, requires more analytical investigations. This paper aims at providing a contribution to such investigations by developing a theoretical description of streaming velocity in standing wave thermoacoustic devices. This study has been motivated in part by recent laser Doppler anemometry measurements in a standing wave thermoacoustic engine.[6]

The term *acoustic streaming* refers to the second-order steady velocity that is induced by and superimposed on the dominating first-order acoustic velocity. Streaming leads to nonzero time-averaged mass flows so that it is a mechanism for convective heat transfer that can reduce the efficiency of thermoacoustic devices. It can be generated in the main resonator and also within any stack pore where boundary layer effects dominate. Studies have recently been published on streaming in toroidal thermoacoustic devices[7–9] or in pulse tubes,[10,11] but as pointed out by Swift,[1] little is known about streaming within a regenerator or a stack. Even an order-of-magnitude estimate of the streaming velocity in such component is not available in the literature. Previous theoretical developments of streaming in closed-like thermoacoustic devices have been restricted to the outer streaming description (outside the boundary layer),[10,12] which cannot treat the stack or regenerator region, or have not included the temperature dependence of the viscosity and heat conduction.[13] Such a description is developed in this paper, not only in the analytically tractable parallel plate geometry, but also in the more realistic cylindrical tube one.

Because the literature on acoustic streaming in general is extensive and the literature on acoustic streaming in thermoacoustic devices rather scarce, there is a need to correctly position this application among others. This is done in Sec. II. In Sec. III, the derivation of the acoustic streaming velocity, together with the corresponding second-order pressure gradient and the time-averaged mass flux in closed thermoacoustic devices, is presented both in the case of parallel plate geometry and in the case of cylindrical tubes. Some results of the calculation of streaming in existing thermoacoustic devices are given in Sec. IV.

II. HISTORICAL PERSPECTIVE

The force that drives acoustic streaming owes its origin to Reynolds stresses in the flow and is observed in a number

[a)]Now at: Laboratoire d'Etudes Aérodynamiques, UMR-CNRS 6609, CEAT, 43 route de l'aérodrome, F-86036 Poitiers Cedex, France.

 0001-4966/2001/110(4)/1808/14/$18.00

of situations, generally separated into two main types. In the first case, acoustic energy dissipation occurs within the Stokes boundary layer adjacent to a solid boundary; it gives rise to a vortex-like streaming velocity. This streaming is usually called ''Rayleigh streaming,'' as it was first modeled by Rayleigh[14] to describe Dvorak's phenomenon associated with dust pattern in Kundt's tube. In his theoretical analysis of this phenomenon, Rayleigh[15] considered the streaming induced by standing waves between plane walls. This also includes the case where the nonuniformity of the acoustic wave comes from gradients in the boundary layer created in the vicinity of an obstacle, whether caused by acoustic oscillation in a fluid adjacent to a solid at rest or by vibration of a solid adjacent to a fluid at rest.

On the other hand, ''Eckart streaming'' [16] does not come from boundary layer effects between a solid and a fluid, as does Rayleigh streaming, but it is due to absorption in the main body of an irrotational sound beam.[17] It is generated by a well-collimated traveling-wave ultrasonic beam. Like Rayleigh streaming, Reynolds stresses are at the origin of this streaming (often referred to as ''quartz-wind''). Unlike the other type of streaming, it is a large-scale phenomena.[18]

Nyborg,[19] and later Zarembo,[18] reviewed both theoretical and experimental investigations of these two types of streaming, although as pointed out by Sharpe *et al.*,[20] experimental work on streaming is rather scarce and qualitative. As noted by Riley,[21] streaming is a phenomenon that occurs more widely than its origin suggests and it can find applications for example in hearing processes,[22] design of woodwind instruments,[23] rectified diffusion,[24] ocean acoustics,[25] bioeffects,[26] etc.

One of these applications concerns the study of thermoacoustic devices, where two kinds of streaming have been investigated. These are usually referred to as ''Gedeon streaming'' and ''Rayleigh streaming;'' but actually, the two cases fall in the audible frequency range and bounded medium case. The term Rayleigh streaming has been used to describe streaming in standing wave thermoacoustic devices. In such devices or in a traditional orifice pulse tube refrigerator, the second-order time average of the rate $\dot{M}$ at which the mass flows through any cross section S, that is

$$\dot{M} = \int_S \langle \rho \mathbf{u} \rangle \cdot \mathbf{dS},$$

must be zero in the steady-state operation, otherwise mass would accumulate somewhere in the resonator. On the other hand, Gedeon[27] is concerned with the nonzero mass flow associated with density and velocity fluctuations that occurs whenever the phase shift between those two quantities is not $\pi/2$. He calculated the time average of the product of the first-order density and velocity across a regenerator assuming Darcy area averaged flow and either an isothermal or an adiabatic equation of state. Later on, the term Gedeon streaming has been used[1] to describe streaming in the case when a closed-loop flow path exists in the device; that is, whenever the averaged mass flow across the resonator or pore stack section may not be zero. This is the case in the annular thermoacoustic prime-mover as proposed by Ceperley,[28] that has recently been created.[8] In their Stirling hybrid engine, Swift *et al.*[9] use a ''jet pump'' to suppress the mass flux. The jet pump adds a pressure drop across the regenerator that balances the one created by the fluctuating density and velocity, so that the time-averaged mass flux through the cross section of the resonator is forced to zero. It uses the asymmetry of hydrodynamic end effects along a diverging contraction, as known in the case of a steady flow. Unfortunately, in addition to generating a pressure drop, the jet pump also dissipates acoustic power.[11] A complete theoretical study of acoustic streaming in annular thermoacoustic prime-mover has been developed recently.[7]

In this paper we are concerned with the first kind of streaming in thermoacoustic devices, that is Rayleigh streaming (both in thermoacoustic sense and in the more general sense), as we deal with closed resonator-type of devices, in which the time-averaged mass flow is zero. The first experimental observations of acoustic streaming in a standing wave thermoacoustic device were reported by Gaitan *et al.*[29] Recently, experimental results have confirmed that the particle velocity in such devices can have a significant steady component,[6,30] which motivated this study. Concerning related theoretical development, works by Rott,[12] Olson and Swift,[10] and Waxler[13] are devoted to the calculation of streaming in the case of a fluid supporting a temperature gradient. Olson and Swift[10] based their theoretical development on Rott's work to derive an expression for the streaming velocity and streaming mass flux in the case of widely separated parallel plates. They showed analytically and verified experimentally that tapering a pulse tube slightly can suppress the streaming mass flux.[31] In both the Rott and the Olson and Swift studies, the two-dimensional flow is supposed to be confined between widely separated parallel plates and the temperature dependence of viscosity and heat conduction are taken into account. In the case of pulse tube, Olson and Swift pointed out that the neglect of the temperature dependence of viscosity leads to significant error.[10] They propose the following picture of the contribution of such dependence in the process of thermoacoustic Rayleigh streaming: Consider a parcel of gas oscillating at about a penetration depth from a rigid boundary. The gas between the parcel and the wall has a different temperature during the motion of the parcel at the right of its equilibrium position than during its motion at the left, due to thermal contact with the wall and the phasing between oscillatory pressure and motion. Because the viscosity depends on temperature, the drag experienced by the parcel during left and right motion is different and, after a full cycle, the parcel does not come back to its initial position.

The only study that is not restricted to widely separated boundaries is provided by Waxler,[13] who treats the case of parallel plates geometry but does not take into account the temperature dependence of viscosity and heat conduction.

III. DERIVATION OF STREAMING IN STANDING WAVE THERMOACOUSTIC DEVICES

It is assumed that an acoustic wave propagates laminarly in an ideal gas along the x axis between two infinitely wide rigid plates or in a cylindrical tube. The transverse dimensions (τ) are supposed to be much smaller than the longitu-

dinal (x) ones. In other words, the ratio of the wavelength and the transverse dimension is large: $c_0/R\omega \gg 1$, higher modes are evanescent, and accordingly the wave is plane. Here, R is the typical transverse dimension of the problem, c_0 is the adiabatic speed of sound, and ω is the angular frequency of acoustic oscillations. Another important ratio in thermoacoustic is the ratio of R and the thermal penetration depth $\delta_t = \delta_\nu/\sqrt{\sigma}$, where σ is the Prandtl number and $\delta_\nu = \sqrt{2\mu/\omega\rho}$ is the viscous penetration depth. In a main resonator or pulse tube, $R/\delta_t \gg 1$, whereas in a stack, $R/\delta_t \approx 1$, and finally in a regenerator $R/\delta_t < 1$. This gives an opportunity to describe the different components of thermoacoustic devices we deal with in this study, noting that, generally, pulse tubes, stacks, and regenerators support a temperature gradient. These components of a thermoacoustic device are treated separately here and joining conditions and end effects are not described. Although experiment has recently shown that these effects are very important for the behavior of streaming in thermoacoustic devices,[30] as our purpose is to evaluate the Rayleigh streaming contribution in these devices, we leave their study for further work. Next, the streaming is supposed to be "very slow," that is, slow enough to leave the first-order variables and the temperature profile unperturbed. This implies that $R_s(R/L)^2 \ll 1$ for the Reynolds number of streaming motion, $R_s = \rho_0 U_S l/\mu$, where l is the longitudinal dimension of the system, U_s is a characteristic magnitude of the streaming motion, and μ is the dynamic viscosity. Accordingly, the effect of inertia on the streaming motion is neglected by comparison with viscous effects (see Ref. 32 for a study of the distortion created in a tube by the effect of inertia).

Next, the solid is assumed to have an infinite heat capacity and the solid and the gas are assumed to have a common temperature $T_0(x)$ in the absence of oscillations. There is no mean flow apart from acoustic streaming, and the method of successive approximation is applied. In this method, the excess of pressure, excess of density, and the fluid velocity at any point in the fluid are given by

$$p - p_0 = p_1 + p_2, \quad \rho - \rho_0 = \rho_1 + \rho_2, \quad \mathbf{u} = \mathbf{u}_1 + \mathbf{u}_2,$$

where the first-order variables ρ_1, p_1, $\mathbf{u}_1$ account for oscillation at angular frequency ω and are assumed to have $e^{-i\omega t}$ time dependence. The zeroth-order variables are steady-state mean values; they represent the values the variables would have if there were no acoustic oscillation. The second-order terms are corrections to be added to ρ_1, p_1, $\mathbf{u}_1$ that include time-independent quantities as well as higher harmonics terms.

In a homogeneous fluid, in which the only forces acting on a parcel of fluid are surface stresses due to elasticity and viscosity of the fluid, the governing equation for the motion of fluid particles, the Navier–Stokes equation, has an x component

$$\rho[\partial_t u_x + (\mathbf{u}\cdot\nabla)u_x] = -\partial_x p + \partial_x[\mu\{2\partial_x u_x - \tfrac{2}{3}\nabla\cdot\mathbf{u}\}] + \nabla_\tau\cdot[\mu(\nabla_\tau u_x + \partial_x \mathbf{u}_\tau)]. \quad (1)$$

Here, ∂_t and ∂_x denote respectively the time and axial derivatives, ∇_τ denotes the transverse component of the del operator, u_x and $\mathbf{u}_\tau$ the axial and transverse components of the particle velocity respectively. Note that $\mu = \mu_0 + \mu_1$. Here also the second viscosity coefficient has been neglected in comparison with the first viscosity coefficient.[33]

When using the continuity equation, Eq. (1) can also be written

$$\partial_t(\rho u_x) + \partial_x(\rho u_x^2) + \nabla_\tau\cdot(\rho u_x \mathbf{u}_\tau) = -\partial_x p + \tfrac{4}{3}\partial_x(\mu\partial_x u_x) - \tfrac{2}{3}\partial_x(\mu\nabla_\tau\cdot\mathbf{u}_\tau) + \nabla_\tau\cdot(\mu\nabla_\tau u_x) + \nabla_\tau\cdot(\mu\partial_x\mathbf{u}_\tau). \quad (2)$$

The assumption that transverse dimensions are much smaller than longitudinal ones allows one to assume that the transverse variations are much greater than the longitudinal ones; it follows that the transverse variation of the acoustic pressure can be neglected and that the axial component of the particle velocity is much greater than its transverse component: $u_x \gg u_\tau$. Using these assumptions when writing Eq. (2) to the second order and time averaging, noting moreover that $\langle \partial_t(\rho_1 u_{1x})\rangle = 0$ because ρ_1, $u_{1x} \propto e^{-i\omega t}$, we get

$$\partial_x(\rho_0\langle u_{1x}^2\rangle) + \nabla_\tau\cdot(\rho_0\langle u_{1x}\mathbf{u}_\tau\rangle) = -\partial_x p_2 + \mu_0\nabla_\tau^2\langle\mu_2\rangle + \langle\nabla_\tau\cdot\{\mu_1\nabla_\tau u_{1x}\}\rangle, \quad (3)$$

where $\langle u_2\rangle = \langle u_{2x}\rangle$. Using a nondimensional transverse coordinate $\eta = \tau/R$, Eq. (3) yields

$$\frac{1}{R^2}\mu_0\nabla_\eta^2\langle u_2\rangle = \partial_x p_2 + \partial_x(\rho_0\langle u_{1x}^2\rangle) + \frac{1}{R}\nabla_\eta\cdot(\rho_0\langle u_{1x}u_{1n}\rangle) - \frac{1}{R^2}\nabla_\eta\cdot(\langle\mu_1\nabla_\eta u_{1x}\rangle). \quad (4)$$

From this equation, successive integration with respect to η gives the thermoacoustic streaming. This is presented next in the case of parallel plates and then in the case of cylindrical tubes.

A. Parallel plate case

In the parallel plate case with plates at $y = \pm R$, using Cartesian coordinates, $\eta = y/R$, then $\nabla_\eta = \partial_\eta$ and successive integrations of (4), first from 0 to η using $\partial_\eta u_2(\eta = 0) = 0$ and $u_{1\eta}(\eta = 0) = 0$, and then from 1 to η using $u_2(\eta = \pm 1) = 0$, gives

$$\frac{1}{R^2}\mu_0\langle u_2\rangle = \int_1^\eta\int_0^{\eta'}\partial_x p_2\, d\eta'\, d\eta'' + \int_1^\eta\int_0^{\eta'}\partial_x(\rho_0\langle u_{1x}^2\rangle)\, d\eta'\, d\eta'' + \frac{\rho_0}{R}\int_1^\eta\langle u_{1x}u_{1\eta}\rangle\, d\eta' - \frac{1}{R^2}\int_1^\eta\langle\mu_1\partial_\eta u_{1x}\rangle\, d\eta'. \quad (5)$$

As proposed by Rott,[4] the complex laws that express viscosity and heat conduction as functions of the mean temperature of the fluid can be approximated around a reference temperature using a coefficient β so that $\mu_0, K_0 \propto T_0^{\beta}$. For instance, around ambient temperature, one finds for air $\beta=0.77$, for helium $\beta=0.647$, and for a mixture of 60% helium and 40% argon $\beta=0.72$. Using $\mu_1/\mu_0=\beta(T_1/T_0)$ and $p=p(x)$, Eq. (5) yields

$$\langle u_2\rangle=\frac{R^2}{2\mu_0}(\eta^2-1)\partial_x p_2 + \frac{R^2}{\mu_0}\int_1^{\eta}\int_0^{\eta'}\partial_x(\rho_0\langle u_{1x}^2\rangle)d\eta'\,d\eta'' + \frac{R\rho_0}{\mu_0}\int_1^{\eta}\langle u_{1x}u_{1\eta}\rangle d\eta' - \frac{\beta}{T_0}\int_1^{\eta}\langle T_1\partial_\eta u_{1x}\rangle d\eta'. \tag{6}$$

Next, we need to determine the unknown second-order pressure gradient in (6). In the toroidal topology, this is done by integrating around the torus.[7] In the case of a closed resonator, we use the fact that the second-order time-average $\dot{M}$ of the rate at which mass flows cross the cross section S must be zero

$$\dot{M}=\int_S\langle\rho\mathbf{u}\cdot\mathbf{dS}\rangle=\int_S\langle\rho_0\mathbf{u_2}+\rho_1\mathbf{u_1}\rangle\cdot\mathbf{dS}=0. \tag{7}$$

This expression shows that two terms contribute to the second-order mass flow. One comes directly from the second-order velocity and one is associated with the ''velocity transform'' or ''Stokes drift.'' [34] When divided by ρ_0, this second term represents the difference between the Lagrangian and the Eulerian mean motions.[35] As shown by Rudenko and Soluyan,[17] the streaming velocity is given by $\langle\mathbf{u}_2\rangle+\langle\rho_1\mathbf{u}_1\rangle/\rho_0$.

Equation (7) gives an expression for the second-order velocity averaged over a cross section $\langle\overline{u_2}\rangle$

$$\langle\overline{u_2}\rangle=\frac{1}{2}\int_{-1}^{1}\langle u_2\rangle d\eta=-\frac{1}{2\rho_0}\int_{-1}^{1}\langle\rho_1 u_{1x}\rangle d\eta, \tag{8}$$

and the integration of (6) yields the hydrodynamic pressure gradient

$$\partial_x p_2=\frac{3\nu_0}{R^2}\int_{-1}^{1}\langle\rho_1 u_{1x}\rangle d\eta + \frac{3}{2}\int_{-1}^{1}\int_1^{\eta}\int_0^{\eta'}\partial_x(\rho_0\langle u_{1x}^2\rangle)d\eta\,d\eta'\,d\eta'' + \frac{3\rho_0}{2R}\int_{-1}^{1}\int_1^{\eta}\langle u_{1x}u_{1\eta}\rangle d\eta\,d\eta' - \frac{3\mu_0\beta}{2T_0R^2}\int_{-1}^{1}\int_1^{\eta}\langle T_1\partial_\eta u_{1x}\rangle d\eta\,d\eta', \tag{9}$$

where $\nu=\mu/\rho$ is the kinematic viscosity, so that

$$\langle u_2\rangle=\frac{3}{4\rho_0}(\eta^2-1)\int_{-1}^{1}\langle\rho_1 u_{1x}\rangle d\eta+\frac{3R^2}{4\mu_0}(\eta^2-1)\int_{-1}^{1}\int_1^{\eta}\int_0^{\eta'}\partial_x(\rho_0\langle u_{1x}^2\rangle)d\eta\,d\eta'\,d\eta'' + \frac{3R}{4\nu_0}(\eta^2-1)\int_{-1}^{1}\int_1^{\eta}\langle u_{1x}u_{1\eta}\rangle d\eta\,d\eta'-\frac{3\beta}{4T_0}(\eta^2-1)\int_{-1}^{1}\int_1^{\eta}\langle T_1\partial_\eta u_{1x}\rangle d\eta\,d\eta' + \frac{R^2}{\mu_0}\int_1^{\eta}\int_0^{\eta'}\partial_x(\rho_0\langle u_{1x}^2\rangle)d\eta'\,d\eta''+\frac{R}{\nu_0}\int_1^{\eta}\langle u_{1x}u_{1\eta}\rangle d\eta'-\frac{\beta}{T_0}\int_1^{\eta}\langle T_1\partial_\eta u_{1x}\rangle d\eta'. \tag{10}$$

This gives the second-order velocity as a function of the acoustic quantities, temperature gradient, geometry of the system, and thermophysical properties of the fluid. The associated second-order time-averaged mass flux density is easily obtained from (10) as

$$\dot{m}_2=\rho_0\langle u_2\rangle+\langle\rho_1 u_{1x}\rangle. \tag{11}$$

In Appendix A, the first-order quantities at leading order solution are expressed. Replacing in (10) the particle velocity, instantaneous temperature, density, and transverse velocity by their respective expressions (A1), (A3), (A4), and (A11) allows the evaluation of the acoustic streaming velocity in any thermoacoustic component, providing only that the acoustic pressure, its x derivative, and the mean temperature distribution are known. Indeed, after calculating the involved integrals in (10), it is tedious but manageable to show that the expression for the second-order velocity $\langle u_2\rangle$ is basically composed of four terms

$$\langle u_2\rangle=-\frac{3}{8\omega\rho_0^2c_0^2}(\eta^2-1)\Re(ip_1\partial_x p_1^*\Psi_1) - \frac{1}{2\omega\rho_0^2c_0^2}\Re(ip_1\partial_x p_1^*\Psi_2)+\frac{3}{8\omega^3\rho_0^2}\times(\eta^2-1)\frac{\partial_x T_0}{T_0}|\partial_x p_1|^2\Re(i\Psi_3) + \frac{1}{2\omega^3\rho_0^2}\frac{\partial_x T_0}{T_0}|\partial_x p_1|^2\Re(i\Psi_4), \tag{12}$$

where $\Re$ denotes the real part of a complex number and

where the complex functions Ψ_1, Ψ_2, Ψ_3, and Ψ_4 are expressed as functions of the thermophysical properties of the fluid, the ratio R/δ_t, and η (see Appendix B). Equation (12) also gives an expression for the second-order velocity as a function of the acoustic intensity and the first-order velocity

$$\langle u_2\rangle = -\frac{I}{\rho_0 c_0^2}\Re\left(\frac{1}{F_\eta^*}\left\{\frac{3}{4}(\eta^2-1)\Psi_1+\Psi_2\right\}\right) + \frac{J}{\rho_0 c_0^2}\Im\left(\frac{1}{F_\eta^*}\left\{\frac{3}{4}(\eta^2-1)\Psi_1+\Psi_2\right\}\right) - |u_{1x}|^2\frac{\partial_x T_0}{T_0}\frac{1}{2\omega|F_\eta|^2}\Im\left(\frac{3}{4}(\eta^2-1)\Psi_3+\Psi_4\right), \tag{13}$$

where $\Im$ denotes the imaginary part of a complex number and F_η describes viscous boundary effects [see Eq. (A2)]. Here, I is the active intensity, associated with work flow or equivalently with the propagating component of the acoustic wave, whereas J is the reactive intensity, associated with local energy transfers that do not propagate, or equivalently with the stationary part of the acoustic wave.[33] Their sum forms the total acoustic intensity Π

$$\Pi = I + iJ = \tfrac{1}{2}\Re(p_1 u_{1x}^*) + i\tfrac{1}{2}\Im(p_1 u_{1x}^*).$$

In cases where the stationary component of the acoustic wave is much greater than its progressive part, the first term in (13) may be neglected.

In typical thermoacoustic devices, the term $|u_{1x}|^2(\partial_x T_0/T_0)[1/(2\omega|F_\eta|^2)]$ is about the order of magnitude of $\Pi/\rho_0 c_0^2$ (with $\partial_x T_0/T_0$ being about the order of 1 m^{-1}) so that, in order to get some properties of the second-order velocity behavior when the ratio R/δ_t is reduced, we define

$$\theta = \tfrac{3}{4}(\eta^2-1)\Psi_1+\Psi_2, \tag{14}$$

$$\Phi = \Im(\tfrac{3}{4}(\eta^2-1)\Psi_3+\Psi_4). \tag{15}$$

These coefficients extracted from (13) are functions of η, the ratio R/δ_t, and the thermophysical properties of the fluid. Figure 1 shows the behavior of Φ (plain line), $\Re(\theta)$ (dashed line), and $\Im(\theta)$ (dashed-dotted line) when the ratio R/δ_t decreases in the case of helium as a working fluid. For large ratios R/δ_t, the term that relates to the effect of the temperature gradient, that is Φ, dominates. For ratios around 15 the term which is associated with the reactive intensity, that is $\Im(\theta)$, dominates and for small ratios the term related with the active intensity, that is $\Re(\theta)$, dominates. Of course, this does not provide directly the behavior of the streaming which is given by (13), but it can help in estimating its tendencies, for example when comparing two components of the same system that have different radii like a pulse tube and a regenerator, or when comparing the behavior of streaming in a system with or without a temperature gradient.

Figure 2 shows the behavior of the same coefficients Φ (plain line), $\Re(\theta)$ (dashed line), and $\Im(\theta)$ (dashed-dotted line) in the case of a ratio $R/\delta_t = 100$, when the factor β that represents the temperature dependence of viscosity is changed from its value for helium around ambient temperature ($\beta = 0.647$) to zero. The coefficient θ is not drastically

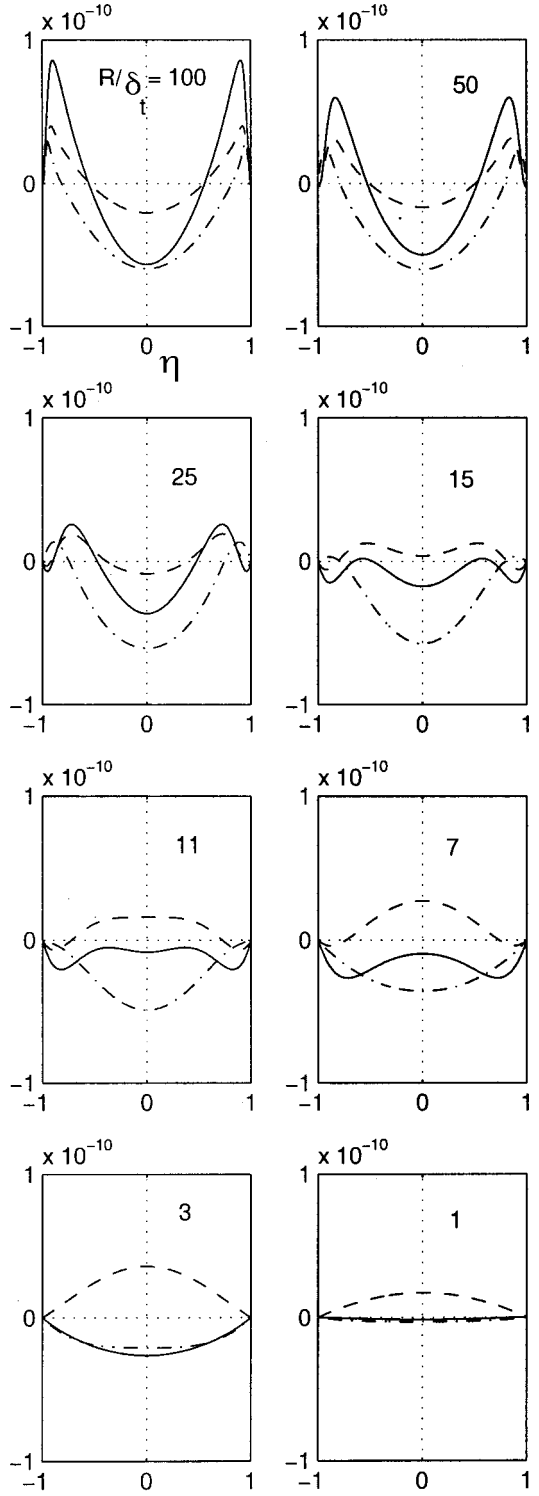

FIG. 1. Coefficients Φ (plain line), $\Re(\theta)$ (dashed line), $\Im(\theta)$ (dashed-dotted line) versus the transverse coordinate η for different ratios R/δ_t.

modified by the neglect of this dependence, but the coefficient that represents the effect of the temperature gradient, that is Φ, experiences a 40% change, indicating as expected that the temperature dependence of viscosity should be taken into account for the description of streaming in thermoacoustic devices.

In order to get some more tractable results, it is possible to simplify the expressions for Ψ_1, Ψ_2, Ψ_3, and Ψ_4 with-

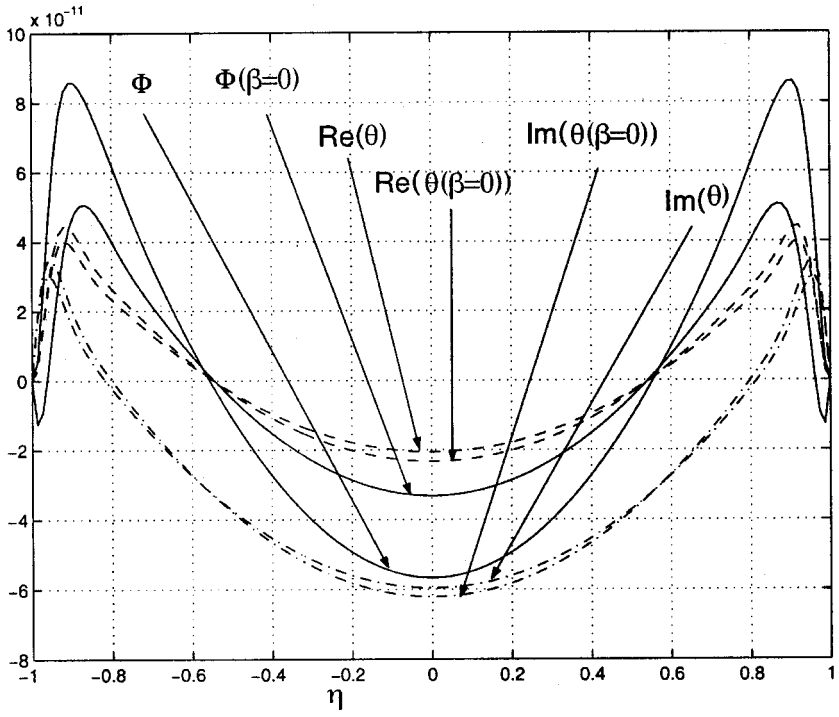

FIG. 2. Coefficients Φ (plain line), $\Re(\theta)$ (dashed line), $\Im(\theta)$ (dashed-dotted line) versus the transverse coordinate η for $\beta=0.647$ and $\beta=0$.

out a drastic approximation for large-enough ratios R/δ_t by assuming that $[\tanh(b)]/b \approx 1/b$. Also, the second-order velocity at the center of the tube can be taken as representative of the whole velocity along η and its expression is much simpler than the latter. For widely enough separated plates, the coefficients $\Psi_{1-4}(\eta=0)$ that give the centerline streaming velocity, also expressed in Appendix B, are functions of the ratio R/δ_t and the thermophysical properties of the fluid only. This approximation gives results for the center-line second-order velocity within 17% for ratios R/δ_t down to 4.

Then, in the case of even larger ratios R/δ_t, it is possible to get a more direct and rapid estimate of the importance of the temperature gradient on streaming by noting that, under this assumption, the first two terms in (12) are equivalent to Rayleigh's law of streaming. That is, under Rayleigh's law assumptions: $\lambda \gg R$ and $\delta_{v,t} \ll R$ and at $\eta=0$, the maximum of the first two terms in (12) is $-3/(8c_0)|u_{1x}|^2$. Also at $\eta=0$, the maximum of the last two terms in (12) is $-(1/2\omega)(\partial_x T_0/T_0)|u_{1x}|^2 \Im(-\frac{3}{4}\Psi_3+\Psi_4)$. Figure 3 shows the behavior of the coefficient $\Phi'=(1/2\omega)\times(\partial_x T_0/T_0)\Im(-\frac{3}{4}\Psi_3+\Psi_4)$ for helium for $\partial_x T_0/T_0=1$ m^{-1}. It appears that the effect of the temperature gradient increases with increasing ratio R/δ_t and decreases with increasing frequency. Also, from this figure it appears that this effect can be very important: for instance, for $R/\delta_t \approx 20$ at a 150 Hz frequency, $\Phi' \approx 3/(8c_0)$.

B. Cylindrical tube

In the case of a cylindrical tube, using polar coordinates, $\eta=r/R$ and then $\nabla_\eta \cdot \mathbf{A}=(1/\eta)\partial_\eta(\eta A_\eta)$ and $\nabla_\eta^2 f=(1/\eta)\partial_\eta(\eta \partial_\eta f)$ so, following the process used in the case of parallel plates, the integration of (10) gives

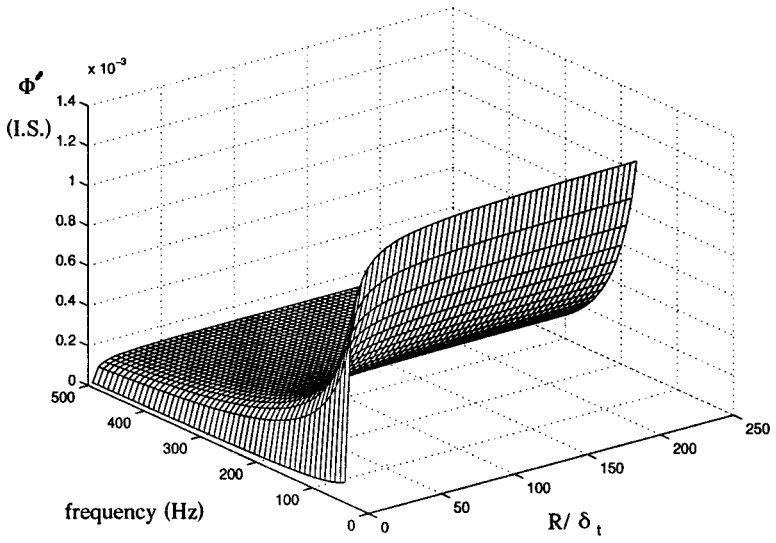

FIG. 3. Coefficient $\Phi'(\partial_x T_0/T_0=1)=[1/(2\omega)]\times(\partial_x T_0/T_0)\Im(-\frac{3}{4}\Psi_3+\Psi_4)$ as a function of the frequency and the ratio R/δ_t.

$$\langle u_2\rangle = \frac{4}{\rho_0}(\eta^2-1)\int_0^1 \langle \rho_1 u_{1x}\rangle \eta d\eta + \frac{4R^2}{\mu_0}(\eta^2-1)$$
$$\times \int_0^1 \eta \int_{-1}^{\eta} \frac{1}{\eta'} \int_0^{\eta'} \partial_x(\rho_0\langle u_{1x}^2\rangle)\,\eta''\, d\eta\, d\eta'\, d\eta''$$
$$+ \frac{4R}{\nu_0}(\eta^2-1)\int_0^1 \eta \int_{-1}^{\eta} \langle u_{1x}u_{1\eta}\rangle d\eta\, d\eta'$$
$$- \frac{4\beta}{T_0}(\eta^2-1)\int_0^1 \int_{-1}^{\eta} \langle T_1 \partial_\eta u_{1x}\rangle d\eta\, d\eta'$$
$$+ \frac{R^2}{\mu_0}\int_{-1}^{\eta}\frac{1}{\eta'}\int_0^{\eta'} \partial_x(\rho_0\langle u_{1x}^2\rangle)\,\eta''\, d\eta'\, d\eta''$$
$$+ \frac{R}{\nu_0}\int_{-1}^{\eta}\langle u_{1x}u_{1\eta}\rangle d\eta' - \frac{\beta}{T_0}\int_{-1}^{\eta}\langle T_1\partial_\eta u_{1x}\rangle) d\eta', \tag{16}$$

where the hydrodynamic pressure gradient expression

$$\partial_x p_2 = \frac{16\nu_0}{R^2}\int_0^1 \langle \rho_1 u_{1x}\rangle \eta\, d\eta$$
$$+ 16\int_0^1 \eta \int_{-1}^{\eta}\frac{1}{\eta'}\int_0^{\eta'} \partial_x(\rho_0\langle u_{1x}^2\rangle)\,\eta''\, d\eta\, d\eta'\, d\eta''$$
$$+ \frac{16\rho_0}{R}\int_0^1 \eta\int_{-1}^{\eta}\langle u_{1x}u_{1\eta}\rangle d\eta\, d\eta'$$
$$- \frac{16\mu_0\beta}{T_0R^2}\int_0^1 \eta\int_{-1}^{\eta}\langle T_1\partial_\eta u_{1x}\rangle d\eta\, d\eta', \tag{17}$$

has been derived similarly.

The first-order axial velocity, instantaneous temperature, and density are given by their respective expressions (A1), (A3), and (A4) similar to the case of parallel plates, but the expressions of the coefficients that describe viscous and thermal boundary layers effect are different (see Appendix A). The expression for the first-order transverse velocity is also given in Appendix A [Eq. (A19)]. Substituting in (16) the expressions for u_{1x}, ρ_1, $u_{1\eta}$, and T_1 as was done previously and calculating the involved integrals, the second-order velocity can be shown to have an expression comparable to (12). But, in the case of cylindrical tubes, some of the integrals have to be calculated numerically, namely integrals of the sort

$$\int_{-1}^{\eta} J_1(b\eta)J_0(b^*\eta)d\eta,$$

or with other arguments so that no analytical results can be presented for this geometry. Still, we find it useful to present results of calculation for this geometry, which is more realistic for many thermoacoustic devices. Before turning to these results, note that other geometries could be studied in a similar manner, provided the expressions for the coefficients that describe viscous and thermal boundary layers effects are known.

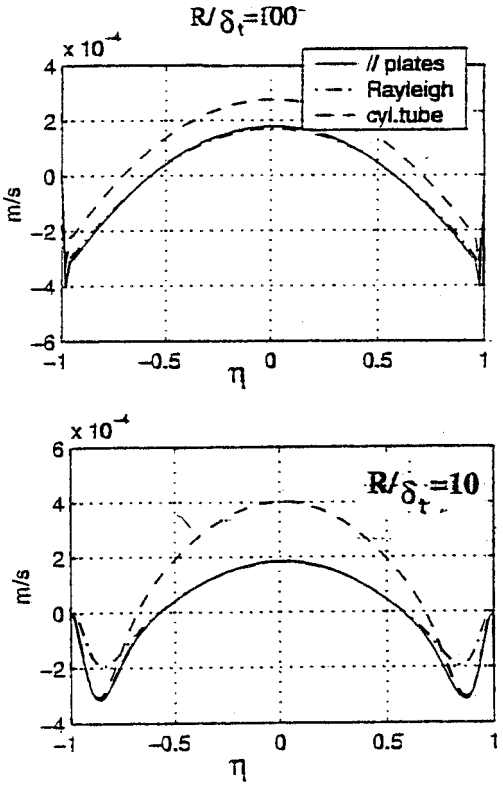

FIG. 4. Calculated second-order velocity $\langle u_2\rangle$ in a quasi-half-wavelength resonator as a function of the transverse coordinate η for $R/\delta_t = 100$ (first figure) and $R/\delta_t = 10$ (second figure).

IV. RESULTS FOR STREAMING IN THERMOACOUSTIC DEVICES

The general shape of acoustic streaming velocity is usually not qualitatively modified by a temperature gradient but the first-order solution is greatly complicated by it; therefore, we begin by comparing results of calculation of streaming velocities in parallel plates and cylindrical tubes without any temperature gradient. Let us consider a 100-Hz standing wave in a 60% helium 40% argon fluid at ambient temperature (291 K) and at a static pressure of 0.724 MPa (100 psia), which are typical of thermoacoustic applications. At $x=0$ the tube (or parallel plates) is rigidly closed $[u(0)=0]$ and the rms first-order pressure is $p_1(0)=2.3$ kPa($\approx$161 dB SPL). At the other end, $x=l$, a volume source is set that compensates losses in the resonator. The acoustic pressure varies along x according to

$$p_1(x) = \frac{p_1(0)}{2}(e^{-ikx}+e^{ikx}),$$

with $k=\omega/c_0\sqrt{[\gamma-(\gamma-1)F_t]/F}$ being the complex wave number and F and F_t being defined by Eqs. (A8) and (A9). Now, the radius of the tube R is varied and the length l of the tube is changed so that $l=\pi/\Re(k)$. In such a quasi-half-wavelength resonator, the calculated second-order velocities in the corresponding cylindrical tubes (dashed lines), parallel plates (plain lines) are presented in Fig. 4. Also, the results of the calculation of the second-order velocity according to Rayleigh's law streaming[18] (valid for large tubes only)

$$\langle u_2\rangle = \frac{A^2}{4c_0}\sin(2kx)\left\{\frac{1}{2}e^{[-2R(1+\eta)]/\delta_\nu} + e^{[-R(1+\eta)]/\delta_\nu}\cos\left(\frac{R(1+\eta)}{\delta_\nu}\right) + 2e^{[-R(1+\eta)]/\delta_\nu}\sin\left(\frac{R(1+\eta)}{\delta_\nu}\right) + \frac{3}{4} - \frac{9\eta^2}{4}\right\},$$

are presented (dashed-dotted curve). For $R/\delta_t = 100$ and $R/\delta_t = 10$, the second-order velocity at $x = 0.55$ m (which corresponds to the maximum of the center-line second-order velocity) across the section is presented.

In the case of tube radius much larger than the penetration depths, in agreement with general findings, an offset parabolic second-order velocity profile results, with the velocity near the wall being equal to the velocity just outside the boundary layer. The fluid near the center moves in the opposite direction to the fluid near the wall. But, when the ratio R/δ_t decreases, the boundary layer effects cannot be simply reduced to a nonslip condition. On the lowest curve, the associated vortices start to emerge. The streaming is a bit smaller between parallel plates than in a cylindrical tube.

Now, let us look closer at the behavior of the streaming when the ratio R/δ_t is further reduced. Figure 5 shows the evolution of the second-order velocity across the section of a cylindrical tube at a fixed position ($x = 0.55$ m) when the ratio R/δ_t varies from 4 to 0.5. The two upper curves (ratios of 4 and 3) clearly depict the four vortices' pattern, the second-order velocity changing sign four times. Then, for lower ratios a first limit is crossed as the second-order velocity changes sign only twice for ratios from 2.75 to 1. Finally, for even smaller ratios a second limit is crossed in the behavior of the second-order velocity as it remains positive across the whole section, tending to a somewhat Poiseuille profile. Note that for any ratio, the product $\langle \rho_1 u_{1x}\rangle$ changes accordingly so that the average of the second-order time-averaged mass flux across the section remains zero. In the case of parallel plates, a similar behavior can be observed when the ratio R/δ_t is decreased, the streaming velocity remaining, as in the case of large ratios, smaller than in cylindrical tube.

When turning to the case of streaming in a fluid that supports a temperature gradient, it is necessary first to solve Eq. (A12) in order to get the necessary acoustic variables. This can be done numerically or by using an approximate analytical solution.[36] Here, we choose to show three examples of the use of the above-presented derivation that concern streaming in a thermoacoustic engine, in a thermoacoustic refrigerator, and in a pulse tube. The first order variables are thus extracted from DeltaE calculations.

First, results of measurements of particle velocity in a thermoacoustic standing wave engine that has been recently built at the National Center for Physical Acoustics[30] motivated the calculation of streaming in the thermoacoustic stack. In this device, the resonator is filled with a mixture of 60% helium and 40% argon gas at an absolute static pressure of 1 MPa and the working frequency is 43 Hz. The honeycomb thermoacoustic stack is modeled as identical cylindrical pores of length $l = 18$ cm and of radius $R = 0.37$ mm,

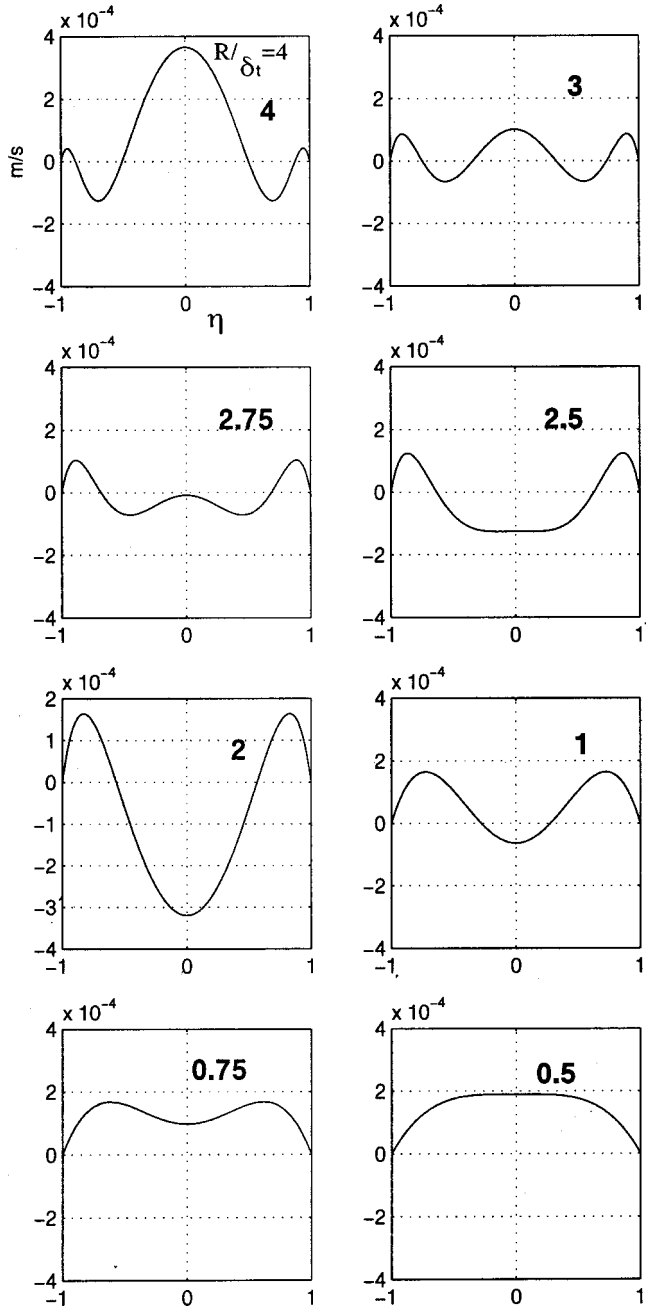

FIG. 5. Calculated second-order velocity $\langle u_2\rangle$ across the section of a cylindrical tube for different ratios R/δ_t.

which corresponds to $R/\delta_t \approx 0.9$. According to results of DeltaE calculation, the mean temperature linearly increases along the pores from 298 to 550 K, the root-mean-square acoustic pressure at the entrance of the stack is $p_1(x=0) = 2900$ Pa (that is, $\approx$163 dB SPL), the rms acoustic volume flow is $U_1(x=0) = u_{1x}(x=0)S_s = 0.0056\ \mathrm{m}^3/\mathrm{s}$, where $S_s = 0.9\pi R_r^2$ is the open fluid area of the stack and $R_r = 10$ cm is the radius of the main resonator. The phase difference between $U_1(x=0)$ and $p_1(x=0)$ is 90 deg. At the other end of the stack, $p_1(x=l) = 2800$ Pa, $U_1(x=l) = 0.0057\ \mathrm{m}^3/\mathrm{s}$, and their phase difference is 80 deg. The acoustic pressure and acoustic volume flow can be fitted to second-order polynomial functions of x. The acoustic volume flow yields the necessary x derivative of the acoustic pressure according to

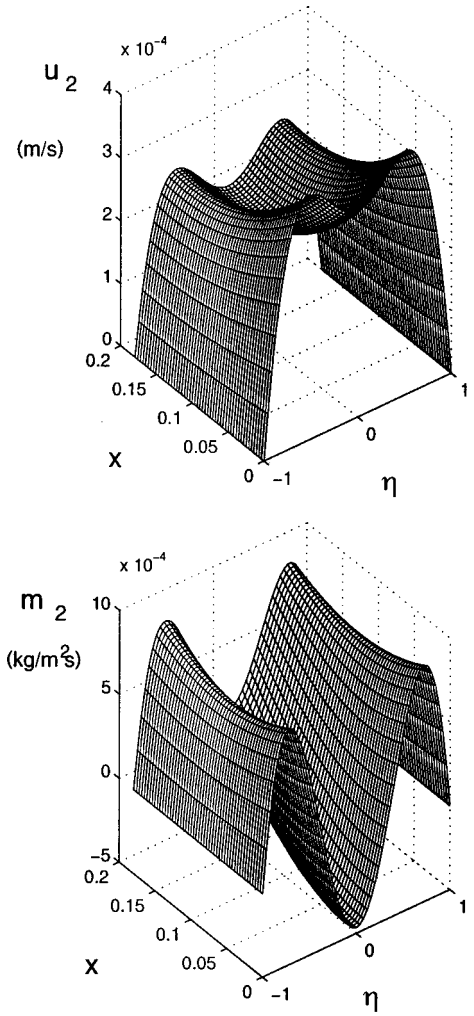

FIG. 6. Calculated second-order velocity $\langle u_2 \rangle$ (upper figure) and second-order time-averaged mass flow (lower figure) as functions of the axial coordinate x and the transverse coordinate η in the stack of a thermoacoustic engine.

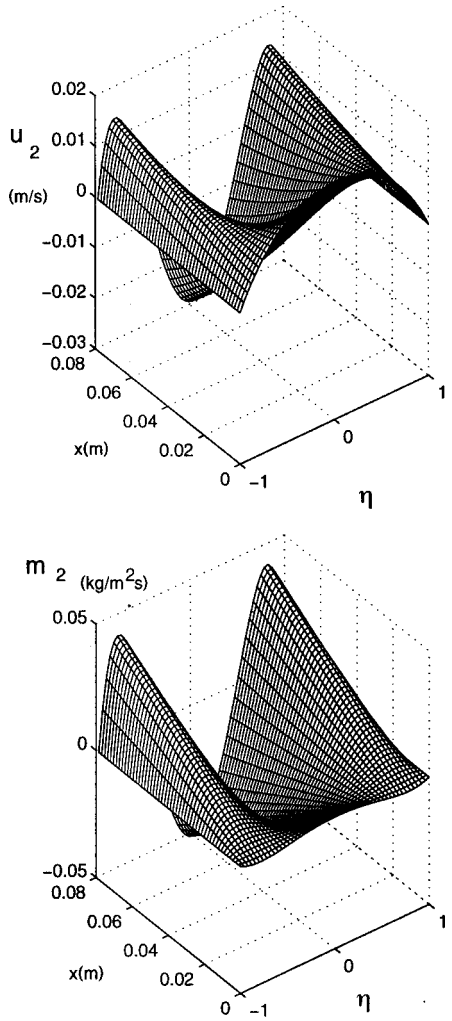

FIG. 7. Calculated second-order velocity $\langle u_2 \rangle$ (upper figure) and second-order time-averaged mass flow (lower figure) as functions of the axial coordinate x and the transverse coordinate η in the stack of a thermoacoustic refrigerator (Hofler's refrigerator).

$\partial_x p_1 = (\rho_0 \omega / i S_s F) U_1$. The associated first-order particle velocity is of the order of 0.4 m/s. Figure 6 shows the results of calculation of the corresponding second-order velocity (upper figure), given by Eq. (16), and second-order time-averaged mass flow (lower figure), given by Eq. (11), as functions of the position inside one stack pore. A similar calculation for the streaming in the main resonator of this device shows that in this component also the second-order velocity is of the order of 0.1 mm/s and the second-order time-averaged mass flow is of the order of 10^{-3} kg/m^2/s. From this calculation, it appears that Rayleigh streaming in a stack pore and in the resonator does not participate significantly in the heat transfer along these components.

But, this is not the case for every situation, even in standing wave thermoacoustic devices. In Hofler's refrigerator, for instance,[37] in which the amplitudes are higher and which is filled with 1 MPa helium driven at a 500-Hz frequency, streaming can be expected to have significant effects on the behavior of the device. Here, the stack is 7.8 cm long and the rectangular pore radius is 0.18 mm so that $R/\delta_t = 1.6$. As in the former example, the first-order quantities are extracted from results of DeltaE calculation and the streaming in a stack pore is calculated between equivalent parallel plates. The temperature linearly decreases along the stack from 330 to 288 K, the acoustic pressure is of the order of 30 000 Pa (that is, $\approx$183 dB SPL), and the first-order particle velocity is of the order of 6 m/s. Figure 7 shows the results of calculations of the corresponding second-order velocity (upper figure) and second-order time-averaged mass flow (lower figure) as functions of the position inside one stack pore. When considering the relative size of the different terms in Eq. (12), it appears that the first two terms are an order of magnitude larger than the last two terms so that the influence of the temperature gradient on streaming is not crucial in this device. In the main resonator, the particle velocity is of the order of 20 m/s and Fig. 8 shows that the calculated second-order velocity in this cylindrical tube is of the order of 0.15 m/s at $\eta = 0$, in agreement with Rayleigh's law. So, in comparison with the first example (NCPA thermoacoustic engine), the cause of the greater streaming in Hofler's refrigerator is its large acoustic amplitude.

Now, as a last example, let's turn to the case of streaming in a regenerator of a typical pulse tube refrigerator. The resonator is filled with helium at a static pressure of 3.1 MPa

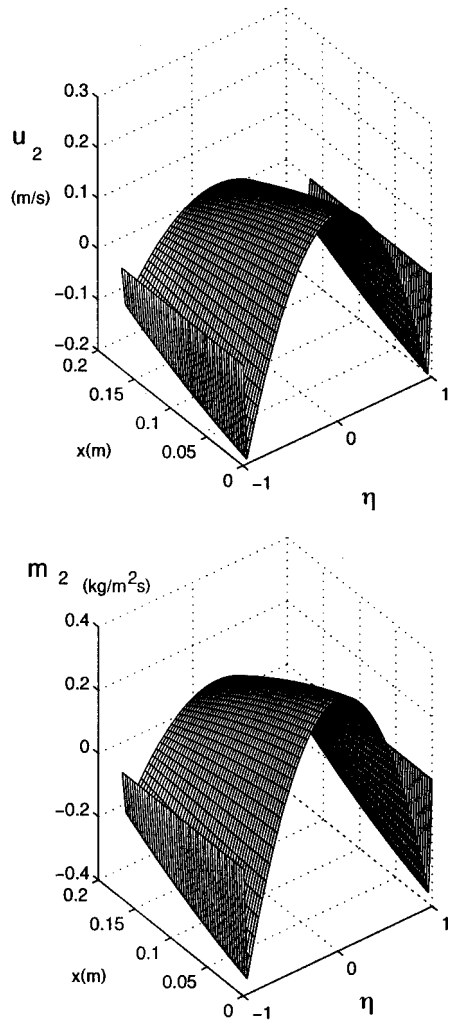

FIG. 8. Calculated second-order velocity $\langle u_2 \rangle$ (upper figure) and second-order time-averaged mass flow (lower figure) as functions of the axial coordinate x and the transverse coordinate η in the main resonator of a thermoacoustic refrigerator.

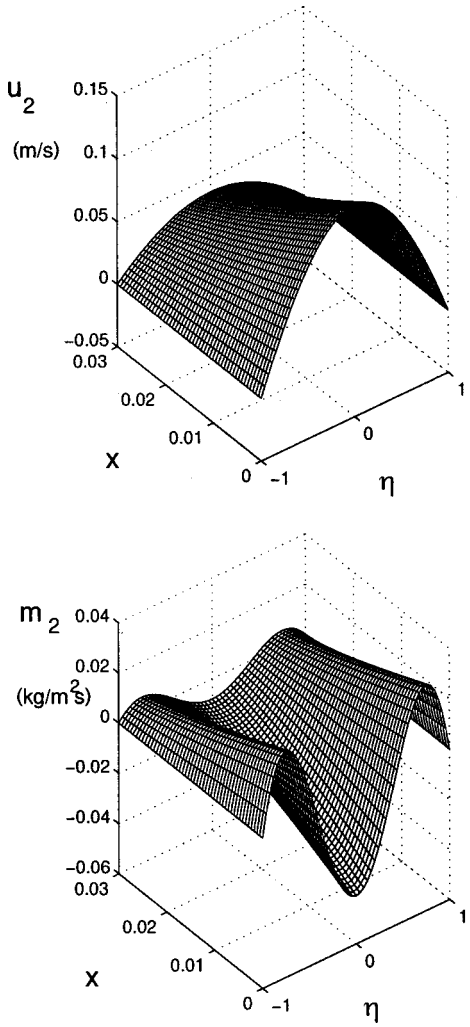

FIG. 9. Calculated second-order velocity $\langle u_2 \rangle$ (upper figure) and second-order time-averaged mass flow (lower figure) as functions of the axial coordinate x and the transverse coordinate η in the regenerator of a pulse tube.

and the working frequency is 100 Hz. For the calculation of streaming, the regenerator is supposed to be composed of identical parallel plates of length $l=3$ cm and of radius $R=0.024$ mm which corresponds to $R/\delta_t \approx 0.37$. According to results of DeltaE calculations, the temperature linearly decreases along the regenerator from 303 to 128 K, the rms acoustic pressure at the entrance of the regenerator is $p_1(x=0)=220$ kPa (that is, $\approx$201 dB SPL), the rms acoustic volume flow $U_1(x=0)=0.0042\,\mathrm{m}^3/\mathrm{s}$, and their phase difference is 48 deg. At the other end of the stack $p_1(x=l)=210$ kPa and $U_1(x=l)=0.0012\,\mathrm{m}^3/\mathrm{s}$, and their phase difference is 26 deg. The acoustic pressure and acoustic volume flow can be assumed to vary linearly along the regenerator. The acoustic volume flow yields the necessary x derivative of the acoustic pressure according to $\partial_x p_1 = [\rho_0 \omega/(iS_s F)]U_1$, where $S_s = 1.6\times 10^{-3}\,\mathrm{m}^2$ is the open regenerator area. The associated first-order particle velocity is about 2 m/s. Figure 9 shows that in the regenerator, the associated second-order velocity is approximately 0.1 m/s and gives rise to a significant second-order average mass flux. As in the previous examples, the second-order velocity profile is qualitatively comparable to the one predicted in the no-temperature-gradient situation. As in the previous example, the most important terms in the expressions of the second-order acoustic velocity (12) are the first two terms. But, when doing the calculation of streaming in the pulse-tube part of this device, in which the acoustic pressure, first-order velocity, and ratio $\partial_x T_0/T_0$ are of the same order of magnitude as in the regenerator (see the results in Fig. 10), the largest contribution in (12) is the last two terms. This is in agreement with Fig. 1, which shows that the temperature-gradient-related terms are dominant for large R/δ_t ratios. In Fig. 10 the center-line second-order velocity is of the order of -0.15 m/s at the middle of the tube, in agreement with results calculated from the Olson and Swift derivation.[10] Also, when using the above-presented large tube approximation to estimate the importance of the temperature gradient in this situation, we get $3/(8c_0) \approx 3.7\times 10^{-4}(\mathrm{m/s})^{-1}$ and $\Phi' \approx 10^{-2}(\mathrm{m/s})^{-1}$, which shows again that the most important term is the one related to the temperature gradient.

V. CONCLUSION

An analytical derivation of acoustic streaming in standing wave thermoacoustic devices has been presented that al-

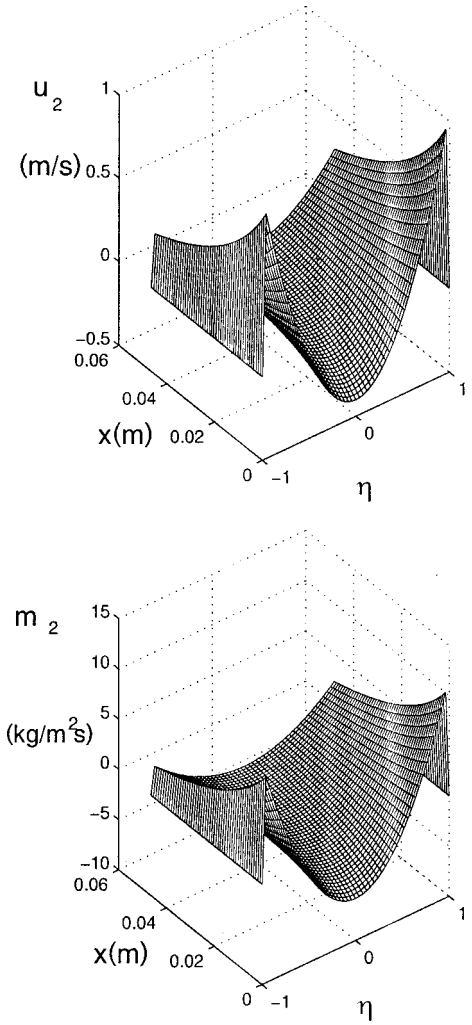

FIG. 10. Calculated second-order velocity $\langle u_2 \rangle$ (upper figure) and second-order time-averaged mass flow (lower figure) as functions of the axial coordinate x and the transverse coordinate η in a pulse tube.

lows calculation of the streaming velocity, associated hydrodynamic pressure gradient, and second-order time-averaged mass flow between parallel plates and in cylindrical tubes of any characteristic transverse dimension. This solution takes into account the effect of a temperature gradient in the fluid. It was shown that in the expression for the second-order particle velocity, the importance of the term related to the temperature gradient is less significant for small ratios R/δ_t than for large ones. Approximate formulas for the case of large ratios R/δ_t allow a more rapid estimation of this term to be added to the classical Rayleigh's law. The behavior of the streaming as the ratio R/δ_t is varied has been discussed. Examples of the use of this calculation for practical thermoacoustic devices have been presented. It appears that streaming can be expected to play an important role in the behavior of high-amplitude closed thermoacoustic devices. The calculation of streaming in the thermoacoustic engine built at the National Center for Physical Acoustics does not give results comparable with experimental results, indicating that in this device the large steady component of the measured particle velocity is not due to Rayleigh streaming. Further research is needed to determine its cause. In particular, joining conditions should be examined. The next step in developing the study of this phenomenon should be to treat the device as a whole; that is, not to consider a stack pore or a resonator as an isolated system. Also, very importantly, there is a need to compute the heat fluxes due to the Rayleigh acoustic streaming in thermoacoustic devices.

ACKNOWLEDGMENTS

This work was supported by the Office of Naval Research. Thanks to G. Smith for providing experimental results and to G. W. Swift for giving DeltaE files for the pulse tube refrigerator.

APPENDIX A: LEADING ORDER

1. Parallel plate geometry

To the first order, the Stokes–Navier equation yields

$$u_{1x} = \frac{\partial_x p_1}{i\omega\rho_0} F_\eta, \tag{A1}$$

where

$$F_\eta = 1 - \frac{\cosh(b\eta)}{\cosh(b)}, \quad b = \frac{(1-i)R}{\delta_\nu} = \frac{(1-i)R\sqrt{\omega}}{\sqrt{2\nu}}. \tag{A2}$$

Note that this notation is similar to that defined by Arnott *et al.*[38]

Also, the equation of heat transfer yields an expression for the instantaneous temperature in the fluid

$$T_1 = \frac{\gamma-1}{\rho_0 c_0^2} T_0 F_{\eta t} p_1 - \frac{\partial_x T_0}{\rho_0 \omega^2} \partial_x p_1 \left[\frac{\sigma F_\eta - F_{\eta t}}{\sigma - 1} \right], \tag{A3}$$

which, in turn, using

$$\rho_1 = -\frac{\rho_0}{T_0} T_1 + \frac{\gamma}{c_0^2} p_1,$$

gives

$$\rho_1 = \frac{\gamma - (\gamma-1)F_{\eta t}}{c_0^2} p_1 - \frac{\partial_x T_0}{T_0 \omega^2} \partial_x p_1 \left[\frac{\sigma F_\eta - F_{\eta t}}{\sigma - 1} \right]. \tag{A4}$$

Here, γ is the ratio of isobaric to isochoric specific heats, and

$$F_{\eta t} = 1 - \frac{\cosh(\sqrt{\sigma} b \eta)}{\cosh(\sqrt{\sigma} b)}. \tag{A5}$$

The continuity equation yields an expression for the transverse velocity $u_{1\eta}$. Indeed, to the first order, under the above-stated assumptions, the continuity equation gives

$$-i\omega\rho_1 + \partial_x(\rho_0 u_{1x}) + \frac{\rho_0}{R} \partial_\eta u_{1\eta} = 0,$$

or, using the previous expressions for u_{1x}, ρ_1, and T_1

$$\partial_\eta u_{1\eta}=\frac{iR}{\omega\rho_0}\left\{\partial_x(F_\eta\partial_x p_1)+\frac{\gamma\omega^2}{c_0^2}p_1-\frac{\omega^2}{C_pT_0}F_{\eta t}p_1+\frac{\partial_x T_0}{T_0}\partial_x p_1\left[\frac{\sigma F_\eta-F_{\eta t}}{\sigma-1}\right]\right\}.$$

Now, $\partial F_\eta/\partial x=(\partial F_\eta/\partial b)(\partial b/\partial T_0)(\partial T_0/\partial x)$, also $\partial b/\partial T_0=-b(\beta+1)/(2T_0)$ [because $\partial\nu_0/\partial T_0=\nu_0(\beta+1)/T_0$] and $\partial F_\eta/\partial b=-\eta b\phi+b(1-F_\eta)(1-F)$. Here, we have used

$$\phi=\frac{1}{b^2}\partial_\eta F_\eta=\frac{\sinh(b\eta)}{b\cosh(b)},\tag{A6}$$

$$\phi_t=\frac{1}{\sigma b^2}\partial_\eta F_{\eta t}=\frac{\sinh(\sqrt{\sigma}b\eta)}{b\sqrt{\sigma}\cosh(b\sqrt{\sigma})},\tag{A7}$$

$$F=\frac{1}{2}\int_{-1}^{1}F_\eta\,d\eta=1-\frac{\tanh b}{b},\tag{A8}$$

$$F_t=\frac{1}{2}\int_{-1}^{1}F_{\eta t}\,d\eta=1-\frac{\tanh(\sqrt{\sigma}b)}{\sqrt{\sigma}b}.\tag{A9}$$

For comparison, note that $F=1-f_\nu^*$ and $F_t=1-f_\kappa^*$, where f_ν and f_κ are used in Swift's notation[2] and the star denotes complex conjugation.

Finally

$$\partial_x F_\eta=-b^2\frac{\beta+1}{2}\frac{\partial_x T_0}{T_0}[-\eta\phi+(1-F_\eta)(1-F)],$$

and therefore

$$\partial_\eta u_{1\eta}=\frac{iR}{\omega\rho_0}\left[\frac{\omega^2\gamma}{c_0^2}p_1-\frac{\omega^2}{T_0C_p}p_1F_{\eta t}+\frac{\partial_x T_0}{T_0}\partial_x p_1\left\{\frac{\sigma F_\eta}{\sigma-1}-\frac{F_{\eta t}}{\sigma-1}\right\}+\frac{\partial^2 p_1}{\partial x^2}F_\eta-\partial_x p_1 b^2\frac{\beta+1}{2}\frac{\partial_x T_0}{T_0}\times\{-\eta\phi+(1-F_\eta)(1-F)\}\right],\tag{A10}$$

and, because $u_{1\eta}(\eta=0)=0$,

$$u_{1\eta}=\frac{iR}{\omega\rho_0}\left[\frac{\partial^2 p_1}{\partial x^2}(\eta-\phi)+\frac{\partial_x T_0}{T_0}\partial_x p_1\left\{\eta+\frac{-\sigma\phi+\phi_t}{\sigma-1}\right\}+\frac{\omega^2}{c_0^2}p_1(\eta+(\gamma-1)\phi_t)-\partial_x p_1\frac{\beta+1}{2}\frac{\partial_x T_0}{T_0}\times\{-\eta(1-F_\eta)+\phi+\phi b^2(1-F)\}\right].\tag{A11}$$

Finally, the equation describing the linear acoustic harmonic pressure field with superimposed temperature gradient is[39]

$$\rho_0\partial_x\left[\frac{F}{\rho_0}\partial_x p_1\right]+\frac{F-F_t}{1-\sigma}\frac{\partial_x T_0}{T_0}\partial_x p_1+\frac{\omega^2}{c_0^2}\times[1+(\gamma-1)(1-F_t)]p_1=0.\tag{A12}$$

Equation (A12) gives an expression for the pressure second derivative

$$\frac{\partial^2 p_1}{\partial x^2}=-\partial_x p_1\frac{\beta+1}{2}\frac{\partial_x T_0}{T_0}\left(1-\frac{b^2(1-F)^2}{F}\right)-k_0^2\left[\frac{1+(\gamma-1)(1-F_t)}{F}\right]p_1+\partial_x p_1\frac{\partial_x T_0}{T_0}\times\left\{-\frac{\sigma}{\sigma-1}+\frac{F_t}{F(\sigma-1)}\right\},\tag{A13}$$

because

$$\rho_0\partial_x\left[\frac{F}{\rho_0}\partial_x p_1\right]=F\partial_x p_1\frac{\partial_x T_0}{T_0}+F\frac{\partial^2 p_1}{\partial x^2}+\partial_x p_1\partial_x F,$$

and

$$\partial_x F=\frac{\beta+1}{2}\frac{\partial_x T_0}{T_0}(F-b^2(1-F)^2).$$

2. Cylindrical tube

In the case of a cylindrical tube, the expressions for the first-order particle velocity, density, and instantaneous temperature are still (A1), (A4), and (A3), but the coefficients that describe the viscous and thermal boundary layers effects are given by

$$F_\eta=1-\frac{J_0(b\eta)}{J_0(b)},\quad b=\frac{(1+i)R}{\delta_\nu},\tag{A14}$$

$$F_{\eta t}=1-\frac{J_0(\sqrt{\sigma}b\eta)}{J_0(\sqrt{\sigma}b)},\tag{A15}$$

$$\phi=\frac{J_1(b\eta)}{bJ_0(b)},\quad \phi_t=\frac{J_1(\sqrt{\sigma}b\eta)}{\sqrt{\sigma}bJ_0(\sqrt{\sigma}b)},\tag{A16}$$

$$F=2\int_0^1 F_\eta\eta\,d\eta=1-\frac{2J_1(b)}{bJ_0(b)},\tag{A17}$$

$$F_t=2\int_0^1 F_{\eta t}\eta\,d\eta=1-\frac{2J_1(\sqrt{\sigma}b)}{\sqrt{\sigma}bJ_0(\sqrt{\sigma}b)}.\tag{A18}$$

Here, J_0 and J_1 are Bessel functions of the first kind of order, respectively, 0 and 1. Similarly, the integration of the continuity equation yields an expression for the first-order transverse particle velocity

$$u_{1\eta}=\frac{iR}{\omega\rho_0}\left[\frac{\partial^2 p_1}{\partial x^2}\left(\frac{\eta}{2}-\phi\right)+\frac{\partial_x T_0}{T_0}\partial_x p_1\left\{\frac{\eta}{2}+\frac{-\sigma\phi+\phi_t}{\sigma-1}\right\}+\frac{\omega^2}{c_0^2}p_1\left(\frac{\eta}{2}+(\gamma-1)\phi t\right)+\partial_x p_1\frac{\beta+1}{2}\frac{\partial_x T_0}{T_0}\times\left\{\eta(1-F_\eta)-\phi+\frac{\phi b^2(1-F)}{2}\right\}\right],\tag{A19}$$

and the equation describing the linear acoustic harmonic pressure field with superimposed temperature gradient is the same as in the parallel plate geometry.

APPENDIX B: DETAIL OF THE DERIVATION

The coefficients that give the second-order velocity between parallel plates for any ratio R/δ_t in a fluid that supports a temperature gradient are

$$\Psi_1=\beta(\gamma-1)\left\{\frac{2\sigma}{\sigma+1}-2(1-F^*)\left(1+\frac{\sigma-1}{(\sigma+1)^2}\right)+\frac{4\sigma(1-F_t)}{(\sigma+1)^2}+2b^2\sigma(1-F_t)\frac{1-F^*}{\sigma+1}\right\}+2(\gamma-1)(1-F_t)$$
$$\times\left(\frac{1}{\sigma}+\frac{1-\sigma}{(\sigma+1)^2}-\frac{1}{\sigma+1}\right)-\frac{2(\gamma-1)(1-F^*)}{\sigma+1}\left(\sigma+\frac{2}{\sigma+1}\right)+2(\gamma-2)(1-F^*)+2+2b^2(1-F^*)-\frac{2(\gamma-1)}{\sigma(\sigma+1)}$$
$$+2b^2(\gamma-1)\frac{(1-F^*)(1-F_t)}{\sigma+1}-\frac{1+(\gamma-1)(1-F_t)}{F}\{3(1-F)-8(1-F^*)+b^2|1-F|^2+5+2b^2(1-F^*)\},$$

$$\Psi_2=\beta(\gamma-1)\left\{\frac{\sigma}{\sigma+1}-(1-F_\eta^*)+(1-F_\eta^*)\frac{1-F_{\eta t}}{\sigma+1}-b^2\phi^*\phi_t\frac{\sigma}{\sigma+1}+\frac{\sigma b^2(1-F_t)(1-F)}{\sigma+1}\right\}+F_\eta^*+(1-F^*)b^2$$
$$-\eta\phi^*b^2-\frac{\gamma-1}{\sigma(1+\sigma)}+\frac{(\gamma-1)(1-F_{\eta t})}{\sigma}-\frac{\gamma-1}{\sigma+1}(1-F_\eta^*)(1-F_{\eta t})+\frac{b^2(\gamma-1)(1-F^*)(1-F_t)}{(\sigma+1)}-b^2\phi_t\phi^*\frac{\gamma-1}{\sigma+1}$$
$$-\frac{1+(\gamma-1)(1-F_t)}{F}\left\{(1-F^*)b^2+3F_\eta^*-\eta\phi^*b^2-\frac{1}{2}+\frac{|1-F_\eta|^2}{2}-b^2\frac{|\phi|^2}{2}+\frac{b^2|1-F|^2}{2}-F_\eta\right\},$$

$$\Psi_3=\frac{(11\sigma+13)(1-F^*)}{2(\sigma+1)}+\frac{(-3\sigma+5)(1-F)}{2(\sigma-1)}+\frac{2(1-F_t)}{\sigma^2-1}-2-2(1-F^*)b^2+\frac{2}{\sigma(\sigma^2-1)}-\frac{2(1-F_t)}{\sigma(\sigma-1)}+\frac{b^2|1-F|^2}{\sigma-1}$$
$$+\frac{4(1-F^*)}{(\sigma-1)(\sigma+1)^2}-\frac{2b^2(1-F^*)(1-F_t)}{\sigma^2-1}+\frac{2(1-F_t)}{(\sigma+1)^2}-\frac{\sigma}{\sigma-1}+(\beta+1)\left\{5-(1-F^*)-4(1-F)+\frac{1}{2}b^2(1-F^*)\right.$$
$$\left.-\frac{3}{2}b^2(1-F)^2-\frac{1}{2}b^4(1-F)|1-F|^2\right\}+\frac{\beta\sigma}{\sigma+1}-2\beta(1-F^*)\left(1-\frac{1}{(\sigma+1)^2}\right)+\frac{\beta\sigma(1-F)}{\sigma-1}+\frac{\beta\sigma b^2|1-F|^2}{\sigma-1}$$
$$-\frac{4\beta\sigma(1-F_t)}{(\sigma+1)^2(\sigma-1)}-2\beta b^2\sigma(1-F_t)\frac{1-F^*}{\sigma^2-1}-\frac{\sigma(1-F^*)}{\sigma-1}+\left\{\frac{\sigma}{\sigma-1}-\frac{F_t}{F(\sigma-1)}-\frac{\beta+1}{2}\left(1-\frac{b^2(1-F)^2}{F}\right)\right\}$$
$$\times[3(1-F)-8(1-F^*)+b^2|1-F|^2+5+2b^2(1-F^*)],$$

$$\Psi_4=-b^2(1-F^*)+\frac{1}{\sigma(\sigma^2-1)}-\frac{1-F_{\eta t}}{\sigma(\sigma-1)}+\frac{b^2(|1-F|^2-|\phi|^2)}{2(\sigma-1)}+\frac{(1-F_{\eta t})(1-F_\eta^*)}{\sigma^2-1}-2F_\eta^*+b^2\eta\phi^*-\frac{F_\eta}{\sigma-1}$$
$$-\frac{b^2((1-F^*)(1-F_t)-\phi_t\phi^*)}{\sigma^2-1}+\frac{\sigma(1-|1-F_\eta|^2)}{2(\sigma-1)}+\frac{b^2}{4}(\beta+1)\left\{\frac{7}{b^2}-\frac{4(1-F_\eta)}{b^2}-\frac{3|1-F_\eta|^2}{b^2}-\eta\phi^*(1-F_\eta)\right.$$
$$\left.+\eta\phi(3-F_\eta^*)+(1-F^*)-(1-F)[|1-F_\eta|^2+2(1-F_\eta)-b^2|\phi|^2+b^2|1-F|^2]\right\}+\beta\left[\frac{\sigma}{2(\sigma+1)}-(1-F_\eta^*)\right.$$
$$\left.+\frac{b^2\sigma(|1-F|^2-|\phi|^2)}{2(\sigma-1)}+\frac{\sigma|1-F_\eta|^2}{2(\sigma-1)}-\frac{(1-F_\eta^*)(1-F_{\eta t})}{\sigma^2-1}-\frac{\sigma b^2[(1-F_t)(1-F^*)-\phi^*\phi_t]}{\sigma^2-1}\right]+\left\{\frac{\sigma}{\sigma-1}-\frac{F_t}{F(\sigma-1)}\right.$$
$$\left.-\frac{\beta+1}{2}\left(1-\frac{b^2(1-F)^2}{F}\right)\right\}\left[(1-F^*)b^2+3F_\eta^*-b^2\eta\phi^*-\frac{1}{2}+\frac{|1-F_\eta|^2}{2}-\frac{b^2|\phi|^2}{2}+\frac{b^2|1-F|^2}{2}-F_\eta\right].$$

Under the approximation $[\tanh(b)/b]\approx 1/b$, the coefficients that give the center-line second-order velocity are

$$\Psi_1(\eta=0)\approx\beta(\gamma-1)\left(\frac{2\sigma}{\sigma+1}+\frac{2i}{b}\left(1+\frac{\sigma-1}{(\sigma+1)^2}\right)+\frac{4\sqrt{\sigma}}{b(\sigma+1)^2}-\frac{2i\sqrt{\sigma}}{\sigma+1}\right)-\frac{2i(\gamma-2)}{b}+\frac{2(\gamma-1)}{b\sqrt{\sigma}}\left(\frac{1}{\sigma}+\frac{1-\sigma}{(\sigma+1)^2}-\frac{1}{\sigma+1}\right)$$
$$+\frac{2i(\gamma-1)}{b(\sigma+1)}\left(\sigma+\frac{2}{\sigma+1}\right)+2-2ib-\frac{2(\gamma-1)}{\sigma(\sigma+1)}-\frac{2i(\gamma-1)}{\sqrt{\sigma}(\sigma+1)}-\left(\frac{b\sqrt{\sigma}+(\gamma-1)}{\sqrt{\sigma}(b-1)}\right)\left(\frac{3+8i}{b}-i+5-2ib\right),$$

$$\Psi_2(\eta=0)\approx\frac{\beta(\gamma-1)\sigma}{\sigma+1}\left(1-\frac{i}{\sqrt{\sigma}}\right)+1-ib-\frac{\gamma-1}{\sigma(1+\sigma)}+\frac{\gamma-1}{i\sqrt{\sigma}(\sigma+1)}-\left(\frac{b\sqrt{(\sigma)}+(\sigma-1)}{\sqrt{\sigma}(b-1)}\right)\left(-ib+\frac{3-i}{2}\right),$$

$$\Psi_3(\eta=0)\approx -\frac{i(11\sigma+13)}{2b(\sigma+1)}+\frac{1}{2b(\sigma-1)}(3\sigma+5+18i\sigma+2\beta\sigma-4\sigma^{3/2})-\frac{4\beta\sqrt{\sigma}}{b(\sigma+1)^2(\sigma-1)}-2+2ib$$
$$+\frac{1}{\sigma-1}(-i+4\sigma-i\sigma-2ib\sigma-i\beta\sigma)+\frac{2(1+ib)}{\sqrt{\sigma}b(\sigma^2-1)}+\frac{2}{\sigma(\sigma^2-1)}-\frac{4i}{b(\sigma-1)(\sigma+1)^2}$$
$$+\frac{2}{\sqrt{\sigma}b(\sigma+1)^2}+(\beta+1)\left(\frac{7}{2}+\frac{i-4}{b}\right)+\frac{\beta\sigma}{\sigma+1}+\frac{2i\beta}{b}\left(1-\frac{1}{(\sigma+1)^2}\right)+\frac{2i\beta\sqrt{\sigma}}{\sigma^2-1}$$
$$+\left(-\frac{b\sqrt{\sigma}-1}{\sqrt{\sigma}(b-1)(\sigma-1)}+\frac{\beta+1}{2(b-1)}\right)\left(\frac{3+8i}{b}-i+5-2ib\right),$$
$$\Psi_4(\eta=0)\approx -\frac{i}{2(\sigma-1)}(1-2i+4i\sigma+2b\sigma+\sigma+\beta\sigma)+ib+\frac{1+i\sqrt{\sigma}+i\sigma^{3/2}\beta}{\sigma(\sigma^2-1)}+\frac{7(\beta+1)}{4}+\frac{\sigma\beta}{2(\sigma+1)}$$
$$+\left(-\frac{b\sqrt{\sigma}-1}{\sqrt{\sigma}(b-1)(\sigma-1)}+\frac{\beta+1}{2(b-1)}\right)\left(-ib+\frac{3-i}{2}\right).$$

[1] G. W. Swift, ''Thermoacoustics: A unifying perspective for some engines and refrigerators,'' Technical Report, Condensed Matter and Thermal Physics Group, Los Alamos National Laboratory. Draft available at http://www.lanl.gov/thermoacoustics/Book/index.html (1999).
[2] G. W. Swift, ''Thermoacoustic engines,'' J. Acoust. Soc. Am. **84**, 1145–1180 (1988).
[3] G. W. Swift, ''Thermoacoustic engines and refrigerators,'' Phys. Today **48**(7), 22–28 (1995).
[4] N. Rott, ''Thermoacoustics,'' Adv. Appl. Mech. **20**, 135–175 (1980).
[5] W. C. Ward and G. W. Swift, ''Fully tested software and users guide available from energy science and technology software center, US Dept. of Energy, Oak Ridge, TN,'' J. Acoust. Soc. Am. **95**, 3671 (1994).
[6] G. Smith, ''Streaming in thermoacoustic engine,'' J. Acoust. Soc. Am. **106**, 2265(A) (1999).
[7] V. Gusev, S. Job, H. Bailliet, P. Lotton, and M. Bruneau, ''Acoustic streaming in annular thermoacoustic prime-movers,'' J. Acoust. Soc. Am. **108**, 934–945 (2000).
[8] T. Yazaki and A. Tominaga, ''Measurement of sound generation in thermoacoustic oscillations,'' Proc. R. Soc. London, Ser. A **454**, 2113–2122 (1998).
[9] G. W. Swift, D. L. Gardner, and S. Backhaus, ''Acoustic recovery lost power in pulse tube refrigerators,'' J. Acoust. Soc. Am. **105**, 711–724 (1999).
[10] J. R. Olson and G. W. Swift, ''Acoustic streaming in pulse tube refrigerators: Tapered pulse tubes,'' Cryogenics **37**(12), 769–776 (1998).
[11] S. Backhaus and G. W. Swift, ''A thermoacoustic-Stirling heat engine: Detailed study,'' J. Acoust. Soc. Am. **107**, 3148–3166 (2000).
[12] N. Rott, ''The influence of heat conduction on acoustic streaming,'' J. Appl. Math. Phys. (ZAMP) **25**, 417–421 (1974).
[13] R. Waxler, ''Stationary velocity and pressure gradients in a thermoacoustic stack,'' J. Acoust. Soc. Am. **109**, 2739–2750 (2001).
[14] Lord Rayleigh, ''On the circulation of air observed in Kundt's tubes and some allied acoustical problems,'' Philos. Trans. R. Soc. London **175**, 1–21 (1884).
[15] J. W. Strutt and Baron Rayleigh, *The Theory of Sound*, 2nd ed. (Dover, New York, 1945).
[16] C. Eckart, ''Vortices and streams caused by sound waves,'' Phys. Rev. **73**(1), 68 (1948).
[17] O. V. Rudenko and S. I. Soluyan, *Theoretical Foundations of Non Linear Acoustics* (Plenum, New York, 1977), English translation.
[18] L. Z. Zarembo, ''Acoustic Streaming,'' in *High Intensity Ultrasonic Fields*, edited by L. D. Rozenberg (Plenum, New York, 1971), Part 3, p. 137.
[19] W. L. Nyborg, ''Acoustic Streaming,'' in *Physical Acoustics*, edited by W. P. Mason (Academic, New York, 1965), Vol. 2, Part b.
[20] J. P. Sharpe, C. A. Greated, C. Gray, and D. M. Campbell, ''The measurement of acoustic streaming using particle image velocimetry,'' Acustica **86**, 168–172 (1989).
[21] N. Riley, ''Acoustic streaming,'' in *Encyclopedia of Acoustics*, edited by M. J. Crocker (Wiley, New York, 1997).
[22] M. J. Lighthill, ''Acoustic streaming in the ear itself,'' J. Fluid Mech. **239**, 551–606 (1992).
[23] D. H. Keefe, ''Acoustic streaming, dimensional analysis of nonlinearities, and tone-hole mutual interactions in woodwinds,'' J. Acoust. Soc. Am. **73**, 1804–1820 (1983).
[24] See, for example, C. C. Church, ''A method to account for acoustic microstreaming when predicting bubble growth rates produced by rectified diffusion,'' J. Acoust. Soc. Am. **84**, 1758–1764 (1988).
[25] See, for example, N. Riley, ''Acoustic Streaming,'' Theor. Comput. Fluid Dyn. **10**, 349–456 (1998).
[26] See, for example, D. L. Miller, ''A review of the ultrasonic bioeffects of microsonations, gas-body activation, and related cavitation-like phenomena,'' Ultrasound Med. Biol. **13**, 443–470 (1987).
[27] D. Gedeon, ''DC gas flows in Stirling and pulse-tube cryocoolers,'' Cryocoolers **9**, 385–392 (1997).
[28] P. H. Ceperley, ''A pistonless Stirling engine—The traveling wave heat engine,'' J. Acoust. Soc. Am. **66**, 1508–1513 (1979).
[29] D. F. Gaitan, A. Gopinath, and A. A. Atchley, ''Experimental study of acoustic turbulence and streaming in a thermoacoustic stack,'' J. Acoust. Soc. Am. **96**, 3220(A) (1994).
[30] G. Smith, ''Examination of streaming regions within a waste-driven thermoacoustic refrigerator,'' Ph.D. thesis, University of Mississippi, 2000.
[31] J. R. Olson and G. W. Swift, ''Suppression of acoustic streaming in tapered pulse tubes,'' 10th International Cryocooler Conference, Monterey, CA, May, 1998.
[32] L. Menguy and J. Gilbert, ''Nonlinear acoustic streaming accompanying a plane stationary wave in a guide,'' Acta Acust. **86**, 249–259 (2000).
[33] M. Brunean, *Précis d'Acoustique Fondamentale* (Hermès, Paris, 1998).
[34] W. L. Nyborg, ''Acoustic streaming,'' in *Nonlinear Acoustics*, edited by M. F. Hamilton and D. T. Blackstock (Academic, New York, 1998), p. 207–231.
[35] J. Lighthill, ''Acoustic streaming,'' J. Sound Vib. **61**(3), 391–418 (1978).
[36] V. E. Gusev, H. Bailliet, P. Lotton, and M. Bruneau, ''Asymptotic theory of nonlinear acoustic waves in thermoacoustic prime-mover,'' Acta Acust. (Beijing) **86**(1), 25–38 (2000).
[37] T. J. Hofler, ''Thermoacoustic refrigerator design and performance,'' Ph.D. thesis, University of California, San Diego, 1986.
[38] W. P. Arnott, H. E. Bass, and R. Raspet, ''General formulation of thermoacoustics for stacks having arbitrarily shaped pore cross sections,'' J. Acoust. Soc. Am. **90**, 3228–3237 (1991).
[39] N. Rott, ''Damped and thermally driven acoustic oscillations in wide and narrow tubes,'' J. Appl. Phys. (ZAMP) **20**, 230–243 (1969).

Experimental observations of the stress experienced by a solid surface when a laser-created bubble oscillates in its vicinity

S. J. Shaw
AMOR Group, Cranfield University, RMCS Shrivenham, Swindon SN6 8LA, United Kingdom

W. P. Schiffers and D. C. Emmony
Department of Physics, Loughborough University, Loughborough LE11 3TU, United Kingdom

(Received 12 November 2000; accepted for publication 29 June 2001)

In an attempt to shed more light on the complex process by which cavities interact destructively with rigid boundaries we consider experimentally the interaction of a laser-generated bubble with a nearby solid boundary. To determine the stresses the surface of the boundary experiences, particularly during the final stages of the first collapse phase, we present a series of pressure transducer traces observed when the laser-created cavity is produced close to the solid boundary. Through careful control of experimental parameters we record pressure increases for cavities created between 0.56 and 1.5 times the maximum bubble radius from the solid boundary. Previous studies have shown this to be a complex process which is particularly sensitive to the working parameters of the problem, which is borne out by our observations. © *2001 Acoustical Society of America.* [DOI: 10.1121/1.1397358]

PACS numbers: 43.25.Yw [MAB]

I. INTRODUCTION

The phenomena of cavitation damage, i.e., the process by which bubbles or vapor cavities can destructively interact with boundaries, has been the subject of much research ever since it was identified as the prime candidate for the observed damage of the great ocean liners' propellers after a surprisingly small time in use.[1] Since this early identification, cavitation bubbles have been found to occur on many scales ranging from microbubbles in the blood stream, other body fluids, or the fluid of the eyes, created as a by-product of laser-induced lithotripsy or laser surgery, to the large explosion bubble, for example, due to depth charges. For solid metallic surfaces like ship's propellers, cavity interaction is erosive leaving, at best, the surfaces pock-marked. In medical applications, the production of microbubbles can result in cell walls being badly damaged, but on the positive side can aid in the breakup of stones (see Ref. 2 and the references therein). The most catastrophic effects of cavitation damage are seen for explosion bubbles where typically bubbles of radius up to 30 m can be created.[3] Although cavities can cause damage on many scales, the evidence suggests the general mechanisms underlying the phenomena are the same, although the detail is still unclear. It should be noted that the larger a bubble is the more important buoyancy effects become, which may hinder or promote the process of interaction. It should also be borne in mind that if a boundary has freedom to move, then dependent upon the amount of movement, the interaction process can be different.

In this study we are not interested in how cavitation bubbles are formed and subsequently approach solid boundaries. Our interests lie in trying to shed more light on the complex process by which bubbles, once they are near a boundary, interact with it in such a way as to cause the observed damage. Much theoretical and experimental research[2,4–13] has shown that if a bubble is undergoing volume oscillations as it approaches a solid boundary, then in the collapse phase, particularly around minimum volume, two physical phenomena are observed, each of which has been put forward as the possible cause of cavitation damage. One of these is the emission of a shock wave when the bubble achieves minimum volume. The second is the development of a wall-directed liquid jet during the later stages of the collapse process, which threads the bubble and may subsequently impact on the boundary. For normal experimental setup scenarios, where experimental reproducibility is achievable, how either of these phenomena can cause the damage is still far from clear due to the rapidity of the event. Typically for a bubble of maximum radius 1.5 mm, all the interesting physics occurs over a timescale of 20 μs or less. At the other end of the scale, explosion bubbles with maximum radii of 30 m may offer a longer timescale for viewing the interesting physics, but monetary cost severely limits experimental reproducibility. Hence it is still far from clear how the bubble actually damages the solid surface.

It should be stressed that in real cavitation damage situations, the interaction of a single bubble with a solid boundary is normally not an isolated event. Indeed, in many cases the bubble population is so numerous that they exist in the form of ''clouds.'' Therefore, a very complex physical situation arises in which bubble–boundary, bubble–bubble, and bubble–shock-wave interactions all have to be evaluated. From both a theoretical and experimental point of view, the enormity of this task cannot be overstated, especially since a single bubble–boundary interaction process is still not fully understood. Hence it is felt that a good starting point to understanding the overall picture is to try and shed more light on the single bubble–boundary interaction process.

In a series of experimental studies we have attempted to

 0001-4966/2001/110(4)/1822/6/$18.00

determine qualitatively what stresses are experienced by a solid boundary and surrounding fluid when a bubble oscillates in the vicinity. Using a combination of schlieren photography, dynamic photoelasticity techniques and a thin film transducer placed on the surface of the boundary, we conducted a study concentrating on times around the first minimum volume.[14] The observations were found to be sensitive to small changes in the stand-off parameter γ, which is the ratio of the distance the laser-generated bubble is created from the boundary to the radius of the bubble at maximum volume. For particular values of γ ($\frac{5}{6}$, 1) a double-peaked pulse with a total positive pressure duration of about 20 μs was recorded by the pressure transducer for the times of interest around the first minimum volume. One surprising observation was the lack of a significant pressure rise corresponding to the possible initial liquid jet impact on the solid boundary. This was partially explained on the grounds that the initial jet radius is expected to be orders of magnitude smaller than the transducer radius.

In a subsequent study combining numerical and experimental observations, Tong *et al.*[15] identified a new phenomenon which they termed a ''splash'' effect and directly linked it with the double-peaked structure. They found that the ''splash'' effect depended directly on whether there was a liquid layer between the boundary and the surface of the bubble closest to this boundary during the collapse phase and also the thickness of this layer. The ''splash'' itself is a splash wave that propagates around the bubble after the wall-directed jet impacts into the sandwiched liquid layer and which subsequently may impact violently upon the opposing bubble wall.

In the present study we present a series of pressure transducer traces to show the possible range (in terms of γ) over which the ''splash'' effect of Tong *et al.*[15] may be valid around the first collapse, by demonstrating the range of the double-peaked structure. In effect we present the evolution of the double-peaked structure with respect to γ. It is felt that having such a record in one paper will be of benefit to other researchers. Consequently, we present a series of results in the range $0.56 \leqslant \gamma \leqslant 1.5$.

In the next section we discuss the experimental setup used to generate the pressure transducer traces. This is followed by the presentation of the results and some discussion.

II. EXPERIMENTAL SETUP

In Fig. 1 we present a schematic representation of the experimental setup used to both create and observe cavitation bubbles. The cavities are generated using a Q-switched Nd:Yag laser operating at a wavelength of $\lambda = 1.06\ \mu$m with an output energy of about 100 mJ, in a pulse approximately 20 ns long, which is adequate to obtain breakdown in water. The coherent beam is expanded using a plano-concave lens and then focused to the chosen bubble creation site in the water cell by a 28-mm focal length, f/2.0 camera lens. The resultant plasma forms over the pulse width of the laser, growing along the laser beam axis. The cavity expands around the plasma, becoming spherical early in its lifetime. In order to observe the resultant interaction of the vapor bubble with the nearby solid boundary (polymethylmethacrylate block) we employ two techniques. The predominant number of results we present are pressure (voltage) traces obtained from a thin film polyvinylidene fluoride (pvdf) transducer fixed to the surface of the PMMA block. The keyhole-shaped transducer has an active circular area of diameter 3 mm and is covered by two silver ink electrodes.

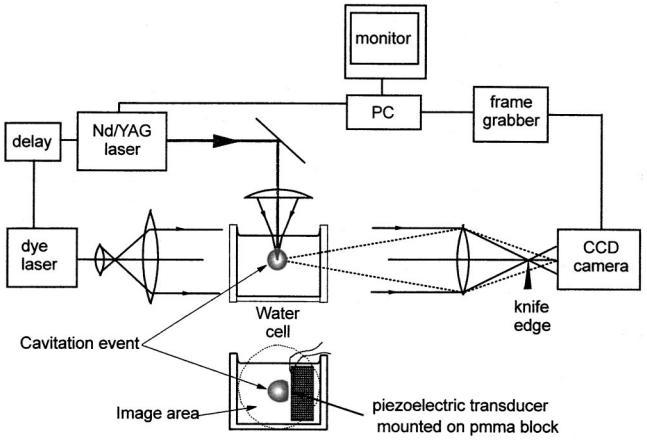

FIG. 1. Experimental setup.

We also present a selection of schlieren images taken for each event when the relevant bubble is at the first maximum volume. In order to illuminate the cavities a pulsed nitrogen gas laser operating at $\lambda = 337$ nm with a pulse duration of 500 ps and energy of about 15 μJ is employed. The nitrogen laser in turn is used to excite green coumarin 500 dye resulting in a green light beam of wavelength $\lambda = 512$ nm and a coherence length of 20 μm. In order to spatially filter the beam it is passed through a $\times 40$ microscope objective and a 25-μm pinhole and the final parallel beam of light is obtained by passing it through a 50-mm focal length camera lens. A CCD camera and video-frame-grabber unit are used to record the schlieren images. The analog video signal is digitized and stored in a 512×512 pixel array.

III. RESULTS AND DISCUSSION

In this section we present a series of transducer pressure (voltage) traces corresponding to the interaction of a single laser-generated bubble in water for values of the stand-off parameter γ in the range $0.56 \leqslant \gamma \leqslant 1.5$, concentrating on times around the first minimum volume. We also present a selection of schlieren pictures displaying the relevant cavities at maximum volume so that we have an idea whether a liquid layer is sandwiched between the bubble and the boundary, the existence and thickness of which appear to play a key role in possible ''splash'' formation and resultant effects.

Figure 2(a) displays a typical low temporal resolution pressure trace from the transducer for the laser-generated cavity taken over several cycles of oscillation and is characterized by distinct pressure spikes. The first spike corresponds to the acoustic transient emitted at laser breakdown. The second and third spikes are due to positive pressure stresses recorded by the transducer around the first and second minimum volumes of the oscillation cycle, respectively. Figure 2(b) is a high temporal resolution trace of the first collapse (corresponding to ''h'' in Fig. 5). In this study we

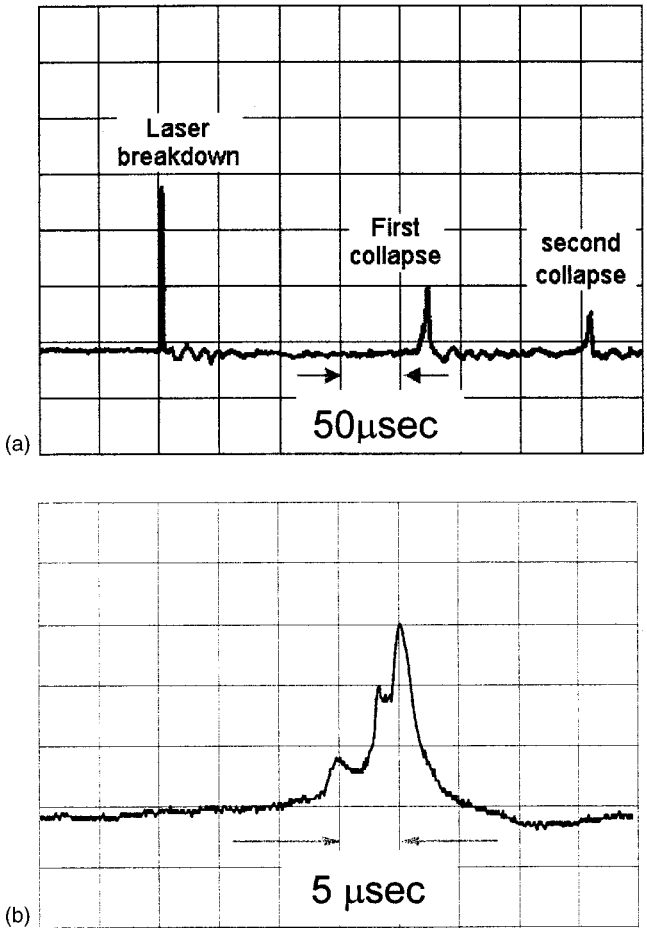

FIG. 2. (a) Transducer plot at low resolution for a typical event. (b) Transducer plot at high resolution of the pressure peak due to the first collapse at $\gamma = 0.72$.

TABLE I. Ranges of experimental parameters employed in this study.

$2T_c$ (μs)	R_{max} (mm)	s (mm)	γ	
		$0.56 \leqslant \gamma \leqslant 0.95$		
370	1.85	1.04	0.56	a
360	1.78	1.04	0.58	b
350	1.72	1.04	0.60	c
340	1.68	1.04	0.62	d
330	1.63	1.04	0.64	e
320	1.58	1.04	0.66	f
310	1.49	1.04	0.70	g
300	1.45	1.04	0.72	h
290	1.39	1.04	0.75	i
280	1.34	1.04	0.78	j
270	1.32	1.04	0.79	k
260	1.28	1.04	0.81	l
250	1.24	1.04	0.84	m
240	1.20	1.04	0.87	n
230	1.17	1.04	0.89	o
220	1.09	1.04	0.95	p
		$0.96 \leqslant \gamma \leqslant 1.50$		
360	1.82	1.75	0.96	A
350	1.78	1.75	0.98	B
340	1.74	1.75	1.00	C
330	1.68	1.75	1.04	D
320	1.63	1.75	1.07	E
310	1.60	1.75	1.09	F
300	1.58	1.75	1.11	G
290	1.53	1.75	1.14	H
280	1.48	1.75	1.18	I
270	1.43	1.75	1.22	J
260	1.39	1.75	1.26	K
250	1.34	1.75	1.31	L
240	1.28	1.75	1.36	M
230	1.24	1.75	1.41	N
220	1.17	1.75	1.50	O

are interested in the development of the second spike only, with respect to the stand-off parameter, γ, for the reasons we outlined in the Introduction. It is also felt that for the γ range of interest this has the most importance as far as cavitation damage is concerned.

In order to vary the stand-off parameter we employ a different approach to our previous work.[14] Normally different values of the stand-off parameter are achieved by creating the cavities at different distances from the boundary but keeping the maximum radius of the bubble the same (the laser energy required to create the bubble is kept fixed). Here we conduct two sets of experiments for the ranges $0.56 \leqslant \gamma \leqslant 0.95$ and $0.96 \leqslant \gamma \leqslant 1.5$, respectively, as shown in Table I. For each set of experiments the distance of bubble creation from the boundary, s, is kept fixed. For the first set (lower range) $s = 1.04$ mm while for the other set (upper range) $s = 1.75$ mm. Then for each range, the maximum bubble radius R_{max} is altered by varying the laser energy used to create the bubbles. The precise reduction in laser energy is evaluated from measurements of the time from bubble creation to the first minimum volume, namely $2T_c$, as shown for each range in Table I. The maximum bubble radius is measured directly from an image taken at time T_c corresponding to maximum bubble radius. Schlieren images of the respective bubble shapes at maximum volume for a selection of stand-off parameter values—eight images for each range—are displayed in Figs. 3 and 4. Using this approach, which is dependent on varying R_{max} (through varying laser energy) as opposed to the distance, s, the bubble is created from the boundary, may help us evaluate whether the stand-off parameter γ truly characterizes bubble-boundary interactions.

We now examine the first collapse spike [Fig. 2(b)], i.e., the second spike in Fig. 2(a), in detail and in particular its sensitivity to γ. In our subsequent pictures the transducer traces are a magnification of the region of interest. Figure 5 displays the relevant pressure outputs for the first set of experiments, i.e., for the range $\gamma = 0.56$ to $\gamma = 0.95$. Note the first result ($\gamma = 0.56$) is in the top right corner and subsequent traces proceed downwards and to the left. The labeling in Fig. 5 corresponds to that in Table I. It is felt that not only does Fig. 5 clearly show how the pressure, as recorded by the transducer, evolves with γ, but it also demonstrates the sensitivity to this nondimensional ratio. We now consider each trace in more detail and give some thought to the implied physics.

The first trace (5a) is dominated by a large positive pressure pulse lasting in total for about 4–5 μs. This signal is superimposed on a second positive pressure, which is much smaller but lasts for about 15 μs. For this value of stand-off

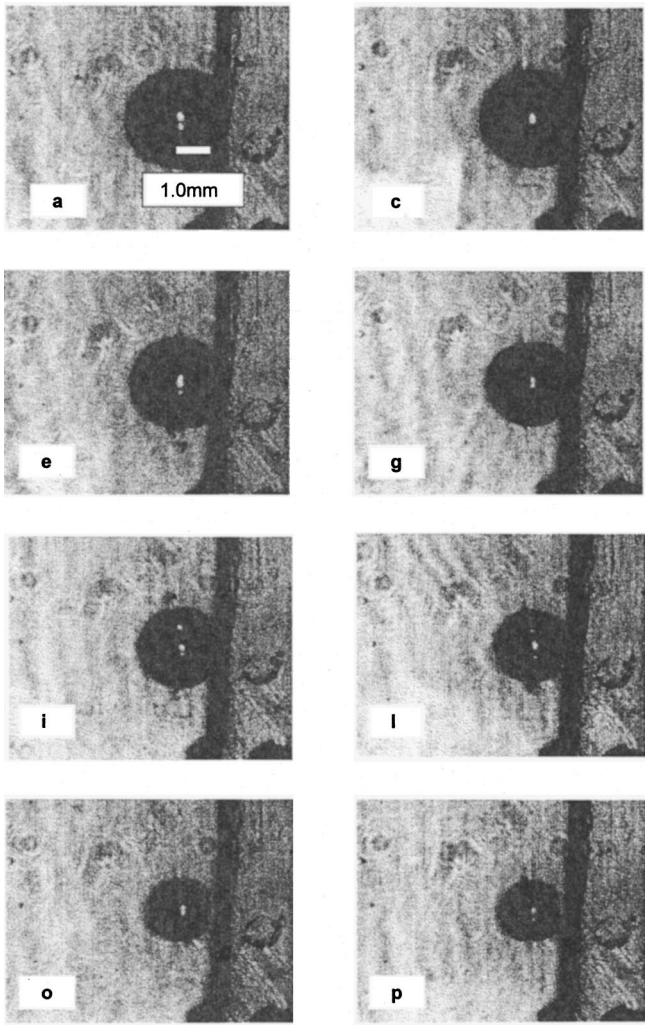

FIG. 3. Schlieren images of an oscillating cavitation bubble in front of a solid boundary at maximum volume.

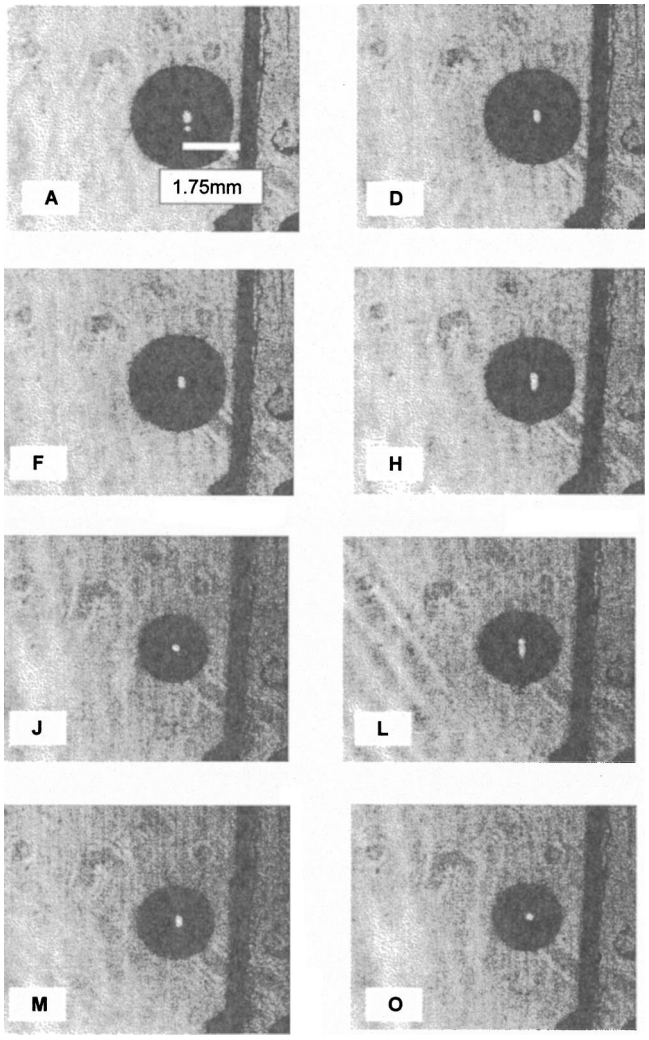

FIG. 4. Schlieren images of an oscillating cavitation bubble in front of a solid boundary at maximum volume.

parameter ($\gamma = 0.56$) it is felt that if a liquid layer is sandwiched between the bubble and the solid boundary during the collapse phase, then it is probably too thin for "splash" effects, if they occur, to have any significant effect. Consequently, there is not much disruption to the continued bubble collapse process, resulting in strong acoustic transient emission at minimum volume. The large pressure spike is most likely due to the summation of a series of large shock wave emissions given its rise time. Philipp and Lauterborn[16] have suggested that for a bubble in the range $0.5 \leqslant \gamma \leqslant 0.6$, a series of shock wave emissions are possible due to, first, emissions at minimum volume and, then, to the disintegration of the bubble torus into a ring of tiny bubbles, which then collapse very quickly with the emission of many more shock waves. We shall review our overall assessment here after considering more transducer output, for larger stand-off parameter values.

The second result we consider is for $\gamma = 0.58$ (5b). The trace is still dominated by one large pressure pulse superimposed on a much smaller but longer lasting stress. We also observe a smaller peak to the left of the dominant pressure pulse. Close examination of the main spike gives some indi-

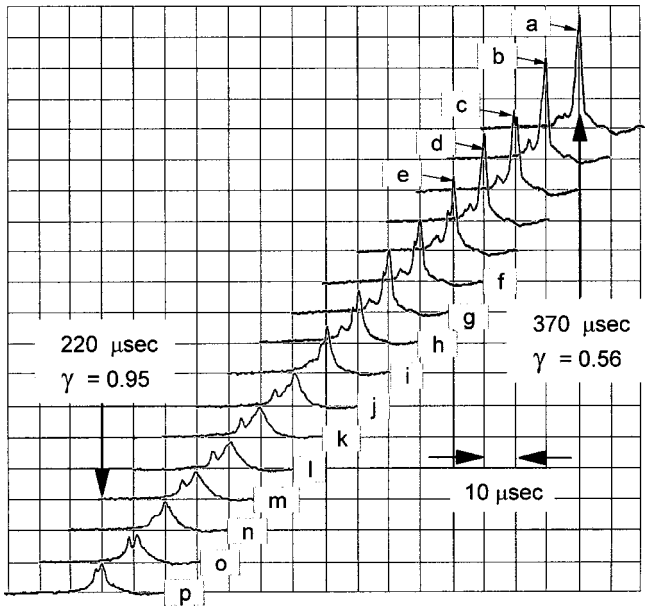

FIG. 5. Transducer trace evolution around the first minimum volume for the range $0.56 \leqslant \gamma \leqslant 0.95$.

cation that there are two pulses which can just be resolved in 5c. Our interpretation of these results is that splash effects have a small but observable effect now. It is felt that a thin liquid layer exists for this value of γ which, when impacted upon by the liquid jet, results in weak splash wave effects, which are observed as the small peak. A consequence of the splash wave having weak effects is that we assume there is not much disruption to the symmetry of the bubble collapse process.

For $\gamma=0.60$ and 0.62 (traces 5c and 5d) we observe the same qualitative features. The first peak is still small but is getting progressively broader, indicating a longer timespan over which splash wave effects are experienced. The dominant pressure pulse of the previous results is reducing in amplitude and is split into two peaks for the $\gamma=0.60$ result. We also interpret this as evidence of the growing influence of splash wave effects.

In trace 5e ($\gamma=0.64$) a slightly different structure is observed. The left-hand peak is similar to previous observations while the dominant stress recorded by the transducer now has one peak with a spike half-way up its rise. Physically we now speculate that we have the following sequence of events. The jet threads the bubble impacting on the trapped liquid layer, causing a splash wave to form. Subsequent splash wave impact effects not only give rise to the left-hand peak, but are also significant enough to influence the collapse process with associated minimum volume shock wave emission. We associate the spike on the large pressure rise with shock wave emission at minimum volume and speculate that the large pressure rise is now due to fluid flow effects through the bubble. Reviewing our previous observations in light of these remarks it is felt that for $\gamma \leqslant 0.62$, the observed large pressure rise could be due to a combination of fluid flow effects through the now toriodal bubbles and minimum volume shock wave emission. This would be due to both effects peaking at approximately the same time. For $\gamma = 0.64$ the influence of the splash wave effects is such that they disrupt the symmetry of the bubble collapse process, resulting in distinct emissions from different parts of the bubble torus at earlier times with reduced amplitude. It is also felt that splash wave effects enhance the fluid flow through the bubble, which is now seen as the largest peak.

This overall structure is maintained as the stand-off parameter is increased up to $\gamma=0.72$ (traces 5f–5h) although the dominant pressure rise decreases in amplitude. In trace 5i the left-hand peak is not so pronounced but this is explained on the grounds that the splash wave impact effects are marked by a series of acoustic emissions which in this case are more evenly distributed in time—in previous examples many of the emissions are concurrent. The result for $\gamma = 0.75$ (5i) also indicates a reduction in the importance of the spike(s) on the rise of the dominate pressure. This reduction continues through traces 5j–5l, with an indentation barely visible on the larger pressure rise in 5k and 5l. By trace 5m ($\gamma=0.84$) this feature is no longer observable. It is also noted in pressure outputs 5j–5m that, while the amplitude of the main pressure amplitude decreases slightly, the importance of the first peak increases significantly. Result 5n is slightly anomalistic in that the left-hand peak is not as

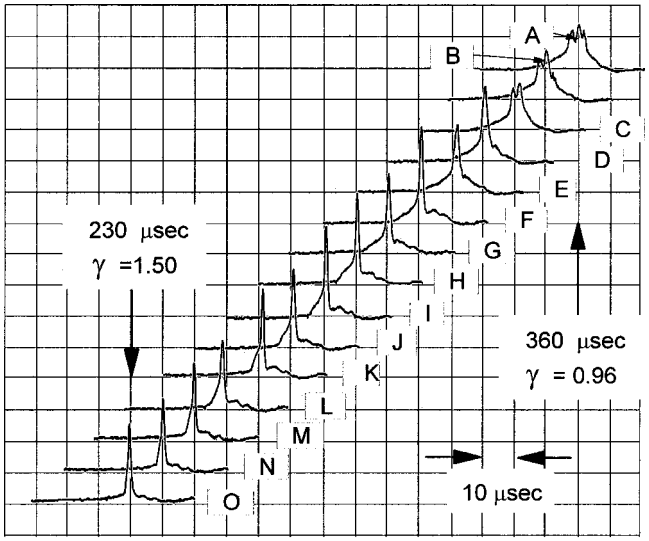

FIG. 6. Transducer trace evolution around the first minimum volume for the range $0.96 \leqslant \gamma \leqslant 1.50$.

pronounced, but in the last two traces 5o and 5p, the two peaks are almost the same size. The two main peaks are also observed to be getting closer together. In 5l ($\gamma=0.81$) they are about 5–6 μs apart, in 5m they are separated by 4 μs, while in trace 5o the two peaks are now separated by a time interval of 2–3 μs. The last result (trace 5p) shown for this sequence corresponds to $\gamma=0.95$ with the two main peaks being approximately 2 μs apart. An interesting observation made on an enhanced scale but not visible in the presented pressure output was the presence of a small spike on the fall of the second pressure evolution. This may have relevance with respect to the first picture of the second sequence of results we present.

For the second set of results the distance the bubble is created from the boundary is changed to $s=1.75$ mm. The laser energy used to create the first bubble in this sequence was comparable to the energy at the beginning of the first sequence, i.e., the bubbles have comparable initial kinetic energy, where for the first result here we now have $R_{\max} = 1.82$ mm. The results obtained for the range $\gamma=0.96$ to $\gamma=1.50$ are presented in Fig. 6, where again the first result is in the top right corner and we progress downwards and to the left. The horizontal and vertical scales are the same as Fig. 5. Our first result in this new sequence in terms of the stand-off parameter is $\gamma=0.96$, which is a value fairly close to the last result of the first experimental sequence (5p), but the creation energies are markedly different. The transducer trace 6A shows surprisingly three peaks which require some explanation. The first and second peaks are separated by about 2 μs, so we associate them with the peaks observed in 5p. We speculate that the third peak could be due to some physical enhancement of the spike on the fall of the second pressure evolution remarked upon above. Curiously the amplitudes of peaks 1 and 2 have increased noticeably. We offer two possible explanations. Either we are witnessing the beginning of a growth trend which can only be verified with more results or the change in laser energy may be having an observable effect. Since the initial bubble here will have

more initial kinetic energy (in comparison to trace 5p), then at maximum volume there will be more potential energy in the fluid to drive the collapse process. Does this mean that the resultant jet, which derives its velocity from this potential energy, has more kinetic energy? Does γ parametrize the exchange of energy correctly, i.e., we raise the question of whether the dimensionless parameter scales the differences in energy correctly over the broad range it is used. It must be realized that each event is generated by a different laser pulse and that breakdown is not exactly the same (as shown by the multiple breakdowns in some images in Figs. 3 and 4); however, the energy of each event is determined by us to be given by $R_{\max}$ in each case. It is also noted that 6A indicates that the surface experiences a total positive pressure over a slightly longer time in comparison to 5p.

In the next trace (6B), two dominant pressure pulses are observed once again with a small spike on the fall of the second positive pressure. The first pressure peak has a similar magnitude to trace 6A, while the second peak has undergone a noticeable increase. We note that the transducer output indicates that the surface experiences a positive stress in total for about 25 μs. Moving onto trace 6C ($\gamma=1.00$) the result is similar apart from the spike on the fall of the second peak being absent.

The physical effects observed by the transducer now undergo a radical change. For $\gamma=1.04$, i.e., trace 6D, only one dominant positive pressure is now observed. Before the main pressure pulse is a slow rise over about 10 μs while after, on the right, is an indication of another small rise. The solid surface experiences a positive stress for about 20 μs here. It is felt that the liquid layer between the lower bubble surface and solid boundary is too thick for splash effects to be significant now when the jet impacts upon it, i.e., the fluid situation is now akin to that described by Tong *et al.*[15] for the larger value of $\gamma=1.2$. Consequently, fluid flow effects and minimum volume shock wave emission are the dominant effects recorded by the transducer now. For further increases of the stand-off parameter this new general profile is maintained. For $\gamma=1.09$ (trace 6F) the surface is again positively stressed in total for about 20 μs, while the $\gamma=1.14$ (6H) result indicates a shorter time period of about 16 μs. In trace 6H we can see that it is the duration of the small but longer lasting pressure which is reduced as opposed to the dominant, in effect superimposed, pressure pulse. These trends continue for the remainder of the results presented from $\gamma=1.18$ (6I) through to $\gamma=1.50$ (6O). The last result presented, i.e., trace 6O, is almost entirely dominated by a large, sharp pressure pulse indicating that the pressure transducer records mainly minimum volume shock wave emission, for this value of stand-off parameter.

IV. CONCLUSIONS

In this article we have presented a pressure (voltage) transducer trace evolution (in terms of the nondimensional parameter γ) of the stresses experienced by a solid boundary when a laser-generated cavitation bubble pulsates in its vicinity, concentrating on times around the first minimum volume. This study was motivated by a desire to determine the range of the previously observed multiple peak structure[14] which Tong *et al.*[15] have associated with splash effects. We have determined the upper limit occurs between stand-off parameter values of 1.00 and 1.04 while the lower limit is around $\gamma=0.58$. In between these limits a variety of pressure stress distributions is observed, but with the common structure of two main peaks, the amplitudes of which vary with stand-off parameter value. For the larger values of γ presented ($\gamma=1.04$ to $\gamma=1.50$) a large pressure peak superimposed on a much smaller, longer lasting pressure is observed.

In order to generate the cavities for different values of stand-off parameter, the laser energy was varied, i.e., the maximum bubble radius was varied, while the bubble creation distance from the solid boundary was kept fixed.

[1] D. Silberrad, "Propeller erosion," Engineering, 33–35 (1912).
[2] A. Vogel, W. Lauterborn, and R. Timm, "Optical and acoustic investigations of the dynamics of laser-produced cavitation bubbles near a solid boundary," J. Fluid Mech. **206**, 299–338 (1989).
[3] R. H. Cole, *Underwater Explosions* (Princeton U.P., Princeton, NJ, 1948).
[4] M. Kornfeld and L. Suvorov, "On the destructive action of cavitation," J. Appl. Phys. **15**, 495–506 (1944).
[5] C. F. Naudé and A. T. Ellis, "On the mechanism of cavitation damage by nonhemispherical cavities collapsing in contact with a solid boundary," Trans. ASME J. Basic Eng. **83**, 648 (1961).
[6] J. K. Walters and J. F. Davidson, "The initial motion of a gas bubble formed in an inviscid liquid. Part 1. The two-dimensional bubble," J. Fluid Mech. **12**, 408–416 (1962).
[7] J. K. Walters and J. F. Davidson, "The initial motion of a gas bubble formed in an inviscid liquid. Part 2. The three-dimensional bubble and the toroidal bubble," J. Fluid Mech. **17**, 321–336 (1963).
[8] T. B. Benjamin and A. T. Ellis, "The collapse of cavitation bubbles and the pressures thereby produced against solid boundaries," Philos. Trans. R. Soc. London, Ser. A **260**, 221–240 (1966).
[9] M. S. Plesset and R. B. Chapman, "Collapse of an initially spherical vapour cavity in the neighbourhood of a solid boundary," J. Fluid Mech. **47**, 283–290 (1971).
[10] W. Lauterborn and H. Bolle, "Experimental investigations of a cavitation-bubble collapse in the neighbourhood of a solid boundary," J. Fluid Mech. **72**, 391–399 (1975).
[11] J. R. Blake, B. B. Taib, and G. Doherty, "Transient cavities near boundaries. Part 1. Rigid boundary," J. Fluid Mech. **170**, 479–497 (1986).
[12] Y. Tomita and A. Shima, "Mechanisms of impulsive pressure generation and damage pit formation by the bubble collapse," J. Fluid Mech. **169**, 535–564 (1986).
[13] S. Zhang, J. H. Duncan, and G. L. Chahine, "The final stage of the collapse of a cavitation bubble near a rigid wall," J. Fluid Mech. **257**, 147–181 (1993).
[14] S. J. Shaw, Y. H. Jin, W. P. Schiffers, and D. C. Emmony, "The interaction of a single laser-generated cavity in water with a solid surface," J. Acoust. Soc. Am. **99**(5), 2811–2824 (1996).
[15] R. P. Tong, W. P. Schiffers, S. J. Shaw, J. R. Blake, and D. C. Emmony, "The role of 'splashing' in the collapse of a laser-generated cavity near a rigid boundary," J. Fluid Mech. **380**, 339–361 (1999).
[16] A. Philipp and W. Lauterborn, "Cavitation erosion by single laser-produced bubbles," J. Fluid Mech. **361**, 75–116 (1998).

A correction to Maekawa's curve for the insertion loss behind barriers

Penelope Menounou[a)]
Department of Mechanical Engineering, The University of Texas at Austin, Austin, Texas 78712-1063

(Received 20 April 2001; revised 1 July 2001; accepted 2 July 2001)

Maekawa's curve is one of the most established methods for predicting the insertion loss (IL) behind barriers. For the simple case of a barrier modeled as a half plane, the IL is given versus a single parameter, the Fresnel number (N_1). Predictions obtained by Maekawa's curve deviate largely from experimental data, and from predictions obtained by analytical solutions, when the receiver is either close to the barrier or at the boundary separating the illuminated from the shadow zone. It is shown that if a second Fresnel number (N_2) is appropriately defined, the IL obtained by the existing analytical solutions can be expressed versus N_1 and N_2 for several types of incident radiation (plane, cylindrical, and spherical). Accordingly, the single curve in Maekawa's chart can be replaced by a family of curves. Each curve corresponds to a different N_2 and provides the IL versus N_1. The Kurze–Anderson formula (a mathematical expression of Maekawa's curve) is also modified to describe this set of curves. Besides providing increased accuracy in the areas where Maekawa's curve does not, the graph proposed here addresses the more general problem of combining the simplicity of empirical models like Maekawa's with the accuracy of sophisticated mathematical models. [DOI: 10.1121/1.1398050]

PACS numbers: 43.28.Js, 43.50.Gf [LCS]

NOMENCLATURE

(r_0,ϕ_0,z_0)	coordinates of the location of the source; based on a cylindrical coordinate system having its z axis on the edge of the barrier; radial distance r_0 measured from the edge of the barrier; angle ϕ_0 measured from the surface of the barrier facing the source; assume $z_0=0$
(r,ϕ,z)	coordinates of the location of the receiver; receiver assumed to be in the shadow zone; r measured from the edge of the barrier; ϕ measured from the surface of the barrier facing the source
δ	diffraction angle; the angular position of the receiver measured from the shadow boundary, $\delta=\phi-(\pi+\phi_0)$
shadow boundary	line separating the illuminated from the shadow zone
R_1	direct distance from source to receiver (as if the barrier were not present)
R_2	direct distance from image source to receiver (as if the barrier were not present)
L	shortest distance from source (or image source) to receiver after diffraction from the edge of the barrier, i.e., the length of the shortest source-edge–receiver path
λ	wavelength of the incident wave
N_1	extra distance sound travels from the source to the receiver after diffraction by the barrier edge, normalized by half the wavelength of the incident wave; $N_1=2[(L-R_1)/\lambda]$
N_2	extra distance sound travels from the image source to the receiver after diffraction by the barrier edge, normalized by half the wavelength of the incident wave; $N_2=2[(L-R_2)/\lambda]$
IL	insertion loss, $\mathrm{IL}=-10\log([P_d^{\mathrm{rms}}(A)]/[P_o^{\mathrm{rms}}(A)])^2$, where $P_d^{\mathrm{rms}}(A)$ is the rms value of the pressure at point A with the barrier present and $P_o^{\mathrm{rms}}(A)$ is the rms value of the pressure at the same point without the barrier
$\mathrm{IL_c}$	part of IL that is *common* for all three types of simple incident radiation (plane, cylindrical, and spherical incident waves)
$\mathrm{IL_{sp}}$	part of IL that depends on the geometrical *spreading* of the incident wave; $\mathrm{IL}=\mathrm{IL_c}+\mathrm{IL_{sp}}$
$\mathrm{IL_s}$	part of $\mathrm{IL_c}$; it appears in the modified version of the Kurze–Anderson formula; it is a function of N_1, which represents the relative position of the *source* to the barrier and the receiver
$\mathrm{IL_b}$	part of $\mathrm{IL_c}$; it appears in the modified version of the Kurze–Anderson formula; it is a function of N_2/N_1, which is a measure of proximity of either the source or the receiver to the surface of the *barrier*
$\mathrm{IL_{sb}}$	part of $\mathrm{IL_c}$; it appears in the modified version of the Kurze–Anderson formula; it is a function of N_2, as N_1 goes to 0; it is computed only when the receiver is very close to the *shadow boundary*; $\mathrm{IL_c}=\mathrm{IL_s}+\mathrm{IL_b}+\mathrm{IL_{sb}}$
F	Fresnel integral, $F(w)=\int_0^w e^{i\pi(t^2/2)}dt$

[a)]Electronic mail: menounou@mail.utexas.edu

 0001-4966/2001/110(4)/1828/11/$18.00

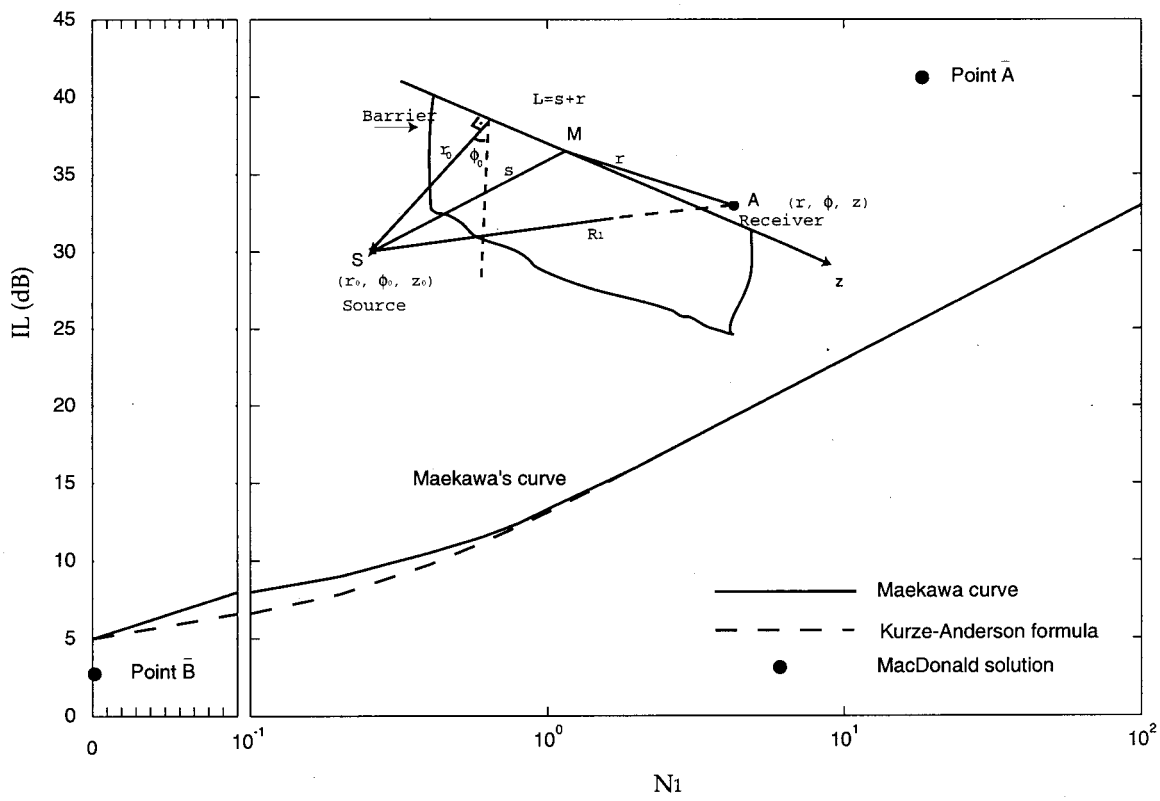

FIG. 1. Cases of large deviations between the Maekawa curve (solid line), the Kurze–Anderson formula (dashed line), and the MacDonald solution (•); point $\bar{A}$: source and receiver close to the barrier, point source S at $(r_0,\phi_0,z_0)=(5,5°,0)$, receiver A at $(r,\phi,z)=(5,355°,0)$; point $\bar{B}$: source and receiver at the shadow boundary, point source S at $(r_0,\phi_0,z_0)=(1,20°,0)$, receiver A at $(r,\phi,z)=(1,200°,0)$; distances r, r_0, z, z_0 normalized by the wavelength of the incident wave; frequency of the incident wave $f=800$ Hz.

I. INTRODUCTION

The subject of the present work is sound diffraction by the top edge of a barrier modeled as an infinitely thin rigid half-plane. Sound generated by a sound source located in front of the barrier is diffracted by the barrier's top edge and reaches the receiver located in the shadow zone behind the barrier (see Fig. 1). The shielding effect of the barrier is quantified by the insertion loss (IL), which is a measure of the sound attenuation due to the presence of the barrier. The insertion loss at a point A is defined as

$$\mathrm{IL}=-10\log\left(\frac{P_d^{\mathrm{rms}}(A)}{P_o^{\mathrm{rms}}(A)}\right)^2, \tag{1}$$

where $P_d^{\mathrm{rms}}(A)$ is the rms value of the pressure at point A with the barrier present and $P_o^{\mathrm{rms}}(A)$ the rms value of the pressure at the same point without the barrier.

Maekawa's work[1,2] is well established for predicting the insertion loss behind rigid, thin barriers. Maekawa's exhaustive experimental investigation resulted in a graph containing a single curve that provides the IL versus a single parameter. A mathematical description of this curve, which involves simple calculations and is therefore often used instead of the Maekawa curve, was suggested by Kurze and Anderson.[3,4] The Maekawa chart and the corresponding Kurze–Anderson formula have found extensive use within the noise community. Their main advantages are their simplicity and the accuracy of their predictions. Studies have shown, however, that in certain cases, experimental data deviate a great deal from Maekawa's curve. For example, Kawai *et al.*[5] conducted experiments similar to Maekawa's and compared their experimental data with Maekawa's curve, as well as with the MacDonald solution,[6] which is the exact analytical solution for diffraction of time-harmonic spherically spreading waves. While their experimental results were in agreement with the MacDonald solution, both deviated a great deal from Maekawa's curve when either the source or the receiver were comparatively near the barrier. This observation addresses a more general problem: although exact analytical solutions exist and agree favorably with measurements, they are not widely used, mainly because of their mathematical complexity. See Refs. 6–11, and references therein, for some, but certainly not all, of the exact solutions for diffraction that have been published and applied in acoustics, as well as in other disciplines. In the context of the present work "exact solutions" means solutions that have been obtained solely by assuming a simple sound source in front of an infinitely thin, rigid half-plane.

The goal of the present work is to combine the simplicity of the Maekawa curve with the accuracy of the exact solutions. In light of this goal, corrections are proposed to the Maekawa chart as well as to the corresponding Kurze–Anderson formula. In Sec. II a systematic comparison between Maekawa's results and the MacDonald solution is presented. Cases of large deviations are demonstrated and identified by their geometrical characteristics and their error amplitude. Subsequently, in Sec. III, it is shown that if ap-

propriate parameters are defined, the IL provided by appropriate approximate forms of the analytical solutions can be presented by a simple equation. This equation lends itself to presentation as a diagram similar to that of Maekawa. A new graph is thus proposed, which, because it stems from the exact analytical solutions, provides accurate predictions in the cases where Maekawa's chart does not. A corresponding correction to the Kurze–Anderson formula is also proposed (Sec. IV). The corrected formula contains elementary functions, involves simple calculations, and provides a reasonably accurate description of the new chart. Finally, in Sec. V, we discuss the relation of the equation for the IL derived in Sec. III with the well-established Kirchhoff theory for diffraction. Attention is drawn to the fact that the equation presented here is more accurate than the Kirchhoff solution, yet as simple.

The new graph presented here provides increased accuracy compared to Maekawa's curve at the expense of utilizing a second parameter. It also addresses the more general problem of combining the simplicity of empirical models with the accuracy of more complicated mathematical models. Unlike other attempts[5] to provide corrections to Maekawa's curve, the graph presented here is simple and can easily be used on a routine basis in the field. Moreover, it is the only one, to the best of the author's knowledge, that can be used for all three types of simple incident radiation: spherical, cylindrical, and planar. It should be further noted that many successful attempts to improve Maekawa's curve have been reported[12–15] (the references here are only a small fraction of these in the literature). However, these studies mostly provide corrections for problems involving effects due to the presence of the ground or due to side edges of a finite length barrier. The work presented here addresses the more elementary problem of diffraction by a half-plane. The corrected graph we propose does not conflict with the aforementioned studies. On the contrary, it can be combined with them as a further improvement of the Maekawa chart.

II. CRITICAL EXAMINATION OF MAEKAWA'S CURVE

In the present section Maekawa's work and the MacDonald solution are briefly described and a systematic comparison between results obtained by both methods is presented.

Maekawa[1,2] used a spherically spreading pulsed tone of short duration and measured the diffracted field behind a thin, rigid barrier in a test room. He measured the sound field in the shadow zone for a variety of frequencies and source–receiver locations. He showed that all his experimental data could be fitted by a single curve that provides the IL versus a single parameter, the Fresnel number N_1 (see Fig. 1). The Fresnel number is defined as the extra distance the sound travels after diffraction by the edge of the barrier, normalized by half the wavelength of the incident wave

$$N_1 = 2\frac{L-R_1}{\lambda}, \tag{2}$$

where R_1 is the direct distance between source and receiver, L is the shortest source-edge–receiver distance, and λ is the wavelength of the incident wave (see the inset of Fig. 1).

The Maekawa curve can be described mathematically by the following formula suggested by Kurze and Anderson:[3,4]

$$\mathrm{IL}_{\mathrm{KA}} = 5 + 20\log\frac{\sqrt{2\pi N_1}}{\tanh\sqrt{2\pi N_1}}. \tag{3}$$

This formula contains elementary functions and utilizes the parameter N_1. It provides an accurate description of the Maekawa curve, having only a small discrepancy of 1.5 dB from the curve for $N_1<1$. Because it is well suited for computations, it is often used instead of the Maekawa curve.

The MacDonald solution, on the other hand, is far more complex mathematically than the Kurze–Anderson formula. Assume a point source that produces the pressure field $P_0 = (e^{ikR_1})/R_1$, where the time dependence of the source signal is assumed to be $e^{-i\omega t}$. The diffracted signal P at a point in the shadow zone behind the barrier is given by the following formula:[6,7]

$$P = ik\int_{m_1}^{\infty}\frac{H_1^{(1)}(kR_1+\mu^2)}{\sqrt{\mu^2+2kR_1}}d\mu + ik\int_{m_2}^{\infty}\frac{H_1^{(1)}(kR_2+\mu^2)}{\sqrt{\mu^2+2kR_2}}d\mu, \tag{4}$$

where $m_1=\sqrt{k(L-R_1)}$, $m_2=\sqrt{k(L-R_2)}$, k is the wave number of the incident wave, R_2 is the direct distance between the image source and the receiver, and $H_1^{(1)}$ is the Hankel function of the first kind. A considerable amount of research has been published on innovative ways to simplify Eq. (4) (see, for example, Refs. 16 and 17). However, even these simplified versions of Eq. (4) are not nearly as simple and easy to apply as Eq. (3). It can be observed that the MacDonald solution requires knowledge of four parameters: k, R_1, R_2, and L. Maekawa's work suggests that all four parameters can be collapsed into one, the Fresnel number. As a result, multiple source–receiver configurations can be found that have the same Fresnel number but result in different IL.

Consider a spherically spreading incident wave, source located at $(r_0,\phi_0,0)$ and receiver at (r,ϕ,z). In the following, the distances r_0, r, z_0, z, are reported in dimensionless form (normalized by the incident wavelength), and the angles, ϕ_0 and ϕ, in degrees. The predictions from the MacDonald solution are inserted in the Maekawa chart in order to provide a graphical illustration of the comparisons, while the arithmetic value of the discrepancies is computed by the Kurze–Anderson formula.

Figure 1 illustrates two cases where Maekawa's chart gives predictions that deviate largely from the analytical solution. Point $\overline{A}$ in the graph represents the IL for a source–receiver configuration where both source and receiver are close to the barrier $[(r_0,\phi_0,z_0)=(5,5°,0)$ and $(r,\phi,z)=(5,355°,0)]$. Point $\overline{B}$ represents the IL for a source–receiver configuration where the receiver is at the shadow boundary $[(r_0,\phi_0,z_0)=(1,20°,0)$ and $(r,\phi,z)=(1,200°,0)]$. The observed discrepancy for the first case is 15 dB, and for the second 3 dB. The deviations presented are representative

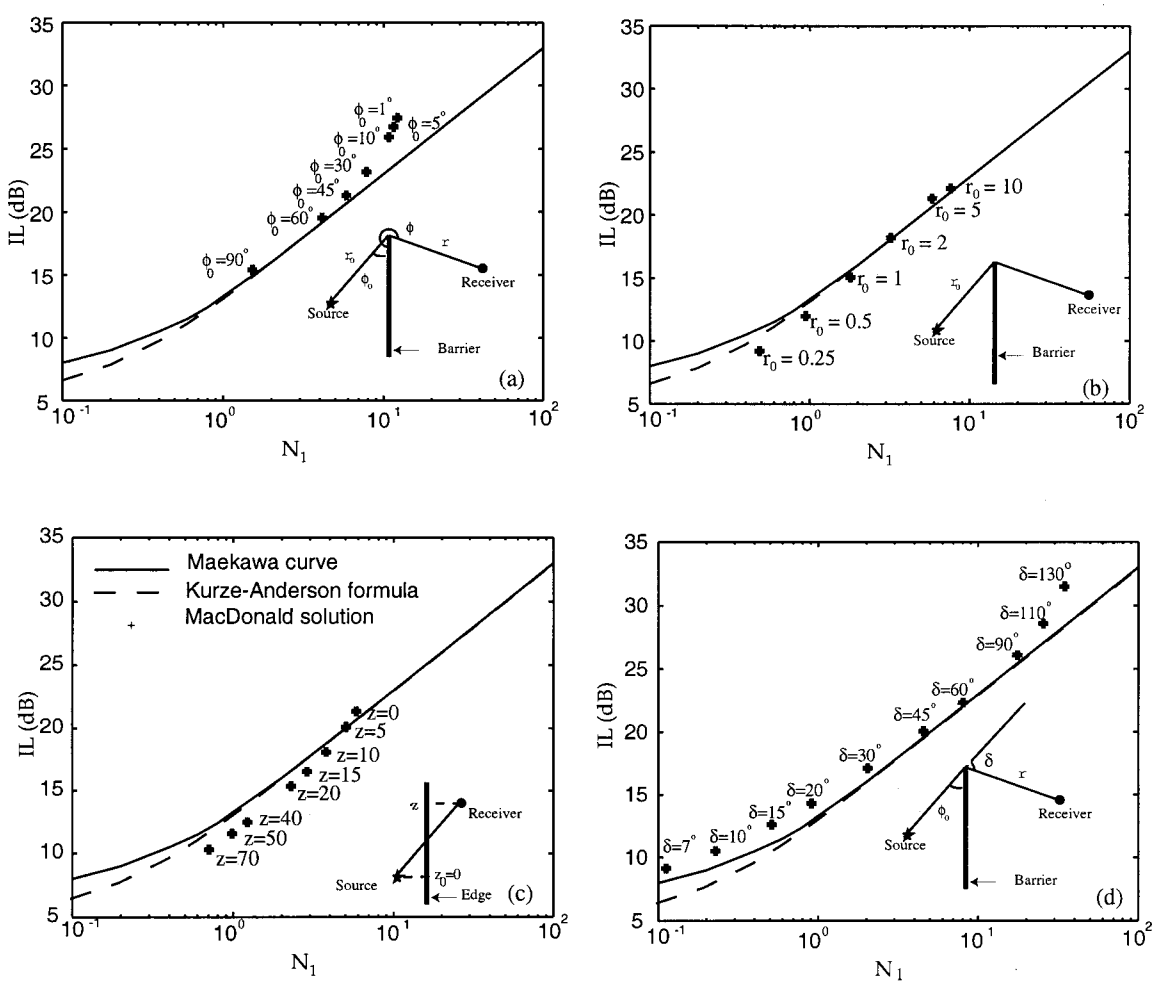

FIG. 2. Comparisons between Maekawa's curve (solid line), the Kurze–Anderson formula (dashed line), and the MacDonald solution ("+"); source moves closer to the barrier surface [(a)]; source moves closer to the edge [(b)]; receiver moves parallel to the edge of the barrier [(c)]; receiver moves away from the shadow boundary towards the surface of the barrier [(d)].

of the two types of geometrical configuration. The first type of configuration can give discrepancies of large amplitude, theoretically infinite as r_0 and r approach infinity and ϕ_0 and ϕ approach 0° and 360°, respectively. The second type of configuration gives discrepancies of modest amplitude, which do not exceed 5–6 dB.

Let us now demonstrate a systematic comparison between Maekawa's results and the MacDonald solution. Figure 2(a) illustrates comparisons between Maekawa's chart, the Kurze–Anderson formula, and the MacDonald solution, as the source moves closer to the barrier. The angle of incidence, ϕ_0, varies from 90° to 1°. The agreement deteriorates as the source moves closer to the barrier. The discrepancy between Maekawa's chart and analytical solution exceeds 3 dB for source locations close to the barrier. Figure 2(b) shows comparisons, as the source moves closer to the edge of the barrier. The radial distance from the source to the barrier edge, r_0, varies from 0.25 to 50 wavelengths. The agreement deteriorates slightly as the source moves closer to the edge, but, nevertheless, remains good for all comparisons (less than 1.5-dB difference). In Fig. 2(c), the effect of changing the receiver's axial position, z, is investigated. The axial position, z, varies from 0 to 70 wavelengths. The agreement is good for all points. Finally, Fig. 2(d) illustrates the same comparisons as the receiver moves from positions very close to the shadow boundary to positions very close to the barrier surface. Accordingly, the angle of diffraction, δ, varies from 7° to 130°. The agreement is good when the receiver is away from both the shadow boundary and the barrier, but it deteriorates (more than 2-dB difference) when the receiver approaches either of them.

In conclusion, it can be observed that Maekawa's curve and the exact solution are in agreement for a broad range of cases. The discrepancies are less than 1.5 dB. Discrepancies greater than that can be found in the following two cases: (i) source or receiver is very close to or at the barrier [see Figs. 1, 2(a), and 2(d)], or (ii) receiver is very close to or at the shadow boundary [see Figs. 1 and 2(d)].

III. A NEW CHART AS A CORRECTION TO MAEKAWA'S CHART

The goal of the present work is to bridge the Maekawa curve with the exact solutions by providing a graph that has both the simplicity of the Maekawa curve and the accuracy of the exact solutions. In the following, appropriate parameters are defined and an equation for the IL obtained by exact solutions is presented. The presentation of this equation in a

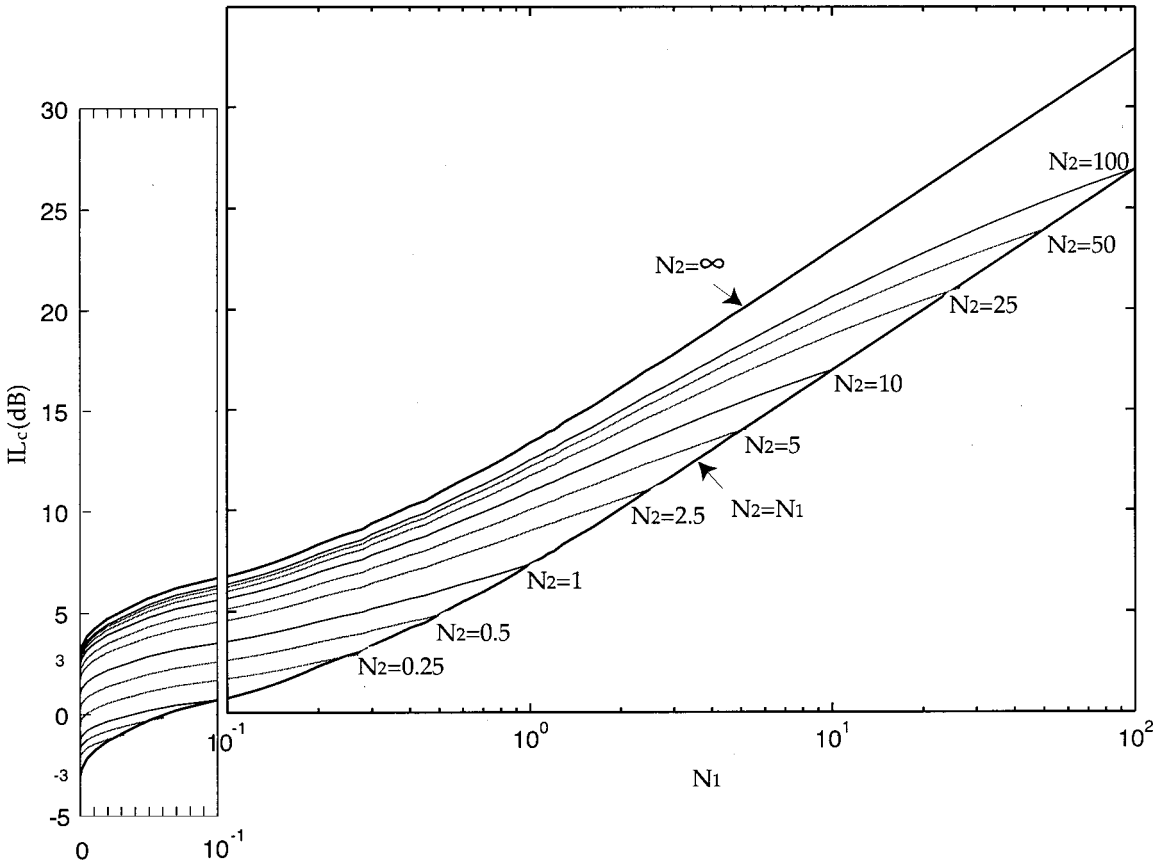

FIG. 3. A new graph as a correction to the Maekawa curve; IL_c is the part of the insertion loss that is common for plane, cylindrical, and spherical incident waves [Eq. (6)]; N_1 is the conventional Fresnel number associated with the source; N_2 is an additional Fresnel number associated with the image source [Eq. (8)]; total insertion loss $IL=IL_c+IL_{sp}$ [IL_{sp} given by Eq. (7)]; barrier modeled as an infinitely thin, rigid half plane.

form of a diagram similar to that of Maekawa is demonstrated and its relation to the Maekawa chart is discussed.

It can be shown (see the Appendix) that the IL behind a barrier for all three types of simple incident radiation (plane, cylindrical, and spherical waves) can be expressed in a unified way as follows:

$$IL = IL_c + IL_{sp}, \tag{5}$$

$$IL_c = -10\log\left|[F(\infty)-F(\sqrt{2N_1})] + e^{i\pi(N_1-N_2)}[F(\infty)-F(\sqrt{2N_2})]\right|^2, \tag{6}$$

$$IL_{sp} = \begin{cases} 3 \text{ dB} & \text{for plane waves,} \\ -10\log\dfrac{1}{\left(\dfrac{L}{R_1}\right)+1} & \text{for cylindrical waves,} \\ -10\log\dfrac{1}{\left(\dfrac{L}{R_1}\right)^2+\left(\dfrac{L}{R_1}\right)} & \text{for spherical waves,} \end{cases} \tag{7}$$

where F denotes Fresnel integrals. It can be observed that the IL is a function of the following three parameters:

$$N_1 = 2\frac{L-R_1}{\lambda}, \quad N_2 = 2\frac{L-R_2}{\lambda}, \quad \frac{L}{R_1}. \tag{8}$$

The parameter N_1 is the conventional Fresnel number, which is associated with the relative position of the source to the barrier and the receiver. The parameter N_2 can be thought of as a second Fresnel number that is associated with the relative position of the image source to the barrier and the receiver. Similar to N_1, N_2 is defined as the extra distance that the sound travels from the image source to the receiver after diffraction by the edge of the barrier, normalized by half the wavelength of the incident wave. The third parameter is the ratio of the distances the sound travels with and without the barrier present. The Appendix provides an appropriate definition of the distances L, R_1, and R_2 in the case of a plane incident wave. It can be observed that the first term in Eq. (5), IL_c, is a function on the two Fresnel numbers, N_1 and N_2, and is the same for all three types of incident radiation. The second term, IL_{sp}, depends on the ratio L/R_1 and is different for the different types of incident radiation.

One of the advantages of Eq. (6) is that is provides the IL behind a barrier in terms of Fresnel integrals, which are well-studied tabulated functions. The second, and perhaps the most important, advantage of Eq. (6) is that it can be presented as an easy-to-use diagram. Equation (6) represents a family of curves as shown in Fig. 3. Each curve corresponds to a different N_2 and provides the IL_c versus N_1. Note that for presentation purposes the N_1 axis in Fig. 3 is on logarithmic scale for $N_1>0.1$ and on linear scale for $N_1<0.1$. It can be observed that the family of curves is bounded by two basic curves. The lower bound is the curve corresponding to $N_2=N_1$ (the minimum value of N_2), while the

upper bound is the curve that corresponds to $N_2 \to \infty$ (the maximum value of N_2). Note that the minimum value of N_2 is obtained when either the source or the receiver (or both) is on the surface of the barrier, while the maximum value of N_2 is obtained when the surface of the barrier is considered absorbent, instead of rigid. In this case, the image source must be placed infinitely far from the barrier rendering the value of N_2 infinite. The mathematical formulations of the bounding curves as obtained from Eq. (6) are

$$\mathrm{IL_c}|_{N_2=N1} = -6 - 10\log|F(\infty) - F(\sqrt{2N_1})|^2, \tag{9}$$

$$\mathrm{IL_c}|_{N_2\to\infty} = -10\log|F(\infty) - F(\sqrt{2N_1})|^2. \tag{10}$$

Note that Eqs. (9) and (10) represent identical curves, but transposed by 6 dB. Therefore, it can be observed that for the same N_1 the value of $\mathrm{IL_c}$ can vary up to 6 dB depending on the value of N_2.

It should be emphasized that the same graph can be used for plane, cylindrical, and spherical incident waves. The total value of IL can be found by adding $\mathrm{IL_{sp}}$ to the value read on the graph, where $\mathrm{IL_{sp}}$ depends on the geometrical spreading of the incident wave [Eq. (7)]. The minimum value of $\mathrm{IL_{sp}}$ is 3 dB for all three types of incident radiation and is obtained when L/R_1 is minimum (equal to 1); that is, when the source is at the shadow boundary. For plane incident waves, $\mathrm{IL_{sp}}$ remains constant, while for cylindrical and spherical waves it increases with increasing L/R_1, yielding, as expected, greater IL for spherically spreading waves than for cylindrically spreading waves.

Figure 4 shows that Maekawa's results can be reproduced from the method presented here by appropriately choosing the parameters N_2/N_1 and L/R_1. For Fig. 4(a) we chose $N_2/N_1 = 1$ and $L/R_1 = 1.6$, while for Fig. 4(b) $N_2/N_1 = 6$ and $L/R_1 = 1$. The underlying assumption in Maekawa's work is that for the majority of source–receiver configurations the values of the ratios N_2/N_1 and L/R_1 are within the stated limits. Errors are introduced whenever one of the two ratios is close to its minimum value. Consider, first, the case where both source and receiver are very close to the barrier. This renders the Fresnel numbers N_2 and N_1 equal. For Maekawa's chart to yield accurate predictions the value of the ratio L/R_1 must be 1.6 [Fig. 4(a)]. This is obviously not always true, and therefore errors are introduced. Consider now the case where the receiver is at the shadow boundary. This renders L/R_1 unity. For Maekawa's chart to yield accurate predictions the value of the ratio N_2/N_1 must be 6 [Fig. 4(b)]. Again, this is not always true.

IV. A NEW FORMULA AS A CORRECTION TO THE KURZE–ANDERSON FORMULA

In the present section the Kurze–Anderson formula is appropriately modified so that is describes the family of curves in Fig. 3. Our goal is to propose a formula that contains elementary functions and describes the new graph with at least the same degree of accuracy that the Kurze–Anderson formula describes the Maekawa chart.

Our extensive numerical experimentation resulted in the following formula:

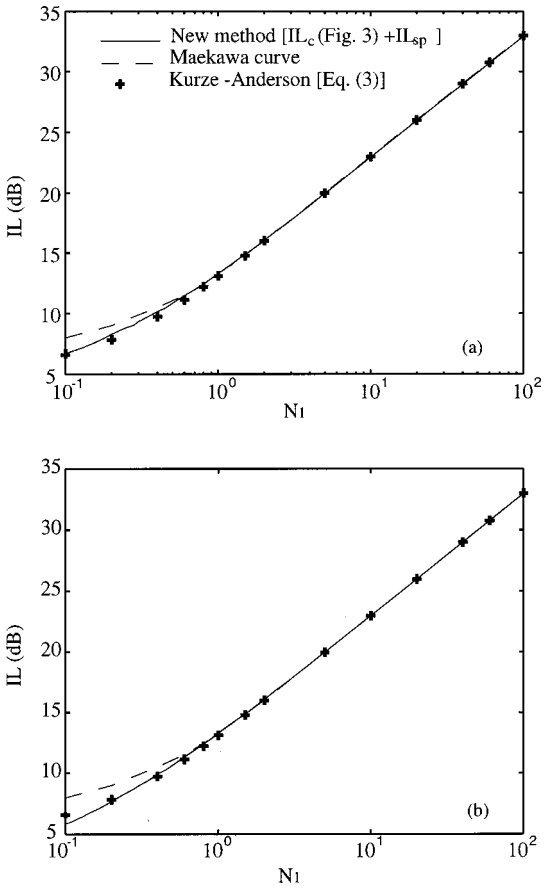

FIG. 4. Maekawa's curve (dashed line) and the Kurze–Anderson formula ("+") can be reproduced from the new method (solid line); in (a) $N_2/N_1 = 1$ and $L/R_1 = 1.6$; in (b) $N_2/N_1 = 6$ and $L/R_1 = 1$.

$$\mathrm{IL} = \mathrm{IL_s} + \mathrm{IL_b} + \mathrm{IL_{sb}} + \mathrm{IL_{sp}} = \mathrm{IL_c} + \mathrm{IL_{sp}}, \tag{11}$$

where

$$\mathrm{IL_s} = 20\log\frac{\sqrt{2\pi N_1}}{\tanh\sqrt{2\pi N_1}} - 1, \tag{12}$$

$$\mathrm{IL_b} = 20\log\left[1 + \tanh\left(0.6\log\frac{N_2}{N_1}\right)\right], \tag{13}$$

$$\mathrm{IL_{sb}} = (6\tanh\sqrt{N_2} - 2 - \mathrm{IL_b})(1 - \tanh\sqrt{10N_1}), \tag{14}$$

and $\mathrm{IL_{sp}}$ is given by Eq. (7). The first term, $\mathrm{IL_s}$, is a function of N_1, which is a measure of the relative position of the receiver to the *source*. The second term is a function of N_2/N_1, which is a measure of the proximity of either the source or the receiver to the *barrier* surface. The third term is appreciable and needs to be computed only when N_1 is very small, which in turn is a measure of the proximity of the receiver to the *shadow boundary*. The first three terms add up to create $\mathrm{IL_c}$. Finally, the fourth term is the only term that depends on the type of incident radiation, is $\mathrm{IL_{sp}}$, and it should be recalled that it is a function of the ratio L/R_1.

Figure 5 shows reasonable agreement between the new family of curves and the proposed formula for $\mathrm{IL_c}$. It should be noted that, because the graph in Fig. 5(a) does not contain values of N_1 less than 0.1, only $\mathrm{IL_s}$ and $\mathrm{IL_b}$ have been used to compute $\mathrm{IL_c}$. The contribution from $\mathrm{IL_{sb}}$ for the values of

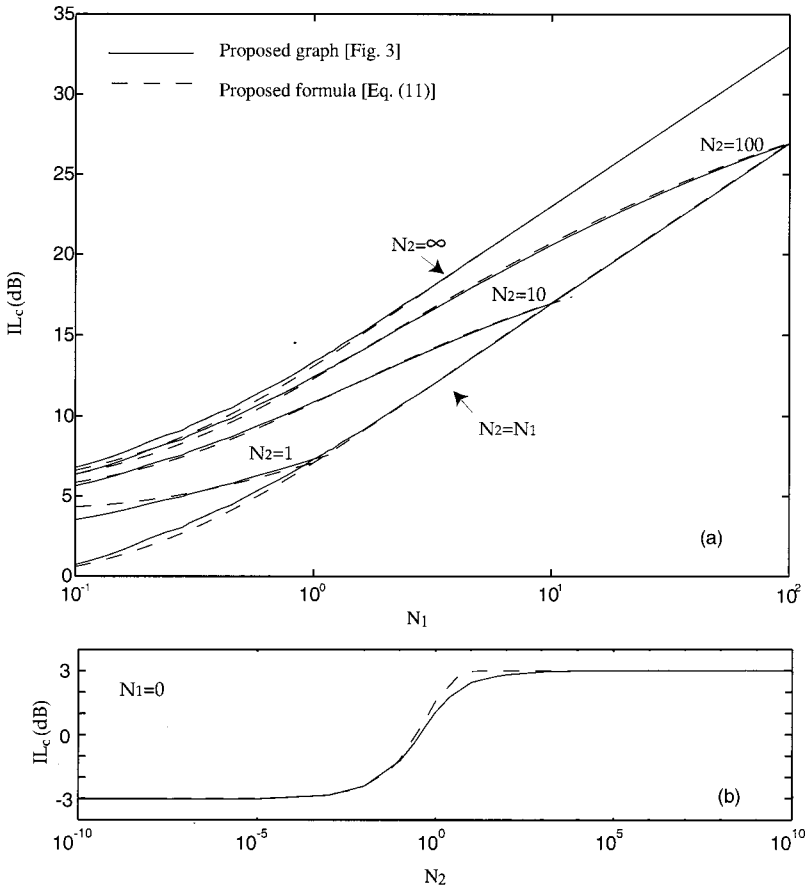

FIG. 5. Reasonably good agreement between the graph in Fig. 3 and Eq. (11), which is a correction to the Kurze–Anderson formula.

N_1 in Fig. 5(a) is negligible. This contribution is appreciable only when $N_1 \rightarrow 0$. Figure 5(b) shows the comparison between the graph and the proposed formula in this specific case.

The suggested formula not only provides a reasonably good description of the new chart, but a careful analysis of its terms offers an understanding for the inaccuracies of Maekawa's chart discussed in this paper. It should be noted that Eq. (12), which represents the first term in Eq. (11), is identical to the original Kurze–Anderson equation [Eq. (3)], but reduced by 6 dB. In other words, Maekawa's work suggests that the sum of the remaining terms in Eq. (11) ($IL_b + IL_{sb} + IL_{sp}$) is always 6 dB. This is the assumption that gives rises to the inaccuracies discussed in this paper. Let us examine each one of the terms in Eq. (11) and particularly their range of values.

The values of IL_s range from -1 to infinity, as can be seen in Fig. 6(a). As expected, the protection offered by the barrier increases as the receiver moves deeper into the shadow zone.

The values of IL_b range from 0 to 6 dB [see Fig. 6(b)]. It should be noted that the minimum contribution of IL_b to IL occurs when $N_2/N_1 = 1$ (source or receiver on the barrier), while the maximum occurs when $N_2/N_1 \rightarrow \infty$ (reflections from the barrier are ignored). In the former case, the pressure field at the receiver is enforced (and thus the shielding effect of the barrier reduced) because of the "pressure-doubling" effect. In the latter case, the shielding effect of the barrier is increased because the contributions from the reflected field at the receiver location are ignored. At any rate, it should be observed that by ignoring the correct value of N_2 in the calculations for the IL, we introduce errors of up to 6 dB.

Equation (14) needs to be computed only when the receiver is at, or very close to the shadow boundary. Maekawa's work suggests that at the shadow boundary the IL is 5 dB [see Eq. (3)]. The present work, however, indicates that the IL can vary from 0 to 6 dB (see Fig. 3 for $N_1 = 0$ and $IL_{sp} = 3$ dB). Ignoring the value of N_2 in the calculations when the receiver is at the shadow boundary can result in a 5-dB error. This type of error was demonstrated in Sec. II (point $\overline{B}$ in Fig. 1).

Finally, the values for IL_{sp} range from 3 dB to infinity [see Fig. 6(d)] as L/R_1 increases from 1 to infinity. It should be emphasized that because IL_{sp} does not have an upper bound, ignoring the correct value of L/R_1, and thus the contributions to Eq. (11) from IL_{sp}, can result in substantial errors. This type of error was also demonstrated in Sec. II (point $\overline{A}$ in Fig. 1).

In conclusion, the proposed formula contains elementary functions, involves simple calculations, and provides a reasonably accurate description of the new graph. Furthermore, the proposed formula, and particularly the analysis of its terms, provides an explanation of the inaccuracies of Maekawa's chart discussed in Sec. II.

V. A NEW EQUATION AS A CORRECTION TO THE KIRCHHOFF SOLUTION

In the following we investigate the relation of the work presented here to the Kirchhoff solution, which is perhaps

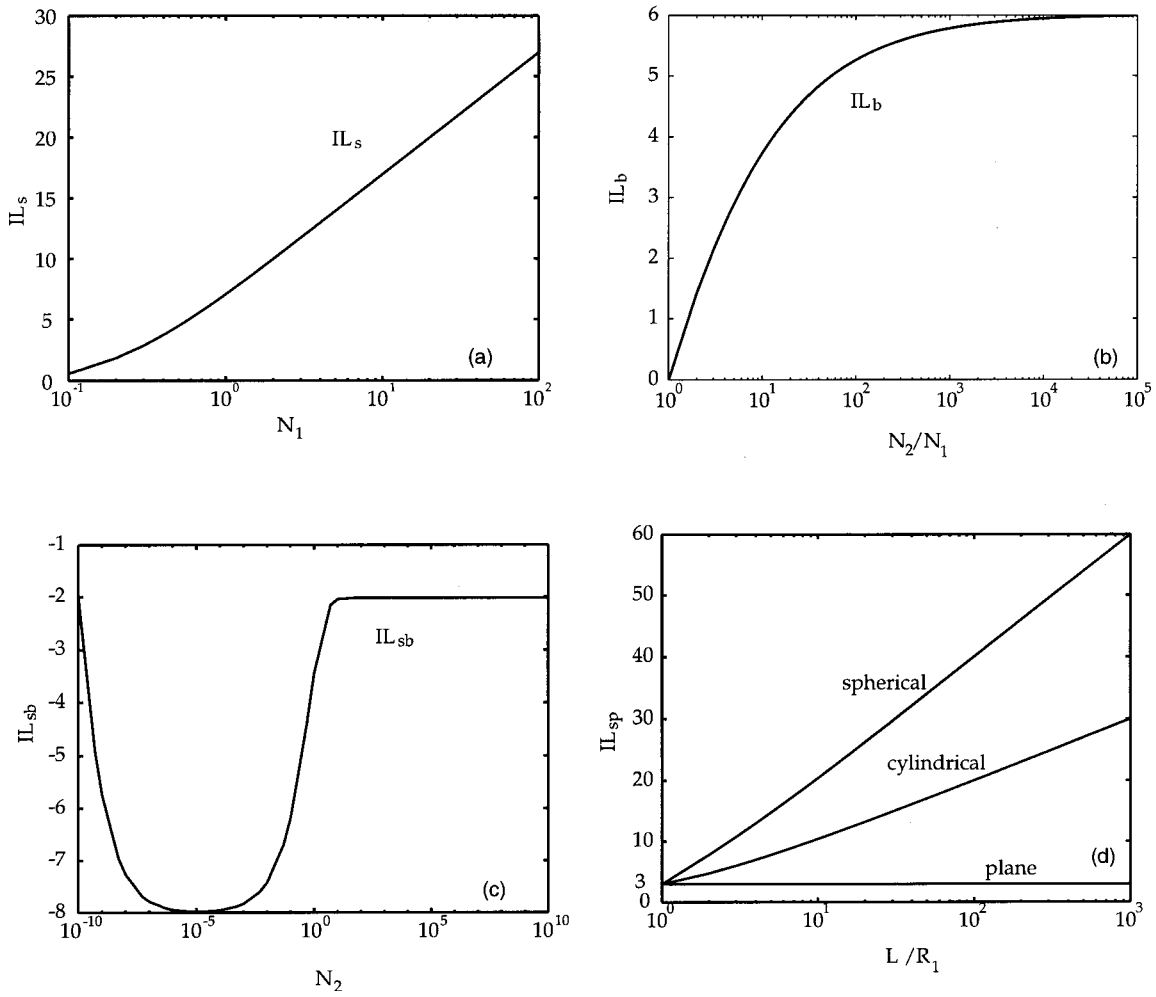

FIG. 6. Graphical representation of Eqs. (12) [(a)], (13) [(b)], (14) [(c)], and (7) [(d)].

the most widely used analytical solution for sound diffraction within the noise communities.

Let us briefly revisit the Kirchhoff solution.[18] For a receiver in the shadow zone, the IL obtained by the Kirchhoff solution can be expressed in terms of Fresnel integrals as follows:

$$\mathrm{IL}_{\mathrm{Kirchhoff}} = -10\log|F(\infty)-F(w)|^2 - 10\log\left|\frac{1-i}{2}\right|^2, \tag{15}$$

where $w = x/\sqrt{\lambda a/2}$ for plane incident waves and $w = \sqrt{2/\lambda(a^{-1}+b^{-1})}h$ for spherical incident waves (see the inset of Fig. 7 for a definition of the distances x, a, b, h). Equation (15) is accurate when the reflections from the surface of the barrier are ignored and the receiver is close to the shadow boundary.[16,18]

Despite the severe restrictions and the reported discrepancies with experimental data,[19] the Kirchhoff solution has found extensive use, mainly because it is expressed in terms of Fresnel integrals, which are well-studied tabulated functions. One of the advantages of Eq. (6), which was presented in Sec. III, is that it provides the IL behind a barrier in terms of Fresnel integrals. Because it stems from the exact solutions, it has none of the above restrictions, yet is as simple as the Kirchhoff solution. We would therefore like to draw attention to this fact and suggest the use of Eq. (6) as a correction to the Kirchhoff solution.

Comparison of Eqs. (15) and (5) leads to the following observations. The second Fresnel number (N_2) does no appear in the Kirchhoff solution. This is explained by the fact that the Kirchhoff theory does not take into account the reflections from the barrier and thus the relative position of the image source to the receiver. It should also be noted that the predictions obtained by the Kirchhoff solution are the same for both plane and spherical incident waves. This is expected, because the Kirchhoff solution is valid at points close to the shadow boundary, where $\mathrm{IL}_{\mathrm{sp}}$ (the only contribution to the IL that depends on the type of the incident wave) is the same for all types of incident radiation. Finally, it can be observed that Eq. (15) is similar in form to Eq. (5). The first term in Eq. (15) corresponds to IL_{c} (with $w = \sqrt{2N_1}$) and the second to $\mathrm{IL}_{\mathrm{sp}}$. Consider, for example, spherical incident waves. The Fresnel number N_1 becomes

$$N_1 = 2\,\frac{a\sqrt{1+\frac{h^2}{a^2}} + b\sqrt{1+\frac{h^2}{b^2}} - a - b}{\lambda}. \tag{16}$$

Now, because the Kirchhoff solution is valid for receiver

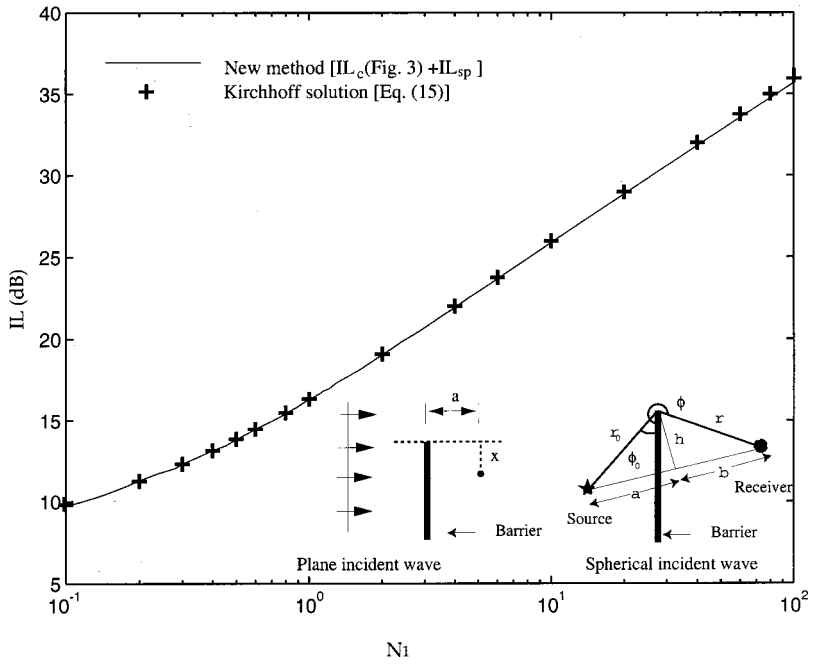

FIG. 7. The new method (solid line) matches results from the Kirchhoff solution ("+") [Eq. (15)] for $N_2 \rightarrow \infty$ and $L/R_1 = 1$.

locations close to the shadow boundary, we have $a \gg h$ and $b \gg h$. This yields

$$N_1 \approx 2\,\frac{a+\frac{h^2}{2a}+b+\frac{h^2}{2b}-a-b}{\lambda} = \frac{h^2}{\lambda}\left(\frac{1}{a}+\frac{1}{b}\right) = \frac{w^2}{2}. \tag{17}$$

Finally, it should be noted that the Kirchhoff solution can be reproduced from the new method, if we assign appropriately the values of N_2 and L/R_1, so that they represent the assumptions embodied in the Kirchhoff theory. We let $N_2 \rightarrow \infty$ to account for the fact that contributions from the image source are ignored and $L/R_1 = 1$ to account for the fact that the receiver is located close to the shadow boundary. Figure 7 shows that the new method matches results from the Kirchhoff solution in the regions where the latter is valid.

VI. SUMMARY/CONCLUSIONS

Maekawa's curve gives predictions that deviate largely from experimental data and analytical solutions when the source or receiver is very close to or at the barrier surface, or when the receiver is very close to or at the shadow boundary. An equation was presented that is based on existing analytical solution for sound diffraction and provides the IL behind barriers using two appropriately defined Fresnel numbers (N_1 and N_2) and the ratio L/R_1. The first Fresnel number (N_1) is the conventional Fresnel number and is associated with the relative position of the source to the barrier and the receiver. The second Fresnel number (N_2) is defined similarly to N_1 and represents the relative position of the image source to the barrier and the receiver. A new graph was thus proposed as a correction to Maekawa's chart. The single curve in Maekawa's chart is replaced by a family of curves. Each curve corresponds to a different N_2 and provides the IL versus N_1. Unlike the Maekawa chart, the graph presented here can be used for all three types of simple incident radiation (plane, cylindrical, and spherical incident waves). The new graph offers increased accuracy in the cases where Maekawa's does not. A modification to the Kurze–Anderson formula was also proposed. The proposed formula contains elementary functions, involves simple calculations, and provides a reasonably accurate description of the new graph. Finally, attention was drawn to the fact that the equation presented here for predicting the IL is similar in form with the well-known Kirchhoff solution, but more accurate. It can, therefore, be used as a correction to the Kirchhoff solution.

ACKNOWLEDGMENT

The work presented here was supported by the Texas Advanced Technology Program and the F. V. Hunt Postdoctoral Research Fellowship from the Acoustical Society of America.

APPENDIX A: COMMENTS ON THE DEFINITION OF THE FRESNEL NUMBERS

The definitions of the Fresnel numbers N_1 and N_2 [as shown in Eq. (8)] are applicable for plane, cylindrical, and spherical incident waves. In cases of cylindrical and spherical incident waves, R_1, R_2, and L are defined in the nomenclature. In the case of plane incident waves, however, these definitions yield infinite values for R_1, R_2, and L. A modified definition is therefore suggested. We define L to be the distance from the diffracting edge to the receiver, R_1 the distance between the receiver and the incident wavefront that grazes the edge [see Fig. 8(a)], and R_2 the distance between the receiver and the wavefront of the reflected signal that grazes the edge [see Fig. 8(b)]. Caution should be exercised when one calculates the extra distance the sound travels due to the presence of the barrier, i.e., the numerator of N_1 and N_2 in Eq. (8). The extra distance the incident signal travels in Fig. 8(a) is $L-R_1$, while the extra distance the reflected signal travels in Fig. 8(b) is $L+R_2$.

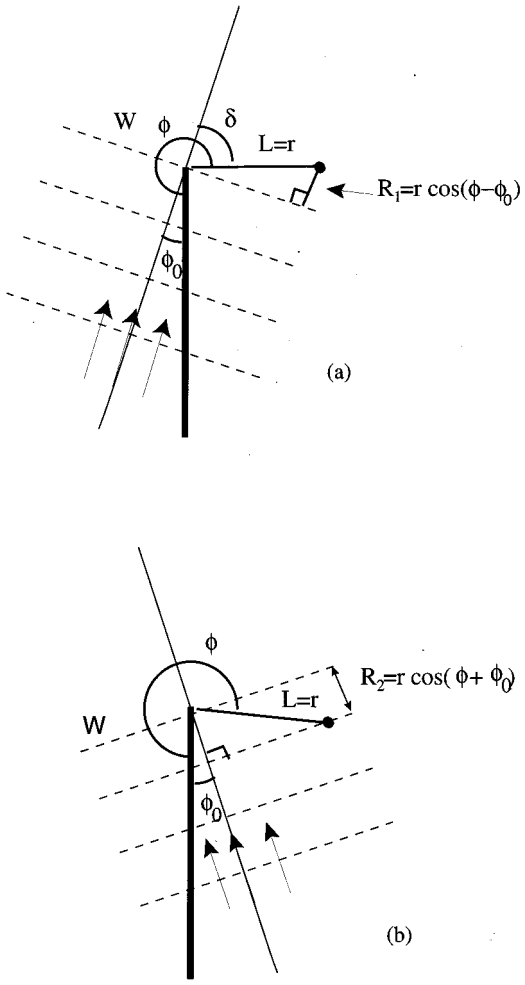

FIG. 8. Plane wave incident on a half-plane; incident wave shown in (a); reflected wave shown in (b).

APPENDIX B: DERIVATION OF EQS. (5), (6), AND (7)

1. Spherical incident waves

Assume a point source S located at (r_0,ϕ_0,z_0) and a receiver A in the shadow zone at (r,ϕ,z). If the shortest diffraction path is longer than one wavelength of the incident wave $(kL\gg 1)$, then the diffracted field at A can be expressed in terms of Fresnel integrals as follows:[7,11]

$$P_d(A)=\frac{ke^{-i(\pi/4)}}{\sqrt{kL}}\frac{e^{ikR_1}}{\sqrt{k(L+R_1)}}[F(\infty)-F(\sqrt{2N_1})]+\frac{ke^{-i(\pi/4)}}{\sqrt{kL}}\frac{e^{ikR_2}}{\sqrt{k(L+R_2)}}[F(\infty)-F(\sqrt{2N_2})]. \tag{B1}$$

The pressure at the same point without the barrier present is

$$P_o(A)=\frac{e^{ikR_1}}{R_1}, \tag{B2}$$

where the time dependence has been assumed to be $e^{-i\omega t}$.

In order to compute the IL behind the barrier [Eq. (1)], the ratio of $P_d(A)$ and $P_o(A)$ is needed

$$\frac{P_d(A)}{P_o(A)}=\frac{e^{-i(\pi/4)}}{\sqrt{\left(\frac{L}{R_1}\right)^2+\left(\frac{L}{R_1}\right)}}[F(\infty)-F(\sqrt{2N_1})]+\frac{e^{-i(\pi/4)}e^{i\pi(N_1-N_2)}}{\sqrt{\left(\frac{L}{R_1}\right)^2+\left(\frac{LR_2}{R_1^2}\right)}}[F(\infty)-F(\sqrt{2N_2})], \tag{B3}$$

where Eq. (8) has been used to substitute $e^{ik(R_2-R_1)}$ with $e^{i\pi(N_1-N_2)}$ in the second term of the above equation. Assume now that we can replace R_2 by R_1 (in other words, $R_2\approx R_1$) in the denominator of the second term. Subsequently, substitution of Eq. (B3) into Eq. (1) yields

$$\mathrm{IL}=-10\log\left|[F(\infty)-F(\sqrt{2N_1})]+e^{i\pi(N_1-N_2)}\times[F(\infty)-F(\sqrt{2N_2})]\right|^2-10\log\frac{1}{\left(\frac{L}{R_1}\right)^2+\left(\frac{L}{R_1}\right)}. \tag{B4}$$

2. Cylindrical incident waves

The diffracted field at a receiver location A behind a barrier at (r,ϕ) that is produced by a line source located at (r_0,ϕ_0) can be also expressed in terms of Fresnel integrals, if $kL\gg 1$[7,11]

$$P_d(A)=\frac{2}{i\pi}\sqrt{\frac{\pi}{2}}\frac{e^{ikR_1}}{\sqrt{k(L+R_1)}}[F(\infty)-F(\sqrt{2N_1})]+\frac{2}{i\pi}\sqrt{\frac{\pi}{2}}\frac{e^{ikR_2}}{\sqrt{k(L+R_2)}}[F(\infty)-F(\sqrt{2N_2})]. \tag{B5}$$

The pressure at the same point without the barrier present is

$$P_o(A)=H_0^{(1)}(kR_1)\approx\sqrt{\frac{2}{kR_1\pi}}e^{ikR_1}e^{-i(\pi/4)}. \tag{B6}$$

In order to compute the IL behind the barrier [Eq. (1)], the ratio of $P_d(A)$ and $P_o(A)$ is needed. The ratio, with the help of Eq. (8), becomes

$$\frac{P_d(A)}{P_o(A)}=\frac{e^{-i(\pi/4)}}{\sqrt{\left(\frac{L}{R_1}\right)+1}}[F(\infty)-F(\sqrt{(2N_1)})]+\frac{e^{-i(\pi/4)}e^{i\pi(N_1-N_2)}}{\sqrt{\left(\frac{L}{R_1}\right)+\left(\frac{R_2}{R_1}\right)}}[F(\infty)-F(\sqrt{2N_2})]. \tag{B7}$$

As in the case of spherical waves, we substitute R_2 with R_1 in the denominator of the second term in Eq. (B7), and then Eq. (B7) into Eq. (1), to obtain

$$\mathrm{IL}=-10\log\left|[F(\infty)-F(\sqrt{2N_1})]+e^{i\pi(N_1-N_2)}\times[F(\infty)-F(\sqrt{2N_2})]\right|^2-10\log\frac{1}{(L/R_1)+1}. \quad \text{(B8)}$$

It should be noted that the first term in Eqs. (B4) and (B8) is the same (regardless of the type of the incident radiation). It is the second term in Eqs. (B4) and (B8), which is a function of L/R_1, that differs.

3. Plane incident waves

Consider a plane wave incident on a barrier at an angle ϕ_0 and a receiver A at (r,ϕ) behind the barrier. The diffracted field at A can be expressed in terms of Fresnel integrals exactly without any approximations[7,11]

$$P_d(A)=e^{-ikr\cos(\phi-\phi_0)}\frac{1-i}{2}\times\left[F(\infty)-F\left(2\sqrt{\frac{kr}{\pi}}\cos\frac{\phi-\phi_0}{2}\right)\right]+e^{-ikr\cos(\phi+\phi_0)}\frac{1-i}{2}\times\left[F(\infty)-F\left(2\sqrt{\frac{kr}{\pi}}\cos\frac{\phi+\phi_0}{2}\right)\right]. \quad \text{(B9)}$$

The definitions of the Fresnel numbers in the case of plane incident waves [see Eq. (8) and Appendix A] yield

$$N_1=2\frac{L-R_1}{\lambda}=2\frac{kr}{\pi}\cos^2\left(\frac{\phi-\phi_0}{2}\right)$$
$$N_2=2\frac{L-R_2}{\lambda}=2\frac{kr}{\pi}\cos^2\left(\frac{\phi+\phi_0}{2}\right). \quad \text{(B10)}$$

The above equations can be used to bring Eq. (B9) into the same form as Eqs. (B1) and (B5)

$$P_d(A)=e^{-ikr\cos(\phi-\phi_0)}\frac{1-i}{2}[F(\infty)-F(\sqrt{2N_1})]+e^{-ikr\cos(\phi+\phi_0)}\frac{1-i}{2}[F(\infty)-F(\sqrt{2N_2})]. \quad \text{(B11)}$$

The pressure at the same point without the barrier present is

$$P_o(A)=e^{-ikr\cos(\phi-\phi_0)}, \quad \text{(B12)}$$

and the ratio of $P_d(A)$ and $P_o(A)$ becomes

$$\frac{P_d(A)}{P_o(A)}=\frac{1-i}{2}[F(\infty)-F(\sqrt{2N_1})]+e^{-ikr[\cos(\phi+\phi_0)-\cos(\phi-\phi_0)]}\frac{1-i}{2}\times[F(\infty)-F(\sqrt{2N_2})]. \quad \text{(B13)}$$

Equation (B11) can be used to bring the exponential in the second term to the familiar form $e^{i\pi(N_1-N_2)}$ [see Eqs. (B3) and (B7)]. By substitution of Eq. (B13) into Eq. (1), we obtain

$$\mathrm{IL}=-10\log\left|[F(\infty)-F(\sqrt{2N_1})]+e^{i\pi(N_1-N_2)}\times[F(\infty)-F(\sqrt{2N_1})]\right|^2-10\log\left|\frac{1-i}{2}\right|^2. \quad \text{(B14)}$$

Again, the first term in Eqs. (B4), (B8), and (B14) is the same (regardless of the type of the incident radiation), while the second depends on the type of incident radiation.

[1] Z. Maekawa, "Noise reduction by screens," Appl. Acoust. **1**, 157–173 (1968).
[2] Z. Maekawa, "Simple design method for various shaped noise barriers," in *Proceedings of the International Conference NOISE & VIBRATION '89*, Osaka, Japan (Elsevier, New York, 1989).
[3] U. J. Kurze, "Noise reduction by barriers," J. Acoust. Soc. Am. **55**, 504–518 (1974).
[4] U. J. Kurze and G. S. Anderson, "Sound attenuation by barriers," Appl. Acoust. **4**, 35–53 (1971).
[5] T. Kawai, K. Fujimoto, and T. Itow, "Noise propagation around a thin half-plane," Acustica **38**, 313–323 (1977).
[6] H. M. MacDonald, "A class of diffraction problems," Proc. London Math. Soc. **14**, 410–427 (1915).
[7] J. J. Bowman and T. B. A. Senior, *Electromagnetic and Acoustic Scattering by Simple Shapes*, edited by J. J. Bowman, T. B. A. Senior, and P. L. E. Uslenghi (North-Holland, Amsterdam, 1969).
[8] S. I. Hayek, "Mathematical modeling of absorbent highway noise barrier," Appl. Acoust. **31**, 77–100 (1990).
[9] H. Medwin and C. S. Clay, *Fundamentals of Acoustical Oceanography* (Academic, San Diego, 1998).
[10] H. Medwin, "Shadowing by finite noise barriers," J. Acoust. Soc. Am. **69**, 1060–1064 (1981).
[11] P. Menounou, I. J. Busch-Vishniac, and D. T. Blackstock, "Directive line source model: A new method for sound diffraction by half planes and wedges," J. Acoust. Soc. Am. **107**, 2973–2986 (2000).
[12] Y. W. Lam, "Using Maekawa's chart to calculate finite length barrier insertion loss," Appl. Acoust. **42**, 29–40 (1994).
[13] A. Muradali and K. R. Fyfe, "A study of 2D and 3D barrier insertion loss using improved diffraction-based methods," Appl. Acoust. **53**, 49–75 (1998).
[14] K. Takagi, "Some remarks on practical methods for calculating acoustical diffraction," Appl. Acoust. **31**, 119–132 (1990).
[15] M. Fukuda, *Noise Control Engineering* (Nikkankoyo, Tokyo, 1976).
[16] A. D. Pierce, *Acoustics: An Introduction to its Physical Principles and Applications* (Acoustical Society of America, American Institute of Physics, New York, 1989).
[17] P. C. Clemmow, "A note on the diffraction of a cylindrical wave by a perfectly conducting half-plane," Q. J. Mech. Appl. Math. **3**, 377–384 (1950).
[18] M. Born and E. Wolf, *Principles of Optics*, 3rd ed. (Pergamon, New York, 1965), pp. 375–382.
[19] G. M. Jebsen and H. Medwin, "On the failure of the Kirchhoff assumption in backscatter," J. Acoust. Soc. Am. **72**, 1607–1611 (1982).

Exact solutions for modeling sound propagation through a combustion zone

R. I. Sujith[a)]
Department of Aerospace Engineering, Indian Institute of Technology Madras, Chennai 600036, India

(Received 14 February 2001; accepted for publication 20 June 2001)

Exact analytical solutions for one-dimensional sound propagation through a combustion zone, taking the effects of mean temperature gradient and oscillatory heat release into account, are presented in this paper. The wave equation is derived starting from the momentum and energy equations. Using appropriate transformations, solutions are derived for the case of an exponential mean temperature gradient in terms of Bessel functions. For the case of a linear mean temperature profile, solutions are derived in terms of confluent hypergeometric functions. Example calculations show that the accuracy in modeling combustion–acoustics interactions can be significantly increased by the use of these solutions. © *2001 Acoustical Society of America.*
[DOI: 10.1121/1.1396332]

PACS numbers: 43.28.Kt [MSH]

NOMENCLATURE

a, b	constants in Eqs. (17) and (21)
B	constant in Eq. (11a)
C, d	constants in Eq. (12)
i	$=\sqrt{-1}$, imaginary number
k	wave number$=\omega/c$
p	pressure
P	acoustic pressure amplitude
q	heat release
Q	oscillatory heat release amplitude
R	gas constant
$\Re$	pressure coupled response
s	transformation variable in Eq. (19)
S	velocity coupled response
u	velocity
U	acoustic velocity amplitude
x	axial distance
t	time
T	temperature
α, β, σ	constants in Eq. (23)
δ	constant in Eq. (15)
ε	transformation variable in Eq. (19)
γ	ratio of specific heats
ν	order of Bessel function
ρ	density
ω	angular frequency
Ω	constant in Eq. (11)

Superscripts

$'$	oscillating quantity
-	time-averaged quantity

Subscript

n	region

I. INTRODUCTION

The occurrence of combustion instabilities has been a plaguing problem in the development of combustors for rockets, jet engines, and power generating gas turbines.[1] Predicting and controlling combustion instability requires an understanding of the interactions between the combustion process and the acoustic waves. In this context, it is important to model sound propagation through an unsteady combustion zone, including the effects of mean temperature gradient and oscillatory heat release.

A physical description of the effect of a mean temperature gradient can be visualized by assuming that the gas in the combustion zone consists of infinitesimally thin gas layers, each at a different (constant) temperature, that are in contact with one another. In this case, the propagation of sound from one layer to another is accompanied by wave transmission and reflection, which modifies the wave structure in the duct. The effect of an oscillatory heat release is to add acoustic energy to the system if it is in phase with the oscillatory pressure, and to remove acoustic energy from the system if it is out of phase with the oscillatory pressure.

During the onset of combustion instability, the unsteady heat release responds to the acoustic velocity and pressure oscillations. In gas-phase systems, often the heat release responds mainly to the acoustic velocity. This response, known as velocity coupling, can be caused by hydrodynamic instabilites[2,3] or by oscillations in flame surface area due to the acoustic oscillations.[4,5] In spray combustion systems, the periodic acceleration associated with a plane acoustic wave propagating normal to the flame surface will give rise to a phase lag between the velocity of the droplets and the velocity of the gas. This phase lag creates a periodic modulation of the flux of fuel which is being vaporized in the preheat zone. This unsteady flux of vaporized fuel is transported by convection and diffusion to the combustion zone, which pro-

[a)]Address for correspondence: DLR Göttingen, Bunsenstraße 10, 37073 Göttingen, Germany; electronic mail: Raman.sujith@dlr.de

duces a modulation in the combustion rate which is a function of the acoustic velocity.[6–9] When there is velocity coupling, the heat release will be proportional to the acoustic velocity, with a phase indicative of a time delay. This time delay depends upon the phenomena involved; for example, in a bluff body stabilized combustor, it will be dependent on the convective velocity,[3,10] and in a spray combustor, it is dependent on the droplet response to the acoustic velocity fluctuations.[6–8]

In solid propellant combustion, there are different types of premixed diffusion and partially premixed flamelets at different heights at different locations on the burning surface. Their response to acoustic (pressure and velocity) oscillations are different in terms of reaction rate, flame location, and thermal feedback to the burning surface. The response of the propellant to externally imposed acoustic oscillations is a collective response of these flamelets to these different processes.[11] In solid propellant combustion,[11,12] and also in certain gas turbine systems,[13–15] the heat release responds to the pressure oscillations also, known as pressure coupling. When there is pressure coupling, the heat release will be proportional to the acoustic pressure, with a phase indicative of a time delay. For example, in gas turbine systems, the time delay is mainly influenced by the equivalence ratio and it has been deduced in the past from blow-off experiments.[13,14] The unsteady combustion process can in general be modeled as a function of the acoustic quantities in the combustion region,[11,12,16] i.e., $Q=\Re P+SU$, where $\Re$ and S are the pressure and velocity coupled responses, respectively.

In most of the analysis, the flame is assumed to be of negligible thickness. When the thickness of a flame approaches zero, the relaxation time goes to zero, so that the interaction between a flame considered as a discontinuity and the external changes takes place instantaneously. In reality, there is a finite relaxation time due to processes such as mixing and chemical reactions. Therefore, changes do not occur instantaneously, and the combustion zone has a finite thickness.[17]

In many practical applications, the heat release is distributed over a significant length of the resonator.[10] For example, when a flame is stabilized in a duct in the wake of a bluff body, the combustion is initiated as the flow passes the flame holder, but the fluid continues to burn throughout the downstream portion of the duct. Langhorne[2] has shown that this can occur over a length which can be an appreciable fraction of the wavelength. In those solutions, where the finite thickness of the combustion zone is taken into account, the variation of mean temperature along this zone is not taken into account. Raun and Beckstead[18] have shown that the accurate estimation of the acoustic mode shape is essential to accurate prediction of growth rate in their instability model of a Rijke tube. They also show that accurate prediction of the mode shape requires integration of the acoustic equations using the accurate mean temperature profile. The same conclusions were arrived at by McIntosh and Rylands.[19]

To date, considerable efforts have been expended on the development of an understanding of wave propagation through inhomogeneous media. Munjal and Prasad[20] and Peat[21] have developed exact analytical solution for ducts with small temperature gradients, in the presence of mean flows. These solutions are used for studying automotive mufflers, but not for combustion zones, due to the restriction of a small temperature gradient. Sujith *et al.*[22] and Kumar and Sujith[23] present exact solutions for inhomogeneous, constant area ducts with specified temperature profiles, with arbitrarily large temperature gradients. Bala Subrahmanyam *et al.*[24] obtained a family of exact solutions for quasi-one-dimensional, transient acoustic wave propagation in ducts with mean temperature and area variations in the absence of mean flow. Lang *et al.*[25] has developed a model which includes the unsteady heat release, but does not take into account the temperature rise. Lieuwen and Zinn[16] investigated the application of multipole expansions to sound generation from ducted unsteady combustion processes.

Essentially all of the available exact solutions of the wave equation in nonconstant temperature ducts ignore the effect of unsteady heat release. Those which take the effect of heat release into account do not take the steep mean temperature gradient into account. Of course, numerical solutions that yield accurate results can be obtained. However, analytical solutions provide better insight and feel for the physics of the problem and can easily be incorporated into combustion instability models. Furthermore, analytical solutions can be used to benchmark numerical results.

A family of exact, explicit solutions for sound propagation in a combustion zone, taking into account the effect of an arbitrarily steep mean temperature gradient and oscillatory heat release, is presented in this paper. The paper is organized in the following manner. First, the one-dimensional wave equation for a constant area duct with an axial temperature gradient and oscillatory heat release in the absence of mean flow is derived for a perfect, inviscid, and non-heat-conducting gas. Using appropriate transformations, this equation is then reduced to Bessel's differential equation for an exponential mean temperature profile and the confluent hypergeometric equation for the case of a linear mean temperature profile. The paper closes with example calculations illustrating the application of the developed solutions. The analysis is valid only for small mean Mach numbers.

II. DERIVATION OF THE WAVE EQUATION

The derivation of the wave equation for a constant area duct in the presence of a mean temperature gradient and oscillatory heat release is presented in this section. Assuming a perfect, inviscid, and non-heat-conducting gas, the one-dimensional momentum, energy[16,26] and state equations can be expressed in the following form:

Momentum:

$$\rho\frac{\partial u}{\partial t}+\rho u\frac{\partial u}{\partial x}+\frac{\partial p}{\partial x}=0; \tag{1}$$

Energy:

$$\frac{\partial p}{\partial t}+u\frac{\partial p}{\partial x}+\gamma p\frac{\partial u}{\partial x}=(\gamma-1)q; \tag{2}$$

State:

$$p=\rho RT. \tag{3}$$

Expressing each of the dependent variables as the sums of steady and time-dependent small amplitude solutions

$$u(x,t)=\overline{u}(x)+u'(x,t), \quad p(x,t)=\overline{p}(x)+p'(x,t),$$
$$\rho'=\overline{\rho}(x)+\rho'(x,t), \quad q=q(x)+q'(x,t), \tag{4}$$

and substituting these equations into the conservation equations yields systems of steady and wave equations. Assuming that the mean flow Mach number is negligible, the solution of the steady momentum equation shows that the mean pressure $\overline{p}$ is a constant in the duct. The resulting linearized acoustic momentum and energy equations are

$$\frac{\partial u'}{\partial t}+\frac{1}{\overline{\rho}}\frac{\partial p'}{\partial x}=0, \tag{5}$$

$$\frac{\partial p'}{\partial t}+\gamma\overline{p}\frac{\partial u'}{\partial x}=(\gamma-1)q'. \tag{6}$$

Assuming that the solution has a harmonic time dependence [i.e., $p'(x,t)=P(x)e^{i\omega t}$, $u(x,t)=U(x)e^{i\omega t}$, $\rho'(x,t)=\hat{\rho}(x)e^{i\omega t}$, and $q'(x,t)=Q(x)e^{i\omega t}$], Eqs. (5) and (6) reduce to

$$i\omega\overline{\rho}U+\frac{\partial P}{\partial x}=0, \tag{7}$$

$$i\omega P+\gamma\overline{P}\frac{\partial U}{\partial x}=(\gamma-1)Q. \tag{8}$$

The acoustic density is decoupled from the momentum and energy equations for small values of mean velocities. Therefore, the continuity equation does not have to be solved simultaneously with the acoustic momentum and energy equations. Instead, the solution obtained by solving the momentum and energy equations can be substituted into the continuity equation to obtain the following expression for acoustic density:[27]

$$\hat{\rho}=\left(\frac{P}{c^2}\right)+\left(\frac{iU}{\omega}\right)\frac{d\overline{\rho}}{dx}+\frac{i(\gamma-1)}{\omega c^2}Q, \tag{9}$$

where $c^2=\gamma R\overline{T}$.

As explained in the previous section, the unsteady combustion process can be modeled as a function of the acoustic quantities in the combustion region, i.e., $Q=\Re P+SU$, where $\Re$ and S are the pressure and velocity coupled responses. The wave equation can then be derived from Eqs. (7) and (8) as

$$\frac{d^2P}{dx^2}+\left[\frac{1}{\overline{T}}\frac{d\overline{T}}{dx}-\frac{(\gamma-1)S}{\gamma\overline{P}}\right]\frac{dP}{d\overline{T}}+\left[\frac{\omega^2+i\omega\Re(\gamma-1)}{\gamma R\overline{T}}\right]P=0. \tag{10}$$

For obtaining solutions, Eq. (9) is rewritten with the mean temperature as the independent variable

$$\left[\frac{d\overline{T}}{dx}\right]^2\frac{d^2P}{d\overline{T}^2}+\left[\frac{1}{\overline{T}}\frac{d}{dx}\left[\overline{T}\frac{d\overline{T}}{dx}\right]-B\frac{d\overline{T}}{dx}\right]\frac{dP}{d\overline{T}}+\frac{\Omega^2}{\gamma R\overline{T}}P=0, \tag{11}$$

where

$$B=\frac{(\gamma-1)S}{\gamma\overline{P}} \quad \text{and} \quad \Omega^2=\omega^2+i\omega\Re(\gamma-1). \tag{11a}$$

Equation (11) cannot be solved for an arbitrarily general $\overline{T}(x)$. Solutions for certain temperature profiles for which Eq. (11) reduces to a standard solvable differential equation are derived in the following sections.

III. SOLUTION FOR AN EXPONENTIAL MEAN TEMPERATURE PROFILE

In this section, solution to wave propagation through a combustion zone with an exponential mean temperature distribution given by the expression

$$\overline{T}=Ce^{dx}, \tag{12}$$

where C and d are constants, are derived.

Using Eq. (12), Eq. (11) can be reduced to the following form:

$$\frac{d^2P}{d\overline{T}^2}+\left[2-\frac{B}{d}\right]\frac{dP}{d\overline{T}}+\frac{\Omega^2}{\gamma Rd^2}\frac{P}{\overline{T}^3}=0. \tag{13}$$

For constant values of $\Re$ and S, Eq. (13) can be reduced to the Bessel's differential equation by transformation of variables. Solution to Eq. (13) can therefore be obtained in terms of Bessel functions,[28,29] as

$$P=\overline{T}^{(B/d-1)/2}\left[c_1J_\nu\left[\frac{\delta}{\sqrt{\overline{T}}}\right]+c_2J_{-\nu}\left[\frac{\delta}{\sqrt{\overline{T}}}\right]\right]$$

if ν is not an integer, (14a)

$$P=\overline{T}^{(B/d-1)/2}\left[c_1J_\nu\left[\frac{\delta}{\sqrt{\overline{T}}}\right]+c_2Y_\nu\left[\frac{\delta}{\sqrt{\overline{T}}}\right]\right]$$

if ν is an integer, (14b)

where

$$\delta=\frac{\Omega}{\sqrt{\gamma Rd^2}} \tag{15}$$

It is interesting to note that, for the case of $B=0$ (which corresponds to $S=0$),

$$P'=\frac{1}{\sqrt{\overline{T}}}\left[c_1J_1\left[\frac{\delta}{\sqrt{\overline{T}}}\right]+c_2Y_1\left[\frac{\delta}{\sqrt{\overline{T}}}\right]\right]. \tag{16}$$

IV. SOLUTION FOR A LINEAR MEAN TEMPERATURE PROFILE

In this section, solution is found for wave propagation in combustion zones with a linear mean temperature profile given by the expression

$$\overline{T}=ax+b. \tag{17}$$

Using Eq. (17), Eq. (11) can be reduced to the following confluent hypergeometric equation, for constant values or $\mathfrak{R}$ and S:

$$s\frac{d^2P'}{ds^2}+(1-s)\frac{dP'}{ds}+\varepsilon P'=0, \tag{18}$$

where

$$s=\frac{B}{a^2}\overline{T}, \quad \varepsilon=\frac{\Omega^2a^2}{\gamma RB}. \tag{19}$$

The solution to Eq. (18) can be expressed in the form of confluent hypergeometric series[30]

$$F(s)=C_1{}_1F_1(\varepsilon;1;s)+C_2U(\varepsilon;1;s). \tag{20}$$

It is interesting to observe that for the special case of $B=0$ (i.e., the heat release is a function of acoustic pressure only) solutions can be obtained for mean temperature profiles of the form

$$\overline{T}=(ax+b)^n, \tag{21}$$

$$P'=\overline{T}^{\alpha}[c_1J_{\nu}(\beta\overline{T}^{\sigma})+c_2Y_{\nu}(\beta\overline{T}^{\sigma})],$$

when ν is an integer, (22a)

$$P'=\overline{T}^{\alpha}[c_1J_{\nu}(\beta\overline{T}^{\sigma})+c_2J_{-\nu}(\beta\overline{T}^{\sigma})],$$

when ν is not an integer, (22b)

where

$$\nu=\frac{1-n}{2-n}, \quad \alpha=\frac{1}{2}\left(\frac{1}{n}-1\right), \quad \beta=\frac{\Omega}{an\sqrt{\gamma R}\sigma}, \tag{23}$$

and

$$\sigma=\frac{1}{n}-\frac{1}{2}.$$

V. EXAMPLE CALCULATIONS

In this section, an example problem is solved in order to illustrate the application of the developed solutions. Specifically, this section will consider the problem discussed in Ref. 1 that applied the first order matching conditions across an infinitely thin sheet. The advantages of using the exact solutions will be illustrated by comparing the error introduced by this approximation.

The mean flow of a combustible mixture through a long duct, closed at one end ($x=0$) and a standing wave pattern of a given frequency and amplitude is established using an acoustic driver at the other end, with a flame stabilized in the wake of a bluff body at the axial location $x=L_1$; see Fig. 1. The combustion is initiated when the flow passes the flame holder, but the fluid continues to burn throughout a significant length downstream of the duct. Oscillations are driven in this duct using an acoustic driver. The portion of the duct upstream of the flame holder is designated as region 1 with a nonreacted gas density of ρ_1 and a sound speed of c_1. Region 2 is the post combustion zone downstream of the flameholder, with a reacted gas density ρ_2 and sound speed c_2. $\overline{T}_1=300\,\mathrm{K}$, $\overline{T}_2=1875\,\mathrm{K}$. $\mathfrak{R}/\omega R=5.53\times10^{-3}$, $B=5.64\times10^{-3}$. (The values of $\mathfrak{R}$ and S are typical numbers estimated in a similar geometry from chemiluminescence measurements of CH radical.) The termination at $x=0$ (Fig. 1 is a hard termination) and the pressure amplitude there is P_0.

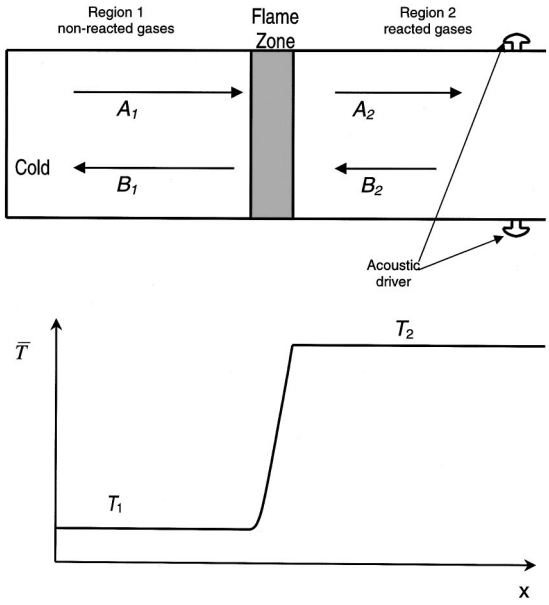

FIG. 1. Schematic diagram of the model geometry.

In the harmonic domain, the solutions may be expressed in the following form:

$$P_n(x)=A_ne^{ik_nx}+B_ne^{-ik_nx}, \tag{24}$$

$$U_n(x)=-\frac{1}{\overline{\rho c}}(A_ne^{ik_nx}-B_ne^{-ik_nx}), \tag{25}$$

where the subscript n denotes the region of interest.

A number of studies (e.g., Refs. 1, 16, 31, and 32) have used conservation conditions relating the one-dimensional[31,32] acoustic field variables for an infinitely thin flame. In these references, the conditions applied across a flame are

$$P_+-P_-=0, \tag{26}$$

$$(U'_+-U'_-)=\frac{(\gamma-1)}{\gamma\overline{p}}\tilde{Q}, \tag{27}$$

where subscripts + and − denote the value of the variables just upstream and just downstream of the flame region, and

$$\tilde{Q}=\int_{L_1}^{L_2}Q\,dx. \tag{28}$$

Figures 2 and 3 compare the spatial dependence of the acoustic pressure and velocity distributions obtained from the exact solutions developed in this study (for an exponential temperature profile) and using the solutions obtained with the jump conditions Eq. (26) and (27) when L/λ_2 is 0.01 and $K_2L_2=5.95$ (L is the thickness of the combustion zone). In this example, the thickness of the combustion zone is small relative to the wavelength. Figures 2 and 3 show that for a thin combustion zone, the acoustic field is well described by the jump conditions. Figures 4 and 5 compare the

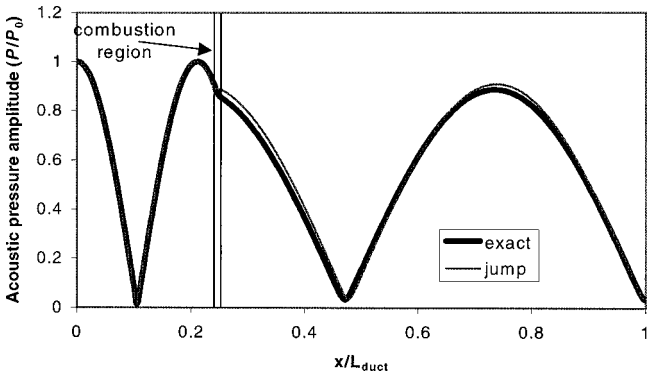

FIG. 2. Variation of acoustic pressure amplitude with axial distance. $L/\lambda_2 = 0.01$.

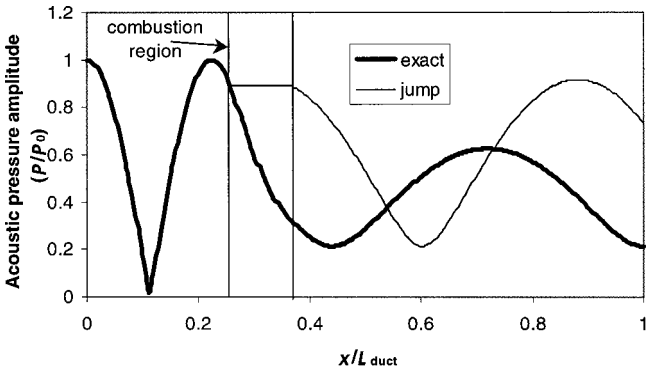

FIG. 4. Variation of acoustic pressure amplitude with axial distance. $L/\lambda_2 = 0.1$.

exact and approximate solutions when L/λ_2 is 0.1 and $K_2L_2 = 5.63$. These results show that significant errors result from the use of the jump conditions. The size of the combustion regions in real combustors is likely to be closer to or larger than that employed in the second example. From the data presented by Langhorne,[2] it can be seen that the combustion zones in bluff body stabilized flames (e.g., an afterburner) can be 25% of the wavelength. The heat release zone can be 50% of the length of the combustor.

In addition, it should be noted that the procedure given by the references (e.g., Refs. 1, 16, 31, and 32) does not provide any information about the values of the acoustic variables within the combustion region. That is, information is obtained about the acoustic quantities only on the boundary of the region. However, the results from the present study can provide the values of the acoustic pressure and velocity inside the combustion zone. Considerable error in the calculation of the modes can occur if the effect of the temperature gradient is neglected. Significant differences can occur in the calculation of the acoustic pressure (P_+) and velocity (U_+) at the end of the flame zone, as can be seen from Figs. 4 and 5. As an example, in Fig. 4, at the end of the flame zone, the acoustic pressure is close to being a pressure minimum, if the effects of temperature gradients are taken into account. However, calculations that do not take the effect of temperature gradient into account show that the acoustic pressure is near a pressure maximum.

It has been shown by Raun and Beckstead[18] and McIntosh and Rylands[19] that accurate estimation of the acoustic mode shape is essential to accurate prediction of growth rate in their analysis of oscillations in a Rijke tube. They have shown that not taking the mean temperature profiles in the burner led to wrong predictions of the growth rate, though the flame-interaction model was accurate. Flame-interaction models need the accurate values of acoustic pressure and velocity. As can be seen from the results presented, not taking the mean temperature profile into account can lead to considerable inaccuracies in the prediction of mode shapes.

The solutions presented in this paper have application in the study of the pressure- and velocity-coupled responses of propellants that undergo distributed combustion. Distributed combustion is the term used to denote the combustion of solid particles, usually metals such as aluminum or boron in the combustion chambers of solid propellant rocket motors after they have been emitted from the burning solid propellant surface, but before they pass through the nozzle.[33] The pressure- and velocity-coupled responses are obtained by burning the propellant at the end of a modulated exhaust combustion chamber. Measurements of unsteady gas velocity using magnetic velocimetry[34] along with measurement of unsteady pressure and the mean temperature distribution in the combustor combined with a one-dimensional linear acoustic analysis of the flow within the chamber[35] is used to measure the propellant responses. The analysis of Cauty *et al.*[35] assumed that all of the propellant combustion occurred in a region very close to the burning propellant surface, allowing the propellant response to be treated as a boundary condition. Such an assumption is not valid for metallized composite propellants. This analysis has been modified to allow for a distributed combustion zone away from the propellant sur-

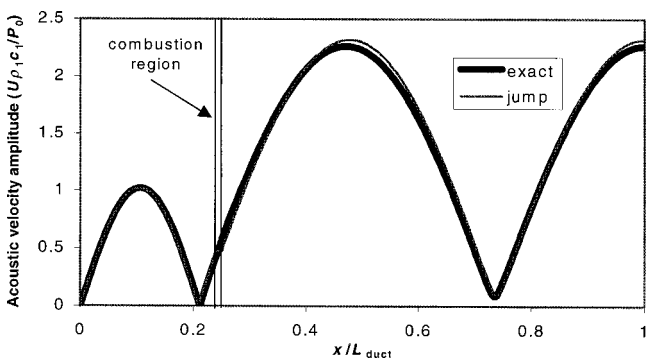

FIG. 3. Variation of acoustic velocity amplitude with axial distance. $L/\lambda_2 = 0.01$.

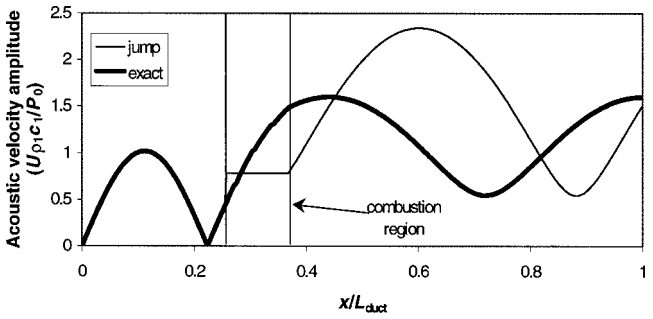

FIG. 5. Variation of acoustic velocity amplitude with axial distance. $L/\lambda_2 = 0.1$.

face, by integrating the acoustic equations numerically.[33,36,37] The solutions presented in this paper can be used in this analysis to take into account the effect of distributed combustion and the mean temperature gradient in the combustor (due to heat transfer to the walls of the combustor), for small mean velocities.

VI. CONCLUSIONS

Exact solutions describing the propagation of one-dimensional acoustic waves in combustion zones including the effects of mean temperature gradient and oscillatory heat release were obtained by applying suitable transformation to the wave equation. Solutions were obtained for exponential and linear mean temperature profiles. The solutions were applied to investigate the sound propagation through a combustion zone. It is shown that not taking the mean temperature profile at the combustion zone into account can lead to considerable inaccuracies in the prediction of mode shapes.

The solutions obtained in this analysis are in terms of special functions (Bessel and hypergeometric functions) and are easy to evaluate. These closed-form expressions presented herein can be used as benchmarks for checking the results obtained from computer programs that are intended for applications for systems with mean temperature gradients and oscillatory combustion.

ACKNOWLEDGMENTS

This work was supported by the Alexander von Humboldt Foundation through a Humboldt fellowship to the author. The author wishes to thank Dr. S. R. Chakravarthy, IIT Madras, with whom he had many interesting discussions.

[1] K. Mcmanus, T. Poinsot, and S. M. Candel, "A review of active control of combustion instabilities," Prog. Energy Combust. Sci. **19**, 1–29 (1993).
[2] P. J. Langhorne, "Reheat buzz: An acoustically coupled combustion instability. I. Experiment," J. Fluid Mech. **193**, 417–443 (1998).
[3] G. J. Bloxsidge, A. P. Dowling, and P. J. Langhorne, "Reheat buzz: An acoustically coupled combustion instability. II. Theory," J. Fluid Mech. **193**, 445–473 (1998).
[4] P. Pelcé and D. Rochwerger, "Vibratory instability of cellular flames propagating in tubes," J. Fluid Mech. **239**, 293–307 (1992).
[5] G. Searby and D. Rochwerger, "A parametric acoustic instability in premixed flames," J. Fluid Mech. **231**, 529–543 (1991).
[6] M. DiCicco and J. Buckmaster, "Role of slip in the generation of acoustic instabilities in gas turbines," J. Propul. Power **12**, 34–40 (1996).
[7] A. Duvvur, C. H. Chiang, and W. A. Sirignano, "Oscillatory fuel droplet vaporization: Driving mechanism for combustion instability," J. Propul. Power **12**, 358–365 (1996).
[8] J. P. Delplanaque and W. A. Sirignano, "Transcritical liquid oxygen droplet vaporization: Effect on rocket combustion instability," J. Propul. Power **12**, 349–357 (1996).
[9] C. Clanet, G. Searby, and P. Clavin, "Primary acoustic instability of flames propagating in tubes: Cases of spray and premixed gas combustion," J. Fluid Mech. **385**, 157–197 (1999).
[10] A. P. Dowling, "The calculation of thermoacoustic oscillations," J. Sound Vib. **180**, 557–581 (1995).
[11] M. Barrere, "Non-steady burning and combustion stability of solid propellants," in *Progress in Astronautics and Aeronautics*, edited by L. DeLuca, E. W. Price, and M. Summerfield (AIAA, Washington DC, 1992), Vol. 143, pp. 17–58.
[12] M. Micci, L. H. Caveny, and W. A. Sirignano, "Linear analysis of forced longitudinal waves in rocket motor chambers," AIAA J. **19**, 198–204 (1981).
[13] T. Poinsot, C. Le Chatelier, S. M. Candel, and E. Esposito, "Experimental determination of the reflection coefficient of a premixed flame in a duct," J. Sound Vib. **107**, 265–278 (1986).
[14] E. E. Zukoski and F. E. Marble, "Experiments concerning the flame stabilization in the wakes of bluff bodies," in Proceedings of the Symposium on Gas Dynamics, North Western University, Evanston, IL, pp. 205–210.
[15] J. Harper, C. Johnson, Y. Neumeier, T. Lieuwen, and B. T. Zinn, "Experimental investigation of the nonlinear flame response to flow disturbances in a gas turbine combustor," AIAA 2001-0486, 39th AIAA Aerospace Sciences Meeting and Exhibit, 8–11 January 2001, Reno, NV.
[16] T. Lieuwen and B. T. Zinn, "Application of multipole expansions to sound generation from ducted unsteady combustion processes," J. Sound Vib. **235**, 405–414 (2000).
[17] A. T. Chu, "On the generation of pressure waves at a plane flame front," Fourth Symposium (International) on Combustion, The Combustion Institute, 603–612 (1953).
[18] R. L. Raun and M. W. Beckstead, "A numerical model for temperature gradient and particle effects on Rijke burner oscillations," Combust. Flame **94**, 1–24 (1993).
[19] A. C. McIntosh and S. Rylands, "A model of heat transfer in Rijke tube burners," Combust. Sci. Technol. **113–114**, 273–289 (1996).
[20] M. L. Munjal and M. G. Prasad, "On plane-wave propagation in a uniform pipe in the presence of a mean flow and a temperature gradient," J. Acoust. Soc. Am. **80**, 1501–1506 (1986).
[21] K. S. Peat, "The transfer matrix of a uniform duct with a linear temperature gradient," J. Sound Vib. **123**, 43–53 (1988).
[22] R. I. Sujith, G. A. Waldherr, and B. T. Zinn, "An exact solution for one-dimensional acoustic fields in ducts with an axial temperature gradient," J. Sound Vib. **184**, 389–402 (1995).
[23] B. Manoj Kumar and R. I. Sujith, "Exact solution for one-dimensional acoustic fields in ducts with polynomial temperature profiles," J. Vibr. Acoust. **120**, 965–969 (1998).
[24] P. Bala Subrahmanyam, R. I. Sujith, and T. Lieuwen, "A family of exact transient solutions for acoustic wave propagation in inhomogeneous, nonuniform area ducts," J. Sound Vib. **240**, 704–715 (2001).
[25] W. Lang, T. Poinsot, and S. Candel, "Active control of combustion instability," Combust. Flame **70**, 281–289 (1987).
[26] F. E. C. Culick, "Acoustic oscillations in solid propellant rocket chambers," Acta Astronaut. **12**, 113–126 (1966).
[27] M. Salikuddin and B. T. Zinn "Adaptation of the impedance tube technique for the measurement of combustion process admittances," J. Sound Vib. **68**, 119–132 (1980).
[28] M. Magnus, F. Oberheittinger, and R. P. Soni, *Formulas and Theorems for the Special Functions of Mathematical Physics* (Springer, Berlin, Heidelberg, New York, 1966).
[29] S. Zhang and J. Jin, *Computation of Special Functions* (Wiley New York, 1996).
[30] J. B. Seaborn, *Hypergeometric Functions and Their Applications* (Springer, New York, 1991).
[31] J. J. Keller, W. Egli, and J. Hellat, "Thermally induced low frequency oscillations," ZAMP **36**, 250–274 (1985).
[32] J. J. Keller, "Thermoacoustic oscillations in combustion chambers of gas turbines," AIAA J. **33**, 2280–2287 (1995).
[33] M. M. Micci, "Linear acoustic analysis of solid propellant pressure-coupled distributed combustion," J. Propul. Power **12**, 1179–1181 (1996).
[34] J. R. Wilson and M. M. Micci, "Direct measurement of high frequency, solid propellant, pressure coupled admittances," J. Propul. Power **3**, 296–302 (1987).
[35] F. Cauty, P. Comas, F. Villot, and M. M. Micci, "Magnetic flow meter measurement of solid propellant pressure coupled responses using an acoustic analysis," J. Propul. Power **12**, 436–438 (1996).
[36] E. H. Cardiff and M. M. Micci, "Distributed combustion response function modeling and measurement," AIAA Paper 99-2497, 35th AIAA/ASME/SAE/ASEE Joint Propulsion Conference, Los Angeles, CA, 20–24 June (1999).
[37] E. H. Cardiff and M. M. Micci, "Distributed combustion response function modeling and measurement," AIAA Paper 2000-3796, 36th AIAA/ASME/SAE/ASEE Joint Propulsion Conference and Exhibit, Huntsville, AL, 16–19 July (2000).

On the sound sources of screech tones radiated from choked circular jets

Yoshikuni Umeda[a)]
Department of Aeronautics and Astronautics, Graduate School of Engineering, Kyoto University, Yoshida Hon-machi, Sakyo-ku, Kyoto 606-8501, Japan

Ryuji Ishii
Department of Resources and Energy, Graduate School of Energy, Kyoto University, Yoshida Hon-machi, Sakyo-ku, Kyoto 606-8501, Japan

(Received 24 February 2001; accepted for publication 20 July 2001)

The generation mechanism of the screech tone in the helical oscillation mode is mainly investigated using a series of instantaneous schlieren photographs. From the photographs, five evanescent sound sources are observed as prominent points along the jet axis. The sound source for the dominant helical oscillation mode is found to be the second prominent point which moves along a circular orbit in a plane perpendicular to the jet axis and just downstream of the rear edge of the third shock cell. It is shown that the speed of a moving sound source is supersonic and that the Mach cone generated by the moving sound source forms the helical-shaped wave front of the screech tone for the helical oscillation mode of the jet. This idea of the moving sound source is well supported by a measured directionality of the screech tone. Sound sources of the other oscillation modes appearing in the other pressure ratio ranges are also described. [DOI: 10.1121/1.1402620]

PACS numbers: 43.28.Mw [MSH]

I. INTRODUCTION

The acoustic emission from an underexpanded supersonic jet generally has a frequency spectrum that contains powerful discrete tones called *screech*. In a supersonic free jet issuing from a circular convergent nozzle, there are several shock cell structures; the large coherent vortical structures are convected downstream and interact with the oblique shock waves at the rear edge of the shock cells. The interaction between the vortical structure and the shock wave is very effective in producing strong acoustic waves. The resultant sound wave propagates upstream and stimulates the thin shear layer near the nozzle lip. In such a manner, we have a well-known feedback loop first proposed by Powell (1953a).

Experimental investigations about the instability of supersonic circular jets have been performed by several researchers. Westley and Wooley (1975, 1976) found that a circular jet oscillates in the helical mode at the pressure ratio $R=4.7$. For the axisymmetric and helical oscillation modes of screech tone, Panda (1998) studied the periodic oscillation of shock waves in screeching underexpanded circular jets by using a new shock detection technique based on laser light scattering by shock waves and showed that the mode of shock motion is the same as that of the emitted screech tone. He calculated the shock oscillation amplitude of the first shock for the helical oscillation mode by using the unsteady, linearized pressure perturbation equation given by Howe and Ffowcs Williams (1978) and obtained reasonably good agreement with his experimental result.

Panda (1999) also found from traversing microphone measurements and schlieren photography that partial interference between the upstream-propagating sound waves and the downstream-propagating hydrodynamic waves manifests itself as a standing wave along the jet boundary. He showed that an exact screech frequency formula could be derived in terms of the standing wavelength [not the shock spacing as was proposed by Powell (1953a)].

Raman (1997, 1999) showed that screech cessation in highly underexpanded rectangular jets is realized by diminishing feedback to the nozzle lip and poor receptivity at the initial shear layer due to excessive expansion of the jet boundary. He also found the same standing wave pattern along the jet boundary as that found by Panda (1999) for circular jets.

For the circular jet, Tam *et al.* (1986) showed theoretically that the feedback acoustic waves were the weakest link of the loop and they obtained the formula of the screech tone frequency predictable at all temperatures except for the staging of tone frequencies. Recently, Shen and Tam (1998) carried out a numerical simulation on the generation of the screech tones for the axisymmetric mode and showed that their numerical results for the principal features of the screech tone such as sound intensity and frequency agree well with the experimental ones obtained by Ponton and Seiner (1992).

In the frequency characteristics of screech tones radiated from a circular underexpanded jet with a thick lip nozzle, Powell (1953a) found several discontinuities. These discontinuities suggest that the circular jet oscillates in different

[a)]Author to whom correspondence should be addressed; electronic mail: umeda@kuaero.kyoto-u.ac.jp

oscillation modes in different pressure ratio ranges. In the investigation about the instability of supersonic circular jets, Davies and Oldfield (1962) found that five stages exist in a pressure ratio range of less than about 6.0 and the first four oscillation modes are axisymmetric, axisymmetric, lateral, and helical, respectively, with increasing pressure ratio. Recently, Powell *et al.* (1990, 1992) showed that the last oscillation mode at the highest pressure ratio R (dominant mode D) is lateral. They also showed that the plane of oscillation of the last lateral mode (mode D) rotates, vibrates, and dwells, while the first lateral mode (dominant mode B) occasionally changes to a helical mode at the same frequency.

Powell *et al.* (1992) also found that the dominant helical mode C is very stable and its frequency is higher ($\approx$14%–23%) than that of the secondary b (or d) mode, which is adjacent to the dominant lateral modes B and D. This is a very strange phenomenon. Furthermore, there are the following riddles about the occurrence of the dominant helical oscillation mode C:

(1) Why does the helical oscillation mode of jet occur?
(2) Where is the sound source?
(3) How does the sound source behave?

Although these riddles are the most basic problems about the generation of the helical oscillation mode of jet, there has been only one approach by Powell *et al.* (1990) to these problems. In the present paper, we will mainly try to solve these fundamental problems by using a series of instantaneous schlieren photographs taken at a pressure ratio of $R=3.90$. It will be shown that the dominant tone in helical oscillation mode C is radiated from a moving sound source along a circular orbit in the plane perpendicular to the jet axis and just downstream of the rear edge of the third shock cell.

Next, sound sources of the secondary screech tones labeled u which was unidentified in the previous investigation (Powell *et al.*, 1990, 1992) and the secondary tone labeled b (or d) observed at the same pressure ratio $R=3.90$ will be identified. Furthermore, the axial positions of sound sources for the lateral and helical oscillation modes appearing in the dominant mode B, and those for axisymmetric mode A and lateral mode D will be addressed.

II. EXPERIMENTAL APPARATUS

The convergent circular nozzle used in this experiment had an internal exit diameter of $d=10$ mm. The external diameter in the exit plane was 26 mm, i.e., the ''lip'' of the nozzle was 8 mm thick, almost equal to the exit diameter. The cold air jet was exhausted from this nozzle. The maximum pressure ratio attainable with this circular nozzle was 5.84.

The positions of the microphones for the measurement of the power spectrum and phase of the sound are shown in Fig. 1. The radial distance r_m of the microphones from the jet axis was set at 77 mm. One microphone M_f was kept at a fixed position, while the other one, M_m, was rotated through the angle θ in steps of 15° about the axis, both microphones being kept in a plane at a fixed distance $x=40$ mm upstream

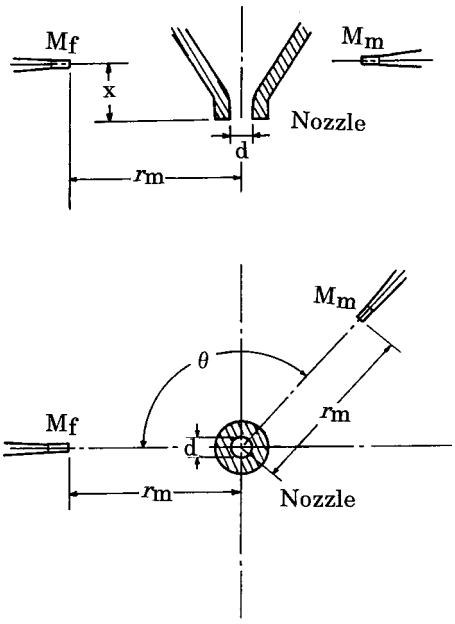

FIG. 1. Position of the fixed and moveable microphones, M_f and M_m, respectively, relative to circular nozzle.

of the face of the nozzle. The fixed microphone M_f was a 6.4-mm-diam B&K type 4135 condenser microphone, and the moveable one M_m was a B&K type 4138, 3.2 mm in diameter.

All the signal outputs from the microphones were analyzed using an Ono Sokki CF-5210 2ch FFT spectrum analyzer. The photographs were taken using a conventional single pass schlieren system. This used 20-cm-diam mirrors of 200-cm focal length, with a Sugawara type MS-230 spark light source of duration about 1 μs for the instantaneous photograph and an Hg monochromatic continuous light source for the long time exposure photograph. The jet was systematically turned off between the taking of each data sample for different microphone separation angles and for different pressure ratios of the jet and between the taking of each photograph.

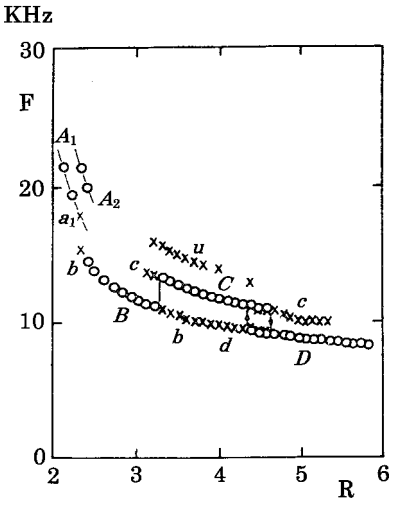

FIG. 2. Screech frequencies at the fixed microphone vs pressure ratio R for the circular jet.

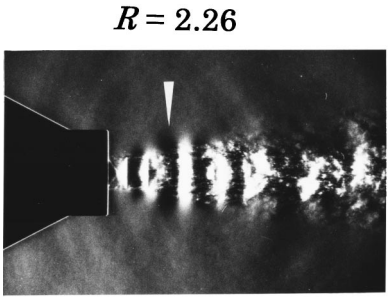

FIG. 3. Photograph of the jet in the axisymmetric oscillation mode A_1 ($R=2.16$).

III. EXPERIMENTAL RESULTS

A. Spectrum analyses and photographs of jet configuration

First, the frequency characteristics of screech tones emitted by the circular jet at various pressure ratios R from 2.0 to 5.84 were measured. These pressure ratios correspond to the common measure of ideally fully expanded jet Mach numbers of 1.05 and 1.81, respectively. Figure 2 shows the experimental result obtained in the previous investigation (Powell *et al.*, 1990, 1992). The open circles indicate *dominant* tones, defined here as those that exceed the local broadband noise by at least 10 dB. The five segments are labeled in turn with capital letters, A_1, A_2, *B*, *C*, and *D*. The crosses mark *secondary* tones that exceed the local broadband noise by 5–10 dB, and these continuous parts are labeled with lower case letters of the dominant tone of which they appear to be a continuation, there being one region where *b* and *d* are equally applicable. There is also another secondary tone labeled *u*. These tones, belonging to six segments (A_1, A_2, *B*, *C*, *D*, and *u*) in the frequency characteristics of the screech tones, are radiated from the jet oscillation in the different oscillation modes. In this figure, tones that are thought to be exact harmonics of dominant tones are not shown.

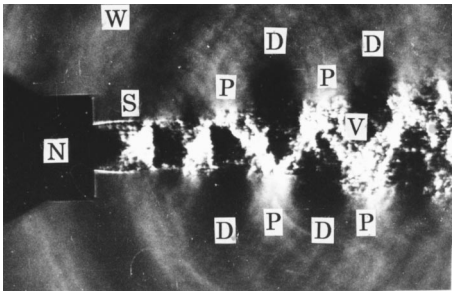

FIG. 5. Schlieren instantaneous photograph of the circular jet ($R=3.90$).

Schlieren photographs with an exposure of about 1 μs showing the jet configuration and associated sound field for each of the dominant modes are shown in Figs. 3 ($R=2.26$, A_1 mode; axisymmetric), 4 ($R=2.93$, *B* mode; lateral/helical), 5–7, 9 ($R=3.90$, *C* mode; helical), and 10 ($R=4.87$, *D* mode; lateral), respectively. From these photographs it is observed that the cell length increases with pressure ratio *R*. In the case of the *A* mode, the sound waves and the coherent vortices are axisymmetrical. In the case of the *B*, *C*, and *D* modes, strong asymmetric sound waves and asymmetric vortices are observed.

B. Identification of the instability modes

It will be reasonably accepted from the optical observations of the present and previous investigations (Powell *et al.*, 1990, 1992) that axisymmetric vortices are generated in connection with the jet oscillation of axisymmetric mode; on the other hand, asymmetric vortices are generated in association with that of asymmetric oscillation mode. The asymmetric oscillation mode includes lateral and helical oscillation modes. However, it is difficult to discriminate the difference between these oscillation modes from photographic observation.

According to Powell's feedback loop theory for the generation of the screech tone, when the discontinuous vortices

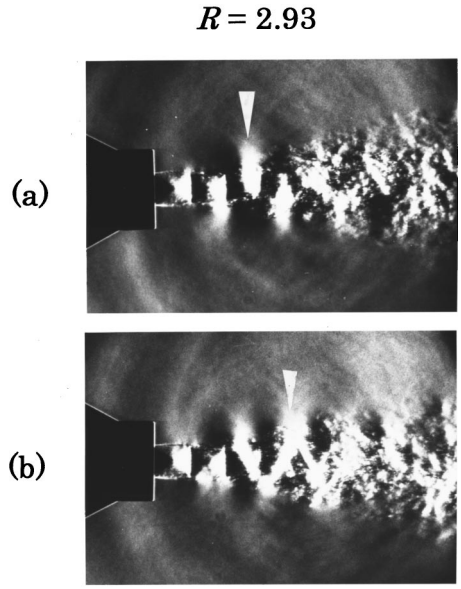

FIG. 4. Photographs of the jets in the dominant oscillation mode *B* ($R=2.93$): (a) lateral mode, (b) helical mode.

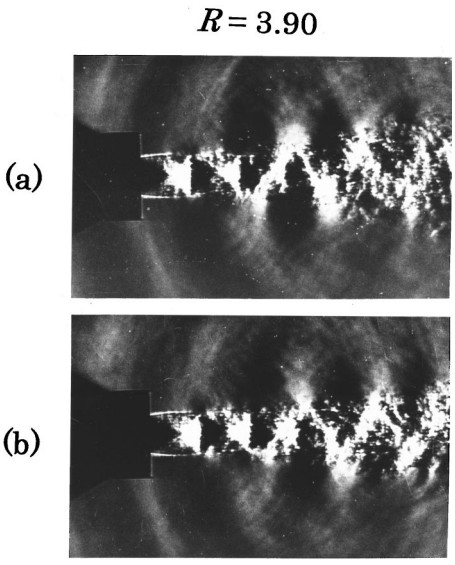

FIG. 6. Reproducibility of feedback phenomenon. These two photographs were taken at a time interval of about 10 s which is much larger than the period of the tone generation (about 10^{-4} s).

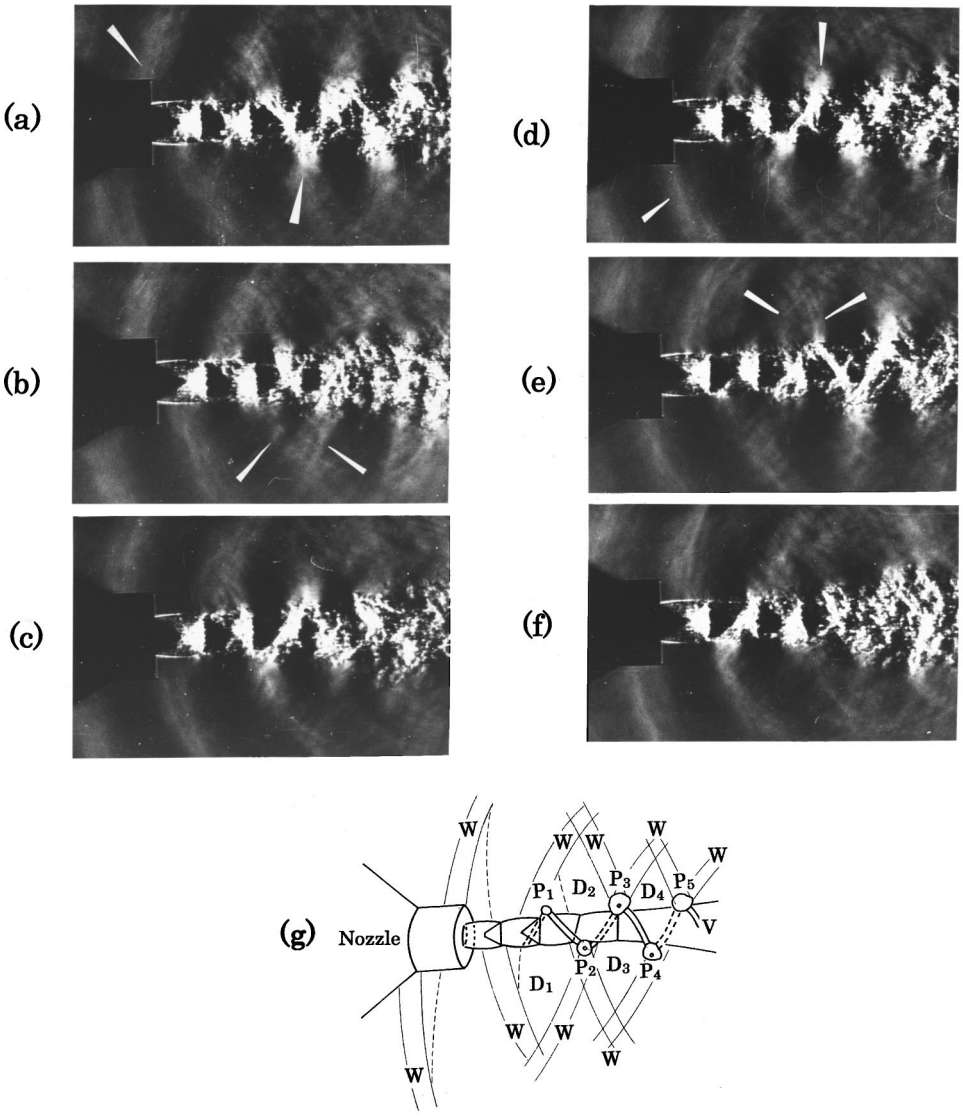

FIG. 7. One cycle of the screech tone generation in helical oscillation mode for $R=3.90$: (a)–(f) instantaneous schlieren photographs; (g) schematic view of the flow field and near-sound field drawn from photograph (a), symbols are the same as those in Fig. 5.

interact with the oscillating oblique shock wave in the cell structure of the supersonic jet, the sound waves are generated alternately from both sides of the jet and the jet oscillates in the lateral oscillation mode. On the contrary, the helical-shaped sound wave front must be generated by an interaction between the vortexlike structure and the oblique shock wave.

Therefore, if the three-dimensional structures of the wave fronts of screech tone radiated from the jet are determined, both oscillation modes can be discriminated exactly. In order to get information on the three-dimensional structures of the wave fronts for both oscillation modes, in the previous investigations (Powell *et al.*, 1990, 1992) the phase differences of the sound waves between two points in the radiation field were measured by using two microphones as shown in Fig. 1. In the phase measurements, one microphone M_f was placed at a fixed position and the other one M_m was rotated about the jet axis. The phase differences ϕ of the sound waves were measured at every 15° of microphone separation angles θ. The phase differences between the sound signals received by the two microphones correspond to a particular three-dimensional structure of the wave fronts as shown in the previous paper (Powell *et al.*, 1990, 1992). By using this technique, lateral and helical oscillation modes could be discriminated clearly. Namely, in the case of lateral oscillation mode, the measured phase differences ϕ are clustered near the values of 0 and π for the microphone separation angles θ. In the case of the helical oscillation mode, the

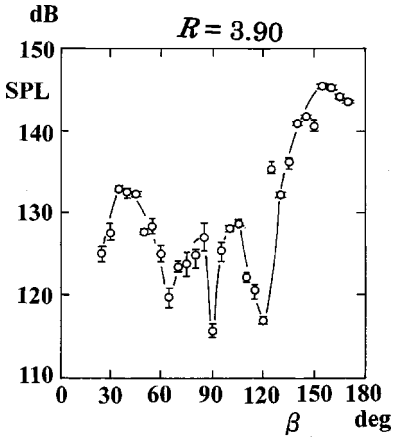

FIG. 8. Directionality of the screech tone for the pressure ratio $R=3.90$.

phase differences ϕ are changed linearly with the microphone separation angles θ.

Furthermore, it was confirmed that the mode of jet instability changes successively from two axisymmetrical modes A_1 and A_2, a lateral mode *B*, a helical mode *C*, and a lateral mode *D* with increasing pressure ratio of the jet. Lateral mode *B* occasionally changes to a helical mode at the same frequency.

For the jet oscillating in *B* mode, in the photograph of Fig. 4(a), several discontinuous vortices are arranged alternately along the jet axis as was described above. In contrast, in the photograph of Fig. 4(b), a continuous zigzag vortexlike structure is observed along the jet axis. Such a zigzag vortexlike structure is also clearly seen in the photographs of the jet oscillating in the dominant *C* mode (Figs. 5, 6, and 7). As shown in the previous investigations (Powell *et al.*, 1990, 1992) and also will be shown in a later section in this paper, in the dominant *C* mode case, it is observed that the phase differences measured by two microphones are changed linearly with the microphone separation angle as shown in Fig. 11(a) and the data points never cluster about the values of 0 and π as is seen in the lateral mode [Fig. 11(c)]. Therefore, this dominant *C* mode is unambiguously helical. These facts strongly support the hypothesis that the zigzag vortexlike structure on the photograph is actually a continuous helical-shaped vortex around the jet and it convects downstream along the jet axis.

Panda (1998) showed that the mode of shock motion is the same as that of the emitted screech tone. It has to be emphasized that Powell *et al.* (1990, 1992), Davies and Oldfield (1962), and Westley and Woolley (1975, 1976) believed that there are helical vortices around the jet oscillating in the helical *C* mode. Thus, it can be confirmed that the configurations of the sound wave fronts and the coherent vortical structure correspond to the shock and jet oscillation modes.

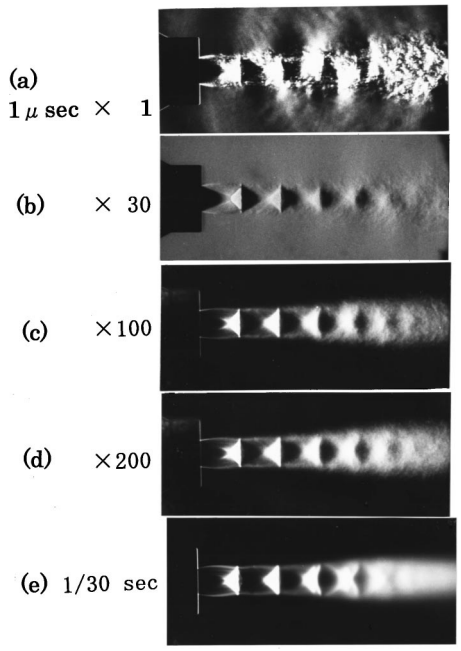

FIG. 9. Circular jet exhausted at a pressure ratio $R=3.90$: (a) instantaneous schlieren photograph (1 μs); (b)–(d) multiple exposure photographs; (e) long time exposure photograph (1/30 s).

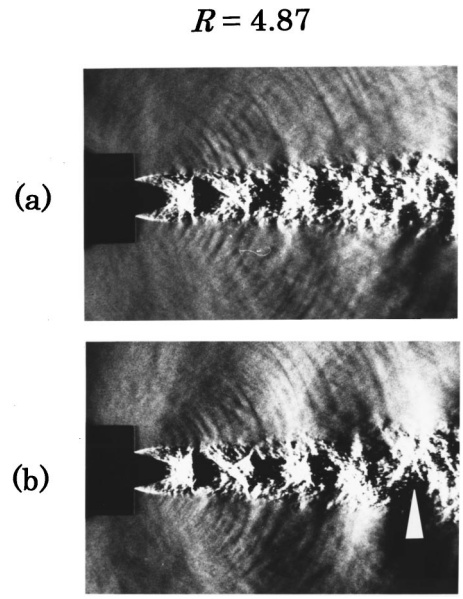

FIG. 10. Photographs of the jets in the lateral oscillation mode *D* ($R=4.87$): (a) looking perpendicularly to the oscillation plane, (b) looking in the oscillation plane.

C. Sound sources of the *C* mode screech

First, in the present section, the generation mechanism of the dominant helical oscillation mode *C* will be investigated by using instantaneous schlieren photographs.

1. Schlieren photographs

From the frequency characteristics shown in Fig. 2, Powell *et al.* (1992) observed that the ratio of the frequency of the dominant *C* mode and the secondary *b* (or *d*) mode was about 1.22 at a pressure ratio $R=3.90$. This fact suggests that the length of the feedback loop for oscillation mode *C* will be shortened compared with that for the secondary oscillation mode *b* (or *d*) at the same pressure ratio. In this study, the locations of the screech tone sound sources in the dominant helical oscillation mode were explored by using instantaneous schlieren photographs.

Figure 5 shows an instantaneous photograph of the free jet issuing from a circular nozzle "*N*" at a pressure ratio $R=3.90$. This photograph was taken by using a Xe flash lamp with an exposure of about 1 μs. In this case, it has already been confirmed that the oscillation mode of the jet is helical (Davies and Oldfield, 1962; Westley and Woolley, 1975, 1976; Powell *et al.*, 1990, 1992). So, in this photograph, we can see several shock cell structures "*S*" in the jet, a downstream-convecting helical vortex "*V*" around the jet, and upstream-propagating very strong sound waves "*W*" in the ambient which have helix wave fronts.

In this photograph, it is also observed that the sound waves are radiated from a few prominent points "*P*" on the helical vortical structure around the jet. This fact seems to indicate that these prominent points are the evanescent sound sources in the helical oscillation mode. A few elliptic-shaped dark portions "*D*" are also seen outside the jet in the downstream region of the second shock cell and are arranged in

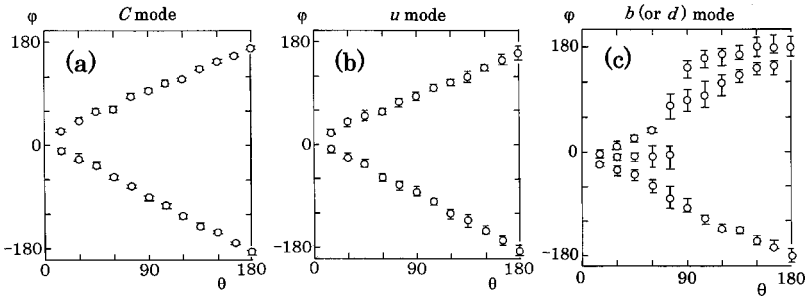

FIG. 11. Variation in phase angle φ at the moveable and fixed microphones, separated by angle θ, for the screech mode as follows (a) mode *C*, (b) mode *u*, (c) mode *b* (or *d*).

the opposite side of the jet to respective prominent points to form a zigzaglike pattern. These dark portions may be respective sound source before a half period of the jet oscillation. This situation will be described in more detail in the next section. Inside the dark portions, the local pressure is lower than the ambient pressure. The sound waves propagate upstream with strong directionality.

2. Feedback loop for the dominant helical oscillation mode C

In the following, the feedback loop of the screech tone generation for the dominant helical oscillation mode *C* will be examined by using a series of photographs showing one cycle of the jet oscillation.

Figures 6(a) and (b) show an underexpanded free jet at a pressure ratio of $R=3.90$. In these photographs, the locations of the upstream-propagating sound wave fronts almost coincide with each other. Although these photographs were taken at a very long time interval compared with the period of the tone generation, the locations and shapes of the large helical vortices, the locations of the prominent points, and the locations and sizes of the dark portions in both photographs almost coincide with each other. Obviously, these photographs are different only in the small scale of flow structures. Such a situation strongly suggests that the predominant large-scale phenomena are repeated periodically and synchronously. Therefore, we can use the location of the upstream-propagating wave front as a reference time in order to investigate the generation mechanism of the screech tone for the helical oscillation mode.

By making use of the above idea, we can demonstrate one cycle of the feedback loop occurring in an underexpanded jet issuing at a pressure ratio of $R=3.90$ by a series of the instantaneous schlieren photographs as shown in Fig. 7 where the time passes in alphabetical order.

In Fig. 7(a), we can see what appears to be a clear helical vortex crossing the rear edge of the third shock cell; it has an inclination decreasing with increasing distance from the nozzle exit. In this photograph, five tiny but very prominent white circles (points) can be seen on the helical vortex. These points can be seen at the bending points of the zigzaglike pattern (actually as the zigzaglike pattern shows the helix, the bending points do not exist) of the vortex appearing in this photograph. The first prominent point appears at a position slightly downstream of the rear edge of the second shock cell. The second prominent point is seen at a position just downstream of the rear edge of the third shock cell. The third one is seen near the rear edge of the fourth cell. The fourth prominent point is seen at the middle of the fifth cell. And, the fifth point is seen at the rear edge of the fifth cell. It is also observed from this photograph that the screech tones are radiated from these very prominent points. In the symmetric positions relative to the jet axis for these prominent points, elliptic-shaped dark portions can be seen.

Near sound field as well as flow pattern at this instant [Fig. 7(a)] is schematically and three-dimensionally shown in Fig. 7(g). In this figure, five prominent points which appeared on the coherent vortical structure "*V*" are denoted by "P_1"–"P_5." Dark portions are indicated by "D_1"–"D_4" and sound waves propagating upstream and downstream are denoted by "*W*" as shown in Fig. 5.

In the next photograph [Fig. 7(b)] which shows the flow pattern of the jet at about one quarter of one cycle later than flow pattern shown in Fig. 7(a), the zigzaglike pattern of the helical vortex moves downstream and becomes somewhat obscure. In this case, since the prominent points exist on the jet axis and optically overlap with the turbulent jet, it is difficult to find them in this photograph. Two wave fronts (denoted by arrows) propagating in the upstream and downstream directions are seen. They seem to be emitted from the second prominent point "P_2" located near the end of the third shock cell [Fig. 7(g)].

In Fig. 7(c), we can see again a clear helical vortex crossing the rear edge of the third shock cell but it has reverse inclination with that for the helical vortex shown in Fig. 7(a). In this case, only one prominent point is visible just downstream of the rear edge of the third cell, but its position is in the opposite side (upper side) of the jet to the second prominent point "P_2" as shown in Fig. 7(g).

In Fig. 7(d), which shows the flow pattern of the jet at about one half of one cycle later than the flow pattern shown in Fig. 7(a), the principal flow pattern becomes opposite to the jet axis and three prominent points [corresponding to "P_1"–"P_3" in Fig. 7(g)] can be seen.

In Fig. 7(e), a clear helical vortex can be seen in the downstream region of the third shock cell and it has an inclination decreasing with increasing distance from the nozzle exit. The third and fourth prominent points can be seen and again two wave fronts (indicated by arrows) propagating in the upstream and downstream directions are observed. They seem to emit from the second prominent point "P_2" located near the end of the third shock cell as shown in Fig. 7(b).

Figure 7(f) shows the flow pattern of the jet at about one half of one cycle later than the flow pattern in Fig. 7(b). In this case, it is also difficult to see the prominent points.

From the detailed analysis of the series photographs presented above, we can say:

First, a helical-shaped vortical structure moves downstream with the passage of time.

Second, the prominent point "P_2" which is denoted by an arrow in Fig. 7(a) and appeared downstream from the third shock cell and disappear the next instant [Fig. 7(b)]. And then, it appears in the upper side of the jet [Figs. 7(c) and (d)]. It disappears again [Figs. 7(e) and (f)] and appears in the lower side of the jet [Fig. 7(a)]. This fact can be understood by considering that the prominent point "P_2" rotates around the jet axis.

Third, although in the photograph of Fig. 7(a) a very prominent point (the second prominent point "P_2") appears on the lower side of the jet, it disappears the next instant [Fig. 7(b)] and two sound waves (indicated by arrows) propagating upstream and downstream appear. Such a situation can also be seen in the upper side of the jet as shown in the photographs of Figs. 7(d) and (e). Therefore, it is concluded that the prominent point "P_2" appearing near the third shock cell end is a dominant sound source of the helical-shaped wave front of the screech tone and rotates about jet axis.

Fourth, considering the dark portion "D_2" which is seen on the opposite side of the second prominent point "P_2" relative to the jet axis, the dark portion "D_2" always appears in the axially symmetric location to the corresponding prominent point. The axial distances from the nozzle exit to the prominent point "P_2" and the dark portion "D_2" are always the same, independent of time. Therefore, the dark portion "D_2" also rotates about the jet axis in the same plane of the second prominent point. Such situations can be seen in the other prominent points ("P_1," "P_3," and "P_4") and dark portions ("D_1," "D_3," and "D_4"). Namely, these dark portions show the marks of the former sound sources.

Fifth, in Figs. 7(a) and (d), the wave front reaches the nozzle lip one and one half (3/2) cycles after its radiation (indicated by arrows). In this case, the sound wave front reaches the opposite side of the nozzle lip relative to the jet axis to the sound source. This is the peculiar characteristic observed in the helical oscillation mode. In the case of the axisymmetrical and lateral oscillation modes, the wave fronts reach the nozzle lip one or two cycles later than their radiation.

Upon reaching the nozzle lip, the helical-shaped sound wave front sweeps the nozzle lip in one turn during one cycle by the screech tone. By stimulating the thin shear layer by this wave front, a new vortical structure is generated near the nozzle lip and is grown up during the convection in the second shock cell as seen in Fig. 7(c). This vortical structure is further convected downstream along the jet axis again and the grown vortical structure can be seen in the third shock cell structure as shown in Fig. 7(a). At this instant, the second prominent point "P_2" appears at a position just downstream from the rear edge of the third shock cell and the lower side of the jet boundary. Then, two sound waves are radiated from this prominent point "P_2" as shown in Figs. 7(a) and (b). One of these sound waves propagates upstream through the ambient again. Thus, the process is repeated and

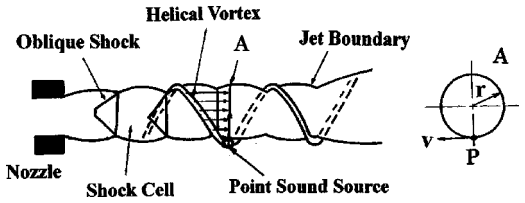

FIG. 12. Schematic view of the oscillating jet in the helical mode and the orbit of the moving sound source.

the feedback loop for the dominant helical oscillation mode *C* is completed.

Although we can see the feedback process of the screech tone generation for the helical oscillation mode *C* from only one direction in the series of the photographs, it must be noted that the helical vortexlike structure and the helical wave front of the sound have a continuous three-dimensional structure. Therefore, such a feedback process must be generated at all times in the constant feedback path between the nozzle exit plane and the plane where the evanescent sound source visible as the second prominent point "P_2" appears. As the successive segments of the helical vortexlike structure pass through the plane in the direction of the jet axis at different instants, the point sound sources are generated continuously and rotate about the jet axis.

In the photographs of Figs. 7(a) and (b) whose time difference is about one half cycle of the jet oscillation, the shock wave at the rear edge of the third cell interacts with helical vortex at two axisymmetric positions on the upper and lower jet boundaries, respectively. As these two photographs look at the jet from one direction, these photographs show that the oscillating shock wave owing to the jet oscillation interacts with the helical vortexlike structure in the plane described above just in one cycle of the jet oscillation. Therefore, it is confirmed that this dominant helical mode tone is generated by the resonance caused by the interaction between the downstream-convecting coherent helical vortexlike structure and the synchronously oscillating oblique shock wave in the jet.

3. Moving sound source along a circular orbit

In the case of helical oscillation mode *C*, when the helical coherent vortexlike structure travels a constant length of the feedback loop, each part of the helical vortexlike structure must travel the same distance at the different radial position to keep a constant axial length of the feedback loop at every instant. So, the screech tone must be generated by the sound source rotating about the jet axis at a constant speed in a plane labeled "*A*" perpendicular to the jet axis as shown in the left hand figure of Fig. 12. In this case, infinite numbers of point sources are generated successively in adjacent points on a circle around the jet boundary by the interaction between the helical vortical structure and the oblique shock near the rear edge of the third shock cell. As soon as a point source is generated, a spherical sound wave is radiated from the point source and then it disappears. So, the point source is an evanescent one. Therefore, such a sound source seems to act as if it was a moving point source along a circular orbit and its frequency is equal to the screech tone.

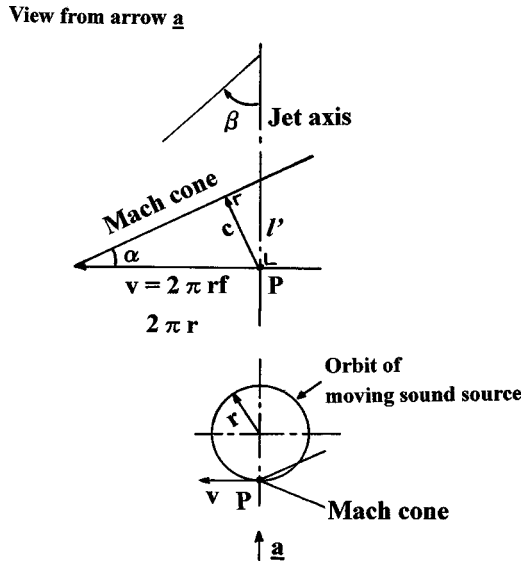

FIG. 13. Schematic view of the Mach cone and the orbit of moving sound source.

If this image of the moving sound source is correct and the speed of the moving sound source is subsonic, the Doppler shifted frequency of the screech tone would be detected in the near sound field in plane "*A*" perpendicular to the jet axis. If the speed of the moving sound source is supersonic, a Mach cone moving with the sound source would be generated.

In the right hand side of Fig. 12, the schematic view of the moving sound source looking downstream from the jet is shown. The source "*P*" moves at a speed of v along a circular orbit whose radius is r. Speed v of the moving sound source is calculated by using the value of the radial distance r of the prominent point on the coherent vortical structure and the frequency of the screech tone f. Namely, we have

$$v = 2\pi r f. \tag{1}$$

From the photograph shown in Fig. 7, the value of radial displacement r was determined to be 0.96 cm. The frequency of screech tone f was measured as 11.85 kHz. So, velocity v is calculated to be 715 m/s, namely, the speed of moving sound source is supersonic. Therefore, it is inferred that the Mach cone is generated behind the moving sound source as shown in the lower part of Fig. 13. The upper part of Fig. 13 shows a side view of the moving Mach cone with the point sound source. In this figure, the speed of point source "*P*" and the sound velocity are denoted by letters v and c, respectively. Referring to this figure, a half angle of the Mach cone, α, is calculated by

$$\sin\alpha = c/v = 340/715 = 0.476, \tag{2}$$

which yields

$$\alpha = 28.4°. \tag{3}$$

The envelope of the Mach cone extends in the upstream and downstream directions in the ambient as the sound source moves along the circular orbit. A half distance l' of the Mach cone extending along the jet axis during one turn of the moving sound source is calculated as

$$l' = 2\pi r \tan\alpha = 2\pi \times 0.96 \times 0.54 = 3.26 \text{ cm}. \tag{4}$$

In the series photograph of Fig. 7, it is observed that the wave front of the screech tone arrives at the nozzle lip 1.5 cycles after its emission. Then, the transfer distance l of the envelope of the Mach cone along the jet axis during a 1.5 turn of the moving sound source is obtained as

$$l = 1.5 \times l' = 4.89 \text{ cm}. \tag{5}$$

This value is very close to the axial distance ($x = 4.7$ cm) from the sound source to the nozzle exit obtained by the Schlieren photograph.

From the abovementioned facts, it will be confirmed that the envelope of the Mach cone rotating with sound source forms the helical-shaped wave front of the screech tone. Using this idea, the directionality of the screech tone in the helical oscillation mode *C* can be considered. As shown in Fig. 13, the envelope of the Mach cone or the helical-shaped wave front of the screech tone inclines to the plane where the sound source rotates about jet axis by about 30°. Then, the directions of propagation of the helical-shaped wave fronts are about $\beta = 30°$ and 150°, where angle β is measured from the jet axis in the downstream direction. Therefore, maximum sound pressure level (SPL) will be observed at about $\beta = 30°$ and 150° and the minimum SPL will be obtained at about $\beta = 60°$ and 120°.

Figure 8 shows the directionality of the screech tone for the pressure ratio $R = 3.90$. In this figure, open circles indicate the average values of the SPL of the dominant tone (*C* mode, 11.85 kHz) and the error bars represent the limit of the scatter of individual measurements, six in number. From this figure, it is observed that the directionality of the dominant screech tone agrees very well with the prediction mentioned above. Therefore, the measured directionality of the screech tone supports the idea of the moving sound source at a supersonic speed.

4. Sound source of the C mode screech

In the series of the schlieren photographs shown in Fig. 7, five sound sources are observed. From this figure, it is confirmed that the second prominent point "P_2" that appears slightly downstream from the third shock cell is the very strong sound source of the dominant *C* mode tone. What physical conditions determine the axial position of the sound source of this dominant screech tone? In order to clarify this problem, a long time exposure photograph was examined.

Samples of the instantaneous and the long time exposure photographs of the jet exhausted at a pressure ratio $R = 3.90$ are shown in Fig. 9. For the instantaneous schlieren photograph [Fig. 9(a)], a stroboscopic flash unit having a duration of about 1 μs was used. For the long time exposure photograph [Fig. 9(e)], an Hg monochromatic continuous light source was used and the duration time was 1/30 s. At first glance, these two photographs seem to show completely different phenomenon. It is difficult to find a relation between the flow structures especially in the downstream region in these two photographs. The flow shown in the instantaneous photograph seems to be very turbulent, and the

three-dimensional helical structure can be seen. It is difficult to identify the fourth, the fifth, etc. shock-cell patterns seen in the long time exposure photograph.

On the other hand, the long time exposure photograph shows a rather smooth and regular shock-cell pattern. The butterfly pattern seen in the fourth and the fifth cells indicate that the shocks are oscillating axially as well as radially. In the present experiments, the shock pattern in the long time exposure photographs did not change its shape and location even when the exposure time was varied from 1/1000 s to 1/4 s. It suggests that the shock pattern seen in Fig. 9(e) shows some time mean feature of the jet structure.

In order to find a more distinct relationship between the instantaneous photograph and the long time exposure one, photographs with multiple exposures were taken, as shown in Figs. 9(b)–(d). The duration of each flash is about 1 μs and the time interval between two successive flashes is about 1 s. The numbers of flashes are denoted in each photograph. With increasing number of flashes, the shock pattern becomes more clear and the sound field surrounding the jet becomes quieter. When the number of flashes is 200 [Fig. 9(d)], the structure of the jet is almost the same as that shown in the long time exposure photograph [Fig. 9(e)]. Since the time interval of two successive flashes is long enough, we may assume that each flash was substantially distributed uniformly in one cycle of the jet oscillation.

In the long time exposure photograph [Fig. 9(e)], a butterfly pattern can be seen in the fourth cell. This pattern shows that the fourth cell vibrates violently. At an axial position of the leading edge of the axisymmetrical antennalike pattern of the butterfly, it can be seen that the spreading ratio of the jet boundary increases abruptly and takes its maximum value.

The observed large widening of the jet boundary near the rear edge of the third shock cell is considered as follows: As experimental investigations by Minota (1993) and Szumowski and Sibieraj (1996) and the numerical simulation by Inoue and Hattori (1999) showed, when a vortex interacts with a shock wave, the shock wave is deformed and very strong sound waves are generated. In this dominant helical mode case, segments of the continuous helical vortical structure interact with the oscillating oblique shock successively at the rear edge of the third shock cell and segments of the vortical structure collapse and then, infinite numbers of point sound sources are generated successively. Thus, the jet boundary is widened just downstream of the rear edge of the third shock cell, as observed in the long time exposure photograph of Fig. 9(e) and sound sources surely exist at the axial distance where the spreading ratio of the jet boundary is a maximum. In this case, the axial distance x/d of the sound source is determined as 4.7 from the photograph.

5. Sound sources of u and b (or d) modes

In the previous sections, the second prominent point "P_2" appearing near the end of the third shock cell was decided as a sound source of the dominant helical *C* mode tone by surveying a series of instantaneous schlieren photographs in Fig. 7. So, it became clear that this dominant *C* mode tone is generated by the feedback loop between the nozzle exit and the second prominent point "P_2" rotating around the jet axis. In a spectrum shown in Fig. 14, this dominant helical *C* mode tone is observed as a very large peak, which exceeds the broadband noise by about 20 dB. This spectrum was obtained by using a fixed microphone M_f shown in Fig. 1. Furthermore, we can see that the helical *C* mode tone has double sideband frequencies at a distance Δf on the abscissa. The oscillation modes of jets at these sideband frequencies are denoted by *u* and *b* (or *d*) after Fig. 2. If the frequency of the helical *C* mode tone is denoted by f_C, the frequencies of the sideband are $f_C+\Delta f$ and $f_C-\Delta f$, respectively.

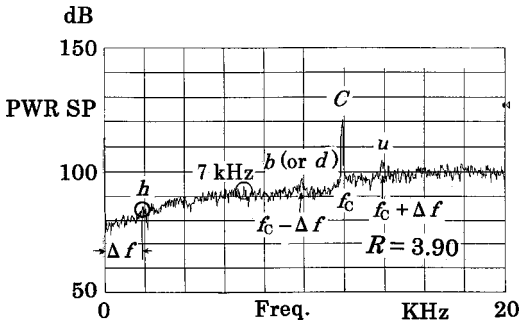

FIG. 14. Spectrum measured by a fixed microphone M_f shown in Fig. 1 ($R=3.90$).

We can also see in this spectrum that a discrete frequency component *h*, which has a very small peak, and the frequency nearly equal to the frequency difference Δf ($=1.9$ kHz) between the frequencies of the helical *C* mode tone f_C($=11.85$ kHz) and the secondary *u* mode tone f_u ($=13.8$ kHz) or *b* (or *d*) mode tone $f_{b,d}$($=9.9$ kHz). This fact indicates that the signal *C* is amplitude-modulated by the signal *h* of frequency Δf.

Now, consider the sound source for the secondary *b* (or *d*) mode tone. In the case of the dominant helical *C* mode, it has already been determined that the feedback length is about 4.7 times the nozzle diameter and the fundamental resonant frequency is 11.85 kHz. If the third prominent point "P_3" is assumed to be the sound source of the secondary *b* (or *d*) mode tone, the feedback length for this tone is 5.7 times nozzle diameter. Further, if the resonant frequency is inversely proportional to the feedback length, it is calculated to be 9.8 kHz. In the spectrum shown in Fig. 14, the frequency of a small peak labeled *b* (or *d*) is 9.9 kHz and agrees very well with the calculated one. Therefore, it is confirmed that the third prominent point is identified as the sound source of the secondary mode *b* (or *d*). Thus, it is concluded that the large ratio (1.2) of two frequencies of the screech tones between the dominant *C* mode (11.85 kHz) and the secondary *b* (or *d*) mode (9.9 kHz) is caused by the different positions of the respective sound sources generated in the same jet.

Further, in the photograph of Fig. 7(a), the other three prominent points ("P_1," "P_4," and "P_5") are observed at the positions of 3.5, 6.7, and 7.7 times the nozzle diameter, respectively, from the nozzle lip. The corresponding resonant frequencies to these sound sources are estimated as 15.9 kHz, 8.3 kHz, and 7.2 kHz, respectively. But, although a

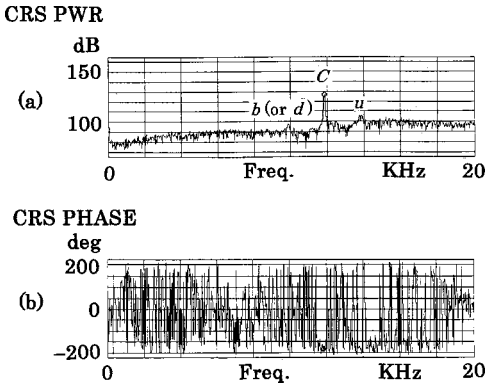

FIG. 15. Cross spectrum of sound signals from two microphones ($R=3.90$): (a) magnitude; (b) phase difference.

very small peak with a frequency of about 7 kHz is seen in a circle, a peak corresponding to the frequency of the *u* mode tone (13.8 kHz) and the peaks for the other two frequencies cannot be seen in the spectrum shown in Fig. 14. Therefore, the sound source for the *u* mode does not exist. So, the sound wave for the *u* mode is considered as a higher sideband frequency wave due to amplitude modulation.

6. Identification of the instability modes u and b (or d)

In the previous section, it is confirmed that the generation of the secondary tones of *u* and *b* (or *d*) modes is accompanied by the generation of the dominant tone of *C* mode. Therefore, it is expected that the oscillation modes of these secondary tones may be the same as that of the dominant helical *C* mode. However, in the previous investigation (Powell *et al.*, 1990, 1992), it was inferred without direct phase measurement of the sound that as dominant *B* and *D* modes were connected by secondary *b* (or *d*) mode, this mode was actually the same as dominant *B* and *D* modes (lateral).

Thus, in this section, in order to examine which supposition is correct, phase measurements of the sound waves were carried out using two microphones as shown in Fig. 1. In this experiment, three-dimensional structures of the sound wave fronts which correspond to respective oscillation modes of jets could be determined as was described in Sec. III B.

Powell *et al.* (1990, 1992) carried out the phase measurement by drawing a correlogram of the cross correlation of the sound signals from the two microphones. Therefore, only the phase difference of the dominant *C* mode could be measured at the pressure ratio $R=3.90$.

In the present experiment, the phase differences of the two sound signals were measured by calculating the cross spectrum on the 2ch FFT analyzer. In this case, both calculated results of the magnitudes of the cross correlation and phase differences were indicated as two graphs on the screen of the analyzer. So, the resonant frequencies of the jets could be detected as peaks in the magnitude of the correlation; the corresponding phase differences of the sound signals could be measured by scanning a cursor to these peaks no matter how low their levels were if they were detected. An example of the cross spectrum is shown in the two parts of Fig. 15. As can be seen in Fig. 15(a), three peaks of the magnitude of the correlation were detected. Frequencies of these peaks correspond to the oscillation modes of *C*, *u*, and *b* (or *d*). Therefore, in the present experiment, the phase differences of the sound waves for these modes were measured in Fig. 15(b).

Although there is no meaning to measure the secondary oscillation mode of *u* because the sound source for it does not exist, as mentioned in Sec. III C 5, Fig. 11 shows the results of the phase measurement for oscillation modes *C*, *u*, and *b* (or *d*) derived from the data shown in Fig. 15. These results were obtained for the same samples of the data. The open circles denote the average values of the 18 data sets and the bars indicate the limit of the scatter. In Figs. 11(a) and (b), the linear relationship between the phase difference φ and the microphone separation angle θ is obtained for modes *C* and *u*, respectively. These linear relationships indicate a helical oscillation mode of jet as was indicated for the oscillation mode *C* in the previous investigations (Powell *et al.*, 1990, 1992).

However, in the case of the secondary *b* (or *d*) mode [Fig. 11(c)], the result shows that there are data points clustering about $\varphi=0$ and π, and data points which form the pattern of the helical structure as was seen in modes *C* and *u*. This result shows that the secondary *b* (or *d*) mode oscillates in the lateral mode and it occasionally changes to the helical one at the same frequency as was shown in the case of the dominant *B* mode in the previous investigation (Powell *et al.*, 1990, 1992).

In the result of the dominant *C* mode shown in Fig. 11(a), if the sense of rotation of the helix is defined as positive when the value of φ is positive, the sense of rotation of the helix is the reversal to the former one when the value of φ is negative. In the present experiment, it was found that when the values of φ for the dominant *C* mode is positive, the values of φ for the secondary *u* and *b* (or *d*) modes also are positive, and *vice versa*. Therefore, it is confirmed that the senses of rotation for *C*, *u*, and *b* (or *d*, when the oscillation mode is a helical one) modes are the same.

D. Sound source of the *A* mode screech

Next, the sound source of the jet oscillating in the axially symmetric mode was investigated. Figure 3 shows a photograph of the jet oscillating in the axially symmetric A_1 mode for a jet pressure ratio $R=2.16$. In this photograph, the sound source is seen as a barbell-like dark portion at the rear edge of the third shock cell (indicated by an arrow). The distance from the nozzle exit to the center of the dark portion is $1.9d$. It is observed that wavelength λ of this screech is also $1.9d$. Thus, the distance from the nozzle exit to the sound source in the axisymmetric oscillation mode is the same as the wavelength of the screech.

E. Sound sources of the dominant *B* mode screech

Powell *et al.* (1992) have shown that the first lateral mode (dominant *B* mode) occasionally changes to a helical mode at the same frequency. What does occur in the change of oscillation modes at the same pressure ratio *R* and at the same frequency? In order to understand this mysterious phe-

nomenon, two schlieren photographs of the jet taken at a pressure ratio $R=2.93$ were carefully investigated. These photographs are shown in Fig. 4. Figure 4(a) shows the jet oscillating in the lateral mode, while Fig. 4(b) demonstrates the jet in the helical oscillation mode. The difference between both oscillation modes can easily be discriminated by the observation of the vortical structures in these photographs.

In the lateral mode, several discontinuous vortices are arranged alternately along the jet axis. In contrast to this, in the helical oscillation mode, a continuous helical vortex is seen around the jet. Comparing these photographs, it is observed that the wavelength λ of these sound waves is nearly equal to $2.8d$. However, axial distances from the nozzle exit to the prominent points and the centers of dark portions as the sound sources are different from each other.

By careful examination of these photographs, it was found that the axial spacing between two adjacent sound sources is nearly the same in both photographs. Namely, in Fig. 4(a) (lateral mode), the spacing between the centers of two adjacent dark portions seen on either side of the rear edge of the fourth cell is $1.6d$. In Fig. 4(b) (helical mode), the spacing between the adjacent two prominent points seen in the upper or lower part of the jet is also $1.6d$. Therefore, it is believed that the sound waves in both oscillation modes are generated at the same time interval during which the vortices pass through this distance of $1.6d$, which is just the period of these sound waves.

In the case of the lateral mode shown in Fig. 4(a), a prominent point (denoted by an arrow) exists near the rear edge of the third shock cell. The axial distance from the nozzle exit to this prominent point is $2.8d$, which is equal to one wavelength of the sound in this case. In contrast to this, for the case of the helical oscillation mode shown in Fig. 4(b), a prominent point (denoted by an arrow) is seen near the rear edge of the fourth shock cell. The axial distance from the nozzle exit to this prominent point is $4.2d$ which is equal to 1.5 times wavelength of the sound. The former situation is easily understood by a feedback process proposed by Powell (1953a). As the feedback loop for the dominant helical oscillation mode of *C* has been investigated in the previous section, the latter situation can also be reasonably understood.

Therefore, it is confirmed that for the lateral and helical oscillation modes appearing in dominant mode *B*, the sound sources exist at different axial distances from the nozzle exit. Namely, for the lateral oscillation mode, the sound source exists at one wavelength of the sound downstream of the nozzle exit (near the rear edge of the third shock cell). In the case of the helical oscillation mode, the sound source exists at one and one half wavelengths of the sound downstream of the nozzle lip (slightly downstream of the fourth cell) and it rotates around the jet axis.

F. Sound source of the dominant *D* mode screech

Finally the sound source for the dominant mode *D* was examined. Powell *et al.* (1990, 1992) have shown that in this oscillation mode, the jet oscillates laterally and the plane of oscillation rotates, vibrates, and dwells. Figure 10 shows the jets oscillating in this lateral mode. The pressure ratio of the jet is $R=4.87$.

Figure 10(a) is a view of the jet looking perpendicularly to the oscillation plane. In this photograph, it is observed that the sound waves with very short wavelength (high frequency) propagate in the direction about 30 deg downstream to the jet axis. Those high frequency sound waves are known to be radiated by the small vortices moving downstream around a jet at a supersonic velocity.

Figure 10(b) is a view of the jet looking in the oscillation plane. In this photograph, it is observed that the jet oscillates violently in the lateral oscillation mode and the very high frequency sounds are radiated. It is also observed that a very prominent point is seen at the rear edge of the fifth shock cell (denoted by an arrow). At this point, the jet axis bends significantly. The screech tone is radiated from this prominent point. So, it is confirmed that the dominant sound source in this lateral oscillation mode *D* exists at the rear edge of the fifth cell. From this photograph, it is also observed that in this case the screech tone emitted from the prominent point (sound source) at the rear edge of the fifth shock cell reaches the nozzle exit two cycles later.

Last, it must be noted that in the cases of the axially symmetric and lateral oscillation modes, the screech tones are generated intermittently by the interaction between the downstream-convecting discontinuous vortices around the jet and the oblique shock waves in the rear edge of the shock cells, while in the case of the helical oscillation mode, the screech tones are produced continuously by the interaction between a downstream-convecting helical vortex and the oscillating oblique shock waves in the shock cells.

IV. DISCUSSIONS

In this experimental study, mainly the generation of the screech tone in the dominant helical oscillation mode *C* was investigated using a series of instantaneous schlieren photographs and it is observed that the moving sound source for mode *C* appears as the prominent point "P_2" on the helical-shaped coherent vortical structure. This sound source is generated by the interaction between the helical-shaped coherent vortical structure and the oscillating oblique shock at the rear edge of the third shock cell. As soon as the point sound source is generated, a spherical sound wave is radiated from it. So, the sound source is an evanescent one and only one point source exists at every instant. Infinite numbers of such evanescent sound sources are generated at adjacent circumferential places in the plane perpendicular to the jet axis and just downstream of the end of the third shock cell. From these evanescent sound sources, infinite numbers of spherical sound waves are radiated successively. Therefore, these sound sources seem to act as if they were moving point sources along a circular orbit on the plane at a constant supersonic speed and an envelope of the sound waves forms a Mach cone moving along the circular orbit.

Prominent points appear at two instants in one cycle of the screech tone as shown in Fig. 7. They appear on upper and lower sides of jet. So, these prominent points indicate the front and back views of a head of the moving Mach cone.

The envelope of the Mach cone is widened both in the upstream and downstream directions as the sound source moves along the circular orbit and forms two helical-shaped wave fronts propagating in the upstream and downstream directions. This situation is observed in the photographs of Figs. 7(b) and (e). The distance from the nozzle exit to the plane of the circular orbit of the moving sound source could be estimated using this idea.

The idea of the moving Mach cone with sound source at the supersonic speed is not only capable of predicting the formation of the helical-shaped wave front of the screech tone, but can also explain the directionality of the screech tone in the helical oscillation mode of jet: maximum SPL at angles of 30° and 150°, minimum SPL at angles of 60° and 120° as shown in Fig. 8.

But, why is the observed directionality of the screech tone in the helical *C* mode antisymmetric in the upstream and downstream directions as shown in Fig. 8? It is difficult to understand this fact using the idea of the single moving sound source at a supersonic speed, because the sound waves produced as the envelope of the moving Mach cone must have the same intensity both in the upstream and downstream directions. Such situations are observed in the upper side of the jet shown in Fig. 7(a) and in the lower side of the jet shown in Fig. 7(b).

To understand the antisymmetry of the directionality of the screech tone in the helical *C* mode, the series of schlieren photographs shown in Fig. 7 must be investigated carefully: In Fig. 7(b), it is observed that two strong sound waves with symmetrical wave fronts are generated from the second prominent point "P_2" and are propagated in the upstream and downstream directions on the lower side of the jet. When the upstream-propagating sound wave passes through the rear edge of the second shock cell, as observed in Figs. 7(c) and (d), the original sound wave generated by the second prominent point "P_2" is intensified by the superposition with the sound wave produced by the first prominent point "P_1" appearing in the slightly downstream of the rear edge of the second shock cell.

Likewise, in Fig. 7(e), it is observed that two strong sound waves are produced from the prominent point "P_2" and are propagated in the upstream and downstream directions in the upper side of the jet. When the upstream-propagating sound wave passes through the rear edge of the second shock cell, it is observed from Fig. 7(b) that the original sound wave is also reinforced by superposition with the sound wave generated by the first prominent point "P_1."

In such a way, it can be understood that the screech tone in the helical oscillation mode is intensified in the upstream direction by the superposition of the sound waves generated by the second and first prominent points "P_2" and "P_1." The intensifying mechanism of the screech tone in the dominant helical *C* mode observed in the above series of photographs partly supports the usefulness of the idea of the superposition of the sound waves from the phased array of two sources ("P_1" and "P_2") as proposed by Powell (1953b).

Use of the only one idea of the superposition of the sound waves from the several sources, however, seems to be inadequate to explain the directionality of the screech tone in the helical oscillation mode, because it cannot predict maximum SPL at angles of 30° and 150° and minimum SPL at angles of 60° and 120° as shown in Fig. 8. Furthermore, the experimental result obtained by Norum (1983) for the directionality of the screech tone in the helical oscillation mode shows discrepancy with the calculated one using the idea of superposition of the sound waves, especially for the angular positions less than 60° and greater than 150° from the jet axis.

Therefore, to satisfactorily understand the whole directionality of the screech tone in dominant helical mode *C*, both ideas of the moving sound source at a supersonic speed and the superposition of the sound waves from the phased array are needed.

Incidentally, Powell *et al.* (1990) described an idea of the rotating sound source about the jet axis at a supersonic speed in conjunction with the helical oscillation mode of jet. But, they did not describe explicitly the concept of the Mach cone moving with the sound source. So, it was difficult to understand why the helical-shaped wave front is formed. They overestimated the feedback frequency, because they did not use the exact value for the diameter of the circular orbit of the moving sound source. They used nozzle diameter d as the diameter of the circular orbit. Actually, the diameter of the circular orbit was found to be $1.92d$ by the schlieren photograph in the present investigation. So, overestimation of the feedback frequency by Powell *et al.* (1990) was corrected using the value $1.92d$ as the diameter of the circular orbit. Powell *et al.* (1990) estimated the inclination angle α of the helical-shaped wave front of the screech tone as about 66°. This value did not agree at all with that observed in the schlieren photograph. The calculated value of α should become about 28°, if the value of $1.92d$ was used instead of d. This inclination angle of the helical-shaped wave front agrees very well with that observed in the schlieren photograph.

Here, some accompanying phenomena occurring with the dominant helical oscillation mode *C* of the jet were investigated. In the sound spectrum for a pressure ratio $R=3.90$ (Fig. 14), the dominant *C* mode tone and the secondary *u* and *b* (or *d*) mode tones are observed. In these tones, sound sources actually exist for the dominant *C* mode and the secondary *b* (or *d*) mode, but the sound source does not exist for the secondary *u* mode. This secondary tone belonging to the *b* (or *d*) mode is generated from the third prominent point "P_3" appearing at the rear edge of the fourth cell. The large ratio of 1.2 of the frequencies of screech tones between the dominant mode *C* and the secondary mode *b* (or *d*) is caused by the difference of the distances from the nozzle exit to the respective sound sources.

The sound wave for the *u* mode is observed as that with a higher sideband frequency owing to the amplitude modulation. The phenomenon of the amplitude modulation was reported in our previous papers on the hole-tone generation from choked jets (Umeda *et al.*, 1988; Umeda and Ishii, 1993). In these papers, it was suggested that the frequency of the amplitude modulation f_M is nearly equal to the frequency difference between the frequency of the dominant hole-tone f_0 and that of the screech tone f_S radiated from the free jet.

In the case of the screech tone, it is considered that the amplitude modulation of the helical *C* mode tone occurs when the jet is excited by the sound wave having a beat frequency Δf. This beat frequency is occurred by the frequency difference between the frequencies of the real sound waves in the dominant helical *C* mode (f_C) and the secondary *b* (or *d*) mode ($f_{b,d}$).

Now, consider the reason why the tone in the *b* (or *d*) mode is secondary one. In the photographs shown in Figs. 7(a) and (d), it can be seen that the sound source "P_3" for this mode exists near the rear edge of the fourth cell. At this place, the helical vortical structure is fairly disintegrated after interaction between the vortical structure and a shock wave at the rear edge of the third shock cell. So, the sound source in this case will be relatively weak. Therefore, it is concluded that the tone belonging to the *b* (or *d*) mode and the other two tones becomes a secondary tone.

Next, since the helical mode *C* of the jet oscillation is dominant, it was supposed that the secondary oscillation mode of *b* (or *d*) accompanied with the dominant helical mode was also helical one. From the present experiment, however, it was observed that the secondary *b* (or *d*) mode is the lateral and occasionally changes to the helical one [see Fig. 11(c)]. The result partly supports the above supposition. Namely, we could expect the helical oscillation mode, but could not expect the lateral one which occasionally occurred.

The reason this lateral mode occurs may be considered as follows: In the photograph of Fig. 7(a), it is observed that the second prominent point "P_2," which is the sound source of the tone for the dominant *C* mode, appears slightly downstream from the rear edge of the second shock cells. So, at this place, the sound wave is generated from the jet oscillating tightly in the helical mode. But, the third prominent point "P_3," which is the sound source of the tone for the secondary *b* (or *d*) mode, appears at the rear edge of the fourth shock cell. At this location, it is suggested that the jet has two degrees of freedom of oscillation in the helical and lateral modes. This occurs because the adjacent shock cells move in opposite directions to each other about the rear edge of the shock cell, as was shown in Fig. 7. But, since this sound generation process in the lateral mode is the secondary one, as shown in the power spectrum of Fig. 14, the dominant mode of jet oscillation becomes a helical one.

In the case of the dominant *B* mode, it is observed that the helical mode occasionally changes to the lateral mode at the same frequency, and *vice versa*. Therefore, the helical mode appearing in the *B* mode is unstable unlike the dominant helical *C* mode. The instability of the helical mode appearing in the *B* mode may be constructed in the following manner: As Powell *et al.* (1992) described, when two lateral oscillation modes of jet with the same frequency and almost the same amplitude occur in two planes perpendicular to each other, the linear combination of them results in the helical oscillation mode of jet. In this case, the point sound source moves at supersonic speed along a circular orbit about the jet axis.

However, by the jet instability, the separation angle between the two oscillation planes in the lateral mode and the amplitude of the jet oscillation are changed from time to time. Then, the helical oscillation mode cannot persist and the mode changes to the lateral one. If the conditions for the creation of the helical oscillation of the jet are satisfied again, helical oscillation mode appears again.

Furthermore, for the lateral and helical oscillation modes appearing in the dominant *B* mode, it is observed that the dominant sound sources exist at different axial distances from the nozzle exit for the respective oscillation modes. In the lateral oscillation mode, the sound source exists at one wavelength of the sound wave downstream from the nozzle exit. In the case of the helical oscillation mode, it exists at one and one half wavelengths downstream from the nozzle lip and rotates around the jet axis. But the reason why the change in the axial distance from the nozzle exit to the dominant sound source appearing in the different two oscillation modes (helical and lateral) occurs remains unsolved; further experimental study is necessary.

In the cases of the axisymmetric *A* and the lateral *D* oscillation modes, the dominant sound sources of the screech exist at one wavelength and two wavelengths downstream from the nozzle exit, respectively.

Finally, it is found from the instantaneous schlieren photographs taken in each oscillation mode of the jets that for the axially symmetric and lateral oscillation modes, the axial distances from the nozzle exit to the sound sources take the values of $n\,[=1,2]$ times the wavelengths λ of the screech tones, while in the case of the helical oscillation mode, they take the values of $(n+1/2)$ times the wavelength λ.

Therefore, it is considered that the convection Mach number M_{con} of the coherent vortices is automatically controlled by changing the spreading ratio of the jet boundary so that the wavelengths Λ of the vortices (defined as the spacing between the adjacent vortices) times $n\,[=1,2$, in the cases of the axially symmetric and lateral modes] or $(n+1/2)$ [in the case of the helical mode] become equal to the distances from the nozzle exit to the respective sound sources. Thus, considering the variation of the convection Mach number M_{con} of the vortices with the pressure ratio *R* of the jet shown by Powell *et al.* (1992), the feedback mechanism of the generation of the screech tone can be understood quite reasonably.

For this point, Panda (1999) proposed the standing wave pattern formed by the partial interference between the downstream-propagating hydrodynamic wave and the upstream-propagating acoustic wave based on his experimental result and showed that an exact screech frequency formula could be derived. But, as he described, the fact that his exact relation for the screech frequency does not require shock spacing is somewhat puzzling.

V. CONCLUSIONS

The present experimental study was performed to solve mainly the fundamental problems about the generation of the dominant helical oscillation mode *C* of the jet:

(1) Why does the helical oscillation mode of jet occur?
(2) Where is the sound source?
(3) How dose the sound source behave?

We believe that these problems are solved by introduc-

ing the moving sound source found in a series of photographs of the flow field along with the near-sound field. The moving sound source is generated as follows: a helical-shaped coherent vortex passes through the rear edge of the third shock cell; each segment of the helical vortex produces point sound source on the different radial places in the plane perpendicular to the jet axis. In this way, the axial distance of the feedback loop is kept to be constant at every instant.

The sound source of the screech tone for the dominant helical oscillation mode *C* can be observed as the second prominent point "P_2" appeared just downstream of the rear edge of the third shock cell. This sound source rotates about the jet axis at a constant supersonic speed in a plane perpendicular to the jet axis and forms a Mach cone with moving sound source. The envelope of the Mach cone is widened upstream and downstream as the sound source moves along the circular orbit and forms two helical-shaped wave fronts of the screech tone for the dominant helical oscillation mode of jet. This idea of the moving sound source predicts partly the directionality of the screech tone in the helical oscillation mode. Therefore, we believe that three riddles about the dominant helical oscillation mode of jet are made clear in this investigation.

The sound sources for the secondary *u* and *b* (or *d*) mode tone generated in conjunction with the generation of the dominant helical *C* tone were investigated. It is found that although the sound source for the secondary *b* (or *d*) mode tone exists, the sound source for the *u* mode tone does not exist.

For the dominant *B* mode tone, it is clarified by the schlieren photographs that the axial distance from the nozzle exit to the location of the dominant sound source differs with each other depending on the oscillation mode at the same frequency (lateral or helical mode).

Finally, it has to be stressed that our main conclusions require the presence of the helical vortex around the jet oscillating in the *C* mode. In other words, the frequency characteristics and the directionality of the screech tone and also the corresponding oscillating behavior of the jet in the *C* mode cannot be explained consistently and successfully without the presence of the helical vortex. In this respect, the presence of the vortex has been established rather indirectly. Although there is ample circumstantial evidence for the existence of the helical vortex, we confidently expect that detailed measurements of the vorticity distribution in the jet will confirm the presence of the helical vortex.

ACKNOWLEDGMENTS

The authors would like to thank Professor A. Powell at Houston University for valuable discussions and comments on this paper.

Davies, M. G., and Oldfield, D. E. S. (**1962**). "Tones from a choked axisymmetric jet. II. The self-excited loop and mode of oscillation," Acustica **12**, 267–277.

Howe, M. S., and Ffowcs Williams, J. E. (**1978**). "On the noise generated by an imperfectly expanded supersonic jet," Philos. Trans. R. Soc. London, Ser. A **289**, 271–314.

Inoue, O., and Hattori, Y. (**1999**). "Sound generation by shock-vortex interactions," J. Fluid Mech. **380**, 81–116.

Minota, T. (**1993**). "Interactions of a shock wave with a high-speed vortex ring," Fluid Dyn. Res. **12**, 335–342.

Norum, T. D. (**1983**). "Screech suppression in supersonic jets," AIAA J. **21**, 235–240.

Panda, J. (**1998**). "Shock oscillation in underexpanded screeching jets," J. Fluid Mech. **363**, 173–198.

Panda, J. (**1999**). "An experimental investigation of screech noise generation," J. Fluid Mech. **378**, 71–96.

Ponton, M. K., and Seiner, J. M. (**1992**). "The effects of nozzle exit lip thickness on plume resonance," J. Sound Vib. **154**, 521–549.

Powell, A. (**1953a**). "On the mechanism of choked jet noise," Proc. Phys. Soc. London, Sect. B **66**, 1039–1056.

Powell, A. (**1953b**). "On the noise emanating from a two-dimensional jet above the critical pressure," Aeronaut. Q. **4**, 103–122.

Powell, A., Umeda, Y., and Ishii, R. (**1990**). "The screech of round choked jets, revisited," AIAA Paper 90-3980.

Powell, A., Umeda, Y., and Ishii, R. (**1992**). "Observation of the oscillation modes of circular choked jets," J. Acoust. Soc. Am. **92**, 2823–2836.

Raman, G. (**1997**). "Cessation of screech in underexpanded jets," J. Fluid Mech. **336**, 69–90.

Raman, G. (**1999**). "Supersonic jet screech: Half-century from Powell to the present," J. Sound Vib. **225**, 543–572.

Shen, H., and Tam, C. K. W. (**1998**). "Numerical simulation of the generation of axisymmetric mode jet screech tones," AIAA J. **36**, 1801–1807.

Szumowski, A. P., and Sobieraj, G. B. (**1996**). "Sound generation by a ring vortex-shock wave interaction," AIAA J. **34**, 1948–1949.

Tam, C. K. W., Seiner, J. M., and Yu, J. C. (**1986**). "Proposed relationship between broadband shock associated noise and screech tones," J. Sound Vib. **110**, 309–321.

Umeda, Y., and Ishii, R. (**1993**). "Hole tone generation from highly choked jets," J. Acoust. Soc. Am. **94**, 1058–1066.

Umeda, Y., Maeda, H., and Ishii, R. (**1988**). "Hole tone generation from almost choked to highly choked jets," AIAA J. **26**, 1036–1043.

Westley, R., and Woolley, J. H. (**1975**). "The near-field sound pressures of a choked jet when operating in the spinning mode," AIAA 2nd AeroAcoustics Conference, AIAA Paper 75-479.

Westley, R., and Woolley, J. H. (**1976**). "Sound pressures of a choked jet oscillating in the spinning mode," AIAA Aeroacoustics Specialists Conf., 2nd, Prog. Astronaut. Aeronaut. **43**, 185–202.

Quasisteady aero-acoustic response of orifices

P. Durrieu[a)]
Laboratoire d'Acoustique Université du Maine, URA CNRS 1101, BP 535 Av. O. Messiaen, 72017 Le Mans Cedex, France

G. Hofmans
Applied Physics, CC.2.24, Technische Universiteit Eindhoven, Postbus 513, 5600 MB Eindhoven, The Netherlands

G. Ajello
Laboratoire d'Acoustique Université du Maine, URA CNRS 1101, BP 535 Av. O. Messiaen, 72017 Le Mans Cedex, France

R. Boot
Applied Physics, CC.2.24, Technische Universiteit Eindhoven, Postbus 513, 5600 MB Eindhoven, The Netherlands

Y. Aurégan
Laboratoire d'Acoustique Université du Maine, URA CNRS 1101, BP 535 Av. O. Messiaen, 72017 Le Mans Cedex, France

A. Hirschberg[b)]
Applied Physics, CC.2.24, Technische Universiteit Eindhoven, Postbus 513, 5600 MB Eindhoven, The Netherlands

M. C. A. M. Peters
PULSIM, TNO-TPD, Postbus 155, 2600 AD Delft, The Netherlands

(Received 20 October 1999; revised 18 June 2001; accepted 8 July 2001)

The low frequency response of orifices (slit, circular diaphragm, and perforated plate) in the presence of mean flow is well predicted by a quasisteady theory. A refinement is brought to the theory by considering a Mach number dependent vena contracta coefficient. The measurements of the vena contracta coefficient of a slit agree well with the simple analytical expression existing in the case of the Borda tube orifice. The measured scattering matrix coefficients do not depend strongly on the geometry of the element. If the frequency is increased the moduli remain relatively unaffected while the arguments exhibit a complex behavior which depends on the geometry. From these considerations an anechoic termination efficient at high mass flow is designed. © *2001 Acoustical Society of America.* [DOI: 10.1121/1.1398058]

PACS numbers: 43.28.Py, 43.28.Ra [LCS]

I. INTRODUCTION

Orifices and perforated plates are generic elements in silencers which take care of sound absorption. The quasisteady theory assumes that the acoustic response of such elements can be described as a succession of steady flow states. This approach has been used by, among others, Ingard and Ising,[1] Cummings[2] for orifices, by Ronneberger[3] for sudden expansions in pipe cross sections and grazing flow along wall perforations.[4] A general discussion of engineering applications is provided by Davies.[5] The absorption of sound in such devices has been explained in terms of vortex shedding by Bechert.[6] Bechert[6] showed also that a properly designed orifice placed at the end of a pipe is an anechoic (nonreflecting) termination at a specific Mach number. While more elaborate theories are now available, which describe the frequency dependence of the aero-acoustic response of orifices[7–10] the quasisteady theory remains a most useful design tool. In this paper we provide some information about the frequency range in which this theory is valid. The influence of the orifice geometry (slit, circular hole, and perforated plate) is considered. While we restrict ourselves to low frequencies, relatively high Mach numbers, as found in mufflers, are considered. Finally the theory is applied to design an anechoic termination which has been used in scale experiments of combustion in long pipe-lines.

A simplified model of the steady flow through an orifice placed in a pipe is presented in Fig. 1.

At the orifice, a free jet is formed by separation of the flow. After flow separation the jet contracts from the orifice cross sectional area S_d to a final cross section S_j, the vena contracta. Further downstream the jet flow becomes unstable and a turbulent mixing region is observed before a fully developed pipe flow is recovered. In practice the turbulent mixing region can be quite long, we however assume that all the

[a)]Now at: PSA Peugeot Citroën, Direction Organes, 18, rue des Fauvelles, 92256 La Garenne-Colombes Cedex, France.
[b)]Author to whom correspondence should be addressed; electronic mail: A.Hirschberg@tue.nl

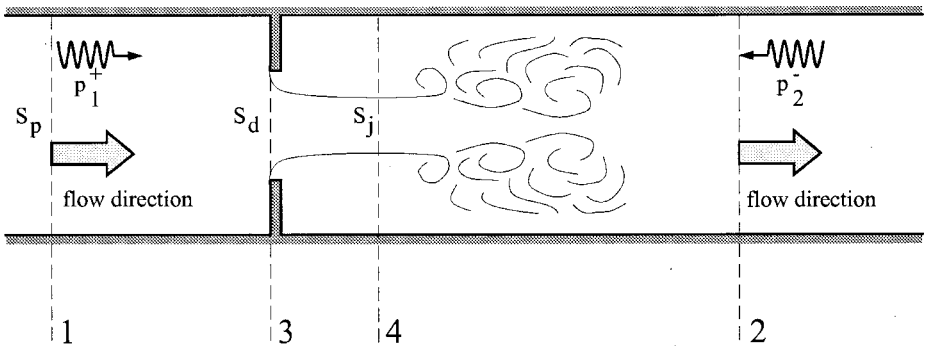

FIG. 1. Harmonic perturbation of a flow passing through a diaphragm. Description of the phenomenon and notations. Regions 1 and 2: one-dimensional flow, region 3: jet formation, region 4: turbulent flow.

relevant acoustical phenomena occur within a few pipe diameters.

A quantitative prediction of the aero-acoustic performance of an orifice involves the knowledge of the ratio S_j/S_d of jet to orifice cross sectional areas, which is called the vena contracta factor Γ_0. Often the theoretical value $\Gamma_0=\pi/(2+\pi)$ for an incompressible flow through a slit shaped orifice in an infinite baffle is quoted. We propose a semiempirical approach allowing us to predict both the effect of compressibility of the flow (Mach number dependency) and of the confinement in the pipe. The key idea is to use an interpolation formula between limit cases which has been derived by Hofmans[10] for the case of a Borda tube orifice (sharp edged pipe segment of cross sectional area S_d placed in the orifice).

The theory is validated by means of scattering matrix measurements obtained by means of a two-load method[11] at the TUE (Technische Universiteit Eindhoven) and TA-HGE (Tenneco Automotive-Heinrich Gillet GmbH & Co. KG) and a two-source method.[11–13] at the LAUM (Laboratoire d'Acoustique de l'Université du Maine).

Finally the design of a robust anechoic pipe termination effective over a broad range of Mach numbers and frequencies is discussed.

II. PREDICTION OF AERO-ACOUSTICAL RESPONSE

A. Wave propagation

Consider a diaphragm as a discontinuity between two uniform pipe segments of cross sectional area S_p. The flow upstream of the discontinuity is assumed to be one-dimensional and is determined by the flow velocity u_1, the pressure p_1, and the density ρ_1. This flow is assumed to be isentropic, there are no incoming fluctuations of the entropy convected with the flow. Downstream of the discontinuity, we assume again a one-dimensional flow with velocity u_2, pressure p_2, and density ρ_2. This flow is assumed to be adiabatic but not isentropic. The modulation of the dissipation in the turbulent mixing region downstream of the jet (see Fig. 1) induces fluctuations in the entropy.

The flow is perturbed by incident acoustic waves p_1^+ and p_2^- corresponding to a wave travelling in the downstream direction at the upstream side and a wave travelling upstream at the downstream side. These perturbations generate acoustic waves p_1^- and p_2^+ travelling upstream at the upstream side and downstream at the downstream side. The pressure perturbations travel with the local speed of sound c_i ($i=1,2$). The entropy perturbation σ_2' is convected with the flow velocity u_2.

The present discussion is further restricted to harmonic perturbations of radial frequency ω. The sign convention $\exp[i\omega t]$ is used. The amplitude of the perturbations are indicated by a prime. We furthermore neglect sound production by the discontinuity which is not correlated with the incoming perturbations. In such a case the pressure waves generated at the discontinuity can be expressed in terms of the scattering matrix:

$$\begin{pmatrix} p_2^+ \\ p_1^- \end{pmatrix} = \begin{pmatrix} t^+ & r^- \\ r^+ & t^- \end{pmatrix} \begin{pmatrix} p_1^+ \\ p_2^- \end{pmatrix}. \tag{1}$$

The elements t^+ and r^+ are the transmission and reflection coefficients of a wave p_1^+ measured for $p_2^-=0$. This condition is achieved for a sound source placed upstream and an anechoic termination placed downstream of the discontinuity. The elements t^- and r^- are the equivalent transmission and reflection coefficients of a p_2^- wave measured when $p_1^+=0$.

Frequencies such that only plane acoustic waves propagate in the pipe segments are considered. The highest frequencies considered are about one tenth of the cut-off frequency for propagation of higher order acoustic modes. Far from any discontinuities, this implies that the acoustic pressure $p'(x)$ is given by

$$p_i'=p_i^+ \exp[-ik_i^+x]+p_i^- \exp[ik_i^-x] \tag{2}$$

with $i=1,2$. The frequencies considered are so high that visco-thermal dissipation can be described in terms of a small correction to the wave numbers:

$$k^\pm=\frac{\omega}{c_i\pm u_i}+(1-i)\alpha_i^\pm, \tag{3}$$

where $\alpha_i^\pm$ is the damping coefficient and u_i the mean velocity of the flow. Complex wave numbers k_i^+ and k_i^- are given in the Appendix.

When calculating the velocity perturbations u' due to the acoustic waves we neglect the effect of friction:

$$u_i'=\frac{p_i^+-p_i^-}{\rho_i c_i} \tag{4}$$

while the density fluctuations ρ' are related to the pressure fluctuation by using the equation of state:

$$c_i^2\rho_i' = p_i' + \sigma_i', \tag{5}$$

where σ' are the entropy waves introduced by Ronneberger.[3] Note that $\sigma_1' = 0$ in our applications.

B. Steady flow through an orifice

Consider now a steady flow through an orifice as sketched in Fig. 1. The flow is assumed from the upstream region (1) until the vena contracta (j) of the free jet to be homentropic and frictionless. Furthermore the turbulent mixing region is assumed between the vena contracta (j) and the downstream region (2), to be adiabatic and we neglect wall friction in this region. Using a one-dimensional flow approximation we derive from the integral mass conservation law, the equations

$$\rho_1 u_1 = \rho_2 u_2 \tag{6}$$

and

$$\rho_1 u_1 = \Gamma_0 \frac{S_d}{S_p} \rho_j u_j \tag{7}$$

with $\Gamma_0 = S_j/S_d$. As the flow is adiabatic the total enthalpy is conserved. Assuming an ideal gas with constant γ we have

$$\frac{1}{2}u_1^2 + \frac{\gamma}{(\gamma-1)}\frac{p_1}{\rho_1} = \frac{1}{2}u_2^2 + \frac{\gamma}{(\gamma-1)}\frac{p_2}{\rho_2} \tag{8}$$

and

$$\frac{1}{2}u_1^2 + \frac{\gamma}{(\gamma-1)}\frac{p_1}{\rho_1} = \frac{1}{2}u_j^2 + \frac{\gamma}{(\gamma-1)}\frac{p_j}{\rho_j}. \tag{9}$$

The momentum conservation applied to the mixing region yields

$$p_j + \Gamma_0 \frac{S_d}{S_p}\rho_j u_j^2 = p_2 + \rho_2 u_2^2. \tag{10}$$

This system of equation is complemented by the isentropic flow condition in the jet

$$(p_j/p_1) = (\rho_j/\rho_1)^\gamma. \tag{11}$$

The flow is determined when four variables are specified by boundary conditions. One of these boundary conditions is that the upstream flow is assumed to be homentropic. The numerical procedure for solving this set of equation involves an iterative procedure for which a Newton method is used. In this iterative procedure we take into account the fact that the vena contracta factor Γ_0 depends on the Mach number.

C. Linear perturbation of the flow

We introduce small perturbations p_i', ρ_i', and u_i' of the stationary flow state p_i, ρ_i, and u_i (with $i=1$, 2 or j at the upstream, downstream side or at the jet). The time dependence of the vena contracta factor Γ_0 which is induced by fluctuations in the Mach number is neglected. The linear perturbation of the mass balance equations (6) and (7) yields

$$\frac{1}{c_1}[p_1^+(1+M_1) - p_1^-(1-M_1)] = \frac{1}{c_2}[p_2^+(1+M_2) - p_2^-(1-M_2) + \sigma_2' M_2] \tag{12}$$

and

$$\frac{1}{c_1}[p_1^+(1+M_1) - p_1^-(1-M_1)] = \frac{\Gamma_0}{c_j}\frac{S_d}{S_p}[p_j' M_j + u_j' \rho_j c_j], \tag{13}$$

where the ideal gas law is used to calculate the speed of sound $c_i^2 = \gamma p_i/\rho_i$. The conservation of total enthalpy (8) and (9) can be written in terms of linear perturbations as

$$\frac{1}{\rho_1}[p_1^+(1+M_1) + p_1^-(1-M_1)] = \frac{1}{\rho_2}\left[p_2^+(1+M_2) + p_2^-(1-M_2) - \frac{\sigma_2'}{\gamma-1}\right] \tag{14}$$

and

$$\frac{1}{\rho_1}[p_1^+(1+M_1) + p_1^-(1-M_1)] = \frac{1}{\rho_j}[p_j' + u_j' \rho_j c_j M_j]. \tag{15}$$

The momentum conservation low (10) in terms of linear perturbations becomes

$$\left[p_j'\left(1 + \Gamma_0 \frac{S_d}{S_p} M_j^2\right) + 2u_j' \Gamma_0 \frac{S_d}{S_p}\rho_j c_j M_j\right] = p_2^+(1+M_2)^2 + p_2^-(1-M_2)^2 + \sigma_2' M_2^2. \tag{16}$$

For given incident waves p_1^+ and p_2^-, this set of equations can be solved for the unknowns p_1^-, p_2^+, σ_2', p_j', and u_j'. In principle, the elements t^+, r^+, t^-, and r^- of the scattering matrix of Eq. (1) can be deduced from these results. Explicit expressions are so complex that they do not provide much insight and are therefore not presented.

D. Vena contracta factor

In the present section we provide information on the dependence of the vena contracta factor $\Gamma_0 = S_j/S_d$ on the Mach number M_1, the ratio S_d/S_p of orifice to pipe cross sectional areas, the Reynolds number and the geometry.

As starting point of the discussion, we assume that the orifice has sharp edges and that the Reynolds number is high so that the effect of S_d/S_p and M_1 are mainly considered. Some insight on the influence of the geometry are provided by considering both the slit and the circular orifice. Our analysis is based on the theory for an orifice in which the opening has been replaced by a thin walled pipe of cross section S_d. This corresponds to a Borda tube confined in a pipe of section S_p as shown in Fig. 2.

Using a theoretical approach similar to that of Sec. I B we have the following equation:

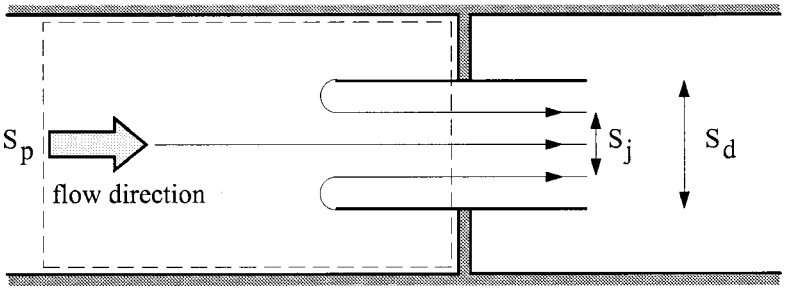

FIG. 2. Confined Borda tube used to derived a theory of the dependence of the vena contracta factor on the Mach number M_1 and the confinement ratio S_d/S_p.

$$\rho_1 u_1 = \Gamma_0 \frac{S_d}{S_p} \rho_j u_j \tag{17}$$

from the mass conservation law, and the equation

$$S_p(p_1 + \rho_1 u_1^2) = (S_p - S_d)p_0 + S_d(p_j + \Gamma_0 \rho_j u_j^2) \tag{18}$$

from the integral momentum equation applied on a control volume enclosing the orifice (see Fig. 2). In this equation the pressure p_0 is the pressure on the upstream side of the orifice plate which is assumed to be uniform and equal to the stagnation pressure of the upstream flow:

$$p_0 = p_1 \left(1 + \frac{\gamma - 1}{2} M_1^2 \right)^{\gamma/(\gamma-1)}. \tag{19}$$

As we assume an homentropic flow down to the vena contracta, we have also the isentropic flow condition (11)

$$p_j / p_1 = (\rho_j / \rho_1)^{\gamma}. \tag{20}$$

Using Eqs. (11), (17), and (18) p_j, ρ_j, and u_j are eliminated to obtain an expression relating Γ_0 to M_1 and S_d/S_p. It is however more convenient to use the jet Mach number $M_j = u_j/c_j$ as a parameter. The jet Mach number M_j is related to the upstream Mach number M_1 by the relationship

$$1 + \gamma M_1^2 = \left(1 - \frac{S_d}{S_p} \right) \left(1 + \frac{\gamma - 1}{2} M_1^2 \right)^{\gamma/(\gamma-1)} + \frac{S_d}{S_p} \left(\frac{1 + \frac{\gamma - 1}{2} M_1^2}{1 + \frac{\gamma - 1}{2} M_j^2} \right)^{\gamma/(\gamma-1)} + \gamma M_j M_1 \left(\frac{1 + \frac{\gamma - 1}{2} M_1^2}{1 + \frac{\gamma - 1}{2} M_j^2} \right)^{1/2}. \tag{21}$$

Once M_j has been determined for given M_1 and S_d/S_p the vena contracta factor is easily calculated from

$$\Gamma_0 = \frac{S_0}{S_d} \frac{M_1}{M_j} \left(\frac{1 + \frac{\gamma - 1}{2} M_j^2}{1 + \frac{\gamma - 1}{2} M_1^2} \right)^{(\gamma+1)/2(\gamma-1)}. \tag{22}$$

For $S_d/S_p < 0.6$ Hofmans[10] found that this formula can be approximated by

$$\Gamma_0 \simeq \frac{1}{1 + \sqrt{1 - (S_d/S_p)}} + \frac{\left(1 + \frac{\gamma - 1}{2} M_j^2 \right)^{\gamma/(\gamma-1)} - 1}{\gamma M_j^2} - \frac{1}{2} \tag{23}$$

which corresponds to an extrapolation formula

$$\Gamma_0(S_d/S_p, M_j) \simeq \Gamma_0(S_d/S_p, 0) + \Gamma_0(0, M_j) - \Gamma_0(0,0) \tag{24}$$

which is assumed to be valid for any orifice. We therefore discuss further the limiting values $\Gamma_0(0,0)$, $\Gamma_0(0,M_j)$, and $\Gamma_0(S_d/S_p,0)$ for both the slit and the circular orifice. For further reference note that the vena contracta factor of a Borda tube in an infinite baffle is in the incompressible limit $\Gamma_0(0,0) = \frac{1}{2}$.

The vena contracta factor of a slit in an infinite baffle can easily be calculated for an incompressible flow ($M_j = 0$) by means of the hodograph method.[14] One finds $\Gamma_0(0,0) = \pi/(2+\pi) \simeq 0.61$. The same value is often quoted for circular diaphragms but the theory predicts following Gilbarg[14] $\Gamma_0 = 0.58$. This discrepancy between the commonly reported vena contracta factor and the theory is expected to be due to Reynolds number effects in the experiments. Some information about Reynolds number dependence has been correlated by Blevins,[15] but we further ignore this effect. Higher vena contracta factors can also be due to the lack of sharpness of the edges of the orifice. An edge radius r to orifice diameter D of $r/D = 10^{-2}$ already explains the difference between experiment and theory.[15]

For a slit using the hodograph method, Busemann[16] found the implicit solution

$$\Gamma_0\left(\frac{S_d}{S_p}, 0 \right) = \frac{\pi}{\pi + 2\left(\frac{1}{\Gamma_0} \frac{S_p}{S_d} - \Gamma_0 \frac{S_d}{S_p} \right) \arctan\left[\Gamma_0 \frac{S_d}{S_p} \right]}. \tag{25}$$

For a circular orifice Idelchik[17] proposes the use of the equation

$$\Gamma_0\left(\frac{S_d}{S_p}, 0 \right) = \frac{1}{1 + \sqrt{0.5(1 - (S_d/S_p))}} \tag{26}$$

which provides in the range $0.1 \leqslant S_d/S_p \leqslant 0.7$ a good fit to the experimental data collected by Gilbarg.[14] For $\Gamma_0(0,0)$, this formula yields the value 0.586 which is the theoretical value obtained by Gilbarg[14] with a simplified theory. The formula for $\Gamma_0(S_d/S_p,0)$ has also a structure similar to the structure which was obtained for the Borda tube in Eq. (23). Also the value $\Gamma_0(S_d/S_p,0) - \Gamma_0(0,0)$ obtained with the for-

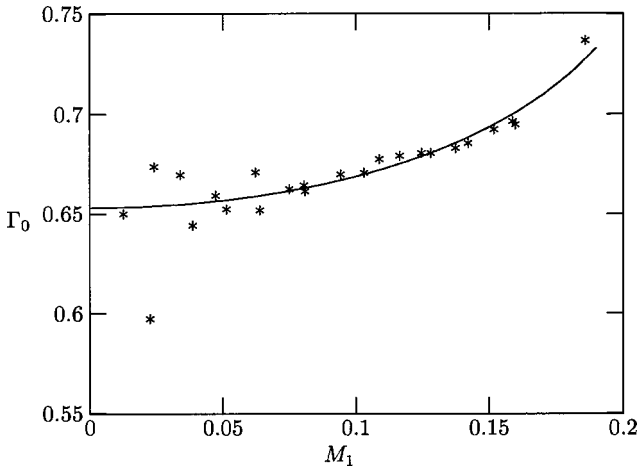

FIG. 3. Vena contracta coefficient Γ_0 of a slit with respect to M_1. *, measurements; —, relation 24 using formula 25 for the term $\Gamma_0(S_d/S_p,0)$ and formula 27 for the term $\Gamma_0(0,M_j)-\Gamma_0(0,0)$. The slit has a height of 10.8 mm and a width of 30 mm. The circular pipe has a diameter of 30 mm.

mula of Idelchik[17] is a good fit of the result of Busemann[16] in the range $0<S_d/S_p\leqslant 0.7$.

The Mach number dependence $\Gamma_0(0,M_j)-\Gamma(0,0)$ appears also to be quite insensitive to the geometry. For a slit Busemann[16,18] proposes an analytical expression based on a simplified model for the gas compressibility. While quite elegant this simplified theory is not very accurate. The value of $\Gamma(0,M_j)-\Gamma(0,0)$ obtained with the Borda tube model [Eq. (23)] appears to be a good fit of the experimental data for a circular orifice reported by Shapiro[18] and the two-dimensional theory without approximation for the gas compressibility. We propose to use the fit formula of Shapiro's solution:

$$\Gamma_0(0,M_j)-\Gamma_0(0,0)=0.13M_j^2 \tag{27}$$

which is a good fit to the theory up to $M_j=0.9$.

In Fig. 3 experimental data obtained with a slit shaped orifice in a circular pipe are compared with the proposed theory. The vena contracta factor has been derived from total pressure losses Δp_t using the Borda–Carnot formula $\Gamma_0=1/[1-\sqrt{(\Delta p_t/p_0)}]$ where p_0 is the upstream stagnation pressure.

For further reference the vena contracta factors measured for a perforated plate and a single orifice with the same (total) value of S_d/S_p are compared in Fig. 4. The perforated plate has 45 holes. We observe that the vena contracta factor of the perforated plate is higher than that of the orifice with a single hole. The difference can be due to the influence of the Reynolds number or to the difference in relative sharpness r/D of the edges of the perforations. Following Blevins,[15] a value $r/D=0.05$ is sufficient to explain this effect. This corresponds to $r=0.175$ mm in the case of the perforated plate. This stresses the importance of accurate geometry of the test elements whereas theoretical works on industrial devices must be based on measured pressure losses coefficients.

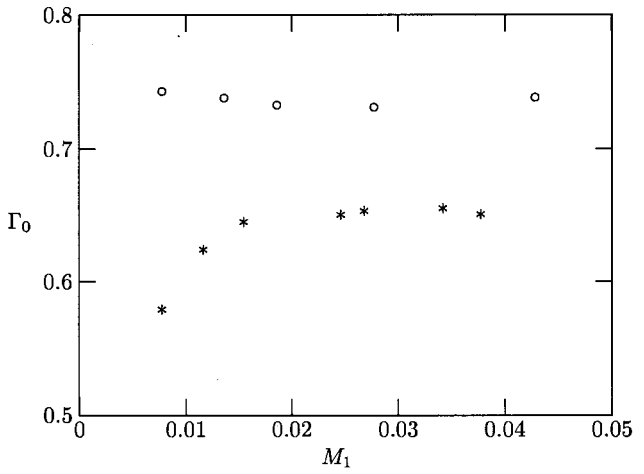

FIG. 4. Vena contracta coefficient Γ_0 with respect to M_1. Comparison between the vena contracta of a single hole orifice and a perforated plate of the same open area ratio. *, round edged single hole orifice inserted in a pipe; ○, perforated plate inserted in a pipe. The single hole orifice diameter is 23.3 mm, the plate is made of 45 holes of diameter 3.5 mm and the pipe diameter is 47 mm. The open area ratio is then 25%.

III. EXPERIMENTAL SET-UPS

A. Measurement method

The reflection coefficient data presented have been obtained by means of the two-microphone method.[19] The scattering matrix data was obtained by means of the two-load method at the TUE and TA-HGE while the two-source method was used at the LAUM. In the scattering matrix experiments two sets of microphones are placed at x_{11} and x_{12} upstream of the discontinuity and at x_{21} and x_{22} downstream of the discontinuity. At each side of the discontinuity the acoustic field is described by Eq. (2). The reflection coefficient R_i follows from the measurement of the transfer function $(H_{21})_i=p_i'(x_{i2})/p_i'(x_{i1})$:[19]

$$R_i=\frac{p_i^-}{p_i^+}=\frac{(H_{21})_i\exp[-ik_i^+x_{i1}]-\exp[-ik_i^+x_{i2}]}{-(H_{21})_i\exp[ik_i^-x_{i1}]+\exp[ik_i^-x_{i2}]}. \tag{28}$$

Note that we have chosen the origin $x=0$ at the discontinuity which we are characterizing. When the reflection coefficient has an absolute value close to unity, which corresponds to a standing wave pattern, the equation becomes singular when $|(x_{i2}-x_{i2})\omega/c_i|=n\pi$ with $n=1,2,\ldots$. Furthermore, as shown by Åbom and Bodén,[19] the accuracy of the measurement decreases strongly when $|(x_{i2}-x_{i2})\omega/c_i|>\pi/2$. This limits the frequency range in which we can measure. At the TUE, three microphones were used which allows us to check the accuracy of the data. At the LAUM, measurements were performed with anechoic terminations upstream and downstream of the discontinuity which reduces the standing wave pattern and makes measurements less sensitive to errors.

When two microphone pairs are placed at both sides of the discontinuity, the transmission coefficient $T_{21}=p_2^+/p_1^+$ can be in addition to the reflection coefficients R_1 and R_2 determined from

$$T_{21}=\frac{p_2'(x_{21})[\exp(-ik_1^+x_{12})+R_1\exp(ik_1^-x_{12})]}{p_1'(x_{12})[\exp(-ik_2^+x_{21})+R_2\exp(ik_2^-x_{21})]}. \tag{29}$$

When two experiments A and B have been performed for the same mean flow conditions but with different acoustic

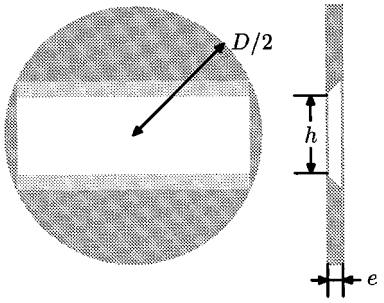

FIG. 5. Sketch of the measured slits. The dimensions are given in Table I.

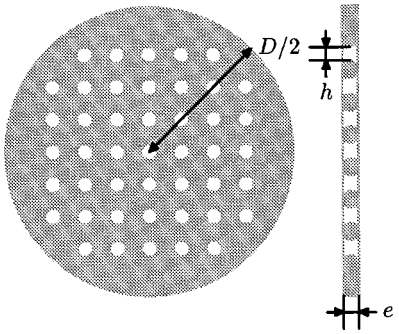

FIG. 6. Sketch of the measured perforated plate. The dimensions are given in Table II.

boundary conditions the scattering matrix is obtained from the set of linear equations

$$T_{21}^{A}=t^{+}+r^{-}R_{2}^{A}T_{21}^{A}, \tag{30}$$

$$R_{1}^{A}=r^{+}+t^{-}R_{2}^{A}T_{21}^{A}, \tag{31}$$

$$T_{21}^{B}=t^{+}+r^{-}R_{2}^{B}T_{21}^{B}, \tag{32}$$

$$R_{1}^{B}=r^{+}+t^{-}R_{2}^{B}T_{21}^{B}. \tag{33}$$

In the case of the two-load method the sound was produced by modulating the main flow by means of a siren (TUE) or a rotating valve (TA-HGE). At the downstream side the setup was terminated by an open pipe end at $x=L$. Two linearly independent experiments were achieved by using two different lengths, respectively $L=L_A$ and $L=L_B$. Optimal conditioning of the experiment is obtained for $|(L_B-L_A)\omega/c_2|=\pi/2$, which corresponds to a quarter wavelength. For $|L_B-L_A|$ equal to a multiple of a half wavelength the method is singular. At the TUE the measurements were restricted to a single optimal frequency. At TA-HGE additional experiments with different length were carried out to extend the frequency range.

When a pipe segment is actually mounted between the two experiments the operation is rather long which requires a corresponding stability of the mean flow conditions. The procedure can be accelerated by using a pipe segment of a quarter wave length placed downstream of a side branch closed by a piston. When the side branch length is increased from zero to a quarter wave length one achieves conditions which are similar to the ones obtained by changing the main pipe length by a quarter wave length. A nice feature of this method is that it can be used at high pressures, replacing the open pipe termination by a vessel with damping material. Drawback of this method is that it is only optimal at a single frequency.

The two-source method removes much of the problems of the two-load method. Loudspeakers were used as sources,[13] one placed upstream and the second placed downstream of the discontinuity. The use of anechoic terminations makes the setup insensitive to frequency. The use of loudspeakers makes it possible to use an automatic source control and therefore to reduce considerably the stability constraint of the main flow by speeding up the measurement procedure.

While the two-source method is more convenient, we did carry out experiments with the two-load method because the use of a siren or a rotating valve allows reproducing flow conditions which are closer to those found in industrial applications such as car mufflers. In particular a siren is a very powerful sound source at low frequencies where a loudspeaker cannot be used.

B. Setups

The technical details of the TUE setup have been provided by Peters.[20] The TA-HGE setup is described in the thesis of Durrieu.[21] The LAUM setup is described in the thesis of Ajello.[13] Some essential differences between the setups are now given.

At the TUE, we focused on the Mach number dependence of the scattering matrix at low frequency and high mass flow and the test of the anechoic termination for combustion experiments. The siren frequency and flow are stable within the experimental accuracy ($\Delta f/f=10^{-4}$, $\Delta M/M=10^{-2}$) during each experiment. A FFT procedure was used with a frequency discretisation corresponding to the experimental accuracy. Measurements were only carried out at the fundamental frequency generated by the siren. The coherence of the signals was larger than 0.999 99 (in most cases at least 0.999 999). The gas temperature T was deduced from the measured wall temperature T_w assuming a recovery factor for a turbulent boundary layer:[18]

$$T_w=T\left(1+\mathrm{Pr}^{1/3}\frac{\gamma-1}{2}M^2\right). \tag{34}$$

The accuracy of this temperature has been estimated to be 0.2 °C. The pipe diameter was $D=3.001$ cm. The test diaphragms used are slit shaped as shown in Fig. 5. The accuracy of the slits geometry was 0.01 mm. Special care

TABLE I. Labeling and dimensions of the orifices measured at the TUE and at the LAUM. The test pipe has a diameter of 30.01 mm.

Label	Width (mm)	Height (mm)	Thickness (mm)	Open area ratio (%)
Large slit (I)	30.01	10.8	4	45.76
Narrow slit (II)	30.01	2.7	4	11.46

TABLE II. Labeling and dimensions of the orifices measured at TA-HGE. The test pipe has a diameter of 47 mm.

Label	Diameter (mm)	Holes number	Thickness (mm)	Open area ratio (%)
Perforated plate	3.5	45	2	24.95
Diaphragm	23.3	1	2	24.6

was take to keep the edges as sharp as possible. The air was dry and dry air properties as reported by Peters[20] were used. The dimensions of the orifices investigated at the TUE are summarized in Table I.

The test section of the setup of the LAUM is the same as that of Eindhoven. The same microphones and signal conditioning is used. The main difference is that the sources (loudspeakers) are driven by a swept (stepwise) sine software procedure of the HP3565s analyzer. Two-hundred frequencies are scanned step by step within a relatively short time. As three microphones are placed on both sides of the discontinuity the air temperature can be determined from acoustical measurements. It is assumed that this temperature remains constant for all measured frequencies during one experiment, which leaves a considerable redundancy in the experimental data. This information is used by means of a least square procedure. Because the air is not dry, the effect of moisture is taken into account as specified by Ajello.[13]

The setup at TA-HGE has a larger diameter of the main pipe $D=4.7$ cm. This allows mounting the 1/2 inch condensator microphones (B&K 4133) flush to the pipe wall. The transfer functions were measured by means of a tracking method (analyzer DIFA DSA 204). The flow noise limited the frequency to the first few harmonics. The accuracy of the geometry of the test objects is of the order of 0.1 mm. Because the edges are not very sharp, the presented theoretical curves are based on measured pressure loss coefficients $C_D=\Delta p_t/p_0$. The focus of this part of the research was the investigation of the difference between single hole orifices and perforated plates as shown in Fig. 6.

The plate thickness is 1.5 mm the perforation diameter is 3.5 mm. Hence the plate remains relatively thin compared to the diameter of the perforations so that turbulent dissipation in the jets occurs downstream of the plate.[17] The dimensions of the orifices investigated at TA-HGE are summarized in Table II.

IV. VALIDATION OF THE THEORY

The Mach number dependent measurements performed on slits were carried out at the TUE. Figure 7 shows the modulus of the scattering matrix coefficients t^+, r^-, r^+, and t^- of a narrow and a large slit whose open area ratio are 11% and 46%, respectively. The measurement frequency was 77 Hz which is the optimum frequency for the two-microphone when considering the setup arrangement as described in the preceding section. The measurements are compared to three different theoretical predictions. An incompressible theory has been derived by Ajello.[13] The terms of the order of M^2 have been discarded and consequently the term accounting for the fluctuation of entropy is dropped since it is proportional to the square of the Mach number. Two compressible theories are distinguished. Both are derived by using the linearized compressible conservation equations written in Sec. II C: one approach considers a constant vena contracta factor while the second uses the relation (27). The value for the vena contracta coefficient at Mach 0 has been calculated by using the relation (25) a correction being made to account for the geometry of the tested element because relation (25) is valid for a two-dimensional slit. Hence Γ_0 has been calculated by integrating the relation (25) for a pipe diameter varying from h to D. The calculation leads to a value for Γ_0 of 0.653 for the large slit which seems coherent with the experimental data shown in Fig. 3. Note that the value predicted by the relation (26) is 0.658 which is close to 0.653 whereas relation (26) does not take into account the object geometry but only the open area ratio. The value of the vena contracta coefficient is 0.618 for the narrow slit.

As emphasized by the flow dependent theories, matrix coefficients depend strongly on the Mach number. This is all the more the case as the slit open area ratio decreases. The compressibility is expected to have an important influence for a Mach number in the jet above 0.3. Indeed the incompressible and compressible theoretical behaviors start to diverge for a Mach number of about 0.08 for the large slit and at about 0.02 for the narrow slit. Next the relevance of using a compressible vena contracta coefficient seems to be confirmed by the measurements of the direct coefficients t^+ and r^+ whereas it is less obvious for the reverse coefficients t^- and r^-. The compressible theory with $\Gamma_0(S_d/S_p,M_j)$ is however in all cases better than the compressible theory ignoring the Mach number dependence of the vena contracta coefficient. Moreover it can be concluded that a quasisteady theory predicts well the response of the slits at the frequency of measurements. Significant deviations have been observed by Ronneberger[8] at higher frequencies. Therefore some frequency dependent measurements were carried out in order to check the limit of the validity of the quasisteady modelling. These measurements were performed at the LAUM for frequencies up to 800 Hz.

Figure 8 presents the measured modulus of the scattering matrix coefficients with respect to frequency. The plots emphasize a weak frequency dependence. This tendency which is not explained by a one-dimensional theory has been reported by Ajello[13] for a circular diaphragm and by Ronneberger[3,8] for a perforated plate and at higher Mach numbers. The deviation is more accentuated as the Mach number increases. At high frequencies the distance over which the jet develops is no longer much shorter than the hydrodynamic wavelength: for the conditions of Fig. 8 the Strouhal number $\mathrm{Sr}=fh/u_d$ (where u_d is the mean flow velocity at the orifice) is about 1/4 at 800 Hz. The variation of the coefficients does not exceed 5% on the curves shown and

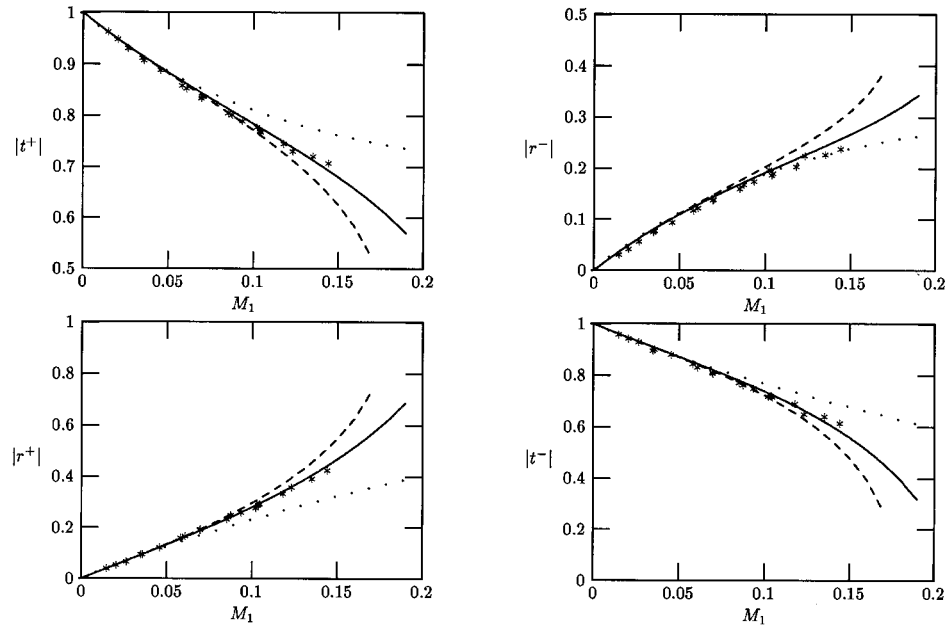

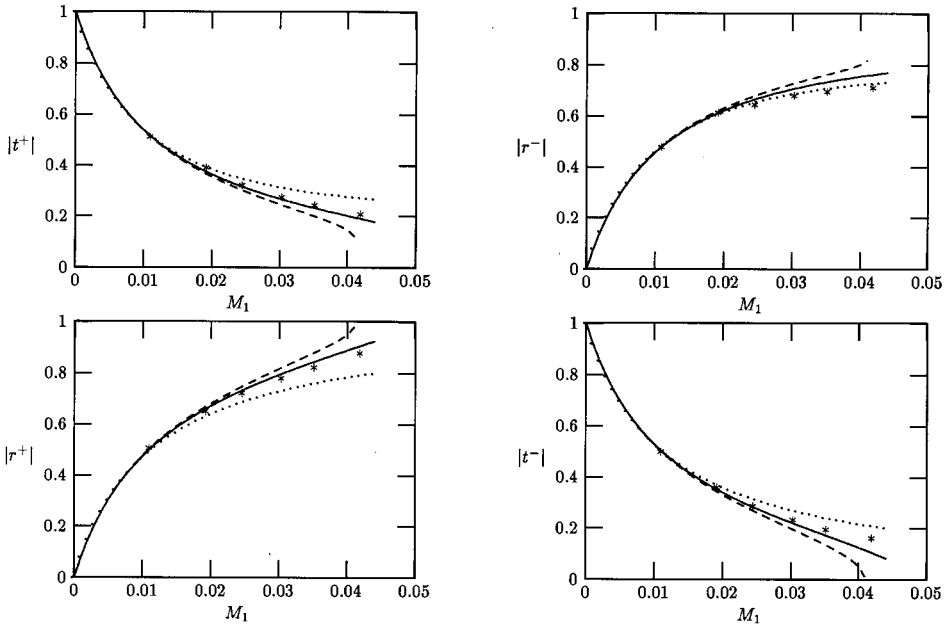

FIG. 7. Modulus of the scattering matrix coefficients with respect to M_1. —: Compressible theory with $\Gamma_0(S_d/S_p, M_j)$; ---, compressible theory with $\Gamma_0(S_d/S_p, 0)$; $\cdots$, incompressible theory. $f = 77$ Hz.

we chose not to investigate this phenomenon giving regard both to its relatively small importance at the frequencies of interest and to the complexity of the existing theories (see the introduction).

Figure 9 presents the argument of the matrix coefficients with respect to M_1 for a frequency of 77 Hz. It is not easy to extract pertinent information from the curves describing the Mach number dependence of the arguments. In particular the variation of the arguments of the reflection coefficients are much weaker than those observed by, e.g., Hofmans[10] and Ronneberger.[8] These variations have been predicted by Hofmans[10] by using a numerical code based on the vortex-blob method. They occur for Sr of the order of 1.0 which is much larger than the Strouhal numbers measured here (in our experiments $0.0008 < \mathrm{Sr} < 0.06$). At Mach 0 the frequency dependence of the argument is well predicted by the addition of an acoustic mass. This is illustrated by Fig. 10 in which are plotted the arguments of the matrix coefficients with respect to frequency for $M_1 = 0$. The theoretical curves shown in Fig. 10 are derived by using the expression of the acoustic mass given by Morse and Ingard[22] and whose length is written as

$$\Delta l = \frac{2h}{\pi} \ln\left(\frac{1}{2} \tan\frac{\pi h}{4D} + \frac{1}{2} \cot\frac{\pi h}{4D} \right). \tag{35}$$

In this case Δl is equal to about 4.3 mm which is almost 2 times larger than the well-known approximation of Fock[23]

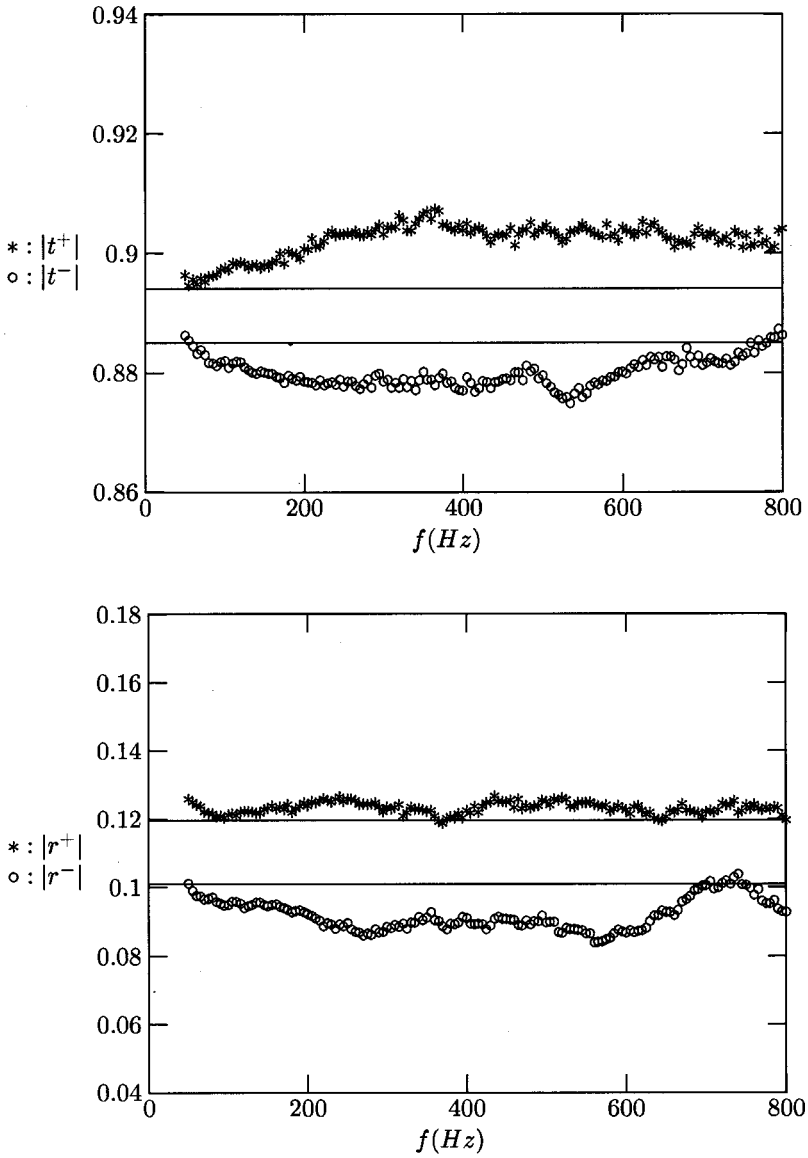

FIG. 8. Modulus of the scattering matrix coefficients of the slit (I) with respect to frequency. ∗, t^+ and r^+; ○, t^- and r^-; —, theoretical predictions. $M_1 = 0.045$.

for the circular diaphragm. This is an illustration of the important geometrical dependence of the acoustic mass (e.g., Refs. 24 and 25). As for the Mach number dependence of the acoustic mass it is emphasized in Fig. 11 which shows the argument of the reflection coefficient with respect to frequency for a Mach number equal to 0.045. Again the theoretical curves are derived by using the expression of Morse and Ingard[22] at Mach 0. These authors suggest that in a presence of flow the acoustic mass is divided by 2. This quantitative assumption is contradicted by our measurements. At high frequencies (200 Hz). it is close to the value at Mach 0. Below 100 Hz, negative values of $\varphi(r^-)$ are observed. A similar complex behavior has been reported by Ajello[13] for circular diaphragms and Peters[20] for open pipe terminations.

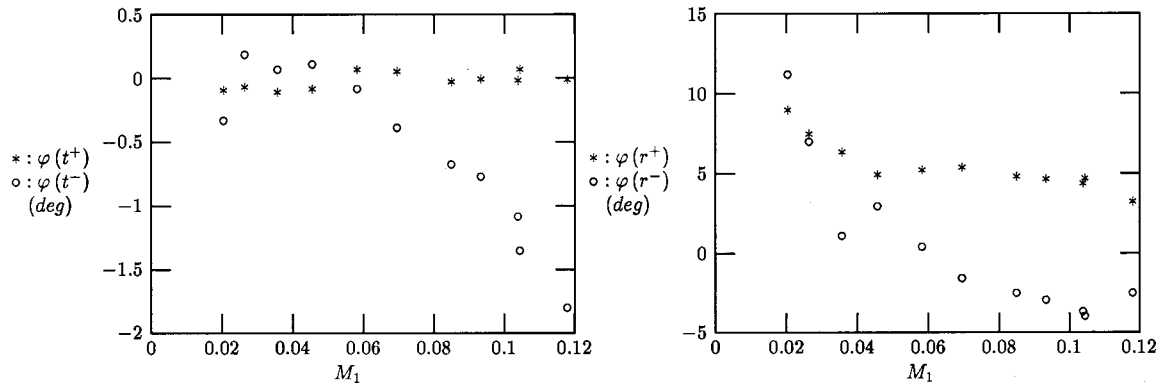

FIG. 9. Argument of the scattering matrix coefficients of the slit (I) with respect to the Mach number. $f = 77$ Hz.

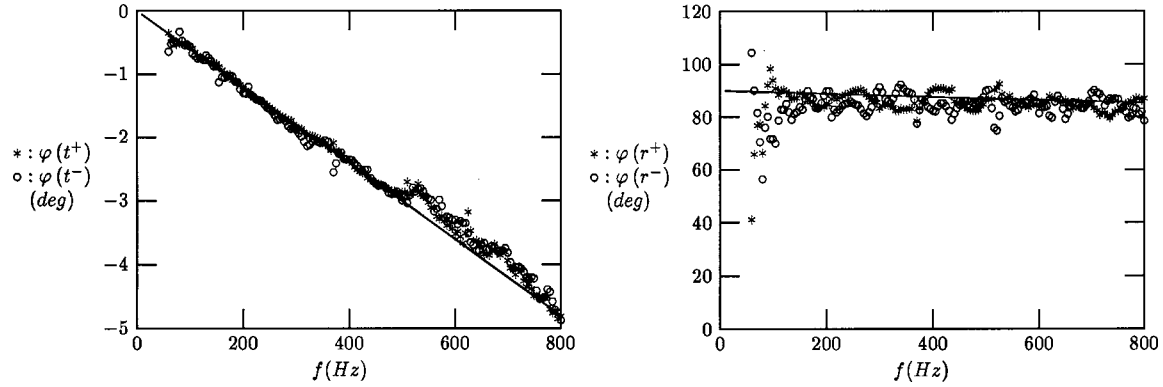

FIG. 10. Argument of the scattering matrix coefficients of the slit (I) with respect to frequency. ∗, ○, measurements; —, theory derived by using the acoustic mass given by Morse and Ingard. $M_1=0$.

Further measurements have been carried out at TA-HGE in order to investigate the behavior of diaphragmlike elements that are commonly used in the design of car silencers. These elements are the rounded edged diaphragm and the perforated plate. Figure 12 presents the comparison of a perforated plate and a rounded edged diaphragm of equal open area ratio of about 25%. The measurements were carried out by using four microphones working in pairs. For each pair the distance between the microphones is about 90 cm so that optimum measurements are obtained for frequencies of 100 Hz, 300 Hz,..., where the points at which the two-microphone method fails have been discarded. Predictions are also shown in the Figure: they are calculated by using a vena contracta coefficient directly extracted from the measured static pressure difference presented in Fig. 4. The frequency dependence of the modulus discussed above is also seen in the Figure, although it is much less clear than in Fig. 8. The interesting feature is that this frequency dependence seems to be weak in the case of the perforated plate. This behavior is also reported by Ronneberger[8] for measurements performed at much higher frequencies. It can be predicted by the addition of an acoustic mass: indeed contrary to the modulus of the circular diaphragm, $|t^+|$ and $|t^-|$ slightly decrease linearly with frequency and $|r^+|$ and $|r^-|$ slightly increase with frequency. This suggests that the frequency and mass flow limits of the validity of a quasisteady modelling of perforates are beyond those existing for a single hole diaphragm. Furthermore the measurements of the static pressure difference of perforated plates that we performed stress a very weak dependence of the vena contracta coefficient on the Mach number.

The arguments of r^+ and t^+ are shown in Fig. 12. For the circular diaphragm we use the approximation calculated by Fock[23] while for the perforated plate we use the expression given by Allard[26] which is written as

$$\Delta l = 0.48 S^{1/2}(1-1.14\Phi^{1/2}), \tag{36}$$

where S is the area of one aperture and Φ is the open area ratio, called porosity in the case of perforates. Due to the measurement accuracy, it is difficult to draw conclusions from the measurements. It seems however that the measured acoustic masses are smaller than those predicted by the acoustic masses, even if, as suggested by Morse and Ingard[22] they are corrected by a factor 2.

V. REFLECTION COEFFICIENT OF A DIAPHRAGM

Diaphragms have been used for many years as devices to reduce low frequency pulsations created, for example, behind compressors. One of the most recent works on this topic is the low frequency nonreflecting endplate presented by Bechert.[6] Bechert studied the sound absorption which occurs at a discontinuity in the presence of flow. For this purpose he derived a simple low frequency model of the flow past an orifice placed at the end of a duct. In this approach, all the kinetic energy is assumed to be absorbed by the turbulence

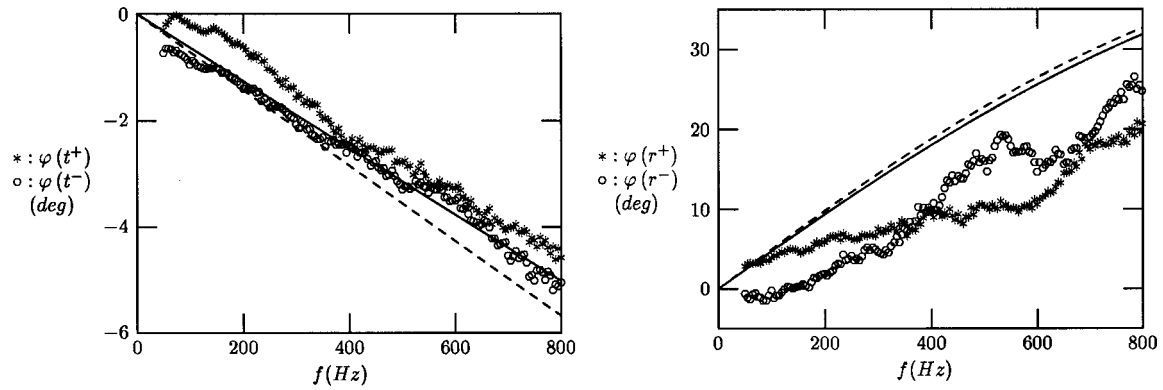

FIG. 11. Argument of the scattering matrix coefficients of the slit (I) with respect to frequency. ∗, t^+ and r^+; ○, t^- and r^-; —, theoretical predictions for t^+ and r^+ using the formula 35; ---, theoretical predictions for t^- and r^- using the formula 35. $M_1=0.045$.

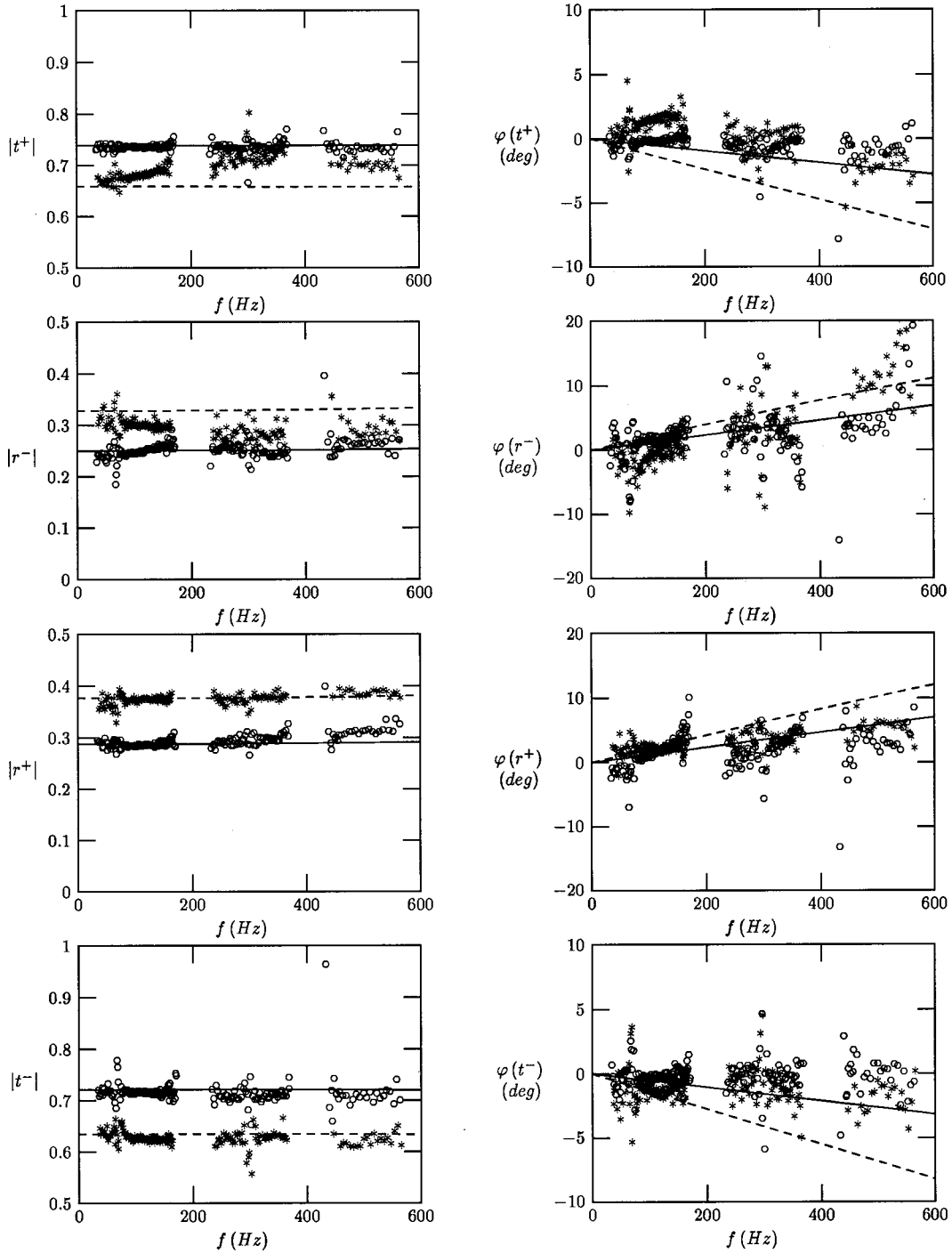

FIG. 12. Modulus and argument of the scattering matrix coefficients of circular orifices of same open area ratio with respect to frequency. ○, perforated plate; *, diaphragm; —, theoretical prediction for the perforated plate; ---, theoretical prediction for the diaphragm. $M_1 = 0.036$. The orifices dimensions are given in Table II.

generated at the edges of the diaphragm. The term $\frac{1}{2}\rho o u_j^2$ disappears in the integral momentum equation derived over the orifice and the pressure in the jet equals the pressure outside. Then if we assumed that the transmitted wave is negligible at low frequencies the reflection coefficient R_1 is expressed by the following relation:

$$R_1 \approx -\frac{1-M_1[(S_p/S_j)^2-1]}{1+M_1[(S_p/S_j)^2-1]}. \tag{37}$$

For an upstream Mach number M_1 equal to $S_j^2/(S_p^2 - S_j^2)$ there is no reflection. For a Mach number belonging to the neighborhood of $S_j^2/(S_p^2-S_j^2)$, the reflection is low but this anechoic region is rather narrow. Only a combination of different open area ratio diaphragms will ensure an effective anechoic termination over a large Mach number range. If we describe the acoustic response of each diaphragm by the scattering matrix relation 1 the upstream reflection coefficient $R_1 = p_1^-/p_1^+$ is given by the following relation:

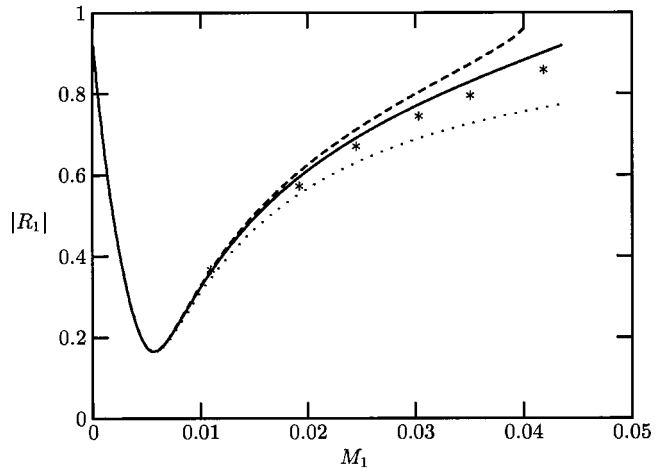

FIG. 13. Modulus of the acoustic reflection coefficient of the slit (II) with respect to M_1. The slit is placed in the pipe at a distance of about 1.8λ from the end pipe, λ being the wave length. *, measurements; —, compressible theory with $\Gamma_0(S_d/S_p, M_j)$; ---, compressible theory with $\Gamma_0(S_d/S_p, 0)$; ⋯, incompressible theory. $f=77$ Hz.

$$R_1 = r^+ + \frac{t^+ t^-}{1 - r^- R_2} R_2, \tag{38}$$

with $R_2 = p_2^-/p_2^+$. It is clear that the upstream reflection coefficient depends on the downstream reflection coefficient R_2, that is it depends on the downstream load. For example, if the diaphragm is inserted in an infinite pipe we have $R_1 = r^+$ and this has a minimum only for $S_j^2/(S_p^2 - S_j^2) = 0$. The case of a diaphragm inserted in an open ended pipe is interesting because the reflection coefficient of such a termination, and therefore R_2, is well known.[5,20] This situation is illustrated in Fig. 13 which presents the modulus of R_1 for a slit inserted in a straight pipe at different positions. Both the measurements and the previously discussed theories are shown. The slit is placed in the pipe at a distance of about 1.8λ from the end pipe, λ being the wavelength. $|R_1|$ presents a minimum which is different from zero. The minimum is zero if the downstream pipe length is equal to half the excitation wavelength. Therefore the zero reflection is obtained only at a single frequency. Whatever the diaphragm position is in the pipe the minimum occurs for M_1 close to $1/(S_p/S_j - 1)^2$. This value differs from the one found when the diaphragm is placed at the end of a pipe.

For completeness, note that the compressible expression for the reflection coefficient of a diaphragm placed at the end of a pipe is written as[27]

$$R_1 = -\frac{(1-M_1)[1-(S_p/S_j)^2(\rho_1/\rho_j)^2 M_1]}{(1+M_1)[1+(S_p/S_j)^2(\rho_1/\rho_j)^2 M_1]}. \tag{39}$$

VI. DESIGN OF AN ANECHOIC TERMINATION

Experiments have been carried out at Shell Research (Koninklijke Shell Exploratie en Produktie Laboratorium) on the interaction of combustion and low frequency acoustic pulsations ($1\,\text{Hz} < f < 5\,\text{Hz}$) in long pipe lines. Typical length of the pipes are in full scale a few kilometers. A 1/10 scale model experiment was designed. Obviously pipes of a few hundred meters are still prohibitive in laboratory experiments. We designed mufflers with a length of less than 5 m which mimic reasonably well the almost anechoic behavior of the actual pipe. The use of four to five diaphragms allowed a fair result over a broad frequency range $5\,\text{Hz} < f < 50\,\text{Hz}$ and for a broad range of Mach numbers $0.02 < M < 0.20$. As combustion involves soot formation and large temperatures, it was not possible to use porous media in the damper. The position and dimensions of the orifices was calculated by means of an optimization program using the quasisteady theory. The actual damper performed as predicted. We show here results of comparison of theoretical prediction and measurements carried out at the TUE with an accurately manufactured prototype (see Fig. 14 and Fig. 15). Please note that this prototype was not optimized.

We see that the theory provides a fair prediction of the muffler performances.

VII. CONCLUSIONS

We have presented a quasisteady analysis of the aeroacoustic response of orifices in pipes. Special attention was given to the Mach number dependence and confinement effect on the vena contracta factor both for slits and circular orifices. Experiments with three different setups confirm the significance of Mach number effects. The data for slits and circular orifices has been complemented with results obtained for a perforated plate, which provides information on the influence of the geometry on the response. It appears that only the argument of the scattering matrix parameters is strongly dependent on the geometry. This corresponds to the dependence of the effective mass on the geometry which is well known from the literature in the absence of mean flow. In the presence of mean flow the effective mass of the orifice is not simply half that without flow as suggested by Morse

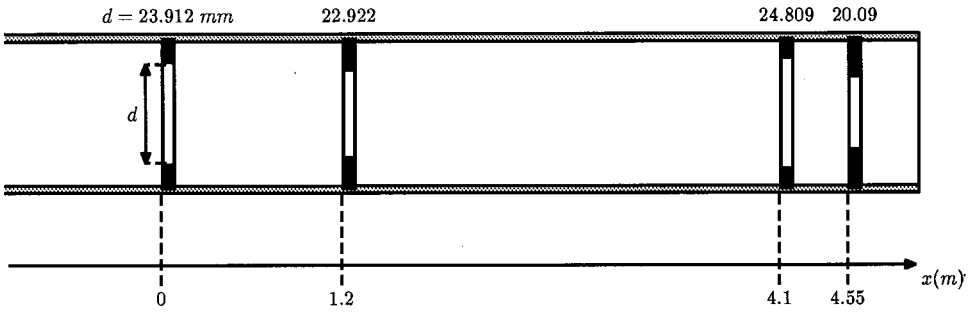

FIG. 14. Geometry of the prototype anechoic termination for combustion experiments in long pipes. The pipe diameter is 30.01 mm.

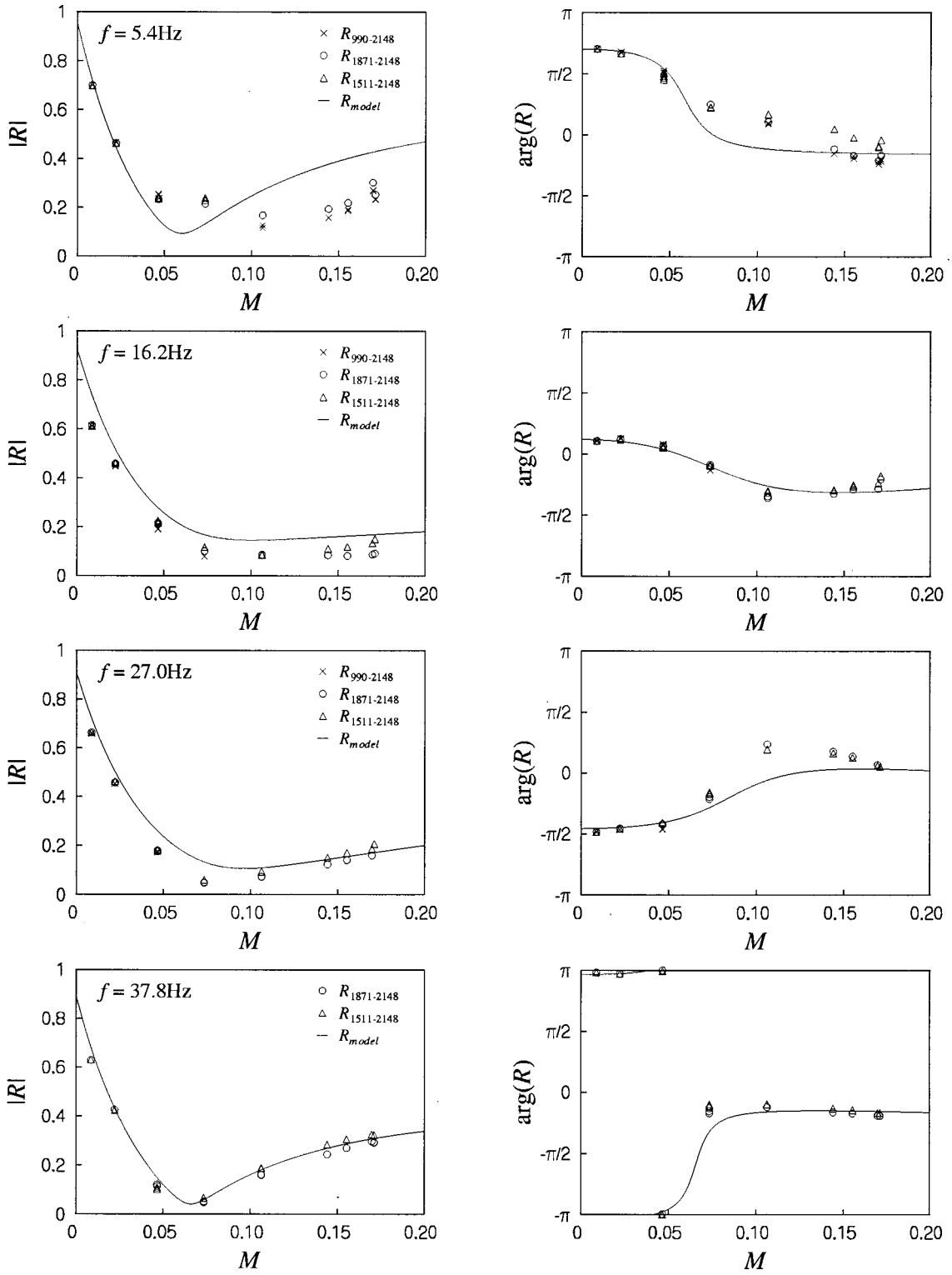

FIG. 15. Comparison of measured Mach number dependence of the reflection coefficient of the anechoic termination with the theory assuming a quasisteady response of the orifices. The different symbols account for different microphones pairs.

and Ingard.[22] A much more complex behavior is observed leading at low frequencies to value lower than half the effective mass without flow. This is analogous to the results obtained by Peters[20] for an open pipe termination. The usefulness of the theory was illustrated by predicting the performance of an anechoic termination consisting of several orifices placed along a pipe.

APPENDIX: VISCO-THERMAL DISSIPATION IN A TURBULENT MAIN FLOW

Complex wave numbers $k^{\pm}$ are given by the following relation:

$$k^{\pm}=\frac{\omega}{c\pm u}+(1-i)\alpha^{\pm}, \tag{A1}$$

where $\alpha^{\pm}$ is the damping coefficient c the speed of sound and u the mean velocity of the flow.

For typical conditions considered here the damping is determined by visco-thermal dissipation in thin boundary layers at the pipe wall. For a kinematic viscosity ν, the value of the damping coefficient is determined by the ratio of the Stokes layer thickness $\delta_{ac}=\sqrt{2\nu/\omega}$ and the thickness δ_l of the viscous sublayer of the turbulent main flow. We use the value of δ_l proposed by Peters:[20]

$$\delta_l = 1.25\nu\sqrt{\rho/\tau_w}, \tag{A2}$$

where ρ is the mean density of the flow and where the wall shear stress τ_w is calculated for a pipe of diameter D by means of the formula of Blasius:[28]

$$\tau_w = \tfrac{1}{8}\psi\rho u^2 \tag{A3}$$

with the friction coefficient ψ given by

$$\psi = 0.3164\left(\frac{\nu}{uD}\right)^{1/4}. \tag{A4}$$

Ronneberger and Ahrens[29] propose a simple model in which the shear waves generated at the wall by the acoustic perturbations are assumed to propagate in the viscous sublayer as in a laminar flow and to reflect on the turbulent core of the flow as if it was a rigid wall. Peters[20] proposes a modification of the rigid core model of Ronneberger and Ahrens[29] by including a phase shift in the reflection of the shear waves which corresponds to the memory of the turbulent flow. In the limit of low Mach numbers $\lim_{M\to 0}\alpha^{\pm}=\alpha$, Peters[20] obtained the formula

$$\frac{\alpha}{\alpha_0} = \frac{1+\exp[-2(1+i)(\delta_l/\delta_{ac})-200i(\delta_l/\delta_{ac})^2]}{1-\exp[-2(1+i)(\delta_l/\delta_{ac})]}, \tag{A5}$$

where α_0 is the damping in a stagnant gas ($M=0$) which is given by Kirchhoff's formula[30]

$$\alpha_0 = \frac{w\delta_{ac}}{cD}\left(1+\frac{\gamma-1}{\sqrt{\mathrm{Pr}}}\right), \tag{A6}$$

where γ is the ratio of specific heats and Pr the Prandtl number. The factor 12.5 in the definition (A2) of δ_l has actually been chosen by Peters[20] in order to obtain a reasonable fit to the experimental data available.[29,20] The correction of the damping coefficient for the influence of convective effects has been successfully predicted by Ronneberger and Ahrens[29] in the case $\delta_{ac}/\delta_l<1$ by means of a ''quasilaminar'' theory. A theory including the influence of turbulence has been proposed by Howe.[31] As such theories are quite complex and we only need the damping as a correction in the interpretation of our experiments, we decide to use the intuitive correction

$$\alpha^{\pm} = \frac{\alpha}{1\pm M}, \tag{A7}$$

where $M=u/c$ is the Mach number.

[1] U. Ingard and H. Ising, ''Acoustic non-linearity of an orifice,'' J. Acoust. Soc. Am. **42**, 6–17 (1967).

[2] A. Cummings and W. Eversman, ''High amplitude acoustic transmission through duct terminations: theory,'' J. Sound Vib. **91**, 503–518 (1983).

[3] D. Ronneberger, ''Experimentelle Untersuchungen zum akustischen Reflexionfaktor von unstetigen Querschnittänderungen in einem luftdurchströmten Rohr,'' Acustica **19**, 222–235 (1967).

[4] D. Ronneberger, ''The acoustical impedance of holes in the wall of flow ducts,'' J. Sound Vib. **24**, 133–150 (1972).

[5] P. O. A. L. Davies, ''Practical flow ducts acoustics,'' J. Sound Vib. **124**, 91–115 (1988).

[6] D. W. Bechert, ''Sound absorption caused by vorticity shedding, demonstrated with a jet flow,'' J. Sound Vib. **70**, 389–405 (1980).

[7] M. S. Howe, ''On the theory of unsteady high Reynolds number flow through a circular aperture,'' Proc. R. Soc. London, Ser. A **366**, 205–223 (1979).

[8] D. Ronneberger, Theoretische und experimentelle Untersuchung Schallausbreichtung durch Querschnittssprünge und Lochplatten in Strömungkanälen, Abschlußbericht zum DFG-Forschungvorhaben Ro 369/11, 12, 14, Drittes Physikalisches Institut, Göttingen, 1987.

[9] I. J. Hugues and A. P. Dowling, ''The absorption of sound by perforated linings,'' J. Fluid Mech. **218**, 205–235 (1990).

[10] G. C. J. Hofmans, ''Vortex sound in confined flows,'' Ph.D. thesis, Eindhoven University of Technology, 1998.

[11] M. Åbom, ''Measurement of the scattering matrix of acoustical two ports,'' Mech. Syst. Signal Process. **5**, 89–104 (1991).

[12] M. L. Munjal and A. G. Doige, ''Theory of a two source-location method for direct experimental evaluation of the four-pole parameters of an aeroacoustic element,'' J. Sound Vib. **141**, 323–333 (1990).

[13] G. Ajello, ''Acoustic measurements in pipe systems with flow: design of a flow bench and applications to measurement of discontinuities,'' Ph.D. thesis, Université du Maine, 1997.

[14] D. Gilbarg, *Encyclopedia of Physics; Volume IX, Fluid Dynamics III. Jets and Cavities* (Springer-Verlag, Berlin, 1960).

[15] R. D. Blevins, *Applied Fluid Dynamics Handbook* (Van Nostrand Reinhold, New York, 1984).

[16] A. Busemann, ''Hodographenmethode der Gasdynamik,'' Z. Angew. Math. Mech. **17**, 73–79 (1937).

[17] I. E. Idelchik, *Handbook of Hydraulic Resistance*, 2nd ed. (Springer-Verlag, Berlin, 1986).

[18] A. H. Shapiro, *The Dynamics and Thermodynamics of Compressible Fluid Flow* (Ronald, New York, 1953), Vol. I.

[19] M. Åbom and H. Bodén, ''Error analysis of two microphone measurements in ducts with flow,'' J. Acoust. Soc. Am. **83**, 2429–2438 (1988).

[20] M. C. A. M. Peters, ''Aeroacoustic sources in internal flows,'' Ph.D. thesis, Eindhoven University of Technology, 1993.

[21] P. Durrieu, ''Development of experimental and predictive tools aimed at investigating the acoustical behaviour of car silencer components,'' Ph.D. thesis, Université du Maine, 1999.

[22] P. M. Morse and K. U. Ingard, *Theoretical Acoustics* (Princeton University Press, Princeton, NJ, 1968).

[23] V. A. Fock, ''A theoretical investigation of the acoustical conductivity of a acoustical conductivity of a circular aperture in a wall put across a tube,'' C. R. (Dokl.) Acad. Sci. URSS **31**, 875–878 (1941).

[24] J. Kergomard and A. Garcia, ''Simple discontinuities in acoustic waveguides at low frequencies: critical analysis and formulae,'' J. Sound Vib. **114**, 465–479 (1987).

[25] C. L. Morfey, ''Acoustic properties of openings at low frequencies,'' J. Sound Vib. **9**, 357–366 (1969).

[26] J. F. Allard, *Propagation of Sound in Porous Media: Modeling Sound Absorbing Materials* (Chapman-Hall, London, 1993).

[27] R. J. J. Boot, ''Aeroacoustic behaviour of diaphragms,'' Master's thesis, Report R-1370-A, Eindhoven University of Technology, 1995.

[28] H. Schlichting, *Boundary-layer Theory*, 7th ed. (McGraw-Hill, New York, 1979).

[29] D. Ronneberger and A. Ahrens, ''Wall shear stress caused by small amplitude perturbations of turbulent boundary layer flow: an experimental investigation,'' J. Fluid Mech. **83**, 433–464 (1977).

[30] A. D. Pierce, *Acoustics: An Introduction to its Physical Principles and Applications* (McGraw-Hill, New York, 1981).

[31] M. S. Howe, ''The damping of sound by wall turbulent shear layers,'' J. Acoust. Soc. Am. **98**, 1723–1730 (1995).

Oscillation modes of supersonic multijets exhausting from very adjacent multiple nozzles

Yoshikuni Umeda[a)]
Department of Aeronautics and Astronautics, Graduate School of Engineering, Kyoto University, Yoshida Honmachi, Sakyo-ku, Kyoto 606-8501, Japan

Ryuji Ishii
Department of Resources and Energy, Graduate School of Energy, Kyoto University, Yoshida Honmachi, Sakyo-ku, Kyoto 606-8501, Japan

(Received 9 June 2000; revised 17 May 2001; accepted 24 July 2001)

The oscillation modes of a supersonic circular twin jet and multijet with square configuration where the center-to-center spacing of nozzles was fixed to 1.4 times the nozzle diameter were investigated experimentally. It is found that the twin jet oscillates simultaneously in three different oscillation modes for the pressure ratios of about 4.1. From the acoustical observation, these oscillation modes are identified as one lateral oscillation mode perpendicular to a plane composed of the twin jet axes and two lateral oscillation modes parallel to this plane. For a multijet with a square configuration, only one lateral oscillation mode was observed. In this case, it is observed that when the spacing between *two facing sides* of the square formed by four jets is stretched, the spacing between the other two sides shrinks and vice versa. © *2001 Acoustical Society of America.*
[DOI: 10.1121/1.1404380]

PACS numbers: 43.28.Ra, 43.50.Nm, 43.28.Py [LCS]

I. INTRODUCTION

It has been well known that the acoustic emission from an underexpanded jet has a broad frequency band component as well as a few discrete ones called screech tones in its spectrum. Powell (1953) proposed that a feedback mechanism governs the emission of the screech tone. It consists of downstream-convecting coherent vortical structures around the jet and upstream-propagating sound waves in the ambient. He also reported that the frequencies of the screech for the circular jet exhibit several discontinuities at particular pressure ratios R.

These discontinuities of the frequencies of the screech tone suggest that the jet oscillates in different oscillation modes in the different pressure ratio ranges. Davies and Oldfield (1962) have found that five stages exist in the case of the circular underexpanded jet in the pressure ratio range less than 6.0. They have established that the first four modes of oscillation are, respectively, axisymmetric, axisymmetric, lateral, and helical. The last one at the highest pressure ratio was established to be lateral by Powell *et al.* (1990, 1992). They also clarified that the first lateral mode observed in the pressure ratio range from 2.3 to 3.3 occasionally changes to the helical mode at the same frequency and that the last lateral oscillation mode in the highest pressure ratio range shows a very strong amplitude modulation. This phenomenon was caused by the fact that the plane of oscillation rotates about the jet axis, vibrates, and dwells.

When such circular jets are closely spaced, the level of the screech can be greatly amplified or suppressed due to a coupling process between them. Therefore, recently the noise and coupling process between two closely spaced jets has been studied by a few researchers. Seiner *et al.* (1988) showed that a resonant interacting twin jet can generate dynamic pressures exceeding the fatigue failure limit for nearby metallic aircraft structures. Wlezien (1989) found that for the closely spaced jets, coupling occurs at low Mach numbers and is suppressed at high Mach numbers. Umeda and Ishii (1997) showed that for the twin jet whose center-to-center spacing is 2.8 times nozzle diameter, two counter-rotating helical oscillation modes and two reversed lateral oscillation modes generated in a plane composed of two jets were observed in the different pressure ratio ranges. They also showed that for the multijet with square configuration, the quadrupolelike oscillation mode where four jets oscillate laterally along the diagonal lines of the square, four counter-rotating helical oscillation mode, and the symmetric oscillation mode are observed with increasing pressure ratio.

In the present experiment, the oscillation modes of the twin jet and a multijet with square configuration for the center-to-center spacing of $s/d=1.4$, which is half as large as that used in the previous investigation (Umeda and Ishii, 1997), were studied and very interesting unexpected phenomena were observed.

II. EXPERIMENT

The experimental apparatus and methods are the same as those in the previous investigations (Umeda and Ishii, 1997) except for the center-to-center spacing of the nozzles. The schematic views of the nozzle configuration used in this experiment are shown in Fig. 1. Two and four cylindrical nozzles were composed as one body. The nozzles had internal diameter of $d=5$ mm. The length of cylindrical nozzles was $l=50$ mm. The minimum thickness of nozzle lip outside

[a)]Author to whom correspondence should be addressed; electronic mail: umeda@kuaero.kyoto-u.ac.jp

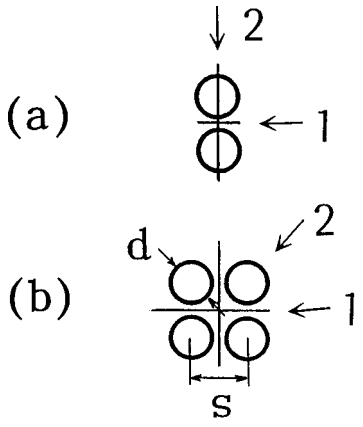

FIG. 1. Schematic views of nozzles ($s/d=1.4$): (a) twin jet, (b) multijet with square configuration.

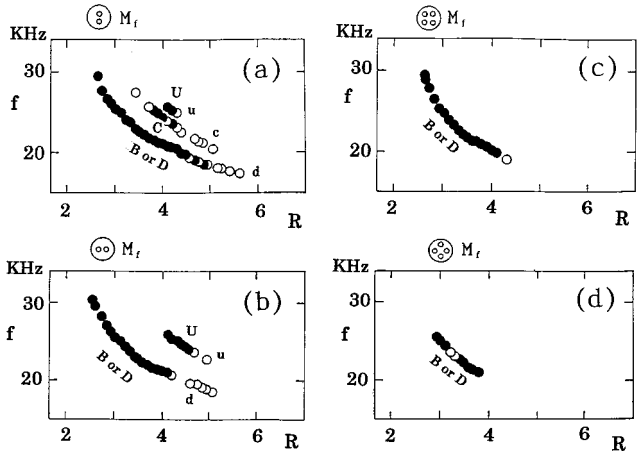

FIG. 2. Frequency characteristics: (a), (b) twin jet; (c), (d) multijet with square configuration.

the nozzle configuration was 1 mm and the center-to-center spacing of the nozzles was fixed to $s=7$ mm ($s/d=1.4$). In these figures, arrows 1 and 2 show the directions of acoustical and optical observations.

First, the frequency characteristics of the screech tones emitted by these multiple jets were measured by using a fixed microphone M_f (0.64 cm diam B & K type-4135) in order to find the pressure ratios where discontinuities occur in the frequency characteristics of the screech tone. Next, acoustical observation using two microphones were made at various pressure ratios associated with individual oscillation modes in order to discriminate the jet oscillation mode. Finally, the optical observations were carried out to confirm the results of the acoustical observations and also to clarify the unexpected phenomena observed in the acoustical observation.

III. EXPERIMENTAL RESULTS

A. Frequency characteristics of screech tone

In general, since the characteristics of the radiation field of the multijet depend on the plane of measurement with respect to the nozzle configuration. The frequency characteristics of the screech tones radiated by the two jet configurations shown in Fig. 1 were measured by the fixed microphone M_f placed in the two directions shown by arrows 1 and 2 in the near-sound field while changing the pressure ratios R of the jets from 2.00 to 6.33.

Figure 2 shows the experimental results measured for the twin jet and multijet with square configuration. The solid circles indicate dominant tones and are labeled with capital letters *B*, *C*, *D*, and *U*. The open circles mark secondary tones and are labeled with lowercase letters *c*, *d*, and *u*. In the present experiment, mode *A*, which is observed in the case of the single jet (Powell *et al.*, 1990, 1992; Umeda and Ishii, 1997), was not observed at all. In the case of the twin jet, two or three oscillation modes were observed for the pressure ratio range R from about 4 to 5 depending on the microphone direction to the nozzles as shown in Figs. 2(a) and (b). On the contrary, only one oscillation mode was observed in the case of the multijet with square configuration as shown in Figs. 2(c) and (d).

B. Acoustical observations

Next, the acoustical observations were carried out to discriminate the oscillation modes of jet instability. In order to discriminate the oscillation modes of these jets, it is necessary to get information on the three-dimensional structures of wave fronts radiated from jets as shown in the previous investigations (Powell *et al.*, 1990, 1992; Umeda and Ishii, 1997). The information can be obtained by measuring the phase differences of the screech tone radiated by the jets. In this acoustical observation, two microphones were placed concentrically with the central axis of nozzles. The first microphone M_f was kept in a fixed position at $\theta=0°$, and the second microphone M_m (0.32 cm diam B & K type-4138) was rotated about the central axis of nozzles in 15 deg increments up to 180 deg relative to the first one. The phase difference between the sound signals received by the two microphones was measured on a Yokogawa AR1100 Analyzing Recorder. The phase differences between the signals so obtained will correspond to a particular three-dimensional structure of wave fronts. The relationship between the phase difference ϕ and the microphone separation angle θ were measured at two different positions of the fixed microphone M_f for the nozzle configurations.

1. Twin jet (R=2.93)

Applying this technique to the twin jet, first the relationship between the phase difference ϕ and the microphone separation angle θ was measured at the pressure ratio $R=2.93$, where only one oscillation mode (stage *B* or *D*) occurred. The experimental results are shown in Figs. 3(a) and (b). The solid circles show the average value of the ten data sets and the bar represents the scatter. These results show that the phase difference ϕ is 0° at the microphone separation angles $\theta=0°$ and 180°, and $\phi=\pm 180°$ at $\theta=90°$. In the figures on the right side, the phase differences ϕ are revealed with the angular position of the moving microphone M_m and arrows show the instantaneous oscillation directions of the jets. From these figures, it will be concluded that at a pressure ratio $R=2.93$ the twin jets oscillate laterally in antiphase to each other in a plane composed of the two jets.

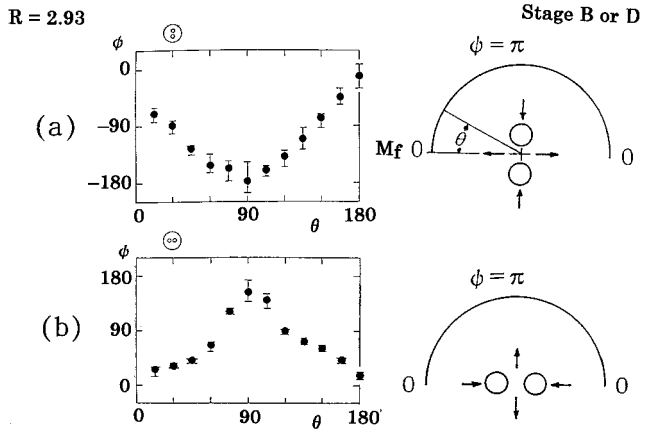

FIG. 3. Relationship between phase difference ϕ and separation angle θ of microphones for twin jet at pressure ratio $R=2.93$ (stage B or D).

2. Twin jet (R=4.10)

From the frequency characteristics shown in Figs. 2(a) and (b) it is found that the twin jet at the pressure ratio R of about 4.10 oscillates in three oscillation modes, B or D, C, and U, simultaneously. Figure 4 shows three relationships between the phase difference ϕ and the microphone separation angle θ corresponding to the three different oscillation modes of the jets which were obtained from the same acoustical data. Figures 4(a) and (b) show the results for the stage B or D. These results are similar to those as shown in Figs. 3(a) and (b). Therefore, these results indicate that the twin jets for the stage B or D observed in this case also oscillate laterally in antiphase to each other in the same plane composed of the two jets.

Figure 4(c) shows the result of the acoustical observation for stage C. However, the result when the nozzles were rotated around the central axis of two nozzles by 90° to the nozzles shown in this figure could not be obtained, because the sound pressure level for the stage C mode at the fixed microphone M_f was too low to get the cross-correlation between the signals from the two microphones shown in Fig. 2(b). But, the result shown in Fig. 4(c) clearly indicates that the twin jet oscillates in a lateral oscillation mode perpendicular to the plane composed of two jets.

Figures 4(d) and (e) represent the results of the acoustical observation for the stage U mode. Figure 4(d) shows that the phase difference ϕ is 0° for the microphone separation angle $\theta=0°$ and 180°, and $\phi=-180°$ at and around $\theta=90°$. But, the result shown in Fig. 4(e) indicates that the phase difference ϕ is fixed at about 0° for $\theta<90°$, and is kept at about $-180°$ for $\theta>90°$. These results indicate that for the stage U mode, the twin jet oscillates laterally in phase in the plane composed of two jets.

Thus three oscillation modes occurring simultaneously in the twin jet at the pressure ratio $R=4.10$ were discriminated by the acoustical observation. But, from only an acoustical observation, it cannot be understood why these oscillation modes occurred simultaneously.

3. Multijet with square configuration (R=3.51)

In the case of the multijet with square configuration, only one oscillation mode is observed as shown in Figs. 2(c) and (d). This stage is determined to be B or D by comparing these results with those for the twin jet as shown in Figs. 2(a) and (b). Figures 5(a) and (b) show the results of the acoustical observation measured at a pressure ratio $R=3.51$. The result shown in Fig. 5(b) almost overlaps those shown in Fig. 5(a) when the angle θ is shifted by 45° corresponding to the nozzle configuration. From Fig. 5(a), it can be seen that the phase differences ϕ are about 0° at $\theta=0°$ and 180°, and $\phi=-180°$ at and around $\theta=90°$. This result shows that when the spacing between two facing sides of the square composed of four jets is stretched, the spacing between the other two sides shrinks and vice versa.

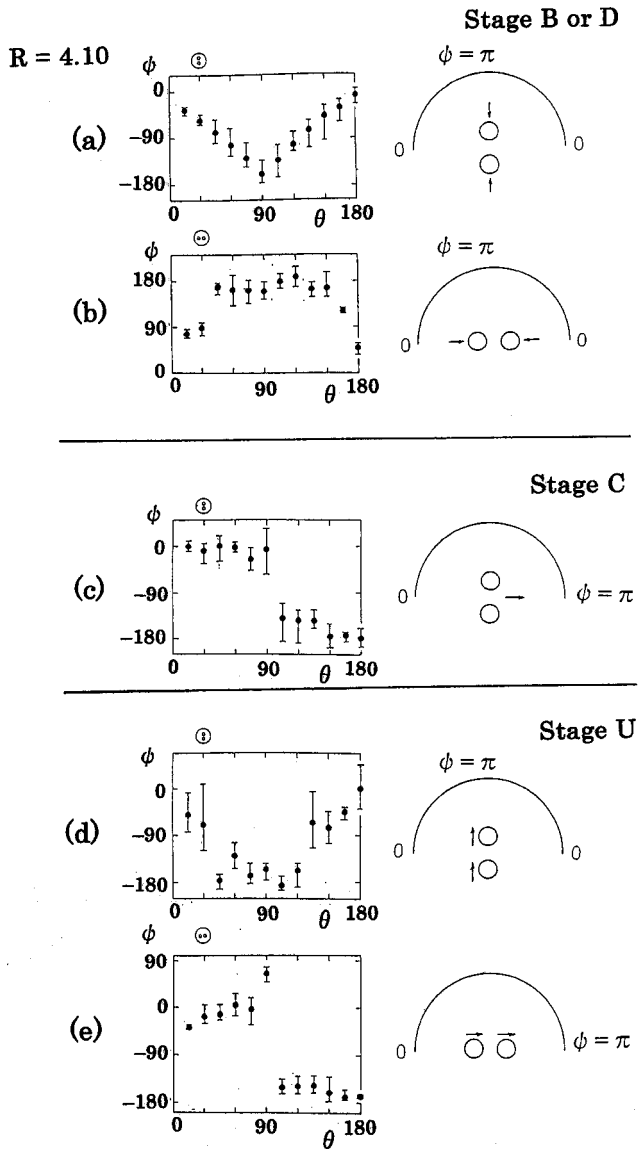

FIG. 4. Relationship between phase difference ϕ and separation angle θ of microphones for twin jet at pressure ratio $R=4.10$: (a), (b) stage B or D; (c) stage C; (d), (e) stage U.

C. Optical observations

Finally, in order to check the accuracy of above result for the twin jet and the multijet with square configuration, instantaneous Schlieren photographs with an exposure of about 1μs were taken to display the jet configuration and the

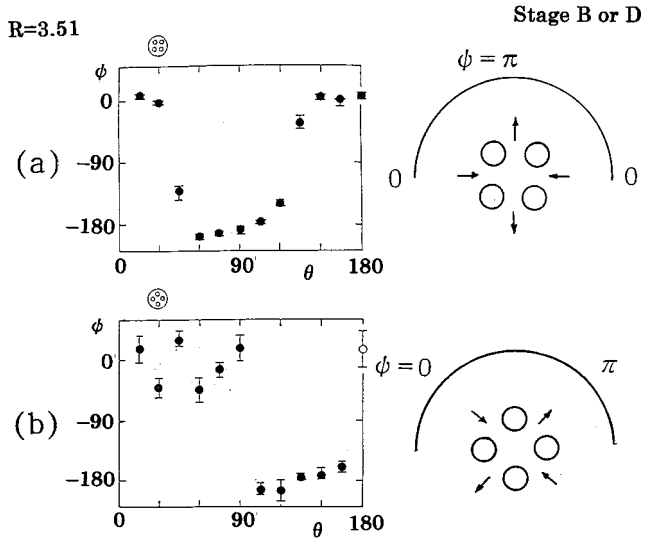

FIG. 5. Relationship between phase difference ϕ and separation angle θ of microphones for multijet with square configuration at pressure ratio $R = 3.51$ (stage B or D).

associated near-sound field. In this visualization, the jet configurations were observed from two different directions of arrows 1 and 2 [Fig. 1(a)], respectively.

1. Twin jet (R=2.93)

The photographs of the twin jet at the pressure ratio $R = 2.93$ (stage B or D) are shown in Figs. 6(a) and (b). The arrows outside the photograph indicate the instantaneous oscillations of the parts of two jets. It is observed from the photographs that in this stage, two jets oscillate laterally in antiphase to each other in the plane composed of two jets as shown by the acoustical observation. Also, at the same instant, it is found that the phases reverse along the jet axis by almost the same spatial interval, say one shock cell length.

2. Twin jet (R=4.10)

In the previous section, it is found that three oscillation modes occurred simultaneously in the twin jet at the pressure ratio $R = 4.10$. But, from only acoustical observation, it cannot be understood why these oscillation modes occurred simultaneously. In order to understand this unexpected phenomenon, the visualization was carried out for this twin jet.

Figures 6(c) and (d) show the photographs of the twin jet for the pressure ratio $R = 4.10$ which were observed from the directions of arrows 1 and 2 [Fig. 1(a)], respectively. From these photographs, it can be seen that this twin jet oscillates simultaneously in three different oscillation modes. Namely, from Fig. 6(c), in the relatively upstream region of the jets (downstream of the nozzle lip by 3–4 shock cell lengths), the same parts of two jets oscillate laterally in-phase in the plane composed of two jets. On the contrary, in the downstream region (downstream of the nozzle lip by 7–8 shock cell lengths), the corresponding parts of two jets oscillate laterally in antiphase to each other in the same plane. From Fig. 6(d) which was observed from the direction of arrow 2 [Fig. 1(a)], it can be seen that in the middle region of the axial distance (downstream of the nozzle lip by 5–6 shock cell lengths), these jets oscillate perpendicularly to the plane.

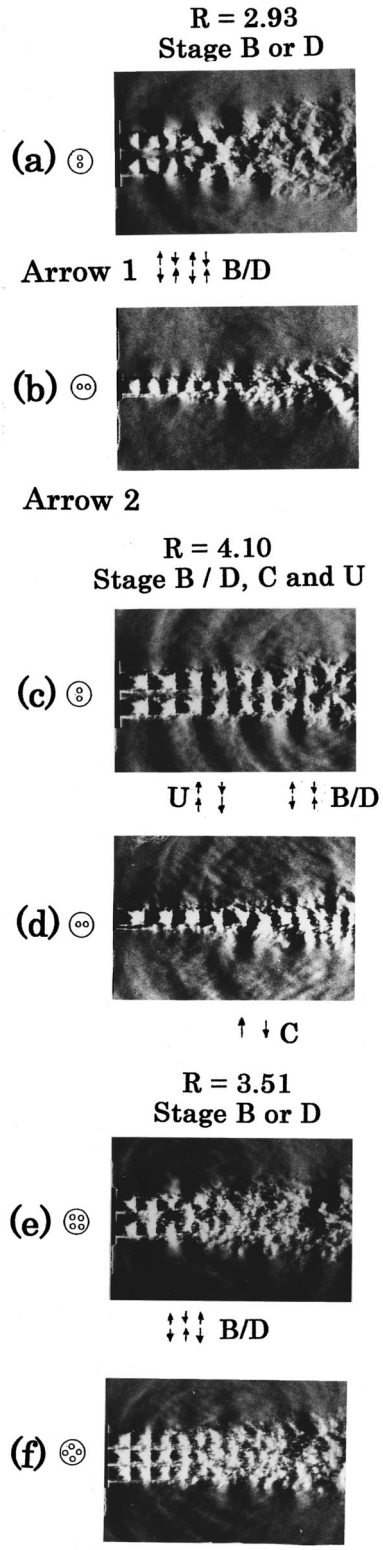

FIG. 6. Schlieren photographs: (a), (b) twin jet oscillating in B or D mode ($R = 2.93$); (c), (d) twin jet oscillating in B or D, C, and U modes ($R = 4.10$); (e), (f) multijet with square configuration oscillating in B or D mode ($R = 3.51$).

These photographs completely coincide with the above results of acoustical observation. Therefore, it may be concluded that three different oscillation modes occur simultaneously in the different regions of the twin jet at a pressure ratio around 4.1.

3. Multijet with square configuration (R=3.51)

Figure 6(a) shows a photograph of the multijet with square configuration for a pressure ratio $R=3.51$ observed from the direction of arrow 1 [Fig. 1(b)]. This photograph shows that two facing sides of the square composed of four jets oscillate laterally in antiphase. So, this photograph supports the above acoustical observation. It also shows that the oscillation directions of the jets reverse periodically along the jet axis. Figure 6(f) shows a photograph of the same jet observed from the direction of arrow 2 [Fig. 1(b)].

Therefore, the multijet with square configuration oscillate as follows: when the spacing between two facing sides of the square formed by four jets is stretched, the spacing between the other two sides shrinks and vice versa, and the oscillation direction of the jets reverses periodically along the jet column.

IV. CONCLUSION

In the experimental study of the oscillation modes of the circular multijets with center-to-center spacing of $s/d=1.4$, the following very interesting phenomena were observed. Namely:

(1) The twin jet oscillates in three different oscillation modes simultaneously at pressure ratios of about $R=4.1$. These three oscillation modes occur at the different ranges of the axial distance from the nozzle exit. For the stage *U* mode, the twin jet oscillate laterally in phase in the plane composed of two jets. For the stage *B* or *D* modes, the jets oscillate laterally in antiphase to each other in the same plane. Concerning to *C* mode, the twin jet oscillates laterally in the direction vertical to the plane.

(2) The multijet with square configuration oscillates in only one lateral oscillation mode. In this case, the multijet oscillate as follows; when the spacing between two facing sides of the square composed of four jets is stretched, the spacing between the other two sides shrinks and vice versa.

ACKNOWLEDGMENT

The authors received support from the Ministry of Education and Culture of Japan [Grant No. C(2)-08650201].

Davies, M. G., and Oldfield, D. E. S. (**1962**). ''Tones from a choked axisymmetric jet. II. The self-excited loop and mode of oscillation,'' Acustica **12**, 267–277.

Powell, A. (**1953**). ''On the mechanism of choked jet noise,'' Proc. Phys. Soc. London, Sect. B **66**, 1039–1056.

Powell, A., Umeda, Y., and Ishii, R. (**1990**). ''The screech of round choked jets, revisited,'' AIAA paper 90-3980 (unpublished).

Powell, A., Umeda, Y., and Ishii, R. (**1992**). ''Observation of the oscillation modes of circular choked jets,'' J. Acoust. Soc. Am. **92**, 2823–2836.

Seiner, J. M., Manning, J. C., and Ponton, M. K. (**1988**). ''Dynamic pressure loads associated with twin supersonic plume resonance,'' AIAA J. **26**, 954–960.

Umeda, Y., and Ishii, R. (**1997**). ''Oscillation modes of supersonic multijets,'' J. Acoust. Soc. Am. **101**, 3353–3360.

Wlezien, R. W. (**1989**). ''Nozzle geometry effects on supersonic jet interaction,'' AIAA J. **27**, 1361–1367.

An examination of the parameters that govern the acoustic behavior of sea bed sediments containing gas bubbles

T. N. Gardner and G. C. Sills
Department of Engineering Science, University of Oxford, Parks Road, Oxford OX3 7LD, United Kingdom

(Received 28 June 1999; revised 1 May 2001; accepted 29 May 2001)

The acoustic properties of sea bed sediments containing occluded gas are dominated by the volume of gas contained in bubbles, the size of bubbles, and the elastic properties of the soil matrix. This study evaluated current theory developed by Anderson and Hampton to determine the sound speed and resonance frequency of gassy soils, and the models they used to determine the elastic properties of the soils. It compared calculated sound speeds, based on material properties simulated by the models, with measured sound speeds on ''large bubble'' laboratory soils produced in a similar manner to natural sea bed gassy soils. There was some evidence that the Anderson and Hampton equations accurately predicted sound speed at lower frequencies of bubbles resonance and below, but results were sensitive to inappropriate values for the elastic and damping properties of the soil. The bounds of sound speed based on the elastic properties of models that simulate ''compressible fluid'' or ''suspension'' behavior were grossly misleading when applied to large bubble soils. Conversely, sound speed based on models that correctly simulate the ''bulk'' or ''matrix'' properties of large bubble soils, at strain magnitudes and strain rates equivalent to acoustic signals, agreed well with measured data. [DOI: 10.1121/1.1388005]

PACS numbers: 43.30.Ma, 43.30.Pc, 43.30.Vh [DLB]

I. INTRODUCTION

Sea bed sediments containing occluded gas in the form of small bubbles are referred to as gassy soils. As gassy sediments can be highly dispersive and attenuative mediums acoustically, this has initiated much interest from acousticians involved in marine engineering and survey work. Surveys and site investigations routinely involve acoustic methods, and where layers of gassy sediments are difficult to penetrate acoustically the concealment of underlying sea beds is of some concern. Gassy sediments are also a major hazard during sea bed drilling operations, because of the sudden buoyancy caused by the release of sediment gas under pressure. Gas is also released naturally,[1–3] and the resulting disturbances to the overlying water and air arising from sudden density gradients may explain the disappearances of boats and airplanes in the south Atlantic region of the Bermuda Triangle. Therefore, in order to survey the properties of a sea bed it is essential to detect the presence of any gassy sediment and to estimate its gas content. To perform this acoustically, it is necessary to acquire knowledge of the relationship between the acoustic and the material properties of these sediments.

Gas may be present in soil as ''small'' bubbles that are smaller than particle size and are wholly contained in fluid within interparticle spaces. Or it may be present as ''large'' bubbles' that are greater than particle size and are formed within pockets fashioned by the saturated soil matrix (or particles and fluid). The small bubble soil may be modeled mechanically as a skeletal framework of solid particles fully saturated with a compressible fluid, while the large bubble soil that is the focus of the present study may not. Studies such as those by Anderson and Hampton[4,5] examined the acoustic behavior of gassy sediments and those material properties influenced by phasal structure. Anderson and Hampton[4,5] further developed existing theory on bubble resonance for bubbles wholly contained within fluids but applied it to sediments characterized by the large bubble model for bubbles contained within a solid/fluid matrix. As with fluids, three different compressional wave responses were predicted relating to signal frequency. At frequencies of resonance, gas bubbles in sediment pulsate radially in response to a signal frequency dependent on bubble diameter. Over the range of resonance frequencies (of wavelengths 10π to 100π times bubble diameter) the medium was shown to be highly dispersive and attenuative. At frequencies below this, the bulk material properties of the medium dominated its mechanical behavior producing an acoustic response equivalent to a very compressible monophasic material of low sound speed. At frequencies above bubble resonance, the saturated soil matrix dominated the mechanical behavior of the medium, producing a response equivalent to fully saturated sediment (containing no gas) with a sound speed of approximately 1500 m/s.

They defined the sound speed of gassy sediment in terms of its composition and material properties at frequencies below, at, and above bubble resonance. In the absence of data on bulk material properties relevant to a large bubble soil at frequencies below resonance, they approximated the range of sound speed by calculating lower and upper bound values. The lower bound was derived from comparatively spongy suspensions (Wood[6]) which are solids suspended loosely in fluids, and the upper bound was derived from comparatively stiff saturated soils (Gassman,[7] Smith,[8] Hamilton[9]) modified by introducing a compressible pore fluid. At frequencies of resonance, they added a term to the dynamic fluid properties defined by Silberman[10] for bubbles in water to accommodate the shear rigidity of the saturated soil matrix in gassy sediment. They used the equations of Gassman[7] to calculate the material properties of this matrix.

The theory developed by Anderson and Hampton has

not been validated. Nor has a similar study carried out by Bedford and Stern[11] who applied the theory of energy conservation to derive equations of motion for gassy soil. This accommodated resonance within an expression for the kinetic energy associated with the pulsating radial motion of bubbles. However, the model is not relevant to a large bubble soil since it assumes the acoustic response of a medium comprising a solid and a compressible pore fluid, as does the upper bound approximation of Anderson and Hampton.

To validate models that are based on the relationship between acoustic and material properties, controlled measurements of sound speed may be compared with model predictions based on known material properties. Although many laboratory and *in situ* acoustic measurements have been made on gassy soils,[12–19] little information is provided on soil compositions and material properties. More recently, however, laboratory measurements were made by Gardner[20] to determine the acoustic and material properties of a large bubble soil. In this study, methane gas was released in estuarine silty clay under controlled conditions replicating the natural process of bubble formation in sediment. This produced a gassy soil with uniformly distributed bubbles of between 0.2 and 1.8 mm diameter, in which gas fraction, bubble size distribution, and sound speed was measured over frequencies of bubble resonance and below. Wheeler and Gardner[21] reported measured sound speeds in these large bubble soils at frequencies below resonance. These were shown to agree well with sound speeds calculated by the bulk compressional wave equation. Material properties were determined from the elastic theory and test data of Wheeler[22–24] and Jardine *et al.*[25] on similar soils. No similar approach has been made to examine the theoretical model of Anderson and Hampton[4,5] at frequencies of resonance.

The aim of the present study was to evaluate this model. The first objective was to evaluate the Anderson and Hampton equation for sound speed at frequencies of resonance by comparing measured sound speeds reported by Gardner[20] with sound speeds of the Gardner soils calculated by the Anderson and Hampton model. Model sound speeds were initially based on material properties of the Gardner soils estimated by the method adopted by Anderson and Hampton appropriate to a small bubble model. For comparison, sound speeds were calculated that were based on material properties of large bubble soils estimated from Wheeler[22–24] and Jardine *et al.*[25] The second objective was to examine the possibility of refining the material properties (damping and elastic moduli) of the Gardner soils, by improving the correlation between sound speeds calculated by the Anderson and Hampton model at frequencies of bubble resonance and below. The third objective was to calculate the resonance frequencies of bubbles in the Gardner soils from the model of Anderson and Hampton. The fourth objective was to calculate sound speeds at frequencies below resonance using the model of Anderson and Hampton with their bulk material properties based on suspensions and saturated soils, and to evaluate these against measured data. The behavior of their suspension and compressible fluid models was examined and compared with the behavior of the ''large bubble'' model (reported by Wheeler and Gardner[21]).

TABLE I. Physical properties of the soils.

Soil	Gas fraction	Degree of saturation (%)	Bulk density (kg/m^3)	Void ratio
50-1	0.198	72	1322	2.311
50-2	0.173	75	1363	2.215
52-1	0.082	87	1513	1.899
52-2	0.115	83	1459	2.003
53-1	0.005 11	99.18	1639	1.674
53-2	0.004 07	99.35	1640	1.674
51-1	0.004 84	99.23	1640	1.674
51-2	0.003 57	99.43	1643	1.667

II. METHOD

A. Gassy soils from the experimental study of Gardner (Ref. 20)

The physical properties of eight laboratory soils containing occluded gas in the form of large bubbles are shown in Tables I and II (from Gardner[20]). Table I shows soil gas fractions (the proportion of methane gas volume to total soil volume) from 0.003 57 to 0.198, which encompass the range of gas contents found in naturally occurring gassy soils. Table II shows the range of bubble diameters contained in each soil, and Figs. 1(a)–(d) show the sound speeds of the soils measured by piezoelectric compression wave transducers. Two soils are presented in each figure (in Fig. 1 are E50-1 and E50-2). Both soils originated from the same subsoil preparation and were tested concurrently since they contained similar gas contents and bubble sizes. Two complementary methods were used to measure sound speed to enhance the frequency range of data in view of the substantial dispersion and attenuation of the soil.[20] These are indicated as TTC where signal transit time was measured and corrected for phase shift and sound speeds were determined using path length, and FT where sound speeds were obtained from Fourier Transforms. Although sound speeds and frequency ranges fluctuate a great deal, there is reasonable concurrence between TTC and FT data sets, particularly for the soils of large gas content. It can be seen that the ''*transition point*'' between frequencies that are below bubble resonance and the lowest frequencies of bubble resonance were indicated by an upturn in the sound speed curve at between 15 and 20 kHz for soils 50-1 and 53-1.

TABLE II. Resonance frequencies of bubble groups.

	Bubble diameter (μm)		Resonance frequency (kHz)	
Soil	Minimum	Maximum	Minimum	Maximum
50-1	229	1746	793	104
50-2	247	1746	734	104
52-1	276	807	653	223
52-2	348	1605	516	112
53-1	137	458	1302	391
53-2	137	276	1297	649
51-1	137	385	1297	463
51-2	174	669	1039	270

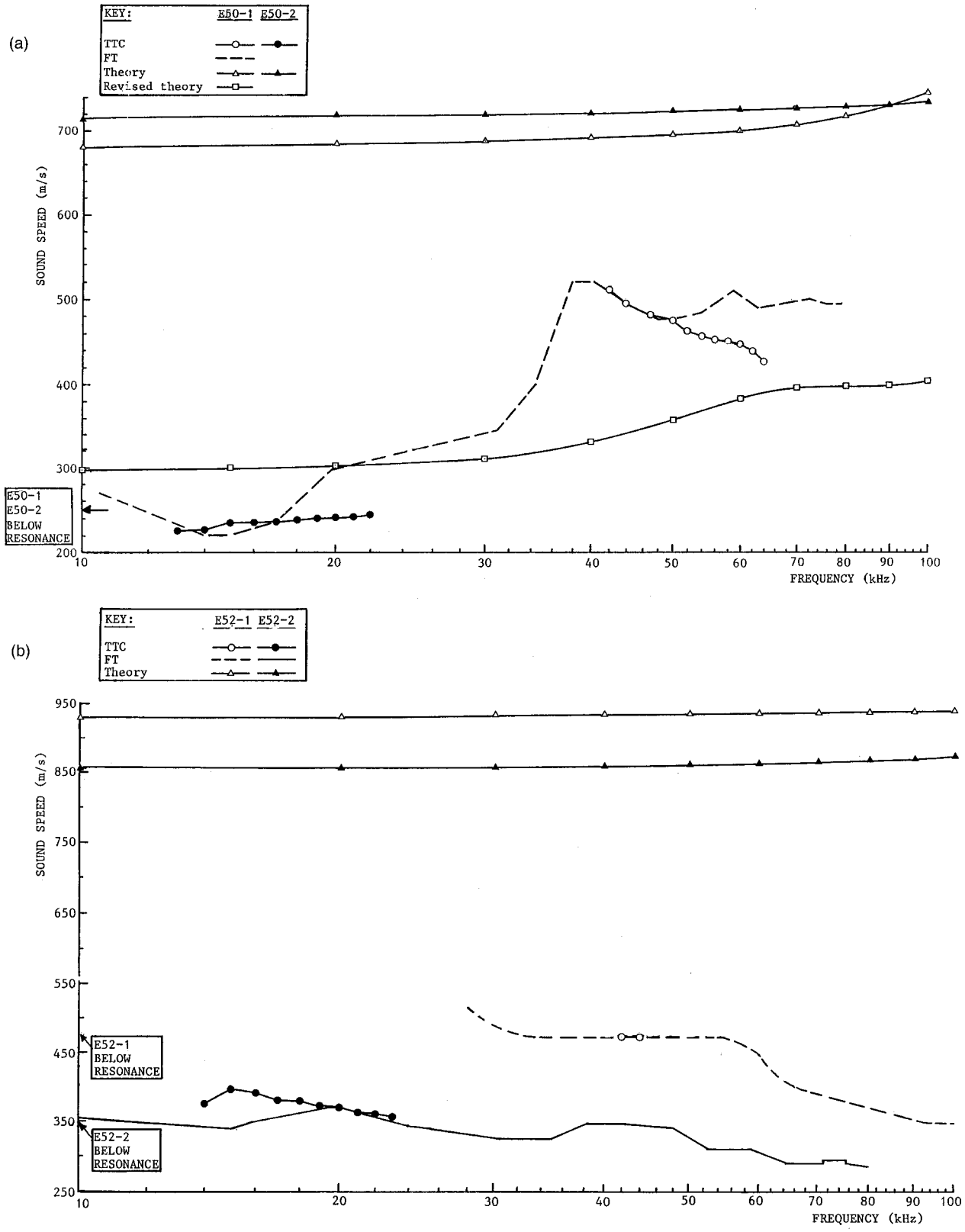

FIG. 1. A comparison at frequencies of gas bubble resonance between measurements of sound speed on laboratory gassy soils by Gardner (Ref. 20) (using two measurement techniques, TTC and FT), and sound speeds calculated using Eq. (1) based on material properties of the soil matrix defined by Anderson and Hampton (Refs. 4, 5).

B. Equations used in the present study—from Anderson and Hampton (Refs. 4, 5)

For sound speed at frequencies below resonance, the exact solution of the equation of motion for elastic, homogeneous, and isotropic solids is:

$$c = \sqrt{\frac{K + (4G/3)}{\rho}}, \tag{1}$$

where K and G are the **bulk** dilatational and shear moduli of the soil, and ρ is its density.

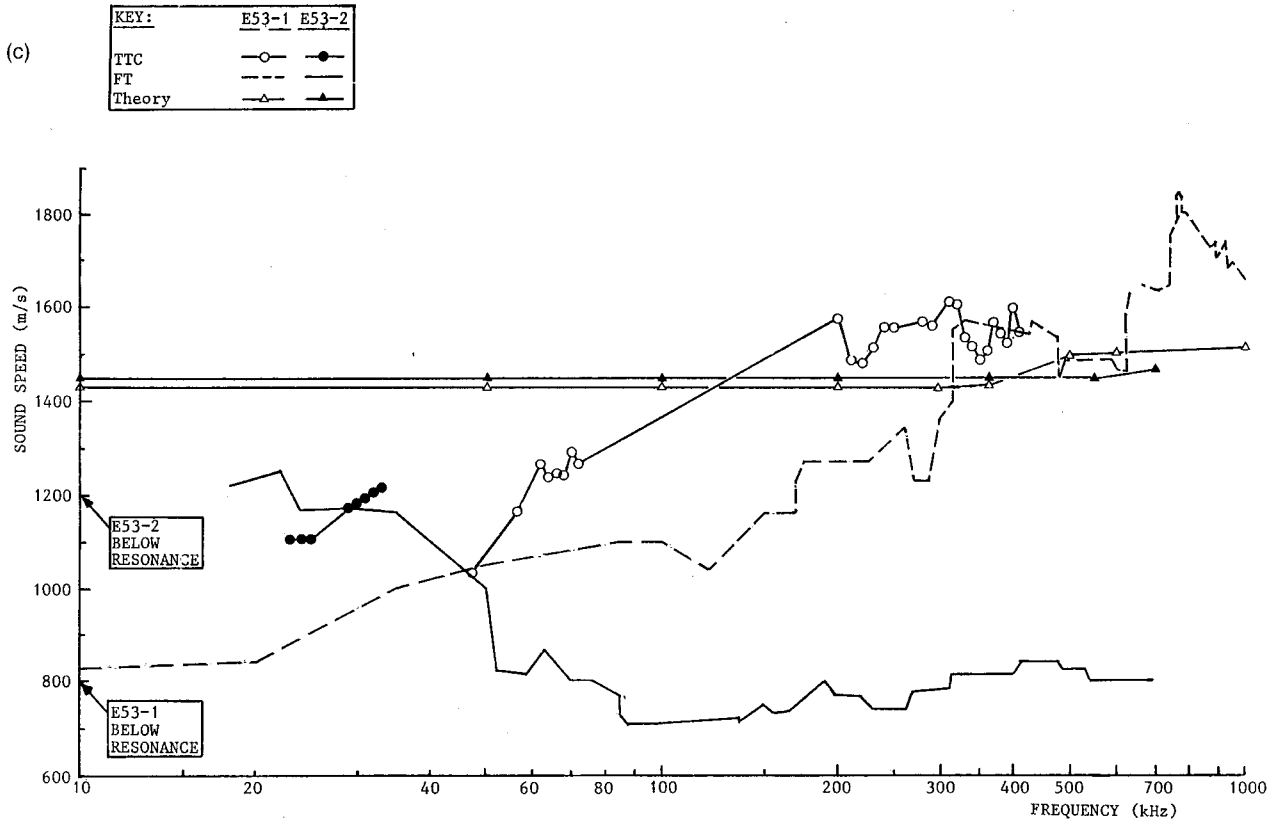

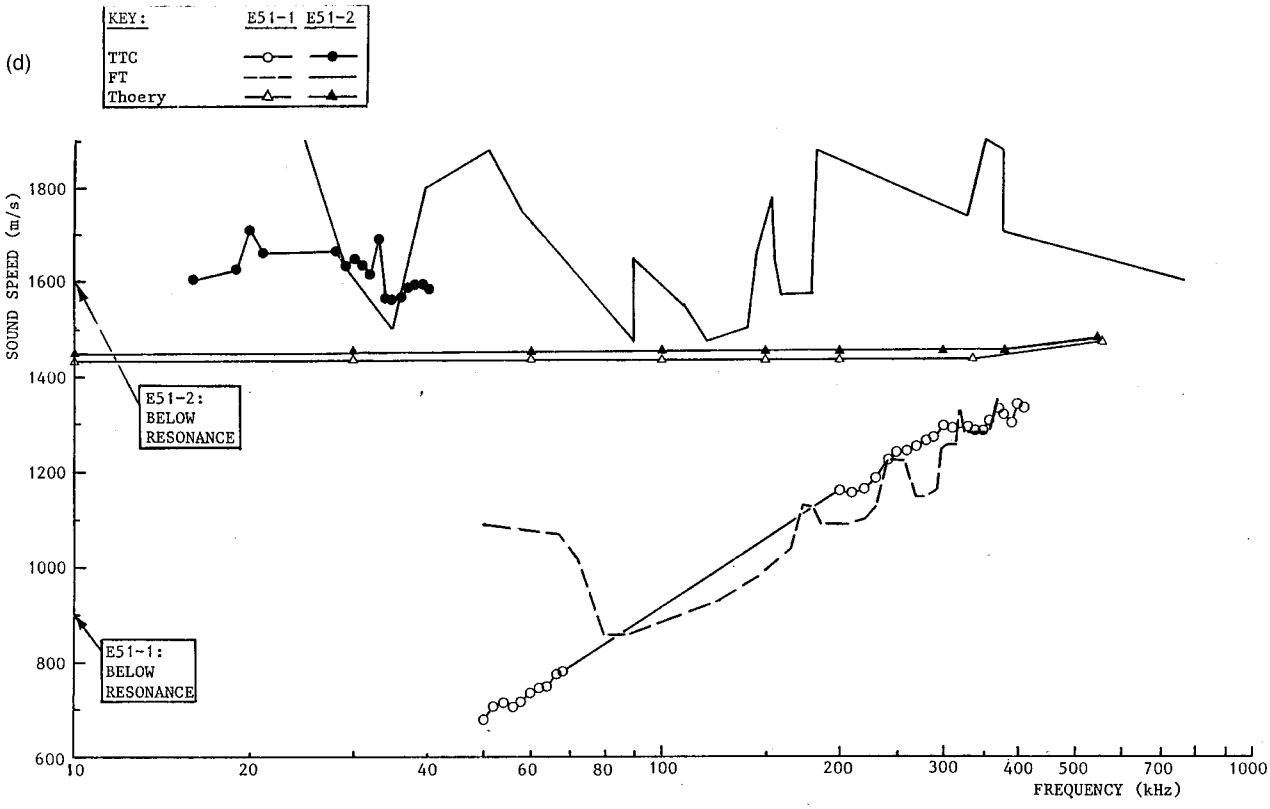

FIG. 1. (*Continued.*)

At frequencies of bubble resonance the Anderson and Hampton equation is:

$$\left(\frac{c_0}{c}\right)^2=\frac{1}{2}(1+WX_1)\left\{1\pm\left(1+\left[\frac{WY_1}{1+WX_1}\right]^2\right)^{1/2}\right\}, \qquad (2)$$

where c_0 is the sound speed in saturated sediment, and X_1 and Y_1 are coefficients of a gassy medium for which bubble size distribution may be expressed as a histogram. Also,

$$W=\frac{K_{\text{sat}}}{\gamma P_0+4G_{\text{sat}}/3},$$

γ is the specific heat ratio for gas (adiabatic constant), P_0 is the ambient hydrostatic pressure, and K_{sat} and G_{sat} are the dilatational and shear moduli of the soil matrix (**not** the *bulk* material properties). The Anderson and Hampton equation for the frequency of resonance (f_0) is:

$$f_0 = \frac{1}{2\pi r}\sqrt{\frac{3\gamma P_0}{A\rho_s} + \frac{4G_{sat}}{\rho_s}} \tag{3}$$

for a bubble radius r. ρ_s is the soil matrix bulk density and A is defined as a coefficient. They believed the product $f_0 r$ ("r" is bubble radius) to be a constant for a given soil matrix.

C. Calculating acoustic parameters—Anderson and Hampton model (Refs. 4, 5)

Acoustic parameters were calculated from the Anderson and Hampton equations based on the material properties of the Gardner soils provided, except for the elastic moduli K_{sat} and G_{sat} (dilatational and shear) that were estimated from two sources: case (i) Anderson and Hampton[4,5] and case (ii) Wheeler,[22–24] Jardine *et al.*,[25] and Wheeler and Gardner.[21]

D. Sound speed at frequencies of resonance

Sound speed for frequencies up to 2000 kHz were calculated by Eq. (2), based on properties of the Gardner soils (listed briefly in Tables I and II and the Appendix,[26] and in more detail in Gardner).[27] The volume concentration of gas in each bubble size provided by Gardner[20] is accommodated within the constants X_1 and Y_1. The dilatational modulus of the (solid–fluid) saturated soil matrix (K_{sat}) is used in the Anderson and Hampton acoustic equations, rather than the bulk modulus of the gassy soil (K). This is because the Anderson and Hampton equations were developed from Silberman[10] where K was defined as the modulus of the host component in a biphasic gassy medium. The same argument applies for the matrix shear rigidity (G_{sat}), which was used instead of G. Two cases were considered based on different estimates of K_{sat} and G_{sat}.

1. Case i—Upper bound estimates used by Anderson and Hampton (Refs. 4, 5)

Dynamic measurements on saturated mediums were used to provide upper bound values of sound speed. G_{sat} (0.13 GPa) was estimated from dynamic measurements on saturated surficial sediments by Smith[8] and Hamilton,[9] and the corresponding K_{sat} (3.65 GPa) was calculated from Gassman.[7]

2. Case ii—Lower bound estimate taken from Jardine et al. (Ref. 25) and Wheeler (Refs. 22–24)

G_{sat} (0.05 GPa) was estimated from the high rate load–displacement soil tests of Jardine *et al.*[25] at strains of 0.01%, since this was appropriate to acoustic signals of strain 0.01% to 0.001%. The value of K_{sat} (4.211 GPa) that corresponded with this value of G_{sat} was obtained from the experimental work of Wheeler[22–24] on saturated soils prepared from the same soil batch and in the same manner as the Gardner large bubble soils. This procedure is justified, since it is evident from Wheeler and Gardner[21] that bulk properties of the Gardner soils estimated from these sources produce sound speeds that agree well with the measured data at frequencies below bubble resonance.

Resonance frequencies (f_0), based on the measurements by Gardner[20] of bubble radii (r) in the large bubble soils, were calculated using Eq. (3). Properties of the Gardner soils are listed briefly in Tables I and II and the Appendix, or in more detail in Gardner.[27] For comparison, the constant was calculated from the product of (f_0) at the lowest frequencies of resonance found by Gardner[20] and the radius (r) of the largest size of bubbles, since the largest bubbles should be responsible for the lowest frequencies of resonance. The product was also calculated using the bubble size containing most gas (since these bubbles may generate the greatest kinetic energy during resonance) and the frequency at which peak sound speed occurs (since at this frequency these bubbles may exert the greatest influence upon sound speed in each soil). Products for the two soils with the largest bubbles and the two with the smallest bubbles were compared, since it was expected that their $f_0 r$ products would be the same as all soil specimens produced from the same silty–clay medium consolidated by the same vertical stress (Anderson and Hampton).[4,5]

E. Sound speed at frequencies below resonance

Sound speeds for the eight Gardner soils at frequencies below resonance were calculated in Eq. (1). Two cases were considered based on different soil models to estimate the bulk elastic moduli (K and G).

1. Case (i)—Upper and lower bound using Anderson and Hampton (Refs. 4, 5)

Anderson and Hampton equations were used for calculating the bulk properties K and G of the Gardner gassy soils (Table III) consistent with the rationale of Anderson and Hampton for producing upper and lower bounds. For the lower bound, modeled on soil suspensions, G was considered to be zero since a fluid has no shear rigidity. The corresponding K was calculated by Eq. (A1) [and Eq. (A2) for bulk density, see the Appendix] since each phase (solid, liquid, and gas) was assumed to contribute to the bulk property of the soil in proportion to its volume. For the upper bound values, modeled as saturated soils modified with a compressible fluid, K was calculated by Eqs. (A3) and (A4) (Gassman,[7] the Appendix). Dynamic G was taken from measurements of G made by Smith[8] and Hamilton.[9] The bulk modulus K_w' for fluid was redefined to allow for the presence of gas in proportion to its gas–fluid volume [Eq. (A5), the Appendix]. Therefore the upper bound simulated a biphasic medium formed from "solids" and a "compressible fluid."

2. Case ii—Upper and lower bound using Wheeler and Gardner (Ref. 21)

The bulk properties K and G of the Gardner soils used by Wheeler and Gardner[21] were employed to reproduce their sound speed curves. This enabled sound speeds based on the material properties of the large bubble model of Wheeler and Gardner[21] to be compared with sound speeds based on the

TABLE III. Elastic moduli of the soils (below resonance).

Soil	G (MPa)	K (MPa)	G (MPa)	K (MPa)
	(a) Anderson upper bound (compressible fluid model)		(b) Anderson lower bound (suspensioin theory)	
51-2	130	116.46	0	36.884
53-2	130	111.99	0	32.394
51-1	130	106.89	0	27.279
53-1	130	105.46	0	25.848
52-1	130	81.32	0	1.622
52-2	130	80.85	0	1.157
50-2	130	80.47	0	0.769
50-1	130	80.37	0	0.672
	(a) Wheeler upper bound (large bubble model, dynamic)		(b) Wheeler lower bound (measured static)	
51-2	19.880	2360	1.988	685
53-2	19.870	2250	1.987	600
51-1	19.840	2140	1.984	510
53-1	19.830	2070	1.983	490
52-1	17.170	230	1.718	26.0
52-2	16.000	160	1.601	15.0
50-2	13.850	80	1.388	7.0
50-1	12.910	67	1.298	6.8

suspension and compressible fluid models proposed by Anderson and Hampton [case (i) above]. The Wheeler and Gardner lower bound bulk properties K and G for the Gardner soils were extrapolated from large strain static load tests and their upper bound values were from the dynamic tests of Jardine *et al.*[25] at low strains representative of acoustic signals. Sound speeds of the Gardner soils based on these upper bound bulk properties of G and K were shown by Wheeler and Gardner[21] to agree well with measured sound speeds in the same soils.

III. RESULTS

A. Sound speed at frequencies of resonance

Figure 2 presents sound speeds calculated by Eq. (2), based on the properties of the eight Gardner soils. In the high gas content soils ($E50$,$E52$), upper bound estimates of moduli [case (i)] produced sound speeds approximately 100 m/s higher than the lower bound of case (ii) at frequencies below 100 kHz (this is not apparent in the figure because of axis scaling). Resonance frequency at peak sound speed was between 500 and 1000 kHz for both cases in all eight soils. For both cases (i) and (ii), the Anderson and Hampton model when applied to the high gas content soils ($E50$,$E52$) produced peak sound speeds that were implausibly high, but peaks were more credible when the model was applied to the low gas content soils ($E51$,$E53$). The low gas content soils of case (i) did not peak at resonance, but those of case (ii) exhibited the same profile below, at, and above resonance as the data calculated by Anderson and Hampton[4,5] based on harbor mud of low gas content.

Calculated sound speeds have been superimposed on Fig. 1 (indicated as ''theory'') to compare with the corresponding measured data for the same soils from Gardner.[20] Case (i) only is used since this model utilizes the method for predicting G and K proposed by Anderson and Hampton.[4,5] The correlation between data sets is weak. The transition points on the calculated curves, indicated by an upturn in sound speed, occurred at 60–90 kHz for $E50$, $E52$ and at 350–500 kHz for $E51$, $E53$. These occurred at higher frequencies than the corresponding transition points identified by the measured curves (15–20 kHz). Thus bubbles were resonating at lower frequencies and producing lower sound speeds than the current theory of Anderson and Hampton[4,5] predicts. Also, sound speeds at the transition points of measured data were 40%–70% less than corresponding sound speeds in the calculated data. Since the measured data of Gardner[20] covers only the frequencies of large bubble resonance and below, the correlation between measured and calculated data at peak sound speed and at frequencies above resonance could not be examined.

B. Frequencies of bubble resonance

Table II shows the resonance frequencies of the maximum and minimum bubble sizes of each soil that were calculated using Eq. (4) based on the properties of the Gardner soils and the moduli of case (i). Again, the lowest frequencies of resonance (for the largest bubbles) for each soil are higher than the corresponding (transition point) frequencies from the measured data. Table IV provides $f_0 r$ values for the largest size of bubbles and for the bubble size containing most gas. Neither was constant.

C. Refining material properties to improve the correlation at frequencies of resonance

Figure 3(a) shows the influence upon sound speed of varying K_{sat} above and below 3.65 GPa (while holding G_{sat} constant at 0.013 GPa). An increase in K_{sat} improves the correlation with measured data by producing a drop in sound speed below resonance frequencies, but a further increase in peak sound speed and a shift of the peak upward in frequency causes further disparity. Since the converse occurs for a reduction in K_{sat}, K_{sat} cannot be refined in all respects to produce a better fit between calculated and measured data. Figure 3(b) shows the influence upon sound speed of varying G_{sat} above and below 0.013 GPa (while holding K_{sat} constant at 4.221 GPa). A reduction in G_{sat} produces propitious reductions in sound speed below frequencies of resonance and in the lowest frequency of resonance, which improves the correlation with measured data. Therefore, revised moduli were required that reduced G_{sat} and allowed K_{sat} to remain largely unchanged. These were obtained from measurements of G_{sat} performed on laboratory saturated soils (Wheeler[22–24]) from the same batch of estuarine silty clay as the Gardner soils and prepared in the same manner. The value of G_{sat} was then modified to ensure that the modulus corresponded with small strain acoustic measurements (Jardine *et al.*[25]), giving 20 MPa. Wheeler[22–24] was again used to find the value of K_{sat} that corresponded with this G_{sat} in a saturated soil prepared from the same soil batch in the same manner. This gave 3570 MPa, which was close to the unrefined value and therefore did not influence the correlation between sound speeds and measured data.

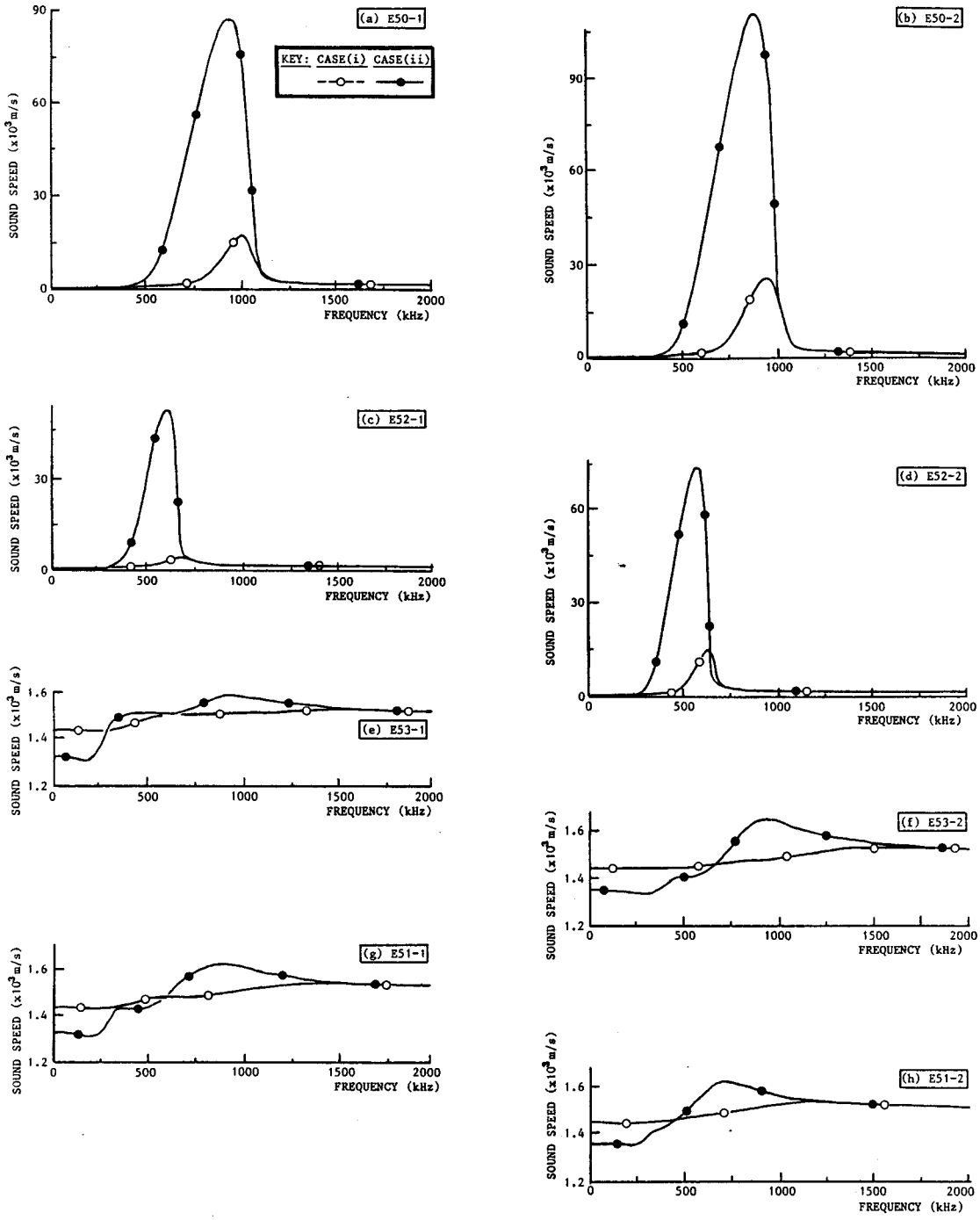

FIG. 2. Calculated values of sound speed at frequencies of gas bubble resonance (the symbols do not denote data points; actual points are at 2.44 kHz intervals). Calculations are based on material properties of the soil matrix defined by Anderson and Hampton (Refs. 4, 5) [case (i)], or from Wheeler (Refs. 22–24) and Jardine *et al.* (Ref. 25) [case (ii)].

TABLE IV. $f_0 r$ values produced using parameters from experiments.

		Bubble size—Peak gas content		Bubble size—Largest	
Soil	Transition point (kHz)	Average bubble diameter (μm)	$f_0 r$ (Hz cm)	Average bubble diameter (μm)	$f_0 r$ (Hz cm)
50-1	20	312	312	1746	1746
50-2	20	422	422	1746	1746
53-1	20	-	-	458	458
51-1	80	137	548	385	1540

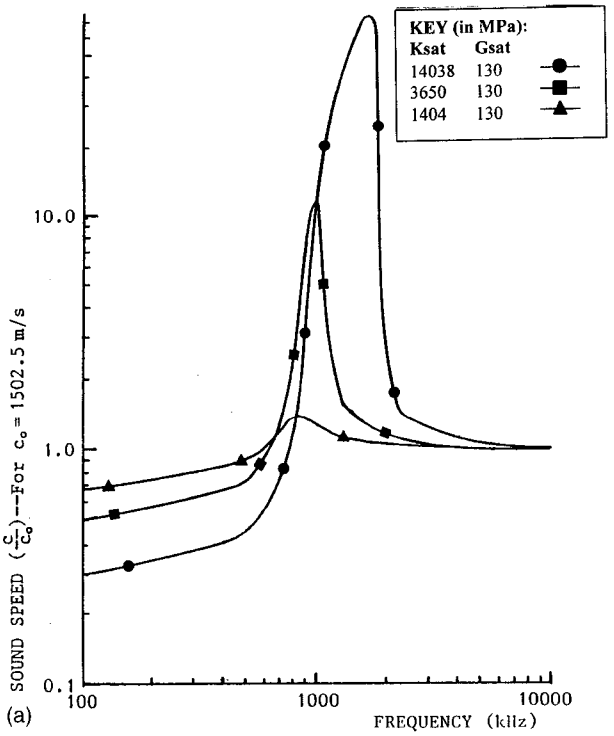

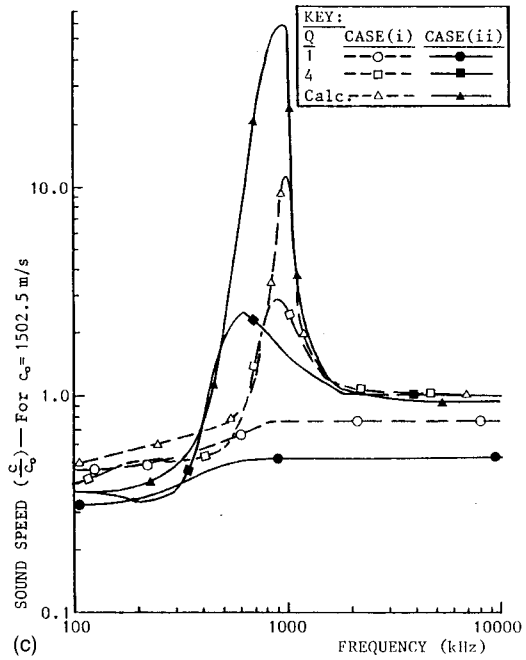

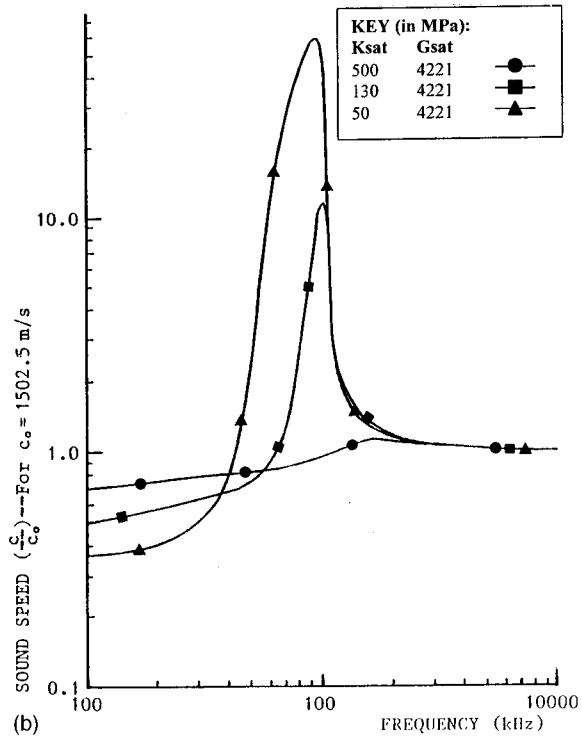

FIG. 3. Perturbation of soil material properties to examine sound speed sensitivity. (a) Varying K_{sat} above and below 3.65 GPa (while holding G_{sat} constant at 0.013 GPa). (b) Varying G_{sat} above and below 0.013 GPa (while holding K_{sat} constant at 4.221 GPa). (c) Varying the specific dissipation function (Q), the inverse of the damping constant (d) defined by Anderson and Hampton (Refs. 4, 5).

Sound speeds based on these refined moduli were not found to improve the correlation at all frequencies. Since the mechanical behavior of soil is also influenced by its signal damping property, this may also be refined to improve the correlation between measured and modeled data. Figure 3(c) shows the influence upon sound speed of varying the specific dissipation function (Q), the inverse of the damping constant (d) defined by Anderson and Hampton.[4,5] The original sound speed curve calculated without amending damping (and without estimating Q separately) is shown alongside curves generated from $Q=1$ and 4. A value of one is appropriate to stiff ocean sediments (Anderson and Hampton[4,5]), whereas a value of four is more appropriate to the softer laboratory soils of Gardner.[20] Since a value of four propitiously reduces the frequency at which peak sound speed occurs, the sound speed below frequencies of resonance, and the peak sound speed (thus compensating for the slight increase due to reducing G_{sat}), revised values of Q, G_{sat}, and K_{sat} (4, 20 MPa, 3570 MPa) were used to calculate sound speed by Eq. (2). This improved the match between calculated and measured data for soil E50-1 [see "revised theory" Fig. 1(a)], through reducing sound speed below resonance by

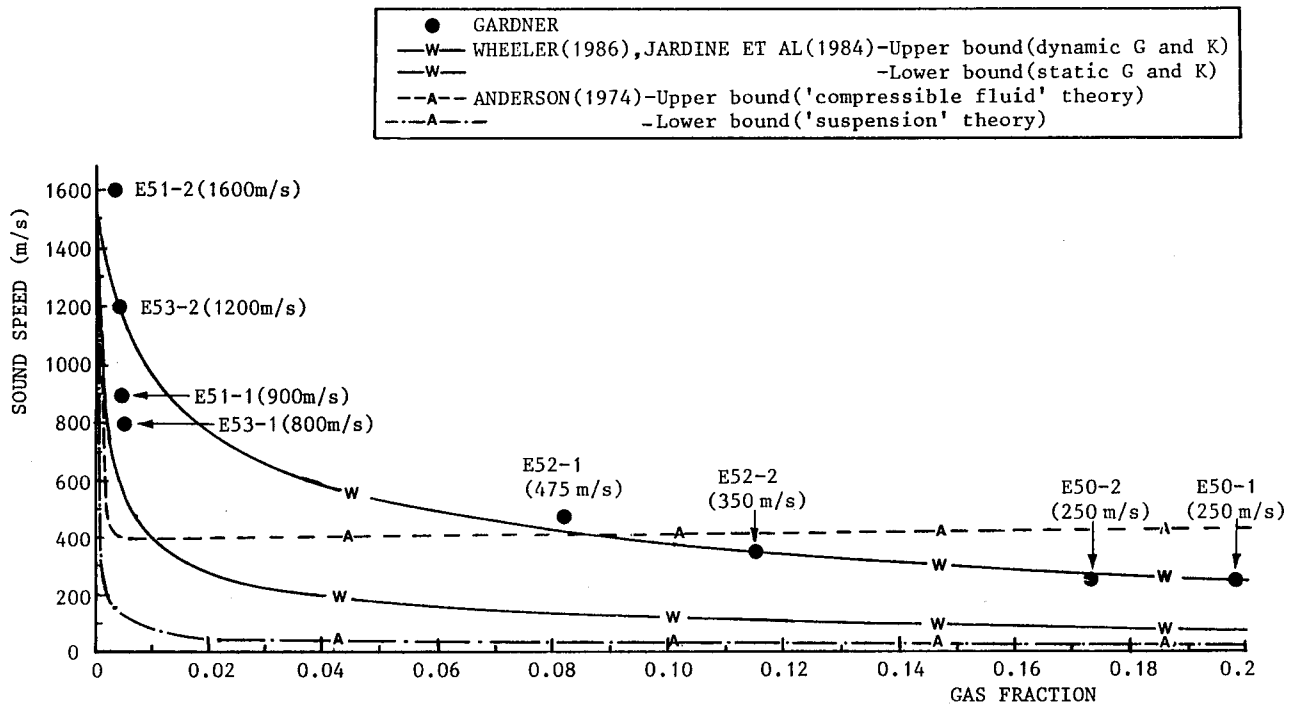

FIG. 4. A comparison between theoretical calculations and measurements of sound speed at frequencies below bubble resonance. Calculations were based on bulk elastic properties defined by Anderson and Hampton (Refs. 4, 5) [case (i)], or were based on Wheeler and Gardner (Ref. 21) [case (ii)] using the work of Wheeler (Refs. 22–24) and Jardine *et al.* (Ref. 25).

55% and through reducing the lowest frequency of resonance (for the largest bubbles); although the match was not exact in respect of the rate of variation of sound speed with frequency. Since sound speed varies directly in response to adjustments in Q, G_{sat}, and K_{sat}, sound speeds for the remaining soils based on these refined values will similarly improve the correlation with the corresponding measured data.

D. Sound speed at frequencies below resonance

Figure 4 shows calculated upper and lower bound sound speeds below frequencies of resonance, based on properties of the Gardner soils and the Anderson and Hampton equations defining the bulk properties G and K [case (i)]. Comparative data are shown for upper and lower bound sound speeds [case (ii)], and for measured sound speeds (Wheeler and Gardner[21]). The single measurements for each soil are analogous to the measured sound speeds shown in Fig. 1 at approximately 10 kHz. Sound speeds at 10 kHz are below the frequency of resonance in all soil samples. This is deduced because, in the soils of largest bubble diameter (50-1, 50-2, and 52-2, Table II) that resonate at the lowest frequencies, the measured curve data and the refined theoretical curve data appear to indicate zero gradients or troughs at around 15 to 20 Hz or above. Thus the transition points marking the lowest frequencies of bubble resonance for all eight soils must be above 10 kHz. The best fit with the experimental data from the eight large bubble soils of different gas content was case (ii)—upper bound data, modeled correctly as a gas surrounded by a solid–fluid matrix at an acoustic strain level of 0.01%. Case (ii)—lower bound, from the same large bubble model but based on static load tests at large strains, substantially underestimated sound speed at all gas fractions indicating the importance of strain rate and magnitude. The worst indicator was case (i)—lower bound data based on the bulk properties of a soil suspension, proving inappropriate even as a lower bound for large bubble soils. Additionally, the upper bound (suspension) and lower bound (compressible fluid) data of case (i) show abrupt reductions in sound speed between a saturated soil and a gassy soil of only minimal gas content. This happens to a lesser extent with the upper and lower bounds of case (ii) for the large bubble soil that behaves as a monophasic medium below resonance. The case (i) data indicate little variation in sound speed for gas fractions greater than those causing the initial abrupt reductions, whereas the case (ii) data indicate progressively reducing sound speeds for increasing gas contents. As a result, case (i)—upper bound underestimates measured sound speed substantially at low gas fractions (<0.06) and overestimates sound speed substantially at high gas fractions (>0.12). It should be noted that at frequencies below resonance, the sound speeds calculated by Eq. (1) were substantially lower than the corresponding sound speeds initially calculated by Eq. (2), since initially different values of G_{sat} were used for the saturated soil matrix. The refinement of G eradicated the difference.

IV. DISCUSSION

A. Sound speeds at frequencies of resonance and material properties of the soil matrix

It is evident from Figs. 1 and 3 that the acoustic response of a gassy soil at frequencies of resonance is dominated by its gas volume and to a much lesser extent by its

elastic moduli and the damping activity of the soil matrix. Substantial variations in sound speed between the soils arise from relatively small differences in gas content, and much smaller variations arise from substantial differences in the soil matrix properties. There is also evidence that sound speeds at the lower frequencies of bubble resonance and at frequencies below resonance may be predicted with some success using the theory of Anderson and Hampton.[4,5] However, sound speed predictions by the model must be based on material properties of the saturated soil matrix that accurately simulate the load-displacement behavior of the soil at strain magnitudes and strain rates consistent with the acoustic signal propagated. It has been demonstrated that the study of Wheeler[22–24] on gassy soils of the large bubble type at high strain levels, and the study by Jardine *et al.*[25] on saturated soils at low strains, may be used to estimate elastic moduli which simulate the acoustic behavior of the Gardner soils.

As the Gardner soils were consolidated by a total stress of 25 kPa under atmospheric hydrostatic pressure, they simulated lightly consolidated surficial layers of sediment in relatively shallow water. The properties obtained from the Anderson and Hampton estimates may be more appropriate to relatively stiff marine sediments consolidated by the weight of overlying material. Such gassy soils may have greater matrix shear rigidity, but may not have correspondingly high matrix dilatational rigidity, Wheeler[22–24]). For these soils, the Anderson and Hampton Eq. (2) will predict high sound speeds at frequencies below resonance and high frequencies of large bubble resonance in comparison with the measured sound speeds of the softer Gardner soils. As Gardner's frequency range of measured sound speeds was limited, it was not possible to evaluate the accuracy of Eq. (2) for predicting peak sound speeds at frequencies of resonance. However, peak sound speeds based on both unrefined estimates of G_{sat} and K_{sat} appeared unreasonably high in comparison with the data produced by Anderson and Hampton based on ocean bottom silt and harbor mud. This will be the case unless G_{sat} is increased substantially to simulate the mechanical behavior of more consolidated soils (without adjusting K_{sat}), or damping is adjusted within the range $(1 < Q < 4)$. Such an increase in G_{sat} is inappropriate for simulating the mechanical behavior of the Gardner soils, and although the adjustment of Q may be appropriate evidence of this is unavailable.

B. Resonance frequencies and the constant $f_0 r$

The resonance frequencies of the largest and smallest bubbles should provide an indication of the frequency range over which bubble resonance influences sound speed. In practice the range will be greater than this as the resonances of single-sized bubbles affect sound speed over a range of frequencies near resonance (as indicated by the data on harbor muds from Anderson and Hampton[4,5]). It is therefore unsurprising that resonance frequencies of the largest bubbles [from Eq. (3)] are greater than transition point frequencies indicated by corresponding measured data. This level of disparity is reduced for transition points based on the refined material properties of the soil, to a level that reveals the extent of resonance effects in the Gardner soil below the peak resonance frequency of the largest bubble.

C. Sound speed at frequencies below resonance, models and bulk material properties

At frequencies below resonance sound speeds based on bulk material properties of ''large bubble'' soils (Wheeler and Gardner[21]) were shown to match the measurements made by Gardner[20] better than sound speeds based on Anderson and Hampton approximations. Sound speeds based on material properties simulating the ''compressible fluid'' and ''suspension'' models of Anderson and Hampton are not helpful and misleading when applied as upper and lower bound estimates for ''large bubble'' soils. This is because their load-displacement behavior is fundamentally different. The abrupt change in sound speed from a saturated soil to a gassy one arising from a minimal amount of gas content is caused by an equally abrupt increase in the bulk compressibility $(1/K)$. This arises from the substantial compressibility of gas within fluid in their compressible fluid (upper bound) and suspension (lower bound) models. It happens to a lesser extent with the Wheeler and Gardner large bubble models (upper and lower bounds) because gas is contained in structural pockets in the saturated matrix, and a pocket structure formed by the saturated soil matrix has a lower compressibility than a gas bubble formed in fluid. Additionally, suspension models are misleading since they employ a shear modulus of zero, which is unrealistic when applied to sea bed soils since even the softest soils have some shear rigidity. Without shear rigidity and with a high compressibility, the Anderson and Hampton suspension model produces sound speeds of almost zero at all gas contents, other than minimal. The magnitude and trend of variation in sound speed is therefore very different to the behavior of large bubble soils, and is uninformative as a lower bound guide. Even the compressible fluid model proved not to be an effective lower bound guide, since sound speeds determined by the model were less than measured sound speeds in soils with gas fractions of less than 0.09.

APPENDIX A: FURTHER PROPERTIES USED IN THE EQUATIONS

At resonance

Values of parameters used to calculate sound speed or resonance frequency by Eqs. (1), (2) and (3) (note—the list includes parameters not contained in the main text that are defined below and discussed in Anderson[4,5]):

Case i—Anderson and Hampton

Ratio of specific heats of gas in bubbles $\gamma = 1.333$ (Kaye and Laby[26]).

Reciprocal of thermal diffusivity of gas for bubbles in water (where for the gas s_p is specific heat at constant pressure, ρ_g is density, and C_g is thermal conductivity)—Anderson and Hampton:[4,5]

$$\frac{\rho g^s p}{Cg} = 500 \text{ s/m}$$

Soil matrix bulk density $\rho_s = 1597 \text{ kg/m}^3$ (measured from saturated soil sample, Gardner[27])
Water density $\rho_w = 1020 \text{ kg/m}^3$ (measured from water sample, Gardner[27])
Gas density $\rho_g = 0.6623 \text{ kg/m}^3$ (CRC Handbook[28])
Sound speed in bubble free water $c_0 = 1502.5$ (measured, Gardner[27])
Soil shear modulus $G_{\text{sat}} = 1.3 \times 10^8 \text{ N/m}^2$ (Measurement from saturated surficial sediment—Smith[8] and Hamilton[9])
Imaginary part of complex modulus $G' = 0.325 \times 10^8 \text{ N/m}^2$ (25% of G—Anderson and Hampton[4,5])
Soil dilatational modulus $K_{\text{sat}} = 3.649\,86 \times 10^9 \text{ N/m}^2$ (from Gassman[7] equations—saturated medium)
Soil frame bulk modulus $K_f = 0.007\,97 \times 10^{10} \text{ N/m}^2$ saturated soil (Anderson and Hampton[4,5])
Mineral particle bulk modulus $K_m = 5.0 \times 10^{10} \text{ N/m}^2$ saturated soil (Anderson and Hampton[4,5])
Water bulk modulus $K_w = 0.23 \times 10^{10} \text{ N/m}^2$ saturated soil (Anderson and Hampton[4,5])
Ambient hydrostatic pressure $P_0 = 1.013\,25 \times 10^5 \text{ N/m}^2$
Total void porosity $n = 0.625$ (measured from saturated soil sample, Gardner[27])

Case ii—Wheeler (Refs. 22–24) and Jardine *et al.* (Ref. 25)

As above, except for G_{sat} and K_{sat} as follows:
Soil shear modulus $G_{\text{sat}} = 0.5 \times 10^8 \text{ N/m}^2$ ($G'_{\text{sat}} = 0.125 \times 10^8 \text{ N/m}^2$)
Soil dilatational modulus $K_{\text{sat}} = 4.211 \times 10^9 \text{ N/m}^2$

Below resonance

$$K = \frac{K_g K_w K_m}{n_g K_w K_m + (1-n) K_w K_g + (n-n_g) K_m K_g} \tag{A1}$$

$$\rho = n_g \rho_g + (1-n)\rho_m + (n-n_g)\rho_W \tag{A2}$$

where:

K_g = gas bulk modulus

K_w = water bulk modulus

K_m = mineral particle bulk modulus

n = total void porosity

n_g = gas porosity

ρ_g = gas density

ρ_m = mineral density

ρ_w = water density

$$K = K_m \left(\frac{K_f + Q'}{K_m + Q'} \right), \tag{A3}$$

where K_f = sediment frame bulk modulus, and

$$Q' = \frac{K'_w (K_m - K_f)}{n(K_m - K'_w)}, \tag{A4}$$

$$K'_w = \frac{K_w \gamma P_0}{n'_g K_w + (1-n'_g)\gamma P_0}, \tag{A5}$$

where:

γ = ratio of specific heats

ρ_0 = ambient hydrostatic pressure

n'_g = fraction of sediment pore volume occupied by gas.

[1] A. A. Yakubov, A. A. Ali-Zade, and M. M. Zeinalov, "Mud volcanos of the Azerbaijan," SSR; Atlas Academy of Science of Azerbaijan, SSR; Baku, U.S.S.R., Vol. 258 (1971).
[2] R. S. Newton, R. C. Cunningham, and C. E. Schubert, "Mud volcanoes and pockmarks: Sea floor engineering hazards or geological curiosities?" Offshore Techn. Conf. **3729**, 425–435 (1980).
[3] L. H. King and B. Maclean, "Pockmarks of the Scotian shelf," Geol. Soc. Am. Bull. **81**, 3141–3148 (1970).
[4] A. L. Anderson and L. D. Hampton, "Acoustics of gas bearing sediments, I. Background," J. Acoust. Soc. Am. **67**, 1865–1889 (1980).
[5] A. L. Anderson and L. D. Hampton, "Acoustics of gas bearing sediments, II. Measurements and models," J. Acoust. Soc. Am. **67**, 1890–1903 (1980).
[6] A. B. Wood, *A Textbook of Sound*, 3rd ed. (McGraw-Hill, New York, 1930).
[7] F. Gassman, "Elastic waves through a packing of spheres," Geophysics **16**, 673–685 (1951).
[8] D. T. Smith, "Acoustic and mechanical loading of marine sediments," O.N.R. Symposium on Physics of Sound in Marine Sediments, Austin, TX (1973).
[9] E. L. Hamilton, "Elastic properties of marine sediments," J. Geophys. Res. **76**, 579–604 (1971).
[10] E. Silberman, "Sound velocity and attenuation in bubbly mixtures measured in standing wave tubes," J. Acoust. Soc. Am. **29**, 925–933 (1957).
[11] A. Bedford and M. Stern, "A model for wave propagation in gassy sediments," J. Acoust. Soc. Am. **73**, 409–417 (1983).
[12] P. E. Kepkay, "Preliminary investigation of free gas as the control of a sub-bottom acoustic reflector in the fine-grained sediments of Halifax Harbor and St Margaret's Bay, Nova Scotia," MSc Thesis, Dalhousie University (1977).
[13] J. L. Jones, C. B. Leslie, and L. E. Barton, "Acoustic characteristics of a lake bottom," J. Acoust. Soc. Am. **30**, 142–145 (1958).
[14] J. L. Jones, C. B. Leslie, and L. E. Barton, "Acoustic characteristics of underwater bottoms," J. Acoust. Soc. Am. **36**, 154–157 (1964).
[15] F. Press and M. Ewing, "Low-speed layer in water-covered areas," Geophysics **13**, 127–132 (1948).
[16] J. L. Worzel and C. L. Drake, "Structure section across the Hudson River at Nyack, N.Y. from seismic observations," Ann. N.Y. Acad. Sci. **80**, (1959).
[17] F. K. Levin, "The seismic properties of Lake Maracaibo," Geophysics **27**, 35–47 (1962).
[18] T. S. Edrington and T. M. Calloway, "Sound speed and attenuation measurements in gassy sediments in the Gulf of Mexico," Geophysics **49**, 297–299 (1984).
[19] M. P. Hochstein, "Seismic measurements in Suva Harbor (Fiji)," N. Z. J. Geol. Geophys. **13**, 269–281 (1970).
[20] T. N. Gardner, "An acoustic study of soils that model sea-bed sediments containing gas bubbles," J. Acoust. Soc. Am. **107**, 163–176 (2000).
[21] S. J. Wheeler and T. N. Gardner, "Elastic moduli of soils containing large gas bubbles," Geotechnique **39**, 333–342 (1989).
[22] S. J. Wheeler, "A conceptual model for soils containing large gas bubbles," Geotechnique **38**, 389–397 (1988a).
[23] S. J. Wheeler, "The undrained shear strength of soils containing large gas bubbles," Geotechnique **38**, 399–413 (1988b).
[24] S. J. Wheeler, "The stress strain behavior of soils containing gas bubbles," DPhil thesis, University of Oxford (1986).

[25] R. J. Jardine, M. J. Symes, and J. B. Burland, ''The measurement of soil stiffness in the triaxial apparatus,'' Geotechnique **34**, 323–340 (1984).
[26] J. V. C. Kaye and T. H. Laby, *Tables of Physical and Chemical Constants*, 14th ed. (Longman, New York, 1973).
[27] T. N. Gardner, ''The acoustic properties of gassy soil,'' DPhil Engineering Thesis, University of Oxford (1988).
[28] *CRC Handbook of Chemistry and Physics* (CRC Press, Boca Raton, FL, 1999).

Dispersion of interface waves in sediments with power-law shear speed profiles. I. Exact and approximate analytical results[a)]

Oleg A. Godin[b)]
NOAA/Environmental Technology Laboratory, Ocean Remote Sensing Division, Boulder, Colorado 80305-3328 and Acoustic Wave Propagation Laboratory, P. P. Shirshov Oceanography Institute of the Russian Academy of Sciences, Moscow 117851, Russia

David M. F. Chapman
Defence Research Establishment Atlantic, Dartmouth, Nova Scotia B2Y 3Z7, Canada

(Received 5 October 2000; revised 13 April 2001; accepted 12 July 2001)

In the upper tens of meters of ocean bottom, unconsolidated marine sediments consisting of clay, silt, or fine sand with high porosity are ''almost incompressible'' in the sense that the shear wave velocity is much smaller than the compressional wave velocity. The shear velocity has very large gradients close to the ocean floor leading to strong coupling of compressional and shear waves in such ''soft'' sediments. The weak compressibility opens an avenue for developing a theory of elastic wave propagation in continuously stratified soft sediments that fully accounts for the coupling. Elastic waves in soft sediments consist of ''fast'' waves propagating with velocities close to the compressional velocity and ''slow'' waves propagating with velocities on the order of the shear velocity. For the slow waves, the theory predicts the existence of surface waves at the ocean-sediment boundary. In the important special case of the power-law depth-dependence of shear rigidity, phase and group velocities of the interface waves are shown to scale as a certain power of frequency. An explicit, exact solution was obtained for the surface waves in sediments characterized by constant density and a linear increase of shear rigidity with depth, that is, for the case of shear speed proportional to the square root of the depth below the sediment-water interface. Asymptotic and perturbation techniques were used to extend the result to more general environments. Theoretical dispersion relations agreed well with numerical simulations and available experimental data and, as demonstrated in a companion paper [D. M. F. Chapman and O. A. Godin, J. Acoust. Soc. Am **110**, 1908 (2001)] led to a simple and robust inversion of interface wave travel times for shear velocity profiles in the sediment.
[DOI: 10.1121/1.1401776]

PACS numbers: 43.30.Ma, 43.30.Dr, 43.30.Pc [DLB]

I. INTRODUCTION

There is a theoretical understanding and a compelling experimental evidence[1–13] that shear rigidity of unconsolidated marine sediments increases continuously with depth near the water-sediment interface and it is often proportional to a certain power z^{ν} of depth z below the interface as long as the composition of the sediments remains unchanged. Owing to their shear rigidity, unconsolidated sediments support seismo-acoustic interface waves. The study of such waves in surficial marine sediments is of considerable interest because dispersion of the interface waves provides an insight into geoacoustic properties of the sea floor that are difficult to measure by other means.[10,14–16] In addition, the interface waves exhibit some intriguing physical properties that are directly related to the power-law depth-dependence of shear rigidity.[12,17]

Previous techniques of interface wave analysis involved cumbersome numerical modeling. Numerical models usually rely on approximating the depth-dependence of geoacoustic parameters by a stack of homogeneous layers. (We will call this a *stacked-layer model*, for simplicity.) In the present paper, an analytical theory of elastic waves in continuously stratified soft sediments is developed. The theory is based on the existence of a small parameter, namely, the ratio of shear and compressional wave velocities in soft sediments. Owing to this small parameter, soft sediments are rubberlike or jellylike, as far as their elastic properties are concerned, and they can be treated mathematically as an incompressible or almost-incompressible solid. With regard to interface waves, the major result of the theory is a set of analytical dispersion relations that specify the phase and group speed of the interface waves as a function of frequency, mode number, and the geophysical parameters of the medium. These formulas can be used in the direct inversion of experimental data to provide estimates of shear speed profiles having a power-law characteristic. The application of the theoretical results to experimental data sets is the topic of a companion paper,[17] hereafter called paper CG.

[a)]Parts of this work have been previously reported at Acoustics Week in Canada (Victoria, B. C., October 1999) and at the 139th ASA Meeting (Atlanta, May–June 2000).

[b)]Author to whom correspondence should be addressed; electronic mail: Oleg.Godin@noaa.gov

This paper is organized as follows. In Sec. II, the fundamental equations of motion are analyzed for linear mechanical waves in stratified elastic media in the limit of compressibility tending to zero. A wave equation is derived that is exact for linear waves in incompressible stratified solids and which fully accounts for continuous *P-SV* wave coupling. Scaling techniques are applied to the wave equation in Sec. III to determine the frequency dependence of group and phase velocities of surface waves in solids with power-law profile of shear velocity with arbitrary exponent ν. In Sec. IV, exact analytical dispersion relations and mode shape functions are obtained for surface waves in the special case $\nu=\frac{1}{2}$. The effects of wave polarization and boundary conditions on the interface waves are also discussed. Asymptotic techniques are applied in Sec. V to derive the dispersion relation of high-order modes for arbitrary ν. Variational perturbation theory is utilized in Sec. VI to quantify the effects of small but finite compressibility and to determine dispersion relations for the exponent ν values close to but different from $\frac{1}{2}$. In Sec. VII, exact and approximate theoretical dispersion relations are compared with the results of the numerical simulations for stacked-layer models, with the design of stacked-layer models appropriate to simulate a continuous profile being discussed in Appendix. Section VIII summarizes major findings of this work.

II. GOVERNING EQUATIONS

Small-amplitude (linear) waves in solids obey the following equation of motion (Ref. 18, Sec. 1.3)

$$\rho\frac{\partial^2 u_j}{\partial t^2}=\sum_{i=1}^{3}\frac{\partial}{\partial x_i}\sigma_{ij},\quad j=1,2,3, \tag{1}$$

which is essentially Newton's second law. Here ρ is the density, $\mathbf{u}=(u_1,u_2,u_3)$ is the displacement vector, and σ_{ij} is the stress tensor. Displacements and stresses are related by Hooke's law, which takes the following form for the isotropic solid:

$$\sigma_{ij}=\lambda\delta_{ij}\nabla\cdot\mathbf{u}+\mu\left(\frac{\partial u_i}{\partial x_j}+\frac{\partial u_j}{\partial x_i}\right). \tag{2}$$

In a layered medium having horizontal boundaries and with density and Lamé parameters λ and μ that are independent of time t and the horizontal coordinates x and y, the wave field consists of *P-SV* and *SH* waves. Assuming harmonic dependence $\exp(i\xi x-i\omega t)$ of the wave field on horizontal coordinates and time, for *P-SV* waves, Eqs. (1) and (2) reduce to (Ref. 18, Sec. 1.3)

$$\begin{aligned}-\rho\omega^2 u_1&=i\xi[(\lambda+2\mu)\nabla\cdot\mathbf{u}+\mu' u_3-\mu u_3']+(\mu u_1')',\\ -\rho\omega^2 u_3&=[(\lambda+2\mu)\nabla\cdot\mathbf{u}-i\xi\mu u_1]'-\xi^2\mu u_3-i\xi\mu' u_1,\end{aligned} \tag{3}$$

where $\rho=\rho(z),\lambda=\lambda(z),\mu=\mu(z)$, and the prime stands for the derivative d/dz with respect to the vertical coordinate. At $\mu=0$ the Eq. (3) set reduces to equations for sound waves in a layered fluid.

Consider soft sediments for which $\mu/\lambda\ll 1$. Then the terms with $\nabla\cdot\mathbf{u}$ dominate on the right sides in Eq. (3) unless $\nabla\cdot\mathbf{u}$ is very small or, more precisely, unless $|\nabla\cdot\mathbf{u}|\lesssim\xi\mu u/\lambda$. In the first approximation, one can discard the terms with μ in Eq. (3). Hence, in soft sediments, the waves with nonzero $\nabla\cdot\mathbf{u}$ are much like compressional waves (sound) in fluid with the sound speed $c=(\lambda/\rho)^{1/2}$. The perturbations in the displacement and stress fields as well as in the phase velocity caused by the shear rigidity are small compared with those in the sound wave in the fluid. We refer to such waves as *fast seismo-acoustic waves*. We demonstrate that this is not the only type of *P-SV* wave supported by soft sediments.

When $\nabla\cdot\mathbf{u}$ is small enough, the terms with μ in Eq. (3) may become significant and, in fact, dominant. The corresponding waves have phase velocities V of the order of the shear wave velocity $c_t=(\mu/\rho)^{1/2}\ll c$. We refer to such waves as *slow seismo-acoustic waves*[19,20] and represent their displacement field as

$$\mathbf{u}=\sum_{s=0}^{\infty}\left(\frac{\omega}{\xi c_r}\right)^{2s}\mathbf{u}^{(s)},\quad |\mathbf{u}^{(s)}|=O(1), \tag{4}$$

$$i\xi u_1^{(s)}+\partial u_3^{(s)}/\partial z=\frac{\rho c_r^2}{\lambda}\xi q^{(s-1)},\quad s=0,1,2,...,\quad q^{(-1)}\equiv 0. \tag{5}$$

This particular representation of the displacement field follows from the requirement that there is a balance between the terms with and without λ in Eq. (3). Here the constant c_r is a representative value of the compressional wave velocity c. The development in Eq. (4) is essentially in powers of the small parameter $(V/c)^2$, which tends toward zero when $\mu\to 0$ (for all z) at fixed λ or when $\lambda\to\infty$ at fixed $\mu(z)$. We stress that the slow waves exist even in the incompressible solid with $\lambda=\infty$. The idealization of solid being incompressible is often used, for instance, in geotechnics and soil mechanics. Equations (4) and (5) represent the slow wave field at large but finite λ as a perturbation of the field in an incompressible solid.

Substituting Eq. (4) into Eq. (3), one obtains

$$\begin{aligned}&-\rho\omega^2[u_1^{(s)}+iq^{(s)}]-i\xi[\mu' u_3^{(s)}-\mu\partial u_3^{(s)}/\partial z]\\ &\quad-(\mu\partial u_1^{(s)}/\partial z)'=2i\xi^2\mu\rho c_r^2 q^{(s-1)}/\lambda,\\ &-\rho\omega^2 u_3^{(s)}+2i\xi\mu' u_1^{(s)}+i\xi\mu\partial u_1^{(s)}/\partial z+\xi^2\mu u_3^{(s)}\\ &\quad-(\rho\omega^2 q^{(s)}/\xi)'=2\xi(\mu\rho c_r^2 q^{(s-1)}/\lambda)'.\end{aligned} \tag{6}$$

Taken together, Eqs. (6) and (5) provide a full set of equations to consecutively determine $\mathbf{u}^{(0)}$ and $q^{(0)}$, $\mathbf{u}^{(1)}$ and $q^{(1)}$, and so on. Similar equations have been used in Ref. 21 to study waves in three-dimensionally inhomogeneous solid.

Consider the equations for $\mathbf{u}^{(0)}$ and $q^{(0)}$ in more detail. These two functions completely describe the displacements and stresses of the wave in the limit of the incompressible solid, and provide leading-order terms in the case of finite λ. Note that the displacement is purely solenoidal (i.e., $\nabla\cdot\mathbf{u}=0$) in this approximation, as in a pure shear wave, but the stresses are distinct from those in a shear wave as long as $q^{(0)}\not\equiv 0$. We suppress the superscript in $\mathbf{u}^{(0)}$ and $q^{(0)}$ in what follows to simplify notation. Using Eq. (5) to eliminate u_1 from Eq. (6), one finds

$$\xi q + u_3' = (\xi^2 \mu u_3' - \mu u_3''' - \xi^2 \mu' u_3 - \mu' u_3'')/\rho\omega^2, \quad (7)$$

$$q' + \xi u_3 = \xi(\xi^2 \mu u_3 - 2\mu' u_3' - \mu u_3'')/\rho\omega^2 - \rho' q/\rho. \quad (8)$$

By differentiating Eq. (8) and subtracting the product of ξ and Eq. (7) from the result, one has

$$q'' - \xi^2 q = \frac{-2\xi}{\rho\omega^2}(\mu' u_3'' + \mu'' u_3' - \xi^2 \mu' u_3) - \left(\frac{\rho'}{\rho}\right)' q + \frac{\xi\rho'}{\rho^2\omega^2}(2\mu' u_3' + \mu u_3'' - \xi^2 \mu u_3). \quad (9)$$

Equations (8) and (9) constitute a set of two ordinary second-order differential equations that describes slow waves in a layered solid in the limit $\mu/\lambda \to 0$. We have a set of two equations rather than a single second-order equation because the slow wave generally consists of coupled *P* and *SV* waves.

As an alternative to the set of Eqs. (8) and (9), by excluding q from Eqs. (7) and (8), we obtain a fourth-order wave equation in terms of the vertical displacement:

$$(\mu u_3'')'' + [(\rho\omega^2 - 2\xi^2\mu)u_3']' + \xi^2(\mu\xi^2 - \rho\omega^2 + \mu'')u_3 = 0. \quad (10)$$

The equation can be also written as

$$(\partial^2/\partial z^2 - \xi^2)(\rho\omega^2 u_3 + \mu u_3'' - \mu\xi^2 u_3) = \rho''\omega^2 u_3 + \rho'\omega^2 u_3' - 2\xi^2\mu'' u_3. \quad (11)$$

Having solved the fourth-order wave equation for u_3, it is straightforward to calculate u_1 from Eq. (5) and q from Eq. (7) and, thus to fully determine the wave field in the given incompressible solid.

In the case of the uniform solid, the right side of Eq. (11) equals zero, and the wave equation factors into two second-order equations:

$$u_3'' - \xi^2 u_3 = 0, \quad (12)$$

$$u_3'' + (\rho\omega^2/\mu - \xi^2)u_3 = 0. \quad (13)$$

Any solution to either of Eqs. (12) and (13) is a solution to Eq. (11). Obviously, Eq. (12) is the limit at $\lambda \to \infty$ of the well-known equation for *P* waves in the uniform solid, whereas Eq. (13) coincides with the exact equation for *SV* waves in the uniform solid. When derivatives of the medium parameters are bounded, the right side of Eq. (11) becomes negligible, compared with the left side, for high-frequency waves. Then, Eq. (11) *asymptotically* reduces to uncoupled Eqs. (12) and (13) in the case of inhomogeneous media. Consequently, *P* and *SV* slow waves are asymptotically uncoupled in the incompressible solid like these waves are known to be in a solid with finite λ.[22]

There exists a special case of a layered solid where the right side of Eq. (11) vanishes and the fourth-order equation factors exactly into the second-order Eqs. (12) and (13). This is the case when the density is constant and the shear modulus is a linear function of depth. [For Eqs. (12) and (13) to be valid, the depth-dependence of λ is insignificant as long as λ is large enough compared with μ.] As a cautionary note, for a solid with linear $\mu(z)$—unlike the uniform solid—it would be wrong to assume that solutions to Eq. (12) always represent *P* waves while solutions to Eq. (13) always represent *SV* waves. In the linear $\mu(z)$ case, solutions to both Eqs. (12) and (13) are generally a superposition of continuously coupled *P* and *SV* waves. This can be verified by calculating the stress tensor by using Eqs. (2), (5), and (7) and comparing the result to the stress tensor due to pure compressional and pure shear waves.

III. DIMENSIONAL ANALYSIS

Consider slow *P*-*SV* elastic waves in a solid half-space $z>0$ with a constant density and a power-law depth-dependence of the shear modulus:

$$\mu = \rho B^2 (z/l)^{2\nu}, \quad 0 < \nu < 1. \quad (14)$$

B represents the shear-wave velocity at the depth $z=l$.[23] The shear rigidity vanishes at $z \to 0$; its gradient tends toward zero, remains finite, or diverges as $z \to 0$ if $\nu > \frac{1}{2}$, $\nu = \frac{1}{2}$, or $\nu < \frac{1}{2}$, respectively. The exponent ν values we consider are bounded by 1 from above because, as it can be shown, at $\nu \geqslant 1$ the medium does not support slow waves in the vicinity of the interface $z=0$.

Introducing the dimensionless depth $y = \xi z$, Eqs. (8) and (9) can be written in a dimensionless form:

$$\frac{dq}{dy} = -u_3 - My^{2\nu}\left(\frac{d^2u_3}{dy^2} + \frac{4\nu}{y}\cdot\frac{du_3}{dy} - u_3\right), \quad (15)$$

$$\frac{d^2q}{dy^2} - q = -4\nu My^{2\nu-1}\left(\frac{d^2u_3}{dy^2} + \frac{2\nu-1}{y}\cdot\frac{du_3}{dy} - u_3\right), \quad (16)$$

where

$$M = \omega^{-2} B^2 \xi^2 (\xi I)^{-2\nu}. \quad (17)$$

Hence, $q = \xi^{-1} F_1(\nu, M, y)$, $u_3 = \xi^{-1} F_2(\nu, M, y)$ where $F_{1,2}$ are some dimensionless functions of their dimensionless arguments. We see that displacements in the wave depend on various dimensional parameters of the problem, not directly, but only through their combination M. In mathematical terms, solutions to the governing Eqs. (8) and (9) are *self-similar*.[24] The implied similarity is between the wave field at various frequencies, wave numbers, and parameters of the power-law Eq. (14).

The self-similarity enables us to establish some general properties of the dispersion relation of surface waves. Let a homogeneous fluid with density ρ_f and sound speed c occupy the half-space $z<0$. The boundary conditions at $z=0$ are continuity of the vertical displacement u_3 and the normal stress σ_{33}. According to Hooke's law Eq. (2), in the solid

$$\sigma_{33}(0) = \xi^{-1}\rho\omega^2 q(0). \quad (18)$$

In the fluid,

$$\sigma_{33}(z) = -p(z) = Ce^{\xi z}, \quad C = \text{const}; \quad u_3(z) = (\rho_f\omega^2)^{-1}\,\partial p/\partial z, \quad (19)$$

where p stands for acoustic pressure.

We assumed that phase velocity $V = \omega/\xi$ of the surface wave is small compared with the sound speed c, i.e., μ

$\ll \lambda_f \equiv \rho_f c^2$. This is certainly the case when compressional wave velocities in fluid and solid have the same order of magnitude. With the help of Eqs. (18) and (19), the boundary conditions for the waves in a solid reduce to a single equation:

$$q(0)+Ru_3(0)=0, \quad R\equiv \rho_f/\rho. \tag{20}$$

The boundary condition Eq. (20) does not contain ω, ξ, B, or l and, hence, does not violate the self-similarity of the problem. Substituting the solutions for q and u_3 in terms of $F_{1,2}$ into Eq. (20), we find that, if a surface wave exists, its dispersion relation is given by

$$M=\Phi(R,\nu), \tag{21}$$

where Φ is a yet undetermined function. In terms of the phase velocity, the dispersion relation Eq. (21) becomes

$$V=[B^{-1}\omega^{\nu} l^{\nu}\Phi^{1/2}(R,\nu)]^{-1(1-\nu)}. \tag{22}$$

We will refer to Eq. (22) as *the scaling law*. For the group velocity

$$U=\frac{\partial\omega}{\partial\xi}=V\left[V-\frac{\omega}{V}\frac{\partial V}{\partial\omega}\right]^{-1}, \tag{23}$$

a remarkably simple expression results from Eq. (22)

$$U=(1-\nu)V. \tag{24}$$

Equations (22) and (24) determine phase and group velocities of a slow surface wave up to a factor that depends on the density ratio R and the power-law exponent ν but not on B, l, or wave frequency. The factor also depends on the mode order if the medium can support a sequence of surface waves.

The next step in the analysis of the dispersion relation can be made for surface waves that are not coupled to fluid. In this special case, $C=0$ in Eq. (19). Hence, $q(0)=u_3(0)=0$. Then, we again obtain Eqs. (22) and (24) but now with Φ independent of R. (Which is natural, as long as the wave does not "feel" the fluid.) The latter result also applies to the case when solid half-space $z>0$ is bounded by a rigid or free boundary $z=0$. This is not to say that the phase velocity does not depend on the type of boundary. Certainly, the function Φ is different for different boundary conditions and accounts for the effect of the boundary conditions on the surface wave.

When applied to the wave equation (Ref. 18, Sec. 1.3)

$$\frac{\partial^2 u_2}{\partial z^2}+\frac{1}{\mu}\frac{\partial\mu}{\partial z}\frac{\partial u_2}{\partial z}+\left(\frac{\omega^2\rho}{\mu}-\xi^2\right)u_2=0 \tag{25}$$

of *SH* waves, quite similar considerations show that the scaling law Eq. (22) also holds for *SH* waves in the half-space $z>0$. For all the three types of the boundary conditions considered above, Φ in Eq. (22) is independent of R for the *SH* modes.

We emphasize that the assumption of an incompressible solid is necessary for the scaling law Eq. (22) to be rigorously valid for *P-SV* waves. Below we show that the exact scaling is violated when the Lamé parameter λ is finite, but corrections to the phase velocity are very small as long as the phase velocity of the surface wave is small compared with the velocity of compressional waves. In addition, the position of the interface is essential; an additional dimensional parameter enters the problem, and the scaling law is violated if the boundary is not at $z=0$ where the shear modulus Eq. (14) vanishes.

IV. THE CASE $\nu=\frac{1}{2}$: AN EXACT SOLUTION

In this case of constant gradient of shear rigidity $\mu(z)$, the shear velocity is proportional to the square-root of depth, and its derivative has a singularity at the interface $z=0$.

A. Vertically polarized surface waves near a fluid–solid interface

At $\nu=\frac{1}{2}$ the set of governing Eqs. (8) and (9) for *P-SV* waves becomes

$$\begin{aligned}(M\xi z-1)\xi u_3' &= \xi^2(q+Mu_3)+M(zu_3'')',\\ (M\xi z-1)\xi u_3 &= (q+Mu_3)'+M(zu_3')'.\end{aligned} \tag{26}$$

These have a first integral. Indeed, differentiating the second equation with respect to z and subtracting the first equation from the result, one finds

$$(q+2Mu_3)''=\xi^2(q+2Mu_3). \tag{27}$$

From Eq. (27) and the boundedness of the field at $z\to+\infty$, we have

$$q+2Mu_3=Ae^{-\xi z}; \quad A=\text{const}. \tag{28}$$

From Eq. (28) and the second equation in the set Eq. (26), it follows

$$Mzu_3''+\xi(1-M\xi z)u_3=\xi Ae^{-\xi z}, \tag{29}$$

$$u_3(0)=A, \quad q(0)=A(1-2M). \tag{30}$$

Consider first the case $A\neq 0$ where the surface wave in the solid is coupled to the fluid. Then, substituting Eq. (30) into the boundary condition Eq. (20), we arrive at the dispersion relation Eq. (21) with

$$\Phi(R,1/2)=(1+R)/2. \tag{31}$$

For the phase velocity we have

$$V=\frac{2B^2}{\omega l(1+R)}. \tag{32}$$

This result agrees with the scaling law Eq. (22). Note that in deriving Eqs. (32) and (34) below, we have not *assumed* but rather *proved* the existence of a surface wave. We see that, in the fluid–solid medium considered, only one surface wave exists that is coupled to the fluid.

To find the displacement field of the surface wave, Eq. (29) needs to be solved. The general solution to this inhomogeneous second-order ordinary differential equation is

$$u_3(z)=Ae^{-\xi z}+B_1U_1(z)+B_2U_2(z), \tag{33}$$

where the first term on the right side is a particular solution to the inhomogeneous equation, $U_{1,2}$ are linear-independent solutions of the homogeneous equation, and $B_{1,2}$ are arbitrary constants. A particular solution to Eq. (29) that satisfies the boundary condition Eq. (30) is obtained with $B_1=B_2=0$. Then, from Eqs. (28) and (33),

$$u_3(z)=Ae^{-\xi z},\quad q(z)=A(1-2M)e^{-\xi z}. \tag{34}$$

Soon we show that, for $A\neq 0$, Eq. (34) is the only solution that satisfies Eq. (26) and the physical requirement for the displacements to be bounded.

Consider now the case $A=0$. In this case, $q(0)=u_3(0)=0$ according to Eq. (30). Hence, the acoustic field in the fluid is identically zero; the surface wave is uncoupled from the fluid. Equations (31), (32), and (34) do not apply to this case. According to Eq. (28), $q(z)=-2Mu_3(z)$, and the problem reduces to solving the differential equation (29), which is now a homogeneous one. The homogeneous equation has been previously considered in the study (Ref. 18, Sec. 3.2) of exact solutions to acoustic wave equations in a continuously stratified fluid. Linear-independent solutions to the equation are $U_1=M_{1/(2M),\ \frac{1}{2}}(2\xi z)$ and $U_2=W_{1/(2M),\ \frac{1}{2}}(2\xi z)$, where $M_{l,m}(y)$ and $W_{l,m}(y)$ are Whittaker functions (Ref. 25, Chap. 13). The function $W_{l,m}(y)$ has a logarithmic singularity at $y=0$. Therefore, B_2 must equal zero in Eq. (33) for the displacements to be finite at $z\to 0$. The function $M_{l,m}(2\xi z)$ tends to infinity at $z\to+\infty$ unless $\frac{1}{2}+l-m$ is a positive integer (Ref. 25, Chap. 13). Hence, from the conditions at infinity we have:

$$M=(2n)^{-1},\quad n=1,2,\ldots. \tag{35}$$

[Note that for $M=(1+R)/2>\frac{1}{2}$ that corresponds to the fluid-coupled surface wave, the differential equation considered has no solution that is bounded throughout the half-space $z>0$. Therefore, $u_3(z)$ in Eq. (34) is *the only* bounded solution to the inhomogeneous differential equation (29).] For M given by Eq. (35), the Whittaker function can be expressed in terms of Laguerre polynomials L_{n+1} or Generalized Laguerre polynomials $L_{n-1}^{(l)}$ (Ref. 25, Chaps. 13 and 22), and we have for the vertical displacement

$$\begin{aligned} u_3(z)&=\frac{B_1\zeta e^{-\zeta/2}}{n}L_{n-1}^{(1)}(\zeta)\\ &=-\frac{B_1\zeta e^{-\zeta/2}}{n}\frac{d}{d\zeta}L_n(\zeta)\\ &=\frac{B_1 e^{\zeta/2}}{n!}\frac{d^{n-1}}{d\zeta^{n-1}}(e^{-\zeta}\zeta^n),\quad \zeta=2\xi z. \end{aligned} \tag{36}$$

The solution Eq. (36) satisfies the respective wave equation and the boundary conditions at $z=0$; it is uniformly bounded and vanishes at $z\to+\infty$. Consequently, it defines a surface wave for each n. In particular, for lower order modes, we have from Eq. (36)

$$\begin{aligned} &u_3(z)=2\xi B_1 z e^{-\xi z},\ \ n=1;\\ &u_3(z)=2\xi B_1 z(1-\xi z)e^{-\xi z},\quad n=2. \end{aligned} \tag{37}$$

It follows from Eq. (36) that the horizontal displacement $u_1=i\xi^{-1}du_3/dz$ is nonzero at the interface for all n while $u_3(0)=0$.

Hence, there is an infinite, countable number of surface waves that are not coupled to fluid. From Eqs. (35) and (17), for their phase velocities we find

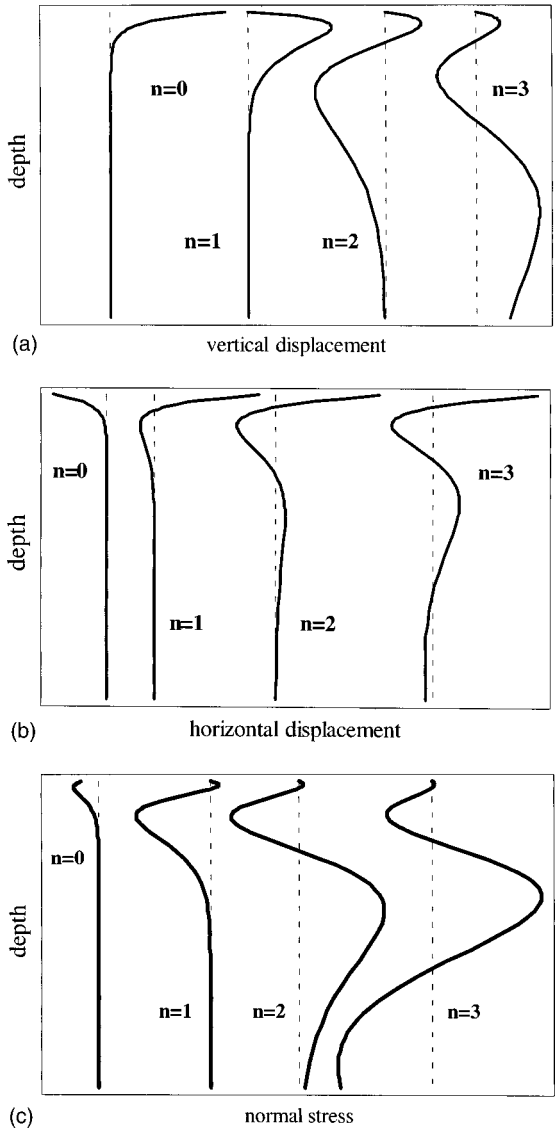

FIG. 1. Mode shape functions of monochromatic P-SV interface waves in the sediment with the linear depth-dependence of shear rigidity. Vertical displacement, u_3 (a), horizontal displacement, u_1 (b), and normal stress at a horizontal interface, σ_{33} (c) are shown for the fundamental mode ($n=0$) and three first main-sequence modes ($n=1,2,3$). Dashed lines indicate zero value of wave field for each mode. Relative mode amplitudes correspond to the choice $A=B_1$ in Eqs. (34) and (36); $R=2/3$.

$$V_n=\frac{2B^2}{\omega l}n,\quad n=1,2,\ldots. \tag{38}$$

This result is, again, in agreement with the scaling law Eq. (22). The normal modes are numbered in Eq. (38) in the order of increasing phase velocity and, hence, increasingly deep penetration into the solid.

It should be stressed that the fluid-coupled mode Eq. (34) is *fundamental*; its phase velocity Eq. (32) is lower than that of any other mode. Formally, the fundamental mode can be included in the sequence Eq. (38) by introducing a fractional mode order $n=(1+R)^{-1}$ that is a function of the density ratio.

Wave fields in the fundamental and main sequence modes are illustrated by Fig. 1.

B. Horizontally polarized surface waves near a fluid–solid interface

At $\nu=\frac{1}{2}$ it is convenient to introduce a new dependent variable $\psi=(2\xi z)^{1/2}u_2$. Then the wave equation (25) for *SH* waves becomes

$$\frac{d^2\psi}{d\zeta^2}+\left(-\frac{1}{4}+\frac{1}{2M\zeta}+\frac{1}{4\zeta^2}\right)\psi=0, \quad \zeta=2\xi z. \tag{39}$$

The equation can be solved in terms of the Whittaker functions. The solution to Eq. (39) that meets the physical requirement $\psi(0)=0$ is

$$\psi=B_1 M_{1/(2M),0}(\zeta). \tag{40}$$

The solution tends to infinity at $z\to+\infty$ unless $\frac{1}{2}+1/(2M)$ is a positive integer (Ref. 25, Chap. 13). Hence, from the conditions at infinity, we have [cf. Eq. (35)]:

$$M=(2n-1)^{-1}, \quad n=1,2,\ldots. \tag{41}$$

Under the condition Eq. (41), the Whittaker function in Eq. (40) can be expressed in terms of Laguerre polynomials L_{n-1} (Ref. 25, Chaps. 13 and 22), and the vertical dependence of the displacement is given by

$$u_2(z)=-\frac{B_1 e^{-\zeta/2}}{n}L_{n-1}(\zeta)$$
$$=\frac{B_1 e^{\zeta/2}}{n!}\frac{d^{n-1}}{d\zeta^{n-1}}(e^{-\zeta}\zeta^{n-1}), \quad \zeta=2\xi z. \tag{42}$$

For *SH* waves, the boundary conditions at a fluid–solid boundary consist in the requirement that the component σ_{12} vanishes (Ref. 18, Sec. 1.3). The solution Eq. (42) satisfies the boundary condition at $z=0$ because $\mu(0)=0$. The solution also satisfies the wave equation (25), is uniformly bounded throughout the solid, and tends toward zero at $z\to+\infty$. Consequently, it defines a surface wave for each n. In particular, for lower-order modes we have from Eq. (42)

$$u_2(z)=B_1 e^{-\xi z}, \quad n=1;$$
$$u_2(z)=0.5B_1(1-2\xi z)e^{-\xi z}, \quad n=2. \tag{43}$$

The displacement is nonzero at the interface for all n.

Hence, there is an infinite, countable number of surface waves of the *SH* type. The *SH* waves are not coupled to the fluid. From Eqs. (41) and (17), for their phase velocities, we find

$$V_n=\frac{2B^2}{\omega l}\left(n-\frac{1}{2}\right), \quad n=1,2,\ldots. \tag{44}$$

This result agrees with the scaling law Eq. (22). Comparison of Eq. (44) with Eq. (38) demonstrates that the phase velocities of *SH* surface waves and *P-SV* surface waves uncoupled to fluid interlace, with velocities of a *P-SV* wave being higher than those of the *SH* wave of the same order. The fundamental *P-SV* mode is slower (faster) than the first *SH* mode if fluid density is higher (lower) than the solid density. Depth-dependence of displacements and stresses in the first three *SH* modes is shown in Fig. 2.

The problem of monochromatic surfaces waves in the incompressible solid with linear $\mu(z)$ is closely connected to the classic quantum-mechanical problem of stationary states in the Coulomb potential. With $A=0$, the wave equation (29) for *P-SV* waves is equivalent to the stationary Schrödinger equation for the radial ψ-function[26] when the orbital quantum number is zero. (There is no counterpart to the fundamental *P-SV* mode in the quantum-mechanical problem.) The wave equation (39) for *SH* waves is equivalent to the stationary Schrödinger equation for the radial ψ-function provided that the orbital quantum number takes the nonphysical value $-\frac{1}{2}$. The boundary conditions at $z=0$ and at infinity also turn out to be equivalent in the acoustic and quantum-mechanical problems. Hence, mode shape functions and dispersion relations for the surface waves could have been derived from the textbook results for the Coulomb potential. Not surprisingly, an inspection shows that the dispersion relations Eqs. (38) and (41) we obtained agree with the known solution to the quantum-mechanical problem for the Coulomb potential.[26]

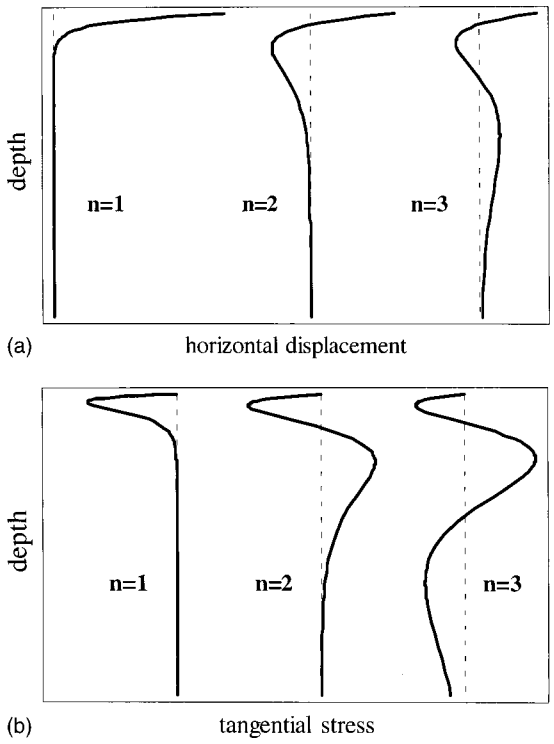

FIG. 2. Mode shape functions of monochromatic *SH* interface waves in the sediment with the linear depth-dependence of shear rigidity. Particle displacement u_2 (a) and tangential stress at a horizontal interface σ_{23} (b) are shown for the first three modes ($n=1,2,3$). Dashed lines indicate zero value of wave field for each mode. Relative mode amplitudes correspond to an n-independent value of the coefficient B_1 in Eq. (42).

C. Surface waves near ideal boundaries

The exact solutions of the governing equations obtained in Secs. IV A and IV B enable one to analyze the existence of and obtain the dispersion relation for the surface waves in other environments involving an incompressible solid with a linear profile of shear rigidity. We limit ourselves here to considering the two simplest cases.

Let us consider surface waves when $z=0$ is a free or rigid boundary. The boundary conditions for elastic waves at a rigid surface require that the displacement is zero at the boundary. It has been demonstrated above that at least one

component of the displacement is necessarily nonzero at $z=0$ for waves that are bounded throughout the solid, that is, waves that have a finite displacement and a stress tensor at both limits $z\to+0$ and $z\to+\infty$. [Horizontal displacement is nonzero at the boundary in *SH* waves and in the *P-SV* waves described by Eq. (36); vertical displacement is nonzero in the *P-SV* wave described by Eq. (34).] Hence, no surface wave exists in the half-space with a rigid boundary.

The boundary conditions for elastic waves at a free surface require that the traction is zero at the boundary, that is $\sigma_{j3}(0)=0$ $j=1,2,3$. This condition is violated by the *P-SV* wave described by Eq. (34) for which $\sigma_{33}(0)\neq 0$. Hence, such surface waves cannot be supported by a free boundary. On the contrary, all *SH* waves described by Eq. (42) and the *P-SV* waves described by Eq. (36) meet the boundary condition of zero traction. Hence, the free surface supports an infinite, countable set of *SH* and *P-SV* surface waves. In fact, the only difference between surface waves in the fluid–solid medium considered and the solid half-space with a free boundary is that the fundamental *P-SV* mode is stripped by the free boundary; all other surface waves are unaffected by substitution of a fluid half–space by a free boundary. This is natural since these waves are fully uncoupled from the (inviscid) fluid.

V. NORMAL MODES OF HIGH ORDER FOR ν ARBITRARY

A. Matched asymptotic expansions of the field

In this section we continue the analysis of interface waves in the fluid–solid medium with the power-law Eq. (14) profile of shear rigidity for general ν. As in Secs. III and IV, the medium density is assumed to be constant. We are interested in high-order modes. For such modes, the right side in the wave equation (11) is negligible. Indeed, at large z, the shear modulus is a slowly varying function compared with u_3, and all the terms containing derivatives of μ are small. In the opposite limit of small z, within paretheses in the left side of Eq. (11) $\mu\xi^2 u_3$ is negligible compared with $\rho\omega^2 u_3$. The terms resulting from applying the operator $(\partial^2/z^2-\xi^2)$ to $\mu\xi^2 u_3$ include $\mu''\xi^2 u_3$, which justifies disregarding the right side of Eq. (11) at small z. These heuristic arguments leave open the question of whether the right side in Eq. (11) is negligible at all z. At the end of this section we demonstrate that, for high-order modes, the domains of z ''small'' and ''large'' (in the above-defined sense) overlap and cover all $z>0$.

With the right side discarded, the wave equation (11) factors into second-order equations (12) and (13). Solutions to Eq. (12) are related to the fundamental mode. In this section, we concentrate on solutions to Eq. (13). The respective normal modes, by definition, constitute *the main sequence* of *P-SV* surface waves. To solve Eq. (13), consider first small z where

$$\mu\xi^2 \ll \rho\omega^2. \tag{45}$$

Then Eq. (13) becomes

$$u_3''+\frac{\omega^2 l^{2\nu}}{B^2 z^{2\nu}}u_3=0 \tag{46}$$

and admits an analytic solution (see, e.g., Ref. 18, Sec. 3.2.). The general solution to Eq. (46) is

$$u_3=z^{1/2}[A_1 J_{m+1}(r)+A_2 Y_{m+1}(r)],$$
$$m=\frac{2\nu-1}{2(1-\nu)},\quad r=\frac{\omega z^{l-\nu}}{Bl^{-\nu}}, \tag{47}$$

where $A_{1,2}$ are arbitrary constants, J_{m+1} and Y_{m+1} are cylindrical functions. Using recurrence relations for the cylindrical functions (Ref. 25, Chap. 9), for the horizontal displacement, we obtain from Eq. (47) without any approximations

$$u_1=\frac{i\omega l^{\nu}}{\xi B}z^{1/2-\nu}[A_1 J_m(r)+A_2 Y_m(r)]. \tag{48}$$

The same result was reported in Ref. 13 which considered *P-SV* waves in soft sediments under the condition Eq. (45) in connection with ambient noise resonances observed in the ocean.

From Eq. (2) for the stress tensor and the Eq. (46) it follows that the boundary condition of zero horizontal traction at the fluid–solid interface $z=0$ requires $u_3(0)=0$. Taking into account the behavior of the cylindrical functions when their argument tends toward zero (Ref. 25, Chap. 9), we find from the boundary condition that $A_2=0$ and, from Eqs. (7) and (46), that $q(0)=0$. Hence, the waves considered to not interact with the fluid half-space. At $r\gg 1$ one can use an asymptotic expansion of the Bessel function (Ref. 25, Chap. 9) to obtain

$$u_3\approx A_1\left(\frac{2z}{\pi r}\right)^{1/2}\cos\left(r-\frac{2\pi m+3\pi}{4}\right). \tag{49}$$

On the other hand, when the WKB approximation is applicable, the solution to Eq. (46) that vanishes at $z\to\infty$ has the form (Ref. 18, Secs. 8.1 and 9.2)

$$u_3=D\left(\frac{\rho\omega^2}{\mu}-\xi^2\right)^{-1/4}$$
$$\times\cos\left(\phi(z)-\phi(z_t)+\frac{\pi}{4}\right),\quad 0<z<z_t. \tag{50}$$

Here

$$\phi(z)=\int_0^z\sqrt{\frac{\rho\omega^2}{\mu(z_1)}-\xi^2}\,dz_1 \tag{51}$$

is the phase integral and z_t is the turning point defined as a solution to the equation

$$\mu(z_t)\xi^2=\rho\omega^2. \tag{52}$$

In deriving Eq. (50) we took into account that there is a single turning point in Eq. (46) and that the inapplicability of the WKB approximation in the vicinity of $z=z_t$ results in a $\pi/2$ phase loss of the reflected wave at $0<z<z_t$.

The WKB solution Eq. (50) does not correctly predict the u_3 behavior at $z\to 0$, and it is not applicable in the vicinity of $z=0$. As discussed in detail in Ref. 13, these limitations are due to the singularity the coefficient of the wave equation has at $z=0$ for the power-law profile. However, as z increases, Eq. (50) becomes applicable and matches Eq. (49). Indeed, under the condition Eq. (45) $\phi(z)\approx r$ and

$(\rho\omega^2/\mu-\xi^2)^{-1/4}\approx \text{const}\cdot(z/r)^{1/2}$. For Eqs. (49) and (50) to represent the same solution [that is, for $u_3(z)$ to simultaneously obey conditions at the boundary $z=0$ and at infinity], it is necessary that $\phi(z_t)=\pi(n+m/2)$ where n is an integer. This equation enables one to determine the phase velocity of the normal mode as a function of frequency, medium parameters, and the mode order n. Calculating the integral in Eq. (51) for the power-law profile, we have

$$\phi(z_t)=\frac{\sqrt{\pi}}{2}\frac{\Gamma\left(\frac{1-\nu}{2\nu}\right)}{\Gamma\left(\frac{1}{2\nu}\right)}M^{-(1/2\nu)}=\frac{\sqrt{\pi}}{2}\frac{\Gamma\left(\frac{1-\nu}{2\nu}\right)}{\Gamma\left(\frac{1}{2\nu}\right)}\frac{\omega l}{B^{1/\nu}}V^{1/\nu-1}. \tag{53}$$

Hence,

$$V_n=\left[\sqrt{\pi}\left(2n+\frac{2\nu-1}{2(1-\nu)}\right)\frac{B^{1/\nu}}{\omega l}\Gamma\left(\frac{1}{2\nu}\right)\Big/\Gamma\left(\frac{1-\nu}{2\nu}\right)\right]^{\nu/(1-\nu)}. \tag{54}$$

Compared with the scaling law Eq. (22), the new information provided by Eq. (54) consists of the phase-velocity dependence on the power-law exponent ν and also on the mode order n.

The matching of the WKB solution Eq. (50) and the solution Eq. (47), which is valid at small z, is not accidental. Owing to the singularity in the wave equation at $z=0$, the WKB approximation is applicable apart from the singularity where $\phi(z)\gg 1$ (Ref. 13 and Ref. 18, Sec. 9.2). Using Eq. (54), we write this condition as

$$\xi z\gg n^{-\nu/(1-\nu)}, \tag{55}$$

whereas the applicability condition Eq. (45) of the approximate solution Eq. (47) becomes

$$\xi z\ll n. \tag{56}$$

Both applicability conditions become less restrictive as n increases. The conditions Eqs. (55) and (56) are compatible, and the two solutions have a common domain of validity as long as n is large. Hence, the validity of the dispersion relation Eq. (54) is assured for high-order modes at any $\nu\in(0,1)$.

In fact, the dispersion equation has a broader applicability. At $\nu=\frac{1}{2}$ Eq. (54) reduces to the exact dispersion relation Eq. (38). Hence, Eq. (54) is also approximately valid for low-order main sequence normal modes, at least where $\nu\approx\frac{1}{2}$.

The dispersion relation can be obtained quite similarly for horizontally polarized surface waves, starting from their exact wave equation (25). The result differs from the dispersion relation for *P-SV* waves by merely substituting $n-\frac{1}{2}$ for n in Eq. (54). Note that the phase velocities of consecutive *P-SV* and *SH* surface waves interlace. The group velocities of the *P-SV* and *SH* surface waves possess the same property. As in the *P-SV* case, the asymptotic dispersion relation for *SH* waves becomes exact for all n when $\nu=\frac{1}{2}$.

B. A streamlined approach

From very general considerations it follows that, for rapidly varying wave fields, the WKB approximation is valid throughout the continuously stratified medium with the exception of narrow vicinities of certain critical depths, where caustics occur or coefficients of the wave equation become singular. In problems on guided propagation, the assumption of rapid variation of the wave field compared with the variation of medium parameters translates into the requirement that normal mode order be large compared with unity. In the specific problem we are interested in, there are two critical depths where the WKB approximation breaks down: $z=0$ [due to $\mu(z)$ singularity] and the turning depth $z=z_t$. For the wave field at $z<z_t$ and away from the turning depth, the inapplicability of the WKB approximation in the vicinity of z_t is known to simply result in the phase loss of $\pi/2$ by the wave reflected from the turning depth. Quite similarly, for the wave field at $z>0$ and away from the interface $z=0$, the inapplicability of the WKB approximation in the vicinity of $z=0$ results in a phase loss by the wave reflected from the interface. (Energy conservation guarantees that the reflected wave amplitude is not affected.) The value of the phase loss at $z=0$ has been determined in Ref. 13 with the assumption that the inequality Eq. (45) holds. This phase loss depends on ν and is given by $\pi(m-\frac{1}{2})$. We can use this result in considering surface waves because, as we have demonstrated above, the inequality Eq. (45) holds throughout the vicinity of $z=0$ where the WKB approximation is inapplicable and the additional phase loss occurs.

Given the phase losses at reflection from the "boundaries" $z=0$ and $z=z_t$ of the waveguide, a dispersion relation of guided modes can be easily derived within the WKB approximation by calculating the phase increment of a quasi-plane wave that successively reflects from both boundaries and returns to its starting depth. Requiring that the round-trip phase increment is an integer times 2π, we again obtain the dispersion relation $\phi(z_t)=\pi(n+m/2)$ [see the text before Eq. (53)] that immediately leads to Eq. (54) for the phase velocity.

Although this approach is less rigorous than the one presented in Sec. V A and does not provide an expression for the wave field, it leads to the correct dispersion relation of the main sequence modes in a much more economical way than the matched asymptotic expansions technique.

VI. PERTURBATION ANALYSIS

A. Fundamental mode in media with $\nu\approx\frac{1}{2}$

Consider *P-SV* waves in the fluid–solid medium of constant density when the exponent in the power-law Eq. (14) is close to unity. Then $|\nu-\frac{1}{2}|$ can be viewed as a small parameter, and the dispersion relations for various modes can be obtained by using a perturbation theory. The exact results obtained in Sec. IV for $\nu=\frac{1}{2}$ will serve as reference (unperturbed) solutions.

A perturbation theory has been developed in Ref. 27 that enables the calculation of corrections to propagation constants of elastic waves due to variations in either or both material parameters and the position of boundaries and inter-

faces in stratified fluid–solid systems. Let the shear modulus profiles in two media be different and all the other parameters be the same. Then difference of modal propagation constants in the two media is given by Ref. 27 as

$$\delta\xi = I_1/I_2 + O(\xi^{-1}(\delta\xi)^2), \tag{57}$$

where

$$I_1 = \int_0^\infty dz\left[\xi^2 u_1^2 \delta\left(\frac{4\mu(\lambda+\mu)}{\lambda+2\mu}\right) - \sigma_{13}^2\delta\left(\frac{1}{\mu}\right) - 2i\xi u_1\sigma_{33}\delta\left(\frac{\lambda}{\lambda+2\mu}\right) + \sigma_{33}^2\delta\left(\frac{1}{\lambda+2\mu}\right)\right], \tag{58}$$

$$I_2 = \frac{2\xi}{\omega^2}\int_{-\infty}^0 \frac{dz}{\rho_f}p^2 - 2i\int_0^{+\infty} dz(\sigma_{13}u_3 - \sigma_{11}u_1). \tag{59}$$

Here δF stands for perturbation in the physical quantity F, that is, the difference in values this quantity takes in the given medium and in the reference state. In Eqs. (58) and (59), the propagation constant ξ, the acoustic pressure p in the fluid, and the displacements and stresses in the solid are those in the reference state.

Equation (58) can be simplified by taking into account $\lambda \gg \mu$. Discarding terms proportional to $1/\lambda$, we have

$$I_1 = \int_0^{+\infty} dz[4\xi^2 u_1^2 + (i\xi u_3 + u_1')^2]\delta\mu. \tag{60}$$

The perturbation in the shear modulus due to ν variation is given by

$$\delta\mu = \rho B^2 (z/l)^{2\nu} - \rho B^2 z/l. \tag{61}$$

For the fundamental mode, using the Eqs. (19) and (34) for the unperturbed field, we obtain from Eqs. (57), (59)–(61)

$$\delta\xi/\xi = 1 - (2\xi l)^{1-2\nu}\Gamma(1+2\nu) + O((\nu-1/2)^2). \tag{62}$$

In terms of the phase velocity, taking into account the identity $(\delta\xi/\xi)_\omega = -(\delta V/V)_\omega$ and the value of Gamma-function derivative at an integer argument (Ref. 25, Chap. 6), we obtain from Eq. (62)

$$\left(\frac{\partial}{\partial\nu}\ln V_0\right)_{\omega,B,l} = 2(1-\gamma) - 2\ln(1+R) + 4\ln\frac{B}{\omega l}. \tag{63}$$

This result is exact in the limit of the incompressible media. Here $\gamma = 0.577\,21...$ is the Euler's constant.

For comparison, it follows from the scaling law Eq. (22) that

$$\left(\frac{\partial}{\partial\nu}\ln V\right)_{\omega,B,l} = \frac{-1}{2(1-\nu)^2}\ln\Phi - \frac{1}{2(1-\nu)}\frac{\partial}{\partial\nu}\ln\Phi + \frac{1}{(1-\nu)^2}\ln\frac{B}{\omega l}. \tag{64}$$

It should be emphasized that dependence of the phase velocity derivative on frequency and the parameters B and l is fully determined by the scaling law. The new information obtained with the perturbation theory consists in the value of the function $\Phi(\nu,R)$ derivative at $\nu = \frac{1}{2}$:

$$\left(\frac{\partial}{\partial\nu}\ln\Phi\right)_{\nu=1/2} = 2\ln 2 - 2(1-\gamma). \tag{65}$$

It is interesting that the logarithmic derivative turns out to be independent of the density ratio R.

B. Main sequence modes in media with $\nu \approx \frac{1}{2}$

For the main sequence P-SV modes, the wave number perturbation is given by the same Eqs. (57), (59)–(61) as for the fundamental mode, but the integrals I_1 and I_2 are now functions of the mode order n, and their evaluation turns out to be more complicated.

The first integral on the right side of Eq. (59) for I_2 equals zero because the main sequence modes are not coupled to the fluid. By using the wave equation

$$Mz(u_3'' - \xi^2 u_3) + \xi u_3 = 0 \tag{66}$$

for the main sequence modes at $\nu = \frac{1}{2}$ [see Eq. (29)] and taking into account $u_3(0) = 0$, the second integral on the right side of Eq. (59) can be simplified, leading to

$$I_2 = 2\rho V^2\int_0^{+\infty} u_3^2\, dy. \tag{67}$$

Then, by differentiating both sides of Eq. (57) with respect to ν, we have for the phase velocity derivative at $\nu = \frac{1}{2}$

$$\left(\frac{\partial}{\partial\nu}\ln V_n\right)_{\omega,B,l} = \frac{B^2}{\omega V_n}\left(\int_0^{+\infty} u_3^2\, dy\right)^{-1}\left(J_1 + J_2\ln\frac{V_n}{\omega l}\right), \tag{68}$$

where

$$J_1 = \xi^{-4}\int_0^{+\infty} dy[4\xi^2(u_3')^2 + (\xi^2 u_3 + u_3'')^2]y\ln y;$$
$$J_2 = \xi^{-4}\int_0^{+\infty} dy[4\xi^2(u_3')^2 + (\xi^2 u_3 + u_3'')^2]y. \tag{69}$$

After some algebra involving integrations by parts and the use of the wave equation (66), the integrals J_1 and J_2 become

$$J_1 = 2\int_0^{+\infty}(1+2n^2\ln y)u_3^2\frac{dy}{y}, \quad J_2 = 4n\int_0^{+\infty} u_3^2\, dy. \tag{70}$$

From Eqs. (68) and (70), we obtain:

$$\left(\frac{\partial}{\partial\nu}\ln V_n\right)_{\omega,B,l,\nu=1/2} = 4\ln\frac{B}{\omega l} + 2\ln 2n + \frac{J_1}{2n\int_0^{+\infty} u_3^2\, dy}. \tag{71}$$

This exact expression enables the calculation of phase and group velocities of the main sequence normal mode when ν is close to but different from $\frac{1}{2}$. Note that the last term in the right side of Eq. (71) is a function of the mode order n only. Hence, Eq. (71) is in agreement with Eq. (64) which is a corollary of the scaling law.

For instance, let $n = 1$. For this mode, the vertical displacement is given by Eq. (37), and Eq. (71) becomes

$$\left(\frac{\partial}{\partial\nu}\ln V_1\right)_{\omega,B,l,\nu=1/2}=4\ln\frac{B}{\omega l}+3-2\gamma. \tag{72}$$

As another example, consider the opposite case with $n\gg 1$. For high-order modes, the main contributions to the integrals in Eq. (71) originate from the domain above the turning point z_t, which is defined by Eq. (52). At $0<z<z_t$ one can use the WKB expression Eq. (50) for the vertical displacement. The field is a rapidly oscillating function of depth and, therefore, in the integrands, the vertical displacement squared and similar quantities can be substituted by their averages over distances of the order of the reciprocal vertical wave number:

$$\langle u_3^2\rangle=\frac{D^2}{2}\left(\frac{\rho\omega^2}{\mu}-\xi^2\right)^{-1/2};\quad \langle (u_3')^2\rangle=\frac{D^2}{2}\left(\frac{\rho\omega^2}{\mu}-\xi^2\right)^{1/2}. \tag{73}$$

After calculating the resulting integrals, we find from Eq. (71)

$$\left(\frac{\partial}{\partial\nu}\ln V_n\right)_{\omega,B,l,\nu=1/2}=4\ln\frac{nB}{\omega l}+O(n^{-1}). \tag{74}$$

Note that the rate of relative variation of phase velocity as a function of ν increases with increasing mode order.

The derivative of the phase velocity with respect to ν can be independently calculated for high-order modes from the asymptotic dispersion relation Eq. (54), which is valid at arbitrary ν. Taking into account the derivatives of the Gamma function at arguments $\frac{1}{2}$ and 1 (Ref. 25, Chap. 6), we obtain from Eq. (54)

$$\left(\frac{\partial}{\partial\nu}\ln V_n\right)_{\omega,B,l,\nu=1/2}=4\ln\frac{nB}{\omega l}+\frac{1}{n}. \tag{75}$$

Equation (75) is consistent with Eq. (74). Hence, the perturbation results provide a check of validity of the asymptotic analysis of Sec. V. Equation (75) shows also that the dispersion relation Eq. (54)—although valid for all n at $\nu=\frac{1}{2}$—is only asymptotic rather than exact at $\nu\neq\frac{1}{2}$. Indeed, for $n=1$ the derivative Eq. (75) deviates from the exact result Eq. (72).

To calculate the logarithmic derivative of the phase velocity Eq. (71) for arbitrary n, we substitute the expression for the vertical displacement in terms of Generalized Laguerre polynomials Eq. (36) into Eq. (70) and use standard integrals involving products of the polynomials[28] as well as their recurrence relations (Ref. 25, Chap. 22) to obtain

$$\int_0^{+\infty}u_3^2\,dy=B_1^2,\quad \int_0^{+\infty}u_3^2\frac{dy}{y}=\frac{B_1^2}{n},$$
$$\int_0^{+\infty}u_3^2\ln y\,\frac{dy}{y}=\frac{B_1^2}{n}\left[\frac{1}{n}-\ln 2+\psi(n)\right] \tag{76}$$

and

$$\left(\frac{\partial}{\partial\nu}\ln V_n\right)_{\omega,B,l,\nu=1/2}=4\ln\frac{nB}{\omega l}+2\psi(n)-2\ln n+\frac{2}{n}+\frac{1}{n^2}, \tag{77}$$

where ψ stands for Digamma function, i.e., the logarithmic derivative of the Gamma function; $\psi(n)=-\gamma+1+\frac{1}{2}+\frac{1}{3}+\ldots+1/(n-1)$ (Ref. 25, Chap. 6). Equation (77) is exact. It is easy to verify that it agrees with Eqs. (72) and (74) in the respective special cases. At large n, Eq. (75) obtained from the asymptotic dispersion relation Eq. (54) differs from the exact result Eq. (77) by terms $O(n^{-2})$, as expected from the matched-asymptotics analysis presented in Sec. V. By combining Eqs. (54) and (77), we obtain an approximate dispersion equation

$$V_n=\left\{\sqrt{\pi}\left[2n+(2\nu-1)\left(\frac{3-2\nu}{2-2\nu}+\frac{1}{n}+2n\psi(n)-2n\ln n\right)\right]\times\frac{B^{1/\nu}}{\omega l}\Gamma\left(\frac{1}{2\nu}\right)\Big/\,\Gamma\left(\frac{1-\nu}{2\nu}\right)\right\}^{\nu/(1-\nu)} \tag{78}$$

of main sequence modes that is accurate up to the factor $1+O[(\nu-\frac{1}{2})^2/n^2]$. The dispersion equation is consistent with the scaling law and, being accurate to the second order with respect to $1/n$ for arbitrary ν and with respect to ν for arbitrary n, it is anticipated to be a good approximation to (as yet unknown) exact dispersion relation for most ν and n of practical interest. We discuss the accuracy of the dispersion equation (78) further in Sec. VII.

C. Weakly compressible media

In this subsection, we consider a different kind of perturbation. Specifically, we want to quantify the effect that small but finite compressibity of the medium has on dispersion of interface waves. For simplicity, we assume that $\nu=\frac{1}{2}$ and that the Lamé parameter $\lambda(z)$ is constant in solid and in fluid. Values of the Lamé parameter in the solid and fluid are designated $\lambda=\rho\ c_l^2$ and $\lambda_f=\rho_f\ c_f^2$, respectively. Physical meaning of c_l and c_f is, respectively, the (fast) compressional wave velocity in the solid and the sound velocity in the fluid.

From the perturbation theory,[27] for the difference in wave numbers between a mode in a weakly compressible medium and a mode of the same order in an incompressible medium, we have

$$\delta\xi=I_3/I_2+O[\xi^{-1}(\delta\xi)^2], \tag{79}$$

where

$$I_3=\frac{1}{\rho_f c_f^2}\int_{-\infty}^{0}dz p^2(z)+\frac{1}{\rho c_l^2}\int_0^{+\infty}dz(2\mu\xi u_3+\sigma_{33})^2. \tag{80}$$

Density and shear rigidity profiles in the two media are assumed to be the same. The field quantities entering Eq. (80) are those in the reference (unperturbed) state, i.e., in the incompressible medium. The integral I_2 in Eq. (79) is defined in Eq. (59) and has been considered in the preceding subsections. According to Eqs. (2) and (5),

$$2\mu\xi u_3+\sigma_{33}=\rho\omega^2\xi^{-1}q \tag{81}$$

under the second integral in Eq. (80).

For the fundamental mode, evaluation of the integral I_3 is straightforward, and one obtains from Eqs. (79)–(81)

$$V_0=\frac{2B^2}{\omega l(1+R)}\left[1-\frac{2B^4R}{\omega^2l^2(1+R)^3}\left(\frac{1}{c_f^2}+\frac{R}{c_l^2}\right)\right]+V_0^5O\left(\frac{1}{c_f^4}+\frac{1}{c_l^4}\right). \tag{82}$$

For the main sequence modes, $q=-2Mu_3=-n^{-1}u_3$. Then, one has from Eqs. (79)–(81) and (70)

$$V_n=\frac{2nB^2}{\omega l}\left(1-\frac{2B^4}{\omega^2l^2c_l^2}\right)+V_nO(V_n^4/c_l^4). \tag{83}$$

Quite naturally, the phase velocity of the main sequence modes is independent, to the first order, of the density and sound speed in the fluid.

We see from Eqs. (82) and (83) that the scaling law is violated when the medium is compressible. Indeed, in the compressible medium, modal phase velocities are no longer proportional to $B^2/\omega l$. On the other hand, corrections to the phase velocity due to medium compressibility are proportional to the squared ratio of the phase velocity to sound velocity, and they are rather small when $V\ll c_l$, c_f. In practice, when compressional wave velocities are of the order of 1500 m/s, the results obtained for incompressible sediments remain reasonably accurate for interface waves with velocities up to 250 m/s. The accuracy of the theoretical dispersion relations can be further improved by accommodating the first-order corrections Eqs. (82), (83) for finite compressibility.

According to the perturbation theory,[27] first-order corrections to the dispersion relation are additive. Therefore, the results of subsections VI A–VI C can be combined in a straightforward manner to predict the effect of finite compressibility on dispersion of interface waves in media with $\nu\approx\frac{1}{2}$. Quite similarly, we can account for density gradients in the sediment or, say, a nonzero but small value of shear rigidity at $z=0$. Without discussing these in detail, we note that the perturbations cause interface waves to deviate from the scaling law, but corrections to the phase velocities remain small as long as the relative variation of density is small in the layer $0<z\lesssim z_t$ and $\mu(0)\ll\mu(z_t)$, where z_t stands for the turning depth Eq. (52) of the mode.

D. Second-order corrections

When first-order perturbation theory does not provide sufficient accuracy in modeling interface wave dispersion, calculation of second-order corrections may be required to improve the accuracy and account for larger environmental variations. The perturbation theory[27] is not limited to first-order corrections, although the complexity of the analysis rapidly increases with the order of the correction. Here we consider only second-order corrections to the phase velocity of the fundamental mode due to deviations of ν from $\frac{1}{2}$. Assuming, as before, homogeneous fluid half-space $z<0$ and constant sediment density, from Ref. 27 we have

$$V_0^2-(V_0^{(p)})^2=\frac{B^2}{K_1}\int_0^{+\infty}dy\left[\frac{y}{\xi l}-\left(\frac{y}{\xi l}\right)^{2\nu}\right]K_2(y), \tag{84}$$

where

$$K_1=Ru_3(0)u_3^{(p)}(0)+\int_0^{+\infty}dy[u_3u_3^{(p)}+\dot u_3\dot u_3^{(p)}],$$
$$K_2=4\dot u_3\dot u_3^{(p)}+\ddot u_3\ddot u_3^{(p)}+\ddot u_3u_3^{(p)}+u_3\ddot u_3^{(p)}+u_3u_3^{(p)}. \tag{85}$$

Here V and u_3 refer to the mode in the unperturbed medium, i.e., when $\nu=\frac{1}{2}$, and superscript p indicates the mode parameters in a medium characterized by an arbitrary ν value. A dot signifies the derivative with respect to the dimensionless depth $y=\xi z$. It is convenient to assume that modes in the two media have the same value of ξ and different frequencies. Equations (84)–(85) are exact. They are analogous to Eqs. (57)–(61), but differ by retaining all high-order terms. For the fundamental mode $\ddot u_3=u_3$, and K_1 in Eq. (85) simplifies to

$$K_1=(1+R)u_3(0)u_3^{(p)}(0). \tag{86}$$

To determine terms $O[(\nu-\frac{1}{2})^2]$ in the phase velocity from Eqs. (84)–(86), $u_3^{(p)}(y)$ must be known to first order in $\nu-\frac{1}{2}$. For the derivatives $Q=(\partial q/\partial\mu)_{M,\nu=\frac{1}{2}}$ and $W=(\partial u_3/\partial\nu)_{M,\nu=\frac{1}{2}}$ we have from Eqs. (15), (16), and (34) the differential equations

$$My(\ddot W-W)+W=-\dot w+4M(1+\ln y)e^{-y}, \tag{87}$$

$$\ddot w-w=4My^{-1}e^{-y},\quad w\equiv Q+2mW. \tag{88}$$

Here and below we assume that the solutions at $\nu=\frac{1}{2}$ are normalized by the condition $A=1$ in Eq. (34). At $y\to+\infty$ the functions w and W should tend toward zero. In addition, for stresses and horizontal and vertical displacements in the interface wave to be finite at the interface, $w(0)$, $W(0)$, and $\dot W(0)$ must be bounded.

Equation (88) is easily solved. Its solution satisfying the condition at infinity can be written as

$$w=Ce^{-y}-2Mf(y),\quad f\equiv e^{-y}\ln y+E_1(2y), \tag{89}$$

where C is an arbitrary constant and E_1 stands for the exponential integral (Ref. 25, Chap. 5). Note that f satisfies the equation $\dot f-f=-2e^{-y}\ln y$; tends toward zero at $y\to+\infty$; and $f(y)=-\gamma-\ln 2-2y\ln y+O(y)$ as $y\to+0$. The inhomogeneous equation (87) has a particular solution $W=[C+4M(1+M)]e^{-y}+2Mf(y)$. As discussed in Sec. IV A, the homogeneous equation (87) can be solved in confluent hypergeometric functions. The solution to Eq. (87) meeting conditions at $y=0$ and at infinity is

$$W=[C+4M(1+M)]e^{-y}+2Mf(y)+4M\Gamma\left(\frac{-1}{2M}\right)ye^{-y}U\left(1-\frac{1}{2M},2,2y\right), \tag{90}$$

where U is a Kummer's function (Ref. 25, Chap. 13). It has an integral representation

$$U(a,b,2y)=\int_1^\infty e^{-2y(t-1)}(t-1)^{a-1}t^{b-a-1}\,dt. \tag{91}$$

Note that the vertical displacement at $\nu \neq \frac{1}{2}$ has, by far, more complicated depth-dependence than in the reference case $\nu = \frac{1}{2}$. In particular, unlike Sec. IV, a confluent hypergeometric function enters Eq. (90) because the derivative of the partial solution to inhomogeneous Eq. (87) has a logarithmic singularity at $y \to +0$.

From Eqs. (88)–(90) and the definitions of Q and W we have

$$\begin{aligned} u_3(0) &= 1 + (\nu - \tfrac{1}{2})[C + (1+R)(2 - \gamma - \ln 2)] \\ &\quad + O[(\nu - \tfrac{1}{2})^2]; \\ q(0) &= 1 - 2M + (\nu - \tfrac{1}{2})[-RC + (1+R)(2+R) \\ &\quad \times (\gamma + \ln 2) + (1+R)^2] + O[(\nu - \tfrac{1}{2})^2]. \end{aligned} \tag{92}$$

Substituting Eq. (92) into the boundary condition Eq. (20) and using Eq. (21), we immediately obtain the first derivatives Eqs. (63) and (65) derived in Sec. VI A from different considerations. Further, from Eqs. (85) and (86) we have

$$\begin{aligned} K_1 &= (1+R)[1 + (\nu - \tfrac{1}{2})C + (\nu - \tfrac{1}{2})(1+R) \\ &\quad \times (2 - \gamma - \ln 2)] + O[(\nu - \tfrac{1}{2})^2], \\ K_2 &= 4e^{-2y}[2 + (\nu - \tfrac{1}{2})S] + O[(\nu - \tfrac{1}{2})^2], \\ S &= 2\ln y - y^{-1} + 2C + 2(1+R)(2+R) \\ &\quad + 2(1+R)\Gamma(-s)[2yU(1-s,3,2y) \\ &\quad - (1+s)U(1-s,2,2y)], \\ s &= (1+R)^{-1}. \end{aligned} \tag{93}$$

Using the integral representation Eq. (91) of Kummer's functions and interchanging the order of integration over t and y, all integrals in Eq. (84) can now be solved in terms of Gamma functions, leading to the following exact expressions:

$$\left(\frac{\partial^2}{\partial \nu^2} \ln \Phi\right)_{R, \nu = 1/2} = 4 - \frac{2\pi^2}{3}(2+R) - 4(1+R)^2 \times \left[\gamma + \Psi\left(\frac{R}{1+R}\right)\right]; \tag{94}$$

$$\begin{aligned} \left(\frac{\partial^2 \ln V_0}{\partial \nu^2}\right)_{\xi, R, B, l} &= -\frac{1}{2}\left(\frac{\partial^2 \ln \Phi}{\partial \nu^2}\right)_R; \\ \left(\frac{\partial^2 \ln V_0}{\partial \nu^2}\right)_{\omega, R, B, l} &= 8(\ln 2 + \gamma - 1) - \left(\frac{\partial^2 \ln \Phi}{\partial \nu^2}\right)_R. \end{aligned} \tag{95}$$

The relations between derivatives of the phase velocity and of Φ given by Eq. (95) are corollaries of the scaling law Eq. (22). The second logarithmic derivative of Φ Eq. (94) is always positive. It decreases monotonically with R and, for fluid-sediment density ratios of practical interest $0 < R \leqslant 1$, its minimum value $2(2 - \pi^2 + 16\ln 2) \approx 6.4415$ occurs at $R = 1$.

We finally use knowledge of Φ Eq. (31) and its first two derivatives Eqs. (65) and (94) at $\nu = \frac{1}{2}$ to obtain from the scaling law an approximate dispersion relation

$$\begin{aligned} V_0 &= 2\left(\frac{B^2}{1+R}\right)^{1/2(1-\nu)} (\omega l)^{-\nu/(1-\nu)} \\ &\quad \times \exp\left(\frac{2\nu - 1}{2(1-\nu)}(1-\gamma) + \frac{(2\nu-1)^2}{4(1-\nu)} \right. \\ &\quad \left. \times \left\{\frac{\pi^2}{6}(2+R) - 1 + (1+R)^2\left[\gamma + \psi\left(\frac{R}{1+R}\right)\right]\right\}\right) \end{aligned} \tag{96}$$

for the fundamental mode that is accurate up to a factor $1 + O[(\nu - \frac{1}{2})^3]$. The accuracy of the dispersion relation Eq. (96) is further discussed in Sec. VII.

E. Horizontally polarized interface waves in media with $\nu \approx \frac{1}{2}$

When applying perturbation theory to *SH* waves, we again obtain Eq. (57)[27,29] for the first-order variation in wave number of the surface wave due to small perturbations in the shear rigidity profile; the integrals I_1 and I_2 now given by

$$I_1 = \int_0^{+\infty} dz[\xi^2 u_2^2 + (u_2')^2]\delta\mu, \tag{97}$$

$$I_2 = -2\xi^2 \int_0^{+\infty} dz\, \mu u_2^2. \tag{98}$$

Here u_2 is the only nonzero component of displacement in *SH* waves corresponding to the reference (nonperturbed) state. We are interested in variations in the wave number due to deviations of the power-law exponent ν from its reference value $\nu = \frac{1}{2}$. Then perturbation in the shear rigidity profile is given by Eq. (61). Using Eq. (42) for $u_2(z)$ in terms of Laguerre polynomials, the integrals Eqs. (97) and (98) can be evaluated analytically for arbitrary mode order n, leading to the exact expression

$$\left(\frac{\partial}{\partial \nu} \ln V_n\right)_{\omega, B, l, \nu = 1/2} = 4\ln\frac{(n - \frac{1}{2})B}{\omega l} + 2\psi(n) - 2\ln\left(n - \frac{1}{2}\right) + \frac{2}{2n-1} \tag{99}$$

for the derivative of the mode phase velocity with respect to ν. Details of the transformations are similar to those outlined in Sec. VI B for the main sequence of *P-SV* interface waves and are not reproduced here. The derivatives Eqs. (99) and (77) for *SH* and *P-SV* waves are very similar but differ in their dependence on mode order n.

Together with Eq. (44) for the phase velocity in the reference state, Eq. (99) describes the dispersion of *SH* interface waves of arbitrary order at $\nu \approx \frac{1}{2}$. An asymptotic dispersion relation valid for high-order modes ($n \gg 1$) and arbitrary ν has been discussed at the end of Sec. V A. These two results can be combined, giving an approximate dispersion equation

$$V_n = \left\{\sqrt{\pi}\left[2n - 1 + (2\nu - 1)(2n-1)\left[\psi(n) - \ln\left(n - \frac{1}{2}\right)\right] + \frac{2\nu - 1}{2 - 2\nu}\right]\frac{B^{1/\nu}}{\omega l}\frac{\Gamma(1/(2\nu))}{\Gamma((1-\nu)/(2\nu))}\right\}^{\nu/(1-\nu)} \tag{100}$$

that is accurate up to the factor $1+O[(\nu-\frac{1}{2})^2/n^2]$. The approximate dispersion equation is consistent with the scaling law and reproduces the exact results Eqs. (44) and (99) as well as the WKB-type asymptotics of Sec. V. The dispersion equation differs from Eq. (78) for *P-SV* waves only in its n dependence. It has been shown in Sec. IV that, at $\nu=\frac{1}{2}$. the dispersion equation of *SH* interface waves becomes that of the main sequence of *P-SV* modes if $n-\frac{1}{2}$ is substituted for n. From Eq. (100) and the asymptotic expansion of the Digamma function $\psi(n)$ (Ref. 25, Chap. 6), it follows that the same correspondence between phase velocities holds, to within the factor $1+O[(\nu-\frac{1}{2})/n^2]$, at arbitrary ν for high-order modes. However, for the more frequently observed lower modes, no simple correspondence exists between dispersion relations at different wave polarizations, unless $\nu=\frac{1}{2}$.

F. Truncated power-law profile

In geoacoustic inversions of experimental data available in a finite frequency band, it is important to know in what depth interval the inversion results are reliable. For a slow interface wave supported by a sediment with monotonically increasing shear rigidity $\mu(z)$, the maximum depth H up to which the environment is reliably probed is determined by the turning point z_t of the lowest-frequency, deepest-penetrating wave. Coefficient of proportionality between H and z_t depends on the mode shape function and accuracy to which phase or group velocity is measured.

To quantify the above considerations for sediments with a power-law profile of shear rigidity, let us introduce the following criterion: Inversion does not apply to depths $z>H$ if relative change in the phase (or group) velocity is less than a certain given number ϵ, $0<\epsilon\ll 1$, when medium below $z=H$ is substituted by a homogeneous half-space. It is assumed that shear velocity and other parameters remain continuous at $z=H$. We refer to resulting $\mu(z)$ dependence as *truncated power-law profile*.

For the truncated profile and $\nu=\frac{1}{2}$ exact dispersion relations can be easily determined using the results of Sec. IV for arbitrary H. Here we are interested in the case when H considerably exceeds z_t. Then perturbations to the interface wave group and phase velocities due to truncation are small and, to first order, are given by the perturbation Eqs. (57), (59), and (60) for *P-SV* waves and Eqs. (57), (97), and (98) for *SH* waves. The truncated profile is described as a perturbation

$$\delta\mu=0, \quad 0<z\leqslant H; \quad \delta\mu=\rho B^2(H-z)/l, \quad z>H \quad (101)$$

to the linear profile. Although $\delta\mu$ Eq. (101) increases indefinitely with depth, integrals in Eq. (57) converge because of the exponential decrease of the wave field at large z. After some algebra, we obtain $\delta\xi/\xi[1+O(\delta\xi/\xi)]=\exp(-2\xi H)$, $\exp(-2\xi H)(1+2\xi^2H^2)$, and $\exp(-2\xi H)$, respectively, for the fundamental mode, first *P-SV* mode, and first *SH* mode. Not surprisingly, the difference between the mode propagation constants for power-law and truncated power-law profiles decrease exponentially with H for large H. The exponential decay is modified by a polynomial multiplier for higher-order modes.

The equations for the propagation constant perturbation are easily inverted to determine the limiting depth of the sediment up to which the interface wave is sensitive to shear velocity variations. Using the definition of the turning point Eq. (52), we obtain

$$\frac{H}{z_t}=\frac{1+R}{4}|\ln\epsilon|, \quad \frac{1}{4}\left|\ln\frac{2\epsilon}{(\ln 2\epsilon)^2}\right|, \quad \frac{1}{2}|\ln\epsilon|, \qquad (102)$$

respectively, for the fundamental mode, first *P-SV* mode, and first *SH* mode.

VII. COMPARISON OF ANALYTICAL AND NUMERICAL RESULTS

We have derived analytical dispersion relations for interface waves at the boundary between a fluid and an incompressible solid with a power-law shear modulus. The *P-SV* modes considered include the fundamental mode, which is coupled to the fluid, and the main sequence modes, which are not. For the square-root profile ($\nu=\frac{1}{2}$), these relations are exact; for other cases ($\nu\neq\frac{1}{2}$), the relations are approximate. To apply these relations (especially the approximate ones) to practical calculations such as the geoacoustic inversions of paper CG,[17] it is necessary to demonstrate that the analytical formulas give results that are acceptably close to trustworthy results obtained from numerical models. As there are no numerical models that directly admit a power-law shear speed profile, we are compelled to tackle the numerical simulations with a model that uses a stack of homogeneous layers that approximates a continuous profile.

The first step is to develop a procedure to generate stacked-layer models equivalent, in effect, to continuous power-law profiles; this is described in the Appendix, in which we validate the stacked-layer numerical model against the exact results for the square-root profile. We find that 30 progressively thicker intermediate layers (each providing the same travel time for a vertically traveling shear wave) yield a phase speed accuracy of about 0.1% for a reasonable computation time. Using the same procedure to generate accurate and time-efficient stacked-layer models for cases in which $\nu\neq\frac{1}{2}$, we now investigate the agreement of the approximate analytic dispersion relations with numerical results for a range of cases.

To calculate the phase speeds of the interface wave modes for the stacked-layer models, we used a variation of the method used to numerically investigate seismo-acoustic noise resonances.[13] In that study, to calculate the acoustic reflection coefficient of a stack of elastic layers, it was necessary to compute the inverse of a large matrix representing the continuity conditions on the *P* and *SV* fields at the boundaries between the many layers. The basis of the approach is described by Brekhovskikh and Godin (Ref. 18, Chap. 4), and the calculations were implemented in the software package MATHEMATICA.[30] Certain transformation coefficients of plane waves at the boundary become singular at precisely those horizontal wave number values that correspond to the normal modes of the system, that is, the interface waves (Ref. 18, Chap. 4). Mathematically speaking, the determinant of the above matrix vanishes at the wave num-

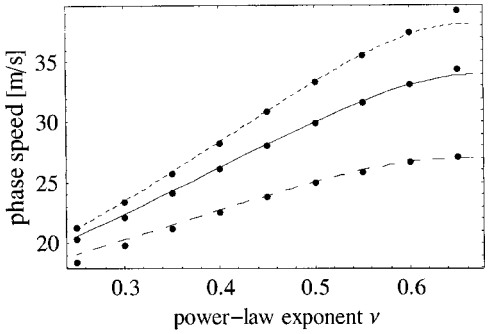

FIG. 3. Numerical values (dots) and analytical values (curves) of the phase speed of the fundamental mode in the power-law profile $c(z)=10\sqrt{\pi}z^{\nu}$ (SI units) as a function of the exponent ν: $R=1$ (large dash), $R=\frac{2}{3}$ (solid curve), and $R=\frac{1}{2}$ (small dash).

bers (angular frequency divided by phase speeds) of the interface waves. In a monotonically increasing profile, at any given frequency, there are an infinite number of modes. To find a root associated with a given mode, we choose a reasonably accurate initial estimate and then let the MATHEMATICA's FINDROOT function search for the solution, that is, the value of the phase speed that makes the determinant vanish. Fortunately, it turns out that the analytical formulas derived in this paper provide very good starting values for the cases of interest.

First, we consider the fundamental mode at 2 Hz in the shear speed profile $c(z)=10\sqrt{\pi}z^{\nu}$, with ν taking values between 0.25 and 0.65 with increments of 0.05. This range matches experimentally observed values. Since the fundamental mode is sensitive to R, we show results for $R=1$, $R=\frac{2}{3}$, and $R=\frac{1}{2}$. (These correspond to sediment/water density ratios of 1, 3/2, and 2, respectively.) The numerical stacked-layer phase speed values are plotted in Fig. 3 as points, while the corresponding analytical estimates from Eq. (96) are plotted as curves. The agreement is quite good (perfect for $\nu=\frac{1}{2}$), showing some variation at extreme values of ν and R.

Next, we consider the main sequence of modes. Figure 4 compares the numerical stacked-layer phase speeds of modes 1 and 2 (dots) with the analytical estimates from Eq. (78). The $R=\frac{2}{3}$ fundamental mode results from Fig. 3 are repeated. Again, the agreement is very good (perfect for $\nu=\frac{1}{2}$), showing some variation at extreme values of ν. Investigation of

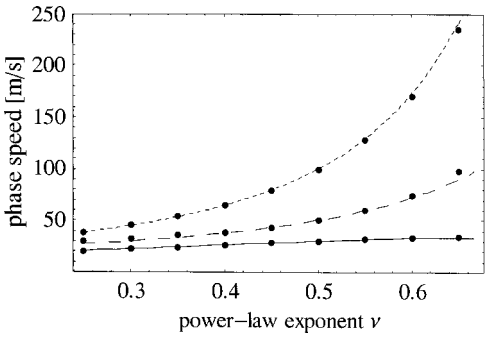

FIG. 4. Numerical values (dots) and analytical values (curves) of the phase speed of modes in the power-law profile $c(z)=10\sqrt{\pi}z^{\nu}$ (SI units) as a function of the exponent ν: $n=0$ (solid curve), $n=1$ (large dash), and $n=2$ (small dash).

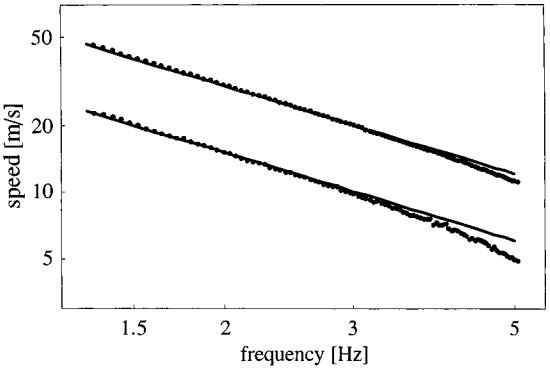

FIG. 5. SAFARI results (dots) and analytical curves (lines) showing the frequency scaling of the dispersion of the fundamental mode in the square-root profile $c(z)=10\sqrt{\pi z}$ (SI units) with $R=\frac{2}{3}$: phase speed (upper), group speed (lower).

the stacked-layer results reveals no appreciable variation of the main sequence phase speeds for different values of R, in agreement with theory. Further investigation shows that the agreement between stacked-layer results and the analytical formula improves with increasing mode order, as expected.

To illustrate the frequency-scaling effect, we compare the analytical formulas for the phase and group speeds of the fundamental mode in the square-root profile $c(z)=10\sqrt{\pi z}$ with those generated by the well-known SAFARI code[31] used in many seismo-acoustic modeling applications. For this comparison we use an equal-travel-time model with $m=21$, $H=2.26\,\mathrm{m}$, and $R=\frac{2}{3}$. (See the Appendix for explanation of the parameters m and H of the stacked-layer model.) Figure 5 shows the SAFARI phase and group speed results between 1.3 Hz and 5 Hz, along with the ideal curves, which are $V_0=60/f$ and $U_0=30/f$ (SI units), respectively. The data are plotted in log–log format to accentuate the frequency scaling of the dispersion. Note that the agreement is best at intermediate frequencies, where the stacked-layer model is properly "tuned," but it degrades at low and high extremes of frequency.

In summary, comparison of analytical and numerical calculations of the phase speed of interface waves in power-law shear speed profiles in almost-incompressible media indicates that the analytical formulas provide good estimates of the dispersion relations. The scaling of the phase and group speeds with frequency is confirmed; however, it is difficult to construct a stacked-layer goacoustic model that will simulate a power-law shear speed profile and remain accurate over a wide range of frequencies. Given the natural uncertainties in the experimental interface-wave dispersion data, the analytical formulas are deemed to be accurate enough for the purposes of analytical inversion of the shear speed profile, when the profile is, indeed, of the power-law form.

VIII. DISCUSSION AND CONCLUSIONS

We have demonstrated theoretically that soft marine sediments support slow seismo-acoustic interface waves. Their phase and group velocities are determined by density and shear wave speed stratification and, depending on wave polarization, either insensitive to or independent of compressional wave speed. Phase velocity of the interface waves is

of the order of magnitude of the shear speed in the sediment. In the case of constant density and the power-law profile of shear speed, interface wave dispersion follows the *scaling law* Eq. (22). The scaling law predicts modal phase and group velocities V and U up to a factor that is a function of the exponent ν, the mode order n, and, for the fundamental mode, the ratio of the sediment and water densities R. The dependence of the velocities on frequency and material parameters B and l is fully determined by the scaling law. In particular, phase and group velocities are proportional to a certain power of frequency, with ratio of the velocities being independent of the mode order, wave polarization, and environmental parameters except for ν.

For the environmental model considered, the scaling law applies at all wave frequencies. In practice, however, it can be valid for a finite frequency band only. At low frequencies, the scaling law ceases to be valid when the interface wave penetrates into deep sediment layers where shear rigidity deviates from the power-law profile. At high frequencies, the assumption of a vertically stratified environment becomes questionable, and one has to account for surface roughness and, possibly, for horizontal gradients of volumetric parameters of the sediment. In addition, the very concept of an effective solid underlying our theory does not apply when wavelength becomes comparable to the sediment grain size.

The dimensional analysis leading to the scaling law is rigorous for *SH* (horizontally polarized or Love) interface waves. For *P-SV* (vertically polarized) waves it holds in the limit of an incompressible solid. Strictly speaking, finite compressibility violates the scaling law. However, relative corrections to the interface-wave phase velocity prove to be of the second order in the ratio of V to the compressional speed c_l. The corrections and, hence, effects of finite compressibility are typically negligible unless the phase velocity exceeds 150–250 m/s.

The abovementioned multiplicative factor in the scaling law Eq. (22) cannot be found from dimensional considerations. A detailed dynamic analysis is required to determine the factor. We obtained an *exact, explicit analytical solution* to the equations of motion for interface waves in the case of incompressible solid with the power-law profile of shear speed and $\nu=\frac{1}{2}$, that is, in the case of linear dependence of the shear rigidity on depth. It is proved that an infinite, countable number of interface waves exists in such a medium. Wave fields in each of the interface waves are expressed in terms of elementary functions. The exact solution may be used as a benchmark to verify numerical models of seismo-acoustic fields in stratified marine sediments.

No exact solution is available for $\nu\neq\frac{1}{2},0$. To determine the multiplicative factor, asymptotic methods and perturbation theory have been used. Dispersion relations valid for higher-order modes ($n\gg 1$) at arbitrary ν have been obtained by the method of matched asymptotic expansions that extends the WKB method to the wave equation having singularities and turning points. The perturbation theory enabled us to derive approximate dispersion relations valid for arbitrary n and ν close to $\frac{1}{2}$. Calculation of the second-order corrections in $\nu-\frac{1}{2}$ were necessary to accurately reproduce the dispersion relation of the fundamental mode throughout the range of ν values encountered in marine sediments. The perturbation theory can be also used to account for finite compressibility, density gradients, and other deviations from the ideal geoacoustic model that admits the exact solution. The final results are the *approximate dispersion relations* given by Eqs. (78), (96), and (100), which combine the information obtained from asymptotic and perturbation analyses. By comparing analytical predictions to numerical simulations, we demonstrated that the analytical results reproduce, with sufficient accuracy, the dispersion relations of the interface waves for all values of ν that are of practical interest. The analytical dispersion relations Eqs. (78), (96), and (100) serve as the basis for the goacoustic inversions of experimental data reported in the companion paper.[17]

Two kinds of *P-SV* interface waves are supported by the power-law shear speed profile. Whereas the fundamental interface mode is strongly coupled to water-borne sound, the main sequence modes are essentially uncoupled from water; vertical displacement and normal stress at the water-sediment interface are nonzero in the fundamental mode only. The fundamental mode is the only mode sensitive to the water density. (These properties of the main sequence modes are a consequence of the singularity in the power-law profile at the water-sediment interface and of the assumed vertical stratification of the medium. Surface roughness, three-dimensional volumetric inhomogeneities in the ocean bottom, or both can couple sound waves to the main sequence modes and may make the modes observable with a hydrophone situated in water. The coupling also occurs if the shear speed profile deviates from the power law in such a way that shear rigidity is nonzero at $z=0$.) The vertically polarized main sequence modes are similar to horizontally polarized interface waves supported by the same medium. Qualitatively, the fundamental mode has much in common with the Rayleigh wave (Ref. 18, Sec. 4.4) at the interface between homogeneous fluid and solid half-spaces: both are vertically polarized surface waves; they manifest themselves as an evanescent sound wave in fluid; and they have phase velocities of the order of the shear speed in solid. Dispersion properties of the two waves, however, are entirely different. Whereas the Rayleigh wave have frequency-independent velocities $V=U$, the fundamental mode is strongly dispersive; V and U are proportional to certain power of frequency; and the phase velocity always exceeds the group velocity (by factor of 2 at $\nu=\frac{1}{2}$). The two interface waves have different displacement and stress fields. For instance, in the incompressible solid with a light fluid load ($R\ll 1$) the ratio of amplitudes of horizontal and vertical displacements in the Rayleigh wave varies from 0.5436 at the surface to 0.2955 at large depth (Ref. 18, Sec. 4.4.2). In the fundamental mode, the ratio is 1, independent of depth. Velocity of the Rayleigh wave is primarily determined by the *value* of shear speed at the interface; in the incompressible solid, $V=0.9554c$. The velocity of the fundamental mode is determined by the *rate* of shear speed (or shear rigidity) *variation* at the interface,

specifically, by the shear rigidity gradient in the case when $\nu=\frac{1}{2}$. Consider an incompressible solid half-space with a light fluid load and a shear speed profile $c(z)=c(0)+B(z/l)^{\frac{1}{2}}$. At high frequencies, the medium supports a Rayleigh-type surface wave with velocity $0.9554c(0)$. Velocity of the Rayleigh-type wave tends toward zero when $c(0)\to 0$ and no Rayleigh-type wave exists at $c(0)=0$. On the contrary, the velocity of the fundamental mode is insensitive to $c(0)$ when this quantity is small; it is given by Eq. (32). The fundamental mode exists whether $c(0)=0$ or not. Arguably, the Rayleigh wave and the fundamental interface wave described in this paper should be considered as distinct types of surface waves.

It should be emphasized that, in spite of unconsolidated marine sediments being almost incompressible, coupling between shear and (evanescent) compressional waves materially affects the dispersion relation of vertically polarized interface waves. Continuous coupling between shear waves of vertical polarization and compressional waves is reflected in the wave equation (11) for *P-SV* waves being of the fourth order as opposed to second-order wave equations for uncoupled compressional and shear waves. As far as interface waves of given mode order are concerned, the coupling is equally important at low and high frequencies. In the limit of an incompressible solid, the particle displacement $\mathbf{u}$ is akin that in pure shear wave in the sense that $\nabla\cdot\mathbf{u}=0$. However, the compressional component of the wave field is as important as its shear component in the stress field. The relative contributions of shear and compressional components in a given interface wave can be quantified as a dimensionless ratio of depth-averaged values of vertical displacement u_3 and quantity q defined by Eq. (5) with $s=1$. With such a criterion, one can say that the contributions of compressional and shear components are roughly equal in both the fundamental mode and the first main sequence *P-SV* mode. With mode order n increasing, the contribution of the compressional component decreases as $1/n$, and higher-order main sequence modes are almost pure shear waves. It is insightful to compare the main sequence *P-SV* modes with the *SH* modes of the same order for the power-law profile with $\nu=\frac{1}{2}$. The *SH* modes are, of course, pure shear waves. At $n=1$, when there is a strong *P-SV* coupling, the phase and group speeds of the vertically polarized mode are twice as large as speeds of the horizontally polarized mode. At $n\gg 1$, when the coupling is weak, the relative difference between speeds of the two modes is $O(1/n)$ just like the contribution of the compressional-wave component of the *P-SV* interface wave.

ACKNOWLEDGMENTS

Stimulating discussions with N. Ross Chapman (University of Victoria, British Columbia, Canada), Marshall V. Hall (DSTO, Sydney, New South Wales, Australia), and Ron Kessel (DREA, Dartmouth, Nova Scotia, Canada) are gratefully acknowledged. OAG's research reported in this paper was originally supported in part by the Natural Sciences and Engineering Research Council of Canada and has been completed while he held a Senior NRC-NOAA/ETL Research Associateship.

APPENDIX: DESIGNING, OPTIMIZING, AND VALIDATING A STACKED-LAYER MODEL

To fashion a stacked-layer geoacoustic model that is equivalent, in effect, to a model with continuous parameters, we first choose a sequence of boundary depths $\{z_1,z_2,z_3,\ldots,z_m\}$ that define the lower limits of the homogeneous layers, where layer 1 is the upper (water) half-space, and layer m is the lower half-space. By default, $z_1=0$ and $z_m=\infty$. Then we assign a corresponding sequence of shear speeds $\{c_1,c_2,c_3,\ldots,c_m\}$ in the layers, producing a "staircase" profile of shear speed versus depth. By default, $c_1=0$. We choose the layer speeds in such a way that the numerical results from the stacked-layer model converge to those of the ideal continuous model as the number of intermediate layers is increased. This process can be validated for an incompressible solid with a square-root shear speed profile, for which we have analytical expressions for the mode phase speeds. We demonstrate that a sequence of progressively thicker layers is more computationally efficient than a sequence of layers of identical thickness.

In either case, we require that the vertical travel time through a given homogeneous layer is the same as the travel time in the power-law profile between the same depths. In the power-law profile, the vertical travel time between depth zero and depth z is

$$\tau(z)=\int_0^z\frac{dz'}{c(z')}=\frac{l}{(1-\nu)B}\left(\frac{l}{z}\right)^{\nu-1}. \tag{A1}$$

The thickness of layer k is $\Delta z_k=z_k-z_{k-1}$ and the travel time between z_{k-1} and z_k is $\Delta\tau_k=\tau(z_k)-\tau(z_{k-1})$, so the appropriate speed in layer k is $c_k=\Delta z_k/\Delta\tau_k$. Once we choose the boundary depths (or, equivalently, the layer thicknesses), the shear speeds follow. The staircase design task reduces to optimally choosing the sequence $\{z_1,z_2,z_3,\ldots,z_m\}$ for a particular problem, to yield the highest numerical accuracy with the fewest layers (to reduce computation time). We have considered two prescriptions: (a) equal layer thickness, and (b) equal layer travel time.

1. Equal layer thickness

In this case, the layers are equally thick, that is,

$$z_k=(k-1)h, \tag{A2}$$

in which h is the thickness of the first intermediate layer, which is directly below the water. The combined thickness of the intermediate layers is $H\equiv z_{m-1}=(m-2)h$, that is, the depth at which the lower half space begins. The corresponding layer speeds are

$$c_k=\frac{(1-\nu)B(h/l)^{\nu}}{(k-1)^{1-\nu}-(k-2)^{1-\nu}};\quad k=2,3,\ldots,m. \tag{A3}$$

TABLE AI. Convergence of fundamental mode phase speed.

Layers		Equal layer thickness				Equal layer travel time			
n	$n-2$	h [m]	V [m/s]	% error	Compute time[a)]	h [m]	V [m/s]	% error	Compute time[a]
12	10	1.00	22.1865	26	0.2	0.100	29.7383	0.9	0.1
22	20	0.50	26.9033	10	0.8	0.025	29.9261	0.2	0.4
32	30	0.33	28.5632	5	1.6	0.011	29.9653	0.1	1
42	40	0.25	29.1736	3	3.2	0.007	29.9759	0.07	2.1
52	50	0.20	29.4587	2	5.4	0.004	29.9837	0.04	3.6
62	60	0.17	29.6147	1	9.2	0.003	29.9857	0.03	4.1
continuous			29.9960				29.9960		

[a]Relative to the 32-layer equal-layer-travel-time case.

2. Equal layer travel time

In this case, the layers are chosen to be progressively thicker with depth, so that the travel time in each layer is the same, for which it is necessary that

$$z_k=(k-1)^{1/(1-\nu)}h, \tag{A4}$$

where $h\equiv z_2$. The combined thickness of the intermediate layers is $H\equiv z_{m-1}=(m-2)^{1/(1-\nu)}h$. In this case, the layer speeds are

$$c_k=(1-\nu)B(h/l)^{\nu}[(k-1)^{1/(1-\nu)}-(k-2)^{1/(1-\nu)}],$$
$$k=2,3,...,m. \tag{A5}$$

3. Tuning the stacked-layer profile

In either case, to optimize the layering to solve a particular problem, one needs to appropriately choose h (or H) and the total number of layers n; then the stacked layer profile follows from applying Eqs. (A2) and (A3) or Eqs. (A4) and (A5). The tuning depends on the mode order and the frequency: as a rule-of-thumb, for low-order modes, H must be much greater than the mode turning depth (where the mode phase speed equals the shear speed), then the number of layers needs to be increased until the desired accuracy is achieved, at which point h is typically much less than the mode turning depth.

We illustrate this by considering the phase speed of the fundamental mode in an almost-incompressible solid with the square-root profile $c(z)=10(\pi z)^{\frac{1}{2}}$ (SI units), having a sediment/water density ratio of 1.5. At 2 Hz, assuming incompressibility, the phase speed of the fundamental mode is exactly 30 m/s, which matches the shear speed profile at a depth of 2.86 m; incorporating the correction Eq. (82) for finite compressibility, with $c_f=1500$ m/s and $c_f=1550$ m/s, the phase speed is reduced to 29.9960 m/s. We choose H to be 10 m, then consider models with 10 to 60 intermediate layers. The results of numerical computation with our stacked-layer model are shown in Table AI and illustrated in Fig. A1. Note that the computations using the model with equal layer travel times are always much more accurate and faster than those using the model with equal layer thicknesses. The better model converges to the ideal result as the number of layers is increased, such that the product of computation time and the percentage error remains roughly constant. Also, note how very thin the upper layers must be made to achieve the stated accuracy.

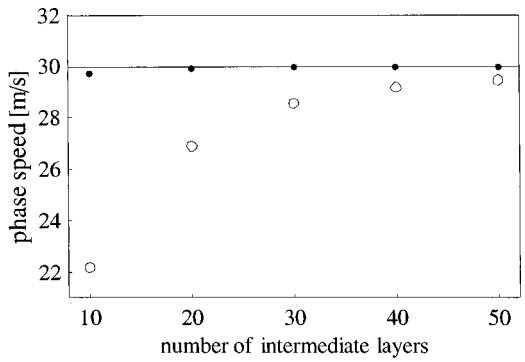

FIG. A1. FIG. A1. Convergence of stacked-layer models to analytic result (solid line) with increasing number of layers: equal layer travel time (upper points) and equal layer thickness (lower points).

Accordingly, for the numerical normal mode calculations presented elsewhere in this paper, we use a stacked-layer geoacoustic model based on equal layer travel times for shear waves, with 30 intermediate sediment layers. Sediment density and sound speed are held constant in all layers for these calculations, but it would be straightforward to incorporate staircase approximations to depth-dependent profiles of these parameters, if desired.

[1] E. I. Hamilton, "Attenuation of shear waves in marine sediments," J. Acoust. Soc. Am. **60**, 334–338 (1976).

[2] B. O. Hardin, "The nature of stress-strain behavior for soils," in *Proceedings of the Specialty Conference on Earthquake Engineering and Soil Dynamics* (ASCE, Pasadena, 1978), pp. 30–90.

[3] J. E. White, *Underground Sound Application of Seismic Waves* (Elsevier, Amsterdam, 1983), pp. 67–68.

[4] D. T. Smith, "Geotechnical characteristics of the sea bed related to seismo-acoustics," in *Ocean Seismo-Acoustics*, edited by T. Akal and J. M. Berkson (Plenum, New York, 1986), pp. 483–500.

[5] G. M. Bryan and R. D. Stoll, "The dynamic shear modulus of marine sediments," J. Acoust. Soc. Am. **83**, 2159–2164 (1988).

[6] M. D. Richardson, E. Muzi, B. Miaschi, and F. Turgutcan, "Shear wave velocity gradients in near-surface marine sediments," in *Shear Waves in Marine Sediments*, edited by J. M. Hovem, M. D. Richardson, and R. D. Stoll (Kluwer, Dordrecht, 1991), pp. 295–304.

[7] M. V. Hall, "Acoustic reflectivity of a sandy seabed: A semianalytic model of the effect of coupling due to shear modulus profile," J. Acoust. Soc. Am. **98**, 1075–1079 (1995).

[8] T. Iwasaki and F. Tatsuoka, "Effects of grain size and grading on dynamic shear moduli of sands," Soils Found. **17**, 19–35 (1997).

[9] D. Huns, A. Davis, and J. Pyrah, "Relating *in situ* shear wave velocity to void ratio and grain size for unconsolidated marine sediments," in *High Frequency Acoustics in Shallow Water*, edited by N. G. Pace, E. Poul-

iquen, O. Bergem, and A. P. Lyons (SACLANTCEN, La Spezia, Italy, 1997), pp. 251–258.
[10] J. C. Osler and D. M. F. Chapman, "Seismo-acoustic determination of the shear-wave speed of surficial clay and silt sediments on the Scotian Shelf," Can. Acoust. **24**, 11–22 (1996).
[11] F. A. Bowles, "Observations on attenuation and shear-wave velocity in fine-grained, marine sediments," J. Acoust. Soc. Am. **101**, 3385–3397 (1997).
[12] D. M. F. Chapman, "Shear speed gradients and resonances in ocean seismo-acoustic modelling," in *Theoretical and Computational Acoustics '97*, edited by Y. C. Teng, E. C. Shang, Y. C. Pao, M. H. Schultz, and A. D. Pierce (World Scientific, Singapore, 1999), pp. 147–158.
[13] O. A. Godin and D. M. F. Chapman, "Shear speed gradients and ocean seismo-acoustic noise resonances," J. Acoust. Soc. Am. **106**, 2367–2382 (1999).
[14] A. Caiti, T. Akal, and R. D. Stoll, "Estimation of shear wave velocity in shallow marine sediments," IEEE J. Ocean. Eng. **19**, 58–72 (1994).
[15] R. D. Stoll and T. Akal, "Experimental techniques for bottom parameter inversion in shallow water," in *Full Field Inversion Methods in Ocean and Seismo-Acoustics*, edited by O. Diachok, A. Caiti, P. Gerstoft, and H. Schmidt (Kluwer Academic, Dordrecht, 1995), pp. 311–316.
[16] S. A. Frivik, R. Allnor, and J. M. Hovem, "Estimation of shear wave properties in the upper seabed using seismo-acoustical interface waves," in *High Frequency Acoustics in Shallow Water*, edited by N. G. Pace, E. Pouliquen, O. Bergem, and A. P. Lyons (SACLANTCEN, La Spezia, Italy, 1997), pp. 155–162
[17] D. M. F. Chapman and O. A. Godin, "Dispersion of interface waves in sediments with power-law shear speed profiles. II. Experimental observations and inverse modeling," J. Acoust. Soc. Am. **110**, 1908 (2001).
[18] L. M. Brekhovskikh and O. A. Godin, *Acoustics of Layered Medium. I: Plane and Quasi-Plane Waves* (Springer-Verlag, Berlin, 1990).
[19] To avoid misunderstanding, the slow waves we consider have nothing to do with slow compressional waves in porous media predicted by Biot theory (Ref. 20). We assume throughout this paper that unconsolidated sediments can be described as an effective solid with depth-dependent density and effective Lamé parameters λ and μ. If it were not for gradients of ρ, λ, or μ, slow seismo-acoustic waves in soft sediments would be nothing else than familiar *SV* elastic waves in homogeneous solid.
[20] R. D. Stoll, *Sediment Acoustics* (Springer-Verlag, Berlin, 1989), pp. 5–36.
[21] G. P. Panasenko, "Averaged systems of equations of the theory of elasticity in a medium with weakly compressible inclusions," Matem. Zametki **51**, 126–133 (1992) [in Russian].
[22] K. Aki and P. G. Richards, *Quantitative Seismology. Theory and Methods* (Freeman, San Francisco, 1980), Chap. 8.
[23] The depth scale l can be chosen arbitrary in Eq. (14); it has been introduced solely to make the dimensionality and value of B independent of ν. Parameters B and l are related to the quantity c_0 used to specify the power-law profile in the companion paper (Ref. 17) by $c_0 = Bl^{-\nu}$. The two parametrizations of the power-law profile are equivalent as long as ν is constant. When dependence of wave fields on ν is studied, the use of parameters B and l instead of c_0 arguably provides a more intuitive description of the environment.
[24] G. I. Barenblatt, *Similarity, Self-Similarity, and Intermediate Asymptotics* (Consultants Bureau, New York, 1979).
[25] *Handbook of Mathematical Functions with Formulas, Graphs, and Tables*, Appl. Math. Ser., Vol. 55, edited by M. Abramovitz and I. A. Stegun (National Bureau of Standards, Washington, 1964).
[26] L. D. Landau and E. M. Lifshitz, *Course of Theoretical Physics, Vol. 3: Quantum Mechanics, Nonrelativistic Theory* (Pergamon, New York, 1972), Sec. 36.
[27] O. A. Godin, "Acoustic mode reciprocity in fluid/solid systems: Implications on environmental sensitivity and horizontal refraction," in *Theoretical and Computational Acoustics '97*, edited by Y. C. Teng, E. C. Shang, Y. C. Pao, M. H. Schultz, and A. D. Pierce (World Scientific, Singapore, 1999), pp. 59–76.
[28] A. P. Prudnikov, Yu. A. Brychkov, and O. I. Marichev, *Integrals and Series, Vol. 2: Special Functions* (Gordon and Breach, New York, 1986), Sec. 2.19.14.
[29] H. Takeuchi and M. Saito, "Seismic surface waves," in *Seismology: Surface Waves and Earth Oscillations*, edited by B. A. Bolt (Academic, New York, 1972), pp. 217–295.
[30] S. Wolfram, *The Mathematica Book*, 3rd ed. (Wolfram Research, Inc., Champaign, 1996).
[31] H. Schmidt and F. B. Jensen, "Efficient numerical solution technique for wave propagation in horizontally stratified environments," Comput. Math. Appl. **11**, 699–715 (1985).

Dispersion of interface waves in sediments with power-law shear speed profiles. II. Experimental observations and seismo-acoustic inversions[a)]

David M. F. Chapman[b)]
Defence Research Establishment Atlantic, P.O. Box 1012, Dartmouth, Nova Scotia B2Y 3Z7, Canada

Oleg A. Godin
NOAA/Environmental Technology Laboratory, Ocean Remote Sensing Division, 325 Broadway, Boulder, Colorado 80303-3328 and Acoustic Wave Propagation Laboratory, P. P. Shirshov Oceanography Institute of the Russian Academy of Sciences, Moscow 117851, Russia

(Received 5 October 2000; revised 23 April 2001; accepted 12 July 2001)

The propagation of seismic interface waves is investigated in soft marine sediments in which the density is constant, the shear modulus is small, and the profile of shear speed c_s versus depth z is of the power-law form $c_s(z)=c_0 z^{\nu}$, in which c_0 and ν are constants $(0<\nu<1)$. Both the phase speed V and the group speed U of interface waves scale with frequency as $f^{\nu/(\nu-1)}$ and they obey the simple relation $U=(1-\nu)V$. These relations are derived in a simple way using ray theory and the WKB method; a companion paper [O. A. Godin and D. M. F. Chapman, J. Acoust. Soc. Am. **110**, 1890 (2001)] rigorously derives the same result from the solutions to the equations of motion. The frequency scaling is shown to exist in experimental data sets of interface wave phase speed and group speed. Approximate analytical formulas for the dispersion relations (phase and group speed versus frequency) enable direct inversion of the profile parameters c_0 and ν from the experimental data. In cases for which there is multi-mode dispersion data, the water-sediment density ratio can be determined as well. The theory applies to vertically polarized (P-SV) modes as well as to horizontally polarized (SH) modes (that is, Love waves). © *2001 Acoustical Society of America.* [DOI: 10.1121/1.1401739]

PACS numbers: 43.30.Ma, 43.30.Dr, 43.30.Pc [DLB]

I. INTRODUCTION

The shear rigidity of surficial marine sediments affects both acoustic and geo-technical seabed properties:[1,2] acoustically, the reflectivity of the seabed is sensitive to shear waves in some environments; geo-technically, shear rigidity governs the ease of excavation for engineering installations or burial operations. In soft marine sediments—that is, unconsolidated sediments consisting of clay, silt, and sometimes sand—there is evidence (reviewed below in Sec. II) that the shear speed profile has a power-law depth dependence: $c_s(z)=c_0 z^{\nu}$, in which c_s is the shear speed, z is the depth below the water-sediment boundary, and c_0 and ν are constants. The parameter c_0 is the shear speed at unit depth and the parameter ν, which must be in the range $0<\nu<1$, governs the rate of increase of shear speed with depth. In this paper, we do not dwell on the physical conditions required for such sediments to exhibit power-law shear speed profiles; rather, we consider the consequences of power-law profiles on the propagation and dispersion of seismic interface waves at the water-sediment boundary.

In homogeneous elastic media, the wave equations of motion reduce to separate wave equations for compressional (P) waves, vertically polarized shear (SV) waves, and horizontally polarized shear (SH) waves. When the medium becomes vertically stratified, the SH waves remain independent, but the P and SV waves become coupled through the gradient of the shear modulus. There are two varieties of seismo-acoustic (P-SV) waves: "slow" seismo-acoustic waves that propagate at speeds of the order of the shear speed in the sediment[3] and "fast" waves that propagate at speeds in the range of the compressional speeds in the water and the sediment. In this paper, we focus on the "slow" seismo-acoustic waves in the vicinity of the water-sediment boundary.

If the sediment layer were a homogeneous half-space, there would be only a single, slow, seismo-acoustic mode: the Scholte wave.[4,5] This wave is nondispersive, as waves at all frequencies travel at the same phase speed, which is identical to the group speed. In a depth-dependent shear speed profile, there is a fundamental mode akin to the Scholte mode, but this mode is now dispersive: for a monotonically increasing shear speed, the phase speed decreases with increasing frequency. In addition to the fundamental mode, there may be other modes that superficially appear to be pure shear waves trapped by the upward-refracting profile. The measurement of the phase or group speed of these dispersive interface waves enables the determination of the shear speed profile through inverse modeling techniques.

The power-law shear speed profile is a special case in which the shear speed increases from zero at the interface

[a)]Portions of this paper have been presented orally at the Third International Conference on Theoretical and Computational Acoustics (Trieste, Italy, May 1999) and Acoustics Week in Canada (Victoria, B.C., October 1999).
[b)]Author to whom correspondence should be addressed: electronic mail: chapman@drea.dnd.ca

 0001-4966/2001/110(4)/1908/9/$18.00

with infinite gradient, that is, the speed increases with depth at an infinite rate. (This is radically different from the environment that supports a Scholte wave, which has finite shear speed at the boundary with zero gradient.) Theoretical investigation of the fundamental and main sequence modes in the power-law profile reveals some unexpected and remarkable properties: The phase and group speeds of all modes scale with frequency as $f^{\nu/(\nu-1)}$. Moreover, the relation between group speed U and phase speed V is $U=(1-\nu)V$ for all modes at any frequency. The fundamental mode is the true interface wave in the sense that it is coupled to the water layer and has finite vertical displacement at the boundary. The main sequence modes are trapped P-SV waves that are decoupled from the water layer; that is, the vertical displacement of these modes is zero at the boundary. Admittedly, in their precise form, these relations hold true only for the ideal circumstances in which the medium is perfectly stratified according to a power-law depth dependence, the density is constant, and the shear speed is vanishingly small; however, these conditions exist in Nature to a sufficient degree of approximation that the theoretically derived attributes are observed in experimental data.

A companion paper[6] (Paper I) rigorously derives the dispersion relations for the interface wave modes under the ideal conditions stated above, presenting exact analytical expressions for mode functions and phase speeds for all modes in the case of the square-root profile ($\nu=\frac{1}{2}$). When $\nu\neq\frac{1}{2}$, approximate dispersion relations are developed using two distinct analytical methods. This paper presents some elementary arguments based on ray theory and the Wentzel–Kramers–Brillouin (WKB) method that persuasively support the frequency-scaling hypothesis, at least. We also present sets of experimental dispersion data that exhibit this property.

The fact that the phase and group speeds scale with frequency provides a direct method of inverting experimental data for one of the parameters: the exponent ν. When phase (or group) speed is plotted versus frequency in log–log format, data exhibiting the frequency-scaling property form a straight line of slope $\nu/(1-\nu)$. Thus ν is easily estimated from experimental data using a simple procedure, without recourse to numerical modeling. Determining the parameter c_0 from the log–log plot requires more work; for this, we need the explicit expressions for the dispersion relations from Paper I.

It is customary to invert for the shear speed profile using a numerical seismo-acoustic propagation model based on a notional geo-acoustic model consisting of many stacked, homogeneous sediment layers.[7–11] Such a ''staircase'' shear speed profile has multiple shear speed parameters that must be collectively varied to obtain a good fit between model and data. Special care must be taken to ensure a reasonably unique estimate of the shear speed profile. In cases where the shear speed profile is truly continuous, stacked layer models are necessarily approximate and large numbers of fine layers are required to treat high shear speed gradients. If the shear speed profile were actually of the power-law form, then the method described in this paper would provide a unique, fast, inversion involving significantly fewer parameters.

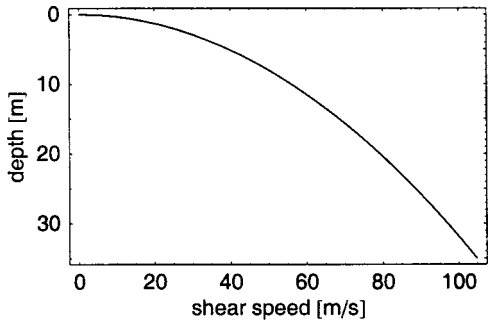

FIG. 1. The power-law shear speed profile $c_s(z)=10\sqrt{\pi}z^{1/2}\approx 17.7z^{1/2}$.

Apart from its utility as an inversion tool, the analytical investigation of interface wave dispersion provides additional physical insight that can be difficult to glean from the results of numerical simulation alone. In particular, it turns out that the speed of the fundamental mode is particularly sensitive to the value of the water-sediment density ratio, while the speeds of the main sequence modes—at least in the ideal case considered—are entirely insensitive to this ratio. This fact may not have been sufficiently appreciated before now. Our analysis confirms that the P-wave speeds in the water and the sediment are truly ''passive'' geo-acoustic parameters in this context, while showing that the density ratio is an ''active'' parameter insofar as the fundamental mode is concerned. This observation is not merely academic, as an incorrect assignment of the value for density would result in a bias in the shear speed profile, regardless of the inversion method used.

With this introduction, the paper is organized as follows: Section II further describes the power-law shear speed profile, considers aspects of ray tracing in such a profile, presents a simple (although nonrigorous) derivation of the frequency-scaling dispersion law, and derives a WKB approximation to the dispersion relations. Section III summarizes the analytical mode dispersion formulas, both exact ($\nu=\frac{1}{2}$) and approximate ($\nu\neq\frac{1}{2}$), derived in Paper I. Section IV applies these formulas to several experimental data sets, inverting the data to give estimates of the parameters of the shear speed profile and—for multi-mode data sets—the density ratio. Section V presents our discussion and conclusions.

II. INSIGHTS PROVIDED BY RAY THEORY AND THE WKB METHOD

A. Relevance of the power-law profile

We consider dispersion of seismo-acoustic interface waves in marine sediments of constant density with the shear speed profile

$$c_s(z)=c_0 z^{\nu}, \tag{1}$$

which is related to the shear modulus profile

$$\mu(z)=\rho c_0^2 z^{2\nu}, \tag{2}$$

in which ρ is the density (that is, $c_s=\sqrt{\mu/\rho}$).

Laboratory measurements of shear speed in sediment samples, interpreted with the aid of semi-empirical physical models,[12] show a power-law dependence of dynamic shear

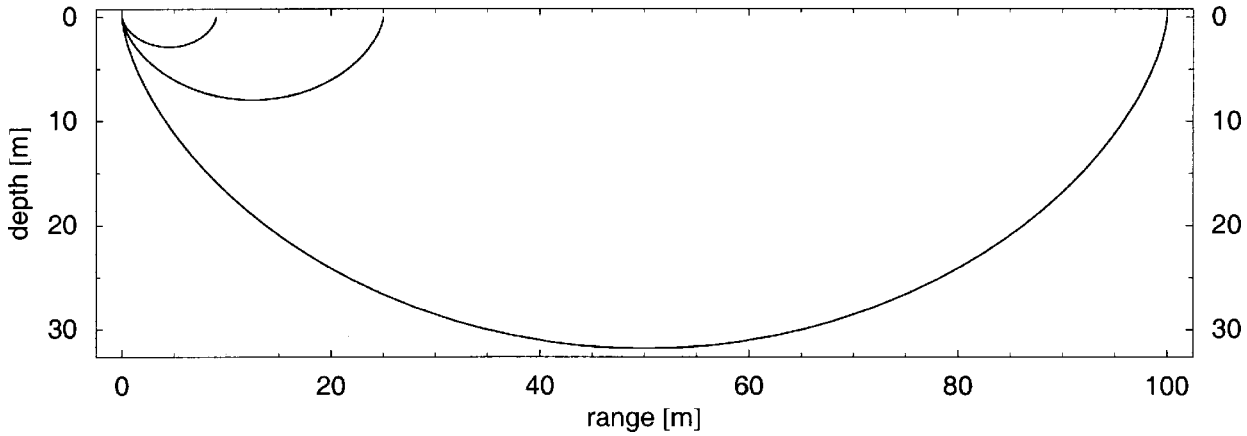

FIG. 2. Three rays propagating in the shear speed profile of Fig. 1, with the same point of origin but with different turning depths, as summarized in Table I.

modulus on confining pressure. One expects that natural sediments with depth-independent composition would exhibit an overburden pressure that increases linearly with depth; hence there should exist power-law profiles of shear speed versus depth *in situ* (assuming constant density). Indeed, surveys of geo-acoustic properties of soft marine sediments[13] often report shear speed profiles in power-law form. Some experimental seismo-acoustic inversions[14] have produced ''staircase'' shear speed profiles strongly suggestive of an underlying continuous power-law profile. Naturally, one would expect to see some variation from the ideal case, but in any event a nonuniform layer with a continuously varying power-law shear speed profile is likely to be a better first approximation than a single homogeneous layer, as is often assumed in geo-acoustic models for computational convenience.[15]

B. Ray tracing in a power-law profile

The power-law profile of Eq. (1) is singular, in the sense that the shear speed approaches zero with infinite gradient at zero depth. Contrary to expectation, this does not create mathematical difficulties. In fact, the singularity is *essential* for certain features of the solution. In particular, the ray theory integrals associated with this profile evaluate easily and result in simple expressions for complete cycles. One peculiarity of such profiles is that all rays always arrive at the upper boundary in the normal direction, regardless of their starting point. Thus the ray angle at zero depth is not a good ray parameter. As the power-law profile is an upward-refracting profile, all downward-traveling rays must eventually turn around at some depth and begin to travel upward. The turning depth z_t (or, equivalently, the shear speed at the turning depth, $c_t = c_0 z_t^{\nu}$) makes a convenient ray parameter: for a given profile, z_t or c_t uniquely define a ray.

Snell's law defines the local ray angle θ (relative to the horizontal plane) through the relation $\cos\theta(z) = c_s(z)/c_t = (z/z_t)^{\nu}$. The horizontal distance traveled by a ray leaving the surface and traveling to depth z is

$$x(z) = \int_0^z \frac{\cos\theta(z')\,dz'}{\sin\theta(z')} = \frac{z_t}{2\nu}\int_0^{(z/z_t)^{2\nu}} y^{1/2\nu-1/2}(1-y)^{-1/2}\,dy \tag{3}$$

and the associated travel time is

$$t(z) = \int_0^z \frac{dz'}{c_s(z')\sin\theta(z')} = \frac{z_t}{2\nu c_t}\int_0^{(z/z_t)^{2\nu}} y^{1/2\nu-3/2}(1-y)^{-1/2}\,dy, \tag{4}$$

in which the integration variable has been changed from z' to $y = (z'/z_t)^{2\nu}$.

Numerical evaluation of Eq. (3) enables us to trace rays in a given profile. Figure 1 shows the power-law profile $c_s(z) = 10\sqrt{\pi z} \approx 17.7 z^{1/2}$. Figure 2 shows three rays in this profile, all having the same starting point at the surface, with different turning depths ($z_t = 2.9$ m, 8.0 m, and 31.8 m). Note that all three rays leave their common departure point in the normal direction, but end up at different points down range, according to their different turning depths.

C. Derivation of the frequency-scaling law for phase and group speed

When the upper limit of the integrals in Eqs. (3) and (4) is z_t, the integrals turn out to be Beta functions expressible in terms of the gamma (Γ) function.[16] Accordingly, the horizontal skip distance and cycle time of a ray are given by the simple expressions

TABLE I. Parameters of rays (Fig. 2) in the square-root profile (Fig. 1).

Turning depth z_t [m]	Turning speed c_t [m/s]	Skip distance X [m]	Cycle time T [s]	Speed of advance X/T [m/s]
2.865	30	4.5	0.3	15
7.958	50	12.5	0.5	25
31.831	100	50	1.0	50

$$X = 2x(z_t) = \frac{1-\nu}{\nu} B_\nu z_t \tag{5}$$

and

$$T = 2t(z_t) = \frac{1}{\nu c_t} B_\nu z_t, \tag{6}$$

in which B_ν is the number

$$B_\nu = \sqrt{\pi}\Gamma\left(\frac{1-\nu}{2\nu}\right) \Big/ \Gamma\left(\frac{1}{2\nu}\right). \tag{7}$$

The average horizontal speed of advance of a ray is just the skip distance divided by the cycle time, or

$$X/T = (1-\nu)c_t. \tag{8}$$

Note that the ray cycle time becomes infinite as $\nu \to 1$, while the skip distance stays finite; accordingly the average speed of advance approaches zero, and the problem is not physical for $\nu > 1$. Table I presents z_t, c_t, X, T, and X/T for the rays in Fig. 2.

All rays (including those equivalent to modes) obey Eq. (8), and it is tempting to identify X/T with the mode group speed U, and c_t with the mode phase speed V, so that

$$U = (1-\nu)V. \tag{9}$$

However, by definition, the group speed of a mode is governed by the frequency dependence of the phase speed, that is,

$$U = V\left(1 - \frac{f}{V}\frac{dV}{df}\right)^{-1}. \tag{10}$$

Accordingly, if both Eq. (8) and Eq. (9) apply, both the phase speed and the group speed are compelled to scale with frequency as

$$V, U \propto f^{\nu/(\nu-1)}. \tag{11}$$

It is remarkable that such an elegant result could be derived from simple ray considerations; however, this law is a manifestation of the fundamental equations of motion of the slow seismo-acoustic waves in this ideal environment, to which ray theory is an approximate solution. In fact, the authors' initial ray-based derivation of the frequency-scaling law provided the motivation for the complete wave-theoretic analysis of Paper I, which proves that the frequency scaling of phase and group speeds is a fundamental property of the slow waves in the power-law shear speed profile. Frequency-scaling applies to both the fundamental mode and the main sequence of modes that are trapped by the shear speed profile.

D. Approximate dispersion relation for the main sequence modes

We now extend the ray analysis to derive a WKB-style solution to this problem. As we are more interested in dispersion relations (eigenvalues) than mode amplitudes (eigenfunctions), we need only to consider the WKB phase condition, which in generic form is

$$\phi_{\mathrm{WKB}} = n\pi + \phi_u/1 + \phi_1/2, \tag{12}$$

in which ϕ_{WKB} is the integral of the vertical wave number between the upper and lower turning points of the mode, and ϕ_u and ϕ_1 are the phase lags of a plane wave at the upper and lower turning points, respectively.

We previously investigated seismo-acoustic ambient noise resonances in sediments with power-law shear speed profiles bounded below by a strong reflector.[17] This phenomenon is distinct from the propagation of interface waves, but the treatment of the upper boundary condition is identical. The modified WKB solution of the noise resonance problem requires the introduction of a ν-dependent phase lag at the upper boundary of the form

$$\phi_u = \pi m(\nu) - \pi/2, \tag{13}$$

in which

$$m(\nu) = (2\nu - 1)/(1-\nu). \tag{14}$$

For the interface wave problem, the lower boundary is a true turning point induced by the upward-refracting profile, so the phase lag there is simply $\phi_1 = \pi/2$. The WKB phase integral is related to Eqs. (3) and (4):

$$\phi_{\mathrm{WKB}} = 2\pi f \int_0^{z_t} \frac{\sin\theta(z')dz'}{c_s(z')} = \pi f(T - X/c_t) = \pi f B_\nu c_0^{1/\nu}/c_t^{1-1/\nu}, \tag{15}$$

in which we have used the identity $\sin\theta/c_s = 1/c_s \sin\theta - \cos\theta/c_t \sin\theta$. Putting these together, the mode phase speeds V_n are those values of the phase speed c_t that satisfy the WKB phase condition Eq. (12); that is,

$$V_n = \left(\frac{c_0^{1/\nu}[n + m(\nu)/2]}{fB_\nu}\right)^{\nu/(1-\nu)}. \tag{16}$$

This expression, which applies only to the main sequence modes and not to the fundamental mode, has the correct frequency dependence, shows the dependence of phase speed on the parameter c_0, and nicely anticipates the full wave theory solution of this problem, which is summarized below. The corresponding expression for group speed follows from applying Eq. (10).

III. SUMMARY OF THE FULL WAVE THEORY SOLUTION

Paper I, through a rigorous mathematical analysis of the equations of motion in this medium, not only justifies the insight provided by the preceding approach, but develops the analysis much further. In this section, we review some of the significant results of Paper I, especially those used to reduce the experimental data in Sec. IV. The complete derivation of the expressions in this section can be found in that paper.

A. Vertically polarized (*P-SV*) modes

The generic dispersion relation for slow *P-SV* waves in a power-law profile is

$$V_n = \left(\frac{c_0^{1/\nu} n_{\mathrm{eff}}(n,\nu,R)}{fB_\nu}\right)^{\nu/(1-\nu)}, \tag{17}$$

in which n is the mode number (0,1,2,3,...), $R=\rho_w/\rho$ is the ratio of the water density to the sediment bulk density, and n_{eff}, the ''effective'' mode number is a dimensionless function of n, ν, and R that is determined by the solution of the wave equation with appropriate boundary conditions. The frequency scaling of the group speed follows directly from applying Eq. (10), as does the simple relation between U and V first derived from ray considerations in Eq. (9). The superiority of the wave theory approach is demonstrated by its inclusion of the fundamental mode along with the main sequence of modes: strictly speaking, there is no ray equivalent to the fundamental mode in such problems.

Furthermore, exact solutions exist (under the stated conditions) for the case $\nu=\frac{1}{2}$, the square-root profile. These solutions consist of mode functions for the horizontal and vertical stress and displacement, and exact expressions for the effective mode number, which turn out to be

$$n_{\text{eff}}(n,1/2,R)=\begin{cases}\dfrac{1}{1+R} & (n=0)\\ n & (n=1,2,3,..).\end{cases} \tag{18}$$

Accordingly, the phase speeds for the modes in the square-root profile are

$$V_n(\nu=1/2)=\begin{cases}\dfrac{c_0^2}{\pi f(1+R)} & (n=0)\\ \dfrac{nc_0^2}{\pi f} & (n=1,2,3,...),\end{cases} \tag{19}$$

and the group speeds are just one-half of these values. The fundamental mode is coupled to the water column and is sensitive to R; the main sequence modes are not coupled to the water and are insensitive to R. Furthermore, the main sequence modes are harmonically spaced in phase speed. Since $1/(1+R)<1$, the fundamental mode appears to have a ''fractional'' mode order, in relation to the main sequence of phase speeds at any given frequency. These results for the square-root profile could be used to validate and benchmark numerical seismo-acoustic propagation models. For example, Paper I favourably compares the phase speed and group speed of the fundamental mode in a square-root profile with dispersion curves generated by the SAFARI model.[18]

At the time of writing, no exact dispersion relations have been derived for the case $\nu\neq\frac{1}{2}$; however, application of perturbation theory to the $\nu=\frac{1}{2}$ case provides the approximate formulas

$$n_{\text{eff}}(n,\nu,R)=\begin{cases}\dfrac{B_\nu}{2\pi}\left(\dfrac{2}{1+R}\right)^{1/2\nu}\exp\left[a\left(\nu-\dfrac{1}{2}\right)+b\left(\nu-\dfrac{1}{2}\right)^2+\ldots\right] & (n=0)\\ n+\dfrac{\nu-\frac{1}{2}}{2(1-\nu)}+\left(\nu-\dfrac{1}{2}\right)\left\{1+\dfrac{1}{n}+2n[\Psi(n)-\ln n]\right\}+\cdots & (n=1,2,3,...),\end{cases} \tag{20}$$

in which

$$a=(1-\gamma-\log 2)/\nu,$$

$$b=\frac{1}{\nu}\left\{\frac{2+R}{6}\pi^2-1+(1+R)^2\left[\gamma+\Psi\left(\frac{R}{1+R}\right)\right]\right\}, \tag{21}$$

$$\gamma=0.577\,21...\quad\text{(Euler's constant)}$$

$\Psi(x)$ being the Digamma function.[16]

Of course, Eq. (20) reduces to Eq. (18) when $\nu=1/2$, and the complicated second-order correction factors are needed only for extreme values of ν. Also, for the main sequence modes, the first two terms of Eq. (20) are identical to the WKB approximation of Eq. (16). (The terms in curly brackets vanish for infinite n.)

In the following section, we employ Eqs. (17), (18), and (19) in to invert experimental interface wave dispersion data for the shear profile parameters c_0 and ν; in one case (multimode data) we also determine the parameter R, but in other

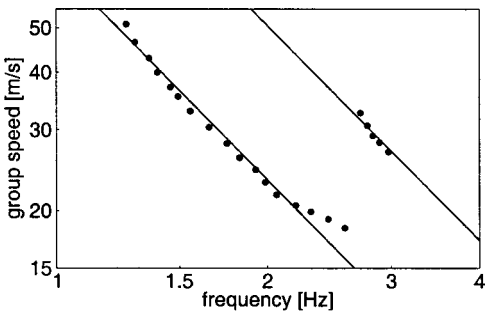

FIG. 3. Log–log plot of the dispersion data of the fundamental mode and the first main sequence mode of the Eastern Shore data (Ref. 14), with a model fit showing the frequency dependence $f^{-1.55}$. This site has layers of fine clay and silt.

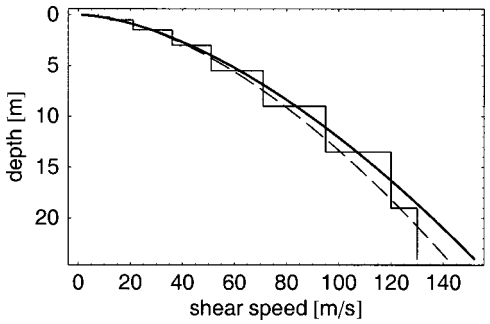

FIG. 4. The staircase profile at Eastern Shore (Ref. 14) compared with the power-law profile $22.0z^{0.608}$ (solid curve) from analytic inversion of the same dispersion data and the power-law profile $21.7z^{0.59}$ (dashed curve) from ambient noise analysis (Ref. 17).

TABLE II. Summary of experimental data sets and inversion parameters.

Site	Ref.	Modes	c_0 [m/s][a]	ν	ρ [kg/m^3][b]	$V_{\max}$ [m/s]	$z_{\max}$ [m]
Eastern Shore	14	2	22.0 ± 0.2	0.608 ± 0.008	1620 ± 80	130	37
Orkanger	20, 21	1	76.7 ± 0.3	0.421 ± 0.003	1800[c]	214	23
Straits of Sicily	10, 11	1	161 ± 5	0.349 ± 0.012	1800[c]	670	119
Gulf of Mexico	23, 24	1[d]	121.5 ± 0.2	0.253 ± 0.002	-	132	2.8

[a]Owing to the fractional power law, the units of c_0 are odd: think of c_0 as the shear speed at unit depth.
[b]The actual inversion parameter is $R=\rho_w/\rho$.
[c]This is an assumed value.
[d]This is the first *SH* (Love) mode, rather than a *P-SV* mode, as in the other cases.

cases (fundamental mode only) we must assume a value. Paper I also derives correction formulas for the phase speed of *P-SV* modes in weakly compressible media. (That is, when the shear speed is an appreciable fraction of the compressional speeds in the water and sediment.) These corrections are not significant in the experimental cases considered in this paper.

B. Horizontally polarized (*SH*) modes, or Love waves

An analysis similar to the case of *P-SV* waves summarized above can also be applied to the case of trapped *SH* waves (also called *Love waves*). In this case, there is no coupling of *SH* waves to *P* waves either in the water or in the sediment, and there is no fundamental mode corresponding to the *P-SV* fundamental mode. However, there is a main sequence of trapped modes corresponding to the main sequence of *P-SV* modes. For the special case $\nu=\frac{1}{2}$. The phase speed of the *SH* modes is still given by Eq. (17); however, the effective mode number is $n-\frac{1}{2}$ rather than n. The *SH* and *P-SV* modes are thus interleaved in the square-root profile.

For $\nu\neq\frac{1}{2}$, the effective mode number is approximately

$$n_{\text{eff}}=n-\frac{1}{2}+\frac{\nu-\frac{1}{2}}{2(1-\nu)}+(\nu-\tfrac{1}{2})(2n-1)\times[\Psi(n)-\ln(n-\tfrac{1}{2})]+\ldots\ . \tag{22}$$

(The terms in square brackets vanish for infinite n.) In the following section we use Eqs. (17) and (22) in Sec. III to invert experimental data of a single *SH* mode for the shear profile parameters c_0 and ν. As there is no coupling to the water, the water-sediment density ratio R plays no role in the dispersion of Love waves. Generally speaking, the sediment density is not relevant to the dispersion of Love waves, provided the density gradient is not large.

C. Depth limitation of the theory

Extended indefinitely in depth, the power-law profile increases without bound, which is unlikely to hold true in Nature. However, interface wave dispersion experiments probe the speed profile effectively only up to a depth horizon determined by the lowest-frequency, highest-speed waves. Below this horizon, the actual shear speed profile has little influence on the measurements. At a given frequency f, every interface mode has a turning depth z_t at which the mode phase speed $V(f)$ equals the shear speed. Paper I considers the error in phase speed introduced by replacing the power-law profile below a certain depth by a uniform half-space. As a rule-of-thumb, for the phase speed error to be less than 1%, that depth should be about twice the turning depth. Accordingly, with this error criterion, inversion in a power-law profile is trustworthy only to a maximum depth given by

$$z_{\max}\approx 2(V_{\max}/c_0)^{1/\nu}, \tag{23}$$

in which $V_{\max}=V(f_{\min})$ is the maximum measured phase speed, which occurs at the lowest frequency of measurement $f_{\min}$. [The quantity $V_{\max}$ should be replaced by $U_{\max}/(1-\nu)$ for experiments in which group speed is measured.] Once a power-law inversion is performed, Eq. (23) can be used to estimate the depth to which the inversion is valid.

IV. INTERPRETATION AND INVERSION OF EXPERIMENTAL DATA

We use four sets of previously published dispersion data to validate the frequency scaling of interface waves in ma-

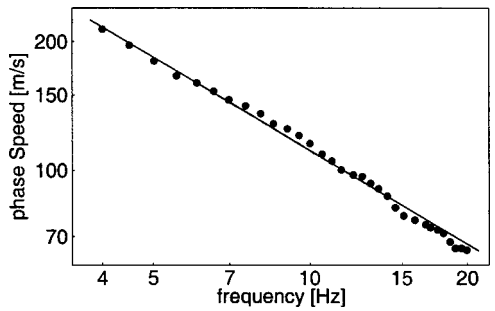

FIG. 5. Log–log plot of the fundamental mode dispersion data from the Orkanger data (Ref. 20) with a model fit showing the frequency dependence $f^{-0.727}$. This site has layers of silt and fine sand over gravel.

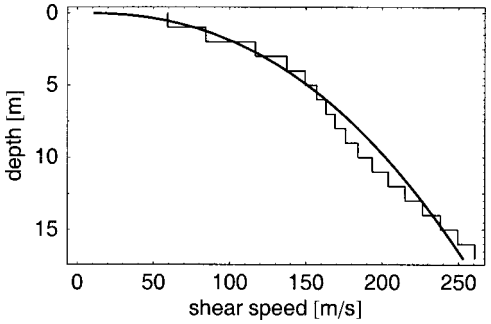

FIG. 6. The staircase profile at Orkanger (Ref. 20) compared with the power-law profile $76.7z^{0.421}$ inverted analytically from the same dispersion data.

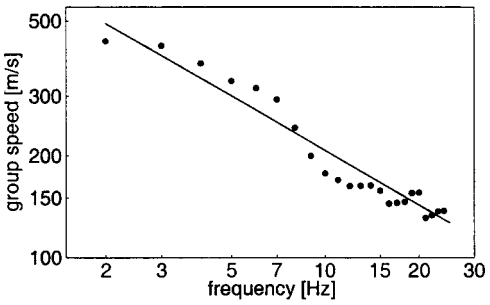

FIG. 7. Log–log plot of the fundamental mode dispersion data at Sicily B (Ref. 11) with a model fit showing the frequency dependence $f^{-0.536}$. This site has layers of coarse sand.

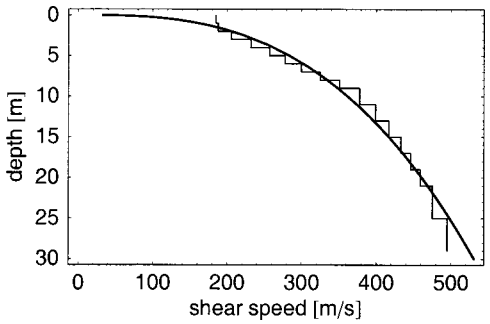

FIG. 8. The staircase profile from Sicily B (Ref. 11) compared with the power-law profile $162z^{0.349}$ inverted analytically from the same dispersion data.

rine sediments. We then apply the approximate analytical dispersion relations to the data to invert for the geo-acoustic parameters c_0 and ν. In one case we independently determine R; in two other cases, we must assume a value for R; in the fourth case the inversion is independent of R. The original inversions used a variety of experimental techniques and data reduction methods, but all were based on stacked-layer geoacoustic models. We compare our continuous power-law profiles with the previously determined staircase profiles. Our inversion results are summarized in Table II.

To fit our model to the data, we use the NONLINEARREGRESS package of MATHEMATICA.[19] This package automatically searches for the best fit of a nonlinear multiparameter model to supplied data, based on an initial guess for the parameters. NONLINEARREGRESS uses the Levenberg–Marguardt method, which begins with a steepest-descent approach and changes to quadratic minimization to converge on a solution. The algorithm provides not only the best-fit model parameter values, but a summary report of regression diagnostics, including estimates of parameter variance. If the number of model parameters were large, there is the possibility of finding only a local (rather than global) fit, depending on the initial estimate; however, in this application, there are only three parameters and their influence on the model is well understood. No inconsistent results were encountered in the following data reduction.

The measurements are organized as a list of elements of the form {mode number, frequency, speed}, and the theoretical phase or group speeds are defined as functions of mode number, frequency, c_0, ν, and R according to Eqs. (20)–(22) above. Rough initial estimates of c_0, ν, and R are provided to NONLINEARREGRESS, and the algorithm iterates to a best fit, which yields final estimates of c_0, ν, and R with standard errors. These error estimates are based on the scatter in the data set relative to the target model; they do not incorporate the uncertainty in the experimental data points themselves. In the case of single-mode (fundamental mode) data, the method is modified: A value for R is assumed, and the fit proceeds as before, with one less free parameter. The derived parameters are used to compute model dispersion curves to lay over the original data as a visual check of goodness-of-fit. In some cases, the agreement is judged to be too unsatisfactory to declare that the geoacoustic parameter inversion has been successful.

Note that the continuous profiles are expected to be valid only up to the depth $z_{\max}$ calculated according to Eq. (23). In Cases A–C, $z_{\max}$ exceeds the maximum depth of the staircase profile, and the staircase profiles agree reasonably well with the corresponding continuous profile. The apparent disagreement in Case D will be discussed. For ease of comparison, the shear profiles are plotted to the maximum depth of the staircase data.

A. Osler and Chapman: Eastern Shore data

On the wide continental shelf east of Nova Scotia, there are basins partially filled with layers of fine sediments, mostly clay and silt. Osler and Chapman[14] reported interface wave dispersion results from two sites: Eastern Shore and Emerald Basin. They used an ocean bottom seismometer to receive signals generated several hundred meters from small explosions on the seabed. They processed the geophone time series to produce a time-frequency-intensity plot (sometimes called a *Gabor diagram*), from which they picked sample points that defined ridges of high intensity corresponding to the fundamental mode and the first main sequence mode. The latter was not as distinct as the former, but the data were sufficient to generate a stacked-layer model through an inversion procedure that consisted of running SAFARI[18] multiple times and individually adjusting profile parameters to achieve an acceptable fit of modelled dispersion curves to the experimental ''picks.'' Their staircase profile for the Eastern Shore data suggests an underlying power-law profile of the form $(21.1\pm0.5)z^{(0.62\pm0.01)}$ (SI units), with the assumption of material densities in the range 1500 kg/m^3 to 1600 kg/m^3. Independently, Godin and Chapman[17] analyzed the seismo-acoustic noise resonances at the same site, which suggested a power-law profile of the form $(21.7\pm1.5)z^{(0.59\pm0.06)}$. Using the same data ''picks'' as Ref. 14, the power-law inversion method produces the three-parameter fit shown in Fig. 3, with an estimated density of 1620 ± 80 kg/m^3 and an estimated profile of $(22.0\pm0.2)z^{(0.608\pm0.008)}$. This profile is shown in Fig. 4 along with the original ''staircase'' profile and the ''noise'' profile. All three are in very good agreement.

B. Frivik *et al.*: Orkanger data

Frivik *et al.*[20,21] analyzed seismic survey data from a river delta site near Orkanger in the Trondheim fjord, the seabed consisting of silt and fine sand over sand and gravel.

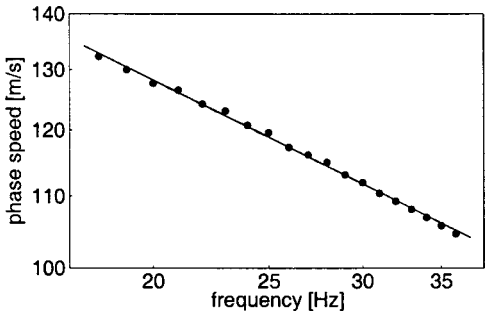

FIG. 9. Log–log plot of the dispersion of the first Love mode at the Gulf of Mexico site (Ref. 23) with a model fit showing the frequency dependence $f^{-0.339}$. This site has layers of sand.

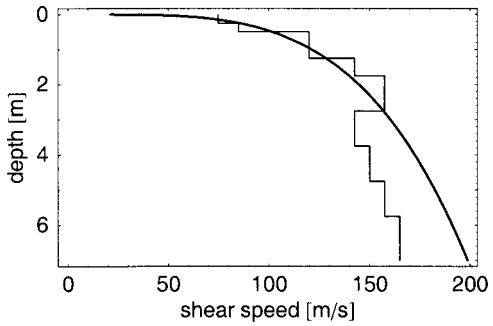

FIG. 10. The staircase profile from the Gulf of Mexico site (Ref. 23) compared with the power-law profile $121.5z^{0.253}$ inverted analytically inverted from the same dispersion data.

They studied dispersion data in the form of phase speed versus frequency for interface waves generated by small explosives. They detected two modes (fundamental and first main sequence) in the data, and inverted the data to obtain a shear speed profile using the method of Refs. 10 and 11, assuming a density of 1800 kg/m^3. Our fit to their data is shown in Fig. 5, although we decided not to use the first main sequence mode in the final fit, due to the difficulty they experienced interpreting this mode from the raw data.[22] Instead, we adopted their value for the density and used their fundamental mode data, which scales well with frequency. Overall, the resulting power-law profile $(76.7\pm0.3)z^{(0.421\pm0.003)}$ agrees well with their staircase profile in Fig. 6.

C. Caiti *et al.*: Sicily B data

In a shallow water area of the Straits of Sicily, Caiti *et al.*[10,11] performed interface wave experiments in sediments of coarse sand. Their group speed data is replotted in log–log format in Fig. 7, along with our power-law fit. They did not report the sediment density used in their inversion, and we have assumed a value of 1800 kg/m^3, consistent with coarse sand. The resulting continuous profile $(161\pm4)z^{(0.365\pm0.013)}$ is shown in Fig. 8 along with their staircase profile. Considering the scatter in the dispersion data, the agreement between the profiles is remarkably good.

D. Stoll and Akal: Gulf of Mexico data

Using a torsional source, Stoll and Akal[23] generated and measured *SH* modes (Love waves) in sand sediments in the Gulf of Mexico. Their phase speed data is replotted in log–log format in Fig. 9 along with our power-law fit to the same data. The resulting continuous profile $(121.5\pm0.2)\times z^{(0.253\pm0.002)}$ is shown in Fig. 10 along with the staircase profile determined by Stoll and Akal. Note that the profiles are comparable down to 2.5 m, but diverge below that depth; however, Table II shows that the effective inversion horizon for this case is only about 2.8 m at these relatively high frequencies, as calculated by Eq. (23). It is unlikely that either inversion method would yield a trustworthy result below this depth from these data. In fact, there is some suggestion[24] of the existence of two distinct sand layers at this site, one coarse and one fine, possibly having different porosities and different densities.

V. DISCUSSION AND CONCLUSIONS

Starting from elementary considerations of ray-tracing in media with power-law shear speed profiles of the form $c_s(z)=c_0z^\nu$, we derived the remarkable result that both the phase speed V and the group speed U of interface waves should scale with frequency as $f^{\nu/(\nu-1)}$ and that $U=(1-\nu)V$. A companion paper[6] rigorously investigated this hypothesis on a wave theoretical basis and proved that indeed this is so, provided that the sediment density is constant and that the sediment is effectively incompressible, that is, the shear speed is very much smaller than the compressional speed.

The analytical approach provided approximate expressions for the phase and group speed of the *P-SV* interface waves in such environments, including the fundamental mode (which is coupled to the water and is sensitive to the water-sediment density ratio R), and the main sequence of modes (which are decoupled from the water and are insensitive to R). The existence of these expressions made it possible to perform analytical inversions of experimental dispersion data to determine the geo-acoustic parameters c_0, ν, and sometimes R. In the special case $\nu=\frac{1}{2}$, the analytical expressions for phase and group speed turned out to be exact (under the assumptions of constant density and vanishingly small shear speed). Further development of the theory provided analogous expressions for *SH* modes (Love waves) and also corrections to account for weakly compressible media.

We applied these formulas to four data sets whose dispersion data exhibited the frequency-scaling property indicative of a power-law profile. In all cases, the analytically inverted continuous power-law profiles agreed well with the staircase profiles determined using methods employing repetitive forward modelling based on stacked-layer geo-acoustic inputs. Two inversions used phase speed; the other two used group speed. In one case in which two modes were observed, we independently determined the sediment density; in two other cases, in which only fundamental mode data was available, we needed to assume a reasonable value for density. The fourth inversion used Love wave data, and did not need (and could not provide) a density estimate.

We do not suggest that all marine sediments should exhibit a perfect power-law shear speed profile; indeed, it is evident that many do not. However, there are realistic conditions under which some sediments very nearly exhibit the

qualities required for the approach in this paper to be valid. Moreover, by plotting the dispersion data in log–log format (log speed versus log frequency), it is easy to test the dispersion data for the desired frequency-scaling property before proceeding. Even in cases where analytical inversion does not seem worthwhile, log–log dispersion plots would accentuate (through their nonlinear nature) the departure from an ideal power-law form. Finally, in cases where a multiparameter stacked-layer geo-acoustic model is unavoidable, an analytical inversion based on these principles might provide a practical starting model.

The analytical analysis of interface wave dispersion in power-law profiles has provided insights into the physics of this problem that are only glimpsed through numerical modelling. Apart from the practical applications just discussed, one principal result has not been sufficiently appreciated before now: the significant role that sediment density plays in the dispersion of the fundamental mode of *P-SV* interface waves. Whether analytic or numerical inversions are being contemplated, this fact must be respected.

ACKNOWLEDGMENTS

The authors would like to acknowledge the contributions of the following individuals: DMFC thanks Jack Dodds for initially drawing attention to the frequency scaling of interface wave dispersion in the special case $\nu = \frac{1}{4}$ and John Osler for collecting and analyzing the DREA dispersion data (and for suggesting that we perform seismo-acoustic inversion on them). Both authors thank Svein Frivik, Rune Allnor, and Andrea Caiti for supplying data in electronic form, and Ron Kessel for validating some key calculations. Thanks to Bob Stoll for commenting on a portion of the manuscript. We especially thank Professor Ross Chapman of the University of Victoria and Dr. Harold M. Merklinger of DREA for their long-standing support and encouragement. OAG's research was originally supported in part by the Natural Science and Engineering Research Council of Canada and has been completed while the author held a Senior NRC-NOAA/ETL Research Associateship.

[1] *Shear Waves in Marine Sediments*, edited by Jens M. Hovem, Michael D. Richardson, and Robert D. Stoll (Kluwer Academic, Dordrecht, 1991).
[2] *Ocean Seismo-Acoustics*, edited by Tuncay Akal and Jonathan M. Berkson (Plenum, New York, 1986).
[3] Not to be confused with the ''slow'' compressional wave predicted by the Biot–Stoll sediment acoustics model, described by (for example) R. D. Stoll and T. K. Kan, ''Reflection of acoustic waves at a water-sediment interface,'' J. Acoust. Soc. Am. **70**, 149–156 (1981).
[4] Dieter Rauch, ''Seismic interface waves in coastal waters: A review,'' SACLANTCEN Report SR-42 (NATO SACLANT ASW Research Centre, Italy, November 1980).
[5] L. Cagniard, *Reflection and Refraction of Progressive Seismic Waves* (McGraw-Hill, New York, 1962).
[6] Oleg A. Godin and David M. F. Chapman, ''Dispersion of interface waves in sediments with power-law shear speed profiles. I. Exact and approximate analytical results,'' J. Acoust. Soc. Am. **110**, 1890 (2001).
[7] Finn B. Jensen and Henrik Schmidt, ''Shear properties of ocean sediments determined from numerical modeling of Scholte wave data,'' in *Ocean Seismo-Acoustics*, edited by Tuncay Akal and Jonathan M. Berkson (Plenum, New York, 1986), pp. 683–692.
[8] R. D. Stoll, G. M. Bryan, R. Flood, D. Chaynes, and P. Manley, ''Shallow seismic experiments using shear waves,'' J. Acoust. Soc. Am. **83**, 93–102 (1988).
[9] S. E. Dosso and G. H. Brooke, ''Measurement of seismo-acoustic ocean-bottom properties in the high Arctic,'' J. Acoust. Soc. Am. **98**, 1657–1666 (1995).
[10] A. Caiti, R. D. Stoll, and T. Akal, ''Estimation of shear wave velocity in shallow marine sediments,'' IEEE J. Ocean. Eng. **19**, 58–72 (1994).
[11] A. Caiti, T. Akal, and R. D. Stoll, ''Shear wave velocity in seafloor sediments by inversion of interface wave dispersion data,'' SACLANTCEN Report SR-205 (NATO SACLANT Undersea Research Centre, Italy, May 1993).
[12] G. M. Bryan and R. D. Stoll, ''The dynamic shear modulus of marine sediments,'' J. Acoust. Soc. Am. **83**, 2159–2164 (1988).
[13] Frederick A. Bowles, ''Observations on attenuation and shear-wave velocity in fine-grained, marine sediments,'' J. Acoust. Soc. Am. **101**, 3385–3397 (1997).
[14] John C. Osler and David M. F. Chapman, ''Seismo-acoustic determination of the shear-wave speed of surficial clay and silt sediments on the Scotian Shelf,'' Can. Acoust. **24**, 11–22 (1996).
[15] N. Ross Chapman and David M. F. Chapman, ''A coherent ray model of plane-wave reflection from a thin sediment layer,'' J. Acoust. Soc. Am. **94**, 2731–2738 (1993).
[16] Milton Abramowitz and Irene A. Stegun, *Handbook of Mathematical Functions*, 9th ed. (Dover, New York, 1972), p. 258.
[17] O. A. Godin and David M. F. Chapman, ''Shear-speed gradients and ocean seismo-acoustic noise resonances,'' J. Acoust. Soc. Am. **106**, 2367–2382 (1999).
[18] H. Schmidt and F. B. Jensen, ''Efficient numerical solution technique for wave propagation in horizontally stratified environments,'' Comput. Math. Appl. **11**, 699–715 (1985).
[19] Steven Wolfram, *The Mathematica Book*, 3rd ed. (Wolfram Research, Inc., Champaign, 1996).
[20] S. A. Frivik, R. Allnor, and J. M. Hovem, ''Estimation of shear wave properties in the upper sea-bed using seismo-acoustical interface waves,'' in *High Frequency Acoustics in Shallow Water*, edited by N. G. Pace, E. Pouliquen, O. Bergem, and A. P. Lyons (NATO SACLANT Undersea Research Centre, Italy, 1997), pp. 155–162.
[21] Svein Arne Frivik, ''Determination of shear wave properties in the upper seafloor using seismo-acoustic-interface waves,'' Ph.D. thesis, Norwegian University of Science and Technology, Department of telecommunications, N-7034, Trondheim, Norway, January 1998.
[22] Rune Allnor, ''Seismo-acoustic remote sensing of shear wave velocities shallow marine sediments,'' Ph.D. thesis, Norwegian University of Science and Technology, Department of telecommunications, N-7034, Trondheim, Norway, September 2000.
[23] R. D. Stoll and T. Akal, ''Experimental techniques for bottom parameter inversion in shallow water,'' in *Full Field Inversion Methods in Ocean and Seismo-Acoustics*, edited by O. Diachok, A. Caiti, P. Gerstoft, and H. Schmidt (Kluwer Academic, The Netherlands, 1995), pp. 311–316.
[24] Robert D. Stoll, Lamont-Doherty Earth Observatory, Columbia University, Rte. 9W, Palisades, NY 10964, personal communication, 2000.

Necessary conditions for a maximum likelihood estimate to become asymptotically unbiased and attain the Cramer–Rao Lower Bound. Part I. General approach with an application to time-delay and Doppler shift estimation

Eran Naftali and Nicholas C. Makris
Massachusetts Institute of Technology, Room 5-222, 77 Massachusetts Avenue, Cambridge, Massachusetts 02139

(Received 17 October 2000; revised 20 April 2001; accepted 29 May 2001)

Analytic expressions for the first order bias and second order covariance of a general maximum likelihood estimate (MLE) are presented. These expressions are used to determine general analytic conditions on sample size, or signal-to-noise ratio (SNR), that are *necessary* for a MLE to become asymptotically unbiased and attain minimum variance as expressed by the Cramer–Rao lower bound (CRLB). The expressions are then evaluated for multivariate Gaussian data. The results can be used to determine asymptotic biases, variances, and conditions for estimator optimality in a wide range of inverse problems encountered in ocean acoustics and many other disciplines. The results are then applied to rigorously determine conditions on SNR necessary for the MLE to become unbiased and attain minimum variance in the classical active sonar and radar time-delay and Doppler-shift estimation problems. The time-delay MLE is the time lag at the peak value of a matched filter output. It is shown that the matched filter estimate attains the CRLB for the signal's position when the SNR is much larger than the *kurtosis* of the expected signal's energy spectrum. The Doppler-shift MLE exhibits dual behavior for narrow band analytic signals. In a companion paper, the general theory presented here is applied to the problem of estimating the range and depth of an acoustic source submerged in an ocean waveguide.
[DOI: 10.1121/1.1387091]

PACS numbers: 43.30.Pc, 43.60.Gk, 43.60.Pt [DLB]

I. INTRODUCTION

In many practical problems in ocean acoustics, geophysics, statistical signal processing, and other disciplines, nonlinear inversions are required to estimate parameters from measured data that undergo random fluctuations. The nonlinear inversion of random data often leads to estimates that are biased and do not attain minimum variance, namely the Cramer–Rao lower bound (CRLB), for small sample sizes or equivalently low signal-to-noise ratio (SNR). The maximum likelihood estimator (MLE) is widely used because if an asymptotically unbiased and minimum variance estimator exists for large sample sizes, it is guaranteed to be the MLE.[1] Since exact expressions for the bias, variance, and error correlation of the MLE are often difficult or impractical to derive analytically, it has become popular in ocean acoustics and many other areas to simply neglect potential biases and to compute limiting bounds on the mean square error, such as the CRLB, since these bounds are usually much easier to obtain. The CRLB, however, typically provides an unrealistically optimistic approximation to the MLE error correlation in many nonlinear inverse problems when the sample size is small, or equivalently the SNR is low. A number of bounds on the error correlation exist that are tighter than the CRLB.[1–5] Some of these bounds are based on Bayesian assumptions[4,5] and so require the *a priori* probability density of the parameters to be estimated, which can be problematic when the *a priori* probability density is not known.[6]

The purpose of the present paper is not to derive a new parameter resolution bound, but rather to determine, within the framework of classical estimation theory[1,6,7] the conditions on sample size, or SNR, *necessary* for the MLE to become asymptotically unbiased and attain minimum variance. The approach is to apply the tools of higher order asymptotic inference, which rely heavily on tensor analysis, to expand the MLE as a series in inverse orders of sample size or equivalently inverse orders of SNR.[7] From this series analytic expressions for the first order bias, second order covariance and second order error correlation of a general MLE are presented in terms of joint moments of the log-likelihood function and its derivatives with respect to the parameters to be estimated. Since the first order error correlation is shown to be the CRLB, which is only valid for unbiased estimates, the second order error correlation can provide a tighter error approximation to the MLE than the CRLB that is applicable in relatively low SNR even when the MLE is biased to first order. These expressions are then used to determine general analytic requirements on sample size, or SNR, that are *necessary* for an MLE to become asymptotically unbiased and attain minimum variance. This is done by showing when the first order bias becomes negligible compared to the true value of the parameter and when the second order covariance term becomes negligible compared to the CRLB.

The first order bias is evaluated for general multivariate Gaussian data. The second order covariance and error correlation terms are evaluated for two special cases of Gaussian data that are of great practical value in ocean acoustics, geophysics, and statistical signal processing. The first is for a deterministic signal vector embedded in additive noise and the second is for a fully randomized signal vector with zero mean in additive noise. These cases have been widely used in ocean acoustic inversions, spectral estimation, beamforming, sonar and radar detection, and localization problems, as well as statistical optics.[8–10] In a companion paper, each of these cases is applied to determine the asymptotic bias and covariance of maximum likelihood range and depth estimates of a sound source submerged in an ocean waveguide from measured hydrophone array data as well as necessary conditions for the estimates to attain the CRLB.[11]

In the present paper, these expressions are applied to the active sonar and radar time-delay and Doppler-shift estimation problems, where time delay is used for target range estimation and Doppler shift is used for target velocity estimation. Attention is focused on the commonly encountered scenario of a deterministic signal with unknown spatial or temporal delay received together with additive white noise. The time-delay MLE is then the time lag at the peak value of a matched filter output. The matched filter estimate for a signal's time delay or position is widely used in many applications of statistical pattern recognition in sonar, radar, and optical image processing. This is because it has long been known that the matched filter estimate attains the CRLB in high SNR. *Necessary* analytic conditions on how high the SNR must be for the matched filter estimate to attain the CRLB have not been previously obtained but are derived here using the general asymptotic approach developed in Secs. II–IV.

A number of authors have derived tighter bounds than the CRLB for the time-delay estimation problem to help evaluate performance at low SNR where the CRLB is not attained by the MLE, as, for example, in Refs. 5, 12, 13. The present paper follows a different approach by providing explicit expressions for the second order variance of the time-delay and Doppler-shift MLEs that are attained in lower SNR than the CRLB. The first order bias is also derived. These expressions are then used to provide analytic conditions on SNR necessary for the time-delay MLE, namely the matched filter estimate, and Doppler-shift MLE to become unbiased and attain minimum variance in terms of properties of the signal and its spectrum. Illustrative examples for standard linear frequency modulated (LFM), hyperbolic frequency modulated (HFM), and canonical waveforms are provided for typical low-frequency active-sonar scenarios in ocean acoustics.

II. GENERAL ASYMPTOTIC EXPANSIONS OF THE MLE AND ITS MOMENTS

Suppose the random data vector $\mathbf{X}$, given m-dimensional parameter vector $\boldsymbol{\theta}$, obeys the conditional probability density function (pdf) $p(\mathbf{X};\boldsymbol{\theta})$. The log-likelihood function $l(\boldsymbol{\theta})$ is defined as $l(\boldsymbol{\theta})=\ln(p(\mathbf{X};\boldsymbol{\theta}))$ when evaluated at measured values of $\mathbf{X}$. Let the rth component of $\boldsymbol{\theta}$ be denoted by θ^r. The first log-likelihood derivative with respect to θ^r is then defined as $l_r=\partial l(\boldsymbol{\theta})/\partial\theta^r$. If $R_1=r_{11}\ldots r_{1n_1},\ldots\ldots,R_m=r_{m1\ldots mn_m}$ are sets of coordinate indices, joint moments of the log-likelihood derivatives can be defined by $v_{R_1,\ldots,R_m}=E[l_{R_l}\ldots l_{R_m}]$, where, for example, $v_{s,tu}=E[l_s l_{tu}]$ and $v_{a,b,c,de}=E[l_a l_b l_c l_{de}]$.

The expected information, known as the Fisher information, is defined by $i_{rs}=E[l_r l_s]$ where the indices r, s are arbitrary. Lifting the indices produces quantities that are denoted by $v^{R_1,\ldots,R_m}=i^{r_{11}s_{11}}\ldots i^{r_{mn_m}s_{mn_m}}v_{s_{11}\ldots s_{1n_1},\ldots,s_{m1}\ldots s_{mn_m}}$, where $i^{rs}=[\mathbf{i}^{-1}]_{rs}$ is the r, s component of the inverse $\mathbf{i}^{-1}$ of the expected information matrix $\mathbf{i}$. The inverse of the Fisher information matrix $\mathbf{i}^{-1}$ is also known as the Cramer–Rao lower bound (CRLB). Here, as elsewhere, the Einstein summation convention is used. That is, if an index occurs twice in a term, once in the subscript and once in the superscript, summation over the index is implied.

The MLE $\hat{\boldsymbol{\theta}}$, the value of $\boldsymbol{\theta}$ that maximizes $l(\boldsymbol{\theta})$ for the given data $\mathbf{X}$,[1,6,7] can now be expressed as an asymptotic expansion around $\boldsymbol{\theta}$ in increasing orders of inverse sample size n^{-1} or equivalently SNR. Following the derivation of Barndorff-Nielsen and Cox,[7] the component l_r is first expanded around $\boldsymbol{\theta}$ as

$$\hat{l}_r=l_r+l_{rs}(\hat{\theta}-\theta)^s+\tfrac{1}{2}l_{rst}(\hat{\theta}-\theta)^s(\hat{\theta}-\theta)^t+\tfrac{1}{6}l_{rstu}(\hat{\theta}-\theta)^s(\hat{\theta}-\theta)^t(\hat{\theta}-\theta)^u+\cdots, \tag{1}$$

where $(\hat{\theta}-\theta)^r=\hat{\theta}^r-\theta^r$. Equation (1) is then inverted to obtain an asymptotic expansion for $(\hat{\theta}-\theta)^r$, as shown in Appendix D. After collecting terms of the same asymptotic order, this can be expressed as[7]

$$(\hat{\theta}-\theta)^r=\underbrace{i^{rs}l_s}_{O_p(n^{-1/2})}+\underbrace{\tfrac{1}{2}v^{rst}l_s l_t+i^{rs}i^{tu}H_{st}l_u}_{O_A(n^{-1})}+\underbrace{\tfrac{1}{6}(v^{rstu}+3v^{rsv}i_{vw}v^{wtu})l_s l_t l_u}_{O_A(n^{-3/2})}$$
$$+\underbrace{v^{rsu}i^{tv}H_{uv}l_s l_t+\tfrac{1}{2}i^{rs}v^{tuv}H_{st}l_u l_v+\tfrac{1}{2}i^{rs}i^{tu}i^{vw}H_{stv}l_u l_w}_{O_A(n^{-3/2})}+\underbrace{i^{rs}i^{tu}i^{vw}H_{st}H_{uv}l_w}_{O_A(n^{-3/2})}+O_A(n^{-2})+\cdots, \tag{2}$$

where $H_R \equiv l_R - v_R$. The terms are organized in decreasing asymptotic order. The drops occur in asymptotic orders of $n^{-1/2}$ under ordinary repeated sampling, which is equivalent to an asymptotic drop of $(\mathrm{SNR})^{-1/2}$. The asymptotic orders of each set of terms are indicated by symbols such as $O_A(n^{-m})$ which denotes a polynomial that will be of order n^{-m} when n is large but may contain higher order terms, i.e., $O_p(n^{-(m+1)})$, that can be significant when n is small. Here the symbol $O_p(n^{-m})$ denotes a polynomial of exactly order n^{-m} for all values of n.

The first order bias of the MLE is then the expected value of Eq. (2), as derived by Barndorff-Nielsen and Cox,[7]

$$b(\hat{\theta}^r) = E[(\hat{\theta}-\theta)^r] = \underbrace{\tfrac{1}{2} i^{ra} i^{bc} (v_{abc} + 2v_{ab,c})}_{O_p(n^{-1})} + O_p(n^{-3/2}) + \cdots . \tag{3}$$

Here we take a further step and use Eq. (2) to derive the error correlation of the MLE to second order as given by the order-separated expression

$$\begin{aligned}
\mathrm{Cor}(\hat{\theta}^r, \hat{\theta}^a) = E[(\hat{\theta}-\theta)^r (\hat{\theta}-\theta)^a] \\
= \underbrace{[i^{ra}]}_{O_p(n^{-1})} + [\underbrace{2 i^{mb} i^{nc} v_{lmn} (i^{rs} i^{la} + i^{as} i^{lr}) v_{s,b,c}(n^1) + \tfrac{1}{2} i^{cd} i^{ef} (i^{rs} i^{ab} + i^{as} i^{rb}) v_{bce,d,f,s}(n^2)}_{O_p(n^{-2})} \\
\underbrace{+ i^{tu} (i^{rs} i^{ab} i^{cd} + i^{rd} i^{ab} i^{cs} + i^{ad} i^{rb} i^{cs}) v_{st,u,bc,d}(n^2)}_{O_p(n^{-2})} \\
\underbrace{+ i^{bm} i^{cq} i^{tp} v_{lmn} v_{opq} (\tfrac{1}{4} i^{rl} i^{ao} i^{sn} + \tfrac{1}{2} i^{rs} i^{al} i^{on} + \tfrac{1}{2} i^{as} i^{rl} i^{on}) v_{s,t,b,c}(n^2)}_{O_p(n^{-2})} \\
\underbrace{+ \tfrac{1}{2} i^{sm} v_{lmn} (i^{tn} i^{cd} (i^{rl} i^{ab} + i^{al} i^{rb}) + 2 i^{bn} i^{cd} (i^{rl} i^{at} + i^{al} i^{rt}) + i^{cl} i^{tn} (i^{rd} i^{ab} + i^{ad} i^{rb})) v_{s,t,bc,d}(n^2)}_{O_p(n^{-2})} \\
\underbrace{+ \tfrac{1}{6} i^{mb} i^{nc} i^{od} v_{lmno} (i^{rs} i^{la} + i^{as} i^{rl}) v_{s,b,c,d}(n^2) + 4 i^{bm} (i^{rs} i^{al} + i^{as} i^{rl}) v_{s,m,lb}(n^1)}_{O_p(n^{-2})}] + O_p(n^{-3}) + \cdots ,
\end{aligned} \tag{4}$$

where notation such as $v_{bce,d,f,s}(n^2)$ means the n^2 order terms of the joint moment $v_{bce,d,f,s}$.

Using the identity $\mathrm{Cov}(\hat{\theta}^r, \hat{\theta}^a) = \mathrm{Cor}(\hat{\theta}^r, \hat{\theta}^a) - b(\theta^r) b(\theta^a)$, we obtain the following expression for the covariance of the MLE to second order:

$$\begin{aligned}
\mathrm{Cov}(\hat{\theta}^r, \hat{\theta}^a) = E[(\hat{\theta}^r - E[\theta^r])(\hat{\theta}^a - E[\theta^a])] \\
= \underbrace{[i^{ra}]}_{O_p(n^{-1})} + [\underbrace{2 i^{mb} i^{nc} v_{lmn} (i^{rs} i^{la} + i^{as} i^{lr}) v_{s,b,c}(n^1) + \tfrac{1}{2} i^{cd} i^{ef} (i^{rs} i^{ab} + i^{as} i^{rb}) v_{bce,d,f,s}(n^2)}_{O_p(n^{-2})} \\
\underbrace{+ i^{tu} (i^{rs} i^{ab} i^{cd} + i^{rd} i^{ab} i^{cs} + i^{ad} i^{rb} i^{cs}) v_{st,u,bc,d}(n^2)}_{O_p(n^{-2})} \\
\underbrace{+ i^{bm} i^{cq} i^{tp} v_{lmn} v_{opq} (\tfrac{1}{4} i^{rl} i^{ao} i^{sn} + \tfrac{1}{2} i^{rs} i^{al} i^{on} + \tfrac{1}{2} i^{as} i^{rl} i^{on}) v_{s,t,b,c}(n^2)}_{O_p(n^{-2})} \\
\underbrace{+ \tfrac{1}{2} i^{sm} v_{lmn} (i^{tn} i^{cd} (i^{rl} i^{ab} + i^{al} i^{rb}) + 2 i^{bn} i^{cd} (i^{rl} i^{at} + i^{al} i^{rt}) + i^{cl} i^{tn} (i^{rd} i^{ab} + i^{ad} i^{rb})) v_{s,t,bc,d}(n^2)}_{O_p(n^{-2})} \\
\underbrace{+ \tfrac{1}{6} i^{mb} i^{nc} i^{od} v_{lmno} (i^{rs} i^{la} + i^{as} i^{rl}) v_{s,b,c,d}(n^2) + 4 i^{bm} (i^{rs} i^{al} + i^{as} i^{rl}) v_{s,m,lb}(n^1)}_{O_p(n^{-2})} \\
\underbrace{- \tfrac{1}{4} i^{rs} i^{tu} i^{aw} i^{yz} (v_{stu} v_{wyz} + 2 v_{stu} v_{wy,z}(n^1) + 2 v_{st,u} v_{wyz}(n^1) + 4 v_{st,u} v_{wy,z}(n^1))}_{O_p(n^{-2})} + O_p(n^{-3}) + \cdots .
\end{aligned} \tag{5}$$

The first order covariance term i^{ra} is the *r, a* component of the inverse of the Fisher information, or the *r, a* component of the CRLB. A bound on the lowest possible mean square error of an *unbiased scalar* estimate that involves inverse sample size orders higher than n^{-1} was introduced by Bhattacharyya.[2] While it involves derivatives of the likelihood function, it is quite different from the multivariate covariance derived in Eq. (5) that is valid for multivariate estimates that may be biased. For discrete random variables, expressions equivalent to Eqs. (3)–(5) have been obtained in

a significantly different form via a different approach by Bowman and Shenton.[14]

A *necessary* condition for the MLE to become asymptotically unbiased. This is for the first order bias of Eq. (1) to become much smaller than the true value of the parameter θ^r. Similarly, a *necessary* condition for the MLE to asymptotically attain minimum variance is for the sum of second order terms in Eq. (5) to become much smaller than the first order term, which is the CRLB.

III. ASYMPTOTIC BIAS, ERROR CORRELATION AND COVARIANCE OF THE MLE FOR GAUSSIAN DATA

The asymptotic expressions presented for the bias, error correlation, and covariance of the MLE in Sec. II are now evaluated for real multivariate Gaussian data. General multivariate Gaussian data can be described by the conditional probability density

$$p(\mathbf{X};\boldsymbol{\theta}) = \frac{1}{(2\pi)^{nN/2}} \frac{1}{|\mathbf{C}(\boldsymbol{\theta})|^{n/2}} \exp\left\{ -\frac{1}{2} \sum_{i=1}^{n} (\mathbf{X}_i - \boldsymbol{\mu}(\boldsymbol{\theta}))^T \times \mathbf{C}^{-1}(\boldsymbol{\theta})(\mathbf{X}_i - \boldsymbol{\mu}(\boldsymbol{\theta})) \right\}, \tag{6}$$

where the data $\mathbf{X} = [\mathbf{X}_1^T \mathbf{X}_2^T \mathbf{X}_3^T \ldots \mathbf{X}_n^T]^T$ are comprised of n independent and identically distributed N-dimensional data vectors $\mathbf{X}_i$ to show an explicit dependence under normal repeated sampling for convenient reference. It is noteworthy that the CRLB is always proportional to $1/n$ but may be proportional to a more complicated function of the length of the data vector N.

We begin by deriving the first order bias for the general multivariate Gaussian case where the data covariance $\mathbf{C}$ and the data mean $\boldsymbol{\mu}$ depend on the parameter vector $\boldsymbol{\theta}$. The joint moments required to evaluate both the error correlation and covariance for the general case are quite complicated but not of great relevance in most standard ocean acoustic and signal processing problems.[8] They are not derived in this paper, but are the subject of another work where the second order bias is also derived.[15] We instead define two special cases that have great practical value, since they describe a deterministic signal in additive noise and a fully randomized signal in noise, respectively. In the former the data covariance $\mathbf{C}$ is independent of the parameter vector $\boldsymbol{\theta}$, while the mean $\boldsymbol{\mu}$ depends on $\boldsymbol{\theta}$ which is the subject of the estimation problem. In the latter, the data mean $\boldsymbol{\mu}$ is zero while the covariance $\mathbf{C}$ depends on the parameter vector $\boldsymbol{\theta}$ to be estimated. In the latter case, the sample covariance of the data is a sufficient statistic that contains all measurement information about the parameters to be estimated.[1,16]

The assumption of Gaussian data is valid, by virtue of the central limit theorem even for small n and N, when the total received field is the sum of a large number of statistically independent contributions. In the case of a deterministic signal in additive noise, the additive noise typically arises from a large number of independent sources distributed over the sea surface.[17] These noise sources may be either caused by the natural action of wind and waves on the sea surface, or they may be generated by ocean-going vessels.[18]

A particular fully randomized Gaussian signal model that is very widely used and enjoys a long history in acoustics, optics, and radar[19,20] is the circular complex Gaussian random (CCGR) model. The basic assumption in this model is that at any time instant, the received signal field is a CCGR variable.[9,19] This means that the real and imaginary parts of the instantaneous field are independent and identically distributed zero-mean Gaussian random variables. In active detection and imaging problems, this model is typically used to describe scattering from fluctuating targets[21,22] and surfaces with wavelength scale roughness.[9] When the target or resolved surface patch is large compared to the wavelength, the total received field can be thought of as arising from the sum of a large number of independent scatters so that the central limit theorem applies. Since World War II, the CCGR signal model has been used to describe ocean-acoustic transmission scintillation in what is known as the saturated region of multi-modal propagation.[19,23,24] In this regime, natural disturbances in the waveguide, such as underwater turbulence and passing surface or internal gravity waves, lead to such randomness in the medium that the waveguide modes at the receiver can be treated as statistically independent entities. The central limit theorem can then be invoked for the total received field, which behaves as a CCGR process in time.[16,19] In passive source localization problems in ocean-acoustics, the source signal is typically mechanical noise that is accidentally radiated into the ocean by a vessel. This noise typically has both narrow and broadband components that arise from a broad distribution of independent mechanical interactions that lead to a signal that can be represented as a CCGR process in time. The CCGR signal model has become a very standard model in ocean-acoustic matched field processing.[16,25,26]

A. The general multivariate Gaussian case

We obtain the following expression for the first order bias of the MLE given general multivariate Gaussian data

$$b(\hat{\theta}^r) = \tfrac{1}{2} i^{rs} i^{tu} (v_{stu} + 2v_{st,u}) + O_p(n^{-3/2})$$

$$= \sum_{s=1}^{m} \sum_{t=1}^{m} \sum_{u=1}^{m} \frac{2}{n} [\mathbf{i}^{-1}]_{rs} [\mathbf{i}^{-1}]_{tu} \left\{ \frac{1}{2} \mathrm{tr}\left(\mathbf{C}^{-1} \frac{\partial^2 \mathbf{C}}{\partial\theta^s\,\partial\theta^t} \mathbf{C}^{-1} \frac{\partial \mathbf{C}}{\partial\theta^u} \right) + \left(\frac{\partial^2 \boldsymbol{\mu}}{\partial\theta^s\,\partial\theta^t} \right)^T \mathbf{C}^{-1} \left(\frac{\partial \boldsymbol{\mu}}{\partial\theta^u} \right) + \left(\frac{\partial \boldsymbol{\mu}}{\partial\theta^s} \right)^T \mathbf{C}^{-1} \left(\frac{\partial \mathbf{C}}{\partial\theta^u} \right) \mathbf{C}^{-1} \left(\frac{\partial \boldsymbol{\mu}}{\partial\theta^t} \right) \right.$$

$$\left. - \sum_{s,t} \left(\frac{\partial^2 \boldsymbol{\mu}}{\partial\theta^s\,\partial\theta^u} \right)^T \mathbf{C}^{-1} \left(\frac{\partial \boldsymbol{\mu}}{\partial\theta^t} \right) - \sum_{s,t} \left(\frac{\partial \boldsymbol{\mu}}{\partial\theta^s} \right)^T \mathbf{C}^{-1} \left(\frac{\partial \mathbf{C}}{\partial\theta^t} \right) \mathbf{C}^{-1} \left(\frac{\partial \boldsymbol{\mu}}{\partial\theta^u} \right) - \frac{1}{2} \sum_{s,t} \mathrm{tr}\left(\mathbf{C}^{-1} \frac{\partial^2 \mathbf{C}}{\partial\theta^s\,\partial\theta^u} \mathbf{C}^{-1} \frac{\partial \mathbf{C}}{\partial\theta^t} \right) \right\}, \tag{7}$$

by substituting Eqs. (A1)–(A3) for the relevant joint moments into Eq. (3) for the first order bias, where $\Sigma_{s,t}$ indicates a sum over all possible permutations of s, t orderings, a total of two. For example, $\Sigma_{s,t} v_{st} = v_{st} + v_{ts}$.

It should be noted that the expression contains both tensor notation, denoted by the indices s, t, and u, and vector-matrix notation. For the first order bias, only first and second order parameter derivatives are required of the mean and covariance.

Suppose, for example, the bias of the vector

$$\hat{\theta} = \begin{bmatrix} \hat{\mu} \\ \hat{C} \end{bmatrix}$$

is desired, where $\hat{\mu}$ and $\hat{C}$ are the maximum likelihood estimates of the mean and variance, respectively, from a set of n independent and identically distributed Gaussian random variables x_i. The bias obtained from Eq. (6) is zero for the mean component and $-(C/n)$ for the variance component. This result can be readily verified by taking expectation values directly.[27]

It is noteworthy that the first order bias of a *scalar* parameter estimate always vanishes for general Gaussian data as can be seen by inspection of Eq. (7).

B. Deterministic signal in additive noise, parameter-independent covariance

The multivariate error correlation and covariance of the MLE can be obtained to second order for a deterministic signal vector in additive Gaussian noise by substituting Eqs. (B1)–(B10) into Eqs. (4) and (5), respectively. In this case, $\mathbf{C}$ is independent of $\boldsymbol{\theta}$ in Eq. (6). For scalar parameter and data, the following simple expressions for the mean-square error and variance are obtained

$$\mathrm{MSE}(\hat{\theta}) = \underbrace{\frac{C}{n(\mu')^2}}_{O_p(n^{-1})} + \underbrace{\frac{15C^2(\mu'')^2}{4n^2(\mu')^6} - \frac{C^2(\mu''')}{n^2(\mu')^5}}_{O_p(n^{-2})}, \tag{8}$$

$$\mathrm{var}(\hat{\theta}) = \underbrace{\frac{C}{n(\mu')^2}}_{O_p(n^{-1})} + \underbrace{\frac{14C^2(\mu'')^2}{4n^2(\mu')^6} - \frac{C^2(\mu''')}{n^2(\mu')^5}}_{O_p(n^{-2})}. \tag{9}$$

Suppose, for example, that the bias, mean-square error and variance of the MLE of the parameter $\theta = \mu^2$ are desired, where the x_i are again n independent and identically distributed Gaussian random variables, and C is independent of θ. The corresponding bias C/n, mean-square error $4C\mu^2/n + 3C^2/n^2$, and variance $4C\mu^2/n + 2C^2/n^2$, obtained using Eqs. (3)–(5) can be readily shown to correspond to those obtained by taking expectation values directly.[27] Since the MLE for $\theta = \mu^2$ is biased, the Bhattacharyya bound does not hold for this example and in fact can exceed the actual variance of the MLE.[27]

C. Random signal in noise: Zero-mean and parameter-dependent covariance

Similarly, the error correlation and covariance of the MLE can be obtained to second order for a zero-mean Gaussian random signal vector in Gaussian noise by substituting Eqs. (C1)–(C10) into Eqs. (4) and (5), respectively. In this case, $\boldsymbol{\mu}$ is zero in Eq. (6). For scalar parameter and data, the following simple expressions for the mean-square error and variance expressions are obtained:

$$\mathrm{MSE}(\hat{\theta}) = \underbrace{\frac{2C^2}{n(C')^2}}_{O_p(n^{-1})} - \underbrace{\frac{8C^3(C'')}{n^2(C')^4} + \frac{15C^4(C'')^2}{n^2(C')^6} - \frac{4C^4(C''')}{n^2(C')^5}}_{O_p(n^{-2})}, \tag{10}$$

$$\mathrm{var}(\hat{\theta}) = \underbrace{\frac{2C^2}{n(C')^2}}_{O_p(n^{-1})} - \underbrace{\frac{8C^3(C'')}{n^2(C')^4} + \frac{14C^4(C'')^2}{n^2(C')^6} - \frac{4C^4(C''')}{n^2(C')^5}}_{O_p(n^{-2})}. \tag{11}$$

Suppose, for example, that the bias, mean-square error, and variance of the MLE of the parameter $\theta = C^2$ are desired, where the x_i are n independent and identically distributed Gaussian random variables with zero-mean. It can be readily shown that the corresponding bias $2C^2/n$, mean-square error $8C^4/n + 44C^4/n^2$, and variance $8C^4/n + 40C^4/n^2$, obtained using Eqs. (3)–(5), correspond to those obtained by taking expectation values directly.[27]

IV. CONTINUOUS GAUSSIAN DATA: SIGNAL EMBEDDED IN WHITE GAUSSIAN NOISE

Let a real signal $\mu(t;\theta)$ that depends on parameter θ be received together with uncorrelated white Gaussian noise of power spectral density $N_0/2$ that is independent of θ. Suppose the real signal has Fourier transform $\mu(t;\theta) \leftrightarrow \Psi(f;\theta)$. The complex analytic signal and its Fourier transform $\tilde{\mu}(t;\theta) \leftrightarrow \tilde{\Psi}(f;\theta)$ are conventionally defined such that $\tilde{\Psi}(f;\theta) = 2\Psi(f;\theta)$ for $f > 0$, $\tilde{\Psi}(f;\theta) = 0$ for $f < 0$, and $\tilde{\Psi}(f;\theta) = \Psi(f;\theta)$ for $f = 0$, so that $\mu(t;\theta) = \mathrm{Re}\{\tilde{\mu}(t;\theta)\}$. The total received analytic signal, $\tilde{\varphi}_i(t)$, then follows the conditional probability density[28]

$$p(\tilde{\varphi}_i(t);\theta) = k \exp\left\{ -\frac{1}{2N_0} \int_0^T |(\tilde{\varphi}_i(t) - \tilde{\mu}(t;\theta))|^2 \, dt \right\}, \tag{12}$$

where k is a normalization constant. The bias, the mean-square error, and the variance of the MLE $\hat{\theta}$ are obtained from Eqs. (3)–(5) as

$$b(\hat{\theta}) = -\frac{N_0}{2} \frac{\mathrm{Re}\{\tilde{I}_2\}}{\tilde{I}_1^2}, \tag{13}$$

$$\mathrm{MSE}(\hat{\theta})=\underbrace{\frac{N_0}{\tilde{I}_1}}_{O_p(n^{-1})}+\underbrace{\frac{15N_0^2\,\mathrm{Re}\{\tilde{I}_2\}^2}{4\tilde{I}_1^4}-\frac{N_0^2\,\mathrm{Re}\{\tilde{I}_3\}}{\tilde{I}_1^3}}_{O_p(n^{-2})}, \tag{14}$$

$$\mathrm{var}(\hat{\theta})=\underbrace{\frac{N_0}{\tilde{I}_1}}_{O_p(n^{-1})}+\underbrace{\frac{14N_0^2\,\mathrm{Re}\{\tilde{I}_2\}^2}{4\tilde{I}_1^4}-\frac{N_0^2\,\mathrm{Re}\{\tilde{I}_3\}}{\tilde{I}_1^3}}_{O_p(n^{-2})}, \tag{15}$$

after evaluating the joint moments for the parameter-independent covariance, where $\tilde{I}_1$, $\tilde{I}_2$, $\tilde{I}_3$ are defined as follows:

$$\tilde{I}_1=\int\left(\frac{\partial\tilde{\mu}(t;\theta)}{\partial\theta}\right)^*\left(\frac{\partial\tilde{\mu}(t;\theta)}{\partial\theta}\right)dt, \tag{16}$$

$$\tilde{I}_2=\int\left(\frac{\partial\tilde{\mu}(t;\theta)}{\partial\theta}\right)^*\left(\frac{\partial\tilde{\mu}^2(t;\theta)}{\partial\theta^2}\right)dt, \tag{17}$$

$$\tilde{I}_3=\int\left(\frac{\partial\tilde{\mu}(t;\theta)}{\partial\theta}\right)^*\left(\frac{\partial\tilde{\mu}^3(t;\theta)}{\partial\theta^3}\right)dt. \tag{18}$$

There are two important issues to note. First, we are now working with continuously measured data as opposed to the discrete data vectors of Sec. III. Second, the fact that we are only estimating a scalar rather than a vector parameter greatly simplifies the evaluation of the joint moments.

V. TIME-DELAY ESTIMATION

Suppose $\tilde{\mu}(t;\theta)=\tilde{\mu}(t-\tau)$ in Eq. (12) so that the scalar time delay $\theta=\tau$ is to be estimated. The MLE $\hat{\theta}=\hat{\tau}$ of time-delay τ corresponds to the peak output of a matched filter for a signal received in additive Gaussian noise.[8] Estimates of the time delay between transmitted and received signal waveforms are typically used in active-sonar and radar applications to determine the range of a target in a nondispersive medium. The asymptotic bias, mean-square error, and variance of $\hat{\tau}$ are obtained by substituting τ for θ in Eqs. (13)–(18).

The following alternative expressions are obtained for Eqs. (16)–(18) by applying Parseval's Theorem

$$\tilde{I}_1=\int\left(\frac{\partial\tilde{\mu}(t-\tau)}{\partial\tau}\right)^*\left(\frac{\partial\tilde{\mu}(t-\tau)}{\partial\tau}\right)dt$$
$$=(2\pi)^2\int_0^\infty f^2|\tilde{\Psi}(f)|^2\,df, \tag{19}$$

$$\tilde{I}_2=\int\left(\frac{\partial\tilde{\mu}(t-\tau)}{\partial\tau}\right)^*\left(\frac{\partial\tilde{\mu}^2(t-\tau)}{\partial\tau^2}\right)dt$$
$$=j(2\pi)^3\int_0^\infty f^3|\tilde{\Psi}(f)|^2\,df, \tag{20}$$

$$\tilde{I}_3=\int\left(\frac{\partial\tilde{\mu}(t-\tau)}{\partial\tau}\right)^*\left(\frac{\partial\tilde{\mu}^3(t-\tau)}{\partial\tau^3}\right)dt$$
$$=-(2\pi)^4\int_0^\infty f^4|\tilde{\Psi}(f)|^2\,df. \tag{21}$$

Noting that the first order bias of Eq. (13) is directly proportional to $\mathrm{Re}\{\tilde{I}_2\}$, where $\mathrm{Re}\{\tilde{I}_2\}=0$ from Eq. (19), we find that *the first order bias for the maximum likelihood time-delay estimation problem is identically zero*, as expected by inspection of Eq. (7).

To evaluate the mean-square error and the variance, all three integrals are needed. Noting that $\mathrm{Re}\{\tilde{I}_2\}=0$ and $\mathrm{Re}\{\tilde{I}_3\}=\tilde{I}_3$ the following results are obtained:

$$\mathrm{MSE}(\hat{\tau})=\mathrm{var}(\hat{\tau})=\underbrace{\frac{N_0}{\tilde{I}_1}}_{O_p(n^{-1})}-\underbrace{\left(\frac{N_0}{\tilde{I}_1}\right)^2\frac{\mathrm{Re}\{\tilde{I}_3\}}{\tilde{I}_1}}_{O_p(n^{-2})}+O_p(n^{-3}), \tag{22}$$

where $\tilde{I}_1$, $\tilde{I}_3$ are evaluated in Eqs. (19) and (21), respectively. The mean-square error can also be expressed explicitly in terms of $\mathrm{SNR}=2E/N_0$ and signal parameters via

$$\mathrm{MSE}(\hat{\tau})=\mathrm{var}(\hat{\tau})$$
$$=\underbrace{\frac{1}{(2E/N_0)(\beta^2+\omega_c^2)}}_{O_p(n^{-1})}$$
$$+\underbrace{\frac{1}{(2E/N_0)^2}\frac{\gamma^4+8\omega_c^2\beta^2+3\omega_c^4}{(\beta^2+\omega_c^2)^3}}_{O_p(n^{-2})}+O_p(n^{-3}), \tag{23}$$

where $f_c=\omega_c/(2\pi)$ is the carrier frequency, E is the total energy of the real signal, β is commonly defined as the signal's root mean square (rms) bandwidth, and γ^4 is the fourth moment of the expected signal's energy spectrum.

$$2E=\int_{-f_c}^\infty|\tilde{\Psi}(v+f_c)|^2\,dv, \tag{24}$$

$$\beta^2=\frac{(2\pi)^2\int_{-f_c}^\infty v^2|\tilde{\Psi}(v+f_c)|^2\,dv}{2E}, \tag{25}$$

$$\gamma^4=\frac{(2\pi)^4\int_{-f_c}^\infty v^4|\tilde{\Psi}(v+f_c)|^2\,dv}{2E}. \tag{26}$$

Equation (23) explicitly shows the asymptotic dependence of the MLE time-delay variance on increasing orders of $(\mathrm{SNR})^{-1}$. For a base-banded signal, where $\omega_c=0$, the first order variance term of Eq. (23) is proportional to the inverse of β^2, while the second term is proportional to the ratio γ^4/β^6. While it is well known that the first order variance or CRLB decreases with increasing rms bandwidth at fixed SNR, the behavior of the second order variance term has a more complicated interpretation since it involves both γ and β.

The time-delay MLE asymptotically attains the CRLB when $(\gamma^4+8\omega_c^2\beta^2+3\omega_c^4)/(\beta^2+\omega_c^2)^2 \ll 2E/N_0 = \text{SNR}$. For a base-banded signal, this condition means that the SNR must be much larger than the *kurtosis* γ^4/β^4 of the expected signal's energy spectrum. This can be interpreted as meaning that as the signal's energy spectrum becomes more peaked, higher SNR is necessary to attain the CRLB.

Example 1

Assume a real Gaussian base-banded signal with a constant energy. Its waveform can be represented as

$$h(t)=\frac{1}{\sqrt{\tau_s}}\exp(-\pi(t^2/\tau_s^2)), \quad |t|\leqslant T/2,$$

where $h \leftrightarrow H$. For real signals, $2E$ is replaced by $E/2$, and Ψ replaces $\tilde{\Psi}$ in Eqs. (24)–(26), where in the present case $\Psi = H$. Under the assumption that τ_s/T is sufficiently small that the limits of integration $[-T/2,T/2]$ can be well approximated as $[-\infty,\infty]$, Eq. (23) for the variance of the time-delay MLE can be written to second order as

$$\text{var}(\hat{\tau})=\underbrace{\frac{N_0}{2}\frac{\sqrt{2}}{\pi}\tau_s^2}_{O_p(n^{-1})}+\underbrace{\left(\frac{N_0}{2}\right)^2\frac{6}{\pi}\tau_s^2}_{O_p(n^{-2})}.$$

Since the signal's energy is $1/\sqrt{2}$, the first and second order terms equalize when the SNR is 3, which is the kurtosis of a Gaussian density, where the $\text{SNR}=2E/N_0$. This makes sense because a Gaussian signal has a Gaussian energy spectrum by the convolution theorem. For SNRs less than 3, or in decibels for $10\log\text{SNR}<5$ dB, the second order term is higher than the first and the CRLB is a poor estimate of the true mean-square error. Moreover, since $1/\tau_s$ is a measure of the signal's bandwidth, decreasing τ_s, or increasing the signal's bandwidth, will decrease both first and second order variance terms, and so improve the time-delay estimate.

VI. DOPPLER SHIFT ESTIMATION

Suppose now that a *narrow band* signal waveform is transmitted in a nondispersive medium and measured with additive Gaussian noise at a receiver that is moving relative to the source at low Mach number $u/c \ll 1$, where u is the speed of relative motion and c the speed of wave propagation. The expected analytic signal waveform at the receiver $\tilde{\mu}(t;f_D)$ is then frequency shifted with Doppler-shift parameter $f_D=-2u/c$. The total signal and noise measured at the receiver will then obey the conditional probability density of Eq. (12) with $\theta=f_D$. The goal now is to examine the asymptotic statistics of the MLE $\hat{f}_D$ for the Doppler-shift parameter.

With the given assumptions, the signal waveform can be represented as

$$\tilde{\mu}(t;f_D)=\tilde{g}(t)e^{j2\pi t(f_c+f_D)}, \tag{27}$$

where the complex envelope $\tilde{g}(t)$ is known and is zero outside the interval $-T/2\leqslant t\leqslant T/2$. By applying Parseval's Theorem, the following expressions are obtained:

$$\tilde{I}_1=\int\left(\frac{\partial\tilde{\mu}(t;f_D)}{\partial f_D}\right)^*\left(\frac{\partial\tilde{\mu}(t;f_D)}{\partial f_D}\right)dt$$
$$=(2\pi)^2\int_{-T/2}^{T/2}t^2|\tilde{g}(t)|^2\,dt, \tag{28}$$

$$\tilde{I}_2=\int\left(\frac{\partial\tilde{\mu}(t;f_D)}{\partial f_D}\right)^*\left(\frac{\partial\tilde{\mu}^2(t;f_D)}{\partial f_D^2}\right)dt$$
$$=j(2\pi)^3\int_{-T/2}^{T/2}t^3|\tilde{g}(t)|^2\,dt, \tag{29}$$

$$\tilde{I}_3=\int\left(\frac{\partial\tilde{\mu}(t;f_D)}{\partial f_D}\right)^*\left(\frac{\partial\tilde{\mu}^3(t;f_D)}{\partial f_D^3}\right)dt$$
$$=-(2\pi)^4\int_{-T/2}^{T/2}t^4|\tilde{g}(t)|^2\,dt. \tag{30}$$

To evaluate the bias, $\tilde{I}_1$ and $\text{Re}\{\tilde{I}_2\}$ are substituted into Eq. (13). Noting that $\text{Re}\{\tilde{I}_2\}=0$, we find that *the first order bias for the Doppler-shift MLE* $\hat{f}_D$ *is identically zero*, as expected by inspection of Eq. (7).

Equations (28)–(30) are then substituted into Eqs. (14)–(15) to evaluate the mean-square error and the variance to second order. The resulting relations for the second order mean-square error and variance of the Doppler-shift MLE are similar to those obtained for the time-delay MLE:

$$\text{MSE}(\hat{f}_D)=\text{var}(\hat{f}_D)$$
$$=\underbrace{\frac{N_0}{\tilde{I}_1}}_{O_p(n^{-1})}-\underbrace{\left(\frac{N_0}{\tilde{I}_1}\right)^2\frac{\text{Re}\{\tilde{I}_3\}}{\tilde{I}_1}}_{O_p(n^{-2})}+O_p(n^{-3}), \tag{31}$$

since the two problems are related through the time-frequency duality principle. Expressing $\tilde{I}_1$, $\tilde{I}_3$ in terms of SNR and signal parameters then explicitly yields the Doppler-shift MLE mean-square error in terms of increasing orders of $(\text{SNR})^{-1}$ as

$$\text{MSE}(\hat{f}_D)=\text{var}(\hat{f}_D)$$
$$=\underbrace{\frac{1}{(2E/N_0)\alpha^2}}_{O_p(n^{-1})}+\underbrace{\frac{1}{(2E/N_0)^2}\frac{\delta^4}{\alpha^6}}_{O_p(n^{-2})}+O_p(n^{-3}), \tag{32}$$

where

$$2E=\int_{-T/2}^{T/2}|\tilde{g}(t)|^2\,dt, \tag{33}$$

$$\alpha^2=\frac{(2\pi)^2\int_{-T/2}^{T/2}t^2|\tilde{g}(t)|^2\,dt}{2E}, \tag{34}$$

$$\delta^4=\frac{(2\pi)^4\int_{-T/2}^{T/2}t^4|\tilde{g}(t)|^2\,dt}{2E}. \tag{35}$$

The Doppler-shift MLE then asymptotically attains the CRLB when $\delta^4/\alpha^4 \ll 2E/N_0 = \text{SNR}$. For an analytic signal

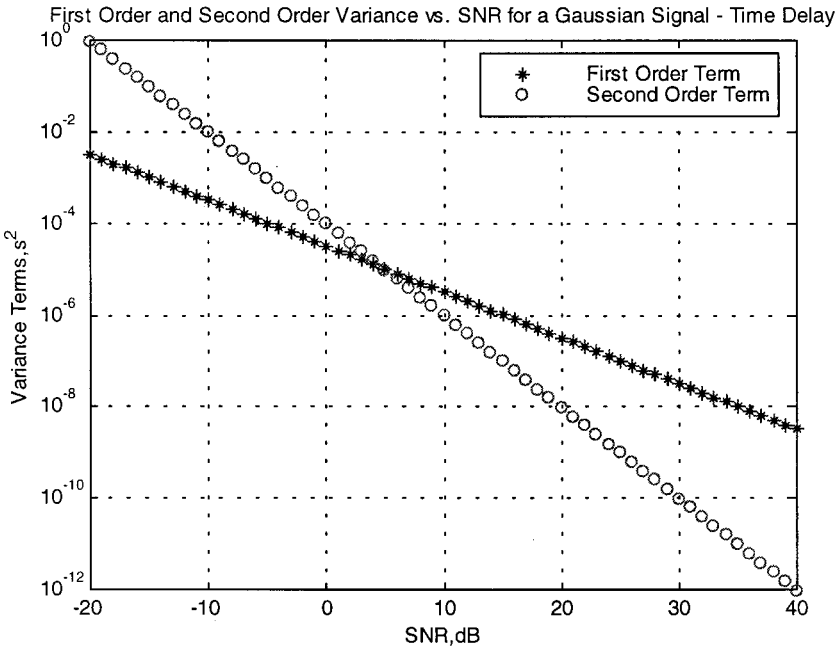

FIG. 1. Gaussian signal time-delay variance terms as a function of SNR.

with symmetric magnitude, this can be interpreted as meaning that the SNR must be large compared to the *kurtosis* of the signal's squared magnitude.

Example 2

For real signals where $\mu(t;f_D)=g(t)\cos 2\pi t(f_c+f_D)$, Eq. (32) can be used when $2E$ is replaced by $4E$ in Eqs. (34)–(35), and the real signal envelope $g(t)$ replaces $\tilde{g}(t)$ in Eqs. (33)–(35). For the CRLB to be attained in this real signal case, the SNR must be large compared to *twice* the *kurtosis* of the squared magnitude of the real signal envelope, assuming a symmetric magnitude. Computing E, α^2, and δ^4 for the real signal envelope $g(t)=h(t)$ of example 1, by Eq. (32), the variance of the Doppler-shift MLE can be written to second order as

$$\mathrm{var}(\hat{f}_D)=\underbrace{\frac{N_0}{2}\frac{2\sqrt{2}}{\pi}\frac{1}{\tau_s^2}}_{O_p(n^{-1})}+\underbrace{\left(\frac{N_0}{2}\right)^2\frac{24}{\pi}\frac{1}{\tau_s^2}}_{O_p(n^{-2})}+O_p(n^{-3}).$$

The first and second order terms equalize when the SNR is 6, twice the Gaussian kurtosis as expected, where SNR $=2E/N_0$. For SNRs less than 6, or in decibels when $10\log \mathrm{SNR}<7.8$ dB, the second order term is higher than the first, and the CRLB provides a poor estimate of the true MSH. Increasing τ_s decreases the signal's bandwidth and so also decreases both first and second order variance terms, which improves the Doppler-shift estimate.

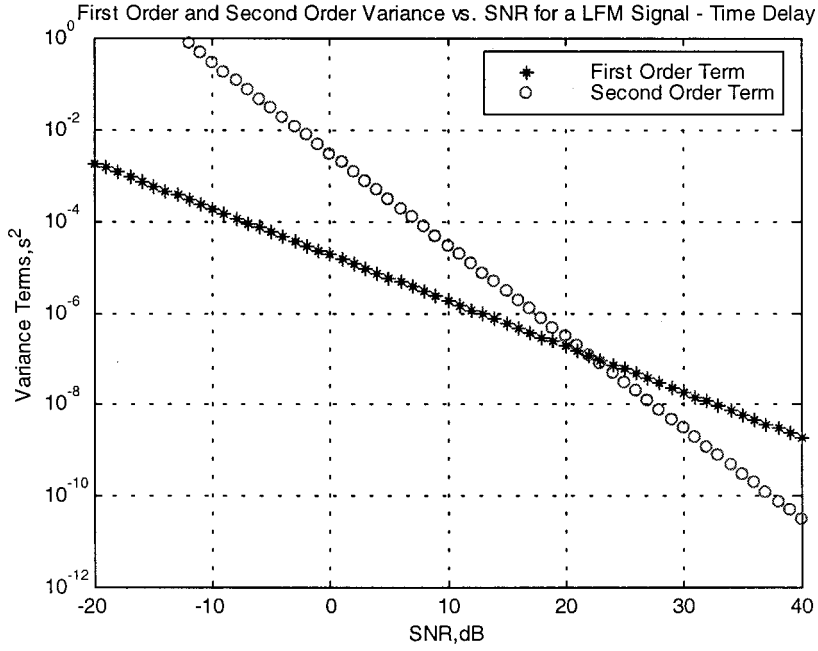

FIG. 2. LFM signal time-delay variance terms as a function of SNR.

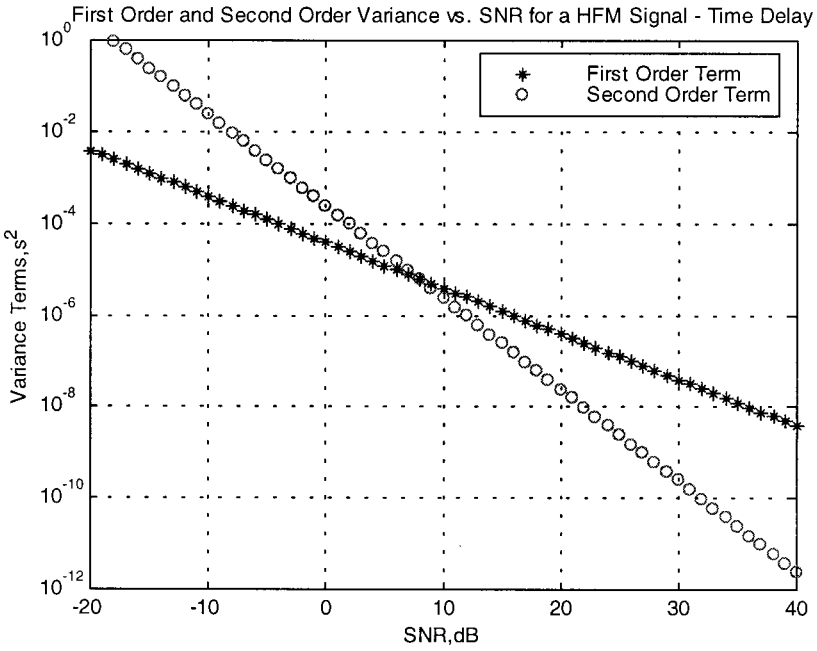

FIG. 3. HFM signal time-delay variance terms as a function of SNR.

VII. ASYMPTOTIC OPTIMALITY OF GAUSSIAN, LFM AND HFM WAVEFORMS IN MAXIMUM LIKELIHOOD TIME-DELAY AND DOPPLER-SHIFT ESTIMATION

The general expressions for the second order variance for both the MLE time-delay and the Doppler-shift estimators, Eqs. (22) and (31), are now implemented for the Gaussian linear frequency modulated (LFM) and hyperbolic frequency modulated (HFM) waveforms. All waveforms are demodulated.

The Gaussian signal is described in examples 1 and 2 above. The LFM signal is defined by

$$\mu(t)=\cos(\omega_0 t+\tfrac{1}{2}bt^2), \quad |t|\leqslant T/2, \tag{36}$$

where $f_0=\omega_0/2\pi$ is the carrier frequency and the bandwidth is given by $bT/2\pi$. The signal is demodulated when multiplied by $\cos(\omega_0 t)$ and low-pass filtered. The HFM signal is defined by

$$\mu(t)=\sin(\alpha\log(1-k(t+T/2))), \quad |t|\leqslant T/2, \tag{37}$$

where $k=(f_2-f_1)/f_2T$, $\alpha=-2\pi f_1/k$, and f_1 and f_2 are the frequencies that bound the signal's spectrum. This signal is demodulated when multiplied by $\cos(\omega_0 t)$, where $f_0=\sqrt{f_1 f_2}$, and is low-pass filtered. To control sidelobes in the frequency domain, the signal is often multiplied by a temporal window function, or taper. We use the modified Tukey window that has the form

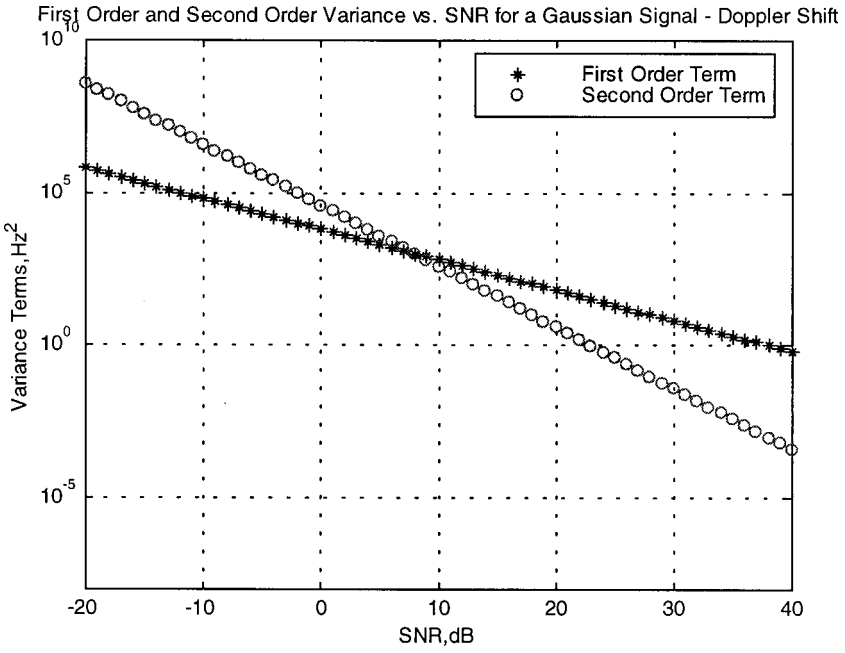

FIG. 4. LFM signal Doppler-shift variance terms as a function of SNR.

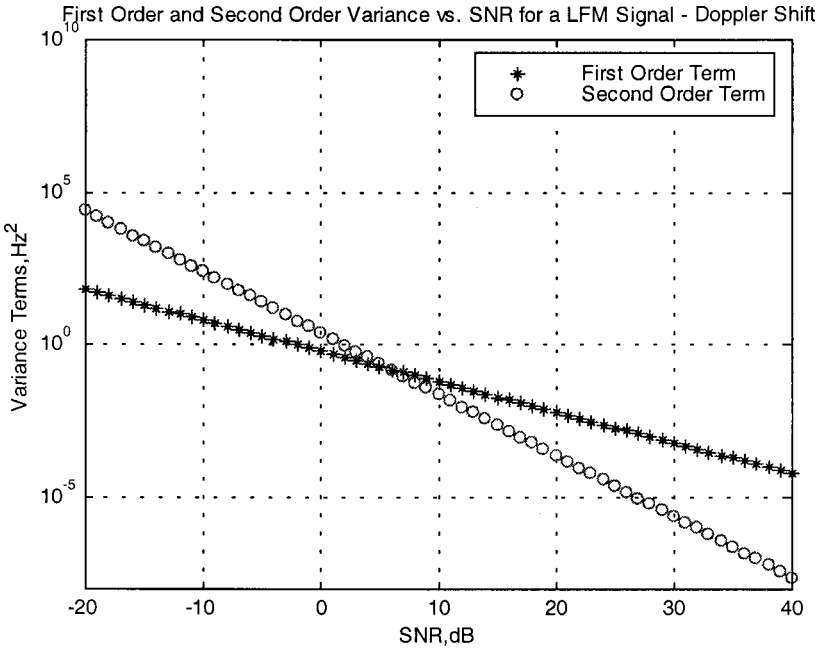

FIG. 5. Gaussian signal Doppler-shift variance terms as a function of SNR.

$$w(t) = \begin{cases} p+(1-p)\sin^2\left(\pi\dfrac{t+T/2}{2T_w}\right) & \text{for } 0\leqslant t\leqslant T_w \\ 1 & \text{for } T_w\leqslant t\leqslant T-T_w \\ p+(1-p)\sin^2\left(\pi\dfrac{(t+T/2)-(T-2T_w)}{2T_w}\right) & \text{for } T-T_w\leqslant t\leqslant T \end{cases}, \tag{38}$$

where $T_w=0.125T$ is the window duration and $p=0.1$ is the pedestal used.

The dependence of the first and second order variance terms on SNR is presented in Figs. 1–3 for the time-delay MLE and in Figs. 4–6 for the Doppler-shift MLE for the three signals. The bandwidth is fixed at 100 Hz in Figs. 1–6, for a typical low-frequency active-sonar scenario.[29] The figures illustrate some important characteristics of the variance terms for both the time-delay and the Doppler-shift MLE. As SNR increases, the first order variance exhibits the expected linear fall-off and the second order variance falls off with the expected second order power law as can be seen more generally in Eqs. (23) and (32) where the second order term is proportional to $-20\log_{10}(N_0/2E)$, and the first to $-10\log_{10}(N_0/2E)$. The value of either term at a specific bandwidth and SNR can then be used to determine its value at the same bandwidth for all SNRs.

Table I specifies the SNR's values beyond which the second order variance can be neglected relative to the first by

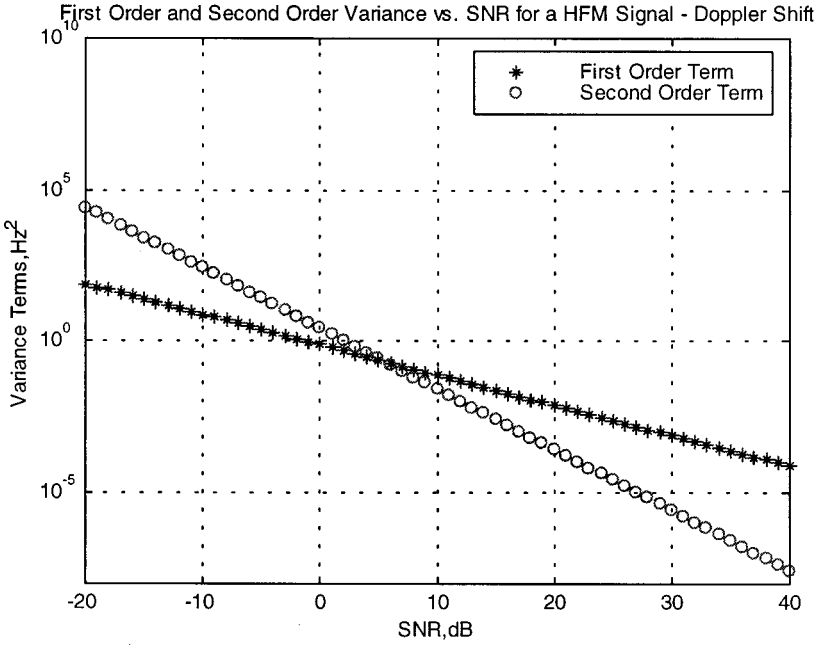

FIG. 6. HFM signal Doppler-shift variance terms as a function of SNR.

TABLE I. Minimum signal-to-noise ratios (SNRs) *necessary* for the MLE to asymptotically attain the CRLB. The given values are the minimum SNRs needed for the CRLB to exceed the second order MLE variance by 10 dB. All signals have 100 Hz bandwidth.

	Gaussian signal	LFM signal	HFM signal
Time Delay	15 dB	32 dB	18 dB
Doppler Shift	18 dB	16 dB	15 dB

showing where the former is an order of magnitude less than the latter. Table I then provides conditions *necessary* for the MLE to attain the CRLB in time-delay and Doppler-shift estimation for the given signals. It also specifies conditions *necessary* for the MLE to be approximated as a linear function of the measured data.

VIII. CONCLUSION

By employing an asymptotic expansion of the likelihood function, expressions for the first order bias, as well as the second order covariance and error correlation of a general MLE, are derived. These expressions are used to determine conditions *necessary* for the MLE to become asymptotically unbiased and attain the CRLB. The approach is then applied to parameter estimation with multivariate Gaussian data. Analytic expressions for the general first order bias of the multivariate Gaussian MLE and the second order error covariance and correlation of the MLE for two special cases of multivariate Gaussian data that are of great practical significance in acoustics, optics, radar, seismology, and signal processing. The first is where the data covariance matrix is independent of the parameters to be estimated, the standard deterministic signal in additive noise scenario. The second is where the data mean is zero and the signal as well as the noise undergo circular complex Gaussian random fluctuations. In a companion paper, the expressions derived here are applied to determine the asymptotic bias, covariance, and mean-square error of maximum likelihood range and depth estimates of a sound source submerged in an ocean waveguide from measured hydrophone array data.[11] Necessary conditions for these source localization estimates to attain the CRLB are also obtained.[11]

In the present paper, general expressions for the first order bias, second order mean-square error, and variance of scalar maximum likelihood time-delay and Doppler-shift estimates are obtained for deterministic signals in additive Gaussian noise. The time-delay MLE is the peak value of a matched filter output. Both time-delay and Doppler-shift MLEs are shown to be unbiased to first order. Analytic conditions on SNR necessary for the time-delay and Doppler-shift MLEs to attain the CRLB are provided in terms of moments of the expected signal's squared magnitude and energy spectrum. For base-banded signals, the time-delay MLE, namely the matched filter estimate, attains the CRLB when the *kurtosis* of the expected signal's energy spectrum is much smaller than the SNR. This can be interpreted as meaning that higher SNR is necessary to attain the CRLB as a demodulated signal's energy spectrum becomes more peaked. The Doppler-shift MLE is found to have dual behavior for narrow band analytic signals.

APPENDIX A: JOINT MOMENTS FOR ASYMPTOTIC GAUSSIAN INFERENCE: GENERAL MULTIVARIATE GAUSSIAN DATA

For the *general multivariate Gaussian* case of Eq. (6), both the mean $\boldsymbol{\mu}$ and the covariance matrix $\mathbf{C}$ depend on the parameter vector $\boldsymbol{\theta}$. The joint moments required to evaluate the first order bias are

$$i_{ab}=\frac{n}{2}\mathrm{tr}(\mathbf{C}^{-1}\mathbf{C}_a\mathbf{C}^{-1}\mathbf{C}_b)+n\boldsymbol{\mu}_a^T\mathbf{C}^{-1}\boldsymbol{\mu}_b, \tag{A1}$$

$$\begin{aligned} v_{abc}=&\frac{n}{3}\sum_{a,b,c}\mathrm{tr}(\mathbf{C}^{-1}\mathbf{C}_a\mathbf{C}^{-1}\mathbf{C}_b\mathbf{C}^{-1}\mathbf{C}_c)\\ &-\frac{n}{4}\sum_{a,b,c}\mathrm{tr}(\mathbf{C}^{-1}\mathbf{C}_{ab}\mathbf{C}^{-1}\mathbf{C}_c)-\frac{n}{2}\sum_{a,b,c}\boldsymbol{\mu}_{ab}^T\mathbf{C}^{-1}\boldsymbol{\mu}_c\\ &+\frac{n}{2}\sum_{a,b,c}\boldsymbol{\mu}_a^T\mathbf{C}^{-1}\mathbf{C}_b\mathbf{C}^{-1}\boldsymbol{\mu}_c, \end{aligned} \tag{A2}$$

$$\begin{aligned} v_{ab,c}=&-\frac{n}{2}\sum_{a,b}\mathrm{tr}(\mathbf{C}^{-1}\mathbf{C}_a\mathbf{C}^{-1}\mathbf{C}_b\mathbf{C}^{-1}\mathbf{C}_c)+n\boldsymbol{\mu}_{ab}^T\mathbf{C}^{-1}\boldsymbol{\mu}_c\\ &+\frac{n}{2}\mathrm{tr}(\mathbf{C}^{-1}\mathbf{C}_{ab}\mathbf{C}^{-1}\mathbf{C}_c)\\ &-n\sum_{a,b}\boldsymbol{\mu}_a^T\mathbf{C}^{-1}\mathbf{C}_b\mathbf{C}^{-1}\boldsymbol{\mu}_c, \end{aligned} \tag{A3}$$

where, for example, $\Sigma_{a,b,c}$ indicates a sum over all possible permutations of *a*, *b* and *c* orderings, leading to a total of six terms. Terms such as $\mathbf{C}_{ab}$ and $\boldsymbol{\mu}_{ab}$ represent the derivatives of the covariance matrix $\mathbf{C}$ and the mean vector $\boldsymbol{\mu}$ with respect to θ^a and θ^b, respectively.

APPENDIX B: JOINT MOMENTS FOR ASYMPTOTIC GAUSSIAN INFERENCE: MULTIVARIATE GAUSSIAN DATA WITH PARAMETER-INDEPENDENT COVARIANCE: DETERMINISTIC SIGNAL IN INDEPENDENT ADDITIVE NOISE

For this case the covariance matrix of Eq. (6) is independent of the parameters to be estimated, i.e., $\partial\mathbf{C}/\partial\theta^i=0$ for all *i*. The joint moments required to evaluate the first order bias, as well as the second order error correlation and covariance are

$$i_{ab}=n\boldsymbol{\mu}_a^T\mathbf{C}^{-1}\boldsymbol{\mu}_b, \tag{B1}$$

$$v_{abc}(n^1)=-\frac{n}{2}\sum_{a,b,c}\boldsymbol{\mu}_{ab}^T\mathbf{C}^{-1}\boldsymbol{\mu}_c, \tag{B2}$$

$$v_{a,b,c}(n^1)=0, \tag{B3}$$

$$v_{ab,c}(n^1)=n\boldsymbol{\mu}_{ab}^T\mathbf{C}^{-1}\boldsymbol{\mu}_c, \tag{B4}$$

$$\begin{aligned} v_{abcd}(n^1)=&-\frac{n}{8}\sum_{a,b,c,d}\boldsymbol{\mu}_{ab}^T\mathbf{C}^{-1}\boldsymbol{\mu}_{cd}\\ &-\frac{n}{6}\sum_{a,b,c,d}\boldsymbol{\mu}_{abc}^T\mathbf{C}^{-1}\boldsymbol{\mu}_d, \end{aligned} \tag{B5}$$

$$v_{a,b,c,d}(n^2)=\frac{n^2}{8}\sum_{a,b,c,d}\boldsymbol{\mu}_a^T\mathbf{C}^{-1}\boldsymbol{\mu}_b\boldsymbol{\mu}_c^T\mathbf{C}^{-1}\boldsymbol{\mu}_d, \tag{B6}$$

$$v_{a,b,cd}(n^1)=0, \tag{B7}$$

$$v_{a,b,c,de}(n^2)=\frac{n^2}{2}\sum_{a,b,c}\boldsymbol{\mu}_a^T\mathbf{C}^{-1}\boldsymbol{\mu}_b\boldsymbol{\mu}_c^T\mathbf{C}^{-1}\boldsymbol{\mu}_{de}, \tag{B8}$$

$$v_{a,b,cd,ef}(n^2)=\frac{n^2}{2}\sum_{(a,b)\times(cd,ef)}\boldsymbol{\mu}_a^T\mathbf{C}^{-1}\boldsymbol{\mu}_{cd}\boldsymbol{\mu}_b^T\mathbf{C}^{-1}\boldsymbol{\mu}_{ef}+n^2\boldsymbol{\mu}_{cd}^T\mathbf{C}^{-1}\boldsymbol{\mu}_{ef}\boldsymbol{\mu}_a^T\mathbf{C}^{-1}\boldsymbol{\mu}_b, \tag{B9}$$

$$v_{a,b,c,def}(n^2)=\frac{n^2}{2}\sum_{a,b,c}\boldsymbol{\mu}_a^T\mathbf{C}^{-1}\boldsymbol{\mu}_b\boldsymbol{\mu}_c^T\mathbf{C}^{-1}\boldsymbol{\mu}_{def}, \tag{B10}$$

where the notation $\Sigma_{(a,b)\times(cd,ef)}$ indicates a sum over all possible permutations of a and b orderings combined with permutations of cd and ef orderings, leading to a total of four terms.

APPENDIX C: JOINT MOMENTS FOR ASYMPTOTIC GAUSSIAN INFERENCE; MULTIVARIATE GAUSSIAN DATA WITH ZERO-MEAN: RANDOM SIGNAL IN NOISE

For this case the mean is zero in Eq. (6). The joint moments required to evaluate the first order bias, as well as the second order error correlation and covariance are then

$$i_{ab}=\frac{n}{2}\mathrm{tr}(\mathbf{C}^{-1}\mathbf{C}_a\mathbf{C}^{-1}\mathbf{C}_b), \tag{C1}$$

$$v_{abc}(n^1)=\frac{n}{3}\sum_{a,b,c}\mathrm{tr}(\mathbf{C}^{-1}\mathbf{C}_a\mathbf{C}^{-1}\mathbf{C}_b\mathbf{C}^{-1}\mathbf{C}_c)-\frac{n}{4}\sum_{a,b,c}\mathrm{tr}(\mathbf{C}^{-1}\mathbf{C}_{ab}\mathbf{C}^{-1}\mathbf{C}_c), \tag{C2}$$

$$v_{a,b,c}(n^1)=\frac{n}{6}\sum_{a,b,c}\mathrm{tr}(\mathbf{C}^{-1}\mathbf{C}_a\mathbf{C}^{-1}\mathbf{C}_b\mathbf{C}^{-1}\mathbf{C}_c), \tag{C3}$$

$$v_{ab,c}(n^1)=-\frac{n}{2}\sum_{a,b}\mathrm{tr}(\mathbf{C}^{-1}\mathbf{C}_a\mathbf{C}^{-1}\mathbf{C}_b\mathbf{C}^{-1}\mathbf{C}_c)+\frac{n}{2}\mathrm{tr}(\mathbf{C}^{-1}\mathbf{C}_{ab}\mathbf{C}^{-1}\mathbf{C}_c), \tag{C4}$$

$$v_{abcd}(n^1)=-\frac{3n}{8}\sum_{a,b,c,d}\mathrm{tr}(\mathbf{C}^{-1}\mathbf{C}_a\mathbf{C}^{-1}\mathbf{C}_b\mathbf{C}^{-1}\mathbf{C}_c\mathbf{C}^{-1}\mathbf{C}_d)+\frac{n}{2}\sum_{a,b,c,d}\mathrm{tr}(\mathbf{C}^{-1}\mathbf{C}_{ab}\mathbf{C}^{-1}\mathbf{C}_c\mathbf{C}^{-1}\mathbf{C}_d)-\frac{n}{16}\sum_{a,b,c,d}\mathrm{tr}(\mathbf{C}^{-1}\mathbf{C}_{ab}\mathbf{C}^{-1}\mathbf{C}_{cd})-\frac{n}{12}\sum_{a,b,c,d}\mathrm{tr}(\mathbf{C}^{-1}\mathbf{C}_{abc}\mathbf{C}^{-1}\mathbf{C}_d), \tag{C5}$$

$$v_{a,b,c,d}(n^2)=\frac{n^2}{32}\sum_{a,b,c,d}\mathrm{tr}(\mathbf{C}^{-1}\mathbf{C}_a\mathbf{C}^{-1}\mathbf{C}_b)\mathrm{tr}(\mathbf{C}^{-1}\mathbf{C}_c\mathbf{C}^{-1}\mathbf{C}_d), \tag{C6}$$

$$v_{a,b,cd}(n^1)=-\frac{n}{2}\times\sum_{(a,b)\times(c,d)}\mathrm{tr}(\mathbf{C}^{-1}\mathbf{C}_a\mathbf{C}^{-1}\mathbf{C}_b\mathbf{C}^{-1}\mathbf{C}_c\mathbf{C}^{-1}\mathbf{C}_d)+\frac{n}{2}\sum_{a,b}\mathrm{tr}(\mathbf{C}^{-1}\mathbf{C}_a\mathbf{C}^{-1}\mathbf{C}_b\mathbf{C}^{-1}\mathbf{C}_{cd}), \tag{C7}$$

$$v_{a,b,c,de}(n^2)=-\frac{n^2}{24}\sum_{(a,b,c)\times(d,e)}\mathrm{tr}(\mathbf{C}^{-1}\mathbf{C}_d\mathbf{C}^{-1}\mathbf{C}_e)\times\mathrm{tr}(\mathbf{C}^{-1}\mathbf{C}_a\mathbf{C}^{-1}\mathbf{C}_b\mathbf{C}^{-1}\mathbf{C}_c)-\frac{n^2}{8}\sum_{(a,b,c)\times(d,e)}\mathrm{tr}(\mathbf{C}^{-1}\mathbf{C}_a\mathbf{C}^{-1}\mathbf{C}_b)\times\mathrm{tr}(\mathbf{C}^{-1}\mathbf{C}_c\mathbf{C}^{-1}\mathbf{C}_d\mathbf{C}^{-1}\mathbf{C}_e)+\frac{n^2}{8}\sum_{a,b,c}\mathrm{tr}(\mathbf{C}^{-1}\mathbf{C}_a\mathbf{C}^{-1}\mathbf{C}_b)\times\mathrm{tr}(\mathbf{C}^{-1}\mathbf{C}_c\mathbf{C}^{-1}\mathbf{C}_{de}), \tag{C8}$$

$$v_{a,b,cd,ef}(n^2)=\frac{n^2}{8}\sum_{(cd,ef)\times(a,b)\times(c,d)\times(e,f)}\left\{\mathrm{tr}(\mathbf{C}^{-1}\mathbf{C}_c\mathbf{C}^{-1}\mathbf{C}_d)\left[\mathrm{tr}(\mathbf{C}^{-1}\mathbf{C}_a\mathbf{C}^{-1}\mathbf{C}_b\mathbf{C}^{-1}\mathbf{C}_e\mathbf{C}^{-1}\mathbf{C}_f)-\frac{1}{2}\mathrm{tr}(\mathbf{C}^{-1}\mathbf{C}_a\mathbf{C}^{-1}\mathbf{C}_b\mathbf{C}^{-1}\mathbf{C}_{ef})\right]\right\}$$
$$+\frac{n^2}{8}\sum_{(cd,ef)\times(a,b)\times(c,d)\times(e,f)}\left\{\mathrm{tr}(\mathbf{C}^{-1}\mathbf{C}_a\mathbf{C}^{-1}\mathbf{C}_b)\left[\frac{1}{2}\mathrm{tr}(\mathbf{C}^{-1}\mathbf{C}_c\mathbf{C}^{-1}\mathbf{C}_d\mathbf{C}^{-1}\mathbf{C}_e\mathbf{C}^{-1}\mathbf{C}_f)\right.\right.$$
$$\left.\left.-\frac{1}{2}\mathrm{tr}(\mathbf{C}^{-1}\mathbf{C}_c\mathbf{C}^{-1}\mathbf{C}_d\mathbf{C}^{-1}\mathbf{C}_{ef})+\tfrac{1}{8}\mathrm{tr}(\mathbf{C}^{-1}\mathbf{C}_{cd}\mathbf{C}^{-1}\mathbf{C}_{ef})\right]\right\}$$
$$+\frac{n^2}{8}\sum_{(cd,ef)\times(a,b)\times(c,d)\times(e,f)}\mathrm{tr}(\mathbf{C}^{-1}\mathbf{C}_a\mathbf{C}^{-1}\mathbf{C}_c\mathbf{C}^{-1}\mathbf{C}_d)\mathrm{tr}(\mathbf{C}^{-1}\mathbf{C}_b\mathbf{C}^{-1}\mathbf{C}_e\mathbf{C}^{-1}\mathbf{C}_f)$$

$$+\frac{n^2}{8}\sum_{(cd,ef)\times(a,b)}\mathrm{tr}(\mathbf{C}^{-1}\mathbf{C}_a\mathbf{C}^{-1}\mathbf{C}_{cd})\mathrm{tr}(\mathbf{C}^{-1}\mathbf{C}_b\mathbf{C}^{-1}\mathbf{C}_{ef})$$

$$-\frac{n^2}{8}\sum_{(cd,ef)\times(a,b)\times(c,d)\times(e,f)}\mathrm{tr}(\mathbf{C}^{-1}\mathbf{C}_a\mathbf{C}^{-1}\mathbf{C}_{cd})\mathrm{tr}(\mathbf{C}^{-1}\mathbf{C}_b\mathbf{C}^{-1}\mathbf{C}_e\mathbf{C}^{-1}\mathbf{C}_f), \tag{C9}$$

$$v_{a,b,c,def}(n^2)=\frac{n^2}{18}\sum_{(a,b,c)\times(d,e,f)}\mathrm{tr}(\mathbf{C}^{-1}\mathbf{C}_a\mathbf{C}^{-1}\mathbf{C}_b\mathbf{C}^{-1}\mathbf{C}_c)\mathrm{tr}(\mathbf{C}^{-1}\mathbf{C}_d\mathbf{C}^{-1}\mathbf{C}_e\mathbf{C}^{-1}\mathbf{C}_f)$$

$$-\frac{n^2}{24}\sum_{(a,b,c)\times(d,e,f)}\mathrm{tr}(\mathbf{C}^{-1}\mathbf{C}_a\mathbf{C}^{-1}\mathbf{C}_b\mathbf{C}^{-1}\mathbf{C}_c)\mathrm{tr}(\mathbf{C}^{-1}\mathbf{C}_{de}\mathbf{C}^{-1}\mathbf{C}_f)$$

$$+\frac{n^2}{8}\sum_{(a,b,c)\times(d,e,f)}\{\mathrm{tr}(\mathbf{C}^{-1}\mathbf{C}_a\mathbf{C}^{-1}\mathbf{C}_b)[\mathrm{tr}(\mathbf{C}^{-1}\mathbf{C}_c\mathbf{C}^{-1}\mathbf{C}_d\mathbf{C}^{-1}\mathbf{C}_e\mathbf{C}^{-1}\mathbf{C}_f)$$

$$-\mathrm{tr}(\mathbf{C}^{-1}\mathbf{C}_c\mathbf{C}^{-1}\mathbf{C}_{de}\mathbf{C}^{-1}\mathbf{C}_f)+\tfrac{1}{6}\mathrm{tr}(\mathbf{C}^{-1}\mathbf{C}_c\mathbf{C}^{-1}\mathbf{C}_{def})]\}. \tag{C10}$$

The notation $\Sigma_{(a,b,c)\times(d,e,f)}$ indicates summation over all possible permutations of *d*, *e*, *f* and *a*, *b* and *c*, leading to a total of 36 terms.

APPENDIX D: DERIVATION OF THE ASYMPTOTIC EXPANSION OF THE MAXIMUM LIKELIHOOD ESTIMATE

Following Barndoff-Nielsen and Cox,[7] Eq. (1) is first inverted for $(\hat{\theta}-\theta)^r$ to obtain the expansion

$$(\hat{\theta}-\theta)^r=j^{rs}l_s+\tfrac{1}{2}j^{rs}l_{stu}(\hat{\theta}-\theta)^t(\hat{\theta}-\theta)^u+\tfrac{1}{6}j^{rs}l_{stuv}\times(\hat{\theta}-\theta)^t(\hat{\theta}-\theta)^u(\hat{\theta}-\theta)^v+\cdots, \tag{D1}$$

where j^{rs} is the inverse of the observed information matrix $j_{rs}=-l_{rs}$. Iterating this procedure leads to an expression for $(\hat{\theta}-\theta)^r$ that is solely in terms of the derivatives of the likelihood function

$$(\hat{\theta}-\theta)^r=j^{rs}l_s+\tfrac{1}{2}j^{rs}j^{tu}j^{vw}l_{stv}l_ul_w+\tfrac{1}{6}j^{rs}j^{tu}j^{vw}j^{xy}(l_{suyw}+3l_{swp}j^{pq}l_{quy})l_tl_vl_x+\cdots. \tag{D2}$$

The difficulty with this expression is that j^{rs} is not well defined for all likelihood functions and all values of $\hat{\theta}$. This problem is circumvented by expanding j^{rs} in terms of well-defined quantities. First, note that

$$\mathbf{j}=\mathbf{i}\{\mathbf{I}-\mathbf{i}^{-1}(\mathbf{i}-\mathbf{j})\}, \tag{D3}$$

where $\mathbf{I}$ is the identity matrix. The inverse is then

$$\mathbf{j}^{-1}=\{\mathbf{I}-\mathbf{i}^{-1}(\mathbf{i}-\mathbf{j})\}^{-1}\mathbf{i}^{-1}. \tag{D4}$$

which can be expanded as

$$\mathbf{j}^{-1}=\mathbf{i}^{-1}+\mathbf{i}^{-1}(\mathbf{i}-\mathbf{j})\mathbf{i}^{-1}+\mathbf{i}^{-1}(\mathbf{i}-\mathbf{j})\mathbf{i}^{-1}(\mathbf{i}-\mathbf{j})\mathbf{i}^{-1}+\cdots, \tag{D5}$$

or equivalently as

$$j^{rs}=i^{rs}+i^{rt}i^{su}H_{tu}+i^{rt}i^{su}i^{vw}H_{tv}H_{uw}+\cdots, \tag{D6}$$

where $H_R=l_R-v_R$ for any set of coordinate indices $R=r_1\ldots r_m$, where, for example, $H_{tu}=l_{tu}-v_{tu}$. Inserting Eq. (D6) into Eq. (D2) then leads to Eq. (2).

[1] C. R. Rao, *Linear Statistical Inference and its Applications* (Wiley, New York, 1966).
[2] A. Battacharya, "On some analogues of the amount of information and their uses in statistical estimation," Sonkhya **8**, 1–14, 201–218, 315–328 (1946).
[3] E. W. Barankin, "Locally best unbiased estimators," Ann. Math. Stat. **20**, 477–501 (1949).
[4] D. Chazan, M. Zakai, and J. Ziv, "Improved lower bounds on signal parameter estimation," IEEE Trans. Inf. Theory **IT-21**, 90–93 (1975).
[5] A. J. Weiss and E. Weinstein, "Fundamental limitations in passive time delay estimation," IEEE Trans. Acoust., Speech, Signal Process. **ASSP-31**, 472–485 (1983).
[6] R. A. Fisher, *Statistical Methods and Scientific Inference* (Hafner, New York, 1956).
[7] O. E. Barndorff-Nielsen and D. R. Cox, *Inference and Asymptotics* (Chapman & Hall, London, 1994).
[8] H. L. Van Trees, *Detection, Estimation, and Linear Modulation Theory—Part III* (Wiley, New York, 1971).
[9] J. W. Goodman, *Statistical Optics* (Wiley, New York, 1985).
[10] O. Diachok, A. Caiti, P. Gerstoft, and H. Schmidt, Eds., *Full Field Inversion Methods in Ocean and Seismic Acoustics* (Kluwer, Dordrecht, 1995).
[11] A. Thode, E. Naftali, Ian Ingram, P. Ratilal, and N. C. Makris, "Necessary conditions for a maximum likelihood estimate to attain the Cramer-Rao lower bound. Part II: Range and depth localization of a sound source in an ocean waveguide," J. Acoust. Soc. Am. (submitted).
[12] A. Zeira and P. Schultheiss, "Realizable lower bounds for time delay estimation," IEEE Trans. Signal Process. **41**, 3102–3113 (1993).
[13] A. B. Baggeroer, "Barankin bound on the variance of estimates of the parameter of a Gaussian random process," M.I.T. Res. Lab., Cambridge, MA, Electron, Quart. Prog. Rep. **92**, 324–333 (1969).
[14] L. R. Shenton and K. O. Bowman, *Maximum Likelihood Estimation in Small Samples* (Charles Griffin, London, 1977).
[15] M. Zanolin, E. Naftali, and N. C. Makris, "Second order bias of a multivariate Gaussian maximum likelihood estimates with a chain rule for higher moments," J. Roy. Statist. Soc. B (submitted).
[16] N. C. Makris, "Parameter resolution bounds that depend on sample size," J. Acoust. Soc. Am. **99**, 2851–2861 (1996). The misstatement in this paper that the distribution for the sample covariance of a CCGR data vector is unknown is corrected in Ref. 17 below. The distribution in question is the complex Wishart distribution.
[17] N. C. Makris, "The statistics of ocean-acoustic ambient noise," in *Sea Surface Sound '97*, edited by T. Leighton (Kluwer Academic, Dordrecht, 1997).
[18] B. R. Kerman, Ed., *Sea Surface Sound, Natural Mechanisms of Surface Generated Noise in the Ocean* (Kluwer, Boston, 1987).
[19] N. C. Makris, "The effect of saturated transmission scintillation on ocean-acoustic intensity measurements," J. Acoust. Soc. Am. **100**, 769–783 (1996).
[20] N. C. Makris, "A foundation for logarithmic measures of fluctuating intensity in pattern recognition," Opt. Lett. **20**, 2012–2014 (1995).
[21] N. C. Makris and P. Ratilal, "A unified model for reverberation and sub-

merged target scattering in a stratified ocean waveguide,'' J. Acoust. Soc. Am. **109**, 909–941 (2001).
[22] P. Swerling, ''Probability of detection for fluctuating targets,'' Rand Report RM 1217 (1954); reissued in Trans. IRE Prof. Group Inf. Theory **IT-6**, 269–308 (1960).
[23] P. G. Bergmann, ''Intensity fluctuations,'' in *The Physics of Sound in the Sea, Part I: Transmission* (National Defense Research Committee, Washington, DC, 1946).
[24] I. Dyer, ''Statistics of sound propagation in the ocean,'' J. Acoust. Soc. Am. **48**, 337–345 (1970).
[25] A. B. Baggeroer, W. A. Kuperman, and H. Schmidt, ''Matched field processing: Source localization in correlated noise as an optimum parameter estimation problem,'' J. Acoust. Soc. Am. **83**, 571–587 (1988).
[26] A. B. Baggeroer, W. A. Kuperman, and P. H. Mikhalevsky, ''An overview of matched field methods in ocean acoustics,'' IEEE J. Ocean Eng. **18**, 401–424 (1993).
[27] Naftali, ''First order bias and second order variance of the Maximum Likelihood Estimator with application to multivariate Gaussian data and time delay and Doppler shift estimation,'' SM Thesis, MIT, Cambridge, MA, 2000.
[28] P. M. Woodward, *Probability and Information Theory, with Application to Radar* (Pergamon, New York, 1964).
[29] N. C. Makris, C. S. Chia, and L. T. Fialkowski, ''The bi-azimuthal scattering distribution of an abyssal hill,'' J. Acoust. Soc. Am. **106**, 2491–2512 (1999).

Computed narrow-band azimuthal time-reversing array retrofocusing in shallow water

Michael R. Dungan and David R. Dowling
Department of Mechanical Engineering and Applied Mechanics, University of Michigan, Ann Arbor, Michigan 48109-2121

(Received 15 May 2000; revised 29 November 2000; accepted 25 June 2001)

The process of acoustic time reversal sends sound waves back to their point of origin in reciprocal acoustic environments even when the acoustic environment is unknown. The properties of the time-reversed field commonly depend on the frequency of the original signal, the characteristics of the acoustic environment, and the configuration of the time-reversing transducer array (TRA). In particular, vertical TRAs are predicted to produce horizontally confined foci in environments containing random volume refraction. This article validates and extends this prediction to shallow water environments via monochromatic Monte Carlo propagation simulations (based on parabolic equation computations using RAM). The computational results determine the azimuthal extent of a TRA's retrofocus in shallow-water sound channels either having random bottom roughness or containing random internal-wave-induced sound speed fluctuations. In both cases, randomness in the environment may reduce the predicted azimuthal angular width of the vertical TRA retrofocus to as little as several degrees (compared to 360 degrees for uniform environments) for source-array ranges from 5 to 20 km at frequencies from 500 Hz to 2 kHz. For both types of randomness, power law scalings are found to collapse the calculated azimuthal retrofocus widths for shallow sources over a variety of acoustic frequencies, source-array ranges, water column depths, and random fluctuation amplitudes and correlation scales. Comparisons are made between retrofocusing on shallow and deep sources, and in strongly and mildly absorbing environments. [DOI: 10.1121/1.1397359]

PACS numbers: 43.30.Vh, 43.30.Yj, 43.30.Ft [DLB]

I. INTRODUCTION

Acoustic time reversal is a promising technique for acoustic-array beamforming in unknown multipath environments. The transducer array that produces the time-reversed field (a time-reversing array or TRA) may be of nearly any size or shape and can operate in any frequency range. Recent computational and experimental TRA studies in underwater acoustics (Kuperman *et al.*, 1998; Song *et al.*, 1998a; Khosla and Dowling, 1998; Song *et al.*, 1999; Hodgkiss *et al.*, 1999) suggest that TRAs can robustly retrofocus sound on remote sound sources in shallow ocean waters. TRA research has also been pursued in the area of biomedical ultrasound (Fink, 1997, 1999; Tanter *et al.*, 1998; Rose *et al.*, 1999; Roux *et al.*, 1999a), nondestructive evaluation (Chakroun *et al.*, 1995; Draeger *et al.*, 1998; Yönak and Dowling, 1999), and other areas (Draeger *et al.*, 1999; Draeger and Fink, 1999; Ohno *et al.*, 1999; Yamamoto *et al.*, 1999; Roux *et al.*, 1999b). The basic formulation of acoustic time reversal is provided in Jackson and Dowling (1991). Overviews are provided in Fink (1997, 1999).

Unlike ordinary beamforming techniques (Steinberg, 1976; Ziomek, 1985), time reversal actually utilizes the acoustic environment to retrofocus sound so TRAs perform better when random scattering and multipath propagation are present, although TRA performance is generally degraded in time-dependent (Dowling and Jackson, 1992; Khosla and Dowling, 1998; Dungan and Dowling, 2000) and noisy environments (Song *et al.*, 1998a; Khosla and Dowling, 2000). This article presents new computational results and scaling laws for azimuthal beam forming by a linear vertical TRA responding to a harmonic point source at a range R from the TRA in a low-noise time-independent shallow-water sound channel. When the environment is horizontally uniform, this source-TRA configuration produces a retrofocus ring of radius R with an azimuthal angular extent of 360 degrees. However, this same array placed in a horizontally inhomogeneous environment can produce a time-reversed field that includes significant azimuthal focusing (beamforming) in the direction of the point source. The purpose of this article is to provide predictions of the extent of this environmentally produced retrofocusing in shallow-water sound channels having either bottom roughness or containing sound speed fluctuations produced by a linear superposition of random internal waves convecting a sound speed gradient.

This azimuthal environmentally produced retrofocusing is generated by the two-step propagation algorithm for a time-reversing array. During the source-to-array propagation step, the sound signal is imprinted with the environmental characteristics between the source and the array. The array receives the imprinted signal, time reverses it (i.e., first-in becomes last-out), and rebroadcasts it. During this rebroadcast step, the vertical TRA directs acoustic energy uniformly into all azimuthal angles ($0 \leqslant \phi < 360°$). However, only the sound that retraces the direction ($\phi = 0$) back toward the source focuses because the TRA's rebroadcast field is mismatched to the details of the environment in all other directions ($\phi \neq 0$). This preferred-direction focusing phenomena is essentially the same as the environmental signal-

processing gain described in Perkins and Kuperman (1990) in the context of matched field processing; the difference is the present article emphasizes the effects of randomness as opposed to deterministic three-dimensional features of the ocean sound channel. Acoustic underwater communication is one application area where the benefits of robust focusing in unknown and changing environments are important and where TRA techniques are currently receiving attention.

Previous studies of TRA horizontal focusing have been limited. Song *et al.* (1998b) investigated the horizontal dimension of a retrofocus spot in their unique experiments conducted in the Mediterranean Sea (Kuperman *et al.*, 1998; Song *et al.*, 1998a, 1999; Hodgkiss *et al.*, 1999). However, their efforts on this topic were confined to a single source-array track, acoustic frequency, and source-array range. Past analytical and computational studies of time reversal in shallow ocean waters (Khosla and Dowling, 1998; Dungan and Dowling, 2000) have emphasized vertical retrofocus size without considering horizontal focusing in any detail, although a tenuous theoretical prediction was advanced in Khosla and Dowling (1998). The computational results and scaling laws presented here are intended to complement these previous studies to provide a means of quantitatively predicting the horizontal or azimuthal retrofocus size produced by vertical TRAs in horizontally nonuniform environments.

The remainder of this article is organized into three sections. In the next section we describe the acoustic environment used in this study, the bottom variation and internal wave models, and the computational technique. In Sec. III we present the vertical and azimuthal retrofocus simulation results along with proposed scaling laws and comparisons. In the final section we summarize the findings and state the conclusions drawn from this study.

II. COMPUTATIONAL APPROACH

This study utilizes repeated two-dimensional (2D) simulations in depth-range planes that fan out from the array to predict azimuthal TRA retrofocusing, a three-dimensional (3D) phenomena. This technique, commonly called the N×2D approach to 3D simulations, has been successfully exploited in previous underwater simulation studies. Here, each propagation slice is computed with the wide-angle parabolic-equation code RAM (Collins, 1993, 1994, 1998). The goal of this study is to predict how vertical-TRA azimuthal retrofocus size is influenced by environmental parameters, source-array geometry, and acoustic frequency (f). The following four subsections describe the environment investigated, the bottom variation model, the internal wave model, and the implementation of these within RAM.

A. Average environment

The shallow ocean is a complicated acoustic environment. Here, the main parametric complication is random bottom roughness added to a static baseline range-independent sound channel. Figure 1 shows a 3D representation of the simulation environment with bottom roughness and mean depth $D=75$ m. Water column and smooth-bottom properties are based on oceanic measurements taken near the center

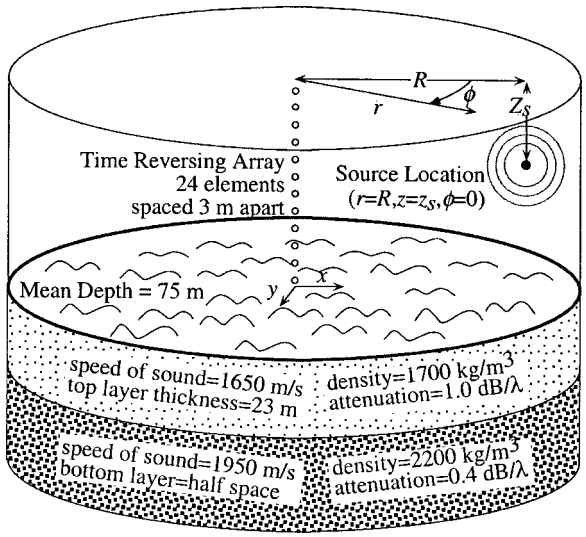

FIG. 1. Schematic of the sound channel and time-reversing array (TRA) geometry. The radial coordinate is r. The vertical coordinate, z, increases downward. The azimuthal angle is denoted by ϕ. A harmonic omnidirectional source is located at ($r=R$, $\phi=0$, $z=z_s$). The TRA receives the signal at ($r=0$, $\phi=0$, $z=z_n$) and retransmits it to form a retrofocus back near the source. The $z=0$ plane represents a pressure release surface. The ocean bottom has two layers.

of the SWARM (shallow-water acoustics in a random medium) site (see Apel *et al.*, 1997). The SWARM experiment was conducted off the coast of New Jersey in the late summer of 1995 during a seasonally active time for internal waves. The actual SWARM water column depth was range dependent (seaward sloping bottom) and the bottom contained multiple layers, but these complexities were not included in the present study. The speed of sound profile used here, shown in Fig. 2(a), is calculated from smoothed temperature and salinity measurements made at the center of the SWARM site in the absence of internal wave solitons. Figure 2(b) shows the calculated root-mean-square speed of sound fluctuations when synthetic internal waves (see Sec. II C) are included in the sound channel. For all the simulations, the average bottom is a two-layer model with properties extrapolated from core and chirp measurements at the SWARM site (Apel *et al.*, 1997). The 23-m-thick upper layer has a speed of sound of 1650 m/s and a density of 1700 kg/m^3, and the

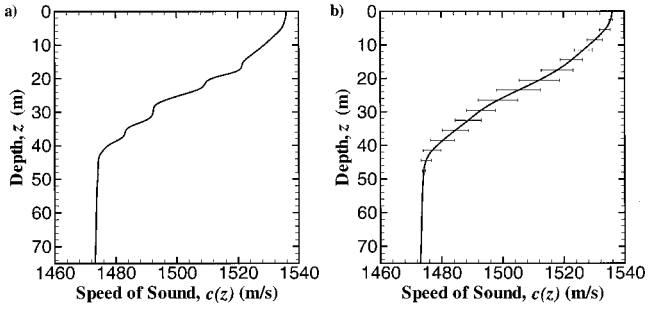

FIG. 2. Speed of sound versus depth for the baseline sound channel. (a) This profile is based on measurements made during the 1995 SWARM experiment that were provided to the authors by Dr. Steven Finette of the Naval Research Laboratory. (b) Average and fluctuating speed of sound in the synthetic internal wave field. The horizontal bars lie at ±1 standard deviation.

lower layer is modeled as a half-space with a speed of sound of 1950 m/s and a density of 2200 kg/m^3. Attenuation values were extrapolated from tabulations in Jensen *et al.* (1994) and are 1.00 dB per wavelength and 0.40 dB per wavelength for the upper and lower layers, respectively. The roughness model (described in the next subsection) was not based on SWARM measurements.

The ocean surface is treated as a flat pressure-release surface. Although this is clearly an approximation for acoustic frequencies in the kHz range and above, the complications posed by bubble scattering, bubble absorption, and dynamic rough ocean-surface scattering are beyond the scope of this study. Assessments of rough surface scattering and TRA performance are provided in Kuperman *et al.* (1998) and Khosla and Dowling (1998).

The parameters just described will be the same throughout the rest of this article unless stated otherwise. The exceptions will be for (*i*) variations in attenuation values that illustrate the role of bottom absorption, (*ii*) different bottom roughness levels (described in the next subsection), (*iii*) vertical stretching (see discussion of Fig. 11), and (*iv*) fluctuations in the speed of sound profile caused by random linear internal waves.

B. Bottom variation

In this study, the ocean bottom is taken to be flat, on average, with a zero-mean spatially varying random roughness height $H(r,\phi)$ of the first bottom layer. The local depth, z_b, of the sound channel at a given (r,ϕ) location is the sum of the mean depth $D=75$ m and H:

$$z_b(r,\phi)=D+H(r,\phi). \tag{1}$$

Most ocean-bottom surveys agree on a statistical variation model involving a power law distribution of the spectrum of H, $\Phi_H(k_h)$, with horizontal spatial frequency k_h:

$$\Phi_H(k_h)\propto k_h^{-b}. \tag{2}$$

Bell (1975) tabulated bottom roughness spectral data from various experiments. Berkson and Matthews (1984), Fox and Hayes (1985), Jackson *et al.* (1986), and Medwin and Clay (1998) also present or use bottom roughness spectral data in the form of a power law, but some differences exist between recommended values of the exponent *b*.

In this study, H is synthesized from a random superposition of sinusoidal roughness height fluctuations whose statistics are azimuthally isotropic:

$$H(r,\phi)=\sum_{k_h}\sum_{\theta}F(k_h)e^{ik_hr\cos\phi\cos\theta+ik_hr\sin\phi\sin\theta}, \tag{3}$$

where θ represents the azimuthal angles of the roughness height sinusoids ($0<\theta<360°$), and $F(k_h)$ is a random complex amplitude having a power spectrum in k_h given by

$$\langle|F(k_h)|^2\rangle=C_0^2H_{\rm rms}^2\left(\frac{k_h^2}{k_h^2+k_l^2}\right)^{\alpha}k_h^{-b}\left(\frac{k_u^2}{k_h^2+k_u^2}\right)^{\beta}. \tag{4}$$

The real and imaginary components of $F(k_h)$ are Gaussian distributed with zero mean, and the angle brackets denote an expected value. The power law exponent used here is $b=2.0$ and the maximum root-mean-square (rms) depth variation is $H_{\rm rms}=3.0$ m. These values are based on Table I in Berkson and Matthews (1984) (see also Table 13.1 in Medwin and Clay, 1998). The extra factors in (4) compared to (2) exist to smooth the depth fluctuation spectrum in the regions of the lower- and upper-cutoff horizontal wave numbers, k_l and k_u, respectively. The normalization constant in (4), C_o^2, is chosen so that

$$H_{\rm rms}^2=\int_0^{\infty}\langle|F(k_h)|^2\rangle\,dk_h. \tag{5}$$

The remaining parametric choices necessary to evaluate (4) consist of rolloff exponents ($\alpha=3$ and $\beta=2$) and upper and lower wave numbers ($k_u=0.06\,\mathrm{m}^{-1}$ and $k_l=0.001\,\mathrm{m}^{-1}$). The final depth fluctuation spectrum is shown in Fig. 3 for $H_{\rm rms}=3.0$ m. The correlation length Λ produced by this bottom roughness model was 280 m, and was computed from

$$\Lambda=\frac{1}{H_{\rm rms}^2}\int_0^{\infty}\langle H(r,\phi)H(r+\Delta r,\phi)\rangle\,d\Delta r. \tag{6}$$

In computing the sum shown in (3), discrete k_h steps of $\Delta k_h=0.0005\,\mathrm{m}^{-1}$ were taken. The number of θ-direction waves increased linearly with k_h to attain nearly uniform tiling of the $k_h-\theta$ plane. One realization of the bottom roughness with $H_{\rm rms}=3.0$ m and rms slope of 0.02 is shown in Fig. 4. Although some remnants of the discrete sinusoid sum are apparent, the depth variations are not unrealistic. Superimposed on Fig. 4 is a sample retrofocus grid with the TRA on the left and the various source locations (white dots) and azimuthal sample points on the right. Notice that the bottom roughness profile found between the various return paths and the initial source-array path may differ significantly. This article presents the results of investigations into the importance of such variations in bottom roughness on TRA retrofocusing.

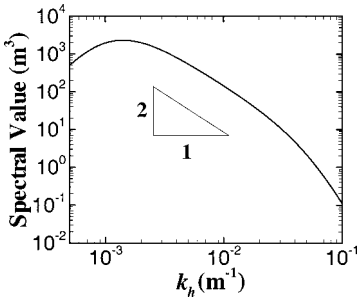

FIG. 3. Synthetic bottom variation spectrum for a power law of exponent $b=2$. The inset triangle indicates slope of a curve with a slope of -2.

C. Linear internal waves

To compare the importance of bottom roughness and water-column random refraction on azimuthal retrofocusing by vertical TRAs, linear internal waves were inserted into the baseline sound channel described in Sec. II A. The internal-wave model is a superposition of random linear waves having a Garrett–Munk spectrum that is adjusted for shallow ocean conditions. It is the model used by Dungan and Dowl-

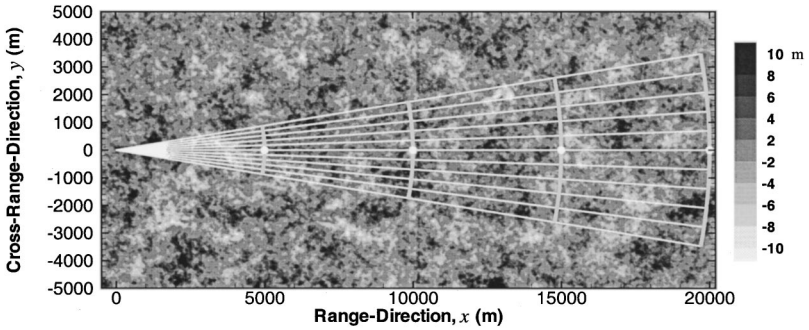

FIG. 4. Sample synthetic bottom variation floor map over a 10×20-km^2 area for $H_{\rm rms}=3.0$ m. The TRA is located on the left, with several azimuthal return paths superimposed. Several source locations are indicated by white dots. The gray-scale changes from black (more than $+10$ m upward deflection) to white (less than -10 m downward deflection).

ing (2000) and is a simple extension on the formulation of Dashen *et al.* (1979) and Tielbürger *et al.* (1997).

Internal waves cause heaving motions within the water column that alter the local sound speed by lifting and lowering the otherwise static contours of constant sound speed. These imposed variations produce a 3D sound-speed field that depends on r and ϕ, as well as z. The vertical deflections produced by internal waves are governed by a second-order differential equation (Dashen *et al.*, 1979)

$$\frac{d^2}{dz^2}W(z)+k_h^2\left[\frac{N^2(z)-\omega^2}{\omega^2-f_c^2}\right]W(z)=0, \tag{7}$$

which, along with the waveform boundary conditions of $W(0)=W(D)=0$, creates an eigenvalue problem. Here, $W(z)$ is the vertical displacement produced by an internal wave having radian frequency ω, k_h is the horizontal wave number of the internal wave, and $f_c=2\Omega\sin(°\text{latitude})$ is the inertial frequency with Ω equal to the rotation rate of the earth. For these calculations, f_c was evaluated at a latitude of 39.25°, corresponding to the center of the SWARM site. When ω and k_h are independent parameters, (7) has eigenmode solutions $W(k_h,j,z)$ at a discrete set of frequency eigenvalues $\omega_j(k_h)$. The internal wave modes and frequencies particular to this study were calculated from (7) numerically using shooting techniques (see Press *et al.*, 1986). Hence, a dynamic three-dimensional simulation of the internal-wave-induced vertical displacement η can be obtained by a triple sum over internal-wave modes (j), horizontal wave numbers (k_h), and azimuthal angles (θ),

$$\eta(r,\phi,z,t)=\mathrm{Re}\Bigg\{\sum_j\sum_{k_h}\sum_\theta F(k_h,j)W(k_h,j,z)\times\exp[ik_hr\cos\theta\cos\phi+ik_hr\sin\theta\sin\phi-i\omega(k_h,j)t]\Bigg\}. \tag{8a}$$

The F-term is a Gaussian random complex weighting having a uniform distribution in θ and a Garrett–Munk spectrum in mode number and horizontal wave number

$$\langle|F(k_h,j)|^2\rangle=\frac{4}{\pi}E_0M[j^2+j_*^2]^{-p/2}k_jk_h^2(k_h^2+k_j^2)^{-2}, \tag{8b}$$

where

$$k_j=\frac{\pi jf_c}{\int_0^D N(z)\,dz} \tag{8c}$$

and

$$M=\left\{\sum_{j=1}^{\infty}(j^2+j_*^2)^{-p/2}\right\}^{-1}. \tag{8d}$$

Here, E_0 is the internal-wave energy level, j_* is the mode weighting parameter, and p is the mode weighting exponent. As with (3), the sum given in (8a) was calculated using a variable azimuthal resolution so that random numbers were assigned to approximately equal tile areas of the $k_h-\theta$ plane for each value of j. Hence the number of θ-evaluations in (8a) increased linearly with increasing k_h. The parametric ranges and increments used for summation were $1\leqslant j\leqslant15$, $5\times10^{-4}\,\mathrm{m}^{-1}\leqslant k_h\leqslant1.5\times10^{-1}\,\mathrm{m}^{-1}$ with steps of $\Delta k_h=5\times10^{-4}\,\mathrm{m}^{-1}$, and $0\leqslant\theta\leqslant360°$ with $\Delta\theta=2°$ when $k_h=1.5\times10^{-1}\,\mathrm{m}^{-1}$. The internal wave mode shapes $W_j(z,k_h)$ evolve gradually with increasing k_h, so mode shapes were interpolated between the minimum and maximum values of k_h with intervening calculations every $10^{-2}\,\mathrm{m}^{-1}$.

The Garrett–Munk spectrum parameters (E_0,p,j_*) were chosen to match a temporal power spectrum of vertical displacements measured at the SWARM site in 75 m of water without soliton activity. This was accomplished by using (8a) at a fixed depth of 25 m to generate a synthetic vertical displacement time series, computing the power spectrum from this synthetic time series, and then comparing the resulting synthetic spectrum with the SWARM measurements. Adjustments were made to the spectrum parameters until a visually acceptable match of the two spectra was achieved (see Dungan and Dowling, 2000). The final parameter choices are $j_*=1$, $p=4$, and $E_0=24.6\,\mathrm{J/m}^2$. Other independent research suggests similar values for these parameters (Tielbürger *et al.*, 1997; Yoo and Yang, 1998; Yang and Yoo, 1998). The final speed of sound fluctuation levels, shown in Fig. 2(b), are confined to the upper half of the sound channel.

D. Propagation model

Acoustic propagation in the roughened and internal-wave containing sound channels was computed with RAM, a wide-angle parabolic equation (PE) code (Collins, 1993, 1994, 1998). Previous use of RAM in the context of narrow-band TRA simulations has been described in Dungan and Dowling (2000). The use of RAM here was nearly identical, the only difference being the extension to N×2D calculations to determine the azimuthal extent of the TRA retrofocus region.

To summarize, a modified version of RAM that outputs the real and imaginary components of the pressures was used so that amplitudes at the TRA locations could be complex conjugated before the back-propagation was computed. Complex conjugation is the equivalent of time reversal for narrow-band signals (Jackson and Dowling, 1991). In the forward propagation step (at time t_1), a point source with radian frequency ω located at $(r,\phi,z)=(R,0,z_s)$ ensonifies the sound channel. Elements of the TRA located at $(0,0,z_n)$ record this field, complex conjugate it, amplify it, and rebroadcast it (at time t_2). The response of such an array is entirely described by the conjugate Green's function, $G_{c\omega}$ [see Dowling and Jackson (1992), Eq. (10), or Kuperman *et al.* (1998), Eq. (7)]:

$$G_{c\omega}(r,\phi,z,t_2-t_1)=\sum_{n=1}^{N} G_{2\omega}(r,\phi,z;0,0,z_n) \times G^{*}_{1\omega}(0,0,z_n;R,0,z_s), \quad (9)$$

where N is the number of array elements and the coordinates are shown in Fig. 1. Here, $G_{1\omega}(0,0,z_n;R,0,z_s)$ is the Green's function at radian frequency $\omega=2\pi f$ for acoustic propagation from the source at $(R,0,z_s)$ to an array element at $(0,0,z_n)$ for time t_1, and the asterisk denotes complex conjugation. Similarly, $G_{2\omega}(r,\phi,z;0,0,z_n)$ is the Green's function for acoustic propagation from an array element at $(0,0,z_n)$ to (r,ϕ,z) for time t_2. For all retrofocusing computations in the baseline sound channel, the array has 24 elements with 3-m vertical spacing, and the time delay, t_2-t_1, is set to be zero for simplicity.

The use of the N×2D approach to calculate the 3D features of $G_{2\omega}(r,\phi,z;0,0,z_n)$ requires some consideration. Much work has been done to determine the applicability of N×2D approximations to 3D problems. Buckingham (1984) and Sturm *et al.* (1998) have shown that this approximation does not fare well in a full-wedge sound channel. However, Kuperman *et al.* (1991), Smith (1998), Orris and Perkins (1998), and others have shown that for mild range-dependence, the N×2D approach closely models three dimensions and even predicts some 3D effects like horizontal refraction (Smith, 1996, 1998). The bottom roughness and internal wave-field environments generated to obtain the current results are mild enough to be treated with acceptable accuracy by the N×2D approximation.

III. TRA RETROFOCUSING RESULTS

The results of this investigation into the environment's effect on the retrofocusing capability of a time-reversing array are presented in three parts. The first two subsections investigate an environment with a varying bottom and its impact on vertical and azimuthal retrofocusing, respectively. The final subsection explores the impact of linear internal waves on azimuthal retrofocusing. A more thorough study of TRA retrofocus amplitude and vertical extent in static and dynamic shallow-water sound channels is provided in Dungan and Dowling (2000).

TABLE I. Bottom roughness effect on vertical full-width at half-maximum size of retrofocus, z_{FWHM}, at a source array range of $R=10$ km for various frequencies and two source depths $z_s=25$ m (a) and $z_s=50$ m (b). Notice that only small changes in mean vertical retrofocus sizes occur at each frequency, but large variations can occur in 50% confidence levels for the vertical retrofocus sizes (in parentheses) as the rms depth fluctuation increases.

	Frequency			
H_{rms} (m)	250 Hz $z_{\mathrm{FWHM}/\lambda}$	500 Hz $z_{\mathrm{FWHM}/\lambda}$	1000 Hz $z_{\mathrm{FWHM}/\lambda}$	2000 Hz $z_{\mathrm{FWHM}/\lambda}$
	(a) Source depth=25 m			
0.0	2.8 (0.0)	2.7 (0.0)	2.7 (0.0)	2.4 (0.0)
1.0	2.9 (0.2)	2.7 (0.1)	2.7 (0.1)	2.6 (0.1)
2.0	3.1 (0.9)	2.6 (0.1)	2.6 (0.1)	2.7 (0.3)
3.0	3.3 (1.1)	2.6 (0.2)	2.7 (0.2)	2.6 (0.3)
	(b) Source depth=50 m			
0.0	3.7 (0.0)	4.0 (0.0)	4.8 (0.0)	3.4 (0.0)
1.0	3.7 (0.1)	4.0 (0.1)	4.1 (0.2)	4.5 (0.4)
2.0	3.8 (0.3)	4.1 (0.3)	3.9 (0.4)	4.0 (0.3)
3.0	3.9 (0.5)	4.1 (0.4)	3.6 (0.4)	3.2 (0.2)

A. Vertical retrofocusing with random rough bottom

The performance of the TRA in the $\phi=0$ vertical plane of the baseline sound channel with varying bottom geometry was investigated as a preliminary study to the azimuthal retrofocusing investigations. The results are found by calculating $G_{c\omega}$ from (9) at $r=R$ and $\phi=0$, and determining the vertical size of the retrofocus region. The parameters varied in this case include source depth ($z_s=25$ and 50 m), acoustic frequency ($f=250$, 500, 1000, and 2000 Hz), and rms depth fluctuation ($H_{\mathrm{rms}}=0$, 1.0, 2.0, and 3.0 m). The parameters cover a range $0\leqslant kH_{\mathrm{rms}}\leqslant 25$, where k is the acoustic wave number. For these initial studies, the source-array range was held fixed at $R=10$ km.

The vertical retrofocus size results are given in Table I which lists the TRA-retrofocus-peak full-width at half-maximum (FWHM) values through the depth, z_{FWHM}, divided by the acoustic wavelength λ. These results show that z_{FWHM} lies in the range of three to four wavelengths for the entire parameter range with the shallow source ($z_s=25$ m), providing a somewhat smaller retrofocus. These results are based on ten realizations of the bottom roughness at each H_{rms} value.

Interestingly, increasing rms depth fluctuation does not lead to consistent changes in z_{FWHM} or even to higher uncertainty values for z_{FWHM}. Thus, the main conclusion to be drawn from these results is that bottom roughness does not have a significant effect on vertical retrofocus size in this parameter range when $\phi=0$.

B. Azimuthal retrofocusing with a random rough bottom

The azimuthal extent of the TRA retrofocus was investigated for the baseline sound channel with varying levels of bottom roughness. The results are found by calculating $G_{c\omega}$ from (9) at $r=R$ and $\phi\neq 0$, and determining the azimuthal angular size of the retrofocus peak. The parameters varied in

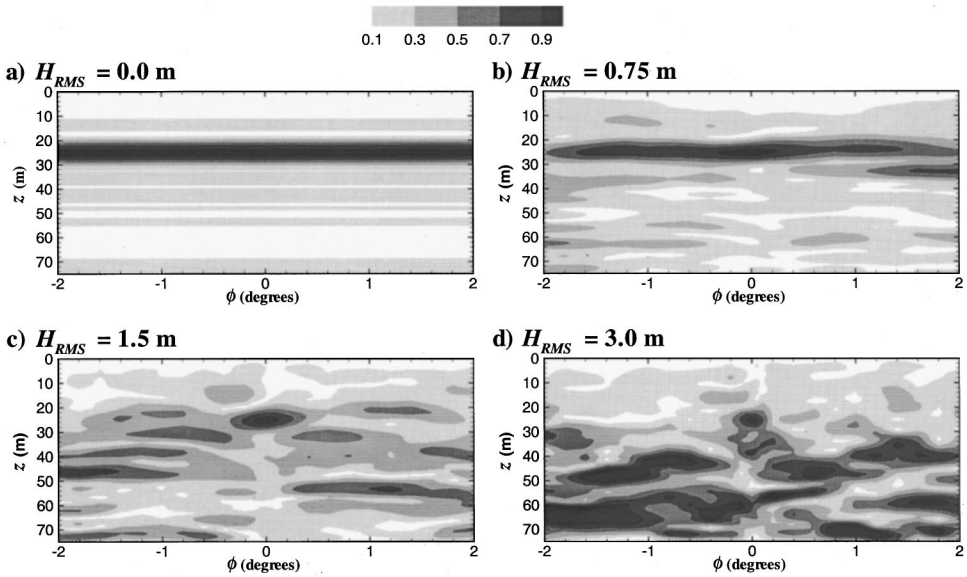

FIG. 5. Retrofocus field amplitude through the channel depth on a vertical screen as shown in Fig. 6 at a source-array range of $R=10$ km for various bottom rms height variations: $H_{\rm rms}=0.0$ m (a), 0.75 m (b), 1.5 m (c), and 3.0 m (d). The acoustic frequency is $f=500$ Hz and the source depth is $z_s=25$ m. Each field is self-normalized and black corresponds to the highest 10% of field amplitudes.

this case cover the same parametric range as the vertical retrofocus size study but also include four source-array ranges $R=2.5$, 5, 10, and 20 km.

Whereas the increase in bottom roughness has little or no effect on the TRA's vertical retrofocus size, the azimuthal retrofocus size is strongly dependent on both roughness and range, and decreases as both increase. An example is shown in Fig. 5 for the results of one bottom roughness realization captured by looking at different ϕ-angles at a constant range ($R=10$ km) to produce an N×2D composite image. The projected geometry for the images shown in Fig. 5 is sketched in Fig. 6. The TRA's retrofocus for the baseline smooth-bottom sound channel [$H(r,\phi,)=0.0$ m] is an unvarying 360-degree ring as partially shown for a 500-Hz source at $z_s=25$ m in Fig. 5(a). As the bottom roughness increases ($H_{\rm rms}=0.75$ m, $H_{\rm rms}=1.5$ m, and $H_{\rm rms}=3.0$ m), the azimuthal retrofocus size decreases [Figs. 5(b)–(d), respectively]. This environment-enhanced focusing becomes stronger as $H_{\rm rms}$ increases. Sidelobes that occur in the lower half of the sound channel when $\phi\neq 0$ are caused by acoustic energy that was unintentionally broadcast at that azimuthal angle by the linear vertical TRA. These azimuthal sidelobes are not caused by mode stripping and would contribute to the 360-degree ring retrofocus if $H_{\rm rms}=0$. They occur in the lower half of the sound channel because of the channel's strongly downward-refracting sound speed profile.

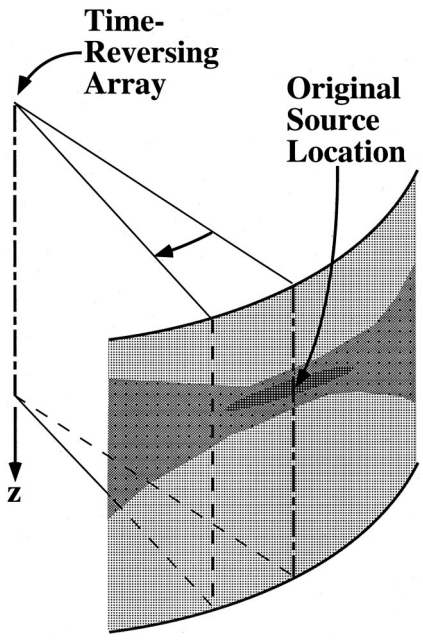

FIG. 6. Sketch of a vertical screen illustrating the viewing orientation of the field plots in Figs. 5 and 7. The TRA is at the left with propagation paths compiled at small ϕ intervals to produce the field values displayed on the curved vertical screen (at $r=R$) shown at the right. The images in Figs. 5 and 7 represent the field on the curved screen from the vantage point of the TRA ($r=0$).

The azimuthal retrofocus size also decreases as the source-array range increases (up to a point where absorption degrades the retrofocus). Figure 7 shows this development for a 500-Hz source at $z_s=25$ m for $R=2.5$, 5, 10, and 20 km. As R increases, the importance of bottom scattering increases and the acoustic waves traveling on bottom-interacting paths become increasingly more imprinted with the particular bottom roughness profile lying between the source and the array. On the array-to-source propagation step, the TRA's rebroadcast field only retrofocuses in the angular region where the bottom roughness profile felt by the back-propagating waves is closely matched to the source-array bottom roughness profile. At longer ranges, this angular region of bottom-profile match is reduced because of increased bottom scattering and geometrical considerations. The linear vertical TRA still spreads acoustic power uniformly into all possible azimuthal directions (i.e., 360 degrees); however, the rebroadcast field fails to focus in any direction except that towards, or nearly towards, the original source ($\phi\approx 0$). The misdirected acoustic energy leads to the side lobe structure in Figs. 5 and 7.

The azimuthal retrofocus size can be quantified in terms of an angular full-width at half-maximum (FWHM), $\phi_{\rm FWHM}$, defined as the angular extent over which the TRA-produced pressure amplitudes are more than half of the peak pressure found at $(R,0,z_s)$. Figure 8 displays the range de-

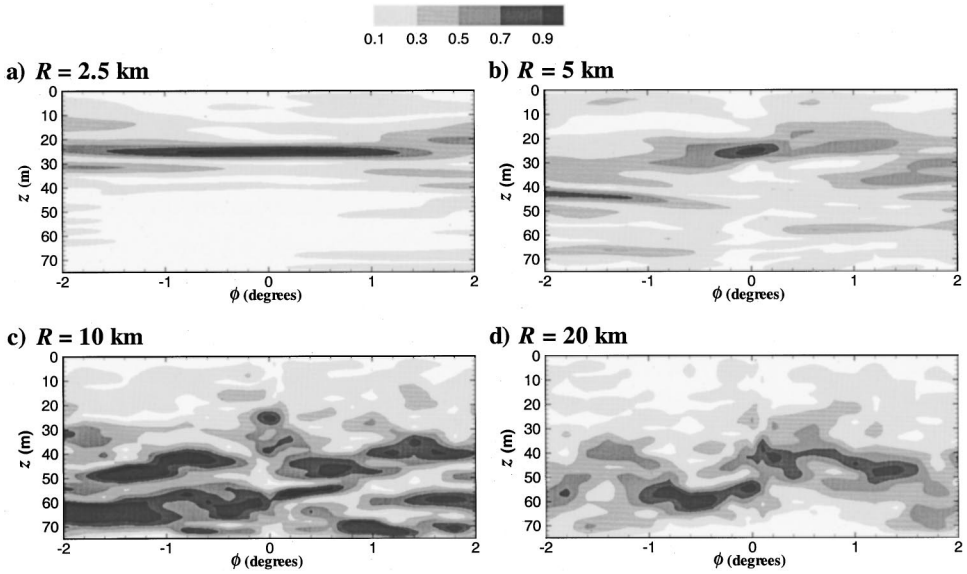

FIG. 7. Retrofocus field amplitude through the channel depth on a vertical screen as shown in Fig. 6 for various source-array ranges: $R=2.5$ km (a), 5 km (b), 10 km (c), and 20 km (d). The acoustic frequency is $f=500$ Hz, the source depth is $z_s=25$ m, and the rms bottom roughness is $H_{\rm rms}=3.0$ m. Each field is self-normalized and black corresponds to the highest 10% of field amplitudes.

pendence of $\phi_{\rm FWHM}$ for source depths of 25 and 50 m at four acoustic frequencies for $H_{\rm rms}=3.0$ m based on ten different realizations of the bottom roughness. The range values on the horizontal axes in Fig. 8 are both scaled by the acoustic wave number $k=2\pi f/c$ where $c=1500$ m/s. The slope triangle provided in Fig. 8 suggests $\phi_{\rm FWHM}\propto(kR)^{-3/2}$. These scaled plots show that the shallow source case [Fig. 8(a)] produces a frequency-independent rate of decrease in $\phi_{\rm FWHM}$ with increasing source-array range followed by an upturn that depends on frequency. The pattern is similar but less well defined for the deep source [Fig. 8(b)]. This difference is believed to arise from the comparative dominance of low-order modes for deep-source retrofocusing when compared to shallow-source source retrofocusing in the same channel. The low-order propagating modes are less susceptible to bottom absorption and perturbations from bottom roughness so the deep source ($z_s=50$ m) produces larger azimuthal retrofoci than the shallow source ($z_s=25$ m). Recall that vertical-TRA azimuthal retrofocusing is only possible when there is significant propagation perturbations caused by variations in the bottom (or water column).

The frequency dependent upturns in $\phi_{\rm FWHM}$ shown in Fig. 8 occur because of bottom absorption that preferentially effects the higher-order modes. To verify this claim, cases were run at 500 Hz and $H_{\rm rms}=3.0$ m with varying attenuation values in the two bottom layers. The cases studied include one-quarter (0.25 and 0.10 dB/λ), one-half (0.50 and 0.20 dB/λ), one (1.00 and 0.40 dB/λ), and two (2.00 and 0.80 dB/λ) times the nominal attenuation values specified in Sec. II A. Figure 9 shows these results for $z_s=25$ m [Fig. 9(a)] and $z_s=50$ m [Fig. 9(b)]. As in Fig. 8, the horizontal axis is kR. For the shallow source [Fig. 9(a)] as the attenuation values drop, there is an increase in the range at which the azimuthal sharpening trend reverses. For the deep source [Fig. 9(b)], the results also show sharper azimuthal retrofocusing for lower attenuation values. These results support the contention that the upturns in $\phi_{\rm FWHM}$ with increasing R are caused by the absorption of the higher-order propagating modes.

To quantify the effect of bottom roughness height on azimuthal retrofocusing, $\phi_{\rm FWHM}$ was calculated at 500 Hz for $H_{\rm rms}=0.75$, 1.5, and 3.0 m. Figure 10 displays these results for $z_s=25$ m [Fig. 10(a)] and $z_s=50$ m [Fig. 10(b)], respectively. As in Figs. 8 and 9, the horizontal axis is kR. A smooth-bottom case produces a 360 degree retrofocus and therefore does not appear on either frame of Fig. 10. The

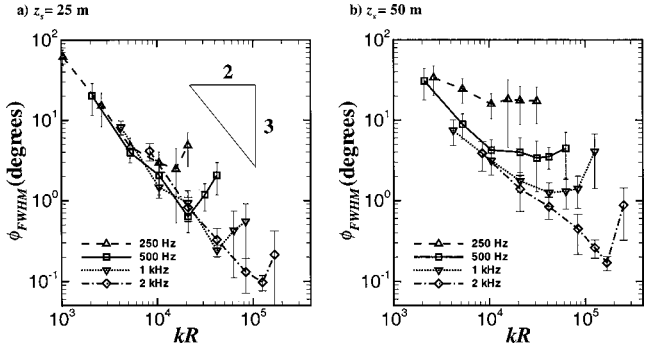

FIG. 8. TRA retrofocus azimuthal full-width at half-maximum angles, $\phi_{\rm FWHM}$, versus acoustic-wave-number-scaled source-array range (kR) for varying frequencies at source depths of $z_s=25$ m (a) and 50 m (b). The rms bottom roughness is $H_{\rm rms}=3.0$ m. The inset triangle illustrates a $-3/2$ slope. The results suggest $\phi_{\rm FWHM}\propto(kR)^{-3/2}$.

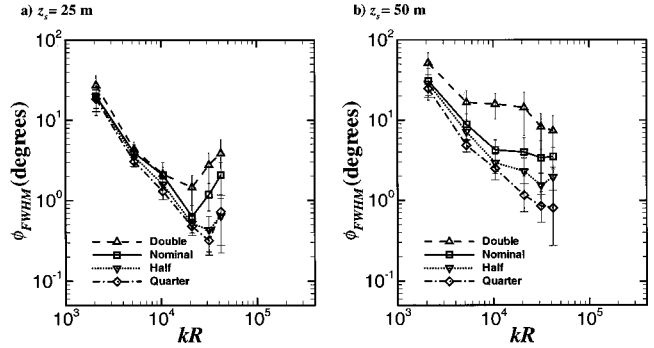

FIG. 9. TRA retrofocus azimuthal full-width at half-maximum angles, $\phi_{\rm FWHM}$, versus acoustic-wave-number-scaled source-array range (R) for varying bottom attenuation values at source depths of $z_s=25$ m (a) and 50 m (b). The rms bottom roughness is $H_{\rm rms}=3.0$ m, and the acoustic frequency is $f=500$ Hz.

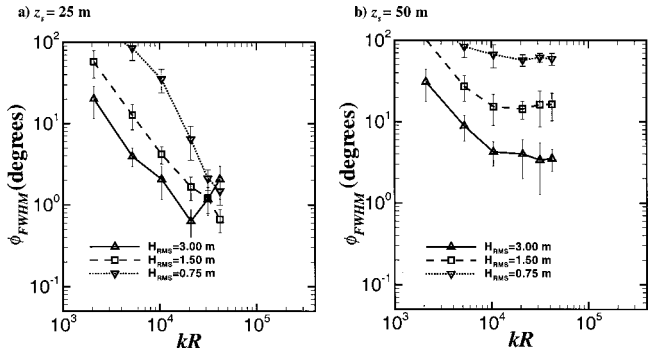

FIG. 10. TRA retrofocus azimuthal full-width at half-maximum angles, ϕ_{FWHM}, versus acoustic-wave-number-scaled source-array range (R) for varying rms bottom roughness at source depths of $z_s=25$ m (a) and 50 m (b). The acoustic frequency is $f=500$ Hz.

remaining curves indicate an impressive sharpening of the retrofocus as the bottom roughness increases with the shallow ($z_s=25$ m) source leading to consistently smaller retrofoci than the deep ($z_s=50$ m) source for ranges greater than 5 km ($kR\approx 10^4$) and $H_{\mathrm{rms}}=3.0$ m. Interestingly, the predicted azimuthal extent of the vertical TRA's retrofocus falls below 5 degrees for both source depths when $H_{\mathrm{rms}}=3.0$ m. In addition, the effects of absorption are delayed to longer ranges for smaller H_{rms}. This is due to the higher amount of bottom absorption present when H_{rms} is greater, since local grazing angles for bottom scattering and penetration are increased by increased bottom roughness.

The trends found in Figs. 8–10 suggest a simple power-law scaling is possible for the azimuthal size of the TRA retrofocus. Arguments leading to such a scaling law are presented in the next few paragraphs along with figures showing the scaling law's effectiveness for TRA retrofocusing on shallow and deep sources.

A TRA retrofocus field forms when the phase of the original forward-propagated field is precisely cancelled by the back-propagated field. Thus, the net phase at a TRA retrofocus is zero when the propagation is reciprocal and scattering from the bottom roughness along the source-array path ($\phi=0$) is compensated. If the phase of the back-propagated field is sufficiently altered compared to the forward propagated field, the constructive interference that forms the retrofocus will not occur and the retrofocus will be weakened or even lost. When the ocean bottom is rough, such uncompensated phase variations will occur in the TRA's back-propagated field along azimuthal directions ($\phi\neq 0$) other than that toward the source ($\phi=0$) because of uncompensated scattering from the differing bottom roughness features lying along $\phi\neq 0$ paths.

The extent of such phase variations can be estimated by comparing the TRA's back-propagated field that travels at $\phi=0$, $G_{c\omega}(r,0,z)$, and the TRA's back-propagated field that travels at a small nonzero azimuthal angle ϕ, $G_{c\omega}(r,\phi,z)$. Here, the phase difference at the source depth, z_s, between these two field values is denoted by η, i.e., $G_{c\omega}(r,0,z_s,0)G^*_{c\omega}(r,\phi,z_s,0)\propto e^{i\eta}$. Although the expected value of η will be zero, its variance, $\langle\eta^2\rangle$, increases with increasing k, R, ϕ, and H_{rms} because of uncompensated bottom scattering along the $\phi\neq 0$ path. When $\langle\eta^2\rangle$ is of order unity or greater, the TRA retrofocus in the ϕ-direction will have been weakened or even eliminated because of uncompensated bottom scattering. Therefore, ϕ_{FWHM} should be proportional to the value of ϕ that produces $\langle\eta^2\rangle\approx 1$.

To determine how $\langle\eta^2\rangle$ depends on ϕ, an estimate is needed for the phase fluctuations developed by the nth propagating mode traveling in the ϕ direction. Here, the approach of Clay (1964) is adopted; a ray with bottom-grazing angle θ_n is associated with each of the N_p propagating modes of the sound channel and a simple statistical model is built from the I_n interactions of each ray with the rough ocean bottom. A more sophisticated approach based on the work of Kuperman (1975) and Kuperman and Ingentio (1977) may be possible but was not found necessary.

At the nth ray's ith bottom interaction, the ray's phase will be modified by a random increment γ that depends on the acoustic wave number k, the local bottom roughness profile $H(r,\phi)$, and the ray's grazing angle θ_n, i.e., $\gamma=\gamma[k,H(r_{i,n},\phi),\theta_n]$. For the ith bottom interaction, the difference in the phase increment between the nth ray at ϕ and the nth ray at $\phi=0$ will be

$$\Delta\gamma_{i,n}=\gamma[k,H(r_{i,n},\phi),\theta_n]-\gamma[k,H(r_{i,n},0),\theta_n]$$
$$\approx r_{i,n}\phi\frac{\partial\gamma}{\partial H}\frac{\partial H}{\partial y}, \tag{10}$$

where $r_{i,n}$ is the distance from the array to the nth ray's ith bottom interaction, the approximate equality follows from a Taylor series expansion of $\gamma[k,H(r_i,\phi),\theta_n]$ with $\phi\ll 1$, and the y axis is horizontal and transverse to the $\phi=0$ direction (see Fig. 1). The total phase difference, η, can be estimated by summing (10) over bottom interactions and rays. Thus, if all the bottom interactions produce independent phase fluctuations, the variance of η is approximately

$$\langle\eta^2\rangle\approx N_pN_b\left\langle\left(r_{i,n}\phi\frac{\partial\gamma}{\partial H}\frac{\partial H}{\partial y}\right)^2\right\rangle, \tag{11}$$

where N_b is the average number of bottom interactions per ray and N_p is the number of rays.

To determine how $\langle\eta^2\rangle$ depends on acoustic and sound channel parameters, proportionalities and scaling relationships can be inserted in (11). Here, $N_p\propto kD$, $N_b\propto R/D$, $r_{i,n}\sim R$, $\partial\gamma/\partial H\sim\gamma_{\mathrm{rms}}/H_{\mathrm{rms}}$, and $\partial H/\partial y\sim H_{\mathrm{rms}}/\Lambda$ are used to find

$$\langle\eta^2\rangle\propto kD\frac{R}{D}R^2\phi^2\left(\frac{\gamma_{\mathrm{rms}}}{H_{\mathrm{rms}}}\right)^2\left(\frac{H_{\mathrm{rms}}}{\Lambda}\right)^2\propto\frac{kR^3\gamma^2_{\mathrm{rms}}}{\Lambda^2}\phi^2. \tag{12}$$

When $\langle\eta^2\rangle$ is set equal to unity, (12) can be inverted to find the parametric dependence of ϕ_{FWHM}:

$$\phi_{\mathrm{FWHM}}\propto\frac{\Lambda}{k^{1/2}R^{3/2}\gamma_{\mathrm{rms}}}. \tag{13}$$

In general, γ_{rms} will be proportional to kH_{rms} (see Ishimaru, 1978) and a function g that depends on the statistics of the scattering geometry: $\gamma_{\mathrm{rms}}=kH_{\mathrm{rms}}g(H_{\mathrm{rms}}/\Lambda,\overline{\theta})$ where H_{rms}/Λ represents the surface slope, and $\overline{\theta}$ is an appropriate average model-propagation grazing angle. Making this substitution for γ_{rms} produces the final scaling law for ϕ_{FWHM}:

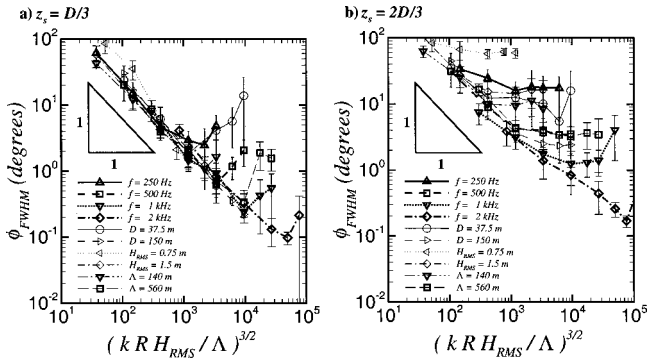

FIG. 11. TRA retrofocus azimuthal full-width at half-maximum angles, ϕ_{FWHM}, versus the dimensionless parameter $(kRH_{\mathrm{rms}}/\Lambda)^{+3/2}$ for a variety of acoustic frequencies f, source array ranges R, and root-mean-square bottom roughnesses heights H_{rms} for bottom correlation lengths $\Lambda = 140$, 280, and 560 m and sound channel depths $D = 37.5$, 75, and 150 m with a source depth of $z_s = D/3$ (a) and $2D/3$ (b). Where not specified, the nominal parameters of $f = 500$ Hz, $H_{\mathrm{rms}} = 3.0$ m, $D = 75$ m, and $\Lambda = 280$ m were used in the simulations. The inset slope triangle shows a -1 slope. The collapse is better for the shallower source where ϕ_{FWHM} is typically smaller than for the deeper source.

$$\phi_{\mathrm{FWHM}} \propto \frac{\Lambda}{(kR)^{3/2} H_{\mathrm{rms}} g(H_{\mathrm{rms}}/\Lambda, \overline{\theta})}. \tag{14}$$

This scaling law matches the kR power-law dependence shown in Fig. 8(a) and predicts ϕ_{FWHM} to be independent of D.

The accuracy of (14) and the remaining dependence of ϕ_{FWHM} on H_{rms}/Λ was determined by plotting calculated results for ϕ_{FWHM} vs. the right side of (14) assuming a power-law behavior for the scattering function g. First, new simulations were carried out in sound channels that were vertically stretched and compressed by factors of 2 and $\frac{1}{2}$, respectively ($D = 150$ and 37.5 m). For these simulations, the vertical TRA remained water-column-spanning with constant 3-m spacing and the acoustic frequency was 500 Hz. The source depth and speed of sound gradients were scaled, but the bottom roughness height was not changed. Additional simulations were also completed with the bottom roughness profiles stretched and compressed in the horizontal plane by factors of 2 and $\frac{1}{2}$, respectively ($\Lambda = 560$ and 140 m), compared to the nominal case ($\Lambda = 280$). Here, too, the roughness height was unchanged.

Figure 11 presents all of the computed results on a single plot for the shallower (a) and deeper (b) source. Figure 11 is similar in format to Figs. 8–10 except that the inset triangle shows a slope of -1 and the horizontal axis is $(kRH/\Lambda)^{3/2}$. This scaling factor was found by trial and error to produce the best collapse of the computed results for the shallower source. It implies $g(H_{\mathrm{rms}}/\Lambda, \overline{\theta}) \sim \sqrt{H_{\mathrm{rms}}/\Lambda}$.

Given the sophistication of the arguments leading to (14), the collapse of results in Fig. 11(a) is good with the exception of the attenuation upturns at longer ranges and the shorter-range results at the lowest roughness level. In fact, a quantitative power-law relationship for the azimuthal retrofocus size of the shallower source can be proposed:

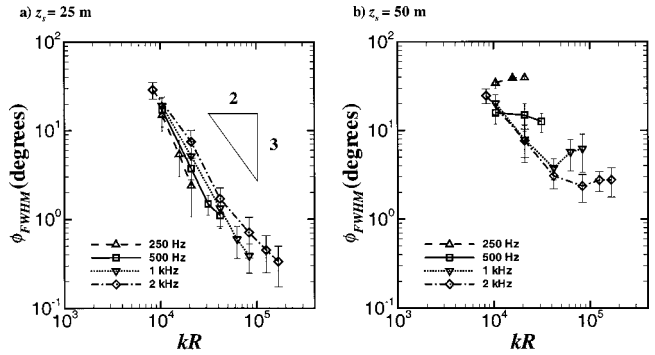

FIG. 12. TRA retrofocus azimuthal full-width at half-maximum angles, ϕ_{FWHM}, versus acoustic-wave-number-scaled source, array range (R) for SWARM strength internal waves at various frequencies for source depths of $z_s = 25$ m (a) and 50 m (b) without bottom roughness.

$$\phi_{\mathrm{FWHM}}(\mathrm{degrees}) \approx 2500 \left(\frac{\Lambda}{kRH_{\mathrm{rms}}} \right)^{3/2}, \tag{15}$$

where the empirical constant (2500) was chosen by eye to fit the bulk of the calculations for ϕ_{FWHM} that are not influenced by absorption. This scaling law accounts for ϕ_{FWHM} in terms of five length scales ($1/k$, D, R, H_{rms}, and Λ) and should be applicable to a wide variety of shallow-water sound channels when absorption effects are minimal.

The collapse of the ϕ_{FWHM} results for the deeper source ($z_s = 50$ m) shown in Fig. 11(b) are favorable but not as compelling as for the shallow source. Here the retrofocus is mostly formed by the lowest-order modes that are least likely to be perturbed by bottom interactions and the azimuthal retrofocus sizes are larger than that found for the shallower source ($z_s = 25$ m). The influence of the mode-averaged grazing angle on ϕ_{FWHM}, which is not predicted in (14), is the most likely cause for the less successful collapse of results shown in Fig. 11(b). However, (15) does provide a consistent lower limit for ϕ_{FWHM} for the deeper source.

In summary, bottom roughness encourages environment-enhanced retrofocusing. Higher acoustic frequencies, greater bottom roughness, and longer ranges sharpen azimuthal retrofocusing except when absorption of the high-order propagating modes reverse these trends.

C. Azimuthal retrofocusing with static internal waves

Variations in the water column properties caused by internal waves may also lead to environment-enhanced retrofocusing. In a sound channel with vertical variation in the sound speed, internal waves raise and lower the contours of constant sound speed to produce a fully three-dimensional (3D) sound-speed field. This subsection describes the effects of a random superposition of linear internal waves on vertical-TRA azimuthal retrofocusing in the baseline sound channel without bottom roughness. The parameters varied here include the source depth (z_s), the source-array range (R), and the acoustic frequency (f). These internal-wave retrofocusing results are provided for comparison with the bottom roughness results presented in the previous subsection, and for comparison with the simplified theory in Kholsa and Dowling (1998).

Figure 12 shows the azimuthal retrofocus width,

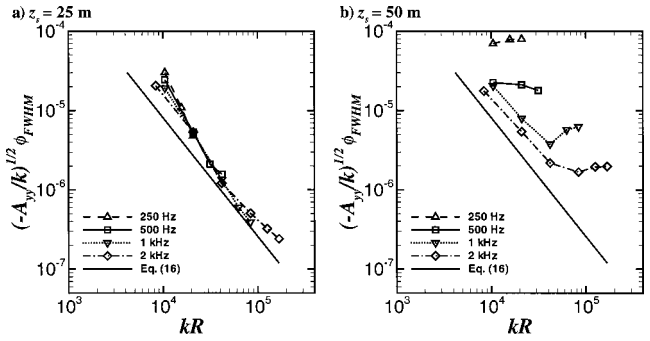

FIG. 13. Comparison of (16) to the computed retrofocus azimuthal full-width at half-maximum angles, ϕ_{FWHM}, versus acoustic-wave-number-scaled source-array range (R) for SWARM strength internal waves at various frequencies for source depths of $z_s=25$ m (a) and 50 m (b). The collapse is unsuccessful for the deeper source because the back-propagating field interacts little with the sound speed fluctuations.

ϕ_{FWHM}, versus scaled source-array range, kR, for source depths of $z_s=25$ m [Fig. 12(a)] and $z_s=50$ m [Fig. 12(b)]. The logarithmic range on both axes and the scaling of this figure allow it to be directly compared to Figs. 8–10. The shallow source data plainly show that as the range increases, ϕ_{FWHM} decreases for a random linear super-position of internal waves whose strength is matched to measurements made during the SWARM experiment. This trend is not as strong and then appears to slightly reverse at long ranges for the deep source. Comparison of Figs. 10 and 12 shows that a rms depth fluctuation of 1.5 m leads to nearly the same azimuthal retrofocus extent as the SWARM-strength internal waves for both the shallow and deep sources.

These internal-wave retrofocusing results can also be compared to the simple single-path straight-ray theory developed in Khosla and Dowling (1998). Their Eq. (5a) predicts that horizontal retrofocusing will be produced by a linear vertical TRA operating in a randomly refracting free-space environment. For small retrofocus angles, their prediction for ϕ_{FWHM} (in radians) becomes

$$\phi_{\mathrm{FWHM}}(\mathrm{radians}) \approx \frac{2.35 w_y}{R} = 8.14\left(\frac{k}{-A_{yy}}\right)^{1/2}(kR)^{-3/2}, \tag{16}$$

where w_y is the horizontal standard deviation width of the retrofocus, and A_{yy} is the second spatial derivative of the projected autocorrelation function of index of refraction fluctuations with respect to the horizontal coordinate [see Ishimaru (1978), A_{yy} is negative]. Figure 13 shows a comparison of (16) (solid straight line) with the current computed results (curves with symbols) for the shallow source ($z_s=25$ m). The value of A_{yy} used to construct this figure ($-1.4\times10^{-8}\,\mathrm{m}^{-1}$) was obtained from a water-column average of the simulated internal wave fluctuations. The scaling suggested by (11) produces a remarkable collapse of the computational results for ϕ_{FWHM} at the various acoustic frequencies and source-array ranges even though the predicted power law exponent and retrofocus sizes do not perfectly match the computational results. The simulation results for ϕ_{FWHM} are approximately a factor of 2 larger than the predictions of (16).

Like the bottom roughness cases, the scaled internal-wave-field results for ϕ_{FWHM} with the deeper ($z_s=50$ m) source shown in Fig. 13(b) do not collapse as well as the scaled shallower ($z_s=25$ m) source results. Here, the low-order modes forming the deeper retrofocus predominantly pass underneath the sound speed variations shown in Fig. 2(b). Thus, the scaling law (16), which is based on a water-column average of sound-speed fluctuations, overpredicts the azimuthal scattering effects of the internal waves when the source is deep in the sound channel. However, when taken together, the deep and shallow source results suggest that random refraction has similar effects on azimuthal TRA retrofocusing in both free-space (single-path) and sound channel (multi-path) environments when the propagating sound fields interact with the random media.

IV. SUMMARY AND CONCLUSIONS

This article reports the findings of a computational study of the azimuthal (or horizontal) extent of the retrofocus formed by a vertical narrow-band water-column-spanning time-reversing array operating in a static random shallow ocean. The influences of source depth, source-array range, acoustic frequency, bottom absorption, random bottom roughness, and internal-wave-induced fluctuations have all been addressed. Moreover, two power law scalings for the azimuthal size of the TRA retrofocus have been found.

The results presented here lead to several conclusions. First of all, random depth variations in a sound channel environment sharpen the retrofocusing in the azimuthal direction while leaving the vertical retrofocus size essentially unchanged. This occurs because modal propagation dominates the vertical character of shallow-water sound fields so that the more delicate effects of weak horizontal environmental variations can only be ascertained in the azimuthal (or horizontal) retrofocus size. Second, the environment's ability to enhance (i.e., decrease) a vertical TRA's azimuthal retrofocus size increases with increasing acoustic frequency, environmental fluctuation levels, and source-array range. While this conclusion is strongly supported by the rough bottom results shown in Figs. 8–11, it also applies to retrofocusing with random internal waves. Third, the extent to which vertical-TRA azimuthal retrofocusing is influenced by random environmental fluctuations in a shallow ocean sound channel is determined by the depth of the source and the character of the channel's propagating modes. Deep (shallow) source retrofocusing relies more heavily on the lower (higher) order propagating modes that are less (more) susceptible to scattering from bottom roughness and internal waves. Thus, deep (shallow) sources produce larger (smaller) azimuthal retrofocus sizes. And, the shallow-source azimuthal sizes are amenable by simple power law scalings which form lower bounds for deeper source retrofocus sizes. Fourth, bottom absorption eventually reverses the trend toward better azimuthal retrofocusing with increasing bottom roughness and range.

And, finally, the good (perhaps even fortuitous) agree-

ment found between the simple theory of (16) and the calculated azimuthal retrofocus sizes for the shallower source suggests that retrofocusing through random media in single-path and multipath environments shares some common features. In this circumstance, the connection between single-path and multipath environments may lie in the fact that the calculated sound channel results only incorporate vertical multipath propagation. When viewed in the usual vertical r-z plane, multipath propagation is apparent in the sound channels of this study. However, when sound propagation in the same environments is viewed from above (i.e., looking down on the r-ϕ plane), there is only one propagation path; all of the various bottom and surface bounce paths seen in the r-z plane follow the same r-ϕ path. Moreover, this lone path is a straight line in the horizontal r-ϕ plane. Weak horizontal propagation variations lead to azimuthal retrofocusing, and (16) is based on there being a single straight average propagation path through the random medium between any two points. Interestingly, both of these phenomena (weak horizontal propagation variations, and straight r-ϕ plane rays) are captured in the current N×2D calculations. Thus, the main reason that (16) was found successful in the internal-wave perturbed sound channels simulated here is because the dominant multipath propagation occurs in vertical planes while the phenomena necessary for vertical-array azimuthal retrofocusing are reasonably well simulated by single-path propagation in the horizontal r-ϕ plane. Therefore, although (16) is surprisingly effective, it will likely fail in more complicated three-dimensional environments that support both horizontal (i.e., azimuthal) and vertical multipath propagation.

ACKNOWLEDGMENTS

This work was sponsored by the Office of Naval Research Ocean Acoustics Program through contract Nos. N00014-96-1-0040 and N00014-97-1-0628. The authors also wish to thank Dr. Michael Collins for his guidance in utilizing RAM and Dr. Steven Finette for providing the SWARM measurements.

Apel, J. R., Badiey, M., Chiu, C.-S., Finette, S., Headrick, R., Kemp, J., Lynch, J. F., Newhall, A., Orr, M. H., Pasewark, B. H., Tielbürger, D., Turgut, A., von der Heydt, K., and Wolf, S. (**1997**). ''An overview of the 1995 SWARM Shallow-water internal wave acoustic scattering experiment,'' IEEE J. Ocean Eng. **22**, 465–500.

Bell, T. H. (**1975**). ''Statistical features of sea floor topography,'' Deep-Sea Res. Oceanogr. Abstr. **22**, 883–892.

Berkson, J. M., and Matthews, J. E. (**1984**). ''Statistical Characterization of Seafloor Roughness,'' IEEE J. Ocean Eng. **9**, 48–52.

Buckingham, M. J. (**1984**). ''Acoustic propagation in a wedge-shaped ocean with perfectly reflecting boundaries,'' in *Hybrid Formulation of Wave Propagation*, edited by L. B. Felsen (Nijhoff, Dordrecht).

Chakroun, N., Fink, M., and Wu, F. (**1995**). ''Time reversal processing in ultrasonic nondestructive testing,'' IEEE Trans. Ultrason. Ferroelectr. Freq. Control **42**, 1087–1098.

Clay, C. S. (**1964**). ''Effect of a slightly irregular boundary on the coherence of waveguide propagation,'' J. Acoust. Soc. Am. **36**, 833–837.

Collins, M. D. (**1993**). ''A split-step Padé solution for parabolic equation method,'' J. Acoust. Soc. Am. **93**, 1736–1742.

Collins, M. D. (**1994**). ''Generalization of the split-step Padé solution,'' J. Acoust. Soc. Am. **96**, 382–385.

Collins, M. D. (**1998**). ''New and improved parabolic equation models,'' J. Acoust. Soc. Am. **104**, 1808(A).

Dashen, R., Munk, W. H., Watson, K. M., and Zachariasen, F. (**1979**). In *Sound Transmission Through a Fluctuating Ocean*, edited by S. M. Flatté (Cambridge U. P., Cambridge).

Dowling, D. R., and Jackson, D. R. (**1992**). ''Narrow-band performance of acoustic phase-conjugate arrays in dynamic random media,'' J. Acoust. Soc. Am. **91**, 3257–3277.

Draeger, C., and Fink, M. (**1999**). ''One channel time-reversal in chaotic cavities: Theoretical limits,'' J. Acoust. Soc. Am. **105**, 611–617.

Draeger, C., Aime, J.-C., and Fink, M. (**1999**). ''One channel time-reversal in chaotic cavities: Experimental results,'' J. Acoust. Soc. Am. **105**, 618–625.

Draeger, C., Cassereau, D., and Fink, M. (**1998**). ''Theory of the time-reversal process in solids,'' J. Acoust. Soc. Am. **102**, 1289–1295.

Dungan, M. R., and Dowling, D. R. (**2000**). ''Computed narrowband time-reversing array retrofocusing in a dynamic shallow ocean,'' J. Acoust. Soc. Am. **107**, 3101–3112.

Fink, M. (**1997**). ''Time-Reversed Acoustics,'' Phys. Today **50**(3), 34–40.

Fink, M. (**1999**). ''Time-Reversed Acoustics,'' Sci. Am. **281**(5), 91–97.

Fox, C. G., and Hayes, D. E. (**1985**). ''Quantitative Methods for Analyzing the Roughness of the Seafloor,'' Rev. Geophys. **23**(1), 1–48.

Hodgkiss, W. S., Song, H. C., Kuperman, W. A., Akal, T., Ferla, C., and Jackson, D. R. (**1999**). ''A long-range and variable focus phase-conjugation experiment in shallow water,'' J. Acoust. Soc. Am. **105**, 1597–1604.

Ishimaru, A. (**1978**). *Wave Propagation and Scattering in Random Media* (Academic, San Diego), Vol. 2.

Jackson, D. R., and Dowling, D. R. (**1991**). ''Phase-conjugation in underwater acoustics,'' J. Acoust. Soc. Am. **89**, 171–181.

Jackson, D. R., Winebrenner, D. P., and Ishimaru, A. (**1986**). ''Application of the composite roughness model to high-frequency bottom backscattering,'' J. Acoust. Soc. Am. **79**, 1410–1422.

Jensen, F. B., Kuperman, W. A., Porter, M. B., and Schmidt, H. (**1994**). *Computational Ocean Acoustics* (AIP, New York), p. 41.

Khosla, S. R., and Dowling, D. R. (**1998**). ''Time-reversing array retrofocusing in simple dynamic underwater environments,'' J. Acoust. Soc. Am. **104**, 3339–3350.

Khosla, S. R., and Dowling, D. R. (**2000**). ''Time-reversing array retrofocusing in noisy environments,'' J. Acoust. Soc. Am. **109**, 538–546.

Kuperman, W. A. (**1975**). ''Coherent component of specular reflection and transmission at a randomly rough two-fluid interface,'' J. Acoust. Soc. Am. **58**, 365–370.

Kuperman, W. A., and Ingenito, F. (**1977**). ''Attenuation of the coherent component of sound propagating in shallow water with rough boundaries,'' J. Acoust. Soc. Am. **61**, 1178–1187.

Kuperman, W. A., Porter, M. B., Perkins, J. S., and Evans, R. B. (**1991**). ''Rapid computation of acoustic fields in three-dimensional ocean environments,'' J. Acoust. Soc. Am. **89**, 125–133.

Kuperman, W. A., Hodgkiss, W. S., Song, H. C., Akal, T., Ferla, C., and Jackson, D. R. (**1998**). ''Phase-conjugation in the ocean: experimental demonstration of an acoustic time reversal mirror,'' J. Acoust. Soc. Am. **103**, 25–40.

Medwin, H., and Clay, C. S. (**1998**). *Fundamentals of Acoustical Oceanography* (Wiley–Academic, Boston), Chap. 13.

Ohno, M., Yamamoto, K., Kokubo, A., Sakai, K., and Takagi, K. (**1999**). ''Acoustic phase conjugation by nonlinear piezoelectricity. I. Principle and basic experiments,'' J. Acoust. Soc. Am. **106**, 1330–1338.

Orris, G. J., and Perkins, J. S. (**1998**). ''Three-dimensional propagation modeling in shallow water,'' J. Acoust. Soc. Am. **103**, 3029(A).

Perkins, J. S., and Kuperman, W. A. (**1990**). ''Environmental signal processing: Three dimensional matched field processing with a vertical array,'' J. Acoust. Soc. Am. **87**, 1553–1556.

Press, W. H., Flannery, B. P., Teukolsky, S. A., and Vetterling, W. T. (**1986**). *Numerical Recipes* (Cambridge U.P., Cambridge), Chap. 16.

Rose, J. H., Bilgen, M., Roux, Ph., and Fink, M. (**1999**). ''Time-reversal mirrors and rough surfaces: Theory,'' J. Acoust. Soc. Am. **106**, 716–723.

Roux, Ph., De Rosny, J., Fink, M., and Rose, J. R. (**1999a**). ''Time-reversal mirrors and rough surfaces: Experiment,'' J. Acoust. Soc. Am. **106**, 724–732.

Roux, Ph., Derode, A., Peyre, A., Tourin, A., and Fink, M. (**1999b**). ''Acoustic imaging through a multiple scattering medium using a time-reversal mirror,'' J. Acoust. Soc. Am. **107**, L7–L12.

Smith, K. B. (**1996**). ''Modeling the effects of azimuthal coupling on acous-

tic propagation in the presence of 3-dimensional, rough ocean interfaces using the parabolic approximation,'' Special Issue of Theoretical and Computational Acoustics, edited by D. Lee, Y.-H. Pao, M. H. Schultz, and Y. C. Teng (World Scientific, Singapore), pp. 115–131.

Smith, K. B. (**1998**). ''Three-dimensional propagation effects: Modeling, observations, and suggested benchmark cases,'' J. Acoust. Soc. Am. **103**, 2989(A).

Song, H. C., Kuperman, W. A., and Hodgkiss, W. S. (**1998a**). ''A time-reversal mirror with variable range focusing,'' J. Acoust. Soc. Am. **103**, 3234–3240.

Song, H. C., Kuperman, W. A., Hodgkiss, W. S., and Gerstoft, P. (**1998b**). ''Out-of-plane defocusing in a time reversal mirror,'' J. Acoust. Soc. Am. **104**, 1748(A).

Song, H. C., Kuperman, W. A., Hodgkiss, W. S., Akal, T., and Ferla, C. (**1999**). ''Iterative time reversal in the ocean,'' J. Acoust. Soc. Am. **105**, 3176–3184.

Steinberg, B. D. (**1976**). *Principles of Aperture and Array System Design* (Wiley, New York), Chaps. 1, 12.

Sturm, F. B., Fawcett, J. A., Jensen, F. B., and Pélissier, M.-C. (**1998**). ''Benchmarking Two Three-Dimensional Parabolic Equation Methods,'' J. Acoust. Soc. Am. **103**, 2990(A).

Tanter, M., Thomas, J.-L., and Fink, M. (**1998**). ''Focusing and steering through absorbing and aberrating layers: Application to ultrasonic propagation through the skull,'' J. Acoust. Soc. Am. **103**, 2403–2410.

Tielbürger, D., Finette, S., and Wolf, S. (**1997**). ''Acoustic propagation through an internal wave field in a shallow water waveguide,'' J. Acoust. Soc. Am. **101**, 789–808.

Yamamoto, K., Ohno, M., Kokubo, A., Sakai, K., and Takagi, K. (**1999**). ''Acoustic phase conjugation by nonlinear piezoelectricity. II. Visualization and application to imaging systems,'' J. Acoust. Soc. Am. **106**, 1339–1345.

Yang, T. C., and Yoo, K. (**1998**). ''Frequency spectrum of linear internal waves in shallow water and a modified Garrett-Munk model,'' J. Acoust. Soc. Am. **104**, 1765(A).

Yönak, S. H., and Dowling, D. R. (**1999**). ''Photoacoustic detection and localization of small gas leaks,'' J. Acoust. Soc. Am. **105**, 2685–2694.

Yoo, K., and Yang, T. C. (**1998**). ''Measurements of modal spectrum of linear internal waves in shallow water and comparison with the Garrett-Munk model,'' J. Acoust. Soc. Am. **104**, 1765(A).

Ziomek, L. J. (**1985**). *Underwater Acoustics* (Academic, Orlando, FL), Chaps. 3 and 4.

Surface acoustic waves in the GHz range generated by periodically patterned metallic stripes illuminated by an ultrashort laser pulse

B. Bonello[a] and A. Ajinou
Laboratoire des Milieux Désordonnés et Hétérogènes (UMR CNRS 7603), Université Pierre et Marie Curie (boîte 86), 4, place Jussieu, 75252 Paris cedex 05, France

V. Richard, Ph. Djemia, and S. M. Chérif
Laboratoire des Propriétés Mécaniques et Thermodynamiques des Matériaux (UPR CNRS 9001), Université Paris-Nord, Bd. Jean-Baptiste Clément, 93430 Villetaneuse, France

(Received 29 November 2000; revised 24 May 2001; accepted 6 July 2001)

The photoelastic response of periodic arrays of stripes attached to the surface of a substrate and illuminated by an ultrashort laser pulse were investigated. The samples were gold arrays on silicon and aluminum arrays either on crystalline quartz or on silicon. The metallic stripes had submicrometer lateral dimensions and the spatial periods ranged from about 1 μm up to 5 μm. The substrate being transparent (quartz) or slightly absorbing (silicon) at the laser wavelength ($\lambda = 750$ nm), a laterally modulated thermal stress is generated near the surface of the substrate when a light pulse illuminates the structure. The studies of vibrations involved by the subsequent relaxation processes show that surface acoustic waves at frequency as high as about 5 GHz are excited with the samples consisting of aluminum stripes. In the case of the aluminum samples with the largest lateral spatial periods (aluminum on quartz), the surface acoustic wave propagates outside the illuminated area. In the case of the gold samples, a normal mode of individual bars is observed instead. Experimental evidence shows that these behaviors are mainly governed both by the lateral spatial period of the structure and by the density of the metal.
[DOI: 10.1121/1.1399034]

PACS numbers: 43.35.Pt, 43.35.+d, 43.38.Rh, 68.35.Gy [SGK]

I. INTRODUCTION

Various techniques, including mechanical and optical methods, have been developed for exciting surface acoustic waves (SAW) onto nonpiezoelectric solid substrates.[1–3] As far as waves at low frequencies are concerned, the simplest procedure consists in launching a longitudinal bulk wave into a wedge attached to the substrate; the longitudinal acoustic mode impinging on the interface is converted into a Rayleigh mode, provided that the longitudinal sound velocity in the wedge is less than the one in the substrate. However, on account of the large ultrasonic damping of the bulk acoustic modes it involves, this method is only efficient at frequencies less than a few tens of MHz. This limitation can be overcome by optical excitation. If the surface of an absorbing material is illuminated by a short laser pulse, both bulk and surface waves are generated by thermal expansion mechanisms. The intense radial temperature gradient in the illuminated area results in a strong stress on the surface, which in turn causes a SAW to radiate over 360° as a broadband pulse. The frequency is determined by the optical pulse duration and experiments in the GHz range are commonly achieved with picosecond laser pulses. As for the directivity, it can be improved by several means. The use of a cylindrical lens to focus the laser beam into a line source[4,5] or illumination through a noncontacting mask simulating an interdigital transducer[6] both allow to concentrate the elastic energy in the direction normal to the line source and to investigate the nonlinear regime.[7] The interference pattern resulting from the crossing of two laser beams is a widely used technique, too.[8–10] These optical methods are effective for opaque—or covered by an opaque layer—materials and in materials exhibiting strong electrostrictive properties.

An alternative approach suitable for transparent materials consists of exciting SAW by illuminating with a laser pulse, a periodic metallic array of stripes attached to the surface of the sample.[11,12] The rapid nonradiative relaxation following the partial absorption of the optical pulse generates a temperature distribution that has the same spatial shape as the metallic array. If the substrate is transparent, or less absorbing than the stripes, the illumination results in a laterally modulated temperature rise which in turn causes a modulated thermal expansion underneath the surface; counterpropagating SAW are thus expected to be launched in the direction normal to the stripes. Their frequency is given by the ratio of the lateral spatial period to the velocity of the Rayleigh wave in the substrate and hence, SAW at several GHz can be resonantly excited by nanostructures with a submicrometer spatial period. Unfortunately, it has been experimentally demonstrated that this scenario does not hold in certain situations. Lin *et al.*[13] have used the picosecond ultrasonic technique to study the photoelastic response of nanometric arrays of gold bars on silica substrates, set into vibration by an ultrashort laser pulse. Instead of the expected SAW, they observed the

[a]Author to whom correspondence should be addressed; electronic mail: bbo@ccr.jussieu.fr

normal modes of individual stripes without coupling among them. They attributed the lack of SAW to the radiation of elastic energy in the bulk of the substrate resulting from the periodicity of the gold arrays. A simple calculation showed that the rate of radiation strongly depends both on the periodicity of the array and on the density of the metal, so that the excitation of SAW is inhibited in gold arrays (density $\rho_{\mathrm{Au}}=19.3\ \mathrm{g\,cm^{-3}}$) with nanometric lateral dimensions.

In this article, we show that SAW in the GHz range can be optically excited with aluminum arrays. We first find out how the power flow in the Rayleigh wave varies with the lateral spatial period and we compare it with the rate of radiation in the substrate originating from the propagation under the periodic structure. This allows us to establish under which conditions SAW are actually excited. We then report on experimental results obtained by using the picosecond ultrasonics. We compare the photoelastic response of aluminum arrays with a spatial period of a few micrometers or less, with the one of gold arrays having a lateral period of about 1 μm. We show that , owing to the low density of aluminum ($\rho_{\mathrm{Al}}=2.7\ \mathrm{g\,cm^{-3}}$), SAW at several GHz are excited and propagate out of the illuminated area at the surface of the substrate, whereas they do not in the case of gold.

II. THEORETICAL BACKGROUND

Although the involved physical processes are quite different, SAW optically excited and Rayleigh waves launched at the surface of a piezoelectric plate by conventional interdigital transducers have similar features. In particular, the larger the number of stripes affected by the excitation process, the narrower the bandwidth of the SAW. In our experiment, up to about a hundred metallic bands were illuminated, therefore accurately fixing the wavelength. One can thus consider that the angular frequency ω of the excited Rayleigh wave is given by

$$\omega=\frac{2\pi V_R}{d}, \tag{1}$$

where V_R is the Rayleigh wave velocity in the substrate and d the lateral spatial period.

Besides the Rayleigh surface wave, the normal modes of the individual metallic bars are also excited, provided that the period of the corresponding vibration is larger than the optical pulse duration. The displacements associated with these modes, their amplitude, and their frequencies depend both on the cross section of the bars and on the excitation process but they do not depend on the spatial period.

In order to estimate the efficiency of the excitation process, we compare in this section the power flow in the SAW with the rate of radiation in the bulk of the substrate due to the propagation of the wave under the periodic structure. Although the experiments described in the next section have been performed in anisotropic substrates, we present the calculation for the isotropic case since it can be analytically completed in that case; the main results allow for qualitative comparisons which remain valid whatever the symmetry of the substrate.

The power flow in the surface wave an be easily derived from the expressions for the displacements in the sagittal plane associated with the Rayleigh wave, together with the Poynting's theorem. In the case of a wave propagating in the x direction at the surface of an isotropic solid lying in the $(x-y)$ plane, the displacement vector $\mathbf{u}$ has nonzero components along the x axis and in the direction perpendicular to the surface, which is the z axis. The components are[14]

$$u_x=u_0\left(\exp\left(-\alpha_1\frac{z}{d}\right)-a\exp\left(-\alpha_2\frac{z}{d}\right)\right)\times\exp\left(i\omega\left(t-\frac{x}{V_R}\right)\right), \tag{2a}$$

$$u_y=0, \tag{2b}$$

$$u_z=-iu_0\left(1-\frac{V_R^2}{V_L^2}\right)^{1/2}\left(\exp\left(-\alpha_1\frac{z}{d}\right)-\frac{1}{a}\exp\left(-\alpha_2\frac{z}{d}\right)\right)\exp\left(i\omega\left(t-\frac{x}{V_R}\right)\right), \tag{2c}$$

where the constants α_1, α_2, and a are defined by $\alpha_1=2\pi(1-V_R^2/V_L^2)^{1/2}$, $\alpha_2=2\pi(1-V_R^2/V_T^2)^{1/2}$, and $a=1-(V_R^2/2V_T^2)$. u_0 is the amplitude of the wave; V_R, V_L, and V_T are, respectively, the Rayleigh longitudinal, and shear wave velocities in the substrate.

On the other hand, the components $P_k(k=x,y,z)$ of the complex acoustic Poynting vector $\mathbf{P}$ are related to the components of the stress tensor σ by

$$P_k=-\frac{1}{2}\frac{\partial u_j^*}{\partial t}\sigma_{jk}, \tag{3}$$

in which the use of repeated indices indicates summation. Combining Eqs. (2) and (3), one easily finds that the only real component of $\mathbf{P}$ lies along the x axis and reduces to the form

$$P_x=i\frac{\omega}{2}\left(c_{11}\frac{\partial u_x}{\partial x}+C_{12}\frac{\partial u_z}{\partial z}\right)u_x^*, \tag{4}$$

where C_{11} and C_{12} are the elastic constants of the material. It is then straightforward to show that P_x depends on the spatial period d through

$$P_x=f(z/d)d^{-2}. \tag{5}$$

The factor $f(z/d)$, which corresponds to the exponential decay of the elastic energy in the depth of the substrate, is positive and depends on the physical parameters of the material. This coarse approach therefore allows the prediction that the elastic energy near the surface $(z=0)$ is proportional to d^{-2}.

The Rayleigh wave radiates elastic energy into the bulk as it propagates under the metallic array. Indeed, the normal component of the stress σ_{zz} is null in between two consecutive stripes at the surface of the sample, but is different from zero under the metallic bands: as a consequence of this stress, the metallic stripes follow the motion of the surface and generate longitudinal waves (assumed to be plane waves), which propagates along the z axis with the velocity

V_L. This in turn leads to the damping of the SAW; it is thus important to estimate the rate of radiation for a given nanostructure and to compare it with the power flow in the surface wave. This can be done in a straightforward way by first calculating the stress underneath the stripes and then by applying again Poynting's theorem. The only nonzero component[15,16] of the stress tensor, namely σ_{zz}, was deduced from the equation of motion in the metal

$$\rho_M \frac{\partial^2 u_z}{\partial t^2} = \frac{\partial \sigma_{zz}}{\partial z}, \tag{6}$$

where ρ_M is the density of the metal. As long as the thickness h of the metallic stripes remains small (this condition is always fulfilled in our experiments), the displacement in the metal along the z axis is constant and Eq. (6) can be solved: the normal component of the stress tensor is found to be[13]

$$\sigma_{zz} = 4\pi^2 \rho_M h u_z V_R^2 d^{-2}. \tag{7}$$

As for the particle velocity $\partial u_z/\partial t$ in the substrate, it was also deduced from the equation of motion. Assuming that u_z has the form $u_z = u_z^0 \exp(i\omega(t - z/V_L))$, we obtained

$$\frac{\partial u_z}{\partial t} = -i(\rho_s \omega)^{-1} \frac{\partial \sigma_{zz}}{\partial z}, \tag{8}$$

where ρ_s is the density of the substrate. Combining Eqs. (1), (3), (7), and (8), one finds that the rate of radiation per unit area in the substrate is given by[13]

$$P_z = A \frac{h^2 \rho_M^2}{d^4}. \tag{9}$$

The constant A depends on the density and on the sound velocities V_R and V_L in the substrate $[A = 8\pi^4 V_R^4 \times u_z^{0^2} (\rho_s V_L)^{-1}]$. The point in Eq. (9) is that the rate of radiation into the substrate is proportional to the squared density of the metal and inversely proportional to the fourth power of d. This is to be compared to the asymptotic d^{-2} dependence of the power flow in the Rayleigh wave predicted by Eq. (5). As a consequence of this d^{-4} behavior, the corresponding damping prevents the Rayleigh waves from propagating under a periodic nanostructure made up of a heavy material and/or for small spatial periods. The mechanical vibration of individual bars is observed instead.

III. EXPERIMENTAL DETAILS

Two sets of samples were prepared to check the validity of the preceding arguments. Gold specimens were fabricated using the electron beam lithography.[17] They consisted of 1-mm-long bands, periodically deposited onto silicon substrates. The bands were about 400 nm thick and the spatial period was 1 micrometer for all the samples. The width of the bands went from about 290 nm up to 500 nm, so that the covering rate (i.e., the ratio of the metallic surface to the total surface of the nanostructure) varies from 29% up to 50%.

The aluminum samples were deposited either on silicon or on quartz substrates by the same method we used for the fabrication of the gold specimens. In order to investigate the influence of the density, we prepared aluminum samples on silicon substrates. Both their thickness and spatial period were identical to those of the gold samples, i.e., 400 nm and 1 μm, respectively, therefore allowing comparisons; the width of the bands ranged from 300 nm up to 680 nm. The metallic bands were perpendicular to the [110] crystallographic axis of silicon.

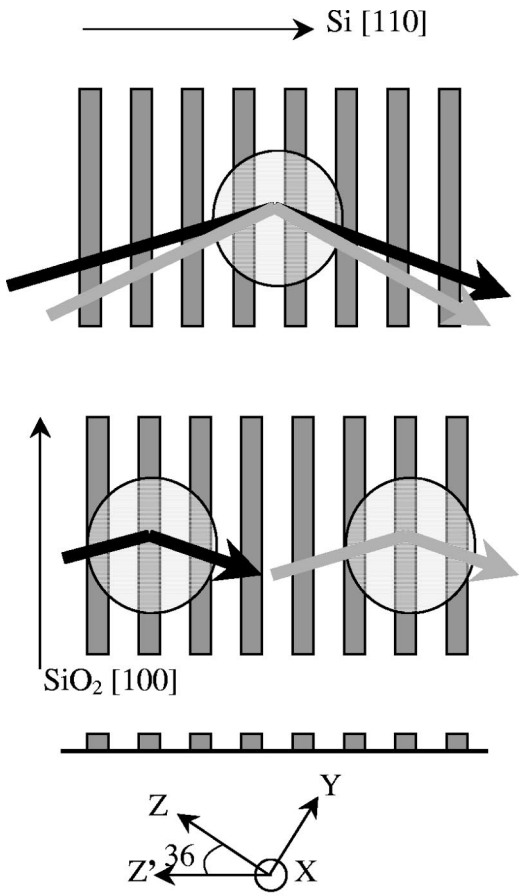

FIG. 1. Geometry of the experiment. The top plot holds for all the samples: gold and aluminum samples on silicon, and aluminum on quartz as well. In some experiments performed with aluminum on quartz, the metallic bands were parallel to the plane of incidence. This geometry is not represented here. The middle plot corresponds to the configuration in experiments proving that the SAW propagates outside the illuminated area (see the text). The bottom plot describes the cut of the crystalline quartz substrates (AT cut).

We also prepared aluminum gratings on crystalline quartz. The plane of the substrate was at an angle of 36° with respect to the crystallographic plane XY, corresponding to the so-called AT cut. The metallic bands were parallel to the [100] direction. The geometry is shown in Fig. 1. This cut is particularly interesting since a Rayleigh wave cannot be piezoelectrically excited in the direction normal to the stripes (this direction is referenced as Z' in Fig. 1). A surface transverse wave, corresponding to a displacement of the matter parallel to the [100] direction, is excited instead. This shear wave propagates along Z' at a velocity of 5100 ms^{-1}. All the bands deposited on this substrate had identical cross sections but different spatial periods. The cross section of the stripes was about 100 nm thick and 1.5 μm across; the spatial period was either 2.5 or 5 μm.

The quality of the samples, the dimensions, the period, and the sharpness of the edges were characterized by scanning electron microscopy.

We used the picosecond acoustics to investigate the photoelastic response of the nanostructures. This technique involves the excitation of the sample by an ultrashort optical pulse (the pump pulse) and the monitoring of the subsequent reflectivity changes by measuring the intensity of a reflected pulse (the probe pulse) delayed with respect to the pump by means of a variable optical path. Details on our apparatus can be found in Ref. 16. Briefly, it allows for a delay up to 4 ns with a temporal resolution only limited by the duration of the laser pulse, namely 100 fs. In most experiments, we focused both pump and probe beams at nearly normal incidence on the same area of the surface sample by means of a lens (f:62 mm) or a Cassegrain objective. However, in some experiments performed with aluminum on quartz, we probed the change in optical reflectivity a few micrometers away from the excited area (Fig. 1). The diameter of the laser spot was measured to be 70 μm when the lens was used; it was reduced to 15 μm with the Cassegrain objective.

When a light pulse is incident on the surface of the sample, the temperature of the absorbing parts of the heterostructure rises by a few Kelvin, which in turn creates stress- and strain fields by thermal expansion. Actually, the initial temperature distribution within the sample depends on the optical absorption lengths ζ of the two materials making up the sample, through a term of the form $\zeta^{-1}\exp(-z/\zeta)$, where z is the direction normal to the surface.[15] All the samples under investigation exhibited a strong contrast in the optical properties of the stripes and the substrate, at the wavelength of our sapphire:Ti laser source ($\lambda=750$ nm). This is obvious for the aluminum samples on crystalline quartz since the substrate is transparent. The case of the metallic stripes (aluminum and gold as well) on silicon requires further analysis. Indeed, a rigorous description of the initial stress and strain fields near the surface of these samples should include both the transport and the recombination of the carriers in the silicon. This is far beyond the scope of this article. However, a simpler approach consists of comparing the optical parameters of the silicon with the ones of the metals. The absorption length of silicon, for $\lambda=750$ nm, is $\zeta_{Si}=6.6$ μm. This is about 10^3 times the value in aluminum ($\zeta_{Al}=7$ nm). The contrast is less important with gold ($\zeta_{Au}=13$ nm) but still meaningful. We can thus consider that the initial temperature distribution in the direction perpendicular to the metallic bands—and consequently the initial strain field—has the same spatial period as the sample itself.

The optical properties of the sample are slightly altered when a strain field affects the surface. In all the experiments presented here, we took advantage of this modulation of the refractive index to monitor the photoelastic response of the gratings: the intensity of the reflected probe beam was recorded as a function of the delay with respect to the pump, using a PIN silicon photodiode associated to a conventional lock-in amplifier scheme. It is to be noticed here that the light on the photodiode mainly comes from reflection by the metallic stripes. So, one can consider in first approximation that the recorded signal originates from the change in the optical properties of the metal. However, in the case of gratings on silicon, some additional contribution from the substrate should be considered for an accurate analysis of the intensity of the reflected light.

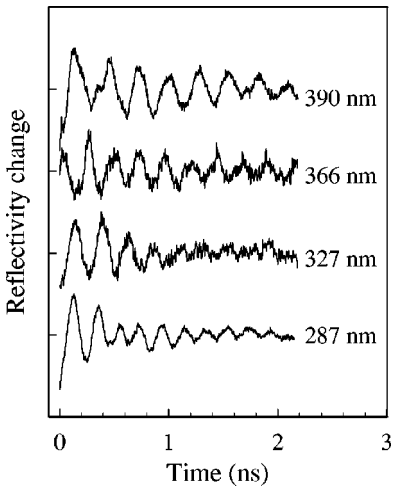

FIG. 2. Change in optical reflectivity as a function of time for samples consisting of gold stripes onto a silicon substrate. The spatial period is 1 μm for all the samples; the width of the bands is indicated near each curve. A background of thermal origin has been subtracted.

IV. RESULTS

A. Gold samples

We show in Fig. 2 the time dependence of the photoelastic response of the gold samples. For all the samples, the signal consists of a single damped oscillation whose frequency does not obey Eq. (1). We report in Fig. 3 the measured frequency against the width of the bands. It is found to depend almost linearly on the width. Since the spatial period was identical for all the samples ($d=1$ μm), this oscillation is not the Rayleigh wave at the surface of the silicon but is rather attributed to the normal mode of individual bars. For a stripe bonded to a substrate, flexural, and longitudinal modes might be excited as well. Both of them induce a slight change in the optical properties of the bar and consequently they both could be detected by our method. However, it is hard to determine, using simple arguments, which of these vibrations is involved in the photoelastic response of the structure. Indeed, there is no analytical solution to the prob-

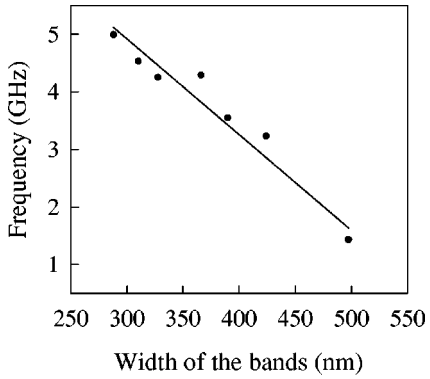

FIG. 3. Frequency of the normal mode as a function of the width of the metallic bands for samples consisting of gold arrays on silicon. The thickness of the bands was 400 nm and the lateral repeat distance was 1 μm for all the samples.

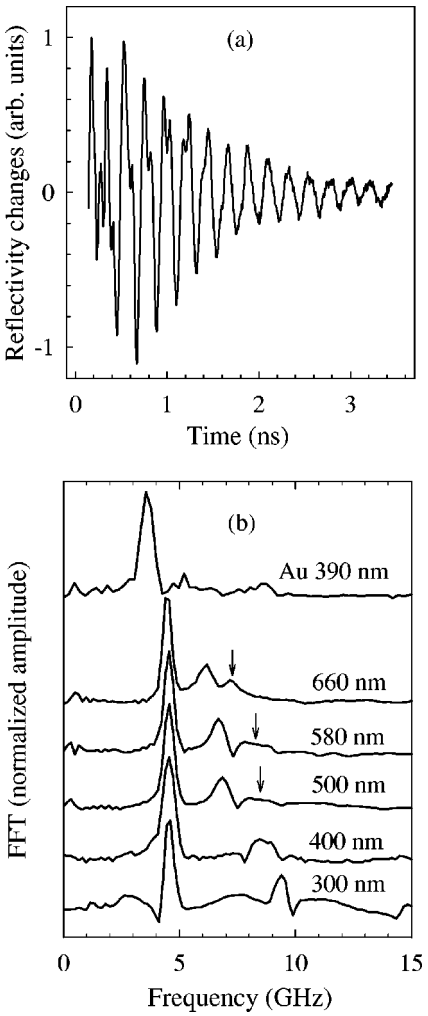

FIG. 4. (a) Change in optical reflectivity as a function of time for a sample consisting of aluminum stripes 300 nm wide. A background of thermal origin has been subtracted. (b) Magnitude of the Fourier transform of reflectivity changes, for samples consisting of aluminum stripes on silicon. The spatial period is 1 μm for all the samples. The arrows indicate the position of a likely normal mode. The Fourier transform of a gold sample (width of the metallic stripes: 390 nm) is plotted for comparison.

lem of the normal modes of a free bar with arbitrary rectangular cross section. The difficulty is further increased by the bonding to the substrate, even an order of magnitude for the expected frequency of these modes is difficult to be made. A finite-element analysis is therefore required to identify the displacements associated with the normal mode actually excited.

B. Aluminum samples

We show in Fig. 4 a typical photoelastic response in the time domain of the aluminum gratings on silicon [Fig. 4(a)] and the magnitudes of the Fourier transform [Fig. 4(b)]. The Fourier transform of a gold grating on silicon (spatial period: 1 μm, width of the stripes: 390 nm) is plotted for comparison in Fig. 4(b). It is apparent from this comparison that the photoelastic responses of the aluminum samples have many more components than the one of the gold specimens. The most important feature of the spectra is the sharp peak at a frequency which does not depend on the width of the metallic bands. This peak definitely corresponds to the Rayleigh wave excited by the absorption of the laser pulse. Indeed, the measured frequency (4.9 GHz) is in good agreement with the frequency expected for a SAW with 1-μm wavelength, propagating at the surface of the silicon substrate. The velocity of the Rayleigh wave in the direction [110] of silicon being 5080 ms^{-1}, the expected frequency is 5.08 GHz [see Eq. (1)]. The small discrepancy between these two frequencies is easily attributed to the uncertainty in the repeat distance. In contrast to the case of gold, the small density of aluminum causes only a low radiation into the substrate [see Eq. (9)] and the Rayleigh wave is actually excited, even at a frequency as high as 4.9 GHz.

Besides the Rayleigh wave, at least one vibration is excited too. In some specimens, a second vibration indicated by an arrow in Fig. 4(b) is clearly observable in the Fourier transform (width 660 nm) or appears in the spectrum as a broad peak (widths 500 and 580 nm). The frequency of both these modes depends on the width of the bands: it decreases with increasing mass of the metallic band. We thus believe that both these vibrations are normal modes of individual bars. However, as for the gold samples, finite-element methods are required to unambiguously identify the displacements associated with each mode. As for the 400-nm sample, it seems that the two normal modes have almost identical frequencies, which leads to a single broad feature centered at about 8.5 GHz. We think that the same explanation holds also for the 300-nm sample, but in that case one cannot exclude that the peak at 9.5 GHz could partially be attributed to the second harmonic of the Rayleigh wave. Although the resolution in the frequency domain is not good enough to draw definite conclusions, it is noteworthy that the ratio of the magnitudes of the two main peaks displayed in Fig. 4(b) is almost constant. This suggests that the elastic energy identically shares among collective and individual modes, whatever the width of the bands, and hence that the efficiency of the SAW excitation process does not depend on the covering rate.

We have also studied the photoelastic response of aluminum samples on quartz having identical cross section (0.1 $\times 1.5$ μm^2) but different lateral spatial periods ($d=2.5$ or 5 μm). The experimental recordings are displayed in Fig. 5(a); the magnitudes of the Fourier transforms of the reflectivity changes are shown in Fig. 5(b). These samples are found to vibrate at 1.8 and 1.05 GHz, respectively. These vibrations cannot be the normal modes of individual bars since the stripes had identical cross section in both samples. We rather attribute these vibrations to a collective response of the gratings, since the measured frequencies are in fairly good agreement with the expected frequencies of the surface transverse wave in these samples. Indeed, this mode propagates in the direction normal to the stripes at a velocity of 5100 ms^{-1}, which in the 2.5- and 5-μm samples yields to vibrations at 2.04 and 1.02 GHz, respectively. On the other hand, according to Eq. (9), the 2.5-μm spatial period sample radiates 16 times as much elastic energy into the substrate as the 5-μm spatial period sample. As a consequence, the surface wave is less efficiently excited in the former sample than it is in the latter; besides the peak corresponding to the SAW, the spec-

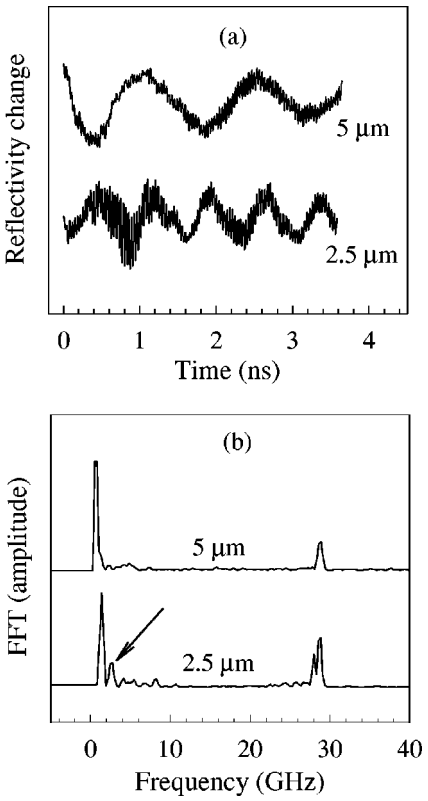

FIG. 5. (a) Photoelastic response of aluminum samples on crystalline quartz in the time domain (thermal background subtracted) and (b) in the frequency domain. The arrow indicates a vibration attributed to a normal mode of the individual bars. The cross sections of the metallic bands are identical for both the samples. The plane of incidence for the probe beam was either parallel (sample 5 μm) or perpendicular (sample 2.5 μm) to the metallic bands.

trum has a strong component [indicated by an arrow in Fig. 5(b)] which we attribute to the mechanical vibration of individual bars.

It is to be noticed that the observed oscillation are standing waves in the area excited by the pump, but that they can propagate in the adjacent regions. We have checked this property with an aluminum grating on quartz substrate having a spatial period of 2.5 μm. To do this, we measured the change in optical reflectivity a few tens of micrometers away from the pump spot. We show in Fig. 6 the recorded data for three different positions of the probe beam. As can be seen clearly in this figure, the phase of the oscillation depends on the lateral position of the probe, as expected for propagating waves. Another interesting feature of the data is the amplitude of the oscillation, which either increases [Fig. 6(a)] or decreases [Figs. 6(b), (c)] within the observation window, depending whether the SAW enters or leaves the probed area. Finally, we close this section with the remark that it is not so surprising that there is an oscillatory part of the response several micrometers away from the excited area, even immediately after the pump has been absorbed. To understand this, one should remember that our detection scheme involves optical probe pulses delayed with respect to the pump by means of the variable optical path (i.e., 4 ns maximum with our experimental setup), modulo the time τ separating two consecutive optical pules at the output of the laser source (τ=12 ns for our Spectra Physics laser). The SAW is

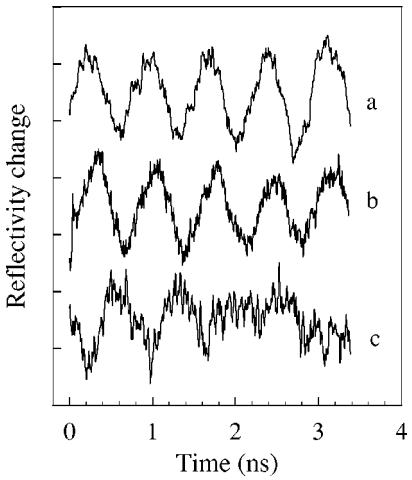

FIG. 6. Photoelastic response of an aluminum sample on quartz (lateral spatial period 2.5 μm) for three positions of the probe beam. The distance between the illuminated and probed areas increases from top to bottom.

detected far from the excited region by an optical pulse emitted with a delay $n\tau$ (n integer) with respect to the pump pulse. The constant delay $n\tau$ should therefore be added to the time scale.

The quartz being transparent for the wavelength of the laser source, the response of the aluminum gratings on this material presents an additional feature around 30 GHz [see Fig. 5(b)]. It consists of at least one oscillation whose frequency depends on the angle of incidence of the probe, but not the lateral spatial period d. We attribute this oscillation to the interference between the part of the light reflected at the metallic surface and the part which enters the substrate through the openings between the stripes. The latter is partially reflected by the acoustic strain originating from the expansion of the aluminum at initial time and which propagates within the quartz at longitudinal sound velocity. As a consequence, the two parts constructively interfere with a frequency ν given by[18]

$$\nu = 2V\lambda_0^{-1}(n^2 - \sin^2\theta)^{1/2}. \tag{10}$$

Here V, n, λ_0, and θ are, respectively, the longitudinal sound velocity in quartz, the refractive index, the wavelength of light, and the incidence of the probe. We measured how the frequency of this mode is modified as the incidence of the probe is changed and we found a good agreement with the behavior predicted by Eq. (10). As the frequency ν is not related to the spatial period, it provides no information on the SAW. It is to be noticed that the interference pattern strongly depends on the orientation of the metallic bands with respect to the plane of incidence of the probe beam. This is clearly apparent in Fig. 5(b), where we show the photoelastic response in the frequency domain, the stripes being parallel (d=5 μm) or perpendicular to the plane of incidence of the probe beam (d=2.5 μm; this configuration is as described by the top plot in Fig. 1). In the latter case, the spectrum presents an additional peak at about 28 GHz. Lin *et al.* have described this mode in Ref. 13. They have shown that it comes from light that passes through an opening between the stripes, is partially reflected by the elastic strain propagating in the substrate, and emerges from the sample by a different

opening. This light interferes with the part of the beam reflected by the metallic bands. The frequency of this mode thus depends on the spatial period, but it is not related to the SAW.

V. CONCLUSIONS

All the experimental results confirm that Rayleigh waves at a frequency as high as 4.9 GHz are excited when a periodic nanostructure is illuminated by an ultrashort laser pulse, provided that the loss of energy by elastic radiation into the substrate is low enough to allow the SAW to propagate. Indeed, when a light pulse is incident on the surface of the sample, stress- and strain-fields are created in the illuminated area by thermal expansion. These fields are determined by the initial temperature distribution. In the case of our samples, the stress- and strain fields show the same periodicity as the metallic gratings, since the optical absorption length is by several orders of magnitude larger in the substrates (quartz and silicon as well) than it is in the metal. Moreover, the experimental results are consistent with the qualitative behavior predicted by Eq. (9): the rate of radiation into the substrate is prohibitive whenever the spatial period is small and the material making up the nanostructure has a large density. As a consequence, the photoelastic response of a gold array with a submicrometer spatial period is essentially related to a normal mode of the individual bars, whereas a collective response is observed in the case of a light material.

The method opens the possibility to use periodic nanostructures to optically generate and to detect very high-frequency SAW. This is particularly interesting whenever the conventional SAW devices are ineffective. This is the case when the material under study is either a solid or a liquid film having submicrometer thickness, deposited onto a nonpiezoelectric material. This situation is encountered with some organic compounds which, owing to chemical compatibility, must be deposited onto specific substrates. This also opens the possibility to use a conducting material as a substrate, provided that its optical properties are in strong contrast to the ones of the material making up the gratings.

However, some questions require further investigation. The most important problem to deal with is the influence of the substrate, both on the generation and on the propagation of the SAW. A preliminary response is given by the form of the coefficient A, appearing in Eq. (9): the lowest rate of radiation in the bulk of the substrate is obtained for materials with a high density and a low Rayleigh velocity. In connection to this, it should be interesting to study how these properties influence the generation process of the initial stress. Another point to develop is the effect of the piezoelectricity on the SAW generation. Our first results on aluminum on quartz suggest that the surface waves are of identical nature whatever the excitation, optical or electrical. This must be confirmed by further experiments in piezoelectric samples with different crystallographic orientations.

ACKNOWLEDGMENTS

We are indebted to Dr. X. Jia for fruitful discussions and to Professor E. Bigler for providing us with several samples.

[1] R. M. White, Proc. IEEE **58**, 1238–1276 (1970).
[2] D. A. Hutchins, *Ultrasonic Generation by Pulsed Lasers*, Physical Acoustics XVIII, edited by W. P. Mason and R. N. Thurston (Academic, San Diego, 1988), Chap. 2.
[3] C. B. Scruby and L. E. Drain, *Laser Ultrasonics* (Hilger, Bristol, 1990).
[4] A. M. Aindow, R. J. Dewhurt, and S. B. Palmer, Opt. Commun. **42**, 116–120 (1982).
[5] Al. A. Kolomenskii, A. M. Lomonosov, R. Kuschnereit, P. Hess, and V. E. Gusev, Phys. Rev. Lett. **79**, 1325–1328 (1997).
[6] E. A. Ash, E. Dieulesaint, and H. Rakouth, Electron. Lett. **16**, 470–472 (1980).
[7] A. Lomonosov, V. G. Mikhalevich, P. Hess, E. Yu. Knight, M. F. Hamilton, and E. A. Zabolotskaya, J. Acoust. Soc. Am. **105**, 2093–2096 (1999).
[8] C. Edwards, A. C. Bushell, S. B. Palmer, and H. Nakano, Nondestr. Test. Eval. **10**, 15–23 (1992).
[9] A. Harata, H. Nishimura, and T. Sawada, Appl. Phys. Lett. **57**, 132–134 (1990).
[10] K. Yamanaka, H. Nishino, Y. Tsukahara, Y. Nagata, and T. Koda, Proc. Ultrason. Int. **93**, 807–810 (1993).
[11] R. E. Lee and D. W. Jackson, Proc.-IEEE Ultrason. Symp. 126–129 (1975).
[12] A. Royer and E. Dieulesaint, J. Phys. (Paris) **C6-44**, 79–83 (1983).
[13] H.-N. Lin, H. J. Maris, L. B. Freund, K. Y. Lee, H. Luhn, and D. P. Kern, J. Appl. Phys. **73**, 37–45 (1993).
[14] See, for example, B. A. Auld, *Acoustic Fields and Waves in Solids* (Krieger, Malabar, FL, 1990), p. 63.
[15] C. Thomsen, H. T. Grahn, H. J. Maris, and J. Tauc, Phys. Rev. B **34**, 4129–4138 (1986).
[16] B. Bonello, B. Perrin, E. Romatet, and J.-C. Jeannet, Ultrasonics **35**, 223–231 (1997).
[17] S. M. Chérif and J.-F. Hennequin, J. Magn. Magn. Mater. **165**, 504–507 (1997).
[18] H.-N. Lin, R. J. Stoner, H. J. Maris, and J. Tauc, J. Appl. Phys. **69**, 3816–3822 (1991).

Lumped-element technique for the measurement of complex density

A. Petculescu and L. A. Wilen
Department of Physics and Astronomy, Ohio University, Athens, Ohio 45701

(Received 31 October 2000; revised 9 May 2001; accepted 6 July 2001)

A novel lumped-element technique is employed to measure the complex density of a gas in circular pores. The complex density expresses the geometry-dependent viscous coupling between the gas and the pore walls and is related to the thermoacoustic function f_μ, or equivalently, $F(\lambda_V)$. The acoustic impedance of a compliant region coupled to a pore (or pore-array) is measured and the impedance of the compliant region is subtracted to yield the impedance of the pore(s) alone, which is directly related to $F(\lambda_V)$. Pores of different lengths are measured in order to eliminate end effects. Working down to very low frequencies achieves a wide range of values for the ratio of the viscous penetration depth to the mean pore size. The results agree very well with analytical solutions for circular pores. The technique is also applied to two porous foam materials. Comparing the results to previous measurements of the complex compressibility, it is shown that two different shape factors (or equivalently, characteristic dimensions) are required to account for the data. © *2001 Acoustical Society of America.* [DOI: 10.1121/1.1401743]

PACS numbers: 43.35.Ud, 43.20.Mv, 43.20.Ye, 43.55.Ev [SGK]

I. INTRODUCTION

Sound propagation in a random medium is often described with ''capillary-tube-based'' theories which model the medium as an array of circular pores or parallel plates.[1–4] These models rely on the solution for sound propagation in a single pore, which was first given by Kirchhoff.[5] In the so-called ''reduced frequency'' limit, a simpler treatment introduced by Zwikker and Kosten[6] can be employed. In this treatment, complex density and complex compressibility functions are defined which completely determine the propagation constant and characteristic impedance of the system. The complex density and compressibility describe the crossover from Poiseuille flow to boundary layer flow (due to viscous effects), and isothermal to adiabatic compression/expansion (due to thermal effects), respectively.

Many experiments have been performed to test the applicability of capillary-based theories. The results have shown that most random media are reasonably well-described by circular, or other uniform, pores, although some modifications may be required such as dynamic shape factors and tortuosity parameters.[4] The majority of experiments to date has employed standing wave or transfer function techniques to extract the wave vector and characteristic impedance of the medium.[7–17] They have the advantage of being able to measure both quantities simultaneously and can be used to test a variety of porous materials. On the other hand, there are a number of complications with these techniques that can sometimes limit both the range of frequency over which they may be applied and their absolute accuracy. Also, they tend to be somewhat laborious in that many pressure measurements are often needed to determine a result at a single frequency.

We recently developed a new lumped-element technique to measure directly the complex compressibility of a gas in a medium. We applied the technique first to a variety of pores of uniform cross section,[18] and later to a porous carbon foam (reticulated vitreous carbon).[19] We found that we could get extremely accurate measurements over a wide range of thermal penetration depths relative to the pore size. These results were discussed in the context of capillary-based porous media and also thermoacoustic stacks. The same formalism used to describe sound propagation in porous media has been applied to the study of thermoacoustic devices.[20] The complex compressibility alone is enough to completely characterize a stack consisting of pores of uniform cross section, but to characterize more complicated stacks, the gain and viscous damping in the stack must be measured independently. Recently, we described a technique to measure the thermoacoustic gain of different model stack geometries.[21]

To complete the picture describing an arbitrary porous medium or thermoacoustic stack, it is necessary to characterize viscous effects. In this paper, we describe a simple new technique to allow the direct measurement of the complex density of a gas. In parallel with our earlier developments, we first test this technique on circular pores of uniform cross section for which the analytical solution is known.[3,6,22] Our results agree well with the theory as well as with earlier work by Nolle[23] and Thurston,[24] both of whom measured similar quantities using different techniques. We also measure the complex density of air in Duocel aluminum, an open-cell metal foam, and reticulated vitreous carbon (RVC), an open-cell carbon foam.[25] The results are compared to previous measurements of the complex compressibility and are discussed in the context of capillary-pore-based models. The measurements we present here, in conjunction with our earlier ones, can completely characterize a medium with regard to either sound propagation or efficacy as a thermoacoustic stack.

II. THEORY

Consider gas in a porous medium with an imposed uniform oscillatory pressure gradient along the z axis, dp_1/dz.

 0001-4966/2001/110(4)/1950/8/$18.00

All acoustic quantities are assumed to have a time dependence of $e^{-i\omega t}$. The resulting flow profile of the gas, **v**, is described by the linearized Navier–Stokes and continuity equations

$$-i\omega\rho_0\mathbf{v}=-\nabla p_1+\tfrac{4}{3}\eta\nabla(\nabla\cdot v)-\eta\nabla\times\nabla\times v,$$
$$-i\omega\rho_1=-\rho_0\nabla\cdot\mathbf{v}, \tag{1}$$

with the boundary condition that the gas velocity be zero at any solid boundary. ρ_0 is the equilibrium density of the gas and η is the gas viscosity. ρ_1 and p_1 are the acoustic variations of the density and pressure, respectively. In general, the complex density is defined to be[20,26]

$$\tilde{\rho}(R/\delta_v)=\frac{dp/dz}{i\omega\hat{v}_z}, \tag{2}$$

where $\hat{v}_z$ is the cross-sectional average of the velocity in the z direction. We will typically work with the normalized complex density which we define as $\rho_0^{-1}\tilde{\rho}(R/\delta_v)$, where $\delta_v=\sqrt{2\eta/\omega\rho_0}$ is the viscous penetration depth. R is the characteristic radius of the system defined as twice the ratio of the open volume to surface boundary area for the medium. For a circular pore, this coincides with the radius of the pore. $F(\lambda_V)$ is defined as the inverse of the normalized complex density, with $\lambda_V=\sqrt{2}R/\delta_v$. The solution to Eq. (1) for a circular pore is[22]

$$v_z(r)=\frac{1}{i\omega\rho_0}\frac{dp_1}{dz}\left(1-\frac{J_0[(1+i)r/\delta_v]}{J_0[(1+i)R/\delta_v]}\right). \tag{3}$$

The cross-sectional average of the velocity is easily calculated to be

$$\hat{v}_z=\frac{1}{i\omega\rho_0}\frac{dp_1}{dz}\left(1-\frac{2}{(1+i)R/\delta_v}\frac{J_1[(1+i)R/\delta_v]}{J_0[(1+i)R/\delta_v]}\right). \tag{4}$$

Hence, for the circular pore case, the normalized complex density and $F(\lambda_V)$ are given by

$$\left.\frac{\tilde{\rho}(R/\delta_v)}{\rho_0}\right|_{\text{circ pores}}=\left(1-\frac{2}{(1+i)R/\delta_v}\frac{J_1[(1+i)R/\delta_v]}{J_0[(1+i)R/\delta_v]}\right)^{-1}$$

$$F(\lambda_V)|_{\text{circ pores}}=1-\frac{2}{\sqrt{i}\lambda_V}\frac{J_1[\sqrt{i}\lambda_V]}{J_0[\sqrt{i}\lambda_V]}. \tag{5}$$

The complex density describes the viscous coupling of the gas in the pore to the pore walls. At low frequencies, the viscous penetration depth is large, resulting in Poiseuille flow. At high frequencies, the viscous penetration depth is small and the resulting flow approaches the inviscid limit. The crossover from one limit to the other is described by the function $F(\lambda_V)$.

One can also define the complex compressibility for a system. Suppose that the system is subjected to uniform pressure oscillations P_1, with resulting density oscillations ρ_1. The complex compressibility $\tilde{C}(\omega)$ is defined as[20,26]

$$\tilde{C}(\omega)=\frac{1}{\rho_0}\frac{\rho_1}{P_1}. \tag{6}$$

Generally it is more convenient to work with the normalized compressibility given by $P_0\tilde{C}(\omega)$, where P_0 is the equilibrium pressure. The compressibility can be written in terms of the thermal dissipation function $F(\lambda_T)$

$$P_0\tilde{C}(\omega)=\left[1-\frac{\gamma-1}{\gamma}F(\lambda_T)\right], \tag{7}$$

where $\lambda_T=\sqrt{2}R/\delta_\kappa$, $\delta_\kappa=\sqrt{2\kappa/\omega\rho_0 c_p}$. κ is the thermal conductivity and c_p is the heat capacity at constant pressure. For a circular pore, the function $F(\lambda_T)$ is given by Eq. (5) with λ_V replaced by λ_T. It is important to emphasize that, for an arbitrary random porous medium, the functions $F(\lambda_T)$ and $F(\lambda_V)$ cannot be calculated and must be determined experimentally. Also, they are not in general the same function for anything other than uniform cross-section pores.

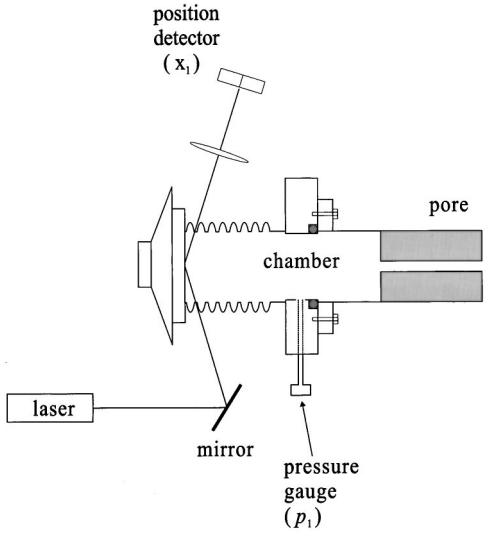

FIG. 1. Experimental apparatus.

III. EXPERIMENT

The apparatus is shown in Fig. 1. Many of its features are similar to the setup used previously to measure the compressibility of single pores and other samples.[18,19] The geometry is essentially that of a Helmholtz resonator: a compliant volume attached to an open porous sample. A loudspeaker oscillates a bellows which is part of the compliant volume. To detect the displacement of the loudspeaker, a laser beam is bounced from a mirror on the cone onto a position-sensitive detector. The oscillatory pressure in the compliant volume is measured with a piezoresistive pressure sensor. Each of the signals is monitored with a vector lock-in interfaced to a computer. A typical run consists of a frequency sweep from 0.5 to 96 Hz in equal $f^{1/2}$ increments. The equilibrium pressure and temperature are measured with a capacitive gauge and mercury thermometer, respectively. The humidity is measured with a digital hygrometer. The complete system is housed in a Plexiglas box which can be flushed with dry nitrogen. Some runs were taken in air, with corrections for humidity; others were performed in dry nitrogen. To within experimental error, both types gave the same result. The apparatus is designed so that samples of different shapes and sizes can easily be interchanged. Five pairs (long and short) of different samples were measured, as shown in Fig. 2. Two were different-diameter single circular pores; the third was a circular pore array; the fourth was Duocel alumi-

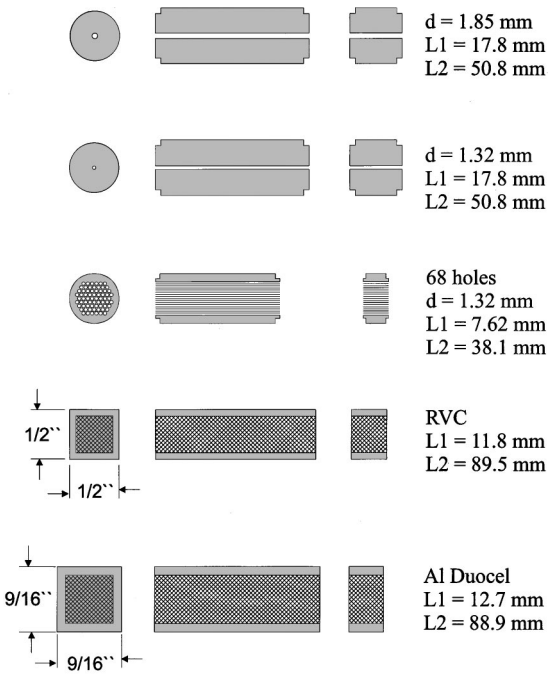

FIG. 2. Pore geometries used in the experiment.

num, a porous open-cell aluminum foam; the fifth was RVC, a porous open-cell carbon foam. The manufacturer specified the pore sizes of the aluminum and carbon samples to be 40 pores per inch (ppi) and 20 pores per inch, respectively. We also took measurements with the compliant volume alone, as well as with a second cylindrical compliant volume of known dimensions acoustically in parallel with the first.

IV. ANALYSIS

For simplicity, we will describe the analysis referring to the single pore samples. A simple lumped-element circuit model for the experimental system is shown in Fig. 3. The larger diameter region including the bellows can be thought

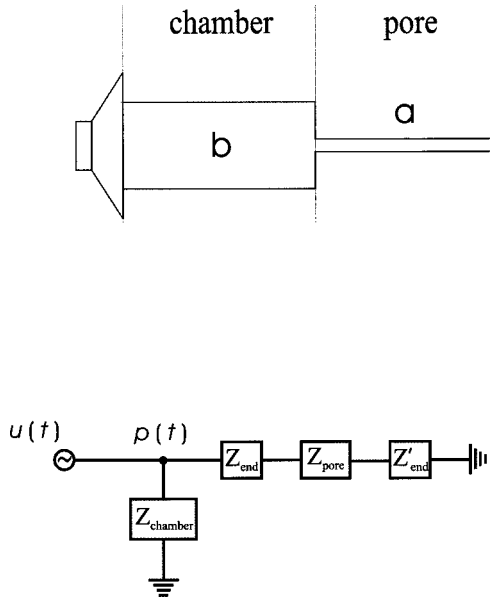

FIG. 3. Simplified circuit model.

of as a compliant chamber. On each side of the pore, and in series with it, are elements which represent the impedances of the pore ends. The series combination of the pore (Z_{pore}) and end impedances ($Z_{\text{end}}+Z'_{\text{end}}$) are in parallel with the chamber. This simple model neglects the compliance of the pore, and also the inertance of the chamber. The appropriateness of the model will be discussed in a later section. If the pore is short compared to the acoustic wavelength, then its impedance can be written in terms of $F(\lambda_V)$ as follows:[20]

$$Z_{\text{pore}}=-\frac{i\omega\rho_0 L}{AF(\lambda_V)}. \tag{8}$$

Consequently, once the pore impedance is measured, $F(\lambda_V)$ can be determined. With this simple circuit model, there are three unknowns to be calculated. (The end impedances appear in series and can be combined together into one unknown term.) Hence, three measurements suffice to determine all of the impedances as follows.

Since we measure both acoustic pressure and displacement (and hence velocity), we can determine the input impedance $Z_{\text{in}}=p_1/i\omega A_{\text{bellows}}X_1$ to the system. The input impedance Z_{in} with an attached open pore of length L and area A is given by

$$\left.\frac{1}{Z_{\text{in}}}\right|_{\text{open}}=\frac{1}{Z_{\text{compliance}}}+\frac{1}{Z_{\text{end}}+Z'_{\text{end}}-\dfrac{i\omega\rho_0 L}{AF(\lambda_V)}}. \tag{9}$$

By plugging the pore at the end near the compliant volume, we also measure the input impedance of the compliant volume alone

$$\left.\frac{1}{Z_{\text{in}}}\right|_{\text{plugged}}=\frac{1}{Z_{\text{compliance}}}. \tag{10}$$

Subtracting the two yields the input impedance of the pore+ends

$$\left.\frac{1}{Z_{\text{in}}}\right|_{\text{plugged}}-\left.\frac{1}{Z_{\text{in}}}\right|_{\text{open}}=\frac{1}{Z_{\text{pore+ends}}}=\frac{1}{Z_{\text{end}}+Z'_{\text{end}}-\dfrac{i\omega\rho_0 L}{AF(\lambda_V)}}. \tag{11}$$

To eliminate the end effects, we must measure two pores of different length but identical diameter, denoted by L_α and L_β. One more subtraction then yields an expression for the impedance of the uniform pore which is simply related to $F(\lambda_V)$

$$Z^{L_\alpha}_{\text{pore+ends}}-Z^{L_\beta}_{\text{pore+ends}}=-\frac{i\omega\rho_0(L_\alpha-L_\beta)}{AF(\lambda_V)}. \tag{12}$$

The experimentally measured quantities are complex voltages proportional to the pressure and to the speaker displacement, denoted by V_{p_1} and V_{X_1}. To get an accurate result for $F(\lambda_V)$, we must have an accurate calibration relating these voltages to the actual pressure (p_1) and displacement (X_1). Actually, since all quantities involve the ratio of the pressure to the displacement, we need only a single calibration factor which relates the ratio p_1/X_1 to the ratio V_{p_1}/V_{X_1}. To achieve this calibration, we perform one additional measure-

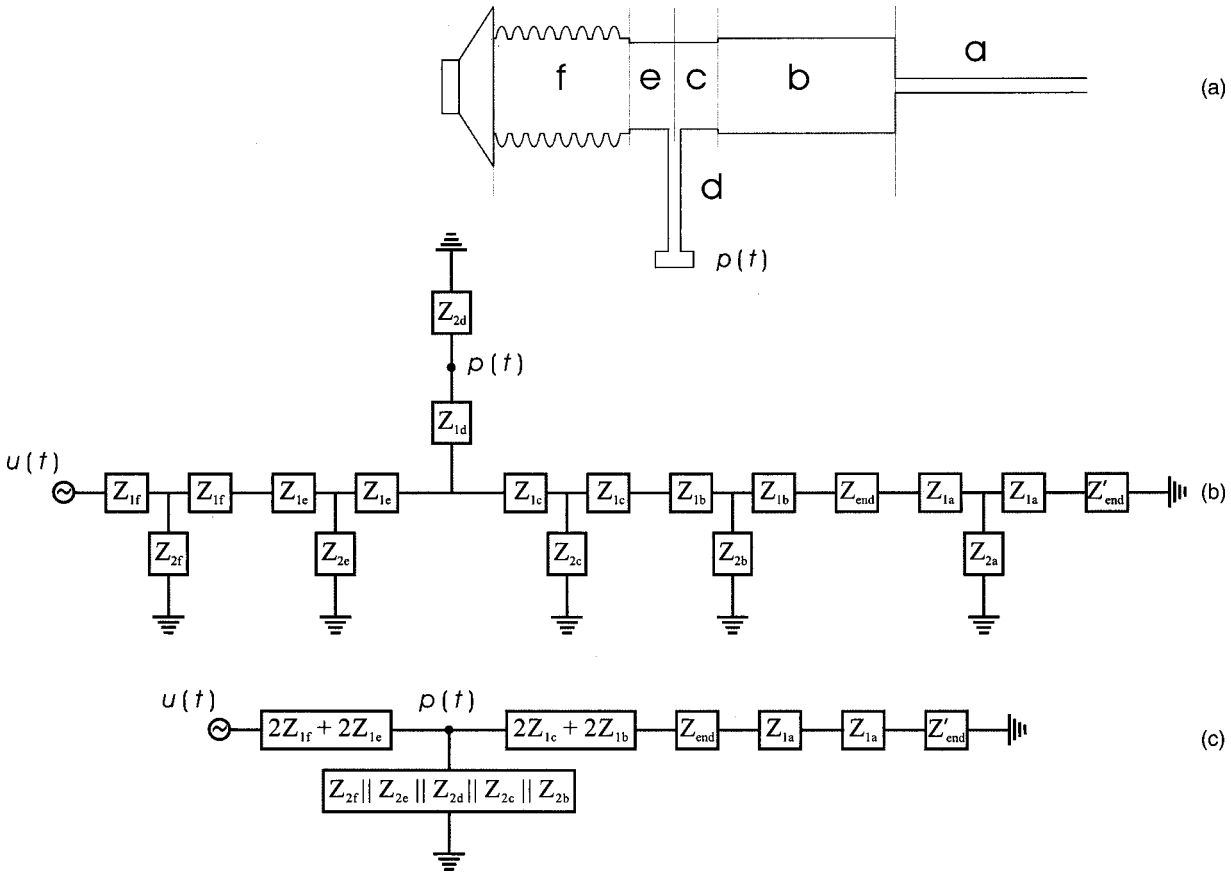

FIG. 4. (a) Schematic diagram. (b) Complete equivalent circuit model. (c) Intermediate circuit model.

ment. We attach a cylindrical compliant volume of known dimensions (denoted by the subscript ''calib'') to the system and measure the input impedance at 96 Hz. By subtracting the compliant volume, we measure the impedance of the calibrated volume

$$\left.\frac{1}{Z_{\text{in}}}\right|_{\text{calib.}} = \left.\frac{1}{Z_{\text{in}}}\right|_{\text{compliance and calib.}} - \left.\frac{1}{Z_{\text{in}}}\right|_{\text{compliance}}. \tag{13}$$

Assuming the acoustic wavelength is much larger than the cell, we can write a theoretical expression for $1/Z_{\text{in}}|_{\text{calib.}}$

$$\left.\frac{1}{Z_{\text{in}}}\right|_{\text{calib.}} = -\frac{i\omega V_{\text{calib}}}{\gamma p_0}[\gamma-(\gamma-1)F(\lambda_T)]. \tag{14}$$

Because the radius of the calibrated volume is large compared to the thermal penetration depth at 96 Hz, we can use the asymptotic form for $F(\lambda_T)$ appropriate to this case

$$\left.\frac{1}{Z_{\text{in}}}\right|_{\text{calib.}} = -\frac{i\omega V_{\text{calib}}}{\gamma p_0}\left[1+\frac{\delta_\kappa}{R_{\text{cal}}}(\gamma-1)(1+i)\right]. \tag{15}$$

Now, since we prefer to work with an expression which depends on as few gas properties as possible, we note

$$\text{Re}\left[\left.\frac{1}{Z_{\text{in}}}\right|_{\text{calib.}}\right] - \text{Im}\left[\left.\frac{1}{Z_{\text{in}}}\right|_{\text{calib.}}\right] = -\frac{i\omega V_{\text{calib}}}{\gamma p_0}. \tag{16}$$

We calibrate the ratio of the measured pressure and displacement signals so that Eq. (16) holds exactly.

V. CIRCUIT MODELS

Gillis *et al.*[27] and Mehl[28] have discussed Helmholtz resonators and their analysis in a number of recent papers. Although the present measurements differ in many respects from those they discuss, there are also many similarities; we are guided heavily by their formalism in our analysis.

The circuit model of Fig. 3 is a simplification of the actual situation. Figure 4(a) shows a detailed diagram of the apparatus with a single pore installed. The complete electrical circuit analog is shown in Fig. 4(b). Following Gillis *et al.*, the circuit elements are identified as follows:

$$Z_1 = Z_0 \tanh\left(\frac{\Gamma L}{2}\right), \quad Z_2 = \frac{Z_0}{\sinh(\Gamma L)},$$

$$Z_0 = \frac{\rho_0 c}{A\sqrt{[F^*(\lambda_V)][\gamma-(\gamma-1)F^*(\lambda_T)]}}, \tag{17}$$

$$\Gamma = \frac{i\omega}{c}\sqrt{\frac{\gamma-(\gamma-1)F^*(\lambda_T)}{F^*(\lambda_V)}},$$

where c is the adiabatic speed of sound, L is the length of a circular region, A is the area of the region, γ is the ratio of specific heats, and the function F is defined in Eq. (5) above. The asterisk denotes complex conjugate. Z_{end} and Z'_{end} represent the unknown impedances of the two ends of the pore. The impedance of the pore can be identified with $2Z_{1a}$ and

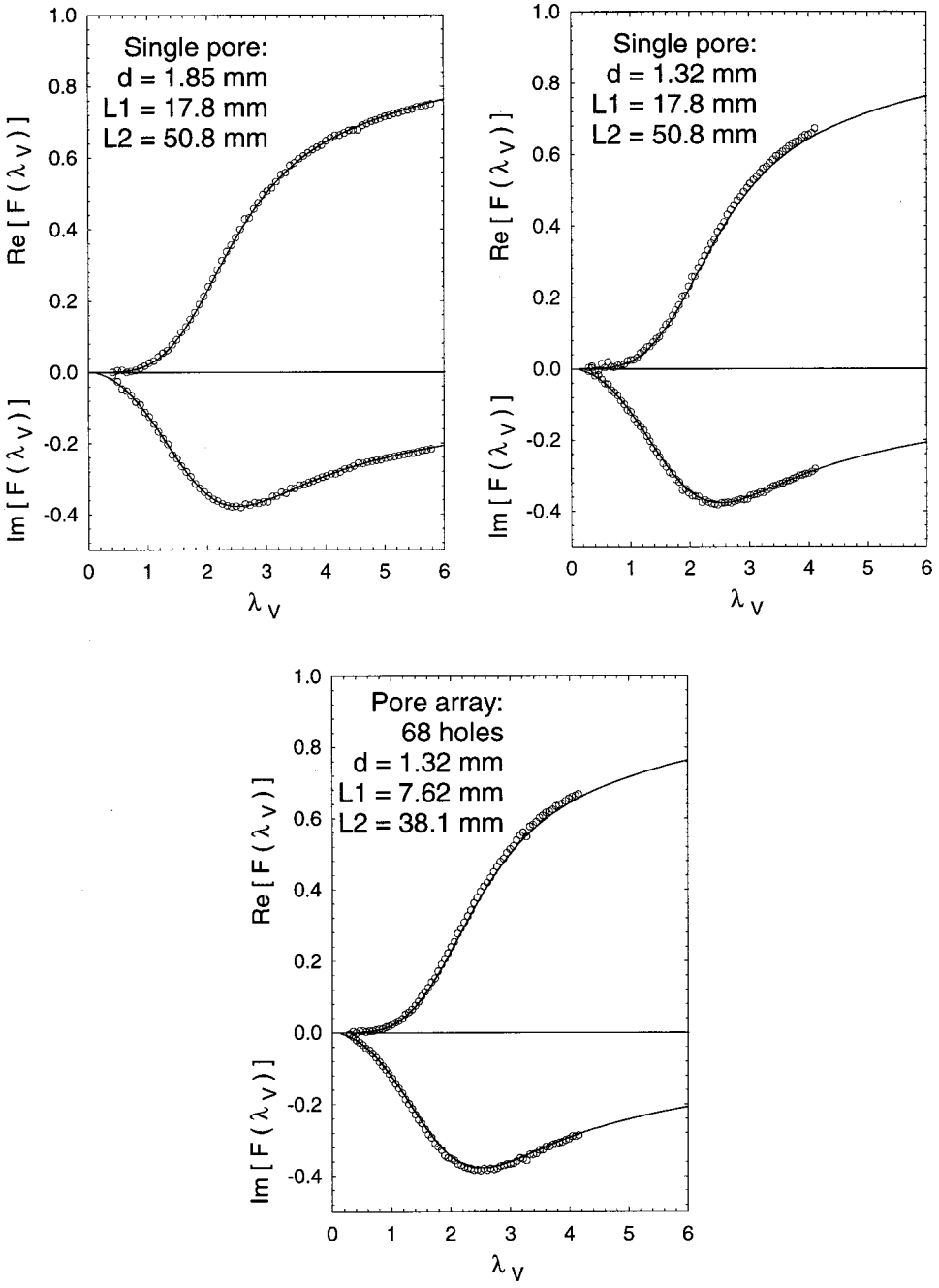

FIG. 5. Results for $F(\lambda_V)$ vs λ_V using the single circular pores and the circular pore array.

the impedance of the chamber can be identified with the parallel combination of Z_{2b}, Z_{2c}, Z_{2d}, Z_{2e}, and Z_{2f}. A careful consideration of this complete circuit model shows that the system can also be described extremely well by the intermediate circuit model shown in Fig. 4(c), as long as the inertance/resistance of the chamber region is small compared to its compliance. Using this intermediate circuit model, it is straightforward to show that if one analyzes the data according to Eqs. (11) and (12), the only difference is that $Z_{\text{pore+ends}}$ should be replaced by $Z_{\text{pore+ends}}+2Z_{1b}+2Z_{1c}$. The extra impedance $(2Z_{1b}+2Z_{1c})$ can be lumped into the end impedances, and drops out when two different-length pores are used to eliminate end effects.

As the ultimate check of the validity of the model used, we generate "synthetic" data for the input impedance to the system using the full T-network of Fig. 4(b) and then analyze the data using the simplified model of Eqs. (8)–(12) to determine $F(\lambda_V)$. The results show that for a wide range of pore impedances, including those measured in the experiment, the simplified model gives the correct results to within 1%.

VI. RESULTS AND DISCUSSION

It is very important to avoid nonlinear effects when performing these measurements. A number of studies have considered nonlinear effects at flange ends and orifices.[29–35] Nonlinearities at sharp edges can occur at relatively low amplitudes. We will defer a discussion of such effects to a future publication. Here, we simply note that all measurements were performed below the threshold for nonlinear effects. In Fig. 5, we have plotted the results for $F(\lambda_V)$ using the two

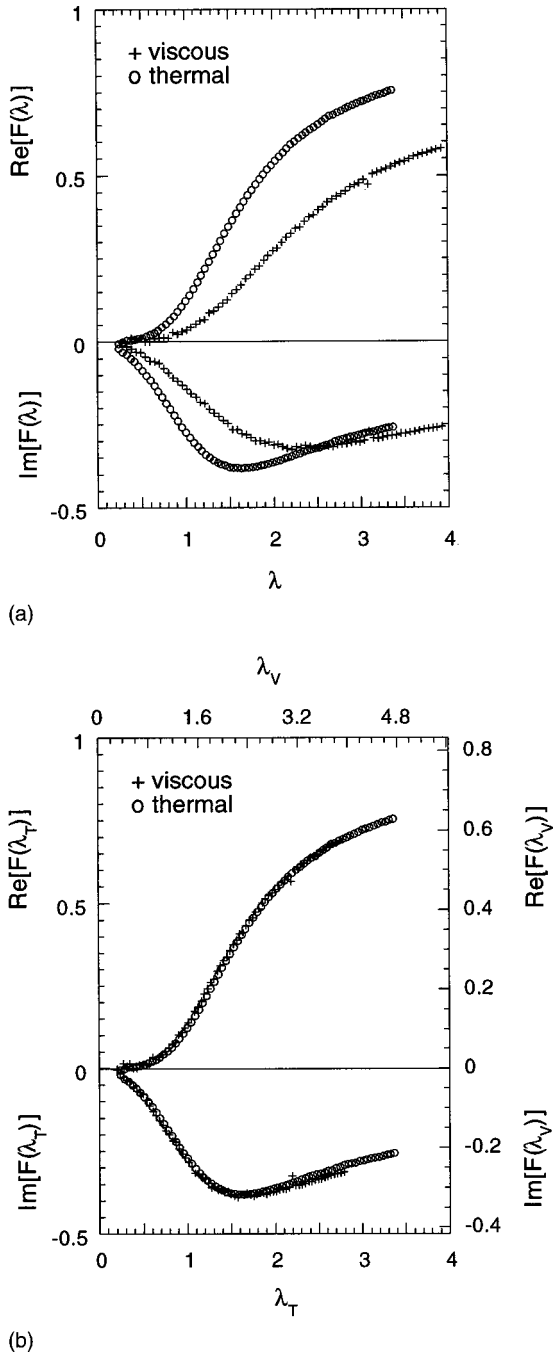

FIG. 6. (a) Results for the Duocel aluminum sample. (b) Scaling of $F(\lambda_V)$ to fit $F(\lambda_T)$.

different-diameter single pores, and also the circular pore array. For each, we show the results obtained from a subtraction involving the longer and the shorter sample. To within experimental error, the curves agree with each other and also with the theory.

In Fig. 6(a), we have plotted the results for the Duocel aluminum sample. We also plot the results for the thermal dissipation function obtained using the method discussed previously.[18,19] For this sample, we used two lengths to subtract out end effects but made no attempt to subtract out the perimeter boundary. Effects of the latter are expected to be small, based on our experience with compressibility measurements. We have no independent measurement for the characteristic radius of these samples and therefore take it to be given by the nominal pore spacing specified by the manufacturer [$R=1/(40\ \text{ppi})=0.635\ \text{mm}$]. The area and volume used in the calculations were taken to be the measured geometric values multiplied by the sample porosity. We determined the porosity independently by comparing the low-frequency compressibility of the Duocel sample to that of another sample of calibrated volume.

The viscous and thermal curves are of similar shape, but differ in scale along both axes. This point is emphasized in Fig. 6(b), where we have scaled the two axes of the viscous function to fit the thermal function as closely as possible. In particular, after scaling, the position of the dip in the imaginary part of F is the same for the two curves. There is no physical reason to expect that the two curves should match up exactly after a scaling of the axes (and indeed, a careful examination shows that they do not). Nevertheless, the scaling is compelling, and useful for comparisons, as discussed below.

In the context of capillary-based porous media theories, a difference in scale in the y axis can be related to the tortuosity q of the sample if the scaling holds rigorously in the high-frequency (large λ) limit. Our measurements do not extend high enough in frequency to determine the tortuosity; we perform the scaling on the y axis to facilitate comparison of the two curves. The vertical scale factor applied to $F(\lambda_V)$ is 1.20.

The scale factor applied to the λ_V axis is 1.41. A difference in scale in the x axis is related to the idea of a ''shape factor,'' or alternatively, ''characteristic dimension.'' Shape factors were originally discussed by Zwikker and Kosten,[6] and later by numerous authors.[2–4,9,10,36] Although the exact definition of the shape factor depends on the particular model used, the results of Fig. 6 imply generally that two different shape factors (one viscous and one thermal) are required to fit the two curves. Such a scenario was discussed by Zwikker and Kosten[6] (and later by Champoux and Stinson,[10] and Allard and Champoux[37]), who pointed out that viscous behavior is dominated by narrower regions which tend to restrict flow while the thermal behavior is dominated by wider parts which have more volume. More recent theoretical models have made these ideas precise by defining thermal and viscous characteristic dimensions which can be calculated (in principle) from the system geometry and which describe the system exactly in the high-frequency limit.[38–41] These dimensions can be measured using acoustic or other techniques. Such theories also predict that the characteristic viscous dimension should be dominated by narrower spaces and hence will be smaller than the analogous thermal dimension.

The above ideas are consistent with our results in Fig. 6(a), which show that the crossover in behavior from Poiseuille to inviscid flow occurs at a higher value of λ than the crossover from isothermal to adiabatic compressibility.[42] Champoux and Stinson[10] found similar results from measurements on a model porous material. However, in their measurements of two real porous materials,[10,11] they were able to fit the results with a single shape factor. Attenborough has also fit measurements of sound propagation in granular media with a model using a single shape factor, but with a

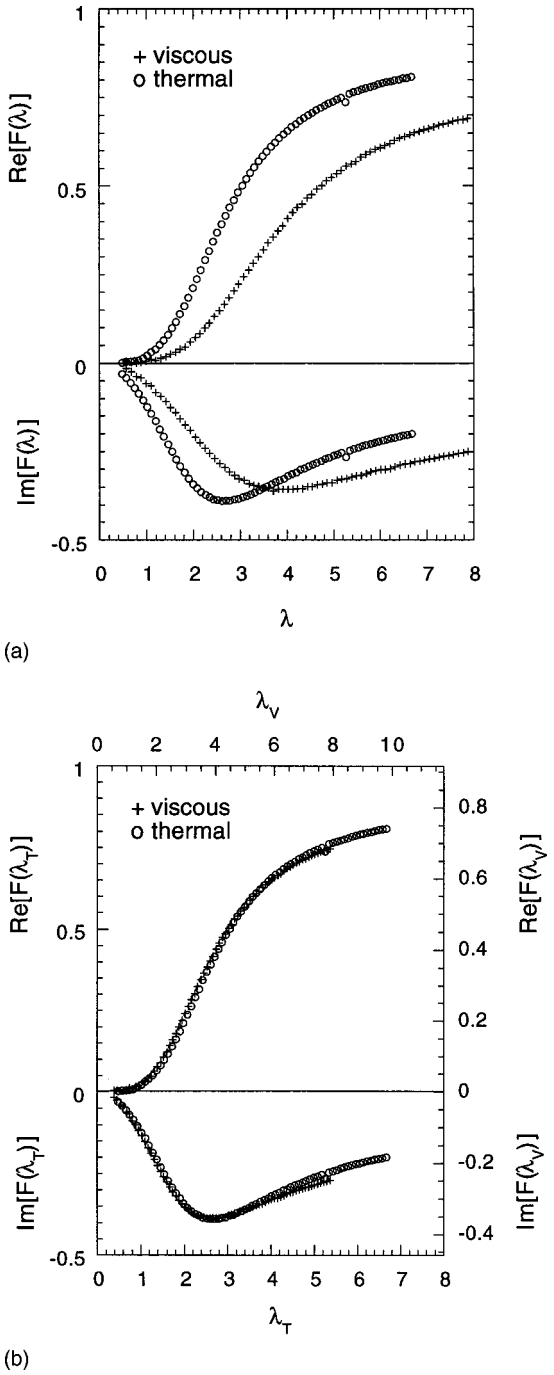

FIG. 7. (a) Results for the RVC sample. (b) Scaling of $F(\lambda_V)$ to fit $F(\lambda_T)$.

distribution of pore sizes.[43] Our results provide an example of a real porous material which unequivocally requires two shape factors to account for the measured behavior.

This last point also has important implications for thermoacoustics. One can speculate on the possibility of engineering a stack geometry which has enhanced thermoacoustic gain with decreased viscous loss.

Finally, in Figs. 7(a) and (b), we show the results for RVC. Here, the characteristic radius is taken to be $R = 1/(20\,\text{ppi}) = 1.27\,\text{mm}$. The discussion above pertaining to Duocel aluminum applies in an analogous way to the results for RVC. The vertical scale factor is determined to be 1.08 and the scale factor applied to the λ_V axis is 1.47.

VII. SOURCES OF ERROR

Statistical errors are mainly due to noise in the electronics used to measure the pressure and displacement. At the lowest frequencies there is additional noise due to fluctuations in the local atmospheric pressure. The total statistical error is about twice the size of the data points or approximately 0.02 in absolute units.

Systematic errors are due to a variety of sources. These include errors incurred by using the simple circuit model in lieu of the more complicated one, drifts in the sensitivity of the detectors, errors in measuring the calibrated volume, and errors in measuring the lengths and radii of the pores. The last item is potentially a large source of error because of the small radii involved. To measure them, we purchased steel pins with diameters calibrated in increments of 0.0025 ± 0.001 mm. By finding the largest pin which fits into the pore, we measure the diameter to a resolution of better than 0.2%. However, the absolute accuracy is estimated to be a few times larger due to surface roughness. Other dimensions can be measured with similar or better accuracy. The largest sources of systematic error are the drifts in the detector sensitivity, errors in measuring the pore radius, and those due to using the simplified circuit model. These result in total errors of about 2%. The errors discussed in this section refer to the viscous measurements only. Errors in the results for $F(\lambda_T)$ are smaller and are discussed in Ref. 19.

VIII. CONCLUSIONS

We have measured the complex density of air in single circular pores with a simple new technique and found good agreement with theory. The technique is easily applied to other model geometries and also random porous media. As an example, we measured the complex density of air in two porous open-cell foam materials. A comparison with previous measurements of the complex compressibility showed that, in the context of capillary-based porous media models, two different shape factors (or equivalently, different thermal and viscous characteristic dimensions) are required to explain the data. Our measurements can characterize a given porous sample completely with regard to acoustic propagation, and we hope to extend the technique to allow the determination of low-frequency thermal and viscous permeabilities. Additional measurements with a temperature difference applied across the sample would completely determine thermoacoustic behavior. We have also used this technique to measure the impedance of orifices, and to characterize jet pumps for use in acoustic Stirling engines; both will be topics of future papers.

ACKNOWLEDGMENTS

We gratefully acknowledge support from the Office of Naval Research. We would like to thank the thermoacoustics group at the National Center for Physical Acoustics for RVC samples, and Energy Research and Generation, Inc. for supplying samples of both RVC and Duocel aluminum. The authors would also like to the thank the reviewers for very useful comments and suggestions.

[1] J. W. Strutt (Lord Rayleigh), *Theory of Sound*, 2nd ed. (Dover, New York, 1945), Vol. II, Sec. 351.
[2] M. A. Biot, ''Theory of propagation of elastic waves in a fluid-saturated porous solid. I. Low frequency range,'' J. Acoust. Soc. Am. **28**, 168–178 (1956).
[3] M. A. Biot, ''Theory of propagation of elastic waves in a fluid-saturated porous solid. II. Higher frequency range,'' J. Acoust. Soc. Am. **28**, 179–191 (1956).
[4] K. Attenborough, ''Acoustical characteristics of porous materials,'' Phys. Rep. **82**, 179–227 (1982).
[5] G. Kirchhoff, ''Ueber den Einflufs der Wärmeleitung in einem Gase auf die Schallbewegung,'' Ann. Phys. Chem. **134**, 177–193 (1868).
[6] C. Zwikker and C. W. Kosten, *Sound Absorbing Materials* (Elsevier, Amsterdam, 1949), Chap. 2.
[7] H. Utsono, T. Tanaka, and T. Fujikawa, ''Transfer function method for measuring characteristic impedance and propagation constant of porous materials,'' J. Acoust. Soc. Am. **86**, 637–643 (1989).
[8] J. D. McIntosh, M. T. Zuroski, and R. F. Lambert, ''Standing wave apparatus for measuring fundamental properties of acoustic materials in air,'' J. Acoust. Soc. Am. **91**, 685–695 (1992).
[9] M. R. Stinson and Y. Champoux, ''Propagation of sound and the assignment of shape factors in model porous materials having simple pore geometries,'' J. Acoust. Soc. Am. **88**, 1929–1938 (1992).
[10] Y. Champoux and M. R. Stinson, ''On acoustical models for sound propagation in rigid frame porous materials and the influence of shape factors,'' J. Acoust. Soc. Am. **92**, 1120–1131 (1992).
[11] Y. Champoux and M. R. Stinson, ''Measurement of the characteristic impedance and propagation constant of materials having high flow resistivity,'' J. Acoust. Soc. Am. **90**, 2182–2191 (1991).
[12] H.-S. Roh, W. P. Arnott, J. M. Sabatier, and R. Raspet, ''Measurement and calculation of acoustic propagation constants in arrays of small air-filled rectangular tubes,'' J. Acoust. Soc. Am. **89**, 2617–2624 (1991).
[13] R. F. Lambert and J. S. Tesar, ''Acoustic structure and propagation in highly porous, layered, fibrous materials,'' J. Acoust. Soc. Am. **76**, 1231–1237 (1984).
[14] A. Cummings and I.-J. Chang, ''Acoustic propagation in porous media with internal mean flow,'' J. Sound Vib. **114**, 565–581 (1987).
[15] V. Tarnow, ''Measurement of sound propagation in glass wool,'' J. Acoust. Soc. Am. **97**, 2272–2281 (1995).
[16] S. L. Yaniv, ''Impedance tube measurement of propagation constant and characteristic impedance of porous acoustical material,'' J. Acoust. Soc. Am. **54**, 1138–1142 (1973).
[17] C. Bordone-Sacerdote and G. G. Sacerdote, ''A method for measuring the acoustic impedance of porous materials,'' Acustica **34**, 77–80 (1975).
[18] L. A. Wilen, ''Measurements of thermoacoustic functions for single pores,'' J. Acoust. Soc. Am. **103**, 1406–1412 (1998).
[19] L. A. Wilen, ''Dynamic measurements of the thermal dissipation function of reticulated vitreous carbon,'' J. Acoust. Soc. Am. **109**, 179–184 (2001).
[20] W. P. Arnott, H. E. Bass, and R. Raspet, ''General formulation of thermoacoustics for stacks having arbitrarily shaped pore cross sections,'' J. Acoust. Soc. Am. **90**, 3228–3237 (1991).
[21] G. Petculescu and L. A. Wilen, ''Thermoacoustics in a single pore with an applied temperature gradient,'' J. Acoust. Soc. Am. **106**, 688–694 (1999).
[22] I. B. Crandall, *Theory of Vibrating Systems and Sound* (Van Nostrand, New York, 1927), pp. 229–241.
[23] A. W. Nolle, ''Small-signal impedance of short tubes,'' J. Acoust. Soc. Am. **25**, 32–39 (1953).
[24] G. B. Thurston, ''Periodic fluid flow through circular tubes,'' J. Acoust. Soc. Am. **24**, 653–656 (1952).
[25] Duocel aluminum foam and RVC carbon foam, manufactured by Energy Research and Generation, Inc., 900 Stanford Avenue, Oakland, CA 94608.
[26] M. Stinson, ''The propagation of plane sound waves in narrow and wide circular tubes, and the generalization to uniform tubes of arbitrary cross-sectional shape,'' J. Acoust. Soc. Am. **89**, 550–558 (1991).
[27] K. A. Gillis, J. B. Mehl, and M. R. Moldover, ''Greenspan acoustic viscometer for gases,'' Rev. Sci. Instrum. **67**, 1850–1857 (1996).
[28] J. B. Mehl, ''Greenspan acoustic viscometer: Numerical calculations of fields and duct-end effects,'' J. Acoust. Soc. Am. **106**, 73–82 (1999).
[29] G. B. Thurston and C. E. Martin, Jr., ''Periodic flow through circular orifices,'' J. Acoust. Soc. Am. **25**, 26–31 (1953).
[30] M. R. Stinson and E. A. G. Shaw, ''Acoustic impedance of small, circular orifices in thin plates,'' J. Acoust. Soc. Am. **77**, 2039–2042 (1985).
[31] L. J. Sivian, ''Acoustic impedance of small orifices,'' J. Acoust. Soc. Am. **7**, 94–101 (1935).
[32] G. B. Thurston, L. E. Hargrove, Jr., and B. D. Cook, ''Nonlinear properties of circular orifices,'' J. Acoust. Soc. Am. **29**, 992–1001 (1957).
[33] R. L. Panton and A. Y. Goldman, ''Correlation of nonlinear orifice impedance,'' J. Acoust. Soc. Am. **60**, 1390–1396 (1976).
[34] U. Ingard and S. Labate, ''Acoustic circulation effects and the nonlinear impedance of orifices,'' J. Acoust. Soc. Am. **22**, 211–218 (1950).
[35] G. B. Thurston, ''Nonlinear acoustic properties of orifices of varied shapes and edge conditions,'' J. Acoust. Soc. Am. **30**, 452–455 (1958).
[36] P. G. Smith and R. A. Greenkorn, ''Theory of acoustical wave propagation in porous media,'' J. Acoust. Soc. Am. **52**, 247–253 (1972).
[37] J-F. Allard and Y. Champoux, ''New empirical equations for sound propagation in rigid frame fibrous materials,'' J. Acoust. Soc. Am. **91**, 3346–3353 (1992).
[38] D. L. Johnson, J. Koplik, and L. M. Schwartz, ''New pore size paramter characterizing transport in porous media,'' Phys. Rev. Lett. **57**, 2564–2567 (1986).
[39] D. L. Johnson, J. Koplik, and R. Dashen, ''Theory of dynamic permeability and tortuosity in fluid saturated porous media,'' J. Fluid Mech. **176**, 379–402 (1987).
[40] Y. Champoux and J-F. Allard, ''Dynamic tortuosity and bulk modulus in air-saturated porous media,'' J. Appl. Phys. **70**, 1975–1979 (1991).
[41] D. Lafarge, P. Lemarinier, and J. F. Allard, ''Dynamic compressibility of air in porous structures at audible frequencies,'' J. Acoust. Soc. Am. **102**, 1995–2006 (1997).
[42] In other words, the scaling we used to make the curves match in Fig. 6(b) was equivalent to using a smaller characteristic radius for the viscous function.
[43] K. Attenborough, ''Models for the acoustical properties of air-saturated granular media,'' Acta Acust. (Beijing) **1**, 213–226 (1993).

Exact solutions for free vibration of shear-type structures with arbitrary distribution of mass or stiffness

Q. S. Li[a)]
Department of Building and Construction, City University of Hong Kong, Tat Chee Avenue, Kowloon, Hong Kong

(Received 22 May 2000; revised 19 March 2001; accepted 25 March 2001)

In this paper, shear-type structures such as frame buildings, etc., are treated as nonuniform shear beams (one-dimensional systems) in free-vibration analysis. The expression for describing the distribution of shear stiffness of a shear beam is arbitrary, and the distribution of mass is expressed as a functional relation with the distribution of shear stiffness, and vice versa. Using appropriate functional transformation, the governing differential equations for free vibration of nonuniform shear beams are reduced to Bessel's equations or ordinary differential equations with constant coefficients for several functional relations. Thus, classes of exact solutions for free vibrations of the shear beam with arbitrary distribution of stiffness or mass are obtained. The effect of taper on natural frequencies of nonuniform beams is investigated. Numerical examples show that the calculated natural frequencies and mode shapes of shear-type structures are in good agreement with the field measured data and those determined by the finite-element method and Ritz method. [DOI: 10.1121/1.1372225]

PACS numbers: 43.40.Cw [CBB]

I. INTRODUCTION

Vibration of non-uniform beams has been a subject of numerous investigations because of its relevance to structural, mechanical and aeronautical engineering. The field measurements conducted by Korqingskee,[1] Ishizaki and Hatakeyana,[2] Wang,[3] Li *et al.*,[4] and Jeary[5] revealed that shear deformation of a multistory frame building is usually dominant in the total deformation in its transverse vibration, and such a building may be simplified as a cantilever shear beam for free vibration analysis. Korqingskee[1] investigated the free vibrations of frame buildings that are treated as a multistep cantilever shear bar and each step of the bar has constant parameters (mass and stiffness). He derived the closed-form solutions for such a shear bar. Wang[6] suggested that a frame building could be treated as a one-step cantilever shear bar with continuously varying distributions of mass and stiffness along its height for the analysis of free vibration. But, he assumed that the mass of the shear bar is proportional to its stiffness. This assumption is not reasonable for many multistory buildings, because this type of shear bar is different from a solid bar, for which the mass is proportional to its stiffness. This is due to the fact that the floor mass of a multistory building is usually about 80% or even more of the total mass of the building in many cases; so, the variation of mass of such a building along the height is not necessarily proportional to its stiffness. Wang[7] suggested that the distribution of mass of a frame building that is simplified as a shear beam for free-vibration analysis can be assumed as uniform, but the distribution of shear stiffness is nonuniform. Li *et al.*[4,8] and Li[9] studied free vibrations of frame buildings that were treated as a shear bar with variably distributed stiffness and mass. By selecting suitable expressions, such as power functions and exponential functions, for describing mass and stiffness distributions, the governing differential equations for free vibration of such bars were reduced to Bessel's equations and other solvable equations.[4,8,10] The exact analytical solutions of such equations for particular shapes of nonuniform bars were thus obtained.

A literature review for this problem indicates that the authors of the previous studies have generally directed their investigations to special functions for describing the distributions of mass and shear stiffness to derive closed-form solutions. Exact analytical solution for free vibration of nonuniform shear beams with arbitrary distribution of mass or stiffness has not been obtained in the literature in the past. In this paper, classes of exact solutions for free vibration of cantilever shear beams, including one-step beams and multistep beams, with arbitrary distribution of mass or stiffness, are derived and an approach to determining natural frequencies and mode shapes for such nonuniform shear beams is proposed. Numerical examples show that the calculated natural frequencies and mode shapes of shear-type structures are very close to the corresponding field-measured data and those determined by the finite-element method and Ritz method, suggesting that the proposed methods are appropriate for engineering application and practice.

The objective of this paper is to present exact solutions for free vibration of nonuniform shear beams with arbitrary distribution of mass or stiffness. In the absence of the exact solutions, this problem can be solved using approximated methods (e.g., the Ritz method) or numerical methods (e.g., the finite-element method). For example, Liew *et al.*[11–13] have developed efficient two- and three-dimensional Ritz algorithms for the free-vibration analysis of elastic solids. Their work provided sets of frequency data and mode shapes for various types of elastic solids subject to different bound-

[a)]Electronic mail: bcqsli@cityu.edu.hk

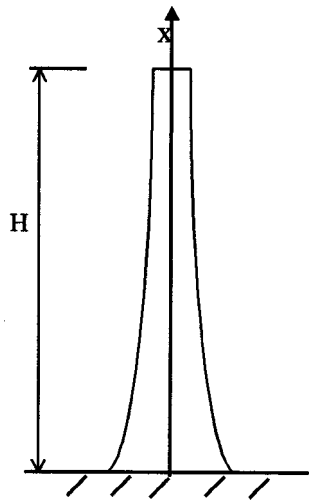

FIG. 1. A cantilever beam with varying cross section.

ary constraints. However, the exact solutions presented here can provide insight into the physics of the problem and help in examining the accuracy of the approximated or numerical solutions. Therefore, it is always desirable to obtain exact solutions to such problems.

II. FREE VIBRATION OF ONE-STEP NONUNIFORM SHEAR BEAMS

The governing equation for undamped free vibration of a one-step shear beam with continuously varying cross section can be written as

$$\frac{\partial}{\partial x}\left[K(x)\frac{\partial y}{\partial x}\right]-\overline{m}(x)\frac{\partial^2 y}{\partial t^2}=0. \tag{1}$$

It is assumed that

$$y(x,t)=X(x)\sin(\omega t+\gamma_0), \tag{2}$$

where $X(x)$ is the undamped vibration mode shape function, ω is the undamped circular natural frequency, and γ_0 is the initial phase.

Substituting Eq. (2) into Eq. (1) yields

$$\frac{d}{dx}\left[K(x)\frac{dX}{dx}\right]+\overline{m}(x)\omega^2 X=0. \tag{3}$$

It is difficult to obtain the exact analytical solution of Eq. (3) for general cases, because the coefficients in the equation vary with the coordinate x. In order to get closed-form solutions of Eq. (3) for arbitrary distribution of $K(x)$ or $\overline{m}(x)$, it is assumed that

$$\begin{aligned} &X(x)=X(r), \quad K(x)=\text{arbitrary function},\\ &\overline{m}(x)=K^{-1}(x)p(r), \quad r=\int K^{-1}(x)dx, \end{aligned} \tag{4}$$

or

$$\begin{aligned} &X(x)=X(r), \quad \overline{m}(x)=\text{arbitrary function},\\ &K(x)=\overline{m}^{-1}(x)p(r), \quad r=\int K^{-1}(x)dx. \end{aligned} \tag{5}$$

In Eq. (4), the expression for describing the distribution of shear stiffness of a shear beam is arbitrary, and the distribution of mass is expressed as a functional relation with the distribution of shear stiffness, and vice versa [see Eq. (5)].

Substituting Eq. (4) or Eq. (5) into Eq. (3) gives

$$\frac{d^2X(r)}{dr^2}+\omega^2 p(r)X(r)=0. \tag{6}$$

It is noted that r is a function of x, and $p(r)$ is a functional expression. Thus, a solution of Eq. (6) actually represents a class of solution for the title problem. On the other hand, it is easier to find the exact solution of Eq. (6) than to solve Eq. (3). It is thus decided to derive the solution of Eq. (6). However, the solution of Eq. (6) is dependent on the expression of $p(r)$. The following six important cases will be considered.

A. Case 1

$$p(r)=a(1+br)^c, \tag{7}$$

where a, b, c are parameters that can be determined by the values of $\overline{m}(x)$ and $K(x)$ at control sections.

In this case, Eq. (6) becomes

$$\frac{d^2X(r)}{dr^2}+\omega^2 a(1+br)^c X(r)=0. \tag{8}$$

Setting

$$g=(1+br)^{1/2\nu}, \quad X=g^\nu Z, \quad \nu=\frac{1}{c+2}, \tag{9}$$

and substituting Eq. (9) into Eq. (8) leads to

$$\frac{d^2Z}{dg^2}+\frac{1}{g}\frac{dZ}{dg}+\left(\alpha^2-\frac{\nu^2}{g^2}\right)Z=0, \tag{10}$$

in which

$$\alpha=\frac{2\nu\omega a^{1/2}}{|b|}, \quad a>0. \tag{11}$$

Equation (10) is a Bessel's equation of the νth order. The general solution of vibration mode shape functions can be expressed as

$$\begin{aligned} X=(1+br)^{1/2}\{&C_1 J_\nu[\alpha(1+br)^{1/2\nu}]\\ &+C_2 J_{-\nu}[\alpha(1+br)^{1/2\nu}]\}, \quad \nu=\text{a noninteger}, \end{aligned} \tag{12}$$

or

$$\begin{aligned} X=(1+br)^{1/2}\{&C_1 J_\nu[\alpha(1+br)^{1/2\nu}]\\ &+C_2 Y_\nu[\alpha(1+br)^{1/2\nu}]\}, \quad \nu=\text{an integer}, \end{aligned} \tag{13}$$

where J_ν and Y_ν are the Bessel function of the first and second kind of order ν, respectively.

Considering the cantilever beam with variable cross section shown in Fig. 1, its two known boundary conditions are

$$X=0 \quad \text{at } x=0, \tag{14}$$

$$\frac{dX}{dx}=0 \quad \text{at } x=H. \tag{15}$$

According to the boundary conditions, Eqs. (14) and (15), and the general solution of mode shape functions, Eq. (12), one obtains the frequency equation as

$$J_\nu[\alpha(1+br_0)^{1/2\nu}]J_{-(\nu-1)}[\alpha(1+br_H)^{1/2\nu}] = -J_{-\nu}[\alpha(1+br_0)^{1/2\nu}]J_{\nu-1}[\alpha(1+br_H)^{1/2\nu}], \quad (16)$$

for ν=noninteger or

$$J_\nu[\alpha(1+br_0)^{1/2\nu}]Y_{(\nu-1)}[\alpha(1+br_H)^{1/2\nu}] = Y_\nu[\alpha(1+br_0)^{1/2\nu}]J_{\nu-1}[\alpha(1+br_H)^{1/2\nu}], \quad (17)$$

for ν=an integer, where $r_0=r_{x=0}$, $r_H=r_{x=H}$.

Solving the frequency equation yields a set of α_j ($j=1,2,...$) and substituting α_j into Eq. (11) yields the following frequency expression:

$$\omega_j=\frac{\alpha_j|b|}{2\nu\sqrt{a}}. \quad (18)$$

If $c=-2$, $\nu=\infty$, then the general solutions given in Eqs. (12) and (13) are not valid for this case; however, Eq. (8) becomes an Euler equation as follows:

$$\frac{d^2X(r)}{dr^2}+\omega^2a(1+br)^{-2}X(r)=0. \quad (19)$$

The general solution of Eq. (19) can be written as

$$X=(1+br)^{1/2}\{C_1\sin[\alpha\ln(1+br)] + C_2\cos[\alpha\ln(1+br)]\} \quad \text{for } 4\omega^2a-b^2>0, \quad (20)$$

or

$$X=C_1(1+br)^{1/2+\alpha}+C_2(1+br)^{1/2-\alpha} \quad \text{for } 4\omega^2a-b^2<0, \quad (21)$$

or

$$X=C_1(1+br)^{1/2}+C_2(1+br)^{1/2}\ln(1+br) \quad \text{for } 4\omega^2a-b^2=0, \quad (22)$$

in which

$$\alpha=\frac{|4\omega^2a-b^2|^{1/2}}{2|b|}. \quad (23)$$

The frequency equations for the case 1 and $c=-2$ are found as

$$\tan[\alpha\ln(1+br_0)-\alpha\ln(1+br_H)]=2\alpha \quad \text{for } 4\omega^2a-b^2>0, \quad (24)$$

$$(1-2\alpha)(1+br_0)^{2\alpha}=(1+2\alpha)(1+br_H)^{2\alpha} \quad \text{for } 4\omega^2a-b^2<0, \quad (25)$$

$$\ln\frac{1+br_0}{1+br_H}=2b \quad \text{for} \quad 4\omega^2a-b^2=0. \quad (26)$$

If $c=0$, then Eq. (8) becomes

$$\frac{d^2X(r)}{dr^2}+\omega^2aX(r)=0. \quad (27)$$

The general solution of the above equation is

$$X=C_1\sin(\omega\sqrt{a}r)+C_2\cos(\omega\sqrt{a}r). \quad (28)$$

The frequency equation for this special case is found as

$$\cos[\omega\sqrt{a}(r_H-r_0)]=0. \quad (29)$$

The above equation requires that

$$\omega\sqrt{a}(r_H-r_0)=\frac{j\pi}{2}, \quad j=1,3,5,.... \quad (30)$$

Substituting this expression into Eq. (11), one obtains the frequency expression

$$\omega_j=\frac{j\pi}{2\sqrt{a}(r_H-r_0)}, \quad j=1,3,5,.... \quad (31)$$

B. Case 2

$$p(r)=ae^{br}, \quad (32)$$

where a and b are parameters that can be determined by the values of $\overline{m}(x)$ and $K(x)$ at control sections.

In this case, Eq. (6) becomes

$$\frac{d^2X(r)}{dr^2}+\omega^2ae^{br}X(r)=0. \quad (33)$$

Setting

$$g=e^{br/2} \quad (34)$$

and substituting Eq. (34) into Eq. (33) leads to

$$\frac{d^2X}{dg^2}+\frac{1}{g}\frac{dX}{dg}+\lambda^2X=0, \quad (35)$$

in which

$$\lambda=\frac{2\omega a^{1/2}}{|b|}, \quad a>0. \quad (36)$$

Equation (35) is a Bessel's equation of the zeroth order. The mode shape function can be written as

$$X=C_1J_0(\lambda e^{br/2})+C_2Y_0(\lambda e^{br/2}). \quad (37)$$

The frequency equation for case 2 is found as

$$J_0(\lambda e^{br_0/2})Y_1(\lambda e^{br_H/2})=Y_0(\lambda e^{br_0/2})J_1(\lambda e^{br_H/2}). \quad (38)$$

C. Case 3

$$p(r)=ae^{br}-c, \quad c>0. \quad (39)$$

Substituting Eq. (39) into Eq. (6) and using the functional transformations given in Eq. (34), one obtains the general solution of mode shapes as

$$X=\begin{cases} C_1J_\nu(\lambda e^{br/2})+C_2J_{-\nu}(\lambda e^{br/2}), & \nu=\text{a noninteger,} \\ C_1J_\nu(\lambda e^{br/2})+C_2Y_\nu(\lambda e^{br/2}), & \nu=\text{an integer,} \end{cases} \quad (40)$$

in which

$$\nu^2=\frac{4c}{b^2}, \quad (41)$$

and the parameter λ can be determined by Eq. (36).

D. Case 4

$$p(r)=(a+br)^c. \tag{42}$$

Substituting Eq. (42) into Eq. (6) and using the following functional transformation:

$$X=g^{\nu}Z, \quad Z=(a+br)^{1/2\nu}, \quad \nu=\frac{1}{c+2}, \tag{43}$$

leads to a Bessel equation the same as Eq. (10). The general solution of mode shape functions is

$$X=\begin{cases}(a+br)^{1/2}\{C_1J_{\nu}[\overline{\alpha}(a+br)^{1/2}] \\ \quad +C_2J_{-\nu}[\overline{\alpha}(a+br)^{1/2}]\}, & \nu=\text{a noninteger}, \\ (a+br)^{1/2}\{C_1J_{\nu}[\overline{\alpha}(a+br)^{1/2}] \\ \quad +C_2Y_{\nu}[\overline{\alpha}(a+br)^{1/2}], & \nu=\text{an integer},\end{cases} \tag{44}$$

in which

$$\overline{\alpha}=\frac{2\nu\omega}{|b|}.$$

E. Case 5

$$p(r)=a(r^2+b)^{-2}, \quad a>0, \quad b>0. \tag{45}$$

The general solution of mode shape functions for this case is given by

$$X=(r^2+b)^{1/2}(C_1\sin\xi+C_2\cos\xi), \tag{46}$$

where

$$\xi=\left(\frac{a+b}{b}\right)^{1/2}\arctan\frac{r}{b^{1/2}}. \tag{47}$$

F. Case 6

$$p(r)=a(r^2-b)^{-2}, \quad a>0, \quad b>0 \tag{48}$$

The general solution of mode shape functions for this case is given by

$$X=(b-r^2)^{1/2}(C_1\sin\xi+C_2\cos\xi), \tag{49}$$

where

$$\xi=\frac{1}{2}\left(\frac{a-b}{b}\right)^{1/2}\ln\frac{b^{1/2}+r}{b^{1/2}-r}. \tag{50}$$

III. FREE VIBRATION OF MULTISTEP SHEAR BEAMS

A multistep shear beam is shown in Fig. 2, each step of which has variably distributed stiffness and mass. The governing differential equation for mode shape function of the ith step can be written as

$$\frac{d}{dx}\left[K_i(x)\frac{dX_i(x)}{dx}\right]+\overline{m}_i(x)\omega^2X_i(x)=0. \tag{51}$$

Equation (51) has the same form as Eq. (3). The general solutions of Eq. (51) are expressed as

$$X_i(x)=C_{i1}S_{i1}(x)+C_{i2}S_{i2}(x) \quad (i=1,2,...,n), \tag{52}$$

where i denotes the ith step and n is the total number of steps of the beam (Fig. 2), and $S_{i1}(x)$ and $S_{i2}(x)$ are special solutions of the mode shape of the ith step. For example, if $\overline{m}_i(x)$ is given by

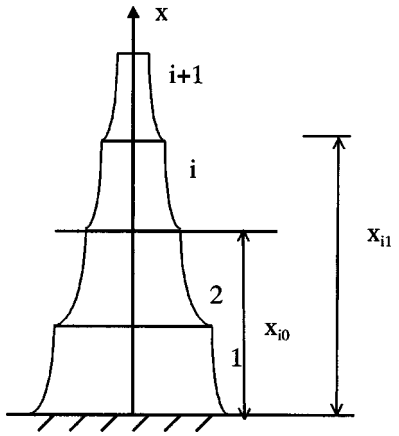

FIG. 2. A multistep shear beam.

$$\overline{m}_i(x)=a_i(1+b_ir)^{c_i}K_i^{-1}(x), \quad r=\int K_i^{-1}(x)dx, \tag{53}$$

then $S_{i1}(x)$ and $S_{i2}(x)$ can be found from Eqs. (12) and (13). Thus, the solutions derived in the last section can be used for free-vibration analysis of multistep nonuniform beams.

The relation between the parameters X_{i1} (shear displacement) and Q_{i1} (shear force) at the end x_{i1} and the parameters X_{i0}, Q_{i0} at the end x_{i0} of the ith step (Fig. 2) can be expressed as

$$\begin{bmatrix}X_{i1}\\Q_{i1}\end{bmatrix}=[T_i]\begin{bmatrix}X_{i0}\\Q_{i0}\end{bmatrix}, \tag{54}$$

in which

$$[T_i]=\begin{bmatrix}S_{i1}(X_{i1}) & S_{i2}(X_{i1})\\ K_{i1}S'_{i1}(X_{i1}) & K_{i1}S'_{i2}(X_{i1})\end{bmatrix} \times\begin{bmatrix}S_{i1}(X_{i0}) & S_{i2}(X_{i0})\\ K_{i0}S'_{i2}(X_{i0}) & K_{i0}S'_{i2}(X_{i0})\end{bmatrix} \tag{55}$$

$$X_{i1}=X_i(x_{i1}), \quad X_{i0}=X_i(x_{i0}), \quad Q_{i1}=Q_i(x_{i1}), \quad Q_{i0}=Q_i(x_{i0})$$

$$K_{i1}=K_i(x_{i1}), \quad K_{i0}=K_i(x_{i0}), \quad S'_{i1}(x_{i1})=\left.\frac{dS_{i1}(x)}{dx}\right|_{x=x_{i1}},$$

$[T_i]$ is called the transfer matrix because it transfers the parameters at the end x_{i0} to those at the end x_{i1} of the ith step. Since

$$X_{i0}=X_{i-1,1}, \quad Q_{i0}=Q_{i-1,1}, \tag{56}$$

X_{i1} and Q_{i1} can be written as

$$\begin{bmatrix}X_{i1}\\Q_{i1}\end{bmatrix}=[T_i][T_{i-1}]\cdots[T_1]\begin{bmatrix}X_{10}\\Q_{10}\end{bmatrix}. \tag{57}$$

Setting $i=n$ obtains the relation between the parameters at the top and those at the base of the beam as follows:

$$\begin{bmatrix}X_{n1}\\Q_{n1}\end{bmatrix}=[T]\begin{bmatrix}X_{10}\\Q_{10}\end{bmatrix}, \tag{58}$$

in which

$$[T]=[T_n][T_{n-1}]\cdots[T_1]. \tag{59}$$

$[T]$ is a matrix of the second order

$$[T]=\begin{bmatrix} T_{11} & T_{12} \\ T_{21} & T_{22} \end{bmatrix}. \tag{60}$$

The element T_{ij} $(i,j=1,2)$ in Eq. (60) can be found according to Eqs. (59) and (55).

The frequency equation can be obtained by use of Eq. (58) and the boundary conditions, Eqs. (14) and (15), as follows (Fig. 2):

$$T_{22}=0. \tag{61}$$

If there is a lumped mass, M_i, attached at x_{i1} of the ith step, then the transfer matrix $[T_i]$ should be replaced by $[T_{mi}]$.

$$[T_{mi}]=\begin{bmatrix} 1 & 0 \\ M_i\omega^2 & 1 \end{bmatrix}[T_i]. \tag{62}$$

Clearly, setting $n=1$ in Eqs. (52)–(59) obtains the solutions for free vibrations of a one-step beam.

IV. STIFFNESS AND MASS EXPRESSIONS

As mentioned above, the stiffness expression can be selected as an arbitrary function and the mass distribution is expressed as a functional relation with the distribution of stiffness, and vice versa.

In general, the stiffness or the mass distribution of a structure or a structural member, such as a beam, a column, can be considered as one of the following functions:

$$(1)\quad K(x)=\alpha\left(1+\beta\frac{x}{H}\right)^{\gamma}. \tag{63}$$

If the sections at $x=0,H/2,H$ are considered as control sections, then

$$\begin{aligned} \alpha&=K(0) \\ \beta&=\left[\frac{K(H)}{K(0)}\right]^{1/\gamma}-1 \\ \gamma&=\frac{\ln K(H/2)-\ln K(0)}{\ln\left(1+\frac{\beta}{2}\right)}, \end{aligned} \tag{64}$$

where $K(0)$, $K(H/2)$ and $K(H)$ are the values of stiffness at $x=0$, $H/2$, and H, respectively.

In this case, if $p(r)$ is given by Eq. (7), then substituting Eq. (63) into Eq. (4) yields

$$\overline{m}(x)=\frac{a}{\alpha}\left(1+\beta\frac{x}{H}\right)^{-\gamma}(1+br)^{c}, \tag{65}$$

in which

$$\begin{aligned} r&=\frac{H}{\alpha\beta}\frac{1}{1-\gamma}\left(1+\beta\frac{x}{H}\right)^{-\gamma+1}, \quad \gamma\neq 1 \\ r&=\frac{H}{\alpha\beta}\ln\left(1+\beta\frac{x}{H}\right), \quad \gamma=1. \end{aligned} \tag{66}$$

If $p(r)$ is given in Eq. (32), then

$$\overline{m}(x)=\frac{a}{\alpha}\left(1+\beta\frac{x}{H}\right)^{-\gamma}e^{br}. \tag{67}$$

The expression of r is the same as that given in Eq. (66).

$$(2)\quad K^{-1}(x)=\alpha e^{\beta(x/H)}+\gamma. \tag{68}$$

The values of $K^{-1}(x)$ at $x=0$, $H/2$, and H are considered as control ones; then

$$\begin{aligned} \gamma&=\frac{K^{-1}(0)K^{-1}(H)-[K^{-1}(H/2)]^2}{K^{-1}(0)+K^{-1}(H)-2K^{-1}(H/2)} \\ \alpha&=K^{-1}(0)-\gamma \\ \beta&=\ln\left[\frac{K^{-1}(H)-\gamma}{\alpha}\right]. \end{aligned} \tag{69}$$

If $p(r)$ is given in Eq. (7) or Eq. (37), then

$$\overline{m}(x)=\alpha a\left(e^{\beta(x/H)}+\frac{\gamma}{\alpha}\right)(1+br)^{c}, \tag{70}$$

or

$$\overline{m}(x)=\alpha a e^{br}\left(e^{\beta(x/H)}+\frac{\gamma}{\alpha}\right), \tag{71}$$

in which

$$r=\frac{\alpha H}{\beta}e^{\beta(x/H)}+\gamma x.$$

$$(3)\quad K^{-1}(x)=\sum_{i=0}^{n}\alpha_i\left(\frac{x}{H}\right)^{i}. \tag{72}$$

If $p(r)$ is given in Eq. (7), then

$$\overline{m}(x)=a\left(1+b\frac{r}{H}\right)^{c}\sum_{i=0}^{n}\alpha_i\left(\frac{x}{H}\right)^{i}, \tag{73}$$

where

$$r=\frac{1}{H}\sum_{i=0}^{n}\frac{\alpha_i}{i+1}x^{i+1}. \tag{74}$$

There are $(n+4)$ independent parameters, α_i $(i=0,1,...,n)$ and a, b, c, in the expressions of $K^{-1}(x)$ and $\overline{m}(x)$, which can be determined by the values of $K^{-1}(x)$ and $\overline{m}(x)$ at critical sections.

If $p(r)$ is given in Eq. (32), then

$$\overline{m}(x)=ae^{br}\sum_{i=0}^{n}\alpha_i\left(\frac{x}{H}\right)^{i}. \tag{75}$$

The expression of r is the same as that given in Eq. (74).

For a multistep shear beam (Fig. 2), the above expressions can be used for describing the distributions of mass and shear stiffness of the ith step of the beam.

V. EFFECT OF TAPER ON NATURAL FREQUENCIES OF NONUNIFORM BEAMS

In order to study the effect of taper on natural frequencies of nonuniform beams, a special case is considered herein, i.e., it is assumed that

TABLE I. The first six eigenvalues ($\lambda_j\beta$) for $\beta>0$.

	Mode					
β	1	2	3	4	5	6
0	1.5708	4.7124	7.8540	10.9956	14.1372	17.2787
0.5	1.3241	4.6406	7.8117	10.9644	14.1120	17.2582
1	1.1653	4.6038	7.7893	10.9492	14.1010	17.2483
2	0.9014	4.5610	7.7670	10.9342	14.0890	17.2368
3	0.8475	4.5471	7.7562	10.9263	14.0832	17.2340
4	0.7676	4.5376	7.7468	10.9208	14.0796	17.2311
5	0.6940	4.5315	7.7463	10.9185	14.0770	17.2292
6	0.6576	4.5252	7.7436	10.9164	14.0754	17.2277
7	0.6055	4.5182	7.7413	10.9144	14.0742	17.2268
8	0.5712	4.5176	7.7392	10.9136	14.0734	17.2261
9	0.5427	4.5153	7.7391	10.9125	14.0724	17.2253
10	0.5210	4.5130	7.7390	10.9120	14.0720	17.2248

$$K(x)=K\left(1+\beta\frac{x}{l}\right)^2, \quad \bar{m}(x)=\bar{m}\left(1+\beta\frac{x}{l}\right)^2. \tag{76}$$

According to Eq. (5), one yields

$$r=-\frac{l}{\beta K}\left(1+\beta\frac{x}{l}\right)^{-1}, \tag{77}$$

$$p(r)=\bar{m}K^{-3}\beta^{-4}l^4r^{-4}. \tag{78}$$

Obviously, Eq. (78) is a special case of Eq. (42), i.e., setting $c=-4$, $a=0$, $b^{-4}=\bar{m}K^{-3}\beta^{-4}l^4$; then, Eq. (42) has the same form as Eq. (78).

The general solution of mode shape functions can be expressed as

$$X=\frac{1}{1+\beta\frac{x}{l}}\left[C_1\sin\lambda\left(1+\beta\frac{x}{l}\right)+C_2\cos\left(1+\beta\frac{x}{l}\right)\right]. \tag{79}$$

Using the boundary conditions, Eqs. (14) and (15), one yields the frequency equation as

$$\tan\lambda\beta=\lambda(1+\beta), \tag{80}$$

where

$$\lambda=\frac{\bar{m}\omega^2}{k\beta^2}.$$

The jth circular natural frequency, ω_j, can be expressed as

$$\omega_j=\frac{\lambda_j\beta}{l}\sqrt{\frac{K}{\bar{m}}}, \quad j=1,2,3,\ldots. \tag{81}$$

TABLE III. The fundamental mode shape.

	x/H	0	0.2	0.4	0.5	0.6	0.8	1.0
X_1	Calculated values	0	0.2365	0.5120	0.6465	0.7671	0.9417	1.0
X_1	Measured values	0	0.226	0.497	0.645	0.763	0.941	1.0

The first six eigenvalues, $\beta\lambda_j$ ($j=1,2,3,4,5,6$), are calculated and listed in Table I. It can be seen from the results presented in Table I that the lowest natural frequency is affected most by the taper. For higher modes, the natural frequencies are close to and less than those of the corresponding uniform beams ($\beta=0$).

VI. NUMERICAL EXAMPLE 1

A tall frame building of 190-m height is located in Moscow. The values of shear stiffness and mass per unit length of this building, which were published by Korqingskee,[1] are listed in Table II.

The procedure for determining natural frequencies and mode shapes of this building is as follows:

(1) Selection of expressions for describing the distributions of shear stiffness and mass per unit length. According to the values of shear stiffness at several sections listed in Table II, we select that

$$K(x)=\alpha_1\left(1+\beta\frac{x}{H}\right)^r, \quad H=190\,\text{m},$$

in which H is the total height of this building, α, β, γ are determined by Eq. (64) based on the values at the sections at $x=0$, $H/2$, and H as follows:

$\alpha_1=1.299\times10^{11}$, $\beta=-0.662, \gamma=2$.

The expression of $\bar{m}(x)$ is

$$\bar{m}(x)=K^{-1}(x)p(r), \quad p(r)=ae^{br}, \tag{82}$$

in which the parameter, r, can be found by use of Eq. (54) as

$$r=2.209\left(1-0.662\frac{x}{H}\right)^{-1}\times10^{-6}. \tag{83}$$

Substituting Eq. (83) into Eq. (82) leads to

$$\bar{m}(x)=\frac{a\times10^{-8}}{1.299}\left(1-0.662\frac{x}{H}\right)^{-2}\times e^{2.209b[1-0.662\,(x/H)]^{-1}\times10^{-6}}.$$

According to Eq. (69) and the values listed in Table II, one obtains

TABLE II. The values of shear stiffness and mass.

x/H	0	0.2	0.4	0.5	0.6	0.8	1.0
$K(x/H)\times10^{11}$ (N)	1.299 (1.299)[a]	0.974 (0.978)	0.698 (0.702)	0.579 (0.579)	0.470 (0.472)	0.283 (0.287)	0.148 (0.148)
$\bar{m}(x/H)\times10^5$ (kg)	10.430 (10.430)	9.421 (9.536)	7.895 (7.997)	6.864 (6.950)	5.620 (5.728)	2.806 (3.006)	0.761 (0.761)

[a]The values in parentheses are calculated ones.

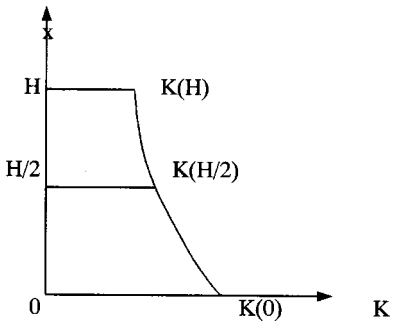

FIG. 3. The stiffness distribution.

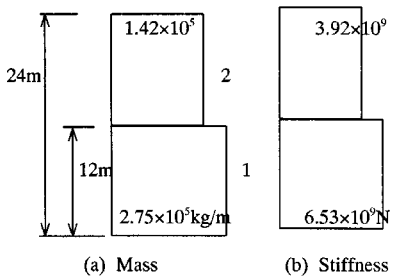

FIG. 4. The distributions of mass and stiffness. (a) Mass; (b) Stiffness.

$a=1.5604\times10^{15}$, $b=-1.1069\times10^{6}$.

The calculated values of $K(x)$ and $\overline{m}(x)$ are also listed in Table II. It can be seen from Table II that the selected expressions are suitable for describing the distributions of shear stiffness and mass of this building.

(2) Determination of frequency equation. Because the expression of $p(r)$ selected belongs to case 2 discussed previously, the frequency equation is Eq. (38). The parameters in Eq. (38) are determined as

$$r_0=2.209\times10^{-6}, \quad r_H=6.537\times10^{-6}. \tag{84}$$

Substituting Eq. (84) into Eq. (38) yields the frequency equation as

$$J_0(0.2947\alpha)Y_1(0.0269\alpha)=Y_0(0.2947\alpha)J_1(0.0269\alpha). \tag{85}$$

Solving Eq. (85), one obtains a set of α_i ($i=1,2,...$); the minimum value, α_1, is found as $\alpha_1=8.29$. Substituting the value of α_1 into Eq. (36) yields the fundamental circular natural frequency and the corresponding natural period as

$\psi_1=3.6699\ \mathrm{rad\,s^{-1}}$, $T_1=1.7121$ s.

Using the Ritz method and assuming that

$$X(x)=\sum_{i=1}^{n} a^i\varphi_i(x), \quad \varphi_i(x)=e^{\beta x/2H}\sin\frac{(2i-1)\pi x}{2H}, \tag{86}$$

one obtains

$T_1=1.7118$ s, if $n=2$.

The above result is almost the same as that obtained by the proposed method. The fundamental natural period experimentally measured by Korqingskee[1] is

$T_1=1.70$ s.

It is clear that the natural period calculated by the proposed method is very close to the field-measured one, suggesting that the proposed methods are appropriate for engineering application and practice.

(3) Determination of mode shape. The mode shape can be determined from Eq. (37). As the one for C_1 and C_2 is arbitrary, we set $C_1=1$. According to the boundary condition, Eq. (14), one obtains

$$C_2=-\frac{J_0(\alpha e^{br_0/2})}{Y_0(\alpha e^{br_0/2})}. \tag{87}$$

Substituting α into Eq. (87) yields

$C_2=-0.0358$.

The first mode shape can be expressed as

$$X_1=J_0(8.29e^{br/2})+0.0358Y_0(8.29e^{br/2}). \tag{88}$$

The calculated values of the fundamental mode shape at several sections and the measured data published by Korqingskee[1] are listed in Table III. It can be seen from Table III that the calculated values of the fundamental mode shape of this building are very close to the measured data. It should be noted that the higher natural frequencies and corresponding mode shapes can also be obtained by using the same procedure mentioned above.

VII. NUMERICAL EXAMPLE 2

An 8-story frame building of 24-m height is located in Wuhan, China. Based on the field measurement,[4] this building can be simplified as a cantilever shear beam for free-vibration analysis. The values of shear stiffness and mass per unit length of this building are determined and shown in Fig. 3.

The procedure for determining the natural frequencies and mode shapes of the two-step shear beam shown in Fig. 4 is as follows:

(1) Determination of special solutions for free vibration of each step. Because the distributions of mass per unit length and shear stiffness of each step are uniform, the special solutions can be found from Eq. (28), i.e.,

TABLE IV. The fundamental mode shape.

	x/H	0	0.125	0.25	0.375	0.50	0.625	0.75	0.875	1.0
X_1	Calculated values	0	0.1854	0.3621	0.5257	0.6871	0.7576	0.9134	0.9798	1.0
X_1	Measured values	0	0.187	0.365	0.526	0.689	0.750	0.910	0.975	1.0

$$S_{11}(x)=\sin(64.89\omega x), \quad S_{12}(x)=\cos(64.89\omega x),$$
$$S_{21}(x)=\sin(60.19\omega x), \quad S_{22}(x)=\cos(60.19\omega x).$$

(2) Evaluation of natural frequencies. Using Eq. (54) and the boundary condition described in Eq. (14) leads to

$$\begin{bmatrix} X_{11} \\ Q_{11} \end{bmatrix} = [T_1] \begin{bmatrix} 0 \\ Q_{10} \end{bmatrix}, \tag{89}$$

$$\begin{bmatrix} X_{21} \\ Q_{21} \end{bmatrix} = [T_2][T_1] \begin{bmatrix} 0 \\ Q_{10} \end{bmatrix} \tag{90}$$

in which $[T_i]$ is given in Eq. (55), and

$x_{10}=0, \quad x_{11}=x_{20}=12, \quad x_{21}=24.$

Substituting x_{10}, x_{11}, x_{20}, x_{21}, and S_{11}, S_{12}, S_{21}, S_{22} into Eq. (55), one obtains

$$[T_1]=\begin{bmatrix} \sin 778.68\omega & \cos 778.68\omega \\ 5.085\times 10^{12}\cos 778.68\omega & -5.085\times 10^{12}\sin 778.68\omega \end{bmatrix} \begin{bmatrix} 0 & 1 \\ 2.141\times 10^{8} & 0 \end{bmatrix}^{-1},$$

$$[T_2]=\begin{bmatrix} \sin 1444.56\omega & \cos 1444.56\omega \\ 5.663\times 10^{12}\cos 1444.56\omega & -5.663\times 10^{12}\sin 1444.56\omega \end{bmatrix} \times \begin{bmatrix} \sin 722.28\omega & \cos 722.28\omega \\ 2.831\times 10^{12}\cos 722.28\omega & -2.831\times 10^{12}\sin 722.28\omega \end{bmatrix}^{-1}.$$

The frequency equation is Eq. (61); solving Eq. (61), one obtains a set of ω_j ($j=1,2,...$); the minimum value, ω_1, is found as

$\omega_1=11.0941$ rad/s.$^{-1}$

The fundamental natural period is

$T_1=0.5664$ s.

The field-measured one[4] is

$T_1=0561$ s.

It is shown that the calculated fundamental natural period is very close to the field-measured one.

(3) Determination of mode shape. The mode shapes of this building can be determined based on the value of ω_j, Eq. (89), and setting $Q_{10}=1$ (or other values). The fundamental mode shape is determined and listed in Table IV. It can be seen from Table IV that the calculated values of the fundamental mode shape of this building are very close to field-measured ones.

VIII. NUMERICAL EXAMPLE 3

The objective of presenting this numerical example is to compare the exact results obtained by the present method with those determined by the finite-element method (FEM).

TABLE V. The first six eigenvalues ($\lambda_j\beta$).

Elements	Mode 1	2	3	4	5	6
Exact values	1.3241	4.6406	7.8117	10.9644	14.1120	17.2582
10 elements	1.3086	4.6098	7.6612	10.7836	13.8861	16.0792
15 elements	1.3208	4.6301	7.7964	10.8102	14.0928	17.1832
20 elements	1.3227	4.6387	7.8001	10.9278	14.1101	17.2476
30 elements	1.3240	4.6404	7.8115	10.9642	14.1116	17.2581
40 elements	1.3241	4.6406	7.8117	10.9643	14.1119	17.2581

It is assumed that the stiffness and mass distributions of a nonuniform beam are described by

$$K(x)=K\left(1+0.5\frac{x}{l}\right)^2, \quad \overline{m}(x)=\overline{m}\left(1+0.5\frac{x}{l}\right)^2.$$

The nonuniform beam is divided into different elements for conducting the numerical computation using the FEM. The first six eigenvalues of the beam obtained by the present exact method and the FEM are presented in Table V for comparison purposes.

It can be seen from Table V that if the nonuniform beam is divided into 40 elements for the numerical computation, the results calculated by the FEM are almost the same as the exact solutions presented in this paper.

IX. CONCLUSIONS

An efficient and exact method is presented herein to determine the natural frequencies and mode shapes of nonuniform shear beams. The function for describing the distribution of mass is arbitrary, and the distribution of shear stiffness is expressed as a functional relation with the mass distribution, and vice versa. Using appropriate functional transformation, the governing differential equations for free vibration of nonuniform shear beams are reduced to Bessel's equations or ordinary differential equations with constant coefficients for several functional relations between shear stiffness distribution and mass distribution. The exact solutions are thus obtained. Since the relation between the mass distribution and stiffness distribution is a functional expression, an exact solution derived herein actually represents a class of exact solutions for the title problem. Numerical examples demonstrate that the calculated natural frequencies and mode shapes of shear-type buildings are very close to the corresponding full-scale measurements and those determined by FEM and the Ritz method, illustrating that the proposed methods are appropriate for engineering application and practice.

ACKNOWLEDGMENTS

The work described in this paper was supported by a grant from the Research Grants Council of the Hong Kong Special Administrative Region, China [Project No. 9040521] and a grant from City University of Hong Kong [Project No. 7001058].

[1] E. L. Korqingskee, *Vibrations of Tall Buildings* (Moscow Press, Moscow, 1952), pp. 25–36.
[2] H. Ishizake and N. Hatakeyana, ''Experimental and numerical studies on vibration of buildings,'' in *Proceedings of the Second World Conference on Earthquake Engineering* (1960).
[3] G. Y. Wang, *Vibration of Buildings and Structures* (Science and Technology, Beijing, P. R. China, 1978).
[4] Q. S. Li, H. Cao, and G. Li, ''Analysis of free vibrations of tall buildings,'' ASCE J. Eng. Mech. **120**(9), 1861–1876 (1994).
[5] A. P. Jeary, *Designer's Guide to the Dynamic Response of Structures* (E & FN Spon, London, 1997).
[6] G. Y. Wang, ''The calculation of earthquake loads acting on buildings,'' J. Civil Eng. **5**(2), 16–32 (1958).
[7] G. Y. Wang, ''Free vibrations of multi-story buildings,'' J. Harbin Univ. Architec. Civil Eng. **1**, 1–10 (1963).
[8] Q. S. Li, H. Cao, and G. Li, ''Static and dynamic analysis of straight bars with variable cross-section,'' Comput. Struct. **59**(6), 1185–1191 (1996).
[9] Q. S. Li, ''Free vibration analysis of shear-type buildings,'' Adv. Struct. Eng. Int. J. **2**(3), 163–172 (1998).
[10] Q. S. Li, J. Q. Fang, and A. P. Jeary, ''Calculation of vertical dynamic characteristics of tall buildings with viscous damping,'' Int. J. Solids Struct. **35**(24), 3165–3176 (1998).
[11] K. M. Liew, K. C. Hung, and M. K. Lim, ''Free vibration studies on stress-free three-dimensional elastic solids,'' ASME J. Appl. Mech. **62**, 159–165 (1995).
[12] K. M. Liew, K. C. Hung, and M. K. Lim, ''Modeling three-dimensional vibration of elliptic bars,'' J. Acoust. Soc. Am. **98**, 1518–1526 (1995).
[13] K. M. Liew, K. C. Hung, and M. K. Lim, ''Vibration of thick prismatic structures with three-dimensional flexibilities,'' ASME J. Appl. Mech. **65**, 619–625 (1998).

Evaluation of impulse noise criteria using human volunteer data

Philemon C. Chan, Kevin H. Ho, Kit K. Kan, and James H. Stuhmiller
Jaycor, 3394 Carmel Mountain Road, San Diego, California 92121

Maria A. Mayorga
Division of Medicine, Walter Reed Army Institute of Research, Building 511, Trailers-Forest Glen Annex, Silver Spring, Maryland 20910

(Received 13 January 1999; revised 14 March 2001; accepted 12 June 2001)

Four impulse noise auditory injury criteria adopted by NATO countries, namely, the MIL-STD-1474D (USA), Pfander (Germany), Smoorenburg (Netherlands), and L_{Aeq8} (France), are evaluated against human volunteer data. Data from subjects wearing single-hearing protection exposed to increasing blast overpressure effects were obtained from tests sponsored by the US Army Medical Research and Material Command. Using logistic regression, the four criteria were each correlated with the test data. The analysis shows that all four criteria are overly conservative by 9.6–21.2 dB for the subjects as tested. The MIL-STD-1474D for single-hearing protection is 9.6 dB lower than the observed injury threshold for 95% protection with 95% confidence for this particular group of subjects as tested. Similar conclusions can be drawn for the other three criteria. © *2001 Acoustical Society of America.* [DOI: 10.1121/1.1391243]

PACS numbers: 43.50.Qp, 43.50.Pn [MRS]

LIST OF SYMBOLS

$\hat{C}$	Hosmer–Lemeshow goodness-of-fit statistic for logistic regression
g	Logit function
$g_{\pm}$	Confidence interval in logit space
L	Effective exposure level
L_{Aeq8}	Eight hour equivalent A-weighted sound-exposure level
L_M	Effective exposure level for MIL-STD-1474D
L_P	Effective exposure level for Pfander criterion
L_{pk}	Peak sound-pressure level
L_S	Effective exposure level for Smoorenburg criterion
m_o	Observed number of failures in a test group
m_p	Presumed failures in a test group
n	Sample size of a test group
n_k	Number of data points in a data group
o_k	Total number of failures in a data group
$P_{\max}$	Peak pressure of the free-field incident wave
P_{ref}	Reference value of 20 μPa
T_B	B duration
T_C	C duration
T_D	D duration
β	Parameter coefficients for the logistic fit
$\hat{\beta}$	Predicted values of β
$\Phi(z_x)$	Accumulative standardized normal distribution function
$\sigma_0, \sigma_1, \sigma_{01}$	Standard errors and covariance
π	Probability of failure
$\overline{\pi_k}$	Average predicted failure rate in the kth data group
$\hat{\pi}$	Predicted failure rate

I. INTRODUCTION

Evaluation of impulse noise criteria is becoming more critical as new weapons tend to exceed exposure levels for single-hearing protection set forth by auditory damage risk criteria (DRC), such as the MIL-STD-1474D in the USA (1991). Previous man-rating studies have consistently shown that auditory injury does not occur at these levels (Patterson *et al.*, 1985, 1987). Consequently, there is a general belief that the current standards underpredict the threshold at which injury occurs. Occupational standards for field application still use free-field pressure because there is still no validated standard method to correlate pressure measured under the protector with observed injury. Previous effort to evaluate the current standards using human data with adequate statistics has been limited.

The objective of this paper is to evaluate four impulse noise auditory injury criteria used by NATO countries against data obtained from human volunteers wearing single-hearing protection. The four criteria evaluated are the MIL-STD-1474D in the USA, Pfander in Germany (Pfander *et al.*, 1980, 1994; Brinkman, 1994), Smoorenburg in The Netherlands (Smoorenburg, 1982, 1992), and L_{Aeq8} in France (Dancer, 1995). Two data sets from human volunteer tests sponsored by the US Army Medical Research and Material Command (USAMRMC) (Johnson, 1994, 1997; and Patterson *et al.*, 1994) were used. The data cover free-field and bunker tests with modified earmuffs. The results will guide future revision of impulse noise DRCs.

II. METHOD

A. Criteria definition

Each injury criterion defines its effective exposure level that is to be kept within a limit, as shown in Table I. Nor-

TABLE I. Criteria definition.

Criteria	Effective exposure level (dB)	Limit (dB)
MIL-STD-1474D (1991)	$L_M = L_{pk} + 6.64 \log(T_B/200) + 5 \log N$	$L_M \leqslant 177$
Pfander (1980, 1994)	$L_P = L_{pk} + 10 \log T_C + 10 \log N$	$L_P \leqslant 175$[a]
Smoorenburg (1982)	$L_S = L_{pk} + 10 \log T_D + 10 \log N$	$L_S \leqslant 181.2$[a]
L_{Aeq8} (1995)	L_{Aeq8}	$L_{Aeq8} \leqslant 100$[a]

[a]With 15-dB attenuation assumed for modified earmuff.

malized to dB, each effective exposure level is calculated from waveform parameters, such as the peak incident pressure and some form of duration. Peak sound-pressure level (SPL) is defined as

$$L_{pk} = 10 \log(P_{max}/P_{ref})^2, \quad (1)$$

where P_{max} is the peak incident pressure and P_{ref} is the reference value of 20 μPa. Figure 1 shows the definition of the four waveform durations commonly used to characterize blast overpressures, namely, the *A*-duration T_A, the *B*-duration T_B, the *C*-duration T_C, and the *D*-duration T_D. While T_A only captures the primary positive phase, T_C, T_B, and T_D provide some measures for complex waveforms. If the same shot is repeated N times, some form of trading rule is used. Figure 2 presents the three peak-based criteria, MIL-STD-1474D, Pfander, and Smoorenburg as the variation of L_{pk} with the corresponding duration for $N=1$.

The MIL-STD-1474D calculates its effective exposure level L_M using the peak sound-pressure level L_{pk} and T_B, with a 5 log N trading rule (Table I). For single-hearing protection, the limit for MIL-STD-1474D is $L_M \leqslant 177$ dB (Table I). As shown in Fig. 2 for MIL-STD, the decrease of L_{pk} with T_B levels off to a constant when T_B exceeds 200 ms. To model this behavior, MIL-STD normalizes T_B by 200 ms and sets T_B to 200 ms when it exceeds 200 ms (Table I). The MIL-STD-1474D does not distinguish between different types of protectors.

Pfander calculates the effective exposure level L_P using L_{pk} and T_C with 10 log N trading where T_C is normalized by 1 ms (Table I). The Pfander (German) criterion was first presented in Pfander *et al.* (1980), and later modified by 5-dB reduction of the limit while retaining the same functional form of the exposure level definition (Brinkmann, 1994; Pfander, 1994). To account for a single-hearing protector, the limit on L_P is raised by an average attenuation, Att_M, in the frequency range from 500 to 2000 Hz (Brinkmann, 1994). The data being analyzed were taken using modified earmuffs with an average attenuation Att_M of 15 dB (Johnson, 1994). Consequently, the Pfander limit is raised by 15 dB to $L_P \leqslant 175$ dB (Table I). The Pfander criterion with 15-dB single-hearing protection is shown in Fig. 2.

Similarly, Smoorenburg uses L_{pk} and T_D with a 10 log N trading to calculate its effective exposure level L_S with T_D normalized by 1 ms. For the selected data with single-hearing protection, 15 dB is added to raise the Smoorenburg limit to $L_S \leqslant 181.2$ dB, following the use of an averaged attenuation as for the Pfander criterion explained above (Table I) (Pfander *et al.*, 1980, 1994; Smoorenburg, 1982). The Smoorenburg criterion with 15-dB single-hearing protection is shown in Fig. 2.

The *B* durations were calculated according to the procedure described in MIL-STD-1474D (1991). The same procedure was used to calculate *D* duration by imposing the 10-dB drop from the peak instead of 20 dB [Figs. 1(b) and (d)]. The *C*-duration was calculated in a straightforward way, as shown in Fig. 1(c).

Using the A-weighted energy concept, L_{Aeq8} was proposed by the French Committee for Weapon Noises (FCWN) with a limit of 85 dB for unprotected ears. The effective exposure level for L_{Aeq8} is the 8-h equivalent A-weighted sound exposure level (Table I). Sound exposure level is the integral of pressure squared over the entire pulse normalized by 1 s. If a shot is repeated N times, the sound exposure level of a single shot is multiplied by N, which is equivalent to using 10 log N equal energy trading. If an exposure involves pulses that are different, L_{Aeq8} will sum up the energies from all individual pulses. To account for single-hearing protec-

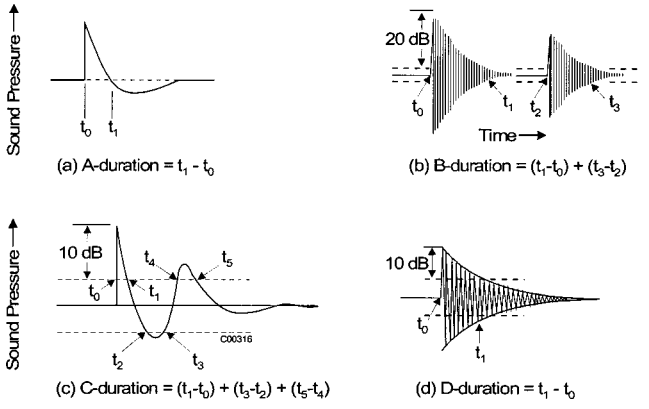

FIG. 1. Definition of impulse noise duration (Smoorenburg, 1992).

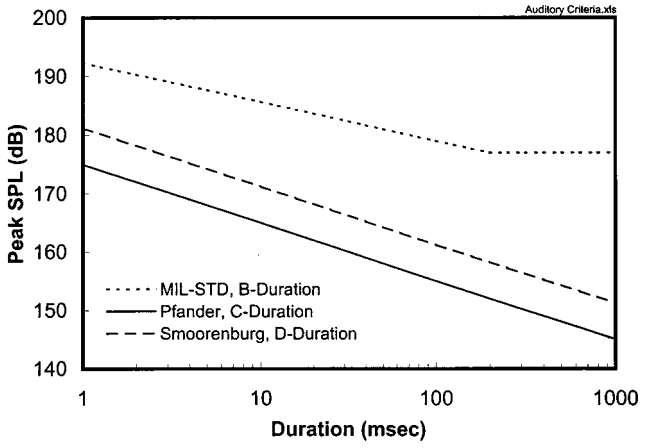

FIG. 2. Peak-based auditory criteria with single-hearing protection and $N=1$. (1.5 dB added to Pfander and Smoorenburg for modified muff.)

tion for the selected data, an assumed theoretical attenuation of 15 dB is added to raise the limit to $L_{\mathrm{Aeq8}} \leqslant 100$ dB following the procedure previously used by Dancer (Dancer, 1995) for using free-field data (Table I).

It appears that L_{Aeq8} should be evaluated by calculating the attenuated A-weighted energy using the insertion loss data taken with an artificial test fixture (ATF) with the protectors as suggested by Dancer (1995, 1998), but this method could not be used for the present work because no insertion loss data were taken for the protectors used at the actual test conditions. Although real-ear-at-threshold (REAT) data were available, the use of such data is not suitable for high-intensity impulse conditions, as Dancer concluded that artificial test fixtures should be used to measure the attenuation effects of the protectors at the actual exposure conditions (Dancer, 1998, 1992). It has not been validated that the use of REAT is equivalent to ATF data for the L_{Aeq8} criterion. We still consider the use of insertion loss data as ongoing research where the procedure, instrumentation requirements, and the threshold are not yet standardized. The limited work presented by Dancer *et al.* (1995, 1998) was based on small sample sizes with the number of subjects ranging from only 8–24. Therefore, we chose to evaluate L_{Aeq8} using the free-field pressure with a theoretical global attenuation factor as previously done by Dancer (1995), and the results will be interpreted accordingly. Such an evaluation is qualitative but it is valuable to compare the L_{Aeq8} method with the other three peak-based criteria using the human data.

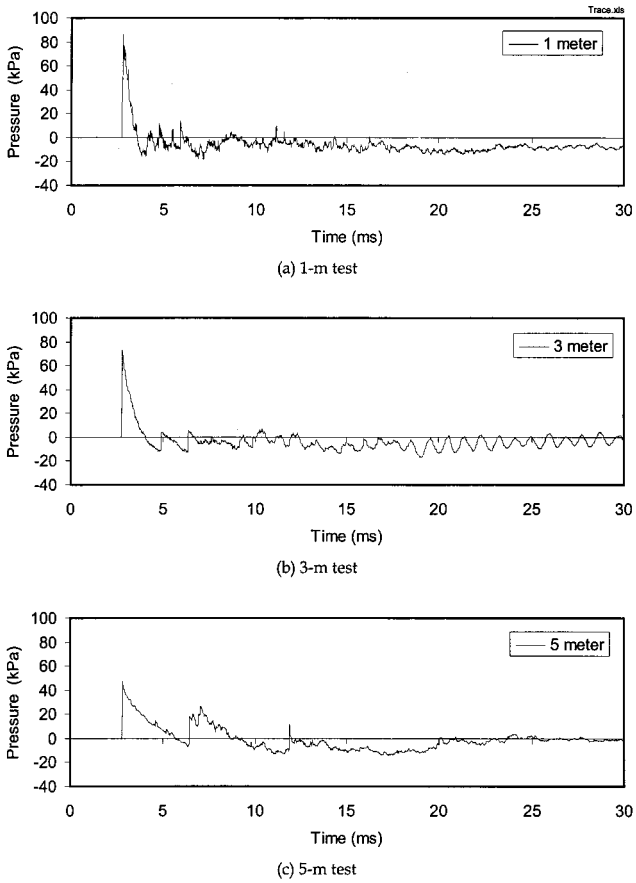

FIG. 3. Typical waveforms from free-field tests (level 7).

B. Human volunteer data

Two human volunteer data sets were used for the present work, and they were obtained from volunteers wearing modified earmuffs in free-field and bunker conditions (Johnson, 1994, 1997). The data can be considered to represent impulse noise due to large-caliber weapons with high intensity and low frequency. The *B*-duration for the blast overpressure (BOP) free-field tests is approximately from 10–22 ms, while that for the Bunker tests reaches 400 ms due to confined reflections. The selected data sets and the tests are described briefly as follows, where the details of the experiments can be found in the cited references.

1. BOP free-field tests

To obtain systematic data for criteria evaluation, the US Army Medical Research and Materiel Command sponsored a test program from 1990–1997 at the Albuquerque blast overpressure (BOP) site (Johnson, 1994). Human volunteers wearing single-hearing protection were tested. For free-field data, we selected the series of tests with subjects wearing the US Army RACAL muffs modified by inserting plastic tubes into the seals to introduce leaks to simulate poor fitting. Compared to the unmodified muffs, the REAT for the modified muff was reduced by about 10 dB across all frequency (Johnson, 1994).

The free-field tests were conducted at three distances, 1, 3, and 5 m, each with seven intensity levels, with L_{pk} increasing by about 3 dB per level, corresponding to a doubling of P^2_{max} [Eq. (1)]. The typical waveforms at the three distances resulted in *A*-durations of about 0.8, 1.5, and 2.8 ms, respectively (Fig. 3). The range of L_{pk} is 174–196 dB. Using the MIL-STD-1474D, doubling *N* results in a 1.5-dB increase in the effective exposure level L_M (Table I). The exposure levels were all above the unprotected auditory threshold of $L_{\mathrm{pk}} = 140$ dB. The right ear was the test ear facing normal to the charge. A small subset of tests was conducted using the unmodified muff at 5 m that resulted in no injury, but these data were excluded, since the modified muff represents a more realistic situation that will yield more conservative results.

For each distance, the subjects were exposed in a walk-up procedure with stepwise increase in the effective exposure level. Three separate groups of subjects were selected for the three distances, respectively, each with an initial group size *n* ranging from 59–68. Table II presents the test matrices and the derived data used for the present analysis. As shown, each box in a matrix refers to a test for a specified distance, peak sound-pressure level, and number of shots (Table II). For each distance, starting with six shots ($N=6$), the subjects were first exposed to increasing L_{pk} levels, from 1–7, followed by stepwise increase of *N* to 100 shots at level 6 (Table II). Tests were also conducted for level 5 at 100 shots at 1 and 3 m. For these two distances, the subjects passing the tests at level 6 at 50 shots were separated into two groups for the 100 shot tests at levels 5 and 6, respectively (Table IIa, b). A subject was tested no more than once a day. A small number of subjects dropped out at higher levels and *N* shots due to auditory failures or subjects' choice (Table II). A total of 192 male subjects participated, with

TABLE II. Free-field walk-up test matrix and results.

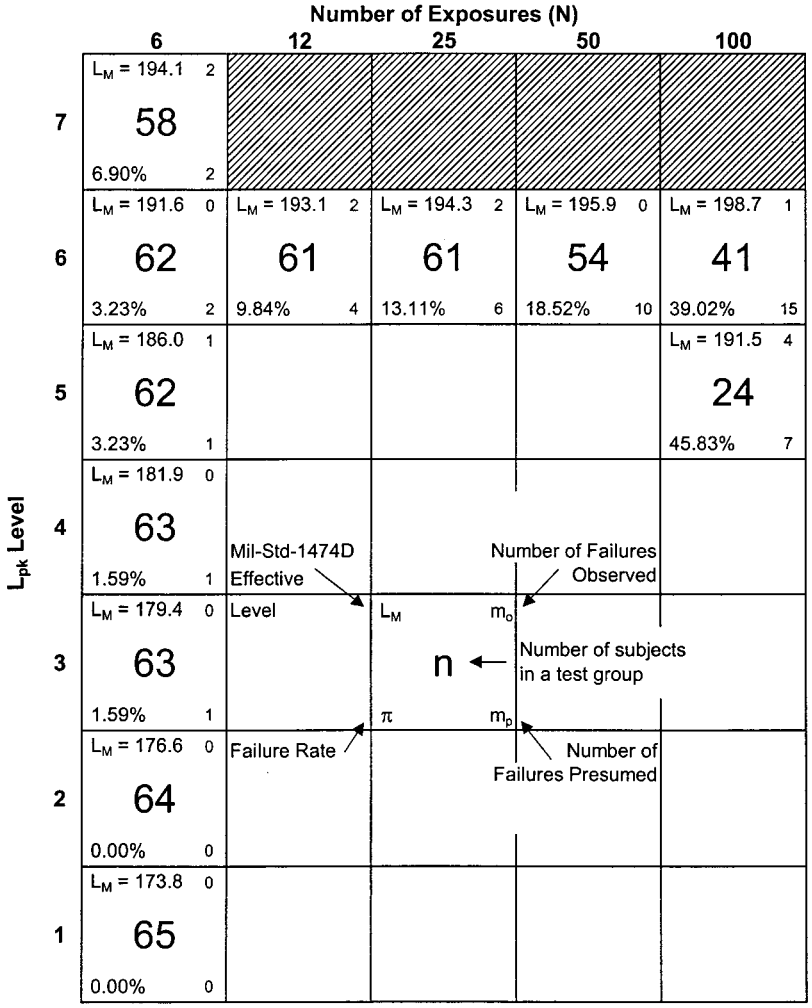

(a) 1-Meter Distance

over 2000 subject-test exposures. Each subject carried a pass/fail condition for each test condition.

Failure threshold was taken as a temporary threshold shift (TTS) $\geqslant$ 25 dB at any frequency, which was measured 2 min after the test (TTS_2). A conditional failure was defined as TTS $\geqslant$ 15 dB but was not a failure. However, when a subject experienced a failure or a conditional failure at a certain L_{pk} level and N shots, he would be presumed to fail at all higher L_{pk} levels and higher N exposures without actually being exposed (Table II). Likewise, according to the original test design, a pass at a certain test condition presumed passes at all lower L_{pk} levels and N. For the present work, presumed failures were included for regression analysis, but presumed passes were excluded. This approach is considered conservative. Therefore, for each test in the test matrix (Table II), the total number of failures is the sum of observed and presumed failures (m_o+m_p). The total number of subjects in each test, n, is the sum of subjects actually tested plus presumed failures (Table II). Hence, the failure rate π for each test is $(m_o+m_p)/n$.

As shown in Table IIa–c, we only consider the data from the test boxes where the group of subjects walked up together for each distance, representing a complete test sequence. A small subset of tests was conducted at the empty boxes below level 6 with $N>6$ for a small number of selected subjects with prior failures or conditional failures. Since these tests were biased, the data were not included in our analysis (Table II). The outcomes of these tests primarily confirm the validity of the presumed failures for these subjects at level 6 and 5 for $N>6$ (Table II).

2. BOP bunker tests

The second data set was also from the BOP human volunteer tests using the modified muff performed inside a bunker to study the effects of complex waves (Johnson, 1997). As shown in the test matrix in Table III, the test was designed to have seven intensity levels similar to the free-field tests. Beginning with one shot, the subjects were first exposed with increasing L_{pk} up to level 7 (Table III). At level 6, N was then increased to 2 and 3, respectively. Failure was defined in the same way as the free-field tests above. However, the Bunker tests resulted in no auditory failures (Table III).

TABLE II. (*Continued.*)

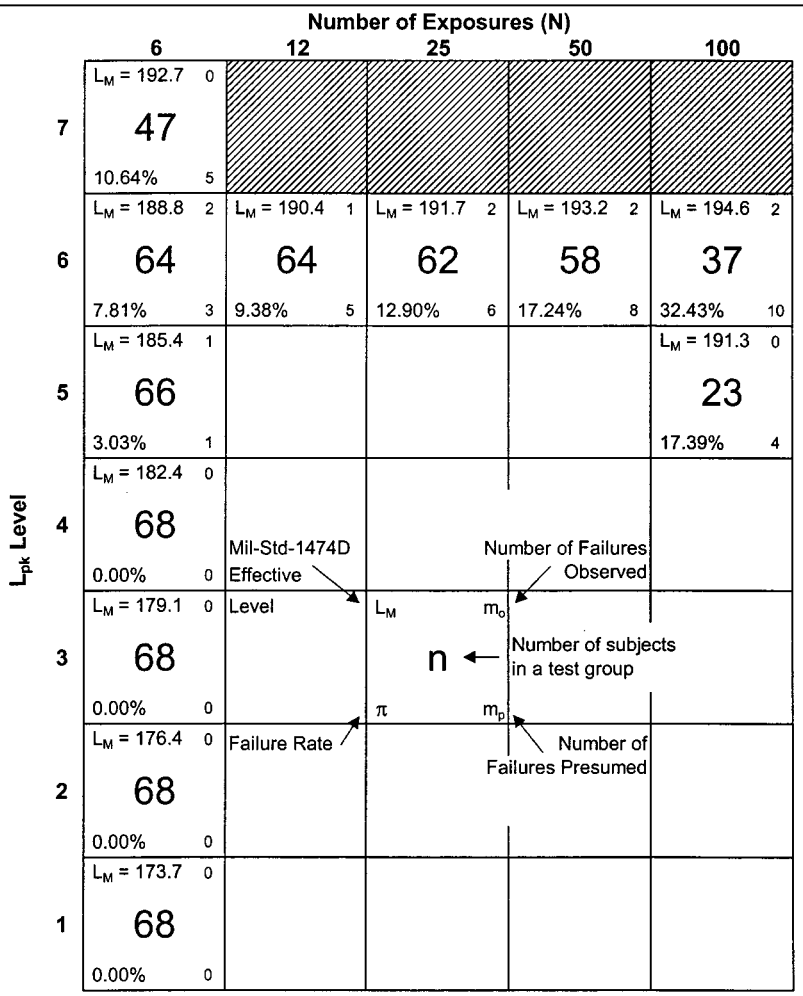

(b) 3-Meter Distance

C. Statistical analysis

The data were analyzed by logistic regression (Hosmer and Lemeshow, 1989). Since the data were longitudinal, the population-averaged model with exchangeable autocorrelation was also used (Zeger and Liang, 1986; Hosmer, 1999). The data were treated as longitudinal since the subjects ''walked'' through a test series from low to high exposure levels with repeated testing. Hence, the subject responses were not independent between tests. The autocorrelation relationship of a subject's outcomes between different exposure levels was modeled as a constant exchangeable coefficient in the correlation matrix. The statistical computation was carried out using the STATA software (STATA, 1999).

We define the logit g as a function of the probability of failure, π

$$g=\ln[\pi/(1-\pi)], \tag{2}$$

and we model g as a linear function in the logit space

$$g=\beta_0+\beta_1 L, \tag{3}$$

where L is the effective exposure level for each criterion (L_M and L_P, etc. in Table I), and β_0 and β_1 are the model coefficients. The covariant variable L is assumed to be continuous. For the regression analysis, the values of L were calculated from the measured waveform parameters. From the regression calculations using the data, we will only obtain the estimated values $\hat{\beta}_0$ and $\hat{\beta}_1$ for the coefficients β_0 and β_1 in Eq. (3). If g is known, π is calculated as

$$\pi=\frac{e^g}{1+e^g}. \tag{4}$$

The regressions were assessed by calculating the Hosmer–Lemeshow goodness-of-fit statistic $\hat{C}$. To accomplish this, the data are divided into ten groups each with approximately equal number of subjects sorted by increasing predicted failure rate. The Hosmer–Lemeshow (H–L) statistic $\hat{C}$ is

$$\hat{C}=\sum_{k=1}^{10}\frac{(o_k-n_k\overline{\pi}_k)^2}{n_k\overline{\pi}_k(1-\overline{\pi}_k)}, \tag{5}$$

where o_k is the total number of failures in each group (m_o+m_p), n_k is the number of data points in the kth group, and the corresponding average predicted failure rate is

TABLE II. (*Continued.*)

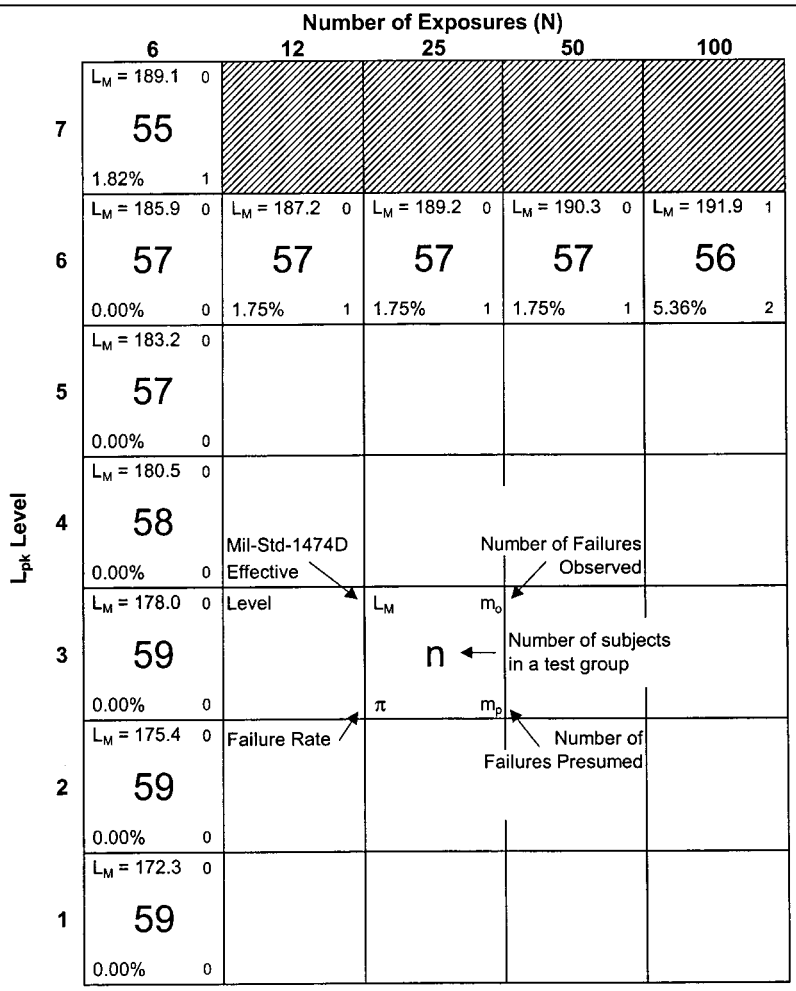

(c) 5-Meter Distance

$$\overline{\pi}_k = \frac{1}{n_k} \sum_{j=1}^{n_k} \hat{\pi}_j, \tag{6}$$

with $\hat{\pi}_j$ obtained by using the fitted logit value $\hat{g}_j = \hat{\beta}_0 + \hat{\beta}_1 L_j$ in Eq. (4). The goodness of fit can be judged by the p value, $P[\chi^2 \geqslant \hat{C}]$, according to the chi-square distribution with 8 degrees of freedom.

The confidence interval (CI) for the fitted model was calculated based on the assumption of normal distribution of the error of the regression, since we had quite a large number of data points from two data sets. Thus, the $(1-\alpha)100\%$ confidence interval estimate of g can be written as a function of L as

$$\hat{g}_{\pm} = \hat{\beta}_0 + \hat{\beta}_1 L \pm z_{1-\alpha/2}\sigma, \tag{7}$$

with

$$\sigma^2 = \sigma_0^2 + 2\sigma_{01}L + \sigma_1^2 L^2, \tag{8}$$

where z_x satisfies the accumulative standardized normal distribution function $\Phi(z_x) = x$.

The standard errors σ_0, σ_1, and the covariance σ_{01} for β_0 and β_1, respectively, are calculated by a robust formula according to Huber and Royall (Huber, 1967; Royall, 1986; Hosmer, 1999), which relaxes the assumption of binomial error structure. The confidence interval for the probability of injury, π, is obtained by using Eq. (4)

$$\hat{\pi}_{\pm} = \frac{e^{\hat{g}_{\pm}}}{(1+e^{\hat{g}_{\pm}})}. \tag{9}$$

Let $L[100(1-a),100(1-\alpha)]$ denote the threshold of L for $100(1-a)\%$ of protection with $100(1-\alpha)\%$ of confidence. Then, $L[100(1-a),100(1-\alpha)]$ can be obtained by solving Eq. (9) with $\hat{\pi}_+ = a$.

III. RESULTS

The logistic regression correlation results are summarized in Table IV, which compares the current criteria limits to the corresponding calculated thresholds for 95% protection with a 95%-confidence interval, $L(95,95)$. If we begin with the free-field data set, Table IV shows a slight increase of 1.3–2.5 dB for the $L(95,95)$ values when the bunker data are included, which is labeled as all-data analysis. The last column in Table IV shows that satisfactory p values were obtained from the Hosmer–Lemeshow (H–L) goodness-of-fit test for the all-data results. The best-fit model regression results are indicated in the last row in Table IV.

TABLE III. Bunker walk-up test matrix and results.

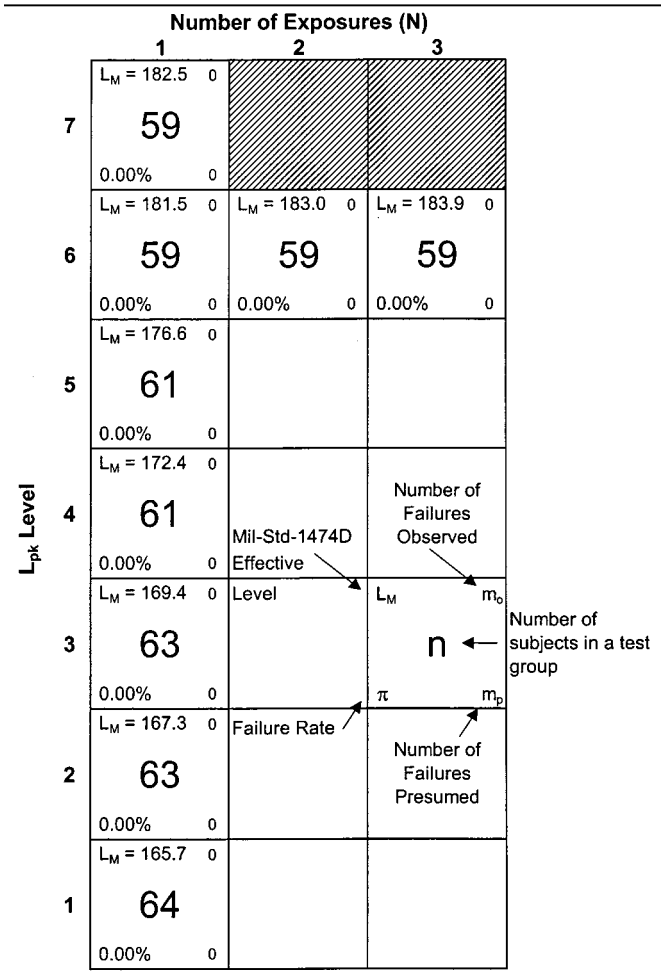

Logistic regression results based on all data indicate that the four NATO criteria are overly conservative by 9.6–21.2 dB for the subjects as tested (Table IV). The MIL-STD-1474D limit of 177 dB underpredicts the observed $L(95,95)$ injury threshold of 186.6 dB by 9.6 dB. Pfander and Smoorenburg underpredict their $L(95,95)$ thresholds by 19.9 and 21.2 dB, respectively (Table IV). Likewise, the energy-based L_{Aeq8} criterion underpredicts the observed $L(95,95)$ threshold of 114.7 dB by 14.3 dB (Table IV).

For visual verification, Figs. 4–7 present the data comparison with the all-data correlations and the 95% CI for the four NATO criteria, where 5% failure is equivalent to 95% protection and the $L(95,95)$ values are taken from the upper bound of the CI. As shown, each plotted data symbol represents one actual test, and the legend indicates the range of the corresponding sample sizes (n). For the MIL-STD, as shown in Fig. 4, the farthest data point from the correlation is the 1-m mortar test at level 5 with 100 shots with $n=24$, resulting in the highest injury rate of 46% (see Table IIa). This data point also shows considerable deviation from the other three criteria correlations (Figs. 5–7).

TABLE IV. Logistic regression results.

Criteria	Current limit (DB)	$L(95,95)$ dB: Free field	$L(95,95)$ dB: Free field and bunker (all data)	H–L test p-value (all data)
MIL-STD-1474D	177	185.3	186.6	0.255
Pfander	175	192.7	194.9	0.276
Smoorenburg	181.2	199.9	202.4	0.165
L_{Aeq8}	100	112.7	114.3	0.247
Best-fit model $L_{\mathrm{pk}}-10.9\log(T_B/200)+3.44\log N$ (all data)	N/A	200.0	200.0	0.929

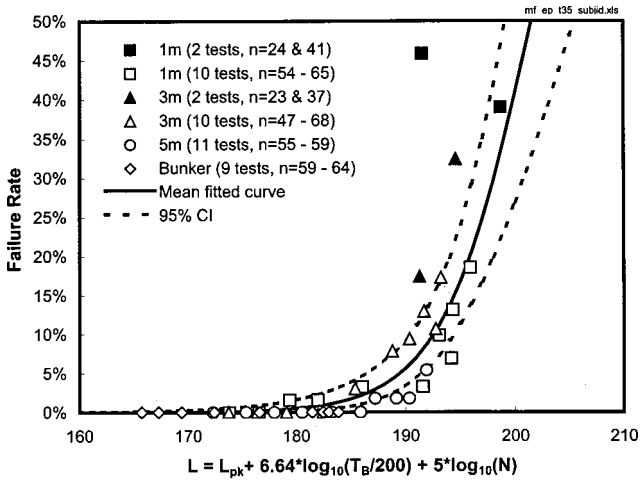

FIG. 4. Data comparison with MIL-STD-1474D correlation.

Figure 8 shows the data comparison with the best-fit model where the coefficients for T_B and N trading were obtained from the regression calculation, instead of just using those defined by MIL-STD (Table IV). That is, these coefficients were freed up to be determined by the actual logistic regression of the data. Furthermore, T_C and T_D were initially included for the regression fitting but eventually eliminated by the tests of statistical significance. Compared to Figs. 4–7, the data are much closer to the best-fit correlation, as shown in Fig. 8, with no apparent ''outliers.'' Consequently, it is not surprising that the best-fit model also results in the best p value (0.971) for the Hosmer–Lemeshow test (Table IV). The best-fit model results in the $L(95,95)$ threshold of 200.0 dB, but this should not be compared with the current MIL-STD threshold of 177 dB, because the best-fit model

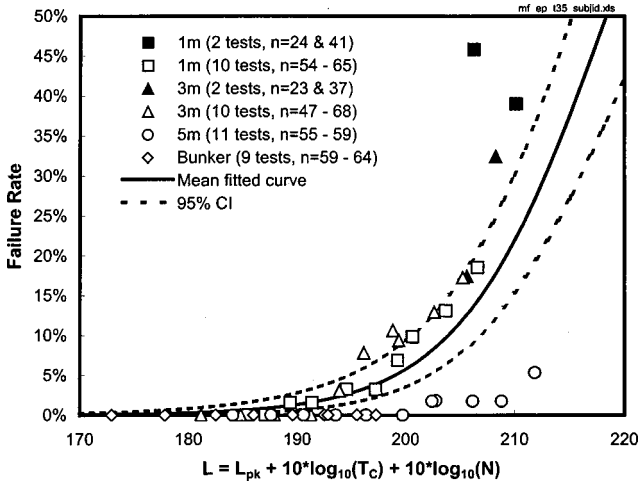

FIG. 5. Data comparison with Pfander correlation.

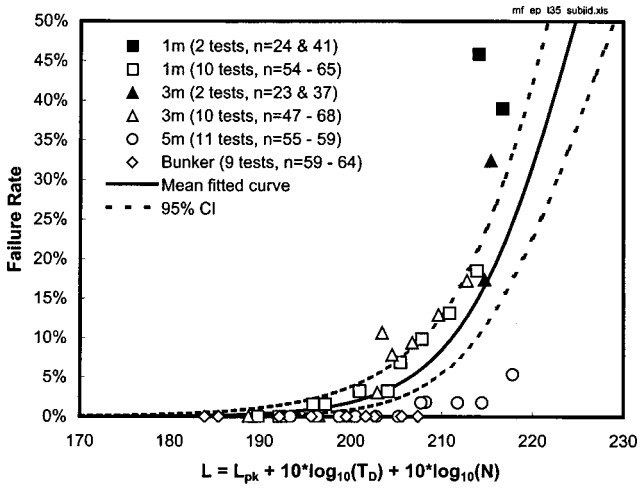

FIG. 6. Data comparison with Smoorenburg correlation.

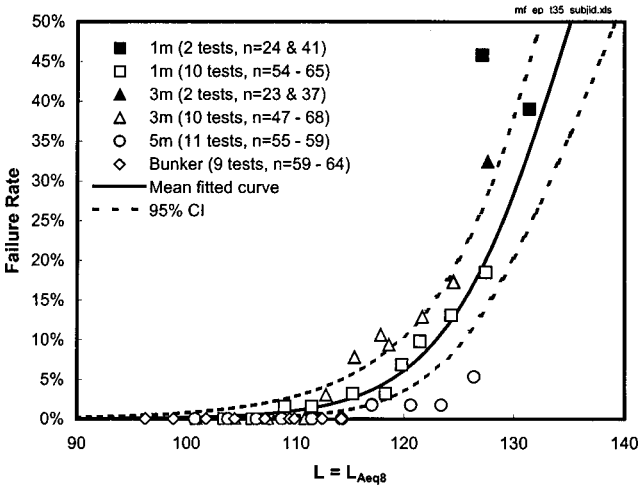

FIG. 7. Data comparison with L_{Aeq8} correlation.

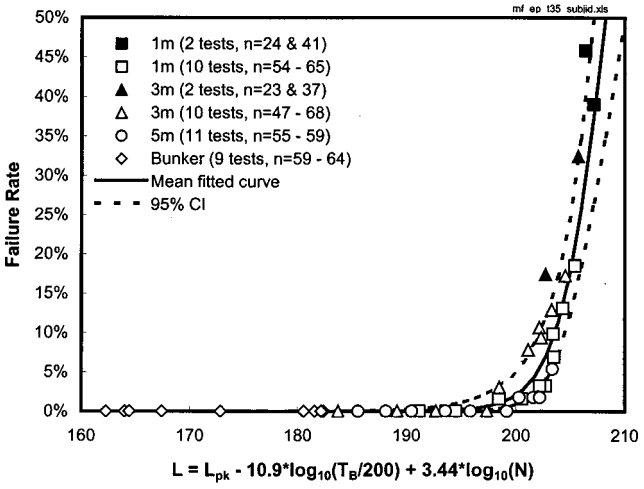

FIG. 8. Data comparison with best-fit model.

TABLE V. Logistic regression results without presumed failures.

Criteria	Thresholds (dB) Current limit	$L(95,50)$	$L(95,95)$	H–L test p-value
MIL-STD-1474D	177	195.8	193.5	0.444
Pfander	175	210.1	206.6	0.591
Smoorenburg	181.2	216.2	213.1	0.358
L_{Aeq8}	100	126.6	124.1	0.960
Best-fit model $L_{\mathrm{pk}}-16.67\log(T_B/200)+3.08\log N$	N/A	208.9	208.1	0.906

has changed the MIL-STD definition of effective exposure level (Table IV). The best-fit model has a negative coefficient (-10.93) for the B duration, which is counter to the positive coefficient specified by MIL-STD (Table IV). Furthermore, the best-fit model indicates a $3.44\log N$ trading, instead of $5\log N$ for MIL-STD and $10\log N$ for the other three criteria (Table IV).

The conservatism of including the presumed failure data was confirmed by a sensitivity study where the presumed failures were excluded. The logistic regression results without presumed failures are shown in Table V. Comparison between Tables IV and V indicates that the $L(95,95)$ values for the four criteria and the best-fit model without presumed failures are much higher than with presumed failures. For example, the $L(95,95)$ threshold for MIL-STD will be raised by another 6.9 dB to 193.5 dB, which is 16.5 dB higher than the present limit (Table V). Therefore, the test data should be analyzed with presumed failures included (Table IV).

IV. DISCUSSION

The objective of the present work is to evaluate the four given NATO criteria for impulse noise against the data from human exposure tests. The thresholds for the criteria and the confidence intervals were determined using established statistical methods. In addition, a ''best-fit'' criterion using peak, T_B, and N was fitted to yield a $L(95,95)$ threshold that also resulted in the best goodness of fit (Table IV).

The assumption that hearing protection reduces the global effective levels by a constant 15 dB may not be adequate. For the peak-based criteria, this attenuation factor can change depending on the type of protectors (Pfander, 1980; Brinkmann, 1994). However, the use of a 15-dB attenuation factor does not affect the evaluation of the functional form of the peak-based criteria. The use of a global attenuation factor for L_{Aeq8} is a simplified approach due to the lack of insertion loss data. Nevertheless, the $L(95,95)$ values for all four criteria were successfully calculated from the statistical data correlation for the subjects as tested, and they were all found to be significantly higher than the current criteria limits.

Other research has indicated hearing protectors are sensitive to both intensity levels as well as spectral effects (Dancer *et al.*, 1992). REAT data are inadequate for evaluating attenuation effects at high intensity levels. Results from some recent studies using the insertion loss measured with an artificial test fixture have advanced some understanding, but the studies were based on a small sample (Dancer *et al.*, 1995, 1998). No injury standard has been established using

pressures measured under the protector in a human ear. Consequently, the undermuff pressures taken for some selected tests cannot be compared against any standard. The work presented here is consistent with the ongoing practice of using free-field pressure for field applications.

The change of the *N*-trading rule by the best-fit model indicates that the study of *N* trading by fixing the other parameter coefficients is of limited use and may lead to misleading conclusions in the discussion of so-called ''equal energy hypothesis.'' The coefficients for *N* should be optimized, together with the other parameter coefficients in the way the best-fit model was determined in the present work. The present best-fit model (Table IV) is still peak-and duration based and has not been tested against other data sets. Nevertheless, the negative coefficient for T_B suggests that longer pulses are less hazardous, which is contrary to all peak-and duration-based criteria. This could also be due to the fact that the pulses for the selected data sets cover only a narrow range of durations with similar spectral behavior representing low-frequency impulses. Spectral effects are probably difficult to be fully captured by peak-and duration-based methods.

The data sets analyzed do not address the issues of variable presentation rates for multiple shots or the effects of the combination of different blast waves with different peak and durations. Previous work on this issue has been limited (Patterson, 1997). It may appear that the energy-based L_{Aeq8} method may be more appropriate for these complex exposure conditions. Animal data can help understand injury correlations (Hamernik *et al.*, 1998).

It is realized that the definition of injury is not uniform between the four criteria, although the tests conducted in the US generally take the injury threshold as TTS $\geqslant$25 dB at 2 min. Pfander uses recovery within 24 h as the indicator (Pfander *et al.*, 1980), and there are studies on the change of TTS with time (Dancer *et al.*, 1991). However, Pfander's data indicate recovery will complete within 24 h if TTS_2 is less than 25 dB (Pfander *et al.*, 1980). Using the present data, our study has evaluated all the criteria based on the injury threshold of $\mathrm{TTS}_2 \geqslant 25$ dB.

In summary, for the occupational standard in the US, the current MIL-STD-1474D for single-hearing protection was found to be 9.6 dB below the $L(95,95)$ threshold for observed injury in the subject group as tested in the selected conditions. Similar conclusions can be drawn for the other three criteria. This result is consistent with the findings of previous man-rating studies and helps quantify the amount of conservatism in the standard (Patterson *et al.*, 1985, 1987). Since the sample size is still limited, the pressure waves come from a limited class of blasts, and the test population may have been better fitted with hearing protection than typical field conditions, there must be judgment exercised in extending the present results to different blast conditions.

ACKNOWLEDGMENTS

The present work was sponsored by USAMRMC under Contract No. DAMD17-96-C-6007. The authors also wish to express their thanks to Dr. David Hosmer, Professor of Biostatistics in the School of Public Health at the University of Massachusetts, and Dr. Doug Tang, Chief of Biostatistics at the Walter Reed Army Institute of Research, for the review and constructive discussions on the statistical method used.

Brinkman, H. (**1994**). ''Current Status Report of the German-DRC,'' Exploratory Group Meeting on the Effects of Impulse Noise, soOl 16–17 May 1994.

Dancer, A., Grateau, P., Cabanis, A., Valliant, T., and Lafont, D. (**1991**). ''Delayed Temporary Threshold Shift Induced by Impulse Noises (Weapon Noises) in Men,'' Audiology **30**, 345–356.

Dancer, A., Grateau, P., Cabanis, A., Barnabe, G., Cagnin, G., Vaillant, T., and Lafont, D. (**1992**). ''Effectiveness of Earplugs in High-Intensity Impulse Noise,'' J. Acoust. Soc. Am. **91**, 1677–1689.

Dancer, A. L. (**1995**). Acta Acust. (Beijing) **3**, 539–547.

Dancer, A. L., and Hamery, P. J. F. (**1998**). ''Results of Human Studies with Linear and Nonlinear Earplugs: Implications for Exposure Limits,'' J. Acoust. Soc. Am. **103**, 2878(A).

Hamernik, R. P., Patterson, J. H., and Ahroon, W. A. (**1998**). ''Use of Animal Test Data in the Development of a Human Auditory Hazard Criterion for Impulse Noise,'' Final Report (Parts 1 and 2), Auditory Research Laboratory, State University of New York, August.

Hosmer, D., and Lemeshow, S. (**1989**). *Applied Logistic Regression* (Wiley, New York).

Hosmer, D. W. (**1999**). Private communication, University of Massachusetts.

Huber, P. J. (**1967**). ''The Behaviour of Maximum Likelihood Estimates Under Nonstandard Conditions,'' Proceedings of the 5th Berkeley Symposium, pp. 221–223.

Johnson, D. (**1994**). ''Blast Overpressure Studies with Animals and Men: A Walk-up Study,'' USAARL Report 94-2.

Johnson, D. (**1997**). ''Blast Overpressure Studies,'' Final Task Report for US Army Medical Research and Material Command, Contract No. DAMD17-93-C-3101.

MIL-STD-1474D. (**1991**). Noise Limits for Military Material (Metric).

Patterson, J. H., Mozo, B., Marrow, R., McConnell, R., Lomba-Gautier, I., Curd, D., Phillips, Y., and Henderson, R. (**1985**). ''Direct Determination of the Adequacy of Hearing Protective Devices for use with the M198, 155-mm Towed Howitzer,'' USAARL Report No. 85-14.

Patterson, J. H., and Mozo, B. (**1987**). ''Direct Determination of the Adequacy of Hearing Protection for Use with the Viper,'' USAARL Report No. 87-9.

Patterson, J. H., Mozo, B. T., and Johnson, D. L. (**1994**). ''Actual Effectiveness of Hearing Protection in High Level Impulse Noise,'' USAARL Report No. 94-48.

Patterson, J. H. (**1997**). ''Proposed New Procedure for Estimating Allowable Number of Rounds for Blast Overpressure Hazards Assessment,'' USAARL Report No. 98-03.

Pfander, F., Bongartz, H., Brinkmann, H., and Kietz, H. (**1980**). ''Danger of Auditory Impairment for Impulse Noise: A Comparative Study of the CHABA Damage-Risk Criteria and Those of the Federal Republic of Germany,'' J. Acoust. Soc. Am. **67**, 628–633.

Pfander, F. (**1994**). ''Reaktion des Ohres auf akustische Belastungen,'' Das Schalltrauma, Bonn in Juni 1994, 17–34.

Royall, R. M. (**1986**). ''Model Robust Confidence Intervals Using Maximum Likelihood Estimators,'' Int. Statist. Rev. **54**(2), 221–226.

Smoorenburg, G. F. (**1982**). ''Damage Risk Criteria for Impulse Noise,'' in *New Perspective on Noise-Induced Hearing Loss*, edited by for R. P. Hamernik, D. Henderson, and R. Salvi (Raven, New York).

Smoorenburg, G. F. (**1992**). ''Damage Risk for Low-frequency Impulse Noise,'' in *Noise-Induced Hearing Loss*, edited by A. Dancer, D. Henderson, R. Salvi, and R. P. Hamernik, Sait-Louis, Mosby Year Book, pp. 313–324.

STATA for Windows (**1999**). Release 6.0, Stata Corporation.

Zeger, S. L., and Liang, K. (**1986**). ''Longitudinal Data Analysis for Discrete and Continuous Outcomes,'' Biometrics **42**, 121–130.

Regularization methods for near-field acoustical holography

Earl G. Williams[a)]
Code 7137, Naval Research Laboratory, Washington, DC 20375-5350

(Received 4 January 2001; accepted for publication 31 July 2001)

The reconstruction of the pressure and normal surface velocity provided by near-field acoustical holography (NAH) from pressure measurements made near a vibrating structure is a linear, ill-posed inverse problem due to the existence of strongly decaying, evanescentlike waves. Regularization provides a technique of overcoming the ill-posedness and generates a solution to the linear problem in an automated way. We present four robust methods for regularization; the standard Tikhonov procedure along with a novel improved version, Landweber iteration, and the conjugate gradient approach. Each of these approaches can be applied to all forms of interior or exterior NAH problems; planar, cylindrical, spherical, and conformal. We also study two parameter selection procedures, the Morozov discrepancy principle and the generalized cross validation, which are crucial to any regularization theory. In particular, we concentrate here on planar and cylindrical holography. These forms of NAH which rely on the discrete Fourier transform are important due to their popularity and to their tremendous computational speed. In order to use regularization theory for the separable geometry problems we reformulate the equations of planar, cylindrical, and spherical NAH into an eigenvalue problem. The resulting eigenvalues and eigenvectors couple easily to regularization theory, which can be incorporated into the NAH software with little sacrifice in computational speed. The resulting complete automation of the NAH algorithm for both separable and nonseparable geometries overcomes the last significant hurdle for NAH.
[DOI: 10.1121/1.1404381]

PACS numbers: 43.50.Yw, 43.20.Ye, 43.60.Pt [JGM]

I. INTRODUCTION

The theory of regularization for linear problems is a heavily researched area and many books[1] are available on the subject. However, it is clear that there is no holy grail as to the best regularization approach, and the success of any particular approach depends on the nature and the physics of the problem which is being solved. NAH is distinguished by the existence of evanescent waves which decay at various rates from the surface of the vibrator. For planar geometries the evanescent waves decay exponentially. For cylindrical and spherical geometries the evanescent waves exhibit exponential and power law decays. These decays are the root of the ill-posed nature of the inverse problem which turns these exponentiallike decays into exponentiallike amplifications reeking havoc due to noise contained in the measured data.

Some refereed publications are beginning to appear on the application of regularization theories to NAH problems,[2–6] as well as many conference proceedings papers over the past few years. One of the reviewers pointed out that there is another excellent paper soon to appear.[7] These papers represent application of NAH to a very wide range of problems and there is no consensus on which regularization methods are the best. There is little doubt that the search for the best method, if there is one, will occupy researchers for many years to come.

With regard to regularization approaches, one thing is clear: eigenvalue decompositions such as the singular value decomposition (SVD) of the system matrix play a crucial role. Although it may be possible to apply regularization without using an eigenvalue decomposition[8] (resulting in a tremendous savings in computational time), the eigenvalue decomposition provides a very physical grasp to the problem allowing for physical insight. Fortunately, it is not necessary to do a SVD in separable geometries, since the theory of NAH for these geometries can be rewritten as an eigenvalue problem exposing mathematical expressions for the eigenvalues and orthonormal eigenvectors, as we will show in this article. On the other hand, conformal (nonseparable surface geometries) NAH relies on the singular value decomposition (SVD) which must be done by software at a severe penalty in computational speed.

Section II deals with the formulation of the exterior, separable geometry NAH problem and casts it as a eigenvalue decomposition so that it can be treated in the same way as the conformal exterior NAH and interior NAH problems, both of which have been solved using the SVD. This formulation brings both separable and nonseparable NAH problems under the same umbrella so that they all can be treated with a single regularization approach.

In Sec. III we discuss three popular regularization schemes and in Sec. IV apply them to some numerical data generated to be representative of the evanescent wave nature of the NAH problem. The reconstruction errors and reconstruction filters are compared. These are compared with the historical filter used in planar and cylindrical NAH, the exponential filter. The exponential filter provides the best (lowest error) results and is used as a baseline for comparison of the regularization procedures. For a parameter selection routine we use the popular Morozov discrepancy principle. This requires a knowledge of the noise variance. Thus we present

a)Electronic mail: williams@genah.nrl.navy.mil

a simple, accurate, and robust procedure to determine the noise variance. The various procedures are cast in terms of *k*-space, which provides a better physical understanding. In Sec. V we present a modification of the standard Tikhonov procedure which we show is more accurate and possibly the best choice of all. Results of this new method are given in Sec. VI. In this section we study another important parameter selection method which does not require a knowledge of the noise variance, the generalized cross validation (GCV), and compare it to the Morozov discrepancy principle.

II. MATHEMATICAL FORMULATION

Let $\dot{w}$ be the normal velocity of a vibrating surface S' and p be the hologram pressure on the measurement surface S. The harmonic time dependence $e^{-i\omega t}$ is suppressed throughout this article. The following relationship exists between them:[9]

$$p=\mathcal{F}^{-1}G_N\mathcal{F}\dot{w}, \tag{1}$$

where $\mathcal{F}$ represents a two-dimensional Fourier transform operator. We call $\mathcal{F}\dot{w}$ and $\mathcal{F}p$ the *k*-space representations (angular spectra) of the velocity and pressure, respectively. The components of Eq. (1) in planar coordinates (x,y,z) are

$$\mathcal{F}\equiv\int\int dx\,dy\,e^{-ik_x x}e^{-ik_y y}, \tag{2}$$

$$G_N=\frac{\rho ck}{\sqrt{k^2-k_p^2}}e^{i\sqrt{k^2-k_p^2}d},\quad \text{where}\quad k_p^2=k_x^2+k_y^2 \tag{3}$$

and

$$\mathcal{F}^{-1}\equiv\left(\frac{1}{2\pi}\right)^2\int\int dk_x\,dk_y\,e^{ik_x x}e^{ik_y y}, \tag{4}$$

where d is the positive distance between the two surfaces. Thus

$$\mathcal{F}p\equiv\int\int p(x,y,z)e^{-ik_x x}e^{-ik_y y}\,dx\,dy.$$

For a cylindrical coordinate system (r,ϕ,z) we have

$$\mathcal{F}\equiv\frac{1}{2\pi}\int\int d\phi\,dz\,e^{-in\phi}e^{-ik_z z}, \tag{5}$$

$$G_N=\frac{i\rho ck}{k_r}\frac{H_n(k_r r)}{H_n'(k_r r')},\quad \text{where}\quad k_r\equiv\sqrt{k^2-k_z^2} \tag{6}$$

and

$$\mathcal{F}^{-1}\equiv\frac{1}{2\pi}\sum_n\int dk_z\,e^{in\phi}e^{ik_z z}, \tag{7}$$

where r and r' are the radii of the hologram (p) and reconstruction ($\dot{w}$) surfaces, respectively. Equation (1) is very general as long as we use a broad definition of the Fourier transform operator. Thus in spherical coordinates (r,θ,ϕ), for an external problem, the components of Eq. (1) are

$$\mathcal{F}\equiv\int d\Omega\,Y_n^m(\theta,\phi)^*, \tag{8}$$

$$G_N=i\rho c\frac{h_n(kr)}{h_n'(kr')}, \tag{9}$$

and

$$\mathcal{F}^{-1}\equiv\sum_n\sum_m Y_n^m(\theta,\phi), \tag{10}$$

where r and r' are the radii of the hologram and reconstruction surfaces, respectively. In this case the Fourier transform operator is given by integration over a solid angle with the orthonormal spherical harmonic as the kernel in the integrand. One can think of G_N as the Neumann surface Green function for the problem with source and field points on the two defined surfaces, respectively.

The equations given above are exact. In the NAH reconstruction process the infinite integrals are replaced with finite integrals over the finite measurement and reconstruction apertures, which are generally chosen to extend past the vibrator. Furthermore, all finite integrals are discretized and the Fourier transform operators become matrix multiplications (including weighting factors), so that $\mathcal{F}\rightarrow\mathbf{F}$. Symbolically we use the calligraphic letters ($\mathcal{F}$) for operators and boldface letters ($\mathbf{F}$) for matrices in most cases. Each row of the matrix spans the truncated two-dimensional coordinate space.

We need to cast Eqs. (1)–(10) as eigenvalue decompositions and expose the similarity to the singular value decomposition. Recall that if $\mathbf{H}$ is the system matrix, an eigenvalue decomposition is given by $\mathbf{HX}=\mathbf{X\Lambda}$, where the eigenvectors are columns of $\mathbf{X}$ and $\mathbf{\Lambda}$ is a diagonal matrix of eigenvalues. These eigenvalues may be complex. In contrast the SVD does an eigenvalue decomposition of the Hermitian matrix $\mathbf{H}^H\mathbf{H}$ (the superscript H signifies conjugate transpose) resulting in eigenvalues (called singular values) which are real and positive.

After discretization Eq. (1) can be written in matrix form with a column vector of pressure (covering the two-dimensional aperture) p_d ($p_d\in\mathcal{C}^M$ where $\mathcal{C}$ is the space of all complex numbers), a column vector of normal velocity $\dot{w}_d$ ($\dot{w}_d\in\mathcal{C}^M$), and the diagonal Neumann matrix $\mathbf{G}$ ($\mathbf{G}\in\mathcal{C}^{M\times M}$):

$$p_d=\mathbf{F}^{-1}\mathbf{G}\mathbf{F}\dot{w}_d, \tag{11}$$

where we use the subscript d to indicate a discretized quantity. Thus, for example, for a planar coordinate system the spatial Fourier transforms would be carried out using a discrete Fourier transform (DFT) so that $\mathbf{F}$ is a full matrix built from the defining DFT matrix $\mathbf{D}$ given for one coordinate dimension by

$$D_{kq}=\frac{1}{\sqrt{n}}e^{-2\pi i(k-1)(q-1)/n},\quad k,q=1,2,\ldots,n,$$

and its inverse $\mathbf{D}^{-1}=\mathbf{D}^H$. It can be shown that $\mathbf{F}$ has the following important properties:

$$\mathbf{F}^H\mathbf{F}=I_M\quad\text{and}\quad\mathbf{F}^{-1}=\mathbf{F}^H. \tag{12}$$

It is important to realize that $\mathbf{G}$ is a diagonal matrix due to the fact that a single *k*-space component of $\dot{w}$ is related to the same *k*-space component of p via G_N, as indicated in

Eqs. (3) and (6). That is, G_N in Eq. (1) relates a single component of $\mathcal{F}p$ to a single component of $\mathcal{F}\dot{w}$ in k-space.

Since the operations given by $\mathbf{F}^{-1}$ and $\mathbf{F}$ are just matrix multiplications we can define a spatial transfer function $\mathbf{H}^{M\times M}$ which directly relates the pressure vector to the velocity vector:

$$p_d = \mathbf{H}\dot{w}_d, \tag{13}$$

where $\mathbf{H}$ embodies the DFT operations of Eq. (11):

$$\mathbf{H} \equiv \mathbf{F}^{-1}\mathbf{G}\mathbf{F}. \tag{14}$$

We can immediately recognize Eq. (14) as an eigenvalue decomposition of $\mathbf{H}$, $\mathbf{H}\mathbf{X}=\mathbf{X}\mathbf{\Lambda}$, with eigenvalues $\mathbf{\Lambda}=\mathbf{G}$ and orthonormal eigenfunctions $\mathbf{X}=\mathbf{F}^{-1}=\mathbf{F}^{H}$.

For example, for planar geometry with the discretization of $(k_x,k_y)\rightarrow(k_{xi},k_{yj})$, Eq. (3) is a diagonal matrix

$$\mathbf{G} \equiv \mathrm{diag}[\lambda_{11},\lambda_{12},\ldots,\lambda_{ij},\ldots],$$

where

$$\lambda_{ij} = \frac{\rho c k}{\sqrt{k^2-k_{pij}^2}} e^{i\sqrt{k^2-k_{pij}^2}d} \quad \text{and} \quad k_{pij}^2 \equiv k_{xi}^2 + k_{yj}^2 \tag{15}$$

and (i,j) spans all the k-space components used in the discretization. Similarly, for cylindrical geometry the eigenvalues are

$$\lambda_{jn} = \frac{i\rho c k}{k_{rj}} \frac{H_n(k_{rj}r)}{H_n'(k_{rj}r')}, \quad k_{rj} \equiv \sqrt{k^2-k_{zj}^2}. \tag{16}$$

The eigenvalues in the separable geometries are generally complex.

As regards the ordering of eigenvalues, it should be recognized that outside the radiation circle (defined by $k_p=k$) $|\lambda_{ij}|$ decreases as $k_p \equiv \sqrt{k_x^2+k_y^2}$ increases. For the planar case, this is clear from Eq. (3) since

$$|G_N| = \frac{\rho c k}{\sqrt{k_p^2-k^2}} e^{-\sqrt{k_p^2-k^2}d} \tag{17}$$

is a monotonically decreasing function in k_p outside the radiation circle. For the cylindrical case it is also true, although not as obvious, that outside the radiation circle the eigenvalues decay monotonically with helical wave number, $k_h \equiv \sqrt{k_z^2+(n/a)^2}$, where n is the order of the circumferential harmonic and $r'=a$ is the reconstruction surface. Thus, as with the planar case, $|G_N|$ in Eq. (6) decreases with increasing k_h outside of the radiation circle, as long as $r \geqslant r'$ (back propagation). To demonstrate this fact Fig. 1 is a plot of λ_{jn} vs k_h for cylindrical geometry for all values of j, n in the discretized k-space, for a particular case used later in this article. As can be seen outside of the radiation circle at $k=0.647$, the eigenvalues decrease monotonically with the helical wave number k_h.

Now that the eigenvalues in Eqs. (1)–(10) have been identified, we can turn to the application of standard regularization techniques to invert Eqs. (11) and (13). The approach here is to use regularization theory based on the SVD and apply it to planar, cylindrical, and spherical holography using the correspondence demonstrated in Eq. (20). Actual SVD decompositions of the transfer function $\mathbf{H}$ are never computed since $\mathbf{G}$ and $\mathbf{F}$ are known already.

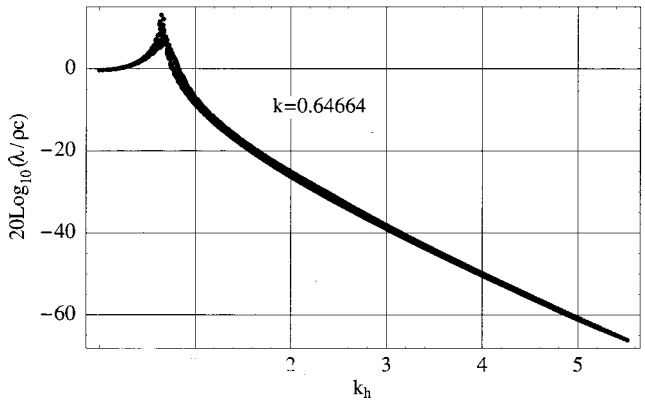

FIG. 1. Relationship between eigenvalues and helical wave number k_h. Four thousand values of $(k_{zj},n/a)$, covering a rectangular mesh in k-space, are plotted. Outside the radiation circle (at $k=0.647$, 6 kHz) $|\lambda_{jn}|$ decreases.

A. Relation to the SVD

Consider now the singular value decomposition (SVD) of the transfer function $\mathbf{H}$ in Eq. (13),

$$\mathbf{H} = U\Sigma V^H, \tag{18}$$

where U and V are left and right unitary (orthonormal) matrices, respectively, and Σ is a diagonal matrix of real singular values. It is sufficient, but not necessary, to assume that the number of reconstruction points N and the number of measurement points M are equal. V^H is the conjugate transpose of V. Since U and V are unitary they satisfy the important relations

$$U^H U = I_M \quad \text{and} \quad V^H V = I_M. \tag{19}$$

Comparison of Eqs. (18) and (19) with Eqs. (14) and (12) reveals the similarity. Thus we make the following associations;

$$V^H \Leftrightarrow \mathbf{F}, \quad U \Leftrightarrow \mathbf{F}^{-1}, \quad \Sigma^2 = \mathbf{G}^H\mathbf{G}. \tag{20}$$

These associations are not equalities, however. That is, if one pictures the modes provided by V^H and U^H from the SVD, they are slightly different from the modes provided by the DFT, the latter being just complex exponentials, as was demonstrated in an earlier paper.[10] Furthermore, the singular values of Σ are all real and positive, whereas the eigenvalues provided by the DFT are complex.

III. REGULARIZATION

The literature for regularization of linear equations, like Eq. (13), is vast. Unfortunately, as we will find below, there appears to be no holy grail with respect to the best regularization technique, since the characteristics of the inversion depend very much on the physics of the problem. Applications to NAH problems are just beginning to appear in the literature which we illuminate later in this work.

We discuss and compare four regularization techniques; standard and modified Tikhonov, Landweber iteration, and

the conjugate gradient approach. These techniques basically determine the shape of the *k*-space (low pass) filter used to eliminate the small-wavelength evanescent waves which blow up due to noise in the inversion process. However, these techniques all contain an undetermined parameter, essentially the break point of the *k*-space filter which must be determined by a separate technique. Parameter selection techniques break up into two categories; ones which depend on a knowledge of the noise variance, and those which do not. We concentrate on the most popular one, the discrepancy principle of Morozov which requires an estimate of the noise variance and we provide a rather simple and computationally robust method to determine the noise from the data. We also consider a second parameter selection technique called the generalized cross validation (GCV) which does not require knowledge of the noise variance. In Sec. V we will compare the Morozov to the GCV applied to two different Tikhonov minimization procedures.

Important to the understanding of regularization theory is the study of the various eigenvalue (*k*-space) filters which arise from these techniques. It will become clear that the taper (slope) of the filter is determined by the procedure chosen whereas the break point (inflection point) of the filter depends on the parameter selection technique, in our case the Morozov discrepancy principle or the GCV.

To simplify the notation we will drop the *d* (discretization) subscript in the equations that follow, as all quantities are discrete in nature. To formulate the effects of noise in the hologram data *p*, assume that spatially uncorrelated random noise ϵ with zero mean and standard deviation σ is present in the measurement. We use a superscript δ to indicate a quantity with noise. Thus p^{δ} is the pressure data with noise. We rewrite Eq. (13) including noise as ($\mathcal{E}$ is expectation)

$$p^{\delta}=\mathbf{H}\dot{w}^{\delta}, \quad p^{\delta}=p+\epsilon, \quad \text{and} \quad \mathcal{E}\|p-p^{\delta}\|=\sigma\sqrt{M}, \tag{21}$$

where from Eq. (13) we have $\mathbf{H}^{M\times M}$.

A. Tikhonov regularization

We begin by studying Tikhonov-based methods and later discuss non-Tikhonov techniques such as Landweber iteration. The standard Tikhonov method was applied to an interior NAH problem in 1996 by Kim and Ih[4] and recently by Nelson and Yoon.[11] In the Tikhonov regularization method we must minimize, with respect to a $\dot{w}$ for a fixed parameter α, the general Tikhonov functional J_{α} given by

$$J_{\alpha}(\dot{w}^{\delta})=\|\mathbf{H}\dot{w}^{\delta}-p^{\delta}\|^2+\alpha\|\mathbf{L}\dot{w}^{\delta}\|^2, \tag{22}$$

where $\|\cdot\|$ represents the L2 norm. The second term in this equation represents a penalty term. It is common to set the matrix $\mathbf{L}=I_M$, in which case Eq. (22) is said to be in standard form.[1] In this case the penalty term prevents the amplitude of the reconstructed normal velocity from growing without bound during the minimization procedure. Indeed, when $\alpha=0$ the reconstruction which results from the minimization is grossly in error. We will consider a different form for $\mathbf{L}$ in Sec. V, which improves the results.

The solution, $\dot{w}^{\alpha,\delta}$ (now depending on α), for the minimization of Eq. (22) is well known[12,1] and is given by

$$\dot{w}^{\delta}=\dot{w}^{\alpha,\delta}=\mathbf{R}_{\alpha}p^{\delta}, \tag{23}$$

where $\mathbf{R}_{\alpha}$ is called the regularized inverse of $\mathbf{H}$ and

$$\mathbf{R}_{\alpha}=(\alpha\mathbf{L}^H\mathbf{L}+\mathbf{H}^H\mathbf{H})^{-1}\mathbf{H}^H=(\alpha I+\mathbf{H}^H\mathbf{H})^{-1}\mathbf{H}^H \quad \text{for} \quad \alpha>0, \tag{24}$$

the second equality occurring when $\mathbf{L}=I_n$, that is, when Eq. (22) is in standard form.

1. Determination of α—The Morozov discrepancy principle

At this point the value of α in Eq. (24) is still undetermined. We discuss two methods for determining α. The first is the discrepancy principle attributed to Morozov (MDP) and the second is the generalized cross validation procedure (GCV). We postpone the discussion of the GCV to Sec. V, however. The discrepancy principle provides a particularly simple method of finding the regularization parameter α when the variance of the noise σ^2 is known, whereas GCV does not require a knowledge of the noise variance. The MDP states that the solution of Eq. (22) must satisfy the following discrepancy equation:

$$\|\mathbf{H}\dot{w}^{\alpha,\delta}-p^{\delta}\|=\delta, \quad \delta=\sqrt{M}\sigma. \tag{25}$$

One can view the first term in the L2 norm in the discrepancy equation as the predicted value of the pressure $p^{\alpha,\delta}$ (now depending on α):

$$p^{\alpha,\delta}\equiv\mathbf{H}\dot{w}^{\alpha,\delta}=\mathbf{H}\mathbf{R}_{\alpha}p^{\delta}, \tag{26}$$

derived from the reconstructed velocity. Returning to Eq. (25), we vary α (and thus $\mathbf{R}_{\alpha}$) until the predicted pressure differs from the measured pressure by just the noise, a result we would expect, in view of Eq. (21), when the predicted pressure $p^{\alpha,\delta}$ is identical to the exact (noiseless) field *p*.

At this point we insert the eigenvalue decomposition Eq. (14) into the problem and study the resulting solutions. In particular, we study the various eigenvalue (*k*-space) filters which arise.

2. Using the eigenvalue decomposition in the Tikhonov solution

Most applications of Tikhonov regularization cast the solution in terms of an eigenvalue decomposition, usually the SVD. This, of course, is critical to our problem since we have already cast the planar and cylindrical NAH equations into a eigenvalue form with the intent of applying regularization tools to them. In what follows we will assume that $\mathbf{H}$ is square so that $M=N$; although this is not a necessary condition, it simplifies the notations. In an attempt to make the SVD solution Eq. (18) and the eigenvalue solution Eq. (14) appear *symbolically* the same we define

$$\overline{\mathbf{U}}\equiv\mathbf{F}^H=\mathbf{F}^{-1}, \tag{27}$$

$$\overline{\mathbf{V}}^H\equiv\mathbf{F}, \tag{28}$$

using bars over the matrices to distinguish them from those in the SVD. We do this because the symbols $\mathbf{U}$ and $\mathbf{V}$ are so commonly used in the literature when dealing with the SVD. Thus when applying results from the literature we are less prone to making errors or confusing the reader already fa-

miliar with regularization theories. Thus we rewrite Eq. (14), realizing that this does **not** represent an SVD, as

$$\mathbf{H}\equiv\overline{\mathbf{U}}\mathbf{G}\overline{\mathbf{V}}^{H}. \tag{29}$$

Using Eq. (29) in Eq. (24) with $\mathbf{L}=I$ we find that

$$\mathbf{R}_{\alpha}=\overline{\mathbf{V}}\,\mathrm{diag}\left(\frac{\lambda_1^*}{\alpha+|\lambda_1|^2},\ldots,\frac{\lambda_M^*}{\alpha+|\lambda_M|^2}\right)\overline{\mathbf{U}}^{H},$$
$$\mathbf{G}=\mathrm{diag}(\lambda_1,\ldots,\lambda_M), \tag{30}$$

where* indicates complex conjugate (we cannot assume the eigenvalues are real). The index of the eigenvalue represents a pair of numbers, that is, λ_{ij} for planar geometry in Eq. (15) and λ_{jn} for cylindrical geometry is Eq. (16).

It is illuminating to consider the *k*-space filter that Tikhonov regularization introduces to the unregularized problem. To this end, consider the unregularized solution R_0. This is found by setting $\alpha=0$ in Eq. (30),

$$R_0=\overline{\mathbf{V}}\,\mathrm{diag}\left(\frac{1}{\lambda_1},\ldots,\frac{1}{\lambda_M}\right)\overline{\mathbf{U}}^{H}.$$

We recognize this as the pseudo-inverse of **H** and note that it fails to produce an accurate solution in the face of noise in the pressure. We define the filter factor F^{α} (a diagonal matrix) as the multiplier which alters the inverted eigenvalues when $\alpha\neq0$, rewriting Eq. (30) as

$$\mathbf{R}_{\alpha}=\overline{\mathbf{V}}F^{\alpha}\,\mathrm{diag}\left(\frac{1}{\lambda_1},\ldots,\frac{1}{\lambda_M}\right)\overline{\mathbf{U}}^{H},$$
$$\text{where}\quad F^{\alpha}=\mathrm{diag}\left(\frac{|\lambda_1|^2}{\alpha+|\lambda_1|^2},\ldots,\frac{|\lambda_M|^2}{\alpha+|\lambda_M|^2}\right). \tag{31}$$

When $\alpha\ll1$ we see that the filter factor is unity, and when $\alpha\gg|\lambda_q|^2$, $q\leqslant M$, the factor goes to zero. The ''break point'' of the filter (when $F^{\alpha}_{qq}=\frac{1}{2}$) occurs for $\alpha=|\lambda_q|^2$. Given that as $|\lambda_q|$ decreases [as $k_p>k$ in Eq. (17) increases] the spatial frequency of the corresponding qth mode U_q increases, where we write $\mathbf{U}$ in terms of the column vectors, U_q,

$$\overline{\mathbf{U}}=(U_1,\ldots,U_q,\ldots,U_M). \tag{32}$$

Then the filter eliminates the highest spatial frequencies in the data, generally due mostly to random noise in the hologram.

To visualize F^{α} we create a parametric plot. That is, we plot (the diagonal of) F^{α} vs $k_p\equiv\sqrt{k_x^2+k_y^2}$ by rewriting Eq. (15):

$$\lambda(k_p)=\frac{\rho ck}{i\sqrt{k_p^2-k^2}}e^{-\sqrt{k_p^2-k^2}d},$$

where we have dropped the index subscript and plot a continuum of values instead. The result for three values of α normalized to $(\rho c)^2$ is shown in Fig. 2. The ''break point'' of the filter [when $F^{\alpha}(k_p)=\frac{1}{2}$] occurs for the value of k_p for which $\alpha=|\lambda(k_p)|^2$. The dashed line in the figure is the exponential *k*-space filter, F^{γ,k_c}, presented later in Eq. (49) with $\gamma=0.15$. This filter has been the filter of choice in NAH reconstructions in the past.[10] When compared with the *k*-space filter we see that the shape of the Tikhonov filter is very similar, differing mostly in the slope at the break point. It turns out that the slope is a critical parameter in the quality of the reconstruction, as we will see later in this article.

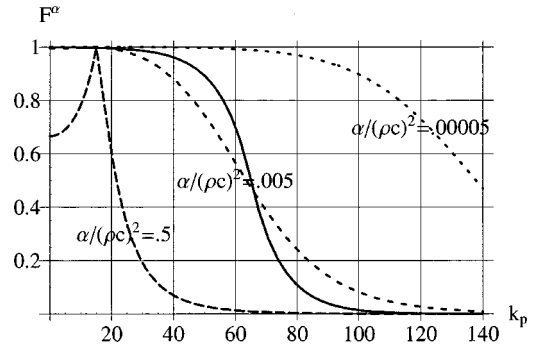

FIG. 2. Plot of $|\lambda(k_p)|^2/(\alpha+|\lambda(k_p)|^2)$ versus k_p with $k=15$ and three values of $\alpha/(\rho c)^2=(0.5, 0.005, 0.00005)$, normalized to ρc. Note the radiation circle is at $k_p=15$. To the left of this point the radiation is supersonic with no decay away from the vibrator, and to the right the radiation is evanescent with a corresponding exponential decay. The solid line is the *k*-space exponential filter with cutoff at $k_c=65$ for comparison with the middle dashed curve.

The left-most curve in Fig. 2 is interesting and points out a flaw in the Tikhonov filter. We see that $F^{\alpha}\neq1$ in the supersonic part of the *k*-space spectrum (inside the radiation circle, $k_p<k$). The plane waves associated with these components propagate to the far field unattenuated. Thus the filter has the unacceptable effect of altering the far field which is calculable from the velocity reconstruction. Fortunately, the fix is trivial. Once the filter factor is computed, the elements for $k_p<k$ are all replaced with unity. Note that this problem with the Tikhonov filter is only severe when $\alpha/(\rho c)^2$ is close to unity.

Returning to Eq. (31) the product $\mathbf{HR}_{\alpha}$ becomes, using Eq. (29),

$$\mathbf{HR}_{\alpha}=\overline{\mathbf{U}}\,\mathrm{diag}\left(\frac{|\lambda_1|^2}{\alpha+|\lambda_1|^2},\ldots,\frac{|\lambda_M|^2}{\alpha+|\lambda_M|^2}\right)\overline{\mathbf{U}}^{H}=\overline{\mathbf{U}}F^{\alpha}\overline{\mathbf{U}}^{H}. \tag{33}$$

Using this result in Eq. (26) we find that

$$p^{\alpha,\delta}=\overline{\mathbf{U}}F^{\alpha}\overline{\mathbf{U}}^{H}p^{\delta}. \tag{34}$$

Thus the *k*-space or Fourier components $\overline{\mathbf{U}}^{H}p^{\delta}$ of the measured pressure are filtered by F^{α} resulting in a smoothed version $p^{\alpha,\delta}$ of the measured pressure. The matrix $\overline{\mathbf{U}}F^{\alpha}\overline{\mathbf{U}}^{H}$ in Eq. (34) is sometimes referred to as the *influence matrix*.[1]

3. The SVD and the discrepancy principle

The discrepancy equation [Eq. (25)] can be written as

$$\|p^{\alpha,\delta}-p^{\delta}\|=\sigma\sqrt{M}, \tag{35}$$

which looks like Eq. (21) if the smoothing effect of F^{α} in Eq. (34) completely eliminates the noise in the measured pressure, a result which would delight any signal processer. Thus we see that the MDP is a very physical principle.

The discrepancy equation is robust computationally since the left-hand side represents a monotonic function in α.[12] That is, when $\alpha=0$, then $F^{\alpha}=I_M$ and Eq. (34) leads us to the conclusion that the left-hand side of the discrepancy

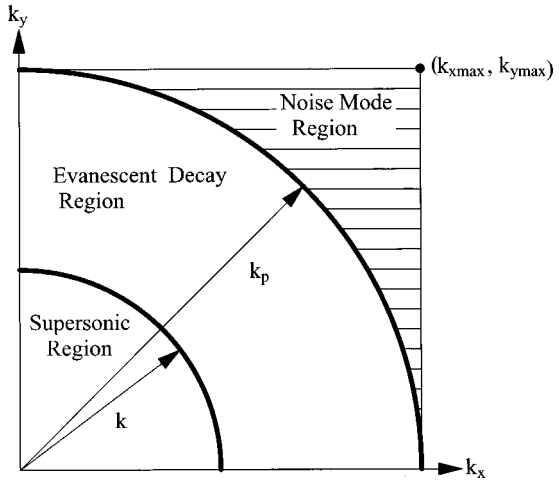

FIG. 3. One quadrant of *k*-space showing the region in which the noise is computed using Eq. (38).

equation is zero. When $\alpha\to\infty$, then $F^\alpha=0$ and the left-hand side is $\|p^\delta\|$. Certainly, $\|p^\delta\|/\sqrt{M}>\sigma$ unless the signal-to-noise ratio (SNR) of the measured pressure is close to or less than unity (an unacceptable measurement condition). Given these two bounds we are guaranteed that at some value of α the equality in the discrepancy equation will be satisfied, yielding a robust determination of α.

We now discuss a simple and robust procedure to determine the standard deviation of the noise.

4. Determination of variance of the hologram noise

As pointed out by Hansen,[1] the expected value of the Fourier coefficients of the noise is given by

$$\mathcal{E}(|U_i^H\boldsymbol{\epsilon}|)=\sigma,\quad i=1,...,N \tag{36}$$

[the column vector U_i was defined in Eq. (32)], so that the Fourier coefficients of the measured pressure will level off at

$$\mathcal{E}(|U_q^H p^\delta|)\approx\sigma\quad\text{for small }|\lambda_q|, \tag{37}$$

since the Fourier coefficients are dominated by $|U_q^H\boldsymbol{\epsilon}|$ for small $|\lambda_q|$ (that is, for large k_p). This latter result is clear from Eq. (17) and Fig. 1, for cylindrical holography, which indicates that the Fourier coefficients of the pressure ($\mathcal{F}p=G_N\mathcal{F}\dot{w}$) must exhibit the same decay as G_N as long as $\mathcal{F}\dot{w}$ remains bounded. This bounding follows from the fact that, since $\|\dot{w}\|$ must be bounded, then $\|\mathcal{F}\dot{w}\|=\|\dot{w}\|$ (Parseval's theorem) is also bounded.

As an example we consider the planar case. The region covered by the wave numbers associated with the eigenvalues is shown in Fig. 3 (only one quadrant shown for simplicity) bounded by $(k_{x\,\max},k_{y\,\max})$, the maximum *k*-space values due to the spatial discretization and the DFT. The shaded corner Ω [that is, $k_p>\max(k_{x\,\max},k_{y\,\max})$] is used to compute σ using

$$\|U_q^H p^\delta\|/\sqrt{Q}\approx\sigma,\quad q\in\Omega, \tag{38}$$

where the norm is taken only over the Q eigenvalues which lie in Ω. Of course it is assumed that the Fourier coefficients of p have dropped off sufficiently into the noise in Ω so that Eq. (37) is valid. It is important to realize that this technique is completely general and will work in any geometry, for interior or exterior NAH problems. It was initially used successfully in the interior of an aircraft fuselage in a conformal NAH application using the SVD.[13]

5. Discrepancy principle in k-space

Returning to the discrepancy principle we seek to understand it in *k*-space. Use Eq. (34) to rewrite Eq. (35) as

$$\|(\overline{\mathbf{U}}F^\alpha\overline{\mathbf{U}}^H-I)p^\delta\|=\sigma\sqrt{M},$$

which becomes in *k*-space (a bar over a vector represents the quantity in *k*-space, $\overline{p^\delta}\equiv\overline{\mathbf{U}}^H p^\delta$)

$$\|F_1^\alpha\overline{p^\delta}\|=\sigma\sqrt{M}, \tag{39}$$

where

$$F_1^\alpha\equiv I-F^\alpha=\text{diag}\left(\frac{\alpha}{\alpha+|\lambda_1|^2},\ldots,\frac{\alpha}{\alpha+|\lambda_M|^2}\right). \tag{40}$$

We recognize $\overline{p^\delta}$ as the *k*-space representation of the measured pressure. The *high-pass filter* F_1^α in Eq. (40) goes to unity for vanishing eigenvalue, and tends towards zero for the largest eigenvalues, opposite to the filter F^α. Equation (39) is remarkably similar to the equation used to construct the noise, Eq. (38). In the latter case the passband components are given in Eq. (38) by the set of modes U_q contained in the region Ω, and the filter is a rectangular one, being zero in the region excluding Ω. The utility of Eq. (39) is that all the computation is done in *k*-space and there is no need to compute the reconstructed velocity.

B. Landweber iteration

This popular technique[12] rewrites $p=\mathbf{H}\dot{w}$ as

$$\dot{w}=(I-\beta\mathbf{H}^H\mathbf{H})\dot{w}+\beta\mathbf{H}^H p,$$

where β is a positive number to be determined. Note that the right-hand side is exactly $\dot{w}$ since the second and third terms cancel (when p is replaced by $\mathbf{H}\dot{w}$). This iteration procedure was studied recently for NAH problems by Kim and Ih.[5] The iteration procedure is set up by using the right-hand side to compute the left-hand side starting with the first iteration solution of $\dot{w}^0=0$. Thus we have

$$\dot{w}^m=(I-\beta\mathbf{H}^H\mathbf{H})\dot{w}^{m-1}+\beta\mathbf{H}^H p,\quad m=1,2,\ldots. \tag{41}$$

Using Eq. (14) to decompose $\mathbf{H}$ the solution to Eq. (41) is

$$\dot{w}^m=\mathbf{R}_\mathbf{m}p$$
$$=\overline{\mathbf{V}}\,\text{diag}\left(\frac{1-(1-\beta|\lambda_1|^2)^m}{\lambda_1},\ldots,\frac{1-(1-\beta|\lambda_M|^2)^m}{\lambda_M}\right)\overline{\mathbf{U}}^H p, \tag{42}$$

from which, in analogy to Eq. (31), we can derive the filter factor F^m:

$$\mathbf{R}_\mathbf{m}=\overline{\mathbf{V}}F^m\,\text{diag}\left(\frac{1}{\lambda_1},\ldots,\frac{1}{\lambda_M}\right)\overline{\mathbf{U}}^H,$$
$$F^m=\text{diag}(1-(1-\beta|\lambda_1|^2)^m,\ldots,1-(1-\beta|\lambda_M|^2)^m). \tag{43}$$

In order for convergence to occur we must choose $\beta < 1/|\lambda_{\max}|^2$.

1. Discrepancy principle for Landweber iteration

The discrepancy equation, Eq. (25), is easily written for Landweber iteration. The filtered pressure similar to Eq. (26) after m iterations is

$$p^{m,\delta} \equiv \mathbf{H}\dot{w}^{m,\delta} = \mathbf{H}\mathbf{R}_{\mathbf{m}} p^{\delta},$$

and the discrepancy equation is

$$\|p^{m,\delta} - p^{\delta}\| = \delta. \tag{44}$$

Note that Eq. (33) is still valid:

$$\mathbf{H}\mathbf{R}_{\mathbf{m}} = \overline{\mathbf{U}} F^m \overline{\mathbf{U}}^H, \tag{45}$$

so that the discrepancy principle can be written in k-space as

$$\|\overline{\mathbf{U}}(F^m - I)\overline{\mathbf{U}}^H p^{\delta}\| = \delta \quad \text{or} \quad \|F_1^m \overline{p^{\delta}}\| = \delta, \tag{46}$$

where

$$F_1^m \equiv I - F^m = \text{diag}((1-\beta|\lambda_1|^2)^m, \ldots, (1-\beta|\lambda_M|^2)^m). \tag{47}$$

As before F_1^m acts as a high-pass filter going to unity for small singular values, and approaching zero for large eigenvalues.

C. Conjugate gradient approach

The method used here is referred to as CGLS.[1] The algorithm consists of five statements, not reproduced here, which are easily programmed. These statements were translated into k-space using Eq. (29). Again the Morozov discrepancy principle was applied to find a stopping point in the iterations. Since no explicit form of the filter factor F is available, it is determined from Eq. (34), where α represents the iteration number, by comparison of the measured pressure to the filtered hologram pressure resulting from the reconstructed velocity. F remains diagonal in the CG approach.

IV. COMPARISON OF RESULTS

In our simulations it is important to generate a test problem which contains evanescent waves decaying away from the vibrating surface. It is the evanescent waves which lead to the ill-posed nature of the inverse NAH problem. To emphasize the generality of our approach we consider a cylindrical hologram geometry for the first study. In a later section we will consider a planar example using a simply supported plate mode below coincidence as the vibrator.

The numerical model consisted of four linear arrays (equally spaced circumferentially) of 36 point sources located slightly within/below (4.34 cm) the reconstruction cylinder of radius 36.6 cm. Each array was 254 cm long and was phased to be subsonic with phase speeds of -150, 300, 450, -600 m/s in water with $c = 1481$ m/s. Thus adjacent point sources are in acoustic short circuit and create radiating fields which tend to decay evanescently. The normal velocity was computed exactly on the reconstruction cylinder. The hologram, computed easily from the radiation from the four line arrays, was placed 1.3 cm from the reconstruction surface. The lattice spacing was 1.6 cm and the hologram consisted of 256 axial points and 60 circumferential points. Random Gaussian noise was added to the hologram with predetermined variance to simulate a measurement with a 15-dB signal-to-noise ratio at frequencies of 2–12 kHz in 2-kHz steps.

To clarify the accuracy of the regularization procedures we plot the results as error versus the regularization parameter α. Note that α can be related to the cutoff of the k-space filter in the following way. Given α, determine the value of $|\lambda_{jn}|^2 = \alpha$. This sets the break point ($F_{qq}^{\alpha} = \frac{1}{2}$) of the filter given in Eq. (31). The wave number (the abscissa) corresponding to this cutoff is given by $k_c = \sqrt{k_{zj}^2 + (n/a)^2}$. For each value of k_c, scanning through the values of (j,n), the error E^{α} between the reconstructed velocity and the true velocity $\dot{w}_{ex}$ is calculated using the formula

$$E^{\alpha} = \|\dot{w}_{ex} - \dot{w}^{\alpha,\delta}\| / \|\dot{w}_{ex}\|. \tag{48}$$

The results of the comparison of the three regularization procedures are shown in Fig. 4. The horizontal axis is the radius of the k-space circle (the helical wave number) $k_c = \sqrt{k_z^2 + (n/a)^2}$, where k_z and n/a are the wave numbers in the two orthogonal coordinate directions. The vertical axis is the percent error between the reconstructed normal velocity and the known solution.

The baseline for comparison is the NAH filter used in both cylindrical and planar holography[9] which we call the exponential filter. This solution corresponds to curves marked with a star. The taper of this filter follows an exponential shape and the filter is defined by

$$F^{\gamma,k_c} = \begin{cases} 1 - \frac{1}{2} e^{-(1-k_p/k_c)/\gamma}, & 0 < k_p \leqslant k_c, \\ \frac{1}{2} e^{(1-k_p/k_c)/\gamma}, & k_p \geqslant k_c, \end{cases} \tag{49}$$

where k_c is the break point and γ determines the slope at the break point. Note that this filter is not determined through a regularization procedure, and that the two unknown parameters, k_c and γ, are chosen by hand. With the proper selection of these parameters we believe that this baseline solution represents the best which can be achieved. Returning to Fig. 4 three conclusions are evident. (1) Tikhonov regularization (diamond), which represents the highest error curve at all six frequencies, does not do as well as Landweber (LW) and CG, (2) the LW (box) and CG (triangle) solutions have similar errors with the CG doing slightly better as the frequency increases, and (3) the exponential filter always has the smallest minimum error.

The results from the discrepancy principle used for the parameter selection (k-space cutoff) are also displayed in Fig. 4 by short vertical lines, one for each of the procedures. These lines indicate the value of k_c (and hence α or m) chosen when the discrepancy principle is applied. As can be seen, MDP fails to find the minimum in almost all of the cases, and almost always finds a value which oversmooths (smaller values of k_c) the solution. This oversmoothing is a well-known fact.[1] However, the discrepancy principle appears to locate closer to the minimum for the Tikhonov solution than for the others, although this solution has the highest error.

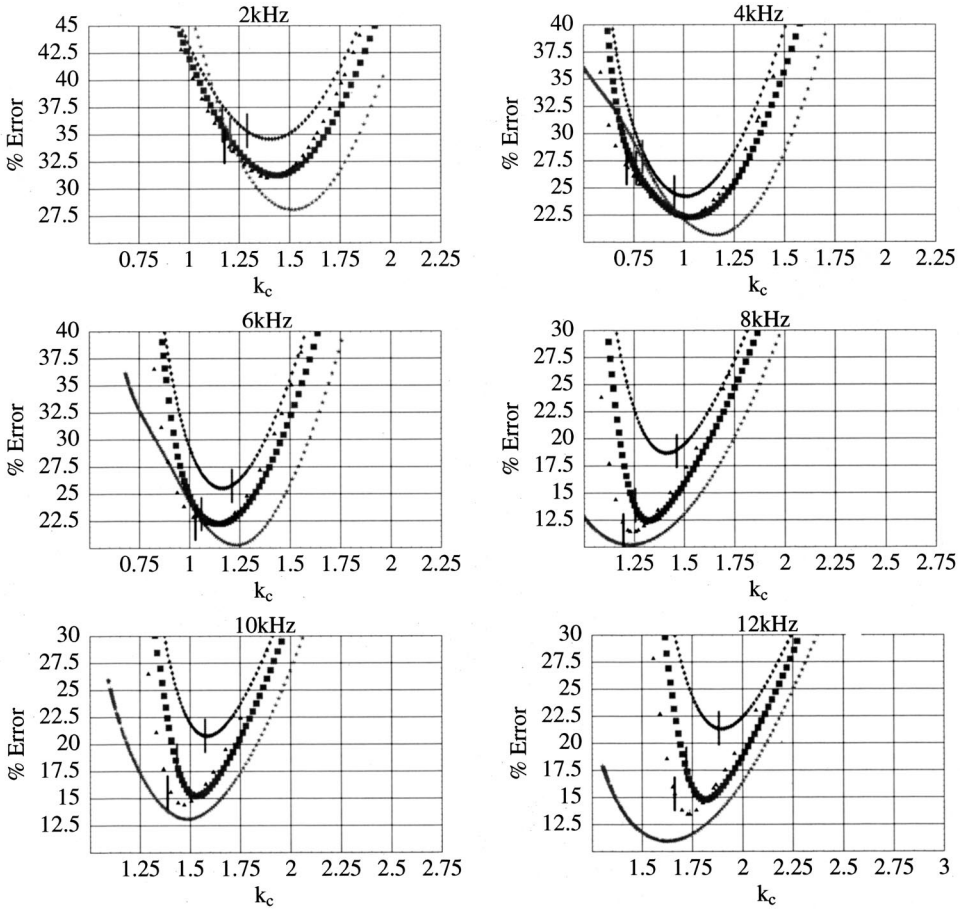

FIG. 4. Comparison of percent errors versus cutoff wave number ($k_c = \sqrt{k_z^2 + (n/a)^2}$) for three regularization techniques given snr=15 dB. The key for the curves is ◇ standard Tikhonov, □ Landweber, △ conjugate gradient, ⋆ exponential filter. The short vertical lines indicate the cutoff determined by the Morozov discrepancy principle.

Although not shown, we found that when the SNR is high, the LW, the CG, and the exponential filters all produce about the same minimum error; however, the standard Tikhonov still has a larger minimum error. To understand these results we need to study the actual filters which are generated in the minimization procedures.

A. Comparison of filter factors

It is very instructive to look at the tapers involved with the various *k*-space filters which arise from the four procedures. Figure 5 compares the four filters plotting the filter factor F against k_p for a SNR of 15 dB for the 2-kHz case. The equations for the filter factors are given by Eq. (31) for standard Tikhonov, Eq. (43) for Landweber, and Eq. (49) for exponential. No equation exists for the conjugate gradient filter. Note that the horizontal axis is wave number, k_p [see Eq. (17)], although the filters are defined in terms of eigenvalues not wave numbers. However, as was indicated in Fig. 1 and by Eq. (17) there is a one-to-one relationship between them outside the radiation circle. Note that $1/k_p$ is proportional to the resolution of the reconstruction. The units of k_p are radians per inch.

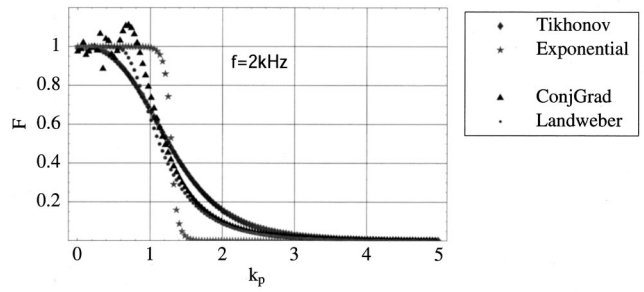

FIG. 5. The filter shapes for the four cases with snr=15 dB. The break points of the filters are determined by the discrepancy principle, corresponding to the vertical lines in Fig. 4 at 2 kHz. The baseline filter is the exponential with $\gamma=0.15$.

What is immediately apparent from Fig. 5 is that the shape of the filter depends on the regularization procedure used. Furthermore, there is a clear correlation between the steepness of the filter and the errors shown in Fig. 4; the lowest error solution (exponential) has the steepest filter through the break point whereas the highest error solution (Tikhonov) has the least steep filter. Thus we conclude that the failure of the Tikhonov procedure is due to the broad nature of the filter taper. The shapes of the CG and LW filters are nearly the same except for the oscillation of the CG filter to levels above $F=1$. The overshoot of the CG filter is surprising and undesirable.

1. Slope at the break point

Given that it is the slope of the filter at the break point which seems to govern the best solution, it is useful to derive some expressions for the slope for the various regularization methods. The break point is defined as the value of $k_p = k_c$ for which $F^{\alpha} = \frac{1}{2}$. For the exponential window defined in Eq. (49) the slope at the break point is given by

$$\frac{\partial F^{\gamma,k_c}}{\partial k_p} = -\frac{1}{2k_c\gamma}, \tag{50}$$

which has a slope tending to infinity when $\gamma \to 0$.

For the other windows we need to have an expression for the singular values. We assume a planar NAH case and that $k_c \gg k$ so that

$$\sigma \approx e^{-k_p d} k/k_p .$$

Thus for Tikhonov we have

$$F^{\alpha}(k_p) = \frac{1}{1+\alpha k_p^2 e^{2k_p d}/k^2},$$

with a break point ($k_p = k_c$) given by $\alpha = (k e^{-k_c d}/k_c)^2$ and a slope at the breakpoint

$$\frac{\partial F^{\alpha}}{\partial k_p} = -\frac{1+k_c d}{2k_c}. \tag{51}$$

Furthermore, for Landweber iteration we find that

$$\frac{\partial F^{m}}{\partial k_p} = -\frac{m(2^{1/m}-1)(1+k_c d)}{k_c},$$

and as $m \to \infty$ we have

$$\frac{\partial F^{m}}{\partial k_p} \to -\frac{(1+k_c d)\log(2)}{k_c}. \tag{52}$$

Two important facts emerge: (1) the slope of the Landweber iteration reaches a finite limiting value and (2) the slope exceeds the Tikhonov slope by a multiplicative factor of $2\log(2) = 1.39$, and thus is only slightly steeper at the break point. This explains why the Landweber iteration provides a better solution, although the slope is still not sharp enough to give the minimum error solution.

For pressure to pressure reconstructions ($\sigma \approx e^{-k_p d}$ for large k_p) these slopes are even simpler given by $-d/2$ for Tikhonov and by $-d\log(2)$ for Landweber. The same conclusions are drawn in this case as identified in the last paragraph.

Although these conclusions are strictly true for the planar NAH case, we assume that similar results will be found with respect to the sharpness of the various filters for any reconstruction problem which involves evanescent or strongly decaying fields.

V. AN IMPROVED TIKHONOV APPROACH AND GCV PROCEDURE

We return to the Tikhonov problem, with the added information that its failure is due to the fact that the filter produced is too broad. We will derive a physically based modification of the penalty (cost) function in the Tikhonov equation which will sharpen up this filter.

The penalty function provided by Tikhonov regularization is given by the second term in Eq. (22). In the foregoing analysis we have chosen the standard form of the Tikhonov functional, with $\mathbf{L} = I_M$. Considering the cost function in k-space we use Parseval's theorem and write

$$\alpha \|\dot{w}^{\delta}\|^2 = \alpha \|\overline{\mathbf{V}}^H \dot{w}^{\delta}\|^2 = \alpha \|\overline{\dot{w}^{\delta}}\|^2, \tag{53}$$

where we have defined the k-space velocity, $\overline{\dot{w}^{\delta}} \equiv \overline{\mathbf{V}}^H \dot{w}^{\delta}$. Thus we see that limiting the growth of the norm of the reconstructed velocity, which forms the basis of the cost function, is equivalent to limiting the growth of all the k-space components of the surface velocity. However, it would be much more logical to restrict only the growth of the high wave number components (components with small eigenvalues) and leave the lower wave number components unaltered in the minimization. As we have seen it is the high wave number components which blow up in the reconstruction and thus are filtered out by the low-pass filter F^{α} defined in Eq. (31). As a result we consider the choice of $\mathbf{L} = F_1^{\alpha}\mathbf{V}^H$, where F_1^{α} is the *high-pass* k-space filter defined in Eq. (39) which resulted from the solution of Tikhonov's equation when $\mathbf{L} = I_M$. Thus the functional [Eq. (22)] which we want to minimize is now given by

$$J_{\alpha}^{1}(\dot{w}^{\delta}) = \|\mathbf{H}\dot{w}^{\delta} - p^{\delta}\|^2 + \alpha \|F_1^{\alpha}\overline{\mathbf{V}}^H \dot{w}^{\delta}\|^2, \tag{54}$$

where F_1^{α} is given from the solution of

$$J_{\alpha}(\dot{w}^{\delta}) = \|\mathbf{H}\dot{w}^{\delta} - p^{\delta}\|^2 + \alpha \|\dot{w}^{\delta}\|^2.$$

The solution to Eq. (54) is obtained by substituting $F_1^{\alpha}\overline{\mathbf{V}}^H$ for $\mathbf{L}$ into the first equality of Eq. (24) [where $\mathbf{H} = \overline{\mathbf{U}}\mathbf{G}\mathbf{V}^H$ and $\mathbf{G}$ was defined in Eq. (30)], resulting in

$$\mathbf{R}_{\alpha}^{1} = \overline{\mathbf{V}}(\alpha(F_1^{\alpha})^2 + \mathbf{G}^H\mathbf{G})^{-1}\mathbf{G}\overline{\mathbf{U}}^H, \tag{55}$$

yielding

$$\mathbf{H}\mathbf{R}_{\alpha}^{1} = \overline{\mathbf{U}}F^{\alpha,1}\overline{\mathbf{U}}^H$$

where

$$F^{\alpha,1} \equiv \mathrm{diag}\left(\cdots \frac{|\lambda_i|^2}{|\lambda_i|^2 + \alpha(\alpha/(\alpha+|\lambda_i|^2))^2} \cdots \right). \tag{56}$$

Comparison with Eq. (31) indicates the change in the solution which results with the new cost function. The high-pass filter, $I - F^{\alpha,1}$, which results [compare with Eq. (39)] is

$$F_1^{\alpha,1} \equiv \mathrm{diag}\left(\cdots \frac{\alpha}{\alpha + |\lambda_i|^2((\alpha+|\lambda_i|^2)/\alpha)^2} \cdots \right). \tag{57}$$

Note that we could derive a whole set of new filters by just continuing this procedure. That is, we could substitute the new filter equation (57) for F_1^{α} in the Tikhonov equation (54) and easily derive a second-order filter, $F_1^{\alpha,2}$. However, it is questionable whether or not the solutions improve.

The discrepancy principle is given in Eq. (35), where $p^{\alpha,\delta}$ is the smoothed pressure resulting from the regularization procedure which now becomes

$$p_1^{\alpha,\delta} = \overline{\mathbf{U}}F^{\alpha,1}\overline{\mathbf{U}}^H p^{\delta}.$$

Using the new high-pass filter the discrepancy equation becomes in k-space, following the analysis which led to Eq. (39),

$$\|F_1^{\alpha,1}\overline{p^{\delta}}\| = \sigma\sqrt{M}.$$

Before we proceed with the results from the simulations, we want to consider another parameter selection procedure besides the MDP. This procedure is called the generalized

cross validation (GCV) and is important because it does not require an estimate of the noise for its application.

A. The generalized cross validation and an improvement

The fundamental paper on the subject was published in 1979.[14] The GCV relies on Tikhonov regularization. It has seen application in NAH recently by Yoon and Nelson.[2] This method determines the value of α in Eq. (22) for the case $\mathbf{L}=I$ using a technique different from the discrepancy principle and is important since it does not require knowledge of the noise variance. Golub calls the solutions (24) a one-parameter family of ridge estimates. This method basically removes a measurement point at a time and compares the reconstruction at the missing data point with the actual data there, minimizing this difference. The resulting function to be minimized for the standard form Tikhonov is

$$J(\alpha)=\frac{\|(\mathbf{H}\dot{w}^{\alpha,\delta}-p^{\delta}\|^2}{[Tr(I-\mathbf{HR}_{\alpha})]^2}=\frac{\|(I-\mathbf{HR}_{\alpha})p^{\delta}\|^2}{[Tr(I-\mathbf{HR}_{\alpha})]^2}=\frac{\|F_1^{\alpha}\overline{p^{\delta}}\|^2}{[Tr(F_1^{\alpha})]^2}, \tag{58}$$

where F_1^{α} was defined in Eq. (39). This equation is closely related to the MDP, in fact, the numerator is just the left-hand side of the MDP in Eq. (39). The denominator of Eq. (58) takes the place of the noise term. As $\alpha\rightarrow 0$ the numerator goes to zero. However, at the same time the denominator also goes to zero in such a way that a minimum of the ratio is formed.

We use Eq. (58) as the stopping criteria for selection of α in the Tikhonov method. We will find in the next section that the cutoff determined by the GCV seems to grossly undersmooth the solution with errors significantly above the minimum error. However, this result uses the filter from the standard Tikhonov minimization with $\mathbf{L}=I_M$. Thus we consider a modified GCV approach, consistent with the modified Tikhonov approach which we just outlined here.

Consistent with the modification of the Tikhonov equation using the high-pass filter in the penalty term ($\mathbf{L}=F_1^{\alpha}\mathbf{V}^H$), we can modify the GCV functional given in Eq. (58) replacing F_1^{α} in numerator and denominator with Eq. (57). Thus we now seek to minimize

$$J^1(\alpha)=\frac{\|F_1^{\alpha,1}\overline{p^{\delta}}\|^2}{[Tr(F_1^{\alpha,1})]^2}. \tag{59}$$

There is no closed form solution to this minimization which must be done computationally. We will find that the results of this new GCV are much better than with the original (standard Tikhonov).

B. Results with the modified Tikhonov and GCV

We consider the example used previously, four lines of 36 monopoles phased so that the axial phase velocities are subsonic. However, we restrict ourselves to the Tikhonov methods—the standard Tikhonov with $\mathbf{L}=I_M$ in Eq. (22) and the modified Tikhonov with $\mathbf{L}=F_1^{\alpha}\mathbf{V}^H$ discussed above. We apply two stopping (parameter selection) criteria, the Morozov discrepancy principle (MDP) and the generalized cross validation (GCV), for each Tikhonov method. We reran the model used before using the standard and modified Tikhonov methods as well as the MDP and GCV parameter selection methods. The results are shown in Fig. 6. These results should be compared directly to Fig. 4.

Since the value of α derived from the MDP is usually too large representing oversmoothing, we also investigate a different version of MDP which we call the compensated MDP (CMDP), which seems to undersmooth the solution. In this case we write the discrepancy principle as

$$\|F_1^{\alpha}\overline{p^{\delta}}\|=\sigma\sqrt{M}, \tag{60}$$

using the high-pass filter for the regular Tikhonov solution ($\mathbf{L}=I_M$). Using F_1^{α} instead of $F_1^{\alpha,1}$ sometimes leads to a better solution, although none of the examples in this article demonstrated this.

The first conclusion evident from Fig. 6 is that the modified Tikhonov produces better results than the standard Tikhonov with the minimum error dropping by about 5%. Close comparison with Fig. 4 indicates that the modified Tikhonov does at least as well as the best of the three regularization procedures, the conjugate gradient approach, although never doing as well as the exponential filter.

Second we conclude that the GCV from Eq. (58) (cutoff shown by the tall ellipses in the figure) does quite poorly in finding the minimum in the curve for the standard Tikhonov and much worse than the MDP (shown with the small circles) at all six frequencies. However, for the modified Tikhonov (lower curves) the corresponding GCV minimization from Eq. (59) is excellent and the best for all six frequencies. It falls close to the actual minimum in the error curve and slightly undersmooths the reconstruction compared to the optimum. The CMDP Eq. (60) (shown by the right-most circle on each curve) and MDP yield fairly good results with the former undersmoothing and the latter oversmoothing.

1. Comparisons using a planar hologram

We consider in this section a different test case generated for planar geometry. In this case the vibrating source is a simply supported square plate mode (nine half-wavelengths in the *x* and seven in the *y* direction). The medium is air. The square plate is 16.3 cm on a side and was baffled. The hologram plane was 0.25 cm above and was square with a width of 32.5 cm. The lattice spacing was 0.25 cm and the hologram was 128 by 128 points. The same mode was used to generate the pressure fields from 2 to 12 kHz in 2-kHz steps. These frequencies are below the coincidence frequency so that the radiation from the plate is strongly evanescent, an essential condition to test regularization theories. Again noise was added to the holograms to generate an SNR of 15 dB, and the surface velocity was reconstructed using the two Tikhonov procedures studied in the last section. The results are shown in Fig. 7.

We see again that the modified Tikhonov (lower curve) provides better results than the standard Tikhonov for all the frequencies, and again the GCV for the standard Tikhonov does poorly. We also draw the same conclusion as before—

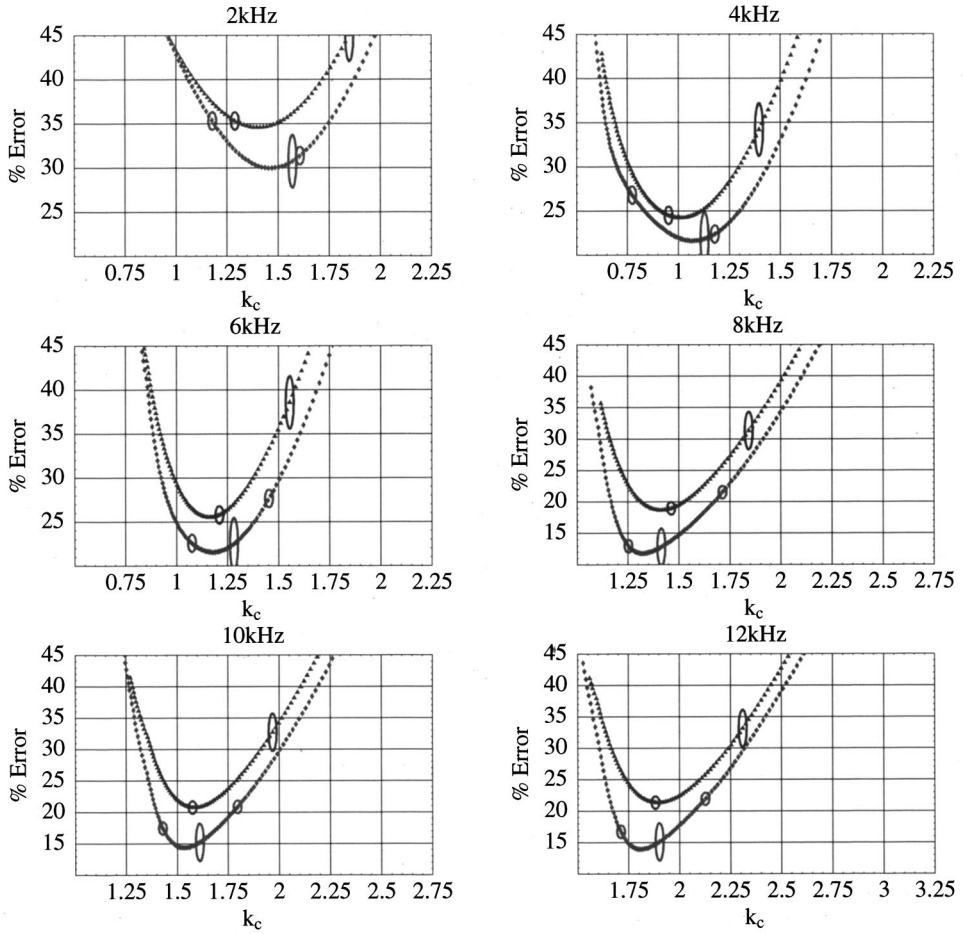

FIG. 6. Results for standard Tikhonov (repeated from Fig. 4) $\mathbf{L}=I_M$ shown with triangles, and the modified Tikhonov with $\mathbf{L}=F_1^{\alpha}\bar{\mathbf{V}}^H$ shown with diamonds. The results for MDP are indicated with small circles (instead of short vertical lines) and GCV with the long ellipses. A second circle to the right of the ellipse on the lower curves is the compensated MDP given by Eq. (60).

the GCV for the modified Tikhonov is better than the MDP and the CMDP. The only exception was the 12-kHz case.

The 12-kHz result illuminates some very important considerations. In planar and cylindrical holography it is critical to apply a Tukey window at the ends of the hologram aperture in order to taper the data to zero at the rim of the hologram. This window is generally eight points wide at each edge.[9] Thus when the errors are computed using Eq. (48) the reconstructed data around the rim is not included. This is done to eliminate the effects of the Tukey window on the error calculation. These effects are generally small as long as the hologram pressure around the rim is small compared to the maximum pressure. (We generally adjust the aperture size so that the pressure drops by 30 dB at the edges in a hologram measurement.) However, for the 12-kHz case the (10,8) mode of the plate is close to coincidence and the pressure field has not decayed sufficiently to meet the 30-dB criteria. Thus the reconstructed field at the edge is grossly in error.

To make this clear consider Fig. 8 which shows a gray-scale rendition of the reconstructed velocity (real part) at 8, 10, and 12 kHz from left to right. The Tukey window does not completely eliminate the edge field blowup in the 12-kHz reconstruction due to the large pressure field present at the edges of the hologram. In the 8-kHz case, however, the edge discontinuity is nearly eliminated by the window. In this case the mode is sufficiently below coincidence that the pressure field at the edges is small. Returning to the 12-kHz GCV result in Fig. 7, we claim that the modified Tikhonov and the GCV do less well (minimum errors are around 25% instead of 10%) in this case precisely due to the large edge discontinuity. In other words, the Tikhonov functional of Eq. (22) uses the velocity over the whole aperture, including the rims. Since the penalty term thus includes the fictitious edge field, the minimization procedure begins to fail. This fact was consistently evident in the research leading to this article. We found that whenever the Tukey window failed to suppress the edge discontinuities the regularization procedures began to give erroneous and inconsistent results. In order to avoid this problem mathematically one would have to reformulate the Tikhonov functional Eq. (22) to exclude the rim of the reconstruction in the $\|\mathbf{L}\dot{w}^{\delta}\|$ term. How to derive a regularized inverse Eq. (24) in this case is presently not known.

Finally, we provide one last figure, the filter shapes for the standard and modified Tikhonov procedures which led to Fig. 6. As we can see from Fig. 9 the modified Tikhonov filter is always sharper than the standard Tikhonov, which leads to the improvement in the reconstruction errors. Also the taper of the modified Tikhonov filter is steeper between $\frac{1}{2}$ and 1 then it is between 0 and $\frac{1}{2}$.

Although we have found that a sharper filter does better, it is not true that the truncated SVD approach in which the filter is rectangular [$\gamma\rightarrow 0$ in Eq. (49)] does even better. We found that as the taper of the filter gets sharper than the exponential filter used in the results of Fig. 5 the minimum

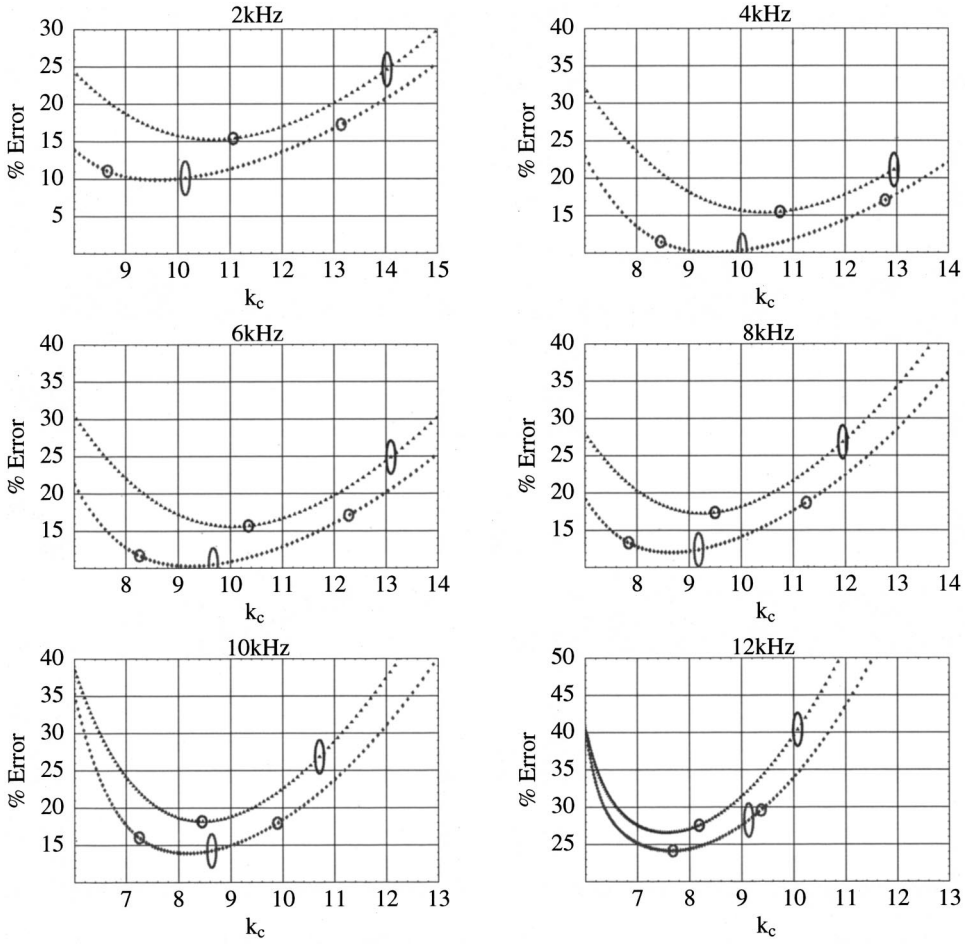

FIG. 7. Planar holography results for the vibration of a square plate in a 10×8 mode. Results for standard Tikhonov $\mathbf{L}=I_M$ shown with triangles, and the modified Tikhonov with $\mathbf{L}=F_1^a\overline{\mathbf{V}}^H$ shown with diamonds. The results for MDP are indicated with small circles (instead of short vertical lines) and GCV with the long ellipses. A second circle to the right of the ellipse on the lower curves is the CMDP given by Eq. (60). The SNR was 15 dB.

error increases. Some amount of taper is always necessary to produce an optimum solution.

VI. CONCLUSIONS

We have presented a robust approach for solving the inverse NAH problem using regularization theory. In particular, we have shown how separable geometry NAH can make use of these theories without computational penalties by making use of an explicit eigenvalue decomposition arising out of the theory of NAH. Application to experiments in which thousands of holograms have been processed to yield velocity reconstructions in planar geometries have suffered no failures in choosing sensible filters and *k*-space cutoffs for the regularization. These experiments cover a wide range of signal-to-noise ratios, even ratios close to unity. The significance of this accomplishment is that velocity reconstructions are now a completely automated procedure with no need for user input except the hologram data and the geometry of the experiment. This removes the tedious and now archaic procedure of manually selecting the *k*-space cutoff for the exponential filter.

We recommend the modified Tikhonov approach with the high-pass filter discussed in Sec. V as the best approach, although the Landweber and conjugate gradient approaches often do equally as well in the cases that we looked at. In this approach, it appears that the GCV gave slightly better results than the Morozov discrepancy principle in terms of finding the absolute minimum in the error. It is perhaps surprising, given this success, that the GCV gives poor results when used for the standard Tikhonov approach. But this is not a concern since the modified Tikhonov solution is always better. The GCV has the added advantage that it does not require an estimate of the standard deviation of the noise in the

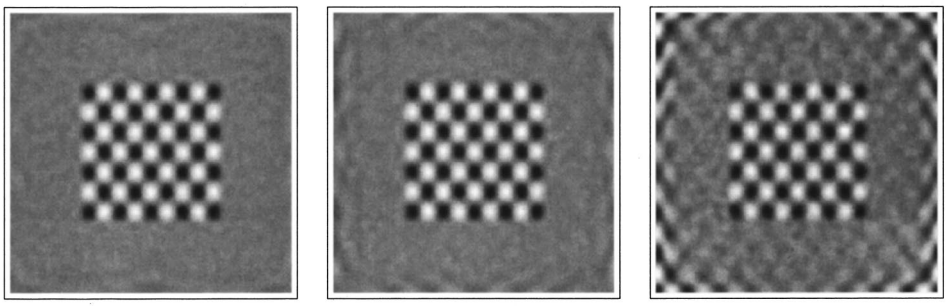

FIG. 8. Velocity reconstruction from the modified Tikhonov using the GCV for 8, 10, and 12 kHz, respectively, for the (10,8) simply supported plate mode.

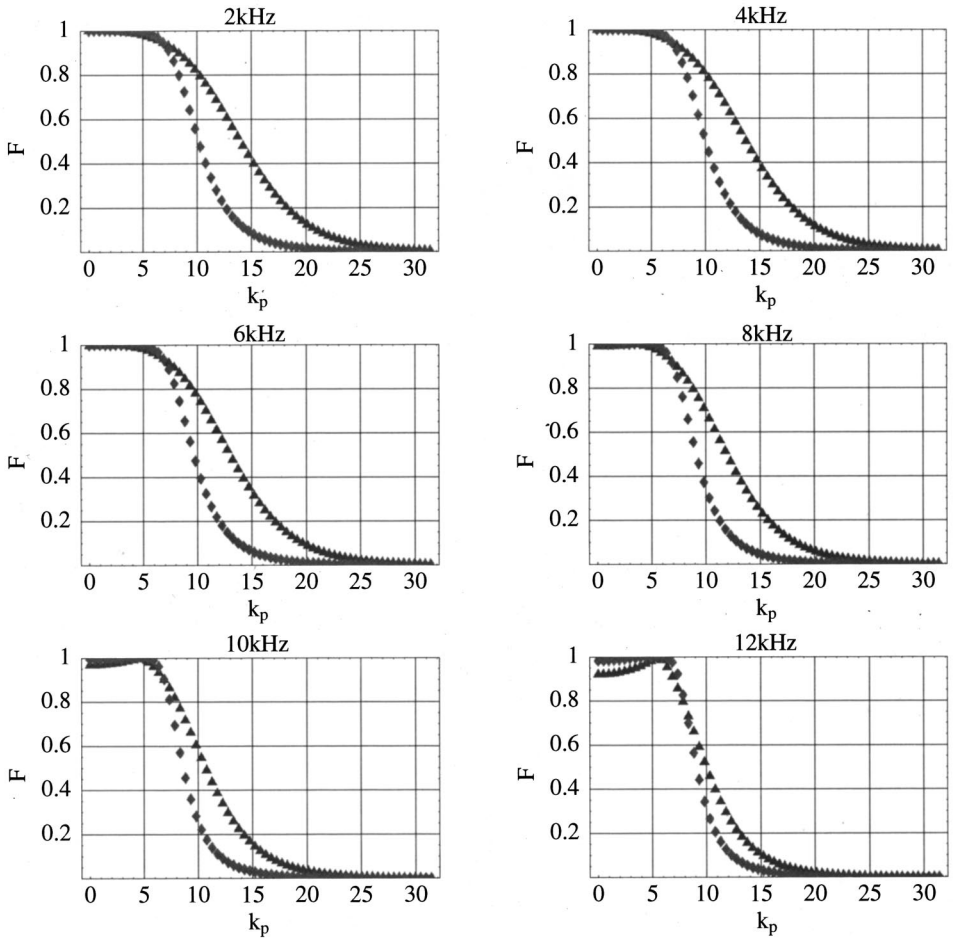

FIG. 9. Filter shapes for the standard and modified Tikhonov regularization procedures. Results for standard Tikhonov $\mathbf{L}=I_M$ shown with triangles, and the modified Tikhonov with $\mathbf{L}=F_1^{\alpha}\overline{\mathbf{V}}^H$ shown with diamonds. The inflection points ($F^{\alpha}=\frac{1}{2}$) were determined by the GCV for both cases.

measurement hologram. However, we have shown a simple and robust method to determine the noise, and we believe the SNR is a very useful measure to have available in the experimental world. Furthermore, it is somewhat easier to determine the solution of the Morozov equation which requires finding a zero crossing of a monotonic function compared with finding the minimum of the GCV equation, the latter requiring finding points on either side of the minimum to begin a search procedure.

As the results with the exponential filter show, none of the regularization theories which we studied found the absolute minimum error for the reconstructed velocity. And there is no proof that the minimum found with the exponential window yields is the absolute minimum. It would be interesting to determine what constraint equation is satisfied by this special window and back out a regularization procedure which has a filter with the exponential taper.

ACKNOWLEDGMENTS

Work supported by the Office of Naval Research. We wish to thank Dilip Ghosh Roy for his valuable input.

[1] P. C. Hansen, *Rank-Deficient and Discrete Ill-Posed Problems* (SIAM, Philadelphia, PA, 1998).
[2] P. A. Nelson and S. H. Yoon, ''Estimation of acoustic source strength by inverse methods: Part i, conditioning of the inverse problem,'' J. Sound Vib. **233**, 643–668 (2000).
[3] S. H. Yoon and P. A. Nelson, ''Estimation of acoustic source strength by inverse methods: Part ii, experimental investigation of methods for choosing regularization parameters,'' J. Sound Vib. **233**, 669–705 (2000).
[4] B-K. Kim and J-G. Ih, ''On the reconstruction of the vibro-acoustic field over the surface enclosing an interior space using the boundary element method,'' J. Acoust. Soc. Am. **100**, 3003–3016 (1996).
[5] B.-K. Kim and J.-G. Ih, ''Design of an optimal wave-vector filter for enhancing the resolution of reconstructed source field by nah,'' J. Acoust. Soc. Am. **107**, 3289–3297 (2000).
[6] F. Augusztinovicz, ''Reconstruction of source strength distribution by inversing the boundary element method,'' in *Boundary Elements in Acoustics, Advances and Applications*, edited by O. von Estorff (WIT, Southhampton, UK, 2000).
[7] P. A. Nelson, ''Some inversion problems in acoustics,'' to appear in J. Acoust. Vib. (2001).
[8] T. K. Delillo, V. Isakov, N. Valdivia, and L. Wang, ''Computational methods for the detection of the source of acoustical noise,'' in *Proceedings of ASME2000*, Orlando, FL, November 2000.
[9] E. G. Williams, *Fourier Acoustics: Sound Radiation and Nearfield Acoustical Holography* (Academic, London, UK, 1999).
[10] E. G. Williams, B. H. Houston, P. C. Herdic, S. T. Raveendra, and Bryce Gardner, ''Interior nah in flight,'' J. Acoust. Soc. Am. **108**, 1451–1463 (2000).
[11] P. A. Nelson, ''Some inverse problems in acoustics,'' in *Proceedings of the 6th International Congress on Sound and Vibration*, Copenhagen, Denmark, July 1999, pp. 7–32.
[12] A. Kirsch, *An Introduction to the Mathematical Theory of Inverse Problems* (Springer-Verlag, New York, 1996).
[13] E. G. Williams, B. H. Houston, and P. C. Herdic, ''Reconstruction of the surface velocity and interior acoustic intensity from an aircraft fuselage using nah,'' in *Proceedings of the NOISE-CON96*, Seattle, WA, October 1996.
[14] G. H. Golub, M. Heath, and G. Wahba, ''Generalized cross-validation as a method for choosing a good ridge parameter,'' Technometrics **21**, 215–223 (1979).

Spatially extended sound equalization in rectangular rooms

Arturo O. Santillán[a)]
Department of Acoustic Technology, Technical University of Denmark, Building 352, DK-2800 Lyngby, Denmark

(Received 23 January 2001; revised 11 July 2001; accepted 12 July 2001)

The results of a theoretical study on *global* sound equalization in rectangular rooms at low frequencies are presented. The zone where sound equalization can be obtained is a continuous three-dimensional region that occupies almost the complete volume of the room. It is proved that the equalization of broadband signals can be achieved by the simulation of a traveling plane wave using FIR filters. The optimal solution has been calculated following the traditional least-squares approximation, where a modeling delay has been applied to minimize reverberation. An advantage of the method is that the sound field can be estimated with sensors placed in the limits of the equalization zone. As a consequence, a free space for the listeners can be obtained. [DOI: 10.1121/1.1401740]

PACS numbers: 43.55.Br, 43.60.Gk, 43.60.Pt [JDQ]

I. INTRODUCTION

The motivation of the presented study is the fact that sound reproduced in a normal listening room undergoes a spectral coloration. Since this implies a linear distortion of the reproduced sound, the effect is undesirable. Reducing the spectral coloration is particularly important at low frequencies in small enclosures, where the acoustic response of the listening space is dominated by distinct normal modes.

The equalization of the frequency response at one or several receiving points has been studied by several authors.[1–7] It has been shown that these systems can achieve a high performance at the exact receiving points; however, if the distance between the target positions is relatively large, the resulting zone of equalization becomes small spheres around each control point. Moreover, the size of this region scales with the wavelength. As a consequence, the resulting system is very sensitive to changes in the position of the listener's head.

The general objective of the work described in this paper has been to study the extent to which minimizing the acoustic response of a rectangular room is possible at low frequencies in an extended and continuous three-dimensional region. The underlying idea is that this zone should be as large as possible in order to include several listeners and allow for their movements. In addition, the error detection microphones should preferably be located at unintrusive positions.

In previous theoretical and experimental studies by Santillán[8,9] the effect of the acoustic response of the room has been minimized in an extended and continuous region. In these studies it was attempted to obtain the same signal (in amplitude and phase) in the entire target zone. However, one of the conclusions was that the zone where equalization can be achieved is limited to regions with dimensions not larger than half a wavelength of the reproduced sound.

In this paper a theoretical investigation on the equalization of sound in a continuous region that occupies almost the complete volume of a rectangular room is presented. The method is based on the simulation of a plane wave moving along the room. Experimental verification of the presented method has been obtained by Santillán and Lydolf.[10]

II. CONDITIONS FOR THE SIMULATION OF A TRAVELING PLANE WAVE

Consider a rectangular room, and a Cartesian coordinate system with its axes parallel to the sides of the room and the origin in one of the lower corners. The complex sound pressure amplitude p in steady state at any position $\mathbf{r}=(x,y,z)$ inside the room produced by L single sources can be described by[11]

$$p(\mathbf{r})=\frac{i\rho\omega}{V}\sum_{l=0}^{\infty}\sum_{m=0}^{\infty}\sum_{n=0}^{\infty}\frac{1}{\Lambda_{lmn}}\frac{1}{\mathbf{k}_{lmn}^2-k^2}\times\sum_{\mu=1}^{L}q_\mu\Psi_{lmn}(\mathbf{r}_\mu)\Psi_{lmn}(\mathbf{r}). \tag{1}$$

Here ω is the angular driving frequency, ρ is the ambient density, $V(=LxLyLz)$ is the volume of the room, Ψ_{lmn} is the mode shape, and $\mathbf{k}_{lmn}$ its complex eigenvalue, k is the wave number, Λ_{lmn} is a scaling factor, and q_μ is the strength of the μth source placed at the position $\mathbf{r}_\mu=(x_\mu,y_\mu,z_\mu)$. For a lightly damped room, the modes are roughly equal to[11]

$$\Psi_{lmn}(\mathbf{r})=\cos(l\pi x/L_x)\cos(m\pi y/L_y)\cos(n\pi z/L_z). \tag{2}$$

Assuming that the specific acoustic admittance β is uniform over the boundaries of the room, $\mathbf{k}_{lmn}^2$ can be approximated to first order as

$$\mathbf{k}_{lmn}^2\simeq(l\pi/L_x)^2+(m\pi/L_y)^2+(n\pi z/L_z)^2+2ik\beta(\epsilon_l/L_x+\epsilon_m/L_y+\epsilon_n/L_z), \tag{3}$$

where $\epsilon_j=2$ if $j=0$, and $\epsilon_j=1$ if $j>0$.

For the equalization of sound in the room, a plane wave propagating in the y direction is desired. Thus under the assumption that only the axial modes in the y direction are excited, Eq. (1) can be simplified as

a)Now at: Department of Acoustics, Aalborg University, Fredrik Bajers Vej 7 B4, DK-9220 Aalborg Ø, Denmark.

$$p(\mathbf{r})=\frac{i\rho\omega}{V}\sum_{m=0}^{\infty}\sum_{\mu=1}^{L}\frac{1}{\Lambda_m}\times\frac{q_\mu\cos(m\pi y_\mu/L_y)\cos(m\pi y/L_y)}{(m\pi y/L_y)^2+2ik\beta(1/L_x+1/L_y+1/Lz)-k^2}. \quad (4)$$

With the condition that there are N sound sources on the wall at $y=0$ and $L-N$ sound sources on the wall at $y=L_y$, and introducing $\mathbf{k}^2=k^2-2ik\beta(1/L_x+1/L_x+1/L_x)$, Eq. (4) can be written as

$$\begin{aligned}p(\mathbf{r})&=\sum_{m=0}^{\infty}\frac{\rho}{V\Lambda_m}\frac{-i\omega}{\mathbf{k}^2-(m\pi/L_y)^2}\sum_{\mu=1}^{N}q_\mu\cos(m\pi y/L_y)\\&+\sum_{m=0}^{\infty}\frac{\rho}{V\Lambda_m}\frac{-i\omega}{\mathbf{k}^2-(m\pi/L_y)^2}\times\sum_{\alpha=N+1}^{L}q_\alpha(-1)^m\cos(m\pi y/L_y)\\&=-\frac{i\omega\rho}{2L_xL_z}\frac{1}{\mathbf{k}\sin(\mathbf{k}L_y)}\left[e^{i\mathbf{k}y}\left(\sum_{\alpha=0}^{N}q_\alpha e^{-i\mathbf{k}L_y}+\sum_{\beta=N+1}^{L}q_\beta\right)+e^{-i\mathbf{k}y}\left(\sum_{\alpha=0}^{N}q_\alpha e^{i\mathbf{k}L_y}+\sum_{\beta=N+1}^{L}q_\beta\right)\right],\end{aligned} \quad (5)$$

where use has been made of the following relations:

$$\begin{aligned}\sum_{m=0}^{\infty}\frac{1}{\Lambda_m}\frac{1}{\mathbf{k}^2-(m\pi/L_y)^2}\cos(m\pi y/L_y)&=L_y\frac{\cos[\mathbf{k}(L_y-y)]}{\mathbf{k}\sin(\mathbf{k}L_y)},\\\sum_{m=0}^{\infty}\frac{1}{\Lambda_m}\frac{(-1)^m}{\mathbf{k}^2-(m\pi/L_y)^2}\cos(m\pi y/L_y)&=L_y\frac{\cos(\mathbf{k}y)}{\mathbf{k}\sin(\mathbf{K}L_y)}.\end{aligned} \quad (6)$$

These Fourier expansions are valid from $y=0$ to $y=2L_y$ for the first expression and from $y=-L_y$ to $y=L_y$ for the second one.

Since the condition $p(\mathbf{r})=P_\alpha e^{-i\mathbf{k}y}$, where P_α is a constant, should be satisfied to simulate a plane wave propagating in the y direction, the coefficient of $e^{i\mathbf{k}y}$ in Eq. (5) has to be zero. This implies that

$$\sum_{\beta=N+1}^{L}q_\beta=-e^{-i\mathbf{k}L_y}\sum_{\alpha=0}^{N}q_\alpha. \quad (7)$$

From the theoretical results above, it can be seen that to simulate a plane wave traveling in the y direction, only the y-axial modes should be excited and, according to Eq. (7), the sound sources on the wall $y=L_y$ should move in antiphase with the sound pressure on that wall.

On the other hand, it should be noticed that the results above are independent of the number of sound sources, the individual values of their strengths, and the position of the sources in the x and z coordinates on the walls at $y=0$ and $y=L_y$. Consequently, these factors can be used to avoid exciting the modes with l or n different from zero.

In a real situation, a good approximation to the conditions needed to simulate a traveling plane wave can be obtained at low frequencies, where relatively few modes contribute significantly to the generated sound pressure. Therefore, the excitation of the undesired modes can be reduced significantly at low frequencies by an appropriate choice of the number of loudspeakers, their position and their strength.

In the next sections, the simulation of the sound equalization in a real situation is analyzed by using a modal model of the sound field in a rectangular room. It should be observed that since only the axial y-modes should be excited, the sound equalization will be practically independent of the length L_y of the room.

III. EQUALIZATION AT SINGLE FREQUENCIES

To analyze the fundamental physical limitations and to visualize the spatial distribution of the sound pressure level, the study of the sound equalization has been complemented in the frequency domain.

A. Optimal solution

For a given distribution of loudspeakers in the room, the optimal solution is obtained by minimizing the difference between the actual sound field that is produced in the listening zone and the desired sound field. For this purpose, the traditional least-squares approximation has been used to calculate the optimal strength of the loudspeakers. This method has been presented by Elliot *et al.*[12] and by Asano and Swason.[13] Thus following the so-called multiple-point method, the actual sound field is estimated by means of M receiver positions in the listening zone. The error e_m at the mth receiving position $\mathbf{r}_m$ is given by

$$e_m=p(\mathbf{r}_m)-p_d(\mathbf{r}_m)=\sum_{l=1}^{L}Z_l(\mathbf{r}_m)q_l-p_d(\mathbf{r}_m), \quad (8)$$

where the complex amplitude of the actual sound pressure $p(\mathbf{r}_m)$ at the receiver position m has been expressed in terms of the individual strength q_l of each of the L sound sources and the transfer impedances Z_l from the lth source to the mth receiving point; $p_d(\mathbf{r}_m)$ is the desired complex sound pressure at that point.

To obtain the best solution for the sound equalization, the cost function

$$J=\frac{1}{M}\sum_{m=1}^{M}|e_m|^2=\frac{1}{M}\sum_{m=1}^{M}|p(\mathbf{r}_m)-p_d(\mathbf{r}_m)|^2 \quad (9)$$

is minimized. Thus this cost function can be expressed in a quadratic form in terms of the individual strengths of the L sound sources. It has been shown that the cost function has a unique global minimum, which corresponds to the optimal solution.

B. Conditions for the simulations

A room with dimensions $L_x=2.7$ m, $L_y=5.0$ m, and $L_z=2.5$ m has been considered for the example presented in this paper. All the modes, axial, tangential, and oblique, with a natural frequency up to 1000 Hz (3846 modes) were used to simulate the sound pressure. The damping ratio was as-

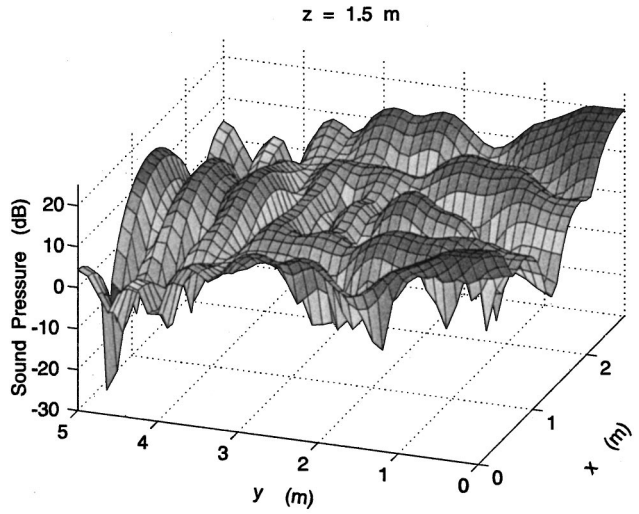

FIG. 1. Amplitude of the sound pressure before equalization for a driving frequency of 300 Hz. The graph corresponds to the sound field in the plane $z=1.5$ m produced by two loudspeakers placed at (0.05,0,2.00) and (2.65,0,2.00) m, respectively.

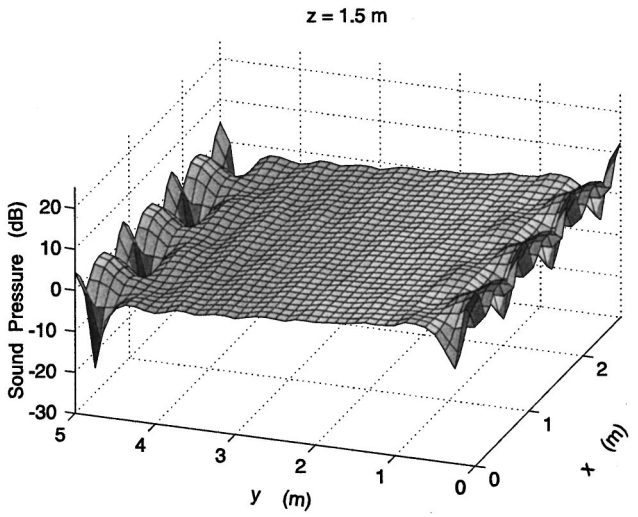

FIG. 2. Optimal equalization in the frequency domain for a driving frequency of 300 Hz. The sound pressure level in the plane $z=1.5$ m is shown.

sumed equal to 0.03 for all the modes; this value corresponds to a reverberation time of approximately 0.2 s at frequencies around 180 Hz. The loudspeakers were modeled as square pistons with a side length of 0.1 m. The value of the sound speed was 346.4 m/s, for an ambient temperature of 25 °C.

C. Distribution of loudspeakers

It was found out that in order to excite mainly the axial modes in the y direction and reduce significantly the amplitude of the other modes, the loudspeakers should be placed equidistantly in the x and the z directions on each of the two walls perpendicular to the y axis. In addition, to minimize the reflection of sound on the surface at $y=L_y$, a condition expressed by Eq. (7), the same number of loudspeakers should be used in each of those two walls.

For the simulations shown below, a number of 16 loudspeakers were placed on each wall perpendicular to the y axis. The 16 loudspeakers in each set were distributed in 4 horizontal lines at the heights $z=0.05$ m, $L_z/3$, $2L_z/3$, and $L_z-0.05$ m, respectively; four loudspeakers in each horizontal line with their respective centers at the coordinates $x=0.05$ m, $L_x/3$, $2L_x/3$, and $L_x-0.05$ m.

D. Spatial distributions of the sound field

The spatial distributions of the sound pressure amplitude in the enclosure before and after equalization for a pure tone of 300 Hz are presented as an example. Before equalization, the sound field in the room was assumed to be produced by two loudspeakers fed with the same input signal. The positions of these loudspeakers are, respectively, (0.05,0,2.00) m and (2.65,0,2.00) m. The amplitude of the sound field in the plane $z=1.5$ m before equalization is shown in Fig. 1. It can be seen that the sound pressure amplitude depends on the position inside the room. The graph of Fig. 1 can be compared with the distribution of the sound pressure amplitude in the same plane after sound equalization, which is depicted in Fig. 2. It can be observed in this figure that the sound pressure amplitude is almost constant in nearly the entire plane with exception of the region close to the walls perpendicular to the y direction. The deviations of the obtained sound pressure amplitude from the desired value were relatively high within a distance of about 0.6 m from the sound sources though. It was found out that this distance of about 0.6 m where a good sound equalization cannot be achieved is practically independent of the reproduced frequency; therefore, the listening zone was assumed as the region from 0.6 m up to 4.4 m in the y direction that occupies all the width L_x of the room and from the floor to the ceiling. The sensor positions for the calculation of the optimal equalization were placed only inside the listening zone equidistantly distributed. The number of these sensor positions was $7\times12\times7$ (588 in total); this means that the sensor positions were arranged in 7 horizontal planes, with 12 lines parallel to the x direction in each plane, and 7 sensors in each of these lines. A good estimation of the sound field can be obtained with fewer sensor positions; however, such a number was used to reduce the error in the estimation of the sound field as much as possible. The amplitude of the desired sound pressure was set to unity at each sensor position; the phase depended on the position in the y direction of the error sensor corresponding with a plane traveling wave.

It should be mentioned that after equalization the sound pressure level in the listening zone was practically independent of the z direction; the spatial distribution of the sound field in any plane xy was basically the same as the one shown in Fig. 2.

E. Values of the least-squares error

To evaluate the results of the sound equalization, the square root of the minimum value of the cost function, given by Eq. (9), has been used. In what follows, this parameter is called the least-squares error (E_{LS}). It was observed that if the value of E_{LS} was less than 0.3 in the presented example, the deviations of the sound pressure from the desired value were within ±3 dB in almost the entire listening zone. Thus the condition $E_{\mathrm{LS}}<0.3$ has been used here as a criterion for

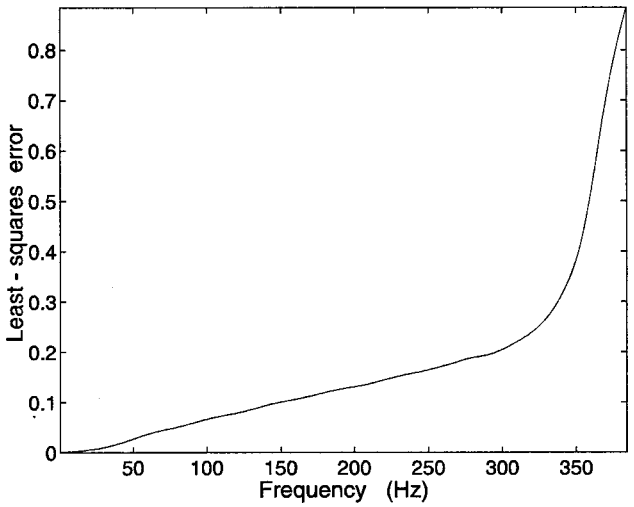

FIG. 3. The least-squares error as a function of the driving frequency for the sound equalization by simulating a plane wave moving in the *y* direction.

a good sound equalization. The least-squares error as a function of the frequency for the considered example is shown in Fig. 3. It can be seen in this figure that the least-squares error increases with increasing frequency, and that the maximum frequency that can be equalized properly is around 343 Hz.

IV. SOUND EQUALIZATION OF RANDOM SIGNALS

Since echoes are undesirable in the reproduction of transient signals, the duration of the impulse response in the listening zone should be minimized. For this reason a modeling delay has been used to approximate the impulse response in the listening zone to a delayed delta function.[14] As a plane wave traveling in the *y* direction is desired to be simulated, the length of the delay depends on the ordinate of the listening position corresponding with the propagation of the plane wave.

A. Optimal solution

A matrix formulation for the reproduction of sound in a least-squares sense has been developed by Nelson *et al.*;[4,14] this formulation has been followed for the equalization of broadband signals in the work presented in this paper. A block diagram of the equalization problem is depicted in Fig. 4. Here the input signal is reproduced by using L loudspeakers. The sound field in the listening zone is represented by M sample signals measured with M microphones. The aim is to design L digital FIR filters with impulse responses $h_l(n)$, one for each sound source, such that the obtainable signal $d'_m(n)$ at the microphone m is the best approximation to the

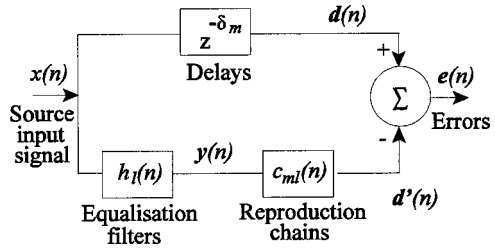

FIG. 4. Block diagram of the equalization problem of broadband signals.

desired signal $d_m(n)$ at that sensor. Here $d_m(n)$ is a delayed version (δ_m samples) of the original input signal $x(n)$ (modeling delay). This procedure has been discussed by Elliott *et al.*[2] In Fig. 4, $\mathbf{y}(n)$ is the vector of input signals to the L sound sources, $\mathbf{d}'(n)$ is the vector of the M actual signals at each of the microphones, $\mathbf{d}(n)$ is the vector of the M desired signals, and $c_{ml}(n)$ is the electroacoustic impulse response from the input to the lth source to the output of the mth sensor. It is assumed that these impulse responses can be accurately modeled as FIR digital filters with J coefficients. In addition, the equalization filters will have a FIR structure as well with I coefficients.

The optimal coefficients of these filters are determined by minimizing a performance index defined by[2,12]

$$\Gamma = E\left\{\sum_{m=1}^{M} e_m(n)^2\right\} = E\{\mathbf{e}(n)^T\mathbf{e}(n)\}, \tag{10}$$

where E represents the expectation operator, and $e_m(n) = d_m(n) - d'_m(n)$. It has been shown that the performance index can be expressed as a quadratic function in terms of all the individual coefficients in the equalization filters. It has also been concluded that it has a unique global minimum value, which corresponds to the optimal control filter coefficients.

B. Conditions for the simulations

It should be noticed that by minimizing the performance error defined in Eq. (10), the optimal solution in statistical sense is calculated. Thus considering that the desired signal is a delayed version of the source input signal, for the described method the only required information on the source input signal is the autocorrelation function. In the simulations that were carried out, an input signal with a delta function as the autocorrelation function has been assumed. It should be noticed, however, that the input signal has to be low-filtered in order to avoid the aliasing effect. For the simulations, the sampling frequency was equal to 770 Hz. The loudspeakers were modeled as first-order analog high pass filters with one pole at 100 Hz.

The classical modal reconstruction model was used to calculate the discrete electroacoustic impulse responses $c_{ml}(n)$. The conditions for the computer simulations are the same described in Sec. II B and in Sec. II C. First, the frequency response functions from the input to each loudspeaker to the output of each sensor were calculated with the modal model. These frequency response functions were multiplied by the frequency response of the antialiasing filter and by the frequency response of the loudspeakers. Eventually, an inverse FFT was applied to obtain the desired discrete impulse responses $c_{ml}(n)$. An FIR filter with 400 coefficients was used to represent each of the impulse responses $c_{ml}(n)$. It was observed that the results of the equalization were highly dependent on the minimization of the aliasing effect. Therefore, a 14th-order analog low pass Butterworth filter with a cutoff frequency of 260 Hz was applied.

It has been found out that the best simulation of the plane wave moving across the room was obtained by placing the error sensors in two planes perpendicular to the direction

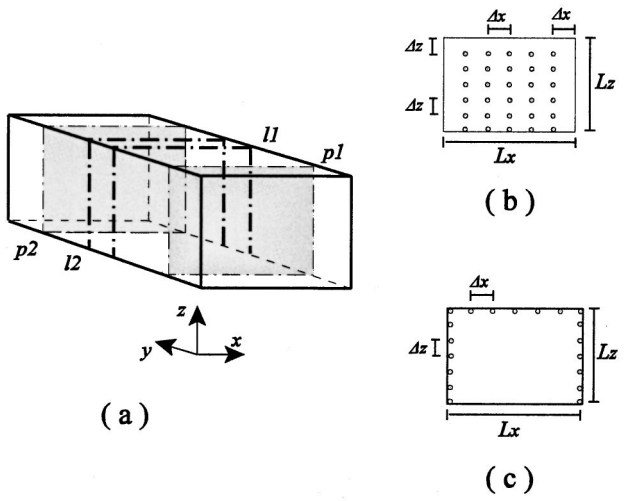

FIG. 5. Diagram of the distribution of the error sensors. These sensors were placed in two planes, indicated by *p1* and *p2* in (a), and along two lines on the walls and the ceiling of the room, denoted by *l1* and *l2*. In each plane there were 30 sensors arranged as shown in (b). The distribution of the sensors along the lines is depicted in (c). The distance between two adjacent sensors were $\Delta x = 0.45$ m and $\Delta z = 0.41$ m.

of propagation of this wave. These two planes should be separated from each other by the distance that the sound travels during one sampling period. In addition, the error in the simulation is reduced if these planes are located close to the middle of the room.

The reason to place the sensor positions very close to each other in the direction of propagation of the simulated wave is the following one: the simulation of a traveling plane wave cannot be carried out appropriately if the distance between two error sensor positions in the direction of propagation of the plane wave is equal to multiples of half a wavelength of the sound to be simulated. In this case the delays applied in the original input signal to obtain the desired signals at those sensors will produce a difference in phase between those two desired signals equal to multiples of pi radians. However, this difference in phase is the same as the one that corresponds to a stationary wave at the two sensor positions. As a consequence, a standing wave pattern will result in the obtained sound field at those frequencies.

Since a free listening zone was desired, the sensor positions should be placed as close as possible to the limits of the listening zone. An appropriate distribution that corresponds to the example presented in the paper is as follows: 19 sensors placed in each of two lines parallel to each other on the walls and the ceiling, one line at $y = 2.73$ m and the other at $y = 3.18$ m. In addition, 30 sensors placed in a plane at $y = 0.93$ m and other 30 sensors on a plane at $y = 4.08$ m. A diagram illustrating the distribution of these 98 sensor positions is shown in Fig. 5. The distances between to adjacent sensors were equal to 0.45 m in the x direction and 0.41 m in the z direction. It was found that, in general, the distance in the x and in the z directions between two adjacent microphones should be less than half a wavelength of the frequency to be equalized. It should be pointed out that an alternative to reduce the number of the error sensors was not analyzed. A possibility is to consider the symmetries in the problem.

A delay of 18 samples was applied to obtain the desired signal for all the sensors placed in the plane at $y = 0.93$ m. Additional delays of four, five, and seven samples were used for the sensors in the two lines in the middle of the room and in the second plane. These additional delays are equal to the time that the simulated plane wave should take to travel from the plane $y = 0.93$ m to reach the corresponding error sensor positions.

C. Impulse and frequency responses before and after equalization

The impulse and frequency responses at four positions in the listening zone before and after equalization are shown in Fig. 6. In this case the sound equalization was carried out with the error sensor positions placed in the limits of the listening zone as described above. The original impulse and frequency responses include the effect of the antialiasing filter, and the impulse responses after equalization are shown with an offset of -2 units in the y axis for clarity. These four positions are different from the locations of the error sensors. Before equalization the sound field was assumed to be produced by two loudspeakers fed with the same input signal and placed, respectively, at the positions (0.05,0,2.0) m and (2.65,0,2.0) m, as in the previous sections. A number of 100 coefficients were used in each of the control filters.

It can be seen in Fig. 6 that the frequency responses have been significantly improved after equalization. The peaks and troughs in the curves without equalization were practically removed after applying the control filters. Thus the frequency responses became approximately flat from about 20 Hz to approximately 340 Hz. In this frequency interval, the deviations from the desired value of 0 dB are within approximately ± 3 dB. It should be noticed that the peaks and troughs in the frequency responses that are not common to all the different error sensor positions can be successfully suppressed, in contrast to the case of sound equalization at discrete points, where only the common peaks and troughs can be removed. It can also be observed in the graphs of Fig. 6 that the impulse responses approximate quite well a delayed delta function. The echoes have been reduced significantly. It can be seen that the delays in the obtained impulse responses after equalization are not the same for the shown positions, but the delay depends on the value of the ordinate of the position according to the simulated plane progressive wave. It should be mentioned that the results at any other position in the listening zone are very similar to the ones shown in Fig. 6.

D. Results of the sound equalization in terms of the least-squares error

To evaluate the results of the sound equalization in terms of the frequency and the spatial distribution of the sound pressure in the listening zone, the impulse responses of the optimal control filters that produced the results of Fig. 6 were transformed to the frequency domain. Thus the frequency responses of the optimal filters were used in Eq. (9) to cal-

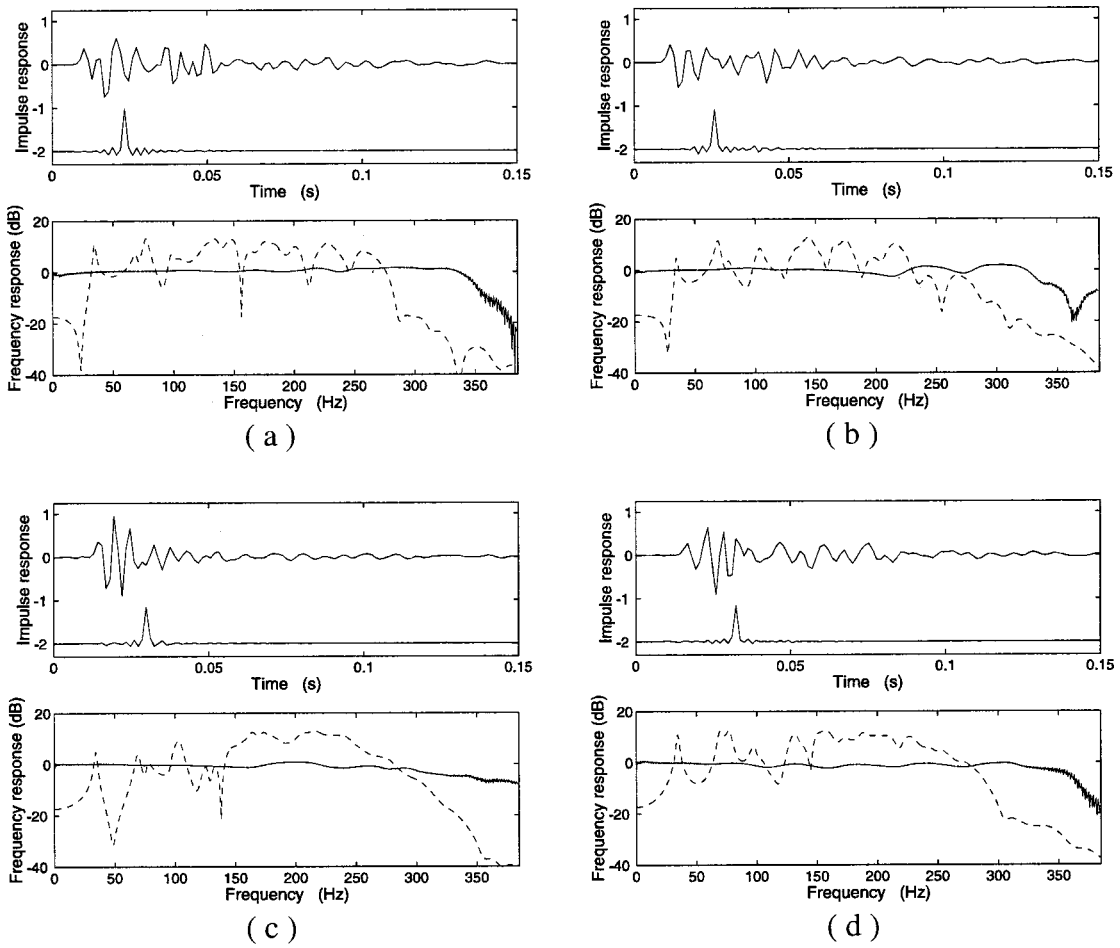

FIG. 6. Impulse and frequency responses at four different positions before and after sound equalization, (a) (0.3,0.9,0.3) m, (b) (1.0,1.8,0.9) m, (c) (1.7,3.2,1.5) m, (d) (2.4,4.1,2.2) m. The impulse response after equalization is shown with an offset of minus two units in the *y* axis for clarity. The solid lines in the frequency response represent the results after equalization and the dashed lines correspond to the results before equalization, which include the response of the antialiasing filters.

culate the least-squares error as a function of the frequency. In this calculation only the amplitude of the sound pressure was taken into account; the error at the *m*th receiver was defined as $e_m = |p(\mathbf{r}_m)| - |p_d(\mathbf{r}_m)|$ instead of Eq. (8). A number of $7 \times 12 \times 7$ sensor positions in listening zone were used to approximate the sound field in the complete three-dimensional region. The resulting cost function is depicted in Fig. 7, where the curve of Fig. 3, which corresponds to the equalization in the frequency domain, is included for comparison. The sound equalization was also carried out with the error sensor positions placed in two parallel planes in the middle of the room, 49 sensor positions in each plane. The graph of the least-squares error calculated for this case is shown as well in Fig. 7.

As it can be seen in Fig. 7, the results of sound equalization obtained with the error sensors placed in two planes in the middle of the room are very similar to the results of the equalization carried out in the frequency domain for frequencies higher than approximately 20 Hz. The least-squares error was higher with the error sensor positions near the limits of the listening zone. Two are the main causes for the higher error in this case: (1) a part of the effort of the control filters is used on trying to reduce the error at these sensor positions at the expense of degrading the sound field in the rest of the listening zone; (2) the sound field cannot be estimated properly around certain frequencies due to the distribution of the error sensors as mentioned in Sec. IV B. The second reason contributes more to the relatively high values of the least-squares error at the frequencies around 110 Hz, 165 Hz, and 220 Hz. Here the distance between the two planes with the error sensor positions (4.08 m–0.93 m) is equal to multiples of half a wavelength at those frequencies.

It might be worth placing the error sensors in the limits of the equalization zone. An adaptive algorithm can be implemented since the error sensors are unobtrusive for the listeners. For a particular application, it should be investigated whether it is advantageous to implement the system adaptively. If only a single adjustment during the installation of the audio system is sufficient to achieve a good equalization and then the control filters are held fixed, the obvious position of the error sensors will be in two planes in the middle of the enclosure.

According to Fig. 7, the equalization of the broadband signal is affected at frequencies lower than approximately 15 Hz in comparison to the results from the frequency domain. The reason might be the assumed poor response of the loudspeakers at that frequency range. However, this is not a problem in practice since these frequencies are not audible.

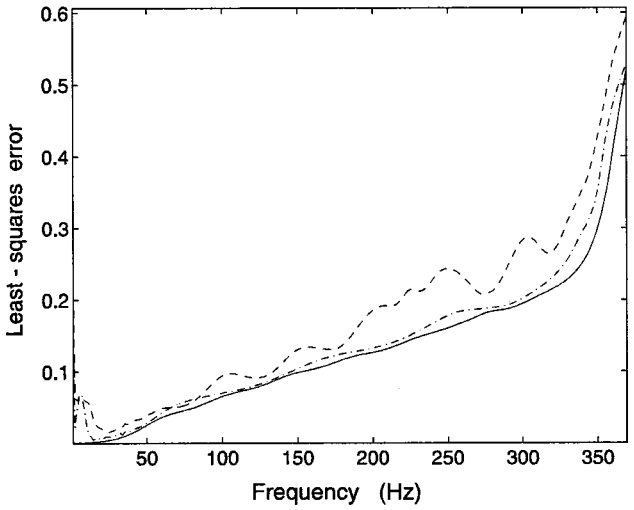

FIG. 7. Least-squares error as a function of the frequency for the sound equalization carried out in the time domain with the sensors placed near the limits of the listening zone (--) and the sensors placed in the middle of that zone (-·-). The results obtained in the frequency domain are shown for comparison (solid line).

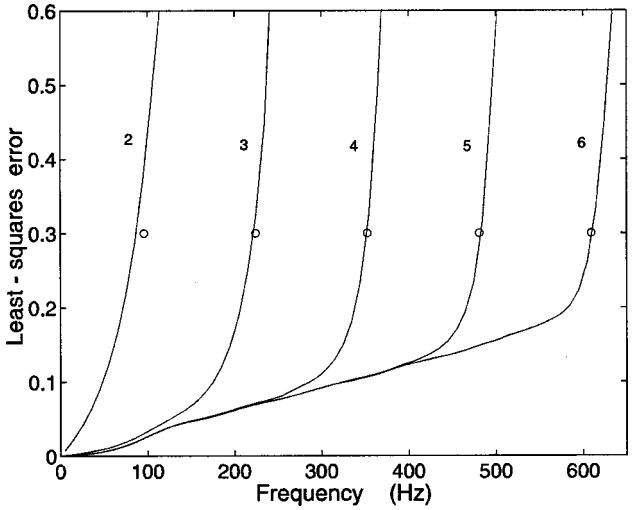

FIG. 9. Least-squares error as a function of the frequency corresponding to different numbers of loudspeakers used in the sound equalization in the frequency domain. The numbers in the figure indicate the total of loudspeakers placed on the wall at $y=0$, and the small circles are predicted values calculated from the distance in the x direction between adjacent sound sources.

The highest value of the least-squares error in the case where the error sensors were placed near the limits of the equalization zone occurred approximately at 300 Hz as can be seen in Fig. 7. Here the least-squares error is equal to 0.29, which is slightly lower than the considered limit of the criterion for a good equalization. The distribution of the sound pressure amplitude in the plane $z=1.5$ m for a driving frequency of 300 Hz after the equalization with the sensor positions in the limits of the listening zone is depicted in Fig. 8. It can be noticed that several dips in the spatial distribution of the sound pressure level appeared along the y direction for this particular frequency. The distance between two adjacent dips is equal to half a wavelength, and therefore, this suggests that the reflection of acoustic energy on the wall at the end of the room was not sufficiently reduced. A very similar graph is obtained if another plane xy is chosen instead of $z=1.5$ m.

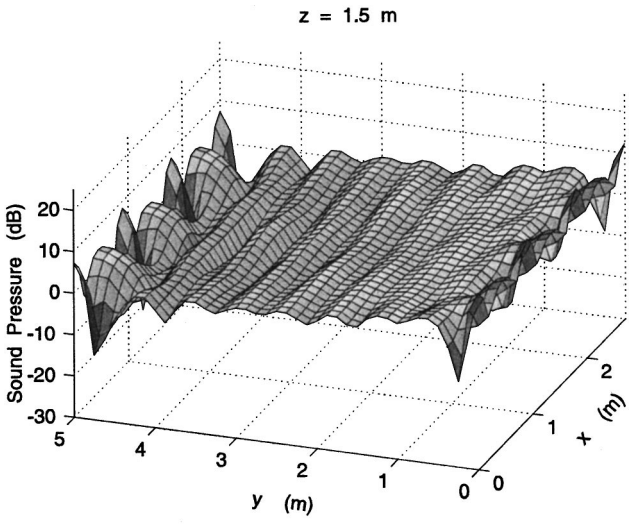

FIG. 8. Distribution of the sound pressure level at the frequency of 300 Hz after sound equalization in the time domain using random noise as the input signal. The result is shown in the plane $z=1.5$ m.

The graph of Fig. 8 can be compared with the graph of the spatial distribution of the sound pressure amplitude at the same frequency before equalization, which is shown in Fig. 1. It can be observed that the spatial distribution of the sound field has been considerably improved after equalization using a broadband signal.

V. NUMBER OF LOUDSPEAKERS AND THE CONTROL OF MODES

To discuss the relation between the number of loudspeakers and the maximum frequency that can be equalized, a two-dimensional problem is considered first for simplicity. An enclosure with dimensions $L_x=2.7$ m, $L_y=3.0$ m, and $L_z=0.15$ m has been used, and a plane wave moving in the y direction has been simulated.

It was found out that, as a first approximation, the maximum frequency that can be equalized is given by

$$f_{\max}=c/d-\Delta_\epsilon, \tag{11}$$

where c is the sound speed, d is the distance in the x direction between two adjacent loudspeakers, and Δ_ϵ is a number that depends on the damping of the room.

The curves of the least-squares error corresponding to different numbers of loudspeakers are plotted as a function of the driving frequency in Fig. 9. The number close to each curve indicates the total of sound sources placed on the wall at $y=0$. The curves in this figure were obtained by minimizing the cost function of Eq. (9) in the frequency domain. A number of $8\times15\times3$ error sensor positions within the equalization zone were used. With the criterion $E_{\mathrm{LS}}<0.3$, the value of Δ_ϵ was determined to be equal to 32 Hz. In this way, the frequencies given by $f_{\max}=c/d-32$ Hz for the different numbers of loudspeakers are plotted by circles in Fig. 9. It can be seen in this figure that each of these circles are

very close to the point in the corresponding curve for which $E_{LS}=0.3$. Thus there is a good agreement between the value of the maximum frequency that can be equalized obtained by minimizing the cost function and the value calculated by using $f_{max}=c/d-32$ Hz.

With the used arrangement of loudspeakers, the filtered signals fed to each of the sound sources at $y=0$ are practically in phase to each other. This fact together with Eq. (11) indicate that the mode with a wavelength equal to the distance between two adjacent sound sources is the mode with $l\neq 0$ whose excitation cannot be reduced significantly and that has the lowest frequency. In this case the loudspeakers are placed at the positions where the oscillations of the mode have the maximum amplitude and the same phase. Thus the loudspeakers are coupled very efficiently to that mode. When the difference between the driving frequency and the frequency of the mode is less than Δ_ϵ, the contribution of this mode becomes significant.

An analog situation occurs for a three-dimensional case. The results of the sound equalization in the vertical direction are mainly affected by the modes with $n\neq 0$ that contribute significantly to the produced sound field. Thus the mode with $n\neq 0$ that has the lowest frequency and whose excitation cannot be reduced appropriately corresponds to a wavelength equal to the distance in the z direction between two adjacent sound sources.

For the simulations presented in the previous sections, the value of Δ_ϵ is 40 Hz. Since the distance between two adjacent loudspeakers in the x direction (0.90 m) was larger than the distance in the z direction (0.83 m), the maximum frequency that can be equalized according to Eq. (11) is $f_{max}=c/0.90\ \text{m}-40\ \text{Hz}=345$ Hz.

VI. DISCUSSION

It has been shown that the simulation of a progressive plane wave moving along a rectangular room is possible. If all the walls are covered with loudspeakers, the presented method can be adapted to simulate plane waves in an arbitrary horizontal direction. Moreover, the simulation of cylindrical waves might be possible as well. Thus the method can be considered as an implementation of wave field synthesis. However, the system will become more complicated since more loudspeakers are required and more error sensor positions will probably be needed.

The possibility to simulate plane waves moving in any desired horizontal direction and cylindrical waves in a rectangular room has been shown theoretically based on computer simulations in the frequency domain by Santillán *et al.*[15]

It should be mentioned that the purpose in the research described in the paper has not been as demanding as to give the listener the perception of direction, but to compensate for the undesired spectral coloration and reverberation in an extended region inside rectangular rooms at low frequencies.

VII. CONCLUSIONS

According to the results presented in this paper, it can be concluded that a good sound equalization at low frequencies can be achieved by the simulation of a traveling plane wave in a rectangular room. The sound equalization can be obtained in a continuous three-dimensional region that occupies almost the complete volume of the room. It has been proved that the equalization of random signals is possible, and that the duration of the impulse response in the listening zone can be reduced significantly. In this way, the impulse response at any point in this zone can be approximated to a delayed delta function.

It has also been shown that the equalization of broadband signals can be achieved with the error sensors placed near the limits of the equalization zone. As a consequence, a free space for the listeners and their movements is obtained.

The number of loudspeakers that are needed for the studied method of sound equalization is, however, relatively large. Since the maximum frequency that can be equalized depends on the distance between two adjacent loudspeakers, more sound sources are required for the equalization of higher frequencies or larger rooms.

ACKNOWLEDGMENTS

The author would like to thank Professor Finn Jacobsen for a number of very useful discussions and suggestions. The work was supported by the Dirección General de Asuntos del Personal Académico, Universidad Nacional Autónoma de México.

[1] M. Miyoshi and Y. Kaneda, "Inverse filtering of room acoustics," IEEE Trans. Acoust., Speech, Signal Process. **36**, 145–152 (1988).
[2] S. J. Elliott and P. A. Nelson, "Multiple-point equalization in a room using adaptive digital filters," J. Audio Eng. Soc. **37**, 899–907 (1989).
[3] S. J. Elliott, L. P. Bathia, F. S. Deghan, A. H. Fu, M. S. Stewart, and D. W. Wilson, "Practical implementation of low-frequency equalization using adaptive digital filters," J. Audio Eng. Soc. **42**, 988–998 (1994).
[4] P. A. Nelson, F. Orduña-Bustamante, and H. Hamada, "Inverse filter design and equalization zones in multichannel sound reproduction," IEEE Trans. Speech Audio Process. **3**, 185–192 (1995).
[5] R. Walker, "Equalization of room acoustics and adaptive systems in the equalization of small room acoustics," Proceedings of AES 15th International Conference, *Audio, Acoustics & Small Spaces*, October 31–November 2, 1998, Snekkersten, Copenhagen, Denmark (Audio Engineering Society, 1998), pp. 32–47.
[6] O. Kirkeby and P. A. Nelson, "Digital filter design for inversion problems in sound reproduction," J. Audio Eng. Soc. **47**, 583–595 (1999).
[7] F. Asano, Y. Suzuki, and T. Sone, "Sound equalization using derivative constraints," Acustica **82**, 311–320 (1996).
[8] A. O. Santillán, "Active equalization of the sound field in an extended region inside a room," Proc. 5th Int. Congress on Sound and Vibration, University of Adelaide, South Australia, December 15–18, 1997, edited by C. H. Hansen and G. Vokalek (International Institute of Acoustics and Vibration, South Australia, 1997), pp. 287–294.
[9] A. O. Santillán, "Experimental low-frequency sound equalization in an extended region of an enclosure using adaptive filters," Proc. 104th Convention Audio Eng. Soc., prep. No. 4755 (1998).
[10] A. O. Santillán and M. Lydolf, "Use of FIR filters to extend the frequency range in a test chamber for low-frequency noise and infrasound exposure," *Proceedings of the 2001 International Congress and Exhibition on Noise Control Engineering* (Inter-Noise 2001), The Hague, The Netherlands, August 27–30, 2001 (Nederlands Akoestisch Genootschap (NAG), The Netherlands, 2001), pp. 2179–2182.
[11] P. M. Morse and K. U. Ingard, *Theoretical Acoustics* (McGraw-Hill, New York, 1968).
[12] S. J. Elliott, I. M. Stothers, and P. A. Nelson, "A multiple error LMS

algorithm and its application to the active control of sound and vibration,'' IEEE Trans. Acoust., Speech, Signal Process. **35**, 1423–1434 (1987).
[13] F. Asano and D. C. Swason, ''Sound equalization in enclosures using modal reconstruction,'' J. Acoust. Soc. Am. **98**, 2062–2069 (1995).
[14] P. A. Nelson, F. Orduña-Bustamante, and H. Hamada, ''Multichannel signal processing techniques in the reproduction of sound,'' J. Audio Eng. Soc. **44**, 973–989 (1996).
[15] A. O. Santillán, M. Uchiyama, and M. Tohyama, ''Sound field control in a rectangular room at low frequencies to simulate the sound radiated by a virtual source,'' Technical Reports IEICE, **98**, 53–60 (1999).

Low-frequency echo-reduction and insertion-loss measurements from small passive-material samples under ocean environmental temperatures and hydrostatic pressures

Jean C. Piquette and Stephen E. Forsythe
Naval Undersea Warfare Center, Division Newport, 1176 Howell Street, Newport, Rhode Island 02840

(Received 26 April 2001; accepted for publication 18 July 2001)

System L is a horizontal tube designed for acoustical testing of underwater materials and devices, and is part of the Low Frequency Facility of the Naval Undersea Warfare Center in Newport, Rhode Island. The tube contains a fill fluid that is composed of a propylene glycol/water mixture. This system is capable of achieving test temperatures in the range of −3 to 40 deg Centigrade, and hydrostatic test pressures in the range 40 to 68 950 kPa. A unidirectional traveling wave can be established within the tube over frequencies of 100 to 1750 Hz. Described here is a technique for measuring the (normal-incidence) echo reduction and insertion loss of small passive-material samples that approximately fill the tube diameter of 38 cm. (Presented also is a waveguide model that corrects the measurements when the sample fills the tube diameter incompletely.) The validity of the system L measurements was established by comparison with measurements acquired in a large acoustic pressure-test vessel using a relatively large panel of a candidate material, a subsample of which was subsequently evaluated in system L. The first step in effecting the comparison was to least-squares fit the data acquired from the large panel to a causal material model. The material model was used to extrapolate the panel measurements into the frequency range of system L. The extrapolations show good agreement with the direct measurements acquired in system L. [DOI: 10.1121/1.1402115]

PACS numbers: 43.58.Vb, 43.20.Fn, 43.20.Ye, 43.58.Bh [SLE]

I. INTRODUCTION

The normal-incidence echo reduction and insertion loss are quantities that are often needed to characterize the performance of passive acoustical materials such as absorbers, decouplers, and acoustic windows. These are often determined in a panel test.[1] Unfortunately as test frequency is lowered, panel size must be increased in order to avoid the disturbing influence of waves originating at the panel edges. For example, conventional panel measurements, as conducted in the Acoustic Pressure Tank Facility (APTF) of the Naval Undersea Warfare Center, Newport, RI (NUWC) are typically limited to frequencies above 10 kHz for samples of 76×76-cm (30×30-in.) lateral dimensions. The lower-frequency limit for panels of this size is reduced to about 3400 Hz if the ONION method is used.[2] However, frequencies even lower than this are often of interest. Panel tests generally must be excluded as test frequency is lowered significantly, owing to the high cost of fabricating large samples and the inability of existing test facilities to accommodate large samples. For example, APTF is limited to panels less than 1.8 m on a side in order that the panel can fit through the facility access port. Even for a panel of this size, tested using conventional methods, the low-frequency limit for echo reduction is about 2 kHz and that for insertion loss is about 3 kHz. The ONION method would only extend the low-frequency cutoff to about 1.5 kHz for both measurements.

An obvious way to attain lower frequencies without increasing sample size is to conduct tests in a rigid-walled tube, such as an impedance or pulse tube.[3] However, such methods, which typically utilize pulsed sound, usually obtain only the echo reduction, not the insertion loss. Such methods also often involve backing the sample with some other material in order to avoid the influence of unwanted reflections from the tube end. Hence, the echo reduction that is measured in this manner is characteristic not only of the sample under test, but also of the backing material. As frequency is lowered significantly the methods employed in pulse tubes clearly become inapplicable, especially once the wavelength in the tube fill fluid exceeds the tube length.

An alternative kind of rigid-walled-tube-based measurement is considered here. System L, one of a group of rigid-walled tubes available for acoustic testing (under ocean environmental conditions of temperature and hydrostatic pressure) at NUWC, has the capability to create a unidirectional traveling wave in steady state. (This is accomplished through the use of active terminations of the tube, thus simulating a tube of infinite length.) Hence, it is possible to place a sample of interest near the tube's center and to test the sample without needing to back the sample in some special way. If desired, the sample can be affixed to a backing plate, or the intrinsic properties of a nonbacked sample can be tested instead.

A description of system L is given in Sec. II. The measurement concept for using system L to determine low-frequency echo reduction and insertion loss is described in Sec. III. Measurements both with and without a sample present in the tube are required to effect the present technique. The required ''without-sample'' measurements, and their use to adjust nominal hydrophone sensitivities and positions as well as the speed of sound of the tube fill fluid, are discussed in Sec. IV. The required ''with-sample'' measurements are discussed in Sec. V. Also described in Sec. V are

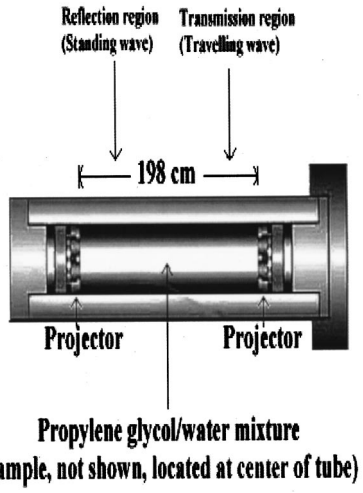

FIG. 1. Schematic representation of the system L tube. The sample under test (not shown) is positioned near the tube center, and must approximately fill the 38-cm tube diameter. Also not shown is a series of hydrophones situated along the upper interior length of the tube. The ''first'' such hydrophone is located at an offset distance of about 15 cm from the projector array nearest the removable tube cover, shown on the right side of the figure. This hydrophone offset was selected to avoid the near-field region of the proximate projector array. This first hydrophone is taken to be the ''reference'' hydrophone. The five other hydrophones are nominally located at 32-, 64-, 104-, 136-, and 168-cm distances from the reference hydrophone. (These values of the nominal hydrophone positions are adjusted, by amounts of less than 1 cm, using a least-squares procedure described in the text.) Positioning the sample near the tube center results in three of these six hydrophones being situated to either side of the sample. The measurements obtained from one such triad of hydrophones (in the reflection region shown) are used to decompose analytically the components of the standing wave that appears in this area of the tube when a sample is present. Measurements obtained from the triad of hydrophones on the other side of the sample (in the transmission region shown) are used both to help establish a unidirectional traveling wave in that region, and to determine the amplitude of the through-the-sample transmitted wave.

comparison measurements acquired from a relatively large test panel, evaluated in APTF. A description of a causal material model used to extrapolate the APTF measurements into the system-L frequency range is also given. A summary and the conclusions are provided in Sec. VI. Finally, the Appendix provides the details of a simple waveguide model that is used to correct the system L measurements for samples that fail to fill completely the cross section of the tube.

II. DESCRIPTION OF SYSTEM L

System L (see Fig. 1) is a horizontal tube designed for acoustical testing of underwater materials and devices, and is part of the Low Frequency Facility of the Naval Undersea Warfare Center in Newport, RI. The tube is of 38 cm inner diameter, and is 243 cm in length. It contains a fill fluid that is composed of a propylene glycol (antifreeze)/water mixture. (The antifreeze is added to the water in a ratio of 1 part antifreeze to 3 parts water. The resulting mixture has a speed of sound of about 1600 m/s, which is slightly greater than that of pure water.) Pressurization apparatus allows hydrostatic test pressures as high as 68 950 kPa, thus simulating an ocean depth of up to about 6.9 km.

Each end of the tube is fitted with a projector array consisting of seven pressure-compensated transducers. Also, an array of six hydrophones is mounted along the upper interior length of the tube to aid in the production of a traveling wave. The first such hydrophone is located at an offset distance of 15 cm from the projector array closest to the tube cover (shown at the right side of Fig. 1). Denoting that hydrophone's position as the zero, or reference, position, the remaining hydrophones are situated at distances of 32, 64, 104, 136, and 168 cm from the reference hydrophone. The last such hydrophone is thus also located about 15 cm from the proximate projector array. By monitoring the amplitudes and phases of the waves received by each of these six hydrophones, more than enough information is acquired to determine the drives that must be applied to each of the two projector arrays in order to establish a unidirectional traveling wave within system L. (The U.S. Navy's first use of active cancellation methods, performed at what was then the Underwater Sound Reference Laboratory in Orlando, Florida, is described in Ref. 4. The current version of the hardware and software in system L is a modern computer-based descendant of the techniques described in this early reference.)

III. MEASUREMENT CONCEPT

A sample is mounted approximately midway between the two projector arrays of the system L tube (note again Fig. 1). The sample is oriented such that a normal to its surface is parallel to, and approximately coincident with, the tube centerline. (If the sample does not entirely fill the cross section of the tube, it is necessary to correct the measurements. A suitable waveguide model is described in the Appendix.) The two projectors in system L are driven in a manner that establishes acoustic waves within the tube that simulate those that are present in a standard normal-incidence panel test.[1] In such a test on one side of the panel there appear two waves, one of which approaches the sample (and which is called the ''incident'' wave), and the other of which recedes from the sample (and which is called the ''reflected'' wave). On the opposite side of the sample there appears only one wave, which recedes from the sample (and which is called the ''through-the-panel transmitted wave''). The two waves appearing in the reflection region of system L combine to create a standing wave; the single wave appearing in the transmission region is a unidirectional traveling wave.

The reflected wave unquestionably loads the projector array that it impinges upon, thereby modifying its output. However, there are three hydrophones situated between that projector and the sample, and both the amplitudes and phases of the received signals are recorded at each of these three hydrophones. Hence, there is more than sufficient information available to decompose analytically the standing wave into its individual, oppositely directed, components. Once the amplitudes of these standing-wave components are known, they can be used to compute the sample's pressure reflection coefficient, and hence the sample's echo reduction (taken here to be -20 times the logarithm to the base 10 of the magnitude of the pressure reflection coefficient).

There are also three hydrophones situated at (approximately) known positions in the transmission region. Amplitude and phase are also accurately measured at these hydro-

phones. The amplitude of the unidirectional traveling wave appearing there can thus be combined with the incident-wave amplitude determined from the reflection-region measurements to compute the sample's pressure transmission coefficient, and hence its insertion loss. (This is taken here to be -20 times the logarithm to the base 10 of the magnitude of the pressure transmission coefficient.)

Pulsed sound would not be an adequate method to achieve the measurements of interest. With the sample located near the tube center as described, the distance between the sample and the projector array in the transmission region is less than 99 cm. Even neglecting turn-on transients of the source(s), and response transients of the sample, this available distance would be only one cycle in the fill fluid at about 1500 Hz. It is clear that sufficient data could not be accurately acquired to characterize the sample to frequencies as low as 100 Hz if it were not possible to create a traveling wave.

IV. "NO-SAMPLE" EXPERIMENTS AND ASSOCIATED LEAST-SQUARES ADJUSTMENTS

A. Background

Even relatively modest errors in sensitivity (of a few tenths of a dB), or in the "known" hydrophone locations (of a few tenths of a cm), can produce several dB of error in the determinations of the amplitudes of the three wave fields (incident, reflected, transmitted) of interest. In order to circumvent this problem, least-squares adjustments of the hydrophone sensitivities and positions, and also of the speed of sound of the tube fill fluid, are required.

The notion behind the least-squares adjustments is the determination of those hydrophone sensitivities and positions, and that speed of sound of the fill fluid, that best satisfy the requirements for echo reduction and insertion loss when no sample is present. Naturally, with no sample present one ideally should find a null reflected wave (infinite echo reduction) and should find a through-the-sample transmitted wave of amplitude equal to the incident wave (zero insertion loss).

Although six hydrophones are present in system L, and although all six are typically used in the creation of a traveling wave within the tube when it is used in its standard mode of transducer calibration, in the present measurement only three hydrophones are available for this purpose. Once a sample has been placed inside the tube near its center, a standing wave will be created in the reflection region. Three of the six hydrophones are located in this region, and thus are unavailable for use in building a traveling wave. The "no-sample" measurements in the system L tube help to establish the fact that a good traveling wave can indeed be built using only these three hydrophones.

B. Determination of the "no-sample" system transfer matrix

Two no-sample data sets are required. The two no-sample data sets involve measurements of the complex voltage responses at each of the six hydrophones for each of two drive conditions. In each of these tests, one of the projectors is driven to steady state while the voltage driving the other projector is held at zero. Of course, driving the system in this manner creates a standing wave within the tube.

Consider the following equation that defines the system-L transfer matrix:

$$\begin{pmatrix} a_{11} & a_{12} \\ a_{21} & a_{22} \\ a_{31} & a_{32} \\ a_{41} & a_{42} \\ a_{51} & a_{52} \\ a_{61} & a_{62} \end{pmatrix} \times \begin{pmatrix} d_1 \\ d_2 \end{pmatrix} = \begin{pmatrix} m_1 \\ m_2 \\ m_3 \\ m_4 \\ m_5 \\ m_6 \end{pmatrix}. \tag{1}$$

Here, the a matrix is the (initially unknown) transfer matrix; the d matrix is the "drive" matrix, i.e., the complex drive voltages applied to each of the two projectors; and the m matrix is the matrix of measured complex responses at each of the six hydrophones in system L. (It should be understood that the elements of the a matrix must be determined not only for the case in which no sample is present, but must also be determined afresh for each sample and each condition of temperature, hydrostatic pressure, and frequency of interest.)

When measurements are acquired as described above, each of the 12 elements of the transfer matrix can be determined, six at a time. For example, when one projector is driven (e.g., the projector that corresponds to element d_1 of the d matrix), while the other projector is shorted out (i.e., $d_2=0$), notice that Eq. (1) reduces to the six equations

$$\begin{aligned} &a_{11}d_1=m_1; \quad a_{21}d_1=m_2; \quad a_{31}d_1=m_3. \\ &a_{41}d_1=m_4; \quad a_{51}d_1=m_5; \quad \text{and} \quad a_{61}d_1=m_6. \end{aligned} \tag{2}$$

Since m_1 through m_6 are the measured hydrophone responses, and since the applied drive d_1 is obviously also known, it is clear that Eq. (2) can be used to determine the unknown (complex) elements a_{11} through a_{61} of the transfer matrix. In a similar manner, the remaining six unknown elements of the transfer matrix are determined when the system is driven under the conditions $d_1=0$ and $d_2\neq 0$. Once all the elements of the a matrix have been determined by this process, projector drives that could be used to create a unidirectional traveling wave in the system L tube can be computed.

In principle, a traveling wave can be built within the tube based on the responses of any two (or more) of the six hydrophones. To do this, a submatrix equation, consisting of only those rows of Eq. (1) that are associated with the hydrophones that are to be used to build the traveling wave, is created. Unlike the situation in which the elements of the transfer matrix were initially determined, in the present case the d elements of the submatrix equation are unknown, but the a elements are known. Also, the m elements of this submatrix equation are "seeded" with the *desired* hydrophone responses, which correspond to the expected hydrophone responses to a unidirectional traveling wave. These desired values are determined by evaluating the unidirectional traveling-wave function $\exp[ikx]$ at the (nominal) "known" hydrophone positions x. (The implied time dependence $\exp[-i\omega t]$ is suppressed.) The resulting submatrix equation can then be solved for the unknown elements of the d matrix.

Since the submatrix equation has only two unknown quantities, *viz.*, d_1 and d_2, but three equations result from the values at each of the three available hydrophones in the transmission region, the problem is solved using linear least-squares methods. The problem must be solved at each measurement frequency and hydrostatic pressure of interest. The best-fit values of d_1 and d_2 obtained at each frequency can then be used to evaluate the ''forward'' problem that would be observed if these two computed drives were in fact applied to the projectors in the system L tube. By substituting these computed drives into Eq. (1), together with the now-known *a*-matrix elements for the no-sample case, the responses at all six hydrophones can then be computed.

C. Least-squares adjustments of hydrophone sensitivities and positions, and of the sound speed of the fill fluid

To effect the required least-squares adjustments, a ''cost'' function must be defined. There is considerable latitude available in the definition of this function. It is important that the cost function be defined in a way that ensures that the adjustments remain relatively small. The principle of ''fitting-to-goal'' was also adopted in designing this function. One such condition is that the amplitude of the reflected wave appearing in the reflection region of the tube when no sample is present should be as small as possible. The second condition is that the amplitude of the wave appearing in the transmission region of the tube when no sample is present should be as close as possible to the amplitude of the incident wave. An auxiliary condition imposes the requirement that the adjustments be small relative to the initial values of the quantities being adjusted, since it is not expected that the initial hydrophone sensitivities and positions, as well as the speed of sound of the tube fill fluid, would ever be grossly in error.

The specific form of the adopted cost function is

$$f=\sum_{i=1}^{n}\left[|R_i|^2+(1-|T_i|)^2+W_1\sum_{j=1}^{5}(1-xc_j)^2+W_2\left[\sum_{j=1}^{5}(1-xc_j)\right]^2+W_3\sum_{j=1}^{5}(1-ec_j)^2+W_4(1-cc)^2\right]. \tag{3}$$

The outermost sum of Eq. (3) is taken over the test frequencies of interest. (This sum excludes certain frequencies at which there are obvious resonances in the system.) The quantities $|R_i|$ are the amplitudes of the *effective* pressure reflection coefficients. The quantities $|T_i|$ are the amplitudes of the *effective* pressure transmission coefficients. The quantities xc_j are hydrophone-position ''correction factors,'' taken initially to be unity. When multiplied times the initial ''known'' hydrophone positions, these factors produce ''corrected'' hydrophone positions. The quantities ec_i are hydrophone calibration correction factors. These are also taken initially to be unity. The quantity *cc* is the tube fill-fluid sound-speed correction factor. The sums that run from $j=1$ to $j=5$ are sums over hydrophones. (One of the six hydrophones in the system is taken to be a reference hydrophone, whose position and calibration are taken to be known exactly.) Finally, the quantities W_1 through W_4 are dimensionless weighting factors, which determine the extent to which the associated sums affect the cost function, and whose values are at our disposal. The following numerical values were found to give good results:

$$W_1=0.2;\quad W_2=0.1;\quad W_3=0.1\quad W_4=0.1. \tag{4}$$

This scheme for determining corrections was found to produce reasonable changes to the initial positions, calibrations, and fill-fluid sound speed. For example, the results of one typical calculation produced the following set of values:

$$\begin{aligned} &xc_1=0.998\,35;\quad xc_2=1.000\,40;\quad xc_3=1.003\,61;\\ &xc_4=0.994\,764;\quad xc_5=1.001\,14;\\ &ec_1=0.988\,471;\quad ec_2=0.997\,562;\quad ec_3=1.006\,29;\\ &ec_4=1.023\,04;\quad ec_5=1.010\,18;\quad cc=0.999\,278. \end{aligned} \tag{5}$$

It can be seen that the correction factors do not differ much from unity, and are distributed mostly randomly, as would be expected of true measurement errors in the adjusted quantities. In this way, it is found that the largest absolute change in hydrophone position is slightly more than 0.7 cm. The largest change in hydrophone calibration is found to be slightly less than 0.2 dB. The change in the speed of sound of the hydrophone fill fluid is less than 1.17 m/s.

The results obtained by applying this procedure to the data acquired with no sample in the system-L tube, for one typical case, are shown in Figs. 2(a) and (b) and Fig. 3. In Fig. 2(a) the effective echo reduction seen at the three hydrophones used to build the traveling wave in the through-the-sample transmitted-wave region is shown. It is seen that typical echo reductions in this region are of the order of 70 dB, except at obvious tube resonances. These extremely high echo reductions are to be expected, since the traveling-wave drives have been computed using the transfer function as determined at these particular hydrophones.

In Fig. 2(b) the effective echo reductions computed at the other triad of hydrophones, that is, the three hydrophones that were *not* used to establish the traveling wave, are shown. The associated pressure reflection coefficients are those used in the computation of the R_i quantities of Eq. (3). The typical value seen in Fig. 2(b) of the associated echo reduction is about 40 dB. (When no corrections are applied to the hydrophone calibrations and positions, and to the sound speed of the tube fill fluid, the typical echo reductions seen at these hydrophones are about 25 dB. Thus, the small corrections to these quantities have a significant impact upon the reduction of measurement error.) The typical value of 40 dB for the echo reduction suggests that a reflected ''error wave'' of amplitude about 1% of that of the incident wave is present in the reflection region of the tube. If an error wave of this same amplitude is also present when a sample of 20-dB intrinsic echo reduction is being measured in system L using the present method, an error of slightly less than 1 dB in the

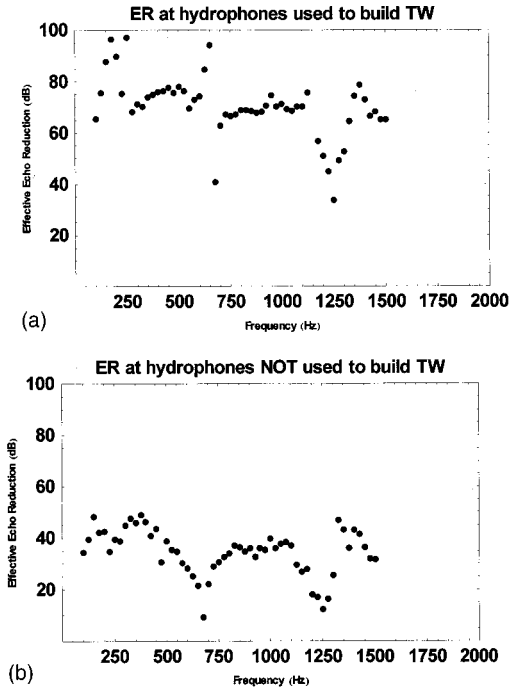

FIG. 2. (a) Effective echo reduction, obtained at the three hydrophones located in the transmission region shown in Fig. 1, when no sample is present in the tube. The very large numerical values are obtained simply because the LS determination of the projector drives is only a slightly overdetermined problem, with the two required drives being determined from the three hydrophones available in the transmission region using a least-squares process. (TW=traveling wave; ER=echo reduction). (b) Effective echo reduction, obtained at the three hydrophones located in the reflection region shown in Fig. 1, when no sample is present in the tube. It can be seen that the typical value obtained for the echo reduction is about 40 dB, ignoring obvious tube resonances. If no adjustments of the hydrophone sensitivities and positions, as well as the speed of sound of the tube fill fluid were performed (as described in the text), the typical echo reduction obtained at these hydrophones for this case is about 25 dB. (TW=traveling wave; ER=echo reduction).

measurement can be expected. For a sample of 30-dB intrinsic echo reduction, the measurement error could be somewhat greater than 3 dB.

In Fig. 3 is shown the effective insertion loss when no sample is present. This is the insertion loss associated with the T_i quantities of Eq. (3). The typical insertion loss seen in this figure is of the order of magnitude of about 0.1 dB. This again suggests that a through-the-sample transmitted error wave of amplitude about 1% of that of the incident wave is present in the transmission region. The respective insertion-loss errors, in samples that are characterized by 20- to 30-dB intrinsic insertion loss, are again in the 1- to 3-dB range, respectively.

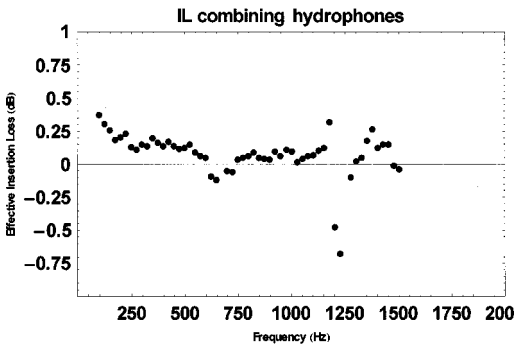

FIG. 3. Effective insertion loss, obtained in the transmission region shown in Fig. 1, when no sample is present. This insertion loss is computed by combining the results obtained from the triad of hydrophones located in this region with those obtained from the triad in the reflection region, required to determine the incident-wave amplitude. It is seen that the typical insertion loss obtained is about 0.1 dB, except at obvious tube resonances. If no adjustments of the hydrophone sensitivities and positions, and the fill-fluid sound speed, were performed, the typical insertion loss obtained is about 1 dB. (TW=traveling wave; IL=insertion loss).

V. "WITH-SAMPLE" EXPERIMENTS

A. Acoustic Pressure Tank Facility (APTF) measurements

Before acquiring any data with samples in system L, a relatively large sample was first tested in APTF. This sample (a decoupler) was measured in order to obtain baseline results that could be used to judge the quality of the system L measurements. The dimensions of the test panel were approximately 82×92 cm $(32\frac{1}{4}\text{ in.}\times36\frac{1}{4}\text{ in.})$, and the sample was of approximately 5-cm (2-in.) thickness. This relatively large panel size enabled the use of standard measurement techniques to approximately determine sample response in the frequency interval of interest. Although highly accurate measurements at the frequencies of interest in system L could not be conducted in APTF, the measurements could be extrapolated into the desired frequency regime. This was possible because the sample of interest consisted of a single-layer material; edge diffraction was found not to be too strong; and new causal theoretical expressions for the sound speed and loss of the material could be employed in the extrapolations. We developed these theoretical expressions using the appropriate Hilbert transform implementation of the causality principle.[5] The transforms were carried out analytically. The results of the analytical calculations were also verified numerically.

The model we used to derive a causal relationship between the sound speed and loss of the sample, based on the use of Kramers–Kronig relations,[5] is of the form

$$\frac{\omega}{c_{\text{phase}}(\omega)}=\frac{\omega}{c_\infty}+[\alpha(\omega)], \tag{6}$$

where ω denotes the angular frequency; $c_{\text{phase}}(\omega)$ and $\alpha(\omega)$ are the phase speed and loss of the sample material expressed as functions of ω, respectively; c_∞ is the phase speed at infinite frequency; and the [ ] notation denotes the Hilbert transform. The numerical value of c_∞ is to be determined by least-squares fitting.

In order that Eq. (6) yield reasonable results without requiring the introduction of specialized methods of analysis,[6] it is helpful to use only functions for $\alpha(\omega)$ that remain finite as $\omega\rightarrow\infty$. We chose to introduce a loss function that is approximately linear with frequency, at least over a major segment of the frequency interval of our experiments, and to use a filtering function to eliminate the divergence for large frequencies. The loss function we chose to introduce is

$$\alpha(\omega)=\frac{a_1|\omega/\omega_0|}{1+b(\omega/\omega_0)^4}, \tag{7}$$

where a_1 is a constant that measures the "strength" of the loss, and which is to be determined by least-squares fitting. [Note that the function defined in Eq. (7) is approximately linear for frequencies below ω_0.] The constants b and ω_0 are parameters that describe the filter characteristics, and their values are at our disposal. The choice of a filter with a fourth-order pole is somewhat arbitrary, but this ensures relatively rapid convergence of the Hilbert-transform integral. Fortunately, the Hilbert transform of $a(\omega)$ as given by Eq. (7) can be carried out analytically in a straightforward fashion. The result is

$$[\alpha(\omega)] = -\frac{a_1\omega_0\omega\left(\pi\sqrt{b}\omega^2+\omega_0^2\ln\left(\frac{b\omega^4}{\omega_0^4}\right)\right)}{2\pi(b\omega^4+\omega_0^4)}. \tag{8}$$

Here ln denotes the natural logarithm.

Panel measurements, as acquired in APTF, directly measure the amplitudes and phases of the incident, reflected, and through-the-panel transmitted waves. Unfortunately, it is not possible to avoid the contaminating influence of the wave originating at the sample edge for the current sample ($32\frac{1}{4}$ in.$\times 36\frac{1}{4}$ in.) at the frequencies of interest. Thus, even if the causal model described above were an exact description of sample performance, exact agreement between theory and measurement would not be expected. However, since the model involves only two adjustable parameters (c_∞ and a_1), it was hoped that least-squares fitting would help to discriminate against edge effects, essentially treating these effects as a form of (coherent) noise. Since many frequencies are involved in the fitting process but only two constants are being adjusted, it was felt that the combined effects of the many test frequencies involved, covering the wide frequency interval of 250 to 15 000 Hz, might reduce the influence of the coherent noise.

The causal dispersion model of Eqs. (6)–(8) was incorporated into a single-layer reflection/transmission model of the sample, and the resulting model was fitted to the APTF data acquired from the panel to determine c_∞ and a_1 at each hydrostatic pressure. In Figs. 4(a) and (b) and Figs. 5(a) and (b) are shown the results of the measurements and of the fitting process for two of the hydrostatic pressures that were tested. Data are shown as dots, while the theoretical results, based on least-squares fitting of the causal model, are shown as solid lines. The solid lines are extended down to 100 Hz in order to cover the low-frequency limit to be tested in system L. (The low-frequency cutoff for the insertion-loss measurements in APTF was 250 Hz, while the low-frequency limit of the echo-reduction measurements was 2000 Hz. These low-frequency limits are well below those usually applied in that facility.) As can be seen, the theory agrees reasonably well with the measurements over much of the data, although the effects of edge diffraction are clearly present, especially in Fig. 5(b).

In fitting the APTF measurements, the filter parameters of the causal model were set such that $\omega_0 = 2\pi 40\,000$ radians/s and $b=0.5$ (dimensionless) in all cases. At the 100 psi hydrostatic test pressure used in the measurements presented in Figs. 4(a) and (b), the two fitted

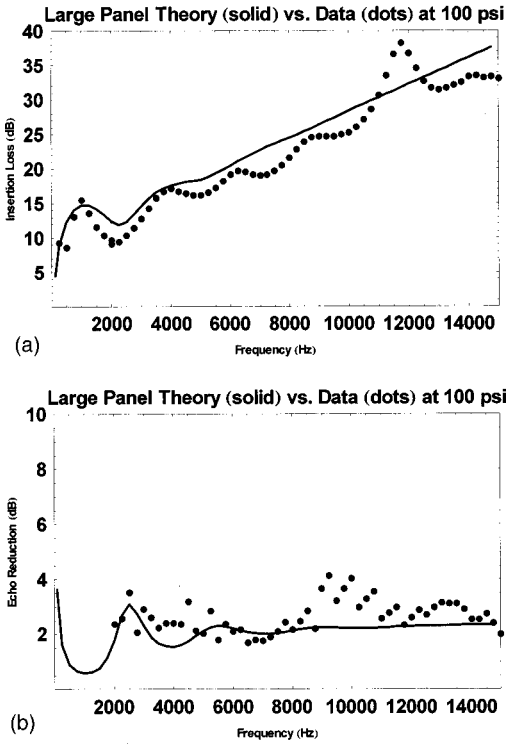

FIG. 4. Insertion loss and echo reduction of the 82×92-cm ($32\frac{1}{4}$-in. $\times 36\frac{1}{4}$-in.) panel at a hydrostatic test pressure of 689 kPa (100 psi). Dots are data; solid lines are from a least-squares fit of a causal panel model to the measurements. Two parameters were adjusted in the fits. (a) Insertion loss. (b) Echo reduction.

model parameters were found to be $c_\infty = 3.5\times 10^4$ cm/s and $a_1 = 2.1\,\mathrm{cm}^{-1}$. At the 500 psi hydrostatic test pressure, shown in Figs. 5(a) and (b), the two fitted model parameters were found to be $c_\infty = 3.9\times 10^4$ cm/s and $a_1 = 1.1\,\mathrm{cm}^{-1}$. These values, and their changes with hydrostatic pressure, are reasonable for the sample under test. At 100 psi, the sound speed in the material, which can be computed from the causal model of Eqs. (6)–(8) using the fitted constants, is about 2.7×10^4 cm/s, while the associated loss factor is about 0.53 cm^{-1}. At 500 psi, the computed sound speed in the material is about 3.3×10^4 cm/s, while the loss factor is about 0.28 cm^{-1}.

B. Sample measurements in system L

An approximately circular subsample of 38-cm (15-in.) diameter was next cut from one corner of the $32\frac{1}{4}$-in. $\times 36\frac{1}{4}$-in. decoupler panel for testing in system L. A corner cut was used to permit retesting of the panel in APTF, should that have proved necessary. The subsample was then mounted in system L, and suitable measurements acquired.

Recall that the basic concept behind the present measurement method involves driving the two transducers to create a traveling wave on one side of the sample and a standing wave on the other. However, there is no need in practice to actually produce such waves within the system when a sample is present. The same kinds of standing-wave measurements used to determine the system transfer function when no sample is present in the tube can also be used when

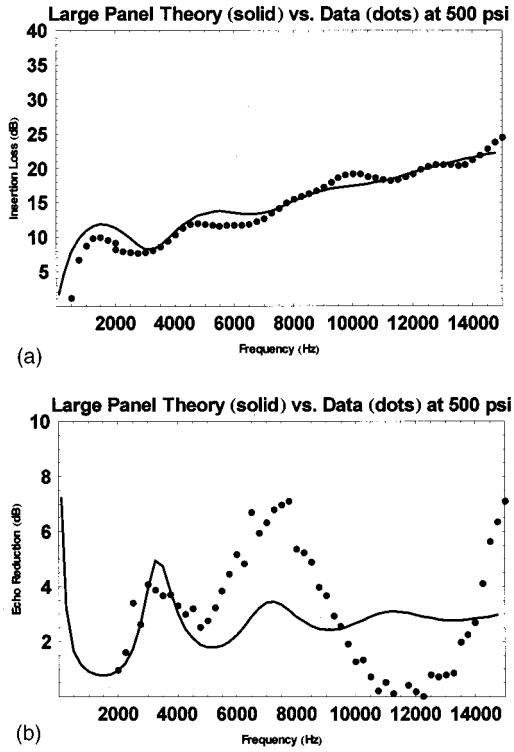

FIG. 5. Insertion loss and echo reduction of the large panel ($32\frac{1}{4}$-in. $\times 36\frac{1}{4}$-in.) at a hydrostatic test pressure of 3450 kPa (500 psi). Dots are data; solid lines from a least-squares fit of a causal panel model to the measurements. Two parameters were adjusted in the fits. (a) Insertion loss. (b) Echo reduction.

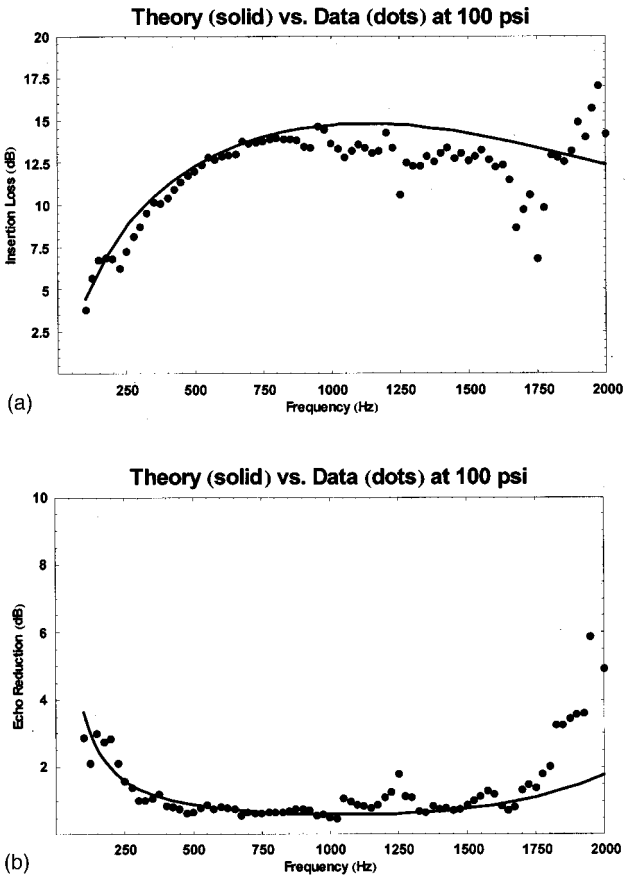

FIG. 6. Insertion loss and echo reduction, at a hydrostatic test pressure of 689 kPa (100 psi), of an approximately circular, 38-cm diameter, subsample cut from the $32\frac{1}{4}$-in.$\times 36\frac{1}{4}$-in. panel, as tested using the new procedure in system L. Dots are data; solid lines are extrapolations of the causal model fitted to the large-panel measurements shown in Fig. 4. (a) Insertion loss. (b) Echo reduction.

a sample is present as well. That is, when a sample is present a transfer-matrix equation of the form of Eq. (1) still applies to the measurements. Of course, the elements of the transfer matrix will obviously be different depending upon whether or not a sample is present, and will obviously be different for each sample and each particular test circumstance. Moreover, the same technique used to determine the projector drives that would produce a unidirectional traveling wave in the transmission region when no sample is present can again be used to determine the drives needed to establish such a wave even when a sample *is* present. Once the measurements that determine the transfer matrix elements for the with-sample case have been acquired, there is no need to actually establish these waves in the tube. The amplitudes of the waves that would appear in each half of the tube can be determined instead from the with-sample transfer matrix, and the amplitudes of these waves can be combined in the usual way to determine sample echo reduction and insertion loss.

The results obtained when the decoupler subsample was evaluated in this way are shown in Figs. 6(a) and (b) and Figs. 7(a) and (b). The dots once again are the measured values, obtained by the present method, and the solid lines are theoretical values based on extrapolating the APTF measurements. The two adjusted parameters determined at each hydrostatic pressure tested in APTF were used in the theoretical expressions of the causal model to compute the solid-line curves shown in the figures. As can be seen, agreement between the measurements and the extrapolations is quite good.

VI. SUMMARY AND CONCLUSIONS

A technique for measuring the echo reduction and the insertion loss of small passive-material samples in NUWC's system L was described. The method allows for the measurements to be acquired over the full range of ocean environmental conditions in the frequency range of 100 to 1750 Hz. ''No-sample'' measurements are acquired in system L and are used to adjust the hydrophone sensitivities and positions. The speed of sound of the tube fill fluid (a propylene glycol/water mixture) is also adjusted. With-sample measurements are obtained and are used to determine the elements of the transfer matrix of the tube/sample system. (The corrected quantities deduced from the no-sample tests are held fixed in determining the elements of the with-sample transfer matrix.) This transfer matrix is then used to determine the echo reduction and the insertion loss of the sample under test.

A causal material model was developed and applied to measurements acquired from a relatively large sample panel evaluated in NUWC's APTF. The model was used to extrapolate the APTF measurements into the frequency range of system L. The extrapolations showed good agreement with the direct measurements acquired using the new method.

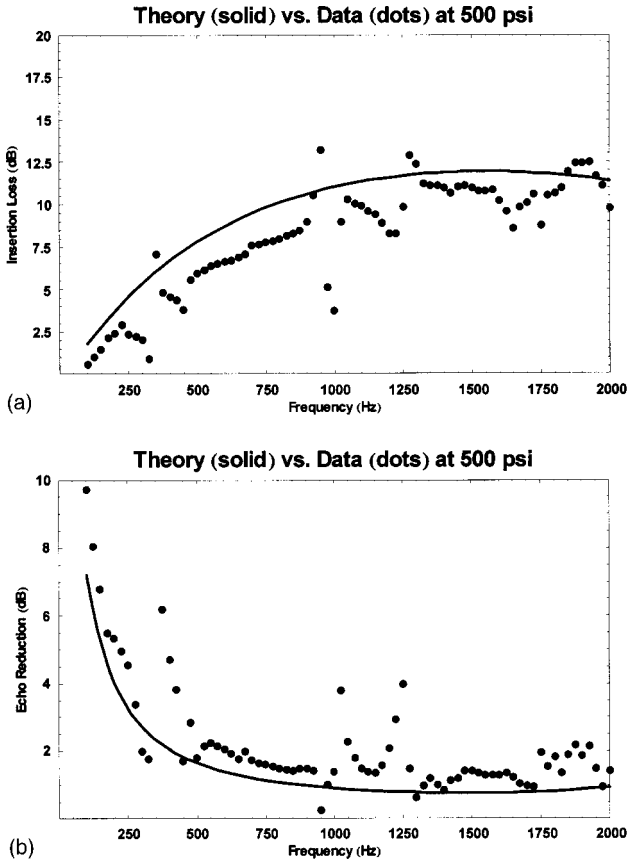

FIG. 7. Insertion loss and echo reduction, at a hydrostatic test pressure of 3450 kPa (500 psi), of an approximately circular, 38-cm diameter, subsample cut from the $32\frac{1}{4}$-in.$\times 36\frac{1}{4}$-in. panel, as tested using the new procedure in system L. Dots are data; solid lines are extrapolations of a causal model fitted to the large-panel measurements shown in Fig. 5. (a) Insertion loss. (b) Echo reduction.

The new technique is currently available for evaluation of customer samples in system L.

ACKNOWLEDGMENTS

We gratefully acknowledge the efforts of Alfred Garceau, who prepared the samples and acquired the data from system L. We are also grateful to Dr. James J. Dlubac, Naval Surface Warfare Center, Carderock Division, West Bethesda, Maryland, for providing material samples and for valuable technical consultation. The work was supported by the Office of Naval Research (Code 321).

APPENDIX: AREA CORRECTION FOR SAMPLES THAT DO NOT FILL THE TUBE COMPLETELY

In our experimental apparatus it is impossible to completely fill the system L tube with a material sample. This results in an experimental error since the effect of the smaller sample is based on a mix of the sample volume and the fluid volume that is replacing the rest of the ideal sample's outer perimeter. For low frequencies, following the analysis in Kinsler and Frey[7] of the effective impedance of a branching pipe, we can define the relevant acoustic quantities following Fig. 8:

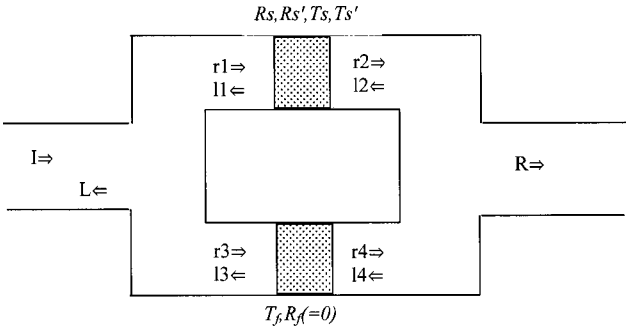

FIG. 8. Boundary conditions and pertinent acoustic variables for a branching pipe.

(1) A is the relative surface area of the sample ($A=1$ completely fills the pipe).
(2) L, R are the complex pressures of the left- and right-moving waves. Here, we assume without loss of generality that an outgoing traveling wave field is established at the right tube end and that the pressure of the incoming wave at the left is unity.
(3) l_1, l_2, r_1, r_2 are the complex pressures of the left- and right-moving waves on either side of the sample in the upper (sample-only) branch of the pipe.
(4) l_3, l_4, r_3, r_4 are the complex pressures of the left- and right-moving waves on either side of the fluid sample in the lower (fluid-only) branch of the pipe.
(5) R_s, T_s, R_s', T_s' are the reflection and transmission coefficients of the sample in the forward and reversed direction. For multilayered samples, R_s and R_s' are in general different, but T_s and T_s' are equal (see Rudgers[8]).
(6) T_f is the transmission coefficient of the fluid (lower branch). This number has magnitude 1.0 but has a phase associated with the travel time through a layer of fluid equal to the thickness of the panel (required to keep the definition of transmission coefficient consistent as a phase shift relative to the incident wave for both fluid and sample). The reflection coefficient of the fluid sample is 0.

The relevant continuity conditions are

(1) $l_1=R_s r_1+T_s' l_2$ (transmission and reflection through the sample),
(2) $r_2=T_s r_1+R_s' l_2$ (transmission and reflection through the sample),
(3) $l_4=T_f l_3$ (transmission through the sample thickness of fluid),
(4) $r_4=T_f r_3$ (transmission through the sample thickness of fluid),
(5) $1+L=l_1+r_1$ (continuity of pressure at the top left fork),
(6) $1+L=l_3+r_3$ (continuity of pressure through the bottom left fork),
(7) $R=l_2+r_2$ (continuity of pressure at the top right fork),
(8) $R=l_4+r_4$ (continuity of pressure at the bottom right fork),
(9) $1-L=A(r_1-l_1)+(1-A)(r_3-l_3)$ (continuity of volume velocity at left fork),

TABLE I. Comparison of analytical and CHIEF results.

Frequency	Analytical R_s	CHIEF R_s	Analytical T_s	CHIEF T_s
500	$-0.034\,154-0.005\,671\,7i$	$-0.034\,106-0.006\,822\,5i$	$0.961\,71+0.135\,58i$	$0.961\,93+0.135\,56i$
1000	$-0.073\,975-0.027\,533i$	$-0.075\,313-0.028\,784i$	$0.906\,18+0.261\,51i$	$0.905\,07+0.261\,33i$
1500	$-0.113\,55-0.066\,766i$	$-0.117\,98-0.068\,186i$	$0.834\,04+0.375\,63i$	$0.832\,08+0.0374\,69i$
2000	$-0.146\,77-0.122\,63i$	$-0.152\,98-0.123\,03i$	$0.746\,61+0.475\,01i$	$0.743\,96+0.471\,84i$
2500	$-0.168\,05-0.192\,29i$	$-0.175\,41-0.199\,75i$	$0.646\,41+0.556\,52i$	$0.641\,03+0.550\,5i$
3000	$-0.173\,14-0.271\,08i$	$-0.181\,64-0.284\,7i$	$0.537\,81+0.617\,52i$	$0.527\,65+0.603\,65i$

(10) $R=A(r_2-l_2)+(1-A)(r_4-l_4)$ (continuity of volume velocity at right fork).

(A1)

The above system can be solved for R_s and T_s, eliminating all but the variables L, R, R_s', T_s', and A. At this point, it can be assumed that two sets of measurements were done: first with the sample in its ''normal'' position, with measured reflected and transmitted amplitudes L_1 and R_1 and then with the sample in the ''flipped'' position (turned 180 deg along the pipe axis to face the other way) with corresponding amplitudes L_2 and R_2 for the reflected and transmitted waves. (In fact, the flipped response can be derived by using the two with-sample measurements to calculate incident, transmitted, and reflected waves with the outgoing wave in the opposite direction, so no more measurements are needed.)

The above-described reflection and transmission coefficients can then be written as

(1) $R_s=R_s(L_1,R_1,A,T_s')$,
(2) $R_s'=R_s'(L_2,R_2,A,T_s)$,
(3) $T_s=T_s(L_1,R_1,A,R_s')$,
(4) $T_s'=T_s'(L_2,R_2,A,R_s)$,

(A2)

where the $R_s(\,)$, etc., are the functional forms derived from Eq. (A1) above with the L_1, L_2, etc. substituted for the L and R in the original solution.

Solving the above system gives

$$(1)\quad R_s=-(L_1L_2)+(R_1-T_f)(R_2-T_f)+A((R_1-T_f)\times(-R_2+T_f)+L_1(1+L_2-T_f^2))/D,$$

$$(2)\quad R_s'=-(L1L2)+(R_1-T_f)(R_2-T_f)+A((R_1-T_f)\times(-R_2+T_f)+L_2(1+L_1-T_f^2))/D,$$

(A3)

$$(3)\quad T_s=A((A-1)(1+L_1)(1+L_2)T_f-R_1((A-1)R_2T_f+T_f^2)-1)/D,$$

$$(4)\quad T_s'=A((A-1)(1+L_1)(1+L_2)T_f-R_2((A-1)R_1T_f+T_f^2)-1)/D,$$

where

$$D=L1L2+A^2(1+L1+L2+L1L2-R1R2)+(R1-Tf)(Tf-R2)-A(L1+L2+2L1L2-2R1R2+R1Tf+R2Tf).$$

Here, T_f is e^{ikd}, the phase correction for traveling through the thickness of fluid, d, at the sample edge; A is the area correction ratio.

The above expressions for transmission and reflection coefficients were tested using a model of the system L tube and a sample with realistic material properties based on our version of CHIEF (combined Helmholtz integral equation formulation.)[9,10] The system L tube and sample were simulated, the ends of the tube were driven by imposing unit surface velocity on the left and right ends of the tube, successively, and the pressure field was measured at points in the tube corresponding to actual hydrophone locations. The sample was defined as being 2-in. thick (two 1-in. layers) with the following material properties (shear was assumed negligible):

$$\rho_1=1800\ \text{kg/m}^3,\quad c_{l1}=2600+520i\ \text{m/s}$$

(imaginary part represents loss), $c_{s1}=0$,

$$\rho_2=800\ \text{kg/m}^3,\quad c_{l2}=1000+200i\ \text{m/s},\quad c_{s2}=0.$$

The radius of the sample was taken to be 0.7071 times the radius of the tube, giving an area ratio of 0.5. The results are given in Table I. As can be seen by inspection, the agreement is good at all frequencies, with deviations increasing with frequency as the assumptions about the plane wave uniformity of the field begin to break down.

[1] R. J. Bobber, *Underwater Electroacoustic Measurements* (U. S. Government Printing Office, Washington, 1970), pp. 287–299.
[2] J. C. Piquette, ''Transmission coefficient measurement and improved sublayer material property determination for thick underwater acoustic panels: A generalization and improvement of the ONION method,'' J. Acoust. Soc. Am. **92**, 468–477 (1992).
[3] See Ref. 1, pp. 305–310.
[4] L. G. Beatty, ''Acoustic impedance in a rigid-walled cylindrical sound channel terminated at both ends with active transducers,'' J. Acoust. Soc. Am. **36**, 1081–1089 (1964).
[5] See, for example, C. W. Horton, ''Dispersion relationships in sediments and sea water,'' J. Acoust. Soc. Am. **55**, 547–549 (1974).
[6] K. R. Waters, M. S. Hughes, J. Mobley, and J. G. Miller, ''On the applicability of Kramers–Kronig relations for untrasonic attenuation obeying a frequency power law,'' J. Acoust. Soc. Am. **108**, 556–563 (2000).
[7] L. E. Kinsler, A. R. Frey, A. B. Coppens, and J. V. Sanders, *Fundamentals of Acoustics*, 3rd ed. (Wiley, New York, 1982), pp. 235–237.
[8] A. J. Rudgers and C. A. Solvoid, ''Apparatus-independent acoustical-material characteristics obtained from panel-test measurements,'' J. Acoust. Soc. Am. **76**, 926–934 (1984).
[9] G. W. Benthien, D. Barach, and D. Gillette, *CHIEF User's Manual* (Naval Oceans System Center, 1988).
[10] H. Schenck, ''Improved integral formulation for acoustic radiation problems,'' J. Acoust. Soc. Am. **44**, 41–58 (1968).

Reduction methods of the reconstruction error for large-scale implementation of near-field acoustical holography[a)]

K. Saijyou[b)]
Fifth Research Center, Technical R & D Institute, Japan Defense Agency, 3-13-1 Nagase, Yokosuka 239-0826, Japan

S. Yoshikawa[c)]
Department of Acoustic Design, Kyushu Institute of Design, 4-9-1 Shiobara, Minami-ku, Fukuoka 815-8540, Japan

(Received 3 March 2000; revised 30 November 2000; accepted 25 July 2001)

New extrapolation methods in real and wave number spaces are proposed to extend near-field acoustical holography (NAH) toward a more quantitative technique applicable to the vibration measurement of actual large-scale structures. The finiteness of the measurement aperture is a serious impediment to such large-scale implementation of NAH because the measurement aperture sufficiently larger than the vibrating structure of interest is usually needed. We should thus investigate how to reduce the reconstruction error when the measurement aperture is restricted to a fraction of the vibrating structure. The following practical suggestions are derived from simulations and underwater experiments: (1) A wave number-space extrapolation method can reduce the reconstruction error to about 25% for the measurement aperture corresponding to 1/16th of the vibrating structure when 10 000 iterations of the extrapolation process are applied. (2) A real-space extrapolation method can reduce the reconstruction error to negligible degree (10^{-10}%) for the measurement aperture corresponding to four times as large as the vibration structure when ten iterations of the extrapolation process are applied. (3) The former method may be widely and safely applied, but many iterations are necessary; the latter method can reduce the reconstruction error very quickly, but a wider measurement aperture than that in the former is needed. Therefore, when the measurement aperture cannot be larger than the vibrating structure, the former method is recommended, while when the measurement aperture is larger than the structure, the latter method is recommended. Summing up, the accuracy of our proposed methods, which is attributed to the property of data extrapolation method that the data inside the measurement aperture is conserved after adequately extrapolating the data outside the aperture, will be relevant to a more quantitative measurement and analysis of real large-scale structures.
[DOI: 10.1121/1.1405417]

PACS numbers: 43.60.Sx, 43.40.Dx, 43.20.Ye [CBB]

I. INTRODUCTION

Near-field acoustical holography (NAH) has been introduced by Williams and Maynard[1] to reconstruct the velocity distribution of a vibrating plate from the acoustic pressure hologram obtained at the near-field points. A conventional acoustic holography suffers from the defect that the spatial resolution of a reconstructed image depends on the wavelength of radiation. NAH enables us to reconstruct the structural vibration without such a limitation on spatial resolution. NAH was extended to the cylindrical geometry,[2] axisymmetric bodies,[3] and an arbitrary geometry.[4] As the result, NAH has been applied to the study of structural vibration and scattering.[5–9]

Although NAH is a very powerful tool for structural acoustics, large-scale implementations of NAH for its application to a large vibrating body such as a ship have not been reported. The finiteness of the measurement aperture is *an* impediment to the large-scale implementation of NAH. In the NAH signal processing, it is assumed that the hologram data are measured over the hologram plane with an infinite size. In practice, the sound pressures are measured on a finite measurement aperture near the vibrating structure. This limitation leads to the errors due to the wraparound and aperture size restrictions. The wraparound error is easily reduced by applying the zero padding, which forms a large virtual aperture by surrounding the measurement aperture with a ''guard band'' of zeros.[10]

However, the discontinuity at aperture edges due to the restriction of the aperture size is amplified in the NAH backpropagation process. Therefore, the discontinuity of the hologram data seriously contaminates the reconstructed result. In order to avoid this discontinuity, an appropriate real-space window may be applied to the zero-padded hologram data.[11] However, the multiplication of a real-space window changes the measured hologram data. The discrepancy of the smoothed hologram from the measured hologram causes new errors, which are inevitable for the application of the real-

[a)]A part of this paper was presented at the 3rd Joint Meeting of the Acoustical Society of America and the Acoustical Society of Japan, 2–6 December 1996, Honolulu, Hawaii [J. Acoust. Soc. Am. **100**, 2653–2654(A) (1996), invited].
[b)]Electronic mail: saijyou@jda-trdi.go.jp
[c)]Electronic mail: shig@kyushu-id.ac.jp

space window. The data outside the measurement aperture are necessary to estimate errors induced by the multiplication of the real-space window. Consequently, this error cannot be estimated in the usual ways. Conventionally, the measurement aperture fully larger than the structure of interest should be prepared to reduce the error. That limits the size of the measured structure.

In this paper, a new data smoothing method based on the data extrapolation is proposed to realize the large-scale implementation of NAH. Our data smoothing method has remarkable advantages, compared with the conventional real-space window method. In the conventional data smoothing, the data outside the measurement aperture are set equal to zero after the rearrangement of the data inside the measurement aperture. This implies that the measured hologram is distorted by the real-space window, and the distortion of the measured data causes reconstruction error. On the other hand, our data smoothing method can be operated in such a way that the measured hologram data are not changed. The data outside the aperture are then adequately extrapolated. Therefore, the hologram would be effectively enlarged without any distortion of the measurement hologram, and the finite aperture effect would be reduced significantly.

To develop the data extrapolation method, we introduced the concept of the ''error norm reduction method'' which is at first presented by Gerchberg.[12] The proposed method is briefly explained as follows.

The coordinate system $\mathbf{r}=(\xi_1,\xi_2,\xi_3)$ is shown in Fig. 1. The radiated pressure $\tilde{p}(\xi_1,\xi_2,\xi_{3m})$ is measured on a measurement aperture S_p that is included in the S_m plane ($\xi_3=\xi_{3m}$), and the vibrating object (S_v) is located at $\xi_3=\xi_{3o}$ (the S_o plane). Vectors $\mathbf{r_0}=(\xi_1,\xi_2,\xi_{3o})$ and $\mathbf{r_m}=(\xi_1,\xi_2,\xi_{3m})$ represent points on the S_o and S_m planes, respectively. The quantity $\tilde{\eta}(\mathbf{r_0})$ indicates the normal component of the displacement of the object surface, and $\tilde{v}(\mathbf{r_0})=\partial\tilde{\eta}(\mathbf{r_0})/\partial t$ defines the normal component of the surface velocity. The tilde over physical quantities indicates that they are complex quantities. The measured pressure $\tilde{p}_{\text{meas}}(\mathbf{r_m})$ on the measurement aperture S_p, which is zero padded, is viewed as the sum of the true pressure $\tilde{p}_{\text{true}}(\mathbf{r_m})$ and an error pressure $\tilde{p}_{\text{error}}(\mathbf{r_m})$:

$$\tilde{p}_{\text{meas}}(\mathbf{r_m})=\tilde{p}_{\text{true}}(\mathbf{r_m})+\tilde{p}_{\text{error}}(\mathbf{r_m}), \tag{1.1}$$

$$\tilde{p}_{\text{error}}(\mathbf{r_m})=-W(\mathbf{r_m})\tilde{p}_{\text{true}}(\mathbf{r_m}), \tag{1.2}$$

$$W(\mathbf{r_m})=\begin{cases}0, & \mathbf{r_m}\in S_p,\\ 1, & \mathbf{r_m}\notin S_p.\end{cases} \tag{1.3}$$

The measurement error may be estimated by defining the ''error norm'' $\|\tilde{p}_{\text{error}}(\mathbf{r_m})\|$ as a square root of the spatial integration of the squared absolute amplitude of the error pressure:

$$\|\tilde{p}_{\text{error}}(\mathbf{r_m})\|=\sqrt{\int_{S_m}|\tilde{p}_{\text{error}}(\mathbf{r}_m)|^2\,d\mathbf{r_m}}. \tag{1.4}$$

The measured pressure $\tilde{p}_{\text{meas}}(\mathbf{r_m})$ is only obtained at first, and the data extrapolation is realized by reducing the error norm while conserving the true pressure. The assumption about the extent of the vibrating object or the highest wave number of the measured pressure is necessary to reduce the error norm. The data extrapolation method is classified by these assumptions.

When the highest wave number is assumed, the error norm is reduced in K (spatial wave number) space by applying a band limitation. This method is called the ''K-space data extrapolation method,'' which is widely applied, because the extent of the object is not generally limited. However, many iterations of the data extrapolation process are necessary, especially to attain higher resolution. Since too many iterations cause an accumulation of computational error, the optimization of the resolution of the reconstructed result should be considered.

On the other hand, when the extent of the vibrating object is assumed, the error norm can be reduced in real space. This method is called the ''real-space data extrapolation method,'' in which it is assumed that the vibrating structure is surrounded by a rigid baffle. The error of the reconstructed surface velocity is made negligibly small by using this method if the assumption above is appropriate. However, the velocity outside the structure always causes the reconstruction error. We note that the extrapolation method, which is based on the assumption that the vibrating object is surrounded by a rigid baffle, has been used by Held[13] and Kwon and Kim.[14] However, they do not present the proof of the convergence of the extrapolation process. In their methods the area of the rigid baffle is just obtained by shifting the complementary window of the measurement aperture toward

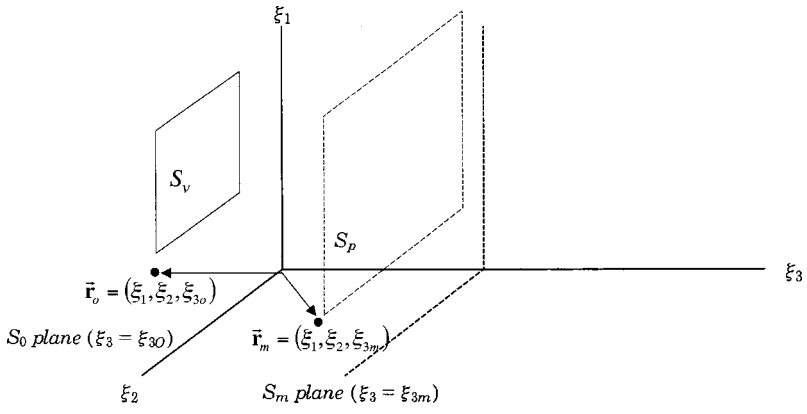

FIG. 1. The general coordinate system applied to the data extrapolation method.

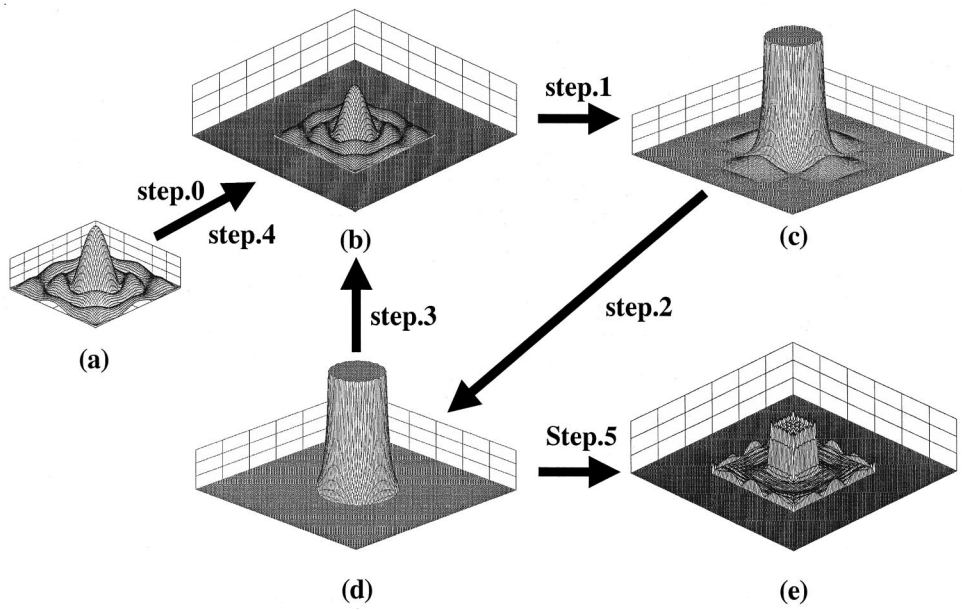

FIG. 2. Schematic diagram of the K-space data extrapolation method. (a) The amplitude of the measured pressure. (b) The amplitude of the corrected pressure on an enlarged aperture. (c) The K-space representation of the corrected pressure. (d) The band-limited K-space representation of the corrected pressure. (e) The amplitude of the reconstructed surface velocity of the structure.

the vibrating object in the direction perpendicular to the measurement plane. The propriety of this assumption is not discussed satisfactorily.

In this paper, we prove the convergence of the extrapolation process and discuss the propriety of the assumption for the extrapolation by introducing the concept of error norm reduction method in Sec. II. And the adaption method of the area of the rigid baffle for reducing the reconstruction error by the data extrapolation is exhibited.

The reconstruction result contains errors due to the restriction of measurement aperture size and the measurement error that is introduced by the sensor or the position mismatch. The problems associated with the measurement error are well addressed in Ref. 15. In the present paper we deal with the reduction method of the reconstruction error caused by the restriction of measurement aperture size, and we assume that the measurement error is zero.

The availability of our proposed methods is justified by simulation and experiment. Since our objective is the application of NAH to real large-scale structures, the size of the measurement aperture is assumed to be considerably smaller than that of the structure in many cases. The error of the surface velocity reconstructed from such a smaller measurement aperture is considered to evaluate the effectiveness of the proposed methods. Algorithms of our data extrapolation methods are first presented in Sec. II. Results of simulations are shown in Sec. III. The model experiment is shown in Sec. IV. The suggestion for the large-scale implementation of NAH is presented in Sec. V. The conclusions drawn from the discussion of them are summarized in Sec. VI.

II. DATA SMOOTHING BASED ON DATA EXTRAPOLATION

A. Algorithm of K-space data extrapolation method

In this section, the algorithm of the K-space data extrapolation method is briefly described. It is assumed that the highest wave number of the true pressure $\tilde{p}_{\text{true}}(\mathbf{r}_m)$ is $k_{\max}$. The coordinate system is shown in Fig. 1. The schematic diagram of the proposed method is shown in Fig. 2, and the procedure is briefly explained below.

(i) **step.0** The measurement aperture size is virtually enlarged by zero padding.

(ii) **step.1** The K-space representation of the pressure on the virtual measurement aperture is obtained by two-dimensional spatial Fourier Transform (abbreviated as 2D-FT hereafter).

(iii) **step.2** If the integration of the squared pressure with high-wave number components ($\sqrt{k_x^2+k_y^2}>k_{\max}$) is smaller than the threshold, then go to step.5. Elsewhere, the high-wave number component is set to be zero. Here, k_x and k_y are the wave numbers of x and y, respectively.

(iv) **step.3** The pressure on the virtual measurement aperture is obtained by two-dimensional spatial inverse Fourier Transform (abbreviated as 2D-IFT hereafter).

(v) **step.4** The pressure of the enlarged aperture is corrected according to the measured pressure. Then, return to step.1.

(vi) **step.5** The surface velocity is reconstructed by the NAH back-propagation of the pressure that is corrected by step.2.

In this study, the threshold is set to 0.01% of the integration of the squared low-wave number components ($\sqrt{k_x^2+k_y^2}<k_{\max}$) of the measured pressure.

The reduction of the error norm is explained as follows.

The radiated pressure is measured on a measurement aperture [Fig. 2(a)]. The zero-padded pressure $\tilde{p}_{\text{meas}}(\mathbf{r}_m)$ [Fig. 2(b)] is expressed by Eq. (1.1) (step.0). It is clear that $\tilde{p}_{\text{true}}(\mathbf{r}_m)$ cannot be modified by the data extrapolation process. On the contrary, $\tilde{p}_{\text{error}}(\mathbf{r}_m)$ is modified by this process. The error pressure, which is zero inside the measurement aperture, has the discontinuity and contains high wave number components. Next, the K-space representation of the zero-padded pressure is obtained by 2D-FT [Fig. 2(c)]. The K-space representation of the error pressure $\tilde{p}_{\text{error}}(\mathbf{r}_m)$ is

$$\tilde{P}_{\text{error}}(k_x,k_y)=F[\tilde{p}_{\text{error}}(\mathbf{r}_m)], \tag{2.1}$$

where F denotes the 2D-FT (step.1). In the K space, high wave number components of the error pressure are set to be zero (step.2). This bandlimited error pressure is given as

$$\tilde{P}_{e,1}(k_x,k_y)=\tilde{P}_{\text{error}}(k_x,k_y)\,\text{circ}\left(\frac{\sqrt{k_x^2+k_y^2}}{k_{\max}}\right), \tag{2.2}$$

$$\text{circ}\left(\frac{\sqrt{k_x^2+k_y^2}}{k_{\max}}\right)=\begin{cases}1, & k_x^2+k_y^2\leqslant k_{\max}^2,\\ 0, & k_x^2+k_y^2>k_{\max}^2.\end{cases} \tag{2.3}$$

The error norm is thus reduced by this band limitation in K space (step.2). The bandlimited error pressure $\tilde{p}_{e,1}(\mathbf{r}_m)$ is then given as

$$\tilde{p}_{e,1}(\mathbf{r}_m)=F^{-1}[\tilde{P}_{e,1}(k_x,k_y)], \tag{2.4}$$

where F^{-1} denotes 2D-IFT (step.3). This bandlimited error pressure will leak into the measurement aperture. Therefore, the pressure on the full measurement aperture is corrected by the measured pressure $\tilde{p}_{\text{meas}}(\mathbf{r}_m)$. Correcting the error pressure in the measurement aperture to zero reduces the error norm again (step.4),

$$\tilde{p}_{\text{error},1}(\mathbf{r}_m)=\tilde{p}_{e,1}(\mathbf{r}_m)W(\mathbf{r}_m), \tag{2.5}$$

where $W(\mathbf{r}_m)$ is given as Eq. (1.3). This new error pressure $\tilde{p}_{\text{error},1}(\mathbf{r}_m)$ has the discontinuity, and the band limitation is applied by the K-space filter [Eq. (2.3)] again. Thus the error norm is reduced in real and K spaces.

In practice, the error pressure norm cannot be obtained directly, however, the cutoff region ($\sqrt{k_x^2+k_y^2}>k_{\max}$) includes the error pressure component only. Therefore, the criterion of the K-space data extrapolation process is introduced as the norm of the pressure component included in the cutoff region, which is defined as

$$\left\|F[\tilde{p}_{\text{error},n}(x,y)]\left[1-\text{circ}\left(\frac{\sqrt{k_x^2+k_y^2}}{k_{\max}}\right)\right]\right\|=\sqrt{\int_{-\infty}^{\infty}\int_{-\infty}^{\infty}\left|F[\tilde{p}_{\text{error},n}(x,y)]\left[1-\text{circ}\left(\frac{\sqrt{k_x^2+k_y^2}}{k_{\max}}\right)\right]\right|^2 dk_x\,dk_y}, \tag{2.6}$$

because $\tilde{p}_{\text{true}}(x,y)$ exists only in the pass region of the K-space filter. This norm, $\|F[\tilde{p}_{\text{error},n}(k_x,k_y)][1-\text{circ}(\sqrt{k_x^2+k_y^2}/k_{\max})]\|$ is removed in step.2. In other words, the K-space data extrapolation process is terminated if the error norm reduction ratio in step.2 is smaller than the threshold.

Now, we discuss the effect that the finiteness of the measurement aperture has on the contamination of the reconstructed results. Let us assume that the distance between the structure and the measurement plane is z, the size of the measurement aperture is $L\times L$, the normal velocity of the structure is $\tilde{v}(x,y)$, and the cutoff wave number of the K-space filter expressed in Eq. (2.3) is k_{cut}. The pressure on the measurement plane $\tilde{p}_{\text{true}}(x,y)$ is expressed as[10]

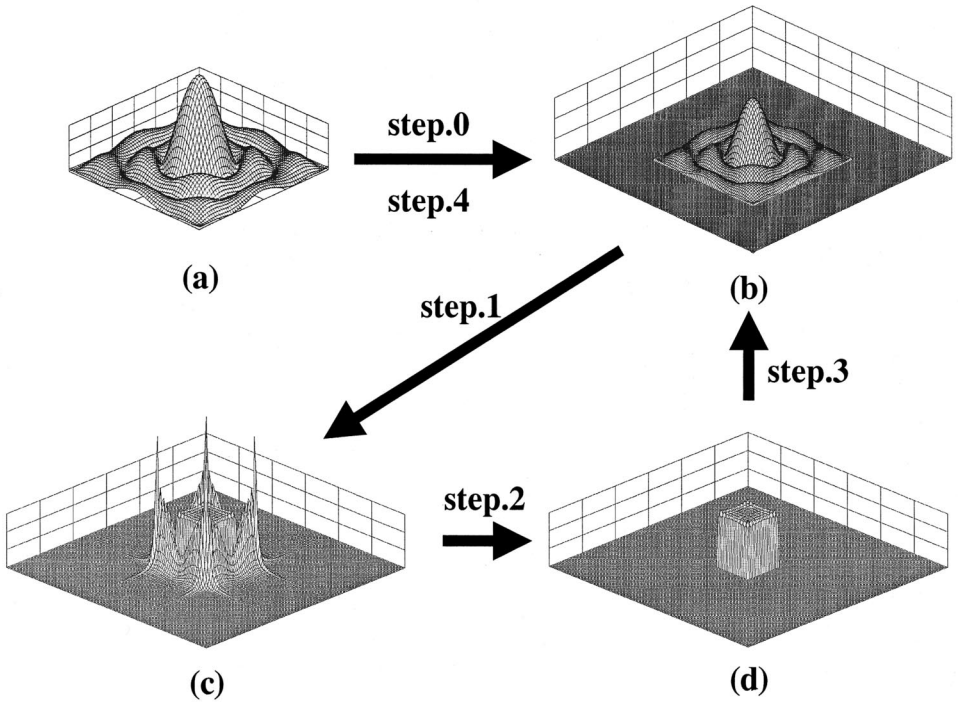

FIG. 3. Schematic diagram of the real-space data extrapolation method. (a) The amplitude of the measured pressure. (b) The amplitude of the corrected pressure on an enlarged aperture. (c) The amplitude of reconstructed surface velocity of the structure. (d) The amplitude of the corrected surface velocity. Note that the velocity outside the structure is set to be zero.

$$\tilde{p}_{\text{true}}(x,y)=F^{-1}\left(F[\tilde{v}(x,y)]\exp(-iz\sqrt{k_0^2-k_r^2})\frac{ik_0\rho c}{\sqrt{k_0^2-k_r^2}}\right), \tag{2.7}$$

$$k_r^2=k_x^2+k_y^2, \tag{2.8}$$

where $k_0=2\pi f/c$, c denotes the sound speed, f the frequency, and ρ the density of the medium (water). The restriction of the measurement aperture is equivalent to the convolution of the K-space representation of the real-space window $F[W_r(x,y)]$ and that of the true pressure $F[\tilde{p}_{\text{true}}(x,y)]$:

$$\begin{aligned}F[\tilde{p}_{\text{true}}(x,y)W_r(x,y)]&=F[\tilde{p}_{\text{true}}(x,y)]*F[W_r(x,y)]\\&=F[\tilde{p}_{\text{true}}(x,y)]*\left[\left(\frac{2L}{\pi}\right)^2\text{sinc}(Lk_x)\text{sinc}(Lk_y)\right],\end{aligned} \tag{2.9}$$

$$W_r(x,y)=[u_{-L/2}(x)-u_{L/2}(x)][u_{-L/2}(y)-u_{L/2}(y)], \tag{2.10}$$

$$u_a(x)=\begin{cases}1, & x\geqslant a,\\ 0, & \text{otherwise.}\end{cases} \tag{2.11}$$

The convolution causes a leakage of low wave number components of the pressure into the high wave number region, and these leaked components are amplified in the NAH back-propagation and velocity reconstruction process. The approximation of reconstructed surface velocity $\tilde{v}_{\text{reconst}}(x,y)$, that is obtained from the pressure measured on the finite aperture $\tilde{p}_{\text{true}}(x,y)W_r(x,y)$, is expressed as

$$\begin{aligned}\tilde{v}_{\text{reconst}}(x,y)&=F^{-1}\left[F[\tilde{p}_{\text{true}}(x,y)W_r(x,y)]\exp(iz\sqrt{k_0^2-k_r^2})\times\frac{\sqrt{k_0^2-k_r^2}}{ik_0\rho c}\right]\\&\approx F^{-1}\left\{\left[F\{\tilde{p}_{\text{true}}(x,y)\}\exp(iz\sqrt{k_0^2-k_r^2})\,\frac{\sqrt{k_0^2-k_r^2}}{ik_0\rho c}\right]*\left(\frac{2L}{\pi}\,\text{sinc}(Lk_r)\exp(iz\sqrt{k_0^2-k_r^2})\,\frac{\sqrt{k_0^2-k_r^2}}{ik_0\rho c}\right)\right\}\\&=F^{-1}\left[F[\tilde{v}(x,y)]*\left(\frac{2L}{\pi}\,\text{sinc}(Lk_r)\exp(iz\sqrt{k_0^2-k_r^2})\times\frac{\sqrt{k_0^2-k_r^2}}{ik_0\rho c}\right)\right].\end{aligned} \tag{2.12}$$

This equation means that the low wave number component of the $\tilde{v}(x,y)$ (wave number $k_{r0}=\sqrt{k_{x0}^2+k_{y0}^2}$ is low) is multiplied by the contamination factor $\tilde{C}(k_{r0};k_{r1})$ and added to the high wave number region (wave number $k_{r1}=\sqrt{k_{x1}^2+k_{y1}^2}$ is high), where

$$\begin{aligned}\tilde{C}(k_{r0};k_{r1})=&\frac{2L}{\pi}\,\text{sinc}\{L(k_{r1}-k_{r0})\}\\&\times\exp[iz(\sqrt{k_0^2-k_{r1}^2}-\sqrt{k_0^2-k_{r0}^2})]\frac{\sqrt{k_0^2-k_{r1}^2}}{\sqrt{k_0^2-k_{r0}^2}}.\end{aligned} \tag{2.13}$$

This added component (which is called the ''contamination velocity component'') contaminates the reconstructed result. If $k_{r1}<k_{\text{cut}}$, this contamination velocity component is not removed by the K-space data extrapolation method. Therefore, we have to make k_{cut} small. On the contrary, if k_{cut} is too small, the reconstruction error becomes large because the resolution of the reconstructed result is deteriorated. The discussion above suggests that k_{cut} should be optimized for the reduction of the contamination velocity component and the resolution improvement of the reconstructed result. The optimization procedure of k_{cut} is discussed in Sec. III in more detail.

Moreover, the mechanism that the distortion of the reconstruction result is caused by the conventional real-space window method may be similarly explained by substituting the window function (Hanning, Tukey, etc.) into Eq. (2.9). However, this explanation departs from the subject of this paper. Therefore, we will postpone the discussion on the problem caused by the conventional real-space window method to another paper.

B. Algorithm of real-space data extrapolation method

In this section, the algorithm of the real-space data extrapolation method is briefly described. First, we assume that the vibrating structure is surrounded by a rigid baffle. The coordinate system is shown in Fig. 1. A schematic diagram of the procedure is shown in Fig. 3, and the procedure is as follows.

(i) **step.0** The measurement aperture size is virtually enlarged by zero padding.

(ii) **step.1** The surface velocity is reconstructed by the NAH back-propagation of the pressure on the virtual measurement aperture.

(iii) **step.2** The reconstructed surface velocity outside the vibrating structure is set to zero.

(iv) **step.3** The pressure on the virtual measurement aperture is calculated by the NAH forward propagation of the surface velocity, which is corrected by step.2.

(v) **step.4** The pressure of the enlarged aperture is corrected according to the measured pressure. Then, return to step.1.

The procedure is iterated until the correction criterion satisfies the requirement that the integration of the squared velocity outside the known extent of the finite plate is smaller than the threshold. In this study, the threshold is set to be 0.01% of the integration of the squared velocity on the finite plate.

The convergence of the zero-padded pressure to the ''true'' pressure by this procedure is explained as follows.

Let us assume that $\tilde{v}(\mathbf{r_0})$ outside the S_v is zero. That is,

$$\tilde{v}(\mathbf{r_0}) = \tilde{v}(\mathbf{r_0}) W_0(\mathbf{r_0}) \begin{cases} \neq 0 & (\mathbf{r_0} \in S_v), \\ = 0 & (\mathbf{r_0} \notin S_v), \end{cases} \tag{2.14}$$

$$W_0(\mathbf{r_0}) = \begin{cases} 1 & (\mathbf{r_0} \in S_v), \\ 0 & (\mathbf{r_0} \notin S_v). \end{cases} \tag{2.15}$$

According to Maynard *et al.*,[10] the relationships between the radiated pressure $\tilde{p}_0(\mathbf{r_m})$ and surface velocity $\tilde{v}(\mathbf{r_0})$ are expressed as

$$\tilde{p}_0(\mathbf{r_m}) = F^{-1}\{F[\tilde{G}_{vp}(\mathbf{r_0};\mathbf{r_m})] F[\tilde{v}(\mathbf{r_0})]\}, \tag{2.16}$$

$$\tilde{v}(\mathbf{r_0}) = F^{-1}\{F[\tilde{G}_{pv}(\mathbf{r_m};\mathbf{r_0})] F[\tilde{p}_0(\mathbf{r_m})]\}, \tag{2.17}$$

where $\tilde{G}_{vp}(\mathbf{r_0};\mathbf{r_m})$ is the Green's function that satisfies the Dirichlet boundary condition on the S_0 plane, and $\tilde{G}_{pv}(\mathbf{r_m};\mathbf{r_0})$ is the Green's function that satisfies the Neumann boundary condition on the S_0 plane. The 2D-FTs of $\tilde{G}_{vp}$ and $\tilde{G}_{pv}$ are termed propagators.[10]

Let us assume that the area of S_p is wide compared with the area of S_v. The radiated pressure is measured on the measurement aperture [Fig. 3(a)]. The zero-padded pressure $\tilde{p}_1(\mathbf{r_m})$ [Fig. 3(b)] is expressed as follows (step.0):

$$\begin{aligned} \tilde{p}_1(\mathbf{r_m}) &= \tilde{p}_0(\mathbf{r_m})[1 - W(\mathbf{r_m})] \\ &= \tilde{p}_0(\mathbf{r_m}) - \tilde{p}_0(\mathbf{r_m}) W(\mathbf{r_m}) \\ &= \tilde{p}_0(\mathbf{r_m}) - \tilde{p}_{e,1}(\mathbf{r_m}), \end{aligned} \tag{2.18}$$

where

$$\tilde{p}_{e,1}(\mathbf{r_m}) = \tilde{p}_0(\mathbf{r_m}) W(\mathbf{r_m}), \tag{2.19}$$

where $\tilde{p}_{e,1}(\mathbf{r_m})$ is the error pressure of the zero-padded pressure, and $W(\mathbf{r_m})$ is given as Eq. (1.3). It is clear that $\tilde{p}_0(\mathbf{r_m})$ cannot be modified by the data extrapolation process. On the contrary, $\tilde{p}_{e,1}(\mathbf{r_m})$ is modified by this process. According to Eq. (2.17), the surface velocity reconstructed from the error pressure $\tilde{p}_{e,1}(\mathbf{r_m})$ is

$$\tilde{v}_{e,1}(\mathbf{r_0}) = F^{-1}\{F[\tilde{G}_{pv}(\mathbf{r_m};\mathbf{r_0})] F[\tilde{p}_{e,1}(\mathbf{r_m})]\}, \tag{2.20}$$

where $\tilde{v}_{e,1}(\mathbf{r_0})$ is infinite in extent (step.1), therefore, the reconstructed surface velocity [Fig. 3(c)] is contaminated. Since the surface velocity outside the S_v is zero [Fig. 3(d)], the new error surface velocity $\tilde{v}'_{e,1}(\mathbf{r_0})$ is given as

$$\tilde{v}'_{e,1}(\mathbf{r_0}) = \tilde{v}_{e,1}(\mathbf{r_0}) W_0(\mathbf{r_0}), \tag{2.21}$$

and the error norm is reduced in the surface velocity domain (step.2). The error pressure $\tilde{p}'_{e,1}(\mathbf{r_m})$ is then reconstructed from $\tilde{v}'_{e,1}(\mathbf{r_0})$ (step.3) as

$$\tilde{p}'_{e,1}(\mathbf{r_m}) = F^{-1}\{F[\tilde{G}_{vp}(\mathbf{r_0};\mathbf{r_m})] F[\tilde{v}'_{e,1}(\mathbf{r_0})]\}, \tag{2.22}$$

where the pressure on the measurement aperture is corrected by the radiated pressure $\tilde{p}_0(\mathbf{r_m})$. Correcting the error pressure $\tilde{p}_{e,1}(\mathbf{r_m})$ in the measurement aperture to zero reduces the error norm again (step.4). The new error pressure $\tilde{p}_{e,2}(\mathbf{r_m})$ is obtained by the correction

$$\tilde{p}_{e,2}(\mathbf{r_m}) = \tilde{p}'_{e,1}(\mathbf{r_m}) W(\mathbf{r_m}). \tag{2.23}$$

Here, let us assume that

$$\|\tilde{v}(\mathbf{r_0})\| > \|\tilde{v}'_{e,1}(\mathbf{r_0})\|, \tag{2.24}$$

where

$$\|\tilde{v}(\mathbf{r_0})\| = \sqrt{\int_{S_0} |\tilde{v}(\mathbf{r_0})|^2 \, d\mathbf{r_0}}, \tag{2.25}$$

$$\|\tilde{v}'_{e,1}(\mathbf{r_0})\| = \sqrt{\int_{S_0} |\tilde{v}'_{e,1}(\mathbf{r_0})|^2 \, d\mathbf{r_0}}, \tag{2.26}$$

and $\|\tilde{v}'_{e,1}(\mathbf{r_0})\|$ is defined as the error velocity norm. Since the evanescent wave component is reduced by the "natural filter effect" in the forward propagation process, then the component of the pressure on S_m plane becomes negligibly small compared with the radiation wave component. Therefore, according to Ref. 10,

$$\|\tilde{v}(\mathbf{r_0})\| \times \rho c k_0 \approx \|\tilde{p}_0(\mathbf{r_m})\|, \tag{2.27}$$

$$\|\tilde{v}'_{e,1}(\mathbf{r_0})\| \times \rho c k_0 \approx \|\tilde{p}'_{e,1}(\mathbf{r_m})\|, \tag{2.28}$$

and

$$\|\tilde{p}_0(\mathbf{r_m})\| > \|\tilde{p}'_{e,1}(\mathbf{r_m})\|, \tag{2.29}$$

$$\begin{aligned} \|\tilde{p}_{e,1}(\mathbf{r_m})\| &= \|\tilde{p}_0(\mathbf{r_m}) W(\mathbf{r_m})\| > \|\tilde{p}'_{e,1}(\mathbf{r_m}) W(\mathbf{r_m})\| \\ &= \|\tilde{p}_{e,2}(\mathbf{r_m})\|, \end{aligned} \tag{2.30}$$

where

$$\|\tilde{p}_0(\mathbf{r_m})\| = \sqrt{\int_{S_m} |\tilde{p}_0(\mathbf{r_m})|^2 \, d\mathbf{r_m}}, \tag{2.31}$$

$$\|\tilde{p}_{e,1}(\mathbf{r_m})\| = \sqrt{\int_{S_m} |\tilde{p}_{e,1}(\mathbf{r_m})|^2 \, d\mathbf{r_m}}. \tag{2.32}$$

Next, let us assume that

$$\|\tilde{v}'_{e,n-1}(\mathbf{r_0})\| > \|\tilde{v}'_{e,n}(\mathbf{r_0})\|, \tag{2.33}$$

then

$$\|\tilde{p}'_{e,n-1}(\mathbf{r_m})\| > \|\tilde{p}'_{e,n}(\mathbf{r_m})\|, \tag{2.34}$$

$$\begin{aligned} \|\tilde{p}_{e,n}(\mathbf{r_m})\| &= \|\tilde{p}'_{e,n-1}(\mathbf{r_m}) W(\mathbf{r_m})\| > \|\tilde{p}'_{e,n}(\mathbf{r_m}) W(\mathbf{r_m})\| \\ &= \|\tilde{p}_{e,n+1}(\mathbf{r_m})\|, \end{aligned} \tag{2.35}$$

$$\begin{aligned} \|\tilde{v}_{e,n}(\mathbf{r_0})\| &= \|F^{-1}\{F[\tilde{G}_{pv}(\mathbf{r_m};\mathbf{r_0})] F[\tilde{p}_{e,n}(\mathbf{r_m})]\}\| \\ &> \|F^{-1}\{F[\tilde{G}_{pv}(\mathbf{r_m};\mathbf{r_0})] F[\tilde{p}_{e,n+1}(\mathbf{r_m})]\}\| \\ &= \|\tilde{v}_{e,n+1}(\mathbf{r_0})\|, \end{aligned} \tag{2.36}$$

$$\begin{aligned} \|\tilde{v}'_{e,n}(\mathbf{r_0})\| &= \|\tilde{v}_{e,n}(\mathbf{r_0}) W_0(\mathbf{r_0})\| > \|\tilde{v}_{e,n+1}(\mathbf{r_0}) W_0(\mathbf{r_0})\| \\ &= \|\tilde{v}'_{e,n+1}(\mathbf{r_0})\|, \end{aligned} \tag{2.37}$$

where $\tilde{p}_{e,n}(\mathbf{r_m})$ and $\tilde{v}_{e,n}(\mathbf{r_m})$ are the error pressure and the error surface velocity yielded by n iterations. As the result, if Eq. (2.24) is satisfied, then

$$\lim_{n\to\infty} \|\tilde{v}_{e,n}(\mathbf{r_0})\| = \lim_{n\to\infty} \|\tilde{p}_{e,n}(\mathbf{r_m})\| = 0. \tag{2.38}$$

Following the above-mentioned discussion, the appropriate measurement aperture S_p and window function $W_0(\mathbf{r_0})$, which satisfy Eq. (2.24), are estimated by computer simulation in Sec. IV.

Here, let us examine the influences of the vibration outside the structure to the reconstruction error of the proposed method. The pressure $\tilde{p}_{\text{true}}(\mathbf{r_m})$ on the S_m plane (cf. Fig. 1), the pressure $\tilde{p}_{\text{inside}}(\mathbf{r_m})$ induced by the velocity of the structure S_v $[\tilde{v}_{\text{inside}}(\mathbf{r_o})]$, and the pressure $\tilde{p}_{\text{outside}}(\mathbf{r_m})$ induced by the velocity of the outside of S_v $(\tilde{v}_{\text{outside}}(\mathbf{r_o}))$ are related as

$$\tilde{p}_{\text{true}}(\mathbf{r_m})=\tilde{p}_{\text{inside}}(\mathbf{r_m})+\tilde{p}_{\text{outside}}(\mathbf{r_m}), \tag{2.39}$$

and

$$\tilde{v}(\mathbf{r_0})=\tilde{v}_{\text{inside}}(\mathbf{r_0})+\tilde{v}_{\text{outside}}(\mathbf{r_0}). \tag{2.40}$$

It is clear that the pressure $\tilde{p}_{\text{inside}}(\mathbf{r_m})$ is not able to be modified by the data extrapolation process because

$$F^{-1}[F[G_{pv}(\mathbf{r_m};\mathbf{r_0})]F[\tilde{p}_{\text{inside}}(\mathbf{r_m})]] = \begin{cases} \tilde{v}_{\text{inside}}(\mathbf{r_0})=\tilde{v}(\mathbf{r_0}) & (\mathbf{r_0}\in S_v), \\ 0 \quad (\mathbf{r_0}\notin S_v). \end{cases} \tag{2.41}$$

On the contrary, $\tilde{p}_{\text{outside}}(\mathbf{r_m})$ is modified by the data extrapolation process. The pressure $\tilde{p}_{\text{outside}}(\mathbf{r_m})$ measured on the measurement aperture is expressed as

$$\tilde{p}_{\text{outside}}(\mathbf{r_m})[1-W(\mathbf{r_m})]=\tilde{p}_{\text{outside}}(\mathbf{r_m})-\tilde{p}_{e,\text{outside},1}(\mathbf{r_m}), \tag{2.42}$$

where

$$\tilde{p}_{e,\text{outside},1}(\mathbf{r_m})=\tilde{p}_{\text{outside}}(\mathbf{r_m})W(\mathbf{r_m}). \tag{2.43}$$

The surface velocity reconstructed from the pressure $\tilde{p}_{\text{outside}}(\mathbf{r_m})-\tilde{p}_{e,\text{outside},1}(\mathbf{r_m})$ is

$$\begin{aligned}\tilde{v}_{\text{outside},1}(\mathbf{r_0}) &= F^{-1}[F[\tilde{G}_{pv}(\mathbf{r_m};\mathbf{r_0})] \\ &\quad \times F[\tilde{p}_{\text{outside}}(\mathbf{r_m})-\tilde{p}_{e,\text{outside},1}(\mathbf{r_m})]], \\ &= \tilde{v}_{\text{outside}}(\mathbf{r_0})-\tilde{v}_{e,\text{outside},1}(\mathbf{r_0}),\end{aligned} \tag{2.44}$$

where $\tilde{v}_{e,\text{outside},1}(\mathbf{r_0})$ is infinite in extent (step.1 in Fig. 3). Since the surface velocity outside the S_v is set to be zero, the new surface velocity $\tilde{v}'_{\text{outside},1}(\mathbf{r_0})$ is given as

$$\begin{aligned}\tilde{v}'_{\text{outside},1}(\mathbf{r_0}) &= \tilde{v}_{\text{outside},1}(\mathbf{r_0})W_0(\mathbf{r_0}) \\ &= -\tilde{v}_{e,\text{outside},1}(\mathbf{r_0})W_0(\mathbf{r_0}).\end{aligned} \tag{2.45}$$

The velocity norm that is induced by $\tilde{p}_{\text{outside}}(\mathbf{r_m})$ is reduced in the surface velocity domain. Therefore, the new error pressure $\tilde{p}'_{e,\text{outside},1}(\mathbf{r_m})$ is reconstructed from the velocity $\tilde{v}'_{\text{outside},1}(\mathbf{r_0})$ as

$$\tilde{p}'_{e,\text{outside},1}(\mathbf{r_0})=F^{-1}\{F[\tilde{G}_{vp}(\mathbf{r_0};\mathbf{r_m})]F[\tilde{v}'_{\text{outside},1}(\mathbf{r_0})]\}, \tag{2.46}$$

where the new error pressure $\tilde{p}'_{e,\text{outside},1}(\mathbf{r_m})$ has the norm in the measurement aperture. Here, the pressure on the measurement aperture is corrected by the true pressure $\tilde{p}_{\text{true}}(\mathbf{r_m})$. The correction when the pressure in the measurement aperture is set to be zero reduces the error norm and also creates new pressure $\tilde{p}_{\text{outside},2}(\mathbf{r_m})$, where

$$\begin{aligned}\tilde{p}_{\text{outside},2}(\mathbf{r_m}) &= \tilde{p}'_{e,\text{outside},1}(\mathbf{r_m})[1-W(\mathbf{r_m})] \\ &\quad +\tilde{p}_{\text{outside}}(\mathbf{r_m})-\tilde{p}_{e,\text{outside},1}(\mathbf{r_m}).\end{aligned} \tag{2.47}$$

The component $\tilde{p}'_{e,\text{outside},1}(\mathbf{r_m})$ is reduced by the iteration of the data extrapolation process, and finally we obtain

$$\lim_{n\to\infty}\tilde{p}'_{e,\text{outside},n}(\mathbf{r_m})=0. \tag{2.48}$$

However, the pressure $-\tilde{p}_{e,\text{outside},1}(\mathbf{r_m})$ is added in the process expressed by Eq. (2.47) to the pressure that is used to reconstruct the velocity of the structure. Therefore, after several times of the iteration, the reconstruction error is induced only by the $\tilde{p}_{e,\text{outside},1}(\mathbf{r_m})=\tilde{p}_{\text{outside}}(\mathbf{r_m})W(\mathbf{r_m})$.

In this case, Eq. (2.24) is modified as

$$\|\tilde{v}(\mathbf{r_0})\|>\|\tilde{v}'_{e,1}(\mathbf{r_0})\|+\|\tilde{v}'_{\text{outside},1}(\mathbf{r_0})\|. \tag{2.49}$$

And if Eq. (2.49) is satisfied, the reconstructed result after several times of the iteration of the extrapolation process is

$$\begin{aligned}\lim_{n\to\infty}\{\tilde{v}(\mathbf{r_0})+\tilde{v}'_{e,n}(\mathbf{r_0})\} &= \tilde{v}_{\text{inside}}(\mathbf{r_0})+\tilde{v}_{\text{outside}}(\mathbf{r_0}) \\ &\quad -\tilde{v}_{e,\text{outside},1}(\mathbf{r_0}) \\ &= \tilde{v}(\mathbf{r_0})-\tilde{v}_{e,\text{outside},1}(\mathbf{r_0}).\end{aligned} \tag{2.50}$$

III. SIMULATIONS

A. Optimization method of the cutoff wave number for data extrapolation method

In this section, we introduce the optimization method of the cutoff wave number for the K-space data extrapolation method. First, we investigate the K-space representation of the velocity in detail based on the average wave number spectrum of the velocity given as follows:

$$\overline{V}(0)=\frac{2\pi\int_0^{3\pi/2L}|F[\tilde{v}(x,y)]|k_r\,dk_r}{\pi\left(\frac{3\pi}{2L}\right)^2}, \tag{3.1}$$

$$\overline{V}\left(\frac{2m\pi}{L}\right)=\frac{2\pi\int_{(2m+1)/2L}^{(2m+3)\pi/2L}|F[\tilde{v}(x,y)]|k_r\,dk_r}{\pi^3\frac{2(m+1)}{L^2}},$$

$$m=1,2,3\ldots\ . \tag{3.2}$$

Figure 4 shows the average wave number spectrum $\overline{V}(2m\pi/L)$, which is normalized by $\overline{V}(0)$. The vibrating object is a rectangular piston of 0.64 m×0.64 m with a rigid baffle, and the vibrating frequency is 3 kHz. The distance between the structure and the measurement plane is 3 cm. The sound velocity in water is 1500 m/s, and the data of the measurement aperture are taken in 2 cm steps along the horizontal and vertical axes. The full aperture is 2.56 m×2.56 m, the measurement aperture is 1.28 m×1.28 m. In order to obtain the measured pressure data, FFT is used to calculate the of the Rayleigh integral of the structural surface velocity[16] in this simulation.

The solid line indicates the average wave number spectrum of the original velocity. This spectrum is monotonically decaying outside the radiation circle. The dotted line means the average wave number spectrum of the velocity reconstructed from the pressure measured on the finite aperture. In the low wave number region, the spectrum of the reconstructed velocity is slightly different from that of the original velocity. However, the spectrum in the high wave number region is very large and different from the spectrum of the

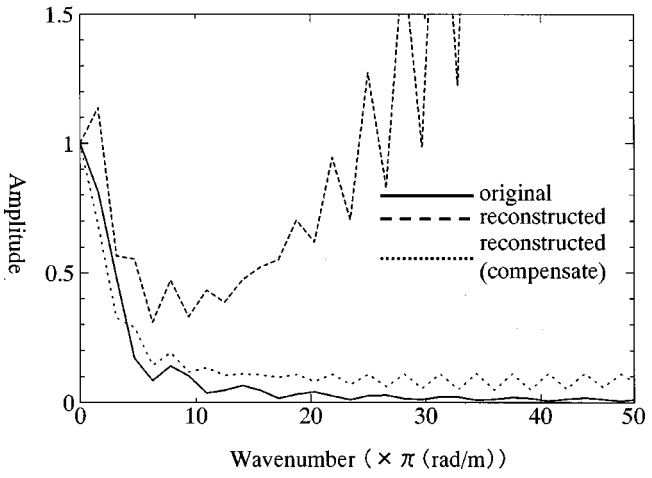

FIG. 4. Average wave number spectrum of the velocity. The solid line shows the original velocity spectrum. The broken line indicates the spectrum of the velocity reconstructed from the pressure measured on the finite aperture. The dotted line means the compensated velocity spectrum. These spectrums are normalized by $\overline{V}(0)$, respectively.

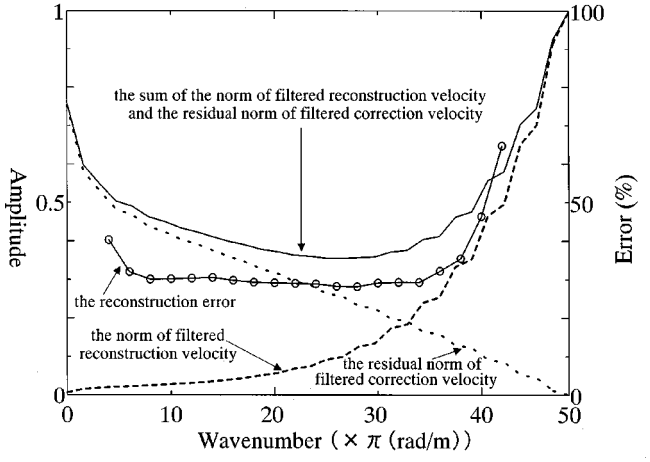

FIG. 5. The relationship between the norm and reconstruction error. The solid line with a circle shows the reconstruction error. The broken and dotted lines indicate the norm of filtered reconstruction velocity and the residual norm of filtered correction velocity, respectively. The solid line corresponds to the sum of the norm of filtered reconstruction velocity and the residual norm of filtered correction velocity.

original velocity. The ratio between the norm of original velocity $\|\tilde{v}(x,y)\|$ and that of the reconstructed velocity $\|\tilde{v}_{\text{reconst}}(x,y)\|$ is 2.02%. Therefore, the norm $\|\tilde{v}_{\text{reconst}}(x,y)\|$ is mostly constituted of the contamination velocity component. The reconstructed error can then be reduced by diminishing the norm of the filtered reconstructed velocity normalized by nonfiltered reconstructed velocity (simply denoted as the ''norm of filtered reconstruction velocity,'' hereafter), which is defined as

$$\|\tilde{v}_{\text{filter}}(x,y;k_{\text{cut}})\| = \frac{\left\| F[\tilde{v}_{\text{reconst}}(x,y)]\,\text{circ}\left(\frac{k_r}{k_{\text{cut}}}\right)\right\|}{\|F[\tilde{v}_{\text{reconst}}(x,y)]\|} = \frac{\sqrt{\int\int |F[\tilde{v}_{\text{reconst}}(x,y)]|^2\,\text{circ}\left(\frac{k_r}{k_{\text{cut}}}\right) dk_x\,dk_y}}{\sqrt{\int\int |F[\tilde{v}_{\text{reconst}}(x,y)]|^2\,dk_x\,dk_y}}. \tag{3.3}$$

Next, an estimation method of the original velocity spectrum is proposed to assure the resolution of the reconstructed result. The cutoff wave number is optimized by calculating the ''norm of filtered corrected velocity.'' In the low wave number region, the spectrum of the reconstructed velocity is slightly different from that of the original velocity. On the other hand, in the high wave number region, the spectrum of the reconstructed velocity is relatively affected by the contamination velocity component, which is approximately obtained as the multiplication of low wave number component in the reconstructed velocity and the contamination factor. To compensate for the influence of the contamination velocity component, the spectrum of the reconstructed velocity is divided by the contamination factor. As a result, we obtain the corrected velocity spectrum, which is expressed as

$$\overline{V}_{\text{correct}}(0) = \frac{\overline{V}_{\text{reconst}}(0)\,\pi}{2L}, \tag{3.4}$$

$$\overline{V}_{\text{correct}}\left(\frac{2m\pi}{L}\right) = \frac{\overline{V}_{\text{reconst}}\left(\frac{2m\pi}{L}\right)}{\tilde{C}\left(k_a;\frac{2m\pi}{L}\right)}, \quad m=1,2,3,\ldots, \tag{3.5}$$

$$k_a = \frac{2\pi\int_0^{3\pi/2L} k_r^2\,dk_r}{\pi\left(\frac{3\pi}{2L}\right)^2} = \frac{2\pi}{\pi\left(\frac{3\pi}{2L}\right)^2}\left[\frac{1}{3}k_r^3\right]_0^{3\pi/2L} = \frac{\pi}{L}. \tag{3.6}$$

The broken line in Fig. 4 shows the corrected velocity spectrum. A good agreement between the spectrum of the original velocity and that of the corrected velocity suggests the validity of the proposed compensation method for the estimation of the velocity spectrum.

Now, let us introduce the norm of filtered corrected velocity normalized by nonfiltered corrected velocity (simply denoted as the ''norm of filtered correction velocity,'' hereafter), which is defined as

$$\|\tilde{v}_{\text{filter,correct}}(x,y;k_{\text{cut}})\| = \frac{\pi\left(\frac{3\pi}{2L}\right)^2\overline{V}_{\text{correct}}(0) + \frac{2\pi^3}{L^2}\sum_{m=1}^{n} m\overline{V}_{\text{correct}}\left(\frac{2m\pi}{L}\right)}{\pi\left(\frac{3\pi}{2L}\right)^2\overline{V}_{\text{correct}}(0) + \frac{2\pi^3}{L^2}\sum_{m=1}^{N} m\overline{V}_{\text{correct}}\left(\frac{2m\pi}{L}\right)}, \tag{3.7}$$

where n is the largest integer that satisfies $n<Lk_{\text{cut}}/2\pi$ and N the largest integer that satisfies $N<\pi/d$ (d: the spatial sampling rate). To reduce the reconstruction error caused by the deterioration of the resolution, we have to make the norm of filtered correction velocity large. In other words, we can reduce the reconstruction error by reducing the residual norm of filtered correction velocity, which is defined as $1-\|\tilde{v}_{\text{filter,correct}}(x,y;k_{\text{cut}})\|$.

According to the discussion above, we can optimize the cutoff wave number k_{cut} by minimizing the sum of the norm of filtered reconstruction velocity and the residual norm of filtered correction velocity. Figure 5 presents that the norm of filtered reconstruction velocity, the residual norm of filtered correction velocity, the sum of these norms, and the reconstruction error. This reconstruction error is defined as $\|\tilde{v}(x,y)-\tilde{v}_{\mathrm{reconst}}(x,y)\|/\|\tilde{v}(x,y)\|$. The estimated optimal cutoff wave number is 26.6π(rad/m), and optimal cutoff wave number that minimizes the reconstruction error is 28π(rad/m). This agreement shows the validity of the proposed optimization method of the cutoff wave number k_{cut}. Therefore, the cutoff wave number for the K-space data extrapolation method is determined by our optimization method proposed in this paper.

In the real-space data extrapolation method, the cutoff wave number k_{cut} is π/d when the measured pressure hologram includes no noise, in other words, s/n$=\infty$, because the real-space data extrapolation method only constrains the extent of the vibrating object. Therefore, the wave number of the measured pressure hologram is only restricted by the spatial sampling rate of the hologram. However, usually the measured pressure hologram includes noise, which distributes uniformly in K-space. This behavior of noise is similar to that of the contamination velocity component. Therefore, it is necessary for the reduction of the noise influence to optimize the cutoff wave number k_{cut}. The optimization algorithm of the k_{cut} is the same as that for the K-space data extrapolation method.

B. The error of K-space data extrapolation method

In this section, the error of the K-space data extrapolation method is examined. The error of the reconstructed surface velocity is defined as follows:

$$\mathrm{error}=\frac{\sqrt{\int\int_S|\tilde{v}_{\mathrm{full}}(x,y)-\tilde{v}_{\mathrm{smoothed}}(x,y)|^2\,dx\,dy}}{\sqrt{\int\int_S|\tilde{v}_{\mathrm{full}}(x,y)|^2\,dx\,dy}}, \qquad (3.8)$$

where S is the structure surface, $\tilde{v}_{\mathrm{full}}(x,y)$ the surface velocity reconstructed from the full aperture pressure, and $\tilde{v}_{\mathrm{smoothed}}(x,y)$ the reconstructed result from the smoothed pressure by the real-space window method and/or data-extrapolation method.

Figure 6 illustrates the simulation result of the K-space data extrapolation method, where the data are normalized by the maximum value. The simulation conditions are the same as those of Fig. 4, and the cutoff wave number k_{cut} is 26.6π(rad/m). This reconstructed result is used as the reference for the comparison between the conventional and proposed data smoothing methods. In this simulation, the structure surface S is set by shifting the measurement aperture to the S_o plane (cf. Fig. 1) in the direction perpendicular to the measurement aperture.

In Fig. 6(b) (conventional method), the measured pressure is smoothed by the Tukey window before being reconstructed.[11,14] The K-space filter for the conventional method is that introduced by Veronesi and Maynard.[17] The measurement aperture is now reduced to a quarter of the reference. The edge discontinuity is depressed, however, the error with respect to the reference (a) is about 73%, which implies a serious influence of the real-space window. Particularly we can easily recognize that the data within the aperture is considerably affected and distorted.

On the other hand, Fig. 6(c) (proposed method) is the result from the K-space data extrapolation method that is applied to the same data as Fig. 4(b). The iteration number is 10 000, because the criterion of the K-space data extrapolation is satisfied. The criterion is expressed in Sec. II A. The reconstruction error with respect to the reference (a) is about 27.8%, where the influence of the discontinuity is sufficiently small. Figure 6(d) displays the outer area of the measurement aperture when our data extrapolation was complete. We may understand that the data extrapolation process

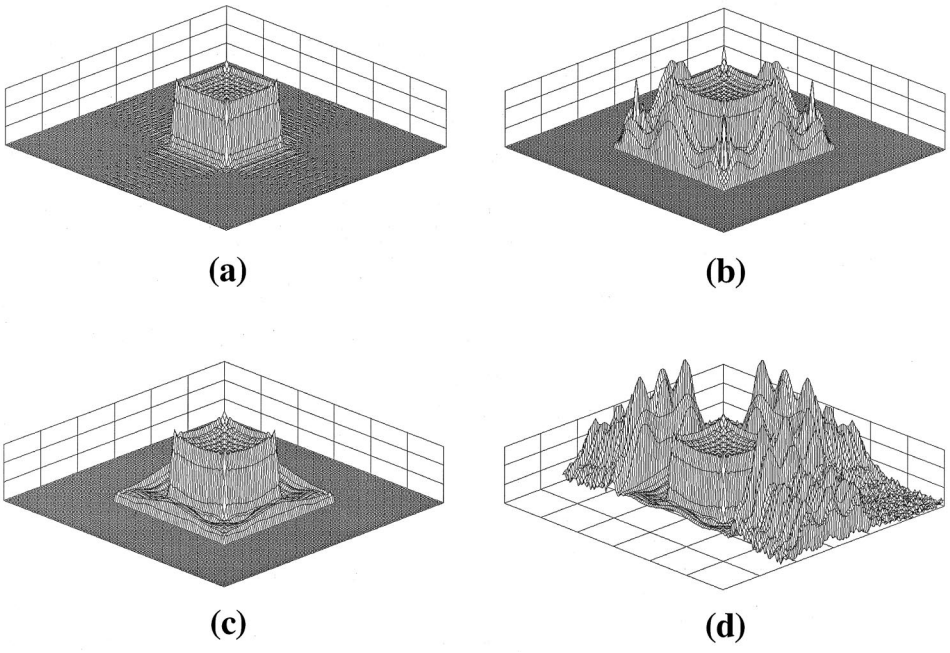

FIG. 6. The simulation result of the surface velocity reconstructed by the K-space data extrapolation method. The structure is uniformly driven at 3 kHz. Full aperture is 2.56 m×2.56 m, and the measurement aperture 1.28 m×1.28 m. The highest wave number $k_{\mathrm{max}}=26.6\,\pi$(rad/m). (a) The amplitude of the surface velocity reconstructed from the full aperture pressure. (b) The amplitude of the surface velocity reconstructed from the measurement-aperture pressure smoothed by the Tukey window. (c) The amplitude of the surface velocity reconstructed from the pressure obtained after 10 000 iterations of data extrapolation of the pressure on the measurement aperture. (d) The same as (c), except that the data over the area outside the measurement aperture is shown.

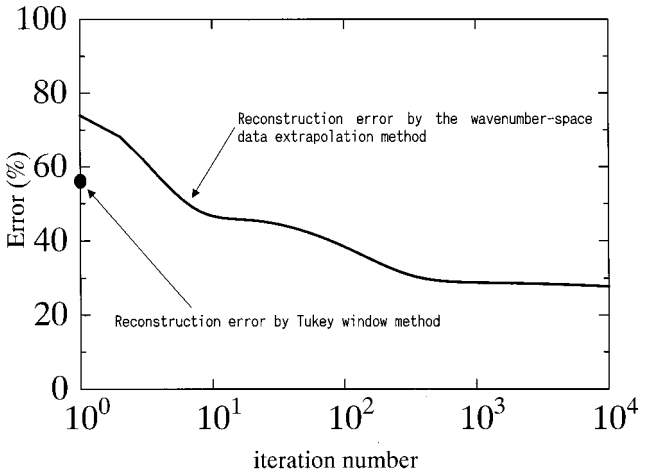

FIG. 7. The error of the reconstructed result of surface velocity. The solid line shows the error by the K-space data extrapolation method. The circle is the error by the conventional window of the Tukey type.

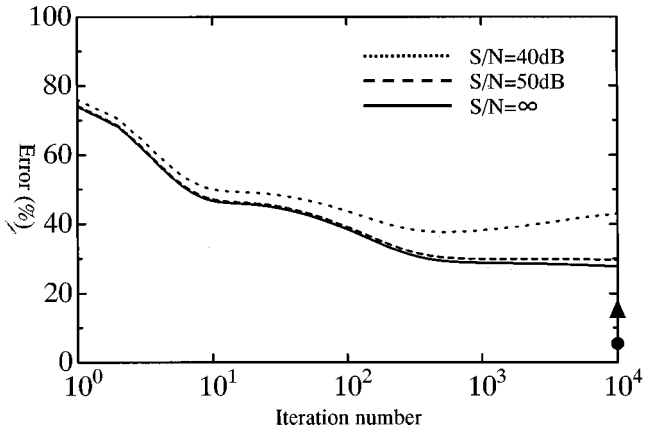

FIG. 8. The effect of the signal-to-noise ratio on the reconstruction error. The solid line shows the error of the surface velocity reconstructed from the measured pressure without noise. The broken and the dotted lines indicate the error of the result reconstructed from the pressure of s/n=50 dB and s/n=40 dB, respectively. A black circle and a triangle indicate that from the pressure of full aperture of s/n=50 dB and s/n=40 dB, respectively.

pushes the edge discontinuity toward the external area while keeping the measured data less affected.

Figure 7 illustrates a relationship between the iteration number and the error of reconstructed surface velocity. The solid line indicates the error of the surface velocity reconstructed by the K-space data extrapolation method, and the circle shows the error by the conventional window of the Tukey type. The results in Fig. 7 show that the error caused by the K-space data extrapolation method is considerably reduced as the iteration number is increased.

Figure 8 shows the dependence of the reconstruction error on the signal to noise ratio (s/n) of the measured pressure. The simulation conditions are the same as those of Fig. 6. The solid line shows the error of the surface velocity from the measured pressure hologram without noise. The broken line is the error of the reconstructed result when s/n=50 dB. The error for 10 000 iterations is 29.6%, while the error from the pressure with a full aperture is 4.8% (shown by a black circle in Fig. 8) when s/n=50 dB. The dotted line indicates the error when s/n=40 dB. The error for 10 000 iterations is 43%, while the error from the pressure with a full aperture is 15.2% (shown by a black triangle in Fig. 8) when s/n=40 dB. These results imply that (1) the error caused by the restriction of the aperture size is dominant when the signal level of the measured pressure is large (s/n>50 dB), and (2) the error caused by the noise is probably dominant when the signal to noise ratio of the measured pressure is small (s/n<50 dB). And in the case of s/n>50 dB, the reconstructed error by the proposed method is smaller than one-half of that by the conventional method. Therefore, the proposed method can be recommended for quantitative analysis.

Figure 9 illustrates the simulation result of K-space data extrapolation method. In this case, the size of the structure (2.56 m×2.56 m) is larger than that of the measurement aperture (0.64 m×0.64 m). The surface velocity of the structure is shown in Fig. 9(a). The white square indicates the measurement aperture. The distribution function of surface velocity for the vibrating structure is given as

$$v(x,y)=\sin\left(2\pi\frac{x}{0.64}\right)\sin\left(2\pi\frac{y}{0.64}\right), \tag{3.9}$$

and $k_{\mathrm{cut}}=6.3\pi$ (rad/m). Figure 9(b) shows the surface velocity on the measurement aperture indicated by the white square in Fig. 9(a), which is reconstructed from the full-aperture pressure data. The surface velocity reconstructed from the smoothed pressure of the measurement aperture using the Tukey window is shown in Fig. 9(c). The reconstruction error is 75%. The comparison between Fig. 9(b) and Fig. 9(c) indicates that the surface velocity distribution is seriously deformed by the Tukey window. Figure 9(d) is the result reconstructed from the pressure that is obtained after 10 000 iterations of our data extrapolation process applied to the pressure on the measurement aperture. The reconstruction error on the measurement aperture is 24.8%, and Fig. 9(d) seems to show a fairly good agreement with Fig. 9(b).

Next, to confirm the availability of the proposed method to quantitative analysis, the spatial derivatives of the reconstructed surface velocity is illustrated in Fig. 10. The left column shows the derivatives of the surface velocity defined by Eq. (3.9), which are used as the reference. The middle and right columns show the derivatives reconstructed from the Tukey window method and the proposed method, respectively. The top, middle, and bottom rows concern the first-, second-, and third-order derivatives with respect to y, respectively. In Fig. 10(b), the edges of the measurement aperture are seriously distorted, and the error relative to the reference (a) is about 61.5%. On the other hand, Fig. 10(c) shows a fairly good agreement with Fig. 10(a), and the error with respect to the reference (a) is about 19.6%. On the second-order derivative, the error by the Tukey window method [Fig. 10(e)] relative to the reference (d) is about 105.7%, while the error by the proposed method [Fig. 10(f)] is reduced to about 19.8%. On the third-order derivative, the error by the Tukey window method [Fig. 10(h)] with respect to the reference (g) is about 140.9%, while the error by the proposed method [Fig. 10(i)] is about 27.4%. As the result, the reconstruction error is significantly reduced by our pro-

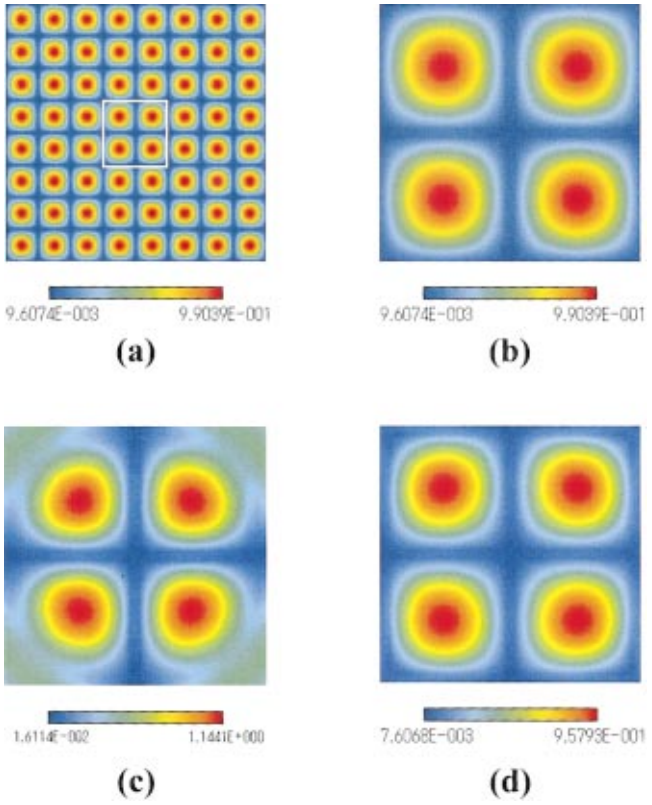

FIG. 9. The simulation result of the surface velocity reconstructed by the K-space data extrapolation method. The structure (2.56 m×2.56 m) is driven at 3 kHz. The full aperture is 2.56 m×2.56 m, and the measurement aperture is 0.64 m×0.64 m. The highest wave number $k_{\max}=6.3\pi$(rad/m) (the resolution is 32 cm). (a) The amplitude of the surface velocity defined by Eq. (3.9). The white square expresses the measurement aperture. (b) The amplitude of the surface velocity of the measurement aperture. (c) The amplitude of the surface velocity reconstructed from the measured pressure smoothed by the Tukey window. (d) The amplitude of the surface velocity reconstructed from the pressure to which 10 000 iterations of the extrapolation process is applied.

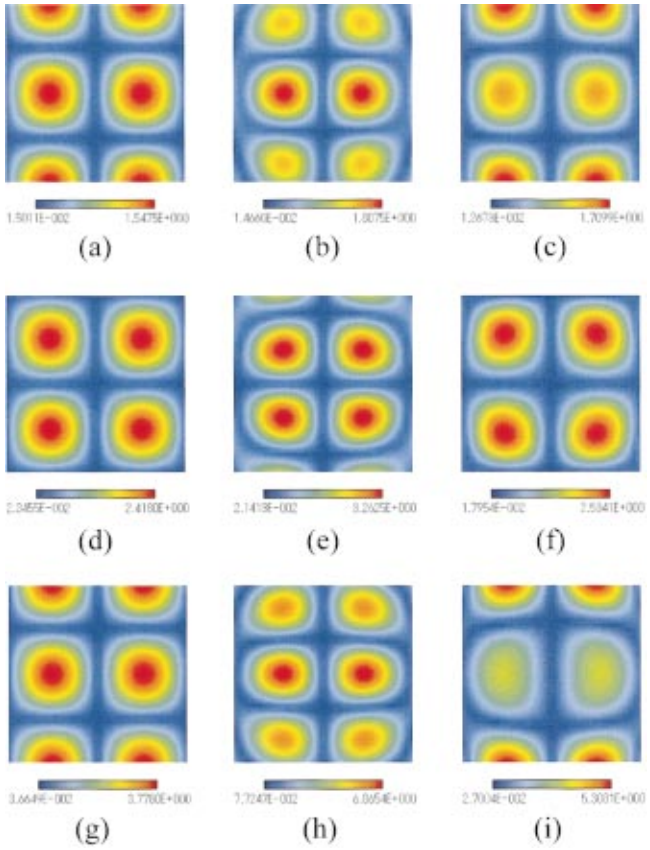

FIG. 10. Spatial derivatives of the reconstructed surface velocity of the measurement aperture. The top row indicates the first-order derivative with respect to y, the middle row the second-order derivative, and the bottom row the third-order derivative. The left column shows the derivatives of the surface velocity defined by Eq. (3.9), the middle column the derivatives of the result reconstructed from the pressure smoothed by the Tukey window, and the right column the derivatives of the result reconstructed from the pressure obtained after 10 000 iterations of the extrapolation process.

posed method. Particularly, even if the order of the derivative becomes higher, the error by the proposed method is almost constant.

In Fig. 9, the edges of the measurement aperture coincide with the nodal lines of the vibrating plate. Here, let us examine that the same simulation except for the distribution function of the surface velocity, which is given as

$$v(x,y)=\cos\left(2\pi\frac{x}{0.64}\right)\cos\left(2\pi\frac{y}{0.64}\right). \tag{3.10}$$

In this case, the edges of the measurement aperture do not coincide with the nodal lines of the vibrating plate. The reconstruction error by Tukey window is 47.7%, and the error of the first-, second-, and third-order derivatives of the reconstructed result by Tukey window are 71.9%, 86.8%, and 158.5%, respectively. On the contrary, the reconstruction error by K-space data extrapolation method is 21.3%, and the error of the first-, second-, and third-order derivatives of the reconstructed result by the proposed method are 23.4%, 27.6%, and 37.2%, respectively.

As a result, if the size of the structure is larger than that of the measurement aperture, the influence of the surface velocity of the structure to the reconstruction error is relatively small. These results suggest the effectiveness of the K-space data extrapolation method for quantitative analysis.

C. The error of the real-space data extrapolation method

In this section, the error of the real-space data extrapolation method is examined. Figure 11 illustrates the simulation result of this method.

The simulation conditions are the same as those of Fig. 4, and the highest wave number k_{cut} is 100 π (rad/m), because the spatial sampling rate is 2 cm.

Figure 11(a) shows the pressure of the full measurement aperture. Figure 11(b) shows the pressure smoothed by the Hanning window, because the reconstruction error by the Hanning window is smaller than that by the Tukey window. The discontinuity of the measurement aperture edge is reduced. However, the pressure outside the measurement aperture is set equal to zero. Figure 11(c) is the extrapolated pressure given after one time iteration of the algorithm, where the discontinuity of the measurement aperture edge is evidently eliminated, and a comparison between the full aperture pressure and the extrapolated result shows good agreement. The surface velocity reconstructed from Fig. 11(a) is shown in Fig. 11(d). This reconstructed result is used as the

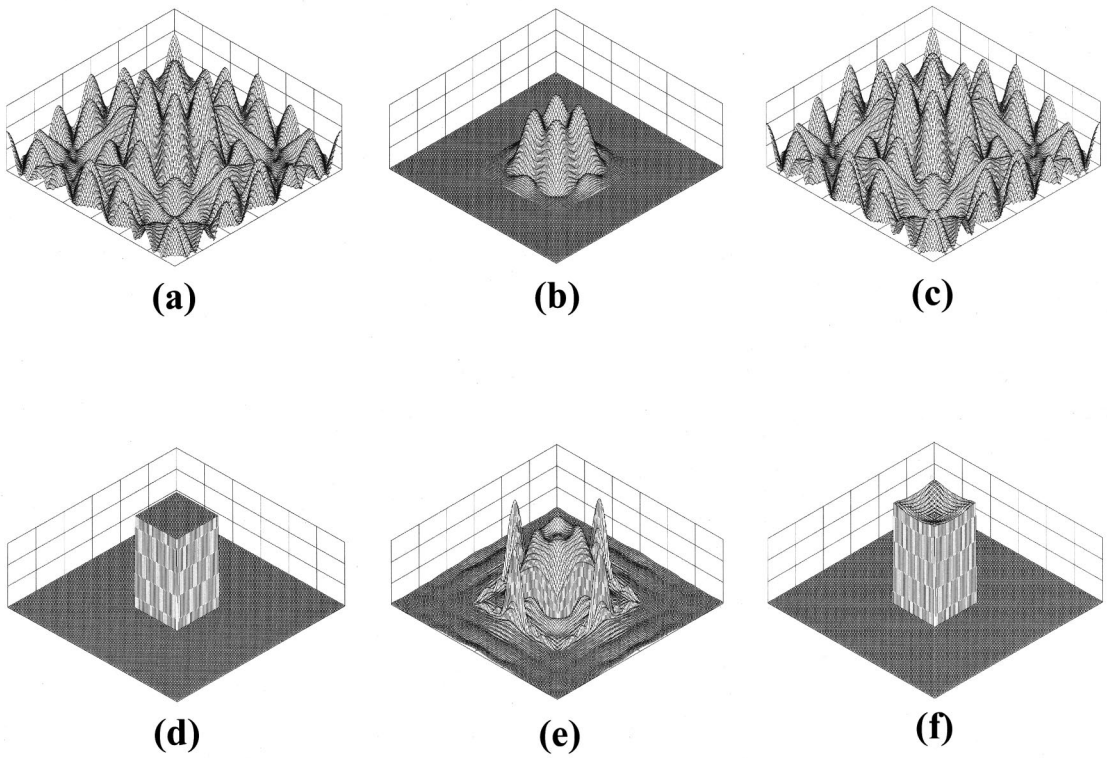

FIG. 11. The simulation result of the surface velocity reconstructed by the real-space data extrapolation method. The structure (0.64 m×0.64 m) is evenly driven at 3 kHz. The full aperture is 2.56 m×2.56 m, and the measurement aperture is 1.28 m×1.28 m. The highest wave number $k_{\max}$ is 100 π (rad/m) (the resolution is 2 cm). (a) The amplitude of the pressure of the full measurement aperture. (b) The amplitude of the pressure smoothed by the Hanning window. (c) The amplitude of the extrapolated pressure after one time iteration. (d) The amplitude of the surface velocity reconstructed from the full aperture pressure. (e) The amplitude of the surface velocity reconstructed from the pressure smoothed by the Hanning window. (f) The amplitude of the surface velocity reconstructed from the pressure obtained after one time iteration of the extrapolation process.

reference for the comparison between the conventional and the proposed data smoothing methods. Figure 11(e) (conventional method) is the reconstructed result from the pressure smoothed by the Hanning window before being reconstructed [Fig. 11(b)]. The edge discontinuity is depressed, however, the error with respect to the reference (d) is about 38.4%, where the influence of the Hanning window is not negligible. Particularly we can easily recognize that the data within the aperture is considerably affected and distorted. On the other hand, Fig. 11(f) (the proposed method) is the result from the pressure smoothed by the real-space data extrapolation method [Fig. 11(c)]. The reconstruction error with respect to the reference (d) is about 3%, where the influence of the discontinuity is sufficiently small. Although only one iteration of the algorithm is used, the reconstruction error is reduced dramatically.

Figure 12 illustrates a relationship between the iteration number and the error of the reconstructed surface velocity. The solid line exhibits the error of the real-space data extrapolation method and the circle indicates the error of the conventional Hanning window method. It is clear that the error norm of the proposed method is decreased with the same reduction rate (about 7.5% per iteration) for each iteration of the algorithm. And the error by the proposed method approaches 10^{-10}% after ten iterations.

Figure 13 shows the relationship between the iteration number and the error of the surface velocity, which is reconstructed with the pressure of s/n=60 dB. The distribution function of surface velocity over the vibrating structure is supposed to be

$$v(x,y)=\begin{cases}\sin\left(2\pi\dfrac{x}{0.64}\right)\sin\left(2\pi\dfrac{y}{0.64}\right), \\ \quad |x|<0.32 \quad \text{and} \quad |y|<0.32, \\ 0, \quad \text{otherwise.}\end{cases} \tag{3.11}$$

The simulation conditions are the same as those of Fig. 4, and $k_{\text{cut}}=36\,\pi(\text{rad/m})$. The solid line shows the error of the surface velocity reconstructed from the full aperture hologram. The dotted line indicates the error of the result reconstructed from the pressure smoothed by the Hanning window. The error is 17.6%. The broken line is the error of the result reconstructed from the pressure smoothed by the real-space data extrapolation method. This result shows that the error of the real-space data extrapolation method is substantially equal to the error from the full-aperture pressure. As the result, the accuracy of the real-space data extrapolation method to the noisy data is close to that of the conventional NAH in which the aperture size is sufficiently larger than that of the source.

To examine the influence of the vibration outside the structure to reconstruction error, another simulation result is shown in Fig. 14. The distribution function of surface velocity over the vibrating structure is expressed as Eq. (3.11). Here, let us define the vibration norm of the structure as

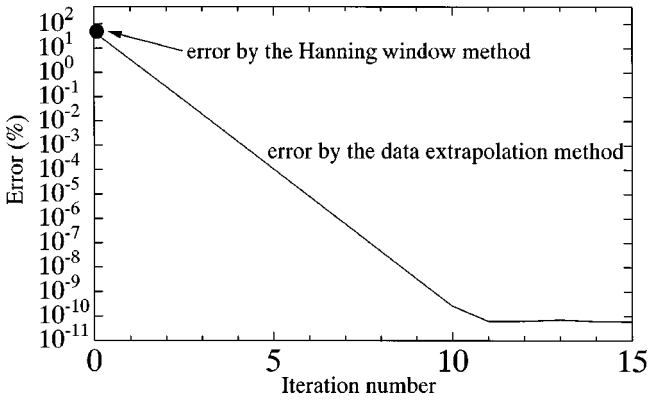

FIG. 12. The relationship between the error degree and iteration number. The solid line: the error of the real-space data extrapolation method; the circle the error of the reconstructed result from the pressure smoothed by the Hanning window. The full aperture is 2.56 m×2.56 m, the measurement aperture is 1.28 m×1.28 m, and the structure size is 0.64 m×0.64 m.

$$\|\tilde{v}_{\text{inside}}(\mathbf{r_0})\| = \sqrt{\int_{S_v} |\tilde{v}(\mathbf{r_0})|^2 d\mathbf{r_0}}, \tag{3.12}$$

and the vibration norm outside the structure as

$$\|\tilde{v}_{\mathbf{outside}}(\mathbf{r_0})\| = \sqrt{\int_{S_0} |\tilde{v}(\mathbf{r_0})|^2 d\mathbf{r_0} - \int_{S_v} |\tilde{v}(\mathbf{r_0})|^2 d\mathbf{r_0}}. \tag{3.13}$$

The ratio of the vibration norm $\|\tilde{v}_{\text{inside}}(\mathbf{r_0})\|/\|\tilde{v}_{\text{outside}}(\mathbf{r_0})\|$ is 23 dB. The structure is driven at 3 kHz. The measurement hologram is parallel to the structure with the distance of 3 cm. The highest wave number k_{cut} is 100 π(rad/m).

Figure 14(a) shows the surface velocity reconstructed from the pressure on the full aperture (2.56 m×2.56 m). When the measurement aperture is reduced to 1.28 m×1.28 m, the surface velocity reconstructed after ten iterations of the proposed method is shown in Fig. 14(b). The discontinuity around the measurement aperture edges is amplified. However, the influence of this discontinuity on the surface velocity of the structure is negligibly small. The reconstruction error is only 1.1%. Figure 14(c) shows the reconstructed result from the pressure that inside the measurement aperture is derived from the velocity on S_0 plane (see Fig. 3), and that outside the aperture is derived from the surface velocity of the structure (S_v) only. The error of the reconstructed result is induced by $\tilde{p}_{e,\text{outside},1}(\mathbf{r_m})$ that is expressed by Eq. (2.43) only. The reconstructed result of Fig. 14(c) is slightly different from that of Fig. 14(b) at the aperture edge. However, the degree of influence of the discontinuity at the aperture edge on the velocity of the structure in Fig. 14(c) is the same as that of the structure in Fig. 14(b). The reconstruction error is 1.1%. Figure 14(d) shows the relationship between the iteration number and the reconstruction error of the proposed method. In this case, the velocity outside the structure is not negligibly small. The solid line shows the error of the surface velocity of Fig. 14(c). The dotted line indicates the error from the Hanning window smoothing. The error is 17.6%. The broken line indicates the error from the proposed method, which converges to 1.1% after 3 iterations of the process. As a result, the error caused by the real-space data extrapolation method is quickly reduced to the degree of the error in Fig. 14(c). In other words, the simulation result confirms Eq. (2.50).

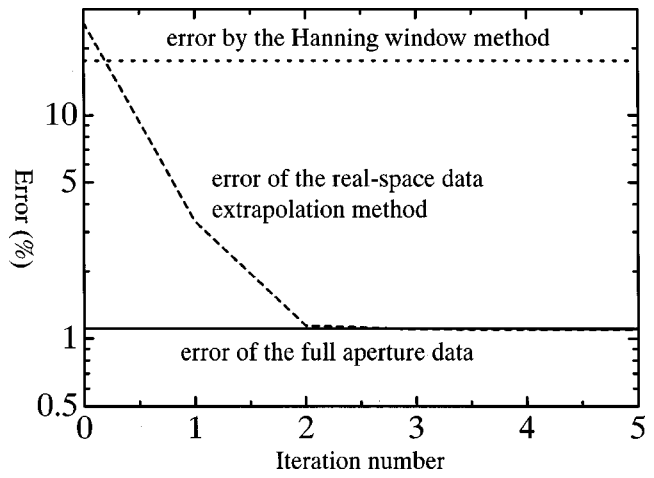

FIG. 13. The error of the reconstructed result of surface velocity (s/n=60 dB). The solid line: the error of the full aperture reconstruction; the dotted line: the error from the pressure smoothed by the Hanning window; the broken line: the error from the pressure smoothed by the real-space data extrapolation method. The full aperture is 2.56 m×2.56 m, the measurement aperture is 1.28 m×1.28 m, and the structure size is 0.64 m×0.64 m.

IV. MODEL EXPERIMENT

In this section, the estimation method of the reconstruction errors by the K- and real-space data extrapolation methods are examined. Since the dependence of the reconstruction error on the measurement aperture size is of primary importance, such dependence is examined by an underwater experiment.

A. Data acquisition system and experimental model

The experiment was carried out in the 5th Research Center's water pool, 15 m long, 9 m wide, and 8 m deep. An automated scanning system was developed for the experiment at this facility (Fig. 15). A sample plate is immersed at about 2 m depth. An accelerator (Wilcoxon F9/Z9/F3) that vibrates the sample plate is attached at the center of the plate. The vibration frequency is 1434 Hz. The full measurement aperture (that is, the location of a hydrophone's [Brüel and Kjaer Type 8103 acoustic center] is set parallel to the sample plate. The distance between the full measurement aperture and the sample plate is 3 cm. The full measurement aperture is scanned by stepwise horizontal and vertical movements with a robotic X-, Y-, and Z-axis scanner. The measured data of the full hologram surface are taken in 2 cm steps along the horizontal and vertical axes. The mesh size is small compared with the acoustic wavelength of interest.

The received and amplified signal from the hydrophone is digitized by a Tektronix RTD-710A digitizer. The digitized signal is transferred to the HP-9000 model 320 computer through a general-purpose interface bas (GP-IB:IEEE-488) line, and input into a floppy diskette. Data sampling inception time is precisely controlled by the computer, which acts as the reference source for holographic interference. All post-experimental data processing is executed on the HP-9000 model 755 computer.

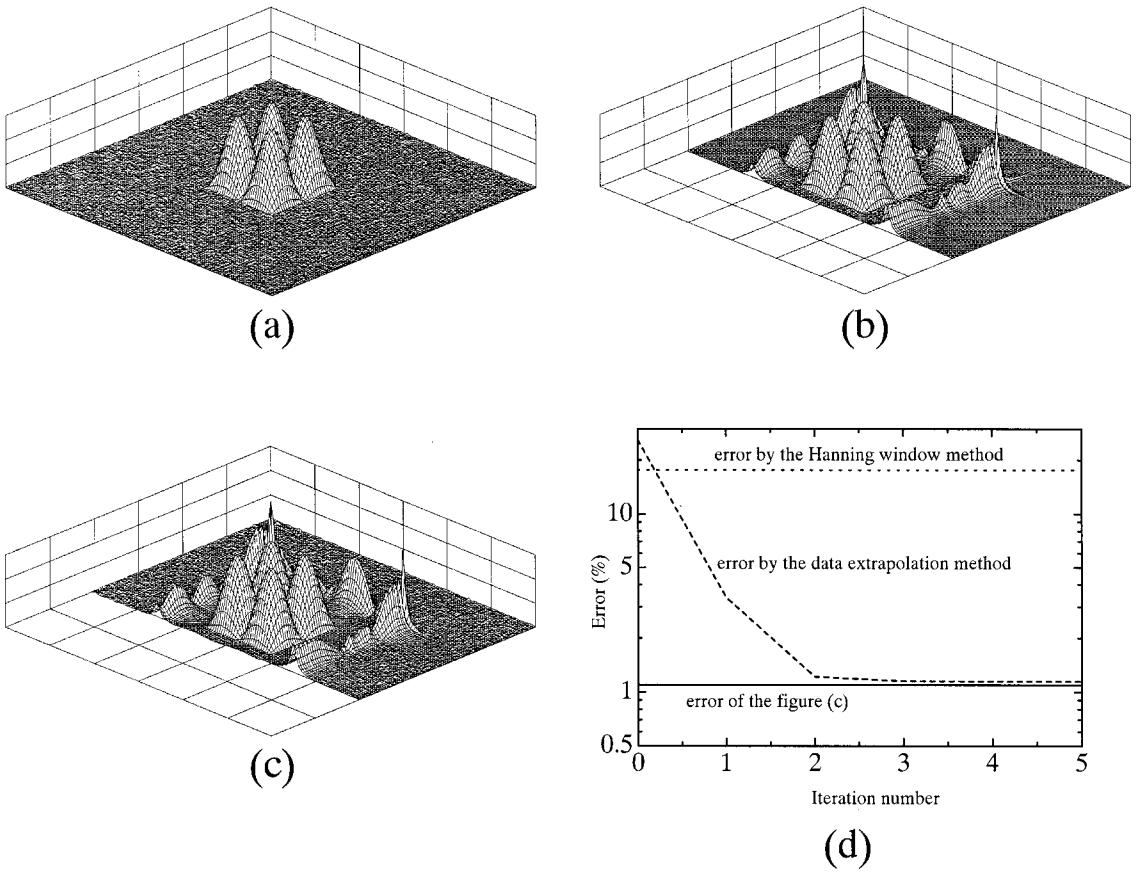

FIG. 14. The influence of the vibration outside the structure upon the reconstruction error of the real-space data extrapolation method. The structure (0.64 m×0.64 m) is driven at 3 kHz. Full aperture is 2.56 m×2.56 m. The highest wave number k_{max} is 100 π (rad/m) (the resolution is 2 cm). (a) The amplitude of the surface velocity reconstructed from the full aperture pressure. (b) The amplitude of the surface velocity reconstructed from the pressure obtained after ten iterations of the extrapolation process. The measurement aperture is 1.28 m×1.28 m. (c) The amplitude of the surface velocity reconstructed from the pressure. The pressure inside the measurement aperture is derived from the velocity on the S_0 plane, and that outside the aperture is derived from the velocity of the structure only. (d) The error of the reconstructed result of surface velocity. The solid line: the error of the surface velocity shown in (c); the dotted line: the error of the result reconstructed from the pressure smoothed by the Hanning window; the broken line: the error of the surface velocity reconstructed from the pressure smoothed by the real-space data extrapolation method.

The model used in the experiment is SUS 304 stainless steel plates (0.54 m×0.44 m).[18] The ends of the plate are sealed with rubber packing to approximate the simply supported boundary condition.

B. Experimental result

Experimental result is shown in Fig. 17. The experimental condition is as follows.

(i) The vibrating plate is 0.54 m×0.44 m (cf. Fig. 16).

(ii) The full measurement aperture is 2.56 m×2.56 m.

(iii) The measurement aperture is varied from 0.76 m ×0.76 m to 2 m×2 m.

(iv) The dynamic range of the measurement apparatus is 50 dB.

(v) The highest wave number is 30π(rad/m).

Figure 17(a) exhibits the surface velocity reconstructed from the full aperture pressure. The vibrational mode appears to be (5,5). Also, a careful inspection of Fig. 17(a) reveals that the plate vibration extends to a small outer area surrounding the plate itself.

Figure 17(b) is the simulated surface velocity. The simulation condition is as follows.

(i) The vibrating plate is assumed to be 0.64 m×0.64 m.

(ii) The highest wave number is 30π(rad/m).

(iii) The vibrational mode is (5,5), which is the same as that of the experiment.

In this simulation, the pressure used to reconstruct the surface velocity is calculated on the measurement plane by the Rayleigh integral of the structural surface velocity.[16]

Figure 17(c) shows the relationship between the error caused by the K-space data extrapolation method and the aperture size. The solid line gives the error of the experimental result; the broken line denotes the error of the simulation result. Both show good agreement. Figure 17(d) shows such a relationship for the real-space data extrapolation method. The simulation result exhibits a good agreement with the experimental result. From the above-mentioned discussion, the reconstruction error may be estimated by simulations before carrying out experiments.

V. SUGGESTIONS FOR LARGE-SCALE IMPLEMENTATION OF NAH

To realize the large-scale implementation of NAH, it is necessary that the reconstruction error be estimated and re-

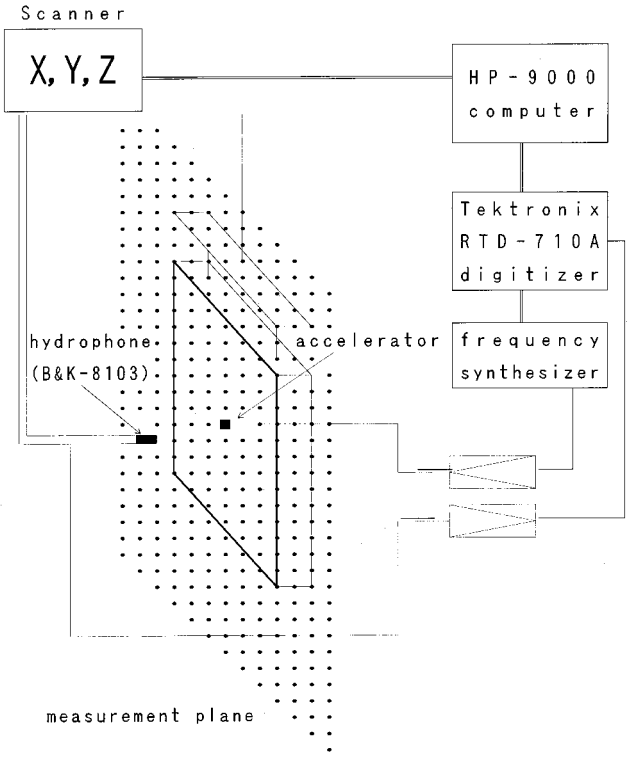

FIG. 15. Block diagram of the NAH experiment.

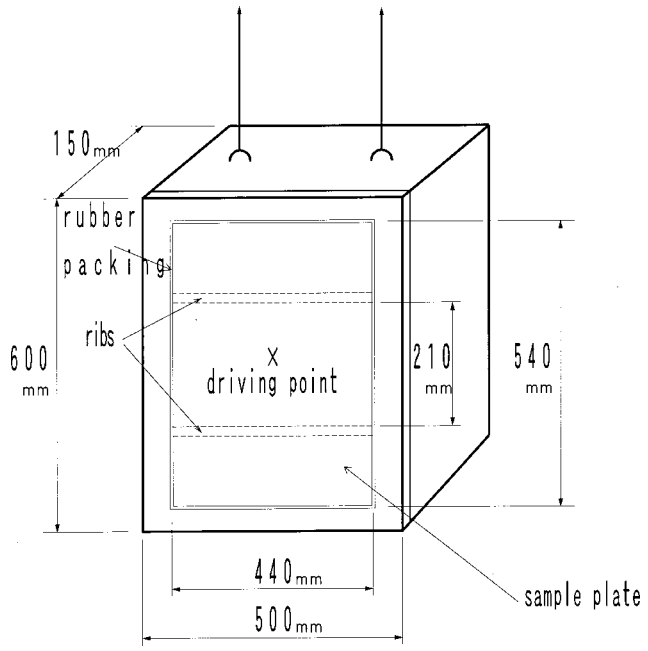

FIG. 16. Experimental model.

duced. The error estimation is important to secure the reliability of the NAH experiment. Therefore, let us discuss the estimation and reduction method of NAH reconstruction error on the basis of the results shown in Sec. III and Sec. IV.

First, the conventional real-space window method and our K-space data extrapolation method are compared with each other. Figure 7 shows that the reconstruction error by the real-space window (Tukey) is about twice as large as that by the K-space data extrapolation method. Also, Fig. 8 shows that the influence of the noise to the result reconstructed by K-space data extrapolation is relatively small. Moreover, Figs. 9 and 10 exhibit that the reconstruction error of the velocity and its spatial derivatives by the real-space window method is very large when the size of the measurement aperture is smaller than that of the structure, and that the error of the higher-order derivatives is larger than that of the lower-order derivatives. On the contrary, the error of the velocity and its spatial derivatives by the real-space data extrapolation method is about 20%, and the error is not varied even if the derivative order is varied. Therefore, the structural intensity of the measured structure may be quantitatively estimated by the K-space data extrapolation method.

Second, the conventional real-space window method and our real-space data extrapolation method are compared with each other. Figure 12 shows that the reconstruction error by the former (Hanning window) is 38.4%, while that by the latter is negligibly small. Also, Fig. 13 shows that the influence of noise on the reconstructed result is negligibly small in the latter. Moreover, the influence of the vibration outside the structure on the reconstruction error by the latter method is small (cf. Fig. 14). Therefore, we may say that our real-space extrapolation method is superior to the conventional real-space window method.

Now, let us discuss the estimation of the reconstruction error. The reason why the reconstruction error by the conventional method cannot be estimated is explained as follows: The reconstruction error by the real-space window method is defined as

$$\begin{aligned}\Delta v(\mathbf{r_0}) &= \|\tilde{v}(\mathbf{r_0}) - \tilde{v}_{\text{wind}}(\mathbf{r_0})\|, \\ &= \sqrt{\int_{S_0} |\tilde{v}(\mathbf{r_0}) - \tilde{v}_{\text{wind}}(\mathbf{r_0})|^2 \, d\mathbf{r_0}}, \\ &> \sqrt{\int_{S_0} |\tilde{v}(\mathbf{r_0})|^2 d\mathbf{r_0} - \int_{S_0} |\tilde{v}_{\text{wind}}(\mathbf{r_0})|^2 \, d\mathbf{r_0}}, \\ &= \sqrt{\int |F\{\tilde{p}(\mathbf{r}_m)[1 - W_{\text{real}}(\mathbf{r}_m)]\} \tilde{G}_{pv}(\mathbf{r}_m; \mathbf{r_0})|^2 \, dk_x dk_y},\end{aligned} \tag{5.1}$$

using the pressure smoothed by the real-space window,

$$W_{\text{real}}(\mathbf{r}_m) = \begin{cases} W_{\text{real}}(\mathbf{r}_m) & (\mathbf{r}_m \in S_p), \\ 0 & (\mathbf{r}_m \notin S_p). \end{cases} \tag{5.2}$$

Because the pressure outside the measurement aperture is not known, Eq. (5.1) cannot be calculated. So, the reconstruction error cannot be estimated by the conventional method. This inevitably requires that the measurement aperture be larger than the structure of interest. On the contrary, Fig. 17 shows that the reconstruction error by the proposed method can be estimated. Therefore, the proposed method can secure the reliability of the experiment and reduce the reconstruction error without such a wide measurement aperture. This implies that the proposed method is applicable to the large-scale implementation of NAH.

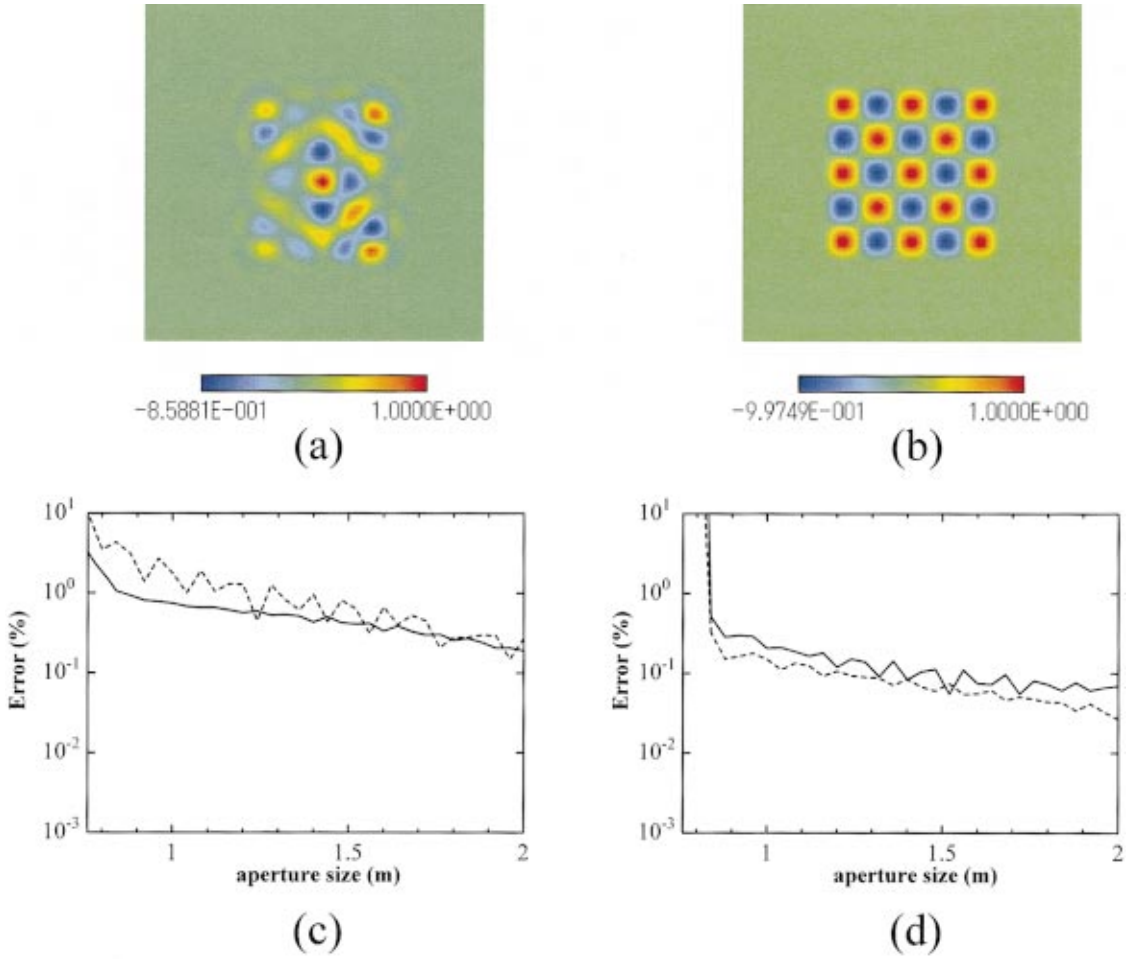

FIG. 17. The relationship between the reconstruction error and the size of measurement aperture. The structure is driven at 1434 Hz. Full aperture is 2.56 m×2.56 m. The highest wave number k_{max} is 30 π(rad/m) (the resolution is 6.6 cm). (a) The real part of the surface velocity reconstructed from the experimental data of the full aperture pressure. The vibrating plate is 0.54 m×0.44 m. (b) The real part of the simulated surface velocity. The vibrating plate is 0.64 m×0.64 m. (c) The error of the surface velocity reconstructed by the K-space data extrapolation method. The solid line shows the error of the experimental result; the broken line the error of the simulated result. (d) The error of the surface velocity reconstructed by the real-space data extrapolation method. The solid line shows the error of the experimental result; the broken line the error of the simulated result.

Also, Fig. 17 illustrates that the reconstruction error reduced by the real-space data extrapolation method is negligibly small. But, if the measurement aperture is smaller than the structure, the reconstruction error cannot converge, as shown in Fig. 17(d). However, many iterations are necessary before the K-space data extrapolation method may be safely applied, particularly to a measurement aperture much smaller than the extent of the vibrating structure, as shown in Fig. 17(c).

As mentioned above, these two methods have complementary properties: (1) For a measurement aperture smaller than the vibrating structure, the K-space data extrapolation method may be applicable. In other words, the K-space data extrapolation method is applicable to a large-scale structure. (2) On the contrary, if the measurement aperture is four times (or more) the size of as the structure, real-space data extrapolation method is preferred because fewer iterations are required.

VI. CONCLUSIONS

The reconstruction error induced by the finiteness of measurement aperture is inevitable for the conventional real-space window method. Also, the degree of error cannot be estimated by the conventional method. We may understand that such a deficiency requires the measurement aperture sufficiently larger than the structure for conventional NAH. This prevents conventional NAH from being applied to an actual large-scale structure.

A data extrapolation method is proposed to estimate and reduce this error. This method is effective even if the measurement aperture is not sufficiently larger than the structure. However, we need *a priori* knowledge about the extent of the vibrating object or the highest wave number of the measured pressure in order to extrapolate the measured pressure. This data extrapolation method may take one of two approaches according to *a priori* knowledge. The first, the K-space data extrapolation method, is widely applied without a severe restriction on the measurement aperture if many iterations are possible. The second, the real-space data extrapolation method can reduce the reconstruction error to a negligibly small degree, but a wider measurement aperture compared with that for the K-space data extrapolation method is necessary. Although there are a few shortcomings like these, NAH supplemented by K-space and real-space data extrapo-

lation methods may be implemented for the measurement of real large-scale structures. Particularly, the measurement aperture may be reduced to about 1/16th of the vibrating structure area if we can optimize our proposed data extrapolation methods.

The availability of these proposed methods is justified by simulations and underwater experiment, where the reconstruction error is adequately estimated and sufficiently reduced. For example, in the K-space data extrapolation method, the reconstruction error of the proposed method is one-quarter of the error for the Tukey window method. On the other hand, in the real-space data extrapolation method, the reconstruction error approaches 10^{-10}%, even when the measurement aperture size is four times as large as the vibrating structure. Moreover, both of the K- and real-space data extrapolation methods are hardly influenced by the noise included in the measured pressure. Our proposed method may thus be recommended to promote a more quantitative analysis based on NAH-oriented structural acoustics as well as a large-scale implementation of NAH.

ACKNOWLEDGMENTS

The first author would like to show his sincere appreciation for helpful suggestions and a great deal of encouragement from Professor Mitsuhiro Ueda of the Tokyo Institute of Technology.

[1] E. G. Williams and J. D. Maynard, ''Holographic imaging without the wavelength resolution limit,'' Phys. Rev. Lett. **45**, 554–557 (1980).
[2] E. G. Williams, H. D. Dardy, and K. B. Washburn, ''Generalized nearfield acoustic holography for cylindrical geometry: Theory and experiment,'' J. Acoust. Soc. Am. **81**, 389–405 (1987).
[3] G. V. Borgiotti, A. Sarkissian, E. G. Williams, and L. Schuetz, ''Conformal generalized near-field acoustic holography for axisymmetric geometries,'' J. Acoust. Soc. Am. **88**, 199–209 (1990).
[4] W. A. Veronesi and J. D. Maynard, ''Digital holographic reconstruction of sources with arbitrary shaped surface,'' J. Acoust. Soc. Am. **85**, 588–589 (1988).
[5] E. G. Williams and H. D. Dardy, ''Mapping of structure-borne intensity using nearfield acoustical holography,'' Proc. Inter-Noise **86**, 1247–1250 (1986).
[6] M. Villot, G. Chaveriat, and J. Roland, ''Phonoscopy: An acoustical holography technique for plane structures radiating in enclosed spaces,'' J. Acoust. Soc. Am. **91**, 187–195 (1992).
[7] S. Yoshikawa, E. G. Williams, and K. B. Washburn, ''Vibration of two concentric submerged cylindrical shells coupled by the entrained fluid,'' J. Acoust. Soc. Am. **95**, 3273–3286 (1994).
[8] K. Saijyou amd S. Yoshikawa, ''Sound scattering of an arbitrary wave incident on a simply-supported cylindrical shell,'' J. Acoust. Soc. Jpn. E **16**, 223–232 (1995).
[9] E. G. Williams, ''Imaging the source on a cylindrical shell from far-field pressure measured on a semicircle,'' J. Acoust. Soc. Am. **99**, 2022–2032 (1996).
[10] J. D. Maynard, E. G. Williams, and Y. Lee, ''Nearfield acoustical holography I: Theory of generalized holography and the development of NAH,'' J. Acoust. Soc. Am. **78**, 1395–1413 (1985).
[11] H.-S. Kwon and Y.-H. Kim, ''Minimization of bias error due to windows in planar acoustic holography using a minimum error window,'' J. Acoust. Soc. Am. **98**, 2104–2111 (1995).
[12] R. W. Gerchberg, ''Super-resolution through error energy reduction,'' Opt. Acta **21**, 709–720 (1974).
[13] J. Held, ''Reduction of spatial windowing effects in acoustical holography,'' Proceedings of Inter-Noise **94**, 1887–1890 (1994).
[14] H.-S. Kwon and Y.-H. Kim, ''Enhanced acoustic holographic sound reconstruction by reducing prediction errors,'' Proceedings of Inter-Noise **95**, 1345–1348 (1995).
[15] K. U. Nam and Y. H. Kim, ''Errors due to sensor and position mismatch in planar acoustics holography,'' J. Acoust. Soc. Am. **106**, 1655–1665 (1999).
[16] E. G. Williams and J. D. Maynard, ''Numerical evaluation of the Rayleigh integral for planar radiators using the FFT,'' J. Acoust. Soc. Am. **72**, 2020–2030 (1982).
[17] W. A. Veronesi and J. D. Maynard, ''Nearfield acoustical holography (NAH) II. Holographic reconstruction algorithms and computer implementation,'' J. Acoust. Soc. Am. **81**, 1307–1322 (1987).
[18] K. Saijyou and S. Yoshikawa, ''Measurement of structural and acoustic intensities using near-field acoustical holography,'' Jpn. J. Appl. Phys. **35**, 3167–3174 (1996).

Representation of harmonic complex stimuli in the ventral cochlear nucleus of the chinchilla

Alberto Recio[a)]
Department of Physiology, University of Wisconsin, 1300 University Avenue, Madison, Wisconsin 53706

(Received 1 February 2001; revised 13 June 2001; accepted 29 June 2001)

The representation of Schroeder-phase harmonic complex sounds in the ventral cochlear nucleus (VCN) of the anesthetized chinchilla was studied. Stimuli consisted of a series of harmonically related sinusoids, multiples of a fundamental frequency (f_0), summed in either negative ($-$SCHR) or positive ($+$SCHR) Schroeder phase. Psychoacoustic experiments performed in humans by other investigators have revealed that masking effects of $-$SCHR stimuli are larger than those found using $+$SCHR stimuli as maskers. In our laboratory, basilar membrane measurements at the base of the chinchilla cochlea show that responses to $-$SCHR stimuli are less ''peaked,'' or modulated, than responses to $+$SCHR stimuli. We also found that suppression of a characteristic-frequency (CF) tone by $-$SCHR stimuli is larger than that evoked by $+$SCHR stimuli. Rate-intensity functions display higher firing rates in responses to $-$SCHR stimuli than in those produced by $+$SCHR stimuli. Firing rates evoked by either $-$SCHR or $+$SCHR stimuli saturate at lower values than those obtained in responses to CF tones. Rate and synchrony suppressions by $-$SCHR stimuli were larger than those evoked by $+$SCHR stimuli. Auditory nerve fiber responses to Schroeder complex stimuli share most of the properties of VCN responses, indicating little additional processing by the VCN. © *2001 Acoustical Society of America.* [DOI: 10.1121/1.1397356]

PACS numbers: 43.64.Qh, 43.64.Pg [LHC]

I. INTRODUCTION

Following the work by Smith *et al.* (1986), there has been a considerable amount of interest in studying the effects of Schroeder-phase complex stimuli as maskers of sounds in the auditory system of mammals (e.g., Kohlrausch and Sander, 1995; Summers and Leek, 1998; Recio and Rhode, 2000a) and birds (Leek *et al.*, 2000). Schroeder-phase complex stimuli (Fig. 1) consist of a sum of sinusoids whose frequency is a multiple of a fundamental frequency (f_0):

$$m(t)=\sum_{k=k_1}^{k_2} A_0 \sin(2\pi k f_0 t+\theta_k).$$

Phase, θ_k, is defined based on an algorithm proposed by Schroeder (1970):

$$\theta_k=\pm\pi k(k-1)/N,$$

where $N=k_2-k_1+1$ represents the number of sinusoids in the waveform. The envelope of the waveform $m(t)$ is flat over almost all of the fundamental period, regardless of the polarity of the starting phase. The instantaneous frequency of $m(t)$, however, depends on the sign of the starting phase. $-$SCHR stimuli [i.e., stimuli with $\theta_k=-\pi k(k-1)/N$] display an instantaneous frequency that increases as a function of time within one cycle of f_0. Alternatively, the instantaneous frequency of $+$SCHR stimuli decreases across the stimulus period.

In psychoacoustic experiments performed in humans, it was found that $-$SCHR stimuli provide a greater amount of masking of sinusoidal probes than $+$SCHR stimuli (Smith *et al.*, 1986; Kohlrausch and Sander, 1995). Using a linear transmission model of basilar membrane (BM) motion (Strube, 1985), it was originally concluded (Smith *et al.*, 1986) that these differences in masking were due to phase characteristics of BM filtering. In fact, BM responses obtained at the base of the chinchilla cochlea (Recio and Rhode, 2000a) showed that the response waveform to $-$SCHR stimuli is less ''peaked,'' or modulated, than that observed in responses to $+$SCHR stimuli. Responses to $-$SCHR stimuli contain a larger amount of energy than responses to $+$SCHR stimuli. This might explain why suppression of a characteristic-frequency (CF) tone was the largest when the $-$SCHR stimulus was used as a suppressor (Recio and Rhode, 2000a). Results at the level of the basilar membrane are therefore consistent with the results of psychoacoustic experiments performed in humans. Nevertheless, any decision variable (e.g., rate- or synchrony-based code) used by humans during psychoacoustic experiments requires a certain representation of these stimuli in the form of neural discharges; hence, it is of great interest to know the representation of the Schroeder-phase complex stimuli at auditory centers, such as the VIII nerve and cochlear nucleus (CN).

Based on what is known about the representation of certain types of sounds, such as single tones and speech, in the cochlear nucleus it is possible to formulate hypotheses about the representation of Schroeder-phase complex stimuli in the CN. For example, a representation of f_0 is expected to prevail, particularly in the case of high-CF neurons. $-$SCHR stimuli evoke BM responses with larger amounts of energy (Recio and Rhode, 2000a) than $+$SCHR stimuli do, therefore differences in firing rates evoked by the two stimuli are expected. We could also expect some differences in the pro-

[a)]Electronic mail: recio@physiology.wisc.edu

 0001-4966/2001/110(4)/2024/10/$18.00

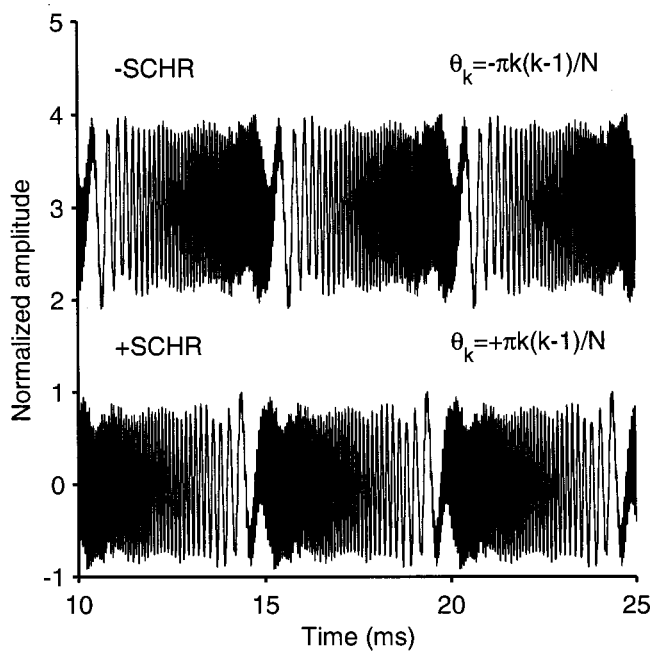

FIG. 1. Waveforms of harmonic complexes for two choices of starting phases. Top waveform: −Schroeder-phase complex (−SCHR), $\theta_k = -\pi k(k-1)/N$. Lower waveform: +Schroeder-phase complex (+SCHR), $\theta_k = +\pi k(k-1)/N$. Total number of components (N) is equal to 96, with harmonics of 5 to 100 of fundamental frequency of 200 Hz. Amplitudes are expressed in arbitrary units.

cessing of ±SCHR stimuli based on the neuron's CF. Results obtained in the base of the cochlea cannot necessarily be used to predict results in other cochlear locations since BM responses in more apical regions of the chinchilla appear to be different from those obtained in the base (Rhode and Cooper, 1996). Because of inherent high CFs that are characteristic of the first turn of the chinchilla cochlea, we could not measure BM responses at lower CF regions (below 6–8 kHz). We therefore measured the responses of individual neurons of the ventral cochlear nucleus (VCN) as a way of studying responses both of the cochlea and of the brainstem auditory nuclei over a wide range of characteristic frequencies to Schroeder-phase complex stimuli.

II. METHODS

A. Animal preparation

Eighteen chinchillas (weight≈500 gm) were anesthetized with intraperitoneal injections of pentobarbital (75 mg/kg) and additional doses were administered as required. A large amount of data has been collected in our laboratory in both cat and chinchilla using this anesthetic, facilitating comparisons with earlier work in this lab. Minimal differences in responses of VCN neurons have been observed in the results of pentobarbital-anesthetized and decerebrate or awake preparations (Evans and Nelson, 1973; Rhode and Kettner, 1987). A thermostatically controlled heating blanket maintained body temperature at 37 °C. After insertion of a tracheal cannula, the left ear was removed and the bulla was vented with 20 cm of a 1-mm plastic tube. Following removal of the overlying cerebellum, the cochlear nucleus was covered with agar. To further reduce brain pulsations, a chamber was mounted over the skull opening and filled with mineral oil. KCl-filled micropipettes, with impedances of 10–20 MΩ, were used to record single-unit activity. Bipolar spike waveforms were generally associated with recordings from cochlear nucleus units (Rhode, 1998). In one experiment, however, we recorded exclusively from auditory nerve fibers (ANFs) in order to compare the responses of auditory nerve fibers to those obtained in the cochlear nucleus. The impedance of the electrodes in auditory nerve fiber recordings was in the 30–70-MΩ range.

We did not confirm the location of most of the recordings. Hence, VCN neurons were classified on the basis of their responses to tones. In some experiments, however, an electrode was left in the location of the last recording. Following a lethal dose of sodium pentobarbital, these animals were perfused transcardially with saline followed by 10% formalin. Coronal sections (60-μm thickness) of the brainstem were then mounted on glass slides and stained with cresyl violet. The electrode track of the last recording was then visualized to confirm that we recorded from the VCN.

B. Unit classification

Post-stimulus time histograms (PSTHs) were obtained from responses to 60 dB SPL short tones at CF. The shape of the PSTH was used to classify units based on the criteria provided by several groups (Blackburn and Sachs, 1989; Rhode and Smith, 1986). We recorded primarily from VCN neurons that were classified as follows: primary-like (PL), primary-like-with-notch (PLN), choppers, onsets with an L-shaped histogram (OL) and onset choppers (OC). Using the coefficient of variation (CV) of the interspike interval histogram (Blackburn and Sachs, 1990), we further classified chopper neurons as transient chopper (CT), if CV$\geqslant$0.3, otherwise as sustained choppers (CS). Since PST histograms of OL neurons often resemble those of PLN neurons, our classification followed the distinguishing procedure given in Recio and Rhode (2000b).

C. Acoustic stimuli and experimental protocol

A RadioShack SuperTweeter speaker was used to present the stimuli. After calibration of the acoustic system (50–20 000 Hz in 50-Hz steps) using a Bruel and Kjær 0.5-in. condenser microphone, stimuli were digitally compensated for the transfer function of the acoustic system before being presented. Both +SCHR and −SCHR stimuli consisted of all harmonics of f_0 between 1000 and 20 000 Hz. This was done to be compatible with the stimuli used in the mechanical studies (Recio and Rhode, 2000a). Two values of f_0 were used: 100 and 200 Hz. Stimuli were presented at several levels 50 times, with a duration of 60 ms and a presentation interval of 150 ms. Rate-intensity functions were obtained in response to a CF tone. When a tone and the Schroeder-phase complex stimuli were played simultaneously, each was presented via a separate speaker.

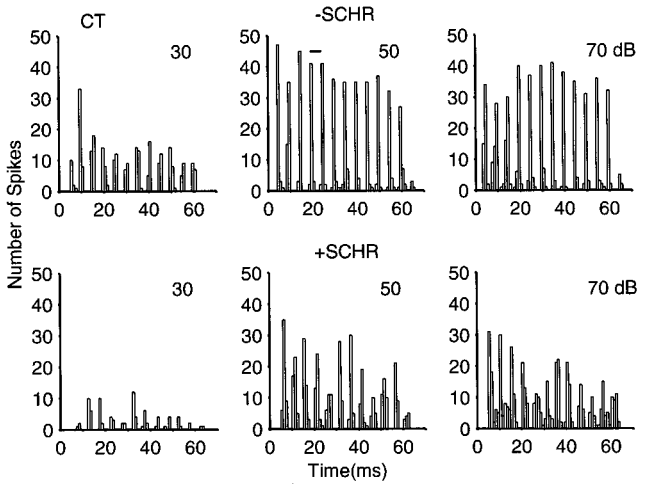

FIG. 2. Post-stimulus time (PST) histograms obtained from responses of a CT neuron (CF=4.8 kHz) to −SCHR (top row) and +SCHR (bottom row) stimuli. Stimulus levels are indicated in each panel. Line located on 50-dB panel (top row) represents 5 ms. Stimulus duration=60 ms. Number of stimulus repetitions=50. Neuron=cn12-6.

III. RESULTS

A. Response characteristics

Results come from the responses of 123 neurons in the VCN. Figure 2 shows PST histograms obtained from responses of a CT neuron (CF=4.8 kHz) to −SCHR (top row) and +SCHR (bottom row) stimuli at three levels. Histograms consist primarily of a series of peaks separated by a time interval equal to the period of f_0 (5 ms). The number of spikes evoked by −SCHR stimuli is larger than the number measured in response to +SCHR stimuli. Results obtained in a PLN neuron (CF=6 kHz; Fig. 3) strongly resemble those of the CT unit shown in Fig. 2: −SCHR stimuli evoked larger firing rates than +SCHR ones (except at 70 dB SPL), and neuronal responses occurred more often at time intervals equal to the period of f_0.

Period histograms based on a 5-ms period from responses to the two Schroeder stimuli are shown in Fig. 4. Phase locking to the fundamental frequency (200 Hz), estimated using the vector strength (Goldberg and Brown, 1969), was largest in responses to −SCHR stimuli for both CT and PLN neurons. Hence, period histograms from responses to −SCHR stimuli appear generally ''peakier,'' or more concentrated, at a particular response phase than those obtained from responses to +SCHR stimuli, as is the case of response of the CT neuron in Fig. 4. In fact, synchronization indices, r, to the fundamental frequency were larger for both neurons in their responses to −SCHR stimulus. Within a stimulus period, responses occurred during different segments since the instantaneous frequency versus time curves differ from each other. Figure 5 shows rate-intensity functions obtained in response to −SCHR (open squares), +SCHR (filled squares) and CF tone (crosses) stimuli for the same two neurons, measured over the duration of the stimuli (60 ms). Similar results were obtained if only the onset (i.e., the first 15 ms) or the steady state (>15 ms) responses were analyzed. Firing rates are usually larger and rate-based thresholds smaller in responses to −SCHR stimuli than to +SCHR stimuli. Responses to Schroeder-phase complex stimuli, however, saturate at a lower maximum firing rate than a CF tone.

Responses of neurons that show significant synchronization to a CF tone were also obtained. Figure 6 shows two period histograms computed from responses of a PL neuron (CF=1.3 kHz) to −SCHR (top row, left column) and +SCHR (top row, right column) stimuli. Peaks in both histograms appear at approximately the same location, which is a consequence of the proximity of the neuron's CF (1.3 kHz) to the lowest frequency value present in the stimulus (1

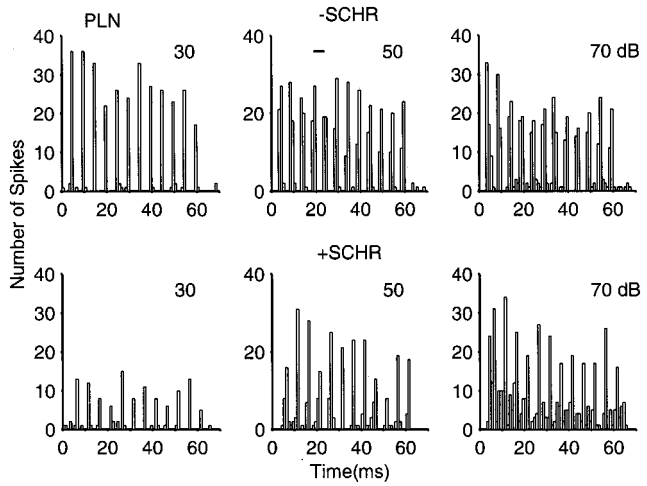

FIG. 3. PST histograms from responses of a PLN neuron (CF=6 kHz) to −SCHR (top row) and +SCHR (bottom row) stimuli. Stimulus duration =60 ms. Number of stimulus repetitions=50. Neuron=cn12-17.

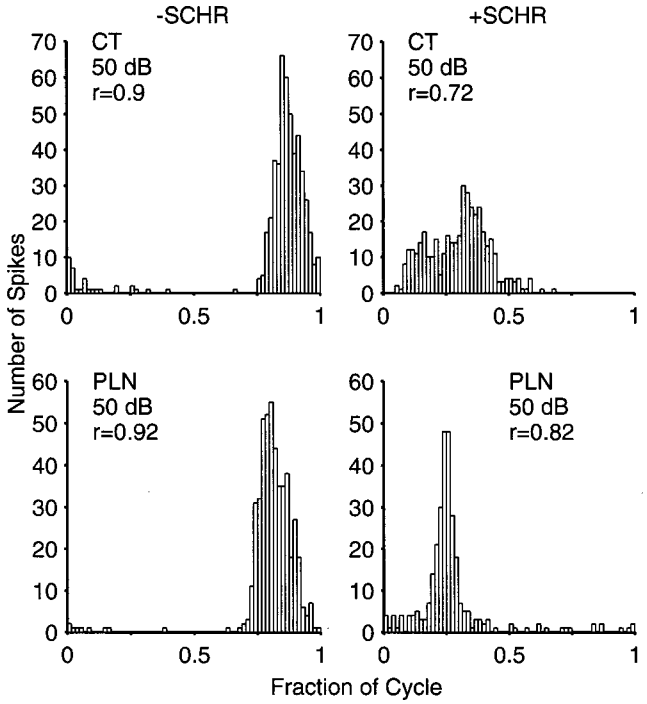

FIG. 4. Period histograms (5-ms period) obtained from responses of neurons shown in Figs. 2 and 3 to −SCHR (left column) and +SCHR (right column) stimulus. Stimulus level=50 dB SPL. Synchronization indices, r, appear in each panel.

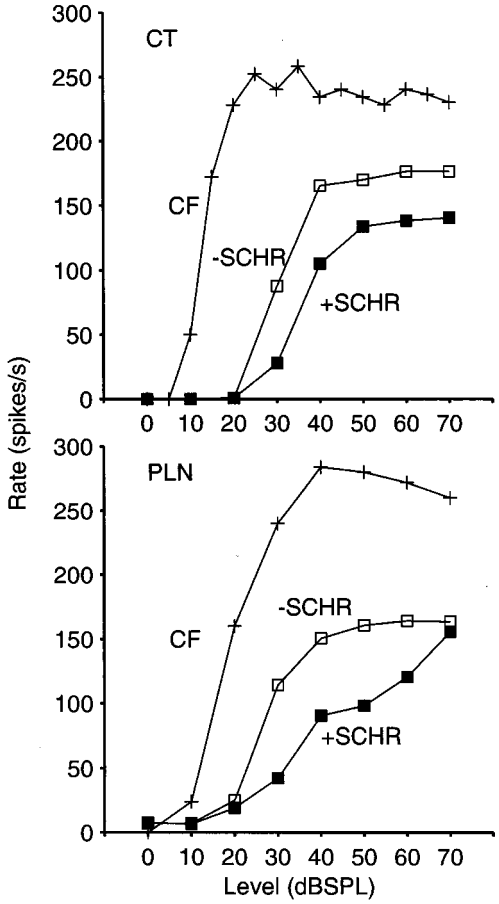

FIG. 5. Rate-intensity functions obtained from responses to −SCHR (open squares), +SCHR (filled squares) and CF tone stimuli. CT and PLN neurons are the ones shown in Figs. 2 and 3, respectively.

kHz). Unlike the period histograms shown in Fig. 4, period histograms of low-CF neurons contain multiple peaks, with not only a representation of f_0 but also a representation of harmonics of the fundamental frequency. Fourier transforms of the autocorrelation histogram of those responses (Fig. 6, lower row) confirm this statement. Spectral peaks occur at $f_0(=200\,\text{Hz})$, $2f_0$ and around the neuron's CF (1200, 1400 and 1600 Hz).

B. Population studies

Figure 7 (left column) shows scatter plots of the firing rate evoked by +SCHR stimuli versus that evoked by −SCHR stimuli at three levels ($f_0=200\,\text{Hz}$). At the intermediate and highest levels of stimulation (50 and 70 dB SPL), firing rates evoked by −SCHR are generally larger than those obtained in response to +SCHR stimuli. Average differences in firing rate ($\text{mean}\{\text{Rate}_{-\text{SCHR}}-\text{Rate}_{+\text{SCHR}}\}$) at 50 and 70 dB SPL are approximately 10 spikes/s. At 30 dB SPL, the average difference decreased, perhaps because for some neurons the stimulus level was below threshold. Using a two-tailed t test ($\alpha=0.05$, $n=123$), differences in rates evoked by −SCHR and +SCHR stimuli were statistically significant. The above statistics were obtained for all the neurons combined, regardless of the neuron's type. This was done since significant differences in responses of different unit types were not seen (Kolmogorov–Smirnov test). For example, at 50 dB SPL, chopper neurons showed the largest average difference (12 ± 18 spikes/s, mean±standard deviation, $N=68$) in favor of −SCHR stimuli, and PLN and OL neurons the smallest difference (9 ± 27 spikes/s, $N=25$). The average difference for primary-like and auditory nerve fibers

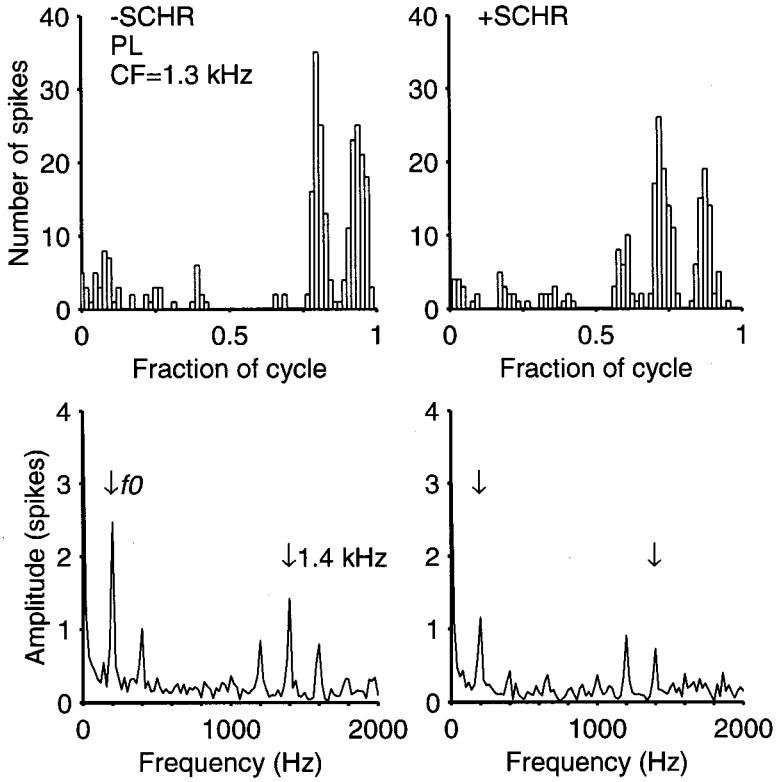

FIG. 6. Period histograms obtained from responses of a PL neuron (CF=1.3 kHz) at 50 dB SPL to a −SCHR (top left panel) and +SCHR (top right panel) stimuli. Fourier transform amplitude of the autocorrelation functions of same responses are shown in the bottom row. Arrows point to responses at f_0 (=200 Hz) and 1400 Hz. Neuron=cn12-3.

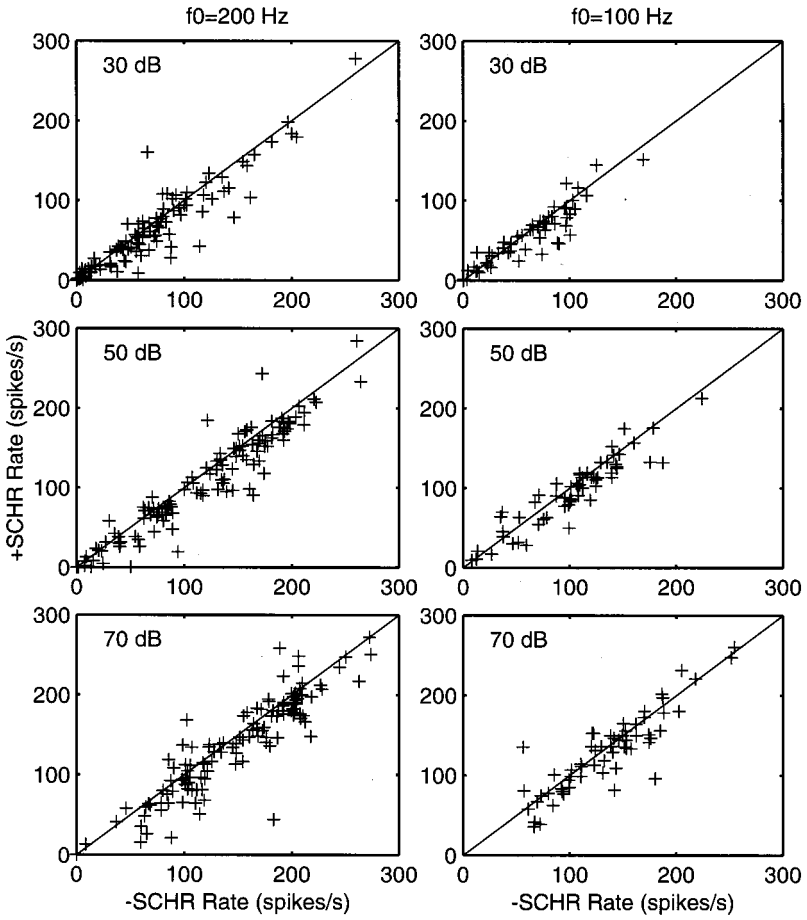

FIG. 7. Firing rates evoked by +SCHR stimuli plotted against firing rates obtained in responses to −SCHR sounds for all the neurons collected. Data in left and right columns were obtained in responses to stimuli synthesized using $f_0 = 200$ and 100 Hz, respectively.

was 10 ± 13 spikes/s ($N = 20$). Distributions of those differences greatly overlapped each other, implying that they are statistically insignificant. For $f_0 = 100$ Hz (Fig. 7, right column), differences in discharge rates were smaller, regardless of the level of stimulation. At 50 dB SPL, the average difference was 7 spikes/s for all neurons. At all levels, however, differences in firing rate evoked by −SCHR and +SCHR stimuli were statistically significant (two-tailed t test, $\alpha = 0.05$ at 30 and 50 dB SPL, and $\alpha = 0.06$ at 70 dB SPL).

Figure 8 (left column) shows synchronization indices measured from responses to −SCHR stimuli plotted against those obtained in responses to +SCHR stimuli ($f_0 = 200$ Hz). Synchronization indices were plotted only if the significance level of the Rayleigh test was $p < 0.005$ (Mardia, 1972). At the three levels analyzed, synchronization to f_0 was larger, on average, in responses to −SCHR stimuli. At 50 dB SPL and $f_0 = 200$ Hz, differences in synchronization were largest for chopper neurons (0.0737 ± 0.14, $N = 68$), followed by OL/PLN neurons (0.0430 ± 0.15, $N = 25$) and PL/ANF neurons (0.0163 ± 0.07, $N = 20$). Figure 8 (right column) shows synchronization indices obtained at $f_0 = 100$ Hz. At 50 dB, the asymmetry in synchronization indices exists but is not as obvious as in the case of $f_0 = 200$ Hz. At 70 dB SPL, however, synchronization indices obtained from responses to −SCHR stimuli are clearly larger on average than those obtained in responses to +SCHR stimuli.

Figure 9 shows firing rate differences (i.e., $\text{Rate}_{-\text{SCHR}} - \text{Rate}_{+\text{SCHR}}$) plotted as a function of the neuron's CF. The effect of CF on firing rate differences is significant based on an ANOVA (analysis of variance) for straight-line regression [$F_{1,116} = 8.71$, $\alpha = 0.0038$]. Results shown in Fig. 9 therefore indicate that asymmetries in firing rates evoked by −SCHR and +SCHR increase in proportion to the neuron's CF.

C. Responses to tones and ±SCHR stimuli

The effects in VCN responses of simultaneously playing a CF tone ("the probe") and a −SCHR or a +SCHR stimulus ("the suppressor") were also studied. Such effects were then compared to the response of the same neuron to a CF tone alone. Figure 10 shows the responses (i.e., the firing rate of the neuron measured during the 60 ms of stimulation) of three CS neurons to a CF tone alone (thin line with symbols), as well as the firing rates to the same tone but in the presence of a −SCHR (continuous lines) or a +SCHR (dashed lines) stimulus. The thickness of the lines is proportional to the level of the Schroeder stimulus (40 or 70 dB SPL). Below a certain probe level, the firing rate of the neurons remained constant, although at a rate larger than the neuron's spontaneous rate, and in proportion to the level of the suppressor. There was also a rightward shift in the rate-intensity functions. At higher probe levels, the firing rate was always lower than that evoked by the probe alone. The amount of suppression, i.e., reduction in firing rate, increases with the level of

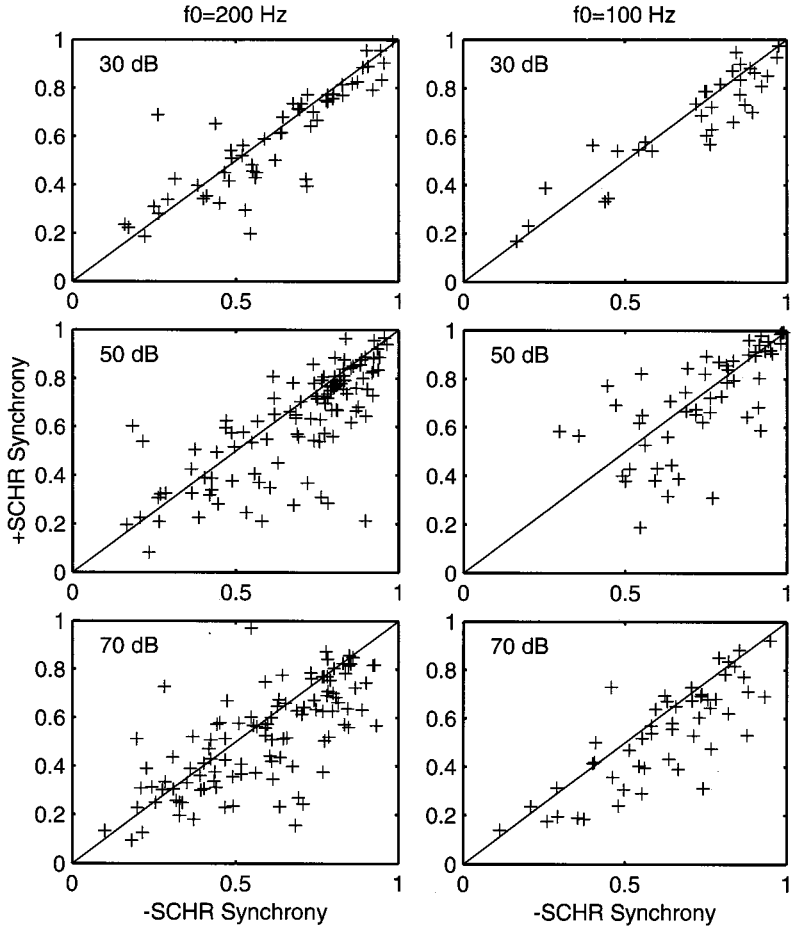

FIG. 8. Synchronization indices measured in responses to +SCHR stimuli versus those measured in responses produced by −SCHR stimuli. Data in left and right columns were obtained in responses to stimuli synthesized using $f_0 = 200$ and 100 Hz, respectively.

the masker. Whereas the amount of suppression evoked by both −SCHR and +SCHR stimuli at 40 dB is similar, at 70 dB SPL, the −SCHR stimulus produces the largest reduction in the firing rate.

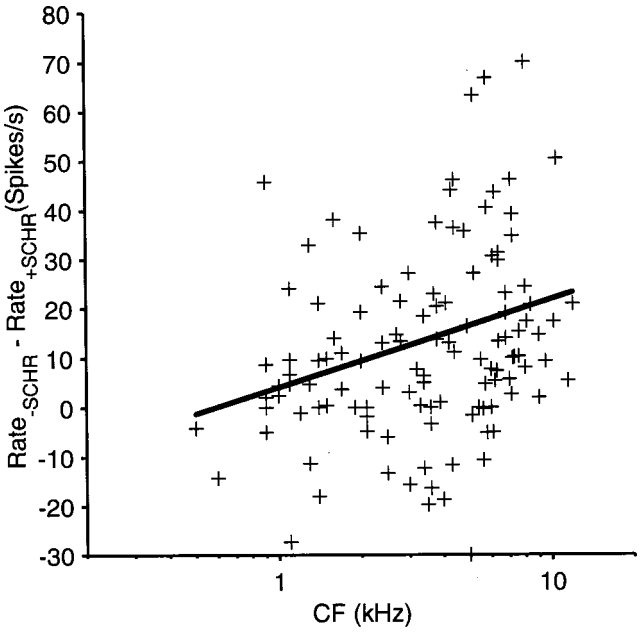

FIG. 9. Effects of CF on the difference between rates evoked by −SCHR and rates evoked by +SCHR. Stimulus level=70 dBSPL. Continuous line shows the least-square fit to the data.

Phase locking to f_0 measured in the responses to either of the two harmonic complexes can be reduced, or suppressed, by the probe stimulus, as shown in Fig. 11. Synchronization to f_0 is always the largest for the responses to the −SCHR stimulus, as expected. At low levels of the probe stimulus, synchronization to f_0 remained constant. Beyond a threshold level there was a reduction in phase locking to the ±SCHR stimuli in proportion to the probe level. For two of the neurons shown in Fig. 11, such thresholds were highest when the −SCHR stimulus was presented.

D. Auditory nerve fibers responses to ±SCHR stimuli

Responses to −SCHR and +SCHR stimuli were also obtained in a number of auditory nerve fibers. Figure 12 (top panel) shows rate-intensity functions obtained from responses to a CF tone alone, and from responses to either of the two harmonic complexes. As in the case of most cochlear nucleus responses, the −SCHR stimulus evoked a larger firing rate than the +SCHR one. The maximum firing rate, moreover, evoked by either of these two stimuli, is less than that elicited by a CF tone, just as in the case of CN neurons. Period histograms (Fig. 12, center and bottom panels) also resemble those obtained in cochlear nucleus neurons, i.e., a representation of f_0 in the discharge pattern of auditory nerve fiber responses. Similar results were found in other

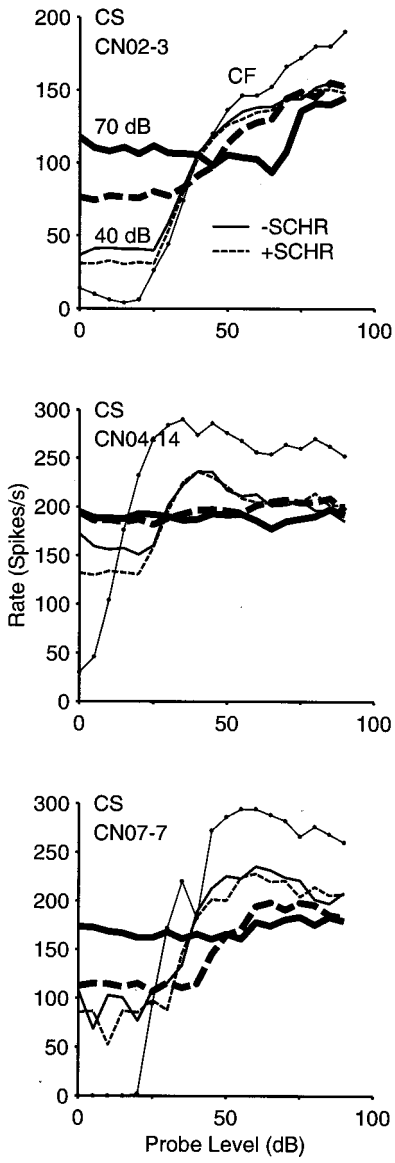

FIG. 10. Discharge rates plotted as a function of stimulus level. The stimulus was either a CF tone alone (thin line with symbols), or a CF tone presented simultaneously with a −SCHR sound (continuous lines) or a +SCHR stimulus (dashed lines). Thickness of lines is proportional to level of harmonic complex. Fifty stimulus repetitions of duration equal to 60 ms. CFs of neurons in top, center and bottom panels are, respectively: 6.1, 1.5 and 6.2 kHz.

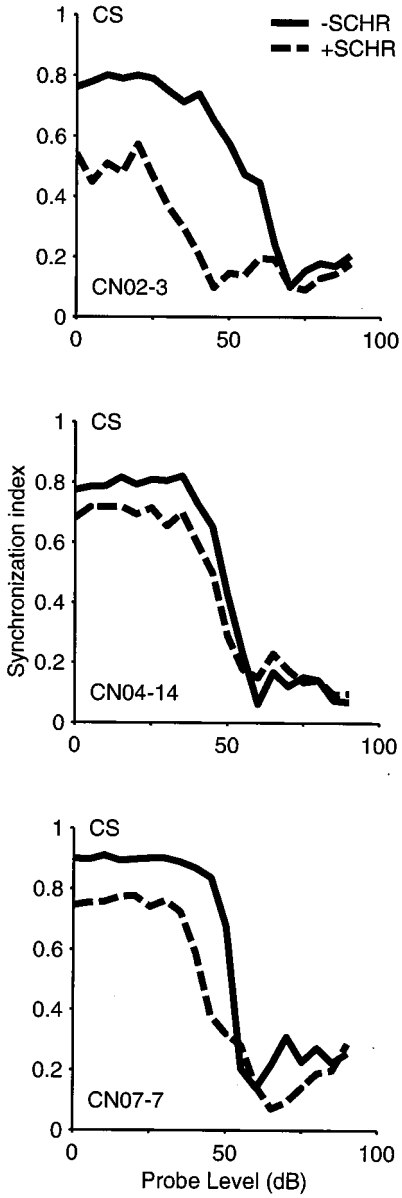

FIG. 11. Synchronization indices to f_0 (=200 Hz) as a function of the level of a CF tone (probe signal). Stimulus consisted of a CF tone played simultaneously with a −SCHR (continuous lines) or a +SCHR (dashed lines) sound of fixed level (70 dB SPL). Same neurons as in Fig. 9.

auditory nerve fiber responses, indicating that VCN neurons perform little processing of ANF responses for this type of stimulus.

IV. DISCUSSION

Responses of cochlear nucleus neurons to −SCHR stimuli differ from responses to +SCHR stimuli in both firing rate and synchronization to f_0. −SCHR stimuli evoked, on average, larger firing rates and synchronization coefficients than +SCHR stimuli. Differences between firing rates evoked by +SCHR and −SCHR complexes appear to be correlated with CF, as these differences increase with the neuron's CF.

Differences in firing rates evoked by −SCHR and +SCHR stimuli are smaller for $f_0=100$ Hz than those measured using $f_0=200$ Hz. Studies of 200% amplitude modulated signals in cat's VCN (Rhode, 1994) have shown discharge rate versus modulation frequency functions that are basically all-pass relations. Temporal modulation transfer functions in the VCN vary between low and bandpass, the latter being more common at high stimulus levels. So, it is not easy to explain the results of this article based on previous results. Note also that stimuli using $f_0=100$ Hz presented in this work have slower instantaneous frequency changes, or sweep rates, than stimuli presented with $f_0=200$. Differences in simultaneous masked thresholds obtained in humans (Kohlrausch and Sander, 1995) are larger

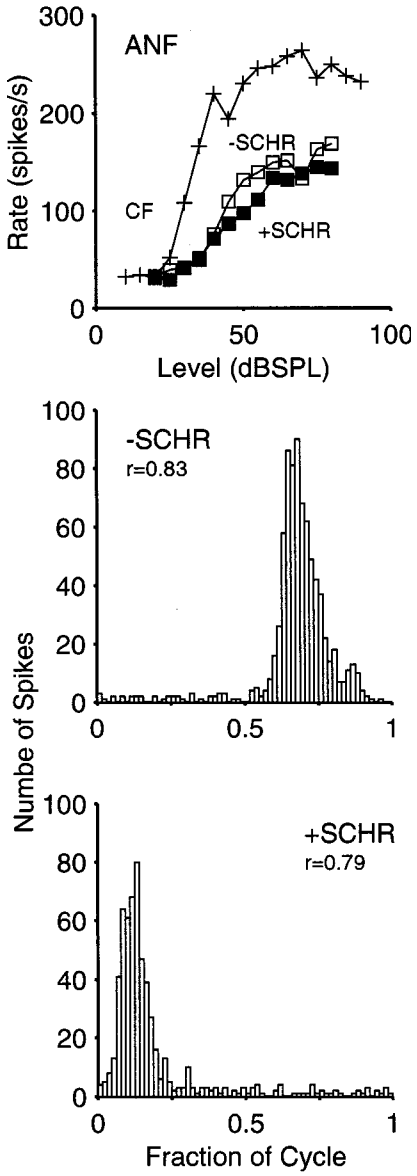

FIG. 12. Rate intensity functions obtained from responses to a CF (=5.8 kHz) tone alone, −SCHR (open squares) and +SCHR (filled squares) symbols (top panel). Period histograms obtained from responses to −SCHR (center panel) and +SCHR (bottom) stimuli along with their respective synchronization indices.

for $f_0=200$ and 100 Hz than for $f_0=50$ Hz, which agrees qualitatively with results shown in this article.

Firing rates evoked by Schroeder stimuli saturate at values that are usually smaller than maximum rates produced by a CF tone alone. This could be due to components in the stimulus suppressing other components that are near CF. The phase versus frequency characteristic of the basilar membrane might also play a role in transmitting pure tones more efficiently than Schroeder stimuli.

Fourier analysis of responses of low-CF neurons to harmonic complex stimuli shows the presence of spectral peaks (harmonics of f_0) around CF. These spectral peaks are more prominent in PL, PLN and OL neurons than in chopper neurons. Because of their poor phase locking, chopper neurons cannot signal the presence of stimuli whose frequency is above 1–1.5 kHz in the temporal structure of their responses.

A. Effects of CF

Differences between firing rates evoked by −SHCR and +SCHR stimuli appear to be correlated with CF (Fig. 9), in spite of the large variability observed. Another effect of CF is shown in Fig. 11, where differences in suppression thresholds are larger for high-CF neurons (top and bottom panels) than for the low-CF neuron (center panel).

Curvatures (i.e., second-order derivatives) of phase versus frequency curves of BM responses to clicks in the base region of the chinchilla cochlea (Recio and Rhode, 2000a) are basically constant around CF and of similar sign and value as curvatures of −SCHR stimuli. Filtering of +SCHR stimuli performed by the BM in the base of the cochlea decreases the amount of curvature (since the curvature of +SCHR stimuli is of the opposite sign and similar absolute value to that of the BM), hence producing peaked, or modulated, waveforms (Kohlrausch and Sanders, 1995). On the other hand, analysis performed on BM click data in the apex of the chinchilla cochlea (Cooper and Rhode, 1996) shows curvatures that are antisymmetric and not constant around CF. Simulations performed using Cooper and Rhode data (results not shown) indicate that, in responses to −SCHR stimuli, the BM in the apex yields waveforms that are very similar, in terms of the amount of modulation, to waveforms obtained in responses to +SCHR stimuli.

In conclusion, differences between responses to −SCHR and +SCHR stimuli appear more obvious for high-CF (>3–4 kHz) than for low-CF neurons (<2 kHz), and this might be attributed to differences in curvatures in the base and apex. It is of interest to note that psychoacoustic experiments performed in humans (Summers and Leek, 1998) have shown that the masking effects of −SCHR stimuli relative to those evoked by +SCHR stimuli are larger for probes in the 2–4-kHz region than for low-frequency ones (~1 kHz).

B. Relation to BM responses

Ventral cochlear nucleus responses to −SCHR and +SCHR stimuli have similarities with basilar membrane responses (Recio and Rhode, 2000a), where the former stimulus elicits larger response root-mean squared (rms) values and smaller modulation, or ''peakiness,'' than the latter stimulus. Because −SCHR stimuli evoke BM responses with larger rms values than those generated by +SCHR stimuli, it is expected that the former stimuli will evoke larger firing rates than the latter. Although the envelope of the stimuli used in this work is basically flat but with an instantaneous frequency that fluctuates over time, the basilar membrane, by virtue of its bandpass characteristic, converts the input stimuli into another waveform with an envelope that is not flat. Synchronization to f_0 in BM responses to −SCHR is, however, *smaller* than the one measured in responses to +SCHR stimuli, which is the opposite of the average response of cochlear nucleus neurons. For example,

at 38 dB SPL, response envelopes shown in Fig. 11 in Recio and Rhode (2000a) yield a synchronization coefficient of 0.04 (0.52 at 88 dB) in responses to −SCHR stimuli and 0.61 (0.72 at 88 dB) when +SCHR was the stimulus. Studies of representation of amplitude modulation in the auditory nerve and cochlear nucleus of cat (Joris and Yin, 1992; Rhode, 1994) have shown that synchronization versus stimulus level curves of ANFs are nonmonotonic functions, going from near zero to a maximum level of synchrony and then decreasing as stimulus level increases. The level at which maximum synchronization occurs is 10–15 dB below the level at which the firing rate of ANFs saturates. Because the maximum firing rate elicited by Schroeder stimuli is below the maximum firing rate evoked by tones, it is conceivable that for stimulation using Schroeder complexes, below saturation synchrony to f_0 is proportional to firing rate. Because overall rate is higher for −SCHR stimuli than for +SCHR, −SCHR stimuli should evoke a larger synchronization index than +SCHR stimuli, if synchrony is proportional to rate. It appears, therefore, that the envelope of basilar membrane responses to −SCHR stimuli is a more effective stimulus since it evokes larger firing rates and synchronization indices in the auditory nerve and in cochlear nucleus neurons than the envelope obtained in responses to +SCHR stimuli. The effectiveness of the stimulus is thus correlated with the rms values of its response. Another possible explanation for this effectiveness comes from the instantaneous frequency versus time curves shown in Fig. 16 in Recio and Rhode (2000a), which depict a slower slope around CF for responses to −SCHR stimuli than for slopes obtained in responses to +SCHR stimuli. That is, the ''dwell time'' around CF is longer in responses to −SCHR than to +SCHR.

C. Suppression effects

Responses to a CF tone in the presence of either −SCHR or +SCHR stimuli show that VCN neurons respond to the harmonic complexes until a certain level of the CF tone is reached. Above this level, the firing rate increased but was always below the firing rate evoked by the tone alone, indicating that suppression in the firing rate occurred. Suppression became larger with increases in suppressor level (i.e., the −SCHR or +SCHR stimulus). Suppression by Schroeder stimuli in cochlear nucleus neurons was larger than suppression by white noise in auditory nerve fibers (Rhode *et al.*, 1978). Synchrony to f_0 in responses to −SCHR or +SCHR stimuli was suppressed when the level of the CF tone increased beyond a threshold value. That is, synchronization indices remained constant below a certain ''threshold,'' which is generally highest when −SCHR stimuli are used. The larger rate suppression and the higher threshold for synchrony suppression evoked by −SCHR stimuli, when compared to suppression produced by +SCHR stimuli, imply that the −SCHR stimuli should be the more effective behavioral masker. This conclusion agrees with the results of relevant psychoacoustic experiments (e.g., Smith *et al.*, 1986; Kohlrausch and Sanders, 1995).

D. Comparison to ANF responses

Responses of auditory nerve and primary-like fibers to ±SCHR stimuli did not show any statistically significant difference from responses of other VCN neuron types, at least in terms of firing rate and synchronization to f_0. For example, although low-CF (i.e., CF$<$4 kHz) chopper neurons can encode in their spike times the value of f_0, they fail to encode the presence of near-CF components. Suppression effects due to Schroeder-phase complex stimuli in the responses to CF tones in the auditory nerve fibers were not studied. Based on previous work (Rhode and Greenberg, 1994), larger suppression effects in the VCN are expected.

The widespread representation of f_0 observed in the majority of VCN responses is a consequence of the existence of the same representation in the auditory nerve. Such representation, which is also related to envelope extraction, in the auditory nerve is possible because of the nature of the response of the basilar membrane, which converts a frequency modulated signal with a flat envelope into another waveform that is both amplitude and frequency modulated.

E. Comparison to previous studies

Because of the changes with time of the instantaneous frequency of Schroeder-phase complex stimuli, obvious similarities exist between this work and studies of auditory nerve fibers and cochlear nucleus responses to frequency-modulated signals. Sinex and Geisler (1981) studied responses of ANFs to sweep tones and found that the number of spikes evoked by upward and downward sweeps was approximately the same, for sweep rates less than about 100 kHz/s. For faster sweep rates (in the order of several hundred kHz/s), Møller (1974) concluded that stimuli with ascending sweep rates, which are similar to −SCHR stimuli, evoked more spikes than stimuli with descending sweeps. The sweep rate of the stimuli used here is around 3.85 MHz/s (Recio and Rhode, 2000a); therefore our results agree with those in Møller (1974). Temporal asymmetries were also found in previous studies (Møller, 1974; Sinex and Geisler, 1981). That is, peak responses (measured as spikes/s) were largest with stimuli with high–low frequency sweeps, yet the overall spike count was the same, which might be a consequence of neural adaptation (Møller, 1974; Sinex and Geisler, 1981).

It is also conceivable that neural adaptation plays a role in the difference in synchronization indices measured in responses to −SCHR and +SCHR stimuli. Nonetheless, it might also be significant that instantaneous frequency curves of BM responses to −SCHR stimuli are different in absolute values of slopes than those measured in responses to +SCHR stimuli.

ACKNOWLEDGMENTS

This work was supported by NIH Grant No. NS-17590 to W. S. Rhode. Thanks to Dan Geisler, Donata Oertel and Bill Rhode for reading an earlier version of this manuscript. I am also thankful to Van Summers and an anonymous reviewer for their many comments.

Blackburn, C. C., and Sachs, M. B. (**1989**). ''Classification of unit types in the anteroventral cochlear nucleus: PST histograms and regularity analysis,'' J. Neurophysiol. **62**, 1303–1329.
Blackburn, C. C., and Sachs, M. B. (**1990**). ''The representation of the steady-state vowel sound /ε/ in the discharge patterns of cat anteroventral cochlear nucleus neurons,'' J. Neurophysiol. **63**, 1191–1212.
Cooper, N. P., and Rhode, W. S. (**1996**). ''Fast travelling waves, slow travelling waves and their interactions in experimental studies of apical cochlear mechanics,'' Aud. Neurosci. **2**, 289–299.
Evans, E. F., and Nelson, P. G. (**1973**). ''The responses of single neurons in the cochlear nucleus of the cat as a function of their localization and anesthetic state,'' Exp. Brain Res. **117**, 402–427.
Goldberg, J. M., and Brown, P. B. (**1969**). ''Response of binaural neurons of dog superior olive complex to dichotic tonal stimuli: Some physiological mechanisms of sound localization,'' J. Neurophysiol. **32**, 613–636.
Joris, P. X., and Yin, T. C. (**1992**). ''Responses to amplitude-modulated tones in the auditory nerve of the cat,'' J. Acoust. Soc. Am. **91**, 215–232.
Kohlrausch, A., and Sander, A. (**1995**). ''Phase effects in masking related to dispersion in the inner ear. II. Masking period patterns of short targets,'' J. Acoust. Soc. Am. **97**, 1817–1829.
Leek, M. R., Dent, M. L., and Dooling, R. (**2000**). ''Masking by harmonic complexes in budgerigars (*Melopsittacus undulatus*),'' J. Acoust. Soc. Am. **107**, 1737–1744.
Mardia, K. V. (**1972**). *Statistics of Directional Data* (Academic, London).
Møller, A. R. (**1974**). ''Coding of sounds with rapidly varying spectrum in the cochlear nucleus,'' J. Acoust. Soc. Am. **55**, 631–640.
Recio, A., and Rhode, W. S. (**2000a**). ''Basilar membrane responses to broadband stimuli,'' J. Acoust. Soc. Am. **108**, 2281–2298.
Recio, A., and Rhode, W. S. (**2000b**). ''Representation of vowel stimuli in the ventral cochlear nucleus of the chinchilla,'' Hear. Res. **146**, 167–184.
Rhode, W. S. (**1994**). ''Temporal coding of 200% amplitude modulated signals in the ventral cochlear nucleus of cat,'' Hear. Res. **77**, 43–68.
Rhode, W. S. (**1998**). ''Neural encoding of single-formant stimuli in the ventral cochlear nucleus of the chinchilla,'' Hear. Res. **117**, 39–56.
Rhode, W. S., and Cooper, N. P. (**1996**). ''Nonlinear mechanics in the apical turn of the chinchilla cochlea *in vivo*,'' Aud. Neurosci. **3**, 101–121.
Rhode, W. S., and Greenberg, S. (**1994**). ''Lateral suppression and inhibition in the cochlear nucleus of the cat,'' J. Neurophysiol. **71**, 493–514.
Rhode, W. S., and Kettner, R. E. (**1987**). ''Physiological study of neurons in the dorsal and posteroventral cochlear nucleus of the cat,'' J. Neurophysiol. **57**, 414–442.
Rhode, W. S., and Smith, P. H. (**1986**). ''Encoding timing and intensity in the ventral cochlear nucleus of the cat,'' J. Neurophysiol. **56**, 261–286.
Rhode, W. S., Geisler, C. D., and Kennedy, D. T. (**1978**). ''Auditory nerve fiber response to wide-band noise and tone combinations,'' J. Neurophysiol. **41**, 692–704.
Schroeder, M. R. (**1970**). ''Synthesis of low peak-factor signals and binary sequences with low autocorrelation,'' IEEE Trans. Inf. Theory **16**, 85–89.
Sinex, D. G., and Geisler, C. D. (**1981**). ''Auditory-nerve fiber responses to frequency-modulated tones,'' Hear. Res. **4**, 127–148.
Smith, B. K., Sieben, U. K., Kohlrausch, A., and Schroeder, M. R. (**1986**). ''Phase effects in masking related to dispersion in the inner ear,'' J. Acoust. Soc. Am. **80**, 1631–1637.
Strube, H. W. (**1985**). ''A computationally efficient basilar-membrane model,'' Acustica **58**, 207–214.
Summers, V., and Leek, M. R. (**1998**). ''Masking of tones and speech by Schroeder-phase harmonic complexes in normally hearing and hearing-impaired listener,'' Hear. Res. **118**, 139–150.

Inner hair cell response patterns: Implications for low-frequency hearing

M. A. Cheatham[a] and P. Dallos

Audiology and Hearing Sciences, Communication Sciences and Disorders, The Hugh Knowles Center, 2-240 Frances Searle Building, 2299 North Campus Drive, Northwestern University, Evanston, Illinois 60208-3550

(Received 26 February 2001; revised 18 June 2001; accepted 29 June 2001)

Inner hair cell (IHC) responses to tone-burst stimuli were measured from three locations in the apical half of the guinea pig cochlea. In addition to the measurement of ac receptor potentials, average intracellular voltages, reflecting both ac and dc components of the receptor potential, were computed and compared to determine how bandwidth changes with level. Companion phase measures were also obtained and evaluated. Data collected from turn 2, where best frequency (BF) is approximately 4000 Hz, indicate that frequency response functions are asymmetrical with steeper slopes above the best frequency of the cell. However, in turn 4, where BF is around 250 Hz, the opposite behavior is observed and the steepest slopes are measured below BF. The data imply that cochlear filters are generally asymmetrical with steeper slopes above BF. High-pass filtering by the middle ear serves to reduce this asymmetry in turn 3 and to reverse it in turn 4. Apical response patterns are used to assess the degree to which the middle ear transfer function, the IHC's velocity dependence and the shunting effect of the helicotrema influence low-frequency hearing in guinea pigs. Implications for low-frequency hearing in man are also discussed. [DOI: 10.1121/1.1397357]

PACS numbers: 43.64.Ld, 43.64.Nf, 43.64.Tk [LHC]

I. INTRODUCTION

Since the time of Fletcher (1940), it has been assumed that the peripheral auditory system can be represented as a large number of independent channels with each channel preceded by an auditory filter. If differences among channels relate primarily to this initial stage of filtering, then characterizing the auditory filter bank should provide insights into the operation of the system as a whole (Rosen and Howell, 1991). Consequently, recordings from different regions along the cochlear partition offer a basis for characterizing individual filters with different center frequencies. Admittedly, most of this information comes from single-unit activity where large numbers of auditory nerve fibers with widely varying best frequencies (BF) can be recorded in a single preparation (Kiang, 1984; Ruggero, 1992). By comparison, recordings from mammalian inner hair cells (IHC) are much less numerous. Nevertheless, they also yield information about different cochlear locations, i.e., information that reflects the best frequency (BF) of any particular recording site. In this report, IHC recordings are used to study how bandwidth changes with level and how the frequency-specific information associated with preceding mechanical events is transformed and modified prior to spike initiation.

Inner hair cell receptor potentials were measured from three locations in the apical half of the guinea pig cochlea. In addition to ac receptor potentials, which are presented in another publication (Cheatham and Dallos, 1998a), average voltages produced by individual cells were computed and compared. These average potentials reflect both ac and dc components of the receptor potential that are integrated at the synapse and that presumably initiate transmitter release. Use of the average potential is appropriate because the ac component of the response cannot by itself initiate transmitter release at high frequencies due to filtering by the cell's basolateral membrane (Russell and Sellick, 1978). Conversely, the dc receptor potential produced by IHCs located at the apex of the cochlea is insufficient to drive transmitter release at levels corresponding to behavioral threshold at low stimulus frequencies (Cheatham and Dallos, 1993, 1999). In previous publications (Cheatham and Dallos, 1993, 1998a), longitudinal comparisons were made for ac responses by using a generic compensation to adjust for decreases in the ac receptor potential due to filtering associated with resistances and capacitances in the cells basolateral membrane. Although not quantitative, this procedure facilitated comparisons at the level of the IHC transducer. Because the average potential includes contributions from voltage- and time-dependent ion channels in the cells basolateral membrane, it may provide a better indication of the signal initiating transmitter release. Hence, our decision was to compute the average potential when comparing hair cell responses recorded at different cochlear locations and when relating these results to behavioral sensitivity.

By collecting iso-input functions and documenting the magnitude and phase changes obtained at a series of levels, it is possible to define the filter properties of each recording location and to determine the factors that influence how these properties vary along the cochlear partition. Although the middle ear shapes cochlear inputs, the primary mechanical frequency analysis is associated with the basilar membrane-outer hair cell-tectorial membrane (BM-OHC-TM) complex

[a]Author to whom correspondence should be addressed; electronic mail: m-cheatham@nwu.edu

that determines the input to the IHC. Because the IHC transduces this information prior to its transfer to the auditory nerve, hair cell measurements are important to our understanding of how frequency and intensity are coded by the peripheral auditory system.

Because mechanical and neural responses obtained at the base of the cochlea are well characterized, the primary focus of this article is to show how apical IHC responses differ from those recorded at more basal locations. The response patterns recorded from IHCs with low BFs are also used to determine how the coding of low-frequency signals impacts behavioral sensitivity in guinea pig. Implications for human hearing are also evaluated.

II. METHODS

The method used in these experiments to record from IHCs is based on that introduced by Dallos *et al.* (1982). In this lateral approach, recordings are made from anesthetized guinea pigs in turns 2–4 where BFs are approximately 4000, 1000 and 250 Hz, respectively. Hence, this procedure allows outputs to be sampled from IHCs having BFs at two-octave intervals. In any given preparation, however, recordings are made from only one cochlear turn. Because second-turn measurements are taken at a location along the cochlear partition that is about half-way between base and apex (Cheatham, 1993), the present results provide information about the apical half of the guinea pig cochlea.

It is acknowledged that the data reported here are obtained from the same cells whose responses are presented elsewhere in a different form (Cheatham and Dallos, 1998a). Although we show representative examples, one for each recording location, these preparations are the best in our collection. The latter contains 12 IHCs from turn 2, 19 from turn 3, and 2 from turn 4. The examples shown in this report are those where the recording time was long enough to acquire frequency response functions at several levels. Further details appear in previous publications (Dallos, 1985, 1986; Cheatham and Dallos, 1992). All of the data reported here were collected in experiments approved by the National Institutes of Health and by Northwestern University's Animal Care and Use Committee.

In the lateral approach for recording IHC responses, a window is made in the cochlear bone overlying the scala media fluid space. This allows the recording electrode to enter the sense organ from the side, along a track that is roughly parallel to, but slightly below, the reticular lamina. Inner hair cell responses to tone-burst stimuli were amplified and capacitance compensated (Cell Explorer Model 8700, Dagan Corp.), low-pass filtered to remove aliasing and gain-controlled to prevent saturation of the analog-to-digital converter. Sound pressure levels, reported in dB *re*: 20 μPa, were determined by placing a probe-tube microphone (BT-1751, Knowles Electronics, Elk Grove Village, IL) close to the tympanic membrane. Averaged response waveforms, obtained for a series of frequencies and levels, were stored for off-line analysis using Igor Pro® (WaveMetrics, Lake Oswego, OR). Although the data were collected using a PDP 11/73 (Digital Equipment Corp.), the results were analyzed on a Macintosh IIfx or a Power Macintosh G3 (Apple Computer, Inc.).

Magnitude and phase data for the fundamental component of the ac receptor potential were taken from fast Fourier transforms of averaged response waveforms. In addition, half-wave rectified, average voltages were computed over an integer multiple of response cycles. The average voltage was then computed by adding together all sampled values above the baseline and dividing by the total number of data points. This procedure is virtually identical to computing the area under each half-cycle and dividing by the stimulus period.

Because data were acquired over many years, the stimulus parameters were not the same for all measurements. Although gated sinusoids were used, the duration was 40 ms for results in turns 3 and 4, but only 10–15 ms in turn 2, where inputs were not presented for frequencies less that 2000 Hz. In addition, the rise/fall time was 0.625 ms in turns 3 and 4, but 2.5 ms in turn 2. The number of samples used in the averaging procedure was also variable. At low levels, at least 30 repetitions were collected while at high levels, and, in some cases, as few as 10 repetitions were averaged. Because hair cell receptor potentials do not adapt, a relatively short interstimulus interval was selected to facilitate data collection, but in no case was it less than 55 ms.

III. RESULTS

A. Frequency response functions

The left panel in Fig. 1 shows the average receptor potential recorded from a third-turn IHC with a BF near 1000 Hz. At the lowest sound pressure level, in this case 20 dB, the cell is narrowly tuned and response magnitude decreases at higher and lower stimulus frequencies. As level increases, however, both low- and high-frequency slopes become flatter and bandwidth increases. The customary measure, Q_{10}, decreases from 1.8 at 20 dB to less than 0.4 at 80 dB. This degradation in frequency selectivity is thought to result from an increase in damping at higher stimulus levels (Anderson *et al.*, 1971; Hubbard and Geisler, 1972; Kim *et al.*, 1973; Hall, 1977).

Relative magnitude functions, obtained by comparing responses at a given sound level with high-level responses at 80 dB, are plotted in the center panel. In other words, plots are given that show how much greater the 80-dB response is than the comparison datum. At each frequency, this magnitude change in dB is plotted relative to the value at 80 dB. If this were a linear system, the three functions would be flat and separated from one another by 20, 40 and 60 dB. The data indicate that the largest magnitude changes, i.e., the most linear responses, are achieved away from BF. In the region around 1000 Hz, the changes are relatively small, indicating that the cell is most nonlinear near BF. This compression reflects that associated with preceding mechanical events (Rhode, 1971; Sellick *et al.*, 1982; Robles *et al.*, 1986; Nuttall and Dolan, 1996; Ruggero *et al.*, 1992, 1997), as well as that produced by the asymmetry inherent in the IHC transducer (Hudspeth and Corey, 1977; Russell and Sellick, 1978). The latter is important because the IHC cannot receive dc inputs due to the free-standing nature of its ste-

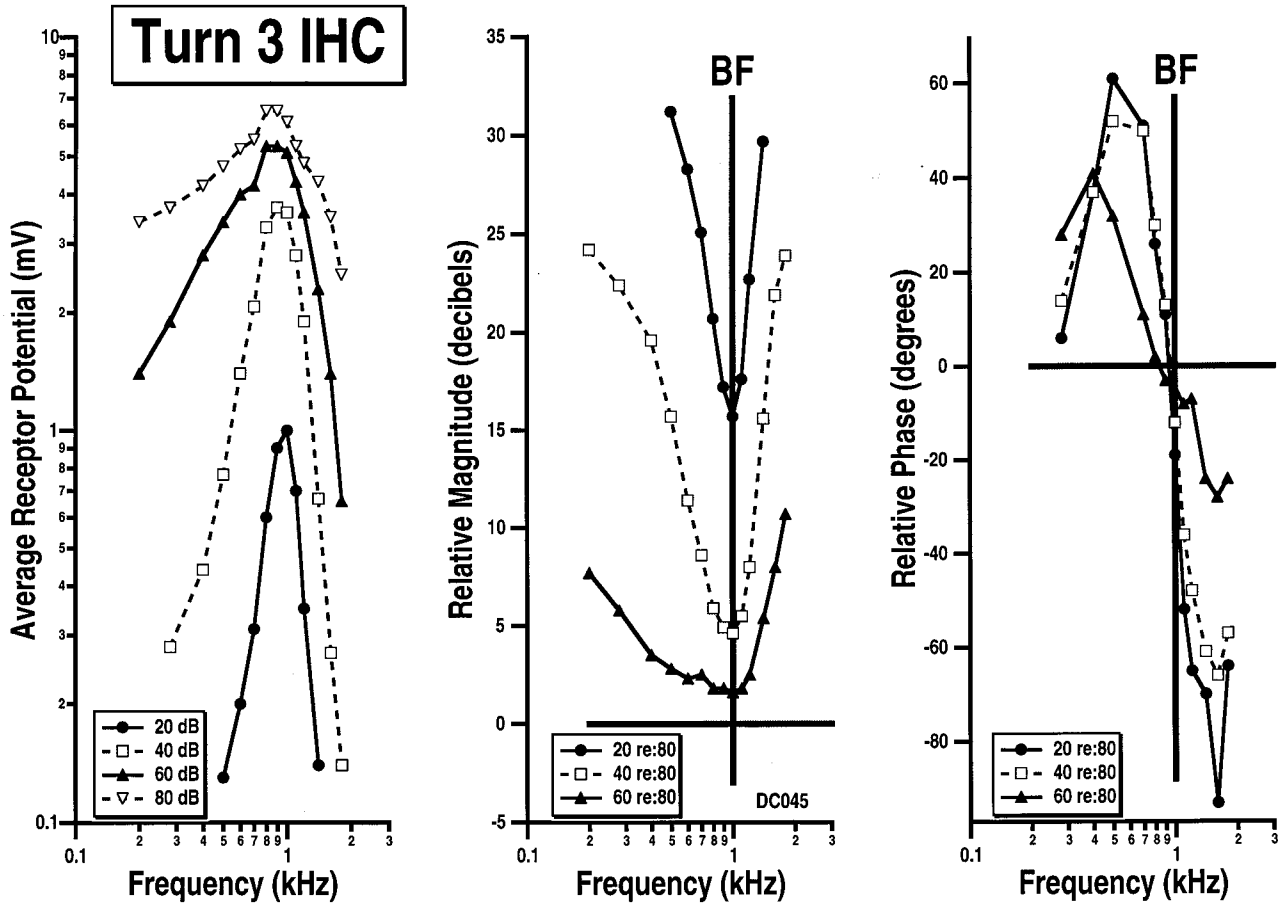

FIG. 1. Iso-input functions are presented for an IHC in the third turn of the guinea pig cochlea. The average receptor potential is plotted for inputs at 20 (circles and solid lines), 40 (open squares and dashed lines), 60 (triangles and solid lines) and 80 (open triangles and dashed lines) dB. The center panel shows magnitude measured relative to the 80-dB condition that is given a value of 0 dB. The vertical line indicates the BF of the cell. Phase data appear on the right where phase changes are also plotted relative to the 80-dB reference condition. By subtracting one measure from another, i.e., 20 from 80 dB, etc., the frequency- and level-dependent changes in magnitude and phase are emphasized.

reocilia (Dallos *et al.*, 1972; Lim, 1972). In other words, the sensory transducer is the source of the IHC's dc receptor potential (Cheatham and Dallos, 1998b), which is included in the average voltage.

Companion phase data are provided in the right panel of Fig. 1. These values were obtained from fast Fourier transforms of averaged IHC responses. The functions show changes in phase for the fundamental component of the ac receptor potential measured relative to the high-level response at 80 dB. The latter was chosen because a high-level reference was used for neural responses in the original description of phase nonlinearity (Anderson *et al.*, 1971). The data indicate phase leads below BF; phase lags above, as reported previously (Dallos, 1986). The phase changes in the BF region are small and the function passes through 0 degrees at this position. In fact, a pivot point at BF can be defined similar to that observed in the single-unit data obtained from neurons with similar BFs (Anderson *et al.*, 1971; Allen, 1983). The existence of a pivot point indicates that response phase is independent of level in the region around BF and that BF is relatively independent of level, except at very high intensities. Data from the third turn are, therefore, consistent with the idea that BF refers to that frequency where the cell is most sensitive and where response phase goes through its lead/lag transition.

Before generalizing from these results, it is prudent to evaluate recordings from other regions along the cochlear spiral, as in Fig. 2 where results are shown for a second-turn IHC with BF around 3800 Hz. The magnitude functions on the left demonstrate that response areas change as level increases from 40 to 80 dB and that high-frequency slopes are steeper than low-frequency slopes. There is also a greater tendency for the peak of the function to shift to lower frequencies, as shown in second turn of the gerbil cochlea (Zwislocki and Chatterjee, 1995) and in the basal turn of the guinea pig cochlea (Russell and Sellick, 1978). This behavior is thought to reflect similar response patterns observed in cochlear mechanics (Rhode, 1971; Sellick *et al.*, 1982; Nuttall and Dolan, 1996; Ruggero *et al.*, 1997). As in Fig. 1, relative magnitude measures are shown in the center and companion phase changes are plotted on the right. Although the latter indicate a lead/lag behavior, the transitions occur above the best frequency of the cell. There is also a tendency for the pivot point to disperse as the zero crossing moves to higher frequencies with increasing level. A similar trend was observed in basilar membrane mechanical responses (Rug-

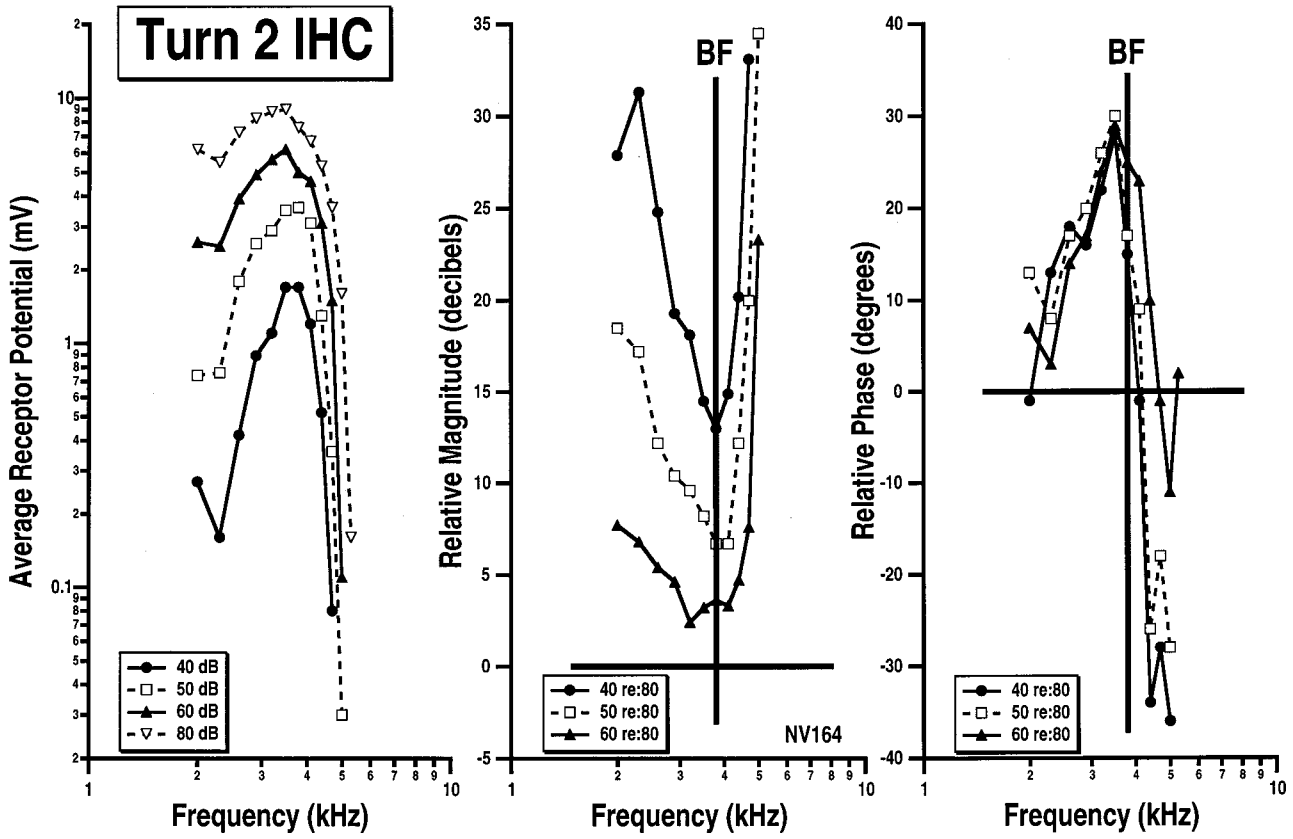

FIG. 2. Data obtained in turn 2 are plotted here for iso-input levels of 40 (circles and solid lines), 50 (squares and dashed lines), 60 (triangles and solid lines) and 80 (open triangles and dashed lines) dB. The BF for this cell is ~3800 Hz. These results are also presented in three panels, as in Fig. 1.

gero *et al.*, 1997) and in auditory nerve fibers with BFs above ~2000 Hz (Allen, 1983). It is acknowledged that we may have underestimated the BF of this second turn IHC because 40 dB was the lowest level used to collect the data shown in Fig. 2.

Measurements from the fourth turn are depicted in Fig. 3 for an IHC with BF near 230 Hz. Again, bandwidth is level dependent and the measurements of relative magnitude, plotted in the center, indicate that the system is nonlinear at this apical recording location. Only at 700 Hz, when the input sound pressure level is decreased from 70 to 50 dB (triangles and solid lines), is response magnitude reduced by 20 dB as expected in linear systems. When compared to center panels in Figs. 1 and 2, the functions from turn 4 are less V-shaped, indicating that the nonlinearity is expressed over more of the response area of the cell. This is consistent with measurements of basilar membrane mechanics at the apex of the cochlea (Rhode and Cooper, 1996). Relative phase changes are plotted on the right. Although a lead/lag behavior is again recorded, the transition occurs *below* the best frequency of the cell. A similar pattern was also observed by Anderson *et al.* (1971) for single units innervating the apex of the cochlea and having low BFs.

Data plotted in Fig. 4 serve to emphasize the level- and frequency-dependent magnitude changes observed in turns 2–4. To facilitate the comparisons, the average receptor potential is normalized to its value at BF, i.e., 3800 Hz in turn 2, 1000 Hz in turn 3, and 230 Hz in turn 4. The frequency scale is also normalized to BF. Plots for the compensated ac receptor potential are provided in a previous publication (Cheatham and Dallos, 1998a). At each recording location, functions are included for the 50- and 90-dB conditions. In turn 2, the largest level-dependent changes are observed below the BF of the cell and the peak of the function shifts to lower frequencies. Conversely, the data in turn 4 exhibit the largest changes above BF and the peak tends to move to higher frequencies. The reverse asymmetry exhibited in turn 4 is consistent with that reported for data from the auditory nerve (Pfeiffer and Molnar, 1970; Rose *et al.*, 1971; Kiang *et al.*, 1977; Gibson *et al.*, 1977; Liberman and Kiang, 1978; Evans, 1981) where the tails of tuning curves for units with BFs below ~1000 Hz are on the high-frequency side of the tuning curve. This contrasts with units with higher BFs where the opposite is true. Data collected in turn 3, and plotted in the center panel, show a more symmetrical expansion of the response area to both lower and higher frequencies as stimulus level increases from 50 to 90 dB.

These place-specific changes in filter shape have important implications for the coding of acoustic signals, especially the reverse asymmetry recorded at the very apex of the cochlea and expressed in both inner hair cell and neural responses. Because filter shape is primarily determined by preceding mechanical events, data for the ac receptor potential are provided in Fig. 5. These results were collected at 50 dB, the lowest level common to all three cells. In order to better represent filter shape at the input to the IHC, ac responses

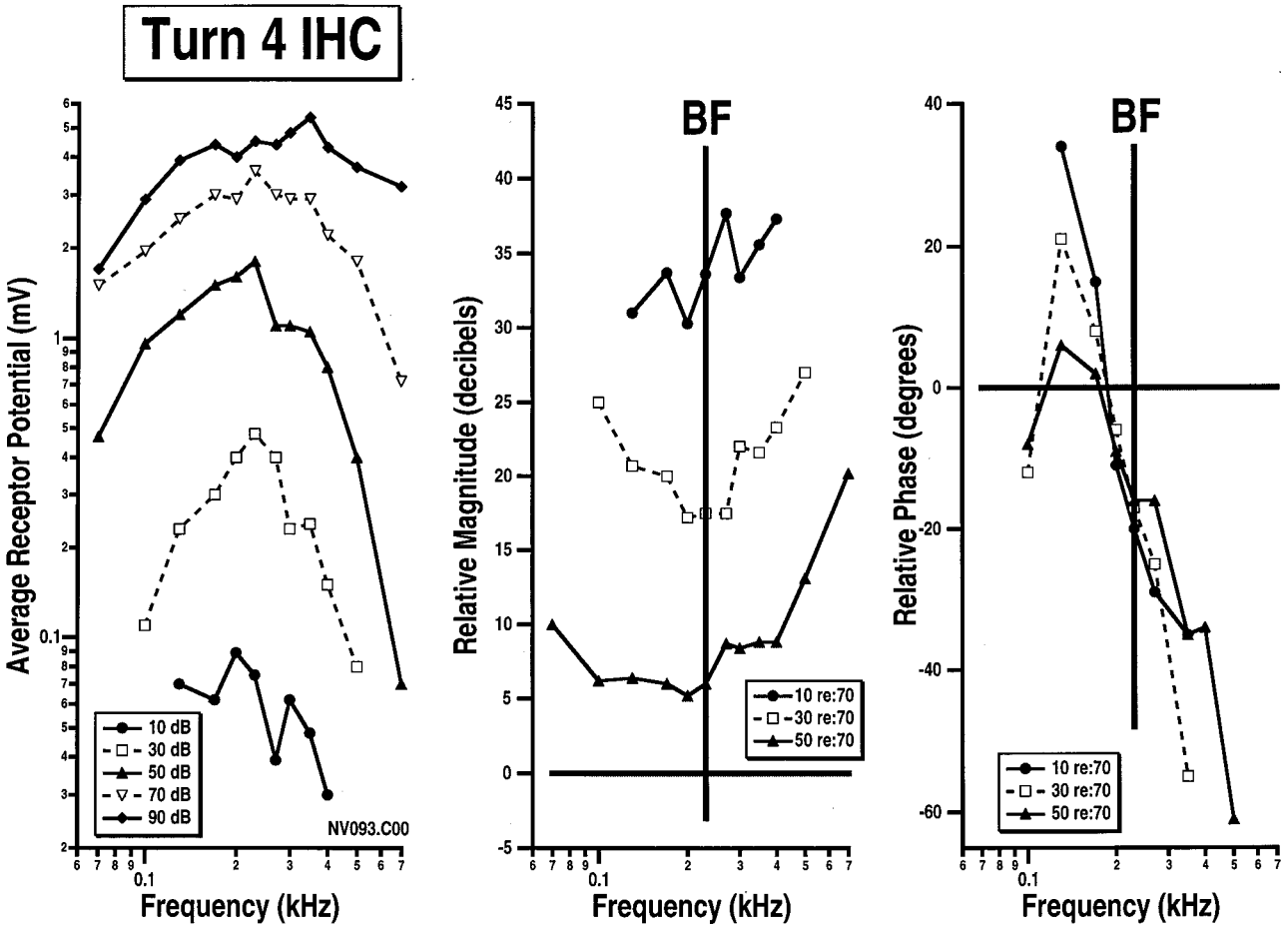

FIG. 3. This plot is similar to those in Figs. 1 and 2 but the data are collected from turn 4 where BF is 230 Hz. The 70-dB condition was used as the reference for the relative magnitude changes plotted in the center panel and for the relative phase changes plotted on the right. The 90-dB condition was not chosen in order to avoid the level-dependent phase changes observed at high input levels (Cheatham and Dallos, 1998b).

were compensated for reductions associated with filtering by the cell's basolateral membrane and by the recording apparatus (Cheatham and Dallos, 1993, Fig. 3C). In addition, the ac magnitude data were normalized at BF and plotted on a normalized, linear frequency scale. The latter choice was made because behavioral data on auditory filter shape are frequently plotted on a linear abscissa. These results are provided to demonstrate changes in filter shape as they appear at the level of IHC transducer.

Data from turn 2 show steeper slopes above BF, while data from turn 4 show steeper slopes below BF. In turn 3, the response area is relatively symmetrical. These shape changes appear to reflect the large variations in high-frequency slope observed at the three cochlear locations. In turn 2, which is approximately 10 mm from the base of the guinea pig cochlea where basilar membrane length is ~18 mm (Cheatham, 1993), the high-frequency slope is ~96 dB/oct. In turn 3, where the center of the cochlear window is ~14 mm from the base, the high-frequency slope is ~32 dB/oct. Finally, in turn 4, which is ~17 mm from the base, the high-frequency slope is only about 10 dB/oct. In contrast, the slopes of the functions below BF are fairly similar at the three recording locations.

B. Implications for behavioral thresholds at low frequencies

Information obtained from the apex of the cochlea is used to construct the schematic shown in Fig. 6, which includes features that would be expected to influence low-frequency responses in the guinea pig cochlea. The middle ear transfer function is represented by the high-pass filter function plotted with dashed lines and decreasing at 6 dB/oct below 600 Hz (Johnstone and Taylor, 1971; Décory *et al.*, 1990; Cooper and Rhode, 1995). In addition, a second high-pass filter also shapes low-frequency responses. This stage of filtering is associated with ciliary mechanics and the resulting velocity dependence of the IHC. In this schematic, input to the IHC is attenuated by 6 dB/oct below a corner frequency of ~470 Hz (Dallos, 1984). In contrast to filtering by the middle ear, this attenuation at the input to the IHC occurs after the frequency analysis that is associated with basilar membrane mechanics. Although more recent studies of hair-cell stereocilia are available (Freeman and Weiss, 1990; Shatz, 2000), these models were primarily designed for and tested in the lizard cochlea. The degree to which these models reflect behavior in the mammalian cochlea has not been

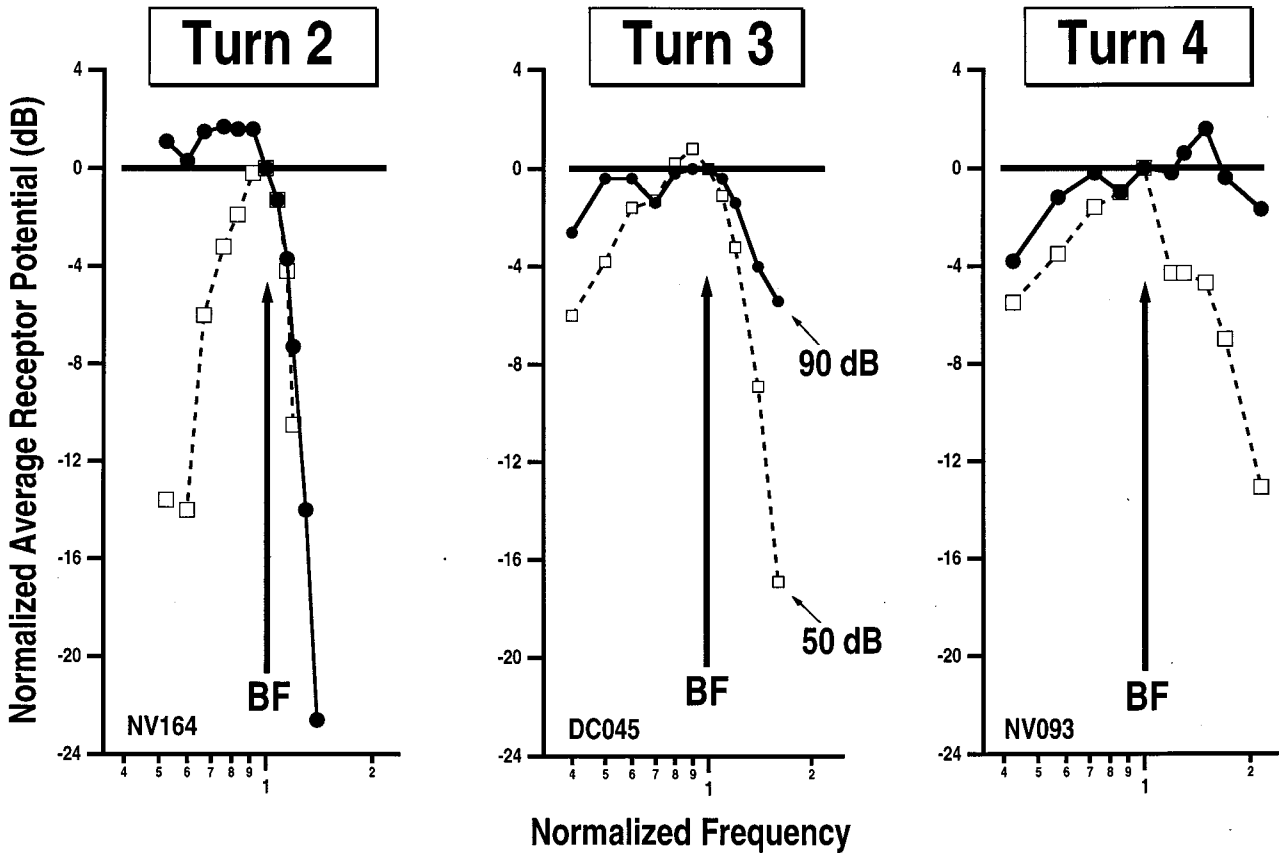

FIG. 4. Iso-input functions obtained in turns 2–4 are compared here at 50 (squares and dashed lines) and 90 (circles and solid lines) dB. To facilitate comparisons, the average receptor potentials are normalized at BF. This is achieved by giving the potential at BF a value of 0 dB and plotting all other values relative to this datum. The abscissa is also normalized by dividing stimulus frequency by BF. Thus, the latter has a value of 1.0 and is designated by the vertical arrow in each panel. Data for turn 3 at 50 and 90 dB were not plotted in Fig. 1 for clarity. The 90-dB condition in Fig. 2 is also missing for the same reason.

evaluated. Hence, our decision is to use the Dallos (1984) model that is based on IHC response patterns recorded in turn 3 of the guinea pig cochlea.

The schematic in Fig. 6 serves to demonstrate how these two high-pass filters affect the shapes of response areas in fourth-turn IHCs. The attenuations due to the middle ear and the velocity dependence of the IHC provide a total, combined attenuation that decreases at a rate of 12 dB/oct. This combined function is plotted with dotted lines. The vertical line demonstrates that the BFs of IHCs in turn 4 are below the corner frequencies of these two high-pass filters. Consequently, input to the cell is reduced by filtering at very low frequencies.

The remaining function, plotted in Fig. 6 with solid lines, represents the behavioral threshold for guinea pigs (Fay, 1988) compiled by averaging data from several investigators (Miller and Murray, 1966; Heffner *et al.*, 1971; Walloch and Taylor-Spikes, 1976; Prosen *et al.*, 1978). These results are normalized at 1000 Hz so that all values are plotted relative to this datum, which is given a value of 0 dB. Behavioral threshold decreases at a rate that exceeds the 6 dB/oct provided by the middle ear transfer function alone, hence the similarities between the combined and behavioral functions. When considering these comparisons, it should be mentioned that the middle ear transfer function for guinea pig was determined with bulla open. This differs from the situation when behavioral thresholds are obtained in intact animals. However, it has been demonstrated that the CM is impervious to many alterations of the middle ear and that the low-frequency slope of the transfer function is not altered (Dallos, 1970, Fig. 8). Dallos also demonstrated that the middle ear muscles do not influence the low-frequency slope of the middle ear transfer function (Fig. 9). Consequently, the comparisons shown in Fig. 6 are not inappropriate.

A similar exercise is provided for humans in Fig. 7. Again, filter functions are plotted with dashed lines. In this figure, the attenuation associated with the middle ear is adapted from Flanagan's computational model (Flanagan, 1962; Dallos, 1973). This effect decreases input to the cochlea at a rate of 6 dB/oct below 1000 Hz. For lack of a better alternative, the function for the IHC velocity dependence is based on guinea pig data and is replotted from the previous figure. Finally, the shunting effect of the helicotrema is appended. This third high-pass filter is required because the helicotrema in man, but not in guinea pig (Dallos, 1970; Zwislocki, 1975), is large with the result that additional attenuation is expected below 100 Hz.

The remaining curve, plotted with solid lines in Fig. 7, approximates the minimum audible pressure (MAP) curve for man (redrawn from Killion, 1978). This curve represents the sound pressure of a tone, at the threshold of audibility, that is presented by an earphone and measured near the tym-

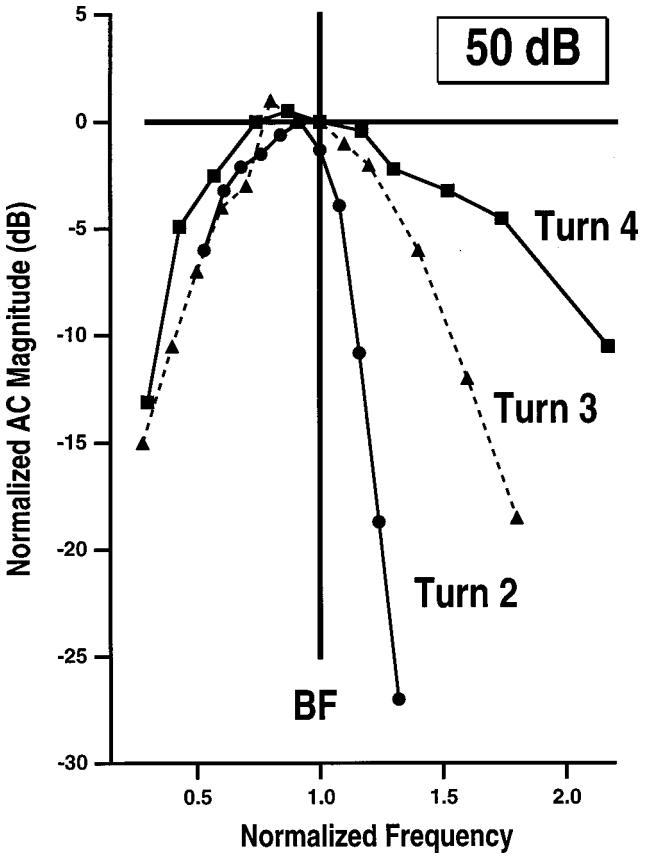

FIG. 5. This figure shows responses at 50 dB for the ac receptor potential obtained from the same three IHCs plotted in Fig. 4. The magnitude data include corrections for filtering associated with resistances and capacitances in the cell's basolateral membrane, as well as low-pass filtering associated with the recording electrode. The latter was required in turn 2 only. As in Fig. 4, the magnitude data are normalized and plotted on a normalized frequency scale. The function for turn 2 is plotted with circles and solid lines; for turn 3, triangles and dashed lines; for turn 4, squares and solid lines.

panic membrane. Because the MAP curve has been normalized, all responses are plotted relative to the response at 1000 Hz. The shape of the MAP curve is similar to the combined curve, which represents the total attenuation due to filtering. Although this schematic shows that these three stages of high-pass filtering approximate the changes in sensitivity exhibited in human subjects, it is acknowledged that the terminal slope of the MAP function is greater than 18 dB/oct (Dadson and King, 1952; Killion, 1978; Puria *et al.*, 1997). This suggests that the additional reduction in sensitivity at very low frequencies (Corso, 1958; Yeowart and Evans, 1974) may relate to physiological noise as suggested by others (Moore, 1989). In other words, the MAP curve represents a masked threshold.

IV. DISCUSSION

A. Comparisons with mechanical and neural responses: Magnitude data

Recordings from mammalian IHCs are consistent with the idea that nonlinearities in the cochlea shape auditory filters in both a frequency- and level-dependent fashion. Even when auditory filter shape is examined psychophysically (Glasberg and Moore, 2000), the changes with level resemble the variations in tuning observed in basilar membrane responses. This association suggests that the fundamental character of auditory filters is determined in the organ of Corti and that this distorted peripheral representation is provided to the central auditory pathway for further analysis. This idea is supported by the similarities between single-unit (Rose *et al.*, 1971; Kiang *et al.*, 1977; Møller, 1977; Gibson *et al.*, 1977; Liberman and Kiang, 1978; Evans, 1981) and IHC data. When response areas are measured at a series of levels, for neurons with BFs around 1000 Hz, the iso-input functions expand symmetrically to both lower and higher stimulus frequencies. This response pattern is reminiscent of that shown in Figs. 1, 4, and 5 for IHCs in turn 3. For neurons with higher BFs, above ~2000 Hz, the response area expands asymmetrically toward lower frequencies with the result that the slopes recorded above BF are steeper than are those below. These results are similar to those from second-turn IHCs and from basilar membrane (Rhode, 1971; Sellick *et al.*, 1982; Robles *et al.*, 1986; Nuttall and Dolan, 1996; Ruggero *et al.*, 1997) and IHC (Russell and Sellick, 1978; Zwislocki and Chatterjee, 1995) responses recorded from more basal regions of the cochlea. Finally, data from neurons with low BFs indicate that response areas expand preferentially toward higher frequencies, i.e., the functions have steeper low-frequency slopes. These response patterns are similar to those shown in Figs. 3–5 for IHCs in the fourth turn. They are also similar to mechanical measurements at the very apex of the cochlea where the frequency of the peak of the response function increases with increasing level (Zinn *et al.*, 2000) and where steeper slopes are recorded below BF (Khanna and Hao, 1999a).

The level-dependent magnitude changes recorded at various cochlear locations should be considered when evaluating the alterations that result from various cochlear manipulations. For example, it has been observed that furosemide-induced changes in neural tuning curves differ depending on BF (Sewell, 1984). When recordings were made from nerve fibers innervating the basal half of the cochlea, a downward shift in BF was observed. However, in nerve fibers with BFs below ~800 Hz, an upward shift was recorded due to the effects of furosemide. Liberman (1984) suggested that this difference in the direction of BF shift may relate to the shape of the tuning curve because the tail is above (below) BF for low (high) BF fibers (Pfeiffer and Molnar, 1970; Rose *et al.*, 1971; Kiang *et al.*, 1977; Møller, 1977; Liberman and Kiang, 1978; Evans, 1981). This implies that the BF shifts seen in compromised auditory systems due to furosemide or acoustic trauma (Liberman and Mulroy, 1982; Liberman and Dodds, 1984) may be a result of the increase in level required to produce a criterion response. The IHC data presented here are consistent with this idea. Data shown in Fig. 4 indicate that responses obtained at the higher input levels required to obtain criterion responses in traumatized cochleae will exhibit magnitude peaks at lower frequencies when recorded at positions with BFs greater than ~1000 Hz. In contrast, at the very apex of the cochlea, for BFs less than ~400 Hz, magnitude peaks should occur at frequencies higher than those observed in healthy cochleae.

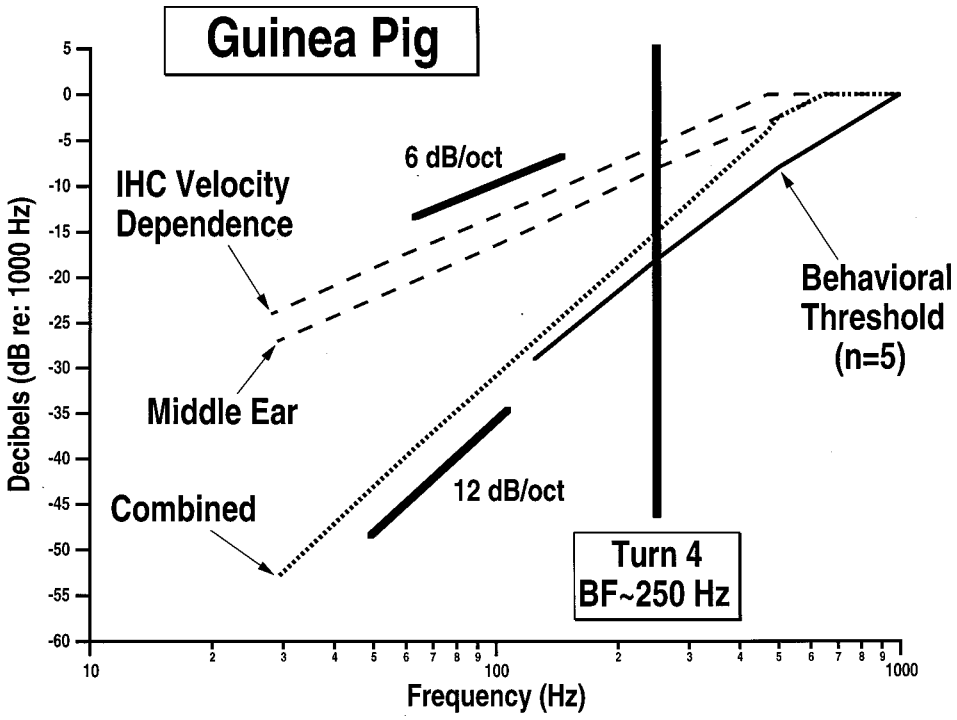

FIG. 6. This schematic depicts factors that influence low-frequency hearing in the guinea pig. The dashed lines indicate the high-pass filter functions associated with the middle ear and with the velocity dependence of the IHC. They decrease at a rate of 6 dB/oct below 600 and 470 Hz, respectively. Their combined effect is plotted with dotted lines and decreases at 12 dB/oct. The average behavioral threshold obtained from five studies (Fay, 1988) is also appended and plotted with solid lines. The vertical bar indicates the BFs of IHCs in turn 4.

Taken together, the data imply that the cochlear filter responsible for mechanical frequency analysis is generally asymmetrical, with steeper high-frequency slopes above BF. As shown in Fig. 5, this asymmetry is reduced in turn 3 and reversed in turn 4 consistent with the high-pass filtering associated with the middle ear transfer function. Although filtering due to the middle ear can account for the reverse asymmetry of apical response patterns and the almost complete symmetry of turn 3 responses at low levels, it cannot account for their reverse nonlinearity. The latter observation refers to the appearance of tuning-curve tails above BF where more linear responses are recorded. This response pattern contrasts with that in the base where tuning-curve tails, and concomitant more linear behavior, are found below BF.

It should also be mentioned that longitudinal variations are observed in the impulse responses of auditory-nerve fibers (Carney *et al.*, 1999). When instantaneous frequency is measured as a function of time, the impulse response exhibits an increasing frequency glide for fibers with BFs greater than ~1500 Hz and a decreasing glide for fibers with BFs less than ~750 Hz. Mechanical measurements recorded at the base of the cochlea also indicate that the frequency of the basilar membrane's impulse response changes with time, increasing from below, up to BF (de Boer and Nuttall, 1997; Recio *et al.*, 1998). Because response envelopes become skewed at high levels, i.e., their center of gravity shifts ear-

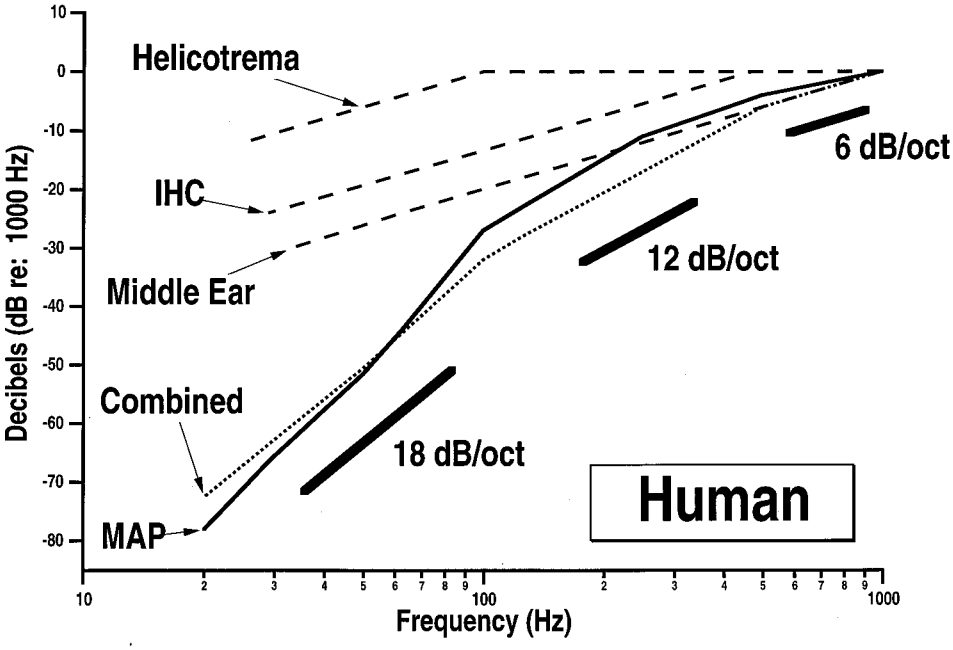

FIG. 7. This schematic for humans is similar to that in Fig. 6 for guinea pigs. In this case, however, the middle ear function decreases at 6 dB/oct below 1000 Hz. A function representing the helicotrema is also included and decreases at 6 dB/oct below 100 Hz. The IHC velocity dependence is appended from Fig. 6. The combined filter function plotted with dotted lines decreases at 6, 12 and finally, 18 dB/oct as frequency decreases below 100 Hz. The function plotted with solid lines is the minimum audible pressure curve (MAP) for humans, re-drawn from Killion (1978).

lier in time (Recio *et al.*, 1998), the increasing glides are consistent with a downward shift in peak frequency as level increases.

These observations imply that cochlear mechanics may differ near the apex of the cochlea. Consistent with this idea, Zinn *et al.* (2000) reported a weak compressive nonlinearity below BF and an expansive nonlinearity above BF when making mechanical measurements near the helicotrema. These authors suggest that the expansive nonlinearity is associated with an active attenuation on the tails of tuning curves, which are above BF when the latter is below ~400 Hz. This idea is compatible with results from experiments in which various cochlear insults are introduced. For example, acoustic overstimulation (Liberman and Dodds, 1984), mechanical damage (Robertson *et al.*, 1980) and/or salicylate ototoxicity (Murugasu and Russell, 1995) all serve to lower the tails of neural tuning curves, i.e., they become hypersensitive. At the base of the cochlea, this behavior is thought to reflect a negative gain below BF provided by the cochlear amplifier (Mountain *et al.*, 1983). Because amplification is vulnerable to insult, many manipulations result in more sensitive responses for the tails of tuning curves well below BF. At the apical end of the cochlea, removal of the active attenuation/negative gain observed in basilar membrane responses above BF (Zinn *et al.*, 2000) could also result in hypersensitive tuning-curve tails when cochlear function is compromised.

It should also be mentioned that IHC responses recorded from turn 4 of the guinea pig cochlea are nonlinear at BF. This is consistent with mechanical data obtained in guinea pig from Reissner's membrane (Cooper and Rhode, 1995) and in chinchilla from tectorial membrane (Rhode and Cooper, 1996) but not with guinea pig results from reticular lamina (Khanna and Hao, 1999a, b). The latter reports indicate that BF responses at the fundamental are linear, inspite of the fact that energy is present for both even and odd harmonic components. The authors argue that the linear behavior at the fundamental reflects negative feedback due to active cochlear mechanics. However, it is also possible that the discrepancy may relate to the observation that frequency response functions in the Khanna and Hao data have two peaks, which the authors acknowledge is associated with preparations that are more broadly tuned. Because Khanna and Hao do not provide data at low levels, it is possible that these preparations are not in good condition. In fact, no harmonic distortion is evident below ~70 dB and most of the frequency response functions are obtained for inputs at 96 dB. Although it could be argued that the IHC results are nonlinear at BF because of asymmetries in the hair cell transducer, this would not explain the discrepancy between the Cooper/Rhode and the Khanna/Hao data. Hence, there is the possibility that the Khanna/Hao results reflect a less than adequate seal between the preparation and the recording/observing apparatus. If the seal is not tight, then notches appear in frequency response functions and more than one peak is evident. In this case, the relatively linear behavior at BF could be explained by interactions between linear ''fast'' and nonlinear ''slow'' responses, as suggested by Cooper and Rhode (1998). If the preparations are not in good condition, then the two peaks on the function may not be very different in magnitude, which facilitates the interactions between ''fast'' and ''slow'' components.

B. Comparisons with mechanical and neural responses: Phase data

The phase data collected from IHCs in turns 2–4 are consistent with previous results (Dallos, 1986) indicating that phase leads (lags) accumulate below (above) BF when stimulus level is reduced. If BF is relatively stable with increasing level, then the lead/lag transition occurs near the BF of the cell and a stationary pivot point can be defined. However, if the peak of the frequency response function is level dependent, the pivot point disperses. For example, in turn 4, the transitions occur below BF and, in turn 2, the transitions occur above BF. These response patterns have their counterparts at the single-unit level (Anderson *et al.*, 1971). These comparisons suggest that one should be cautious when using level-dependent phase changes to define BF (Nuttall and Dolan, 1993, 1996; Cheatham and Dallos, 1995). If BF refers to that frequency where the cell is most sensitive (Galambos and Davis, 1943), then the lead/lag transition in response phase represents BF only when center frequency is relatively independent of level. In the peripheral auditory system, this is observed but only in the region around 1000 Hz. At more basal recording locations, the lead/lag transition tends to overestimate BF; at more apical locations, the transition underestimates BF. In other words, the level-dependent changes in phase move in opposite directions at the two ends of the cochlea.

C. Factors influencing behavioral thresholds at low frequencies

Others have suggested that behavioral threshold correlates with a constant pressure measured inside the vestibule of the inner ear (Lynch *et al.*, 1982; Puria *et al.*, 1997). In fact, the correlations between behavioral threshold and either constant pressure, constant power or constant stapes volume velocity are all very good for inputs between 200 and 1000 Hz. Below ~200 Hz, however, behavioral thresholds increase at a faster rate than any one of these variables (Puria *et al.*, 1997, Fig. 16). The schematic in Fig. 7 indicates that this discrepancy in humans may relate to filtering occurring central to the middle ear/cochlea interface, as suggested by Lynch *et al.* (1982). The most parsimonious explanation for the decrease in sensitivity, shown by the MAP curve at low frequencies, is that reductions are due to high-pass filtering associated with the velocity dependence of the IHC and with the shunting effect of the helicotrema. The latter serves to diminish the pressure difference between scala vestibuli and scala tympani. Because the basilar membrane is displaced as a result of this pressure difference, the helicotrema serves to decrease sensitivity at low frequencies below ~100 Hz (Dallos, 1973; Zwislocki, 1975) in animals where the helicotrema is relatively large. In fact, it has been demonstrated that the slope of the behavioral threshold curve at low frequencies is correlated with helicotrema size. Like humans, both cats and chinchillas have large helicotremas and steeper low-

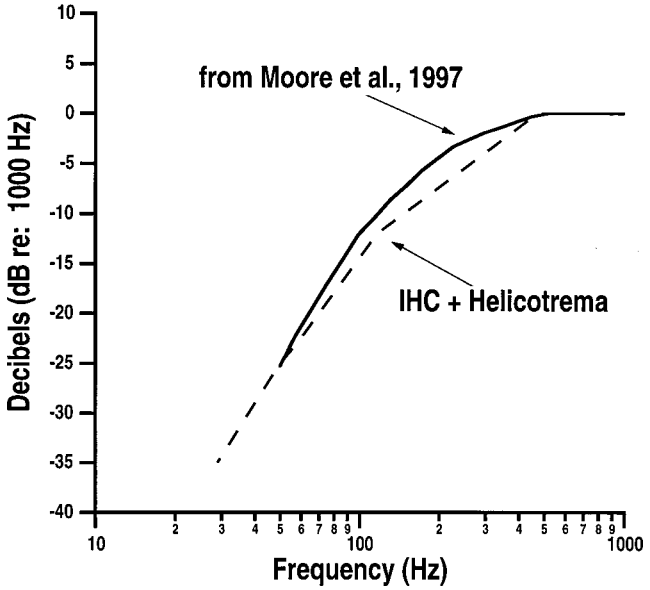

FIG. 8. The arbitrary function used by Moore *et al.* (1997, Fig. 4) is inverted and plotted here along with the combined attenuation due to high-pass filtering by the IHC's velocity dependence and by the shunting effect of the helicotrema. The latter function is plotted with dashed lines and represents the combined reductions plotted individually in Fig. 7 for the helicotrema and IHC. The function from Moore *et al.* was reconstructed using the DIGIMATIC software program.

frequency slopes below 100 Hz when compared to guinea pigs where the helicotrema is small (Dallos, 1970; Fay, 1988). Consequently, high-pass filtering by the helicotrema was not included in the schematic for guinea pigs (Fig. 6).

Finally, Moore and colleagues (1997) developed a phenomenological model for predicting the rise of threshold at low frequencies in human listeners. They acknowledge that this decrease in sensitivity rises more steeply than the transmission characteristic of the middle ear would suggest. This discrepancy is dealt with by assuming that the excitation level at threshold increases with decreasing frequency below 500 Hz according to an arbitrary function (Moore *et al.*, 1997, Fig. 4) designed to match the thresholds specified by an international standard. This arbitrary function is inverted and plotted in Fig. 8 with solid lines to indicate the decreasing input to the central auditory system as stimulus frequency is reduced. Also included is a function showing the high-pass filtering associated with both the IHC's velocity dependence and the helicotrema shunt, as in Fig. 7. The similarity between the two curves suggests that the success of the phenomenological model developed by Moore *et al.* could be due to the incorporation of an arbitrary function that reflects the attenuation of input due to the helicotrema shunt and the free-standing nature of the hair bundle on IHCs (Dallos *et al.*, 1972; Lim, 1972). Although it has previously been suggested that behavioral sensitivity at low frequencies in cat and man can be accounted for by compensating for reductions in cochlear input due to filtering by the middle ear and the helicotrema (Dallos, 1973; Zwislocki, 1975), Fig. 8 suggests that high-pass filtering associated with the IHC's velocity dependence should also be incorporated.

ACKNOWLEDGMENTS

This work was supported (in part) by Research Grant No. 5 R01 DC00089 from the National Institute on Deafness and Other Communication Disorders, the National Institutes of Health. We are grateful to Gulam Emadi for writing the computer program that calculates the average voltage.

Allen, J. B. (**1983**). "A hair cell model of neural response," in *Mechanics of Hearing*, edited by E. de Boer and M. A. Viergever (Delft U.P., Delft, The Netherlands), pp. 193–202.

Anderson, D. J., Rose, J. E., Hind, J. E., and Brugge, J. F. (**1971**). "Temporal position of discharges in single auditory nerve fibers within the cycle of a sine-wave stimulus: Frequency and intensity effects," J. Acoust. Soc. Am. **49**, 1131–1139.

Carney, L. H., McDuffy, M. J., and Shekhter, I. (**1999**). "Frequency glides in the impulse responses of auditory-nerve fibers," J. Acoust. Soc. Am. **105**, 2384–2391.

Cheatham, M. A. (**1993**). "Cochlear function reflected in mammalian hair cell responses," Prog. Brain Res. **97**, 13–19.

Cheatham, M. A., and Dallos, P. (**1992**). "Physiological correlates of off-frequency listening," Hear. Res. **59**, 39–45.

Cheatham, M. A., and Dallos, P. (**1993**). "Longitudinal comparisons of IHC ac and dc receptor potentials recorded from the guinea pig cochlea," Hear. Res. **68**, 107–114.

Cheatham, M. A., and Dallos, P. (**1995**). "Determinations of CF based on response phase," Abs. Assoc. Res. Otolaryngol., p. 95.

Cheatham, M. A., and Dallos, P. (**1998a**). "Auditory filter shape: Implications from IHC recordings," in *Psychophysical and Physiological Advances in Hearing*, edited by A. R. Palmer, A. Rees, A. Q. Summerfield, and R. Meddis (Whurr, London, England), pp. 73–81.

Cheatham, M. A., and Dallos, P. (**1998b**). "The level dependence of response phase: Observations from cochlear hair cells," J. Acoust. Soc. Am. **104**, 356–369.

Cheatham, M. A., and Dallos, P. (**1999**). "Contributions by inner and outer hair cells to the summating potential," Abs. Assoc. Res. Otolaryngol., p. 182.

Cooper, N. P., and Rhode, W. S. (**1995**). "Nonlinear mechanics at the apex of the guinea-pig cochlea," Hear. Res. **82**, 225–243.

Cooper, N. P., and Rhode, W. S. (**1998**). "Apical cochlear mechanics: a review of recent observations," in *Psychophysical and Physiologcial Advances in Hearing*, edited by A. R. Palmer, A. Rees, A. Q. Summerfield, and R. Meddis (Whurr, London, England), pp. 11–18.

Corso, J. F. (**1958**). "Absolute threshold for tones of low frequency," Am. J. Psychol. **71**, 367–384.

Dadson, R. S., and King, J. H. (**1952**). "A determination of the normal threshold of hearing and its relation to the standardization of audiometers," J. Laryngol. Otol. **66**, 366–378.

Dallos, P. (**1970**). "Low-frequency auditory characteristics: species dependence," J. Acoust. Soc. Am. **48**, 489–499.

Dallos, P. (**1973**). *The Auditory Periphery* (Academic, New York).

Dallos, P. (**1984**). "Some electrical circuit properties of the organ of Corti. II. Analysis including reactive elements," Hear. Res. **14**, 281–291.

Dallos, P. (**1985**). "Response characteristics of mammalian cochlear hair cells," J. Neurosci. **5**, 1591–1608.

Dallos, P. (**1986**). "Neurobiology of cochlear inner and outer hair cells; intracellular recordings," Hear. Res. **22**, 185–198.

Dallos, P., Santos-Sacchi, J., and Flock, Å. (**1982**). "Intracellular recordings from cochlear outer hair cells," Science **218**, 582–584.

Dallos, P., Billone, M. C., Durrant, J. D., Wang, C.-y., and Raynor, S. (**1972**). "Cochlear inner and outer hair cells: functional differences," Science **177**, 356–358.

de Boer, E., and Nuttall, A. L. (**1997**). "The mechanical waveform of the basilar membrane. I. Frequency modulations ("glides") in impulse responses and cross-correlation functions," J. Acoust. Soc. Am. **101**, 3583–3592.

Décory, L., Franke, R. B., and Dancer, A. L. (**1990**). "Measurement of eardrum acoustic impedance," in *The Mechanics and Biophysics of Hearing*, edited by P. Dallos, C. Geisler, J. Matthews, M. Ruggero, and C. Steele (Springer-Verlag, New York), pp. 270–277.

Evans, E. F. (**1981**). "The dynamic range problem: Place and time coding at the level of cochlear nerve and nucleus," in *Neuronal Mechanisms of Hearing*, edited by J. Syka and L. Aitkin (Plenum, New York), pp. 69–85.

Fay, R. R. (**1988**). *Hearing in Vertebrates: A Psychophysics Databook* (Hill-Fay, Winnetka, IL).
Flanagan, J. L. (**1962**). ''Models for approximating basilar membrane displacement,'' Bell Syst. Tech. J. **41**, 959–1009.
Fletcher, H. (**1940**). ''Auditory patterns,'' Rev. Mod. Phys. **12**, 47–65.
Freeman, D. M., and Weiss, T. F. (**1990**). ''Hydrodynamic forces on hair bundles at low frequencies,'' Hear. Res. **48**, 17–30.
Galambos, R., and Davis, H. (**1943**). ''The response of single auditory-nerve fibers to acoustic stimulation,'' J. Neurophysiol. **6**, 39–58.
Gibson, M. M., Hind, J. E., Kitzes, L. M., and Rose, J. E. (**1977**). ''Estimation of travelling wave parameters from response properties of cat AVCN neurons,'' in *Psychophysics and Physiology of Hearing*, edited by J. P. Wilson and E. F. Evans (Academic, New York), pp. 57–69.
Glasberg, B. R., and Moore, B. C. (**2000**). ''Frequency selectivity as a function of level and frequency measured with uniformly exciting notched noise,'' J. Acoust. Soc. Am. **108**, 2318–2328.
Hall, J. L. (**1977**). ''Two-tone suppression in a nonlinear model of the basilar membrane,'' J. Acoust. Soc. Am. **61**, 802–810.
Heffner, R., Heffner, H., and Masterton, B. (**1971**). ''Behavioral threshold measurements of absolute and frequency-difference thresholds in guinea pig,'' J. Acoust. Soc. Am. **49**, 1888–1895.
Hubbard, A. E., and Geisler, C. D. (**1972**). ''A hybrid computer model of the cochlear partition,'' J. Acoust. Soc. Am. **51**, 1895–1903.
Hudspeth, A. J., and Corey, D. P. (**1977**). ''Sensitivity, polarity and conductance changes in the responses of vertebrate hair cells to controlled mechanical stimuli,'' Proc. Natl. Acad. Sci. U.S.A. **74**, 2407–2411.
Johnstone, B. M., and Taylor, K. J. (**1971**). ''Physiology of the middle ear transmission system,'' J. Otolaryngol. Soc. Aust. **3**, 226–228.
Khanna, S. M., and Hao, L. F. (**1999a**). ''Reticular lamina vibrations in the apical turn of a living guinea pig cochlea,'' Hear. Res. **132**, 15–33.
Khanna, S. M., and Hao, L. F. (**1999b**). ''Nonlinearity in the apical turn of living guinea pig cochlea,'' Hear. Res. **135**, 89–104.
Kiang, N. Y.-s. (**1984**). ''Peripheral neural processing of auditory information,'' in *Handbook of Physiology, The Nervous System, Vol. 3*, edited by I. Darian-Smith (American Physiological Society, Bethesda, MD), pp. 639–674.
Kiang, N. Y.-s., Liberman, M. C., and Baer, T. (**1977**). ''Tuning curves of auditory nerve fibers,'' J. Acoust. Soc. Am. Suppl. 1 **61**, S27.
Killion, M. C. (**1978**). ''Revised estimate of minimum audible pressure: Where is the missing 6 dB?'' J. Acoust. Soc. Am. **63**, 1501–1508.
Kim, D. O., Molnar, C. E., and Pfeiffer, R. R. (**1973**). ''A system of nonlinear differential equations modelling basilar-membrane motion,'' J. Acoust. Soc. Am. **54**, 1517–1529.
Liberman, M. C. (**1984**). ''Single-neuron labeling and chronic cochlear pathology. I. Threshold shift and characteristic-frequency shift,'' Hear. Res. **16**, 33–41.
Liberman, M. C., and Dodds, L. W. (**1984**). ''Single-neuron labeling and chronic cochlear pathology. III. Stereocilia damage and alterations to threshold tuning curves,'' Hear. Res. **16**, 55–74.
Liberman, M. C., and Kiang, N. Y.-S. (**1978**). ''Acoustic trauma in cats: cochlear pathology and auditory nerve activity,'' Acta Oto-Laryngol., Suppl. **358**, 1–13.
Liberman, M. C., and Mulroy, M. J. (**1982**). ''Acute and chronic effects of acoustic trauma: cochlear pathology and auditory nerve pathophysiology,'' in *New Perspectives on Noise-Induced Hearing Loss*, edited by R. P. Hamernik, D. Henderson, and R. Salvi (Raven, New York), pp. 105–135.
Lim, D. (**1972**). ''Fine morphology of the tectorial membrane: Its relationship to the organ of Corti,'' Acta Oto-Laryngol. **96**, 199–215.
Lynch III, T. J., Nedzelnitsky, V., and Peake, W. T. (**1982**). ''Input impedance of the cochlea in cat,'' J. Acoust. Soc. Am. **72**, 108–130.
Miller, J. D., and Murray, F. S. (**1966**). ''Guinea pig's immobility response to sound: Threshold and habituation,'' J. Comp. Physiol. Psychol. **61**, 227–233.
Møller, A. R. (**1977**). ''Frequency selectivity of single auditory-nerve fibers in response to broadband noise stimuli,'' J. Acoust. Soc. Am. **62**, 135–142.
Moore, B. C. J. (**1989**). *An Introduction to the Psychology of Hearing* (Academic, London).
Moore, B. C. J., Glasberg, B. R., and Baer, T. (**1997**). ''A model for the prediction of thresholds, loudness, and partial loudness,'' J. Audio Eng. Soc. **45**, 224–240.
Mountain, D. C., Hubbard, A. E., and McMullen, T. A. (**1983**). ''Electromechanical processes in the cochlea,'' in *Mechanics of Hearing*, edited by E. de Boer and M. A. Viergever (Nijhoff, The Hague), pp. 119–126.
Murugasu, E., and Russell, I. J. (**1995**). ''Salicylate ototoxicity: the effects on basilar membrane displacement, cochlear microphonics, and neural responses in the basal turn of the guinea pig cochlea,'' Aud. Neurosci. **1**, 139–150.
Nuttall, A. L., and Dolan, D. F. (**1993**). ''Two-tone suppression of inner hair cell and basilar membrane responses in the guinea pig,'' J. Acoust. Soc. Am. **93**, 390–400.
Nuttall, A. L., and Dolan, D. F. (**1996**). ''Steady-state sinusoidal velocity responses of the basilar membrane in guinea pig,'' J. Acoust. Soc. Am. **99**, 1556–1565.
Pfeiffer, R. R., and Molnar, C. E. (**1970**). ''Cochlear nerve fiber discharge patterns: Relationship to the cochlear microphonic,'' Science **167**, 1614–1616.
Prosen, C. A., Peterson, M. R., Moody, D. B., and Stebbins, W. C. (**1978**). ''Auditory thresholds and kanamycin-induced hearing loss in the guinea pig assessed by a positive reinforcement procedure,'' J. Acoust. Soc. Am. **63**, 559–566.
Puria, S., Peake, W. T., and Rosowski, J. J. (**1997**). ''Sound-pressure measurements in the cochlear vestibule of human-cadaver ears,'' J. Acoust. Soc. Am. **101**, 2754–2770.
Recio, A., Rich, N. C., Narayan, S. S., and Ruggero, M. A. (**1998**). ''Basilar-membrane responses to clicks at the base of the chinchilla cochlea,'' J. Acoust. Soc. Am. **103**, 1972–1989.
Rhode, W. S. (**1971**). ''Observations of the vibration of the basilar membrane in squirrel monkeys using Mössbauer technique,'' J. Acoust. Soc. Am. **49**, 1218–1231.
Rhode, W. S., and Cooper, N. P. (**1996**). ''Nonlinear mechanics in the apical turn of the chinchilla cochlea *in vivo*,'' Aud. Neurosci. **3**, 101–121.
Robertson, D., Cody, A. R., Bredberg, G., and Johnstone, B. M. (**1980**). ''Response properties of spiral ganglion neurons in cochleas damaged by direct mechanical trauma,'' J. Acoust. Soc. Am. **67**, 1295–1303.
Robles, L., Ruggero, M. A., and Rich, N. C. (**1986**). ''Basilar membrane mechanics at the base of the chinchilla cochlea. I. Input-output functions, tuning curves, and response phases,'' J. Acoust. Soc. Am. **80**, 1364–1374.
Rose, J. E., Hind, J. E., Anderson, D. J., and Brugge, J. F. (**1971**). ''Some effects of stimulus intensity on response of auditory nerve fibers in the squirrel monkey,'' J. Neurophysiol. **34**, 685–699.
Rosen, S., and Howell, P. (**1991**). *Signals and Systems for Speech and Hearing* (Academic, New York).
Ruggero, M. A. (**1992**). ''Physiology and coding of sound in the auditory nerve,'' in *The Physiology of the Mammalian Auditory CNS*, edited by R. Fay and A. N. Popper (Springer-Verlag, New York), pp. 34–92.
Ruggero, M. A., Robles, L., and Rich, N. C. (**1992**). ''Two-tone suppression in the basilar membrane of the cochlea: Mechanical basis of auditory-nerve rate suppression,'' J. Neurophysiol. **68**, 1087–1099.
Ruggero, M. A., Rich, N. C., Recio, A., Narayan, S. S., and Robles, L. (**1997**). ''Basilar membrane responses to tones at the base of the chinchilla cochlea,'' J. Acoust. Soc. Am. **101**, 2151–2163.
Russell, I. J., and Sellick, P. M. (**1978**). ''Intracellular studies of hair cells in the guinea pig cochlea,'' J. Physiol. (London) **284**, 261–290.
Sellick, P. M., Patuzzi, R., and Johnstone, B. M. (**1982**). ''Measurement of basilar membrane motion in the guinea pig using the Mössbauer technique,'' J. Acoust. Soc. Am. **72**, 131–141.
Sewell, W. F. (**1984**). ''The effects of furosemide on the endocochlear potential and auditory-nerve fiber tuning curves in cats,'' Hear. Res. **14**, 305–314.
Shatz, L. F. (**2000**). ''The effect of hair bundle shape on hair bundle hydrodynamics of inner ear hair cells at low and high frequencies,'' Hear. Res. **141**, 39–50.
Walloch, R. A., and Taylor-Spikes, M. (**1976**). ''Auditory thresholds in the guinea pig: A preliminary report of a behavioral technique employing a food reward,'' Laryngoscope **86**, 1699–1705.
Yeowart, N. S., and Evans, M. J. (**1974**). ''Thresholds of audibility for very low-frequency pure tones,'' J. Acoust. Soc. Am. **55**, 814–818.
Zinn, C., Maier, H., Zenner, H.-P., and Gummer, A. W. (**2000**). ''Evidence of active, nonlinear, negative feedback in the vibration response of the apical region of the in-vivo guinea-pig cochlea,'' Hear. Res. **142**, 159–183.
Zwislocki, J. J. (**1975**). ''The role of the external and middle ear in sound transmission,'' in *The Nervous System, Vol. 3, Human Communication and Its Disorders*, edited by D. B. Tower (Raven, New York), pp. 45–55.
Zwislocki, J. J., and Chatterjee, M. (**1995**). ''On the neural code for loudness and its cochlear correlates,'' in *Advances in Hearing Research*, edited by G. A. Manley, G. M. Klump, C. Köppl, H. Fastl, and H. Oeckinghaus (World Scientific, London), pp. 241–249.

A new procedure for measuring peripheral compression in normal-hearing and hearing-impaired listeners

David A. Nelson,[a] Anna C. Schroder, and Magdalena Wojtczak
Clinical Psychoacoustics Laboratory, Department of Otolaryngology, University of Minnesota, MMC 396, 420 Delaware St. S.E., Minneapolis, Minnesota 55455

(Received 28 November 2000; revised 19 March 2001; accepted 19 July 2001)

Forward-masking growth functions for on-frequency (6-kHz) and off-frequency (3-kHz) sinusoidal maskers were measured in quiet and in a high-pass noise just above the 6-kHz probe frequency. The data show that estimates of response-growth rates obtained from those functions in quiet, which have been used to infer cochlear compression, are strongly dependent on the spread of probe excitation toward higher frequency regions. Therefore, an alternative procedure for measuring response-growth rates was proposed, one that employs a fixed low-level probe and avoids level-dependent spread of probe excitation. Fixed-probe-level temporal masking curves (TMCs) were obtained from normal-hearing listeners at a test frequency of 1 kHz, where the short 1-kHz probe was fixed in level at about 10 dB SL. The level of the preceding forward masker was adjusted to obtain masked threshold as a function of the time delay between masker and probe. The TMCs were obtained for an on-frequency masker (1 kHz) and for other maskers with frequencies both below and above the probe frequency. From these measurements, input/output response-growth curves were derived for individual ears. Response-growth slopes varied from >1.0 at low masker levels to <0.2 at mid masker levels. In three subjects, response growth increased again at high masker levels (>80 dB SPL). For the fixed-level probe, the TMC slopes changed very little in the presence of a high-pass noise masking upward spread of probe excitation. A greater effect on the TMCs was observed when a high-frequency cueing tone was used with the masking tone. In both cases, however, the net effects on the estimated rate of response growth were minimal. © *2001 Acoustical Society of America.* [DOI: 10.1121/1.1404439]

PACS numbers: 43.66.Ba, 43.66.Dc, 43.66.Mk, 43.66.Sr [SPB]

I. INTRODUCTION

Several investigators have recently attempted to obtain psychophysical estimates of cochlear compression in human ears (Stelmachowicz *et al.*, 1987; Nelson and Schroder, 1997; Oxenham and Plack, 1997; Moore and Oxenham, 1998; Plack and Oxenham, 1998; Moore *et al.*, 1999; Hicks and Bacon, 1999a; Plack and Oxenham, 2000; Wojtczak *et al.*, 2001). A common procedure in many of those studies was the use of forward-masking growth functions for low off-frequency and on-frequency sinusoidal maskers to infer estimates of cochlear compression, where the *low off-frequency* masker had a frequency equal to or less than 0.6 of the probe frequency, and the *on-frequency* masker had a frequency equal to the probe frequency. That procedure is exemplified in the work of Oxenham and Plack (1997), who used forward masking from 3-kHz (low off-frequency) and 6-kHz (on-frequency) maskers to obtain estimates of response-growth rates at 6 kHz by measuring masker levels necessary to just mask a probe presented at several fixed levels. We call these functions growth-of-maskability (GMB) functions because the masker level at masked threshold is plotted on the ordinate as a function of the probe level on the abscissa. Based on data from animals indicating that the basilar-membrane response to a tone of a given frequency is linear at a place with a characteristic frequency (CF) well above the tone frequency (Yates, 1990; Yates *et al.*, 1990; Ruggero, 1992; Ruggero *et al.*, 1997; Rhode and Recio, 2000), Oxenham and Plack assumed that the response to the 3-kHz masker at the 6-kHz frequency region was linear. With this assumption, it is reasonable to interpret the slopes of their GMB functions in terms of response-growth rates at the 6-kHz place in the cochlea. For low-level and high-level probe tones the average GMB slope for three normal-hearing listeners was close to 1.0 dB/dB, suggesting linear response growth; for mid-level probe tones the average GMB slope was 0.16 dB/dB, suggesting very gradual response growth and strong peripheral compression. The GMB slope of 0.16 was similar to basilar-membrane (BM) response-growth slopes of 0.20 reported in animals for mid-level CF tones. This implies that the psychophysical measure of response-growth rate reflects BM response-growth rate, both of which are determined by cochlear compression. Where the response-growth rate is the least, cochlear compression is the strongest.

The very gradual GMB slope of 0.16 dB/dB observed by Oxenham and Plack, for a 3-kHz masker frequency (Fm) and a 6-kHz probe frequency (Fp), was obtained in the presence of a background noise intended to mask off-frequency listening at frequencies above and/or below the probe frequency. For the low off-frequency condition (3-kHz masker and 6-kHz probe) they used a high-pass noise; for their on-frequency condition (6-kHz masker and 6-kHz probe) they

[a]Author to whom correspondence should be addressed. Electronic mail: dan@tc.umn.edu

included a low-pass noise intended to mask any cues below the probe frequency. Without a background (high-pass) noise, the comparable low off-frequency GMB slope (in one listener) was not as gradual ($\cong$0.38). This suggests that the estimate of response growth obtained from forward-masking GMB functions, for masker frequencies well below the probe frequency, is strongly dependent upon the spread of excitation from the probe, most likely an upward spread toward higher frequency regions.

Oxenham and Plack (1997) addressed this problem by specifying response-growth rate as the ratio of GMB slopes for the 3-kHz masker and the 6-kHz masker. They tested the notion, in one listener, that the effects of off-frequency listening on GMB slopes are the same for the on-frequency masker as they are for the low off-frequency masker. For that listener, the background noise reduced the GMB slope by about a factor of 2.0 for both the low off-frequency masker (with high-pass noise) and the on-frequency masker (with high-pass and low-pass noise), so the ratio of the low off-frequency and on-frequency GMB slopes and the subsequent estimate of response-growth rate remained about the same (0.17 in quiet and 0.19 in background noise). On the basis of this evidence, the ratios of GMB slopes for low off-frequency versus on-frequency maskers have been used to specify response-growth rates (and peripheral compression) from normal-hearing listeners (Moore *et al.*, 1999; Hicks and Bacon, 1999a, b), although none of the cited studies have demonstrated GMB slope ratios as small as those reported by Oxenham and Plack.

Oxenham and Plack also measured GMB functions at a 2-kHz probe frequency (using a 1-kHz masker), with and without a high-pass noise, in one of their hearing-impaired listeners who exhibited a moderate hearing loss at and above the probe frequency. That subject exhibited no significant difference in the GMB slope with the addition of the high-pass noise. This suggests that the additional high-pass noise is not necessary in hearing-impaired listeners with a hearing loss that increases markedly just above the probe frequency, probably because the hearing loss at the higher frequency regions minimizes the usefulness of upward spread of excitation from the probe toward higher frequencies as probe level increases.

The purpose of this study was twofold. First, we wanted to evaluate the effects of high-pass noise on GMB slopes and to examine more closely the notion that the ratio of GMB slopes for low off-frequency and on-frequency maskers without a background noise accurately specifies response-growth rate. Second, we wanted to explore an alternative procedure for measuring response-growth rate, one in which spread of excitation from the probe might not play such a strong role. For this procedure we made the same assumption as Oxenham and Plack about linear response growth for a low-frequency masker at a higher-frequency probe place, but we minimized spread of excitation effects by fixing the probe at a low level and varying the time delay between masker and probe. With this fixed-level probe procedure, as time delay between masker and probe is increased, a higher masker level is necessary to reach masked threshold, largely because of the increased recovery from forward masking that occurs with increased time delay. The resulting plot of masker level as a function of time delay is referred to here as a temporal masking curve (TMC). For a low off-frequency masker ($Fm \leqslant 0.6Fp$), the increase in masker level with time delay should only reflect recovery from forward masking. This is because the response to the low off-frequency masker at the probe-frequency place is assumed to be linear. For an on-frequency masker ($Fm = Fp$), the increase in masker level with time delay should reflect recovery from forward masking, just as for the low off-frequency case, but it should also reflect any cochlear compression that is applied to the masker. Assuming that recovery from forward masking is the same for low off-frequency and on-frequency maskers, response-growth rates can be estimated by computing the ratio of recovery slopes observed for a low off-frequency masker and an on-frequency masker. The computed rates of response growth can then be used to derive an input/output function. The present study estimates response-growth rates using this alternative procedure in normal-hearing and hearing-impaired listeners. The effects of off-frequency listening and temporal cueing on the estimated response-growth rates are also examined.

II. EXPERIMENT 1: GROWTH OF FORWARD MASKING IN HIGH-PASS NOISE

This experiment was a simple replication of the Oxenham and Plack (1997) forward-masking experiment that examined the effects of background noise on GMB slopes. We wanted to examine further their premise that valid estimates of response-growth rates can be obtained without a background noise by examining the ratios of GMB slopes obtained in quiet for a low off-frequency and on-frequency masker. This requires that spread of excitation above the probe frequency have the same relative effect on GMB slopes for low off-frequency and on-frequency forward maskers in quiet, thus rendering unnecessary the use of a background noise to reduce off-frequency listening.

A. Method

Forward-masking growth functions were obtained for a 6-kHz sinusoidal probe in the presence of a 3-kHz sinusoidal masker or a 6-kHz sinusoidal masker. Each point on the masking functions was obtained by fixing the level of the probe and varying the masker level to reach masked threshold. Probe levels ranged from 35 to 95 dB SPL in 5-dB steps. The resulting function is referred to as a growth-of-maskability (GMB) function to distinguish it from a growth-of-masking (GOM) function in which the masker level is fixed and the probe level is varied to reach masked threshold. This distinction is useful when referring to slopes of masking functions because some authors have reported GOM slopes (Hicks and Bacon, 1999a, b), while others have reported GMB slopes (Oxenham and Plack, 1997; Moore *et al.*, 1999). The masking tones were gated with 2-ms raised-cosine rise and decay times and were at peak amplitude for 100 ms (104-ms total duration). The probe tones were gated with 2-ms raised-cosine rise and decay times with no steady-state portion (4-ms total duration). The time delay between

masker offset and probe offset was 6 ms. These parameters are the same as those used by Oxenham and Plack.

Pure-tone signals for masker and probe stimuli were produced and gated digitally by Tucker Davis Technologies (TDT) D-A converters, routed separately through programmable attenuators, added together in an active mixer, and presented monaurally through a TDH-49 earphone mounted in an MX/AR-1 cushion. Subjects were seated in a double-walled sound-treated booth and conveyed their responses to the computer by pressing buttons on a custom response panel.

A three-interval forced-choice (3IFC) adaptive procedure was used to estimate the masker level needed to just mask the fixed-level probes and to measure absolute sensitivity thresholds. During each 3IFC trial, a subject was presented with three observation intervals demarcated by lights. The masker (or silence, for absolute thresholds) was presented in all three intervals and the probe was presented in only one, randomly selected, interval. The subject indicated which interval contained the probe stimulus by pressing one of three response buttons, after which correct answer feedback was provided.

Masked thresholds were determined using a transformed up–down adaptive procedure (Levitt, 1971). During the first four level reversals, a relatively large step size of 8 dB and a simple up–down stepping rule were used to move into the target masker-level region. Then a 2-dB step size was used for the next two reversals, again with a simple up–down stepping rule. A 2-up, 1-down, stepping rule, still with the 2-dB step size, was followed for the final six reversals to estimate the masker level corresponding to 71% correct detection of the probe. Masked threshold was estimated as the mean of the masker levels for the final six reversals. The final data points were based on the average of three or more such thresholds. Exceptions are noted in the figures for those cases where a subject could not complete at least three threshold measurements.

GMB functions were obtained in quiet and in the presence of a high-pass (HP) noise. The noise was a high-pass filtered white noise with a 3-dB cutoff frequency at 1.117Fp (6702 Hz), which was generated and filtered using TDT equipment (WG1 and PF1). Because the HP noise and the tonal signals were presented through a TDH-49 earphone, the spectrum level of the HP noise in a 6-cc coupler (measured with a Hewlett Packard 4144 1-inch microphone and a Hewlett Packard 3561A dynamic signal analyzer using a 95-Hz bandwidth filter) was relatively constant between 6702 and 9500 Hz and decreased with frequency above about 9500 Hz, such that the spectrum level was about 20 dB less at 12.5 kHz. The overall level of the HP noise was 15 dB below the level of the probe; the spectrum level between 6702 and 9500 Hz was approximately 50 dB below the probe level. At 6 kHz, the probe frequency, the spectrum level of the low-frequency skirt of the HP noise was approximately 90 dB below the probe level. The HP noise was gated on 50 ms before the onset of the masker ramp and gated off 50 ms after the offset of the probe. A GMB function was obtained in a single sitting, with probe levels always presented in ascending order to avoid obvious fatigue effects. The GMB functions were usually remeasured on different days.

In a secondary experiment, GMB functions were measured with a 1-kHz probe tone, both in quiet and in the presence of a HP noise. For those conditions, the noise was a high-pass filtered white noise with a 3-dB cutoff frequency at 1.117Fp (1117 Hz). The spectrum level of the HP noise in a 6-cc coupler was relatively constant between 1117 Hz and 6 kHz and decreased with frequency above 6 kHz, such that the spectrum level was about 10 dB less at 9.5 kHz and 20 dB less at 12.5 kHz. The overall level of the HP noise was 15 dB below the level of the 1-kHz probe tone; the spectrum level of the HP noise between 1117 Hz and 6 kHz was approximately 47 dB below the probe level. The masker-probe gating conditions were the same as those used with the 6-kHz probe.

Two normal-hearing subjects participated in the experiment. Their absolute thresholds were less than 15 dB HL (ANSI, 1989) for octave frequencies between 250 and 8000 Hz. Both subjects received several hours of practice on forward-masking tasks before data collection commenced.

B. Results and discussion

Figure 1 shows the GMB functions for the 6-kHz probe obtained in quiet (open symbols) and in the presence of the HP noise (filled symbols) from two normal-hearing listeners (ksar and yykl). The GMB functions for the 3-kHz (low off-frequency) masker are shown in Figs. 1(a) and (b) and those for the 6-kHz (on-frequency) masker are shown in Figs. 1(c) and (d) [note that the ordinates differ for panels (c) and (d) vs (a) and (b)]. Error bars represent one standard deviation above and below each mean masked threshold. Linear least-squares regression fits to the thresholds at medium probe levels (between about 40 and 80 dB SPL) are shown by the straight lines. The GMB slopes are given by $1/\beta$ (β is the GOM slope).

First notice that in the presence of the HP noise the GMB slopes were essentially identical to those obtained for the average GMB functions in background noise reported by Oxenham and Plack (1997, Fig. 2). The GMB slope of their on-frequency function was 1.0, compared to the GMB slopes of 1.0 dB/dB observed here [black diamonds, Figs. 1(c) and 1(d)]; their low off-frequency GMB slope for probe levels between 50 and 80 dB SPL was 0.16, compared to GMB slopes of 0.11 and 0.16 observed here [black diamonds, Figs. 1(a) and (b)]. Thus, their results in background noise are well replicated in these two subjects. Their ratio of low off-frequency to on-frequency GMB slopes was 0.16, while the slope ratios were 0.11 and 0.16 in the present study. Thus, estimates of response growth at the probe frequency, based on slope ratios of GMB functions that were obtained in the presence of a background noise to reduce off-frequency listening, were similar in both studies.

Oxenham and Plack's on-frequency condition actually included a low-pass noise in addition to a HP noise. Further, the levels of their two noises were not constant relative to each probe level tested. The level of their notched noise essentially increased at a rate that was about half of the rate of increase in the level of the probe. Because we replicated their

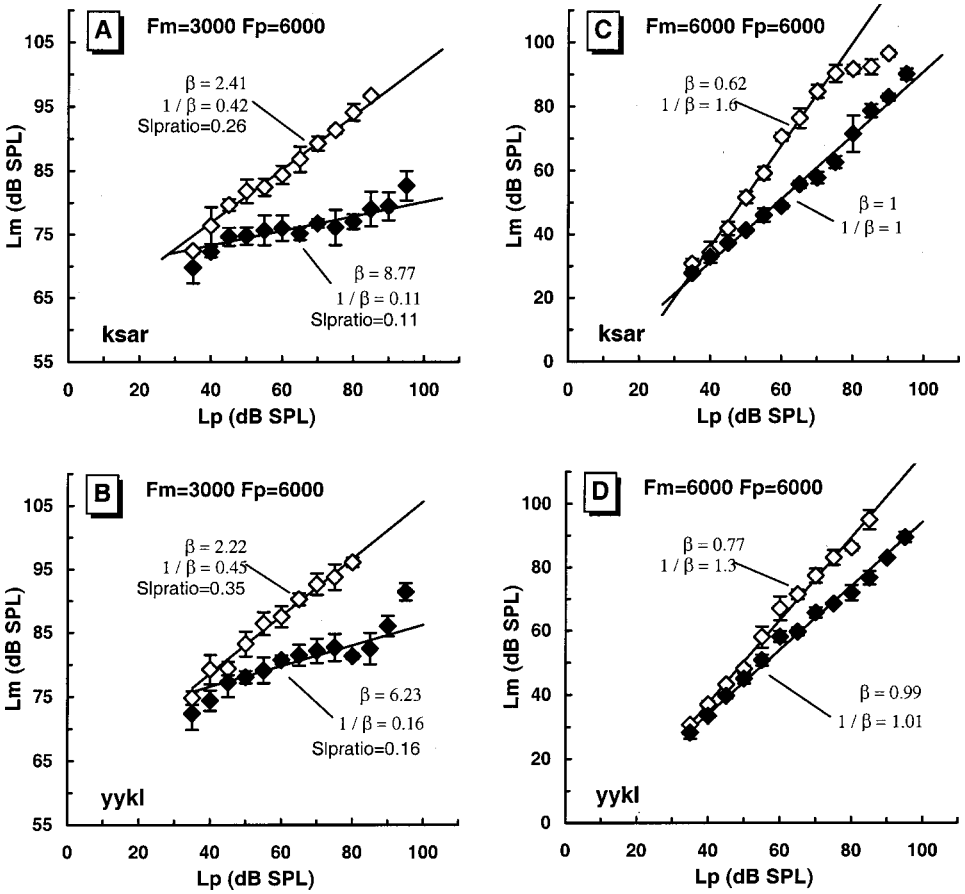

FIG. 1. Growth of maskability (GMB) functions in quiet (open symbols) and in the presence of a high-pass noise (with a low-frequency cutoff at 1.117Fp) to mask spread of excitation toward higher frequencies (closed symbols). The masker level required to mask a 6-kHz probe tone is plotted on the ordinate as a function of probe level on the abscissa. The GMB functions for an off-frequency masker (3 kHz) are shown in (a) and (b) (for normal-hearing subjects ksar and yykl, respectively), and those for an on-frequency masker (6 kHz) are shown in (c) and (d). Solid lines are linear regression fits to each function using only masker levels obtained with mid-level probe tones. The slope of each GMB function is given by $\mathbf{1/\beta}$. The growth-of-masking (GOM) slope, which describes masked threshold as a function of masker level, is given by $\boldsymbol{\beta}$. The slope ratio (Slpratio) is the GMB slope for the off-frequency condition [(a) or (b)] divided by the GMB slope for the corresponding on-frequency condition [(c) or (d)].

findings so well with only a HP noise, the addition of a low-pass noise for the on-frequency condition would seem unnecessary. Similarly, a fixed ratio between the level of the HP noise and the probe level was sufficient to replicate their findings, thus it should not be necessary to employ a varying level ratio as they did.

The GMB functions obtained without the HP noise are shown by the unfilled symbols in Fig. 1. The GMB slopes for the on-frequency condition [Figs. 1(c) and (d)] were 1.6 and 1.3 dB/dB for subject ksar and yykl, respectively, while the GMB slopes for the low off-frequency condition [Figs. 1(a) and (b)] were 0.42 and 0.45 dB/dB. The ratios of on-frequency and low off-frequency GMB slopes were 0.26 and 0.35 in quiet, which are similar to the 0.33 average GMB slope ratio reported for six normal-hearing listeners by Moore *et al.* (1999). If the GMB slope ratio is taken as an estimate of response growth at the probe frequency, then it is more than twice as steep in quiet as it is in HP noise. This result is not consistent with the result reported by Oxenham and Plack (1997). Their single subject, tested both with and without the HP noise, exhibited a GMB slope ratio of 0.17 for the HP noise condition and 0.19 dB/dB for the quiet condition, which led them to conclude that the effects of spread of excitation (as probe level was increased) was the same for low off-frequency and on-frequency maskers. While the HP noise produced about a factor of 2 reduction in GMB slope for both the low off-frequency and the on-frequency maskers in their subject, the two subjects in the present study (ksar and yykl, respectively) exhibited reductions in GMB slopes by factors of 3.8 and 2.8 for the low off-frequency condition and factors of 1.6 and 1.3 for the on-frequency condition. This indicates that, in the present study, the HP noise had a larger effect for the low off-frequency condition than for the on-frequency condition. This can be seen by examining the probe levels, in quiet versus HP noise, corresponding to a fixed masker level in Fig. 1. For example, in subject yykl, at a masker level of 85 dB SPL (Lm on ordinate), the HP noise produced a 35-dB increase in probe level at masked threshold for the low off-frequency condition [Fig. 1(b)] compared to only about a 15-dB increase in probe level for the on-frequency condition [Fig. 1(d)].

A replication of experiment 1 in the same two subjects, using a 1-kHz probe, a 0.6- or 1-kHz masker, and a HP noise with a low-frequency cut-off of 1.117Fp, yielded similar results. The reduction in GMB slope with the HP noise was not as great at 1 kHz as it was at 6 kHz. For subjects yykl and ksar, respectively, the HP noise reduced GMB slopes by factors of 1.5 and 1.4 for the low off-frequency condition and by factors of 1.2 and 1.1 for the on-frequency condition. Thus, without a background noise, upward spread of excitation from the probe still influenced GMB slopes differentially at 1 kHz, just as it did at 6 kHz, but the differential effect was not quite as great.[1]

Moore *et al.* (1999) noted that their GMB slope ratios obtained in quiet were larger than those obtained by Oxenham and Plack (1997) in background noise. They speculated that a possible factor contributing to this difference was off-frequency listening in the quiet condition. For the low-frequency masker, the signal might have been detected using

a region of the basilar membrane with a CF above the signal frequency, which would be slightly less compressive than at the CF region. The present findings support their explanation.

Taken together, the present results and those of previous studies indicate that off-frequency listening to the high-frequency tail of the probe excitation pattern can strongly influence estimates of response-growth rate, and may differ widely among subjects. This is not surprising, considering that the probe level in this experiment is varied from 35 to 95 dB SPL. Spread of excitation varies substantially over such a wide range of probe levels. Thus, it seems precarious to use GMB slope ratios obtained in quiet conditions to specify response growth. The use of background noise to prevent or reduce off-frequency listening seems more prudent. At this point, the results are sufficient to question the validity of procedures for estimating response-growth rates that utilize varying probe levels without the addition of background noise. Therefore, we have examined an alternative procedure for obtaining estimates of response-growth rates, one that does not involve the large changes in spread of excitation associated with varying probe levels.

III. EXPERIMENT 2: RESPONSE GROWTH FROM TMCs

The alternative procedure estimates response-growth rates from the slopes of forward-masking recovery curves for low off-frequency and on-frequency maskers. The TMCs for a fixed-level probe define the masker levels required to just forward mask the probe as a function of the time delay between masker and probe (Nelson and Freyman, 1987). The masker level required to forward mask a probe with an on-frequency masker depends both upon the recovery from forward masking that occurs at the probe-frequency place *and* upon the cochlear compression that exists at the probe-frequency place (Oxenham and Moore, 1995, 1997; Plack and Oxenham, 1998). By way of contrast, the masker level required to forward mask a probe with a low off-frequency masker ($Fm \leqslant 0.6Fp$) depends *only* upon the recovery from forward masking that occurs at the probe-frequency place. This is because the low off-frequency masker that is nearly an octave below the probe frequency produces a linear response at the probe-frequency place in the cochlea (Yates, 1990; Yates *et al.*, 1990; Ruggero, 1992; Nelson and Schroder, 1997; Oxenham and Plack, 1997; Ruggero *et al.*, 1997; Moore and Oxenham, 1998; Rhode and Recio, 2000). If one assumes that the recovery time constant for forward masking at the probe-frequency place on the basilar membrane is independent of masker frequency, then the ratio of the recovery slopes for the on-frequency and the low off-frequency masker, for a given change in time delay, reflects the factor by which the masker level has to be increased in the on-frequency case to overcome cochlear compression. The reciprocal of that factor provides an estimate of response-growth rate that is determined by cochlear compression.

A critical assumption with this procedure is that the recovery time constant for low off-frequency and on-frequency maskers is the same. This assumption has been used to successfully model data for combined simultaneous and nonsimultaneous masking by on-frequency and low off-frequency maskers (Wojtczak *et al.*, 2001). Furthermore, there is evidence that the recovery process at a particular cochlear place, which proceeds exponentially (in decibels) with time delay between masker and probe (Duifhuis, 1973; Nelson and Freyman, 1987), is independent of the frequency difference between masker and probe (Nelson and Pavlov, 1989). Another critical assumption is that the exponential decay of the internal effect of a masker is the same regardless of the magnitude of the internal effect, i.e., the recovery process is well defined by an exponential decay (in decibels) with a level-independent time constant.

A. Method

The TMCs were obtained from four normal-hearing subjects for various masker frequencies surrounding a 1-kHz probe presented at a fixed low level. The fixed-probe or *iso-response* TMC requires a constant response at some central stage in the auditory system, e.g., at the output of a temporal integrator that follows peripheral filtering and compression, which then produces a constant amount of threshold shift (forward masking) at the probe frequency. The input level (masker level) is adjusted to maintain the required response at the probe-frequency place as a function of the time delay between the masker and the probe. As time delay is increased, the amount of forward masking decreases, therefore the masker level must be increased to maintain the same amount of forward masking. A plot of masker level as a function of time delay defines the iso-response TMC (Nelson and Freyman, 1987). A 1-kHz probe frequency was chosen, rather than the 6-kHz probe frequency investigated by Oxenham and Plack (1997), because 1 kHz was the frequency previously investigated by Nelson and Freyman (1987) with hearing-impaired listeners, and 1 kHz is a frequency region that is important for speech perception.

An advantage of the iso-response TMC is that the spatial region in the cochlea being assessed is held constant during an experiment. That region is defined by the excitation pattern produced by the fixed-frequency, fixed-level probe tone. That region is small when the probe is presented at a very low level. Thus, nonlinear spread of probe excitation with increasing level should not affect the estimate of response growth derived from the TMC. A further advantage of the iso-response paradigm is that nonlinearities affecting the probe are constant throughout an experiment. This allows one to infer characteristics of the nonlinearities associated with the masker, as will become apparent during the analysis of the present results.

Forward masking was produced by sinusoidal maskers that varied in frequency from well below to just above the 1-kHz probe tone. Specific masker frequencies examined were 500, 600, 700, 800, 900, 1000, 1012, 1025, 1050, 1100, 1150, and 1200 Hz, although not all masker frequencies were tested in every subject. The masker and probe durations were 200 and 20 ms at peak amplitude, respectively, with 10-ms raised-cosine rise and decay times. During each test session, delay times (between masker offset and probe offset) were tested in the following order: 42, 45, 50, 60, 70, 80, 90, 100,

110, 120, 130, and 140 ms. A minimum temporal separation between masker offset (10% of peak amplitude) and probe onset (10% of peak amplitude) of 2 ms ensured that no physical interaction occurred between masker and probe before reaching the cochlea. For each delay time, the probe level was fixed at a sound pressure level that was about 10 dB SL and the masker level was adjusted adaptively to reach masked threshold.

Pure-tone signals for masker and probe stimuli were produced by frequency synthesizers (Rockland), gated by electronic switches, routed separately through programmable attenuators, added together in a resistive mixer, and presented monaurally through a UTC L-33 transformer and a TDH-49 earphone mounted in an MX/AR-1 cushion. Subjects were seated in a double-walled sound-treated booth and conveyed their responses to the computer by pressing buttons on a custom response panel.

The same 3IFC adaptive procedure described in experiment 1 was used to estimate the level of masker needed to just mask the fixed-level probe and to measure absolute sensitivity threshold. Four normal-hearing subjects participated in the experiment. Their absolute thresholds were less than 15 dB HL (ANSI, 1989) for octave frequencies between 250 and 8000 Hz. All subjects received several hours of practice on forward-masking tasks before data collection commenced.

B. Results and discussion

1. Iso-response TMCs

Figure 2 shows the masker levels required to mask a fixed-level 1-kHz probe, as a function of the time delay between masker offset and probe offset, for maskers varying in frequency from well below to just above the probe frequency. The TMCs are shown from four normal-hearing subjects. Dashed lines indicate three-segment exponential fits to the data.[2]

Several features of these *iso-response* TMCs are evident. The general form of the TMC shows an increase in masker level with masker-probe time delay, which reflects recovery from forward masking over time. At short delay times, considerable forward masking is evident; therefore, relatively low masker levels are required to maintain a fixed amount of forward masking. At longer time delays, more recovery from forward masking is evident; therefore, higher masker levels are required to maintain the same fixed amount of forward masking. For the on-frequency and nearly on-frequency conditions (shaded symbols), the change in masker level with time delay is steep over a range of time delays. For off-frequency maskers, both below (black symbols) and above (unfilled symbols) the probe frequency, the change in masker level with time delay is more gradual.

2. Interpretations of different TMC characteristics

Two aspects of these TMCs are particularly noteworthy: the masker level at the shortest time delay, and the relative steepness of the curve (recovery slope at different time delays). The TMCs for subject KEK are replotted in Fig. 3 to illustrate the main effects that exist, to varying extents, in the data from each of the other three subjects.

First, at the shortest time delay (42 ms), note that high levels are required for the lowest-frequency maskers [Fig. 3(a)] and progressively lower masker levels are required as the masker frequency approaches the probe frequency [Figs. 3(b)–(e)]. At any fixed time delay, masker level differences across frequency define a psychophysical tuning curve (PTC). The PTC approximates an inverted filter function describing gain across masker frequency, a gain that is relative to the gain at the probe frequency. At the shortest time delay, the difference between the level of the lowest off-frequency masker and the level of the on-frequency masker approximates the maximum gain available at and near the probe frequency [approximately 50 dB in Fig. 3(l)]. At longer time delays gain applied to the on-frequency masker decreases, which is evidenced by strong compression, and the difference in gain across masker frequencies diminishes, leading to broader tuning. For masker frequencies very close to the probe frequency, some of the subjects exhibited a large change in the masker level with only a small change in masker frequency (e.g., RXL in Fig. 2 exhibited an increase in masker level of 12 dB for only a 1.2% change in masker frequency from 1000 to 1012 Hz). Such large changes in masker level with small changes in masker frequency could be due to the improved detectability of the probe when small pitch differences exist between masker and probe (Moore, 1980a, b).

If shorter probe tones had been used, the minimum time delay between masker offset and probe offset at which forward masking was measured could have been smaller, but would likely have had little effect on the estimate of maximum gain at the probe place. In the case of shorter probe tones and shorter time delay, less recovery from forward masking may have occurred. Consequently, the masker levels required to mask the probe would have been lower. However, this would be true for both on- and off-frequency maskers. As long as the on-frequency masker falls within a linear region of response growth, the difference between the level for the lowest off-frequency masker and the on-frequency masker should remain the same irrespective of the duration of the probe. Note that for at least two of the subjects [MRM and RXL in Figs. 2(c) and (d)] the slope of the TMC over a range of short time delays, for the on-frequency masker, is approximately the same as the slope of the TMC for the low off-frequency ($Fm \leq 0.6Fp$) masker. Assuming the same recovery time constant for off-frequency and on-frequency forward masking, at least over a range of short time delays, the on-frequency masker produced a linear or nearly linear response. This suggests that the estimate of the maximum gain should not change with decreased probe duration, although additional research with shorter probe tones is needed to examine this premise further. For now, we use the difference between levels of the low off-frequency masker and the on-frequency masker at the shortest time delay to provide an approximation of the maximum gain at the probe frequency place. This is done so that we can express the excitation response produced at the shortest delay by the

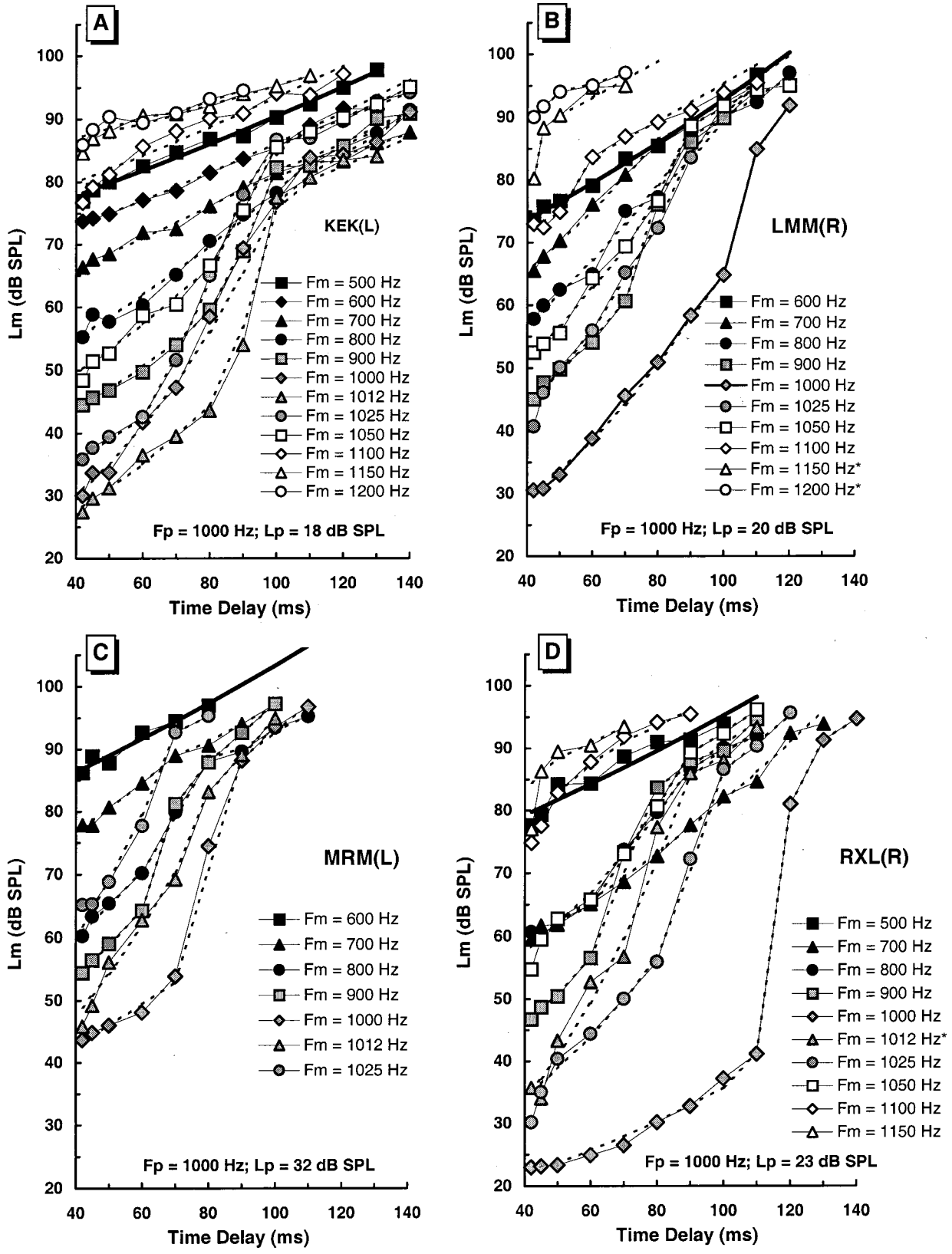

FIG. 2. Fixed-probe-level (*iso-response*) temporal masking curves from four normal-hearing subjects. Each curve shows the masker level (in dB SPL) required to forward mask a fixed-level 1-kHz probe, as a function of the time delay between masker offset and probe offset. The parameter is the frequency of the masking tone. Masker frequencies close to the probe frequency are indicated by shaded symbols, those above the probe frequency are indicated by open symbols, and those well below the probe frequency are indicated by black symbols. An asterisk next to the symbol label indicates that those data were based on only one threshold determination. Dashed lines show three-segment exponential fits to each curve. The wide curve is the single-segment exponential fit to the masker levels for the 0.5- or 0.6-kHz masker frequency.

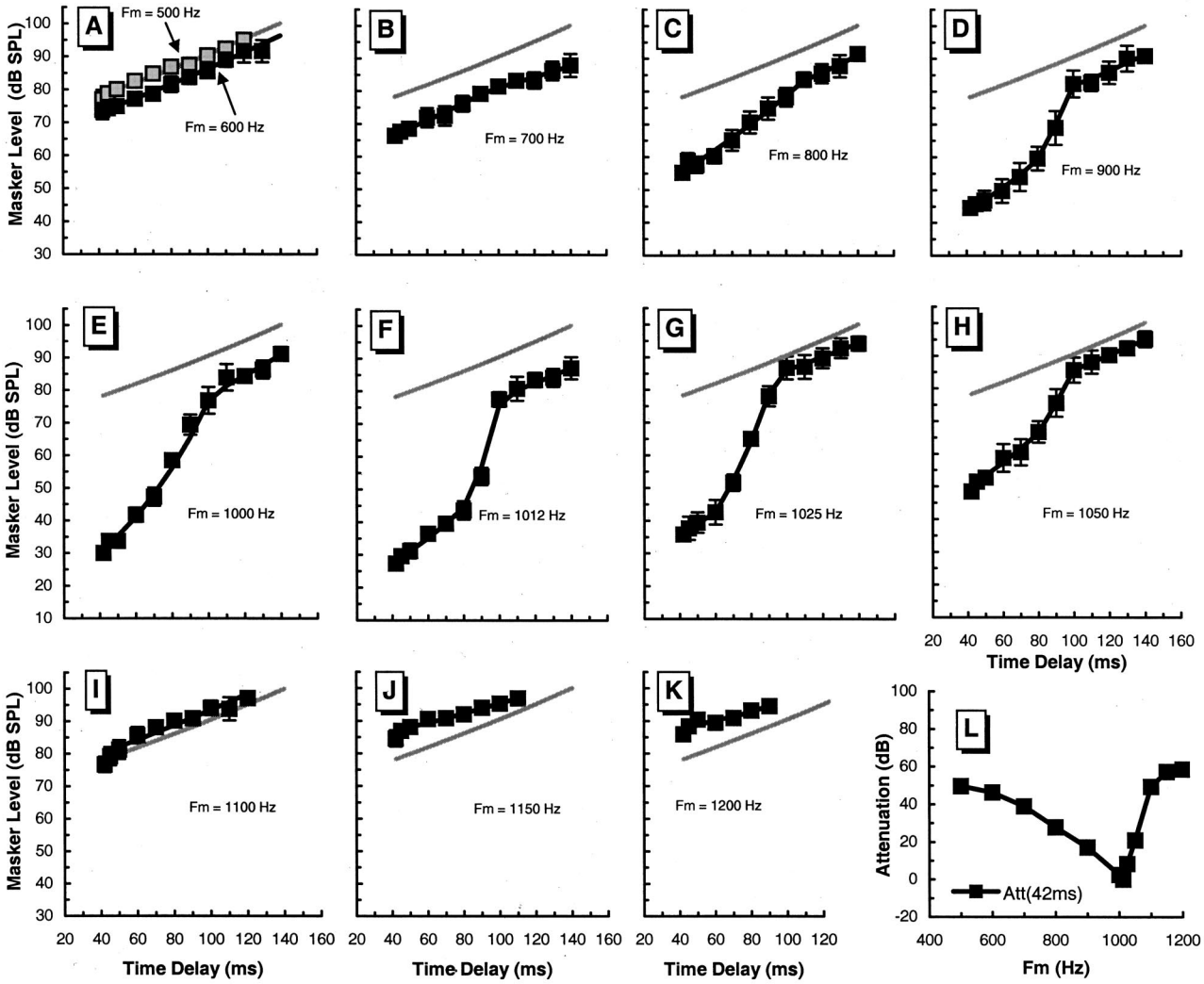

FIG. 3. Temporal masking curves (TMCs) from normal-hearing subject KEK(L), which were used to calculate response-growth slopes as a function of time delay. Each panel shows TMCs for a different masker frequency (Fm). The probe frequency was 1 kHz. Panel (a): Off-frequency TMCs for the 0.5- and 0.6-kHz maskers define the conditions in which the response growth at the 1-kHz probe frequency is linear (by assumption). The 0.5-kHz off-frequency TMC is replicated, for comparison, in (b)–(k) by the wide gray line. (e) On-frequency TMC for the 1-kHz masker. The wide black line shows the three-segment exponential fit to the on-frequency TMC. (b)–(d) and (f)–(k) make the same comparison at other masker frequencies. Panel (l): Attenuation attributed to the auditory filter, which is estimated as the difference in dB between masked thresholds at each masker frequency (Fm) and the masked threshold at 1 kHz, at the 42-ms time delay condition. Maximum gain ($\mathbf{G}_{\max}$) available in the auditory filter is approximated by the difference between the attenuation for the low off-frequency masker and the attenuation for the on-frequency masker.

different frequency maskers in terms of the input level at the probe-frequency place that, at the same time delay, produces an equivalent amount of forward masking.

Consider next the relative steepness of the TMCs at different masker frequencies. As previously proposed, the slopes of the TMCs for the lowest-frequency maskers (Fm≤0.6Fp) are determined only by the amount of recovery from forward masking existing at the probe frequency as a function of the time delay between masker and probe. Therefore, the slope of the TMC reflects the time constant of the recovery process that is represented by an exponential function with a single time constant (τ):

$$\mathbf{L}_m(\text{off}) = \mathbf{L}_p \cdot e^{t/\tau} + \mathbf{G}_{\max}, \tag{1}$$

where t is the time delay between masker and probe, τ is the time constant for recovery from forward masking, $\mathbf{L}_p$ and $\mathbf{L}_m$ are the probe and masker levels in dB SPL, and $\mathbf{G}_{\max}$ is the maximum gain at the probe place (estimated at $t = 42$ ms). The iso-response TMC for the lowest-frequency masker is shown by the shaded squares in Fig. 3(a) (also by the black squares in each panel of Fig. 2). The exponential fit to that curve, using Eq. (1), is indicated by the wide shaded curve in Fig. 3(a) (also by the wide black curve in each panel of Fig. 2). According to our assumptions, for the low off-frequency masker, the change in masker level that occurs with increased time delay between masker and probe is determined solely by recovery from forward masking specified by the time constant, τ.

Because it is assumed that the recovery process at the probe-frequency place is independent of the relative frequencies of masker and probe (Nelson and Pavlov, 1989), then, if there is no compression, the iso-response TMCs for all of the masker frequencies should have the same slope as that shown by the wide shaded curve in Fig. 3 for the 500-Hz masker. Indeed, the recovery-curve slope for the 600-Hz

masker is the same as for the 500-Hz masker [Fig. 3(a)]. At a masker frequency of 700 Hz [Fig. 3(b)], the TMC can no longer be described quite as well by a single exponential curve. And clearly, the slopes of the recovery curves for maskers between 800 and 1050 Hz [wide black curves in Figs. 3(c)–(h)] are not the same as the 500-Hz masker. As the masker frequency moves closer to the probe frequency [Figs. 3(c)–(e)], the TMCs exhibit progressively steeper recovery slopes over a range of time delays. The TMCs for these masker frequencies require three exponential segments to adequately fit the data. For the on-frequency condition, or when the masker frequency is very close to the probe frequency, a pattern emerges in which three segments of the TMC are easily distinguished by different slopes. At short time delays where low masker levels are required, the recovery slope is gradual, close to the recovery slope seen for the lowest-frequency masker. At longer time delays, where moderate masker levels are required, the recovery slopes become very steep. Then, at the longest time delays, where the highest masker levels are required, the recovery slope becomes more gradual again. For subjects LMM, MRM, and RXL, this pattern is evident for the 1000-Hz masker (Fig. 2); for subject KEK this three-segment pattern is most evident for the 1012-Hz masker [Fig. 3(f)]. When the masker frequency is moved above the probe frequency, the steep recovery slopes become progressively flatter with increased masker frequency [Figs. 3(g) and (h)], and the TMCs can again be represented by a single exponential function [Figs. 3(i)–(k)].

A single exponential function was used to fit the TMC for the low off-frequency masker because it reflects one of the traditional models used successfully in the past for quantifying recovery from forward masking (Duifhuis, 1973; Widin and Viemeister, 1979; Abbas and Gorga, 1981; Nelson and Freyman, 1987). The single exponential accounted for most of the variance in the low off-frequency TMCs from these four subjects (99%, 99%, 94% and 92%, respectively, for subjects KEK, LMM, MRM, and RXL). Exponential functions were also used for fitting the other TMCs because it was assumed that the underlying recovery process at the probe-frequency place was the same as that reflected by the low off-frequency masker (i.e., exponential with an identical time constant), regardless of masker frequency, and that compression, when present, would change the apparent slope of that exponential recovery process.[3] Three separate exponential segments were chosen for fitting the other TMCs because it was believed that compression acts differently at low, middle, and high stimulus levels. At time delays where low masker levels are required, gradual recovery slopes indicate little or no cochlear compression. At time delays where moderate-level maskers are required, steep recovery slopes suggest that strong cochlear compression is operating. At time delays where higher masker levels are required, recovery slopes are gradual again. This latter slope reduction is particularly evident for masker levels above about 80 dB for subject KEK, which can be seen in Figs. 3(c)–(h). The more gradual recovery slopes exhibited for these high-level maskers suggest that cochlear response is close to linear at higher levels. This more linear response growth at high levels is consistent with the findings of Oxenham and Plack (1997) in two of three listeners above 80 dB at 2 kHz, and in all three listeners above 80 dB at 6 kHz.

3. Deriving input/output curves from TMC curves

Input/output curves for each masker frequency can be derived from TMCs by determining the output levels for a low off-frequency masker as a function of masker/probe time delay, and then plotting those output levels as a function of input level at each masker frequency. The rationale for this process follows.

For each given time delay along a low off-frequency TMC, the level of a low off-frequency masker that produces the same amount of masking as an on-frequency masker was measured. Thus, for every time delay, it is reasonable to assume that the effective response produced by the low off-frequency masker, at the probe-frequency place, is the same as that produced by the on-frequency masker (or any other off-frequency masker). Therefore, we can express the effective level of a low off-frequency masker, at the probe-frequency place, in terms of the equivalent on-frequency masker level. To illustrate, assume that at a time delay of 42 ms a 78 dB SPL low off-frequency masker (500 Hz) is required to mask an 18 dB SPL probe tone, while a 28 dB SPL on-frequency masker is required to mask the same level probe tone. In this case the effective level for the 500-Hz masker at the probe-frequency place, after being attenuated by the auditory filter, is the same as the level required for the on-frequency masker to mask the probe, which is 28 dB. This level is used as a reference for expressing the relative output at the probe-frequency place produced by the 500-Hz masker at the shortest time delay.

According to our assumptions, any increase in the level of the low off-frequency masker (associated with an increase in time delay) results in a linear increase in the effective output level at the probe-frequency place. Therefore, the changes in masker (input) level with time delay that are observed for a low off-frequency masker will be the same as the changes in effective output level that occur at the probe frequency place. This is illustrated in Fig. 4 by curve (a). The shaded triangles show an input/output function for a 500-Hz masker at the 1-kHz place (Rm500/Lm500): the effective response of the 500-Hz masker at 1 kHz (the output level) is plotted on the ordinate versus the level of the 500-Hz masker (the input level) on the abscissa. Beginning at a low off-frequency input level of 78 dB SPL, which corresponds to an effective output level of 28 dB SPL, the effective output level increases *linearly* with increases in input level. Therefore, sequential increases in output level above 28 dB SPL are the same as the sequential increases in input level that are dictated by the different time delays tested and the time constant for recovery from forward masking.[4]

Since, for the same time delays, output levels are the same for each masker frequency used to measure TMCs, the input/output functions for each masker can be obtained by plotting the 500-Hz masker output levels against each tested masker's (input) levels. Curve (b) in Fig. 4 shows the resulting function for a 1-kHz masker.[5]

Derived input/output response-growth curves for the four normal-hearing subjects are shown in Fig. 5. Response-

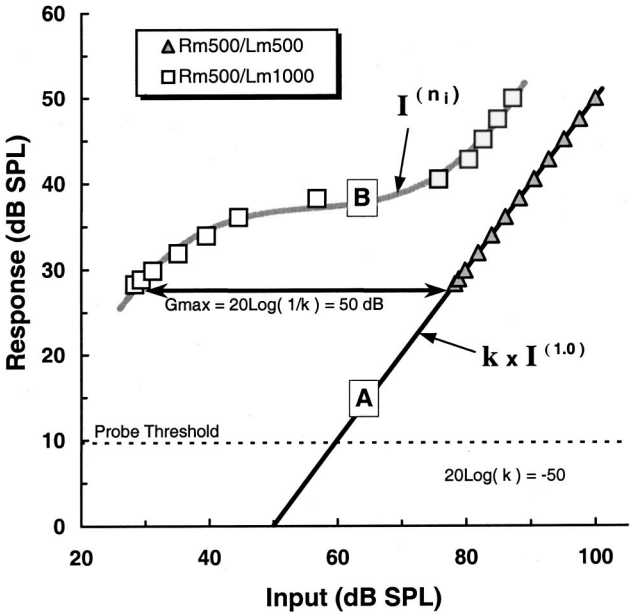

FIG. 4. Derived input/output response growth curves for a 0.5-kHz off-frequency masker [curve (a)] and a 1-kHz on-frequency masker [curve (b)]. Probe threshold is indicated by the dashed line.

growth curves for masker frequencies at and below the probe frequency are shown in the left-hand panels; those for masker frequencies above the probe frequency are shown in the right-hand panels.

4. Response-growth rates calculated from derived input/output curves

Local response-growth rates can be calculated from the derived input/output curves by taking the first derivative of third-order polynomial fits to the input/output curves. Response-growth rates calculated from the derived input/output curves are shown, as a function of input level, for the four normal-hearing listeners in Figs. 6(a)–(d). Response-growth-rate curves are shown at two or three masker frequencies that are close to or equal to the probe frequency for each subject. Typically, response-growth rate varied with input level in a U-shaped fashion, being steep at low and high input levels and gradual for moderate level inputs. The input level at which the minimum response-growth rate occurred varied across subjects, from around 55 dB SPL in subject KEK to around 70 dB in subject MRM. For subject LMM there was no obvious increase in growth rate at the higher levels for the 1000-Hz masker, but there was for the 1025-Hz masker. For subject RXL, negative response-growth rates were estimated when the masker and probe frequencies were the same, but this is an artifact of fitting the input/output curves with a third-order polynomial; none of the local slopes in the raw data in Fig. 5(g) are negative. Some of the extremely gradual growth rates for the 1-kHz masker may have been influenced by the lack of a pitch difference between masker and probe (Moore, 1980a, b), which may have made it more difficult to distinguish the probe from the end of the masker, resulting in lower masker levels at threshold for short and medium delay times. However, the very gradual response-growth rates seen here at moderate input levels are consistent with the 0.16 response-growth rate obtained by Oxenham and Plack (1997).

These computed response-growth rates tended to change with input level and masker frequency in a similar manner to BM response-growth rates. For example, for subject KEK, examination of the input/output curves for maskers with frequencies at or close to the probe frequency [900–1025 Hz in Figs. 5(a) and (b)] indicates that response-growth rates change with input level from near 1.0 at very low input levels, to <0.2 at mid levels, to near 1.0 again at high levels. BM input/output curves obtained by Ruggero *et al.* (1997) for on-frequency stimulation in the base of a chinchilla cochlea are replotted in Fig. 5(a) (a 10-kHz tone stimulating a place in the cochlea corresponding to a 10-kHz best frequency) and Fig. 5(b) (an 11-kHz tone stimulating the 10-kHz place). These functions do not provide strong evidence of a return to linearity at high input levels in healthy animal cochleae. Three subjects out of four tested in this study (KEK, MRM, and RXL) exhibit strong evidence of nearly linear growth rates at input levels above 80 or 90 dB SPL, while that behavior is not as consistent in subject LMM.

As the masker was moved further away in frequency from the probe, the general form of the input/output curve for the masker at the probe-frequency place became more linear. This tendency toward more linear response growth occurred in both frequency directions, i.e., as the masker frequency became either lower or higher than the probe frequency. This result can be seen more clearly in Fig. 7, where the smallest response-growth rate in each input/output curve is plotted against masker frequency.

As the masker frequency below probe frequency became progressively lower, input/output curves became more linear. This tendency was evident in all four subjects, although the exact frequency at which the curves became linear differed across subjects. A similar result has been reported for BM responses as the stimulating tone is lowered below the best frequency (Ruggero *et al.*, 1997; Rhode and Recio, 2000).

As the masker frequency above the probe frequency became progressively higher than the probe frequency, input/output curves also became more linear. This trend is also seen in BM responses, as shown in Fig. 5(b) by the curve for a 17-kHz tone stimulating the 10-kHz place. The separation between the probe frequency and the nearest masker frequency, for which a linear response at the probe place was observed, was smaller on the higher-frequency side of the probe than it was on the lower-frequency side as shown in Fig. 7.

From these comparisons with BM input/output curves, it is clear that the derived input/output curves generated from iso-response TMCs behave generally in the same way as BM response-growth curves in basal regions of the cochlea (Ruggero *et al.*, 1997; Rhode and Recio, 2000). Detailed characteristics of individual input/output curves, e.g., the exact input levels where response-growth rates change from linear to compressive in individual subjects, should be regarded with some caution at this stage of investigation, since subtle cues in forward masking might change them slightly.

The input/output curves derived here are similar to those

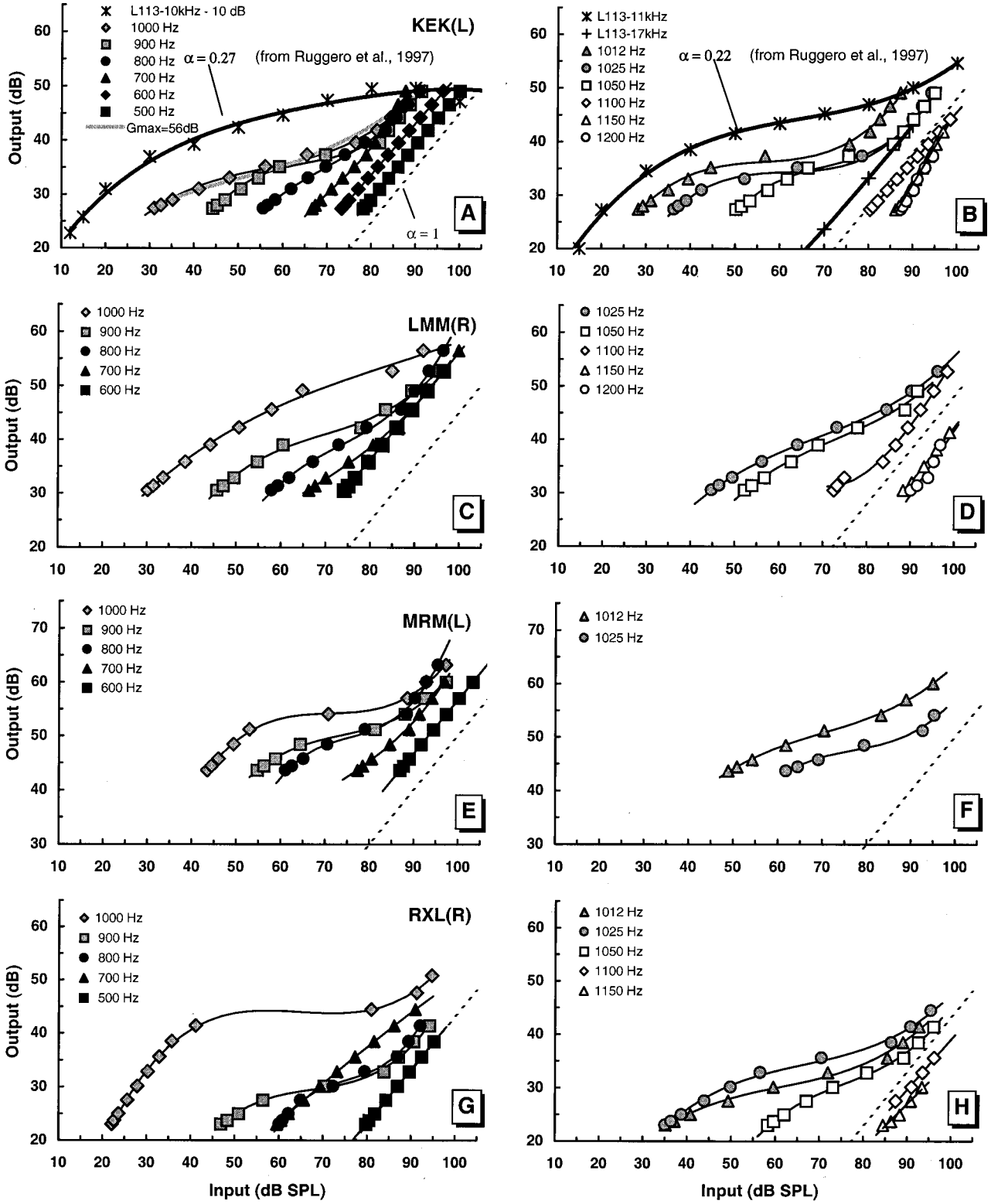

FIG. 5. Derived input/output response-growth curves from four normal-hearing listeners. Response-growth curves for maskers at and below the probe frequency are shown in the left-hand column of panels; those for maskers above the probe frequency are shown in the right-hand column of panels. Solid curves are third-order polynomial fits to the individual input/output curves (linear fits are used for the low- and high-frequency off-frequency curves). Input/output curves from a chinchilla are replotted from Ruggero *et al.* (1997) for comparison. Output for BM curves is velocity (μm/s) less a scaling factor for comparison with psychophysical data. Response-growth slopes at mid levels are indicated by $\boldsymbol{\alpha}$ for Ruggero's near CF curves. A linear growth curve, with $\boldsymbol{\alpha}$=1.0, is shown for reference by the dashed line in each panel. The wide gray curve in (a) is the 1-kHz input/output function predicted by an equation proposed by Glasberg and Moore (2000).

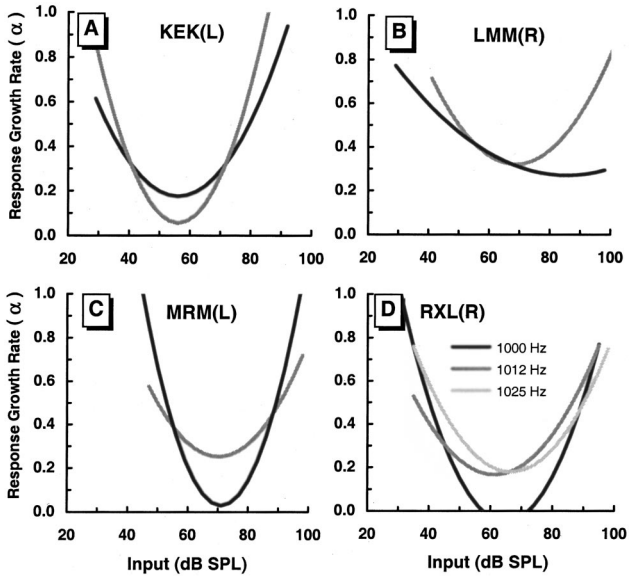

FIG. 6. Response-growth rates estimated from derived input/output curves are shown as a function of input level (masker SPL). The parameter is masker frequency as labeled. Several curves are shown for each subject, one for a masker frequency at the probe frequency and one or two for masker frequencies slightly higher in frequency. For subject RXL(R), the 1000-Hz growth curve exhibited negative growth rates, which was an artifact of the third-order polynomial fitting function.

predicted by an equation published recently by Glasberg and Moore (2000). Their equation (1) describes the gain in dB, for the average normal-hearing listener, that exists at a particular place in the cochlea, as a function of input level (in dB SPL). The free parameter in that equation is $\mathbf{G}_{\max}$, the maximum gain provided by the cochlear amplifier at low input levels. By way of comparison, the input/output function at 1 kHz predicted by their equation, for a $\mathbf{G}_{\max}$ value of 56 dB, is shown by the wide gray curve in Fig. 5(a). For subject KEK the Glasberg and Moore input/output function describes the derived input/output values (shaded diamonds) quite well. A good linear prediction was also achieved for the 0.5-kHz data with a $\mathbf{G}_{\max}$ value of 0.8 dB. However, with only $\mathbf{G}_{\max}$ as a free parameter, the Glasberg and Moore equation did not do a good job of describing the 1-kHz input/output curves derived for the other three subjects. In order to achieve good fits for those subjects, the various parameters in the Glasberg and Moore equation that control the width and center of gravity of the compression region (across input level) would have to be adjusted in addition to the $\mathbf{G}_{\max}$ value.

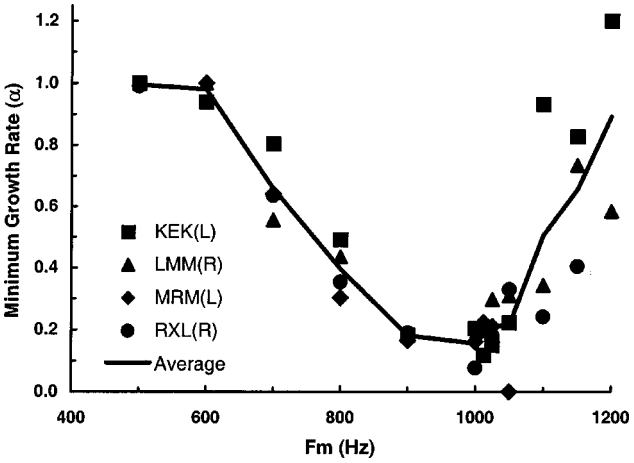

FIG. 7. Minimum response growth rates at 1 kHz as a function of masker frequency, which were taken from the third-order polynomial fits to the derived input/output curves at each masker frequency.

5. Deriving response-growth rates from TMC slope ratios

The response-growth rates calculated from the slopes of derived input/output curves are conceptually equivalent to response-growth rates calculated directly from TMC slope ratios. In the latter case, response-growth rate at any input level is determined by the ratio between the recovery slope for the low off-frequency masker and the recovery slope for any other masker closer in frequency to the probe frequency. Based on Eq. (1), for the lowest off-frequency masker, the change in masker level, $\Delta\mathbf{L}_m(\text{off})$, corresponding to a change in time delay between $t1$ and $t2$ is determined solely by the forward-masking recovery process as described by

$$\Delta\mathbf{L}_m(\text{off}) = (\mathbf{L}_p)e^{t2/\boldsymbol{\tau}} - (\mathbf{L}_p)e^{t1/\boldsymbol{\tau}}, \tag{2}$$

where $t1$ and $t2$ are any consecutive time delays along the TMC.

By assumption, the change in masker level with time delay for an on-frequency masker is controlled by the same recovery process as that operating for a low off-frequency masker, but in addition it is influenced by cochlear compression, which affects the response growth rate with level ($\boldsymbol{\alpha}$) for the masker at the probe-frequency place. Thus, $\boldsymbol{\alpha}$ is a continuously varying function of masker level, which is an exponential function of time delay. Conceptually, for the same two consecutive time delays, $t1$ and $t2$, along the TMC, response growth associated with the on-frequency masker levels at those time delays can be represented by a single exponential and a multiplicative constant as in

$$\boldsymbol{\alpha}\cdot\Delta\mathbf{L}_m(\text{on}) = (\mathbf{L}_p)e^{t2/\boldsymbol{\tau}} - (\mathbf{L}_p)e^{t1/\boldsymbol{\tau}}, \tag{3}$$

From Eqs. (2) and (3), the response-growth rate for the on-frequency masker resulting from a change of $\Delta\mathbf{L}_m$ in masker level can be expressed by

$$\boldsymbol{\alpha} = \Delta\mathbf{L}_m(\text{off})/\Delta\mathbf{L}_m(\text{on}). \tag{4}$$

Thus, for any change to the *input* masker level, $\Delta\mathbf{L}_{mj}$, which corresponds to a change in time delay from t_j and $t_{j'}$, with j and j' corresponding to consecutive time delays along the TMC, there exists a response-growth rate ($\boldsymbol{\alpha}_j$) associated with that change. Response-growth rates calculated in this way are the same as those determined directly from the raw data used to fit the third-order polynomial representing the smoothed input/output curve in the previous section.

6. Response growth and cochlear hearing loss

An important application of the TMC procedure for estimating compression is to evaluate response-growth rates in ears with cochlear hearing loss. This was done by reanalyzing the TMCs from two subjects, EP(R) and RA(R), previously tested by Nelson and Pavlov (1989) in a similar ex-

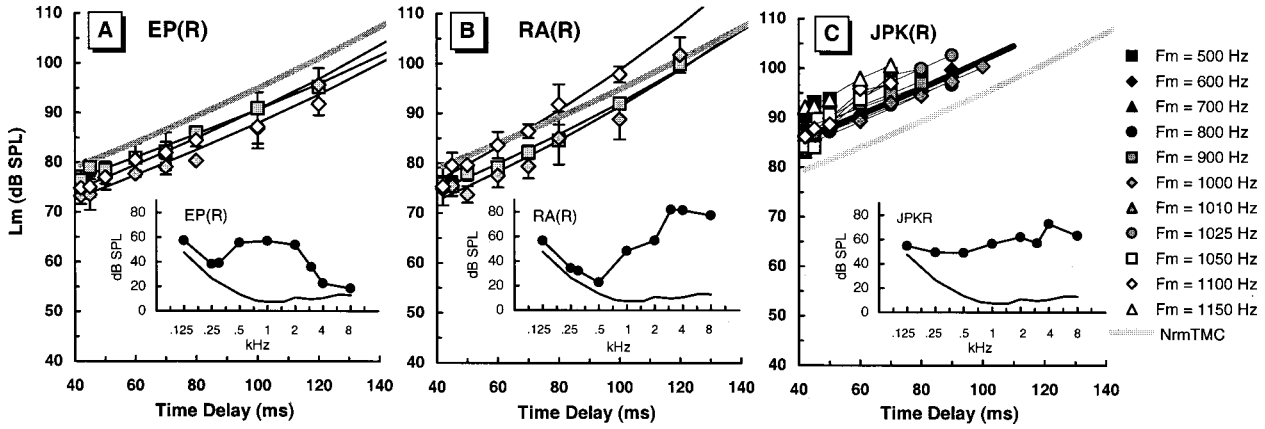

FIG. 8. Results for hearing-impaired listeners. (a) and (b) Fixed-probe-level TMCs for a 1-kHz probe from two hearing-impaired subjects who were previously tested by Nelson and Pavlov (1989) at masker frequencies of 0.9, 1.0, and 1.1 kHz. The parameter is masker frequency, with the on-frequency masker (1 kHz) represented by shaded diamonds. Each curve is fitted with a single-segment exponential, shown by the solid curves. Absolute thresholds for 200-ms tones are plotted as a function of frequency within the inserts. The solid line represents 0 dB HL (ANSI, 1989). The average TMC for low-frequency (0.5–0.6 kHz) maskers in normal-hearing ears (wide shaded curve) is also shown for reference. (c) TMCs for 1-kHz probe tones from a third hearing-impaired listener who was recently tested over a broader range of masker frequencies (0.5–1.15 kHz).

periment using a 4IFC procedure, but at only three masker frequencies (900, 1000, and 1100 Hz). A third subject with cochlear hearing loss, JPK(R), was tested using the same procedure as described for experiment 2, but using the instrumentation from experiment 1. For JPK, the same range of masker frequencies was employed as for the normal-hearing listeners. All three subjects were experienced with forward-masking tasks. Iso-response TMCs obtained from the two previously tested subjects are replotted in Figs. 8(a) and (b); those obtained recently from the third subject using a broader range of masker frequencies are plotted in Fig. 8(c). The average iso-response TMC for the lowest-frequency masker (500 or 600 Hz) from the four normal-hearing listeners is shown, for comparison, by the wide gray curve (labeled NrmTMC).[6] Nearly all of the TMCs from the hearing-impaired listeners are as gradual as those from normal-hearing listeners for a *low off-frequency* masker. The exceptions are the TMCs for maskers above the probe frequency in subjects RA(R) and JPK(R), which exhibited slightly steeper slopes than those exhibited by maskers at and below the probe frequency.

Since the normal-hearing low off-frequency TMC is assumed to reveal linear response growth at the probe frequency, these data suggest that the hearing-impaired listeners also exhibited linear response growth for maskers at and below the probe frequency. In fact, response-growth rate curves derived for all three subjects (not shown) using the methods described for normal-hearing listeners were linear ($\boldsymbol{\alpha}$ close to 1.0) for masker frequencies at and below the probe frequency (the normal-hearing 0.6-kHz frequency curve was used to derive response growth for the two subjects who were not tested at such a low masker frequency). The observed linear response growth at the probe frequency in listeners with cochlear hearing loss is consistent with conclusions reached by other investigators about response growth in cochlear-impaired ears (Stelmachowicz *et al.*, 1987; Oxenham and Moore, 1995; Nelson and Schroder, 1997; Oxenham and Moore, 1997; Moore, 1998; Moore *et al.*, 1999; Hicks and Bacon, 1999b; Wojtczak *et al.*, 2000, 2001).

7. Characterizing compression in the auditory system

Historically, compression effects in the auditory system have been characterized by a compression ratio, which has been defined as the ratio between the change in the input stimulus level and the corresponding change in the output level. For example, a change in the input from 75 to 80 dB SPL that produces a change in the output level from 39 to 40 dB would be defined as a compression ratio of 5:1. This type of relation between input and output has often been described by a power function as in $\mathbf{I}_{\text{out}} = k\mathbf{I}_{\text{in}}^{p}$, where $\mathbf{I}_{\text{out}}$ is output intensity, $\mathbf{I}_{\text{in}}$ is input intensity, and k and p are constants, the former describing the intercept and the latter describing the slope of the input–output function in log–log coordinates (with $0<p<1$). The inverse of the exponent, p, defines the compression ratio.

The use of a power function to describe or simulate the effects of cochlear compression has a rich history (Penner, 1978; Humes and Jesteadt, 1989, 1991; Oxenham and Moore, 1995; Nelson and Schroder, 1996, 1997). In all of these studies a fractional intensity exponent ($\mathbf{I}_{\text{in}}^{p}$, with $0<p<1$) was used to characterize a nonlinearity; usually the exponent was adjusted in order to reduce input intensities sufficiently to account for psychophysical data. Because a single exponent was used, the exponent acted as a constant slope of the input/output function plotted in log–log coordinates.

However, we know from the physiological data that the slope of the BM input/output function is not constant (Yates, 1990; Yates *et al.*, 1990; Ruggero, 1992; Ruggero *et al.*, 1997; Rhode and Recio, 2000); it changes with input level, being linear at low input levels, compressive at mid levels, and perhaps linear again at high input levels. The results of the present study confirm the level dependence of response-growth slopes. Therefore, the use of a power function with a constant exponent, p, independent of input level, cannot accurately characterize compression in the auditory system over a wide range of levels. In order to describe any given output accurately, the slope and the intercept need to change

with input level. Therefore, the output $\mathbf{I}_{out}$ has to be described by

$$\mathbf{I}_{out} = k(\mathbf{I}_{in})\mathbf{I}_{in}^{p(\mathbf{I}_{in})}, \tag{5}$$

where $p(\mathbf{I}_{in})$ is an array of local slopes, and $k(\mathbf{I}_{in})$ is an array of local intercepts in log–log coordinates, which vary with input intensity. It should be noted that by using Eq. (5), we effectively approximate the input/output function by a set of straight lines (in log–log coordinates) defined by local slopes and intercepts.

For the purpose of modeling the effects of compression, it seems more convenient to use one of the following approaches, where compression is level dependent. One is based on a gain function, e.g., similar to the one that was proposed by Glasberg and Moore (2000). Using their equation describing gain in dB for each input level, $\mathbf{L}_{in}$ (expressed in dB SPL), it is possible to compute the corresponding output level, $\mathbf{L}_{out}$ (in dB) by adding gain to the input level. This would be equivalent to expressing the output intensity as

$$\mathbf{I}_{out} = \mathbf{g}(\mathbf{I}_{in}) \cdot \mathbf{I}_{in}, \tag{6}$$

where $\mathbf{g}(\mathbf{I}_{in})$ is obtained by converting gain in dB into linear units.

The exact shape, and thus the local slopes and intercepts of the output function computed with Glasberg and Moore's formula depend on the maximum gain ($\mathbf{G}_{max}$), which is applied to a stimulus of 0 dB SPL. By subtracting the maximum gain (in dB) from each output level, a compressive function will be obtained, in which each output will be equal to (linear response growth) or smaller than the input. In this case, the compressive function could be described by a series of fractions, $n(\mathbf{I}_{in})$, by which the change in the output response relative to the response corresponding to 0 dB output (after subtracting maximum gain) is smaller than the respective change in the input relative to the input of 0 dB SPL. By subtracting the maximum gain from each point on the input/output function, the different intercepts in log–log units corresponding to different values of maximum gain are eliminated and the normalized output intensity can be expressed as

$$\mathbf{I}_{out}/\mathbf{g}_{max} = (\mathbf{I}_{in})^{n(\mathbf{I}_{in})}, \tag{7}$$

where $\mathbf{I}_{in}$ is effectively the intensity obtained by converting the input level from dB SPL into linear intensity units, and $\mathbf{g}_{max}$ is the maximum gain in linear units. Expressed in terms of levels

$$n(\mathbf{L}_{in}) = (\mathbf{L}_{out} - \mathbf{G}_{max})/\mathbf{L}_{in}. \tag{8}$$

Since exponent $n(\mathbf{I}_{in})$ only takes on values between 0 and 1, and it effectively "compresses" a change in input level (*re*: 0 dB SPL) into an equal or smaller change at the output (*re*: the output corresponding to the input of 0 dB SPL normalized by $\mathbf{G}_{max}$), it can be called a compression exponent. This exponent, however, is *not* equivalent to the slope of the input/output function, and, therefore, is *not* equivalent to the reciprocal of the commonly used compression ratio. The only case where this exponent would describe the slope would be if the input/output function had a constant slope for all input levels, as was often assumed in some previous studies. This assumption is not correct given both physiological and psychophysical data. Input/output functions obtained from Eq. (6) normalized by maximum gain, i.e., $\mathbf{I}_{out} = (\mathbf{g}(\mathbf{I}_{in})/\mathbf{g}_{max})\mathbf{I}_{in}$, and those obtained from Eq. (7) for $n(\mathbf{L}_{in}) = (\mathbf{L}_{out} - \mathbf{G}_{max})/\mathbf{L}_{in}$, are identical.

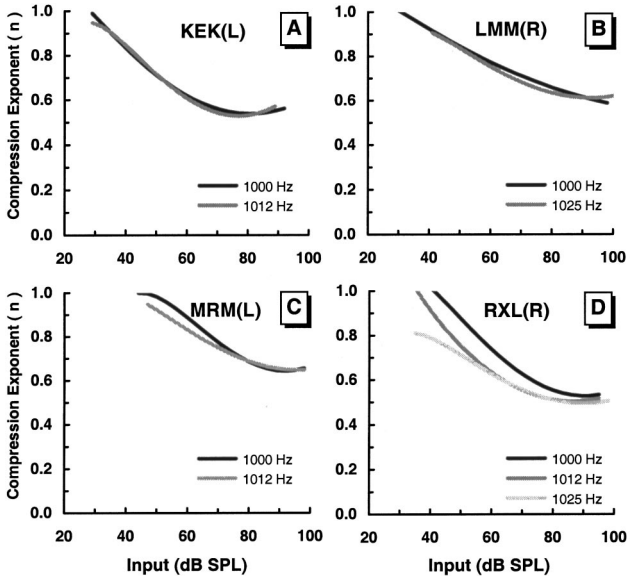

FIG. 9. Compression exponents calculated from the derived input/output curves are shown as a function of input level (masker SPL). The parameter is masker frequency as labeled. Several curves are shown for each subject, one for a masker frequency at the probe frequency and one or two for masker frequencies slightly higher in frequency.

Thus, all three ways of describing the input/output function with a varying slope across levels, presented above [in Eqs. (5)–(7)], are equivalent, and each one of them can be used to make predictions about outputs for different input levels.

Equation (7) characterizes compression as the ratio between output level, normalized by maximum gain, and input level. This is exemplified by curve (b) in Fig. 4. At the input level of 28 dB, the output is equal to the input (by assumption that the response is linear for input levels up to 28 dB SPL), so the compression exponent is 1.0. At 60 dB the output is 38 dB, so the compression exponent is 0.63. At 80 dB the output is about 40 dB, so the compression exponent is 0.50. At 90 dB the output is about 45 dB, so the compression exponent is 0.50. This way of expressing compression, as an exponent applied to input intensity, is consistent with previous descriptions of compression in the auditory system that used a power function with an exponent, *p*, and ignored intercept *k*, to predict the output *at only a single input level* (or only a very restricted range of input levels) (Penner, 1978; Humes and Jesteadt, 1989, 1991; Nelson and Schroder, 1996, 1997).

Figure 9 shows compression exponents (output/input ratios) calculated from third-order polynomial fits to the derived input/output curves, plotted as a function of the input level, for two or three masker frequencies at or near the probe frequency. Compression exponents are large, near 1.0, at low input levels between 25 and 40 dB SPL. As input level rises above about 40 dB SPL, compression exponents de-

crease with input level and gradually saturate at input levels above about 80 dB SPL. The smallest compression exponents were seen for input levels above 80 dB SPL, where the minimum exponents ranged between 0.5 (KEK) and 0.62 (MRM).

IV. EXPERIMENT 3: HIGH-PASS NOISE AND RESPONSE GROWTH

Experiment 1 demonstrated how GMB functions, where forward masker level is varied to reach masked threshold for a range of fixed probe levels, are strongly influenced by spread of excitation from the probe toward higher frequency regions. Consequently, it was concluded that a HP noise is necessary to obtain valid indices of cochlear compression with that procedure. Because probe level is fixed at a relatively low sensation level in the new iso-response temporal masking procedure proposed here for measuring cochlear compression (experiment 2), it was hypothesized that spread of excitation toward higher frequency regions should not be an important factor affecting estimates of cochlear compression. To confirm this hypothesis, normal-hearing subjects were tested in the presence of a HP noise.

A. Method

Three additional normal-hearing subjects participated in the experiment. TMCs were obtained for a 1-kHz probe in quiet, and in the presence of a HP noise with a high-pass cutoff at 1.117 kHz. Masker, probe, and ramp durations were the same as those used to obtain the TMCs in experiment 2. The HP noise was turned on 20 ms before the onset of the masker ramp and was turned off 20 ms after the offset of the probe ramp. The noise was gated with 10-ms raised-cosine ramps. The spectrum level of the HP noise in a 6-cc coupler was relatively constant between 1117 Hz and 6 kHz and decreased with frequency above 6 kHz, so that the spectrum level was about 10 dB less at 9.5 kHz and 20 dB less at 12.5 kHz. Because the probe sensation level was low (10 dB), and the edge of the HP noise was close to the probe frequency, we wanted to ensure that, for each subject, the HP noise would just partially mask the probe, but not completely mask it. Therefore, for each subject, a complete simultaneous growth-of-masking function was measured for the 1-kHz probe in the presence of the HP noise, and then one of two fixed noise levels (25 or 30 dB SPL) was chosen that would produce less than 5 dB of masking. The noise levels used for each subject produced 3.3, 2.6, and 1.7 dB of masking at 1 kHz, respectively, for subjects DYS, KJB, and KSA.

Psychophysical procedures were the same as those described earlier for experiment 2. The instrumentation system was the same as that used in experiment 1. Three TMCs were obtained in each subject: one for a 0.6-kHz (low off-frequency) masker in quiet, one for a 1-kHz (on-frequency) masker in quiet, and one for the 1-kHz masker in the presence of the HP noise.

An obvious control experiment was the measurement of the low off-frequency iso-response TMC in the presence of the HP noise. However, given the large level difference between the 0.6-kHz masker and the 1-kHz probe at masked threshold, the upward spread of excitation above 1 kHz produced by the 0.6-kHz masker was likely to be much greater than any upward spread of excitation produced by the 10-dB SL 1-kHz probe (Kidd and Feth, 1981; Zwicker and Jaroszewski, 1982). The HP noise might partially mask the probe and result in slightly lower 0.6-kHz masker levels, but the likelihood that off-frequency listening might change the slope of the 0.6-kHz TMC is small. Therefore, the HP noise condition with the 0.6-kHz masker was not included in the main experiment.[7]

B. Results and discussion

Figure 10 shows the iso-response TMCs obtained in quiet and HP noise, along with the input/output curves derived from those TMCs, and the response-growth rates calculated from those derived curves. The results in quiet (Q) were similar to those reported above for the other four normal-hearing listeners that were tested in experiment 2. The low off-frequency TMCs obtained in quiet [shaded squares in Figs. 10(a)–(c)] were gradual, presumably because they only reflect recovery from forward masking without any effects of compression. The on-frequency TMCs [black squares and triangles in Figs. 10(a)–(c)] exhibited three segments, reflecting the effects of compression in addition to recovery from forward masking for both the quiet and noise cases. The corresponding derived input/output curves in Figs. 10(d)–(f), exhibit linear response growth for the low off-frequency masker and nonlinear response growth for the on-frequency conditions.

If detection of the probe in quiet involves listening at higher-frequency regions, then the HP noise should mask those frequency regions, and as a result the probe should be more difficult to detect. Consequently, introduction of the noise should result in lower level masking tones to forward mask the probe than during the quiet condition. Except at very short time delays for two of the subjects (DYS and KSA), this was not the case. Masker levels were generally the same or higher in the presence of the HP noise [black triangles in Figs. 10(a)–(c)]. The most consistent effect of the noise was to require higher masker levels in the steeply sloped region of the TMCs (e.g., at a time delay of 80 ms). This could have been due to learning effects, since most of the noise conditions were obtained during later testing sessions, although the subjects were highly practiced at forward masking tasks before beginning the experiments.

Figures 10(g)–(i) show response-growth rates calculated from the derived input/output curves in Figs. 10(d)–(f). Response growth was curvilinear (U-shaped): steep at low and high levels, and very gradual at mid levels (just as in experiment 2). The background noise (N) decreased the minimum growth rate slightly in two of the subjects, but the net effect on response-growth functions was minimal.

From these results it is apparent that the iso-response temporal masking procedure for estimating cochlear compression is relatively free from contamination by the upward spread of excitation from the probe. Thus, it does not appear to be necessary to employ HP noise to obtain valid measures of response growth with this procedure.

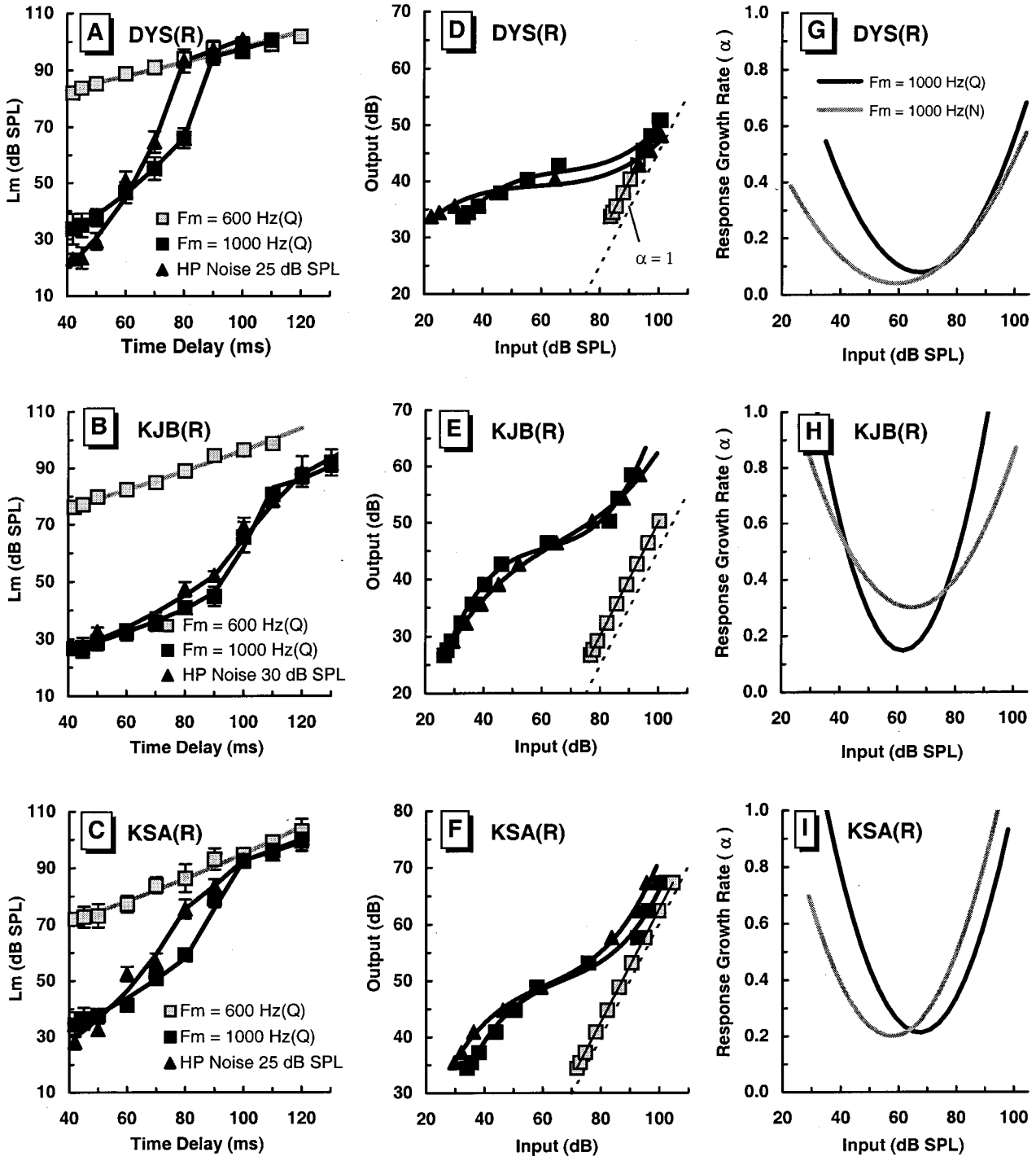

FIG. 10. Effects of high-pass noise on TMCs, derived input/output curves, and response-growth rates, in three normal-hearing listeners. Each row shows results for a different subject. (a)–(c) Fixed-probe-level TMCs at 1 kHz for a low off-frequency masker condition (0.6 kHz) in quiet (shaded squares), an on-frequency masker condition (1 kHz) in quiet (black squares), and an on-frequency masker condition in high-pass noise (black triangles) that was introduced to mask the spread of excitation toward higher frequency regions. (d)–(f) Derived input/output curves for each of the masker conditions. The dashed lines represent linear response growth. (g)–(i) Response growth-rate curves calculated from the derived input/output curves. Black curves are for data obtained in quiet (Q), shaded curves are for data obtained in the high-pass noise (N).

V. EXPERIMENT 4: CUEING TONES AND RESPONSE GROWTH

In forward-masking tasks, when a masker and a subsequent probe are at the same frequency, and consequently have nearly the same pitch, it is often difficult to detect the presence of a short probe immediately following the masker (Terry and Moore, 1977; Moore, 1980a, b; 1981). When the masker and probe are at different frequencies they no longer have similar pitches; therefore, it is easier to detect the presence of the probe tone. Moore (1980a) demonstrated improvements in masked threshold that were as large as 20 dB in some subjects, for maskers at the probe frequency, when a

high-frequency cueing tone was gated synchronously with the masker to mark the masker duration, particularly the end of the masker, by introducing a pitch-difference cue. When masking tones were more than 50 Hz below the probe tone, cueing tones had no effect (Terry and Moore, 1977). Thus, in the present study, the lack of pitch differences between masker and probe for the on-frequency condition could have made it more difficult to hear the probe than in those conditions in which the masker frequency was either below or above the probe frequency, where pitch differences were available.

In experiment 2, the lack of a pitch difference between masker and probe in the on-frequency condition may have made it easier to mask the probe tone. Consequently, adding a pitch-difference cue to an on-frequency masker should raise the masker levels required to mask the probe. Furthermore, it is possible that the lack of pitch differences in experiment 2 may have influenced forward-masked thresholds more at short time delays than at longer time delays. At short time delays the masker and probe are closer together, thus a greater possibility exists for a lack of a temporal distinction between masker and probe. If the lack of pitch differences for on-frequency forward-masking conditions differentially affects masked thresholds at different time delays, then it could influence measurements of response-growth rate. To determine whether or not the lack of pitch difference cues in on-frequency masking influences response-growth rates obtained from iso-response TMCs, the on-frequency masking conditions were tested in the presence of a higher-frequency cueing tone and the results were compared with those obtained earlier without a cueing tone.

A. Method

The three normal-hearing subjects from experiment 3 participated in this experiment. The TMCs were obtained in the presence of a cueing tone. The cueing tone was gated with the masker and on each trial was presented at the same level as the masker. This is slightly different from other experiments with cueing tones because the masker level is varied to reach masked threshold in this experiment. Thus, the level of the cueing tone was also varied with masker level. This method ensured that the cueing tone was always audible. Psychophysical procedures were the same as those described earlier for experiment 2. The instrumentation system was the same as that used in experiment 1. Two TMCs were obtained from each subject for the 1-kHz masker and the 1-kHz probe: one with a 2-kHz cue and one with a 2.5-kHz cue. The 2-kHz cue was an octave above the masker frequency, where suppression of the 1-kHz masker should have been minimal. However, if suppression were involved, the effectiveness of the cue should depend on its proximity in frequency to the main masker and signal. Therefore, moving the cue toward a higher frequency should maintain the cueing effect but reduce any suppression effect. Therefore, a 2.5-kHz cue condition was included.

B. Results and discussion

Figures 11(a)–(c) show the iso-response TMCs obtained in quiet (from experiment 3) and those obtained in the presence of a cueing tone at 2.0 or 2.5 kHz. As noted previously, the TMCs for the 0.6-kHz masker exhibited gradual slopes, reflecting the recovery from forward masking without the influence of cochlear compression. The TMCs for the on-frequency 1-kHz masker, with and without a cue, exhibited the three-sloped characteristics that reflect gradual response growth at short and very long delays and strong compression at mid delays. Presentation of the cueing tones had similar effects across subjects. In general, higher masker levels were required with the cueing tones present than without them, more so at middle time delays than at short time delays.

These effects are shown more clearly in Fig. 12, where the differences between the masker levels obtained with and without a cueing tone are plotted against time delay. At short time delays ($<$60 ms) the 2.0-kHz cueing tones increased masker levels at threshold by about 4–6 dB [Fig. 12(a)]. The 2.5-kHz cueing tones also raised masker levels at threshold at short delays, but by a smaller amount [Fig. 12(b)]. This increase in masker level at threshold for short time delays, in the presence of a cueing tone, was seen in all three subjects.

It might be argued that the effects of the cueing tones could originate from one of two possible sources: pitch difference cues or suppression. However, several factors argue against the suppression explanation. The cueing tones and the masking tones were always at the same overall SPL, a condition for which suppression is typically not observed, except for very small frequency ratios between suppressor and suppressee (Sachs and Kiang, 1967; Geisler *et al.*, 1990). The nearest cueing tone was an octave above the masking tone, which is a fairly wide frequency separation that is unlikely to produce any significant suppression (Houtgast, 1974; Shannon, 1976; Javel *et al.*, 1983; Delgutte, 1990). Increasing the cueing tone frequency to 2.5 kHz only reduced the required masker levels slightly [Fig. 12(b)]. There were still significant effects of the high-frequency cueing tone in all three subjects, despite the additional 500-Hz frequency separation between masker and cueing tone. Significant increases in masker thresholds occurred at short time delays where the masker levels, and therefore the cueing tones, were at low SPLs where the existence region for suppression is even more restricted. Therefore, it seems most likely that the increased masker levels at threshold were caused by improved information about the exact end of the masker.

At middle time delays (60–100 ms), the effects of the cueing tones were considerably larger than at the short time delays (Fig. 12). An increase in masker level as large as 28 dB was required in some subjects to maintain a constant amount of forward masking when the cueing tone was present. The large effects of the cueing tones were then reduced again at still longer time delays ($>$80–100 ms). Notice that the steeply sloped portions of the TMCs [Figs. 11(a)–(c)], and the largest effects of the cueing tones (Fig. 12), occurred over the same range of time delays. In accordance with our earlier reasoning, the steep portion of the TMC is associated with gradual response growth and strong

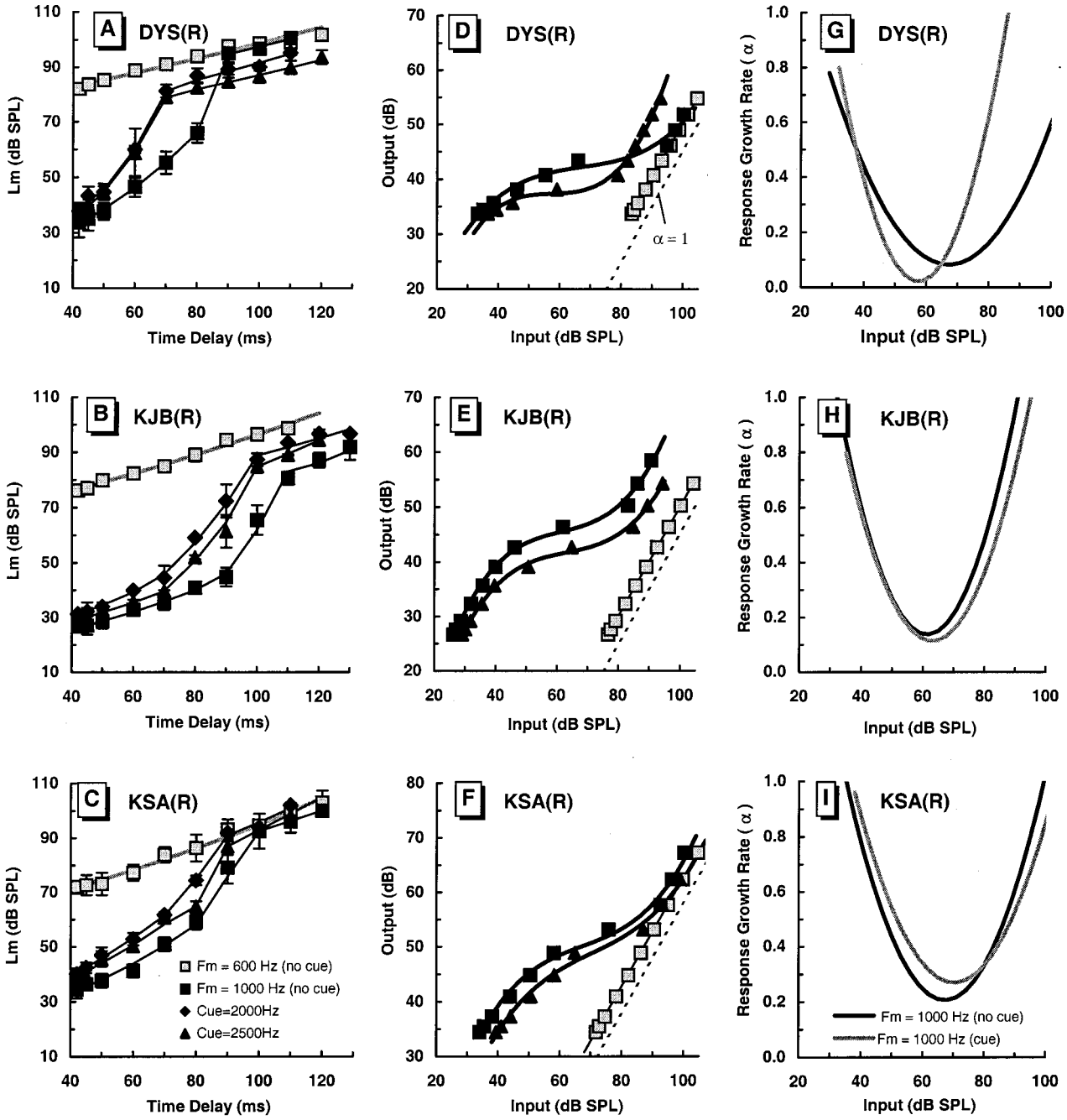

FIG. 11. Effects of cueing tones on TMCs, derived input/output curves, and response growth-rate curves, in three normal-hearing listeners. Each row shows results for a different subject. (a)–(c) Fixed-probe-level TMCs at 1 kHz for a low off-frequency masker condition (0.6 kHz) without any cueing tone (shaded squares), an on-frequency masker condition (1 kHz) with no cueing tone (black squares), an on-frequency masker condition with an additional 2-kHz cueing tone (black diamonds), and an on-frequency masker condition with a 2.5-kHz cueing tone (black triangles). The cueing tones were gated with the masker to introduce a defined pitch cue for the termination of the on-frequency masker. (d)–(f) Derived input/output curves for the masker conditions in quiet and with the 2.5-kHz cueing tone. The dashed lines represent linear response growth. (g)–(i) Response growth rates estimated from the derived input/output curves, as a function of input level (masker SPL). Black curves are for data obtained in quiet, shaded curves are for data obtained in the presence of the 2.5 kHz cueing tone.

cochlear compression. It appears that the small effects of the cueing tones seen at short time delays, where input levels are low, were magnified at the middle time delays where masker levels were higher. At short time delays, where response growth is steep and compression is minimal, only a small increase in masker level was required to maintain constant masking with the addition of a cueing tone. At middle time delays, where compression acting on the masker is strong, a larger increase in masker level was required to maintain the same amount of masking.

The effects of the 2.5-kHz cueing tones on derived input/output curves are shown in Figs. 11(d)–(f) (the results were similar for the 2.0-kHz condition). The general shapes of the fitted input/output curves were not dramatically affected by the cueing tones, although there was a tendency for the input/output curves to be slightly more compressive in

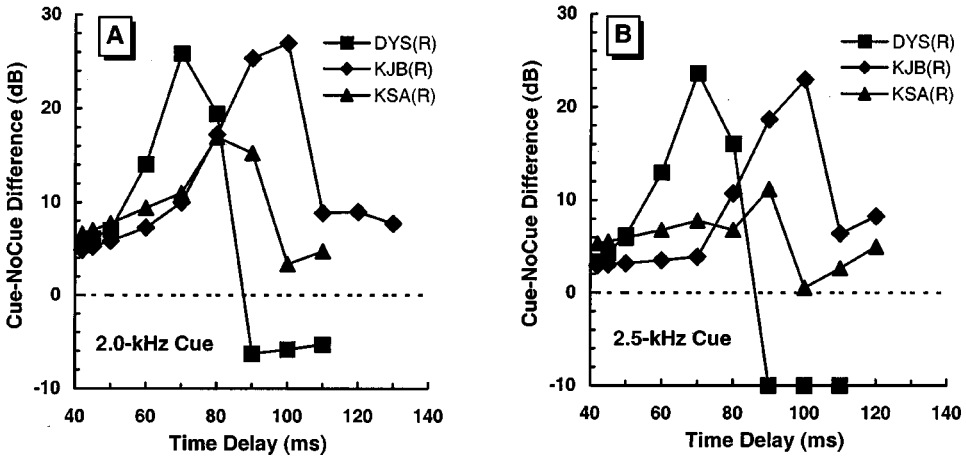

FIG. 12. Effects of cueing tones expressed as masker-level differences. (a) 2.0-kHz cue. (b) 2.5-kHz cue. The differences (in dB) between masker levels, with and without a cueing tone gated with the masker, required to produce a constant amount of forward masking, are plotted on the ordinate as a function of the delay time between masker and probe. The differences are small at short time delays, where masker levels are low and the system is linear. The differences are larger at longer time delays where masker levels are higher and the system is nonlinear.

the presence of the cueing tones for two of the subjects (DYS and KJB). Figures 11(g)–(i) show response-growth rate curves calculated for the quiet and the 2.5-kHz cueing conditions (curves for the 2.0-kHz cueing condition behaved similarly). Response-growth rates changed little in the cueing condition for two subjects (KJB and KSA). For subject DYS, the 2.5-kHz cueing tone made the response-growth curve more compressive and the high-level linearity began at lower input levels.

VI. SUMMARY AND CONCLUSIONS

The GMB forward-masking functions measured in quiet and in the presence of a HP noise, using a 3- or 6-kHz forward masker and a 6-kHz probe, indicated that GMB slope ratios for low off-frequency and on-frequency maskers obtained in quiet do not reflect the same response-growth rates as those obtained in the presence of a HP noise. The estimates of response-growth rate obtained from GMB slope ratios in quiet were at least twice those obtained with a HP noise. Estimates of response-growth rates at 6 kHz obtained in the HP noise are consistent with those observed in animals from basal regions of the cochlea.

An alternative procedure for measuring response-growth rates was presented. That procedure used iso-response TMCs for different masker frequencies around 1 kHz to specify response-growth rates at the 1-kHz place in the cochlea. Input/output curves were derived from the TMCs, and fitted with a polynomial. The first derivative of the fitted input/output curves specified response-growth rate as a function of input level. Response-growth rate varied with input level in a U-shaped fashion, with linear growth at low levels, gradual growth at mid levels, and linear growth again at higher levels. Iso-response TMCs obtained from three subjects with cochlear hearing loss revealed linear response growth throughout the entire range of input levels for on-frequency maskers, indicating the absence of cochlear compression.

Iso-response TMCs obtained in HP noise yielded response-growth rates similar to those obtained in quiet; thus, upward spread of excitation from the probe has little effect on measures of compression with this procedure. Iso-response TMCs obtained in the presence of cueing tones were elevated, more so at time delays where compression existed, which is consistent with the cueing tones facilitating detection of the probe following a masker of the same or nearly the same frequency. However, for two out of three listeners, response-growth rates derived from those curves were similar to those obtained from the TMCs obtained without the cueing tones. Thus, the availability of pitch-difference cues between masker and probe had little effect on measures of response growth obtained with this procedure. From these results we conclude that the iso-response TMC provides a valid psychophysical description of peripheral compression in human subjects.

ACKNOWLEDGMENTS

This work was supported largely by Grant No. DC00149 from NIDCD. This research was also supported in part by the Lion's 5M International Hearing Foundation. We wish to thank Brian Moore and Andrew Oxenham for their thorough and detailed written critiques, as well as Walt Jeasteadt, Gail Donaldson, and Neal Viemeister for their helpful suggestions on previous versions of this manuscript.

[1]The effects of the high-pass noise at 1 kHz should be considered with some caution, because off-frequency listening to splatter below the probe frequency, due to the 2-ms ramp on the probe (4-ms total probe duration), could have affected the measured growth-of-masking slopes. Moore *et al.* (1999) found obvious slope changes in only two out of six subjects when a 5-ms ramp (10-ms total probe duration) was compared with a 2-ms ramp (4-ms total probe duration) on a 2-kHz probe tone. However, at 1 kHz the splatter effects might have been greater for a 2-ms ramp condition.

[2]To facilitate calculation of recovery slopes, from which response-growth slopes were estimated, three different curve segments were used to describe the entire temporal masking curve. An exponential function was fit using least-squares procedures for each segment, in which the masker level decayed exponentially with time delay as in $\ln(\mathrm{Lm}) = b + a(\mathrm{Lp})$. The limits for the fits were adjusted manually until the excellent fits shown in Fig. 2 were achieved. It should be noted that any curve-fitting procedure that fits the data well could have been used.

[3]Any hypothetical function could have been used to fit the low off-frequency and on-frequency TMCs, as long as the fit was excellent, since the ratios of the slopes of the two functions define response growth slopes.

[4]Changes in input level used to calculate associated changes in effective output level were based on the exponential fit TMCs curves rather than the raw data. This was done to smooth the TMCs in order to minimize variability in local slopes.

[5]This procedure for deriving input/output curves is similar to plotting the input level for the low off-frequency masker, on the ordinate, against the input level for the on-frequency masker, on the abscissa. The low off-

frequency masker input levels are then normalized to effective output levels at the probe frequency place by subtracting the maximum gain in the auditory filter estimated at 42 ms, given by $\mathbf{G}_{max}=20\ \mathrm{Log}(1/\mathbf{k})$, which results in the same values as those shown by the open squares in curve b of Fig. 4.

[6]The ''average TMC'' was obtained by fitting each of the normal-hearing curves with a single exponential and then averaging the fitting parameters for that exponential across subjects. Then the average TMC was calculated from those average fitting parameters.

[7]Comments from one of the reviewers led us to verify our reasoning. We obtained iso-response temporal masking curves for 0.6-kHz maskers from three additional normal-hearing subjects, both in quiet and in the presence of the high-pass noise (the original subjects were no longer available for testing at the time). The slope of the 0.6-kHz iso-response TMC did not change in any of the subjects.

Abbas, P. J., and Gorga, M. P. (**1981**). ''AP responses in forward-masking paradigms and their relationship to responses of auditory-nerve fibers,'' J. Acoust. Soc. Am. **69**, 492–499.

ANSI (**1989**). S3.6-1989 ''Specification for Audiometers'' (American National Standards Institute, New York).

Delgutte, B. (**1990**). ''Physiological mechanisms of psychophysical masking: Observations from auditory-nerve fibers,'' J. Acoust. Soc. Am. **87**, 791–809.

Duifhuis, H. (**1973**). ''Consequences of peripheral frequency selectivity for nonsimultaneous masking,'' J. Acoust. Soc. Am. **54**, 1471–1488.

Geisler, C. D., Yates, G. K., Patuzzi, R. B., and Johnstone, B. M. (**1990**). ''Saturations of outer hair cell receptor currents causes two-tone suppression,'' Hear. Res. **44**, 241–256.

Glasberg, B. R., and Moore, B. C. J. (**2000**). ''Frequency selectivity as a function of level and frequency measured with uniformly exciting notched noise,'' J. Acoust. Soc. Am. **108**, 2318–2328.

Hicks, M. L., and Bacon, S. P. (**1999a**). ''Psychophysical measures of auditory nonlinearities as a function of frequency in individuals with normal hearing,'' J. Acoust. Soc. Am. **105**, 326–338.

Hicks, M. L., and Bacon, S. P. (**1999b**). ''Effects of aspirin on psychophysical measures of frequency selectivity, two-tone suppression, and growth of masking,'' J. Acoust. Soc. Am. **106**, 1436–1451.

Houtgast, T. (**1974**). ''Lateral suppression and loudness reduction of a tone in noise,'' Acustica **30**, 215–221.

Humes, L. E., and Jesteadt, W. (**1989**). ''Models of the additivity of masking,'' J. Acoust. Soc. Am. **85**, 1285–1294.

Humes, L. E., and Jesteadt, W. (**1991**). ''Models of the effects of threshold on loudness growth and summation,'' J. Acoust. Soc. Am. **90**, 1933–1943.

Javel, E., McGee, J., Walsh, E. J., Farley, G. R., and Gorga, M. P. (**1983**). ''Suppression of auditory-nerve responses. II. Suppression threshold and growth, isosuppression contours,'' J. Acoust. Soc. Am. **74**, 801–813.

Kidd, G., and Feth, L. L. (**1981**). ''Patterns of residual masking,'' Hear. Res. **5**, 49–67.

Levitt, H. (**1971**). ''Transformed up-down methods in psychoacoustics,'' J. Acoust. Soc. Am. **49**, 467–477.

Moore, B. C. J. (**1980a**). ''Detection cues in forward masking,'' in *Psychophysical, Physiological and Behavioral Studies in Hearing*, edited by G. van den Brink and F. A. Bilsen (Delft U. P., Delft, The Netherlands).

Moore, B. C. J. (**1980b**). ''Relation between pitch shifts and MMF shifts in forward masking,'' J. Acoust. Soc. Am. **69**, 594–596.

Moore, B. C. J. (**1981**). ''On the relation between pitch shifts and MMF shifts in forward masking,'' J. Acoust. Soc. Am. **69**, 594–597.

Moore, B. C. J. (**1998**). *Cochlear Hearing Loss* (Whurr, London).

Moore, B. C. J., and Oxenham, A. J. (**1998**). ''Psychoacoustic consequences of compression in the peripheral auditory system,'' Psychol. Rev. **105**, 108–124.

Moore, B. C. J., Vickers, D. A., Plack, C. J., and Oxenham, A. J. (**1999**). ''Inter-relationship between different psychoacoustic measures assumed to be related to the cochlear active mechanism,'' J. Acoust. Soc. Am. **106**, 2761–2778.

Nelson, D. A., and Freyman, R. L. (**1987**). ''Temporal resolution in sensorineural hearing-impaired listeners,'' J. Acoust. Soc. Am. **81**, 709–720.

Nelson, D. A., and Pavlov, R. (**1989**). ''Auditory time constants for off-frequency forward masking in normal-hearing and hearing-impaired listeners,'' J. Speech Hear. Res. **32**, 298–306.

Nelson, D. A., and Schroder, A. C. (**1996**). ''Release from upward spread of masking in regions of high-frequency hearing loss,'' J. Acoust. Soc. Am. **100**, 2266–2277.

Nelson, D. A., and Schroder, A. C. (**1997**). ''Linearized response growth inferred from growth-of-masking slopes in ears with cochlear hearing loss,'' J. Acoust. Soc. Am. **101**, 2186–2201.

Oxenham, A. J., and Moore, B. C. J. (**1995**). ''Additivity of masking in normally hearing and hearing-impaired subjects,'' J. Acoust. Soc. Am. **98**, 1921–1934.

Oxenham, A. J., and Moore, B. C. J. (**1997**). ''Modeling the effects of peripheral nonlinearity in normal and impaired hearing,'' in *Modeling Sensorineural Hearing Loss*, edited by W. Jesteadt (Erlbaum, Hillsdale, NJ).

Oxenham, A. J., and Plack, C. J. (**1997**). ''A behavioral measure of basilar-membrane nonlinearity in listeners with normal and impaired hearing,'' J. Acoust. Soc. Am. **101**, 3666–3675.

Penner, M. J. (**1978**). ''A power law transformation resulting in a class of short-term integrators that produce time-intensity trades for noise bursts,'' J. Acoust. Soc. Am. **63**, 195–201.

Plack, C. J., and Oxenham, A. J. (**1998**). ''Basilar-membrane nonlinearity and the growth of forward masking,'' J. Acoust. Soc. Am. **103**, 1598–1608.

Plack, C. J., and Oxenham, A. J. (**2000**). ''Basilar-membrane nonlinearity estimated by pulsation threshold,'' J. Acoust. Soc. Am. **107**, 501–507.

Rhode, W. S., and Recio, A. (**2000**). ''Study of mechanical motions in the basal region of the chinchilla cochlea,'' J. Acoust. Soc. Am. **107**, 3317–3332.

Ruggero, M. A. (**1992**). ''Responses to sound of the basilar membrane of the mammalian cochlea,'' Curr. Opin. Neurobiol. **2**, 449–456.

Ruggero, M. A., Rich, N. C., Recio, A., Narayan, S. S., and Robles, L. (**1997**). ''Basilar-membrane responses to tones at the base of the chinchilla cochlea,'' J. Acoust. Soc. Am. **101**, 2151–2163.

Sachs, M. B., and Kiang, N. Y. S. (**1967**). ''Two-tone inhibition in auditory-nerve fibers,'' J. Acoust. Soc. Am. **43**, 1120–1128.

Shannon, R. V. (**1976**). ''Two-tone unmasking and suppression in a forward-masking situation,'' J. Acoust. Soc. Am. **59**, 1460–1470.

Stelmachowicz, P., Lewis, D. E., Larson, L., and Jesteadt, W. (**1987**). ''Growth of masking as a measure of response growth in hearing-impaired listeners,'' J. Acoust. Soc. Am. **81**, 1881–1887.

Terry, M., and Moore, B. C. J. (**1977**). ''Suppression effects in forward masking,'' J. Acoust. Soc. Am. **62**, 781–784.

Widin, G. P., and Viemeister, N. F. (**1979**). ''Pure-tone forward masking,'' J. Acoust. Soc. Am. **66**, 388–395.

Wojtczak, M., Schroder, A. C., and Nelson, D. A. (**2000**). ''Masking period patterns in listeners with cochlear hearing loss,'' J. Acoust. Soc. Am. **107**, 2881(A).

Wojtczak, M., Schroder, A. C., Kong, Y.-Y., and Nelson, D. A. (**2001**). ''The effect of BM nonlinearity on the shapes of masking period patterns in normal and impaired hearing,'' J. Acoust. Soc. Am. **109**, 1571–1586.

Yates, G. K. (**1990**). ''Basilar membrane nonlinearity and its influence on auditory nerve rate-intensity functions,'' Hear. Res. **50**, 145–162.

Yates, G. K., Winter, I. M., and Robertson, D. (**1990**). ''Basilar membrane nonlinearity determines auditory nerve rate-intensity functions and cochlear dynamic range,'' Hear. Res. **45**, 203–220.

Zwicker, E., and Jaroszewski, A. (**1982**). ''Inverse frequency dependence of simultaneous tone-on tone masking patterns at low levels,'' J. Acoust. Soc. Am. **71**, 1508–1512.

Rate and timing cues associated with the cochlear amplifier: Level discrimination based on monaural cross-frequency coincidence detection[a)]

Michael G. Heinz[b)]
Speech and Hearing Sciences Program, Division of Health Sciences and Technology, Massachusetts Institute of Technology, 77 Massachusetts Avenue, Cambridge, Massachusetts 02139 and Hearing Research Center, Biomedical Engineering Department, Boston University, 44 Cummington Street, Boston, Massachusetts 02215

H. Steven Colburn and Laurel H. Carney
Hearing Research Center, Biomedical Engineering Department, Boston University, 44 Cummington Street, Boston, Massachusetts 02215

(Received 1 September 2000; revised 18 July 2001; accepted 23 July 2001)

The perceptual significance of the cochlear amplifier was evaluated by predicting level-discrimination performance based on stochastic auditory-nerve (AN) activity. Performance was calculated for three models of processing: the optimal all-information processor (based on discharge times), the optimal rate-place processor (based on discharge counts), and a monaural coincidence-based processor that uses a non-optimal combination of rate and temporal information. An analytical AN model included compressive magnitude and level-dependent-phase responses associated with the cochlear amplifier, and high-, medium-, and low-spontaneous-rate (SR) fibers with characteristic frequencies (CFs) spanning the AN population. The relative contributions of nonlinear magnitude and nonlinear phase responses to level encoding were compared by using four versions of the model, which included and excluded the nonlinear gain and phase responses in all possible combinations. Nonlinear basilar-membrane (BM) phase responses are robustly encoded in near-CF AN fibers at low frequencies. Strongly compressive BM responses at high frequencies near CF interact with the high thresholds of low-SR AN fibers to produce large dynamic ranges. Coincidence performance based on a narrow range of AN CFs was robust across a wide dynamic range at both low and high frequencies, and matched human performance levels. Coincidence performance based on all CFs demonstrated the ''near-miss'' to Weber's law at low frequencies and the high-frequency ''mid-level bump.'' Monaural coincidence detection is a physiologically realistic mechanism that is extremely general in that it can utilize AN information (average-rate, synchrony, and nonlinear-phase cues) from all SR groups. [DOI: 10.1121/1.1404977]

PACS numbers: 43.66.Ba, 43.64.Bt, 43.66.Fe [MRL]

I. INTRODUCTION

The cochlear amplifier is the name often used to describe an active mechanism within the cochlea that is thought to provide amplification of low-level sounds (Yates, 1995; Moore, 1995). While the mechanism of amplification is not completely understood, several physiological response properties associated with the cochlear amplifier are clear (Ruggero, 1992). The most significant of these is that the active mechanism is vulnerable to cochlear damage and has been shown to be absent in many common forms of sensorineural hearing loss (Patuzzi *et al.*, 1989). This finding raises the question of how the cochlear amplifier benefits normal-hearing listeners, especially in complex listening environments, such as understanding speech in noise, for which hearing-impaired listeners have much difficulty (Moore, 1995). The present study evaluates quantitatively some of the benefits of the cochlear amplifier for extending the dynamic range of the auditory system. The absence of the cochlear amplifier in damaged cochleae is likely responsible for the common report of loudness recruitment by listeners with sensorineural hearing loss and for the associated reduction in dynamic range (see review by Moore, 1995).

It is still not well understood how the auditory system overcomes the dynamic-range problem (for reviews see Evans, 1981; Viemeister, 1988a, 1988b), i.e., the discrepancy between the large dynamic range of human hearing [over 120 dB (Viemeister and Bacon, 1988)], and the limited dynamic range of most auditory-nerve (AN) fibers [less than 30 dB (May and Sachs, 1992)]. A psychophysical experiment in which the dynamic-range problem is clearly evident was examined in the present modeling study: level discrimination of high-level, narrow-band signals in conditions for which information is restricted to frequency regions near the frequency of the signal (e.g., Viemeister, 1974, 1983; Carlyon

[a)]Portions of this work were presented at the Joint Meeting of the Acoustical Society of America and the European Acoustics Association, in Berlin, Germany in 1999.

[b)]Now at: Department of Biomedical Engineering, Johns Hopkins University, 505 Traylor Building, 720 Rutland Avenue, Baltimore, MD 21205; electronic mail: mgheinz@bme.jhu.edu

and Moore, 1984). An influential experiment for level-encoding hypotheses was performed by Viemeister (1983), who found that Weber's law (i.e., constant just-noticeable-difference in level as a function of level) was achieved for high-frequency, narrow-band noise in the presence of band-reject noise. This experiment was designed to prevent the spread of excitation by using a band-reject noise masker and to prevent the use of temporal information by using a high-frequency signal. Viemeister's finding has been taken as evidence that Weber's law must hold in narrow frequency regions and must rely on the use of average-rate information.

Low-spontaneous-rate (LSR), high-threshold AN fibers (Liberman, 1978) have been implicated in the encoding of high sound levels based on average-rate information in narrow frequency regions because of their wide dynamic range (Colburn, 1981; Delgutte, 1987; Viemeister, 1988a, 1988b; Winslow and Sachs, 1988; Winter and Palmer, 1991). However, when models based on cat AN fibers have been used to quantify the total information available in a restricted characteristic-frequency (CF) region with physiological distributions of the SR groups, performance has been predicted to degrade as the level increases above 40 dB SPL (Colburn, 1981; Delgutte, 1987; Viemeister, 1988a, 1988b; Winslow and Sachs, 1988), which is inconsistent with Weber's law and with trends in human performance (Viemeister, 1974, 1983; Carlyon and Moore, 1984). Delgutte (1987) demonstrated that Weber's law could be achieved in single CF-channels by processing high-threshold, LSR AN fibers more efficiently than low-threshold, high-SR (HSR) fibers. He showed that the ''near-miss'' to Weber's law (i.e., a slight improvement in performance as level increases), which is observed in human performance for tones in quiet (e.g., McGill and Goldberg, 1968; Rabinowitz *et al.*, 1976; Jesteadt *et al.*, 1977; Florentine *et al.*, 1987), could be obtained by combining information across CF channels that individually achieved Weber's law. This idea is similar to the assumption made by Florentine and Buus (1981) in their excitation-pattern model.

While there is anatomical evidence that AN fibers with different thresholds and SRs have different patterns of projection to the cochlear nucleus (e.g., Fekete *et al.*, 1984; Rouiller *et al.*, 1986; Liberman, 1991, 1993), there is no strong physiological evidence for the type of preferential processing of LSR fibers used by Delgutte (1987). In addition, the wide dynamic range of LSR fibers depends on the compressive basilar-membrane (BM) responses (Sachs and Abbas, 1974), and there appears to be much less compression at low frequencies than at high frequencies (Cooper and Rhode, 1997; Hicks and Bacon, 1999). Reduced compression at low frequencies is consistent with the absence of nonsaturating (''straight'') rate-level curves at low frequencies in guinea pig (Winter and Palmer, 1991). Thus, it is desirable to investigate other potential sources of information that could produce Weber's law in narrow frequency regions, especially at low frequencies.

The cochlear amplifier is potentially relevant for the encoding of sound level in narrow frequency regions because the associated nonlinear properties influence primarily CFs near the frequency of a tone. Specifically, the nonlinear near-CF response properties include both compressive magnitude responses (Rhode, 1971; Ruggero *et al.*, 1997), as well as level-dependent phase shifts [BM: Ruggero *et al.*, 1997; inner-hair cell (IHC): Cheatham and Dallos, 1998; AN: Anderson *et al.*, 1971]. In evaluating the potential of the cochlear amplifier to extend the dynamic range of the auditory system, it is important to consider several limiting transformations that occur between the BM and the AN. These include (1) saturating rate-level curves (Kiang *et al.*, 1965; Sachs and Abbas, 1974), which act to limit the effect of nonlinear gain on average discharge rate, (2) roll-off of phase-locking at high frequencies (Johnson, 1980; Joris *et al.*, 1994a), which limits nonlinear phase encoding, and (3) randomness of AN responses (Young and Barta, 1986; Miller *et al.*, 1987; Winter and Palmer, 1991; Delgutte, 1996), which limits overall psychophysical performance. Thus, it is important to consider the encoding of information in the AN, not just the compression in BM responses, when evaluating the significance of the cochlear amplifier.

The nonlinear phase changes associated with the cochlear amplifier, which have not been studied in as much detail as the compressive magnitude responses (Sachs and Abbas, 1974; Winter and Palmer, 1991; Moore, 1995; Moore and Oxenham, 1998), are a focus of the present study. These phase cues continue to encode changes in stimulus level at high levels, despite the saturation of average rate above 40 dB SPL for the majority of AN fibers (Sachs and Abbas, 1974; May and Sachs, 1992), and thus may provide a partial solution to the dynamic-range problem. It is important to consider physiologically realistic mechanisms that could make use of the information provided by nonlinear phase shifts. While an absolute phase reference is presumably unavailable to the central nervous system, a relative phase reference can be obtained by comparing across neighboring CFs because the changes in phase are different in adjacent CFs. Carney (1994) demonstrated that nonlinear phase shifts on single AN fibers result in systematic changes in the temporal discharge patterns across CF (i.e., spatio-temporal patterns that vary with level over a wide dynamic range), and hypothesized that changes in spatio-temporal patterns may be important for the encoding of sound level. Any two AN fibers with different CFs have a relative phase difference that varies with level, independent of the absolute phase of the stimulus. Thus, a mechanism that compared the relative timing of two AN fibers would be sensitive to changes in level, without requiring an absolute phase reference.

The present study considers monaural, cross-frequency coincidence detection as a mechanism for decoding the nonlinear phase cues provided by the cochlear amplifier. Coincidence detection is a physiologically realistic mechanism, because any neuron with multiple subthreshold inputs acts as a coincidence detector (Carney, 1994; Joris *et al.*, 1994a). Carney (1990) has shown that several response types in the antero-ventral cochlear nucleus (AVCN) with low CF were sensitive to changes in relative phase across their inputs, consistent with a coincidence detection mechanism. Joris *et al.* (1994a, 1994b) have reported enhanced synchronization in low-CF bushy cells in the AVCN in response to CF tones and in high-CF primary-like-with-notch cells in re-

sponse to low-frequency tones, consistent with coincidence detection at all CFs in globular bushy cells. In addition, there is much evidence for coincidence detection in the binaural system (Yin and Chan, 1990; Goldberg and Brown, 1969; Rose *et al.*, 1966; Yin *et al.*, 1987; Joris *et al.*, 1998). Neurons in the medial superior olive and inferior colliculus have responses that are consistent with coincidence detection between inputs from each ear as a mechanism for decoding interaural time differences that are known to be important for sound localization (reviewed by Colburn, 1996).

In the present study, methods from signal detection theory (SDT) were combined with an analytical nonlinear AN model and a simple coincidence-counting model. Analytical AN models, which represent functional descriptions of neural activity to a well-defined class of stimuli, have been used previously with SDT to evaluate psychophysical performance limits based on the stochastic activity in AN responses (e.g., Siebert, 1965, 1968, 1970; Colburn, 1969, 1973, 1977a, 1977b, 1981). Computational auditory models have also been combined with SDT to evaluate psychophysical performance (e.g., Dau *et al.*, 1996, 1997; Gresham and Collins, 1998; Huettel and Collins, 1999; see Heinz *et al.*, 2001a for review). The present study quantifies the relative contributions of nonlinear magnitude and nonlinear phase responses to level encoding by using four versions of the analytical AN model, which included and excluded the nonlinear gain and nonlinear phase responses in all possible combinations.

II. METHODS

A. Auditory-nerve model

The nonlinear AN model used in the present study is an extension of simple linear analytical AN models used by Siebert (1965, 1968, 1970) and by Colburn (1969, 1973, 1977a, 1977b, 1981). The linear AN model was modified to include the main properties of the cochlear nonlinearities associated with the active process, including (1) nonlinear compressive responses from 30 to 120 dB SPL, (2) compressive nonlinearity restricted to ''near-CF'' regions, (3) compression strength that varies with CF, (4) systematic phase shifts of up to $\pm\pi/2$ above and below CF, (5) no phase shifts at CF, and (6) dynamic range of each SR group that depends on the compressive magnitude response. The response properties of the model are described in the text below, while the assumptions and equations used to specify the model are described in Appendix A. This analytical nonlinear AN model was purposefully kept as simple as possible in order to provide greater intuition and to allow the contribution of each nonlinear property to be investigated separately. The analyses presented below are not limited to this AN model, however, and could be pursued in the future with more complex computational nonlinear models.

The statistics of the AN discharges are modeled by a nonstationary Poisson process with rate function $r(t)$. The phase-locked response of the ith AN fiber (with characteristic frequency CF_i) to a tone burst of level L, frequency f_0, duration T, and phase ϕ, is described by a time-varying rate function similar to that used by Colburn (1981), i.e.,

$$r_i(t;L,f_0,T,\phi) = \frac{\overline{r}[L_{\mathrm{eff}}(L,f_0,\mathrm{CF}_i)]}{I_0\{g[L_{\mathrm{eff}}(L,f_0,\mathrm{CF}_i),f_0]\}} \times \exp\{g[L_{\mathrm{eff}}(L,f_0,\mathrm{CF}_i),f_0] \times \cos[2\pi f_0 t + \theta(L,f_0,\mathrm{CF}_i) + \phi]\}, \quad (1)$$

where $I_0\{g\}$ is the zeroth-order modified Bessel function of the first kind (equal to the time average of the exponential term). Both the average rate $\overline{r}[L_{\mathrm{eff}}]$ and synchrony $g[L_{\mathrm{eff}},f_0]$ are affected by saturating nonlinearities, where the effective level L_{eff} is determined by the nonlinear BM filtering properties and by the level and frequency of the tone. The term $g[L_{\mathrm{eff}},f_0]$ also depends on the stimulus frequency f_0 such that the strength of phase locking decreases at high frequencies. The nonlinear phase response $\theta(L,f_0,\mathrm{CF}_i)$ depends on the level and frequency of the tone as well as on the CF of the AN fiber (see Anderson *et al.*, 1971; Ruggero *et al.*, 1997), and is described similarly to Carney *et al.* (1999). The stimulus is assumed to have random phase ϕ (uniformly distributed) in order to avoid the assumption that the phase of the tone is known to the detector.

Many basic response properties of the AN model are illustrated in Fig. 1. Panels (a)–(c) show the implementation of the nonlinear magnitude responses, which are consistent with physiological data from Ruggero *et al.* (1997). Normalized BM response versus frequency for a 10-kHz CF is shown in Fig. 1(a), for a range of levels. The filters are triangular at low levels, consistent with the linear AN models used by Siebert (1965, 1968, 1970) and Colburn (1969, 1973, 1977a, 1977b, 1981) to fit AN tuning curves in cat. The maximum gain of the cochlear amplifier (i.e., the gain relative to high levels, or equivalently the amount of compression relative to low levels) occurs at CF and is equal to 60 dB for this CF. The nonlinear gain decreases as tone frequency moves away from CF, and the response is linear well away from CF (roughly more than $\pm 1/2$ octaves). Figure 1(b) shows BM output at CF as a function of level for the 10-kHz place. The solid curve represents the nonlinear BM response, while the dashed line represents the linear version of the model. The compressive region extends from 30 to 120 dB SPL, and the model responses are linear below this range. Figure 1(c) shows the cochlear-amplifier gain at CF as a function of CF. The maximum gain decreases as CF decreases, with 60 dB of gain for frequencies above 8 kHz, 20 dB of gain for frequencies below 500 Hz, and a smooth transition for CFs in between. This pattern of nonlinear gain across CF is consistent with both physiological and psychophysical evidence, although the exact amount of gain at low frequencies is still unclear. The majority of BM data has been obtained at high CFs and indicates a maximum gain of roughly 50–60 dB (Ruggero *et al.*, 1997; Nuttall and Dolan, 1996). The BM data at low CFs is less abundant, but indicates reduced nonlinearity at low CFs (e.g., Cooper and Rhode, 1997). Hicks and Bacon (1999) presented psychophysical evidence that cochlear nonlinearity is reduced at low frequencies and is characterized by a gradual, rather than steep, transition as CF decreases.

Figures 1(d) and (f) illustrate how average rate varies

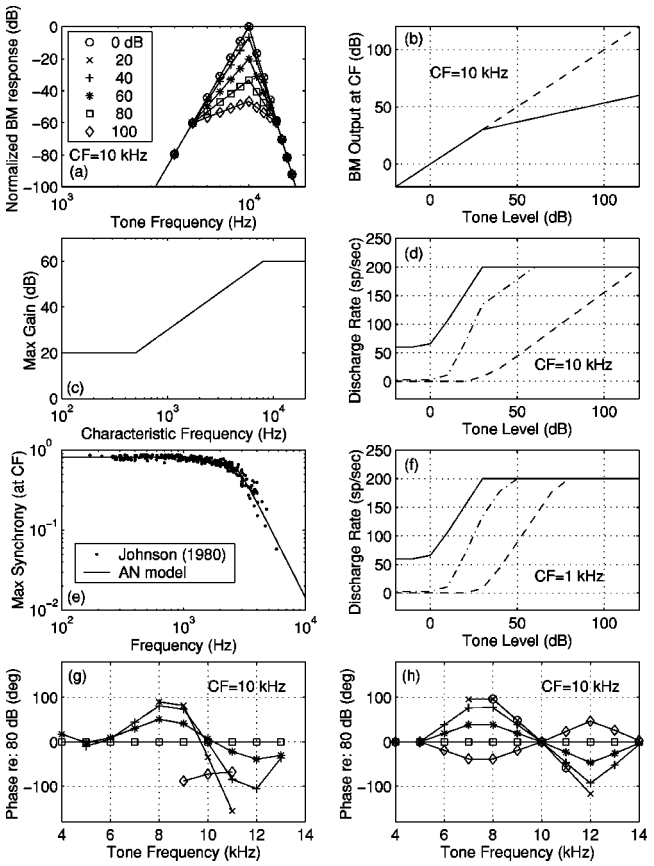

FIG. 1. Nonlinear AN model response properties. (a) Normalized basilar-membrane (BM) response for a 10-kHz place as a function of frequency for levels ranging from 0–100 dB SPL. (b) BM output at CF as a function of level for a 10-kHz place (solid: nonlinear; dashed: linear). (c) Nonlinear gain at CF as a function of CF. (d) Rate-level curves for a 10-kHz tone at CF for three SR groups (HSR: solid, MSR: dashed–dotted, LSR: dashed). (e) Maximum synchrony versus frequency. Model responses are compared to data measured in cat (Johnson, 1980). (f) Rate-level curves for a 1-kHz tone. (g) BM phase-response areas (phase relative to 80 dB SPL) from chinchilla for a 10-kHz CF (data from Ruggero *et al.*, 1997). (h) AN-model phase-response areas for a 10-kHz CF [(g,h): same symbols as in (a)].

with level for the three spontaneous-rate (SR) groups of AN fibers at high and low frequencies, respectively. The AN model represents all fibers within each SR population with a fixed threshold and SR. Based on data from Liberman (1978), SR values of 60, 3, and 0.1 sp/s, thresholds of 0, 10, and 30 dB SPL, and population percentages of 61%, 23%, and 16%, were used for the HSR, medium-SR (MSR), and LSR populations, respectively. A saturated rate of 200 sp/s was used for all three SR groups. Note that the rate-level curves at low frequencies are either ''saturating'' or ''sloping saturating,'' while at high frequencies there is a third class of ''straight'' rate-level curves. This pattern is consistent with rate-level curves in guinea pig described by Winter and Palmer (1991), who found no ''straight'' rate-level curves below 1.5 kHz, and it results from the decrease in cochlear compression as frequency decreases. Figure 1(e) compares the rolloff in phase-locking versus frequency in the model to that in cat (Johnson, 1980).

Figure 1(g) illustrates nonlinear physiological BM phase responses for a 10-kHz CF (Ruggero *et al.*, 1997), while Fig. 1(h) shows the AN-model phase responses. Phase is plotted

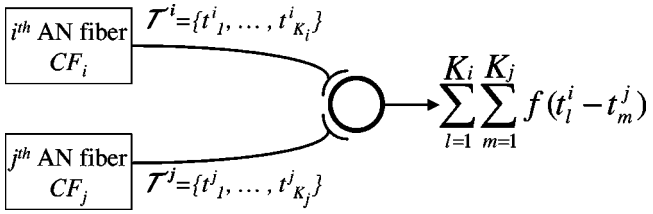

FIG. 2. Simple model of a monaural, cross-frequency coincidence counter. The coincidence detector receives two AN inputs with characteristic frequencies CF_i and CF_j, and discharge times $\mathcal{T}^i=t^i_1,\ldots,t^i_{K_i}$ and $\mathcal{T}^j=t^j_1,\ldots,t^j_{K_j}$, where t^i_l is the lth discharge on the ith AN fiber. The coincidence detector discharges if both inputs discharge within the narrow coincidence window $f(x)$. The output of the coincidence counter is the number of coincidences that occur within the duration of the stimulus.

relative to the phase at a high level (80 dB SPL) in both panels, where each curve represents a different tone level. Thus, any difference from zero represents a phase response that changes with level. The major properties of this nonlinear response, observed for BM responses at high frequencies (Geisler and Rhode, 1982; Ruggero *et al.*, 1997), and IHC (Cheatham and Dallos, 1998) and AN (Anderson *et al.*, 1971) responses at low frequencies, are that (1) phase lags as level increases for $f<\mathrm{CF}$, (2) phase leads as level increases for $f>\mathrm{CF}$, (3) there are no phase changes at CF, (4) the nonlinear-phase region is the same width in frequency as the nonlinear region for the magnitude response, and (5) the maximum phase shifts observed are roughly $\pm\pi/2$ and occur about half way into the nonlinear region. The nonlinear phase responses are consistent with broadened tuning as level increases and the associated changes in the phase-versus-frequency slope (i.e., the slope becomes more shallow as filters broaden).

All predictions in the present study were made with 120 distinct model CFs spaced logarithmically from 300 to 20 000 Hz. It was assumed that the total AN population consists of 30 000 total AN fibers (Rasmussen, 1940) with CFs ranging from 20 to 20 000 Hz (Greenwood, 1990; also see review by Ryugo, 1992). Appendix A describes how the nonlinear-gain and nonlinear-phase properties of the model were included or excluded separately to evaluate the relative contribution of each property to level encoding.

B. Monaural, cross-frequency coincidence counting model

The present study uses a simple coincidence-counting model that was described by Colburn (1969, 1973, 1977a, 1977b) in his studies of binaural phenomena (Fig. 2). A coincidence detector receives two AN-fiber inputs, and is assumed to discharge only when the two input fibers discharge within a narrow temporal window. The output of the coincidence counter is the number of coincident discharges within the duration of the stimulus. The present use of the coincidence-counting model differs from that of Colburn only in the source of the two AN inputs. In the binaural model, each AN fiber was from a different ear and had the same CF. In the present study, the two AN inputs are from the same ear, but can have different CFs. In both studies, performance was assumed to depend only on the number of

coincidences between two AN fibers (i.e., the timing of the coincidences was ignored). The number of coincidences between two AN fibers with discharge times $\mathcal{T}^i=\{t_1^i,\ldots,t_{K_i}^i\}$ and $\mathcal{T}^j=\{t_1^j,\ldots,t_{K_j}^j\}$ is given by

$$\mathcal{C}_{ij}\{\mathcal{T}^i,\mathcal{T}^j\}=\sum_{l=1}^{K_i}\sum_{m=1}^{K_j} f(t_l^i-t_m^j), \tag{2}$$

where t_l^i is the lth discharge out of K_i on the ith AN fiber, and $f(\cdot)$ is a rectangular coincidence window with 10-μs width and unity height (see Colburn, 1969).

C. Evaluation of psychophysical performance limits

1. Optimal processing of AN responses

Psychophysical performance is limited in part by the random nature of AN responses (i.e., different responses are observed for two identical stimulus presentations). Psychophysical performance limits for discrimination experiments have been evaluated with methods from signal detection theory (SDT) by using a nonstationary Poisson process with a time-varying discharge rate $r(t)$ to describe the stochastic nature of AN discharges (e.g., Siebert, 1968, 1970; Colburn, 1969, 1973; Heinz, 2000; Heinz *et al.*, 2001a, 2001b). Heinz *et al.* (2001a) described a general computational method for evaluating psychophysical performance limits using any AN model that describes $r(t)$ for the stimulus conditions of interest. The analytical AN model used in the present study was implemented computationally, and psychophysical performance limits were evaluated based on two hypotheses for the type of information used to perform the task, *all-information* and *rate-place*. The all-information model assumes that the observations used by the optimal processor consist of the complete set of discharge times across the entire AN population, $\mathcal{T}=\{t_l^i\}_{i=1,\ldots,M;l=1,\ldots,K_i}$, where $M=30\,000$ total AN fibers, and K_i is the number of discharges on the ith AN fiber. Thus, the all-information model assumes that the processor makes optimal use of all available information from the AN (e.g., average-rate, synchrony, and phase information). The rate-place model assumes that the optimal processor only uses the number of discharges observed on each AN fiber, $\{K_i\}$.

Optimal performance for single-parameter discrimination experiments can be calculated using a likelihood-ratio test (van Trees, 1968) and has been shown to match the performance limits described by the Cramér–Rao bound (Heinz *et al.*, 2001a). The contribution of each AN fiber to a level discrimination task can be quantified by calculating the normalized sensitivity δ' to changes in stimulus level. [δ' is defined as the sensitivity d' per dB (see Durlach and Braida, 1969; Braida and Durlach, 1988; Heinz *et al.*, 2001a).] The square of the normalized sensitivity of the ith AN fiber in the all-information model is given by

$$(\delta'[\mathrm{CF}_i])^2=\int_0^T \frac{1}{r_i(t)}\left[\frac{\partial r_i(t)}{\partial L}\right]^2 dt, \tag{3}$$

where T is the duration of the stimulus (Siebert, 1970; Heinz *et al.*, 2001a). The total normalized sensitivity based on the population of AN fibers is the sum of the individual normalized sensitivities, $(\delta')^2=\Sigma_i(\delta'[\mathrm{CF}_i])^2$, based on the assumptions of independent AN fibers for deterministic stimuli (Johnson and Kiang, 1976; see also Heinz *et al.*, 2001a), and an optimal combination across AN fibers. The just-noticeable-difference (JND) in level is given by

$$\Delta L=\frac{1}{\sqrt{(\delta')^2}}. \tag{4}$$

Equation (3) describes the normalized sensitivity based on the all-information model; the normalized sensitivity based on rate-place information can be calculated with Eq. (3) by assuming that $r(t)$ is constant across the duration of the stimulus and equal to the average-discharge rate $\bar{r}$ [i.e., setting g to 0 in Eq. (1)]. Thus, the rate-place model does not include information from fine-time or onset responses and therefore predicts inferior performance to the all-information model. The contribution of temporal information in AN discharges can be discerned from a comparison between performance based on the all-information and rate-place models.

2. Performance based on coincidence counts

Performance based on the outputs of a set of coincidence counters was calculated and compared to rate-place, all-information, and human performance. While the all-information predictions represent the optimal performance of any decision device based on the AN discharge times, the coincidence mechanism represents a specific processor that uses the discharge times suboptimally. The number of discharges from a single coincidence detector, $\mathcal{C}_{ij}\{\mathcal{T}^i,\mathcal{T}^j\}$, is a simple function [Eq. (2)] of the two sets of Poisson AN discharge times, $\mathcal{T}^i$ and $\mathcal{T}^j$, and thus the statistics of the coincidence counts can be described (Appendix B). The performance of a single coincidence counter $\mathcal{C}_{ij}$ for level discrimination can be evaluated by calculating the sensitivity index

$$Q_{ij}=\frac{(E[\mathcal{C}_{ij}|L+\Delta L]-E[\mathcal{C}_{ij}|L])^2}{\mathrm{Var}[\mathcal{C}_{ij}|L]}, \tag{5}$$

where the just-noticeable difference for this coincidence counter, $\Delta L_{ij,\mathrm{JND}}$, corresponds to $Q_{ij}=1$. The sensitivity index Q_{ij} represents the commonly used sensitivity index $(d')^2$ if $\mathcal{C}_{ij}$ has a Gaussian distribution with equal variance under both hypotheses, L and $L+\Delta L$ (Green and Swets, 1966; van Trees, 1968). These two assumptions are reasonably accurate for characterizing just-noticeable differences based on a population of independent decision variables (Siebert, 1968, 1970; Colburn, 1969, 1973, 1977a, 1977b, 1981; Heinz *et al.*, 2001a), such as the population of coincidence counts in the present study (see below). Potential deviations from these assumptions do not significantly affect the characterization of performance based on the sensitivity metric Q (Colburn, 1981).

It can be assumed that $E[\mathcal{C}_{ij}|L]$ varies linearly over the incremental level range from L to $L+\Delta L_{\mathrm{JND}}$. Thus, the normalized sensitivity squared for a single coincidence counter, defined as $(\delta'_{ij})^2\triangleq Q_{ij}/(\Delta L)^2$, can be approximated as

$$(\delta'_{ij})^2 \simeq \frac{\left(\frac{\partial}{\partial L} E[C_{ij}|L]\right)^2}{\mathrm{Var}[C_{ij}|L]}. \quad (6)$$

The expectation and variance in Eq. (6) can be evaluated in terms of the stimulus parameters and the two AN CFs (Appendix B). The partial derivative with respect to level in Eq. (6) can be approximated computationally as the difference between the expected value at two slightly different levels divided by the incremental level difference (Heinz *et al.*, 2001a).

The total normalized-sensitivity-squared for a population of coincidence counters is given by the sum of the individual normalized-sensitivities-squared, if it is assumed that the population decision variable is an optimal linear combination of independent (uncorrelated) random variables (or an optimal combination of independent Gaussian random variables). In order to satisfy the independence assumption, it is assumed throughout the present study that no AN fiber innervates more than one coincidence counter. The JND based on coincidence counts is calculated from Eq. (4).

III. RESULTS

A. Distribution of rate, synchrony, and phase information across CF

In order to illustrate the potential benefit of nonlinear phase cues to the encoding of sound level, we first focus on level discrimination at high levels, where the dynamic-range problem is most prominent. Figure 3 illustrates the distribution and relative contributions of rate, synchrony, and phase cues across the AN population of high-spontaneous-rate (HSR) fibers for level discrimination of a 1-kHz, 100-dB SPL tone. The rate responses (i.e., average discharge rate as a function of CF) of the nonlinear-gain, linear-phase model are shown for two tones of slightly different level in panel (b). The more intense tone produces a wider activation pattern; however, the discharge rate for a wide range of CFs near the tone frequency is the same for both tones due to saturation. The distribution of rate information [i.e., normalized sensitivity squared, $(\delta'[\mathrm{CF}])^2$, for the rate-place model] shown in panel (c) illustrates which AN fibers across the population contribute information for level discrimination. The only rate information available for HSR fibers is at frequencies well away from the tone frequency (Siebert, 1965, 1968; also see Stevens and Davis, 1936; Steinberg and Gardner, 1937; Whitfield, 1967).

The situation of primary interest in this study is when information is restricted to AN fibers with CFs near the frequency of the tone. This situation is thought to occur in experiments that use a notched noise masker to limit the spread of excitation (e.g., Viemeister, 1974, 1983; Carlyon and Moore, 1984). A narrow frequency region that will be considered in the current study is indicated by the vertical dotted lines in Fig. 3. This region represents seven model CFs, three above and three below the CF equal to the tone frequency. The narrow frequency region for the 1-kHz tone is 896–1107 Hz and is similar to the notch width used by Carlyon and Moore (1984), which extended ±10% from the

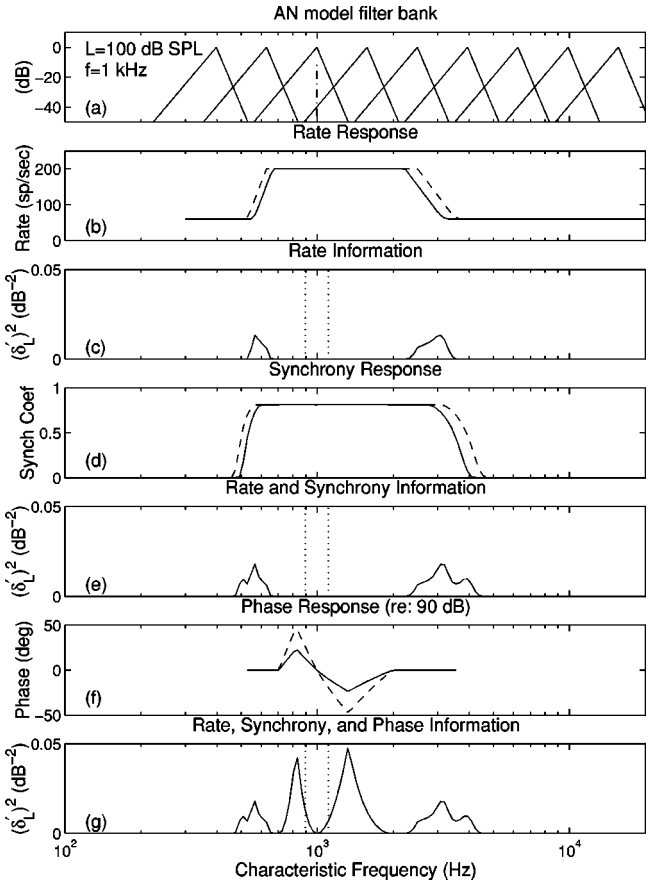

FIG. 3. Distribution of rate, synchrony, and phase information across the AN population of *high-spontaneous-rate fibers* for level discrimination of a low-frequency, high-level tone. (a) AN filter bank with a 1-kHz, 100-dB SPL tone. (b) Average discharge rate as a function of CF for two tones of slightly different level. (c) Average-rate information (normalized sensitivity squared) as a function of CF. The vertical dotted lines indicate the restricted-CF region used in the present study to emphasize the dynamic-range problem. (d) Synchrony coefficient (or vector strength, which ranges from 0 to 1, see Johnson, 1980) as a function of CF for both tones. (e) Information available from both rate and synchrony cues. (f) Normalized phase response (relative to 90 dB) for both tones. (g) Total information from rate, synchrony, and phase cues.

tone frequency. Humans are typically able to perform level discrimination well in the presence of a notched noise (e.g., Viemeister, 1974, 1983; Carlyon and Moore, 1984; Schneider and Parker, 1987); however, Fig. 3(c) shows that there is no average-rate information in HSR AN fibers within the narrow-CF region.

AN phase-locking has a different level dependence than average rate does, and thus it is important to examine the distribution of synchrony information in addition to rate information. Figure 3(d) shows the 1-kHz synchrony coefficient (or vector strength, which ranges from 0 to 1; see Johnson, 1980) for each tone plotted as a function of CF. Synchrony-level curves have thresholds that are roughly 20 dB below rate thresholds, and they typically saturate just above rate threshold (Johnson, 1980). The synchrony-response regions are thus slightly wider than the rate-response regions, but they are also saturated over a wide range of CFs near the tone frequency. The distribution of information available from both rate and synchrony information is shown in panel (e) and represents the all-information

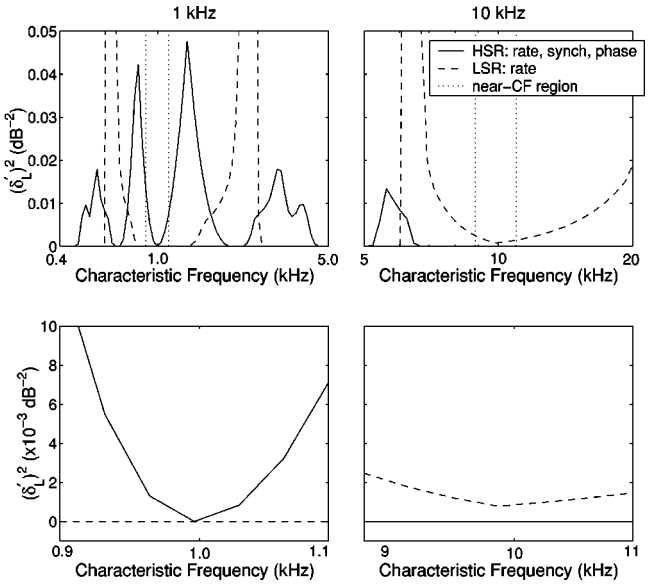

FIG. 4. Comparison of nonlinear phase information in *high-spontaneous-rate (HSR) fibers* and average-rate information in *low-SR fibers* for the encoding of high sound levels in CFs near the tone frequency. The distribution of information across the AN population is shown for level discrimination of 100-dB SPL low- (1 kHz, left column) and high-frequency (10 kHz, right column) tones. The HSR curves (solid) represent rate, synchrony, and phase information, while the LSR curves (dashed) represent only average-rate information. Physiologically realistic properties of HSR and LSR fibers were used to scale the predictions (see text). The vertical dotted lines in the top row represent the narrow-CF region discussed in the present study, which is magnified in the bottom row. Same stimulus conditions were used as in Fig. 3.

normalized sensitivity squared for the nonlinear-gain, linear-phase model. Similar to rate information, there is no synchrony information near the tone frequency for high levels due to saturation of the synchrony coefficient. The useful information from synchrony cues is spread further away from the tone than rate information due to lower synchrony thresholds (Colburn, 1981).

The distribution and relative contribution of nonlinear phase cues is illustrated in panels (f) and (g). The phase responses (relative to the phase at 90 dB SPL) of both tones are shown as a function of CF in panel (f) for the nonlinear-gain, nonlinear-phase model. Auditory-nerve fibers with CFs above and below the tone frequency have phase responses that change with level and thus contribute information. There are no changes in phase at CF, or well away from CF where the BM response is linear. The distribution of the total information provided from rate, synchrony, and phase cues is shown in panel (g), and represents the all-information normalized sensitivity squared for the nonlinear-gain, nonlinear-phase model. By comparing panels (e) and (g), the significant contribution of nonlinear-phase cues to the encoding of level can be seen. While there is no information for the CF equal to the tone frequency, there is significant phase information just below and just above the tone frequency. The amount of phase information is roughly twice as large as the rate and synchrony information. Most importantly for the dynamic-range problem, the only information available in the restricted-CF region is that from nonlinear phase cues.

Figure 4 compares the distribution of information across CF for HSR and LSR fibers at low and high frequencies [see Figs. 1(d) and (f)]. The contribution of nonlinear phase information in HSR fibers is compared to the contribution of average-rate information in LSR fibers. The limited-CF region is indicated by the vertical dotted lines in the top panels, and this region is magnified in the bottom panels. At low frequencies (left column), the HSR fibers (solid curve) contribute significant information from the nonlinear phase cues within the limited CF region. The LSR fibers (dashed curve) do not contribute any information within the limited CF region for the 1-kHz tone because the LSR fibers saturate at 80 dB [see Fig. 1(f)] due to the small amount of compression associated with the cochlear amplifier at low frequencies [Fig. 1(c)]. In contrast, at high frequencies (right column) the HSR fibers contribute no phase information due to the rolloff in phase locking [Fig. 1(e)], while the LSR fibers contribute significant average-rate information within the narrow CF region. The large amount of compression at high frequencies [Fig. 1(c)] results in very shallow (''straight'') rate-level curves for LSR fibers at high frequencies [Fig. 1(d)].

B. Predicted performance based on a narrow CF region

Performance based on a narrow CF region was explored by predicting the JND in level [ΔL; Eq. (4)] using only the information contained in a restricted set of model CFs (seven) surrounding the frequency of the tone. Performance was calculated for a low- (996 Hz) and a high-frequency (9874 Hz) tone, where the tone frequencies were chosen to be equal to one of the 120 model CFs. For the low and high tone frequencies, the near-CF regions used were 896–1107 Hz and 8882–10977 Hz, respectively. Performance was predicted for the HSR, MSR, LSR, and total populations of AN fibers, based on the physiological proportions described by Liberman (1978). Predicted level-discrimination performance is compared for the rate-place and all-information models, where information in the seven model CFs was assumed to be combined optimally, and was scaled to account for the number of AN fibers represented by each model CF. Performance for the monaural-coincidence scheme was calculated based on the same number of total AN fibers as the rate-place and all-information predictions. The seven model CFs in the narrow-frequency region were assumed to innervate a set of four coincidence counters, one of which had both CF inputs equal to the tone frequency. The other three coincidence counters received one CF input above and one below the tone frequency, which were both separated from the tone frequency by an equal number (one, two, or three) model CFs. Based on the assumption that each AN fiber innervates only one coincidence counter, one-half as many same-CF-input coincidence counters were included in the total coincidence population as were coincidence counters with different CF inputs. Thus, rate-place, all-information, and coincidence predictions are all based on the same set of AN fibers with CFs near the tone frequency. Three separate populations of coincidence counters were used associated with the three AN SR groups. This implementation is con-

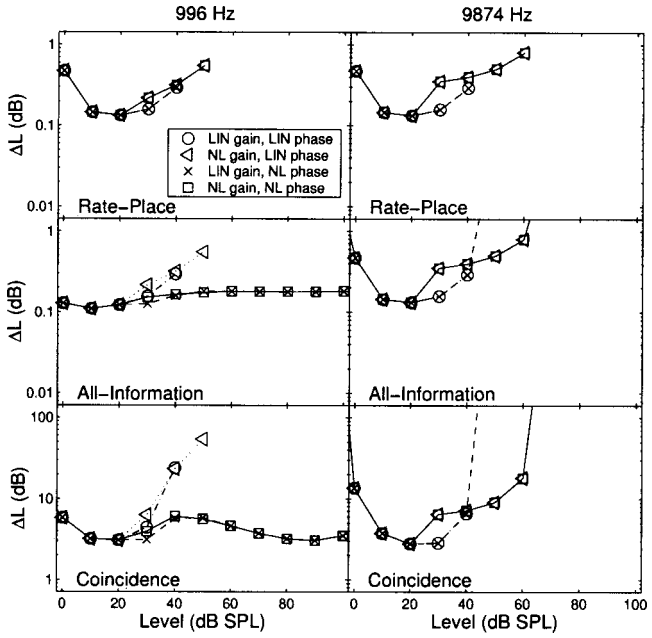

FIG. 5. Level-discrimination performance based on the population of *high-spontaneous-rate (HSR) fibers* in a narrow range of CFs near the tone frequency (see text). The just-noticeable difference ΔL is plotted as a function of stimulus level for a 996 Hz (left column) and a 9874 Hz (right column) tone (500-ms duration). Optimal performance based on average rate and all information is shown in the top and middle rows, respectively. Performance based on a set of monaural coincidence counters is shown in the bottom row. (Note the scale difference between rows.) Four versions of the AN model are shown in each panel to illustrate the effect of nonlinear gain and phase responses. Predictions from the four model versions are identical below 30 dB SPL. Levels for which symbols are not shown represent conditions in which there is no information available for a particular model (i.e., infinite JND).

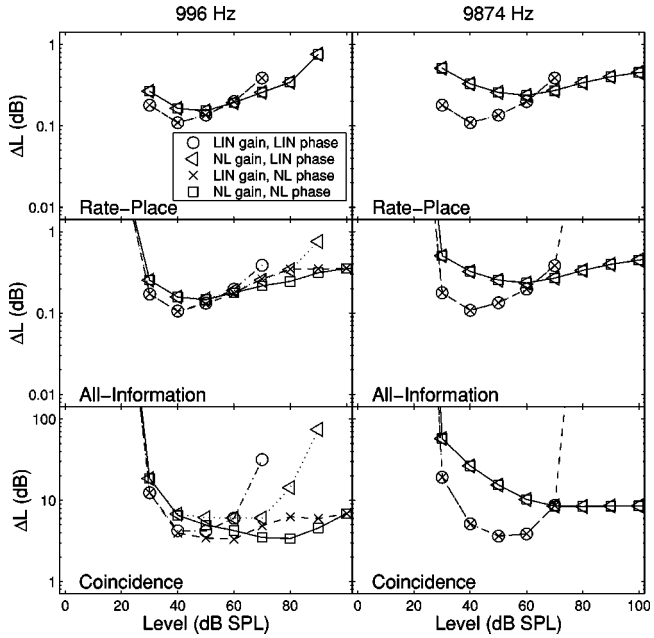

FIG. 6. Level-discrimination performance based on the population of *low-spontaneous-rate (LSR) fibers* in a narrow range of CFs near the tone frequency (see text). The symbols are the same as those used in Fig. 5.

sistent with anatomical studies that have demonstrated distinct projections of the different AN SR groups to the cochlear nucleus (Liberman, 1991, 1993).

Figure 5 shows level-discrimination performance based on the HSR fibers within the narrow frequency region in terms of ΔL as a function of stimulus level L for a low-frequency (left column) and a high-frequency (right column) tone. Rate-place, all-information, and coincidence performance are shown in the top, middle, and bottom panels, respectively. Note that the scale for the ordinate of the coincidence panel is different than those for the rate-place and all-information panels. In order to illustrate the relative contributions from nonlinear-gain and nonlinear-phase properties, performance based on four versions of the AN model is shown in each panel.

Average-rate information in HSR fibers encodes changes in level only over a limited dynamic range (Fig. 5, top row). When the nonlinear gain is included in the AN model, the dynamic range over which changes in level are encoded is extended by 10 dB at low frequencies and by 20 dB at high frequencies. The degradation in performance at 30 dB SPL for the nonlinear-gain models results from the compressive BM response that begins at 30 dB SPL [Fig. 1(b)]. The larger influence of the nonlinear gain at high frequencies compared with low frequencies is due to the CF dependence of the cochlear-amplifier gain.

The contributions of synchrony and nonlinear-phase information are demonstrated by comparing rate-place and all-information predictions (Fig. 5, top and middle rows). The role of synchrony information is most clearly illustrated with the linear-phase versions of the AN model. Synchrony information improves performance at low levels for the low-frequency tone; however, synchrony does not extend the dynamic range to higher levels due to the saturation of synchrony coefficients at lower levels than average rate (Colburn, 1981). The nonlinear phase responses extend the dynamic range for level discrimination up to at least 100 dB SPL at low frequencies. This is in sharp contrast to the range of rate-place information, which does not encode level changes in HSR fibers above 50 dB SPL. At high frequencies, rate-place and all-information predictions are essentially the same because of the sharp rolloff of phase-locking at high frequencies [Fig. 1(e)].

The predictions from the simple coincidence-counter model (Fig. 5, bottom row) follow the same general trends as the all-information predictions for both low and high frequencies, but are more than an order of magnitude worse than optimal all-information performance. The coincidence model utilizes the average-rate (and some of the synchrony) information that dominates performance below 30 dB SPL. The coincidence mechanism also successfully utilizes nonlinear phase cues provided by the cochlear amplifier at low frequencies.

Predictions based on the set of LSR AN fibers within the narrow frequency region are shown in Fig. 6. At both low and high frequencies, the nonlinear gain extends the dynamic range over which changes in level are encoded for the rate-place model; however, performance degrades significantly above 40 dB SPL at low frequencies. Changes in level of a 1-kHz tone are not encoded above 90 dB SPL in the average rate of the set of LSR fibers with CFs near the frequency of the tone. In contrast, LSR rate-place performance for a high-

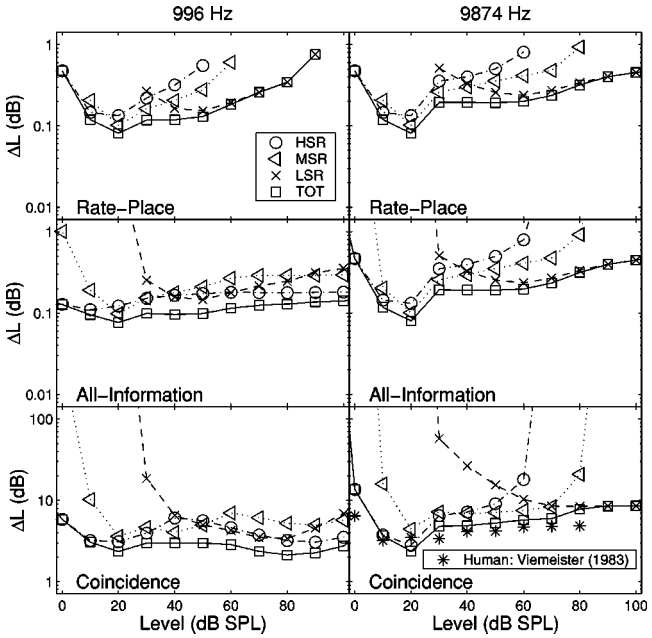

FIG. 7. Level-discrimination performance based on individual and combined spontaneous-rate groups in a narrow range of CFs near the tone frequency (see text). The just-noticeable difference ΔL for the nonlinear-gain, nonlinear-phase AN model is plotted as a function of stimulus level for a 996 Hz (left column) and a 9874 Hz (right column) tone (500-ms duration). Optimal performance based on average rate and all information is shown in the top and middle rows, respectively. Performance based on a set of monaural coincidence counters is shown in the bottom row. (Note the scale difference between rows.) HSR: high-spontaneous-rate; MSR: medium-spontaneous-rate; LSR: low-spontaneous-rate; TOT: optimal combination of all three SR groups. Levels for which symbols are not shown represent conditions in which there is no information available (i.e., infinite JND). Human data for level discrimination of a 200-ms high-frequency noise band (6–14 kHz) in the presence of a notched noise is shown by the stars in the bottom right panel (Viemeister, 1983).

frequency tone is roughly constant across a wide dynamic range, up to 100 dB SPL. The all-information predictions demonstrate that the nonlinear phase responses extend the dynamic range of LSR fibers at low frequencies up to 100 dB SPL. The coincidence predictions (Fig. 6, bottom row) at low frequencies show a small benefit from the nonlinear gain responses; however, performance based on nonlinear gain alone significantly degrades above 70 dB SPL. The benefit from the nonlinear-phase cues is also seen in performance based on the coincidence counters, extending the dynamic range beyond that based on nonlinear gain alone. At high frequencies, coincidence performance is constant above 70 dB SPL when the nonlinear gain is included in the AN model.

The contribution of each of the three SR groups to level-discrimination performance based on the narrow range of CFs is shown in Fig. 7 for both low- and high-frequency tones. The rate-place predictions illustrate that the HSR and MSR fibers are primarily responsible for performance at low levels, while the LSR fibers are responsible at high levels (roughly above 50 dB SPL at both low and high frequencies). Performance based on the combination of average-rate information in the three SR groups degrades by an order of magnitude between 20 and 90 dB SPL at low frequencies, and no changes in level are encoded above 90 dB SPL (see also Colburn, 1981; Delgutte, 1987). Changes in level are encoded much more consistently across level at high frequencies as a result of the large amount of cochlear compression at high frequencies.

The all-information predictions (Fig. 7, middle row) based on all three SR groups are roughly constant across a dynamic range of 100 dB at low frequencies, unlike the rate-place predictions. Thus, Weber's law is achieved based on information within a narrow range of CFs at low frequencies only when nonlinear-phase information is included. Furthermore, performance based on the HSR fibers is as good and often better than performance based on the MSR and LSR fibers for low frequencies, especially at high levels.

Performance at low frequencies based on the populations of coincidence counters (Fig. 7, bottom left panel) demonstrates roughly the same pattern as the all-information predictions, but is roughly an order of magnitude worse than optimal performance. Performance is roughly constant across a wide dynamic range and is primarily determined by the HSR fibers. At high frequencies, performance based on the coincidence counters is also roughly constant from 10 to 100 dB SPL and is determined by HSR fibers at low levels, by MSR fibers at medium levels, and by LSR fibers at high levels. For comparison, human performance for level discrimination of a high-frequency, bandpass noise (6–14 kHz) in a noise masker with a 6–14 kHz notch is shown by the stars (Viemeister, 1983).

C. Predicted performance based on entire population (all CFs)

Predicted performance based on the entire population of AN fibers (i.e., all CFs) was compared to human performance in a pure-tone level-discrimination task in quiet. Rate-place and all-information predictions [Eq. (4)] were based on the optimal combination of information from the 120 model CFs. The same four coincidence counters were used for each CF as in the narrow-CF predictions described above. The total normalized sensitivity squared was the sum of the individual normalized-sensitivities-squared from each of the four coincidence counters at each of the 120 model CFs.[1] In this implementation, each AN fiber innervated only one coincidence counter, and thus the normalized-sensitivities-squared could be summed based on the assumption of independent AN fibers.

Predicted rate-place, all-information, and coincidence performance based on the entire HSR population is shown in Fig. 8 for low- and high-frequency, 500-ms tones. Rate-place performance (top row) based on the linear AN model is flat above 20 dB SPL for the low-frequency tone, consistent with the predictions of Weber's law based on the spread of excitation (Siebert, 1968). For the high-frequency tone, there is a small rise in ΔL above 60 dB SPL for the linear AN model. This rise is due to the upper side of the excitation spreading beyond the highest CF, and it is consistent with the expected $\sqrt{2}$ reduction in ΔL due to the loss of one-half of the information. There is only a small effect of nonlinear gain on rate-place performance based on the population of CFs. The degradation in performance for the high-frequency tone at mid-levels results from the large amount of compression at

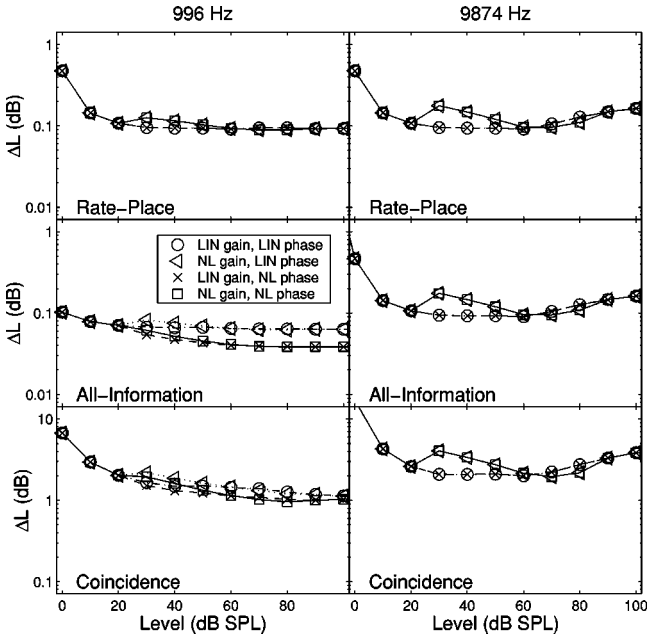

FIG. 8. Level-discrimination performance based on the total population of *high-spontaneous-rate (HSR) fibers*. The symbols are the same as those used in Fig. 5.

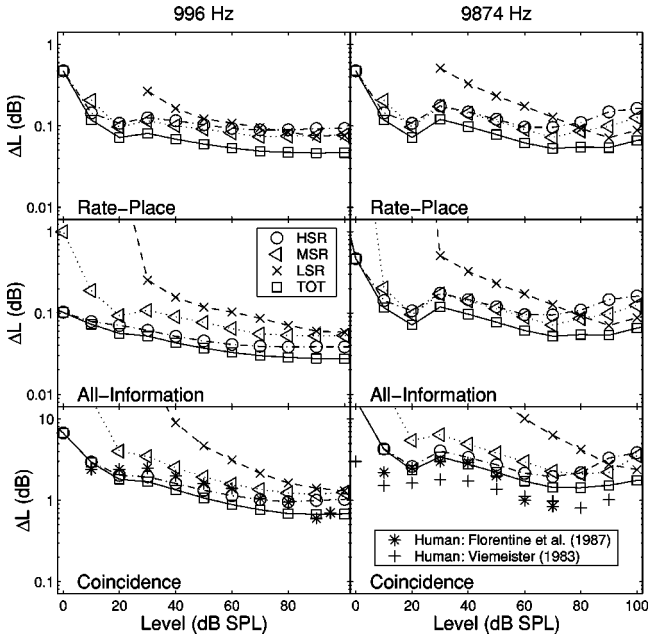

FIG. 9. Level-discrimination performance based on the total population of individual and combined spontaneous-rate groups (same symbols as Fig. 7). Human data for level discrimination of 500-ms tones measured as a function of sensation level is shown by the stars in the bottom left and right panels (Florentine *et al.*, 1987). Human level–discrimination data for a 200-ms high-frequency noise band (6–14 kHz) in quiet is shown by the plus symbols in the bottom right panel (Viemeister, 1983).

high frequencies. The presence of a mid-level bump at high, but not low, frequencies is consistent with human performance (Florentine *et al.*, 1987). At low frequencies, synchrony improves all-information performance (Fig. 8, middle row) for the linear AN model by a factor of five at 0 dB SPL, and by a factor of slightly less than two for higher levels. Weber's law is again predicted above 20 dB SPL based on the contributions of rate and synchrony information.

The near-miss to Weber's law is present in the low-frequency predictions when the nonlinear phase responses are included in the AN model. This is consistent with the nonlinear phase responses producing Weber's law within narrow-CF regions (Fig. 5), and the combination of information across CFs producing the near-miss to Weber's law. Predicted trends based on the population of coincidence counters (Fig. 8, lower row) generally resemble the all-information predictions at both low and high frequencies, with the exception that the benefit from synchrony information at very low levels is not observed. Overall, nonlinear gain and nonlinear phase have only a small effect on predicted level-discrimination performance in quiet due to spread of excitation, which is dominated by *linear*, off-CF responses.

The contribution of the three SR groups to the predicted performance based on the total AN population is shown in Fig. 9 for the nonlinear AN model. The rate-place predictions for the low-frequency tone demonstrate that each of the three SR groups contribute essentially equally above 50 dB SPL. Performance based on the total population of AN fibers (squares) decreases only slightly between 30 and 80 dB SPL. Rate-place predictions at high frequencies show that both the HSR and MSR population have a mid-level bump, while the LSR population does not. Performance below 70 dB SPL is determined primarily by the HSR and MSR fibers, while the LSR fibers determine performance above 90 dB SPL.

Predictions based on the populations of coincidence counters are shown in the bottom row of Fig. 9 and are compared to human performance measured by Florentine *et al.* (1987) as a function of sensation level for the same low- and high-frequency tone conditions.[2] Human performance measured by Viemeister (1983) for level discrimination of a high-frequency, narrow-band noise in quiet is shown for comparison in the bottom right panel. At low frequencies, performance based on the HSR population is always better than performance based on the MSR and LSR populations, similar to the all-information predictions. Above 90 dB SPL, all three SR groups contribute essentially equally. Overall performance based on the total population of coincidence counters is more than an order of magnitude worse than optimal performance, but matches human performance very closely. Predicted performance is slightly better (within a factor of 2) than human performance at most levels. The slope of the near-miss to Weber's law observed in the human performance is matched by the coincidence predictions for the low-frequency tone, as well as by the near-miss beginning at 30 dB SPL. The near-miss in the coincidence predictions results primarily from the nonlinear-phase cues (which begin at 30 dB SPL) in the HSR fibers, and it is not influenced by the population of LSR fibers.

At high frequencies (Fig. 9, bottom right panel), coincidence performance based on the HSR fibers is best among the three SR groups below 80 dB SPL. Coincidence performance based on the total AN population matches the human performance very closely and is within a factor of 2 of both data sets at all levels. The nonmonotonic dependence on level (the "mid-level bump") observed in both sets of human data is also demonstrated in the coincidence predictions. The

level at which the bump occurs is well predicted by the coincidence performance. The size of the bump in the coincidence performance matches the data from Viemeister (1983) and is slightly smaller than the data from Florentine *et al.* (1987). A slight rise in ΔL as level increases at high levels is present in the coincidence performance and is predicted based on the spread of the high-frequency information beyond the highest CF in the model. A slight rise is also often observed in human data when plotted as a function of SPL (Florentine *et al.*, 1987).

IV. DISCUSSION

It has often been suggested that the cochlear amplifier is responsible for the extremely wide dynamic range of the auditory system (e.g., Yates, 1995). However, this suggestion has typically been based solely on the compressive magnitude response observed on the basilar membrane. The present study quantifies the information available for level discrimination in the auditory nerve (AN) with and without the nonlinear gain and nonlinear phase responses that are associated with the cochlear amplifier.

A. The benefit of the cochlear amplifier for extending the dynamic range within narrow CF regions

The encoding of sound level within narrow CF regions has been studied psychophysically using notched-noise maskers; however, understanding mechanisms by which stimulus level within restricted CF regions can be robustly encoded has important implications for wide-band stimuli (such as speech), which often have independent information in many frequency regions.

1. Nonlinear gain

The ability of humans to discriminate changes in level consistently across a wide range of levels in Viemeister's (1983) notched-noise experiment has been interpreted as demonstrating that Weber's law is achieved based on average rate within a narrow range of CFs (e.g., Delgutte, 1987). The notched-noise masker is presumed to mask the CFs away from the signal, and the high-frequency signal is presumed to rule out temporal information. The present predictions support this idea at high frequencies, where the amount of cochlear compression is large enough that the LSR fibers can encode changes in sound level at high levels (Fig. 7). Figure 6 demonstrates that the ability of LSR fibers to encode changes in high sound levels is due to the nonlinear (level-dependent) gain (i.e., compression) associated with the cochlear amplifier. Changes in level of the high-frequency tone were only encoded up to 70 dB SPL in the LSR fibers when the nonlinear gain response was removed from the AN model, but were encoded up to 100 dB SPL with the nonlinear gain.

At low frequencies, however, the average-rate information in a narrow CF region was not adequate to account for Weber's law. There was not enough cochlear compression at low frequencies to encode changes in level across the entire human dynamic range in the average rate of any of the three SR groups (Fig. 7). The model LSR fibers, which have a sloping saturation, only encode changes in level of the low-frequency tone up to 90 dB SPL based on average rate, and performance degrades significantly above 50 dB SPL. This result is consistent with predictions of level-discrimination performance based on cat AN fibers, for which ''straight'' rate-level curves are not observed (e.g., Sachs and Abbas, 1974; Delgutte, 1987; Viemeister, 1988a, 1988b; Winslow and Sachs, 1988). In contrast, Winter and Palmer (1991) predicted that level-discrimination performance for a 1-kHz tone based on guinea-pig AN fibers that innervate a single IHC was better than human performance up to at least 110 dB SPL; however, their model used compression values that were primarily determined from high-frequency fibers, and thus their model may not account for the reduced cochlear compression at low frequencies. Thus, while LSR fibers have been implicated in the encoding of sound level at high levels, they do not appear to quantitatively solve the dynamic-range problem at low frequencies.

2. Nonlinear phase

The nonlinear phase responses associated with the cochlear amplifier have rarely been considered for their ability to extend the dynamic range of the auditory system (Carney, 1994); however, they are significant because the wide dynamic range of their information about changes in level is present in all AN fibers, including the HSR fibers that comprise the majority of the AN population. Such a representation of level is preferred to the level-dependent combination schemes across SR groups that are required for average-rate information to account for level discrimination across a wide range of levels (Delgutte, 1987; Winslow *et al.*, 1987; Viemeister, 1988a, 1988b). For example, Winslow *et al.* (1987) have suggested that level could be encoded based on average rate with a level-dependent selective processor that relies on HSR fibers at low sound levels and LSR fibers at high levels (see review by May *et al.*, 1997). Figure 7 demonstrates that the nonlinear phase responses within a narrow range of CFs support Weber's law at low frequencies based on a combination of the three SR groups that is anatomically realistic (Liberman, 1978). In fact, performance based on the near-CF HSR fibers alone is relatively flat across the entire range of human hearing.

Carney (1994) has illustrated schematically how nonlinear phase shifts on single AN fibers produce systematic temporal patterns across CF (i.e., spatio-temporal patterns). She showed responses for a bank of model AN fibers with different CFs as a function of time for several stimulus levels (Fig. 5 Carney, 1994). The main feature of the spatio-temporal patterns is that, as level increases, the trajectory across CF of the peaks in the discharge probability as a function of time becomes steeper (i.e., the responses across CF become more coincident). This motivated her to propose that sound level may be encoded in the spatio-temporal discharge patterns of AN fibers, and that an across-frequency coincidence mechanism could utilize these level cues at medium to high levels. Figure 7 demonstrates quantitatively that a set of monaural, cross-frequency coincidence counters can encode sound level robustly across the entire range of human hearing based on AN fibers within a narrow range of CFs for both low- and high-frequency tones.

Because the cochlear amplifier acts primarily in near-CF regions, the benefits from both gain and phase cues for extending the dynamic range within narrow-CF regions are particularly useful for complex stimuli such as speech, where spread of excitation is limited. This suggestion is consistent with the general finding that hearing-impaired listeners have the most difficulty with complex stimuli in difficult listening conditions where spread of excitation may not be possible (Moore, 1995). Due to the rolloff in AN phase-locking above 2–3 kHz, the greatest benefit from nonlinear-phase cues is at low frequencies; however, the majority of important speech information is at low frequencies. The ability of nonlinear-phase information to account for Weber's law in narrow-CF regions at low frequencies (and the inability of average-rate information to do so), suggests that nonlinear-phase cues should be considered in the encoding of complex stimuli at high stimulus levels. Loss of the cochlear amplifier would be expected to degrade the representation of complex stimuli in impaired ears due to loss of the nonlinear-phase cues; however, this impairment would not be observed in physiological studies that quantify the reduction of AN information in impaired animals based only on average-rate and synchronized-rate responses (e.g., Miller *et al.*, 1997, 1999). In contrast, analyses of rate representations in the cochlear nucleus would be expected to demonstrate an impairment in the encoding of complex stimuli at high stimulus levels in impaired animals. The ability of monaural coincidence counters to encode changes in sound level at low frequencies across a much wider dynamic range than average-rate information in the AN may provide a basis for reports of enhanced rate representations in the cochlear nucleus. Blackburn and Sachs (1990) and May *et al.* (1998) have reported that rate representations of speech sounds are enhanced in the ventral cochlear nucleus (e.g., chopper neurons and primary-like units with low SR) compared with the AN in normal-hearing animals (reviewed by May *et al.*, 1997). Transient-chopper and primary-like-with-notch neurons in the cochlear nucleus have been shown to be sensitive to phase transitions across frequency, consistent with coincidence detection (Carney, 1990).

B. Pure-tone level discrimination in quiet

1. Near-miss to Weber's law at low frequencies

The present predictions suggest that the only effect of the nonlinear responses associated with the cochlear amplifier for level discrimination of low-frequency tones is that the near-miss, rather than Weber's law, is predicted based on the nonlinear phase responses. The degree of the near-miss in the all-information predictions is larger than in the rate-place predictions, but only matches human performance in the coincidence-detection predictions. Although there are many intuitive reasons to believe that cochlear nonlinearity would strongly influence level discrimination of tones, the predicted effect for tones in quiet is quite small. This nonintuitive finding results from the fact that at medium to high sound levels, where cochlear compression has a strong effect on near-CF BM responses, the primary information about changes in level is contributed by HSR fibers with CFs away from the frequency of the tone. Thus, the CFs that are dominating performance at medium and high sound levels are responding linearly because the nonlinear effects associated with the cochlear amplifier are restricted to near-CF frequencies.

Several other physiological models have produced a near-miss with only low-threshold, HSR fibers. Teich and Lachs (1979) demonstrated the near-miss with a rate-place model that had more rounded filter shapes than Siebert's filters and that incorporated the effects of refractoriness on AN discharge-count variance. Delgutte's (1987) model included average tuning-curve shaped filters and realistic AN-count variance. Heinz *et al.* (2001a) predicted a significant near-miss based on a computational AN model with linear gamma-tone filters and Poisson discharge statistics. The ability of many models to predict the near-miss based on different mechanisms supports the idea suggested by Viemeister (1988a) that the near-miss to Weber's law is not a critical aspect of the dynamic-range problem, and that the robust encoding of sound level in narrow-CF regions is the most important issue.

2. Mid-level bump at high frequencies

A puzzling detail of human level discrimination of tones in quiet is that performance is nonmonotonic at high frequencies, in contrast to the consistent improvement in performance with level at low frequencies (e.g., Carlyon and Moore, 1984; Florentine *et al.*, 1987). Many of the psychophysical experiments exploring the ''mid-level bump'' (or the ''severe departure from Weber's law'') have used short-duration signals in various noise maskers, because the effect (when reported as $\Delta I/I$) is generally larger for short-duration signals (e.g., Carlyon and Moore, 1984) and can be enhanced or reduced by various configurations of notched-noise maskers (e.g., Oxenham and Moore, 1995; Plack, 1998). However, the analytical AN model used in the present study is only appropriate to compare to long duration conditions because onset/offset responses and neural adaptation are not included in the model. In addition, the effects of a notched-noise masker on the different types of AN information must be considered quantitatively using methods that are beyond the present study, as discussed below. Thus, the high-frequency mid-level bump reported by Florentine *et al.* (1987) for level discrimination of 500-ms pure tones in quiet is an appropriate comparison for the present predictions.

Plack (1998) has discussed several explanations for the mid-level bump based on both peripheral and central mechanisms; however, only those that are addressed by the present predictions are discussed here. Carlyon and Moore (1984) have suggested that the mid-level bump at high frequencies may be explained by two populations of AN fibers. They suggested that good performance was provided by the low-threshold, HSR fibers at low levels and by the high-threshold, LSR fibers at high levels, with a degradation in performance at mid levels because neither population encoded changes in sound level. The absence of the mid-level bump at low frequencies was suggested to result from synchrony information providing good performance at mid-levels. The present predictions do not support this explanation by Carlyon and Moore (1984). For the high-frequency

tone, the transition between HSR and LSR fibers determining performance occurs near 80–90 dB SPL (Fig. 9), and no degradation in performance occurs because of the contribution of the third SR group (MSR) reported by Liberman (1978). The contribution of synchrony information at low frequencies is restricted to levels below those where HSR fibers contribute rate information (Fig. 9), and thus cannot be responsible for good performance at mid-levels. It was suggested by von Klitzing and Kohlrausch (1994) that the mid-level bump can be explained based on mid-level compression on the BM; however, their explanation requires that BM responses become linear above roughly 50 dB SPL, which has been shown not to be true in healthy cochleae (Ruggero *et al.*, 1997).

The present predictions demonstrate that a mid-level bump that is consistent with human data results from the large amount of cochlear compression at high frequencies (Figs. 8 and 9). The degradation in model performance at mid-levels is due to the BM input–output function becoming strongly compressed at 30 dB SPL (Fig. 8). As level increases further, the spread of excitation goes beyond the near-CF nonlinear region, and performance is dominated by HSR AN fibers that are responding linearly. Thus, the nonlinear-AN-model predictions for the HSR fibers match those from the linear AN model at levels above 60 dB SPL. The lack of a mid-level bump at low frequencies in the model predictions is consistent with the small amount of cochlear compression at low frequencies [Fig. 1(c)].

Thus, the present predictions suggest that the main effect of compressive magnitude responses on level discrimination of high-frequency tones in quiet is a degradation in performance at mid levels. This hypothesis suggests that hearing-impaired listeners without a healthy cochlear amplifier would not show a mid-level bump. However, this would be difficult to measure due to the typically limited dynamic range in hearing-impaired listeners (Florentine *et al.*, 1993).

In general, the effect of cochlear nonlinearity on level discrimination of tones in quiet was predicted to be small, because the influence of the cochlear amplifier is restricted to near-CF frequencies and the role of spread of excitation is large for tones in quiet. This small predicted effect is consistent with hearing-impaired listeners showing normal JNDs at equal SPL for suprathreshold conditions (Florentine *et al.*, 1993; Schroder *et al.*, 1994).

C. Coincidence detection: A robust, physiologically realistic neural mechanism

The predictions from the present study suggest that a set of monaural, cross-frequency coincidence counters that receive AN inputs from a narrow range of CFs can account for Weber's law across the dynamic range of human hearing, both at low and high frequencies. This finding is significant because Weber's law in narrow-CF regions appears to be required to account for human level-discrimination performance (Florentine and Buus, 1981; Viemeister, 1983); however, an optimal combination of average-rate information across the set of three SR groups in the AN does not produce Weber's law across a wide range of levels, at least at low frequencies (Fig. 7; Colburn, 1981; Delgutte, 1987).

Coincidence detection is a physiologically realistic mechanism, because any neuron with multiple subthreshold inputs acts as a coincidence detector (i.e., several nearly coincident discharges across the inputs are required to produce an output discharge). There is strong evidence that coincidence detection occurs in the binaural auditory system (Yin and Chan, 1990; Goldberg and Brown, 1969; Rose *et al.*, 1966; Yin *et al.*, 1987; Joris *et al.*, 1998), and coincidence detection forms the basis of most models of binaural processing (Colburn, 1996). Carney (1990) showed that several low-CF cell types in the antero-ventral cochlear nucleus (AVCN), primarily globular bushy cells, were sensitive to changes in the relative phase across their inputs. Joris *et al.* (1994a, 1994b) have provided evidence for monaural coincidence detection at all CFs in similar AVCN cell types based on enhanced synchronization in low- and high-CF cells to low-frequency tones.

The simple coincidence-counting mechanism analyzed in the present analysis was shown to utilize the level-dependent phase cues associated with the cochlear amplifier, as suggested by Carney (1994). In addition, the present study demonstrates that monaural, cross-frequency coincidence detection is a robust mechanism for encoding sound level in that both average-rate and nonlinear-phase information from AN discharges are encoded in the coincidence counts, as well as some information from synchrony cues. Thus, coincidence detection may account for level discrimination of noise as well, by decoding average-rate increases at low noise levels and increases in across-CF correlation due to broadened tuning at high levels (see Carney, 1994).

Overall coincidence-based performance depends on the implementation of the coincidence counter population, which was chosen to be simple and conservative in the present study. Inclusion of every AN fiber as an input to the coincidence population allowed the efficiency of the coincidence mechanism to be evaluated. Allowing each AN fiber to innervate only one coincidence neuron created an independent population for which performance could be more easily calculated. This implementation provided a conservative estimate of coincidence-based performance because allowing AN fibers to innervate more than one coincidence neuron could only improve performance (as long as potential across-neuron correlation was accounted for in the combination across coincidence counts).

It is generally accepted that there is far more information in AN responses than is used by humans, and that an inefficient processor is needed to account for human level-discrimination performance (e.g., Colburn, 1981; Delgutte, 1987). The coincidence-counting model processes the AN discharge times inefficiently. Information is lost in the process of coincidence detection because only the times of coincident AN discharges are considered. Additional information is lost by basing performance only on the coincidence counts (i.e., by ignoring the coincidence times). Even though the coincidence mechanism in the present study is far from optimal, the coincidence-performance predictions are typically shifted upward roughly in parallel from the all-information predictions. Figures 7 and 9 illustrate that the degradation in performance that occurs due to the coinci-

dence mechanism results in absolute performance levels for level discrimination that are very close to human performance. In addition, the monaural coincidence mechanism eliminates the requirement of an inefficient processor that varies its inefficiency as a function of level, which has been suggested based on average-discharge rate information in the AN (Colburn, 1981; Delgutte, 1987).

The derivations of performance based on a monaural, cross-frequency coincidence counter described in Appendix B suggest an interesting property that could be useful for physiological studies of neurons that are hypothesized to perform coincidence detection. The ratio of the expected value of coincidence counts [Eq. (B12)] to the variance of counts [Eq. (B13)] is dependent only on the properties of the temporal coincidence window $f(x)$. This ratio would be expected to be independent of stimulus parameters, and therefore the statistics of the observed discharge counts may be used to make inferences about the shape and size of the coincidence window of a given neuron.

D. Limitations of the present study

The analytical AN model was kept simple for the purposes of the present study. The model does not include the effects of external- and middle-ear filtering, or onset/offset and adaptation responses. Also, the model does not include many complex AN response properties, including refractory behavior, the effects of the olivocochlear efferent system (Guinan, 1996), and several complex irregularities in response to high-level tones (e.g., Liberman and Kiang, 1984; Kiang, 1984, 1990; Ruggero *et al.*, 1996) and clicks (Lin and Guinan, 2000). The absence of these properties does not limit the basic conclusions of the present study, but does limit the applicability of the present model at high levels and for more complex stimuli, as discussed further in Heinz (2000).

Predictions in the present study were compared to human data for level discrimination in a notched noise based on the common assumption that the only effect of the notched noise is to eliminate spread of excitation of the tone. In order to accurately evaluate the validity of this assumption, the effect of the noise masker on different types of information must be quantified. This analysis requires two advances beyond the present study: (1) a more complex AN model and (2) an extension of the signal detection theory (SDT) analysis.

In order to accurately evaluate complex stimuli, the AN model must include a description of suppression properties (e.g., Sachs and Kiang, 1968; Delgutte, 1990; Ruggero *et al.*, 1992). The AN response to a CF tone in the presence of a notched-noise masker may be suppressed by the noise, whereas the response of AN fibers with CFs within the noise may be suppressed by the tone. Such complex interactions between the tone and noise maskers could contribute significant information to detection or discrimination of signals in noise and therefore need to be quantified.

For cases in which the stimulus is random, an extension of the SDT analysis beyond the present study is required to quantify the relative effects of physiological (internal) and stimulus (external) variation on psychophysical performance. Heinz *et al.* (2001b) have described an extension of the SDT analysis to discrimination tasks in which a single parameter is randomly varied (e.g., random level variation). In addition, a general theoretical analysis of detection or discrimination of a signal in random noise has been developed and applied to the detection of tones in notched noise by Heinz (2000).

V. CONCLUSIONS

The cochlear amplifier benefits normal-hearing listeners by extending the dynamic range within narrow frequency regions. Nonlinear phase responses near CF associated with the cochlear amplifier encode changes in level across the entire dynamic range of hearing at low frequencies; however, the rolloff in phase locking reduces the effectiveness of phase cues at high frequencies for simple stimuli. Highly compressive basilar-membrane responses at high frequencies allow for the robust encoding of level based on average discharge rate; however, the reduction in cochlear compression at low frequencies reduces the relative ability of average rate to robustly encode sound level at low frequencies.

Cochlear nonlinearity has only a small effect on suprathreshold level discrimination of pure tones in quiet because performance is dominated by spread of excitation to linear off-CF responses. The only effects of cochlear nonlinearity predicted by the model for this task are the ''near-miss'' to Weber's law at low frequencies and the nonmonotonic ''mid-level bump'' at high frequencies.

Monaural coincidence detection is a physiologically realistic mechanism that can utilize the nonlinear gain and phase cues provided by the cochlear amplifier. Performance based on a population of coincidence counters matches human performance for level discrimination of tones across the entire dynamic range of hearing at both low and high frequencies.

ACKNOWLEDGMENTS

The authors thank Dr. Torsten Dau, Dr. Bertrand Delgutte, and Susan Early for providing valuable comments on an earlier version of this paper. We thank Dr. Don Johnson for his synchrony data from cat shown in Fig. 1(e), and Dr. Mario Ruggero for providing the data shown in Fig. 1(g). This study was part of a graduate dissertation in the Speech and Hearing Sciences Program of the Harvard–MIT Division of Health Sciences and Technology (Heinz, 2000). This work was supported in part by the National Institute of Health, Grant T32DC00038, and by the National Science Foundation, Grant 9983567.

APPENDIX A: NONLINEAR ANALYTICAL AUDITORY-NERVE MODEL

The analytical nonlinear auditory-nerve (AN) model used in the present study includes simple descriptions of the most significant properties of the cochlear amplifier. This model was kept as simple as possible so that basic concepts related to rate and timing cues associated with the cochlear amplifier could be demonstrated without the difficulty of interpreting predictions from a more complex model. The as-

sumptions and equations that specify the analytical model are described in this appendix, and basic response properties are shown in Fig. 1.

The discharge statistics of AN fibers are assumed to be described by a nonstationary Poisson process with a time-varying rate function $r(t)$. Equation (1) describes the phase-locked response of an AN fiber in response to a tone burst. The average discharge rate $\bar{r}[L_{\text{eff}}]$ and the strength of phase locking $g[L_{\text{eff}}, f_0]$ both depend on the effective level L_{eff} that drives each AN fiber.

The effective level for the ith AN fiber is determined by the tone level L (dB SPL) and by the nonlinear-filter magnitude response $H_{\text{NL}}(f_0, \text{CF}_i, L)$ for the characteristic frequency CF_i and the tone frequency f_0, i.e.,

$$L_{\text{eff}}(L, f_0, \text{CF}_i) = L + 20\log_{10}[H_{\text{NL}}(f_0, \text{CF}_i, L)]. \tag{A1}$$

The implementation of nonlinear tuning in the present model [see Figs. 1(a)–(c)] represents the idea that the cochlear amplifier produces high sensitivity and sharp tuning at low levels by providing amplification to near-CF frequencies, and that the cochlear-amplifier gain is reduced as level increases (Yates, 1995). At low levels, the magnitude response is described by linear triangular filters that are consistent with those used by Siebert (1968, 1970) to describe tuning curves in cat [see Fig. 1(a)], i.e.,

$$H_S\left(\frac{f_0}{\text{CF}_i}\right) = \begin{cases} \left(\dfrac{f_0}{\text{CF}_i}\right)^{10}, & f_0 \leqslant \text{CF}_i; \\ \left(\dfrac{f_0}{\text{CF}_i}\right)^{-20}, & f_0 \geqslant \text{CF}_i. \end{cases} \tag{A2}$$

Nonlinear compression is incorporated into the magnitude response H_{NL} by multiplying the linear triangular magnitude response H_S by a level- and frequency-dependent attenuation factor, i.e.,

$$H_{\text{NL}}(f_0, \text{CF}_i, L) = (10^{\gamma_{\text{dB}}(f_0, \text{CF}_i, L)/20}) H_S\left(\frac{f_0}{\text{CF}_i}\right). \tag{A3}$$

This form is used so that the level- and frequency-dependent attenuation $\gamma_{\text{dB}}(f_0, \text{CF}_i, L)$ is specified in dB, which allows model properties to be matched directly to experimental descriptions of responses associated with the cochlear amplifier. The next few expressions describe the frequency and level dependence of this attenuation.

The reduction in gain of the cochlear amplifier, γ_{dB}, is specified based on several simple assumptions, consistent with physiological findings (e.g., Ruggero *et al.*, 1997): (1) For a given CF, the maximum gain G provided by the cochlear amplifier is produced for tones presented at CF, and G in dB increases with CF [see Fig. 1(c)] according to

$$G(\text{CF}_i) = \begin{cases} G_{\min}, & \text{CF}_i \leqslant 500\ \text{Hz}; \\ G_{\min} + (G_{\max} - G_{\min}) \dfrac{\log_{10}(\text{CF}_i/500)}{\log_{10}(8000/500)}, & \\ \qquad 500 \leqslant \text{CF}_i \leqslant 8000\ \text{Hz}; & \\ G_{\max}, & \text{CF}_i \geqslant 8000\ \text{Hz}; \end{cases} \tag{A4}$$

where $G_{\min} = 20$ dB, $G_{\max} = 60$ dB. (2) The cochlear amplifier provides full gain for levels below $L_{\text{thr}}^{\text{NL}} = 30$ dB SPL, and the cochlear-amplifier gain is systematically reduced as level increases from $L_{\text{thr}}^{\text{NL}}$ to $L_{\text{sat}}^{\text{NL}} = 120$ dB SPL [see Fig. 1(b)]. (3) The cochlear amplifier only provides amplification for stimulus frequencies near CF, i.e., $f_{lf}^{\text{NL}} \leqslant f_0 \leqslant f_{hf}^{\text{NL}}$, where

$$\begin{aligned} f_{lf}^{\text{NL}} &= \text{CF}_i[10^{-G_{\max}/(20\cdot 10)}], \\ f_{hf}^{\text{NL}} &= \text{CF}_i[10^{G_{\max}/(20\cdot 20)}], \end{aligned} \tag{A5}$$

as shown in Fig. 1(a). This simple implementation of the nonlinear frequency region results in a flat magnitude response between f_{lf}^{NL} and f_{hf}^{NL} at high levels ($L \geqslant L_{\text{sat}}^{\text{NL}}$) and high characteristic frequencies ($\text{CF}_i \geqslant 8000$ Hz). Based on these assumptions, the level- and frequency-dependent reduction in gain is given in dB by

$$\begin{aligned} &\gamma_{\text{dB}}(f_0, \text{CF}_i, L) \\ &\quad = \beta_{\text{mag}}(L, f_0)\left\{-20\log_{10}\left[H_S\left(\frac{f_0}{\text{CF}_i}\right)\right] - G_{\max}\right\}\left[\frac{G(CF_i)}{G_{\max}}\right], \end{aligned} \tag{A6}$$

where

$$\beta_{\text{mag}}(L, f_0) = \begin{cases} 0, & L \leqslant L_{\text{thr}}^{\text{NL}} \quad \text{or} \quad f_0 \notin [f_{lf}^{\text{NL}}, f_{hf}^{\text{NL}}]; \\ \left(\dfrac{L - L_{\text{thr}}^{\text{NL}}}{L_{\text{sat}}^{\text{NL}} - L_{\text{thr}}^{\text{NL}}}\right), & \\ \qquad L_{\text{thr}}^{\text{NL}} \leqslant L \leqslant L_{\text{sat}}^{\text{NL}} \ \text{and} \ f_{lf}^{\text{NL}} \leqslant f_0 \leqslant f_{hf}^{\text{NL}}; & \\ 1, & L \geqslant L_{\text{sat}}^{\text{NL}} \ \text{and} \ f_{lf}^{\text{NL}} \leqslant f_0 \leqslant f_{hf}^{\text{NL}}. \end{cases} \tag{A7}$$

The parameter $\beta_{\text{mag}}(L, f_0)$ is a linear interpolation between the compression threshold $L_{\text{thr}}^{\text{NL}}$ and saturation level $L_{\text{sat}}^{\text{NL}}$ [see Fig. 1(b)], and it represents the reduction in cochlear-amplifier gain as level increases for near-CF frequencies. The second term in Eq. (A6) (in curly brackets) produces maximum gain at CF and reduced gain for tone frequencies off CF, and the third term controls the amount of gain as a function of CF.

In order to evaluate the effect of the nonlinear magnitude response on predictions in the present study, versions of the AN model with and without the nonlinear magnitude responses can be compared. The nonlinear magnitude responses can be excluded by setting $\beta_{\text{mag}}(L, f_0) = 0$ for all levels and frequencies.

The dependence of average discharge rate $\bar{r}$ on the effective level L_{eff} of an AN fiber is specified in terms of a simple saturating nonlinearity (based on Colburn, 1981)

$$\bar{r}[L_{\text{eff}}] = \begin{cases} \text{SR}, & L_{\text{eff}} \leqslant L_{\text{thr}} - 5; \\ \text{SR} + (1/600)(R_{\text{sat}} - \text{SR})(L_{\text{eff}} - L_{\text{thr}} + 5)^2, & \\ \qquad L_{\text{thr}} - 5 \leqslant L_{\text{eff}} \leqslant L_{\text{thr}} + 5; & \\ \text{SR} + (1/30)(R_{\text{sat}} - \text{SR})(L_{\text{eff}} - L_{\text{thr}}), & \\ \qquad L_{\text{thr}} + 5 \leqslant L_{\text{eff}} \leqslant L_{\text{thr}} + 30; & \\ R_{\text{sat}}, & L_{\text{eff}} \geqslant L_{\text{thr}} + 30; \end{cases} \tag{A8}$$

which depends on the spontaneous rate (SR), the saturated rate (R_{sat}), and the rate threshold (L_{thr}). The dependence of average rate on tone level L is shown for a high CF (maximum gain) and a low CF (small gain) in Figs. 1(d) and (f), respectively, for the three SR groups used in this study.

The dependence of phase locking on effective level L_{eff} is specified using the same general form of saturating nonlinearity, i.e.,

$$g[L_{eff},f_0]=\begin{cases}0, & L_{eff}\leqslant L_{thr}-25;\\ [g_{max}(f_0)/600]\,(L_{eff}-L_{thr}+25)^2, & L_{thr}-25\leqslant L_{eff}\leqslant L_{thr}-15;\\ [g_{max}(f_0)/30]\,(L_{eff}-L_{thr}+20), & L_{thr}-15\leqslant L_{eff}\leqslant L_{thr}+10;\\ g_{max}(f_0), & L_{eff}\geqslant L_{thr}+10;\end{cases} \tag{A9}$$

where the dependence of synchrony on frequency, $g_{max}(f_0)$, is matched to data from cat [see Fig. 1(e); Johnson, 1980], and is described by

$$g_{max}(f_0)=\begin{cases}3.1, & f_0\leqslant 1200\ \text{Hz};\\ \dfrac{3.1*1200}{f_0}, & 1200\leqslant f_0\leqslant 2800\ \text{Hz};\\ \dfrac{3.1*1200*2800^2}{(f_0)^3}, & f_0\geqslant 2800\ \text{Hz}.\end{cases} \tag{A10}$$

Note that the threshold for phase locking is specified to be 20 dB below the average-rate threshold in Eq. (A9).

The implementation of the nonlinear phase responses in the present study [see Fig. 1(h)] is based on several simple assumptions: (1) The level-dependent phase responses are limited to the same near-CF frequency region as the magnitude responses, $f_{lf}^{NL}\leqslant f_0\leqslant f_{hf}^{NL}$. (2) Phase varies linearly with tone level. (3) The maximum phase changes occur half way into the near-CF nonlinear frequency region, i.e., at frequencies

$$f_{lf}^{PH}=0.5(CF_i+f_{lf}^{NL}),\quad f_{hf}^{PH}=0.5(CF_i+f_{hf}^{NL}). \tag{A11}$$

(4) The maximum phase shifts between low levels and 80 dB SPL are roughly $\pi/2$. (5) The total traveling-wave delay at high levels ($L>L_{sat}^{NL}$) is compensated for in each CF with neural delays prior to innervation of the coincidence-detection population. This simple assumption is based on strong onset responses to tones for many cell types in the cochlear nucleus (Young, 1984; Rhode and Greenberg, 1992). Based on these simple assumptions, the compensated nonlinear filter phase response [see Fig. 1(h)] is specified by the equation

$$\theta(f_0,CF_i,L)=\begin{cases}0, & f_0\notin[f_{lf}^{NL},f_{hf}^{NL}];\\ \beta_{phase}(L,f_0)\cdot 2\Delta\theta_{max}\left(\dfrac{f_0-f_{lf}^{NL}}{CF_i-f_{lf}^{NL}}\right), & f_{lf}^{NL}\leqslant f_0\leqslant f_{lf}^{PH};\\ \beta_{phase}(L,f_0)\cdot 2\Delta\theta_{max}\left(\dfrac{CF_i-f_0}{CF_i-f_{lf}^{NL}}\right), & f_{lf}^{PH}\leqslant f_0\leqslant CF_i;\\ \beta_{phase}(L,f_0)\cdot 2\Delta\theta_{max}\left(\dfrac{CF_i-f_0}{f_{hf}^{NL}-CF_i}\right), & CF_i\leqslant f_0\leqslant f_{hf}^{PH};\\ \beta_{phase}(L,f_0)\cdot 2\Delta\theta_{max}\left(\dfrac{f_0-f_{hf}^{NL}}{f_{hf}^{NL}-CF_i}\right), & f_{hf}^{PH}\leqslant f_0\leqslant f_{hf}^{NL};\end{cases} \tag{A12}$$

where $\Delta\theta_{max}=\frac{6}{5}\pi$ is the maximum phase change between L_{thr}^{NL} and L_{sat}^{NL}, and $\beta_{phase}(L,f_0)=1-\beta_{mag}(L,f_0)$, where $\beta_{mag}(L,f_0)$ is specified by Eq. (A7).

Versions of the AN model with and without the nonlinear phase changes can be compared in order to evaluate the effect of nonlinear phase responses. The level-dependent phase changes can be excluded by setting $\beta_{phase}(L,f_0)=1$ for all levels and frequencies.

APPENDIX B: PERFORMANCE BASED ON A MONAURAL COINCIDENCE COUNTER

This appendix presents derivations of the expected value and variance of the coincidence counts $\mathcal{C}_{ij}\{\mathcal{T}^i,\mathcal{T}^j\}$ [Eq. (2)] that are needed to calculate the normalized sensitivity δ' of a monaural, cross-frequency coincidence counter [Eq. (6)]. Similar equations and related discussions are presented without derivations by Colburn (1969, 1977b) for a binaural coincidence counter. The expected value and variance in Eq. (6) depend on the Poisson statistics of the two sets of independent AN discharge times, $\mathcal{T}^i$ and $\mathcal{T}^j$, and will be shown to be given by

$$E_{\mathcal{T}^i,\mathcal{T}^j,\phi}[\mathcal{C}_{ij}\{\mathcal{T}^i,\mathcal{T}^j\}]=E_\phi\left[\int_0^T\int_0^T f(x-y)r_i(x;\phi)r_j(y;\phi)dx\,dy\right], \tag{B1}$$

$$\mathrm{Var}_{\mathcal{T}^i,\mathcal{T}^j,\phi}[\mathcal{C}_{ij}\{\mathcal{T}^i,\mathcal{T}^j\}]\simeq E_\phi\left[\int_0^T\int_0^T f^2(x-y)r_i(x;\phi)r_j(y;\phi)dx\,dy\right], \tag{B2}$$

where $r_i(t;\phi)$ and $r_j(t;\phi)$ represent the time-varying rate functions of the two AN inputs to the coincidence counter, ϕ is a random phase imposed on every AN fiber (to force the lack of an absolute time or phase reference), and $f(x)$ is the narrow temporal coincidence window.

The derivations of Eqs. (B1) and (B2) rely on several general results for decision variables of the form

$$X_i(\mathcal{T}^i)=\sum_{l=1}^{K_i}s(t_l^i), \tag{B3}$$

where $s(t_l^i)$ is any function of the lth discharge time t_l^i generated from a Poisson process with rate function $r_i(t)$. It can

be shown (e.g., Rieke *et al.*, 1997) that the expected value and variance of $X_i(\mathcal{T}^i)$ are given by

$$E_{\mathcal{T}^i}[X_i(\mathcal{T}^i)] = \int_0^T s(t) r_i(t)\, dt, \tag{B4}$$

$$\mathrm{Var}_{\mathcal{T}^i}[X_i(\mathcal{T}^i)] = \int_0^T s^2(t) r_i(t)\, dt, \tag{B5}$$

based on the probability density function for Poisson discharge times (see Parzen, 1962; Snyder and Miller, 1991). Equations (B4) and (B5) imply that

$$E_{\mathcal{T}^i}\{[X_i(\mathcal{T}^i)]^2\} = \int_0^T s^2(t) r_i(t)\, dt + \left[\int_0^T s(t) r_i(t)\, dt\right]^2. \tag{B6}$$

The expected value of the coincidence counts [used in Eq. (6) of the text] can be derived as follows:

$$\begin{aligned} E_{\mathcal{T}^i,\mathcal{T}^j,\phi}[\mathcal{C}_{ij}\{\mathcal{T}^i,\mathcal{T}^j\}] &= E_{\mathcal{T}^i,\mathcal{T}^j,\phi}\left[\sum_{l=1}^{K_i}\sum_{m=1}^{K_j} f(t_l^i - t_m^j)\right] \\ &= E_{\mathcal{T}^i,\phi}\left\{\sum_{l=1}^{K_i} E_{\mathcal{T}^j}\left[\sum_{m=1}^{K_j} f(t_l^i - t_m^j)\,\middle|\, \mathcal{T}^i\right]\right\} \\ &= E_{\mathcal{T}^i,\phi}\left[\sum_{l=1}^{K_i}\int_0^T f(t_l^i - y) r_j(y;\phi)\, dy\right]. \end{aligned} \tag{B7}$$

Using Eq. (B4) again, Eq. (B1) is obtained. Similarly, the term $E_{\mathcal{T}^i,\mathcal{T}^j,\phi}[\mathcal{C}_{ij}^2\{\mathcal{T}^i,\mathcal{T}^j\}]$ can be derived as follows:

$$\begin{aligned} &E_{\mathcal{T}^i,\mathcal{T}^j,\phi}[\mathcal{C}_{ij}^2\{\mathcal{T}^i,\mathcal{T}^j\}] \\ &= E_{\mathcal{T}^i,\phi}\left[E_{\mathcal{T}^j}\left(\left\{\sum_{m=1}^{K_j}\left[\sum_{l=1}^{K_i} f(t_l^i - t_m^j)\right]\right\}^2 \middle| \mathcal{T}^i\right)\right] \\ &= E_{\mathcal{T}^i,\phi}\left\{\int_0^T\left[\sum_{l=1}^{K_i} f(t_l^i - y)\right]^2 r_j(y;\phi)\, dy + \left[\sum_{l=1}^{K_i}\int_0^T f(t_l^i - y) r_j(y;\phi)\, dy\right]^2\right\} \\ &= E_\phi\left\{\int_0^T\int_0^T f^2(x-y) r_i(x;\phi) r_j(y;\phi)\, dx\, dy + \int_0^T\int_0^T\int_0^T f(x-y) f(u-y) r_i(x;\phi) r_i(u;\phi) r_j(y;\phi)\, dx\, du\, dy \right. \\ &\quad \left. + \int_0^T\int_0^T\int_0^T f(x-y) f(x-v) r_i(x;\phi) r_j(v;\phi) r_j(y;\phi)\, dx\, dv\, dy + \left[\int_0^T\int_0^T f(x-y) r_i(x;\phi) r_j(y;\phi)\, dx\, dy\right]^2\right\}. \end{aligned} \tag{B8}$$

The variance in Eq. (6) is then equal to

$$\begin{aligned} &\mathrm{Var}_{\mathcal{T}^i,\mathcal{T}^j,\phi}[\mathcal{C}_{ij}\{\mathcal{T}^i,\mathcal{T}^j\}] \\ &= E_{\mathcal{T}^i,\mathcal{T}^j,\phi}[\mathcal{C}_{ij}^2\{\mathcal{T}^i,\mathcal{T}^j\}] - (E_{\mathcal{T}^i,\mathcal{T}^j,\phi}[\mathcal{C}_{ij}\{\mathcal{T}^i,\mathcal{T}^j\}])^2 \\ &= E_\phi\left\{\int_0^T\int_0^T f^2(x-y) r_i(x;\phi) r_j(y;\phi)\, dx\, dy \right. \\ &\quad + \int_0^T\int_0^T\int_0^T f(x-y) f(u-y) r_i(x;\phi) r_i(u;\phi) r_j(y;\phi)\, dx\, du\, dy \\ &\quad \left. + \int_0^T\int_0^T\int_0^T f(x-y) f(x-v) r_i(x;\phi) r_j(v;\phi) r_j(y;\phi)\, dx\, dv\, dy\right\}. \end{aligned} \tag{B9}$$

The two triple-integral terms in the right-hand side of Eq. (B9) can be shown to be negligible relative to the double-integral term if (1) the coincidence window $f(x)$ is much narrower than the period of variation in discharge rate $r(t)$, which is never less than about 0.5 ms given the rolloff in phase locking of AN fibers above 2 kHz [Fig. 1(e); Johnson (1980)], and (2) the following inequality holds:

$$R_{\mathrm{sat}}\left[\int_{-\infty}^{\infty} f(x)\, dx\right]^2 \ll \int_{-\infty}^{\infty} f^2(x)\, dx, \tag{B10}$$

where R_{sat} is the maximum discharge rate of an AN fiber. Both of these conditions are satisfied for the 10-μs rectangular coincidence window in the present study, and thus the approximation in Eq. (B2) holds.

Note that Eqs. (B1) and (B2) can be used with either analytical or computational AN models because they are independent of the AN model used to produce the rate functions. More informative expressions for the expected value and variance can be derived for the present analytical AN model. The expected value can be derived by substituting the rate function $r(t)$ from the analytical AN model [Eq. (1)] into Eq. (B1), i.e.,

$$E_{\mathcal{T}^i,\mathcal{T}^j,\phi}[\mathcal{C}_{ij}\{\mathcal{T}^i,\mathcal{T}^j\}] = \frac{\overline{r_i r_j}}{I_0[g_i]I_0[g_j]} \int_0^T \int_0^T f(x-y)\frac{1}{2\pi}\int_0^{2\pi} \exp[g_i \cos(2\pi f_0 x+\theta_i+\phi)+g_j \cos(2\pi f_0 y+\theta_j+\phi)]\,d\phi\,dx\,dy$$

$$= \frac{\overline{r_i r_j}}{I_0[g_i]I_0[g_j]} \int_0^T \int_0^T f(x-y)\frac{1}{2\pi}\int_0^{2\pi} \exp\Bigg(\sqrt{g_i^2+g_j^2+2g_i g_j \cos[2\pi f_0(x-y)+\theta_i-\theta_j]}$$

$$\times \cos\Bigg\{ \phi + \tan^{-1}\Bigg[\frac{g_i \sin(2\pi f_0 x+\theta_i)+g_j \sin(2\pi f_0 y+\theta_j)}{g_i \cos(2\pi f_0 x+\theta_i)+g_j \cos(2\pi f_0 y+\theta_j)} \Bigg] \Bigg\} \Bigg) d\phi\,dx\,dy$$

$$= \frac{\overline{r_i r_j}}{I_0[g_i]I_0[g_j]} \int_0^T \int_0^T f(x-y) I_0\{\sqrt{g_i^2+g_j^2+2g_i g_j \cos[2\pi f_0(x-y)+\theta_i-\theta_j]}\}dx\,dy, \tag{B11}$$

where $g_i = g[L_{\text{eff}}(L,f_0,\text{CF}_i),f_0]$, $\overline{r_i} = \overline{r}[L_{\text{eff}}(L,f_0,\text{CF}_i)]$, and $\theta_i = \theta(L,f_0,\text{CF}_i)$, and $I_0\{g\}$ is the zeroth-order modified Bessel function of the first kind. The second form follows from writing the sum of cosines as a single cosine, and the last expression follows from the insensitivity of the integral over a period to the phase angle.

Using the assumption that the coincidence window $f(x)$ is narrow relative to the period of stimulus variation, the expected value [Eq. (B1)] and variance [Eq. (B2)] can be shown to be approximated by

$$E[\mathcal{C}_{ij}|L] \simeq \frac{T\overline{r_i r_j}}{I_0[g_i]I_0[g_j]} I_0[\sqrt{g_i^2+g_j^2+2g_i g_j \cos(\theta_i-\theta_j)}] \times \int_{-\infty}^{\infty} f(x)dx, \tag{B12}$$

$$\text{Var}[\mathcal{C}_{ij}|L] \simeq \frac{T\overline{r_i r_j}}{I_0[g_i]I_0[g_j]} I_0[\sqrt{g_i^2+g_j^2+2g_i g_j \cos(\theta_i-\theta_j)}] \times \int_{-\infty}^{\infty} f^2(x)dx. \tag{B13}$$

[1]Coincidence counters for which one input fell outside the model CF range (300–20 000 Hz) were evaluated by using the edge model CF as the input instead. This end effect was not significant for this study's results.

[2]The data from Florentine *et al.* (1987) are plotted as a function of sensation level (SL), which is the most appropriate comparison to the predictions from the analytical AN model that has a fixed threshold at 0 dB SPL. Some of the effects in the human data that occur at a particular sensation level are reduced when the data is averaged across listeners as a function of SPL, rather than SL.

Anderson, D.J., Rose, J.E., Hind, J.E., and Brugge, J.F. (**1971**). "Temporal position of discharges in single auditory nerve fibers within the cycle of a sinewave stimulus: Frequency and intensity effects," J. Acoust. Soc. Am. **49**, 1131–1139.

Blackburn, C.C., and Sachs, M.B. (**1990**). "The representations of the steady-state vowel sound /ε/ in the discharge patterns of cat anteroventral cochlear nucleus neurons," J. Neurophysiol. **63**, 1191–1212.

Braida, L.D., and Durlach, N.I. (**1988**). "Peripheral and central factors in intensity perception," in *Auditory Function: Neurobiological Bases of Hearing*, edited by G.M. Edelman, W.E. Gall, and W.M. Cowan (Wiley, New York), pp. 559–583.

Carlyon, R.P., and Moore, B.C.J. (**1984**). "Intensity discrimination: A severe departure from Weber's law," J. Acoust. Soc. Am. **76**, 1369–1376.

Carney, L.H. (**1990**). "Sensitivities of cells in the anteroventral cochlear nucleus of cat to spatiotemporal discharge patterns across primary afferents," J. Neurophysiol. **64**, 437–456.

Carney, L.H. (**1994**). "Spatiotemporal encoding of sound level: Models for normal encoding and recruitment of loudness," Hear. Res. **76**, 31–44.

Carney, L.H., Heinz, M.G., and Colburn, H.S. (**1999**). "Spatiotemporal coding of sound level: Quantifying the information provided by level-dependent phase cues," Abstracts of the 22nd Midwinter Meeting of the Association for Research in Otolaryngology, pp. 212–213.

Cheatham, M.A., and Dallos, P. (**1998**). "The level dependence of response phase: Observations from cochlear hair cells," J. Acoust. Soc. Am. **104**, 356–369.

Colburn, H.S. (**1969**). Ph.D. dissertation, Massachusetts Institute of Technology, Cambridge, MA.

Colburn, H.S. (**1973**). "Theory of binaural interaction based on auditory-nerve data. I. General strategy and preliminary results on interaural discrimination," J. Acoust. Soc. Am. **54**, 1458–1470.

Colburn, H.S. (**1977a**). "Theory of binaural interaction based on auditory-nerve data. II. Detection of tones in noise," J. Acoust. Soc. Am. **61**, 525–533.

Colburn, H.S. (**1977b**). "Theory of binaural interaction based on auditory-nerve data. II. Detection of tones in noise. Supplementary material," AIP Document No. PAPS JASMA-**61**-525-98.

Colburn, H.S. (**1981**). "Intensity perception: relation of intensity discrimination to auditory-nerve firing patterns," Internal Memorandum, Research Laboratory of Electronics, Massachusetts Institute of Technology, Cambridge, MA.

Colburn, H.S. (**1996**). "Computational models of binaural processing," in *Auditory Computation*, edited by H.L. Hawkins, T.A. McMullen, A.N. Popper, and R.R. Fay (Springer-Verlag, New York), pp. 332–400.

Cooper, N.P., and Rhode, W.S. (**1997**). "Mechanical responses to two-tone distortion products in the apical and basal turns of the mammalian cochlea," J. Neurophysiol. **78**, 261–270.

Dau, T., Püschel, D., and Kohlrausch, A. (**1996**). "A quantitative model of the 'effective' signal processing in the auditory system I. Model structure," J. Acoust. Soc. Am. **99**, 3615–3622.

Dau, T., Kollmeier, B., and Kohlrausch, A. (**1997**). "Modeling auditory processing of amplitude modulation. I. Detection and masking with narrow-band carriers," J. Acoust. Soc. Am. **102**, 2892–2905.

Delgutte, B. (**1987**). "Peripheral auditory processing of speech information: implications from a physiological study of intensity discrimination," in *The Psychophysics of Speech Perception*, edited by M.E.H. Schouten (Nijhoff, Dordrecht, The Netherlands), pp. 333–353.

Delgutte, B. (**1990**). "Two-tone rate suppression in auditory-nerve fibers: Dependence on suppressor frequency and level," Hear. Res. **49**, 225–246.

Delgutte, B. (**1996**). "Physiological models for basic auditory percepts," in *Auditory Computation*, edited by H.L. Hawkins, T.A. McMullen, A.N. Popper, and R.R. Fay (Springer-Verlag, New York), pp. 157–220.

Durlach, N.I., and Braida, L.D. (**1969**). "Intensity perception I: Preliminary theory of intensity resolution," J. Acoust. Soc. Am. **46**, 372–383.

Evans, E.F. (**1981**). "The dynamic range problem: Place and time coding at the level of cochlear nerve and nucleus," in *Neuronal Mechanisms of Hearing*, edited by J. Syka and L. Aitkin (Plenum, New York), pp. 69–85.

Fekete, D.M., Rouiller, E.M., Liberman, M.C., and Ryugo, D.K. (**1984**). "The central projections of intracellularly labeled auditory nerve fibers in cats," J. Comp. Neurol. **229**, 432–450.

Florentine, M., and Buus, S. (**1981**). "An excitation pattern model for intensity discrimination," J. Acoust. Soc. Am. **70**, 1646–1654.

Florentine, M., Buus, S., and Mason, C.R. (**1987**). "Level discrimination as a function of level for tones from 0.25 to 16 kHz," J. Acoust. Soc. Am. **81**, 1528–1541.

Florentine, M., Reed, C.M., Rabinowitz, W.M., Braida, L.D., Durlach, N.I., and Buus, S. (**1993**). ''Intensity perception. XIV. Intensity discrimination in listeners with sensorineural hearing loss,'' J. Acoust. Soc. Am. **94**, 2575–2586.

Geisler, C.D., and Rhode, W.S. (**1982**). ''The phases of basilar-membrane vibrations,'' J. Acoust. Soc. Am. **71**, 1201–1203.

Goldberg, J.M., and Brown, P.B. (**1969**). ''Response of binaural neurons of dog superior olivary complex to dichotic tonal stimuli: Some physiological mechanisms of sound localization,'' J. Neurophysiol. **32**, 613–636.

Green, D.M. and Swets, J.A. (**1966**). *Signal Detection Theory and Psychophysics* (Wiley, New York, reprinted 1988 by Peninsula, Los Altos, CA).

Greenwood, D.D. (**1990**). ''A cochlear frequency-position function for several species—29 years later,'' J. Acoust. Soc. Am. **87**, 2592–2605.

Gresham, L.C., and Collins, L.M. (**1998**). ''Analysis of the performance of a model-based optimal auditory signal processor,'' J. Acoust. Soc. Am. **103**, 2520–2529.

Guinan, J.J., Jr. (**1996**). ''Physiology of olivocochlear efferents,'' in *The Cochlea*, edited by P.J. Dallos, A.N. Popper, and R.R. Fay (Springer-Verlag, New York), pp. 435–502.

Heinz, M.G. (**2000**). Ph.D. dissertation, Massachusetts Institute of Technology, Cambridge, MA.

Heinz, M.G., Colburn, H.S., and Carney, L.H. (**2001a**). ''Evaluating auditory performance limits: I. One-parameter discrimination using a computational model for the auditory nerve,'' Neural Computation **13**, 2273–2316.

Heinz, M.G., Colburn, H.S., and Carney, L.H. (**2001b**). ''Evaluating auditory performance limits: II. One-parameter discrimination with random level variation,'' Neural Computation **13**, 2317–2339.

Hicks, M.L., and Bacon, S.P. (**1999**). ''Psychophysical measures of auditory nonlinearities as a function of frequency in individuals with normal hearing,'' J. Acoust. Soc. Am. **105**, 326–338.

Huettel, L.G., and Collins, L.M. (**1999**). ''Using computational auditory models to predict simultaneous masking data: Model comparison,'' IEEE Trans. Biomed. Eng. **46**, 1432–1440.

Jesteadt, W., Wier, C.C., and Green, D.M. (**1977**). ''Intensity discrimination as a function of frequency and sensation level,'' J. Acoust. Soc. Am. **61**, 169–177.

Johnson, D.H. (**1980**). ''The relationship between spike rate and synchrony in responses of auditory-nerve fibers to single tones,'' J. Acoust. Soc. Am. **68**, 1115–1122.

Johnson, D.H., and Kiang, N.Y.S. (**1976**). ''Analysis of discharges recorded simultaneously from pairs of auditory-nerve fibers,'' Biophys. J. **16**, 719–734.

Joris, P.X., Carney, L.H., Smith, P.H., and Yin, T.C.T. (**1994a**). ''Enhancement of neural synchronization in the anteroventral cochlear nucleus. I. Responses to tones at the characteristic frequency,'' J. Neurophysiol. **71**, 1022–1036.

Joris, P.X., Smith, P.H., and Yin, T.C.T. (**1994b**). ''Enhancement of neural synchronization in the anteroventral cochlear nucleus. II. Responses in the tuning curve tail,'' J. Neurophysiol. **71**, 1037–1051.

Joris, P.X., Smith, P.H., and Yin, T.C.T. (**1998**). ''Coincidence detection in the auditory system: 50 years after Jeffress,'' Neuron **21**, 1235–1238.

Kiang, N.Y.S. (**1984**). ''Peripheral neural processing of auditory information,'' in *Handbook of Physiology, Section I: The Nervous System, Vol. III, Pt. 2*, edited by J.M. Brookhart and V.B. Mountcastle (American Physiological Society, Bethesda, MD), pp. 639–674.

Kiang, N.Y.S. (**1990**). ''Curious oddments of auditory-nerve studies,'' Hear. Res. **49**, 1–16.

Kiang, N.Y.S., Watanabe, T., Thomas, E.C., and Clark, L.F. (**1965**). *Discharge Patterns of Single Fibers in the Cat's Auditory Nerve* (MIT Press, Cambridge, MA).

von Klitzing, R., and Kohlrausch, A. (**1994**). ''Effect of masker level on overshoot in running- and frozen-noise maskers,'' J. Acoust. Soc. Am. **95**, 2192–2201.

Liberman, M.C. (**1978**). ''Auditory-nerve response from cats raised in a low-noise chamber,'' J. Acoust. Soc. Am. **63**, 442–455.

Liberman, M.C. (**1991**). ''Central projection of auditory-nerve fibers of differing spontaneous rate. I. Anteroventral cochlear nucleus,'' J. Comp. Neurol. **313**, 240–258.

Liberman, M.C. (**1993**). ''Central projection of auditory-nerve fibers of differing spontaneous rate. II. Posteroventral and dorsal cochlear nuclei,'' J. Comp. Neurol. **327**, 17–36.

Liberman, M.C., and Kiang, N.Y.S. (**1984**). ''Single-neuron labeling and chronic cochlear pathology. IV. Stereocilia damage and alterations in rate- and phase-level functions,'' Hear. Res. **16**, 75–90.

Lin, T., and Guinan, J.J. Jr. (**2000**). ''Auditory-nerve-fiber responses to high-level clicks: Interference patterns indicate that excitation is due to the combination of multiple drives,'' J. Acoust. Soc. Am. **107**, 2615–2630.

May, B.J., and Sachs, M.B. (**1992**). ''Dynamic range of neural rate responses in the ventral cochlear nucleus of awake cats,'' J. Neurophysiol. **68**, 1589–1602.

May, B.J., Le Prell, G.S., Hienz, R.D., and Sachs, M.B. (**1997**). ''Speech representation in the auditory nerve and ventral cochlear nucleus: Quantitative comparisons,'' in *Acoustical Signal Processing in the Central Auditory System*, edited by J. Syka (Plenum, New York), pp. 413–429.

May, B.J., Le Prell, G.S., and Sachs, M.B. (**1998**). ''Vowel representations in the ventral cochlear nucleus of the cat: Effects of level, background noise, and behavioral state,'' J. Neurophysiol. **79**, 1755–1767.

McGill, W.J., and Goldberg, J.P. (**1968**). ''A study of the near-miss involving Weber's law and pure-tone intensity discrimination,'' Percept. Psychophys. **4**, 105–109.

Miller, M.I., Barta, P.E., and Sachs, M.B. (**1987**). ''Strategies for the representation of a tone in background noise in the temporal aspects of the discharge patterns of auditory-nerve fibers,'' J. Acoust. Soc. Am. **81**, 665–679.

Miller, R.L., Schilling, J.R., Franck, K.R., and Young, E.D. (**1997**). ''Effects of acoustic trauma on the representation of the vowel /ɛ/ in cat auditory nerve fibers,'' J. Acoust. Soc. Am. **101**, 3602–3616.

Miller, R.L., Calhoun, B.M., and Young, E.D. (**1999**). ''Discriminability of vowel representation in cat auditory nerve fibers after acoustic trauma,'' J. Acoust. Soc. Am. **105**, 311–325.

Moore, B.C.J. (**1995**). *Perceptual Consequences of Cochlear Damage* (Oxford University Press, New York).

Moore, B.C.J., and Oxenham, A.J. (**1998**). ''Psychoacoustic consequences of compression in the peripheral auditory system,'' Psychol. Rev. **105**, 108–124.

Nuttall, A.L., and Dolan, D.F. (**1996**). ''Steady-state sinusoidal velocity responses of the basilar membrane in guinea pig,'' J. Acoust. Soc. Am. **99**, 1556–1565.

Oxenham, A.J., and Moore, B.C.J. (**1995**). ''Overshoot and the ''severe departure'' from Weber's Law,'' J. Acoust. Soc. Am. **97**, 2442–2453.

Parzen, E. (**1962**). *Stochastic Processes* (Holden-Day, San Francisco), Chap. 4.

Patuzzi, R.B., Yates, G.K., and Johnstone, B.M. (**1989**). ''Outer hair receptor currents and sensorineural hearing loss,'' Hear. Res. **42**, 47–72.

Plack, C.J. (**1998**). ''Beneficial effects of notched noise on intensity discrimination in the region of the severe departure,'' J. Acoust. Soc. Am. **103**, 2530–2538.

Rabinowitz, W.M., Lim, J.S., Braida, L.D., and Durlach, N.I. (**1976**). ''Intensity perception VI: Summary of recent data on deviations from Weber's law for 1000-Hz tone pulses,'' J. Acoust. Soc. Am. **59**, 1506–1509.

Rasmussen, G.L. (**1940**). ''Studies of the VIIIth cranial nerve in man,'' Laryngoscope **50**, 67–83.

Rhode, W.S. (**1971**). ''Observations of the vibration of the basilar membrane in squirrel monkeys using the Mössbauer technique,'' J. Acoust. Soc. Am. **49**, 1218–1231.

Rhode, W.S., and Greenberg, S. (**1992**). ''Physiology of the cochlear nuclei,'' in *The Mammalian Auditory Pathway: Neurophysiology*, edited by A.N. Popper and R.R. Fay (Springer Verlag, New York), pp. 94–152.

Rieke, F., Warland, D., de Ruyter van Steveninck, R., and Bialek, W. (**1997**). *Spikes: Exploring the Neural Code* (MIT Press, Cambridge, MA).

Rose, J.E., Gross, N.B., Geisler, C.D., and Hind, J.E. (**1966**). ''Some neural mechanisms in the inferior colliculus of the cat which may be relevant to localization of a sound source,'' J. Neurophysiol. **29**, 288–314.

Rouiller, E.M., Cronin-Schreiber, R., Fekete, D.M., and Ryugo, D.K. (**1986**). ''The central projections of intracellularly labeled auditory nerve fibers in cats: an analysis of terminal morphology,'' J. Comp. Neurol. **249**, 261–278.

Ruggero, M.A. (**1992**). ''Physiology and coding of sound in the auditory nerve,'' in *The Mammalian Auditory Pathway: Neurophysiology*, edited by A.N. Popper and R.R. Fay (Springer-Verlag, New York), pp. 34–93.

Ruggero, M.A., Robles, L., and Rich, N.C. (**1992**). ''Two-tone suppression in the basilar membrane of the cochlea: Mechanical basis of auditory-nerve rate suppression,'' J. Neurophysiol. **68**, 1087–1099.

Ruggero, M.A., Rich, N.C., Shivapuja, B.G., and Temchin, A.N. (**1996**). ''Auditory-nerve responses to low-frequency tones: Intensity dependence,'' Aud. Neurosci. **2**, 159–185.

Ruggero, M.A., Rich, N.C., Recio, A., Narayan, S.S., and Robles, L. (**1997**). ''Basilar-membrane responses to tones at the base of the chinchilla cochlea,'' J. Acoust. Soc. Am. **101**, 2151–2163.
Ryugo, D.K. (**1992**). ''The auditory nerve: Peripheral innervation, cell body morphology, and central projections,'' in *The Mammalian Auditory Pathway: Neuroanatomy*, edited by D.B. Webster, A.N. Popper, and R.R. Fay (Springer-Verlag, New York), pp. 23–65.
Sachs, M.B., and Kiang, N.Y.S. (**1968**). ''Two-tone inhibition in auditory-nerve fibers,'' J. Acoust. Soc. Am. **43**, 1120–1128.
Sachs, M.B., and Abbas, P.J. (**1974**). ''Rate versus level functions for auditory nerve fibers in cats: Tone burst stimuli,'' J. Acoust. Soc. Am. **56**, 1835–1847.
Schneider, B.A., and Parker, S. (**1987**). ''Intensity discrimination and loudness for tones in notched noise,'' Percept. Psychophys. **41**, 253–261.
Schroder, A.C., Viemeister, N.F., and Nelson, D.A. (**1994**). ''Intensity discrimination in normal-hearing and hearing-impaired listeners,'' J. Acoust. Soc. Am. **96**, 2683–2693.
Siebert, W.M. (**1965**). ''Some implications of the stochastic behavior of primary auditory neurons,'' Kybernetik **2**, 206–215.
Siebert, W.M. (**1968**). ''Stimulus transformations in the peripheral auditory system,'' in *Recognizing Patterns*, edited by P.A. Kolers and M. Eden (MIT Press, Cambridge, MA), pp. 104–133.
Siebert, W.M. (**1970**). ''Frequency discrimination in the auditory system: Place or periodicity mechanisms?,'' Proc. IEEE **58**, 723–730.
Snyder, D.L., and Miller, M.I. (**1991**). *Random Point Processes in Time and Space* (Springer Verlag, New York), Chap. 2.
Steinberg, J.C., and Gardner, M.B. (**1937**). ''The dependence of hearing impairment on sound intensity,'' J. Acoust. Soc. Am. **9**, 11–23.
Stevens, S.S., and Davis, H. (**1936**). ''Psychophysiological Acoustics: Pitch and Loudness,'' J. Acoust. Soc. Am. **8**, 1–13.
Teich, M.C., and Lachs, G. (**1979**). ''A neural-counting model incorporating refractoriness and spread of excitation. I. Application to intensity discrimination,'' J. Acoust. Soc. Am. **66**, 1738–1749.
van Trees, H.L. (**1968**). *Detection, Estimation, and Modulation Theory: Part I* (Wiley, New York), Chap. 2.
Viemeister, N.F. (**1974**). ''Intensity discrimination of noise in the presence of band-reject noise,'' J. Acoust. Soc. Am. **56**, 1594–1600.
Viemeister, N.F. (**1983**). ''Auditory intensity discrimination at high frequencies in the presence of noise,'' Science **221**, 1206–1208.
Viemeister, N.F. (**1988a**). ''Psychophysical aspects of auditory intensity coding,'' in *Auditory Function: Neurobiological Bases of Hearing*, edited by G.M. Edelman, W.E. Gall, and W.M. Cowan (Wiley, New York), pp. 213–241.
Viemeister, N.F. (**1988b**). ''Intensity coding and the dynamic range problem,'' Hear. Res. **34**, 267–274.
Viemeister, N.F., and Bacon, S.P. (**1988**). ''Intensity discrimination, increment detection, and magnitude estimation for 1-kHz tones,'' J. Acoust. Soc. Am. **84**, 172–178.
Whitfield, I.C. (**1967**). *The Auditory Pathway* (Arnold, London).
Winslow, R.L., Barta, P.E., and Sachs, M.B. (**1987**). ''Rate coding in the auditory nerve,'' in *Auditory Processing of Complex Sounds*, edited by W.A. Yost and C.S. Watson (Erlbaum, New York), pp. 212–224.
Winslow, R.L., and Sachs, M.B. (**1988**). ''Single-tone intensity discrimination based on auditory-nerve rate responses in backgrounds of quiet, noise, and with stimulation of the crossed olivocochlear bundle,'' Hear. Res. **35**, 165–190.
Winter, I.M., and Palmer, A.R. (**1991**). ''Intensity coding in low-frequency auditory-nerve fibers of the guinea pig,'' J. Acoust. Soc. Am. **90**, 1958–1967.
Yates, G.K. (**1995**). ''Cochlear structure and function,'' in *Hearing*, edited by B.C.J. Moore (Academic, New York), pp. 41–74.
Yin, T.C.T., and Chan, J.C.K. (**1990**). ''Interaural time sensitivity in medial superior olive of cat,'' J. Neurophysiol. **64**, 465–488.
Yin, T.C.T. Chan, J.C.K., and Carney, L.H. (**1987**). ''Effects of interaural time delays of noise stimuli on low-frequency cells in the cat's inferior colliculus. III. Evidence for cross-correlation,'' J. Neurophysiol. **58**, 562–583.
Young, E.D. (**1984**). ''Response characteristics of neurons of the cochlear nuclei,'' in *Hearing Science*, edited by C.I. Berlin (College Hill Press, San Diego), pp. 423–460.
Young, E.D., and Barta, P.E. (**1986**). ''Rate responses of auditory-nerve fibers to tones in noise near masked threshold,'' J. Acoust. Soc. Am. **79**, 426–442.

Individual differences in the processing of speech and nonspeech sounds by normal-hearing listeners[a)]

Aimée M. Surprenant[b)]
Department of Psychological Sciences, Purdue University, West Lafayette, Indiana 47907

Charles S. Watson
Department of Speech and Hearing Sciences, Indiana University, Bloomington, Indiana 47405

(Received 21 February 2001; revised 6 July 2001; accepted 30 July 2001)

While a large portion of the variance among listeners in speech recognition is associated with the audibility of components of the speech waveform, it is not possible to predict individual differences in the accuracy of speech processing strictly from the audiogram. This has suggested that some of the variance may be associated with individual differences in spectral or temporal resolving power, or acuity. Psychoacoustic measures of spectral-temporal acuity with nonspeech stimuli have been shown, however, to correlate only weakly (or not at all) with speech processing. In a replication and extension of an earlier study [Watson *et al.*, J. Acoust. Soc. Am. Suppl. 1 **71**, S73 (1982)] 93 normal-hearing college students were tested on speech perception tasks (nonsense syllables, words, and sentences in a noise background) and on six spectral-temporal discrimination tasks using simple and complex nonspeech sounds. Factor analysis showed that the abilities that explain performance on the nonspeech tasks are quite distinct from those that account for performance on the speech tasks. Performance was significantly correlated among speech tasks and among nonspeech tasks. Either, (a) auditory spectral-temporal acuity for nonspeech sounds is orthogonal to speech processing abilities, or (b) the appropriate tasks or types of nonspeech stimuli that challenge the abilities required for speech recognition have yet to be identified. [DOI: 10.1121/1.1404973]

PACS numbers: 43.66.Ba [MRL]

I. INTRODUCTION

It has been known for some time that individuals exhibit a large range of performance on a wide variety of auditory psychophysical tasks (Johnson *et al.*, 1987). These differences become more apparent in the study of complex sounds, especially those with more temporal and spectral complexity. Although the extent of the variability in abilities has not been extensively studied, it has been a common practice in psychoacoustic research to screen observers and discard those who seem unable do the task without extensive training (Green, 1988, p. 94). In contrast, some authors have argued that there is a relatively small range of individual differences in auditory speech-processing ability and that all, or nearly all, people with normal auditory sensitivity have a ''uniformly highly developed auditory ability [to perceive speech] (Summerfield, 1991, p. 126).'' This belief is apparently based on the observation that most people can identify words and sentences perfectly, or nearly perfectly, when they are presented at positive speech-to-noise ratios (S/N).

Perhaps because of the belief that individuals vary little in their speech-processing abilities, most studies investigating the perception of speech under adverse conditions (usually with noise masking) have only reported average discrimination scores at various speech-to-noise ratios. Little attention has been paid to the individual variability in those scores. However, Rupp and Phillips (1969) showed that some individuals who have near-perfect discrimination in the quiet perform very poorly at unfavorable S/N ratios. They coined the term ''normal fragile ear'' to describe such listeners. Middelweerd *et al.* (1990) and Rodriguez *et al.* (1990) reported similar cases of listeners complaining of difficulties in hearing speech in noise despite normal pure-tone audiograms. Participants in these studies were assigned to the ''impaired'' condition on the basis of either complaints of difficulty hearing speech in noise (Middelweerd *et al.*, 1990) or performance on a speech-in-noise test falling below some arbitrary criterion (Rodriguez *et al.*, 1990). Data were then reported as averages for the ''impaired'' and ''normal'' conditions. In both cases, the researchers suggested that there was something pathological about the difficulty of some listeners' experiences in understanding speech in noise.

Research has repeatedly shown that many, if not all, of our cognitive abilities are normally distributed across the population. Intelligence, quantitative, verbal, and spatial abilities are all approximately normally distributed (Spearman, 1927; Horn, 1968, 1989). It might be possible that listeners who have difficulty understanding speech-in-noise simply fall into the lower tail of a normal distribution of speech-recognition abilities. Under the speech-to-noise ratios of most every day conditions, their performance may be perfect (a ceiling effect). However, degraded performance may appear when the task becomes more difficult, as when noise is added. There have been very few published reports describing the range of performance of normal-hearing listeners on speech tasks.

[a)]Portions of this work were presented at the 129th meeting of the Acoustical Society of America, Washington, DC, June 1995.
[b)]Electronic mail: aimee@psych.purdue.edu

Stankov and his colleagues (Stankov and Horn, 1980; Horn and Stankov, 1982; Roberts and Stankov, 1999) have argued that several auditory factors contribute to fluid intelligence. Fluid intelligence is defined as one's ability to learn quickly and thoroughly, to solve problems, reason and remember in ways that are relatively uninfluenced by experience (Horn and Cattell, 1966). It can be contrasted with crystallized intelligence which taps acquired knowledge and ability. Stankov and Horn (1980) identified a separate factor that they called ''speech perception under distraction/distortion,'' which was not highly correlated with any other auditory/perceptual factors. This factor was made up of tests of expanded speech, compressed speech, sound blending, and, most strongly, cafeteria noise masking of speech. Although Stankov and Horn do not discuss the range of performance found on the tasks underlying speech perception under distraction/distortion factor, there must have been a large enough range of performance among the subjects ($N=241$) for this variable to contribute sufficient independent variance to form a distinct factor.

If it is the case that both speech and nonspeech auditory processing are normally distributed across the population, it is of interest to determine the relationship between them. Performance on speech recognition tasks must depend on spectral-temporal analyses by the auditory system. However, psychoacoustic measures of acuity or resolving power for nonspeech stimuli have not been found to correlate significantly with speech processing, or correlate only weakly with it once the audiogram is taken into consideration (Watson, 1987; Christopherson and Humes, 1992). This suggests that some significant amount of the systematic variance in speech recognition abilities may be associated with nonauditory differences among listeners. Thus there are two basic questions addressed in this paper.

(1) What is the distribution of speech-recognition abilities among listeners with normal audiograms (pure-tone sensitivity) in tasks employing masking noise (thereby avoiding ceiling effects)?
(2) Are there systematic relationships between measures of performance on nonspeech psychoacoustic tasks and the ability to understand speech-in-noise?

One area in which individual differences in speech processing have received a great deal of attention is in the study of persons with hearing loss. Listeners with the same severity and configuration of sensorineural hearing loss (SNHL) vary widely in their abilities to understand speech, especially in noise (see Crandell, 1991, for a review). We argue that the individual differences found in persons with hearing loss can be found in the entire population but are usually obscured by the fact that normal-hearing listeners are performing at ceiling levels. Once the system is stressed (by either hearing loss or noise) these individual differences become apparent. Following Crandell (1991), below we discuss a number of possibilities that have been proposed to account for individual differences in speech-processing ability in noise. Although these were meant to apply to individual differences in persons with hearing loss, the data presented here suggest that they may be applicable to persons with normal sensitivity as well.

First, the susceptibility to noise may be due to deficits in auditory processing caused by cochlear damage. For example, Plomp (1978) suggested that a combination of attenuation and distortion were the cause of speech recognition difficulties in the hearing impaired. Cochlear distortion could affect frequency and temporal resolution, as well as frequency or temporal discrimination to different degrees among different hearing-impaired individuals. This hypothesis predicts that difficulties in processing nonspeech and speech materials should occur together: those individuals with distortion at the cochlear level would be expected to have trouble with spectral-temporal resolution of all types of auditory stimuli. The difficulties may become more severe as the stimuli become more spectrally or temporally complex, but there still should be a relationship between difficulties in processing nonspeech and speech materials.

Second, Crandell notes that it is possible that the deficit in speech recognition is due to a more central *auditory* processing disorder (Chermak and Musiek, 1997; Watson, 1994), rather than being entirely a consequence of cochlear pathology. If so, some individuals might have difficulty processing complex sounds in the absence of evidence of brain trauma and without any decline in peripheral sensitivity, linguistic competence, or cognitive abilities. Individuals with central auditory processing disorder are assumed to have no difficulty processing simple auditory or nonauditory stimuli. They are said to show greater difficulties as the task becomes more complex or more ''central'' and that difficulty is assumed to manifest itself in both speech and complex nonspeech processing.

Crandell's third possibility is that individuals may process speech at a general cognitive level differently, resulting in different degrees of efficiency or susceptibility to disruption (Van Rooij and Plomp, 1990, 1992). Given a clear and audible signal, some individuals may perform perfectly, but, under nonoptimal conditions, such as noise or some degree of hearing loss, these individuals may experience difficulty in interpreting the signal. According to this hypothesis, the differences found among individuals with the same degree of hearing loss may be a manifestation of differences that are also present in the population of normal-hearing listeners. This hypothesis does not require any relationship between psychoacoustic processing and speech-processing abilities. However, there might be some nonauditory cognitive task that utilizes the same ability and is affected by the same variables.

Another possibility, one not considered by Crandell, is that the critical properties underlying speech recognition may be *linguistic*, rather than *auditory*, and therefore could be observed with either visual or auditory speech. Finally, it is possible that there is a general ability to make perceptual wholes from fragments, not necessarily speech fragments. This ability, often called ''cloze'' in the reading literature, is the ability to comprehend text or speech in which portions are deleted or distorted. Those individuals who score well on these sorts of tests are making use of top-down contextual information. Both of these hypotheses were given some

modest support by Watson *et al.* (1996) who reported significant correlations ($0.45<r<0.55$, $n=90$, $p<0.001$) between lip-reading (vision-only) abilities of normal-hearing listeners and those listeners' abilities to identify speech in noise (auditory-only). This suggests that one or more common central, or cognitive mechanisms may partially account for the excellence in speech perception by both eye and by ear. Watson *et al.* (1996) argue against a purely modality specific view of speech processing and instead suggest that a portion of the variance in speech processing appears to be associated with nonauditory cognitive abilities. These authors also reported significant correlations between lip-reading, auditory speech processing, and a task in which printed phrases had to be recognized under a condition of ''visual noise.''

Among the important determinants of speech recognition thresholds in noise are the contextual cues available to the listener (Miller *et al.*, 1951; Sumby and Pollack, 1954; Hirsh *et al.*, 1954). Miller *et al.* (1951) found a range in threshold from −14 dB for (closed-set) digits to −4 dB for words in sentences to +4 dB for nonsense syllables. As the stimuli become more complex and the set size increases, listeners' informational capacities and the opportunity for using context increases. Those individuals with good skills in using contextual information may not necessarily do well on less contextually based processing. In the study reported below, we employed a range of speech tests including one that could not benefit from contextual processing or prior knowledge (nonsense syllable recognition), one that could benefit a great deal from contextual cues (sentence recognition), and one that falls in between (closed-set word recognition).

This study determined the individual abilities of 93 normal-hearing college age listeners to process a variety of speech and nonspeech stimuli, and the relation between those auditory performance measures and certain estimates of intellectual or cognitive functioning (SAT-V, SAT-M, GPA). A previously developed test battery, the Test of Basic Auditory Capabilities (TBAC), was used to measure nonspeech auditory processing. The eight sub-tests on this battery have been shown to have good test–retest reliabilities (overall Cronbach's alpha of 0.75 across three groups of subjects; Christopherson and Humes, 1992). Three additional speech tests were added to this battery for the present study. These new tests were constructed from audio recordings included in the Bernstein and Eberhart (1986a, b) lip-reading corpus (a video disk recorded by professional actors). The speech tests were conducted under various levels of speech-to-noise (S/N) ratios and included consonant–vowel (CV) syllable identification (open-set), consonant–vowel–consonant (CVC) word identification (closed-set), and sentence identification (open-set).

II. METHOD

A. Subjects

Ninety-three Indiana University students (Ages: $\mu=20$, range 18–32) served as subjects in this study. All tested within normal limits [<20 dB HL from 250 to 8000 Hz (ANSI, 1989)] on a preliminary hearing screening. Forty-five of the subjects received an additional, 2-dB step audiogram. These 45 subjects also signed a release form to allow access to their academic records and to their scores on the Scholastic Aptitude Test (SAT). The subjects were paid for their participation.

B. Stimuli

The TBAC and speech tests were presented to subjects through a digital audio tape deck (Panasonic, SV-3500). The output of this tape deck was routed to a two-channel amplifier (Macintosh, C24) through a network of attenuator pads and delivered monaurally to 13 pairs of Etymotic ER-3A insert earphones at 75 dB SPL. All stimuli were presented at 75 dB SPL, with the exception of the increments in the intensity-discrimination task. Calibration was accomplished using a 1-kHz tone.

1. Test of basic auditory capabilities (TBAC)

The Test of Basic Auditory Capabilities (TBAC) consists of a series of auditory processing tests including seven discrimination tests and one nonsense syllable identification test. There are eight levels of difficulty in each discrimination test and all tests follow a modified two-alternative forced-choice procedure in which a standard is presented followed by two test stimuli, one of which differs from the standard. Listeners are told that their task is to choose which of the two test sounds is different from the standard. This method is used for seven out of the eight subtests, minimizing listeners' confusions that can result from changes in psychophysical procedures. For the eighth test subjects hear nonsense syllables in cafeteria noise and are asked to identify the sound by choosing one of three written alternatives. The first six tests use tones or tone sequences as stimuli and include a total of 72 trials per test. The seventh test uses sequences of four CV nonsense syllables and the eighth is a portion of the CV/VC nonsense syllable test developed by Resnick *et al.* (1975; see also Dubno *et al.*, 1982). This last test was modified to include three response alternatives on each trial, the actual nonsense syllable that was presented, plus the two most confusable alternatives identified in the study by Dubno *et al.* (1982).

This test has been used to measure the auditory processing capabilities of normal-hearing (Watson *et al.*, 1982a, b; Espinoza-Varas and Watson, 1988), hearing-impaired (Humes and Christopherson, 1991; Christopherson and Humes, 1992) and learning-disabled listeners (Watson, 1991). The eight sub-tests are described below (see Christopherson and Humes, 1992, for a more detailed description).

(a) *Pitch discrimination* (ΔF)—range of Δf from 2 to 256 Hz; standard is a 250-ms, 1.0-kHz tone, presented at 75 dB SPL.
(b) *Single-tone intensity discrimination* (ΔL)—range of from 0.5 to 8.0 dB (same standard as for Pitch discrimination).
(c) *Single-tone duration discrimination* (ΔT)—range from 8 to 256 ms; standard is 100-ms, 1.0-kHz tone, presented at 75 dB SPL.
(d) *Pulse/train discrimination (PT)*—standard is six 20-ms pulses of a 1-kHz tone. The temporal sequences are

varied by increasing the separation between members of one of the test sequences, from 40 ms to 90 ms. (This is a rhythm discrimination test.)

(e) *Embedded test-tone loudness (ET)*—detect the presence of a tone rather than a silent gap in the temporal center of a nine-tone, isochronous pattern. The duration of the target tone is varied between 10 and 200 ms; nontarget tones are all 50 ms in duration.

(f) *Temporal order for tones (TO)*—discriminate the order in which two equal-duration tones are presented, one of which is 550 Hz and the other 710 Hz. The two tones are preceded and followed by equal-duration leading and trailing 600-Hz tones. Duration of the tones in these (isochronous) four-tone sequences are varied from 20 to 200 ms.

(g) *Temporal order for syllables (TOS)*—speech analog of the temporal order for tones test, in which the listener discriminates the syllable sequence /fa/ /ka/ /ta/ /pa/ from /fa/ /ta/ /ka/ /pa/. The durations of the syllables are varied from 75 to 250 ms. (The syllables are natural tokens that were digitally edited.)

(h) *Syllable identification (SI)*—identify nonsense syllables such as ''ooze,'' among three alternatives (adapted from Resnick *et al.*, 1975). The alternatives are the most likely errors, according to the data reported by Resnick *et al.* (1975).

2. Speech tests

All speech materials were recorded from the Bernstein and Eberhardt (1986a, b) lipreading corpus. Speech examples were digitized using an Audiomedia D/A and recorded on a Macintosh. The stimuli were edited and rerecorded onto a DAT. Speech-shaped noise was mixed with the speech. Three types of stimuli were used: CVs, words, and sentences.

a. CVs. The CVs were consonants b, ch, d, f, g, h, k, l, m, n, p, r, s, sh, t, w, and z followed by the vowel /a/. Two examples of each CV (with the exception of k, l, p, and sh which only had one example recorded) were digitized. Each stimulus was recorded at two different speech-to-noise ratios (S/N): 0 and +3 dB. A block of trials consisted of five CVs and blocks alternated in their S/N ratio. Three practice blocks were presented, decreasing in S/N ratio from +6, +3, to 0 dB. There was a 3-s inter-stimulus interval (ISI) and six seconds between blocks. A 0.5-s 1-kHz tone was played to signal the start of each new block. Twelve seconds separated blocks six and seven. Subjects were asked to write the consonants they thought they heard in the blank spaces provided and to be sure to respond on every trial.

b. Words. The words were 50 one-syllable words from the Modified Rhyme test (House *et al.*, 1965) presented in a forced-choice, four-alternative trial structure. The three foils each differed from the target by one feature: the initial and final consonant cluster and the vowel. Words were recorded at two S/N ratios, 0 and −3 dB. A block of trials consisted of five words and the S/N ratio was alternated between blocks. Five seconds separated each word and a 0.5-s 1-kHz tone was played in between each block. Ten seconds separated blocks 25 and 26. Two practice blocks were presented before the test. Subjects were asked to circle the word they thought they heard and were told to respond on every trial.

c. Sentences. Sentences were 20 of the CID sentences (Davis and Silverman, 1970) spoken by a male talker. They ranged in length from 2 to 13 words with an average of 8 words. Sentences were presented in five different levels of noise, +3, 0, −3, −4, and −5 dB S/N ratio. The S/N ratio was decreased systematically within each block of five words. Twenty seconds separated each sentence and a 0.5-s, 1-kHz tone signaled the beginning of each new sentence. Subjects were asked to write down all the words they heard.

C. Procedures

Subjects were tested in groups of 4 to 13 in a sound-treated room. Following a preliminary auditory screening, they were seated at a desk and were given instructions on how to insert the earphones. Testing was completed in two 1-h sessions. The sequence of the tests and of all items within each test were the same for all listeners. This constant test order was chosen to minimize all sources of inter-subject variation in performance other than their individual abilities to perform the tasks.

Instructions for the TBAC are recorded as part of the test and include detailed descriptions of the method for each of the subtests. Subjects are given two practice trials before each test. Instructions for the additional speech tests were given by the experimenter. On each test, subjects were encouraged to guess.

III. RESULTS AND DISCUSSION

A. TBAC

Figure 1 shows the collapsed overall psychometric functions for the seven discrimination tests (dotted lines) and a fitted curve that describes the maximum likelihood probit (solid lines). Estimated thresholds for mean performance at 75% correct are shown for each subtest in Table I (first column). It is clear that the tests do a moderately good job of sampling the transition range (chance-to-perfect) for the 93 normal listeners whose data are shown here. The probit fits are a close description of the data, with all fits but one accounting for greater than 95% of the variance. The exception is the fit to the temporal-order-for-syllables test, which accounts for only 77% of the variance. Later analyses suggest that performance on this last test is not well described by a simple probit function.

Figure 2 shows the mean psychometric functions for listeners falling within each decile when the listeners were ordered by their overall percentages of correct responses on each test. Table I gives an overview of population performance on these tests in terms of the fitted thresholds (intercepts for 50% correct performance expressed in Hz, ms, or dB, as appropriate) for the group of subjects who fall within each decile. These ranges are similar to those reported by Watson *et al.* (1982a) for a comparable sample of normal-hearing listeners (see the Appendix). With the exception of the embedded tone test, the range of thresholds for normal hearing listeners on these stimuli is large.

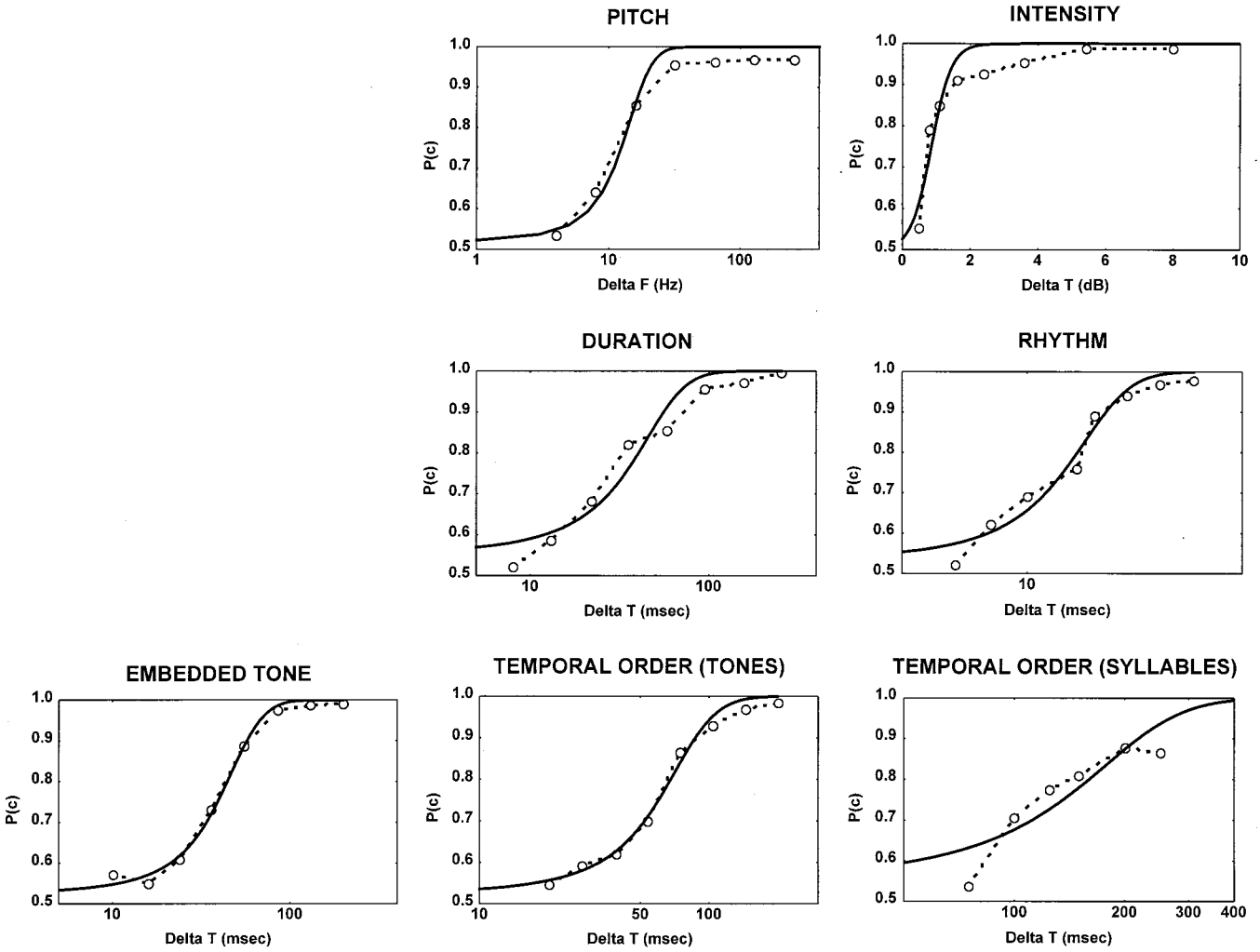

FIG. 1. Collapsed overall psychometric functions for the seven discrimination tests from the TBAC (dotted lines) and a fitted curve which describes the maximum likelihood probit (solid lines).

TABLE I. Population performance on TBAC subtests.

		Thresholds by decile									
Test	Mean	1	2	3	4	5	6	7	8	9	10
Pitch discrimination (Hz)	12.30	[a]	16.00	15.20	13.40	13.40	10.20	8.50	7.80	7.40	5.20
Single-tone intensity discrimination (dB)	0.88	3.00	1.40	1.00	0.90	0.90	0.80	0.70	0.60	0.60	0.40
Single-tone duration discrimination (ms)	34.00	107.00	46.00	36.00	35.00	33.40	33.00	25.20	22.00	18.00	8.00
Pulse/train discrimination (ms)	14.20	26.70	20.30	17.00	15.50	14.30	13.00	10.70	8.40	7.40	5.50
Embedded test-tone loudness (ms)	39.00	54.00	45.00	43.00	39.00	39.00	37.50	37.00	34.00	33.40	33.00
Temporal order (tones) (ms)	61.00	126.00	85.00	75.00	63.50	60.00	58.00	46.00	43.70	35.00	25.70
Temporal order (syllables) (ms)	135.00	[a]	167.00	[a]	157.00	[a]	119.00	101.50	98.00	92.00	75.30
Syllable identification $[P(c)]$	0.74	0.64	0.68	0.71	0.72	0.74	0.75	0.76	0.78	0.80	0.84

[a]Probit fit failed.

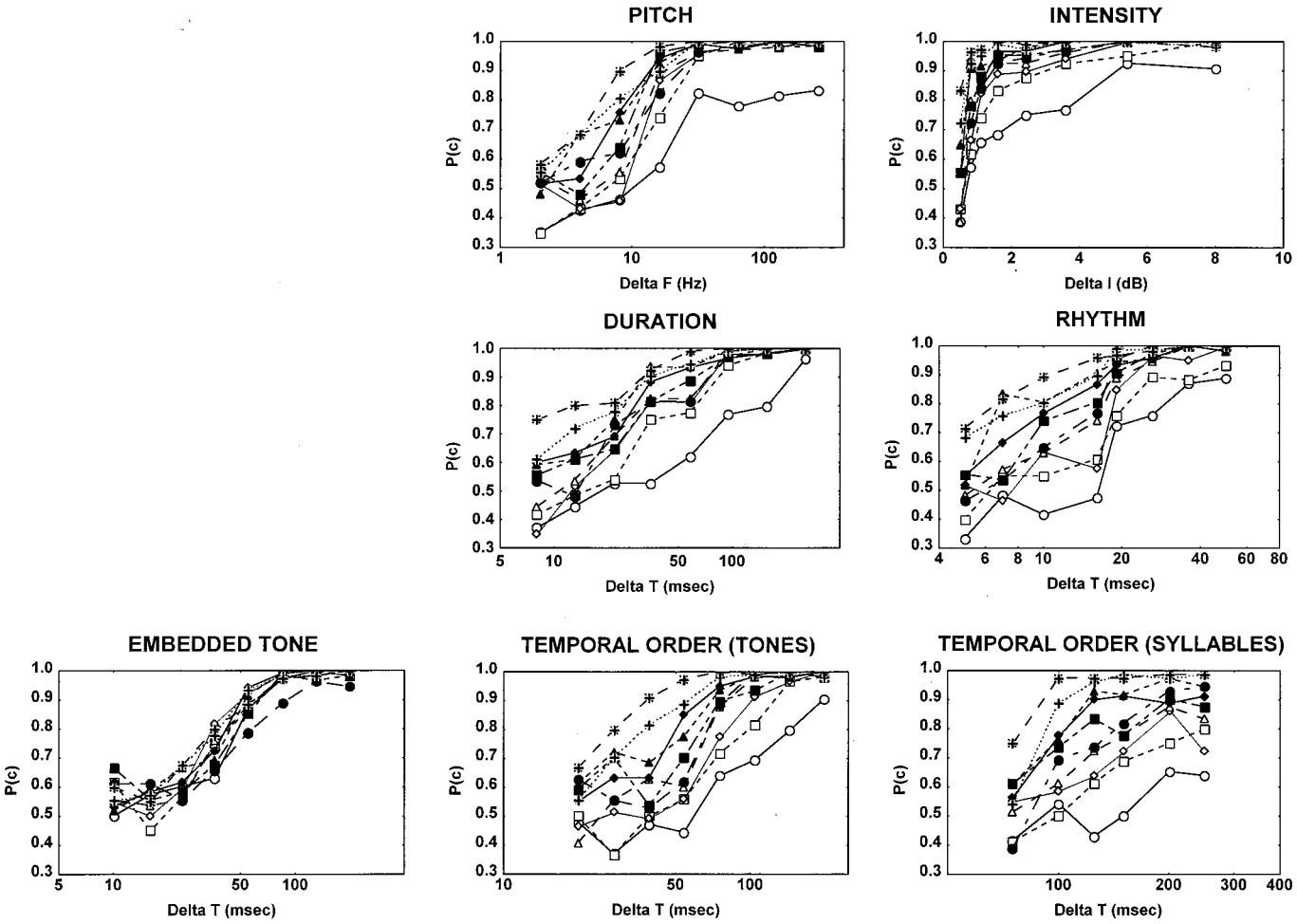

FIG. 2. Mean psychometric functions for listeners falling within each decile for the seven discrimination tests from the TBAC. Deciles were constructed by dividing the individuals into ten groups by their overall percent correct on each test. In general, the leftmost function in the family of curves shows the best 10% of listeners and the rightmost function describes the worst 10% of the listeners.

The families of psychometric functions for all tests except the temporal-order-for-syllables test appear well described by families of probit functions differing primarily in their horizontal displacement. The syllable-order test differs in that the performance by the worst subjects appears to be limited both by the duration of the syllables, yielding horizontal displacement of the function, and also by another factor, which limits maximum performance for long-duration sequences. Although it is not clear what this other factor is, Watson *et al.* (1982a) found a similar result on this test. They noted that their poorest listeners actually performed worse for long-duration sequences than for intermediate-duration ones, on this test. This could reflect a duration-dependent deficiency in working memory for these listeners (Gathercole and Baddeley, 1993).

B. Supplemental speech tests

Means and population statistics, collapsed across noise level, for each of the supplemental speech tests are shown in Table II. The sentences were scored in terms of overall sentences correct and also in terms of total individual words correct. The correlation between those two measures was 0.77. The range of scores for sentences scored by words was larger and more closely approximated a normal distribution. Therefore, for all further analyses, the scores for sentences scored by words have been used.

The range of percent correct $[P(c)]$ for all of the speech tests is about 30 percentage points. This substantial range of performance implies that some of the subjects could understand speech at a much lower S/N ratio than others.

TABLE II. Population performance on supplementary speech tests.

		Means by decile $[P(c)]$									
Test	Mean	1	2	3	4	5	6	7	8	9	10
CVs	0.58	0.45	0.52	0.53	0.56	0.58	0.60	0.61	0.63	0.65	0.71
Words	0.74	0.56	0.66	0.70	0.73	0.75	0.77	0.79	0.80	0.82	0.86
Sentences	0.60	0.39	0.49	0.55	0.57	0.59	0.62	0.64	0.65	0.68	0.75

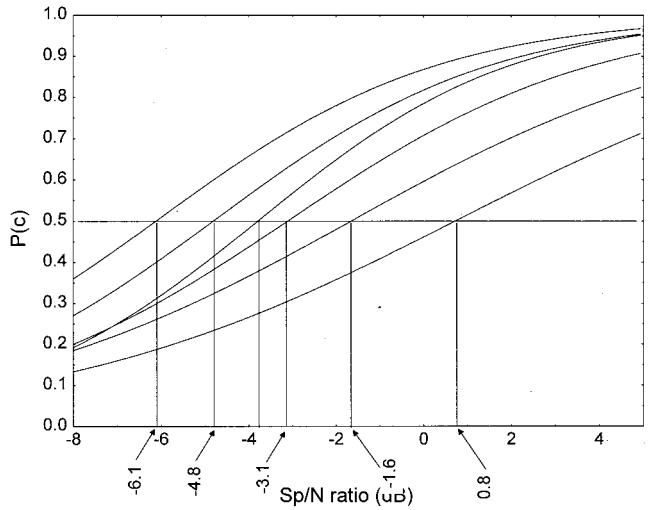

FIG. 3. Mean psychometric functions for listeners falling within each decile for the sentences in noise test. Deciles were constructed by dividing the individuals into ten groups by their overall percent correct on this test. Fifty percent thresholds were interpolated from the fitted functions and are indicated by the arrows. The leftmost curve describes the performance of the best 10% of listeners and the rightmost function describes the worst 10% of the listeners. For maximum clarity, only deciles 1, 2, 3, 7, 9, and 10 are shown.

There were only two levels of noise for the CV and the word test, therefore thresholds could not be accurately estimated. However, there were five levels of noise for the sentences, which allowed the fitting of psychometric functions. Listeners were ordered by overall $P(c)$ into ten groups. A maximum-likelihood normal ogive was fitted to the average data for each decile. Assuming a normal ogive to be representative of this psychometric relationship, ''functional'' S/N ratios were derived by correcting the nominal values to place them on this fitted function.[1] Psychometric functions for decile groups obtained with the resulting functional S/N ratios were then plotted, using maximum-likelihood functions. The probit fits are a close description of the data, with all fits but one accounting for greater than 95% of the variance. The exception is the fit to the eighth decile, which accounts for only 89% of the variance. Fifty-percent thresholds were then interpolated from the fitted functions. Deciles 1, 2, 3, 7, 9, and 10 are shown. As may be seen in Fig. 3, the range of speech-to-noise ratios for 50% correct between the first and tenth decile is approximately 7 dB, and is about 3.2 dB between the second and ninth decile.

C. Correlational analyses

The product-moment correlation coefficients among all of the TBAC subtests and the supplemental speech tests are presented in Table III. Although there are many statistically reliable correlations, there are not many substantial ones.

The reliability of the underlying tests was measured using Cronbach's coefficient *alpha* (Cronbach *et al.*, 1972). This particular measure estimates the proportion of true score variance that is captured by the items by comparing the sum of item variances with the variance of the sum scale. If there is only error in the items (uncorrelated across subjects), then the coefficient will be equal to zero. If all items are perfectly reliable and measure the same thing, then the coefficient is equal to 1. The values of *alpha* were 0.78 for all of the tests together (TBAC and supplemental speech tests); 0.75 for TBAC alone; 0.64 for the supplemental speech tests alone. Although the supplemental speech tests were slightly less reliable than the TBAC scores, all of the reliability measures were high enough to permit interpretation of the inter-test associations.

TABLE III. Correlations (r) among the test ($N=93$).

	1	2	3	4	5	6	7	8	9	10	11
1 CVs	⋯										
2 Words	0.25[a]	⋯									
3 Sentencs	0.41[a]	0.47[b]	⋯								
4 Pitch discrimination	0.23[a]	0.25[a]	0.30[b]	⋯							
5 Single-tone intensity discrimination	0.11	0.20	0.19	0.28[b]	⋯						
6 Single-tone duration discrimination	0.14	0.21[a]	0.10	0.36[b]	0.53[b]	⋯					
7 Pulse/train discrimination	0.14	0.20	0.19	0.28[b]	0.34[b]	0.29[b]	⋯				
8 Embedded test-tone loudness	0.26[a]	0.21[a]	0.20	0.16	0.33[b]	0.33[b]	0.49[b]	⋯			
9 Temporal order (tones)	0.15	0.13	0.12	0.22[a]	0.09	0.33[b]	0.10	0.35[b]	⋯		
10 Temporal order (syllables)	0.18	0.25[a]	0.19	0.26[a]	0.20	0.31[b]	0.17	0.31[b]	0.46[b]	⋯	
11 Syllable identification	0.32[a]	0.31[b]	0.28[b]	0.23[a]	0.30[b]	0.22[a]	0.25[a]	0.31[b]	0.19	0.32[b]	⋯

[a]$p<0.05$.
[b]$p<0.01$.

TABLE IV. Correlations (r) among the supplemental tests ($N=48$).

Test	Threshold (right ear)	Threshold (left ear)	GPA	SAT verbal	SAT math
CVs	−0.10	−0.13	0.11	0.02	0.06
Words	−0.03	−0.05	−0.15	0.09	0.16
Sentences	−0.22	−0.25	0.08	0.18	0.34
Pitch discrimination	0.13	0.11	0.07	0.34[a]	0.23
Single-tone intensity discrimination	0.07	0.13	0.13	0.08	0.27
Single-tone duration discrimination	0.20	0.17	0.25	0.31[a]	0.36
Pulse/train discrimination	0.11	0.06	−0.05	0.02	0.06
Embedded test-tone loudness	0.02	0.06	−0.03	0.29[a]	0.40
Temporal order (tones)	−0.09	−0.05	0.20	0.43[b]	0.42
Temporal order (syllables)	0.15	0.23	0.31[a]	0.65[b]	0.45
Syllable identification	0.17	0.26	−0.04	0.10	0.14
Threshold (rt)	⋯	0.83	0.09	0.22	−0.01
Threshold (lt)	0.83[b]	⋯	0.15	0.32[a]	0.12
GPA	0.09	0.15	⋯	0.52[b]	0.29
SAT verbal	0.22	0.32[a]	0.52[b]	⋯	0.56
SAT math	−0.01	0.12	0.29[a]	0.56[b]	⋯

[a]$p<0.05$.
[b]$p<0.01$.

D. Correlations with other variables

Forty-five of the subjects allowed access to their SAT scores and GPAs and were also given a 2-dB step hearing screening.[2] Table IV shows the correlations among the cognitive/intellectual scores and the TBAC and supplemental speech tests. Interestingly, the temporal order tests from the TBAC correlated quite strongly with the SAT verbal score. This is discussed further below.

E. Factor analyses

Two factor analyses were conducted, one including all of the participants and one restricted to the 45 for whom we obtained SAT scores and GPAs. The analysis including all of the participants was based on the eight TBAC subtests and the three supplementary speech tests described above. The analysis extracted three factors with eigenvalues greater than 1.[3] Varimax-rotated loadings[4] on the three factors are shown in Table V, for each of the auditory tests and other measures.

TABLE V. Three-factor solution for all subtests (eigenvalues>1) $N=93$.

Test	Factor 1	Factor 2	Factor 3
Single-tone intensity discrimination	**0.73**	0.06	0.04
Pulse/train discrimination	**0.73**	0.17	−0.09
Single-tone duration discrimination	**0.67**	0.00	0.35
Embedded test-tone loudness	**0.63**	0.26	0.28
Pitch discrimination	**0.51**	0.33	0.20
Sentences	0.07	**0.83**	−0.03
Words	0.18	**0.68**	0.08
CVs	0.04	**0.67**	0.15
Syllable identification	0.30	**0.52**	0.17
Temporal order (syllables)	0.16	0.21	**0.76**
Temporal order (tones)	0.11	0.06	**0.86**

An interpretation of the three factors is (1) a nonspeech discrimination factor—including most of the TBAC measures, (2) a speech identification factor—including our supplementary speech tests as well as the syllable identification test, and (3) a temporal order discrimination factor—including the two temporal order tests. The three factors accounted for 54% of the variance.

The temporal order discrimination factor is similar to a temporal tracking factor identified by Stankov and Horn (1980). Each of the tasks that loaded on this factor required attention to "a series of successive events for which there is an ordered pattern (p. 37)." Stankov and Horn found this factor to be only moderately correlated with verbal comprehension and musical ability. Tallal (1980; see also Tallal *et al.*, 1985) has identified deficits in temporal integration as a major factor in disordered speech perception in children. The data reported here and also by Stankov and Horn (1980) suggest that temporal-ordering abilities are not intimately related to speech perception.

This analysis also suggests that the abilities measured by the speech and nonspeech tests administered in this study share very little common variance. A four-factor solution (not shown here) did not significantly increase the amount of variance that was accounted for and did not change the interpretation. The speech tests and nonspeech tests were strongly loaded on separate factors; there was also a third factor for the temporal order tests (syllables and tones), and the fourth factor was composed entirely of the Pitch test from the TBAC.

A second factor analysis was performed on the data from those listeners for whom cognitive/intellectual measures were available, as well as the auditory measures ($N=45$). A four factor solution of these data is presented in Table VI. Interestingly, the first factor combined the cognitive/academic measures (GPA, SAT) and the temporal-order variables from the TBAC (Tones and Syllables). As noted earlier,

TABLE VI. Four-factor solution for all variables including cognitive/academic and hearing thresholds ($N=45$).

Test	Factor 1	Factor 2	Factor 3	Factor 4
SAT verbal	**0.86**	0.20	0.01	0.05
Temporal order (syllables)	**0.74**	0.15	0.05	0.09
SAT math	**0.69**	−0.03	0.23	0.23
Temporal order (tones)	**0.66**	−0.22	0.38	−0.04
GPA	**0.62**	0.06	−0.09	−0.11
Pitch discrimination	*0.44*	0.04	0.09	0.08
Hearing threshold (lt)	0.19	**0.92**	0.05	−0.13
Hearing threshold (rt)	0.08	**0.90**	0.06	−0.13
Pulse/train discrimination	−0.10	0.05	**0.82**	−0.08
Embedded test-tone loudness	0.28	−0.07	**0.70**	0.08
Single-tone intensity discrimination	0.04	0.15	**0.63**	0.21
Single-tone duration discrimination	0.42	0.13	**0.57**	0.14
Words	0.04	0.05	−0.01	**0.86**
Sentences	0.18	−0.20	−0.04	**0.82**
CVs	0.02	−0.15	0.23	**0.51**
Syllable identification	0.01	*0.44*	0.22	*0.47*

the importance of temporal variables in developmental language disorders has been repeatedly argued by Tallal and colleagues (e.g., Tallal, 1980; Tallal *et al.*, 1985). However, the association of temporal-order thresholds with intellectual measures in this analysis, and their dissociation from the speech processing factor, suggests an alternative interpretation that temporal-order judgments are more closely related to general cognitive skills than to linguistic ones.

The second factor loaded primarily on hearing thresholds. The range of hearing thresholds in our population was surprisingly large. These ''normal-hearing'' subjects had thresholds ranging from about −10 to +20 dB HL. However, this range of thresholds had little or no association with either speech or nonspeech processing abilities. The third factor consisted mainly of the nonspeech TBAC measures and the fourth factor was made up of the speech tests. This analysis further underscores the independence of abilities underlying speech and nonspeech auditory processing.

F. Summary and conclusions

Several different measures of speech recognition, using nonsense syllables, words, and sentences were significantly correlated, suggesting a common processing mechanism, or mechanisms. These correlations, although statistically significant, were relatively small compared to some previous studies showing substantially stronger relationships among speech processing variables (e.g., Rabinowitz *et al.*, 1992; Demorest *et al.*, 1996). Speech-processing measures are very sensitive to set size, method, and subject population, which could account for the discrepancy. Nevertheless, the factor analysis indicated a strong speech identification factor with the speech tests loading very cleanly on that factor and with very little overlap with the other factors. More importantly, these speech-processing measures correlate only very weakly with measures of spectral and temporal auditory resolving power. These results, together with the significant correlation between lip-reading (visual-only) and auditory-only speech identification in noise (Watson *et al.*, 1996), argue against modality-specific views of speech processing and instead are consistent with theories that postulate a central cognitive factor that is specific either to (a) speech, (b) linguistic tasks, or (c) the recognition of perceptual wholes on the basis of stimulus fragments. Data currently available do not offer a strong reason to choose among these alternatives.

There are significant individual differences in speech processing abilities among normal-hearing college students, yielding a range of speech-to-noise ratios for 50% correct detection of sentences, of about 6.0 dB, for 95% of that population. While apparently modest, given that the dynamic range of the auditory system exceeds 100 dB, this range is not without consequences. Reference to Fig. 3 illustrates, for example, that with a speech-to-noise ratio equal to −1.6 dB, the best ten percent of *normal-hearing listeners* recognize 82% of the words presented to them, while those in the lowest percentile recognize only 38%. This would represent a difference between mostly successful and mostly unsuccessful efforts at sentence-based communication.

From a cognitive perspective, speech processing is a complex skill depending on a variety of subsidiary abilities. Because the speech signal is quite redundant—there are multiple cues to each phonemic distinction—there may be many combinations of strengths and weakness of auditory processing abilities that lead to equivalent levels of speech recognition performance.

While it is tempting to conclude from this work that individual differences in auditory abilities in general have little to do with one's efficiency as a speech processor, that conclusion is probably premature. The discrimination tests included in the TBAC battery, like most nonspeech discrimination tasks that have been found to correlate weakly with speech processing, all encourage ''analytic listening.'' Attempting to detect some subtle spectral or temporal detail of a complex sound (or to judge the pitch of a simple one) may not be examples of the way the auditory system must be employed in identifying spoken words. Thus it is possible that nonspeech discrimination or identification tasks that require the listener to process more global properties of stimuli may be more appropriate for the prediction of individual differences in speech perception.

Another possibility is that the nonspeech tasks that are generally used in psychophysical tasks measure the limits of sensitivity whereas the speech signal contains much larger supra-threshold physical changes. The complexity of the speech signal is such that the ability to detect very small changes in a relatively simple auditory stimulus may not be directly related to speech intelligibility. One approach that one could take towards solving this difference in complexity is to compare discrimination or identification of spectrally-temporally complex nonspeech stimuli to identification of speech sounds. The main difficulty with this approach is that we then have as little control over the exact cues used for solving the task as we do when we use regular speech sounds. A different approach is to limit the speech sounds to the same narrow-band spectral region as the nonspeech tasks (limiting the complexity of the stimuli at least on one dimen-

TABLE VII. Factor analysis for TBAC data on 127 normal-hearing listeners (from Watson *et al.*, 1982a). Loadings less than 0.250 have been replaced by zero.

Test	Factor			
	1	2	3	4
Temporal order (tones)	0.803	0.000	0.000	0.000
Embedded test-tone loudness	0.771	0.000	0.000	0.000
Pitch discrimination	0.659	0.000	0.000	0.000
Temoral order (syllables)	0.522	0.000	0.478	−0.343
Single-tone duration discrimination	0.000	0.878	0.000	0.000
Single-tone intensity discrimination	0.000	0.731	0.325	0.000
Syllable identification	0.000	0.000	0.902	0.000
Pulse/train discrimination	0.000	0.000	0.000	0.876

sion). This is an approach recently taken by Noordhoek *et al.* (2001). Their measure of speech intelligibility was a threshold measure of the bandwidth of speech at 1 kHz required for a 50% intelligibility score. That bandwidth measure was more highly related to their nonspeech auditory tasks than were the common speech reception threshold tasks. This is an interesting result and suggests that auditory resolving power may be more important in certain circumstances than is indicated by our present data. There can be little doubt that if you pare the speech processing task down to the point where you are forced to use some very subtle acoustic details to understand the speech, then eventually individual differences in auditory abilities would have to make a difference in performance.

The applicability of these findings to the practical question of speech perception by the hearing impaired deserves a final comment. The failure of hearing aids to provide useful help to many of the hearing-impaired persons for whom they are provided, has been repeatedly reported for almost 50 years (Humes, 1999). The explanation has commonly been that there is more wrong with the impaired auditory system than its loss of sensitivity (which could be corrected by simple amplification); it also fails to properly analyze the auditory signal (i.e., it is ''distorted''). If true, it would be expected, as noted earlier, that this distortion would also be reflected in the processing of nonspeech stimuli. While the nonspeech tests used here may not have included the correct ''speechlike'' sounds, the data reported here strongly suggest that factors higher in the sequence of processing than the auditory periphery account for significant variance in speech recognition—by both normal hearing and by hearing-impaired listeners. The consequences of being deficient in this higher-level processing ability may become much larger when it is coupled with hearing fragmented speech because of sensorineural (peripheral) hearing loss.

ACKNOWLEDGMENTS

This work was supported by a National Institutes of Health (NIH), Individual National Research Service Award to the first author, by NIH Grant No. DC-00250 and by Air Force Office of Scientific Research Grant No. F49620-92-J-0506DEF to Indiana University.

APPENDIX

The Test of Basic Auditory Capabilities (TBAC, Watson *et al.*, 1982a; Espinoza-Varas and Watson, 1988) was originally standardized with a group of 127 normal-hearing subjects, using free-field stimulus presentation in a relatively uniform acoustic environment. Analysis of that first set of TBAC data suggested a similar factor structure to that reported here, as shown in Table VII. The separation of the speech and nonspeech processing measures shown here was one of the motivations for the present study. While suggestive of a difference in the mechanisms underlying speech recognition and nonspeech auditory discrimination abilities, these results suffered from being based on a single speech recognition task (the nonsense syllable identification test). The present replication and extension of these results clearly support the original conclusion.

[1]We justify this method of smoothing the data on the grounds that variations in the gaussian noise masker were sufficient to explain those small deviations, and that the deviations were also well in excess of the standard errors for these means.

[2]This fine-grained test of auditory sensitivity was introduced because of the possibility that differences in pure-tone thresholds among these listeners might be of some importance, despite all of them being within clinical limits of normal hearing ($x<20$ dB HL). Within such a population it is common to find listeners whose thresholds differ by 15–20 dB or more, at given frequencies. Further analysis showed these large differences in absolute thresholds to have no association whatsoever with speech processing at conventional levels.

[3]In factor analysis an eigenvalue refers to the variance accounted for by each factor as a function of the number of total variables submitted to the factor analysis. In general, the eigenvalues reflect the amount of common variance accounted for by the respective number of factors. Unless a factor extracts at least as much as the equivalent of one original variable (an eigenvalue of 1), it is generally dropped from further consideration.

[4]The goal of rotating the loadings in a factor analysis is to obtain a clear pattern of loadings, that is, factors that are somehow clearly marked by high loadings for some variables and low loadings for others. A varimax rotation of the factor loadings is the most commonly used method of rotating the factors.

ANSI (**1989**). ANSI S3.6-1989, ''Specifications for audiometers'' (American National Standards Institute, New York).

Bernstein, L. E., and Eberhardt, S. P. (**1986a**). *Johns Hopkins Lipreading Corpus I-II: Disc I* (Johns Hopkins, Baltimore, MD).

Bernstein, L. E., and Eberhardt, S. P. (**1986b**). *Johns Hopkins Lipreading Corpus III-IV: Disc I* (Johns Hopkins, Baltimore, MD).

Chermak, G. D., and Musiek, F. E. (Eds.) (**1997**). *Central Auditory Processing Disorders: New Perspectives* (Singular Publishing, San Diego).
Christopherson, L. A., and Humes, L. E. (**1992**). ''Some psychometric properties of the Test of Basic Auditory Capabilities (TBAC),'' J. Speech Hear. Res. **35**, 929–935.
Crandell, C. C. (**1991**). ''Individual differences in speech recognition ability: Implications for hearing aid selection,'' Ear Hear. **12**, 100s–108s.
Cronbach, L. J., Gleser, G. C., Nanda, H., and Rajartnam, N. (**1972**). *The Dependability of Behavioral Measurements: Theory of Generalizability for Scores and Profiles* (Wiley, New York).
Davis, H., and Silverman, S. R. (**1970**). *Hearing and Deafness* (Holt, Rinehart and Winston, New York).
Demorest, M. E., Bernstein, L. E., and DeHaven, G. P. (**1996**). ''Generalizability of speechreading performance on nonsense syllables, words, and sentences: Subjects with normal hearing,'' J. Speech Hear. Res. **39**, 697–713.
Dubno, J. R., Dirks, D. D., and Langhofer, L. R. (**1982**). ''Evaluation of hearing-impaired listeners using a nonsense-syllable test. II. Syllable recognition and consonant confusion patterns,'' J. Speech Hear. Res. **25**, 141–148.
Espinoza-Varas, B., and Watson, C. S. (**1988**). ''Low commonality between tests of auditory discrimination and speech perception,'' J. Acoust. Soc. Am. **84**, S143.
Gathercole, S. E., and Baddeley, A. (**1993**). *Working Memory and Language* (Lawrence Erlbaum, Hillsdale, NJ).
Green, D. M. (**1988**). *Profile Analysis: Auditory Intensity Discrimination* (Oxford, New York).
Hirsh, I. J., Reynolds, E. G., and Joseph, M. (**1954**). ''Intelligibility of different speech materials,'' J. Acoust. Soc. Am. **26**, 530–537.
Horn, J. L. (**1968**). ''Organization of abilities and the development of intelligence,'' Psychol. Rev. **75**, 242–259.
Horn, J. L. (**1989**). ''Cognitive diversity: A framework of learning,'' in *Learning and Individual Differences: Advances in Theory and Research*, edited by P. L. Ackerman, R. J. Sternberg, and R. Glaser (W. H. Freeman, New York), pp. 61–116.
Horn, J. L., and Stankov, L. (**1982**). ''Auditory and visual factors of intelligence,'' Intelligence **6**, 165–185.
Horn, J. L., and Cattell, R. B. (**1966**). ''Refinement and test of the theory of fluid and crystallized ability intelligences,'' J. Educ. Psychol. **57**, 253–270.
House, A. S., Williams, C. E., Hecker, M. H. L., and Kryter, K. (**1965**). ''Articulation-testing methods: Consonantal differentiation with a closed-response set,'' J. Acoust. Soc. Am. **37**, 158–166.
Humes, L. E. (**1999**). ''Dimensions of hearing aid outcome,'' J. Am. Acad. Audiol. **10**, 26–39.
Humes, L. E., and Christopherson, L. (**1991**). ''Speech identification difficulties of hearing-impaired elderly persons: The contributions of auditory processing deficits,'' J. Speech Hear. Res. **34**, 686–693.
Johnson, D. M., Watson, C. S., and Jensen, J. K. (**1987**). ''Individual differences in auditory capabilities. I,'' J. Acoust. Soc. Am. **81**, 427–438.
Middelweerd, M. J., Festen, J. M., and Plomp, R. (**1990**). ''Difficulties with speech intelligibility in noise in spite of normal pure-tone audiogram,'' Audiology **29**, 1–7.
Miller, G. A., Heise, G. A., and Lichten, W. (**1951**). ''The intelligibility of speech as a function of the context of the test materials,'' J. Exp. Psychol. **41**, 329–335.
Noordhoek, I. M., Houtgast, T., and Festen, J. M. (**2001**). ''Relations between intelligibility of narrow-band speech and auditory functions, both in the 1-kHz frequency region,'' J. Acoust. Soc. Am. **109**, 1197–1212.
Plomp, R. (**1978**). ''Auditory handicap of hearing impairment and the limited benefit of hearing aids,'' J. Acoust. Soc. Am. **63**, 533–549.
Rabinowitz, W. M., Eddington, D. K., Delhorne, L. A., and Cuneo, P. A. (**1992**). ''Relations among different measures of speech reception in subjects using a cochlear implant,'' J. Acoust. Soc. Am. **92**, 1869–1881.
Resnick, S. B., Dubno, J. R., Hoffnung, S., and Levitt, H. (**1975**). ''Phoneme errors on a nonsense syllable test,'' J. Acoust. Soc. Am. **58**, 114.
Roberts, R. D., and Stankov, L. (**1999**). ''Individual differences in speed of mental processing and human cognitive abilities: Toward a taxonomic model,'' Learning & Individual Differences **11**, 1–120.
Rodriguez, G. P., DiSarno, N. J., and Hardiman, C. J. (**1990**). ''Central auditory processing in normal-hearing elderly adults,'' Audiology **29**, 85–92.
Rupp, R. R., and Phillips, D. (**1969**). ''The effect of noise background on speech discrimination function in normal-hearing individuals,'' J. Aud. Res. **9**, 60–63.
Spearman, C. (**1927**). *The Abilities of Man* (Macmillian, New York).
Stankov, L., and Horn, J. L. (**1980**). ''Human abilities revealed through auditory tests,'' J. Educ. Psychol. **72**, 21–44.
Sumby, W. H., and Pollack, I. (**1954**). ''Visual contribution to speech intelligibility in noise,'' J. Acoust. Soc. Am. **26**, 212–215.
Summerfield, Q. (**1991**). ''Visual perception of phonetic gestures,'' in *Modularity and the Motor Theory of Speech Perception*, edited by I. G. Mattingly and M. Studdert-Kennedy (Lawrence Erlbaum, Hillsdale, NJ).
Tallal, P. (**1980**). ''Auditory temporal perception, phonics and reading disabilities in children,'' Brain Lang. **9**, 182–198.
Tallal, P., Stark, R. E., and Mellits, D. (**1985**). ''The relationship between auditory temporal analysis and receptive language development: Evidence from studies of developmental language disorder,'' Neuropsychologia **23**, 527–534.
Van Rooij, J. C., and Plomp, R. (**1990**). ''Auditive and cognitive factors in speech perception by elderly listeners: II. Multivariate analyses,'' J. Acoust. Soc. Am. **88**, 2611–2624.
Van Rooij, J. C., and Plomp, R. (**1992**). ''Auditive and cognitive factors in speech perception by elderly listeners: III. Additional data and final discussion,'' J. Acoust. Soc. Am. **91**, 1028–1033.
Watson, B. U. (**1991**). ''Some relationships between intelligence and auditory discrimination,'' J. Speech Hear. Res. **34**, 621–627.
Watson, C. S. (**1987**). ''Uncertainty, informational masking and the capacity of immediate auditory memory,'' in *Auditory Processing of Complex Sounds*, edited by W. A. Yost and C. S. Watson (Lawrence Erlbaum, Hillsdale, NJ).
Watson, C. S. (**1994**). ''Central auditory processing disorders: The view from psychoacoustics,'' Proceedings of ASHA Consensus Conference on Central Auditory Processing Disorders, Albuquerque, NM, March 11–13, 1994. American Speech-Language and Hearing Association, Rockville, MD.
Watson, C. S., Jensen, J. K., Foyle, D. C., Leek, M. R., and Goldgar, D. E. (**1982a**). ''Performance of 146 normal adult listeners on a battery of auditory discrimination tests,'' J. Acoust. Soc. Am. Suppl. 1 **71**, S73.
Watson, C. S., Johnson, D. M., Lehman, J. R., Kelly, W. J., and Jensen, J. K. (**1982b**). ''An auditory discrimination test battery,'' J. Acoust. Soc. Am. Suppl. 1 **71**, S73.
Watson, C. S., Qiu, W. W., Chamberlain, M. M., and Li, X. (**1996**). ''Auditory and visual speech perception: Confirmation of a modality-independent source of individual differences in speech recognition,'' J. Acoust. Soc. Am. **100**, 1153–1162.

Asymmetry of masking between noise and iterated rippled noise: Evidence for time-interval processing in the auditory system

Katrin Krumbholz[a] and Roy D. Patterson
Centre for the Neural Basis of Hearing, Department of Physiology, University of Cambridge, Downing Street, Cambridge CB2 3EG, United Kingdom

Andrea Nobbe
Institute for Human–Machine Communication, Technical University Munich, Arcisstr. 21, D-80333 München, Germany

(Received 9 February 2001; revised 29 May 2001; accepted 26 June 2001)

This study describes the masking asymmetry between noise and iterated rippled noise (IRN) as a function of spectral region and the IRN delay. Masking asymmetry refers to the fact that noise masks IRN much more effectively than IRN masks noise, even when the stimuli occupy the same spectral region. Detection thresholds for IRN masked by noise and for noise masked by IRN were measured with an adaptive two-alternative, forced choice (2AFC) procedure with signal level as the adaptive parameter. Masker level was randomly varied within a 10-dB range in order to reduce the salience of loudness as a cue for detection. The stimuli were filtered into frequency bands, 2.2-kHz wide, with lower cutoff frequencies ranging from 0.8 to 6.4 kHz. IRN was generated with 16 iterations and with varying delays. The reciprocal of the delay was 16, 32, 64, or 128 Hz. When the reciprocal of the IRN delay was within the pitch range, i.e., above 30 Hz, there was a substantial masking asymmetry between IRN and noise for all filter cutoff frequencies; threshold for IRN masked by noise was about 10 dB larger than threshold for noise masked by IRN. For the 16-Hz IRN, the masking asymmetry decreased progressively with increasing filter cutoff frequency, from about 9 dB for the lowest cutoff frequency to less than 1 dB for the highest cutoff frequency. This suggests that masking asymmetry may be determined by different cues for delays within and below the pitch range. The fact that masking asymmetry exists for conditions that combine very long IRN delays with very high filter cutoff frequencies means that it is unlikely that models based on the excitation patterns of the stimuli would be successful in explaining the threshold data. A range of time-domain models of auditory processing that focus on the time intervals in phase-locked neural activity patterns is reviewed. Most of these models were successful in accounting for the basic masking asymmetry between IRN and noise for conditions within the pitch range, and one of the models produced an exceptionally good fit to the data.
[DOI: 10.1121/1.1395583]

PACS numbers: 43.66.Dc, 43.66.Ba, 43.66.Mk, 43.66.Hg [MRL]

I. INTRODUCTION

Over the last 30 years, considerable effort has been devoted to specifying the ''shape'' of the auditory filter in humans, i.e., the magnitude of the transfer function of the filter (e.g., Patterson, 1976), and to constructing filterbanks to simulate cochlear filtering in the spectral domain. These auditory filterbanks are used to convert the long-term power spectra of sounds into ''excitation patterns'' (e.g., Moore and Glasberg, 1987). The excitation pattern is a general term for any representation of the tonotopic distribution of the sound-evoked neural activity at the level of the auditory nerve and above. Excitation patterns based on auditory filter shapes can explain a wide range of auditory phenomena; for example, the roex auditory filter (Patterson *et al.*, 1982) has proven highly successful in predicting the masking of tonal signals by noise (Patterson and Moore, 1986; Rosen and Baker, 1994; Baker *et al.*, 1998; Glasberg and Moore, 2000). When the roles of tone and noise are reversed, however, the tone is found to be a much less effective masker than the noise, and this asymmetry in masker effectiveness is difficult to explain with models based on the excitation patterns of the stimuli. Hellman (1972) showed that a narrow band of noise masks a tone much more effectively than a tone masks a noise, even when the tone and noise maskers have the same power. Patterson and Henning (1977) quantified the discrepancy using the energy detection model of masking, and showed that even when the variability of the energy of the noise is considered, a noise is a more effective masker than a tone. Hall (1997) recently extended Hellman's observations of masking asymmetry to signals and maskers with bandwidths ranging from 0 to 256 Hz. The center frequency of Hall's stimuli was 1 kHz. Hall showed that, when masker level was fixed, masked thresholds for signals with bandwidths greater than that of the masker were much lower than those for signals with bandwidths less than that of the masker. Masked thresholds were essentially independent of signal bandwidth for

[a]Author to whom correspondence should be addressed.

signal bandwidths smaller than or equal to the masker bandwidth, which is compatible with the assumption that detection was based on the level of the stimulus at the output of the auditory filter centered on the signal. For signal bandwidths greater than the masker bandwidth, masked thresholds decreased markedly with increasing signal bandwidth. Hall (1997) attempted to explain the data using excitation patterns that were produced by multiplying the long-term power spectra of the stimuli with the magnitudes of the transfer functions of two of the most recent auditory filters, the two-dimensional, resonant-tectorial-membrane filter of Allen (1980) and the gammatone auditory filter of Patterson (1994a). Nevertheless, the decrease could not be explained in terms of the excitation patterns of the stimuli.

The gammatone auditory filter is defined in the time domain. The magnitude of its transfer function is very similar to that of the roex filter, and it has been successfully used to represent cochlear filtering in physiological models of auditory-nerve fibers (e.g., Hewitt and Meddis, 1991; Zhang *et al.*, 2001). Moreover, the level-dependent version of the gammatone filter, the "compressive gamma*chirp*" auditory filter of Irino and Patterson (1997, 2001), has recently been used to explain not only the level-dependent, human masking data of Rosen and Baker (1994) but also the time-domain recover functions recorded by Carney and Yin (1988) in auditory nerve fibers (Carney *et al.*, 1999). The success of these time-domain filters suggests that the problem Hall (1997) encountered when attempting to model the asymmetry of masking may have less to do with the representation of cochlear filtering, and more to do with the use of excitation patterns as the internal representation of the stimuli. Specifically, models of masking based on excitation patterns ignore the fine-grain timing information at the output of the cochlear filter. In this paper, we investigate this hypothesis using (1) a stimulus referred to as iterated rippled noise which enables us to perform a particularly stringent test of the excitation-pattern model of masking, and (2) a time-domain model of auditory processing that enables us to segregate the effects of filtering and temporal averaging in the production of excitation patterns.

A. Excitation patterns for noise and IRN

Rippled noise (RN) is constructed by delaying a copy of random noise by d ms, and adding it back to the original (Bilsen, 1966). Iterated rippled noise (IRN) is produced by iterating the delay-and-add process n times (Yost, 1996). IRN has a noise-like waveform with a degree of temporal regularity which increases with the number of iterations, n. The stimulus produces a compound perception with a hiss component, typical of the original noise, and a temporally regular component which sounds like a buzzy tone for delays between about 1 and 30 ms, and which elicits a perception of roughness or flutter for delays longer than 30 ms. The pitch of IRN corresponds to the reciprocal of the delay (ROD)[1] and the relative strength of the tone and noise components depends on the degree of temporal regularity in the stimulus. IRN is interesting because it can produce tonal and atonal sounds with the same total energy and very similar excitation patterns. The upper panel of Fig. 1 shows the magnitude of the transfer function of a bandpass filter used in the current study to restrict noise and IRN to the midfrequency region of the audible range. The two lower panels show the excitation patterns produced by noise (middle panel) and an IRN with 16 iterations and a ROD of 64 Hz (lower panel) after they have been passed through the bandpass filter shown in the upper panel. In this case, the cochlear filtering was simulated in the time domain by a gammatone auditory filterbank with 194 channels with center frequencies between 0.8 and 8 kHz, equally spaced on an equivalent rectangular bandwidth (ERB) scale (Glasberg and Moore, 1990; Patterson *et al.*, 1995), and the excitation patterns were produced by calculating the root-mean-square (rms) amplitude of the output of each filter and plotting the rms amplitudes as a function of filter center frequency on the same ERB scale as the bandpass filter in the upper panel. The activity in the excitation patterns is largely restricted to the passband of the initial bandpass filter, as would be expected. The excitation level increases with increasing frequency within the filter passband because the bandwidth of the auditory filter in-

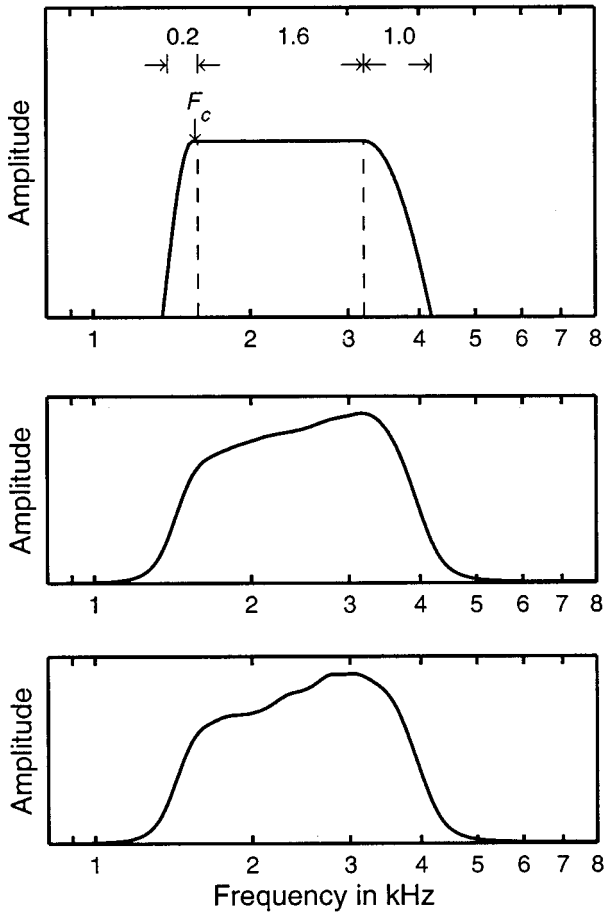

FIG. 1. Upper panel: Schematic diagram of the filter used to restrict the frequency region of the stimuli. The lower cutoff frequency, F_c, was varied from 0.8 to 6.4 kHz. The solid line shows the filter transfer function for the condition where $F_c = 1.6$ kHz. The lower and upper spectral ramps were 0.2- and 1 kHz wide; the flat portion was 1.6 kHz wide. The vertical dashed lines mark the boundaries between the lower and upper spectral ramps and the flat portion. Middle and lower panels: Long-term excitation patterns produced by noise (middle panel) and an IRN with 16 iterations and a ROD of 64 Hz (lower panel) after having been passed through the bandpass filter shown in the upper panel.

creases with increasing center frequency. The excitation patterns of the noise and the IRN are very similar; in particular, when the IRN delay is long and the lower cutoff frequency of the bandpass filter is relatively high, the excitation pattern of the IRN does not reveal a set of harmonically spaced peaks that could be used to determine the pitch of the sound.

Yost *et al.* (1996) showed that it is difficult to explain the discrimination of IRN stimuli with models based on excitation patterns of the stimuli, and Patterson *et al.* (1996) also showed that it is difficult to explain the relative strength of the tone and noise components in the perception of IRN with models based on excitation patterns. In both papers, the authors demonstrated that time-domain models with gammatone auditory filterbanks can explain the perceptions associated with IRN. Moreover, Patterson and Datta (1996) have reported that there is an asymmetry of masking between noise and IRN. They measured masked threshold for noise and for IRN with 256 iterations in the presence of an IRN masker with various numbers of iterations ranging from 0 (noise) to 256. IRN was generated with a delay of 16 ms and all stimuli were high-pass filtered at 0.8 kHz, which is 12.8 times the reciprocal of the delay, so the excitation patterns of the IRNs did not contain any resolved harmonic peaks (Shackleton and Carlyon, 1994). The overall level of the masker was randomly varied over a 10-dB range in order to reduce the salience of loudness as a cue for detection. Threshold signal-to-masker ratio (SMR) for an IRN signal masked by noise was -3 dB, whereas threshold SMR for a noise signal masked by IRN was -13 dB. Since the maskers produce similar excitation patterns, it is difficult to explain the masking asymmetry with traditional power spectrum models of masking.

The study of Patterson and Datta (1996) was limited to a fixed delay of 16 ms and a fixed high-pass cutoff frequency of 0.8 kHz. The pitch of IRN becomes progressively weaker as the delay increases (Yost and Hill, 1978) and as the cutoff of the highpass filter increases (Yost *et al.*, 1998). In the current study, Patterson and Datta's findings are extended by measuring the degree of masking asymmetry between noise and IRN as the reciprocal of the delay varies over the range 16–128 Hz, and as the cutoff of the high-pass filter increases from 0.8–6.4 kHz. We also demonstrate that time-domain models of auditory processing like those reported by Yost *et al.* (1996, 1998) and Patterson *et al.* (1996, 2000) can be extended to explain much of the masking observed in the current experiments.

II. METHODS

A. Stimuli

The stimuli were computed digitally with 16-bit resolution and a sampling rate of 25 kHz [Tucker Davis Technologies (TDT) AP2]. IRN was generated with 16 iterations of the add-original algorithm (Yost *et al.*, 1996) using a gain, g, of unity. The stimuli were filtered into frequency bands with an equivalent rectangular bandwidth of 2.2 kHz and four different lower cutoff frequencies, $F_c = 0.8$, 1.6, 3.2, and 6.4 kHz. The edges of the frequency bands were rounded with a quarter cycle of a cosine function in order to avoid edge

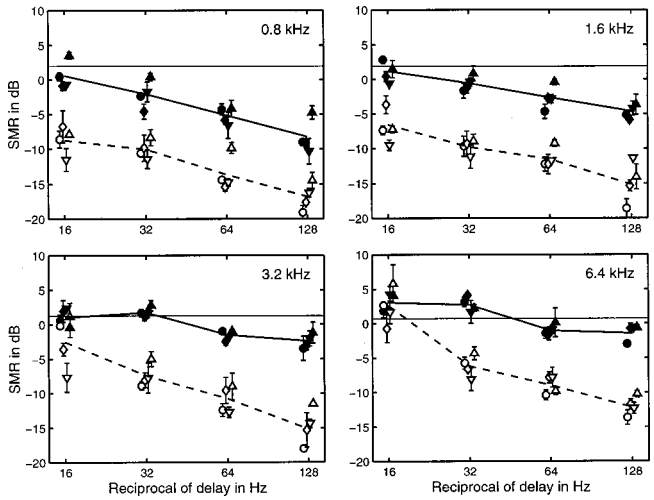

FIG. 2. Individual and average thresholds for the four filter cutoff frequencies ($F_c = 0.8$, 1.6, 3.2, and 6.4 kHz). Threshold is expressed in terms of signal-to-masker ratio, SMR, in dB. Thresholds for IRN masked by noise (filled symbols and solid lines) and for noise masked by IRN (open symbols and dashed lines) are plotted as a function of the reciprocal of the IRN delay (ROD). The results for the individual listeners are presented by different symbols which are shifted relative to each other along the abscissa for clarity; the error bars show the standard error of the threshold estimates. The lines connect the average threshold values for each masker condition across listeners. The average threshold for noise masked by noise in each filter condition is shown by a horizontal, faint solid line.

tones (see the upper panel in Fig. 1). The lower and upper spectral ramps had widths of 0.2 and 1.0 kHz, respectively. The flat portion was 1.6 kHz wide. Filtering was performed digitally in the frequency domain.

In both masking conditions (IRN masked by noise and noise masked by IRN), and in all four filter conditions, masked threshold was measured for four different IRN delays, $d = 7.8125$, 15.625, 31.25, and 62.5 ms, with reciprocals of 128, 64, 32, and 16 Hz. Thresholds were also measured for a noise signal in a noise masker in all four filter conditions, yielding a total of $4 \times 4 \times 2 + 4 = 36$ conditions. In all cases, the signal and masker were gated on and off simultaneously with 25-ms cosine-squared ramps and a flat portion of 750 ms. Three threshold measurements were performed in each condition. The order in which conditions were measured was counterbalanced between the three threshold runs. For the first run, thresholds were measured for ascending filter cutoff frequency; within each filter condition, thresholds were measured first for IRN masked by noise and then for noise masked by IRN; within each masking condition, thresholds were measured for ascending IRN delay. For the second and third threshold runs, the order of the threshold measurements was reversed relative to the previous run. When one threshold run for each of the "IRN masked by noise" and "noise masked by IRN" conditions was completed, thresholds for the "noise masked by noise" condition were measured with the same order of filter cutoff frequencies.

The signal and masker were played out through separate channels of the TDT DD1 D/A converter and low-pass filtered at 10 kHz (TDT FT6-2). They were separately attenuated according to the signal and masker level for the current

trial using two programmable attenuators (TDT PA4). They were added in an analog signal mixer (TDT SM3), where they were also combined with a continuous low-pass noise designed to mask distortion products with frequencies below the stimulus passband. The continuous noise was produced by low-pass filtering (Kemo VBF8) a pink noise from an SRS SR780 spectrum analyzer. The low-pass filter had a slope of 96 dB/octave and a cutoff frequency which was half an octave below the lower cutoff frequency, F_c, of the current filter condition. The unfiltered pink noise had a level of 31.3 dB SPL in the 1/3-octave band around 1 kHz. Finally, the stimuli were fed to a headphone buffer (TDT HB6) and presented diotically via headphones (AKG K 240 DF). The listener was seated in a double-walled, sound-attenuating booth.

B. Procedure

Masked threshold was measured with an adaptive two-alternative, forced-choice procedure. Each trial consisted of two 800-ms observation intervals separated by a silent gap of 500 ms. One of the observation intervals contained the masker alone, the other contained masker plus signal. The listener's task was to choose the interval which contained the signal by pressing one of two buttons on a response box. Feedback was given at the end of each trial. The adaptive parameter was the level of the signal. The nominal overall level of the masker was fixed at 60 dB SPL. However, in order to reduce the usefulness of loudness cues, the levels of the stimuli in both observation intervals were varied randomly within a 10-dB range. The random level rove was intended to encourage listeners to base their decisions on sound quality differences between the two observation intervals in those conditions where signal and masker were of different stimulus type. At the same time, the level rove increased threshold in conditions where a noise signal was presented in a noise masker because loudness was the only cue available to the listeners in these conditions. Signal level was set to a value well above the anticipated threshold at the beginning of each threshold run. After three consecutive correct responses, signal level was reduced and after each incorrect response, signal level was increased to track the signal level that yields 79%-correct responses (Levitt, 1971). The step size of the level increments and decrements was 5 dB up to the first reversal, 3 dB up to the second reversal, and 2 dB for the rest of the ten reversals that made up one threshold run. Each threshold estimate is the average of the last eight reversals of signal level. The data points presented in the figures are the mean of three thresholds estimates and the error bars show their standard errors.

C. Listeners

A total of four listeners participated in the experiment: authors AN and KK as well as two students, NR and RB, who were paid for their services at an hourly rate. The listeners were between 20 and 31 years and reported no history of hearing impairment.

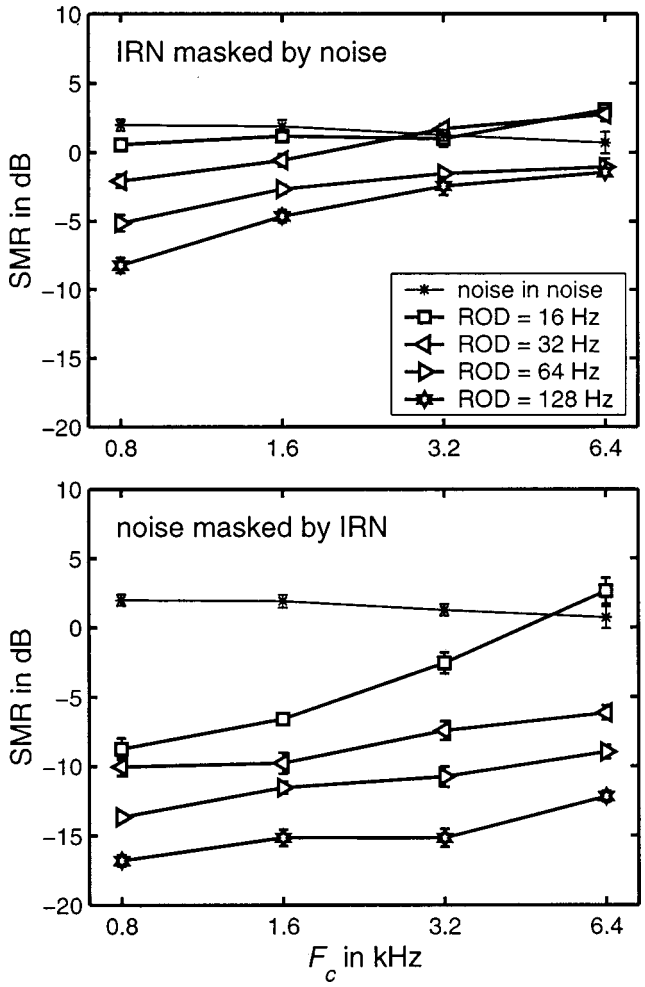

FIG. 3. Average thresholds for IRN masked by noise (upper panel) and noise masked by IRN (lower panel), plotted as a function of filter cutoff frequency, F_c. The parameter is the reciprocal of the IRN delay (see the legend in the upper panel). In both panels, the average thresholds for noise masked by noise are represented by asterisks connected by faint, solid lines.

III. RESULTS

The four panels of Fig. 2 show the experimental results for the four filter conditions ($F_c = 0.8$, 1.6, 3.2, and 6.4 kHz). Threshold for IRN masked by noise (filled symbols and solid lines) and for noise masked by IRN (open symbols and dashed lines) is plotted as a function of the reciprocal of the delay. The individual thresholds for the four listeners are presented by different symbols which are shifted relative to each other along the abscissa for clarity. The lines connect the average threshold values for each masking condition across listeners. For each filter condition, the average threshold for noise masked by noise is indicated by the horizontal, faint solid line. Threshold is expressed in terms of the signal-to-masker ratio, SMR, which is the difference between the overall level of the signal at threshold and the overall level of the masker in dB. The two panels of Fig. 3 show the average thresholds for IRN masked by noise (upper panel) and for noise masked by IRN (lower panel) plotted as a function of the filter cutoff frequency, F_c. The parameter in Fig. 3 is the reciprocal of the IRN delay, ROD. The asterisks connected by faint solid lines in both panels of Fig. 3 show the average thresholds for the noise masked by noise conditions.

For most combinations of filter cutoff frequency and ROD, noise masks IRN much better than IRN masks noise; this *masking asymmetry* is illustrated by the large difference between the bold solid and dashed lines in each panel of Fig. 2. For the lowest cutoff frequency, $F_c = 0.8$ kHz, threshold decreases markedly with increasing ROD for both masking conditions. For IRN masked by noise (solid lines), the slope of the function relating threshold to the ROD becomes shallower as cutoff frequency increases. For most combinations of IRN delay and masking condition, threshold tended to increase with increasing cutoff frequency (Fig. 3). Figure 3 also shows that the functions relating threshold to filter cutoff, F_c, are essentially parallel for delays with reciprocals of 32, 64, and 128 Hz. For 16 Hz, the threshold function for the IRN masked by noise condition is close to the threshold function for the noise masked by noise condition, which is roughly independent of filter cutoff. The loudness difference between masker and masker plus signal was a useful cue for detection at SMRs above the noise masked by noise threshold, and so, threshold for IRN masked by noise and for noise masked by IRN was expected to be bounded by the threshold for noise masked by noise. In the noise masked by noise condition, the loudness difference between masker and masker plus signal was the only detection cue. However, the overall levels of both stimuli were randomized within a 10-dB range. In this case, when the SMR is 1 dB, the level of the masker plus signal will be greater than the level of the masker alone in 79% of the trials. The observed threshold for the noise masked by noise condition is in reasonable accordance with this expectation. For the noise masked by IRN condition, the threshold function for ROD = 16 Hz is markedly steeper than the functions for the other three delays (lower panel in Fig. 3).

Interestingly, in the highest filter condition ($F_c = 6.4$ kHz), the average threshold for IRN masked by noise at 16 and 32 Hz is higher than the threshold for noise masked by noise, where the only detection cue is the loudness difference between masker and masker plus signal. The perceptual correlate of the temporal regularity in IRN with a long delay is not distinct in the highest filter condition, and so the sound quality difference between masker and signal was probably not a reliable cue in the IRN masked by noise condition. It is possible that threshold is elevated in these conditions because listeners still tried to base their decisions on sound quality differences even though they were less useful than loudness differences.

Figure 4 presents the masking asymmetry for each of the IRN delays. Values for different filter cutoff frequencies, F_c, are denoted by different bar infills. When the reciprocal of the delay is 32, 64, or 128 Hz, the masking asymmetry is more or less independent of filter cutoff frequency with an average value of about 9 dB. At 128 Hz, there is a small but progressive increase in masking asymmetry when cutoff frequency increases from 0.8 to 3.2 kHz, which is primarily due to the increase in threshold for the IRN masked by noise condition with increasing cutoff frequency. When the reciprocal of the delay is 16 Hz, the masking asymmetry for the lowest cutoff frequency ($F_c = 0.8$ kHz) is about the same as it is for the higher RODs (about 9 dB), but it decreases

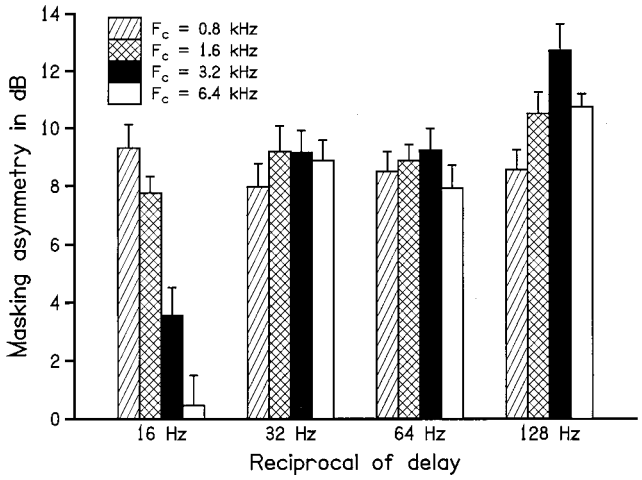

FIG. 4. Masking asymmetry in dB as a function of the reciprocal of the delay for four different filter cutoff frequencies, F_c (denoted by different bar infills). The error bars show the standard errors of the threshold differences.

progressively with increasing cutoff frequency to less than 1 dB when $F_c = 6.4$ kHz. The progressive decrease of the masking asymmetry for the 16-Hz IRN is mainly due to the marked increase in threshold with increasing cutoff frequency in the noise masked by IRN condition (lower panel in Fig. 3). These results suggest that processing of temporal regularity may be based on different principles below and above the pitch–infrapitch boundary, which is at about 30 Hz (Krumbholz *et al.*, 2000).

IV. MASKING ASYMMETRY IN TIME-DOMAIN MODELS OF AUDITORY PROCESSING

Several time-domain models of auditory processing were used to simulate the internal representation of the IRN and noise stimuli in the auditory system and to investigate the neural bases of the observed masking asymmetry. The models are all based on Licklider's (1951) duplex model of pitch, which was the first multichannel autocorrelation model of temporal processing. Several computational versions of Licklider's general model have since been implemented by, for example, Slaney and Lyon (1990), Meddis and Hewitt (1991), and Patterson *et al.* (1992) among others. In general terms, these auditory models produce a multichannel simulation of the neural activity produced by the cochlea, and then they construct a time-interval histogram of the phase-locked activity in each channel. The output is an array of interval histograms referred to as an autocorrelogram or "auditory image."

We will use the terminology described in Patterson and Irino (1998) to distinguish the auditory models described in this section and to separate the processing mechanisms from the representations of internal activity that they produce. For example, the ***g***amma***t***one ***f***ilterbank is a processing module and as such is specified with a lower-case, bold and italic abbreviation, ***gtf***, whereas the output that the module is intended to simulate, basilar membrane motion, is designated by an upper-case, nonbold abbreviation, BMM. A complete model is specified by its processing modules separated by "/" such as the ***gtf/med/ac*** model; the first specifies the mode

of spectral analysis, which is invariably the gammatone auditory filterbank in this paper, the second specifies the method of converting the simulated BMM into a simulated neural activity pattern (NAP), which is the Meddis hair cell (***med***) in this example, and the third specifies the method of processing the time-interval information in the NAP which in this example is autocorrelation (***ac***).

The modeling in the current paper was performed with the AIM/DSAM software package[2] and MATLAB. The model in this section is essentially a modified version of the auditory image model (AIM) presented in Patterson *et al.* (1995). The operation of the middle ear was simulated with a broad, second-order bandpass filter with lower and upper cutoff frequencies of 0.45 and 8.5 kHz, respectively. The spectral analysis performed by the cochlea was simulated with a 60-channel, gammatone filterbank (***gtf***) with center frequencies between 0.1 and 8 kHz, evenly distributed on the ERB scale (Glasberg and Moore, 1990). The filtered waves were half-wave rectified, compressed, and low-pass filtered (***hcl***) to simulate the neural activity pattern (NAP) flowing from the cochlea up the auditory nerve in response to IRN and noise stimuli. We used instantaneous, power-law compression with an exponent of 0.5 (Oxenham and Moore, 1995). A cascade of four low-pass filters, with a fixed cutoff frequency of 0.8 kHz was used to simulate the loss of phase locking at high frequencies (Weiss and Rose, 1988). Finally, a time-interval analysis similar to autocorrelation was applied in each channel of the simulated NAP to produce a two-dimensional time-interval histogram, referred to as an auditory image (AI) (Patterson *et al.*, 1992). Specifically, the conversion from the time dimension of the NAP to the time-interval dimension of the AI was performed with strobed temporal integration (***sti***) (Patterson, 1994b; Patterson and Irino, 1998). Autocorrelation in its original form produces a representation which is analogous to an all-order time-interval histogram. Such histograms are symmetric in the time-interval dimension, and so they are insensitive to temporal asymmetry in the stimulus that listeners often perceive (Patterson, 1994a, b; Akeroyd and Patterson, 1995, 1997). In ***sti***, the analysis is limited to time intervals measured from local peaks within each channel of the NAP. Patterson *et al.* (1996) showed that in the case of pitch perception, where asymmetry is not an issue, autocorrelation and ***sti*** produce virtually indistinguishable results. Consequently, we believe that if autocorrelation were used in place of ***sti*** in the modeling that follows, it would not materially affect the modeling results. Also, ***sti*** takes far less computation time than autocorrelation, which remains a significant advantage when processing a large number of stimuli for a variety of models. This version of AIM is referred to as the ***gtf/hcl/sti*** model (***gtf***: gammatone filterbank; ***hcl***: half-wave rectification, compression, and lowpass filtering; ***sti***: strobed temporal integration).

To summarize the information in the two-dimensional images and to produce a decision measure, the AI was summed across frequency channels to form the summary AI of the stimulus. The summary AIs were normalized to the value at 0 ms because the level rove decreased the salience of overall level as a detection cue. The stimuli used in the modeling were produced in the same fashion as those presented to the listeners in the experiment. For each combination of ROD and filter cutoff, 15 samples of each masker type (noise or IRN) were generated at a fixed level of 60 dB SPL. Simulations were performed for a set of signal levels ranging from values well below to values well above the observed thresholds: For the IRN masked by noise condition, the SMR varied from −16 to 14 dB in 3-dB steps; for the noise masked by IRN condition, the SMR varied from −22 to 14 dB in 3-dB steps. At each signal level and for each combination of ROD and filter cutoff, 15 samples of each signal type (IRN or noise) were generated and added to one of the 15 masker samples for that condition. The stimuli were generated with a duration of 810 ms. For each of the stimuli, a sequence of 20 individual summary AIs was generated in 35-ms steps starting at 105 ms after stimulus onset, where the response of the model has reached steady state. The 20 summary images were averaged to produce a single, overall summary AI for that stimulus. The overall summary AIs for each of the 15 masker or masker-plus-signal samples were averaged to produce the summary AI that was used to calculate the decision measure for each combination of signal level and masker type. The summary AIs were limited to a maximum time interval of 35 ms, as the lower limit of pitch for complex sounds is about 30 Hz, corresponding to a period of 33 ms (Krumbholz *et al.*, 2000). To simulate the reduction in pitch strength near the lower limit of pitch, and to avoid discontinuities at the border of the image, we followed Patterson *et al.* (1996) and Pressnitzer *et al.* (2001) and imposed a linear weighting function which decreased from unity at a time interval of 0 ms, to zero at a time interval of 40 ms. The limitation in time intervals restricted the modeling to stimuli with RODs of 32, 64, and 128 Hz. An attempt to include the 16-Hz data is discussed at the end of this section.

A. *gtf/hcl/sti* model with a Gauss decision measure

The top panel of Fig. 5 shows the summary AIs for the IRN masked by noise condition when the delay is 15.625 ms (ROD = 64 Hz), the filter cutoff is 0.8 kHz, and the SMR is 15 dB. The masker, which is a noise in this case, is shown by the dashed line and the masker plus signal by the solid line. The IRN signal produces a peak at the IRN delay and at integer multiples of the delay, and it reduces the activity in the regions just below and above the peaks. This suggests that the activity levels in the peak regions and adjacent to the peak regions could provide the basis for a decision measure that correlates well with the perceptual cues used in the detection task. The lower panel shows the summary AIs in the noise masked by IRN condition for the same combination of delay and filter cutoff and the same SMR of 15 dB. In this case, the masker (dashed line) is an IRN and the masker plus signal (solid line) is IRN plus noise. Again, the signal produces a difference in the peak regions and the adjacent regions. In this case, however, the signal is a noise and it *reduces* the normalized activity at the IRN delay and its integer multiples, and it *increases* the normalized level in regions just below and above the peaks. Accordingly, we constructed a measure of the relative strength of the tone and

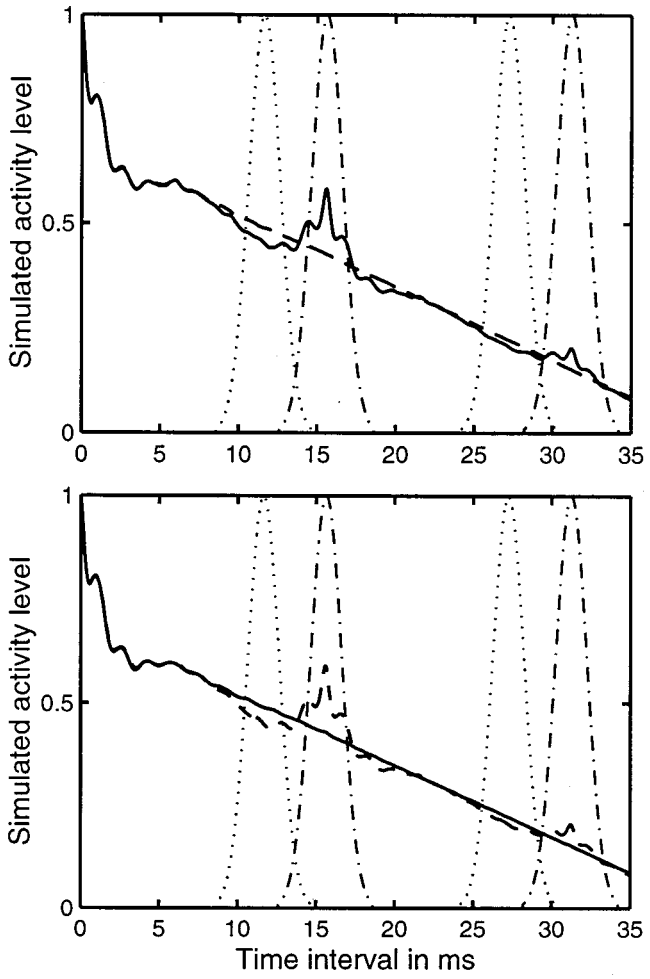

FIG. 5. Summary AIs for masker (dashed line) and masker plus signal (solid line) for IRN masked by noise (left panel) and noise masked by IRN (right panel). In both cases, the IRN delay was 15.625 ms (ROD=64 Hz) and the SMR was 15 dB. The faint dash-dotted and dotted lines show the Gaussian weighting functions used to calculate the level of activity in the peak and background regions.

noise components in the perceptions produced by these stimuli by calculating the activity level in the peak regions and in the adjacent background regions of their summary AIs. Patterson *et al.* (1996) found that the ratio of the peak level to the background level in the summary AI is a good predictor of the perceived tone-to-noise ratio of IRN sounds. Patterson *et al.* restricted their decision measure to the first peak in the image, at the IRN delay. They investigated the tone-to-noise ratio in IRN stimuli for a single delay of 16 ms, and so there was no need to model the effect of IRN delay. We observed that the effect of IRN delay in the current experiment was readily modeled by considering not only the first peak, but also the peaks at integer multiples of the IRN delay that lie within the boundaries of the image, i.e., below 35 ms. The summary AI for a 32-Hz IRN contains only one peak at 31.25 ms, the summary image for a 64-Hz IRN contains two peaks at 15.625 and 31.25 ms (see Fig. 5), and the image for a 128-Hz IRN contains four peaks at integer multiples of 7.8125 ms. The activity in the peak regions of the summary AI, *PA*, was calculated by centering Gaussian weighting functions with a standard deviations of 1 ms on the peaks at integer multiples of the IRN delay below 35 ms,

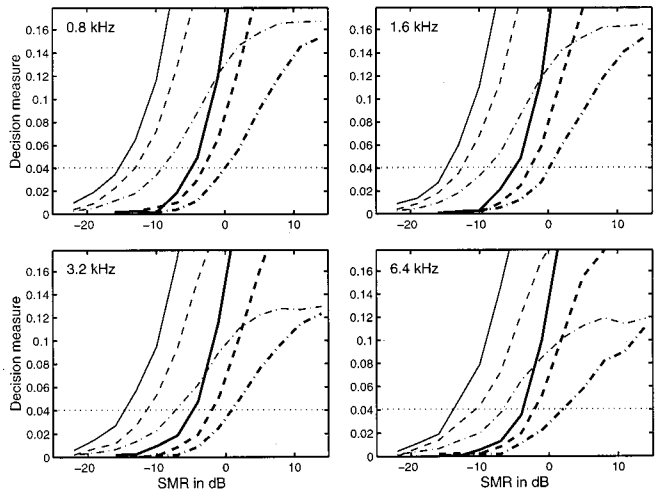

FIG. 6. Decision measure for the ***gtf/hcl/sti***-Gauss model plotted as a function of SMR for the four filter conditions (F_c=0.8, 1.6, 3.2, 6.4 kHz). The bold lines show the decision measure for IRN masked by noise; the thin lines show the results for noise masked by IRN. The reciprocal of the delay is represented by different line types (dash-dotted: 32 Hz; dashed: 64 Hz; solid: 128 Hz). The threshold criterion that minimizes the rms deviation between simulated and measured thresholds is shown by the horizontal, dotted line in each panel.

and then integrating the summary AI within these Gaussian windows. A width of 1 ms was chosen, so that the Gaussian window would encompass the activity in the main peak as well as part of the two side peaks of each peak region in the IRN. *PA* provides a measure of the strength of the tonal component of the stimulus. The activity in the background regions adjacent to the peaks, *BA*, was calculated by applying the same Gaussian weighting functions centered 4 ms below the integer multiples of the IRN delay. The background window was centered on the background region where the difference between masker alone and masker plus signal was greatest (compare the dashed and solid lines in Fig. 5). *BA* provides a measure of the strength of the noise component in the perception. The faint dash-dotted lines in Fig. 5 show the two peak windows, and the faint dotted lines show the two background windows for the 64-Hz IRN. Following Patterson *et al.* (1996), we computed the ratio between peak and background activity for each peak separately and added the ratios for all peaks within the boundary of the image. The peak-to-background ratio of the masker is designated PA_m/BA_m, and for the masker plus signal, it is PA_{m+s}/BA_{m+s}. The absolute value of the difference $PA_{m+s}/BA_{m+s}-PA_m/BA_m$ was used as the decision measure for estimating threshold. The ***gtf/hcl/sti*** model with this decision measure will be referred to as ***gtf/hcl/sti***-Gauss.

The four panels of Fig. 6 show the decision measure plotted as a function of SMR for the four filter conditions (F_c=0.8, 1.6, 3.2, 6.4 kHz). The parameters within each panel are the ROD and the masking condition. The bold lines show the decision measure for IRN masked by noise; the thin lines show the results for noise masked by IRN. Different RODs are represented by different line types (dash-dotted: 32 Hz; dashed: 64 Hz; solid: 128 Hz). Threshold was defined as that SMR at which the peak-to-background difference for masker plus signal deviates from that of the masker

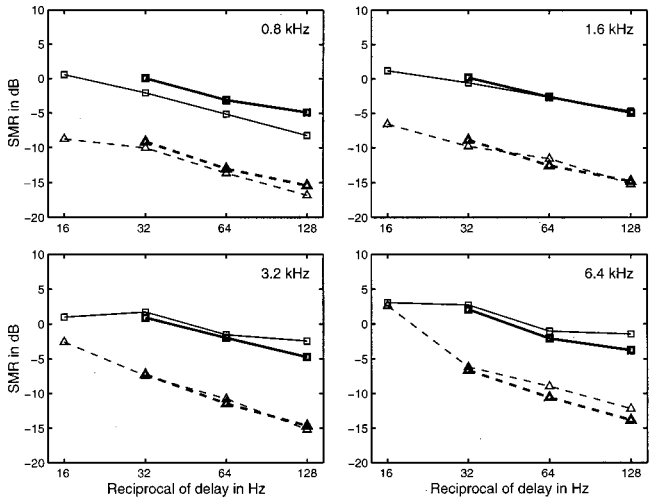

FIG. 7. Simulated threshold for the ***gtf/hcl/sti***-Gauss model as a function of the ROD for the four filter conditions. The bold symbols connected by bold lines show the simulated thresholds for the two masking conditions: IRN masked by noise (squares and solid lines) and noise masked by IRN (triangles and dashed lines). The thin squares and triangles connected by thin, solid, and dashed lines show the corresponding average data from the experiment.

alone by a fixed criterion, *C*. The criterion *C* was the same for all experimental conditions and it was chosen to minimize the root-mean-square (rms) deviation between simulated and measured threshold values for all conditions. In Fig. 6, the criterion is shown by the horizontal, dotted line in each panel.

The four panels of Fig. 7 show simulated threshold as a function of reciprocal of the delay for the four filter conditions. The bold symbols connected by bold lines show the simulated thresholds for the two masking conditions: IRN masked by noise (squares and solid lines) and noise masked by IRN (triangles and dashed lines). The thin symbols connected by thin, solid, and dashed lines show the corresponding average data from the experiment. Comparison of the simulated and observed thresholds shows that, although the ***gtf/hcl/sti***-Gauss model contains no free parameters apart from the criterion, *C*, which was fixed for all conditions, the model can nevertheless explain the basic asymmetry of masking, the effect of the ROD in the range 32–128 Hz, and most of the effect of filter cutoff frequency. The rms deviation between the simulated and observed thresholds is only 1.37 dB. The deviation between the simulated and observed thresholds is concentrated in the IRN masked by noise condition for the lowest filter frequency ($F_c = 0.8$ kHz). Threshold in this condition is overestimated by the model (compare the bold and thin squares in the upper left panel). The fit between the simulated and the observed thresholds in the IRN masked by noise condition is better for the higher filter frequencies, because the observed thresholds increase more strongly with increasing filter frequency than the simulated thresholds.

Patterson *et al.* (2000) used a time-domain model of auditory processing, which was similar to the ***gtf/hcl/sti*** model used in this section, to explain the perceptual tone-to-noise ratio of merged IRNs, i.e., stimuli which consist of two IRNs with different delays, added together. They found that the correspondence between simulated and observed data critically depended on the cutoff frequency of the low-pass filter, which determines the model's loss of phase locking at high frequencies. We examined the effect of the low-pass cutoff frequency, F_{lp}, in the ***gtf/hcl/sti***-Gauss model on the simulation of masking asymmetry, by varying F_{lp} in the four-stage low-pass filter of the ***hcl*** stage of the model between 0.075 and 9.6 kHz in octave steps. The simulation showed that threshold was remarkably insensitive to changes in the low-pass cutoff. Even when F_{lp} was increased from 0.8 kHz (as in the initial version of the ***gtf/hcl/sti*** model above) to 9.6 kHz, the functions relating the decision measure to SMR (as in Fig. 6) remained essentially unchanged, indicating that although the peaks in the summary AIs exhibit an increasing amount of temporal fine structure as F_{lp} is increased, the integral of the activity within the Gaussian windows remains the same. As F_{lp} was decreased below 0.8 kHz, the maximum value of the decision measure at the maximum SMR decreased, because the peaks in the summary AIs became wider and flatter. However, this had little effect on threshold down to $F_{lp} = 0.15$ kHz; the rms deviation between simulated and observed thresholds remained in the range 1.35 to 1.40 dB (compared with 1.37 dB for $F_{lp} = 0.8$ kHz). When the cutoff was reduced to $F_{lp} = 0.075$ kHz, the rms deviation rose to 1.9 dB, because the model lost the ability to account for the effect of IRN delay.

Omitting the compression in the initial version of the ***gtf/hcl/sti***-Gauss model caused only a marginal increase in the rms deviation between simulated and observed thresholds from 1.37 to 1.40 dB. The ***gtf/hcl/sti***-Gauss model without compression still predicts the correct amount of masking asymmetry, indicating that the masking asymmetry in the simulated thresholds is largely determined by the temporal properties of the stimuli. This is in accordance with the findings of Patterson and Irino (1998), who showed that the auditory image model could explain temporal asymmetry in the auditory system. They found that changing the compression in the model did not have a large effect on the predicted asymmetry. Patterson and Irino used a relative decision measure, like the peak-to-background ratio used in the current study. They argued that the effect of instantaneous, monotonic compression is minimized when ratios are computed.

B. *hcl/ac* model with a Gauss decision measure

The fact that the ***gtf/hcl/sti***-Gauss model is insensitive to the low-pass cutoff, F_{lp}, suggests that it is the gammatone filterbank that enables the model to account for the effect of filter condition. In order to test this idea, we calculated the Gauss decision measure directly from the autocorrelation functions (***ac***) of the waves after half-wave rectification, compression, and low-pass filtering. The middle-ear bandpass filter, the compression, and the low-pass filter were the same as in the initial version of the ***gtf/hcl/sti***-Gauss model. The autocorrelation function used to calculate the decision measure was the average of the autocorrelation functions for fifteen 810-ms samples of each stimulus type. The modeling was once again restricted to stimuli with RODs of 32, 64, and 128 Hz. This model will be referred to as the ***hcl/ac***-Gauss model.

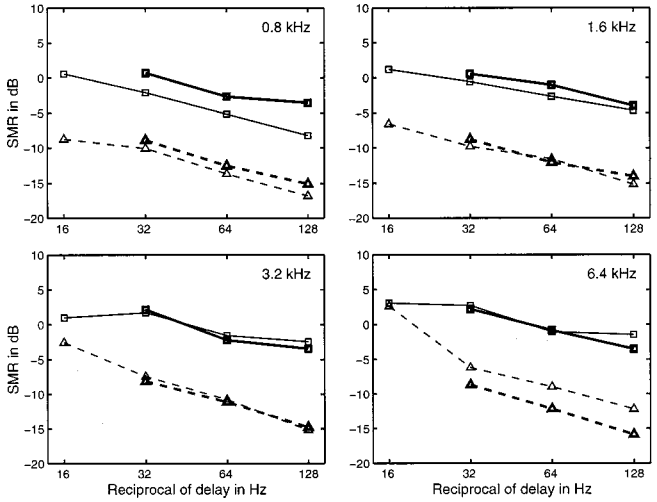

FIG. 8. Simulated threshold for the ***hcl/ac***-Gauss model plotted in the same format as in Fig. 7.

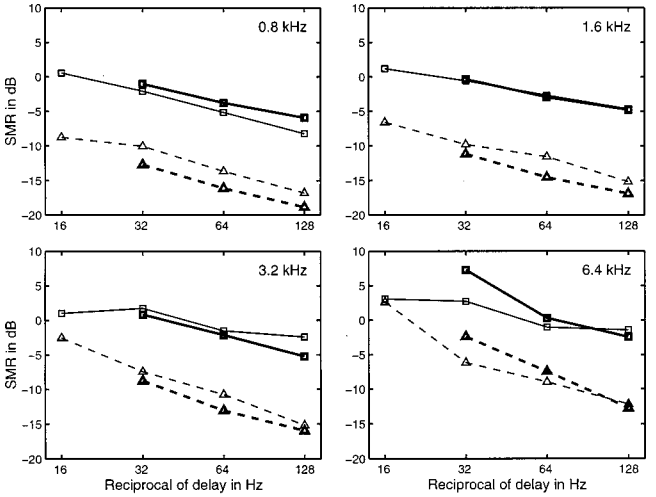

FIG. 9. Simulated threshold for the ***gtf/med/sti***-Gauss model plotted in the same format as in Fig. 7.

Simulated thresholds from the ***hcl/ac***-Gauss model are presented with the average threshold data in Fig. 8. As might be expected, the ***hcl/ac***-Gauss model can account, at least qualitatively, for the basic masking asymmetry and for the effect of IRN delay, but it cannot explain the effect of filter condition. Whereas the observed threshold increases with increasing filter cutoff, the simulated threshold is largely independent of cutoff, so threshold is overestimated in the lowest filter condition ($F_c = 0.8$ kHz) and underestimated in the highest filter condition ($F_c = 6.4$ kHz). Thus, the rms deviation between simulated and observed thresholds increases from 1.37 to 1.89 dB. The simulations were also repeated with a compression exponent of 1 (no compression), in order to determine whether the masking asymmetry in the initial ***hcl/ac***-Gauss model was a result of the compression, or whether it is determined by the temporal structure of the stimuli themselves. As in the case of the ***gtf/hcl/sti***-Gauss model, omitting the compression in the ***hcl/ac***-Gauss model caused only a marginal increase in the rms deviation between simulated and observed thresholds from 1.89 to 1.93 dB.

C. *gft/med/sti* model with a Gauss decision measure

In many time-domain models, the mechano-electrical transduction is simulated with the hair-cell model proposed by Meddis (1986). We repeated the simulations of masking asymmetry described above with a version of AIM where the half-wave rectification, compression, and low-pass filtering were replaced by the Meddis (1986) hair-cell model (***med***). Simulated thresholds from this ***gft/med/sti***-Gauss model are presented with the average threshold data in Fig. 9, which shows that simulated threshold for both masking conditions increases markedly with increasing filter cutoff frequency, F_c. The increase in simulated threshold for the IRN masked by noise condition (filled triangles) is similar to that observed in the data. However, in the noise masked by IRN condition, the simulated threshold increases even more with increasing cutoff frequency which is not observed in the data. Thus, the simulated masking asymmetry decreases with increasing cutoff frequency, whereas the observed masking asymmetry for RODs of 32, 64, and 128 Hz is fairly constant across filter conditions. This discrepancy leads to an increase in the rms error from 1.37 to 2.0 dB. Thus, the ***gtf/med/sti***-Gauss model can explain the main effects in the data qualitatively, but quantitatively, the fit is not as good as that provided by the ***gtf/hcl/sti***-Gauss model. The excess frequency dependence of the ***gtf/med/sti***-Gauss model is probably due to the spontaneous rate of the Meddis (1986) hair cell. In the two-dimensional AIs, the spontaneous rate produces a constant background of activity in channels which do not respond to the stimulus. In the higher filter conditions, the proportion of channels which do not respond to the stimulus becomes greater, because the stimulus passband covers a smaller number of ERBs. Thus, the summary AIs for stimuli in the higher filter conditions have a higher level of background activity and smaller peaks. This illustrates a general limitation of time-domain models that use hair cells with spontaneous rates in conjunction with summary auditory images. Such models could be extended with a routine that determines whether each channel should be included in the summary AI on the basis of whether it makes a useful contribution to the decision measure, but this extension is beyond the scope of the current paper.

D. *gtf/med/sti* with a Euclidean distance measure, D^2

The autocorrelation models described by Meddis and O'Mard (1997) and Pressnitzer *et al.* (2001) are quite similar to the ***gtf/med/sti***-Gauss model, and between them they can account for a wide range of pitch phenomena. There is, however, a difference in the decision measure. Meddis and O'Mard and Pressnitzer *et al.* used a Euclidean distance measure, D^2, rather than the difference between peak-to-background ratios, PA/BA, to summarize the difference between two summary AIs. D^2 is the integral of the squared difference between two summary AIs, and so it compares differences at all time intervals within the image and it gives all differences equal weight. We replaced the Gauss decision measure in the ***gtf/med/sti***-Gauss model with the D^2 measure to determine if this would improve the fit of the ***gtf/med/sti***

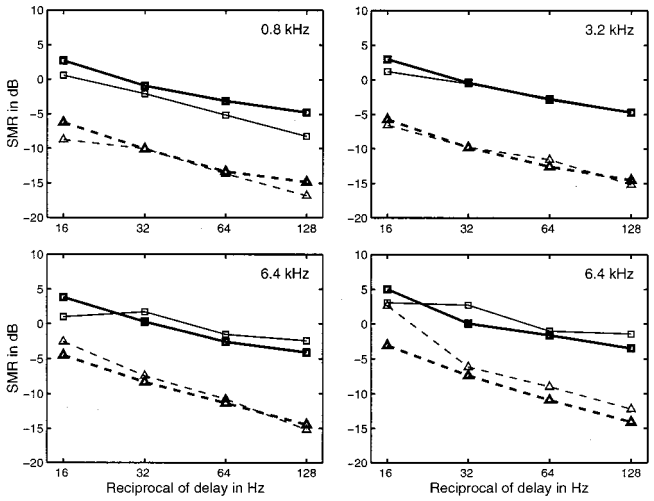

FIG. 10. Simulated threshold for the ***gtf/hcl/sti***-Gauss model with enlarged images plotted in the same format as in Fig. 7.

model. We found that this ***gtf/med/sti***-D^2 model does not predict sufficient masking asymmetry to explain the observed data. The simulated thresholds for IRN masked by noise are greater than those for noise masked by IRN, but the degree of asymmetry is far too small; on average, the masking asymmetry in the simulated thresholds is only 2.5 dB compared to 9.4 dB in the observed thresholds. As a result, the rms deviation between simulated and observed thresholds increases from 2.0 to 3.6 dB when the Gauss measure is replaced by the D^2 measure with the ***gtf/med/sti*** model.

E. Extension of *gft/hcl/sti*-Gauss model to the 16-Hz data

The lower limit of pitch is in the region of 30 Hz and, as a result, the maximum time interval in the AI or the autocorrelogram is typically restricted to about 35 ms (Patterson *et al.*, 1996). This is why the fits described above were restricted to the data for IRN delays with reciprocals greater than 30 Hz. It was also our impression that listeners were using flutter or roughness in the 16-Hz condition rather than the presence of a tonal percept. In the two lower filter conditions ($F_c = 0.8$ and 1.6 kHz), the 16-Hz data appear to be a natural extension of those at the higher RODs; however, in the two higher filter conditions ($F_c = 3.2$ and 6.4 kHz), the thresholds for the two masking conditions converge in the 16-Hz data. Nevertheless, for completeness we extended the ***gtf/hcl/sti***-Gauss model to determine the degree to which it could accommodate the complete data set if we ignored the perceptual data on the lower limit of pitch. The extension was accomplished simply by doubling the maximum time interval in the auditory image to 70 ms by halving the slope of the linear weighting function applied to the summary AI. The simulated and observed thresholds are presented in Fig. 10, which shows that this ***gtf/hcl/sti***-Gauss model with enlarged images does not provide a good fit to the extended data set. At 16 Hz, the model overestimates threshold for IRN masked by noise in all filter conditions. Moreover, the model underestimates threshold for noise masked by a 16-Hz IRN in the two higher filter conditions ($F_c = 3.2$ and 6.4 kHz), and as a result, it overestimates the masking asymmetry at 16 Hz in these two filter conditions. In general, this model predicts that threshold at 16 Hz will simply be an extension of that at 32, 64, and 128 Hz; this is clearly not true for the observed threshold at 16 Hz. The rms deviation between simulated and observed thresholds rises from 1.37 to 1.89 dB when the images are extended to longer time intervals. We interpret this as further evidence that detection for 16 Hz is mediated by different cues than for the higher RODs. This provides some justification for our original decision to limit the model to RODs above 30 Hz.

In summary, the modeling suggests that the most appropriate description of the masking asymmetry observed between noise and IRN in the pitch region is provided by the ***gtf/hcl/sti*** version of Licklider's original model of time-interval processing. The fact that threshold increases with increasing filter cutoff demonstrates that some form of auditory filtering is required to explain the pattern of results across frequency. The standard gammatone auditory filterbank, ***gtf***, was used to perform the spectral analysis, although the asymmetry of masking does not constrain the parameters of the filterbank to the specific values that we have employed. The mechano-electrical transduction in the cochlea was simulated by half-wave rectification, square-root compression, and four stages of low-pass filtering, as suggested by the studies of Yost *et al.* (1998) and Patterson *et al.* (2000) on the perception of pitch and pitch strength. The effects of compression and low-pass filtering were examined but neither was found to play an important role in determining the form of the masking asymmetry as a function either of filter cutoff or IRN delay. However, when the ***hcl*** module was replaced by the Meddis hair cell, ***med***, the spontaneous rate of the hair cell caused the masking asymmetry predicted by the model to decrease as filter cutoff increased—a reduction that is not observed in the data. Similarly, all threshold values increased with cutoff frequency more than they do in the data. The time-interval processing applied by the third stage of the model is required to explain the basic masking asymmetry. The precise form of the processing is not overly constrained by the current data; we used strobed temporal integration, ***sti***, since it is simple and it preserves temporal asymmetry as required by studies of strongly asymmetric sounds (Patterson and Irino, 1998). In order to explain the fact that threshold decreases with IRN delay in all filter conditions for both masker types, it was necessary to include the higher-order peaks of the summary auditory images in the decision measure. This is a new finding that is most likely related to the fact that the experiments included a wide range of delays. Finally, the width of the auditory image was increased to 70 ms in an attempt to explain the data at the longest IRN delay with a reciprocal of 16 Hz, but it was unsuccessful in the sense that the reduction of masking asymmetry at high filter cutoff frequencies in the 16-Hz data was not mirrored in the simulated threshold.

V. CONCLUSIONS

There is a large masking asymmetry between noise and iterated rippled noise (IRN). Noise is about 10 dB more effective in masking IRN than IRN is in masking noise when

the reciprocal of the IRN delay is within the pitch range. For both masking conditions, threshold decreases with decreasing IRN delay, and for most combinations of IRN delay and masking condition, threshold increases as the passband of the stimuli is moved to higher frequencies. When the reciprocal of the delay is 16 Hz, the masking asymmetry decreases progressively as the filter cutoff frequency is increased, from about 9 dB for the lowest cutoff frequency ($F_c = 0.8$ kHz) to less than 1 dB for the highest cutoff frequency ($F_c = 6.4$ kHz). This suggests that masking asymmetry is determined by different cues for delays within and below the pitch range. The fact that a masking asymmetry exists for conditions that combine very long IRN delays with very high filter cutoff frequencies means that it is unlikely that models based on the excitation patterns of the stimuli would be successful in explaining the observed masking asymmetry.

Time-domain models of auditory processing that focus on the time intervals in phase-locked neural activity patterns were quite successful in accounting for the basic masking asymmetry between IRN and noise for conditions within the pitch range. Within this class of models, one of the simplest produced an exceptionally good fit to the data with an rms deviation of only 1.37 dB. This model consisted of a gammatone auditory filterbank, half-wave rectification, square-root compression, low-pass filtering, and a sparse form of autocorrelation. However, the model was unable to explain the change in the pattern of results across frequency for IRN with a delay below the pitch region.

ACKNOWLEDGMENT

Research supported by the Medical Research Council (No. G9901257).

[1]In contrast to a harmonic complex tone, the waveform of IRN is not periodic, so it never repeats itself identically over time. Segments of the waveform separated by *d* ms are correlated, and the correlation increases with the number of iterations, *n*; however, the segements are never identical while *n* is less than infinity. Therefore, strictly speaking, terms that are often used to characterize harmonic tones, like ''period'' and ''repetition rate,'' are inappropriate in the case of IRN. The only correct term is the ''reciprocal of the delay,'' which is often cumbersome, and so, in such cases we use ''ROD'' for reciprocal of the delay.

[2]The AIM/DSAM software package can be acquired over the Internet at http://www.essex.ac.uk/psychology/hearinglab/dsam/index/htm

Akeroyd, M. A., and Patterson, R. D. (**1995**). ''Discrimination of wideband noises modulated by a temporally asymmetric function,'' J. Acoust. Soc. Am. **98**, 2466–2474.

Akeroyd, M. A., and Patterson, R. D. (**1997**). ''A comparison of detection and discrimination of temporal asymmetry in amplitude modulation,'' J. Acoust. Soc. Am. **101**, 430–439.

Allen, J. B. (**1980**). ''Cochlear micromechanics—A physical model of transduction,'' J. Acoust. Soc. Am. **68**, 1660–1670.

Baker, R. J., Rosen, S., and Darling, A. M. (**1998**). ''An efficient characterisation of human auditory filtering across level and frequency that is also physiologically reasonable,'' in *Psychophysical and Physiological Advances in Hearing: Proceedings of the 11th International Symposium on Hearing*, edited by A. Palmer, A. Rees, Q. Summerfield, and R. Meddis (Whurr, London), pp. 81–88.

Bilsen, F. A. (**1966**). ''Repetition pitch: Monaural interaction of a sound with the repetition of the same, but phase shifted sound,'' Acustica **17**, 295–300.

Carney, L. H., and Yin, T. C. T. (**1988**). ''Temporal coding of resonances by low-frequency auditory nerve fibers: Single-fiber responses and a population model,'' J. Neurophysiol. **60**, 1653–1677.

Carney, L. H., Megean, J. M., and Shekhter, I. (**1999**). ''Frequency glides in the impulse responses of auditory-nerve fibers,'' J. Acoust. Soc. Am. **105**, 2384–2391.

Glasberg, B. R., and Moore, B. C. J. (**1990**). ''Derivation of auditory filter shapes from notched-noise data,'' Hear. Res. **47**, 103–138.

Glasberg, B. R., and Moore, B. C. J. (**2000**). ''Frequency selectivity as a function of level and frequency measured with uniformly exciting noise,'' J. Acoust. Soc. Am. **108**, 2318–2328.

Hall, J. L. (**1997**). ''Asymmetry of masking revisited: Generalization of masker and probe bandwidth,'' J. Acoust. Soc. Am. **101**, 1023–1033.

Hellmann, R. P. (**1972**). ''Asymmetry of masking between noise and tone,'' Percept. Psychophys. **11**, 241–246.

Hewitt, M. J., and Meddis, R. (**1991**). ''An evaluation of eight computer models of mammalian inner hair-cell function,'' J. Acoust. Soc. Am. **90**, 904–917.

Irino, T., and Patterson, R. D. (**1997**). ''A time-domain, level-dependent auditory filter: The gammachirp,'' J. Acoust. Soc. Am. **101**, 412–419.

Irino, T., and Patterson, R. D. (**2001**). ''A compressive gammachirp auditory filter for both physiological and psychophysical data,'' J. Acoust. Soc. Am. (in press).

Krumbholz, K., Patterson, R. D., and Pressnitzer, D. (**2000**). ''The lower limit of pitch as determined by rate discrimination,'' J. Acoust. Soc. Am. **108**, 1170–1180.

Levitt, H. (**1971**). ''Transformed up–down methods in psychoacoustics,'' J. Acoust. Soc. Am. **49**, 467–477.

Licklider, J. C. R. (**1951**). ''A duplex theory of pitch perception,'' Experientia **7**, 128–133.

Meddis, R. (**1986**). ''Simulation of mechanical to neural transduction in the auditory receptor,'' J. Acoust. Soc. Am. **79**, 702–711.

Meddis, R., and Hewitt, M. J. (**1991**). ''Virtual pitch and phase sensitivity of a computer model of the auditory periphery. I. Pitch identification,'' J. Acoust. Soc. Am. **89**, 2866–2882.

Meddis, R., and O'Mard, L. (**1997**). ''A unitary model of pitch perception,'' J. Acoust. Soc. Am. **102**, 1811–1820.

Moore, B. C. J., and Glasberg, B. R. (**1987**). ''Formulae describing frequency selectivity as a function of frequency and level, and their use in calculating excitation patterns,'' Hear. Res. **28**, 209–225.

Oxenham, A. J., and Moore, B. C. J. (**1995**). ''Overshoot and the severe departure from Weber's law,'' J. Acoust. Soc. Am. **97**, 2442–2453.

Patterson, R. D. (**1994a**). ''The sound of a sinusoid: Spectral models,'' J. Acoust. Soc. Am. **96**, 1409–1418.

Patterson, R. D. (**1994b**). ''The sound of a sinusoid: Time-interval models,'' J. Acoust. Soc. Am. **96**, 1419–1428.

Patterson, R. D., and Datta, A. J. (**1996**). ''The detection of iterated ripple noise (IRN) masked by IRN,'' Br. J. Audiol. **30**, 148.

Patterson, R. D., and Henning, G. B. (**1977**). ''Stimulus variability and auditory filter shape,'' J. Acoust. Soc. Am. **62**, 649–664.

Patterson, R. D., and Irino, T. (**1998**). ''Modeling temporal asymmetry in the auditory system,'' J. Acoust. Soc. Am. **104**, 2967–2979.

Patterson, R. D. (**1976**). ''Auditory filter shapes derived with noise stimuli,'' J. Acoust. Soc. Am. **59**, 640–654.

Patterson, R. D., and Moore, B. C. J. (**1986**). ''Auditory filters and excitation patterns as representations of frequency resolution,'' in *Frequency Selectivity in Hearing*, edited by B. C. J. Moore (Academic, London), pp. 123–177.

Patterson, R. D., Allerhand, M. H., and Giguère, C. (**1995**). ''Time-domain modeling of peripheral auditory processing: A molecular architecture and a software platform,'' J. Acoust. Soc. Am. **98**, 1890–1894.

Patterson, R. D., Handel, S., Yost, W. A., and Datta, A. J. (**1996**). ''The relative strength of tone and noise components of iterated rippled noise,'' J. Acoust. Soc. Am. **100**, 3286–3294.

Patterson, R. D., Nimmo-Smith, I., Weber, D. L., and Milroy, R. (**1982**). ''The deterioration of hearing with age: Frequency selectivity, the critical ratio, the audiogram, and speech threshold,'' J. Acoust. Soc. Am. **72**, 1788–1803.

Patterson, R. D., Robinson, K., Holdsworth, J., McKeown, D., Zhang, C., and Allerhand, M. (**1992**). ''Complex sounds and auditory images,'' in *Auditory Physiology and Perception, Proceedings of the 9th International Symposium on Hearing*, edited by Y. Cazals, L. Demany, and K. Horner (Pergamon, Oxford), pp. 429–446.

Patterson, R. D., Yost, W. A., Handel, S., and Datta, A. J. (**2000**). ''The perceptual tone/noise ratio of merged iterated rippled noises,'' J. Acoust. Soc. Am. **107**, 1578–1588.

Pressnitzer, D., Patterson, R. D., and Krumbholz, K. (**2001**). ''Lower limit of melodic pitch,'' J. Acoust. Soc. Am. **109**, 2074–2084.
Rosen, S., and Baker, R. J. (**1994**). ''Characterizing auditory filter nonlinearity,'' Hear. Res. **73**, 231–243.
Shackleton, T. M., and Carlyon, R. P. (**1994**). ''The role of resolved and unresolved harmonics in pitch perception and frequency modulation discrimination,'' J. Acoust. Soc. Am. **95**, 3529–3540.
Slaney, M., and Lyon, R. F. (**1990**). ''A perceptual pitch detector,'' in *Proceedings of the IEEE International Conference on Acoustics, Speech, and Signal Processing, Albuquerque, New Mexico* (IEEE, New York), pp. 357–360.
Weiss, T. F., and Rose, C. (**1988**). ''Stages of degradation of timing information in the cochlea: A comparison of hair-cell and nerve-fiber responses in the alligator lizard,'' Hear. Res. **33**, 167–174.
Yost, W. A. (**1996**). ''Pitch strength of iterated rippled noise,'' J. Acoust. Soc. Am. **100**, 3329–3335.
Yost, W. A., and Hill, R. (**1978**). ''Strength of the pitches associated with rippled noise,'' J. Acoust. Soc. Am. **64**, 485–492.
Yost, W. A., Patterson, R. D., and Sheft, S. (**1996**). ''A time domain description for the pitch strength of iterated rippled noise,'' J. Acoust. Soc. Am. **99**, 1066–1078.
Yost, W. A., Patterson, R. D., and Sheft, S. (**1998**). ''The role of the envelope in processing iterated rippled noise,'' J. Acoust. Soc. Am. **104**, 2349–2361.
Zhang, X., Heinz, M. G., Bruce, I. C., and Carney, L. H. (**2001**). ''A phenomenological model for the responses of auditory nerve fibers: Nonlinear tuning with compression and suppression,'' J. Acoust. Soc. Am. **109**, 648–670.

Psychophysical suppression effects for tonal and speech signals

Judy R. Dubno[a] and Jayne B. Ahlstrom
Department of Otolaryngology–Head and Neck Surgery, Medical University of South Carolina, 39 Sabin Street, P.O. Box 250150, Charleston, South Carolina 29425

(Received 8 February 2000; revised 19 March 2001; accepted 19 July 2001)

This experiment assessed the benefits of suppression and the impact of reduced or absent suppression on speech recognition in noise. Psychophysical suppression was measured in forward masking using tonal maskers and suppressors and band limited noise maskers and suppressors. Subjects were 10 younger and 10 older adults with normal hearing, and 10 older adults with cochlear hearing loss. For younger subjects with normal hearing, suppression measured with noise maskers increased with masker level and was larger at 2.0 kHz than at 0.8 kHz. Less suppression was observed for older than younger subjects with normal hearing. There was little evidence of suppression for older subjects with cochlear hearing loss. Suppression measured with noise maskers and suppressors was larger in magnitude and more prevalent than suppression measured with tonal maskers and suppressors. The benefit of suppression to speech recognition in noise was assessed by obtaining scores for filtered consonant-vowel syllables as a function of the bandwidth of a forward masker. Speech-recognition scores in forward maskers should be higher than those in simultaneous maskers given that forward maskers are less effective than simultaneous maskers. If suppression also mitigated the effects of the forward masker and resulted in an improved signal-to-noise ratio, scores should decrease less in forward masking as forward-masker bandwidth increased, and differences between scores in forward and simultaneous maskers should increase, as was observed for younger subjects with normal hearing. Less or no benefit of suppression to speech recognition in noise was observed for older subjects with normal hearing or hearing loss. In general, as suppression measured with tonal signals increased, the combined benefit of forward masking and suppression to speech recognition in noise also increased.
[DOI: 10.1121/1.1403699]

PACS numbers: 43.66.Dc, 43.66.Sr, 43.71.Ky, 43.71.Lz [SPB]

I. INTRODUCTION

Suppression may be responsible for reducing masker effectiveness when additional noise components are introduced at certain frequency locations around the signal. As such, suppression may help maintain normal speech recognition by reducing the effects of background noise and improving the signal-to-noise ratio under certain conditions. Given that individuals with cochlear hearing loss have difficulties understanding speech in noise, and that these individuals may also have reduced or absent suppression (e.g., Wightman *et al.*, 1977; Mills and Schmiedt, 1983; Moore and Glasberg, 1986; Thibodeau, 1991), it is reasonable to assume that a lack of suppression contributes to difficulties in speech understanding. That is, individuals with cochlear hearing loss have relatively poor speech recognition in noise because they do not fully benefit from the reduced effects of background noise and improved signal-to-noise ratios provided by suppression. Although suppression has been demonstrated in psychophysical experiments for many years (e.g., Houtgast, 1974; Shannon, 1976), its functional benefits for speech recognition in noise remain unknown.

Several studies of suppression have used speech or speech-like stimuli as maskers. For example, masking patterns were compared for speech-like stimuli in simultaneous and forward masking (Houtgast, 1974; Tyler and Lindblom, 1982; Moore and Glasberg, 1983b); the patterns of masked thresholds obtained in forward masking showed greater differences between peaks and valleys than those obtained in simultaneous masking, and differences varied with level. This has been interpreted as demonstrating that, at moderate levels, suppression enhanced certain spectral contrasts in the excitation pattern elicited by an auditory stimulus, such as that evoked by vowels. However, this interpretation is currently under debate and the relative contributions to masking of suppression and spread of excitation at various masker levels are not yet known (e.g., Delgutte, 1990a; Beveridge and Carlyon, 1996; Moore and Vickers, 1997; Oxenham and Plack, 1998; Gifford and Bacon, 2000). Excitation patterns estimated from pulsation thresholds or forward masking show reduced spectral contrasts for hearing-impaired subjects (Bacon and Brandt, 1982; Tyler and Lindblom, 1982; Van Tasell *et al.*, 1987). However, an association between the spectral characteristics of excitation patterns evoked by vowels and vowel recognition by hearing-impaired listeners has been difficult to establish (Dubno and Dorman, 1987; Van Tasell *et al.*, 1987; Turner and Henn, 1989).

Whereas speech and speech-like stimuli have been used as *maskers* to estimate suppression, effects of suppression on *perception* of consonants have not been assessed, nor has the impact of reduced or absent suppression on speech recogni-

[a]Author to whom correspondence should be addressed; electronic mail: dubnojr@musc.edu

 0001-4966/2001/110(4)/2108/12/$18.00

tion. Preservation of spectral information in consonant spectra may be critical because, analogous to the vowel's formant structure, the gross shape of the consonant's onset spectrum (Blumstein and Stevens, 1980), as well as spectral information during the formant transition (Kewley-Port *et al.*, 1983), are important acoustic cues for these signals. Furthermore, these cues occur in the initial 20–30 ms of the consonant (Dubno *et al.*, 1987), coinciding with the time period in which forward masking is effective.

To make relevant comparisons of suppression and speech recognition in noise, it is preferable that the same maskers and suppressors be incorporated in both suppression and speech-recognition measurements. In two previous experiments (Dubno and Ahlstrom, 2001a, 2001b), a suppression metric was evaluated wherein forward- and simultaneous-masked thresholds were measured at low and high frequencies in bandlimited maskers as a function of masker bandwidth.[1] Using this method, forward-masked thresholds decreased as masker bandwidth increased, which was attributed to effects of suppression. In both studies, larger estimates of suppression were obtained at a higher than a lower signal frequency, regardless of whether suppression was defined as a change in forward-masked threshold with increasing masker bandwidth or a change in effective masker level. For older subjects with cochlear hearing loss, suppression was reduced relative to normal in regions of elevated thresholds; suppression was correlated with absolute thresholds only at the signal frequency.

In the second study measuring suppression with band limited maskers (Dubno and Ahlstrom, 2001b), masker bandwidths were varied with respect to the signal frequency by extending noise bands below and/or above the signal. The largest reduction in threshold (and, therefore, the most suppression) was observed when noise was added below the signal frequency, consistent with some physiological evidence of stronger suppression below the characteristic frequency (CF) than above (e.g., Delgutte, 1990b). Moreover, for suppressor frequencies below the CF, suppression thresholds are low and suppression regions cover a wide range of levels. Accordingly, suppression may be greater below the signal frequency than above for levels of speech and noise typically encountered in the environment. For older subjects with hearing loss, suppression was reduced to a greater extent above the signal frequency and where thresholds were elevated. Less suppression was observed for older than for younger subjects with normal hearing, consistent with age-related changes in auditory-filter bandwidths attributed to reduced suppression (Sommers and Gehr, 1998). Reduced suppression for older subjects with normal hearing suggested that age contributed to reduced suppression or that suppression was sensitive to changes in cochlear function that did not result in threshold elevation.

The purpose of the current experiment was to assess the benefits of suppression and the impact of reduced or absent suppression on speech recognition in noise. Additional goals were to confirm and extend the earlier findings by assessing changes in suppression with masker level and by comparing results with those from a more conventional tonal measure of suppression (for the latter, see the Appendix). Subjects were younger and older adults with normal hearing and older adults with cochlear hearing loss. The masking procedure for speech signals was analogous to that used to assess suppression with tonal signals. Scores were obtained for filtered consonant–vowel syllables in forward and simultaneous bandlimited maskers as a function of masker bandwidth. Speech-recognition scores in forward maskers should be higher than those in simultaneous maskers, given that forward maskers are less effective than simultaneous maskers. However, if suppression also mitigated the effects of the forward masker and resulted in an improved signal-to-noise ratio, scores should decrease less in forward masking as forward-masker bandwidth increased, and differences between scores in forward and simultaneous maskers should increase with increasing masker bandwidth. If suppression played no role, and results were determined by overall masker energy, scores should decline with increasing forward-masker bandwidth, and differences between scores obtained in forward and simultaneous maskers should remain relatively constant with increasing masker bandwidth.

II. METHODS

A. Subjects

There were three subject groups: (1) 10 younger subjects with normal hearing (mean age: 26.2 years; range: 22–35); (2) 10 older subjects with normal hearing (mean age: 67.4 years; range: 60–73); and (3) 10 older subjects with mild-to-moderate sensorineural hearing loss (mean age: 67.3 years; range: 58–81). Absolute thresholds of normal-hearing subjects (younger and older) were $\leqslant$ 20 dB HL (ANSI, 1989) at octave frequencies from 0.25 to 4.0 kHz and immittance measures were within normal limits. Hearing-impaired subjects were selected from among patients with adult-onset cochlear hearing loss (specific etiology unknown), absolute thresholds within specific ranges, and normal immittance measures. Three subjects wore binaural hearing aids; seven subjects did not have hearing aids, although all but one had been encouraged to use amplification. Thresholds of hearing-impaired subjects were restricted to ensure that (1) as the masker bandwidth increased, noise bands would not be introduced into areas of severe hearing loss or into areas where thresholds were changing abruptly with frequency and (2) subjects' thresholds in the bandpass maskers were higher than their absolute thresholds. For younger subjects, one ear was selected randomly for testing. For older subjects, the test ear was selected based on pure-tone thresholds. For older subjects with normal hearing, the ear with better thresholds was selected. For older subjects with hearing loss, the ear that better met the two criteria listed above was selected. Subjects did not have experience with the psychophysical tasks used in this study. As such, subjects received approximately 2 h of practice with forward masking with noise maskers and 2 h of practice with tonal maskers prior to the start of data collection. Data collection was completed in nine, 2-h sessions. Subjects were paid an hourly rate for their participation.

B. Apparatus and stimuli

1. Tonal signals

Tonal signals were digitally generated (TDT PD1) pure tones, sampled at 50.0 kHz and low-pass filtered at 8.5 kHz. Signals for measuring quiet thresholds were 350-ms pure tones, including 10-ms raised-cosine rise/fall ramps, at selected one-third-octave intervals ranging from 0.25 to 6.3 kHz. Quiet thresholds for frequencies from 8.0 to 18.0 kHz were measured with a Demlar audiometer (signal duration not fixed) and Koss headphones. Signals for forward masking were 20-ms pure tones, including 5-ms raised-cosine rise/fall ramps, at 0.8 and 2.0 kHz. Signal level was varied adaptively.

2. Noise maskers and suppressors

Bandpass noise maskers were created by digitally filtering a broadband noise (filter slopes >100 dB/oct). For each signal, there were three to five bandpass maskers with varying bandwidths. The narrowest bandpass maskers were centered at the signal frequency. Bandwidths ranged from 0.2 to 1.5 kHz (for the 0.8-kHz signal) and from 0.4 to 2.0 kHz (for the 2.0-kHz signal). Bandwidths were increased from narrowest to widest by adding noise bands above or below the signal frequency, that is, varying the masker's high- or low-frequency cutoff. A broadband masker was also included (low-pass cutoff set to 8.0 kHz). Bandpass maskers were presented at three spectrum levels, 35, 40, and 45 dB. Masker duration was 200 ms, including 5-ms raised-cosine rise/fall ramps. In forward masking, the duration between the masker and the signal was 0 ms (at the 0-voltage points). Simultaneous-masked thresholds for 350-ms signals ranging from 1.0–5.0 kHz were also measured in six of the bandpass maskers; these masked thresholds were incorporated in articulation index (AI) computations used to select speech levels (see below). For these measures, masker duration was increased to 356 ms.

3. Speech signals

Speech signals were 66 consonant–vowel syllables formed by combining 22 English consonants with /ɑ,i,u/ spoken by one male and one female talker (a total of 132 syllables). The stimulus set was divided into six subsets to provide a more reasonable listening interval. A more detailed description of the speech materials and procedures is included in Dubno and Schaefer (1992, 1995). Each syllable was presented two times in random order; thus, each speech-recognition score was the average of 264 responses. Digital speech waveforms (without a carrier phrase) were output at a sampling rate of 32.89 kHz, bandpass filtered from 0.89 to 3.55 kHz, routed to an attenuator, mixed with the bandpass masker, and delivered to the earphone. The speech was filtered to increase the difficulty of the task for forward masking, that is, to avoid ceiling effects without the use of very high masker levels.

Recognition of filtered consonant–vowel syllables was measured in quiet, and in simultaneous and forward masking as a function of the bandwidth of the bandpass masker. The masker bandwidths were adjusted in a manner that was similar to that used in the noise suppression measures. The narrowest maskers were centered at 2.0 kHz. Bandwidths ranged from 0.37 to 2.14 kHz. Bandwidths were increased from narrowest to widest by raising the masker's high-frequency cutoff or by lowering the masker's low-frequency cutoff. Bandpass masker spectrum level was fixed at 40 dB, equal to one of the levels used in the noise suppression measurements. For simultaneous masking, the masker was turned on 10 ms before the syllable and was turned off coincident with the offset of the syllable. For forward masking, the syllable onset immediately followed masker offset.

For each subject, filtered consonant–vowel syllables were presented at two levels, one selected for quiet and for forward masking and the other selected for simultaneous masking; different speech levels were necessary because of the substantial difference in the effectiveness of forward and simultaneous masking. Rather than use the same two speech levels for all subjects, levels were selected to correspond to two AI values. The AI values were chosen so that speech levels were not substantially higher for hearing-impaired than for normal-hearing subjects and to avoid floor and ceiling effects across all conditions. Speech levels were determined for each subject using the frequency importance function and normal transfer function relating the AI to speech recognition, measured directly for these stimuli (Dirks *et al.*, 1990a, 1990b). For the quiet condition, speech levels were selected to achieve an AI of 0.58 (~75% correct) for subjects with normal hearing and an AI of 0.31 (~50% correct) for subjects with hearing loss, as computed from each subject's quiet thresholds. The same speech levels were used for forward masking. For simultaneous masking, speech levels for all subjects were selected to achieve an AI of 0.18 (~30% correct) in the widest masker bandwidth (i.e., the most difficult condition), as computed from each subject's thresholds in that masker. Note that the focus of the study is the manner in which speech recognition changes with masker bandwidth in forward and simultaneous masking in the three subject groups, rather than absolute differences in speech recognition between simultaneous and forward masking and among subject groups.

The amplitudes of signals and maskers were controlled individually using programmable and manual attenuators (TDT PA4). The signal was added to the masker or masker plus suppressor (TDT SM3) and delivered through one of a pair of TDH-49 earphones mounted in supra-aural cushions. Spectral characteristics of all signals were verified using an acoustic coupler and a signal analyzer (Stanford Research model SR760).

C. Procedures

For each subject, thresholds were measured in the following order: (1) absolute thresholds for 350-ms pure tones at selected one-third-octave frequencies ranging from 0.25 to 6.3 kHz, followed by thresholds at frequencies from 8.0–18.0 kHz; (2) absolute thresholds for 20-ms tones at 0.8 and 2.0 kHz; (3) forward-masked thresholds for 20-ms tones at 0.8 and 2.0 kHz in bandpass maskers as a function of masker bandwidth, and in a broadband masker, with masker spectrum levels of 35, 40, and 45 dB; (4) forward-masked thresh-

olds for 20-ms tones at 0.8 and 2.0 kHz with the tonal masker alone, and also with the tonal masker and each of four suppressors, for two masker/suppressor level combinations (see the Appendix for these results); and (5) simultaneous-masked thresholds for 350-ms tones for signal frequencies within the speech passband (1.0–5.0 kHz) in six bandpass maskers at a spectrum level of 40 dB, for predictions of speech recognition using the AI. Within each set of measures, the order of signal frequency (0.8 kHz, 2.0 kHz) was counterbalanced and, within these conditions, masker spectrum level, and then masker bandwidth (or suppressor frequency) was randomized. Subjects were tested individually in a sound-treated room.

Thresholds were measured using a single-interval (yes–no) maximum-likelihood psychophysical procedure, similar to that described by Green (1993) and discussed in detail in Leek *et al.* (2000). Each threshold was determined from 24 trials, four of which were catch trials. A monochrome monitor displayed the listen and vote periods. Subjects responded by clicking one of two mouse buttons corresponding to the responses ''yes, I heard the tone'' and ''no, I did not hear the tone.'' Two threshold measurements were obtained in each condition; if these differed by more than 5 dB, a third measurement was obtained. Each data point was the average of the two closest threshold measurements. Thresholds at frequencies from 8.0 to 18.0 kHz were measured using a modified method of limits psychophysical procedure.

Following all threshold measurements, recognition of filtered consonant–vowel syllables was measured in quiet, and in forward and simultaneous masking as a function of masker bandwidth. Subjects were instructed to respond by clicking the mouse on the appropriate alphabetic symbol displayed on the monochrome monitor. All consonants contained in the subset were available alternatives; correct answer feedback was not provided.

It has been suggested that forward-masked thresholds may be affected by confusion if stimulus conditions make it difficult to distinguish the signal from the narrowband masker and if the ability to distinguish the signal from the masker changes with masker bandwidth. As such, in this experiment, stimuli and procedures for forward masking were selected to minimize these effects (Moore and Glasberg, 1986), including: (1) a 20-ms signal, which was long enough to have a tonal quality to differentiate it from the quality of the noise masker; (2) bandpass masker bandwidths which were $\geqslant$20% of the signal frequency, thus avoiding very narrow bandwidths that have envelope fluctuations which are similar to those of the signal; and (3) practice sessions wherein subjects were trained to differentiate quality differences between the masker and the signal, using masker-signal delays $>$0 ms. None of the subjects displayed systematic changes in their forward-masked thresholds during the course of data collection (see Dubno and Ahlstrom, 2001a, 2001b for additional discussion).

III. RESULTS AND DISCUSSION

A. Quiet thresholds

Mean thresholds (in dB SPL) for the three groups of subjects are shown in the top panel of Fig. 1 for 20-ms signals and in the bottom panel of Fig. 1 for 350-ms signals. In the lower right panel, thresholds are shown for pure-tone signals ranging from 8.0 to 18.0 kHz. For these extended high frequencies, if subjects did not respond at the maximum intensity presented (110 dB SPL), thresholds were assigned a value of 115 dB SPL. In the audiometric range, thresholds for the older subjects with normal hearing were higher than those of the younger subjects by about 10 dB (7.5-dB difference for 20-ms signals), although all subjects in these two groups met the criterion of ''normal hearing.'' Thresholds for extended high frequencies were substantially elevated for these older subjects. Hearing-impaired subjects had mild-to-moderate hearing loss which was greater in the higher frequencies than in the lower frequencies; highest thresholds were observed for extended high frequencies.

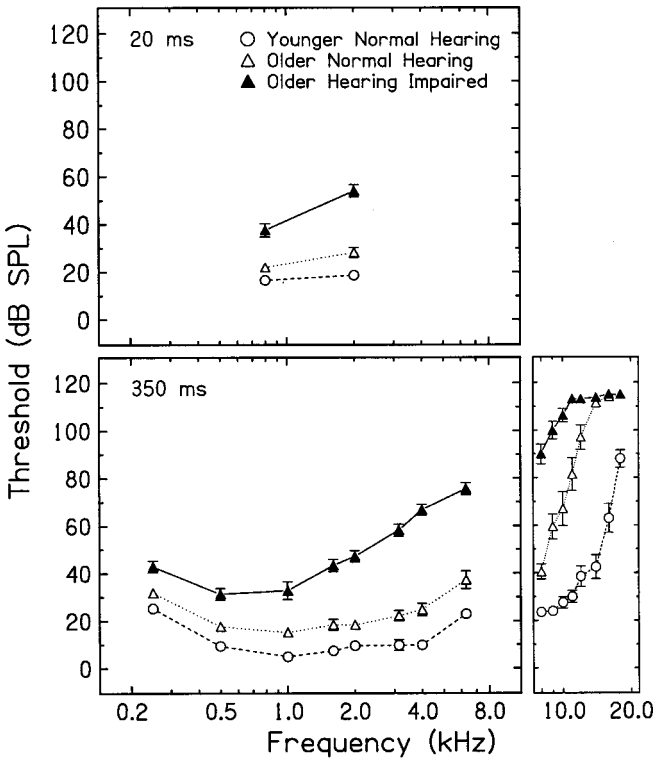

FIG. 1. Mean thresholds (in dB SPL) measured in quiet for younger subjects with normal hearing (open circles), older subjects with normal hearing (open triangles), and older subjects with cochlear hearing loss (filled triangles) for 20-ms signals (top panel) and 350-ms signals (bottom panel). Error bars indicate $\pm$1 standard error of the mean (SE). In the lower right panel, if subjects did not respond at the maximum intensity presented (110 dB SPL), thresholds were assigned a value of 115 dB SPL.

B. Bandpass noise suppression with tonal signals

Figure 2 shows mean suppression of tones as a function of bandpass masker spectrum level for the 0.8-kHz signal for the three subject groups. Figure 3 shows mean suppression for the 2.0-kHz signal, plotted in the same manner as Fig. 2. In both figures, some data points are offset along the abscissa for clarity. Suppression was operationally defined as the decrease in forward-masked threshold with increasing masker bandwidth, as noise bands were added above or below the signal frequency. Thus, each point is the difference in forward-masked threshold (in dB) for the widest and narrow-

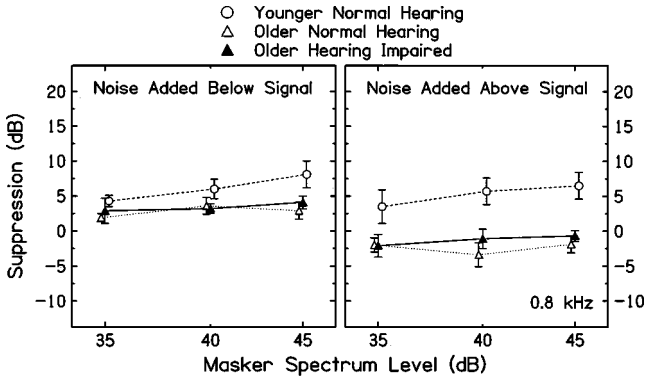

FIG. 2. Mean suppression (±1 SE) as a function of bandpass masker spectrum level for the 0.8-kHz signal for younger subjects with normal hearing (open circles), older subjects with normal hearing (open triangles), and older subjects with cochlear hearing loss (filled triangles). Each point is the difference in forward-masked threshold (in dB) for the widest and narrowest masker bandwidths. The left panel contains results for noise bands added below the signal and the right panel for noise bands added above the signal. Values >0 dB indicate suppression. Some data points are offset along the abscissa for clarity.

est maskers, excluding the broadband masker. The left panel of each figure contains results for noise bands added below the signal and the right panel for noise bands added above the signal. Values >0 dB indicate suppression.

For the younger subjects with normal hearing, measurable suppression was observed for nearly all conditions. However, for the two older groups, suppression was minimal when noise was added below the signal and not present when noise was added above the signal. Suppression measured with noise was assessed by a repeated measures analysis of variance (ANOVA) with subject group as a grouping factor, and masker level and signal frequency as repeated measures. The analysis was conducted only on suppression measured with noise bands added below the signal, given that suppression was measurable here for most subjects. For younger subjects with normal hearing only, an additional ANOVA was conducted with direction of band widening as an additional factor.

For younger subjects with normal hearing, suppression was significantly larger when noise was introduced below the signal than above, but only at 2.0 kHz (0.8 kHz: $F[1,9]=0.26$, $p>0.05$; 2.0 kHz: $F[1,9]=65.97$, $p<0.01$). Suppression was significantly larger at 2.0 kHz than at 0.8 kHz when noise was added below the signal ($F[1,9]=16.94$, $p<0.01$) and above ($F[1,9]=20.99$, $p<0.01$) and increased significantly with masker level ($F[2,18]=7.0$, $p<0.01$).

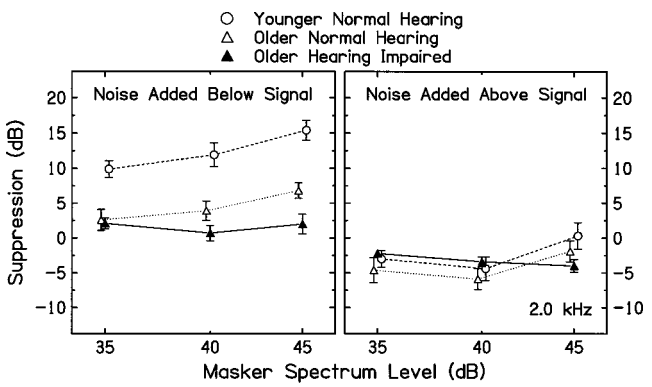

FIG. 3. Same as Fig. 2, but for the 2.0-kHz signal.

At both signal frequencies, suppression was significantly larger for younger subjects with normal hearing than for the two older groups (younger versus older normal: $F[1,27]=15.40$, $p<0.01$; younger versus older hearing impaired: $F[1,27]=22.31$, $p<0.01$; older normal versus older hearing impaired: $F[1,27]=0.64$, $p>0.05$). In contrast to results for younger subjects, suppression for the two older groups was not significantly different at the two signal frequencies (older normal: $F[1,27]=2.77$, $p>0.05$; older hearing impaired: $F[1,27]=0.57$, $p>0.05$) and did not change with level (older normal: $F[1,27]=1.35$, $p>0.05$; older hearing impaired: $F[1,27]=1.87$, $p>0.05$). It was notable that absolute thresholds for older subjects with normal hearing were more similar at both signal frequencies to those of younger subjects than to those of subjects with hearing loss. Nevertheless, suppression for the older subjects with normal hearing was reduced almost as much as for older subjects with hearing loss.

Suppression measured for the three subject groups using the 45-dB masker spectrum level may be compared to earlier results using this technique (Dubno and Ahlstrom, 2001b). The overall results were comparable in that suppression was greater for noise bands introduced below the signal than above, suppression was greater for the 2.0-kHz signal than for the 0.8-kHz signal, and suppression was reduced for older subjects with and without hearing loss relative to that observed for younger subjects with normal hearing.

To assess the influence of confusion effects mentioned previously, forward-masked thresholds were examined in two ways. First, from forward-masked thresholds measured in three masker levels, slopes of growth-of-masking functions were computed for each subject for each masker bandwidth. Neff (1985) suggested that steep slopes (i.e., close to 1.0) were evidence of confusion. Here, for younger subjects, slopes became somewhat shallower as bandwidth increased but remained <0.5 even in the narrowest bandwidth. Overall, slopes were shallower at 2.0 than at 0.8 kHz. For older subjects, slopes for all bandwidths were somewhat steeper than for younger subjects, and were steeper at 2.0 kHz than at 0.8 kHz for older subjects with hearing loss. However, these patterns were observed across all bandwidths, not just for the narrowest bandwidth. Still, slopes ranged from 0.6–0.75, with no systematic relationship with bandwidth. Second, as was observed in Dubno and Ahlstrom (2001b), the decline in forward-masked thresholds with increasing masker bandwidth differed for noise introduced below the signal versus above the signal. Taken together, these two forms of evidence suggest that confusion effects were not influencing forward-masked thresholds.

C. Bandpass noise suppression with speech signals

Figures 4 and 5 plot recognition of filtered consonant–vowel syllables (in percent correct) in quiet and in bandpass maskers as a function of masker bandwidth for the three subject groups. As illustrated by the schematics in the right panels, in Fig. 4, bandwidths were increased by lowering the low-frequency cutoff of the masker, and in Fig. 5, band-

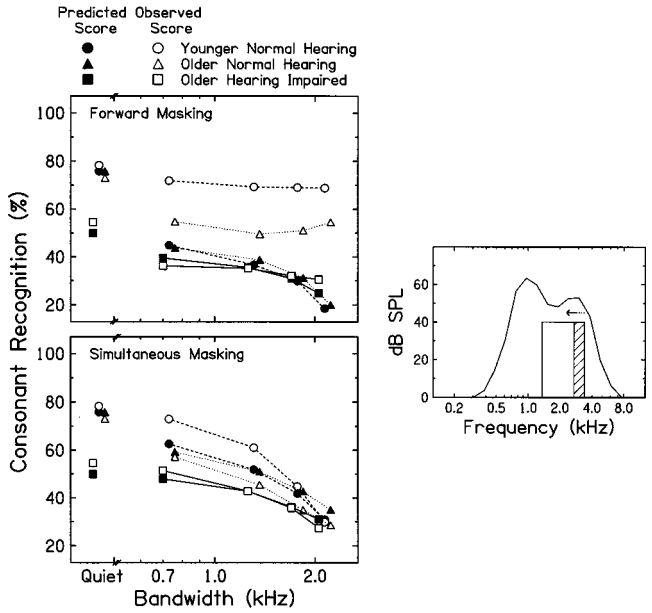

FIG. 4. Recognition of filtered consonant–vowel syllables (in percent correct) in quiet and in bandpass maskers as a function of masker bandwidth for younger subjects with normal hearing (open circles), older subjects with normal hearing (open triangles), and older subjects with cochlear hearing loss (open squares). Filled symbols are scores predicted by the articulation index using each subject's simultaneous-masked thresholds in the relevant masker. Forward-masked conditions are in the top panel and simultaneous-masked conditions are in the bottom panel. The right panel contains a schematic of the long-term spectra of the nonsense syllables and the bandpass maskers. The striped bar represents the masker with the narrowest bandwidth; masker bandwidth was increased by lowering the masker's low-frequency cutoff. Some data points are offset along the abscissa for clarity.

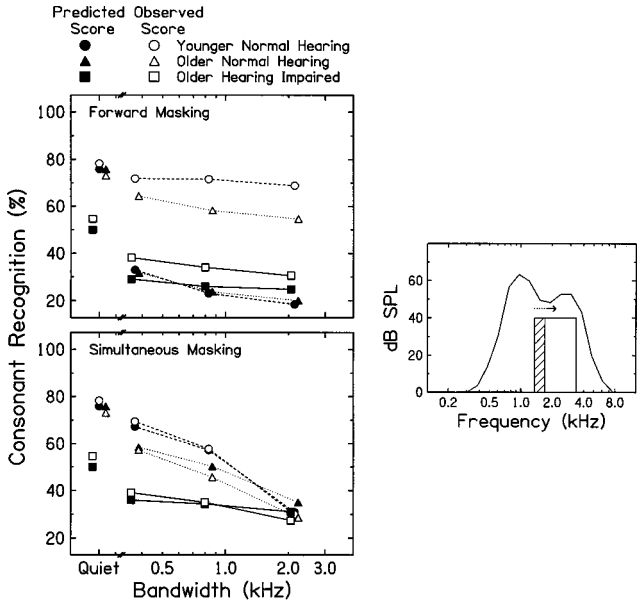

FIG. 5. Same as Fig. 4, but for masker bandwidths increased by raising the masker's high-frequency cutoff.

widths were increased by raising the high-frequency cutoff of the masker. Filled symbols are scores predicted by the AI; open symbols are observed scores. Some data points are offset along the abscissa for clarity. For predictions of scores in simultaneous masking (bottom panels), the speech level presented in simultaneous masking was used to compute the AI. In forward masking, the speech level presented in forward masking was used to compute the AI, but the predictions, of course, assume simultaneous masking of speech.

In simultaneous maskers (bottom panels of Figs. 4 and 5), scores decreased as a function of masker bandwidth, as predicted. That is, as the masker bandwidth increased, overall noise level increased and wider portions of the speech spectrum were masked by the noise. This reduction in signal-to-noise ratio in certain spectral regions resulted in reduced speech recognition. Scores decreased least with increasing masker bandwidth for older subjects with hearing loss when noise was added to the higher frequencies (Fig. 5). This may be attributed to these subjects' elevated thresholds in the higher frequencies; that is, speech audibility in the region above 2.0 kHz was determined by these subjects' absolute thresholds rather than by the band levels of the noise. Scores decreased as expected for subjects with hearing loss when noise was added to the lower frequencies, in regions where absolute thresholds for these subjects were lower. Observed scores in simultaneous masking were generally similar to predicted scores. Exceptions were that younger subjects with normal hearing performed better than predicted in the two narrower bandwidths when noise was added to the lower frequencies (Fig. 4). Older subjects with normal hearing performed somewhat worse than predicted for all but the narrowest bandwidths (Figs. 4 and 5).

Now consider speech recognition in forward masking (top panels of Figs. 4 and 5). There were several aspects of these results that were notable. First, differences between observed scores in quiet and in the narrowest maskers provided a measure of the effectiveness of the forward masker. The forward masker affected speech recognition most for subjects with hearing loss and least for younger subjects with normal hearing. For subjects with hearing loss, scores decreased from those in quiet by 17–18% with the addition of the forward masker, but decreased from quiet by only about 6.5% for younger subjects with normal hearing. For older subjects with normal hearing, the effectiveness of the forward masker depended on the spectrum of the masker. With the addition of a forward masker with a higher frequency passband (Fig. 4), scores decreased from those in quiet by 18%; with the addition of a forward masker with a lower frequency passband (Fig. 5), scores decreased from those in quiet by 9%.

Next, observed scores in forward maskers were better than predicted from simultaneous masking as subjects benefitted in varying degrees from the temporal separation between the masker and signal (open versus filled symbols in *top* panels of Figs. 4 and 5). That is, forward maskers were less effective maskers of speech than simultaneous maskers. For the narrowest masker, the difference between predicted and observed scores was greater with the lower frequency passband (1.41–1.78 kHz, Fig. 5) than with the higher frequency passband (2.82–3.55 kHz, Fig. 4). The influence of the predicted scores themselves on the magnitude of the forward-masking benefit cannot be ruled out. That is, with the lower frequency passband, predicted scores were poorer and the observed-predicted difference in forward masking was greater than with the higher frequency passband.

Younger subjects with normal hearing benefitted most from the temporal separation between the masker and the signal, older subjects with normal hearing benefitted less, and older subjects with hearing loss benefitted least. That is, forward maskers were more effective maskers of speech for older subjects with and without hearing loss than for younger subjects. Estimating from scores in the narrowest higher frequency passband (Fig. 4), scores for younger subjects in forward masking averaged 27% higher than predicted from simultaneous masking, whereas scores for older subjects with normal hearing were only 11% higher. The comparable values for the lower frequency passband (Fig. 5) were 39% and 32%, respectively. For older subjects with hearing loss, scores in forward masking showed only small increases (Fig. 5) or *decreases* (Fig. 4) relative to scores predicted from simultaneous masking. The differences in forward-masking benefit observed among subject groups cannot be attributed to the predicted scores themselves, given that for a particular masker, predicted scores for the three subject groups were nearly equal.

Finally, of greatest interest was the change in forward-masked speech recognition with increasing masker bandwidth. In forward masking of tones, thresholds decreased with increasing masker bandwidth such that thresholds were lowest in the widest forward masker. In a parallel manner, speech-recognition scores should decrease less in forward masking as masker bandwidth increased if the increased masker energy arising from wider masker bandwidths was offset by suppression effects. This was quantified in two ways.

First, differences in scores obtained in the narrowest and widest forward maskers were assessed by repeated measures ANOVA; masker bandwidth was the repeated measure and subject group was the grouping variable. Of interest was the interaction between subject group and bandwidth. For younger subjects with normal hearing, scores in narrow and wide forward maskers were not significantly different, regardless of whether the noise was added to the lower frequency side of the masker ($F[2,27]=1.67$, $p>0.05$) or to the higher frequency side of the masker ($F[1,27]=1.37$, $p>0.05$). That is, with increasing bandwidth of the forward masker, scores for younger subjects with normal hearing remained constant, providing evidence of the benefit of suppression. Scores also remained constant with increasing forward-masker bandwidth for older subjects with normal hearing, but only for noise added to the lower frequency side of the masker (lower frequency side: $F[2,27]=0.009$, $p>0.05$; higher frequency side: $F[2,27]=14.38$, $p<0.01$), consistent with these subjects' larger suppression for noise added below the signal. For older subjects with hearing loss, scores declined significantly as the bandwidth of the forward masker increased, regardless of whether noise was added to the lower frequency side of the masker ($F[2,27]=5.88$, $p<0.05$) or to the higher frequency side of the masker ($F[2,27]=8.83$, $p<0.01$).

Second, as described above, if increased masker energy arising from wider masker bandwidths was offset by suppression effects, scores obtained in the widest forward masker should deviate most from those predicted from simultaneous masking. This was quantified by comparing scores obtained in the widest forward masker with scores predicted from simultaneous masking (i.e., in the widest masker, observed score in forward masking *minus* predicted score in simultaneous masking).

For the younger subjects with normal hearing, simultaneous masking predicted an average score of 19% for the widest masker, whereas in forward masking, scores averaged 69%. Thus, observed scores were 50% higher than those predicted from simultaneous masking. Clearly, the reduced effectiveness of forward maskers provided at least part of the explanation for this improvement, as was the case for the narrowest forward maskers discussed above. However, it may not explain the substantially *greater* difference between observed and predicted scores for the widest maskers than for the narrowest maskers. As discussed above, observed-predicted differences for the narrowest maskers were 27% and 39% for the higher frequency passband and lower frequency passband, respectively. A reasonable explanation is that, in the widest forward masker, the further improvement in score relative to simultaneous masking is attributable to reduced masker effectiveness provided by suppression. Consistent with this explanation was that this ''suppression benefit'' was larger for noise added to the low-frequency side of the masker than to the high-frequency side, given that more suppression of a 2.0-kHz tonal signal was observed for noise added below the signal than above (Fig. 3). However, some ''suppression benefit'' for speech was observed for noise added to the high-frequency side of the masker whereas no suppression at 2.0 kHz was observed for noise added above the signal. Note that masker bandwidths were similar but not identical for tonal and speech masking. For recognition of filtered consonant–vowel syllables, masker passbands were selected to correspond to the speech passband and to provide scores in simultaneous and forward masking that were in the measurable performance range (i.e., avoiding limitations of floor and ceiling). In addition, varying masker effectiveness within a limited range of frequencies may affect detection of a pure tone differently than recognition of a filtered syllable.

Additional tests of the suppression assumption were provided by considering observed–predicted differences for the three subject groups, in light of their differences in suppression at 2.0 kHz (Fig. 3). For older subjects with normal hearing, differences between observed scores in the widest forward masker and scores predicted from simultaneous masking averaged 35%, less than for younger subjects with normal hearing. As noted above, observed–predicted differences for the narrowest forward maskers were also less than for younger subjects. These smaller improvements suggest that forward maskers were generally more effective for these older subjects. The ''suppression benefit'' (comparing observed–predicted differences for narrowest and widest maskers) was measurable for noise added to the low-frequency side of the masker but nearly zero for noise added to the high-frequency side, consistent with these subjects' suppression at 2.0 kHz. However, the ''suppression benefit'' for older subjects with normal hearing was equivalent to that for younger subjects, which was not consistent with younger subjects' larger suppression at 2.0 kHz.

For older subjects with hearing loss, differences between observed scores in the widest forward masker and scores predicted from simultaneous masking averaged only 6%, much less than for subjects with normal hearing. Observed–predicted differences for the narrowest forward maskers were also small or were less than zero; that is, scores in the narrowest forward maskers were nearly equal to or less than scores predicted from simultaneous masking. These subjects' results were entirely consistent with reduced suppression at 2.0 kHz, especially for noise added above the signal.

D. Relationships among suppression measures with tonal and speech signals

In this experiment, suppression measured with speech signals was designed to be similar to suppression measured with tonal signals and bandlimited maskers of varying bandwidths. That is, the benefit of suppression to speech recognition in noise was indicated by the improvement in score in forward masking relative to that predicted in simultaneous masking for the widest minus narrowest masker bandwidths, such that greater observed–predicted differences were associated with greater benefit. Similarly, the magnitude of suppression for tonal signals was indicated by the difference in threshold in forward masking between the widest and narrowest masker bandwidths, such that the greater the reduction in threshold, the greater the suppression. Therefore, it was reasonable to assume that the benefit of suppression to speech recognition in noise would be associated with the magnitude of suppression for tonal signals.

To assess this relationship, Pearson correlation coefficients were computed between suppression measured with tonal and speech signals for all subjects. Suppression for tonal signals was quantified as the difference in forward-masked threshold at 2.0 kHz between the widest and narrowest masker for noise added below the signal (as shown in the left panel of Fig. 3, 40-dB masker). Suppression benefit for speech was quantified as the difference between the score obtained in forward masking and the score predicted by simultaneous masking for the widest minus the narrowest bandwidth, for noise added to the lower frequency side of the masker. Correlation coefficients were also computed between suppression at 2.0 kHz and observed–predicted differences in scores for the narrowest forward maskers. Statistically significant correlations were observed between suppression of a tonal signal for noise added below the signal and (1) observed–predicted differences for the narrowest forward masker ($r=0.633$, $p<0.01$) and (2) observed–predicted differences for the widest forward masker ($r=0.578$, $p<0.01$).

Figure 6 illustrates these relationships. In the top panel, differences between observed and predicted scores for a narrowband forward masker correspond to the effectiveness of forward masking of speech. That is, smaller observed–predicted differences mean that scores in forward masking approach those predicted for simultaneous masking. Thus, the pattern of results in the top panel suggests that subjects with substantial amounts of suppression at 2.0 kHz were those whose speech-recognition scores were less affected by the forward masker; subjects with less suppression were those for whom forward maskers were more effective. In the bottom panel, differences between observed and predicted scores for the widest forward masker reflect the combined benefits of forward masking and suppression. The general trend was that as suppression at 2.0 kHz increased, the combined benefits of forward masking and suppression to speech recognition in noise also increased. Nevertheless, individual differences were substantial. When suppression at 2.0 kHz was small, the combined benefit for speech varied from none (most commonly for subjects with hearing loss) to substantial (for subjects with normal hearing). However, when suppression was greater than ~6 dB, the combined benefit was consistently large.

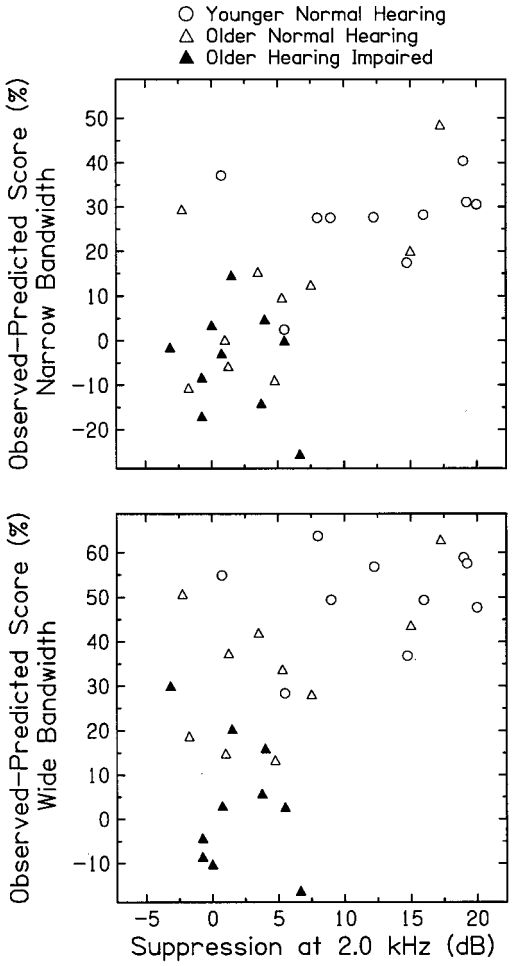

FIG. 6. Differences in observed scores in forward masking and predicted scores in simultaneous masking for three subject groups for a narrowband forward masker (top panel) and a wideband forward masker (bottom panel) plotted against suppression at 2.0 kHz measured with noise added below the signal. See text for description of variables.

E. Estimating suppression as a change in effective masker level

As described above, speech-recognition scores remained relatively constant with increasing masker bandwidth in forward masking which was attributed, in part, to the decrease in masker effectiveness and subsequent improvement in signal-to-noise ratio provided by suppression. It was of interest to determine if the change in effective masker level attributed to suppression could be estimated from the speech-

recognition results. The approach was as follows. It was assumed that the change in effective masker level was equivalent to the amount the masker must be reduced in simultaneous masking to achieve the score obtained in forward masking. For example, for younger subjects with normal hearing, the average score in the widest forward masker was 69%, whereas simultaneous masking predicted a score of 19%. Using the AI and normal transfer function, it was determined that a decrease of 44.3 dB in the level of the simultaneous masker would improve the score to be equal to that achieved in forward masking. Thus, 44.3 dB was the decrease in effective masker level that may be attributed to the combined effects of forward masking and suppression.[2] The comparable values were 22.8 dB for older subjects with normal hearing and 0.3 dB for older subjects with hearing loss. Note that these values do not take into account how scores change with increasing forward-masker level, that is, the slope of the growth-of-masking function in forward masking; this will be assessed further in future experiments.

The decrease in effective masker level attributed to suppression has been estimated previously with tonal signals (e.g., Moore and Glasberg, 1983a; Lee and Bacon, 1998; Dubno and Ahlstrom, 2001a). That is, rather than defining suppression as a change in forward-masked threshold as a function of masker bandwidth, given that the effect of suppression is to reduce masker effectiveness, suppression has been quantified as a change in effective masker level, taking into account the nonlinear growth of forward masking. Here, for the 2.0-kHz signal frequency and the 40-dB masker, suppression was estimated as a change in effective masker level by taking the difference in thresholds for the narrowest and widest maskers and dividing by the slope of the growth-of-masking function measured in forward masking. This computation was conducted only on suppression measured with noise bands added below the signal, given that suppression was measurable here for most subjects. For younger subjects with normal hearing, the change in effective masker level attributed to suppression with tonal signals was 30.5 dB. The comparable values were 8.5 and 1.1 dB for older subjects with normal hearing and older subjects with hearing loss, respectively. These values are smaller than those estimated from forward masking of speech, described above, because the prior estimates included the combined effects of forward masking and suppression. The generally good correspondence between estimates of reduced masker effectiveness for tones and speech suggests that additional investigation of the change in effective masker level attributed to suppression is warranted. A related question that requires further study is the contribution of suppression to improved signal-to-noise ratios in more realistic listening environments where speech interference is a complex combination of forward, backward, and simultaneous masking.

IV. SUMMARY AND CONCLUSIONS

Psychophysical suppression was measured in forward masking using bandlimited noise maskers and suppressors. For noise maskers and tonal signals, suppression was defined as the decrease in forward-masked threshold with increasing masker bandwidth, as noise bands were added above or below the signal frequency. To assess the benefit of suppression and the impact of reduced or absent suppression on speech recognition in noise, scores were obtained for filtered consonant–vowel syllables in forward and simultaneous bandlimited maskers as a function of masker bandwidth. Subjects were younger and older adults with normal hearing, and older adults with cochlear hearing loss. For younger subjects with normal hearing, suppression measured with noise maskers was larger when noise was introduced below the signal than above, increased with masker level, and was larger at 2.0 kHz than at 0.8 kHz. Much less suppression was observed for older subjects with normal hearing or cochlear hearing loss. For younger subjects with normal hearing, scores for forward-masked recognition of filtered consonant–vowel syllables remained constant with increasing masker bandwidth, providing evidence of the benefit of suppression. In addition, scores in forward masking were substantially higher than scores predicted from simultaneous masking, especially in the widest forward maskers. This was attributed to the combined effects of reduced masker effectiveness of forward maskers and suppression. Thus, under nonsimultaneous-masking conditions, suppression may contribute to improved speech recognition in noise. Less or no ''suppression benefit'' for speech was observed for older subjects with normal hearing or hearing loss. In general, as suppression for a tonal signal increased, the combined benefit of forward masking and suppression to speech recognition in noise also increased.

ACKNOWLEDGMENTS

This work was supported (in part) by Grants Nos. R01 DC00184 and P50 DC00422 from NIH/NIDCD. The authors thank Chris Ahlstrom for computer and signal-processing support, Fu-Shing Lee for advice on data analysis, and Amy R. Horwitz, John H. Mills, and Richard A. Schmiedt, for editorial comments. Associate Editor Sid P. Bacon also made helpful suggestions.

APPENDIX: TONAL SUPPRESSION WITH TONAL SIGNALS

A secondary goal of this experiment was to compare suppression measured with bandlimited noise maskers and suppressors to the more conventional measure of suppression using tonal maskers and suppressors. Signals were 20-ms pure tones at 0.8 and 2.0 kHz, as described in the Methods section. Maskers were pure tones at 0.8 and 2.0 kHz; tonal suppressors were fixed at 0.9, 1.1, 1.2, and 1.3 times the signal frequency. Masker levels were 50 and 70 dB SPL; suppressor levels were 20 dB above each masker level. Masker and suppressor durations were both 200 ms, including 5-ms raised-cosine rise/fall ramps, and the duration between the masker and the signal was 0 ms (at the 0-voltage points). Psychophysical procedure was as described in the Methods section.

Suppression measured with tonal maskers and suppressors was smaller in magnitude and less consistently observed among subjects than suppression measured with noise maskers and suppressors (e.g., Lee and Bacon, 1998). Given

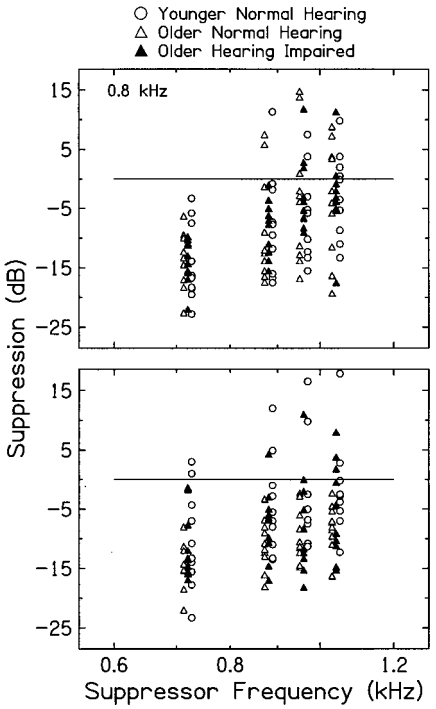

FIG. 7. Suppression as a function of suppressor frequency for the 0.8-kHz signal and masker for younger subjects with normal hearing (open circles), older subjects with normal hearing (open triangles), and older subjects with cochlear hearing loss (filled triangles). Each point is the difference in masked threshold (in dB) with and without the suppressor. The upper panel contains results for masker and suppressor levels of 50 and 70 dB SPL, respectively, and the lower panel for 70 and 90 dB SPL, respectively. Values >0 dB (above the horizontal lines) indicate suppression and values <0 dB (below the horizontal lines) suggest that the suppressor was producing masking. Some data points are offset along the abscissa for clarity.

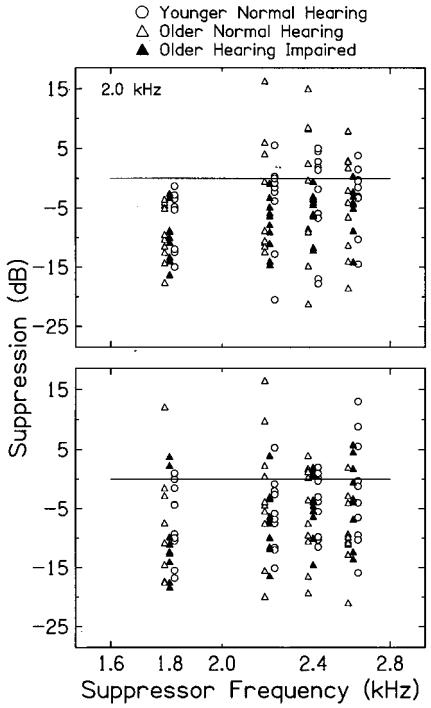

FIG. 8. Same as Fig. 7, but for the 2.0-kHz signal and masker.

that individual differences within subject groups were substantial, results are plotted for individual subjects rather than displaying group means. Figures 7 and 8 plot suppression as a function of suppressor frequency for the 0.8-kHz and 2.0-kHz signal and masker, respectively. The upper panel contains results for masker and suppressor levels of 50 and 70 dB SPL, respectively, and the lower panel for 70 and 90 dB SPL. Suppression (in dB) was operationally defined as the masked threshold without the suppressor minus the masked threshold with the suppressor. Values >0 dB (above the horizontal lines) indicate suppression, because the masked threshold decreased with the addition of the suppressor tone. Values <0 dB (below the horizontal lines) suggest that the suppressor was producing masking, because the masked threshold increased with the addition of the suppressor tone.

Overall, suppression was observed for only a few subjects in each group (the small numbers of subjects with suppression precluded statistical analysis). When observed, suppression was more common with the two higher suppressor frequencies, especially with the lower masker/suppressor levels. Indeed, for those lower levels, no suppression was observed for the suppressor frequency below the signal frequency. This is consistent with suppression thresholds of auditory-nerve fibers that were higher when the suppressor frequency was below the characteristic frequency than above (e.g., Sachs and Kiang, 1968). Suppression was more commonly observed for the 2.0-kHz signal than for the 0.8-kHz signal, consistent with frequency differences in suppression measured with pure tones by Hicks and Bacon (1999a, 1999b) and with greater nonlinear processing in the basal than apical regions of the cochlea (e.g., Rhode and Cooper, 1993; Cooper and Rhode, 1995).

In conditions where suppression was most likely observed, only 4/10 younger subjects with normal hearing and 4/10 older subjects with normal hearing showed suppression for the 0.8-kHz signal (lower masker/suppressor levels, suppressor 1.3 times signal frequency). For the 2.0-kHz signal, 5/10 younger subjects with normal hearing and 5/10 older subjects with normal hearing showed suppression (lower masker/suppressor levels, suppressor 1.2 times signal frequency). These individual differences were consistent with those observed in previous experiments with subjects with normal hearing (see review in Wright, 1996; Lee and Bacon, 1998; Hicks and Bacon, 1999a) and subjects with hearing loss (Hicks and Bacon, 1999b). Wright (1996) suggested that individual differences may be attributed to the interdependence of suppression and tuning. That is, if a tone at the suppressor frequency contributes to masking, due to slight variations in sharpness of tuning, that same tone cannot also provide suppression.

To assess the possible influence of confusion effects in on-frequency forward masking, slopes of two-point growth-of-masking functions were computed for forward-masked thresholds with the masker alone (masker levels of 50 and 70 dB SPL). As noted previously, slopes near 1.0 suggest the influence of confusion effects. Here, slopes averaged ~0.7 for both signal frequencies. Additional evidence against confusion effects was that the signal levels at threshold were lower than the masker levels (Neff, 1985). Thus, as with suppression measures obtained with noise maskers and sup-

pressors, there was little evidence that confusion effects influenced forward-masked thresholds.

To assess the association between suppression measured using tonal maskers and suppressors and suppression measured using noise maskers and suppressors, correlation coefficients were computed within each subject group and signal frequency (for tonal maskers, four suppressor frequencies and two levels; for noise maskers, two band widening directions and three levels). The strongest correlations were observed for younger subjects with normal hearing, which was likely due to their larger range of suppression values. Most correlations were positive, suggesting that younger subjects who demonstrated suppression on one measure also demonstrated suppression on the other. Statistically significant correlations ($r \geqslant 0.632$, $p < 0.05$) were most commonly observed between tonal and noise suppression measured at 0.8 kHz and for suppression measured at the higher levels. Similar trends, but fewer significant correlations, were found for older subjects with normal hearing. Statistically significant correlations between tonal and noise suppression measures were not observed for older subjects with hearing loss, possibly because suppression values were small for these subjects and conditions.

To summarize, suppression measured with tonal maskers and suppressors was observed in a maximum of 50% of subjects in each group and was more commonly observed at 2.0 kHz than at 0.8 kHz, with suppressor frequencies higher than the signal frequency, and in subjects with normal hearing. Suppression measured with tonal maskers and suppressors was smaller in magnitude and less prevalent than suppression measured with noise maskers and suppressors.

[1]The rationale for using noise maskers and suppressors rather than using tonal maskers and suppressors is given in Dubno and Ahlstrom (2001a).

[2]To estimate the decrease in effective masker level that may be attributed to suppression, it is necessary to determine the change in effective masker level between the widest and narrowest maskers. Accordingly, using the same approach as for the widest masker, we attempted to determine the amount the narrowest masker must be reduced in simultaneous masking to achieve the score obtained in forward masking. However, a valid estimate could not be computed for the narrowest maskers because, at these low masker levels, AI values were being determined by the listeners' quiet thresholds rather than by band levels of the noise.

ANSI (**1989**). ANSI S3.6-1989, ''Specifications for Audiometers'' (American National Standards Institute, New York).

Bacon, S. P., and Brandt, J. F. (**1982**). ''Auditory processing of vowels by normal-hearing and hearing-impaired listeners,'' J. Speech Hear. Res. **25**, 339–347.

Beveridge, H. A., and Carlyon, R. P. (**1996**). ''Effects of aspirin on human psychophysical tuning curves in forward and simultaneous masking,'' Hear. Res. **99**, 110–118.

Blumstein, S. E., and Stevens, K. N. (**1980**). ''Perceptual invariance and onset spectra for stop consonants in different vowel environments,'' J. Acoust. Soc. Am. **67**, 648–662.

Cooper, N. P., and Rhode, W. S. (**1995**). ''Nonlinear mechanics at the apex of the guinea-pig cochlea,'' Hear. Res. **82**, 225–243.

Delgutte, B. (**1990a**). ''Physiological mechanisms of psychophysical masking: Observations from auditory-nerve fibers,'' J. Acoust. Soc. Am. **87**, 791–809.

Delgutte, B. (**1990b**). ''Two-tone rate suppression in auditory-nerve fibers: Dependence on suppressor frequency and level,'' Hear. Res. **49**, 225–246.

Dirks, D. D., Dubno, J. R., Ahlstrom, J. B., and Schaefer, A. B. (**1990a**). ''Articulation index importance and transfer functions for several speech materials,'' Asha **32**, 91.

Dirks, D. D., Dubno, J. R., and Bell, T. S. (**1990b**). ''Problems in the prediction of speech recognition among normal-hearing and hearing-impaired listeners,'' J. Acoust. Soc. Am. Suppl. 1 **88**, S32.

Dubno, J. R., and Ahlstrom, J. B. (**2001a**). ''Forward- and simultaneous-masked thresholds in bandlimited maskers in subjects with normal hearing and cochlear hearing loss,'' J. Acoust. Soc. Am. **110**, 1049–1057

Dubno, J. R., and Ahlstrom, J. B. (**2001b**). ''Psychophysical suppression measured with bandlimited noise extended below and/or above the signal: Effects of age and hearing loss,'' J. Acoust. Soc. Am. **110**, 1058–1066.

Dubno, J. R., Dirks, D. D., and Schaefer, A. B. (**1987**). ''Effects of hearing loss on utilization of short-duration spectral cues in stop consonant recognition,'' J. Acoust. Soc. Am. **81**, 1940–1947.

Dubno, J. R., and Dorman, M. F. (**1987**). ''Effects of spectral flattening on vowel recognition,'' J. Acoust. Soc. Am. **82**, 1503–1511.

Dubno, J. R., and Schaefer, A. B. (**1992**). ''Comparison of frequency selectivity and consonant recognition among hearing-impaired and masked normal-hearing listeners,'' J. Acoust. Soc. Am. **91**, 2110–2121.

Dubno, J. R., and Schaefer, A. B. (**1995**). ''Frequency selectivity and consonant recognition for hearing-impaired and normal-hearing listeners with equivalent masked thresholds,'' J. Acoust. Soc. Am. **97**, 1165–1174.

Gifford, R. H., and Bacon, S. P. (**2000**). ''Contributions of suppression and excitation to simultaneous masking: Effects of signal frequency and masker-signal frequency relation,'' J. Acoust. Soc. Am. **107**, 2188–2200.

Green, D. M. (**1993**). ''A maximum-likelihood method for estimating thresholds in a yes-no task,'' J. Acoust. Soc. Am. **93**, 2096–2105.

Hicks, M. L., and Bacon, S. P. (**1999a**). ''Psychophysical measures of auditory nonlinearities as a function of frequency in individuals with normal hearing,'' J. Acoust. Soc. Am. **105**, 326–338.

Hicks, M. L., and Bacon, S. P. (**1999b**). ''Effects of aspirin on psychophysical measures of frequency selectivity, two-tone suppression, and growth of masking,'' J. Acoust. Soc. Am. **106**, 1436–1451.

Houtgast, T. (**1974**). ''Lateral suppression in hearing: A psychophysical study on the ear's capability to preserve and enhance spectral contrasts,'' Ph.D. dissertation, Academische Pers B. V, Amsterdam.

Kewley-Port, D., Pisoni, D. B., and Studdert-Kennedy, M. (**1983**). ''Perception of static and dynamic acoustic cues to place of articulation in initial stop consonants,'' J. Acoust. Soc. Am. **73**, 1779–1793.

Lee, J., and Bacon, S. P. (**1998**). ''Psychophysical suppression as a function of signal frequency: Noise and tonal maskers,'' J. Acoust. Soc. Am. **104**, 1013–1022.

Leek, M. R., Dubno, J. R., He, N.-J., and Ahlstrom, J. B. (**2000**). ''Experience with a yes–no single-interval maximum-likelihood procedure,'' J. Acoust. Soc. Am. **107**, 2674–2684.

Mills, J. H., and Schmiedt, R. A. (**1983**). ''Frequency selectivity: Physiological and psychophysical tuning curves and suppression,'' in *Hearing Research and Theory*, edited by J. V. Tobias and E. D. Schubert (Academic, New York), Vol. 2, pp. 234–336.

Moore, B. C. J., and Glasberg, B. R. (**1983a**). ''Growth of forward masking for sinusoidal and noise maskers as a function of signal delay; implications for suppression in noise,'' J. Acoust. Soc. Am. **73**, 1249–1259.

Moore, B. C. J., and Glasberg, B. R. (**1983b**). ''Masking patterns for synthetic vowels in simultaneous and forward masking,'' J. Acoust. Soc. Am. **73**, 906–917.

Moore, B. C. J., and Glasberg, B. R. (**1986**). ''Comparisons of frequency selectivity in simultaneous and forward masking for subjects with unilateral cochlear impairments,'' J. Acoust. Soc. Am. **80**, 93–107.

Moore, B. C. J., and Vickers, D. A. (**1997**). ''The role of spread of excitation and suppression in simultaneous masking,'' J. Acoust. Soc. Am. **102**, 2284–2290.

Neff, D. L. (**1985**). ''Stimulus parameters governing confusion effects in forward masking,'' J. Acoust. Soc. Am. **78**, 1966–1976.

Oxenham, A. J., and Plack, C. J. (**1998**). ''Suppression and the upward spread of masking,'' J. Acoust. Soc. Am. **104**, 3500–3510.

Rhode, W. S., and Cooper, N. P. (**1993**). ''Two-tone suppression and distortion products on the basilar membrane in the hook region of cat and guinea pig cochleae,'' Hear. Res. **66**, 31–45.

Sachs, M. B., and Kiang, N. Y. S. (**1968**). ''Two-tone inhibition in auditory-nerve fibers,'' J. Acoust. Soc. Am. **43**, 1120–1128.

Shannon, R. V. (**1976**). ''Two-tone unmasking and suppression in a forward-masking situation,'' J. Acoust. Soc. Am. **59**, 1460–1470.

Sommers, M. S., and Gehr, S. E. (**1998**). ''Auditory suppression and frequency selectivity in older and younger adults,'' J. Acoust. Soc. Am. **103**, 1067–1074.

Thibodeau, L. M. (**1991**). ''Performance of hearing-impaired persons on auditory enhancement tasks,'' J. Acoust. Soc. Am. **89**, 2843–2850.
Turner, C. W., and Henn, C. C. (**1989**). ''The relation between vowel recognition and measures of frequency resolution,'' J. Speech Hear. Res. **32**, 49–58.
Tyler, R., and Lindblom, B. (**1982**). ''Preliminary study of simultaneous-masking and pulsation-threshold patterns of vowels,'' J. Acoust. Soc. Am. **71**, 220–224.
Van Tasell, D. J., Fabry, D. A., and Thibodeau, L. M. (**1987**). ''Vowel identification and vowel masking patterns of hearing-impaired subjects,'' J. Acoust. Soc. Am. **81**, 1586–1597.
Wightman, F., McGee, T., and Kramer, M. (**1977**). ''Factors influencing frequency selectivity in normal and hearing-impaired listeners,'' in *Psychophysics and Physiology of Hearing*, edited by E. F. Evans and J. P. Wilson (Academic, London), pp. 295–306.
Wright, B. A. (**1996**). ''Correlated individual differences in conditions used to measure psychophysical suppression and signal enhancement,'' J. Acoust. Soc. Am. **100**, 3295–3303.

Modeling of chaotic vibrations in symmetric vocal folds

Jack J. Jiang[a] and Yu Zhang
Department of Surgery, Division of Otolarynogology, Head and Neck Surgery, University of Wisconsin Medical School, 600 Highland Avenue, K4/769 Clinical Science Center, Madison, Wisconsin 53792-7375

Jennifer Stern
Department of Otolaryngology, Northwestern University Medical School, 303 East Chicago Avenue, Searle Building 12-561, Chicago, Illinois 60611-3008

(Received 24 November 2000; accepted for publication 26 June 2001)

The chaos mechanism of above-range phonation was examined in symmetrically modeled vocal folds by using the traditional two-mass model assumption. The Poincaré map technique was used to display chaotic attractors. This method provided an effective description of irregular vocal-fold movements. The power spectrum, Lyapunov exponent, and Kaplan–Yorke dimension were employed to describe chaotic vibrations in the vocal-fold model. These nonlinear dynamic analyses suggested that, for the positive Lyapunov exponent, chaotic attractors contribute to irregular vocal-fold vibrations. Descriptions of complicated irregular vibrations of the vocal fold yielded evidence of chaos. To investigate the effects of independent parameters such as subglottal pressure, coupling stiffness, and phonation neutral area, bifurcation diagrams based on the Poincaré map were discussed. The results confirmed that the dynamics of the two-mass model was strongly influenced by independent parameters. Nonlinear dynamic methods were expected to provide useful information for better understanding of irregular vocal-fold vibrations as well as of the dynamic mechanism of above-range phonation in excised larynx experimentation. [DOI: 10.1121/1.1395596]

PACS numbers: 43.70.Aj, 05.45.Ac, 05.45.Pq [AL]

I. INTRODUCTION

Chaos theory allows scientists new insights into the irregular phenomena of nature. Many complicated phenomena that were previously attributed to stochastic processes in fact displayed deterministic dynamic behaviors. The deterministic mechanism of the chaotic system has been widely applied to investigate abnormal or disordered behaviors in biological systems in fields such as neurology,[1,2] cardiology,[3,4] and laryngeal physiology.[5–10] These investigations examine the application of chaos theory to irregular vibrations of the vocal fold with the goal of achieving a better understanding of the factors that contribute to vocal abnormalities.

There exists substantial evidence that vocal-fold vibration is a highly nonlinear process.[5,6,10–14] The combined effects of nonlinear biomechanical events and aerodynamic events can produce rich irregular vibratory behaviors such as bifurcation and chaos. Clinical applications of irregularities in vocal-fold vibration have most often involved vocal-fold pathology. Nonlinear dynamic methods may potentially provide a better understanding of the irregular vocal-fold vibration observed in pathological conditions. The study of nonlinear dynamics has recently received considerable attention.

Mathematical models have helped to provide an understanding of the oscillation of the vocal folds during phonation.[6,11–24] Using fluid mechanics theory, partial differential equations can be used to describe nonlinear characteristics of vocal-fold vibration.[6,22–24] However, chaotic dynamics of nonlinear partial differential equations has not been determined. There have been no effective methods to quantitatively describe chaos in partial differential equations. For investigation of the chaotic vibrations of the vocal fold, simple models such as the two-mass model are still very important. Compared with multiple mass models,[20,21] the two-mass model is a simple yet effective way to model vocal-fold vibration, and it has been successfully used to study nonlinear oscillation of the vocal fold in the production of voice.[11–15,18,19] Many interesting phenomena such as the phase difference between the lower and the upper edge of the vocal fold, diplophonia, and other irregular vibration patterns can be modeled by this concept. Studies using the pathological two-mass model, such as the asymmetrical model, have demonstrated that some irregular vocal-fold vibrations are attributed to chaos effects.[12–14]

Previous experiments with excised larynx[25–29] have consistently demonstrated that subglottal pressure determines laryngeal phonation with the following pattern: when subglottal pressure is lower in magnitude than the phonation threshold pressure, phonation does not occur. When the subglottal pressure is above the phonation threshold pressure,[30] the larynx phonates well in a stable range. There exists a maximum subglottal pressure producing the stable, well-defined phonation called the phonation instability pressure.[27] When the subglottal pressure continues to increase and surpasses the phonation instability pressure, irregular vibrations, defined as the above-range phonation (ARP) in this paper, are produced. Although this phenomenon has been previously observed experimentally, its dynamic mechanism remains poorly described.

Chaotic vibrations characterizing models of the patho-

[a]Electronic mail: jiang@surgery.wisc.edu

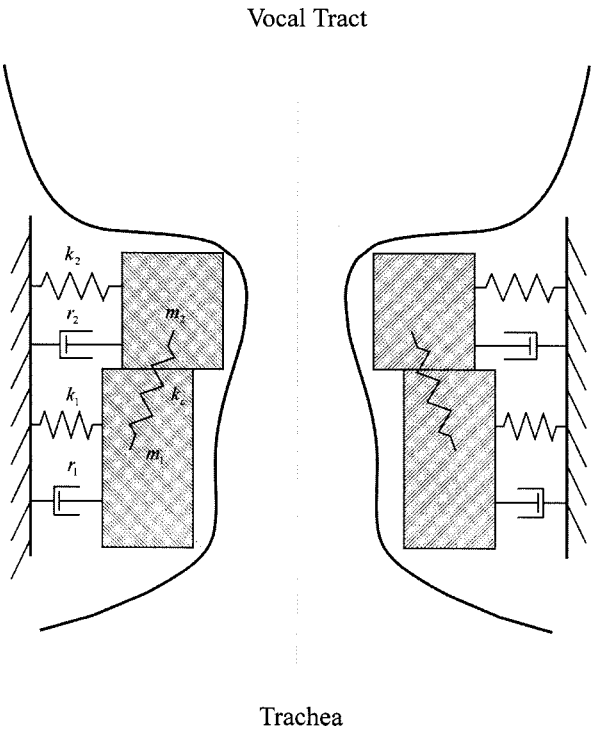

FIG. 1. The schematic diagram of the symmetric two-mass model.

logical larynx also characterize the symmetric vocal fold.[6,10,11] In this paper, the irregular ARP will be modeled as chaotic vibration of symmetric vocal folds for the positive Lyapunov exponent. Several nonlinear dynamic methods are applied to describe nonlinear vibration of vocal fold. Though previous studies have employed the next-maximal map technique,[7,11,12] we will use Poincaré map to display the projection of chaotic attractors, which provides an effective illustration of irregular vocal-fold vibrations. The power spectrum, Lyapunov exponent, and Kaplan–Yorke dimension are also used to describe chaotic vibrations in the two-mass model. Nonlinear dynamic methods demonstrate the chaos mechanism of irregular vibration in the present symmetric vocal-fold model. In order to examine the effects of independent parameters such as subglottal pressure, coupling stiffness, and phonation neutral area, the bifurcation diagrams based on the Poincaré map technique are shown and discussed. The results clearly describe the chaotic nature of above-range phonation as well as the strong dependence of the dynamics of the two-mass model on independent parameters.

II. THE TWO-MASS MODEL OF VOCAL FOLDS

Based on the Ishizaka–Flanagan model,[15] many simplified versions of the two-mass model have been proposed. We used the model of Steinecke and Herzel[12] to investigate the possible chaotic vibration of the vocal-fold system; however, the nonlinear dynamic method used in these analyses can be easily generalized to any of the other versions of the two-mass model.

The systematic diagram of the vocal-fold model is shown in Fig. 1. Deduction of the dynamics requires the following assumptions:

(1) The cubic nonlinearity of the oscillators is small enough to be neglected in the model.
(2) The interaction of the glottal flow with subglottal and supraglottal resonances is negligible. This simplification is based on the excised larynx experiments by Baer,[31] which support the assumptions that subglottal pressure is constant and supraglottal pressure is zero.
(3) The additional pressure drop at the inlet is neglected. Both the viscous losses inside the glottis and the inertia of glottal air are small. The Bernoulli flow is assumed to act only in the narrowest part of the glottis.
(4) The model is considered symmetric. The left side of the vocal fold is assumed to be the same as the right side.

According to these assumptions, the normalized motion equation of the masses can be described by

$$\begin{aligned}
&\dot{x}_1=\nu_1,\\
&\dot{\nu}_1=\frac{1}{m_1}\left(P_1 l d_1-r_1\nu_1-k_1 x_1\right.\\
&\qquad\left.-\Theta(-a_1)c_1\frac{a_1}{2l}-k_c(x_1-x_2)\right),\\
&\dot{x}_2=\nu_2,\\
&\dot{\nu}_2=\frac{1}{m_2}\left(-r_2\nu_2-k_2 x_2-\Theta(-a_2)c_2\frac{a_2}{2l}-k_c(x_2-x_1)\right),
\end{aligned}\tag{1}$$

where x_i $(i=1,2)$ is the displacement of mass m_i, a_{0i} is the phonation neutral area,[15] r_i is the damping constant, k_i is the spring constant, d_i is the thickness of mass m_i, l is the length of the glottis, c_i is the additional spring constant during collision, and k_c is the coupling constant between two masses m_1 and m_2. $a_1=a_{01}+2lx_1$, and $a_2=a_{02}+2lx_2$ denotes the lower and upper glottal areas, respectively. The driving force P_1 describing the action of the pressure in the glottis and the glottal volume flow velocity U can be formulated by the Bernoulli equation

$$P_1=P_s\left[1-\Theta(a_{\min})\left(\frac{a_{\min}}{a_1}\right)^2\right]\Theta(a_1),\tag{2}$$

and

$$U=\sqrt{\frac{2P_s}{\rho}}a_{\min}\Theta(a_{\min}),\tag{3}$$

where P_s is the subglottal pressure and

$$a_{\min}=\begin{cases}a_1, & x_1<x_2\\ a_2, & x_2\leqslant x_1\end{cases}.$$

The function $\Theta(x)$ describing the collision is approximated by

$$\Theta(x)=\begin{cases}\tanh(50x/x_0), & x>0\\ 0, & x\leqslant 0\end{cases}.\tag{4}$$

For the default parameter values $m_1=0.125$, $m_2=0.025$, $r_1=r_2=0.02$, $k_1=0.08$, $k_2=0.008$, $c_1=3k_1$, $c_2=3k_2$, $k_c=0.025$, $d_1=0.25$, $d_2=0.05$, $a_{01}=a_{02}=0.05$, $P_s=0.008$ (≈ 8 cm H_2O), $l=1.4$, and $\rho=0.001\,13$, normal vocal-fold

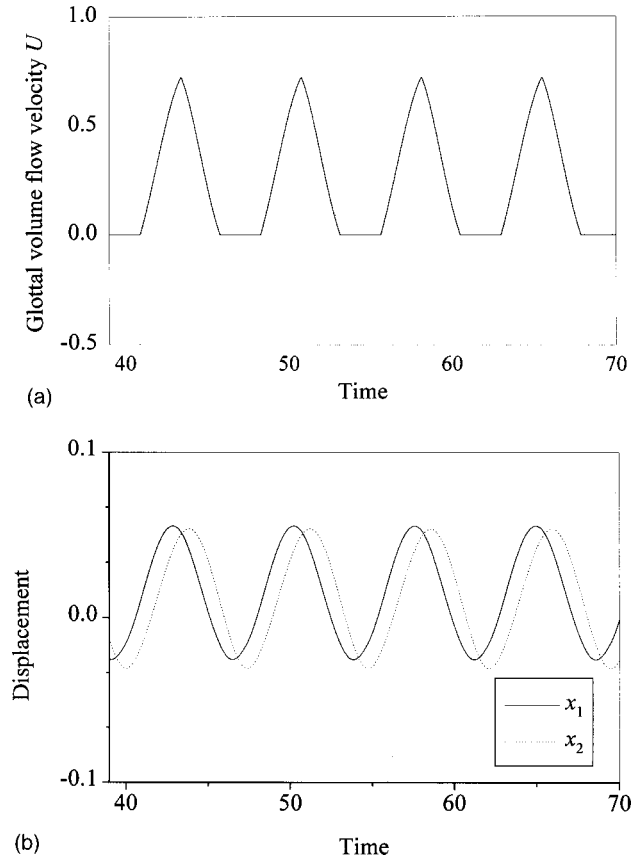

FIG. 2. Normal vocal-fold vibration. (a) The glottal volume flow velocity U; (b) the displacements of the masses m_1 and m_2.

vibration can be observed.[15] All parameters are given in units of cm, g, ms, and their corresponding combinations. The volume flow velocity U and the displacements of the mass m_1 and m_2 are shown in Fig. 2. Here, the glottal volume flow velocity U has the obvious ''valley-cut sinusoid'' shape.[32] During the open phase of the glottic cycle, the vocal folds have no contact with each other, allowing air to flow through the glottis and provide an aerodynamic driving force. This aerodynamic force gives the vocal folds a periodic driving force and sustains the oscillation of the system. However, during the closing stage of the glottic cycle, the vocal folds hit at the midpoint of the glottis and this collision force cuts off the airflow [see Fig. 2(a)]. Figure 2(b) clearly shows the phase difference between the displacement of mass 1 and mass 2. The induced phase difference between the upper and lower masses enables the energy transfer from the airflow to the vocal fold, causing oscillation to then set in.

III. NONLINEAR DYNAMIC METHODS OF THE VOCAL-FOLD MODEL

The recent development of chaos theory provides researchers with methods to describe chaos which include phase space, power spectrum, Poincaré map, dimension, Lyapunov exponents, and others. In this section, these nonlinear dynamic methods will be briefly discussed.

A. Phase space and Poincaré map

A typical mathematical model of a continuous time-evolution process is

$$\frac{d\mathbf{x}}{dt}=\mathbf{v}(\mathbf{x},\mathbf{u}), \quad \mathbf{x}\in R^n, \tag{5}$$

where $\mathbf{x}$ is an n-dimensional vector in the state space, and $\mathbf{u}$ are system parameters. In the two-mass symmetric model of the vocal fold, $n=4$ and vector $\mathbf{x}$ can be written as $\mathbf{x}=\{x_1,\nu_1,x_2,\nu_2\}^T$. With the time evolution of $\mathbf{x}$, the states give a flow $\{\Phi^t(\mathbf{x}_0)|t\in\mathbf{R}^+\}$ in n-dimensional phase space.

In order to reduce the degrees of freedom describing the trajectory, the map technique is applied to project the continuous flow. The method of next-maximum map, has been reported to sample the flow where the maximal value of the variable was recorded.[7,11,12] In this paper, a different method called Poincaré map is applied to project the flow of vocal-fold vibration. The Poincaré map for the n-dimensional flow $\Phi^t(\mathbf{x})$ is an $(n$-1)-dimensional hypersurface. Let Σ transverse to the flow $\Phi^t(\mathbf{x})$ at $\mathbf{x}\in\Sigma\subset R^n$. The Poincaré map $P:\Sigma\rightarrow\Sigma$ is defined as $P(\mathbf{x})=\Phi^T(\mathbf{x})$, where T is the time between two sections. We therefore obtain a series of points $P(\mathbf{x}),P(P(\mathbf{x})),\ldots$. Then, the dynamic types of trajectory can be classified in the Poincaré map as follows: a simple periodic orbit appears as a single fixed point; a periodic orbit with finite commensurable frequency components gives rise to discrete points; a quasiperiodic trajectory draws a closed curve; and chaotic motion is shown as scattered points with some structure.

For the two-mass model of the vocal fold, a plane such as $x_1=0$ is chosen as the Poincaré section. Generally, solving the Poincaré map involves the integration of Eq. (1) and a test of the sign changes for variable x_1. The intersection can be determined by an interpolation between the two points separated by the section $x_1=0$. However, the interpolation procedure inherently leads to an error. To correct for this problem and locate the intersection point with sufficient precision, we use the following methods suggested by Henon.[33,34] Suppose that we have the values $x_1(n\Delta t)<0$, $\nu_1(n\Delta t)$, $x_2(n\Delta t)$, $x_2(n\Delta t)$, $\nu_2(n\Delta t)$ at time $n\Delta t$, and $x_1((n+1)\Delta t)>0$, $\nu_1((n+1)\Delta t)$, $x_2((n+1)\Delta t)$, $\nu_2((n+1)\Delta t)$ at time $(n+1)\Delta t$. Clearly, the intersection must occur between these two time steps. Now, changing the role of x_1 and t, inverting the first equation, and dividing the other three equations by the first one, we have

$$\begin{aligned}
&\frac{dt}{dx_1}=\frac{1}{\nu_1}\\
&\frac{d\nu_1}{dx_1}=\frac{1}{m_1\nu_1}\left(P_1ld_1-r_1\nu_1-k_1x_1\right.\\
&\qquad\left.-\Theta(-a_1)c_1\frac{a_1}{2l}-k_c(x_1-x_2)\right)\\
&\frac{dx_2}{dx_1}=\frac{\nu_2}{\nu_1}\\
&\frac{d\nu_2}{dx_1}=\frac{1}{m_2\nu_1}\left(-r_2\nu_2-k_2x_2-\Theta(-a_2)c_2\frac{a_2}{2l}-k_c(x_2-x_1)\right).
\end{aligned} \tag{6}$$

Taking $\nu_1((n+1)\Delta t)$, $x_2((n+1)\Delta t)$, $\nu_2((n+1)\Delta t)$, and $(n+1)\Delta t$ as initial values and integrating Eq. (6) backward with the step $\Delta x_1 = -x_1((n+1)\Delta t)$, one can locate exactly the values of ν_1, x_2, ν_2 at the $x_1=0$ plane. We therefore obtain the Poincaré map from these values at $x_1=0$.

B. Power spectrum

In addition to the time-domain and phase-space analysis, the study can also be extended into the frequency domain and the tangent space. The former is known as power spectrum analysis. The latter is associated with the Lyapunov exponents. In a sense, power spectrum analysis is a simple qualitative method to judge chaos, where the spectrum of the chaotic signal is represented as a noisy broadband and the spectrums of periodic or quasiperiodic solutions are shown as discrete peaks.

The power spectrum of a scalar signal $u(t)$ can be defined in two different ways.[35] The first definition uses the square of the Fourier transform of $u(t)$ averaged over time

$$P(f) = \lim_{T\to\infty} T^{-1} \left| \int_0^T u(t) e^{-2\pi i f t} dt \right|^2. \tag{7}$$

The second and equivalent way is to define $P(f)$ as a Fourier transform of the time correlation function $R(t)$ according to the Wiener–Khinchin theorem

$$\begin{aligned} P(f) &= \int_{-\infty}^{\infty} R(t) e^{-2\pi i f t}\, dt, \\ R(\tau) &= \lim_{T\to\infty} T^{-1} \int_0^T u(t+\tau) u(t) dt. \end{aligned} \tag{8}$$

For the real-time series $u_0, u_1, \ldots, u_N$, the fast Fourier transform algorithm (FFT) can be used to obtain the power spectrum.

C. Lyapunov exponent and Kaplan–Yorke dimension

There have been many approaches for describing chaos, such as phase portrait analysis, Poincaré map, power spectrum analysis, entropy, fractal dimension, and Lyapunov exponent. Of all of these, the Lyapunov exponent has been shown to be the most effective dynamic descriptor of chaos.[36–42] The Lyapunov exponent is related to the average rate of exponential divergence or convergence of neighboring orbits in phase space. Generally, a system containing at least one positive Lyapunov exponent is defined as chaotic, while the system containing at least one positive Lyapunov exponent is defined as chaotic, while the system with no positive exponent is regular. In dissipative systems, attractors compromise two opposite trends: dissipation plays a global stabilizing or convergent role by contracting the phase space volume, while local orbital instability or divergence forces neighbor orbits to separate exponentially. Therefore, to characterize the convergent or divergent characteristics of vocal-fold systems, Lyapunov exponents should be determined. To describe the tendency of initial conditions with small perturbation, one considers the time evolution of vectors in tangent space. For $\delta\mathbf{x}\to 0$, the local perturbation can be described by the linear variational equation[36]

$$\delta\dot{\mathbf{x}}_0 = D\mathbf{v}(\Phi^t(\mathbf{x}_0))\,\delta\mathbf{x}_0, \tag{9}$$

where $D\mathbf{v}(\Phi^t(\mathbf{x}_0)) = [\partial \mathbf{v}_i / \partial \mathbf{x}_j|_{\Phi^t(x_0)}]$ is the Jacobian matrix of the vector field $\mathbf{v}$ at $\Phi^t(\mathbf{x}_0)$. The solution $\delta\mathbf{x}(t)$ of the linear variational equation (9) is obtained by

$$\delta\mathbf{x}(t) = D\Phi^t(\mathbf{x}_0)\,\delta\mathbf{x}_0, \tag{10}$$

which represents the time dependence of the perturbed vector in tangent space. $D\Phi^t(\mathbf{x}_0)$ is the $n\times n$ fundamental matrix. Considering the convergent or divergent tendency of a set of bases $\{\mathbf{e}_i\}$, $i=1,2,\ldots,n$ in tangent space, we then have the definition of Lyapunov exponent[37]

$$\lambda_i = \lim_{t\to\infty} \frac{1}{t} \log \| D\Phi^t(\mathbf{x}_0) e_i \|. \tag{11}$$

For the equilibrium point of Eq. (1), $D\Phi^t(\mathbf{x}_0)$ is a constant matrix such that the Lyapunov exponents can be reduced to the eigenvalues of the Jacobian matrix. Thus, the stability analysis of the equilibrium position[16–18] can be regarded as a special case of this method. When the chaotic vibration of the vocal fold is considered, $D\Phi^t(\mathbf{x}_0)$ and its eigenvalues vary along the entire chaotic attractor. This condition renders the stability analysis of the fixed point inapplicable. In this case, we should investigate the global stability by calculating Lyapunov exponents of a set of orthonormal directions in tangent space. In chaotic systems, each vector tends to fall along the path of most rapid growth, corresponding to the maximal Lyapunov exponent. To obtain all Lyapunov exponent spectra, the Gram–Schmidt reorthonormalization procedure should be used. Therefore, we use the method of Wolf *et al.* to calculate all Lyapunov exponents of differential equation Eq. (1).[38] For the continuous time system Eq. (5), whose solution is not a fixed point, there always is one Lyapunov exponent equal to zero. The sum of Lyapunov exponents represents the rate of expansion of a volume element, which can be determined by the divergence of the flow $\Sigma_{i=1}^n \lambda_i = \text{div}\ \mathbf{v}(\mathbf{x})$.[37–41] Thus, for four-dimensional symmetric vocal-fold model Eq. (1), the numerical results of Lyapunov exponents can be checked by the relationship

$$\sum_{i=1}^{4} \lambda_i = -\frac{r_1}{m_1} - \frac{r_2}{m_2}. \tag{12}$$

The Lyapunov exponent spectrum was proposed to provide a qualitative classification of attractors.[38–40] When all Lyapunov exponents satisfy $\lambda_i \leqslant 0$, $i=1,2,\ldots,n$, the attractor will reside within the regular invariant set such as fixed point, limit cycle, and quasiperiodic solutions. However, when $\lambda_i > 0$, one or more divergent solutions of perturbation in tangent space will be obtained. One positive Lyapunov exponent demonstrates the presence of chaos. In the four-dimensional vocal-fold model Eq. (1), there are three typical attractors with the following Lyapunov exponent spectrum $(\lambda_1,\lambda_2,\lambda_3,\lambda_4)$: fixed point (-,-,-,-), limit cycle (0,-,-,-), and chaos (+,0,-,-), respectively.

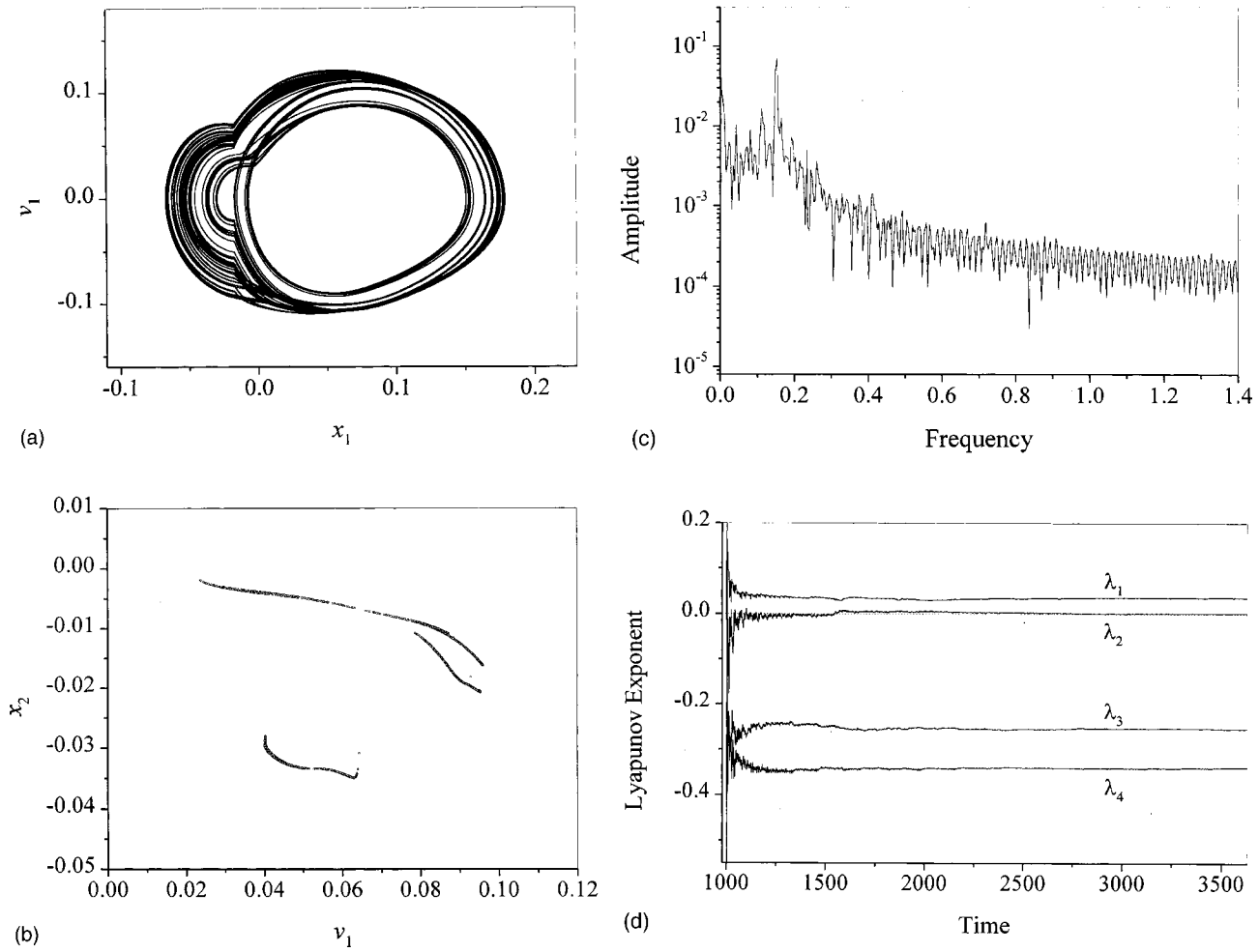

FIG. 3. Chaotic vibration of vocal-fold model where $r_1=0.02$, $r_2=0.01$, $k_c=0.09$, $a_{01}=a_{02}=0.05$, and $Ps=0.05$. (a) Phase space; (b) Poincaré section; (c) power spectrum; (d) time evolutions of Lyapunov exponents.

For the n-dimensional dynamic system Eq. (5), the Kaplan–Yorke dimension or the Lyapunov dimension[43] can be given by

$$D_L=k+\frac{\Sigma_{i=1}^{k}\lambda_i}{|\lambda_{k+1}|}, \tag{13}$$

where k satisfies the condition that

$$\sum_{i=1}^{k}\lambda_i>0$$

and

$$\sum_{i=1}^{k+1}\lambda_i<0.$$

This equation signifies that the i-dimensional volumes in the tangent space will expand if $i\leqslant k$ but will contract if $i>k$. Regarding the relationship of Kaplan–Yorke dimension to the other measures of fractal dimension, generally, there holds an inequality[44]

$$D_2\leqslant D_1\leqslant D_0\leqslant D_L, \tag{14}$$

where D_0, D_1, and D_2 denote the capacity dimension, the information dimension, and the correlation dimension, respectively. The Kaplan–Yorke dimension is an upper bound of the information dimension. The Kaplan–Yorke dimension, as well as correlation dimension, are important parameters for description of the complexity of the dynamic system. For the vocal-fold dynamic model, the Kaplan–Yorke dimension is easily calculated according to Eq. (13), unlike some studies of nonlinear dynamic analysis of the time series of speech in which correlation dimension can be obtained more conveniently.[45–48] Therefore, we will describe the complexity of the vocal-fold model by calculating Kaplan–Yorke dimension instead of correlation dimension.

IV. DISCUSSION OF NUMERICAL CALCULATIONS BASED ON THE SYMMETRIC VOCAL-FOLD MODEL

A. Chaotic vibrations of vocal-fold model

For the symmetric system Eq. (1), chaotic vibrations can be observed in certain values of model parameters. In numerical calculations, a fourth-order Runge–Kutta method is applied to numerically integrate the differential equation Eq. (1) of the symmetric vocal-fold model. The initial conditions are: $x_1(0)=0.1$, $\nu_1(0)=0$, $x_2(0)=0.1$, $\nu_2(0)=0$. We set the time step $H=0.001$, and calculate nonlinear dynamic parameters including Poincaré map, Lyapunov exponent, and Kaplan–Yorke dimension after the 1000-ms transient time.

Figure 3 shows the chaotic vibration of the vocal-fold

model where the typical values of damping and coupling constants are taken as: $r_1=0.02$, $r_2=0.01$, and $k_c=0.09$, respectively.[15] When the high subglottal pressure $Ps=0.05$ ($\approx$51 cm H_2O) is used, chaotic vibration of the model Eq. (1) results. The phase space is shown in Fig. 3(a). The chaotic attractor is shown in the Poincaré map [see Fig. 3(b)]. Figure 3(c) illustrates the power spectrum of vocal-fold vibration where some resonant frequency components are embedded in a broadband ''noisy'' spectrum. Time evolutions of Lyapunov exponents are given in Fig. 3(d), where $\lambda_1=0.036$, $\lambda_2=0$, $\lambda_3=-0.255$, and $\lambda_4=-0.341$. Because one positive Lyapunov exponent is obtained, an irregular vibration, chaos attractor is indicated. The Kaplan–Yorke dimension D_L can be obtained by Eq. (13). The result $D_L=2.14$, as well as Eq. (14), demonstrates that the vibration of the vocal-fold model behaves as the low-dimensional chaos.

We have used a high value of subglottal pressure (51 cm H_2O) to produce irregular phonation in normal vocal folds. The determination that this value is representative is based on experimental observations with larynges in which high subglottal pressure, typically above 20–30 cm H_2O, produced irregular vibration and rough sound.[25–29] In pathologic models of the vocal fold, such as the asymmetric model, the normal value of subglottal pressure, 8 cm H_2O, is sufficient for irregular phonations;[12] in the normal larynx, these irregular vibrations can be produced by phonating at a high subglottal pressure.

B. Bifurcation diagram of independent parameters

Usually, the changes in subglottal pressure, mass, tension, and geometrical size can be treated as independent parameters of the vocal-fold model because the change in these parameters is much slower than the vibration. To describe the influence of independent parameters on induction of a chaotic pattern, Lyapunov exponents and bifurcation diagrams (the Poincaré map of the state versus independent parameters) are calculated for subglottal pressure, coupling stiffness, and phonation neutral area. In bifurcation analysis, we hold independent parameters constant for 1000 ms after the 1000-ms transient time, and calculate the outputs of the vocal-fold model. Subsequently, the independent parameters increase incrementally to produce new groups of output of the vocal-fold model. In this way, the entire bifurcation diagram can be calculated.

1. Subglottal pressure and above-range phonation (ARP)

Subglottal pressure is an important independent parameter that affects the dynamics of the vocal fold. Subglottal pressure must be raised above the phonation threshold pressure for production of ''good phonation.'' However, previous experiments with excised larynx[25–29] found that when subglottal pressure increased to greatly exceed the optimal range of normal phonation, a second range was reached where vibration became very irregular and sound was rough. To give a qualitative description of this experimental phenomenon, the bifurcation diagrams of the symmetric vocal-fold model are presented.

The plots in Fig. 4 illustrate the dependence of nonlinear

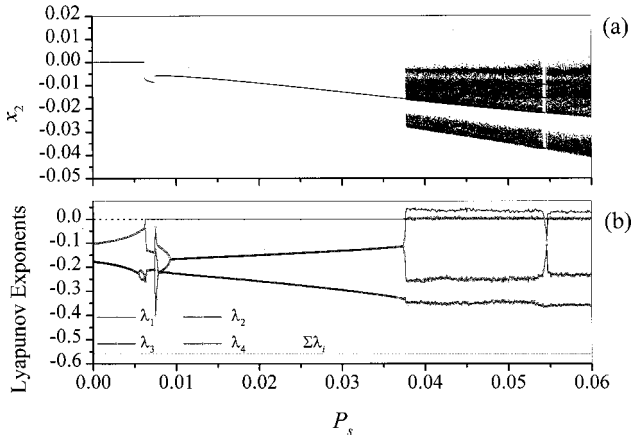

FIG. 4. The influence of the subglottal pressure Ps where $r_1=0.02$, $r_2=0.01$, and $k_c=0.09$; (a) Bifurcation diagram; (b) Lyapunov exponents where the curves correspond to λ_1, λ_2, λ_3, λ_4, and $\Sigma_{i=1}^4\lambda_i$, respectively (λ_1, —; λ_2, $-\square-$; λ_3, $-\triangle-$; λ_4, $-\triangledown-$; $\Sigma_{i=1}^4\lambda_i$, $\cdots$).

dynamic results on the subglottal pressure Ps, where the curves (a) and (b) correspond to bifurcation diagram and Lyapunov exponents, respectively. The independent parameters of the vocal-fold model are taken as: $r_1=0.02$, $r_2=0.01$, and $k_c=0.09$. Here, the bifurcation diagram shows the coexistence of the steady state, period, and chaotic attractor. These sudden changes in the bifurcation diagram are related to various bifurcations of the vocal fold.

The onset of phonation corresponds to the Hopf bifurcation of the vocal-fold system: when subglottal pressure is raised above phonation threshold pressure, the fixed point will become unstable, and a stable limit circle will set in. The conditions necessary for the oscillation threshold of subglottal pressure can be calculated by using perturbation theory.[16–18] However, when subglottal pressure continues to increase and exceeds an optimal range of normal phonation, the second range will be reached in which vibration behaves in an irregular manner. In Fig. 4, we find that when subglottal pressure is above the second threshold pressure 0.0377 [$\approx$38 cm H_2O, i.e., phonation instability pressure (PIP) defined by Jiang *et al.*[27]], the limit cycle loses its stability, and irregular vibrations can be observed. We call this second stage the above-range phonation (ARP). An abrupt transition phenomenon can be seen, which had also been reported in an excised larynx study by Jiang *et al.*[29] The present study further suggests that above-range phonation has a chaotic mechanism. The Lyapunov exponents in Fig. 4(b) confirm the chaotic nature of the irregular ARP in the symmetric vocal-fold model where the curves from the top correspond to λ_1, λ_2, λ_3, λ_4, and $\Sigma_{i=1}^4\lambda_i$, respectively. Despite the continuous increasing of Ps, $\Sigma_{i=1}^4\lambda_i$ keeps equaling the constant -0.48 predicted by Eq. (12). The result

$$\sum_{i=1}^{4}\lambda_i \approx -\frac{r_1}{m_1}-\frac{r_2}{m_2},$$

as well as the fact that there always exists a Lyapunov exponent equal to zero for an autonomous dynamic system whose solution is not a fixed point, ensures the effectiveness of numerical methods for calculating the Lyapunov exponent. The range within which the maximal Lyapunov exponent is

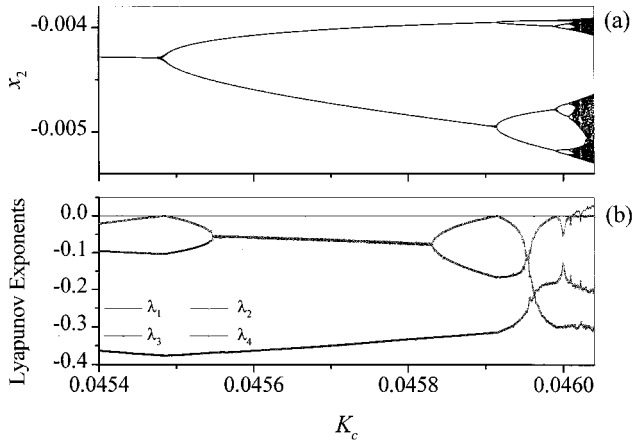

FIG. 5. The influence of the coupling constant k_c where $r_1=r_1=0.01$ and $Ps=0.008$: (a) Bifurcation diagram; (b) Lyapunov exponents where curves correspond to λ_1, λ_2, λ_3, and λ_4, respectively (λ_1, ——; λ_2, $-\square-$; λ_3, $-\triangle-$; λ_4, $-\triangledown-$).

positive defines the chaotic interval of ARP. ARP is observed only at large subglottal pressures. The chaotic model of vocal fold shows a good consistency with the phenomenon of ARP observed in excised larynx experiment.[25–29]

2. Coupling constant

Generally, irregular vibration occurs when system parameters largely deviate from the default values. Chaotic ARP can occur at high subglottal pressure; low damping and large stiffness are also considered to be possible contributions to chaotic vibration.[11,13,14]

To observe the effect of coupling constant k_c on dynamics, the bifurcation diagram and Lyapunov exponents versus k_c are displayed in Figs. 5(a) and (b), respectively, where $Ps=0.008$, and a lower damping constant $r_1=r_2=0.01$ than the default value (0.02) is used. The reduced effective damping might result from vocal-tract inertive coupling.[16] The curves from the top in Fig. 5(b) correspond to λ_1, λ_2, λ_3, and λ_4, respectively. When the coupling constant exceeds a critical value, the well-known period-doubling bifurcation will be observed in the bifurcation diagram [see Fig. 5(a)]. In this case, the limit cycle will become unstable; however, a stable period-doubling oscillation results. As the coupling constant increases, a period-doubling bifurcation scenario is illustrated. Subsequently, chaotic outputs with one positive Lyapunov exponent will appear for the large coupling constant. The dynamic changes of the vocal-fold model can be quantitatively described by the evolution of Lyapunov exponent spectrum in k_c parameter space. The parameter intervals in which $\lambda_1 \approx 0$ define regular vibrations including limit cycle and period-doubling series of period 2^n ($n=1,2,\ldots$). Among the intervals, the period-doubling bifurcation points can be determined when λ_2 approaches zero. When $k_c > 0.046\,012\ldots$, $\lambda_1 > 0$ and $\lambda_2 \approx 0$, such that the vibratory patterns of vocal fold lose the regularity and become chaotic. The k_c parameter intervals of chaos determined by the positive Lyapunov exponent coincide with the illustration in the bifurcation diagram.

The period-doubling scenario has been obtained by Herzel and Knudsen in a study applying the next-maximal map technique.[11] Our study, using a different vocal-fold model and Poincaré map technique, gives the consistent illustrations of period-doubling scenario. The presented evidence of chaos by calculating Lyapunov exponent also characterizes this study.

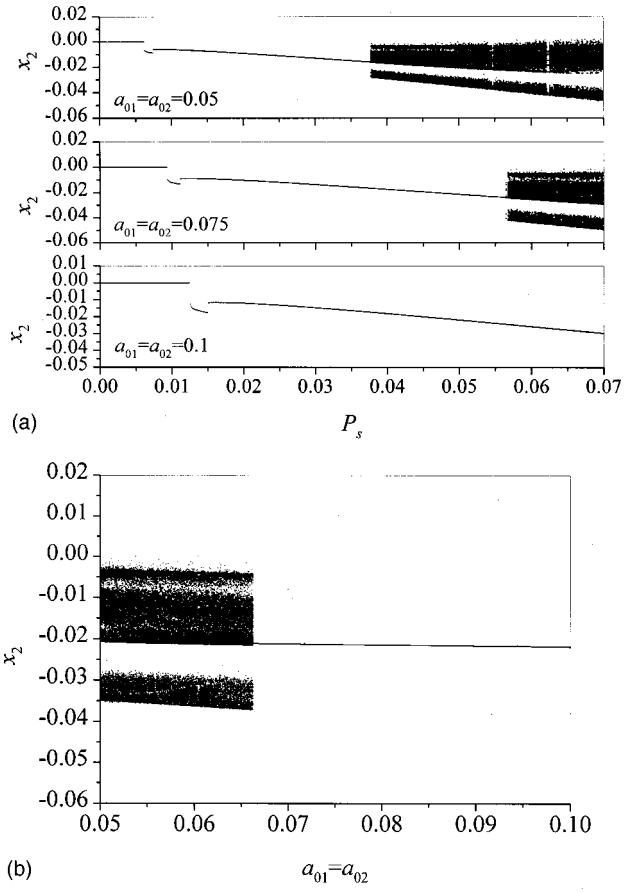

FIG. 6. The influence of phonation neutral area $a_{01}=a_{02}$: (a) The dependence of dynamical output x_2 on subglottal pressure Ps under three sizes of phonation neutral area 0.05, 0.75, and 0.1; (b) the relation between x_2 and $a_{01}=a_{02}$, where $r_1=0.02$, $r_2=0.01$, $k_c=0.09$, and $Ps=0.05$.

3. Phonation neutral area

The interaction of airflow and the glottal area causes the phonation neutral area to play an important role in determining the dynamics of the vocal fold.[15] When the initial area of the glottis increases, the nonlinear interaction between the airflow and glottal area becomes weak. It must then lead to a larger subglottal pressure that excites the periodic oscillation of the vocal fold.[12,16] Figure 6(a) shows the dependence of dynamic output on subglottal pressure Ps under three sizes of phonation neutral area: $a_{01}=a_{02}=0.05$, 0.075, and 0.1, where the parameters of the vocal-fold model are taken as $r_1=0.02$, $r_2=0.01$, and $k_c=0.09$. A larger phonation neutral area would increase the thresholds for periodic and chaotic oscillations. For a large area 0.1 of vocal fold, it is difficult to produce chaotic vibration within the range $Ps<0.07$ of subglottal pressure. To further investigate the influence of neutral area, we show the relation between the output and the phonation neutral area in Fig. 6(b), where the subglottal pressure $Ps=0.05$. For the large phonation neutral area, periodic vibration of vocal fold will oscillate steadily. However, when

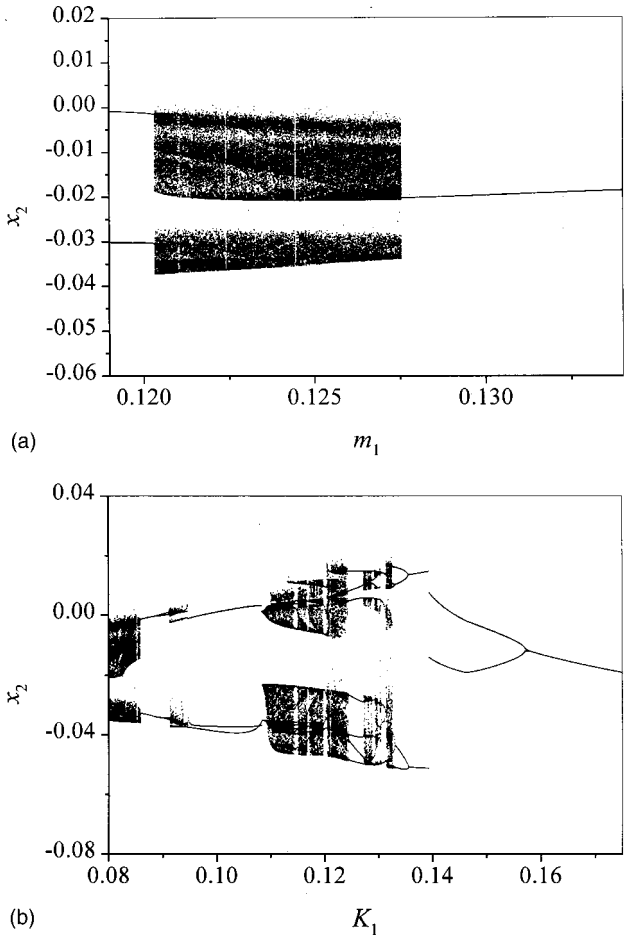

FIG. 7. Bifurcation diagrams where $r_1=0.02$, $r_2=0.01$, $k_c=0.09$, and $Ps=0.05$: (a) The output x_2 versus mass m_1; (b) x_2 versus stiffness k_1.

the phonation neutral area is decreased, the strong interaction between airflow and glottal area will decrease the threshold of irregular vocal-fold vibration and induce chaotic vibration of vocal fold.

Unlike subglottal pressure and phonation neutral area, the exact relationship of mass and stiffness of the two-mass model with the biomechanical properties of the tissue is not clear. Therefore, their influences on nonlinear dynamics of the vocal fold are combined, requiring further research. Examples of their influences are illustrated in the bifurcation diagrams of mass m_1 and stiffness k_1 [see Figs. 7(a) and (b), where $r_1=0.02$, $r_2=0.01$, $k_c=0.09$, and $Ps=0.05$). Similarly, the bifurcation diagrams display the coexistence of steady state, periodic oscillation, period-doubling, period-tripling, and chaotic vibration. In Fig. 7(b), high subglottal pressure $Ps=0.05$ will cause the vocal fold with normal stiffness $k_1=0.08$ to produce chaotic vibration; however, a larger tension $k_1>0.1575$ will produce regular vibration. Therefore, larger tension tends to increase the threshold pressure of irregular vibration, illustrating the strong dependence of vocal-fold vibration on independent parameters.

V. CONCLUSION

In this study, a chaotic mechanism of above-range phonation was suggested in the symmetric vocal-fold model. Nonlinear dynamic methods such as the Poincaré map, power spectrum analysis, Lyapunov exponent, and Kaplan–Yorke dimension, were used to investigate nonlinear vibrations of the two-mass vocal-fold model. Chaotic vibrations with positive Lyapunov exponent were obtained for the symmetric vocal-fold model. To illustrate the influence of independent parameters such as subglottal pressure, coupling constant, and phonation neutral area, bifurcation diagrams were shown. The results suggested the strong dependence of the dynamics of the two-mass model on these independent parameters. Chaotic vibrations occur with obvious changing of the independent parameter from the normal values. Nonlinear dynamic methods provided an effective analysis for describing and quantifying irregular vibration of the vocal fold, and these methods have the potential to develop into a clinical application for the analysis of irregular vocal-fold vibration.

ACKNOWLEDGMENTS

We are very grateful to Professor David G. Hanson for his valuable suggestions and input. This study was supported by NIH Grant No. R29 DC2977 from the National Institute of Deafness and other Communication Disorders.

[1] W. Lutzenberger, H. Preissl, and F. Pulvermuller, "Fractal dimension of electroencephalographic time series and underlying brain processes," Biol. Cybern. **73**, 477–482 (1995).
[2] R. Hornero, P. Espino, A. Alonso, and M. Lopez, "Estimating complexity from EEG background activity of epileptic patients," IEEE Eng. Med. Biol. Mag. **18**(6), 73–79 (1999).
[3] A. L. Goldberger, "Fractal mechanisms in the electrophysiology of the heart," IEEE Eng. Med. Biol. Mag. **11**(2), 47–52 (1992).
[4] Z. Z. Wang, X. B. Ning, Y. Zhang, and G. H. Du, "Nonlinear dynamical characteristics analysis of synchronous 12-lead EGG signals," IEEE Eng. Med. Biol. Mag. **19**(5), 110–115 (2000).
[5] I. R. Titze, R. Baken, and H. Herzel, "Evidence of chaos in vocal fold vibration," in *Vocal Fold Physiology: New Frontier in Basic Science*, edited by I. R. Titze (Singular, San Diego, 1993), pp. 143–188.
[6] D. A. Berry, H. Herzel, I. R. Titze, and K. Krischer, "Interpretation of biomechanical simulations of normal and chaotic vocal fold oscillations with empirical eigenfunctions," J. Acoust. Soc. Am. **95**, 3595–3604 (1994).
[7] H. Herzel, D. Berry, I. R. Titze, and M. Saleh, "Analysis of vocal disorders with methods from nonlinear dynamics," J. Speech Hear. Res. **37**, 1008–1019 (1994).
[8] A. Behrman and R. J. Baken, "Correlation dimension of electroglottographic data from healthy and pathologic subjects," J. Acoust. Soc. Am. **102**, 2371–2379 (1997).
[9] I. Hertrich, W. Lutzenberger, S. Spieker, and H. Ackermann, "Fractal dimension of sustained vowel productions in neurological dysphonias: An acoustic and electroglottographic analysis," J. Acoust. Soc. Am. **102**, 652–654 (1997).
[10] D. A. Berry, H. Herzel, I. R. Titze, and B. H. Story, "Bifurcations in excised larynx experiments," J. Voice **10**, 129–138 (1996).
[11] H. Herzel and C. Knudsen, "Bifurcations in a vocal fold model," Nonlinear Dyn. **7**, 53–64 (1995).
[12] I. Steinecke and H. Herzel, "Bifurcations in an asymmetric vocal-fold model," J. Acoust. Soc. Am. **97**, 1874–1884 (1995).
[13] P. Mergell, H. Herzel, and I. R. Titze, "Irregular vocal-fold vibration—High-speed observation and modeling," J. Acoust. Soc. Am. **108**, 2996–3002 (2000).
[14] P. Mergell and H. Herzel, "Modeling biphonation—the role of the vocal tract," Speech Commun. **22**, 141–154 (1997).
[15] K. Ishizaka and J. L. Flanagan, "Synthesis of voiced sounds from a two-mass model of the vocal cords," Bell Syst. Tech. J. **51**, 1233–1268 (1972).
[16] I. R. Titze, "The physics of small-amplitude oscillation of the vocal folds," J. Acoust. Soc. Am. **83**, 1536–1552 (1988).
[17] K. Ishizaka, "Equivalent lumped-mass models of vocal fold vibration," in

Vocal Fold Physiology, edited by K. N. Steven and M. Hirano (University of Tokyo, Tokyo, 1981), pp. 231–244.
[18] J. C. Lucero, ''Dynamics of the two-mass model of the vocal folds: Equilibria, bifurcations, and oscillation region,'' J. Acoust. Soc. Am. **94**, 3104–3111 (1993).
[19] X. Pelorson, A. Hirschberg, R. R. van Hassel, A. P. J. Wijnands, and Y. Auregan, ''Theoretical and experimental study of quasisteady-flow separation within the glottis during phonation. Application to a modified two-mass model,'' J. Acoust. Soc. Am. **96**, 3416–3431 (1994).
[20] D. Wong, M. R. Ito, N. B. Cox, and I. R. Titze, ''Observation of perturbations in a lumped-element model of the vocal folds with application to some pathological cases,'' J. Acoust. Soc. Am. **89**, 383–394 (1991).
[21] B. H. Story and I. R. Titze, ''Voice simulation with a body-cover model of the vocal folds,'' J. Acoust. Soc. Am. **97**, 1249–1260 (1995).
[22] J. J. Jiang, C. E. Diaz, and D. G. Hanson, ''Finite element modeling of vocal fold vibration in normal phonation and hyperfunctional dysphonia: implications for the pathogenesis of vocal nodules,'' Ann. Otol. Rhinol. Laryngol. **107**, 603–609 (1998).
[23] J. Liljencrants, ''Numerical simulations of glottal flow,'' in Proceedings of EUROSPEECH, Geneva, 1991, pp. 255–258.
[24] H. Iijima, N. Miki, and N. Nagai, ''Glottal impedance based on a finite element analysis of two-dimensional unsteady viscous flow in a static glottis,'' IEEE Trans. Signal Process. **40**, 2125–2135 (1992).
[25] J. van den Berg and T. S. Tan, ''Results of experiments with human larynxes,'' Pract. Oto-Rhino-Laryngologica **21**, 425–450 (1959).
[26] T. Baer, ''Investigation of phonation using excised larynges,'' Ph.D. dissertation, Massachusetts Institute of Technology, Boston (1975).
[27] J. J. Jiang and I. R. Titze, ''A methodological study of hemilaryngeal phonation,'' Laryngoscope **103**, 872–882 (1993).
[28] N. Isshiki, ''Mechanical and dynamic aspects of voice production as related to voice therapy and phonosurgery,'' J. Voice **12**, 125–137 (1998).
[29] J. J. Jiang, J. R. Raviv, and D. G. Hanson, ''Quantitative Measurement of Unstable Phonation,'' Presented at Voice Foundation Meeting, Philadelphia, June 2000.
[30] J. J. Jiang, T. O'Mara, D. Conley, and D. G. Hanson, ''Phonation threshold pressure measurements during phonation by airflow interruption,'' Laryngoscope **109**, 425–432 (1999).
[31] T. Baer, ''Investigation of the phonatory mechanism,'' ASHA Report **11**, 38–47 (1981).
[32] I. R. Titze, J. J. Jiang, and T. Y. Hsiao, ''Measurement of mucosal wave propagation and vertical phase difference in vocal fold vibration,'' Ann. Otol. Rhinol. Laryngol. **102**, 58–63 (1993).
[33] M. Henon, ''On the numerical computation of Poincaré maps,'' Physica D **5**, 412 (1982).
[34] X. J. Li, Y. Zhang, and G. H. Du, ''Influence of perturbations on chaotic behavior of the parabolic ray system,'' J. Acoust. Soc. Am. **105**, 2142–2148 (1999).
[35] S. N. Rasband, *Chaos Dynamics of Nonlinear Systems* (Wiley, Canada, 1989).
[36] J. Holzfuss and W. Lauterborn, ''Liapunov exponents from a time series of acoustic chaos,'' Phys. Rev. A **39**, 2146–2152 (1989).
[37] J.-P. Eckmann and D. Ruelle, ''Ergodic theory of chaos and strange attractors,'' Rev. Mod. Phys. **57**, 617 (1985).
[38] A. Wolf, J. B. Swift, H. L. Swinney, and J. A. Vastano, ''Determining Lyapunov exponents from a time series,'' Physica D **16**, 285–317 (1985).
[39] I. Shimada and T. Nagashima, ''A numerical approach to ergodic problem of dissipative dynamical system,'' Prog. Theor. Phys. **61**, 1605–1616 (1979).
[40] B.-L. Hao, *Chaos* (World Scientific, Singapore, 1984).
[41] E. Ott, T. Sauer, and J. A. Yorke, *Coping with Chaos* (Wiley, New York, 1994).
[42] Y. Zhang, W. H. Jiang, and G. H. Du, ''Chaos behavior of piezoelectric plate vibration,'' J. Acoust. Soc. Am. (in press).
[43] J. L. Kaplan and J. A. Yorke, ''Chaotic behavior of multidimensional difference equations,'' in *Functional Differential Equations and Approximation of Fixed Point*, edited by H.-O. Peitgen and H.-O. Walther, Lecture Notes in Mathematics 730 (Springer, Berlin, 1979).
[44] P. Grassberger and I. Procaccia, ''Measuring the strangeness of strange attractors,'' Physica D **183**, 189–208 (1983).
[45] A. Behrman, ''Global and local dimensions of vocal dynamics,'' J. Acoust. Soc. Am. **105**, 432–443 (1999).
[46] A. Kumar and S. K. Mullick, ''Nonlinear dynamical analysis of speech,'' J. Acoust. Soc. Am. **100**, 615 (1996).
[47] S. S. Narayanan and A. A. Alwan, ''A nonlinear dynamical systems analysis of fricative consonants,'' J. Acoust. Soc. Am. **97**, 2511 (1995).
[48] S. Q. Hu, Y. Zhang, Y. M. Hua, and G. H. Du, ''Nonlinear dynamic characteristic analysis of speech for Chinese,'' Chin. J. Acoust. **19**, 230–239 (2000).

Coherence in children's speech perception

Susan Nittrouer and Court S. Crowther
Boys Town National Research Hospital, 555 North 30th Street, Omaha, Nebraska 68131

(Received 4 October 2000; accepted for publication 26 July 2001)

Studies with adults have demonstrated that acoustic cues cohere in speech perception such that two stimuli cannot be discriminated if separate cues bias responses equally, but oppositely, in each. This study examined whether this kind of coherence exists for children's perception of speech signals, a test that first required that a contrast be found for which adults and children show similar cue weightings. Accordingly, experiment 1 demonstrated that adults, 7-, and 5-year-olds weight *F*2-onset frequency and gap duration similarly in ''spa'' versus ''sa'' decisions. In experiment 2, listeners of these same ages made ''same'' or ''not-the-same'' judgments for pairs of stimuli in an AX paradigm when only one cue differed, when the two cues were set within a stimulus to bias the phonetic percept towards the same category (relative to the other stimulus in the pair), and when the two cues were set within a stimulus to bias the phonetic percept towards different categories. Unexpectedly, adults' results contradicted earlier studies: They were able to discriminate stimuli when the two cues conflicted in how they biased phonetic percepts. Results for 7-year-olds replicated those of adults, but were not as strong. Only the results of 5-year-olds revealed the kind of perceptual coherence reported by earlier studies for adults. Thus, it is concluded that perceptual coherence for speech signals is present from an early age, and in fact listeners learn to overcome it under certain conditions. © *2001 Acoustical Society of America.* [DOI: 10.1121/1.1404974]

PACS numbers: 43.71.Es, 43.71.Ft [KRK]

I. INTRODUCTION

The acoustic signal of speech consists of isolable properties, or cues as they are commonly called. Until recently, prevailing views of speech perception have all proposed that each linguistic element (defined either as a phonemic segment or as a feature) is signaled by specific settings of one or several critical cues. Accordingly, much research in the area of speech perception focused on trying to identify what settings of which cues signal each linguistic element. To be sure, differences of opinion persisted concerning whether the cue settings that define linguistic units would prove to be invariant or not. While some investigators held hope that specific and stable settings of certain properties would be found that signal each linguistic element (e.g., Blumstein and Stevens, 1980; Kewley-Port, 1983; Stevens and Blumstein, 1978), others postulated that there are no invariants, but instead the settings of any one property that signal specific linguistic elements vary depending on the settings of other acoustic properties (e.g., Liberman, 1957; Liberman *et al.*, 1967; Mann and Repp, 1980; Studdert-Kennedy, 1983). Nonetheless, both approaches focused on understanding the relation between isolated cues and linguistic segments.

The question of *how* cues combine was never explicitly addressed in that early work. With hindsight, however, we can suggest that the assumptions underlying all that work clearly fit one of two models, what Best *et al.* (1989) called ''cue extraction'' and ''cue integration.'' The line of work searching for invariant cues to linguistic identity fits under the rubric of cue extraction: listeners extract a specific property, and make a linguistic judgment based on that property. The work attempting to describe the sets of cues that define linguistic elements adheres to notions of cue integration: listeners extract a set of cues, and then sum them to derive the most probable estimate of the linguistic element represented.

Among the predominance of studies seeking to make the connection between isolated acoustic cues and phonetic categories can be found the rare, early study interested in perceptual organization of speech signals (e.g., Broadbent and Ladefoged, 1957). More recently, however, more investigators have focused their work specifically on the question of how acoustic properties are organized in speech perception. One point on which these investigators seem to agree is that acoustic properties cohere in speech perception such that it is difficult, if not impossible, to distinguish stimuli based on the auditory qualities of separate signal components (e.g., Best *et al.*, 1989; Bregman, 1990; Remez *et al.*, 1994). A variety of results support that position. For example, duplex perception experiments demonstrate that when an isolated acoustic property (the cue) is presented to one ear and the rest of the signal (the context) is presented to the other ear, two percepts are reported: a nonspeech percept (consisting of the cue only) and a speech percept (consisting of the context plus the cue). The critical finding of these experiments is that only for the nonspeech percept can listeners describe the auditory quality of the cue (e.g., whether a transition is rising or falling). In other words, even though the cue is needed for labeling the speech percept, it remains inaccessible as a separate perceptual entity (Liberman, Isenberg, and Rackard, 1981; Mann and Liberman, 1983; Whalen and Liberman, 1987).

The question of whether acoustic properties cohere in children's speech perception, according to any principles, has been largely unaddressed, but is important for several reasons. For one, answers to this question can extend our understanding of the general nature of speech perception by informing us as to whether the perceptual organization re-

vealed in studies with adults is present from a young age (possibly birth), or is something that emerges through extensive experience with language. Also, knowing how acoustic properties cohere in children's speech perception will provide some fundamental information for studying other developmental phenomena, such as how perceptual attention changes with age and how access to phonological structure emerges. Thus, the focus of the current investigation was on whether or not acoustic properties cohere in children's speech perception such that stimuli heard as speech cannot be discriminated based on auditory qualities of the signal.

Originally we asked whether children can make discrimination decisions based on the auditory qualities of the signal as well as or better than adults when listening to speech. If children were found to discriminate stimuli better than adults based strictly on auditory qualities, our thinking went, support would be garnered for the position that the perceptual coherence of speech signals demonstrated by adults is a learned phenomenon. This position is represented by the statement of Best *et al.* (1989), ''The infant's task is to discover the phonetic coherence of phonological categories in the surrounding language by focusing attention on recurrent auditory contrasts that signal changes of meaning in that language.'' (p. 249) On the other hand, if children were found to demonstrate the same inability to discriminate stimuli based on auditory qualities that adults demonstrate, then we would suggest that such coherence is an integral aspect of speech perception, present from birth, or at least from a very young age. At the outset of this work, however, we never anticipated the possibility that the strict coherence of signal components reported for adults' speech perception might be even stronger for children. Of course, we never anticipated the possibility that adults would show anything other than strict coherence for speech signals.

From the start we did know that children's perceptual strategies for speech differ in at least one way from those of adults. Experiments have reliably shown that the weights assigned to the several cues involved in a phonetic decision can differ for children and adults. In one of the earliest demonstrations of this difference, Parnell and Amerman (1978) presented various combinations of stop-vowel syllable portions (the release burst, the burst plus aspiration noise, the burst plus aspiration and transition, the transition, the transition plus vowel) for labeling to 4- and 11-year-old children and adults. Four-year-olds labeled stops as accurately as older listeners only when syllable portions included the transitions. Thus, it seemed that children weight formant transitions more, or all other relevant cues less, than adults. Then, three studies investigating differences between young children (3 and 6 years) and adults in the use of vowel duration and syllable-final transitions in decisions of voicing for final stops all concluded that young children's decisions were based more than those of adults on the transitions, and less on vowel duration (Greenlee, 1980; Krause, 1982; Wardrip-Fruin and Peach, 1984). Most recently, experiments on labeling of syllable-initial fricatives have shown both that children weight formant transitions more and fricative-noise spectra less than adults (Nittrouer, 1992, 1996; Nittrouer and Miller, 1997a, 1997b; Nittrouer *et al.*, 2000; Nittrouer and Studdert-Kennedy, 1987). Thus, there is evidence that the relative contributions made to linguistic decisions by the various properties of the acoustic speech signal change as children get older, and gain experience with a native language. However, no study has suggested either that children attend perceptually to properties that are ignored by adults or that children ignore properties to which adults attend. Regardless of the age of the listener, linguistic decisions are based on the same sets of properties for each linguistic decision. Consequently, it was reasonable for us to ask how strongly these signal properties cohere in children's speech perception.

The approach used in this study was pioneered by Fitch *et al.* (1980). They constructed synthetic stimuli that approximated the words ''slit'' and ''split'' by varying each of two cues: the silent interval between the [s] noise and the vocalic portion (which is longer for natural split than for natural slit) and the onset frequencies of the first three formants (which are lower for split than for slit). Specifically, the silent interval varied from 8 to 144 ms in steps of 8 ms, and the transitions at the onset of the vocalic portions were appropriate for either [lɪt] or [plɪt]. Using an oddity paradigm, listeners were asked to choose the stimulus, out of three, that was different. Three conditions were included. In the ''one-cue'' condition, both stimuli in the pair had the same setting for one cue, but had different settings for the other cue. Fitch *et al.* chose to keep the silent interval constant across stimuli within a pair, and varied formant onset frequencies (rather than holding formant onset frequencies constant, and varying the silent interval). In both ''two-cue'' conditions, stimuli within a pair differed on both cues. In the ''two-cooperating-cues'' condition, the settings of both cues within a stimulus biased perception towards either slit or split, relative to settings in the other stimulus: the stimulus with the [lɪt] formant onset frequencies always had the shorter silent interval; the stimulus with the [plɪt] formant onset frequencies always had the longer silent interval. In the ''two-conflicting-cues'' condition, cues were set to oppose each other, such that they biased perception towards different categories: the stimulus with the [plɪt] formant onset frequencies always had the shorter silent interval; the stimulus with the [lɪt] formant onset frequencies always had the longer silent interval. The difference in silent interval between the two members of each pair (in the two-cue conditions) was always 24 ms, a value derived from a labeling experiment showing that 24 ms was the separation in functions for stimuli with the [lɪt] and [plɪt] formant onset frequencies (i.e., the difference in formant onset frequencies was ''worth'' 24 ms of silent interval). Results showed that all listeners were most accurate at discriminating stimuli in the two-cooperating-cues condition: these stimuli showed the familiar peak in discrimination accuracy at the category boundary. Following the two-cooperating-cues condition in discrimination accuracy was the one-cue condition, with discrimination in the two-conflicting-cues condition the poorest. Thus, even though acoustic differences between the two stimuli were identical for the cooperating- and conflicting-cues conditions, whether or not these differences facilitated or inhibited discrimination depended on whether or not cues

biased responses towards the same or different categories.[1]

Best, Morrongiello, and Robson (1981) replicated the findings reported by Fitch *et al.* (1980) using synthetic versions of ''say'' and ''stay,'' where the cues were the silent interval between the [s] noise and the vocalic portion, and the onset frequency of the first formant (*F*1): *F*1 is lower at voicing onset for burstless stay than for say. Presumably by coincidence, labeling data showed that the difference in formant frequencies was worth 24 ms of silent interval for these stimuli, just as it had been in Fitch *et al.* When stimuli were arranged as they had been by Fitch *et al.*, the same ordering of discrimination sensitivity was revealed: two cooperating cues $>$ one cue $>$ two conflicting cues. Noteworthy is the finding of both studies that discrimination for the two-conflicting-cues conditions was barely above chance performance.

Fitch *et al.* (1980) and Best *et al.* (1981) both concluded that the two acoustic properties manipulated in their experiments must be ''perceptually equivalent,'' meaning that both biased responses equally towards specific phonetic labels. Furthermore, it seemed that the auditory qualities of these properties were unavailable to the listeners; instead, listeners were obliged to hear the composite signals according to the phonetic labels they were assigned. In 1989, Best *et al.* explicitly tested four models of how acoustic properties might combine in perception: the ''cue extraction'' and ''cue integration'' models that have already been discussed, and two models of coherence termed ''auditory'' and ''phonetic'' coherence. Both of these latter models suggest that linguistic structure emerges from the speech signal due to principles that mandate signal coherence, but in the case of auditory coherence, these principles guide all of auditory perception. The notion of phonetic coherence, on the other hand, suggests that the components of the speech signal cohere specifically because they arise from the coordinated pattern of articulatory movement that produced them. According to this account, we would not expect the same kind of coherence for a signal with all the properties of speech, if it were not heard as speech. That is, if principles specifically of phonetic coherence explain why speech signals are heard as unitary percepts, then this coherence would be absent for the same signals when they are not heard as speech. According to auditory explanations, these signals should be heard in the same manner regardless of whether they are perceived as speech or nonspeech.

Best *et al.* (1989) tested this hypothesis by comparing the labeling and discrimination of speech-like stimuli when listeners heard these stimuli as music, and when they heard them as speech. Findings across the music and speech conditions led these authors to conclude that ''The results of these three experiments are inconsistent with the claim that speech perception entails the simple extraction, or the extraction and integration, of discrete information-bearing elements or cues.'' (p. 248) Instead, differences in response patterns across the two groups led the authors to conclude that only the model of phonetic coherence could explain how listeners combine separate acoustic properties to derive unitary and distinctive percepts representing linguistic categories. In particular, the listeners in the music group were unable to recover the isolated property that defined the categories, nor could they integrate this property with the rest of the spectral array to derive distinctive percepts. Thus, the general conclusion of this study was that the separate properties of the speech signal cohere according to principles that are unique to speech (i.e., phonetic coherence), and that once a signal is heard in this way, it is difficult, if not impossible, either to recover the individual properties or to have them cohere in a manner that would not be unique to speech (i.e., auditory coherence).

Only two studies have even tried to address the question of signal coherence in children's speech perception. Morrongiello *et al.* (1984) measured discrimination abilities of 5-year-olds for stimuli differing by one cue, two cooperating cues, and two conflicting cues using the same stimuli as those used by Best *et al.* (1981). Unlike the adults of Best *et al.*, children discriminated stimuli in the two-conflicting-cues condition as well as stimuli in the one-cue condition: discrimination abilities were clearly above chance in the two-conflicting-cues condition. Although those authors did not offer possible explanations for this age-related difference in results, we may speculate that it showed that children can hear the auditory qualities of a speech stimulus, independent of its phonetic label, better than adults can. Thus, we may further suggest that the phonetic coherence of speech signals demonstrated by adults may be a phenomenon that emerges as one learns a language. However, there is one caveat to this suggestion. For labeling results, children's data in the Morrongiello *et al.* study showed less separation between functions for the two *F*1-onset conditions than adults' data did in the Best *et al.* study. In other words, the difference in formant onset frequencies was worth less than 24 ms in children's perception. Nonetheless, the difference in silent interval between members of each pair was set according to adults' labeling results, at 24 ms. Therefore, the effective perceptual difference between stimuli in a pair may have been greater for children than for adults. As a result, the Morrongiello *et al.* experiment leaves unanswered the question of whether or not cues cohere in children's speech perception as they do in adults' speech perception.

Eilers *et al.* (1989) asked if infants can discriminate speech stimuli based on their auditory qualities. These investigators manipulated vowel duration and consonant periodicity as cues to voicing for utterance-final alveolar stops, and trained 9-month-old infants to perform a discrimination task. As Fitch *et al.* (1980) and Best *et al.* (1981) reported for adults, Eilers *et al.* found that infants were able to discriminate stimuli better in the two-cooperating-cues condition than in the one-cue condition.[2] As Morrongiello *et al.* (1984) reported for 5-year-olds, Eilers *et al.* found that infants were able to discriminate stimuli as well in the two-conflicting-cues condition as in the one-cue condition. Thus, it might be concluded that infants were making these discriminations based on the auditory qualities of the signal, either because they could recover individual properties of the acoustic signal or because these properties cohered according to principles of general audition. However, a couple findings of the Eilers *et al.* study encourage caution in interpretation. First, different groups of infants participated in the two-

cooperating-cues and the two-conflicting-cues conditions, even though both groups heard the same one-cue stimuli. Overall, infants in the two-cooperating-cues condition performed more accurately than infants in the two-conflicting-cues condition, even in the one-cue condition. Furthermore, adults performed the same discrimination task with the same stimuli as the infants, and they discriminated stimuli as well in the two-conflicting-cues condition as in the two-cooperating-cues condition, a result that conflicts with those of Fitch *et al.* (1980) and Best *et al.* (1981). It might be that results across studies cannot validly be compared because Eilers *et al.* used vowel–stop-consonant syllables as stimuli, whereas Fitch *et al.* and Best *et al.* used stimuli consisting of an [s] noise, followed by a silent interval and then a vocalic portion. However, it is puzzling to have different results based only on the content of the stimuli. Most likely, acoustic properties either cohere according to the principles of phonetic coherence, or they don't. There seems to be no satisfactory explanation for why results might fit this model for some stimuli, but not for others.

For the current study the decision was made to use stimuli that consisted of an [s] noise followed by a silent interval (as appropriate for a stop closure) and a vocalic portion, as Fitch *et al.* (1980) and Best *et al.* (1981) had done. Those are the studies that reported that adults cannot discriminate stimuli based on auditory qualities of the speech signals, and that was the phenomenon under investigation for children in this study. However, the exact choice of stimuli was tricky because, as described earlier, labeling experiments have shown that children and adults weight differently the acoustic properties upon which at least some linguistic decisions rest. For such contrasts, stimuli within a pair would differ by a different perceptual amount across listener age, even though they differed by the same acoustic amount. Thus, the first step of the current study had to be identifying a set of stimuli of the form ([s] noise)–(stop closure)–(vocalic portion) that adults and children label similarly. Only then could we appropriately compare discrimination by children and adults of stimuli differing by one cue, two cooperating cues, and two conflicting cues.

II. EXPERIMENT 1: LABELING

The goal of this experiment was to find a set of stimuli consisting of an [s] noise, followed by a silent interval and then a vocalic portion that children and adults label similarly. In particular, the duration of the silent interval (i.e., the gap duration) and the onset frequency of one or more formant transitions needed to serve as the cues to be manipulated if we were to retain consistency in procedures with those of Fitch *et al.* (1980) and Best *et al.* (1981). While numerous studies (reviewed in the Introduction) have demonstrated that the relative weights assigned to the various signal components for speech can change as children get older (and so gain experience with language), one study has shown that this developmental shift in weighting strategies does not occur for all phonetic contrasts. Nittrouer and Miller (1999) showed that the relative weights assigned to the noise and to formant transitions in decisions of fricative identity are similar for adults and children for /f/-vowel and /θ/-vowel syllables. Nittrouer and Miller argued that this lack of developmental change can be found for any contrasts for which the ''optimal'' strategy (i.e., the one that most effectively facilitates recovery of phonetic structure) is the one used by young children. Consequently, we were hopeful that we would find a contrast for which adults and children would show similar labeling results.

Three studies (Morrongiello *et al.*, 1984; Nittrouer, 1992; Nittrouer, Crowther, and Miller, 1998) have shown that adults and children weight differently the acoustic properties upon which ''say'' versus ''stay'' decisions rest. Therefore, those stimuli could not be used. At the same time, we wanted to avoid using ''slit'' and ''split,'' as Fitch *et al.* had used. Best *et al.* appropriately point out that the production of these syllables is complex articulatorily, and so the resulting signal is complex acoustically. The syllables ''sa'' and ''spa'' were found to meet our requirements.

A. Method

1. Participants

Three groups of listeners participated: 11 adults between the ages of 20 and 40 years; 11 children between the ages of 6 years, 11 months and 7 years, 5 months (the 7-year-olds); and eleven children between the ages of 4 years, 11 months and 5 years, 5 months (the 5-year-olds). All participants were required to pass hearing screenings of the frequencies 0.5, 1.0, 2.0, 4.0, and 6.0 kHz presented at 25 dB HL (ANSI, 1989). All participants were monolingual speakers of American English, had no histories of speech or language problems, and were free from significant early histories of otitis media, defined as six or more episodes before the age of 2 years. In addition, all children participating scored better than the 40th percentile for their age groups on the Goldman-Fristoe Test of Articulation (Goldman and Fristoe, 1986). Participating adults demonstrated a reading level of at least the 11th grade on the Wide Range Achievement Test-Revised [WRAT-R (Jastak and Wilkinson, 1984)]. In addition to these participants, two 5-year-olds and one adult participated, but their data were excluded from the final analysis because they failed to label reliably best exemplars of each category during testing (see Procedures).

2. Equipment

Testing took place in a soundproof booth. Hearing was screened with a Welch Allyn TM262 Auto Tymp tympanometer/audiometer using TDH-39 headphones. Stimuli were stored on a computer, and presented with a Data Translation 2801A digital-to-analog converter, a Frequency Devices 901-F filter, a Crown D-75 amplifier, and AKG-K141 headphones. Cartoon drawings were shown on a color-graphics monitor.

3. Stimuli

Stimuli were created with a SenSyn Laboratory Synthesizer, Version 1.1. They were synthesized at a 10-kHz sampling rate, and presented with low-pass filtering below 4.9 kHz. The [s] noise was a single-pole noise, centered at 3.8 kHz. This noise has been used extensively in labeling experi-

ments in the past, and is known to be a good exemplar of [s]. Two vocalic portions were created. Both were 270 ms long: 40-ms transitions followed by 230-ms steady-state regions. The fundamental frequency of both began at 120 Hz, and fell throughout the vocalic portion to an ending frequency of 100 Hz. For both, *F*1 started at 450 Hz and rose to a steady-state frequency of 650 Hz. *F*3 started at 2100 Hz, and rose to a steady-state frequency of 2500 Hz. *F*2 onset was either 1175 Hz (the ''high *F*2 onset,'' most appropriate for ''sa'') or 950 Hz (the ''low *F*2 onset,'' most appropriate for ''spa''). Steady-state *F*2 was 1130 Hz in both portions. Each vocalic portion was combined with the [s] noise at each of ten gap durations: 0 to 36 ms, varying in 4-ms steps. Thus, there were 20 stimuli: two *F*2 onsets × ten gap durations.

4. Procedures

The hearing screening was done first, followed by either the articulation screening (children) or the reading screening (adults). For the 5-year-olds, recorded stories about each response label (i.e., the animals they named) were presented next. ''Sa'' was a sea creature, and ''spa'' was a horse. These stories were presented both by recorded, natural speech and by synthetic speech. Thus, they served both to teach children the labels and to provide experience listening to synthetic speech. Past experience in this laboratory has shown that children older than 5 years of age do not benefit from these stories, and so 7-year-olds did not hear them. Next, the pictures to be used were introduced. These pictures were 8 × 10 in. Participants were instructed to point to the picture representing the syllable heard, and say the syllable after hearing a stimulus. The experimenter then entered the response into the computer. Two kinds of practice were provided before testing: natural tokens of sa and spa, and the best exemplars of the synthetic stimuli. The natural tokens were five samples each of sa and spa spoken by the second author. The synthetic tokens were the low *F*2 onset with the 36-ms gap (best exemplar of spa) and the high *F*2 onset with the 0-ms gap (best exemplar of sa), presented five times each. Listeners had to respond correctly to nine out of the ten practice items (for both kinds of practice) to move onto either the next practice set or the test set. Testing consisted of ten blocks of the 20 stimuli presented in random order, and children were shown cartoon drawings on the graphics monitor at the end of each block. Participants had to respond correctly to 80% of the best exemplars (i.e., those presented during practice with the synthetic stimuli) during testing for their data to be included in the final analysis. Because all participants demonstrated the ability to label these best exemplars correctly during practice, failure to do so during testing was taken as evidence of a general decrease in attention. A lack of general attention of this sort would diminish the reliability of all responses.

Labeling functions were derived for each *F*2 onset, and were the proportion of sa responses given at each level of gap duration. These proportions were transformed to probit functions (i.e., cumulative normal distributions, represented as probit scores). From these probit functions, distribution means and slopes were computed. Distribution means were the points (given in milliseconds of gap duration) at which the probabilities of sa and spa responses were equal. These values are traditionally termed the ''phoneme boundaries,'' and will be here too. Slope is given as the change in probit units per millisecond of change in gap duration. The difference in location of the two functions at the phoneme boundaries is generally taken as an index of the weight assigned to the dichotomous property (in this case, *F*2 onset), and slope is an index of the weight assigned to the continuous property (in this case, gap duration).

B. Results

Figure 1 shows the labeling functions for all three listener groups, and Tables I and II display the phoneme boundaries and slopes, respectively. As can be seen, all groups performed similarly. Two-way analyses of variance (ANOVAs), with age as the between-subjects factor and transition as the within-subjects factor, done on these data support that conclusion. The main effect of age was not significant, either for phoneme boundaries, $F(2,30)=1.14$, $p=0.333$, or for slopes, $F(2,30)=2.78$, $p=0.078$. Only the main effect of transition was significant, both for phoneme boundaries, $F(1,30)=228.27$, $p<0.001$, and for slopes, $F(1,30)=7.20$, $p=0.012$. The interaction of age × transition was not significant, either for phoneme boundaries, $F(2,30)=0.26$, $p=0.774$, or for slopes, $F(2,30)=0.24$, $p=0.789$. Therefore, adults, 7-year-olds, and 5-year-olds may be said to have weighted the transition and the gap to the same extent in making this phonetic decision, and so these stimuli met our criterion for the discrimination task to be completed in experiment 2.

III. EXPERIMENT 2: DISCRIMINATION

Once stimuli were identified that children and adults label with similar weights assigned to each acoustic property, the next step was to examine discrimination of these stimuli when they differed by only one cue, by two cooperating cues, and by two conflicting cues. Based on the work of Fitch *et al.* (1980) and Best *et al.* (1981), we anticipated that adults would show enhanced sensitivity for stimuli in the two-cooperating-cues condition and diminished sensitivity in the two-conflicting-cues condition, compared to the one-cue condition. However, the most critical condition in this experiment was the two-conflicting-cues condition: this is the one condition in which stimuli cannot be perceived according to the principles of phonetic coherence, if they are to be discriminated. Listeners must either recover the separate properties of the signal or form unique and unitary percepts with these separate properties, percepts that do not neatly correspond to phonetic categories. Because the results of earlier studies (e.g., Best *et al.*, 1981, 1989; Fitch *et al.*, 1980; Remez *et al.*, 1994) suggest that adults do not accomplish either of these perceptual maneuvers (instead forming unitary percepts according to phonetic principles), discrimination in the two-conflicting-cues condition should be poor. We should find a similar response pattern for children, if phonetic coherence is intrinsic to their speech perception.[3] Alternatively, if the phonetic coherence of speech signals found

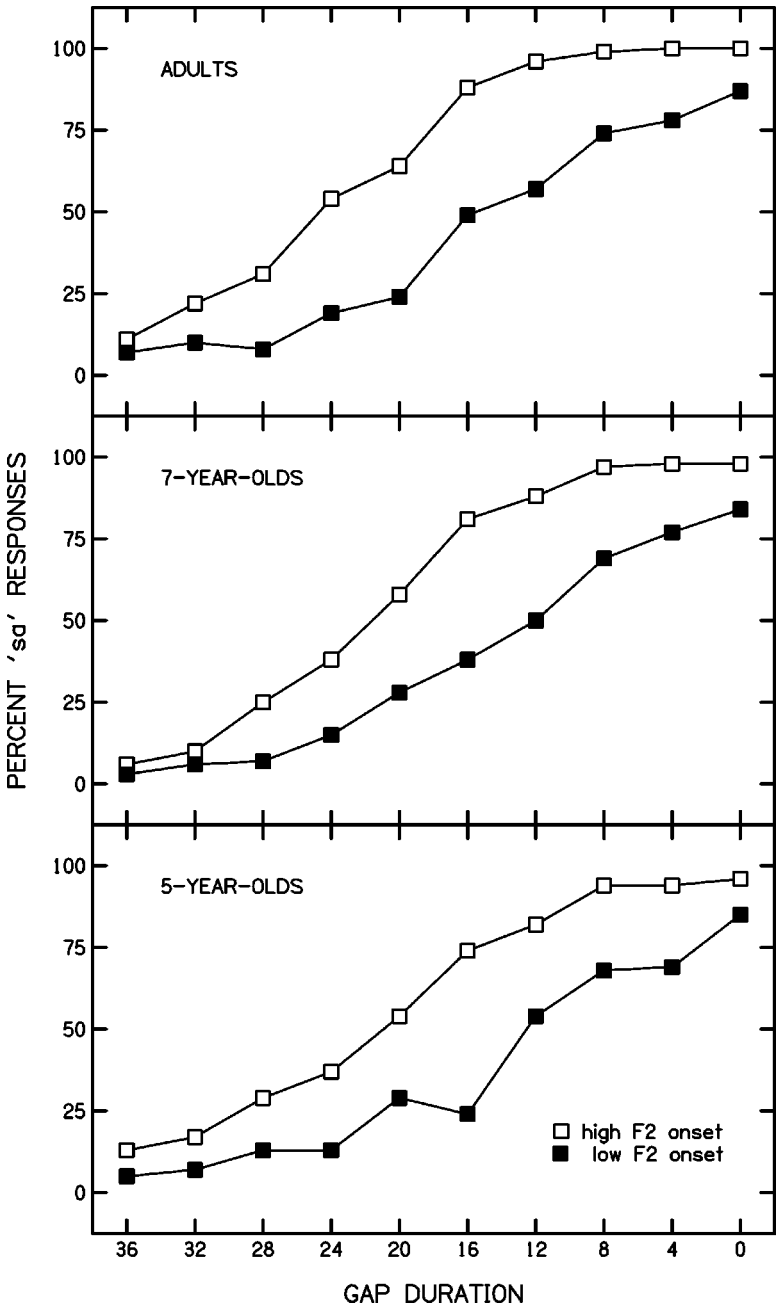

FIG. 1. Mean labeling functions for each age group from experiment 1. Open squares represent results for the high-*F*2 onset condition, and filled squares represent results for the low-*F*2 onset condition.

for adults is a learned phenomenon, then we could find a different pattern of response across the three conditions for children. In particular, we might expect children to demonstrate enhanced sensitivity to signal differences in both two-cue conditions, regardless of whether the cues cooperate or conflict in terms of the category they signal. That is, these children may not have had sufficient experience with speech signals to have discovered phonetic coherence.

TABLE I. Mean phoneme boundaries in ms of gap duration for each age group (with standard deviations in parentheses), for the high *F*2 onset and the low *F*2 onset. Number of participants in each group is given in italics.

	Adults *11*	7-year-olds *11*	5-year-olds *11*
High *F*2 onset	24.8 (3.4)	22.1 (5.1)	22.0 (4.3)
Low *F*2 onset	14.4 (5.3)	12.7 (6.8)	11.6 (4.0)

TABLE II. Mean slopes (in probit units per ms of gap duration) for each age group (with standard deviations in parentheses), for the high *F*2 onset and the low *F*2 onset. Number of participants in each group is given in italics.

	Adults *11*	7-year-olds *11*	5-year-olds *11*
High *F*2 onset	0.14 (0.04)	0.16 (0.05)	0.11 (0.05)
Low *F*2 onset	0.11 (0.06)	0.12 (0.05)	0.09 (0.04)

A. Method

1. Participants

Thirteen adults, and 13 children of each of the ages of 7- and 5 years participated in this experiment. All participants met the same criteria as those described for participants in the first experiment. Four additional 5-year-olds attempted the task, but were unable to perform this discrimination task with natural tokens of spa and sa, and eight additional 5-year-olds and one 7-year-old were unable to discriminate the most different stimuli to be used in any of the three test conditions (see Procedures).

2. Equipment and stimuli

The same equipment was used as in experiment 1. The stimuli used in the first experiment were used in this experiment, but they were presented in pairs in an AX format where A was a constant standard. Three sorts of stimulus pairings were used: those in which stimuli differed by only one cue (the one-cue condition), those in which stimuli differed by two cues such that the settings of both cues biased responses towards the same category label (the two-cooperating-cues condition), and those in which stimuli differed by two cues such that the settings of both cues biased responses towards different category labels (the two-conflicting-cues condition). The ''standard'' stimulus (i.e., the one that remained constant across pairs within any one condition) always had a 36-ms gap. The ''comparison'' stimuli (i.e., those that varied across pairs within any one condition) had gaps varying between 0 and 36 ms. Of course, we could have arranged stimuli so that the standard had a 0-ms gap and the comparisons had longer gaps. However, listeners in experiment 1 were slightly more consistent labeling stimuli with the 36-ms gap and the high *F*2 onset as spa than they were labeling stimuli with the 0-ms gap and the low *F*2 onset as sa. (See Fig. 1: the open squares at the 36-ms gap are closer to 0% than the filled squares at the 0-ms gap are to 100%.) Thus, using stimuli with 36-ms gaps as the standards ensured that the standard was a good exemplar of one of the categories (in this case spa) in every condition, even when cues conflicted. Once the decision was made to use this end of the continuum for standard stimuli, the selection of stimuli (standard and comparisons) for each condition was mandated by the desired arrangement of cues across stimuli within the condition.

In the one-cue condition, all stimuli (standard and comparisons) had the low *F*2 onset, as appropriate for spa; only the duration of the gap varied. In this way, the standard was the clearest exemplar of spa possible. The first stimulus in the pair (the standard) always had the 36-ms gap, and it was followed by a stimulus having another gap duration. Having formant onset frequency remain constant for stimuli within a pair, and the gap duration vary, was one change from the procedures of Fitch *et al.* (1980) and of Best *et al.* (1981). In their one-cue conditions, gap duration remained the same for stimuli within a pair, and formant onset frequencies varied. However, those investigators provided no reason, either procedural or theoretical, for why they did it this way (or why it might matter). Because we wanted our standard to remain constant across pairs, gap duration had to vary. We had no reason, and still do not, to suspect that the arrangement of cues (i.e., which one remains constant and which one varies) would affect listeners' abilities to discriminate speech stimuli based on the auditory qualities of the signals. In any event, if the phenomenon previously reported (that adults have extremely limited access to acoustic properties during speech perception) can only be observed for specific arrangements of cues, then the conclusions reached by those studies need to be reconsidered.

In the two-cooperating-cues condition, the standard had the low *F*2 onset, so both gap-(36 ms) and *F*2 onset biased responses towards spa. All comparison stimuli had the high *F*2 onset, so both gap and *F*2 onset biased responses towards sa (compared to the standard). In the two-conflicting-cues condition, the standard needed to have the high *F*2 onset, to bias responses towards sa. The comparison stimuli in this condition had low *F*2 onsets. Thus, gap and *F*2 onset conflicted in terms of which category they biased responses toward.

3. Procedures

Five-year-olds were provided with a preliminary task that 7-year-olds and adults did not have. Because of this extra task, and their generally shorter attention spans, 5-year-olds were tested over 2 days. Seven-year-olds and adults participated in just one session.

The screening measures were administered first. Next, 5-year-olds were provided with practice labeling pictures as ''same'' or ''not-the-same.''[4] These were hand-drawn pictures of pairs of simple objects, such as flowers and cars. Five of the pictures showed the same object twice, and five showed two different objects. Normally developing children understand the concept of same by age 5 years; this extra practice simply helped familiarize children with the task.

The procedure used here differed from that of Fitch *et al.* (1980) and Best *et al.* (1981), where the stimuli within a pair differed acoustically by the same amount across pairs. We made the decision to use a fixed standard with varied step sizes between stimuli because the method of constant difference (used by Fitch *et al.* and Best *et al.*) leads to the situation where none of the pairs of stimuli has very large acoustic differences between members. As a result, the discriminations to be made are all fairly difficult perceptually, and young children do not tolerate long strings of difficult discriminations. The procedure of using a fixed standard should minimize memory load and decrease stimulus uncertainty, both goals generally viewed as desirable in work with children.

For all discrimination tasks, the response was to point to a picture of two red squares and say ''same'' if the stimuli within a pair were judged to be the same, and to point to a picture of a red square and a black triangle and say ''not-the-same'' if the stimuli within a pair were judged to be different. All participants received practice with this procedure using recorded, natural tokens of sa and spa (five same trials and five different trials) before any testing started at all. If a participant was unable to recognize four of the five ''different'' trials as different (while recognizing that all same trials

TABLE III. Numbers of participants of each age who were unable to hear the most different comparison stimulus as different from the standard in each condition. Total numbers of participants are given in italics.

	Adults *13*	7-year-olds *13*	5-year-olds *13*
Two cooperating cues	0	0	2
One cue	4	2	3
Two conflicting cues	3	3	5

were the same), this natural practice set was presented a second time. If the participant was still unable to meet the criterion, the participant was dismissed. Then, as each stimulus condition was introduced, practice was provided with the most acoustically different stimuli in that condition. Again, five same trials (with both members of the pair being the standard stimulus) and five different trials (with the standard and the most acoustically different stimulus) were provided. If a participant was unable to recognize four of the five different trials as different (while recognizing that all same practice trials were the same), the practice set was presented a second time. If the participant was still unable to meet the criterion, the participant was not tested in that condition. For testing, the standard was paired with all comparison stimuli in that condition (including itself) ten times each (i.e., ten blocks of ten pairs). The order of presentation of conditions was randomized across participants. During testing, participants needed to perform at 80% accuracy for the most different stimuli. Data were discarded for any participant who did not attain this level of performance. Discrimination functions were derived for each condition, and are the percentage of not-the-same responses at each level of gap duration.

B. Results

Table III shows the numbers of participants of each age who were unable to meet the practice or test criteria in each condition, out of the 13 participants of each age who could do the task in at least one condition. Two findings are noteworthy. First, out of all participants, only two 5-year-olds were unable to meet the criteria for the two-cooperating-cues condition. In other words, if a listener was able to discriminate stimuli in only one condition, it was likely to be the two-cooperating-cues condition. Second, there was no participant who was able to do only the two-conflicting-cues condition.

Figure 2 displays the percentage of not-the-same responses at each level of gap duration, for each condition. Table IV lists mean percentages of not-the-same responses for each condition. For each age group, matched *t*-tests were done comparing the percentages of not-the-same responses for the one-cue versus two-cooperating-cues conditions, the two-conflicting-cues versus two-cooperating-cues conditions, and the one-cue versus two-conflicting-cues conditions. For these statistical analyses, missing data were replaced using generally accepted procedures. If a participant was unable to meet the practice or the test criterion in just one condition, that missing value was estimated by regressing that variable on the listener's other two measures (using regression equations derived from the group as a whole). This method of replacing missing data is fairly standard, and did not affect the overall outcome of the study because the estimated values did not change relative percentages across conditions within groups, the result of most interest. If a participant was unable to meet the practice or test criterion in two conditions, those missing values were replaced with the group means for each of those conditions. Again, this method is generally accepted and should not affect overall outcome. The computed *t*-ratios and associated *p*-values are given in Table V.

Looking at adults' responses, the first trend we notice in Fig. 2 and from the percentages provided in Table IV is that adults were much better at discriminating pairs of stimuli in the two-conflicting-cues condition than would have been predicted from Fitch *et al.* (1980) and Best *et al.* (1981): Adults' discrimination was better in the two-conflicting-cues condition than in the one-cue condition. In fact, adults in this experiment discriminated stimulus pairs more readily whenever two cues distinguished the members of the pairs than when only one cue did, regardless of whether the two cues cooperated or conflicted in terms of the category they signaled. This result is commensurate with that of Eilers *et al.* (1989). Looking at the statistical results in Table V we see that the percentage of stimulus pairs discriminated by adults differed across all three conditions, as indicated by the finding that all three *t*-tests were significant. Thus, for adults, the pattern of response was clearly two cooperating cues $>$ two conflicting cues $>$ one cue.

Results for 7-year-olds mirror results of adults in that the order of discrimination functions is similar (two cooperating cues $>$ two conflicting cues $>$ one cue), although the trend is not as strong. In particular, discrimination in the one-cue condition was not as poor as that of adults: the function for the one-cue condition is closer to those of the other two functions than is the case for adults. For 7-year-olds, the only *t*-test to reach statistical significance was the one-cue versus two-cooperating-cues conditions, the best- and the poorest discriminated stimuli.

For 5-year-olds, the order of discrimination functions is different from that of the two older groups: Performance was similar for the two-cooperating-cues and one-cue conditions, but poorer for the two-conflicting-cues condition. Looking at the statistical results in Table V, both *t*-tests involving the two-conflicting-cues condition were statistically significant, indicating that 5-year-olds really were worse at discriminating these stimuli than the stimuli in the other two conditions. The one-cue versus two-cooperating-cues *t*-test was not statistically significant.[5]

Although differences among age groups in discrimination for individual conditions was not the main focus of this study, we did perform ANOVAs on percentages of not-the-same responses for each condition, with age as the factor. Pairwise *t*-tests were also computed. Results of these analyses are shown in Table VI, and indicate that a significant effect of age was found for all conditions. The pairwise *t*-tests confirm impressions from Fig. 2 and Table IV: For the one-cue condition, 7-year-olds showed greater sensitivity to

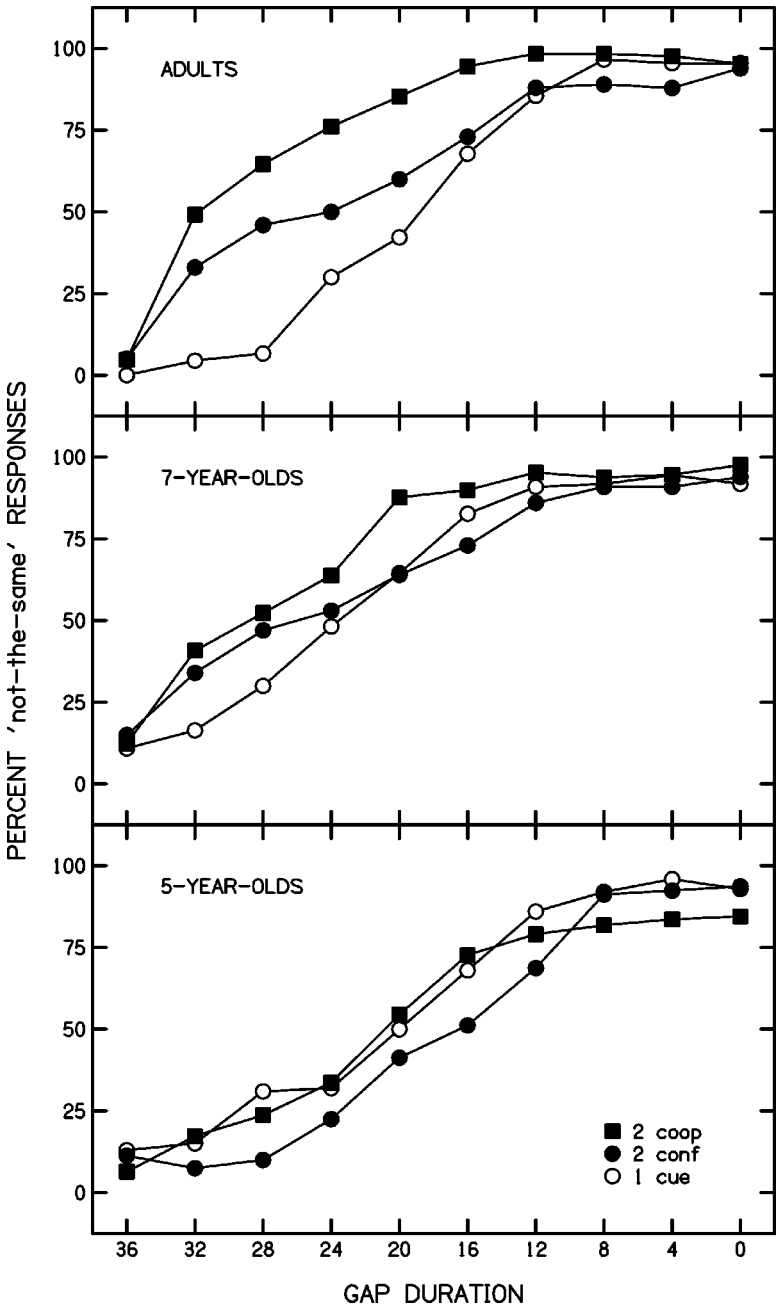

FIG. 2. Mean discrimination functions for each age group from experiment 2. Filled squares represent results for the two-cooperating-cues condition; filled circles represent results for the two-conflicting-cues condition; open circles represent results for the one-cue condition.

TABLE IV. Mean percentages of ''not-the-same'' responses for each age group (with standard deviations in parentheses), for all three conditions. Number of participants in each group included in computations is given in italics.

	Adults	7-year-olds	5-year-olds
	13	*13*	*11*
Two cooperating cues	76.5 (13.4)	72.8 (10.4)	60.9 (15.9)
	12	*12*	*10*
One cue	52.4 (7.8)	61.9 (9.1)	57.6 (10.8)
	12	*12*	*8*
Two conflicting cues	62.6 (12.6)	64.3 (18.1)	49.0 (9.5)

differences between stimuli than adults, but adults and 5-year-olds showed similar sensitivities. For both conditions involving two cues, 5-year-olds showed poorer sensitivities than listeners in the other two groups.

IV. DISCUSSION

This study was originally undertaken to examine whether children would show the same pattern of perceptual coherence for speech that adults showed in studies by Fitch *et al.* (1980) and Best *et al.* (1981). In those studies, adults demonstrated enhanced discrimination for pairs of stimuli in which two cues cooperated in terms of which category they signaled, but a reduction in discriminability when those same cues conflicted in terms of which category they signaled. To use the notation of Best *et al.*, the pattern of results found in

TABLE V. *t*-ratios and *p*-values (given in parentheses) for each matched *t*-test, for each age group. Degrees of freedom are 12 for each group.

	Adults	7-year-olds	5-year-olds
One/ two cooperating	−5.70 (<0.001)	−3.75 (0.003)	−0.72 (0.484)
Two conflicting/ two cooperating	−3.29 (0.007)	−1.77 (0.102)	−3.06 (0.010)
One/ two conflicting	−3.27 (0.007)	−0.57 (0.576)	3.58 (0.004)

TABLE VI. *F*-ratios and *p*-values (given in parentheses) for overall tests of age effect for each condition given in the first row, with Bonferroni significance level of each *t*-test in subsequent rows. Degrees of freedom are 2,36 for the *F*-ratios, and 36 for each *t*-test.

	One cue	Two cooperating	Two conflicting
F-ratio	4.07 (0.026)	5.16 (0.011)	5.53 (0.008)
Adults vs 7 years	0.05	···	···
Adults vs 5 years	···	0.05	0.05
7 vs 5 years	···	0.10	0.05

those studies was two cooperating cues > one cue > two conflicting cues. Unlike those reports, however, the adults in the present study showed enhanced discrimination abilities any time two cues differed between members of the pair, regardless of whether cues were set to cooperate or conflict. Using Best *et al.*'s notation again, the pattern of results was two cooperating cues > two conflicting cues > one cue. This finding indicates that adults could either recover the separate acoustic properties and do a simple summation to obtain a measure of auditory difference, or could derive unitary, distinctive percepts of the stimuli that were not tied to linguistic labels. Deciding between these two possibilities is beyond the scope of this study, but in either case, adults were clearly not obliged to hear these signals strictly according to the principles of phonetic coherence.

It is, of course, tempting to suggest that our conclusions differ from those of Fitch *et al.* (1980) and Best *et al.* (1981) because our procedures differed such that standard stimulus and most comparison stimuli varied more in how acoustically different they were from each other than the two stimuli in any one triad of those earlier experiments. However, the major difference between results of this study and that of both Fitch *et al.* and Best *et al.* (that adults discriminated between stimuli in the two-conflicting-cues condition) was found when the standard and comparison did not differ much in gap duration. In other words, this result was not obtained only for large interstimulus differences. Besides, our results largely replicate those of Eilers *et al.* (1989). Of course, some aspects of the procedures used by Eilers *et al.* differed from those of Fitch *et al.*, of Best *et al.*, and of this study. For example, Eilers *et al.* used a repeating background stimulus that was interrupted for brief periods by comparison stimuli. Nonetheless, both that study and this study found that adults' discrimination was better when two cues differed across stimuli than when only one cue did, regardless of whether the two cues cooperated or conflicted regarding which linguistic category they signaled. Apparently, the procedures of this study and of Eilers *et al.* were simply more sensitive than those of Fitch *et al.* and Best *et al.*

At the same time, adults' discrimination of stimuli in the two-conflicting-cues condition was not as good as in the two-cooperating-cues condition in this study. The proportions of not-the-same responses given to stimuli in the two-conflicting-cues condition were not as high as those in the two-cooperating-cues condition. Also, the shapes of the discrimination functions were different for the two-cooperating-cues and the two-conflicting-cues conditions. Adults were better than expected at judging that two stimuli in the two-conflicting-cues condition were probably not the same when standard and comparison differed in gap durations by only a small amount: The function is never close to ''0% not-the-same responses'' (except of course when the stimuli are physically the same), as it was in the one-cue condition. However, adults never attained the same level of accuracy in judging that stimuli were different from each other in the two-conflicting-cues condition that they attained in the two-cooperating-cues condition: Even at the shortest gap durations (0 to 16 ms), where the largest differences between standard and comparisons existed, adults did not discriminate comparison stimuli from the standard 100% of the time in the two-conflicting-cues condition.

Results for 7-year-olds mirror those of adults, but differences across conditions were not as well-defined. The pattern of results was two cooperating cues > two conflicting cues > one cue, as it had been for adults. However, only the *t*-test for the one-cue versus two-cooperating-cues conditions reached statistical significance. Failure to find a significant difference between the one-cue and the two-conflicting-cues conditions (as was found for adults' data) probably reflects two facts: variability in discrimination performance was high for 7-year-olds in the two-conflicting-cues condition, and the mean function for 7-year-olds in the one-cue condition was at a longer gap duration than that of adults. In other words, a large part of the reason for the difference in statistical findings for 7-year-olds and adults is that 7-year-olds showed *better* discrimination in the one-cue condition, not that they showed poorer discrimination in the two-conflicting-cues condition. The variability in discrimination performance for the two-conflicting-cues condition can probably be offered as the major reason that a significant difference was not found between the two-cooperating-cues and the two-conflicting-cues conditions.

Five-year-olds were the one group that performed as predicted based on Fitch *et al.* (1980) and Best *et al.* (1981), at least with regard to the finding that discrimination was hindered when the two acoustic properties differed across stimuli in terms of which linguistic category they signaled. Unlike the adults in those studies, however, 5-year-olds did not discriminate stimuli any better when the two acoustic properties covaried appropriately in terms of which linguistic category they signaled than when only one property varied across stimuli. As a result, it might be suggested that there

was no coherence of signal components for 5-year-olds, that instead decisions were based solely on gap duration. However, results from the labeling experiment contradict that suggestion: the separation between labeling functions depending on *F*2 onset was exactly the same for 5-year-olds as it was for adults and 7-year-olds, indicating that these children were sensitive to and used both the *F*2-onset cue with the gap-duration cue. Thus we suggest that, in fact, 5-year-olds categorized stimuli, and made their discrimination judgments strictly based on those categories.

It might also be suggested that 5-year-olds were simply poor at discriminating stimuli, perhaps due to general difficulty with the task. However, there is no evidence of that for the 5-year-olds included in the analyses for each condition: Their discrimination thresholds were not at particularly brief gap durations (i.e., far from the gap duration of the standard), and variability was not much greater for 5-year-olds in any condition than it was for the other groups. In sum, we have every reason to believe that these 5-year-olds were discriminating these stimuli with no particular difficulty.

What then are we to conclude about how acoustic properties are integrated in children's speech perception? We suggest that speech perception from a very young age promotes coherence of signal properties. Apparently, it is only with experience that listeners are able to discriminate stimuli in which acoustic properties do not covary together to specify linguistic categories, and so come to discriminate pairs of stimuli that receive the same category labels. In other words, human listeners learn to overcome the coherence of individual cues that normally characterizes speech perception to make the discrimination judgments asked of them in laboratory experiments. Our suggestion that none of the general (i.e., non-speech-specific) principles of auditory organization investigated largely by Bregman and colleagues (Bregman, 1990), and summarized by Remez *et al.* (1994), would explain the signal coherence observed for 5-year-olds' responses is based on the finding that the adults in this study performed better than expected for the two-conflicting-cues condition. From that we conclude that adults were able either to recover the separate acoustic properties or to derive unitary percepts that did not depend on phonetic coherence. In other words, it is possible that the adults were using one of these general-purpose processing strategies. The response patterns of 5-year-olds across conditions did not resemble those of adults, and so we conclude that the perceptual coherence observed in their data was based on different principles, and the principles of phonetic coherence seem the best candidates. Again, principles of phonetic coherence suggest that signal properties cohere when they arise from the same articulatory event. Children must be attentive to these events because they need to recover information that allows them to learn how to move their own vocal tracts in order to produce the sounds of their native language.

The finding that 5-year-olds actually demonstrated evidence of stronger signal coherence than older listeners has implications not only for developmental theories of speech perception, but for general theories of perceptual organization, as well. One view of perceptual coherence holds that multiple attributes come to be perceived as a group following experience with systematic covariation, and this account has been used to explain the role of multiple cues in speech perception (e.g., Holt, Lotto, and Kluender, 2001; Kluender *et al.*, 1998). Earlier descriptions of phonetic coherence made a distinction between coherence in the perception of speech signals and coherence in the perception of other signals largely by suggesting that covariation of signal attributes for speech is specifically a consequence of articulatory movement. Nonetheless, the suggestion has commonly been that phonetic coherence results from extended experience with covariation among acoustic properties (again, see Best *et al.*, 1989). In this experiment, however, the greatest evidence of coherence for these speech signals was demonstrated by the least-experienced listeners. The more experienced listeners in fact showed evidence of having learned how to separate components of the signal.

In summary, we found evidence of strong coherence of separate acoustic cues in the speech perception of young children. With hindsight, perhaps this finding should not have come as a surprise. An important developmental task facing young children is learning how to produce the articulatory gestures required of their native languages, and so those gestures are extremely relevant ecologically. Learning to strip off the individual acoustic properties (which on their own are ecologically irrelevant) is a perceptual skill that may only be acquired later. Thus, children do not discover phonetic coherence; instead, they learn to overcome it when necessary.

ACKNOWLEDGMENTS

This work was supported by research Grant No. R01 DC 00633 from the National Institute on Deafness and Other Communication Disorders to the first author. We thank Donna L. Neff for help in the design of the task in experiment 2, and we are grateful to Donal G. Sinex, Michael Studdert-Kennedy, and Keith R. Kluender for comments on earlier drafts.

[1]It should be borne in mind that whether cues within a stimulus are described as ''cooperating'' or ''conflicting'' is only meaningful in relation to how cues were set for the other stimulus in the triad. For example, in the two-cooperating-cues condition, stimuli with [lit] formant onset frequencies sometimes had silent intervals much longer than would be found for [slit] in natural speech. However, in this condition, these stimuli always had the shorter interval of the two, and so cues are described as cooperating. As another example, in the two-conflicting-cues condition, stimuli with [plit] formant onset frequencies could have silent intervals that would very likely be found for [split] in natural speech. Nonetheless, as long as these stimuli had the shorter interval of the two in the pair, the cues are described as conflicting. Thus, the terms ''cooperating cues'' and ''conflicting cues'' have precise definitions in this context.

[2]Eilers *et al.* (1989) actually included two one-cue conditions by having stimuli in a pair differ only on consonant periodicity or only on vowel duration. However, some infants performed near chance in the one-cue condition where stimuli differed on consonant periodicity, and so we report here only on the one-cue condition where stimuli differed on vowel duration.

[3]Of course, finding similar response patterns for adults and children in this study might indicate something other than that phonetic coherence for speech signals is innate. It could indicate that children had acquired the perceptual strategies of adults by the age of 5 years. However, concern about this alternative explanation would only arise if adults and children were found to respond similarly.

[4]The verbal label not-the-same was used instead of different because the

notion of two items being different is more complex than simply recognizing that two items are not the same. Consequently the youngest children might have difficulty with it. For consistency, listeners in all age groups used the labels same and not-the-same. Morrongiello *et al.* (1984) used the same procedure.

[5]Because only eight 5-year-olds could do this discrimination task in all three conditions, these *t*-tests were also conducted with just those eight children. In that case, no *t*-test reached statistical significance, although the percentage of not-the-same judgments showed the same trend as for the full group of 13: for these eight 5-year-olds, the percentages of not-the-same responses were 57.8 for the two-cooperating-cues condition, 55.4 for the one-cue condition, and 49.0 for the two-conflicting-cues condition.

ANSI (**1989**). ''Specifications for Audiometers'' (American National Standards Institute, New York).

Best, C. T., Morrongiello, B. A., and Robson, R. C. (**1981**). ''Perceptual equivalence of acoustic cues in speech and nonspeech perception,'' Percept. Psychophys. **29**, 191–211.

Best, C. T., Studdert-Kennedy, M., Manuel, S., and Rubin-Spitz, J. (**1989**). ''Discovering phonetic coherence in acoustic patterns,'' Percept. Psychophys. **45**, 237–250.

Blumstein, S. E., and Stevens, K. N. (**1980**). ''Perceptual invariance and onset spectra for stop consonants in different vowel environments,'' J. Acoust. Soc. Am. **67**, 648–662.

Bregman, A. S. (**1990**). *Auditory Scene Analysis: The Perceptual Organization of Sound* (MIT Press, Cambridge, MA).

Broadbent, D. E., and Ladefoged, P. (**1957**). ''On the fusion of sounds reaching different sense organs,'' J. Acoust. Soc. Am. **29**, 708–710.

Eilers, R. E., Oller, D. K., Urbano, R., and Moroff, D. (**1989**). ''Conflicting and cooperating cues: Perception of cues to final consonant voicing by infants and adults,'' J. Speech Hear. Res. **32**, 307–316.

Fitch, H., Halwes, T., Erickson, D., and Liberman, A. (**1980**). ''Perceptual equivalence of two acoustic cues for stop-consonant manner,'' Percept. Psychophys. **27**, 343–350.

Goldman, R., and Fristoe, M. (**1986**). *Goldman Fristoe Test of Articulation* (American Guidance Service, Circle Pines, MN).

Greenlee, M. (**1980**). ''Learning the phonetic cues to the voiced-voiceless distinction: A comparison of child and adult speech perception,'' J. Child Lang. **7**, 459–468.

Holt, L. L., Lotto, A. J., and Kluender, K. R. (**2001**). ''Influence of fundamental frequency on stop-consonant voicing perception: A case of learned covariation or auditory enhancement?'' J. Acoust. Soc. Am. **109**, 764–774.

Jastak, S., and Wilkinson, G. S. (**1984**). *The Wide Range Achievement Test—Revised* (Jastak Associates, Wilmington, DE).

Kewley-Port, D. (**1983**). ''Time-varying features as correlates of place of articulation in stop consonants,'' J. Acoust. Soc. Am. **73**, 322–335.

Kluender, K. R., Lotto, A. J., Holt, L. L., and Bloedel, S. L. (**1998**). ''Role of experience in language-specific functional mappings for vowel sounds as inferred from human, nonhuman and computational models,'' J. Acoust. Soc. Am. **104**, 3568–3582.

Krause, S. E. (**1982**). ''Vowel duration as a perceptual cue to postvocalic consonant voicing in young children and adults,'' J. Acoust. Soc. Am. **71**, 990–995.

Liberman, A. M. (**1957**). ''Some results of research on speech perception,'' J. Acoust. Soc. Am. **29**, 117–123.

Liberman, A. M., Cooper, F. S., Shankweiler, D. P., and Studdert-Kennedy, M. (**1967**). ''Perception of the speech code,'' Psychol. Rev. **74**, 431–461.

Liberman, A. M., Isenberg, D., and Rakerd, B. (**1981**). ''Duplex perception of cues for stop consonants: Evidence for a phonetic mode,'' Percept. Psychophys. **30**, 133–143.

Mann, V. A., and Liberman, A. M. (**1983**). ''Some differences between phonetic and auditory modes of perception,'' Cognition **14**, 211–235.

Mann, V. A., and Repp, B. H. (**1980**). ''Influence of vocalic context on perception of the [ʃ]–[s] distinction,'' Percept. Psychophys. **28**, 213–228.

Morrongiello, B. A., Robson, R. C., Best, C. T., and Clifton, R. K. (**1984**). ''Trading relations in the perception of speech by five-year-old children,'' J. Exp. Child Psychol. **37**, 231–250.

Nittrouer, S. (**1992**). ''Age-related differences in perceptual effects of formant transitions within syllables and across syllable boundaries,'' J. Phonetics **20**, 1–32.

Nittrouer, S. (**1996**). ''Discriminability and perceptual weighting of some acoustic cues to speech perception by 3-year-olds,'' J. Speech Hear. Res. **39**, 278–297.

Nittrouer, S., and Miller, M. E. (**1997a**). ''Developmental weighting shifts for noise components of fricative-vowel syllables,'' J. Acoust. Soc. Am. **102**, 572–580.

Nittrouer, S., and Miller, M. E. (**1997b**). ''Predicting developmental shifts in perceptual weighting schemes,'' J. Acoust. Soc. Am. **101**, 2253–2266.

Nittrouer, S., and Miller, M. E. (**1999**). ''Developmental changes in perceptual weighting strategies for speech are contrast specific,'' J. Acoust. Soc. Am. **106**, S2246.

Nittrouer, S., and Studdert-Kennedy, M. (**1987**). ''The role of coarticulatory effects in the perception of fricatives by children and adults,'' J. Speech Hear. Res. **30**, 319–329.

Nittrouer, S., Crowther, C. S., and Miller, M. E. (**1998**). ''The relative weighting of acoustic properties in the perception of [s]+stop clusters by children and adults,'' Percept. Psychophys. **60**, 51–64.

Nittrouer, S., Miller, M. E., Crowther, C. S., and Manhart, M. J. (**2000**). ''The effect of segmental order on fricative labeling by children and adults,'' Percept. Psychophys. **62**, 266–284.

Parnell, M. M., and Amerman, J. D. (**1978**). ''Maturational influences on perception of coarticulatory effects,'' J. Speech Hear Res. **21**, 682–701.

Remez, R. E., Rubin, P. E., Berns, S. M., Pardo, J. S., and Lang, J. M. (**1994**). ''On the perceptual organization of speech,'' Psychol. Rev. **101**, 129–156.

Stevens, K. N., and Blumstein, S. E. (**1978**). ''Invariant cues for place of articulation in stop consonants,'' J. Acoust. Soc. Am. **64**, 1358–1368.

Studdert-Kennedy, M. (**1983**). ''Limits on alternative auditory representations of speech,'' in *Cochlear Prostheses: An International Symposium*, edited by C. W. Parkins and S. W. Anderson (The New York Academy of Sciences, New York), Vol. 405.

Wardrip-Fruin, C., and Peach, S. (**1984**). ''Developmental aspects of the perception of acoustic cues in determining the voicing feature of final stop consonants,'' Lang. Speech **27**, 367–379.

Whalen, D. H., and Liberman, A. M. (**1987**). ''Speech perception takes precedence over nonspeech perception,'' Science **237**, 169–171.

Vowel formant discrimination II: Effects of stimulus uncertainty, consonantal context, and training[a)]

Diane Kewley-Port[b)]
Department of Speech and Hearing Sciences, Indiana University, 200 South Jordon Avenue, Bloomington, Indiana 47405-7002

(Received 10 January 2001; revised 13 June 2001; accepted 11 July 2001)

This study is one in a series that has examined factors contributing to vowel perception in everyday listening. Four experimental variables have been manipulated to examine systematical differences between optimal laboratory testing conditions and those characterizing everyday listening. These include length of phonetic context, level of stimulus uncertainty, linguistic meaning, and amount of subject training. The present study investigated the effects of stimulus uncertainty from minimal to high uncertainty in two phonetic contexts, /V/ or /bVd/, when listeners had either little or extensive training. Thresholds for discriminating a small change in a formant for synthetic female vowels /I,ɛ,æ,ɑ,ʌ,o/ were obtained using adaptive tracking procedures. Experiment 1 optimized extensive training for five listeners by beginning under minimal uncertainty (only one formant tested per block) and then increasing uncertainty from 8-to-16-to-22 formants per block. Effects of higher uncertainty were less than expected; performance only decreased by about 30%. Thresholds for CVCs were 25% poorer than for isolated vowels. A previous study using similar stimuli [Kewley-Port and Zheng, J. Acoust. Soc. Am. **106**, 2945–2958 (1999)] determined that the ability to discriminate formants was degraded by longer phonetic context. A comparison of those results with the present ones indicates that longer phonetic context degrades formant frequency discrimination more than higher levels of stimulus uncertainty. In experiment 2, performance in the 22-formant condition was tracked over 1 h for 37 typical listeners without formal laboratory training. Performance for typical listeners was initially about 230% worse than for trained listeners. Individual listeners' performance ranged widely with some listeners occasionally achieving performance similar to that of the trained listeners in just one hour. [DOI: 10.1121/1.1400737]

PACS numbers: 43.71.Es, 43.66.Fe, 43.71.An [MRL]

I. INTRODUCTION

Vowel sounds, high in energy and proportionally longer than consonants, are salient portions of ordinary speech. The overall goal of our series of vowel studies has been to model the processing of vowels in the peripheral auditory system and then to describe systematically how factors found in normal conversation affect processing at more central levels. Thresholds for discriminating small changes in vowel formants under optimal listening conditions have been estimated for both male and female vowels (Kewley-Port and Watson, 1994; Kewley-Port *et al.*, 1996). Optimal listening conditions use established psychophysical methods under minimal stimulus uncertainty with highly trained subjects to measure ''best'' performance (see Kewley-Port and Watson, 1994). Our thresholds obtained under optimal conditions have been modeled using excitation patterns (Sommers and Kewley-Port, 1996; Kewley-Port and Zheng, 1998) and shown to be very similar to discrimination thresholds for vowels determined from single unit recordings in the auditory nerves of cats (May *et al.*, 1996). Recently, Kewley-Port and Zheng (1999) employed listening conditions more similar to those found in ordinary conversation where listeners interpret sentences for meaning. Compared to optimal listening conditions, four experimental variables were altered from optimal toward more ordinary listening conditions. The primary stimulus variable was length of phonetic context, and environmental variables included level of stimulus uncertainty, linguistic meaning, and subject training. The present study was designed to extend our knowledge of these four variables gained from Kewley-Port and Zheng (1999) by focusing primarily on stimulus uncertainty and subject training. First, we review our knowledge of these four factors and then provide the motivation for the present experiments.

Vowels in ordinary conversation occur in a variety of phonetic contexts, occasionally in isolation (''Oh'') and typically in words in sentences. Thresholds obtained under minimal-uncertainty testing conditions for vowel formants have been established for isolated steady-state vowels and have yielded replicable estimates across investigations that are essentially constant at 0.1 barks across formant frequency (Kewley-Port and Watson, 1994; Sinnott and Kreiter, 1991; Hawks, 1994). The effect of syllable context on formant discrimination was shown to be highly significant in an early study by Mermelstein (1978) and subsequently in Kewley-Port (1995). In Kewley-Port and Zheng (1999) the resolution of formant frequency under medium uncertainty was determined for isolated vowels and one syllable context (/bVd/), as an isolated word, in a phrase, and in a nine-word sentence. Results showed that the largest effect of increasing phonetic context was from vowel to syllable (36% elevation in thresholds), and the effect of longer context for the phrase and sentence was much smaller (an additional 8% increase). For-

[a)]Portions of these data were presented at the 138th meeting of the Acoustical Society of America [J. Acoust. Soc. Am., **106**, No. 4, Pt. 2, 2275].
[b)]e-mail: kewley@indiana.edu

mant thresholds obtained under minimal uncertainty for syllable context have been published in only one previous report (Kewley-Port, 1995) and for only one vowel, /I/. Results for six consonantal contexts (/b,d,g,m,l,z/) demonstrated that longer consonantal formant transitions substantially elevated formant thresholds. Thresholds measured under optimal conditions are important because they are the baseline of comparison for determining the effects of other stimulus, environmental, or cognitive factors on perception. In Kewley-Port and Zheng (1999), four vowels, /I,ɛ,æ,ʌ/, were investigated, but not under optimal listening conditions. Thus, one goal of this study was to measure and compare formant thresholds under optimal listening conditions for these four vowels in both isolation and in a common syllable context.

Words in natural speech vary in their predictability, meaning that one's ability to predict the next word ranges from rather low in some contexts to very high in others. Watson (Watson *et al.*, 1976; Watson and Kelly, 1981) has investigated the effects of predictability in psychophysical experiments of nonspeech stimuli by varying *stimulus uncertainty*. Watson and Kelly (1981) defined stimulus uncertainty as the predictability of the stimulus to be presented on the next trial, primarily determined by the set size of possible stimuli. Minimal stimulus uncertainty consists of only one stimulus contrast tested within a block of trials and is the method employed in optimal listening conditions. Following terminology from Watson's research, we will categorize stimulus uncertainty into four types according to the number of possible stimuli presented within a trial block: minimal (one contrast); medium (two to ten contrasts); high (greater than 16 contrasts); very high (unique stimuli on every trial). Watson (1987) summarized some of his research on the effects of the level of stimulus uncertainty on the discrimination of intensity, frequency, or time within ten-tone patterns. Discrimination of a change in frequency of a tone, Δf, is most relevant here. In his Table I, Watson (1987) reported that for tones, a change from minimal to medium uncertainty increased Δf by a factor of 2, while a change from minimal to very high uncertainty increased Δf by as much as a factor of 150.

To understand how well vowels are resolved in normal discourse, the effects of stimulus uncertainty on formant discrimination should be quantified. In our report of vowel discrimination in more ordinary listening conditions (Kewley-Port and Zheng, 1999), a medium level of stimulus uncertainty was used with eight possible contrasts presented within one block. This level of stimulus uncertainty was assumed to be somewhat representative of the predictability of words occurring in short sentences. Results suggested that thresholds[1] for formant discrimination under medium uncertainty appear to be degraded by a factor of 2.2 compared to thresholds under minimal uncertainty. The present study systematically examines the effect of increasing the level of stimulus uncertainty from minimal to medium and to high for six vowels when phonetic context is restricted to isolated vowels or CVCs.

Many previous studies of vowel discrimination have been conducted under medium levels of stimulus uncertainty, including Fujisaki and Kawashima (1969), Mermelstein (1978), Macmillian *et al.* (1988), Gagne and Zurek (1988), Iverson and Kuhl (1995), and Coughlin *et al.* (1998), generally without specific justification for the selection of uncertainty level. However, Uchanski and Braida (1998) did examine the effects of uncertainty level on vowel discrimination. While their experimental paradigm is different from ours, it overlaps in important ways. Uchanski and Braida's (1998) goal was to quantify the effects of stimulus variability on pairwise discrimination of similar vowels degraded by noise. Listeners heard either one vowel pair (2AFC), four pairs, or 16 pairs per block. On each trial, listeners heard one vowel in the syllable /hVd/ and had a binary choice of responses. Thus, over a block the number of vowels presented was either 2, 8, or 32, corresponding reasonably to our designations of minimal, medium, and high stimulus uncertainty. Using Uchanski and Braida's calculated estimates of d', discriminability was about three times better for the minimal uncertainty contrasts than for any higher level of uncertainty. Moreover, discriminability was the same for medium and high levels of uncertainty across several measures. They concluded that the perceptual processes operating under minimal uncertainty are quite different than those at higher levels.

Uchanski and Braida's (1998) experiment was not strictly a discrimination paradigm in that the listener's task was to *identify* one of two similar vowels in the /hVd/ words. This is closer to listening in normal discourse where listeners identify words as they extract the meaning from the sentence. Our discrimination tasks have used typical forced-choice responses. For example, in the sentence discrimination task used in Kewley-Port and Zheng (1999), the modified 2AFC trial structure presented three similar sentences, the standard sentence followed by the two test sentences, one of which contained the altered vowel. Although this task does not mimic normal discourse, several experimental conditions were included that asked subjects to identify sentence meaning. Words were modified only in the first sentence occurring in the three stimulus intervals, and subjects wrote down which sentence they heard after completing the discrimination response. In different conditions, either 2, 8, or 16 sentences were in the test set. No differences in the thresholds for vowel discriminability were found among any of the sentence conditions, with or without the identification task. These results that include both discrimination and identification responses in sentences cannot be directly compared to Uchanski and Briada (1998), who employed identification only in single words. Nonetheless, our discrimination-plus-sentence identification conditions did require listeners to extract meaning from sentences and therefore emulate in a limited way that aspect of everyday listening. While the present investigation does not include identification tasks such as those in Kewley-Port and Zheng (1999) or Uchanski and Braida (1998), it does include vowel perception experiments under different levels of stimulus uncertainty similar to Uchanski and Braida (1998).

The fourth variable examined in our studies of more ordinary listening conditions is subject training. Previous experiments at medium levels of stimulus uncertainty have

demonstrated long-term training effects on discrimination for ten-tone patterns (Spiegel and Watson, 1981; Leek and Watson, 1984). Watson and his colleagues have noted that some training strategies are more effective than others in teaching listeners how to attend to the target portions of complex stimuli. In particular, Leek and Watson (1984) investigated long-term training effects with ten-tone patterns using several experimental methods. They noted that the time course of improvement in detection thresholds with training differed considerably among subjects at medium levels of stimulus uncertainty. However, when attention to the target tones was directed by minimal uncertainty training, or by lengthening of the target, large improvements in thresholds were observed.

Kewley-Port and Zheng (1999) measured the effects of extensive training on formant discrimination in sentences. In their experiment 1, listeners participated initially in the sentence discrimination test for 1 h, and then again after 17 h of vowel discrimination tasks. Improvement in performance after training was 65%. In experiment 2, the sentence task was administered twice, after 12 h and 25 h of experience. A small (15%) but significant improvement was obtained after greater than 13 h of additional testing. Kewley-Port and Zheng (1999) concluded that long-term training effects for complex speech stimuli should be expected, and that careful experimental design is required to reduce training effects in multifactor comparisons. Note, however, that for vowel sounds, it is not obvious how to interpret training in psychophysical laboratory experiments given that native speakers already have extensive listening experience ($>$20 years) with speech. On the one hand, estimates of ''best'' discrimination thresholds obtained under optimal listening conditions may provide an estimate of the limits of the neurophysiological resolving power of the auditory system for this class of stimuli. On the other hand, performance by average (already highly experienced) listeners may provide more valid estimates of speech processing abilities in everyday communication. Thus, in the present experiment two training strategies were implemented in order to contrast the abilities of optimally trained subjects with those of typical listeners who received no formal training.

To summarize, the present experiment examines three variables considered important in comparisons of performance under optimal laboratory conditions with that measured during normal discourse: phonetic context, stimulus uncertainty, and subject training. This investigation is intended to extend that of Kewley-Port and Zheng (1999), whose primary focus was the manipulation of phonetic context, with a modest manipulation of the variables of linguistic meaning and subject training, when stimulus uncertainty was fixed. In this study the primary variables are stimulus uncertainty and subject training, while phonetic context is limited to the two that demonstrated large effects in the previous study, namely isolated vowels versus vowels in syllable context.

The design of the present experiment benefited from a preliminary study of uncertainty and training by Kewley-Port (1992). In that study extensive training was given under medium levels of stimulus uncertainty for vowel formants in several CVC contexts. Results from four subjects showed high variability in formant thresholds across both CVC contexts and subjects. Given the unavoidable interaction between levels of uncertainty and duration of subject training, a more systematic design was implemented here. In experiment 1, discrimination performance was optimized using training that began with minimal uncertainty (one formant per block) and then gradually increased uncertainty to 8, 16, and finally 22 formants per block. In experiment 2, performance was measured for many listeners (37) without formal laboratory training under a high level of uncertainty, 22 formants per block. Initial and final performance measures were estimated during a 1-h testing session. The range of discrimination performance for relatively untrained listeners was then compared to that from the highly trained listeners in experiment 1. This design permitted the effects of stimulus uncertainty and training on vowel discrimination to be at least partially separated in the analysis.

II. EXPERIMENT 1

The primary purpose of the first experiment was to systematically explore the effect of stimulus uncertainty on vowel formant discrimination.

A. Method

1. Stimuli

The vowels investigated were the English vowels /I,ɛ,æ,ɑ,ʌ,o/ modeled after a female talker that have been used in several previous discrimination studies (Kewley-Port and Watson, 1994; Kewley-Port *et al.*, 1996). These vowels span a wide range of formant frequencies while generally not including vowels in which two formants are so close together that sometimes there is difficulty in synthesizing a test set with shifted formants. Four of these vowels, /I,ɛ,æ,ʌ/, were studied in Kewley-Port and Zheng (1999) and the same stimuli were used again here. These four vowels were synthesized in two phonetic contexts, either vowel only or in a /bVd/ syllable. The vowels /ɑ/ and /o/ were synthesized in isolation or in the syllables /bob/ and /dɑd/ and were used only in the 22-formant condition. The Klatt (1980) synthesizer was used in the cascade/parallel configuration with a 10 000-Hz sample rate. The formant values for the steady-state portion of the syllables are shown in Table I. The bandwidths for BW1, BW2, and BW3 were 70, 90, and 170 Hz, respectively. The values for F4 and BW4 were 4000 Hz and 250 Hz and were kept constant. Duration for the vowels was 180 ms and for the syllables was 255 ms. The transition parameters for the syllables are shown in Table II. The fundamental frequency ($F0$) contour was the same for isolated vowels and syllables, falling linearly from 220 to 180 Hz. The amplitude contour rose over 15 ms and then fell linearly over the remaining duration. The vowel and syllable stimuli synthesized with these parameters are referred to as the *standard* stimuli.

The test stimuli to be discriminated from the standard stimuli were synthesized in sets of 14, similar to those in Kewley-Port and Watson (1994) and Kewley-Port and Zheng (1999). The test formant, $F1$ or $F2$, was always incremented

TABLE I. Frequencies in Hz for formants $F1$, $F2$, and $F3$ used in synthesizing the six vowels. The last two columns give the range of formant values for the 1st and 14th test stimuli in the test sets for $F1$ and $F2$.

	Standard vowels			Ranges in test set	
Vowel	$F1$	$F2$	$F3$	$F1$	$F2$
/I/	450	2300	3000	455–522	2315–2513
/ɛ/	600	2200	3000	605–671	2210–2341
/ɑ/	875	1175	2850	880–946	1182–1281
/ʌ/	700	1400	2600	705–771	1410–1542
/æ/	1000	1950	3000	1007–1107	1960–2091
/o/	500	800	2000	505–571	807–907

from the standard for 14 steps, using log ratios. The range of the test formants is shown in Table I. For the syllables, changes in formant frequency were made first for the center, steady-state portion of the syllable, and then the formant transitions were linearly interpolated from the onset and offset frequencies shown in Table II to the center frequencies.

The test sets were organized into groups according to uncertainty level (Table III). Sixteen of the test sets were previously investigated in Kewley-Port and Zheng (1999), $F1$ and $F2$ for the vowels /I,ɛ,æ,ʌ/, for isolated vowels (/V/) and /bVd/ syllables. These 16 were tested under all levels of stimulus uncertainty, minimal, medium, and high, and the results are referred to as the 16-formant data. For medium uncertainty testing, these 16 test sets were divided quasirandomly into two groups of eight, medium-1 and medium-2, as shown in Table III. For high uncertainty testing, high-16, all test sets from medium-1 and medium-2 were included. The high-22 uncertainty group included all 22 sets as shown in Table III. Twenty-two test sets was the maximum number that could be run due to computer memory constraints.

2. Subjects

Subjects were college students who were paid for their participation. The five subjects had pure-tone thresholds of 20 dB HL or better at octave intervals from 250 through 8000 Hz.

3. Procedures

Stimuli were presented over calibrated TDH-39 earphones to the right ears of subjects seated in a sound-treated booth. Each subject was run independently on one of four 486 computers. Sound presentation was controlled by TDT equipment including an array processor, a 16-bit D/A converter, a programmable filter, and a headphone buffer. The programmable filter was configured as a low-pass filter with a cutoff frequency of 4300 Hz, and an attenuation level set by the calibration procedure. A synthetic /e/ vowel (3 s in length) was used as the calibration vowel. Output gain was set such that the sound-pressure level measured in the NBS-9A 6-c^3 coupler with a Larson-Davis sound-level meter was 77 dB SPL using the linear weighting scale and the fast reading. Levels for the six standard vowels were within ± 2 dB of the calibration vowel.

Test procedures followed those of Kewley-Port and Zheng (1999). An adaptive-tracking task was used to estimate discrimination thresholds at 71% correct following Levitt (1971). In each trial, stimuli were presented in a modified, two-alternative, forced-choice task with feedback. The standard was presented in the first interval, and subjects indicated on a keyboard which of the next two intervals contained the ''different'' (test) stimulus. Minimal uncertainty testing was conducted in 80-trial blocks. For experiments at

TABLE II. Onset and offset frequencies in hertz and durations in milliseconds for the formant transitions of the syllables.

Formant	Onset (Hz)	Formant transition time (ms)	Offset (Hz)	Formant transition time (ms)
/b/				
$F1$	475	15		
$F2$	1900	55		
$F3$	2750	35		
/d/				
$F1$			300	15
$F2$			2050	55
$F3$			3600	35

TABLE III. Composition of four groups of vowels tested at different levels of stimulus uncertainty is indicated with a check mark for formants in either isolated vowel or /bVd/ context.

Test formant	Medium-1	Medium-2	High-16	High-22
/I/ $F1$		√	√	√
/bId/ $F1$	√		√	√
/ɛ/ $F1$		√	√	√
/bɛd/ $F1$	√		√	√
/ʌ/ $F1$	√		√	√
/bʌd/ $F1$		√	√	√
/æ/ $F1$		√	√	√
/bæd/ $F1$	√		√	√
/ʌ/ $F2$		√	√	√
/bʌd/ $F2$	√		√	√
/æ/ $F2$	√		√	√
/bæd/ $F2$		√	√	√
/ɛ/ $F2$	√		√	√
/bɛd/ $F2$		√	√	√
/I/ $F2$	√		√	√
/bId/ $F2$		√	√	√
/o/ $F1$				√
/bob/ $F1$				√
/o/ $F2$				√
/bob/ $F2$				√
/dad/ $F1$				√
/dad/ $F2$				√

TABLE IV. Protocol for the tasks in experiment 1.

Task	Data	Level of uncertainty	Duration (hours)
(1) Screening	Audiogram		0.5
(2) Training	/I/ $F1$ in /bId/	Minimum	5.0
(3) Thresholds	/V/ or /bVd/ alternating	Minimum	2.5–3.75 per formant (~19 total)
(4) Training medium uncertainty	8-formant test sets	Medium	2.5–6.25
(5) Training higher uncertainty	16- or 22-formant test sets	High	2.5
(6) Testing higher uncertainty	22-, 16-, and 8-formant test sets	Medium and high	3.75

all higher levels of stimulus uncertainty, each of the standard formants was played 14 times per block in a random sequence.

An experimental protocol designed for 1 $\frac{1}{4}$-h testing sessions is shown in Table IV. Because one goal of experiment 1 was to compare the thresholds under optimal listening conditions for /V/ and /bVd/ stimuli, 5 h of training under minimal uncertainty was given each listener with an easy discrimination condition, /I/–$F1$ in /bId/. For threshold testing, a single, randomized test order for the eight formants was used by all listeners. For each formant, test blocks for either /V/ or /bVd/ phonetic context condition alternated during a test session, with the starting order changed daily. Adaptive tracks were continuously monitored and testing was stopped when asymptotic performance was approached over four to five blocks for both /V/ and /bVd/ stimuli, usually after 2 or 3 days of testing.

After the 16 thresholds were determined under optimal listening conditions, training began for the higher uncertainty conditions. Listeners were trained for one session on the medium-1 test group, and then for two to four sessions on alternating blocks of medium-1 and medium-2 to achieve some stability in performance. Next, one session of training with high-16 was followed by a session with high-22 such that training time under the four test sets at higher levels of uncertainty was similar. A final testing order to maximize performance across uncertainty groups was selected to be one block each of high-22, medium-1, and medium-2 and high-16. This test order was run six times each over three sessions.

For each block, a value of ΔF was calculated for each formant as the difference between the standard and the test formant using the average of the step numbers of the reversals and then converted to formant frequency in Hz (geometric mean). An average formant-frequency ΔF for each test formant for each subject was calculated from the last four blocks tested. Group means were calculated as the mean of the average ΔF values across subjects and are the threshold values reported as ΔF in hertz or as transformed to ΔZ in barks.

B. Results

1. Performance measures

The mean values of ΔF for all test sets in experiment 1 are shown in Hz in Table V. The table is arranged to emphasize the comparison among the 16 formants tested in all conditions, with the additional six formants tested only in high-22 shown to the right. Otherwise, this table and all the figures are displayed with center frequency of the test formant, whether $F1$ or $F2$, increasing from left to right.

The well-known effect of increases in ΔF with increasing formant frequency was obtained in this study as well. Kewley-Port and Zheng (1998, 1999) have modeled formant threshold data and have shown that this variability can be removed by transforming Hz to a critical-band rate scale or z scale in barks. Because the present investigation is not focused on variability due to formant frequency but rather on the effects of other variables including stimulus uncertainty and syllable context, the results in this experiment were transformed to the z scale. Specifically, Eq. (6) from Traunmüller (1990) was used to calculate ΔZ in barks from ΔF in Hz for each individual subject. The resulting mean ΔZ values in barks are shown in Table VI (and for 16 formants on Fig. 2). To confirm that this transformation did flatten the slopes of the threshold functions, the slope of the present threshold data under minimal uncertainty for vowel formants (see Fig. 1) was compared to that of Kewley-Port and Watson (1994). Both slopes were nearly flat, smaller than the absolute value of 0.003 $\Delta Z/Z$.

TABLE V. Mean values of ΔF for formant frequency discrimination in Hz. Values for /o/ and /ɑ/ on the right-hand side of the table only tested in the 22-formant condition.

Uncertainty level	/I/ $F1$ 450	/ɛ/ $F1$ 600	/ʌ/ $F1$ 700	/æ/ $F1$ 1000	/ʌ/ $F2$ 1400	/æ/ $F2$ 1950	/ɛ/ $F2$ 2200	/I/ $F2$ 2300	/o/ $F1$ 500	/o/ $F2$ 800	/ɑ/ $F1$ 875	/ɑ/ $F2$ 1175
VOWEL												
Minimum	11.91	14.86	10.33	18.18	35.12	34.97	47.01	15.71				
Medium	18.76	23.15	15.42	22.05	46.94	36.61	40.67	22.52				
High-16	20.48	21.87	13.98	19.21	50.66	38.73	43.00	22.89				
High-22	17.52	26.05	11.92	19.92	50.06	37.63	36.29	16.42	22.94	62.34		
SYLLABLE												
Minimum	10.05	15.20	10.87	15.94	61.21	32.21	47.99	46.01				
Medium	29.99	30.12	14.21	20.47	72.83	26.05	60.62	55.34				
High-16	25.72	21.78	15.82	16.26	44.25	37.52	48.20	57.37				
High-22	29.10	23.80	15.72	18.72	63.64	37.63	59.62	62.70	23.64	64.03	39.56	101.05

TABLE VI. Mean values of ΔZ for formant frequency discrimination in barks. Values for /ɔ/ and /ɑ/ on the right-hand side of the table only tested in the 22-formant condition.

Uncertainty level	/I/ *F*1 4.48	/ɛ/ *F*1 5.75	/ʌ/ *F*1 6.53	/æ/ *F*1 8.53	/ʌ/ *F*2 10.64	/æ/ *F*2 12.84	/ɛ/ *F*2 13.65	/I/ *F*2 13.94	/ɔ/ *F*1 4.92	/ɔ/ *F*2 7.24	/ɑ/ *F*1 7.74	/ɑ/ *F*2 9.52
						VOWEL						
Minimum	0.11	0.12	0.08	0.11	0.16	0.12	0.14	0.05				
Medium	0.17	0.18	0.11	0.13	0.22	0.12	0.12	0.06				
High-16	0.18	0.17	0.10	0.11	0.23	0.13	0.13	0.07				
High-22	0.16	0.21	0.09	0.12	0.23	0.13	0.11	0.05	0.19	0.42		
						SYLLABLE						
Minimum	0.09	0.12	0.08	0.10	0.28	0.11	0.14	0.13				
Medium	0.27	0.24	0.10	0.12	0.31	0.09	0.18	0.16				
High-16	0.23	0.17	0.12	0.10	0.20	0.13	0.14	0.16				
High-22	0.26	0.19	0.12	0.11	0.29	0.13	0.18	0.18	0.20	0.43	0.25	0.52

2. Thresholds for vowels and syllables

This experiment was designed to compare thresholds under optimal listening conditions for vowel formants in isolation and in simple syllable environments. To determine if vowel thresholds for the present data were comparable to those in earlier reports, ΔF values from Kewley-Port and Watson (1994) for the eight vowel formants were converted to barks. The average ΔZ was nearly the same for the 1994 data (0.109 barks) and for the current data (0.110 barks). Statistically, thresholds for the two subject groups were not significantly different by means of a one-way ANOVA [$F(1,14)=0.001$, $p>0.9$]. Thus, under optimal listening conditions subjects in experiment 1 perform comparably to previous subjects.

The results for the vowel and /bVd/ syllable thresholds are shown in Fig. 1. Only two formants had ΔZ thresholds clearly elevated by consonantal context, both for $F2$. The syllable thresholds ($M=0.131$ barks) were not significantly different from the vowel thresholds ($M=0.110$ barks) in a two-way, repeated measures ANOVA of phonetic context by formant frequency [$F(1,4)=4.02$, $p>0.11$]. There was a significant effect of formant frequency [$F(7,28)=6.77$, $p<0.001$] after the bark transform; the slopes of the two functions were essentially zero ($<|0.002|$). A significant interaction of context by formant in the two-way ANOVA [$F(7,28)=6.73$, $p<0.001$] is due to the two elevated $F2$ thresholds for syllables as shown in Fig. 1. These thresholds were elevated for all five listeners and suggest that syllable context sometimes interacts strongly with a listener's ability to discriminate small changes in formant frequency even under optimal listening conditions. These results are similar to Kewley-Port *et al.* (1996) for multiple syllable types and only the /I/ vowel. Although at this time the reason for the variability of the effect of syllable context is not known, it seems to occur only at higher frequencies. Thus, while an average percent increase for syllable context was small, the increase for the two elevated formants was large (>100%).

To determine how individual thresholds differed from one another within context, a one-way ANOVA was calculated separately for the vowel and syllable data. *Post hoc* analysis for vowels (all *post hocs* are Scheffé, $p<0.05$)

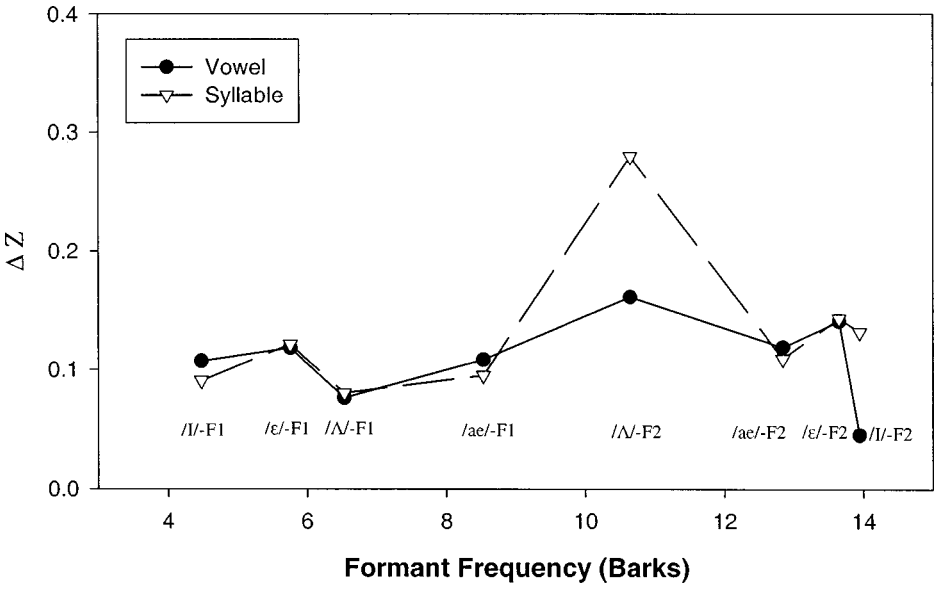

FIG. 1. Thresholds for formant frequency in barks obtained under minimal stimulus uncertainty for either isolated vowel or syllable (/bVd/) context.

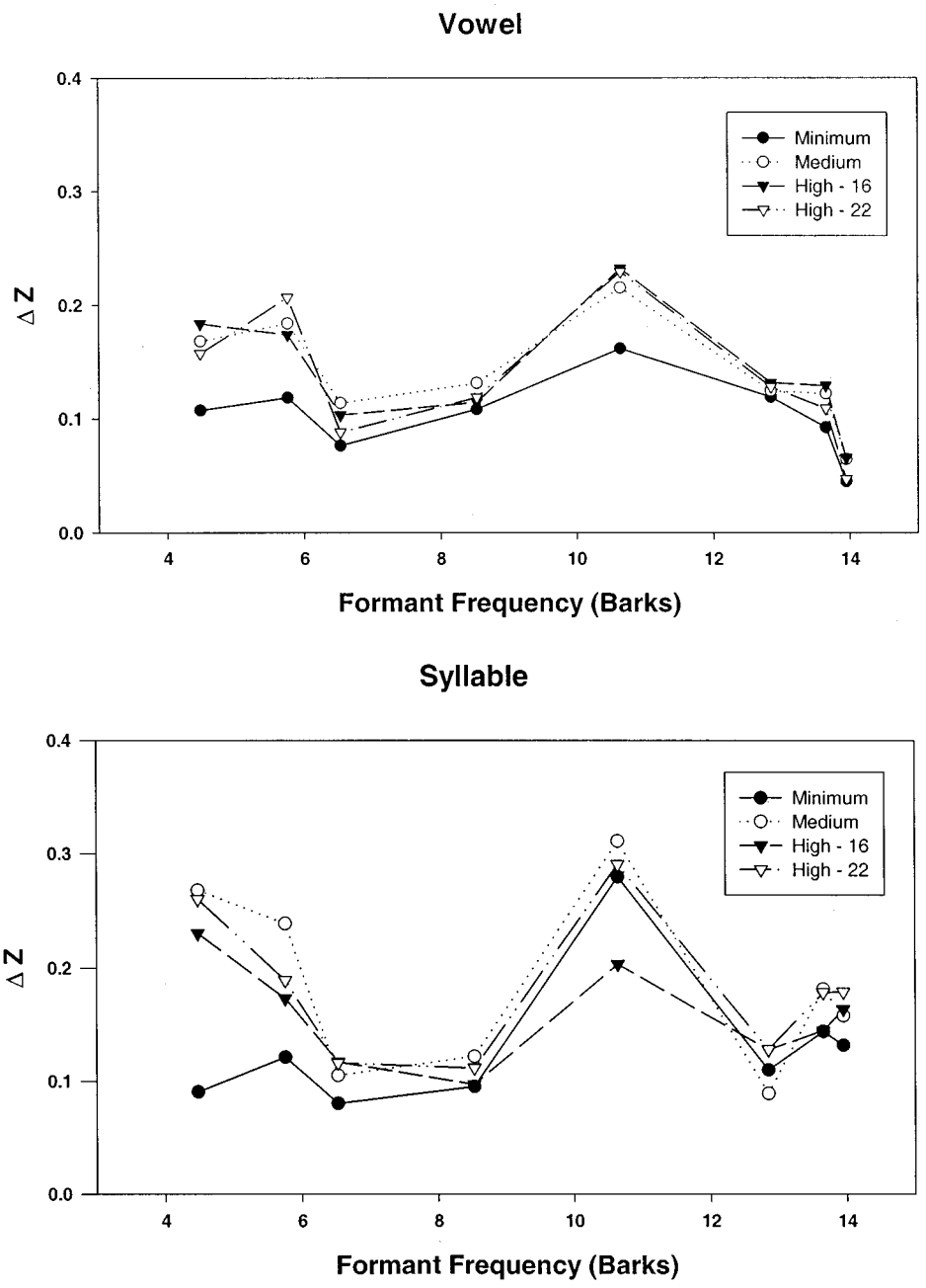

FIG. 2. Thresholds for formant frequency in barks obtained under four levels of stimulus uncertainty for either isolated vowel or syllable (/bVd/) context.

showed that only one vowel pair differed significantly, the highest ΔZ (/ʌ/–$F2$) with the lowest ΔZ (/I/–$F2$). For the syllable context, *post hoc* comparisons indicated that the most elevated threshold (/ʌ/–$F2$) was significantly different for six of the seven other formants. These analyses indicate that generally after the bark transform, thresholds did not differ among the eight test formants within context condition except for the second formant of /ʌ/.

3. Effects of uncertainty and context

The primary goal of experiment 1 was to assess the effects of both stimulus uncertainty and phonetic context on formant discrimination. The thresholds in ΔZ for the 16-formant data are shown in Fig. 2 separately for vowel and syllable contexts. All main effects and interactions were significant, $p<0.05$, in a three-way ANOVA for the variables formant frequency, context, and uncertainty. The significant main effect of formant frequency [$F(7,28)=11.25$, $p<0.001$] was examined with a *post hoc* test. The formant effect appears due once again to one formant that had the poorest thresholds, /ʌ/–$F2$, that was significantly different from five of the other formants.

The significant effects of context and uncertainty are more easily seen in Fig. 3. Formant resolution was consistently degraded [$F(1,4)=42.5$, $p<0.01$] in the syllable context ($M=0.163$ barks) compared to vowel context ($M=0.130$), about 25% poorer. Examining the effects of uncertainty [$F(3,12)=8.46$, $p<0.01$], discrimination was clearly best for stimuli under minimal stimulus uncertainty ($M=0.117$), compared to all higher levels (medium, $M=0.162$; high-16, $M=0.149$; high-22, $M=0.158$). *Post hoc* comparisons confirmed that only two uncertainty contrasts were significantly different, minimal versus medium, and minimal versus high-22. Thus, there were no differences

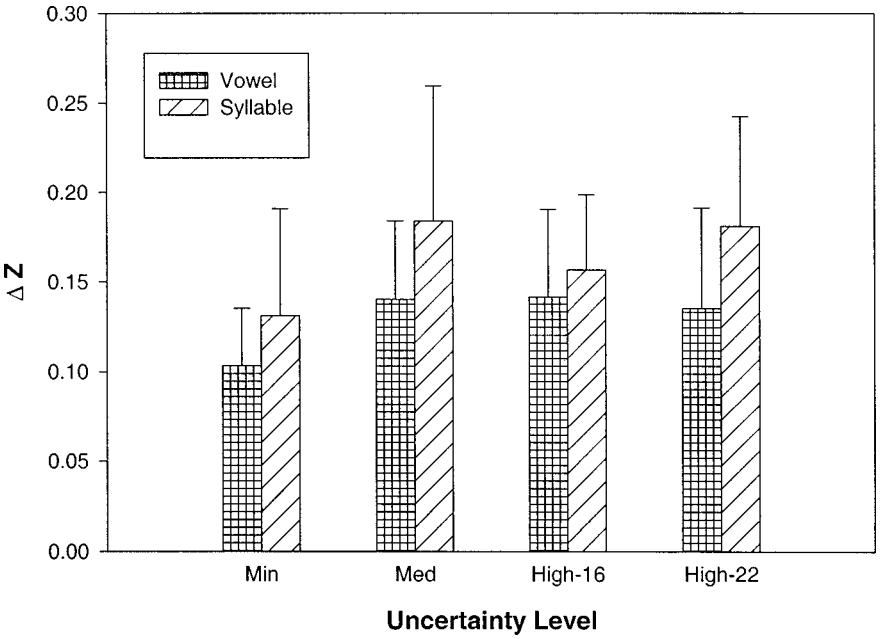

FIG. 3. Average thresholds for formant frequency in barks obtained under four levels of stimulus uncertainty for either isolated vowel or syllable (/bVd/) context. Thresholds are averaged over vowel formants. Error bars are standard deviations.

among the thresholds at the higher levels of uncertainty (see Fig. 2). The average reduction in discrimination due to higher uncertainty was small, about 29%.

There was a significant interaction between context and uncertainty [$F(3,12)=4.30$, $p<0.05$] due primarily to the smaller difference between vowel and syllable contexts for the high-16 condition (the only nonsignificant pair, n.s., see Fig. 3). The overall 25% reduction in resolution in syllable context appears rather well preserved across changes in level of uncertainty. The interaction between context and formant [$F(7,28)=2.63$, $p<0.05$] revealed that syllable context degraded discriminability for just one-half of the formants. The interaction between uncertainty and formant [$F(21,84)=1.89$, $p<0.05$] appears due to small differences in the reduced discriminability at higher levels of uncertainty for specific formants. The three-way interaction of formant, context, and uncertainty observed in Fig. 2 was also significant [$F(21,84)=2.34$, $p<0.05$]. This interaction appears due to a combined effect of syllable context at higher uncertainty degrading discrimination more for a subset of the formants, in particular /I/$-F1$ and /I/$-F2$, and /ɛ/$-F1$ and /ɛ/$-F2$.

Summarizing, for well-trained subjects the effects of stimulus uncertainty on formant discrimination were modest. Only a 30% reduction in discriminability was found between minimal uncertainty thresholds and all the higher levels of uncertainty. This effect was similar to the reduced discrimination of formants in syllable context, which averaged a 25% decrement. However, these two effects combined degraded resolution strongly in a few instances. That is, for /I/$-F1$ and /I/$-F2$ the decrement for syllables at higher uncertainty levels was about 135% and 268% respectively, while only modest differences across conditions were observed for /ʌ/$-F1$, /æ/$-F1$, and /æ/$-F2$.

III. EXPERIMENT 2

Previous discrimination experiments at higher levels of stimulus uncertainty have revealed long-term training effects on performance (Leek and Watson, 1984; Kewley-Port and Zheng, 1999). The primary purpose of the first experiment was to explore systematically the effect of stimulus uncertainty on vowel formant discrimination using training procedures that optimized performance as uncertainty increased. Training on the medium-to-high uncertainty tasks was begun after 37 h testing on minimal uncertainty tasks. This training procedure resulted in very modest performance decrements at higher levels of uncertainty, only about 30%. Experiment 2 was designed to contrast performance by these well-trained listeners with that of typical listeners who have received little formal training. In a previous study (Kewley-Port and Zheng, 1999), four listeners with no previous experience participated in a challenging task to discriminate eight formants in a /bVd/ context in a nine-word sentence. Surprisingly, during just 1 h of testing some subjects rapidly improved their discrimination performance. Apparently individual listeners differ considerably in their initial abilities to discriminate familiar speech sounds in synthesized speech.

The goal of experiment 2 was to assess the effects of training on typical listeners in a complex discrimination task simulating some of the conditions found in normal discourse. In order to include a variety of vowels both in isolation and in syllables, the stimulus group with the highest level of stimulus uncertainty, 22 test formants, was selected. Given the large individual variability observed in previous discrimination experiments, a larger group of subjects was recruited in order to estimate the range of performance found in typical listeners. One hour was selected as the duration of a session in which listeners' performance could be described as reflecting ''little formal laboratory training.''

Improvement of listeners over the hour of testing was measured from the adaptive tracks. Similar to the tracking algorithm in experiment 1, the two-down, one-up rule was used where ΔF was decreased one step for two correct responses and increased one step when one error occurred. Therefore, the first reversal indicated the first instance when a listener did not discriminate a particular ΔF difference. To assess how performance improved over the first hour, two

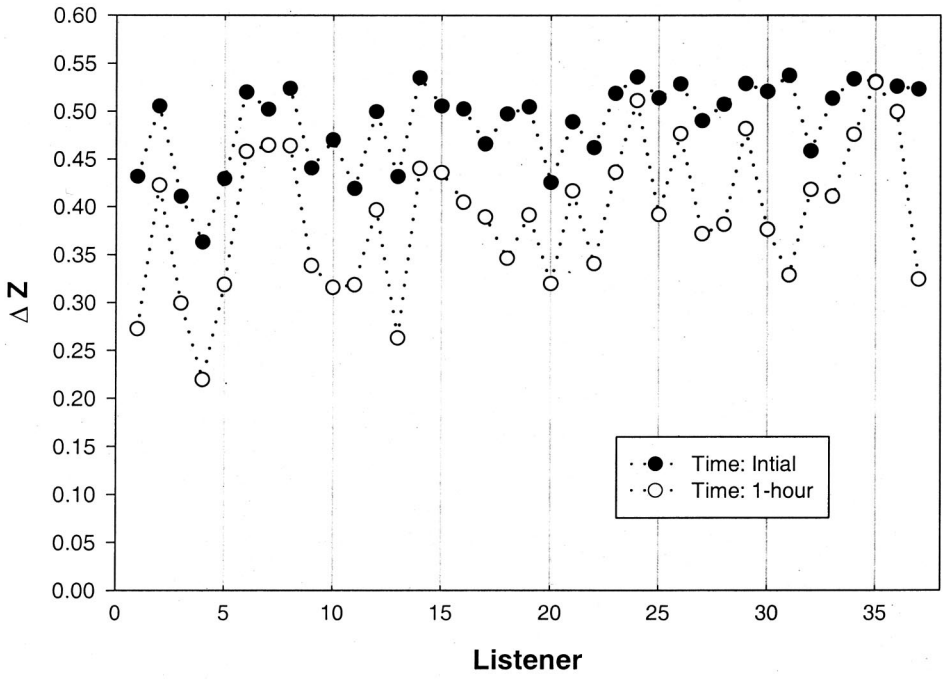

FIG. 4. Average estimates for formant frequency discrimination in barks obtained from 37 typical listeners measured twice during 1 h of testing (see the text). ΔZ values are averaged over 22 formants in both isolated vowels and syllable context.

measures were made. The *initial* estimate of discrimination performance was calculated as the average of the first two reversals. The *1-hour* estimate was calculated from the last two steps visited. The experimental design included sufficient trials for a listener to achieve perfect performance, i.e., error-free responses could, in principle, traverse all 14 ΔF steps in 1 h. Perfect performance did occur ultimately in 0.6% of the formant tracks.

Overall, performance measured in experiment 2 characterized that of a large group of typical listeners during the first hour of a complex formant discrimination task. In addition, these results were compared with those from listeners in experiment 1 who were trained with optimal procedures.

A. Method

1. Stimuli and procedures

The stimuli tested were in the high-22 uncertainty group used in experiment 1 (see Table III). Calibration and adaptive tracking procedures were the same as in experiment 1. The protocol began with $\frac{1}{4}$ h for screening and instructions. Listeners then participated in five blocks of 154 trials for a total of about 1 h testing (excluding breaks).

For each subject, two estimates of performance were made, the first for the initial discrimination ability from the ''first'' two reversals, and the second after 1-h exposure to the task from the last two steps visited. If there were six or more occurrences of the highest step (#14) initially (i.e., at least three errors), then ΔF for step 14 was entered as the initial estimate. The 1-hour estimate was the average of the last two ΔF steps visited in the 35 trials per formant. If there was never a reversal, the initial and 1-hour estimates were both entered as the ΔF for the lowest step (#1). Otherwise, the initial estimate was the average of the first two reversal steps converted to Hz (geometric mean). Given the large amount of data, two research assistants identified the reversals independently from printouts of the adaptive tracks, and any discrepancies were resolved by consensus.

2. Subjects

A total of 37 college students were recruited and paid for their participation. All 37 subjects had pure-tone thresholds of 20 dB HL or better at octave intervals from 250 through 8000 Hz.

B. Results

1. Typical listener performance over 1 h of testing

Discrimination measures in experiment 2 were also converted from ΔF to barks as ΔZ. As a performance benchmark in ΔZ for these listeners without training, it is useful to note that ΔZ thresholds for isolated vowels in optimal conditions (Table VI) are approximately 0.1 barks (one-tenth of a critical band), and that significant experimental differences obtained in Kewley-Port and Zheng (1999) tended to occur when differences in ΔZ exceeded 0.1 barks. For reference purposes, the listeners in experiment 1 with over 47 h of participation are called ''trained listeners'' and listeners in experiment 2 with 1 h of participation are called ''typical listeners.''

The initial and 1-hour ΔZ estimates of discrimination performance averaged over the 22 formants for all the 37 listeners are considered first. As shown in Fig. 4, after just 1 h of participation, estimates did improve for 36 of the 37 listeners, some by large amounts. Initially, the range of the 22-formant average of ΔZ for listeners differed from best listener at the 0.363 barks to worst listener at 0.537 (a range of 0.174 barks). To assess improvement by subjects over time, a two-way ANOVA with subject as a between (random) variable and time as a within variable was calculated. Listeners as a group did significantly improve over the hour of testing $[F(1,36)=157.1,\ p<0.001]$ on the average of 0.099 barks ($\approx$0.1). The distributions of listeners' ΔZ averages were also examined. The distribution for initial ΔZ averages

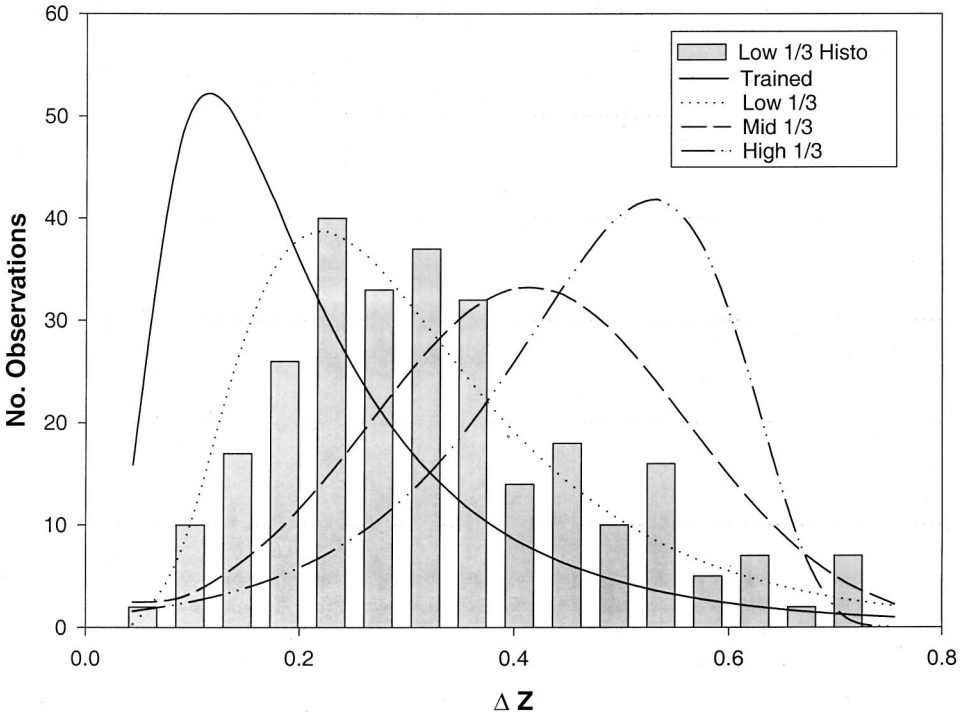

FIG. 5. Distributions of the number of average ΔZ values in barks obtained for the 22-formant test set. Lines indicate the fit to the histograms of the thresholds from four different listener groups (see the text). The trained group from experiment 1 had five subjects, while the other groups from experiment 2 had 12 subjects in each 1/3 group. The histogram shown is only for the group "good 1/3" of the typical listeners which was fit with the log-normal distribution shown with the dotted line.

was very asymmetrical because most subjects (23/37) had quite high values ($\Delta Z > 0.5$). This asymmetrical distribution was well fit by a log-normal curve (after the values were transformed high-to-low as a mirror image). The distribution of 1-hour ΔZ averages was approximately normal. Although six listeners still had many 1-hour ΔZ averages higher than 0.5 barks, about 20% of the listeners had many 1-hour ΔZ averages of about 0.22 barks, which fall well within the distribution of the high-22 thresholds for trained listeners in experiment 1 (Table VI, $M = 0.21$ barks). We can conclude that some typical listeners are able to discriminate vowels in a laboratory task as well as highly trained listeners within the first hour of testing. The pattern of performance across listeners of the average ΔZ for the initial compared to the 1-hour averages appears similar in Fig. 4. In fact, a correlation of $r = 0.79$ for the listeners' ΔZ averages between the two time intervals was significant at the $p < 0.05$ level. This means that variance across listeners observed during the first two reversals of the experiment predicted the variance at the end of the hour with an $r^2 = 0.62$. Apparently, typical listeners exhibit widely differential abilities to perform these complex discrimination tasks immediately upon exposure to the task and listeners' relative performance changes only slightly during the first hour. Given that the typical college-aged listener already has 20+ years of experience listening to vowels, one might not expect such a wide range of abilities. What, then, is the effect of training in the laboratory for typical listeners with medium to poor initial performance? To examine this question, the distributions of ΔZ values for the 22 formants were compared between experiment 1 and experiment 2.

To quantify performance differences for listeners with little formal training, the 37 listeners were divided into three groups of 12 (the median listener was discarded) based on the average 1-hour estimates. There are 22 ΔZ averages per listener in each of three groups (referred to as low-1/3, mid-1/3, and high-1/3 groups). A distribution of 12 listeners×22 formants=264 data points was fit with normal and log-normal functions in STATISTICA (1999) and the Kolmogorov–Smirnov One Sample test was used to select the one with the best fit. The histogram for the best group of listeners (low 1/3) is shown in Fig. 5 along with the best-fitting log-normal function. The fit is statistically a good representation of the underlying histogram of the ΔZ averages that includes the asymmetry of the long tail into poor ΔZ values up to 0.7 barks. Functions for the other two groups, shown in Fig. 5, were equally good statistical fits to the histograms. For the mid 1/3 of the typical listeners, the ΔZ averages were normally distributed. The distribution for the worst group of listeners (high 1/3) was well fit with a log-normal function when the values were transformed high-to-low as a mirror image. The resulting function shown in Fig. 5 has been transformed low-to-high to indicate the location of the high-1/3 distribution. The performance statistics shown in Table VII show that the three group means differ by 0.08 barks, nearly the 0.1-bark threshold for isolated vowels under minimal uncertainty.

To compare the trained and untrained listeners, histograms for the thresholds for the high-22 data in experiment 1

TABLE VII. Basic statistics for ΔZ in barks from three performance groups in experiment 2 for the 1-hour estimates and from the trained listeners in experiment 1 for the high-22 thresholds.

	High 1/3	Mid 1/3	Low 1/3	Trained
Maximum–minimum	0.711–0.133	0.711–0.089	0.711–0.054	0.668–0.054
Range	0.578	0.622	0.657	0.614
Mean	0.473	0.391	0.305	0.208

(5 listeners×22 thresholds=110 data points) were also fit with functions. The best-fitting function was log normal (shown as the solid line in Fig. 5). It is highly asymmetric and reveals that the threshold distribution for trained listeners still has a long tail that extends towards high values of ΔZ. An obvious feature of Fig. 5 is that the distributions for the four listener groups overlap considerably. The overlap is shown in Table VII where ΔZ ranges are greater than 0.5 barks. If we define ''good'' ΔZ values to be near the optimal formant threshold at 0.1 barks, then only the poor performers in the high-1/3 group did not have any good values. If ''poor'' ΔZ values are defined by the high-1/3 group whose mean is near 0.5 barks (five times worse than optimal thresholds), then we note that even the trained listeners had some ΔZ values that exceeded this value. That is, better and poorer performing subjects, trained or untrained, had a wide range of ΔZ averages over the different vowel formants and syllable context conditions in this high uncertainty task.

It appears then, that it is the shapes of the distributions for the four listener groups that are clearly differentiated in Fig. 5, not the ΔZ ranges. Although the means are significantly different in a one-way analysis of variance for listener group [$F(3,934)=120.6$, $p<0.0001$], as well as all *post hoc* binary comparisons ($p<0.001$ level, Scheffé), the shapes of the distributions in Fig. 5 also reveal effects of training. The distribution for the high 1/3 of the typical listeners is very skewed towards low ΔZ values, indicating little improvement in the 1-h session. This contrasts with the trained listeners, whose distribution is very skewed towards high ΔZ values with clearly the most peaked shape of the distributions. The low-1/3 group with only 1 h of training has a mean significantly higher than trained, but the shape is already assuming the skewed shape of the trained group. The mid-1/3 group has a normal distribution with the least peaked shape. Apparently, extensive listener training in this complex task enabled slower learners to achieve not only better performance, but discrimination performance across listeners became more similar. That is, distributions indicate that although some ΔZ averages will be quite high for some stimuli regardless of training, with training listeners who learn at different rates perform more similarly yielding a trained distribution that is quite peaked. The log-normal shape of the trained distribution indicates that geometric means across subjects, or perhaps medians, are probably better descriptors of the basic statistics of formant thresholds than first moment means.

Summarizing these results, typical listeners with little formal training exhibit a wide range of abilities to discriminate vowel formants in complex listening tasks. Some listeners did very well on their first attempts to discriminate formants, with performance close to that of highly trained listeners. On the other hand, 15% of the typical listeners made little improvement in 1 h of training. The effects of extensive training yielded peaked distributions with low thresholds for all listeners, even for those who had poor initial performance. Apparently, individuals learn to perform well in complex listening tasks at very different rates. However, the pattern of performance across listeners for the initial estimates of discrimination (first two reversals) was similar to the performance after 1 h (Fig. 4). This raises the question of whether some of the variance observed in listeners with little formal training is actually systematically different in relation to the experimental variables under investigation. In this experiment there were two stimulus variables manipulated, vowel formant and syllable context. An analysis of the systematic variability of these variables for the typical listeners was done to further clarify the effects of training.

2. Experimental variables

In complex discrimination tasks with speech, some listeners continue to improve over a long time period, even after a month of daily exposure (Kewley-Port and Zheng, 1999). The implication is that asymptotic performance is approached slowly with long time constants. Frequently, an experimental goal is to measure the relative effects of various experimental and stimulus variables on perception, not to estimate the maximum performance of which the listeners are capable. When in the time course of listening to speech can the significant effects of experimental variables be measured? In experiment 1 with highly trained listeners, the variables of formant frequency and syllable context were both significant. Several analyses were performed to determine whether these two variables would also significantly affect discrimination in the first hour of exposure.

In order to calculate an ANOVA for the variables formant and context, the 20 formants that occurred in both vowel and syllable context (all but /ɑ/; see Table VI) were selected. The third variable, time (initial and 1-hour estimates) was also included in a three-way ANOVA (formant ×context×time) for the dependent variable ΔZ. All main effects and interactions were significant. Figure 6 shows the interaction of time with formant frequency (top panel) and context with formant frequency (bottom panel), where the abscissa is displayed with formant labels to more clearly reveal certain patterns. For example, the interaction of time by formant (top of Fig. 6) is most notable in the larger difference in ΔZ for the first compared to the second formants. However, the size of this interaction is small and the main effect of a mean improvement of ΔZ over time [$F(1,36)=141.4$, $p<0.001$] of 0.098 barks (≈0.1 barks) seems to dominate performance. Similarly, small differences are observed in the interaction between context and formant, while the nearly constant difference of 0.0475 (≈0.05 barks) for the significant main effect of vowel versus syllable context [$F(1,36)=48.3$, $p<0.001$] seems to characterize performance in the bottom panel of Fig. 6. Finally, the largest main effect was for formant [$F(1,324)=196.1$, $p<0.001$], with a range of average ΔZ of 0.41 barks (almost $\frac{1}{2}$ a critical band) across the ten formants.

The above analyses and the highly similar functions in the bottom panel of Fig. 6 imply that the factors of context and formant frequency are significant in the initial estimates of ΔZ. To test this, a two-way ANOVA (context×formant) for ΔZ for just the initial estimates was conducted. The effects of context [$F(1,9)=22.7$, $p<0.0001$] and formant [$F(1,9)=165.6$, $p<0.0001$] were both highly significant. Therefore, the clear outcome of this analysis is that the ef-

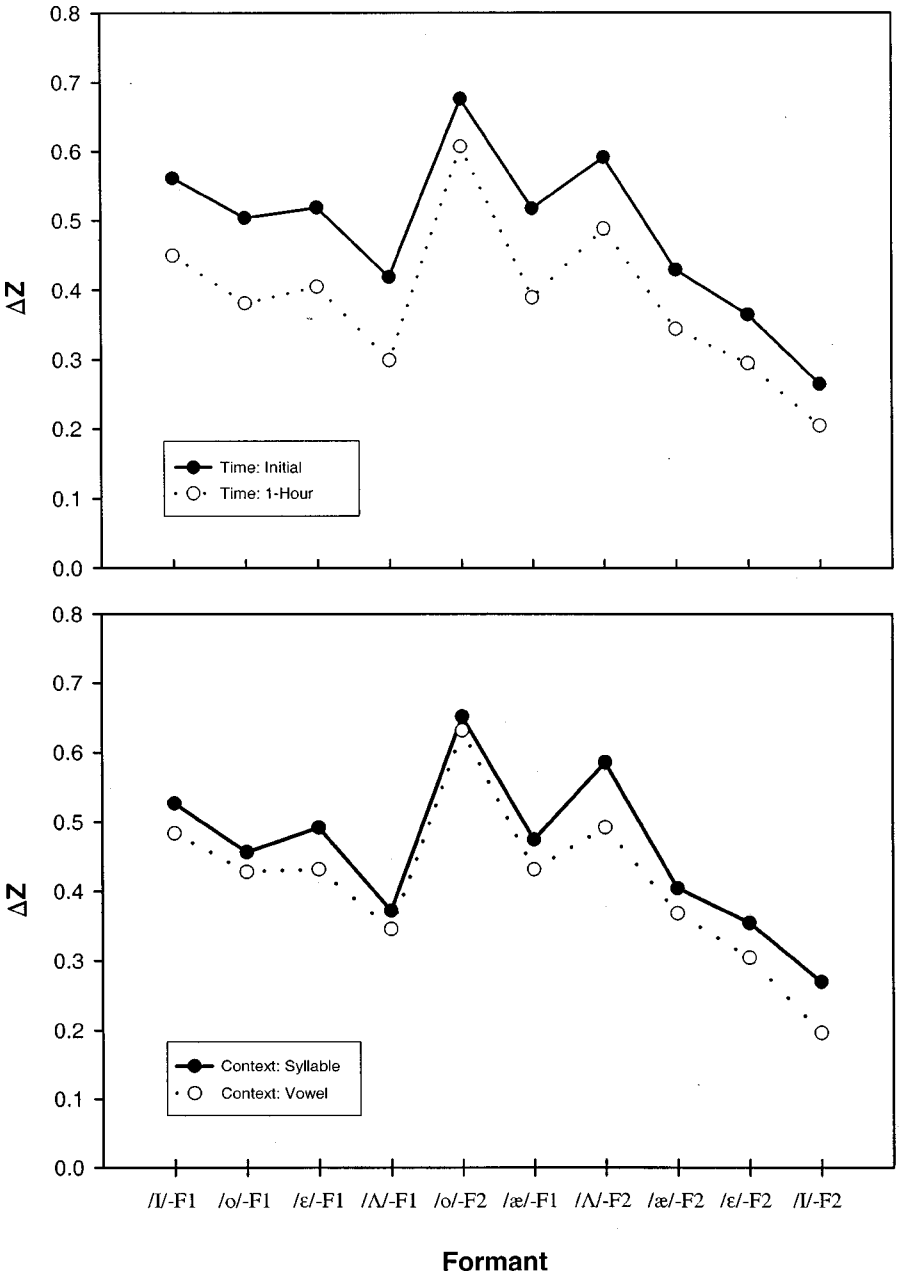

FIG. 6. Average ΔZ values in barks obtained for the high-22 test set are shown for just ten of the formants averaged over 37 typical listeners and different experimental factors. In the upper panel, ΔZ values measured at two different times were averaged over vowel and syllable (/bVd/) context. In the lower panel, ΔZ values obtained for either vowel or syllable (/bVd/) context were averaged over two different measurement times.

fects of the experimental variables are observable and significant in the earliest moment that an observation of discrimination can be taken, namely at the first two reversals. We note, of course, that this is true only when there is a fairly large sample of the population. Given that the variability for our typical listeners in this complex task was large, significant effects in the first hour would not usually occur for the small number of subjects often run in psychoacoustic training studies.

IV. DISCUSSION

A. Comparison of typical and trained listeners

Given that systematic variability was observed in the ability to discriminate formants by typical listeners with little training, how is that performance changed with extensive training? Comparisons of the high-22 ΔZ averages between experiment 2 and experiment 1 with trained listeners can shed light on this question. As expected, extensive training of listeners in a complex speech discrimination task did improve overall performance by large amounts. Averaging over the 22 formants, ΔZ averages for initial reversals ($M=0.489$ barks) were 235% higher than for trained listeners ($M=0.208$ barks). Even though in 1 h they improved quite a bit (0.1 barks), they were still 187% higher than for trained listeners.

Relations between performance for listener groups with different levels of training for the high-22 set were assessed using Pearson correlations. The correlation between the initial and 1-hour performance for all 22 ΔZ averages was high, $r=0.93$ (as expected from the subset of data in Fig. 6, top panel). The correlation between trained and 1-hour ΔZ averages was $r=0.82$ and between trained and initial ΔZ averages was $r=0.67$. This means that while 45% of the variability of thresholds for trained listeners can be predicted from the initial ΔZ estimates, after just 1 h of exposure, 67% of the variability for listeners trained for 47 h can be pre-

dicted. This suggests that while typical listeners encountering a complex task in the laboratory have highly elevated discrimination performance compared to trained listeners, they already have some abilities to attend to small acoustic differences when the stimuli are vowels. To see how much of the remaining 33% of the variance is random ''subject noise'' versus actual differences in perception related to training, additional analyses were conducted.

First, consider the slopes of the formant frequency functions as $\Delta Z/Z$. For all uncertainty conditions for the trained subjects seen in Fig. 2, slopes appear flat, i.e., near zero. For typical subjects ΔZ estimates are clearly lower for higher frequency formants for both initial and 1-hour estimates in Fig. 6, top panel, suggesting negative slopes. For a quantitative comparison, the slopes and significance of deviating from zero slope for the high-22 condition were calculated from the regression between formant frequency and both vowel and syllable data. For trained listeners, slopes were quite flat ($-0.008\,\Delta Z/Z$, n.s.), while typical listeners had significant negative slopes (initial estimates, $-0.02\,\Delta Z/Z$, $p<0.05$; 1-hour estimates, $-0.014\,\Delta Z/Z$, $p<0.05$). Apparently, slopes change towards zero slope in the first hour of training, and with training do approach zero. This implies that listeners with little training find higher-frequency formants easier to discriminate than low-frequency formants (in barks), and that with training, thresholds for low frequencies improve more than for high frequencies.

What were the effects of training in relation to the variable of syllable context? In the bottom panel of Fig. 6, the effect of syllable context was a nearly constant elevation of ΔZ averages by a 0.05 bark difference across all ten formants. While the average elevation for trained listeners in high-22 did not change much (0.0385 barks), the increase for /bVd/ context over /V/ was not constant but rather was either very small or rather large (>0.05 barks for four of the ten formants in Table VI). As a further comparison, under minimal uncertainty, when presumably listeners were even more able to focus their attention, only two of eight formant thresholds were elevated by syllable context (Fig. 1). These results suggest that syllable context has a weak effect on formant discrimination abilities. With little training, listeners consistently have modest elevations for formants in syllable context. With more training, or with other experimental conditions that enable listeners to improve performance, syllable context has no degrading effect for most vowels.

Summarizing, as anticipated, extensive training resulted in improved formant frequency discrimination. Analyses examined whether at initial exposure responses were largely random, thereby implying that listeners were initially unable to focus their attention on the differences among the synthetic stimuli. Results showed, on the contrary, that variability in the initial estimates of discrimination performance exhibited systematic effects related to the stimulus variables of formant frequency and syllable context. Clearly, listeners with extensive experience with natural speech were able to focus attention immediately on the salient properties manipulated in the synthetic speech. However, with additional exposure and feedback in the laboratory task, results showed that training not only reduced random variability (listener noise), but altered listeners' perception. Initially, high frequencies were easier to discriminate, but over time ΔZ thresholds became constant over formant frequency. Initially, syllable context elevated all ΔZ estimates, but over time only a few formants were affected. Since 67% of the variance observed after 47 h of training could be predicted after only 1 h of training, this suggests that moderately reliable measures of experimental variables in speech can be obtained in short-term experiments. On the other hand, to estimate best performance in speech psychophysics tasks, long-term training is needed for low, stable thresholds.

B. Review of factors affecting vowel discrimination in more ordinary listening conditions

Two of the experimental variables investigated in this experiment can be better understood by comparing the results of listeners in the present study with those in Kewley-Port and Zheng (1999). Only the eight formants in /bVd/ syllable context used as stimuli in both experiments and shown in Fig. 7 will be compared. One variable examined in both experiments was listener training. In Kewley-Port and Zheng (1999), one group of listeners participated for the first hour in a discrimination task for syllables in nine-word sentences. The results from the first two blocks were referred to as the ''untrained sentence'' data, as shown in Fig. 7. By comparing this untrained sentence data to the initial ΔZ averages for the high-22 data set, we can more fully answer the question: what are the initial abilities of listeners to discriminate vowels under more ordinary listening conditions? The ΔZ averages for these data sets for the eight formants shown in Fig. 7 largely overlap. In fact, comparing the means for the two data sets averaged over formant frequency reveals they are almost the same [$t(14)=0.777$, $p>0.45$], with means equal to 0.47 and 0.43 barks for the initial and the untrained sentence data, respectively. Even the pattern of variability of ΔZ averages across formant frequency is quite similar, $r=0.90$.

The similarity of these two sets of data from different untrained subjects in rather different complex discrimination tasks helps establish the abilities of typical listeners to discriminate vowels. In Kewley-Port and Zheng (1999), phonetic context was the primary variable manipulated. They argued that the untrained sentence ΔZ averages were quite comparable with those of Mermelstein (1978), who reported formant discrimination for several isolated syllables. The present experiment manipulated level of uncertainty, and results for the high-uncertainty condition yielded very similar results to those of Mermelstein. These comparable results across three experiments bolster the claim that there is an upper limit of performance in tasks simulating ordinary listening for listeners with little formal experimental training. The mean across the three data sets is near 0.5 barks, or one-half a critical band. Thus, there is sufficient evidence to establish 0.5 barks as a typical threshold for formant discrimination by listeners with little training in a variety of experimental conditions.

It was argued in Kewley-Port and Zheng (1999) that closely spaced American vowels in an $F1\times F2$ formant

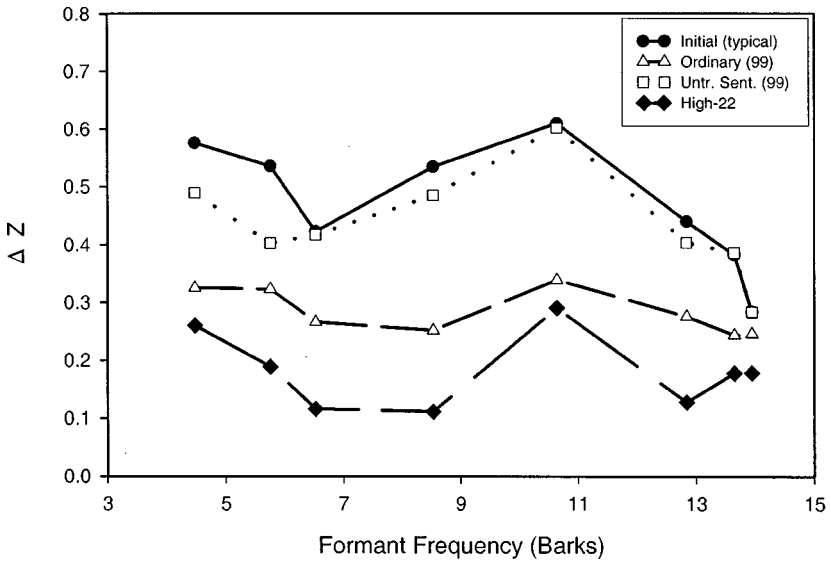

FIG. 7. Average ΔZ values in barks for eight formants in /bVd/ syllables are compared for two experiments. The lines with higher values of ΔZ are for subjects with little formal laboratory training: "Initial" is for 37 typical listeners under high uncertainty in the present experiment, and "Untr. Sent." was for four listeners discriminating vowels in sentences in Kewley-Port and Zheng (1999). "Ordinary (99)" is the norm for listening to ordinary phrases and sentences for trained subjects proposed by Kewley-Port and Zheng (1999). "High-22" is for trained subjects in the present experiment listening to syllables under high uncertainty.

space are only somewhat more than 0.5 barks apart, suggesting that in natural discourse listeners must be able to discriminate formants better than at 0.5 barks. In particular, Kewley-Port and Zheng (1999) claimed to have established a norm for formant discrimination in more ordinary listening of about 0.3 barks as an average of equivalent discrimination for phrases, sentences, and sentences with the addition of an identification task. The primary variable manipulated in the present experiment was level of stimulus uncertainty, a variable fixed in Kewley-Port and Zheng (1999). How do the effects of level of uncertainty compare to the effects for longer phonetic context? In particular, consider the thresholds for the highest level of uncertainty tested, 22 formants, compared to the ordinary norm for formants in phrases and sentences. In Fig. 7 a nearly constant 0.1-bark difference is seen between the ΔZ functions for longer phonetic context [Ordinary (99)] versus higher uncertainty (High-22) [significantly different, $t(14)=3.79$, $p<0.002$]. One way to directly compare the effects is to calculate the ratio representing the increase in ΔZ in relation to optimal, isolated vowel thresholds ($M=0.109$, Kewley-Port and Zheng, 1999). For high-22 thresholds ($M=0.182$), the ratio is 1.7, while for longer phonetic context ($M=0.284$) the ratio is 2.6. (For comparison, the ratio for either the untrained sentence or initial ΔZ averages is 4.0). Clearly, the degrading effect of longer phonetic context on discrimination is much stronger than the effect of higher levels of uncertainty. From the perspective of normal discourse, the implication is that predictability of words in sentences is much less a factor in discriminating formant differences than is length of phonetic context. Thus, the previously established norm for formant frequency discrimination of 0.3 barks continues to be the best estimate of formant discrimination in normal discourse. For comparison with other data presented in hertz, Table VIII converts 0.3 barks to hertz at selected frequencies from 200 to 3000 Hz. Calculating these values as percent yields about 5% for frequencies greater than 1000 Hz, which compares favorably to the commonly cited values of 3%–5% for formant frequency discrimination in isolated vowels (Flanagan, 1955). Note this contrasts with our series of experiments that has demonstrated that optimal formant thresholds for isolated vowels are 1.5% of formant frequency and that 5% is the norm for discrimination of formants in sentences.

V. CONCLUSION

The purpose of this formant discrimination study was to investigate further the effects of four variables that were manipulated to simulate more ordinary listening conditions: phonetic context, stimulus uncertainty, subject training, and linguistic meaning. Our interpretation of the results from both this study, focused on stimulus uncertainty, and those from Kewley-Port and Zheng (1999), focused on phonetic context and linguistic meaning, follows. There is a large variety of listening conditions that is encountered in everyday listening. American English listeners are able to discriminate within-vowel category differences in formants that are greater than 0.3 barks apart in everyday sentences, while simultaneously extracting the linguistic message. Listeners can resolve finer formant differences when speech consists of only single words. However, predictability of words in sentences (measured here by stimulus uncertainty) appears to have only a small effect on the norm for discriminating formants in ordinary listening conditions. This implies that top-

TABLE VIII. Values of the norm for formant discrimination in phrases and sentences (ordinary norm) was shown to be 0.3 barks. This constant value in barks is converted to Hz in this table.

Formant frequency	200	400	600	800	1000	1200	1400	1600	1800	2000	2200	2400	2600	2800	3000
Ordinary norm	27	32	38	44	51	58	66	74	82	92	101	111	122	133	145

down processing has little effect on listeners hearing out small differences in vowels that may signal speaking style, emotion, dialect, etc. Discrimination abilities in everyday sentences improve over a very long time course in laboratory tasks. While there is large variability in the performance of typical listeners who initially participate in laboratory tasks, there is a reasonable percentage (20%) who are almost immediately able to perform some tasks as well as highly trained listeners.

In the larger variety of everyday listening conditions, several important factors have not been explored by the present two studies. The most important is to estimate vowel formant discrimination in natural speech stimuli rather than the artificial-sounding Klatt (1980) synthesized speech used here. A larger set of phrase and sentence types is also needed. These factors are under investigation in a subsequent experiment by Liu and Kewley-Port (2000). Other important factors for future study of vowel discrimination are environmental noise, including poor signal-to-noise ratios and competing voices, especially in relation to their detrimental effects on persons with hearing impairment.

ACKNOWLEDGMENTS

This research was supported by the National Institutes of Health Grant No. DC-02229 to Indiana University. We are grateful to Charles S. Watson for comments on an earlier version of the manuscript. The assistance of Daren Swango, Toby Calandra, and Melissa Coy-Branam in collecting and analyzing data is gratefully acknowledged.

[1]In the previous paper in this series (Kewley-Port and Zheng, 1999), we referred to measures of vowel discriminability obtained under optimal testing conditions as ''thresholds,'' while those obtained under less than optimal conditions were termed ''difference limens.'' While this distinction between two classes of thresholds was useful, it has also produced confusion. Therefore, in this article, only the word threshold appears. Threshold is now generally understood to refer not to a sharp demarcation between stimuli to which persons are sensitive and those stimuli to which they are not, but rather to statistical estimates of sensitivity, in the case of absolute thresholds, or of resolving power or acuity, in the case of difference thresholds. Degradation in discrimination performance, measured under higher levels of stimulus uncertainty, may be interpreted as a consequence of the listener's inability to maintain narrowly focused auditory attention when both target and context vary from trial to trial. In this article we have referred to all measures of sensitivity as thresholds, but distinguish between thresholds obtained under various experimental conditions.

Coughlin, M., Kewley-Port, D., and Humes, L. (**1998**). ''The relation between identification and discrimination of vowels in young and elderly listeners,'' J. Acoust. Soc. Am. **104**, 3597–3607.

Flanagan, J. (**1955**). ''A difference limen for vowel formant frequency,'' J. Acoust. Soc. Am. **27**, 288–291.

Fujisaki, H., and Kawashima, T. (**1969**). ''On the modes and mechanisms of speech perception,'' *Annual Report of the Engineering Research Institute, Faculty of Engineering* (University of Tokyo, Tokyo), Vol. 28, pp. 67–73.

Gagné, J. P., and Zurek, P. M. (**1988**). ''Resonance-frequency discrimination,'' J. Acoust. Soc. Am. **83**, 2293–2299.

Hawks, J. W. (**1994**). ''Difference limens for formant patterns of vowel sounds,'' J. Acoust. Soc. Am. **95**, 1074–1084.

Iverson, P., and Kuhl, P. K. (**1995**). ''Mapping the perceptual magnet effect for speech using signal detection theory and multidimensional scaling,'' J. Acoust. Soc. Am. **97**, 553–562.

Kewley-Port, D. (**1992**). ''Effect of levels of stimulus uncertainty and consonantal context on formant frequency discrimination,'' J. Acoust. Soc. Am. **91**, 2338(A).

Kewley-Port, D. (**1995**). ''Thresholds for formant-frequency discrimination of vowels in consonantal context,'' J. Acoust. Soc. Am. **97**, 3139–3146.

Kewley-Port, D., Li, X., Zheng, Y., and Neel, A. (**1996**). ''Fundamental frequency effects on thresholds for vowel formant discrimination,'' J. Acoust. Soc. Am. **100**, 2462–2470.

Kewley-Port, D., and Watson, C. S. (**1994**). ''Formant-frequency discrimination for isolated English vowels,'' J. Acoust. Soc. Am. **95**, 485–496.

Kewley-Port, D., and Zheng, Y. (**1998**). ''Modeling formant frequency discrimination for isolated vowels,'' J. Acoust. Soc. Am. **103**, 1654–1666.

Kewley-Port, D., and Zheng, Y. (**1999**). ''Vowel formant discrimination: Towards more ordinary listening conditions,'' J. Acoust. Soc. Am. **106**, 2945–2958.

Klatt, D. H. (**1980**). ''Software for cascade/parallel formant synthesizer,'' J. Acoust. Soc. Am. **67**, 971–995.

Leek, M. R., and Watson, C. S. (**1984**). ''Learning to detect auditory pattern components,'' J. Acoust. Soc. Am. **76**, 1037–1044.

Liu, C., and Kewley-Port, D. (**2000**). ''Vowel formant discrimination in natural speech,'' J. Acoust. Soc. Am. **108**, 2601(A).

Levitt, H. (**1971**). ''Transformed up–down methods in psychoacoustics,'' J. Acoust. Soc. Am. **49**, 467–477.

Macmillan, N. A., Goldberg, R. F., and Braida, L. D. (**1988**). ''Resolution for speech sounds: Basic sensitivity and context memory on vowel and consonant continua,'' J. Acoust. Soc. Am. **84**, 1262–1280.

May, B. J., Huang, A., Le Prell, G., and Hienz, R. D. (**1996**). ''Vowel formant discrimination in cats: Comparison of auditory nerve representations and psychophysical thresholds,'' Aud. Neurosci. **3**, 135–162.

Mermelstein, P. (**1978**). ''Difference limens for formant frequencies of steady-state and consonant-bound formants,'' J. Acoust. Soc. Am. **63**, 572–580.

Sinnott, J. H., and Kreiter, N. A. (**1991**). ''Differential sensitivity to vowel continua in Old World monkeys (Macaca) and humans,'' J. Acoust. Soc. Am. **89**, 2421–2429.

Sommers, M., and Kewley-Port, D. (**1996**). ''Modeling formant frequency discrimination of female vowels,'' J. Acoust. Soc. Am. **99**, 3770–3781.

Spiegel, M. F., and Watson, C. S. (**1981**). ''Factors in the discrimination of tonal patterns. III. Frequency discrimination with components of well-learned patterns,'' J. Acoust. Soc. Am. **69**, 223–230.

STATISTICA for Windows [Computer software] (**1999**). StatSoft, Inc., Tulsa, OK.

Traunmüller, H. (**1990**). ''Analytical expressions for the tonotopic sensory scale,'' J. Acoust. Soc. Am. **88**, 97–100.

Uchanski, R. M., and Braida, L. D. (**1998**). ''Effects of token variability on our ability to distinguish between vowels,'' Percept. Psychophys. **60**, 533–543.

Watson, C. S. (**1987**). ''Uncertainty, informational masking, and the capacity of immediate auditory memory,'' in *Auditory Processing of Complex Sounds*, edited by W. Yost and C. S. Watson (Erlbaum, Hillsdale, NJ), pp. 267–277.

Watson, C. S., and Kelly, W. J. (**1981**). ''The role of stimulus uncertainty in the discrimination of auditory patterns,'' in *Auditory and Visual Pattern Recognition*, edited by D. J. Getty and J. N. Howard (Erlbaum, Hillsdale, NJ), pp. 37–59.

Watson, C. S., Kelly, W. J., and Wroton, H. W. (**1976**). ''Factors in the discrimination of tonal patterns. II. Selective attention and learning under various levels of stimulus uncertainty,'' J. Acoust. Soc. Am. **60**, 1176–1186.

Age differences for stop-consonant and vowel perception in adults

Ralph N. Ohde and Rima Abou-Khalil
Department of Hearing and Speech Sciences, Vanderbilt Bill Wilkerson Center for Otolaryngology and Communication Sciences, Vanderbilt University Medical Center, Nashville, Tennessee 37232

(Received 15 January 2001; accepted for publication 28 June 2001)

The purpose of this study was to determine the role of static, dynamic, and integrated cues for perception in three adult age groups, and to determine whether age has an effect on both consonant and vowel perception, as predicted by the ''age-related deficit hypothesis.'' Eight adult subjects in each of the age ranges of young (ages 20–26), middle aged (ages 52–59), and old (ages 70–76) listened to synthesized syllables composed of combinations of [b d g] and [i u *a*]. The synthesis parameters included manipulations of the following stimulus variables: formant transition (moving or straight), noise burst (present or absent), and voicing duration (10, 30, or 46 ms). Vowel perception was high across all conditions and there were no significant differences among age groups. Consonant identification showed a definite effect of age. Young and middle-aged adults were significantly better than older adults at identifying consonants from secondary cues only. Older adults relied on the integration of static and dynamic cues to a greater extent than younger and middle-aged listeners for identification of place of articulation of stop consonants. Duration facilitated correct stop-consonant identification in the young and middle-aged groups for the no-burst conditions, but not in the old group. These findings for the duration of stop-consonant transitions indicate reductions in processing speed with age. In general, the results did not support the age-related deficit hypothesis for adult identification of vowels and consonants from dynamic spectral cues. © *2001 Acoustical Society of America.* [DOI: 10.1121/1.1399047]

PACS numbers: 43.71.Ft, 43.71.An, 43.71.Es [CWT]

I. INTRODUCTION

A. Adult perception of static, dynamic, and integrated cues

The acoustic cues that contribute to the perception of stop consonants and vowels are often classified as static, dynamic, and integrated cues. Static cues are those with limited spectral change over time, while the spectra of dynamic cues vary to a greater extent temporally. Both static and dynamic cues are context dependent, influenced primarily by the following vowel. This context dependency implies the secondary nature of static and dynamic cues in perception. Integrated cues are combinations of static and dynamic properties that, together, form an invariant acoustic property. For example, both the burst and formant transitions contribute to the onset spectrum and thus form a single integrated acoustic property. This property appears invariant and is considered a primary cue to perception (Blumstein and Stevens, 1980; Ohde and Haley, 1997).

In a series of four related experiments, Blumstein and Stevens (1980) presented listeners with stop-consonant–vowel syllables that varied along the parameters of burst duration, formant motion, and vowel context. The results showed that consonant stimuli as brief as 10 ms were reliably identified, even without burst information. However, the addition of the burst clearly enhanced perception of the [d] and [g] stop consonants. Formant motions were shown to be important but secondary cues. Blumstein and Stevens hypothesized that perception of consonant place of articulation is based on invariant properties occurring within a short time window of 10–20 ms adjacent to consonant onset or offset. Thus, it was predicted that the consonant is cued primarily by the gross shape of the acoustic spectrum at onset, and the vowel by the frequencies at formant transition offset.

In another series of four related experiments, Fox (1989) investigated the importance of dynamic information to vowel perception (Strange, 1989). The stimuli consisted of three 7-step /bib/ to /beb/ continua. The three continua consisted of full token, silent-center, and medial vowel stimuli. The results suggested that listeners' vowel perception was accurate even with the presentation of only one pitch period of the silent-center tokens. Moreover, Fox showed that identification of the silent-center stimuli was based on formant changes in the transitions rather than their endpoint or target frequencies. These results underline the importance of dynamic information to accurate vowel perception.

B. Development of speech perception in adults

Our understanding of the perception of static, dynamic, and integrated cues for speech in adults has been generally limited to young adults. Although various cognitive and sensory changes occur with aging, few studies have attempted to examine the impact that these processes may have on consonant and vowel perception in older adults. In fact, there is evidence indicating that cognitive factors independent of hearing loss such as fatigue, changes in memory, motivation, and linguistic capacity affect perception in older adults (Working Group on Speech Understanding and Aging, 1988; van Rooij and Plomp, 1990). For example, research has found age-related declines in consonant perception in the

 0001-4966/2001/110(4)/2156/11/$18.00

absence of pure-tone hearing loss in quiet and in noise (Dubno, Dirks, and Morgan, 1984; Elliott, Busse, and Bailet, 1985; Gelfand, Piper, and Silman, 1985).

If speech perception changes as adults age, there is some indication that the ability to process dynamic acoustic cues is impaired (Price and Simon, 1984; Dorman *et al.*, 1985; Gelfand *et al.*, 1985; Elliott *et al.*, 1989; Fox, Wall, and Gokcen, 1992). For example, age-related differences in perceiving vowels were observed by Fox *et al.* (1992). The researchers studied vowel perception in young adults (ages 19–25) and compared them to perception in older (ages 61–75), normal-hearing adults. The results support an age-related decrement in processing dynamic perceptual cues in vowel perception. The older subjects performed significantly worse at identifying silent-center syllables, indicating a deficit in utilizing dynamic acoustic information during identification tasks. Older subjects also performed worse at identifying lax (marked) than tense (unmarked) vowels. The authors speculated that the differences were based on changes in sensory processing ability; particularly in decreased frequency resolution ability, as well as due to decreased efficiency of processing. Consonant identification by older subjects was also worse in the silent-center condition, again implying that older listeners have greater difficulty utilizing dynamic cues. Based on their findings and others, Fox *et al.* proposed an "*age-related deficit hypothesis*" for processing dynamic cues. This hypothesis predicts that older adults with relatively normal hearing will not process vowel or consonant dynamic cues that change in time similar to young adults.

Earlier findings by Parnell and Amerman (1979) tend to support this age-related deficit hypothesis. In addition, the results of Parnell and Amerman show that older adults were worse than young adults in integrating information from diverse cues such as the stop-consonant noise burst and formant transition onset to derive a consonant and vowel percept. In the Fox *et al.* (1992) and Parnell and Amerman studies, stimulus conditions contained both dynamic and static cues. For example, their natural speech vowel transition tokens included both $F2$ vowel onset (static cue) and vowel transition (dynamic cue). Thus, the independent contribution of either $F2$ onset or vowel transition cannot be assessed. Since static $F2$ onsets have been shown to be salient in perception of both consonants and vowels, it is critical to orthogonally assess static and dynamic cues (Blumstein, Isaacs, and Mertus, 1982; Ohde *et al.*, 1996) when testing the dynamic-cue-based age-related deficit hypothesis.

In summary, for adults over 60 years of age, decreased processing of dynamic cues and decreased efficiency in both consonant and vowel perception were found by Fox *et al.* (1992) and Parnell and Amerman (1979). These results were confirmed in the Price and Simon (1984), Gelfand *et al.* (1985), and Elliott *et al.* (1989) studies, which showed decreased perception based on dynamic information alone, and that temporal information is vulnerable to aging. Based on these developmental adult findings, the age-related deficit hypothesis for processing dynamic cues was proposed (Fox *et al.*, 1992). This hypothesis would also appear to predict poorer identification of sounds by older adults than younger adults due to effects of stimulus duration, because of potential age related reductions in processing speed (Gelfand *et al.*, 1985; Hale, Myerson, and Wagstaff, 1987; Myerson *et al.*, 1992; Wingfield, 1996). Older adults should have greater deficits in processing relatively brief dynamic consonant and vowel properties from shorter duration cues than longer duration cues, if there are age-related reductions in processing speed.

In the current research, synthetic speech-like stimuli were employed that independently assessed static, dynamic, and combinations of static and dynamic cues as a function of duration to directly test the age-related deficit hypothesis for consonant and vowel perception in three adult age groups. The specific questions were the following:

(1) Do young, middle-aged, and older subjects process dynamic cues differently in the perception of consonants and vowels, as predicted by the age-related deficit hypothesis?
(2) Do young, middle-aged, and older subjects process dynamics, static, and integrated cues differently as a function of duration, as predicted by the age-related hypothesis?

II. CONTROL STIMULI: EXPERIMENTS I AND II

The test stimuli were those generated by Ohde and colleagues (1995, 1997), because the present study is concerned with the same variations of parameters in stop consonant and vowel perception. Two experimental conditions, one targeting consonant and the other targeting vowel perception, were administered to subjects. The stimuli were generated with the Klatt cascade/parallel formant synthesizer (Klatt, 1980) at a 10-kHz sampling rate, and with a low-pass filtering of the output at 4 kHz. Consonant–vowel (CV) syllables comprised of the voiced stops [b d g] and the vowels [i *a*] for the first experiment, and [i *a* u] for the second experiment, were synthesized with source and resonance parameters appropriate for an adult male vocal tract. The synthesis parameters were varied according to control and experimental conditions.

The experimental conditions and hypotheses in experiments I and II were focused on the importance of stimulus onsets in consonant and vowel perception, and the effects of parametric changes in dynamic, static, and integrated cues. In particular, the following issues were addressed as a function of these parametric changes: (1) The importance of short duration onsets of consonant–vowel syllables as cues to the perception of place of articulation was examined in experiment I by synthesizing stimuli containing a 5- or 10-ms noise burst (static cue) followed by a brief voiced interval containing moving formant transitions (dynamic cue) with onset characteristics appropriate for [b d g] followed by the vowels [i *a*]. The effect of degree of onset information on consonant identification was determined by varying the voicing from 10 to 46 ms. The effect of different formant transition trajectories on consonant identification was assessed by including two vowel contexts. (2) The influence of formant transition motions was further examined in experiment I by generating stimuli containing a noise burst and formant onset frequencies appropriate for [b d g] in the context of [i *a*], but without

moving transitions (static cue). (3) The role of integrated properties consisting of the noise burst in combination with the onsets of the formant transitions to identification of consonant place of articulation was evaluated in experiment I by generating stimuli similar to those in points (1) and (2), but without noise bursts. (4) In order to determine if cues to vowel identification are present in short-duration stimuli consisting of 10 to 46 ms of voicing, experiment II evaluated the effects of these brief stimuli on vowel identification. The importance of dynamic cues in vowel perception was assessed by generating stimuli with formant transition motion. The role of static cues was determined by examining vowel identification from stimuli containing formants with no motion. The effect of degree of onset information on vowel identification was determined by varying the voicing from 10 to 46 ms.

The control stimuli consisted of either a 5- or a 10-ms noise burst, followed by a 300-ms voicing interval. The voiced portions of the syllables were generated with a cascade configuration of the synthesizer. The onset of the voicing was abrupt and the amplitude remained constant throughout the syllable. The fundamental frequency ($f0$) contour started at 103 Hz and rose in a piecewise linear manner to 125 Hz within 30 ms, after which it remained constant throughout the duration of the voicing. The formant frequency specifications were modeled after Blumstein and Stevens (1980). The onset frequencies of the first four formants were appropriate for the consonants [b d g], and steady-state frequencies of these formants were appropriate for the [i *a* u] vowels. The starting frequency for $F1$ in the [*a*] context was 200 Hz, and a target frequency of 720 Hz was reached after a 20–45-ms transition duration. In the [i] context, the $F1$ starting frequency was 180 Hz, and the target frequency of 330 Hz was reached after a 15–30-ms transition duration. The onset frequency for $F1$ in the [u] context was 180 Hz and reached a steady-state frequency of 370 Hz after a 15–45-ms duration. For both [i] and [*a*] vowel contexts, the $F1$ transition duration was the shortest for the labial ([bi]: 15 ms; [b*a*]: 20 ms), intermediate for the alveolar ([di]: 25 ms; [d*a*]: 30 ms), and longest for the velar ([gi]: 30 ms; [g*a*]: 45 ms) consonant. Transition duration in the [u] context remained the same (15 ms) across all consonants. Transition duration for all other formants ($F2$, $F3$, and $F4$) was 40 ms. Starting frequencies and target frequencies for the manipulated formants are presented in Table I. The frequencies of formants higher than $F4$ were not manipulated because of their limited correspondence to articulatory positions. However, the default value of $F5$ was raised from 3750 to 4500 Hz and its bandwidth changed from 200 to 400 Hz, in order to minimize undesirable influences of the fifth resonator and the amplitude of adjacent formant peaks (Klatt, 1980; Walley *et al.*, 1984).

Linear prediction analyses were obtained with high-frequency pre-emphasis and a 26-ms half-Hamming window positioned at consonantal release (Kewley-Port, 1983; Ohde *et al.*, 1995). Onset spectra and template specification are in accordance with the Blumstein and Stevens (1979) values. Labials had a relatively flat or diffuse-falling spectrum, alveolars a diffuse-rising spectrum, and velars a midfrequency spectral peak (Ohde *et al.*, 1995).

TABLE I. Onset and target frequencies (in Hz) of the first four formants.

Formants	Onset frequency			Target frequency
	[bi]	[di]	[gi]	[i]
$F1$	180	180	180	330
$F2$	1800	2000	2400	2200
$F3$	2600	2800	3000	3000
$F4$	3200	3900	3400	3600
	[b*a*]	[d*a*]	[g*a*]	[*a*]
$F1$	200	200	200	720
$F2$	900	1700	1640	1240
$F3$	2000	2800	2100	2500
$F4$	3500	3500	3500	3500
	[bu]	[du]	[gu]	[u]
$F1$	180	180	180	370
$F2$	800	1600	1400	1100
$F3$	2000	2700	2000	2350
$F4$	3200	3200	3200	3200

A 5- or 10-ms burst was appended to the stimuli 5 to 15 ms prior to the onset of voicing. The burst duration was 5 ms for stops in the [*a*] and [u] context and 10 ms for the [i] context. Like $F1$ transition durations, the voice onset time was shortest for the labial (5 ms), intermediate for the alveolar (10 ms), and longest for the velar (15 ms) context. The bursts were generated by modifying the spectrum of a burst of white noise to be appropriate for each place of articulation, by manipulating frequency-specific amplitude controls within a parallel configuration of the synthesizer. The same noise burst was used to generate all stimuli, and the amplitude and frequency parameters were modeled after those outlined by Klatt (1980). Some modifications were employed in order to enhance the onset spectra (Blumstein and Stevens, 1979), and to obtain adequate burst amplitudes relative to the following vowels (Bush, 1977; Blumstein and Stevens, 1980; Ohde and Stevens, 1983). Table II contains all burst parameters that were manipulated for the control stimuli in the experiments. Linear prediction analyses revealed that the bursts appropriately enhanced the integrated onset properties for each place of articulation, as theoretically and empirically predicted (Blumstein and Stevens, 1979, 1980; Ohde *et al.*, 1995).

Since the energy of the burst for labial stop consonants

TABLE II. Amplitude control levels (A; in dB) and bandwidths (B; in Hz) for the burst synthesis (B3, B5, and B6 were 110, 400, and 1000 Hz, respectively, across stimuli).

	Amplitude controls						Bandwidth	
Stimuli	A2	A3	A4	A5	A6	AB	B2	B4
[bi]	55	0	0	0	0	58	50	250
[di]	0	47	60	62	60	0	70	170
[gi]	0	53	43	45	45	0	70	250
[b*a*]	52	0	0	0	0	58	50	250
[d*a*]	0	48	58	59	55	0	70	170
[g*a*]	52	43	46	46	36	0	70	250
[bu]	52	0	0	0	0	58	50	250
[du]	0	53	60	48	36	0	70	170
[gu]	54	30	43	48	0	0	70	250

TABLE III. Demographic data for the three adult age groups (s.d.=standard deviation).

	Younger subjects Experiment I			Younger subjects Experiment II			Middle-aged subjects			Older subjects		
	Range	Mean	s.d.	Range	Mean	s.d.	Range	Mean	s.d.	Range	Mean	s.d.
Age (years: months)	20:4–25:2	22:7	3.4	21:0–25:9	23:2	4.1	51:7–59:1	54:9	3.1	69:8–76:11	73:7	2:5
Education (in years)	18	18	0	18	18	0	15–18	16.1	1.2	12–18	14.8	2.0

is distributed throughout the spectrum, the AB (bypass path amplitude) parameter of the synthesizer was used. The labial burst amplitude was adjusted to a value approximately 20 dB less than the vowel in the 3500-Hz region (Stevens and Blumstein, 1978). The frequency contents for the alveolar and velar stop bursts were adjusted by manipulating amplitude controls for different formant frequencies. The primary excitation frequency was in the formant that corresponded with spectral peaks of the following vowels. This resulted in an excitation in the region of $F2$ for [g*a*] and [gu], $F3$ and $F4$ for [gi], and $F4$ for [d*a*] and [di]. Although a single formant corresponded to the primary excitation production for the alveolar and velar syllables, weaker energy was distributed throughout the spectrum to ensure a natural continuity between burst release and vowel formants. The amplitudes of the primary excitation for the alveolar and velar consonants were adjusted to be 0–5 dB less than the amplitude of the adjacent formant in the following vowels (Bush, 1977; Blumstein and Stevens, 1980). A total of six control stimuli was generated (2 vowels×3 consonants) for experiment I, and a total of nine control stimuli (3 vowels×3 consonants) for experiment II.

III. EXPERIMENT I: STOP-CONSONANT PERCEPTION

A. Method

1. Test stimuli

The synthesis parameters were varied according to one control condition and four experimental conditions. For the experimental conditions, eight tokens of each syllable were generated. Each stimulus had a voicing duration of either 10 or 46 ms, and formant transitions and bursts were either present or absent in accordance with four experimental conditions: (1) burst+moving transition; (2) burst+straight transition; (3) no burst+moving transition; and (4) no burst +straight transition.

The experimental stimuli were derived from the control stimuli (see Sec. II) by shortening the duration of voicing and by varying the conditions of the burst and formant transitions. As noted, parameters were manipulated according to four experimental conditions. One 10-ms stimulus corresponding to one glottal pulse, and one 46-ms stimulus consisting of five glottal pulses were generated within each condition. For the first condition, the experimental stimuli were generated directly from each control stimulus by reducing the duration of voicing. Thus, these stimuli contained bursts as well as moving formant transitions, and had the same synthesis parameters as the control stimuli. However, the short duration of the 10-ms stimuli prevented the fundamental frequency and formant frequencies from reaching their target values. Instead, they reached values that were interpolated in a piecewise linear manner from the control stimuli. The second stimulus condition contained the burst, but no formant transitions. The generation of the bursts was identical to the moving transition conditions. The stimuli had the same onset frequencies as the corresponding stimuli with formant transitions. However, the frequencies of the second, third, and fourth formants remained constant, i.e., straight, at the onset value throughout the syllable. Only the first formant movement was retained in order to sustain the stop-like quality of the stimuli (Blumstein and Stevens, 1980). The third stimulus condition contained stimuli without bursts and with moving transitions. The stimuli for the fourth condition were equivalent to the third, except for the absence of a formant transition. In all, 48 experimental stimuli were produced (2 vowels×3 consonants×4 conditions×2 durations).

2. Subjects

The subjects were eight young, middle-aged, and older adults. The data for the young adult subjects were obtained in a previous study (Ohde *et al.*, 1995). These subjects ranged in age from 20:4 (years:months) to 25:2 years, with a mean of 22:7 years. Four of the subjects were female and four were male. The middle-aged group ranged from 51:7 to 59:1 years of age with a mean of 54:9 years. Six of the subjects were female and two were male. The older group ranged from 69:8 to 76:11 years of age with a mean of 73:7 years, and all were female. All subjects were native speakers of English and all had completed at least 12 years of schooling (refer to Table III for demographic information). None of the subjects was taking any medication known to affect neurological or hearing functions.

All subjects passed a hearing screening by pure-tone audiometry to establish adequate hearing in both ears for the octave frequencies between 500 and 4000 Hz (Coughlin, Kewely-Port, and Humes, 1998; Ohde and Haley, 1997). All subjects had hearing threshold levels of 30-dB HL or less bilaterally, except for four subjects. Of these, one belonged to the middle-aged group and had a hearing threshold of 35-dB HL at 4000 Hz in the right ear and criterion-level hearing in the left. The remaining three belonged to the older group and they had hearing no worse than 40-dB HL at 4000 Hz in one ear and criterion-level hearing at all tested frequencies in the other ear (Fox *et al.*, 1992). Evaluation of the individual performance of these four subjects showed a high proportion of error-free responses. Thus, it is highly unlikely that the unilateral mild hearing loss at only one frequency

accounts for their response patterns on any individual subtest. As part of the screening, middle-aged and older subjects also had tympanometry to assess middle-ear function. Results showed normal middle-ear functioning for all subjects.

3. Procedure

All practice and testing were conducted binaurally in an IAC booth over headphones (TDH 49). A comfortable listening level at approximately 80-dB SPL was used for all subjects. The stimulus presentation and data collection were controlled by a PDP 11/73 computer. For all conditions, one experimenter outside the booth monitored the accuracy of the control responses and presented the different stimulus conditions.

The two vowel contexts were tested separately, and the order was counterbalanced across subjects. The subjects were asked to identify the initial consonant in a three-alternative forced-choice (3AFC) procedure. The subjects responded by pushing one of three buttons, labeled "b," "d," and "g" on the response box. The experimental stimuli were blocked according to the conditions of the burst and formant transition.[1] The sequence of presentation for a given vowel was burst+moving transition, burst+straight transition, no burst+moving transition, and no burst+straight transition. The six stimuli (3 consonants×2 durations) in each of these conditions were repeated ten times and presented in a random order, with a 3-s interstimulus interval.

Reliable performance throughout the testing was insured by monitoring the subjects' responses to 12 synthesized control stimuli, which were inserted within each experimental condition of 60 stimuli. Across the four conditions for a vowel, average identification of at least 75 percent for these control stimuli was required, i.e., at least 9 of the 12 control stimuli had to be identified correctly. If performance was below this level, the data from that subject would have been discarded, and practice resumed. No subject in this study required additional practice.

4. Statistical analyses

A repeated-measures analysis of variance on the arcsine-transformed percents across place of articulation was used to analyze the data. This analysis included the between-subjects factor of age (young, middle-aged, and old), and within-subjects factors of burst (burst and no burst), vowel ([i] and [*a*]), transition type (straight and moving), and voicing duration (10 and 46 ms). Follow-up analytical comparisons including tests of simple main effects and appropriate Newman Keuls' *post hoc* tests were used to examine relevant significant interactions (Keppel, 1991). Although all significant interactions are reported, not all are analyzed. Significant results at the $p<0.05$ or $p<0.01$ levels are reported below.

B. Results and discussion

Figure 1 illustrates consonant identification across place of articulation for stimuli in the [*a*] and [i] vowel contexts. Identification of stop consonants was high for all listeners in both the [*a*] and [i] burst condition (A and B) contexts, as can be seen from Fig. 1. However, all listeners had worse consonant identification in the [i] context than in the [*a*] context except for the no-burst+moving transition condition, where identification remained high. The longer duration improved identification in the no-burst stimuli, particularly for the young and middle-aged groups. For the no-burst conditions, duration had minimal impact on stop identification for the older group.

A repeated measures analysis of variance revealed significant main effects of the burst [$F(1,21)=45.13$; $p<0.01$], vowel [$F(1,21)=50.80$; $p<0.01$], transition [$F(1,21)=22.69$; $p<0.01$], and duration [$F(1,21)=38.74$; $p<0.01$], and a significant interaction for burst×duration×age [$F(2,21)=9.04$; $p<0.01$].[2] Follow-up comparisons of the burst×duration×age interaction revealed a different pattern of results for the young and middle-aged groups compared to the old group. Simple effects tests showed for the young and the middle-aged groups significant main effects for the burst and duration, and the burst×duration interaction [young: burst[$(1,7)=12.99$; $p<0.01$]; duration[$(1,7)=24.03$; $p<0.01$]; burst×duration[$(1,7)=17.01$; $p<0.01$]; middle: burst[$(1,7)=11.15$; $p<0.01$]; duration[$(1,7)=15.86$; $p<0.01$]; burst×duration[$(1,7)=34.34$; $p<0.01$]. For both groups, Newman Keuls' *post hoc* tests revealed significantly lower stop-consonant identification from the 10-ms no-burst condition compared to the other three conditions. However, for the old group, only the burst main effect was significant [$(1,7)=21.36$; $p<0.01$].

These findings for the burst×duration×age interaction are illustrated in Fig. 2. The strong burst×duration interaction for the young and middle-aged groups is clearly shown in this illustration. As long as there is sufficient duration, the young and middle-aged groups identified consonants from burst- and no-burst stimuli similarly. The old group, however, did not benefit from longer duration stimuli, without a burst. This difference of about 20% in processing no-burst 46-ms stimuli between the old and the young+middle-aged groups was substantial. Thus, the young and the middle-aged groups used both bursts and duration to facilitate stop-consonant identification, whereas the old group relied on the burst+transition integrated property more than the duration cue.

In summary, the results reveal that older listeners rely on the integration of secondary cues to a greater extent than younger and middle-aged listeners. In the absence of a stop-consonant burst, the young and middle-aged subjects were able to utilize stimulus duration for correct identification. Older listeners, on the other hand, were unable to use duration to facilitate correct identification. In regard to dynamic spectral cues, the findings showed contrary to the age-related deficit hypothesis that onset information provided by moving formant transitions was usually a sufficient cue for correct place-of-articulation identification across age groups.

IV. EXPERIMENT II: VOWEL PERCEPTION

A. Method

1. Test stimuli

Nine syllables, comprised of the stops [b d g] followed by vowels [i *a* u], were generated and varied across several

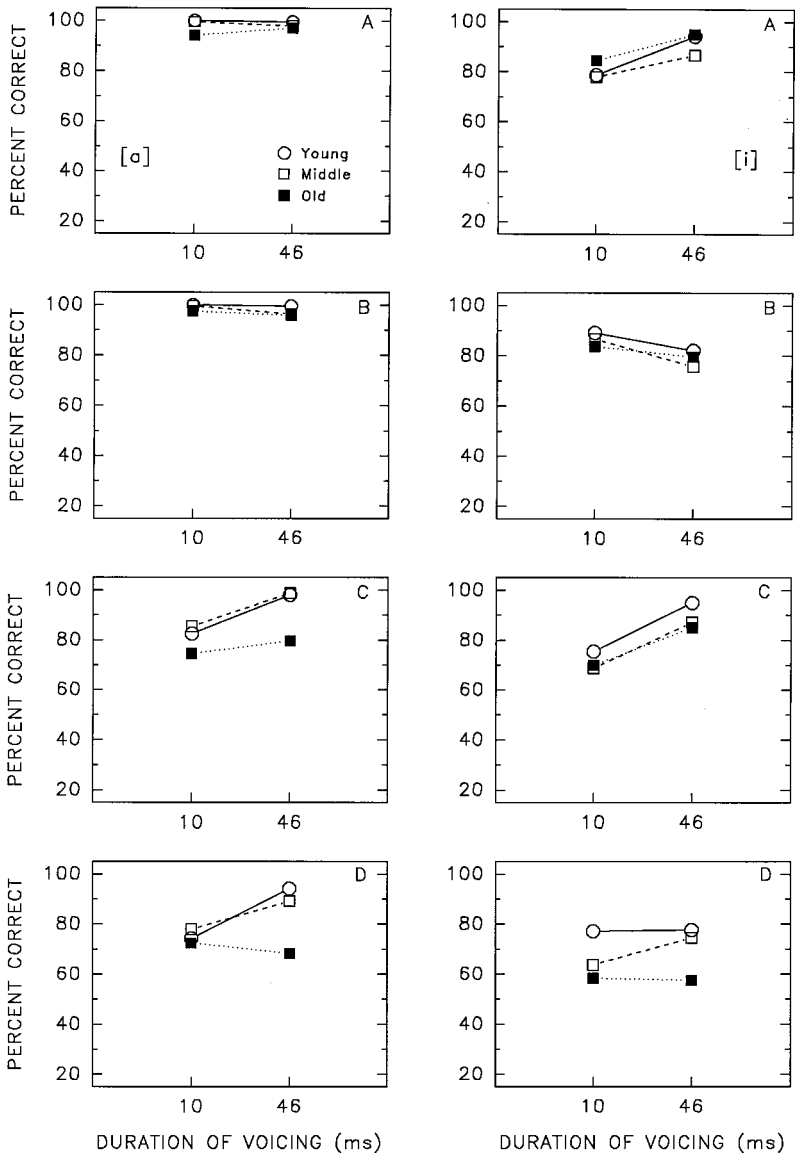

FIG. 1. Percent-correct stop-consonant identification of stimuli with bursts and moving transitions (A), with bursts and straight transitions (B), with no bursts and moving transitions (C), and with no bursts and straight transitions (D) as a function of duration, vowel, and listener age.

parameters. The experimental stimuli had durations of 10, 30, or 46 ms, appropriate bursts, and either moving or straight transitions according to two experimental conditions. The synthesis parameters were modeled after Blumstein and Stevens (1980), and were identical to previous investigations on children's vowel perception (Ohde *et al.*, 1996; Ohde and Haley, 1997). A total of 54 experimental stimuli was produced (3 vowels×3 consonants×3 durations×2 formant transition conditions).

2. Subjects

The subjects in the middle-aged and older groups were the same ones described in experiment I. The subjects in the young group were eight adults ranging in age from 21:0 to 25:9 years, with a mean of 23:2 years (Ohde *et al.*, 1996). Four of the subjects were female and four were male. Two of these subjects (both female) participated in experiment I.

3. Procedure

The two experimental conditions were presented separately within each consonant context. The order of consonant context was counterbalanced across subjects. The stimuli with moving transitions were presented first, followed by the straight transition stimuli (see footnote 1). The nine stimuli (3 vowels×3 durations) in each of these conditions were repeated ten times and presented in a random order with a 3-s interstimulus interval. The subjects were asked to identify the vowel in a 3AFC procedure. The subjects responded by pushing one of three buttons, labeled "i," "u," and "*a*" on the response box. All other testing procedures were identical to experiment I.

Reliable performance throughout the testing was insured by monitoring the subjects' responses to synthesized control stimuli inserted among the experimental stimuli. Fifteen control stimuli were inserted within each experimental condition of 90 stimuli and subjects were required to correctly identify at least 11 of these. If performance was below this level, the

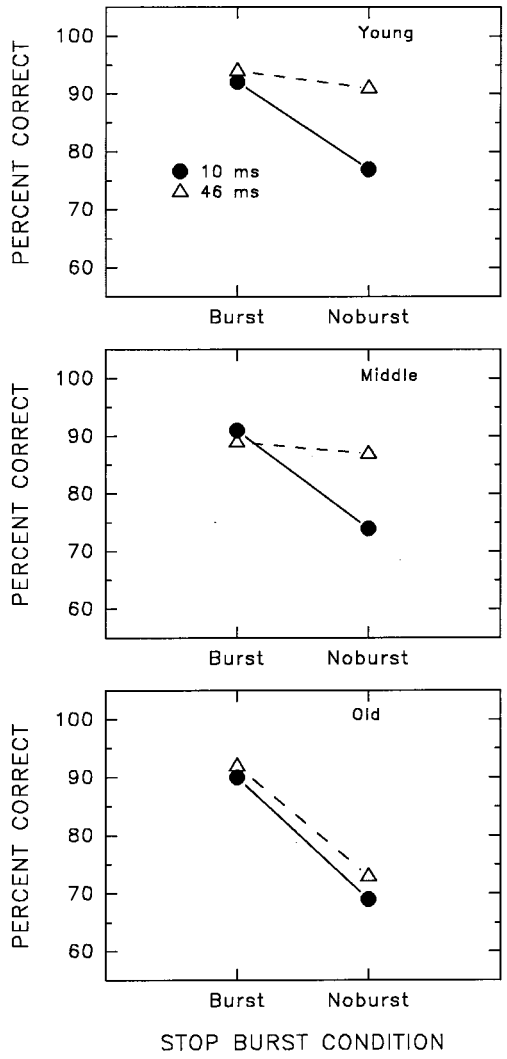

FIG. 2. Percent-correct stop-consonant identification as a function of burst and duration conditions, and listener age.

data from that subject would have been discarded and practice resumed; however, performance was always sufficiently high and practice was not reinstated for any subject.

4. Statistical analyses

A repeated measures analysis of variance on the arcsine-transformed percents collapsed across consonant place of articulation was used to analyze the data. This analysis included the between factor of age (young, middle-aged, and old) and the within factors of vowel ([i], [*a*], and [u]), transition type (straight and moving), and voicing duration (10, 30, and 46 ms). Follow-up analytical comparisons including tests of simple main effects and appropriate Newman Keuls' *post hoc* tests were used to examine relevant significant interactions (Keppel, 1991). Significant results at the $p<0.05$ or $p<0.01$ levels are reported.

B. Results and discussion

As Fig. 3 shows, vowel identification for all age groups was generally high. Vowel identification was somewhat lower for straight transition stimuli. This was particularly the case for the old group and the [u] vowel. An analysis of variance for the vowels across consonant place of articulation showed significant main effects of vowel [$F(2,42)=4.62$; $p<0.05$], transition [$F(1,21)=12.55$; $p<0.01$], and duration [$F(2,42)=16.31$; $p<0.01$].[3] Because there were no significant effects of age or age interactions, vowel identification was comparable across a wide age range of adults.

As reported previously for adults and children (Blumstein and Stevens, 1980; Ohde *et al.*, 1995; Ohde *et al.*, 1996; Ohde and Haley, 1997), formant transition motion improved vowel identification for young, middle-aged, and older adults. However, this improvement with moving transitions over straight transitions for vowel identification was generally small. Thus, the static formant onsets appear salient for the perception of the point vowels examined in this research.

These perceptual findings are consistent with results in production research showing that $F2$ and $F3$ transition onsets differentiate vowels with a wide range of place of articulation (Sussman, 1990). Sussman found that accurate classification of vowel place groups was about 88% using $F2$ and $F3$ onsets as input variables, and 96% using $F2$ and $F3$ vowel targets. Thus, place-of-vowel articulation is clearly present at the first glottal pulse following the release burst.

V. GENERAL DISCUSSION

A. Age differences: Consonant perception

The results of this experiment show that the secondary cues of formant motion, duration, and noise burst are important aids to identification, particularly for consonants. Identification was generally better in the [*a*] context than the [i] context, and longer durations improved identification functions for the young and middle-aged groups. In addition, stop-consonant identification was generally higher for the burst and moving transition conditions.

Developmental differences were observed in consonant identification. In general, the performance of the older group was poorer than the young and middle-aged adults with the absence of secondary cues, particularly the burst, indicating a greater reliance of the older group than young and middle-aged groups on integrated cues for accurate perception. Considering the level of hearing ability in the older group, this finding may help explain why normally hearing older subjects have greater difficulty understanding speech, and is in accordance with previous findings (Price and Simon, 1984; Gelfand *et al.*, 1985; Dorman *et al.*, 1985; Elliott *et al.*, 1989; Fox *et al.*, 1992). The current results show that perceptual integration of the noise burst and vowel onset is important for accurate stop-consonant perception in older subjects. These subjects had relatively normal hearing. Since hearing deficits are common in aging adults, one characteristic of this age-related change in hearing could be problems in perceptual integration. Also, from the Price and Simon (1984), Elliott *et al.* (1989), and Gelfand *et al.* (1985) results, it can be concluded that duration is an important secondary cue to the perception of older subjects. The current results also showed that longer durations were helpful to consonant identification for the young and middle-aged groups, but not the old group.

Hazan and Rosen (1991) found that some young adult

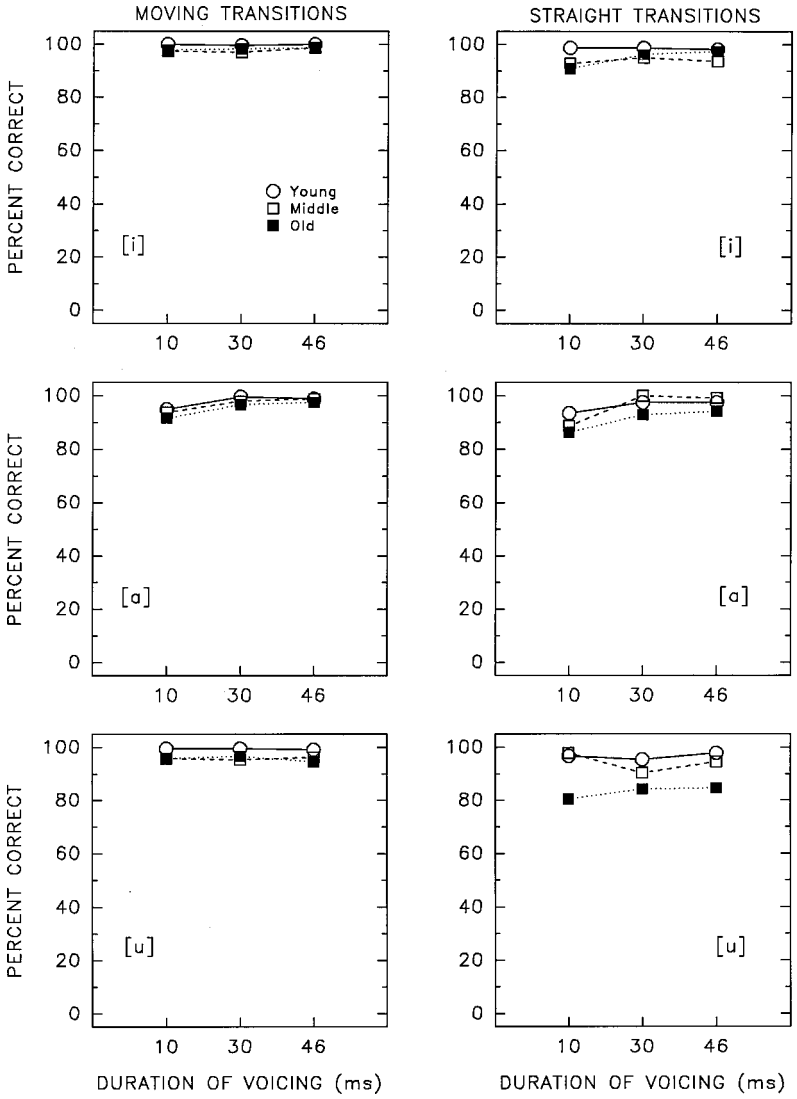

FIG. 3. Percent-correct identification for vowels as a function of duration, transition type, and listener age.

listeners generally had more difficulty labeling the dental stimuli in the reduced cue conditions while others experienced no difficulty. For those listeners who experienced difficulty, some subjects found the no-burst cues more difficult, others the straight transitions, and still others, the reduction of both cues. In the current research, the variability in perception of reduced cue stimuli was attributable to age effects. Older listeners did experience greater difficulty than younger listeners in the no-burst and straight transition conditions, implying that they rely on the integration of static and dynamic cues for accurate perception. This finding may also be attributable to age-related reductions in processing speed (Hale *et al.*, 1987; Myerson *et al.*, 1992; Wingfield, 1996) in older subjects. A consequence of this reduction may be the requirement of additional processing time; hence, the value of integrated cues to this population. Decreased memory efficiency may also be a factor in this finding. Pisoni (1973) noted that phonetic short-term memory is important to the categorization of consonants, and Massaro (1987) showed that short-term memory disturbances affect consonant discrimination. Therefore, decrements in short-term memory in the elderly population may also underlie the difficulty in consonant perception (Gordon-Salant and Fitzgibbons, 1997).

The Dorman *et al.* (1985) study also showed an effect of age on consonant perception. The performance of young adults on perception tasks was compared to that of older listeners with and without hearing impairments. Both elderly groups differed from the young adult group, leading the authors to conclude that identification is highly dependent upon the integration of static and dynamic cues in the older population. In fact, the older listeners were unable to base identification on the dynamic cues alone. However, the present findings showed no formant transition×age interactions indicating that young, middle-aged, or old subjects identified place of articulation of stop consonants from this dynamic cue similarly. The most accurate identification scores occurred in integrated cue conditions for all age groups, particularly the older subjects.

B. Age differences: Vowel perception

In the present study, as in the Dorman *et al.* (1985) one, all groups performed well in the vowel conditions. Because performance on the vowel stimuli was close to ceiling, any other effects may have been masked. Vowel identification remained high in all conditions, showing the saliency of the

vowel signal despite stimulus cue reduction. In fact, vowel perception fell to below 90% for only the old group in the [u] straight transition condition. Moreover, there were no statistically significant differences in vowel identification across age groups.

The results of the study of vowel perception by Fox *et al.* (1992) showed an effect of aging in that older subjects were worse than younger adults at identifying vowels from dynamic acoustic information. The current study generally found no differences in vowel identification across the different age groups. The differences in the results of the two studies may be attributable to the different designs employed. Fox *et al.* (1992) modified natural CVC syllables with the vowels replaced by silence (silent-center syllables), and required listeners to identify the vowel from these tokens as well as from the intact CVC syllables. Subjects were required to say aloud the word corresponding to the stimulus presented. Results showed that older adult listeners were poorer than younger adult listeners at utilizing the dynamic cues preserved in the silent-center conditions. The present study utilized synthesized syllables in which the dynamic cues of formant transition were either preserved or replaced by the constant onset value of the vowel. Because identification remained high for all age groups, it can be concluded that the static formant onsets were salient for vowel identification.

Another potentially important difference between these studies was response choice (Ohde, 1988). In the current research the subjects were required to identify the vowel as belonging to a finite set of three choices [i *a* u], whereas in the Fox *et al.* (1992) study the listeners were required to identify the vowel as being one of any used in the English language. In restricting choices to point vowels and providing static cue information, the current study differs significantly from the Fox *et al.* (1992) research. However, it is unlikely that response task is the basis for the variations in results. In an earlier study, Parnell and Amerman (1979) also used a 3AFC procedure to compare vowel and consonant perception in young adults (25–35 years) and older adults (62–79 years). The stimuli used in this research were edited segments of natural CV syllables comprised of voiceless stops and three vowels [i *a* u], and similar to the burst+moving transition and no burst+moving transition employed in the current research. Parnell and Amerman found that identification of both vowels and consonants were substantially and significantly poorer for older adults than younger adults. Because the response task was identical in the current research and the Parnell and Amerman study, differences in findings are unlikely based on the response paradigm. Overall, the current results do indicate that adults with relatively normal hearing between 25 and 76 years utilize short-duration formant onsets in vowel identification. The high vowel identification from formant onset cues suggests that these properties are equally important in perception as formant offsets and vowel targets, as has been previously claimed (Blumstein and Stevens, 1980).

C. Age-related deficit hypothesis

An important purpose of this research was to assess a hypothesis of adult perception of stop consonants and vowels specifically predicting changes in perception as a function of age for temporally and dynamically changing acoustic cues. The age-related deficit hypothesis predicts that as adults age they will have more difficulty in processing dynamically varying acoustic correlates of sound features such as formant transitions (Fox *et al.*, 1992). This deficit in perceiving dynamic cues could relate to changes with age in sensory processing such as decreased frequency resolution (Lutman, Gatehouse, and Worthington, 1991; Patterson *et al.*, 1982), or age-related reductions in processing speed (Hale *et al.*, 1987; Myerson *et al.*, 1992; Wingfield, 1996). The findings of experiment II for vowels provide no support for this hypothesis. Across all conditions, there were no significant age effects. Contrary to the age-related deficit hypothesis, there was a small but significant increase in vowel identification for the dynamically moving transitions compared to the straight transitions for all age groups, indicating that dynamic frequency change benefited listeners of all ages. Thus, adults ranging from 20 to 70 years of age were very accurate in vowel identification of stimuli with and without dynamic frequency changes.

In addition, the findings of experiment I for consonant perception provide no support for the age-related deficit hypothesis. Strong support for this hypothesis would derive from significant age×transition interactions across stop-consonant place of articulation. Older adults compared to younger adults should have more difficulty perceiving place of articulation of stop consonants from dynamically moving transitions. None of the age×transition interactions was significant, indicating that all age groups processed moving and straight transitions similarly for identification of place of articulation of stop consonants. Contrary to the predictions of this hypothesis, an examination of panels (C) and (D) of Fig. 1 clearly shows that 46-ms moving transitions (C) compared to 46-ms straight transitions (D) improved identification accuracy for all age groups.

It has been proposed that time-varying features are important properties in the identification of stop consonants (Fant, 1973; Kewley-Port, 1983; Stevens, 1985). For example, in the case of velar stops an important property is a prominent midfrequency spectral peak (Fant, 1973; Stevens, 1985). Presumably the long noise burst for [g] provides time for the build-up of the midfrequency spectral peak characteristic of this feature. Thus, an important property of velars is the slow change in spectral energy over a relatively long time interval. The findings showing significant improvement in identification for the no-burst conditions as a function of duration for young and middle-aged groups support the importance of time-varying features in stop-consonant perception. Moreover, the present findings showing that an increase in stimulus duration of the no-burst stimuli did not improve stop identification for the old group may be indicative of age-related reductions in processing speed (Hale *et al.*, 1987; Myerson *et al.*, 1992; Wingfield, 1996) that occur for stop-consonant stimuli containing important time-varying features (Kewley-Port, 1983).

VI. CONCLUSIONS

The findings of this research show that young, middle-aged, and older adults derive important cues from relatively short-duration stimuli for vowel and consonant identification. There were important similarities and differences in vowel and consonant identification as a function of age. Young, middle-aged, and older adults were generally similar in their utilization of dynamic formant transitions for vowel and consonant perception. In regard to timing cues, there was evidence that older adults were less efficient than young and middle-aged adults in the perception of stop consonants-based on temporal properties (Fant, 1973; Kewley-Port, 1983). In addition, there was evidence indicating that older adults relied more on the integration of secondary and primary cues for perception of place of articulation of stop consonants than younger adults. Based on these findings, the following conclusions are supported:

(1) Young, middle-aged, and older adults process dynamic spectral cues similarly contrary to the predictions of the age-related deficit hypothesis.
(2) Older adults' difficulty in identifying stop consonants for the no-burst conditions based on the duration cue indicates reductions in processing speed with age.

ACKNOWLEDGMENTS

This work was supported by NIH Grant No. DC00464 and a Vanderbilt University Research Council grant. The authors thank Dan Ashmead, Chris Turner, Terry Wertz, and two anonymous reviewers for comments on an earlier version of this paper.

[1]The presentation of this sequence was used because it progressed from synthetic sounds that were most natural to least natural. This sequence provided subjects some opportunity to listen to synthetic speech that was most similar to natural productions. Similar blocking procedures have been used in previous perception experiments (Repp, 1986; Ohde, 1994; Ohde *et al.*, 1995).

[2]Other significant interactions were as follows: burst×vowel $[F(1,21)=12.36;\ p<0.01]$, burst×transition $[F(1,21)=6.74;\ p<0.05]$, burst×duration $[F(1,21)=42.14;\ p<0.01]$, transition×duration $[F(1,21)=30.03;\ p<0.01]$, burst×vowel×duration $[F(1,21)=5.29;\ p<0.05]$, vowel×transition×duration $[F(1,21)=25.28;\ p<0.01]$, and burst×vowel×transition×duration $[F(1,21)=5.12;\ p<0.05]$.

[3]Significant interactions were as follows: vowel×transition $[F(2,42)=4.25;\ p<0.05]$, and vowel×duration $[F(4,84)=7.00;\ p<0.01]$.

Blumstein, S. E., Isaacs, E., and Mertus, J. (**1982**). ''The role of the gross spectral shape as a perceptual cue to place of articulation in initial stop consonants,'' J. Acoust. Soc. Am. **72**, 43–50.

Blumstein, S. E., and Stevens, K. N. (**1979**). ''Acoustic invariance in speech production: Evidence from measurements of the spectral characteristics of stop consonants,'' J. Acoust. Soc. Am. **66**, 1001–1017.

Blumstein, S. E., and Stevens, K. N. (**1980**). ''Perceptual invariance and onset spectra for stop consonants in different vowel environments,'' J. Acoust. Soc. Am. **67**, 648–662.

Bush, M. A. (**1977**). ''Integration of cues in the perception of stop consonants,'' SM thesis, M.I.T.

Coughlin, M., Kewley-Port, D., and Humes, L. E. (**1998**). ''The relation between identification and discrimination of vowels in young and elderly listeners,'' J. Acoust. Soc. Am. **104**, 3597–3607.

Dorman, M. F., Marton, K., Hannley, M. I., and Lindholm, J. M. (**1985**). ''Phonetic identification by elderly normal and hearing-impaired listeners,'' J. Acoust. Soc. Am. **77**, 664–670.

Dubno, J. R., Dirks, D. D., and Morgan, D. E. (**1984**). ''Effect of mild hearing loss on speech recognition in noise,'' J. Acoust. Soc. Am. **76**, 87–96.

Elliott, L. L., Busse, L. A., and Bailet, L. L. (**1985**). ''Identification and discrimination of consonant–vowel syllables by younger and older adults,'' Percept. Psychophys. **37**, 307–314.

Elliott, L. L., Hammer, M. A., Scholl, M. E., and Wasowicz, J. M. (**1989**). ''Age differences in discrimination of simulated single-formant frequency transitions,'' Percept. Psychophys. **46**, 181–186.

Fant, G. (**1973**). ''Stops in CV-syllables,'' in *Speech Sounds and Features*, edited by G. Fant (MIT, Cambridge, MA), pp. 110–139.

Fox, R. A. (**1989**). ''Dynamic information in the identification and discrimination of vowels,'' Phonetica **46**, 97–116.

Fox, R. A., Wall, L. G., and Gokcen, J. (**1992**). ''Age-related differences in processing dynamic information to identify vowel quality,'' J. Speech Hear. Res. **35**, 892–902.

Gelfand, S. A., Piper, N., and Silman, S. (**1985**). ''Consonant recognition in quiet as a function of aging among normal hearing subjects,'' J. Acoust. Soc. Am. **78**, 1198–1205.

Gordon-Salant, S., and Fitzgibbons, P. J. (**1997**). ''Selected cognitive factors and speech recognition performance among young and elderly listeners,'' J. Speech Lang. Hear. Res. **40**, 423–431.

Hale, S., Myerson, J., and Wagstaff, D. (**1987**). ''General slowing of non-verbal information processing: evidence for a power law,'' J. Gerontology **42**, 131–136.

Hazan, V., and Rosen, S. (**1991**). ''Individual variability in the perception of cues to place contrasts in initial stops,'' Percept. Psychophys. **49**, 187–200.

Keppel, G. (**1991**). *Design and Analysis: A Researcher's Handbook*, 3rd ed. (Prentice-Hall, Englewood Cliffs, NJ).

Kewley-Port, D. (**1983**). ''Time varying features as correlates of place of articulation in stop consonants,'' J. Acoust. Soc. Am. **73**, 322–335.

Klatt, D. (**1980**). ''Software for a cascade/parallel formant synthesizer,'' J. Acoust. Soc. Am. **67**, 971–995.

Lutman, M. E., Gatehouse, S., and Worthington, A. G. (**1991**). ''Frequency resolution as a function of hearing threshold level and age,'' J. Acoust. Soc. Am. **89**, 320–328.

Massaro, D. W. (**1987**). ''Categorical partition: A fuzzy-logical model of categorization behavior,'' *Categorical Perception: The Groundwork of Cognition*, edited by S. Harnad (Cambridge University Press, Cambridge, England), pp. 254–283.

Myerson, J., Ferraro, F. R., Hale, S., and Lima, S. D. (**1992**). ''General slowing in semantic priming and word recognition,'' Aging **7**, 257–270.

Ohde, R. N. (**1988**). ''Revisiting stop-consonant perception for two-formant stimuli,'' J. Acoust. Soc. Am. **84**, 1551–1555.

Ohde, R. N. (**1994**). ''The development of the perception of cues to the [m]–[n] distinction in CV syllables,'' J. Acoust. Soc. Am. **96**, 675–686.

Ohde, R. N., Haley, K. L., and McMahon, C. W. (**1996**). ''A developmental study of vowel perception from brief synthetic consonant–vowel syllables,'' J. Acoust. Soc. Am. **100**, 3813–3824.

Ohde, R. N., Haley, K. L., Vorperian, H. K., and McMahon, C. W. (**1995**). ''A developmental study of the perception of onset spectra for stop consonants in different vowel environments,'' J. Acoust. Soc. Am. **97**, 3800–3812.

Ohde, R. N., and Haley, K. L. (**1997**). ''Stop-consonant and vowel perception in 3- and 4-year-old children,'' J. Acoust. Soc. Am. **102**, 3711–3722.

Ohde, R. N., and Stevens, K. N. (**1983**). ''Effect of burst amplitude on the perception of stop consonant place of articulation,'' J. Acoust. Soc. Am. **74**, 706–714.

Parnell, M. M., and Amerman, J. D. (**1979**). ''Age and the decoding of coarticulatory cues,'' J. Speech Hear. Res. **22**, 433–445.

Patterson, R. D., Nimmo-Smith, I., Weber, D. L., and Milroy, R. (**1982**). ''The deterioration of hearing with age: Frequency selectivity, the critical ratio, the audiogram and speech threshold,'' J. Acoust. Soc. Am. **72**, 1788–1803.

Pisoni, D. B. (**1973**). ''Auditory and phonetic memory codes in the discrimination of consonants and vowels,'' Percept. Psychophys. **13**, 253–260.

Price, P. J., and Simon, H. J. (**1984**). ''Perception of temporal differences in speech by ''normal-hearing'' adults: Effects of age and intensity,'' J. Acoust. Soc. Am. **76**, 405–410.

Repp, B. H. (**1986**). ''Perception of the [m]–[n] distinction in CV syllables,'' J. Acoust. Soc. Am. **79**, 1987–1997.

Stevens, K. N. (**1985**). ''Spectral prominences and phonetic distinctions in language,'' Speech Commun. **4**, 137–144.
Stevens, K. N., and Blumstein, S. E. (**1978**). ''Invariant cues for place of articulation in stop consonants,'' J. Acoust. Soc. Am. **64**, 1358–1368.
Strange, W. (**1989**). ''Evolving theories of vowel perception,'' J. Acoust. Soc. Am. **85**, 2081–2087.
Sussman, H. M. (**1990**). ''Acoustic correlates of the front/back vowel distinction: A comparison of transition onset versus 'steady state','' J. Acoust. Soc. Am. **88**, 87–96.
van Rooij, J. C. G. M., and Plomp, R. (**1990**). ''Auditive and cognitive factors in speech perception by elderly listeners. II. Multivariate analyses,'' J. Acoust. Soc. Am. **88**, 2611–2624.
Walley, A. C., Pisoni, D. B., and Aslin, R. N. (**1984**). ''Infant discrimination of two- and five-formant voiced stop consonants differing in place of articulation,'' J. Acoust. Soc. Am. **75**, 581–588.
Wingfield, A. (**1996**). ''Cognitive factors in auditory performance: Context speed of processing and constraints on memory,'' J. Am. Acad. Aud. **7**, 175–182.
Working Group on Speech Understanding and Aging (**1988**). ''Speech understanding and aging,'' J. Acoust. Soc. Am. **83**, 859–895.

Application of multidimensional scaling to subjective evaluation of coded speech

Joseph L. Hall
Multimedia Communications Research Laboratory, Bell Labs, Lucent Technologies, Murray Hill, New Jersey 07974-0636

(Received 12 June 2000; revised 20 February 2001; accepted 12 June 2001)

We present results from a pilot study directed at developing an anchorable subjective speech quality test. The test uses multidimensional scaling techniques to obtain quantitative information about the perceptual attributes of speech. In the first phase of the study, subjects ranked perceptual distances between samples of speech produced by two different talkers, one male and one female, processed by a variety of codecs. The resulting distance matrices were processed to obtain, for each talker, a *stimulus space* for the various speech samples. This stimulus space has the properties that distances between stimuli in this space correspond to perceptual distances between stimuli and that the dimensions of this space correspond to attributes used by the subjects in determining perceptual distances. Mean opinion scores (MOS) scores obtained in an earlier study were found to be highly correlated with position in the stimulus space, and the three dimensions of the stimulus space were found to have identifiable physical and perceptual correlates. In the second phase of the study, we developed techniques for fitting speech generated by a new codec under investigation into a previously established stimulus space. The user is provided with a collection of speech samples and with the stimulus space for these speech samples as determined by a large-scale listening test. The user then carries out a much smaller listening test to determine the position of the new stimulus in the previously established stimulus space. This system is anchorable, so that different versions of a codec under development can be compared directly, and it provides more detailed information than the single number provided by MOS testing. We suggest that this information could be used to advantage in algorithm development and in development of objective measures of speech quality.
 [DOI: 10.1121/1.1397322]

PACS numbers: 43.71.Gv, 43.72.Gy, 43.71.Bp [DOS]

I. INTRODUCTION

In order to determine how various speech-processing systems compare with each other, it is necessary to be able to compare the quality of speech produced by these systems. The most sensitive way to making this comparison is to run paired comparisons among all versions; but as the number of versions increases, the number of paired comparisons that need to be made increases sharply. More commonly used methods establish a quality rating. Ratings procedures include the *Diagnostic Acceptability Measure* (DAM) (Voiers *et al.*, 1990), in which trained and calibrated listeners evaluate test material on several carefully developed scales, and the *Mean Opinion Score* (MOS) (ITU-T P.800, 1996, Annex B), an absolute category rating test in which untrained listeners assign scores on a five-point scale. Other tests have been developed to provide higher sensitivity than MOS. These tests include *Degradation MOS* (DMOS) (ITU-T, *op. cit.*, Annex D), a differential category rating test in which each test sample is preceded by a high-quality reference, and subjects rate the degradation of the test sample relative to the reference, and *Comparison MOS* (CMOS) (ITU-T, *op. cit.*, Annex E), a comparison category rating test in which each test sample precedes or follows a fixed reference that may be of higher or of lower quality than the test sample, and listeners rate the quality of the second sample relative to the first. For a discussion and comparison of these category rating tests, the reader is referred to Thorpe (1999).

These methods provide useful results, but each has limitations. The DAM provides information about several attributes of the speech, but it cannot be used with naïve listeners. The category rating tests can be used with naïve listeners, but they share the property that they provide only a single number to describe speech quality. This property is desirable for acceptance testing, but it does not provide the sort of diagnostic information that the DAM can provide and that would appear to be useful for algorithm development and for the development of objective measures of speech quality (Quackenbush *et al.*, 1988; Thorpe and Yang, 1999). A major limitation of MOS testing (but not of DMOS or CMOS) is that a listener's judgment about a test sample can be considered only in the context of the complete test. Listeners differ, and also it seems reasonable to assume that if a particular sample is included among other samples of low quality it will receive a higher rating than if it included among other samples of high quality. The P.800 recommendation specifies that ''Every experiment should include reference conditions so that experiments made in different laboratories or at a different time in the same laboratory can be sensibly compared'' (ITU-T, *op. cit.*, B.2.3). Because of variations among listeners and among speech samples, a listener's rating of a test sample cannot be meaningfully viewed in isolation.

Some very powerful multidimensional scaling techniques have been developed that appear to be applicable to

the determination of speech quality and to overcome some of the limitations mentioned above. Some of these methods are described in Sec. II. The technique we use here is weighted multidimensional scaling (individual differences scaling, or INDSCAL). With this technique, it is possible to determine the perceptual space underlying collections of objects, in this case samples of coded speech. Speech samples that are close together in this perceptual space, called the *stimulus space*, are perceptually close: they sound similar. Samples that are far apart sound different. Furthermore, and this is most important for our present application, the dimensions of this stimulus space correspond to the attributes that listeners use when judging the perceptual distance between samples. The position of a speech sample in this stimulus space is in a very real sense a description of what the speech sample sounds like.

We suggest that this quantitative description of the perceptual attributes of speech processed by various codecs could be useful in the field of algorithm development and in the development of objective measures of speech quality. The single composite judgment of quality provided by MOS testing is essential for acceptance testing, but it does not tell us *why* the quality is good or bad. Weighted multidimensional scaling has the potential of quantifying the performance of codecs relative to the perceptual attributes actually used by listeners in differentiating among speech samples. This is much the same sort of information as is provided by the diagnostic acceptability measure, except that with the DAM the perceptual attributes are specified in advance by the experimenter and with the multidimensional scaling procedure the perceptual attributes are determined by the experiment. The relationship between the two measures should be a fruitful field for future research (Voiers, 2000).

We propose the following as an anchorable speech quality test that utilizes these properties of weighted multidimensional scaling: First, select several, perhaps eight or ten, samples of coded speech that span the perceptual space under question. This is a nontrivial task and should be the subject of future research. We suppose that it would be sufficient to select samples of speech generated by several different systems of the same family as the system under investigation, such as, for example, Code Excited Linear Prediction (CELP) codecs, with different bit rates such that some are superior to and others inferior to the system under investigation. Note that this task would be more feasible for algorithm development, where the properties of the system are known reasonably well in advance, than it would be for acceptance testing, where it might be necessary to compare quite different codecs. Second, carry out a listening experiment to establish the stimulus space for these speech samples. This experiment will be time consuming, because comparisons among all the samples will have to be made by several subjects, but it only has to be done once. To run this test in the field, the user conducts a much shorter listening test in which speech generated by the system under investigation is compared to the eight or ten fixed samples. The speech under test can then be fitted, using methods described in this report, into the previously established stimulus space.

We begin with a brief review of multidimensional scaling techniques. An understanding of these techniques, particularly of individual difference multidimensional scaling, is essential for an appreciation of the test proposed here.

We next present results from a pilot listening experiment in which subjects ranked perceptual distances between samples of speech processed by a variety of codecs. Results for two different talkers, one male and one female, are processed separately by weighted multidimensional scaling to obtain stimulus and subject spaces for the two talkers. In general, the stimulus and subject spaces can be of any number of dimensions; in the present experiment, three dimensions sufficed. The stimulus spaces for the two talkers are highly correlated with each other but are not identical. This result is consistent with the view that different codecs affect different voices differently.[1] There is a close mapping between position in the stimulus space and MOS scores obtained in an earlier study, and the dimensions of the stimulus space have identifiable perceptual and physical correlates. The first and most important of the three dimensions of the stimulus space correlates very highly with MOS. Perceptually, subjects identify it with naturalness. Signals at the ''unnatural'' extreme of this dimension tend to have either very high or very low levels of high-frequency energy. The second and third dimensions are less highly correlated with MOS. The second dimension is identified perceptually with noisiness or distortion and physically with relative amount of high-frequency energy. The third dimension is identified perceptually with fullness or amount of low-frequency sound and physically with relative amount of low-frequency energy.

Finally, we describe a procedure for fitting a new stimulus into a previously established stimulus space. Development of this procedure involved modifying existing multidimensional scaling programs. We evaluated the procedure by appropriate manipulation of the experimental data to simulate the proposed test. Our conclusion is that the proposed procedure is feasible.

II. A BRIEF REVIEW OF MULTIDIMENSIONAL SCALING TECHNIQUES

Multidimensional scaling techniques were developed in the 1960s and 1970s to ''uncover the hidden structure of data bases'' (Kruskal and Wish, 1990). They are a class of techniques that map dissimilarities among objects as input to a spatial representation of these objects as output. They use various optimization procedures to minimize the discrepancy, according to some criterion, between the input dissimilarities and the output distances. The interested reader is referred to Kruskal and Wish (*op. cit.*) or to Young and Harris (1997) for a discussion of these procedures.

The basic concepts of *classical* multidimensional scaling include the *dissimilarity matrix* and the *object* (or *stimulus*) *space*. In an example that is widely cited in the literature (see, for example, Kruskal and Wish, *op. cit.*; and Young and Harris, *op. cit.*), the dissimilarity matrix is a table of flying mileages between 10 U.S. cities. The multidimensional scaling program determines the arrangement of objects (in this case cities) in an n-dimensional object space that minimizes the disparity between the Euclidean distances given in the

dissimilarity matrix and Euclidean distances in the object space, in the least squares sense. In this example, the data are well fitted by a two-dimensional object space, which does not come as a surprise because we know that a map of the United States can be projected onto a plane with little distortion. The two-dimensional object space superimposes almost exactly on a map of the United States, with north at an angle of about 10° from the vertical. This is an example of *classical metric* multidimensional scaling. There is only a single dissimilarity matrix (classical), and the numbers in the dissimilarity matrix are a linear transformation of the distances between objects (metric). An example of the application of classical multidimensional scaling to perceptual evaluation of codecs can be found in Precoda and Meng (1997).

A problem with metric multidimensional scaling in human listening experiments is that listeners are required to associate numbers with dissimilarities. Different listeners use numbers differently, and it is difficult for a listener to use numbers consistently throughout the course of a listening test. A test in which listeners are required to rank order dissimilarities, so that judgments are of the form ''greater than'' or ''less than,'' is more satisfactory in this respect. Tests of this sort can be analyzed by *nonmetric* multidimensional scaling, in which the numbers in the dissimilarity matrix are a rank ordering of the distance between objects. In our example, the two cities that are closest together receive a rank ordering of one, and the two cities that are furthest apart receive a rank ordering of 45. (With 10 cities there are 45 intercity distances.) The criterion used by the multidimensional scaling program is that the rank ordering of distances in the stimulus space agree with the rank ordering of input dissimilarities. According to Young and Harris (*op. cit.*, p. 127), the nonmetric minimization problem is much more difficult than the metric problem and requires an iterative solution. In our airline mileage example, the result of applying nonmetric classical multidimensional scaling to this dissimilarity matrix is an object space that differs only slightly from the first one.

Rank ordering the intercity mileages is easy; it involves simply sorting 45 numbers. In practice, when a listener is asked to make judgment about the relative dissimilarities of auditory stimuli, rank ordering more than a few stimuli becomes very time consuming and puts unacceptable demands on the listener's memory. A technique that has been developed to solve this problem is the *method of triadic comparisons*. Rather than being presented with all n stimuli and being asked to rank order their dissimilarities, the subject is presented with stimuli three at a time and is asked to judge which two of the three are most dissimilar and which two of the three are most similar. The most dissimilar pair is given a score of two, the most similar pair is given a score of zero, and the remaining pair is given a score of one. This process is repeated for all $\binom{n}{3}$ triads of the n stimuli taken three at a time, and the scores resulting from each triad are added up to obtain the dissimilarity matrix. An advantage of this method is that each trial is completely self-contained. The subject's judgment on a given trial is based only on the three stimuli that are presented on that trial. This differs from MOS testing, in which the subject's judgment on a given trial is influenced in an uncontrolled manner by stimuli presented on other trials. The method of triadic comparisons does *not* allow for direct comparison of all $\binom{n}{2}$ stimulus pairs, so that with sparsely populated stimulus spaces some distortion is possible. In our flying-mileages example, the stimulus space resulting from the method of triadic comparisons differs from the original stimulus space; but in spite of the drastically modified task, the basic structure remains unchanged.

The flying-mileage example used so far is in a way unfortunate. It is fortuitous that the dimensions of the object spaces correspond approximately to points of the compass. The only data available is distances between pairs of cities, so that any reflection or rotation of the stimulus space would be equally valid. It happens to turn out this way for this example because the analysis program chooses dimensions such that the first dimension is the longest, and by chance west comes out to the left and north to the top. The only information used by classical multidimensional scaling is a single distance matrix, the solution is rotatable, and no meaning can be ascribed to the dimensions in the solution. This is not the case with *weighted* multidimensional scaling (Carroll and Chang, 1970). In the model used in weighted multidimensional scaling, all subjects base their judgments on the same dimensions but different subjects weight these dimensions differently. Results obtained from weighted multidimensional scaling include not only a stimulus space but also a *subject space*, a space that shows the weight given to each of the dimensions in the stimulus space by each of the subjects. Weighted multidimensional scaling is also referred to as *individual differences* scaling, or INDSCAL.

The solution space generated by weighted multidimensional scaling is not rotatable: the dimensions of the stimulus space and the subject space are dictated by the data and are not arbitrary. This is an extremely important property. It means that we can ask listeners to make judgments about similarities or differences among speech samples without specifying what features they should base these judgments on; and, to the extent that the assumptions of the model are valid, we can determine the relevant features from the experimental results.

A procedure that is in some sense intermediate between classical multidimensional scaling, which produces only a stimulus space, and INDSCAL, which produces separate stimulus and subject spaces, is *multidimensional preference* scaling, or MDPREF (Carroll, 1972). The input to MDPREF is a collection of preference matrices obtained from paired-comparison judgments by several subjects, and the output is a stimulus space. Each subject is represented by a vector in this stimulus space, and the preferences of each subject are represented by the projection of the various stimuli onto this vector. This procedure has much to recommend it, and it has been used in studies of speech quality (McDermott, 1969; Huggins *et al.*, 1977). It differs from INDSCAL in that stimuli are characterized in terms of preference rather than dissimilarity, so that two samples that are degraded equally, but for quite different reasons, could map to the same point in the stimulus space.

In the experiments described in the next section, we used the method of triadic comparisons to elicit judgments

TABLE I. Coders used for male talker. These same coders, except for C00, Q15, and Q25, were also used for the female talker.

Coder	Description
SRC	Original source
C00	13 kb/s CELP
FT8	8 kb/s ACELP
G26	32 kb/s ADPCM
GSM	13 kb/s RPE-LTP
M13	13 kb/s CELP
Q15	15 dB MNRU
Q25	25 dB MNRU
RC50	5 kb/s RCELP
TS	8.5 kB/s CELP

about the perceptual distances between pairs of speech samples, and we analyzed the experimental results using INDSCAL. Analysis of these experimental results has the potential of revealing the underlying perceptual features used by subjects in characterizing these stimuli.

III. LISTENING EXPERIMENT

A. Methods

1. Stimuli

The stimuli used in this experiment were samples of speech processed by various speech codecs (Kroon, 1994). The speech samples were band limited to less than 4 kHz and originally sampled at 8 kHz. They were upsampled to 16 kHz for compatibility with stimulus presentation equipment. Speech for the male talker was an 8.2 s sample, with the talker saying ''The rush for funds reached its peak Tuesday. The birch looks stark white and lonesome. The box is held by a bright red snapper.'' Speech for the female talker was an 8.6 s sample, with the talker saying ''The beam dropped down on the workman's head. Pink clouds floated with the breeze. She danced like a swan, tall and graceful.'' For each talker, the source file was processed by several different codecs. The codecs used for the male talker are given in Table I. A subset of seven of these codecs (SRC, FT8, G26, GSM, M13, RC50, and TS) was used for the female talker.

2. Stimulus presentation

Stimuli were presented by, and the experiment was controlled by, a Hewlett Packard Kayak XU PC outfitted with a Tucker–Davis Technologies System II digital signal processing platform. All stimuli were stored on disk. They were converted with a TDT DA3-4 D/A converter, filtered and amplified with a PA4 programmable attenuator, an FT6-2 6.5 kHz antialiasing filter, and a HB6 headphone buffer, and presented to the subject monaurally at a comfortable listening level through Sennheiser HD-600 headphones. The subject sat inside a double-walled Industrial Acoustics Company soundproof booth.

The subject held a response box with six buttons arranged in a hexagon. Three of these buttons (top, lower left, and lower right) were white, and the other three buttons (upper left, upper right, and bottom) were green. Three coded versions of the speech were used in a given trial. The speech sample was presented in a continuous loop, and the subject could switch from one version to another by pushing one of the three white buttons. This switching could occur at any time during the speech sample. Within 100 ms of the time the subject pushed one of the white buttons, the stimulus faded with a 10 ms linear ramp from one version to another. At all times, the white button corresponding to the version being presented was illuminated.

The subject was instructed to listen to the three versions for as long as desired, and then to push the green button between the two versions that sounded the most different. (For example, if the versions corresponding to the top and lower left white buttons were most different, the subject was to push the upper left green button.) This green button then lit up. The subject continued listening to the three versions for as long as desired and then pushed the green button between the two versions that sounded the most similar. At this point all the lights went out, and after a short pause the next trial began with another three coded versions. Subjects were given a sheet of printed instructions. A typical instruction sheet is reproduced in Appendix A.

There were $\binom{10}{3}=120$ triads for the male talker and $\binom{7}{3}=35$ triads for the female talker. These triads were presented in random order, with a different randomization for each subject. For the male talker, after a five-trial practice session results were typically collected in four sessions of 30 trials each. For the female talker, results were typically collected in a single session. Subjects typically completed a session in 15 minutes or less. Sessions were not allowed to run longer than 30 minutes. If the subject had not completed the assigned triads within 30 minutes, the session was terminated and the remaining triads were presented in another session.

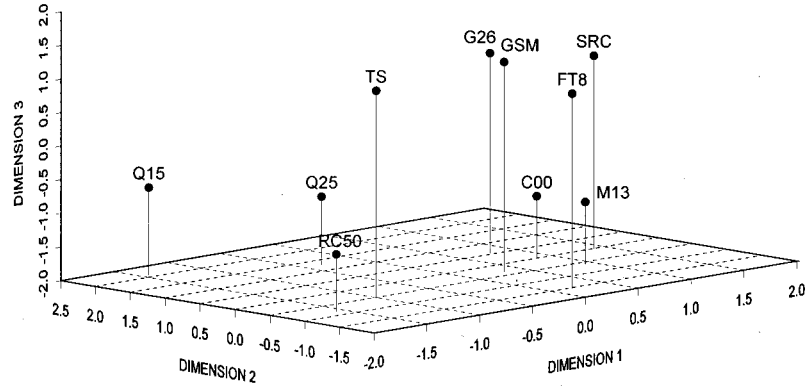

FIG. 1. 3D plot of stimulus space.

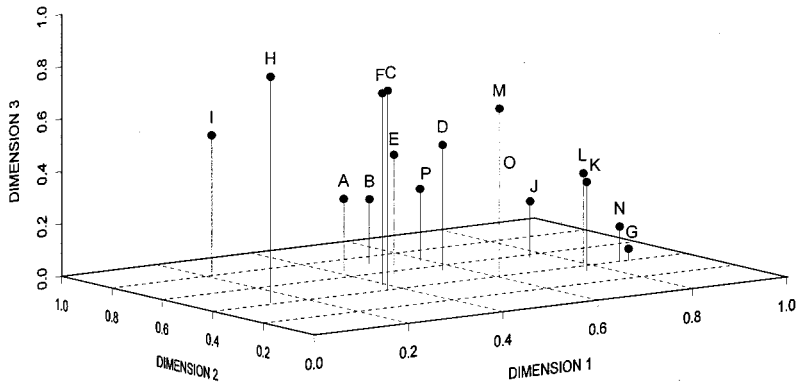

FIG. 2. 3D plot of subject space.

3. Subjects

Sixteen subjects participated in the experiment. They ranged in age from 26 to 67 years. Audiograms were run on both ears of each subject prior to the experiment. If there was any asymmetry between the two ears, the experiment was done using the subject's better ear. Otherwise, the left or right ear was chosen at random. None of the subjects had a threshold elevation greater than 30 dB below 4 kHz, the highest frequency in the speech. In the frequency range from 4 to 8 kHz, the three oldest subjects all had threshold elevations between 40 and 50 dB. Fourteen of the subjects were male and two were female. All were members of the Bell Labs Acoustics and Speech Research Department and had some prior experience in listening to coded speech.

4. Analysis of experimental results

Multidimensional scaling of the experimental results was done by means of SPSS Professional Statistics™ Version 8.0. Further analysis and display of the experimental results was done by means of SPSS Version 8.0 and S-PLUS™ Version 4.5.

B. Results

1. Male talker

a. Stimulus space. The stimulus space derived for the ten speech samples used with the male talker is shown in Fig. 1. The coordinates are given in Appendix B. Several criteria, including variance accounted for, residual stress, and average weight given by the listeners to each dimension, indicate that three is an appropriate number of dimensions.

b. Subject space. Figure 2 shows the derived subject space for the 16 subjects that participated in the experiment. The coordinates are given in Appendix B. These are the weights given to each of the three dimensions by each subject.

As was explained in Sec. II, it is necessary to use weighted multidimensional scaling on experimental results from several subjects if any meaning is to be ascribed to the dimensions of the stimulus space. It is therefore important that the different subjects ascribe different weights to the various dimensions, and Fig. 2 shows that this is the case. Other than that, it is unclear what the importance of the subject space is for our purposes. As will be seen below, the subject spaces obtained for the male and female talkers have little in common. We note in passing that, for the male talker, the older subjects tended to give less weight to dimension 1 than did the younger subjects, and the older subjects tended to give more weight to dimension 3 than did the younger subjects. We have no explanation for this observation; the only measurable distinction of the older subjects was elevated thresholds above 4 kHz, and the stimuli were band limited to less than 4 kHz.

c. Mean opinion scores. Figure 3 is identical to Fig. 1 except that each data point is labeled with an MOS score rather than the name of a codec. These scores were extracted from a large-scale MOS test done at COMSAT Laboratories, Clarksburg, MD (Kroon, *op. cit.*). Each MOS score is an average from 10 listeners and four sentence pairs for this particular talker.

These MOS scores are correlated with dimension 1, as is

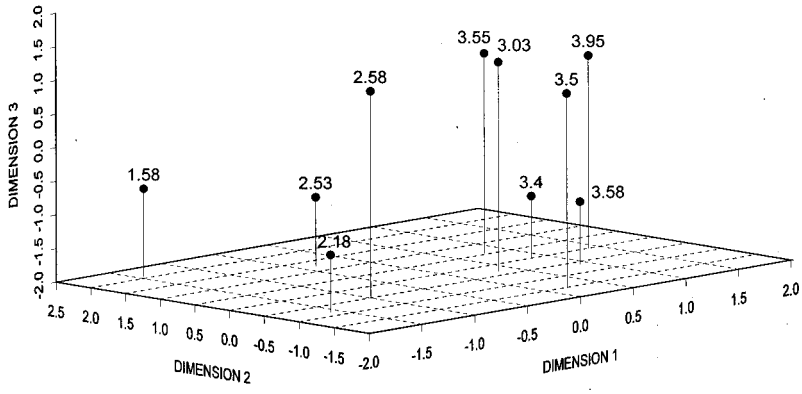

FIG. 3. Similar to Fig. 1, except that data points are labeled with MOS score rather than name of coder.

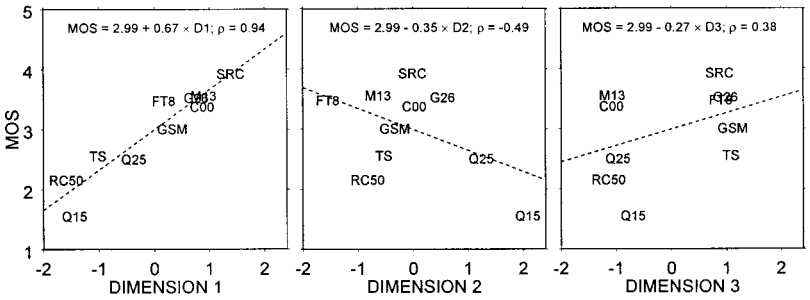

FIG. 4. MOS scores plotted vs dimension 1 (left panel), dimension 2 (center panel), and dimension 3 (right panel).

shown in the left panel of Fig. 4. The correlation coefficient is 0.94. MOS scores are less highly correlated with dimensions 2 and 3, as is shown in the center and right panels. The correlation coefficient with D2 is -0.49, and the correlation coefficient with D3 is 0.38. The dashed line in each panel shows the one-dimensional linear regression of MOS on each dimension.

Figure 5 shows the result of a three-dimensional linear regression of MOS on dimensions 1, 2, and 3. The regression line is

$$\text{PREDICTED MOS} = 2.99 + 0.61 \times \text{D1} - 0.20 \times \text{D2} + 0.05 \times \text{D3}.$$

The rms difference between measured and predicted MOS is 0.11 units. This is a remarkable result. Subjects in the present study were never asked to make any judgment about stimulus quality; the stimulus space is based solely on judgments of perceptual distances between pairs of stimuli. Nevertheless, there is an extremely tight mapping between position in the derived stimulus space and mean opinion scores measured at a different time and place.

2. Female talker

The results presented thus far are encouraging. Perceptual distances between pairs of samples of coded speech can be represented by a three-dimensional stimulus space, and, as stated above, there appears to be a tight mapping between position in this stimulus space and MOS. These results become less interesting if they are valid only for the single talker used so far. If these results do not generalize to different talkers, so that different talkers generate stimulus spaces that have little in common with each other, then the utility of the procedure proposed in this study is called into question.

Accordingly, we repeated the experiment already described using the same procedures, the same subjects, and speech samples generated by a female talker. In order to reduce the size of the experiment, we reduced the number of stimuli from ten to seven by eliminating codecs C00, Q15, and Q25 (Q15 and Q25 because the degradation introduced was of a different type, and C00 because it was similar to M13). This reduced the number of triads that had to be presented from $\binom{10}{3} = 120$ to $\binom{7}{3} = 35$ and meant that we did not have to deal with a major rebellion of subjects.

In order to be able to make meaningful comparisons between the two sets of results, we first reanalyzed the subset of data from the male talker obtained by excluding all judgments that involved one of the excluded codecs. For each of the subjects, we selected the subset of 35 triadic comparisons made among speech from the male talker processed by one of the seven codecs used with the female talker. We then compared results from this modified analysis with results obtained from the female talker. This procedure is valid because, as previously explained, judgments from each triadic comparison are self-contained: because of the design of the experiment, these judgments are not influenced by speech samples presented in other triads.

The conclusion is that results for the male and female talkers are similar but not identical. The two stimulus spaces are highly correlated: the correlation coefficient for dimension 1 is 0.96, for dimension 2 is 0.86, and for dimension 3 is 0.68. Subject spaces for the male and female talkers are not highly correlated. In addition, MOS scores for the female talker are highly correlated with dimension 1 of the stimulus space ($\rho = 0.84$), less highly correlated with dimensions 2 ($\rho = -0.47$) and 3 ($\rho = -0.46$), and can be predicted using three-dimensional linear regression with a residual standard error of 0.27 units.

We should not expect stimulus spaces for the male and female talkers to be identical. Indeed, the observed differences highlight a potential strength of the multidimensional scaling procedure. As is mentioned in footnote 1, the P.800

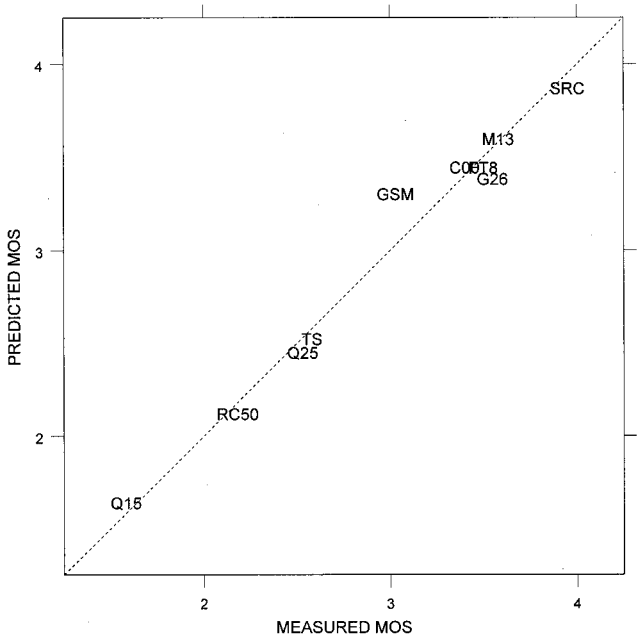

FIG. 5. MOS predicted from three-dimensional linear regression.

recommendation for MOS recognizes that codecs can affect different voices differently and specifies procedures for dealing with these differences. The goal of the multidimensional scaling procedure is not to reproduce MOS scores but rather to provide a quantitative description of perceptual attributes of coded speech, and the observed differences quantify the differences between the two talkers.

C. Subject judgment time

It is instructive to consider the time the subjects took to make the required dissimilarity judgments, both because it tells us something about the nature of the task the subjects are faced with and, at a practical level, it is relevant to the feasibility of using multidimensional scaling in an anchorable context-free speech quality test as described in Sec. I.

The mean time per judgment was 37 seconds. There were 16 subjects and, for the male talker, $\binom{10}{3}=120$ triads. An analysis of variance in which the factors influencing response time are assumed to be subject and triad, with no interactions, leads to the conclusion that both subject and triad effects are highly significant $[\Pr(F_{\text{Triad}})<0.015, \Pr(F_{\text{Subject}})<0.001]$. We will consider these two effects separately.

1. Subject effects

There was a more than three-to-one difference in mean judgment time among subjects, averaged across the 120 triads: the fastest subject took an average of 22 seconds per judgment, while the slowest subject took an average of 70 seconds per judgment. There is an interesting relationship between mean judgment time and proportion of variance in the scaled data that is accounted for by the solution. One group of subjects, the ''careful'' subjects, took between 20 and 70 seconds per judgment and were well fitted by the model: the variance accounted for was generally well above 80%. The other subjects could be described as rushing through the task: they took less than 30 seconds per judgment and were less well fitted by the model, with variance accounted for as low as 63%.

2. Stimulus effects

There was more than a two-to-one difference among mean judgment time for the 120 triads: subjects took an average of less than 25 seconds for the fastest triads and more than 50 seconds for the slowest. The reason for this difference is shown in Fig. 6. This figure is extremely interesting because of what it tells us about the nature of the judgments the subjects are required to make. The three vertical bars to the left, labeled ''FAST TRIAD,'' show the positions in the three-dimensional stimulus space of the three stimuli in one of the triads that subjects were able to judge rapidly. Regardless of which dimension we consider, it is easy to see that the most similar pair is S1 and S2. The most dissimilar pair is not quite as straightforward, but it is clear that it is either S1 and S3 or S2 and S3 (in fact, the distance between S1 and S3 in the stimulus space is slightly greater than the distance between S2 and S3). The three vertical bars to the right, labeled ''SLOW TRIAD,'' show the positions of the three stimuli in one of the triads that took a long time to judge. On

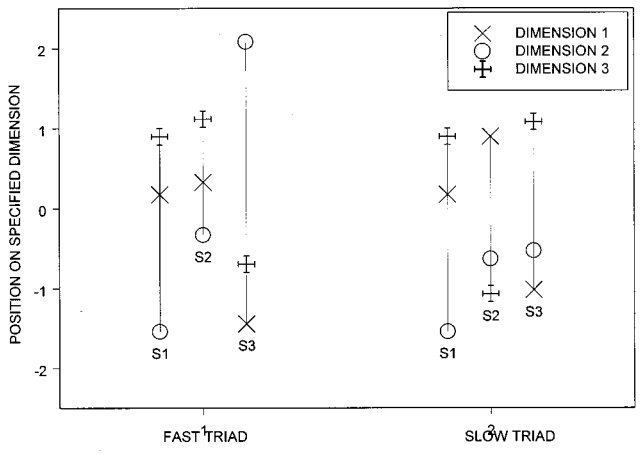

FIG. 6. Position in stimulus space of the three stimuli in a triad that was easy to judge (''FAST TRIAD'') and of the three stimuli in a triad that was difficult to judge (''SLOW TRIAD'').

dimension 1, S1 and S2 are the most similar; on dimension 2, S2 and S3 are the most similar; and on dimension 3, S1 and S3 are the most similar. Similarly, S2 and S3 are the most dissimilar on dimensions 1 and 3 while S1 and S3 are the most dissimilar on dimension 2. Subjects complained that judgments on triads such as this one were difficult because they could not decide what aspect of the stimuli to attend to.

IV. IDENTIFICATION OF DIMENSIONS

The results shown in Sec. III establish that weighted multidimensional scaling can be used to fit speech samples processed by the codecs used in this experiment into a three-dimensional stimulus space. We stated in Sec. II that, to the extent that the assumptions of the underlying model are valid, these dimensions are meaningful: they are in fact the relevant perceptual dimensions that subjects use when making dissimilarity judgments. In this section, we address the question of what the three dimensions of the stimulus space are. What perceptual attributes do they correspond to, and can we identify any physical correlates?

A. Perceptual attributes

In order to determine the perceptual attributes corresponding to the three dimensions, we carried out a second listening experiment, using as subjects the same 16 people who participated in the first experiment. The stimuli were the same coded versions of speech produced by the male talker that were used in the first experiment, and stimulus generation and presentation was the same as in the first experiment. This time, however, the subjects controlled which coded version they were listening to with a button box that had eight buttons in a row. One dimension was investigated at a time. The stimuli were ordered according to their position on the dimension being investigated. The stimuli were associated with the eight buttons monotonically according to their position on the dimension being investigated, so that the leftmost button produced the stimulus that was at one extreme of the dimension being investigated and the rightmost button produced the stimulus that was at the opposite extreme. As in the first experiment, subjects could change from one stimulus

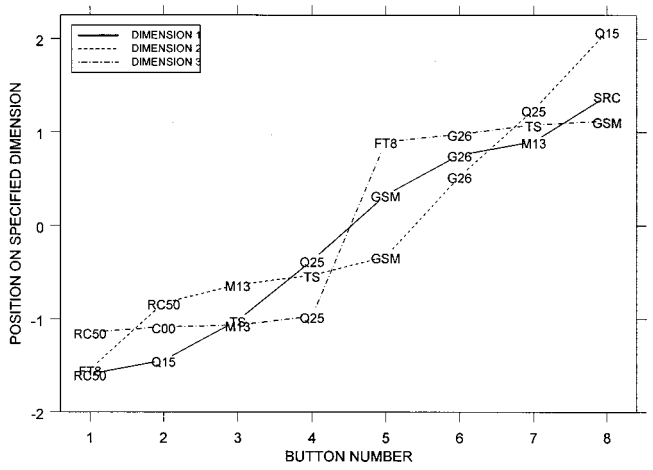

FIG. 7. Ordering of stimuli for identification of perceptual significance of each dimension.

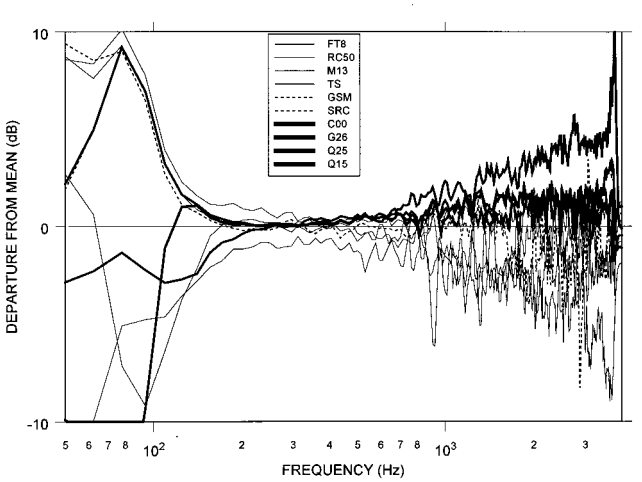

FIG. 9. Departure from average spectrum partitioned on dimension 2.

to another at any time: the stimulus faded from one version to another with a 10 ms linear ramp when a button was pushed. At all times, the button corresponding to the version being played was illuminated.

Since our button box had only eight buttons, we selected 8 of the 10 stimuli for each dimension. The eight stimuli used for dimension 1 were, in order, RC50, Q15, TS, Q25, GSM, G26, M13, and SRC. For dimension 2, they were FT8, RC50, M13, TS, GSM, G26, Q25, and Q15. For dimension 3, they were RC50, C00, M13, Q25, FT8, G26, TS, and GSM. The ordering of stimuli, as well as their position on each specified dimension, are shown in Fig. 7. The order in which the various dimensions were presented, as well as whether button #1 in Fig. 7 was the leftmost or rightmost button, were randomized from subject to subject.

For each dimension, the subjects were instructed to decide what attribute of the stimulus changed monotonically with button position and to describe this attribute in their own words. The instruction sheet for this experiment is reproduced in Appendix C. The subjects were given an answer sheet on which they could write their responses to the following questions.

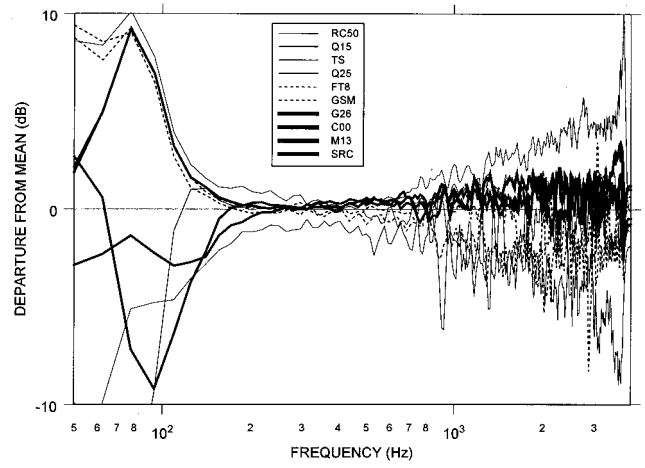

FIG. 8. Departure from average spectrum partitioned on dimension 1.

(i) The perceptual attribute of the stimulus that changes from button #1 to button #8 is: ____

(ii) This attribute increases/decreases (circle one, cross out the other) from button #1 to button #8.

(iii) Comments:

The subjects found this task difficult. In several cases they were not able to identify any attribute that changed monotonically with button position, and in cases where they were able to identify an attribute the responses varied widely. With these qualifications, it appears that the attribute most often identified with dimension 1 is naturalness, the attribute most often identified with dimension 2 is noisiness, and the attribute most often identified with dimension 3 is the amount of low-frequency content. The subjects' responses are summarized in Appendix D.

B. Physical correlates

We considered the average spectrum of each of the 10 speech samples in an effort to determine physical correlates of the three dimensions. We first computed the average power spectrum of each individual speech sample, using a 1024-point Hamming window, then averaged these 10 spectra (on a dB scale) to get the grand average power spectrum. Finally, we subtracted this grand average power spectrum from the average of each of the individual spectra to get the departure of each individual spectrum from the grand average. The results are shown in Figs. 8 (dimension 1), 9 (dimension 2), and 10 (dimension 3). In each figure, results for the 10 codecs are partitioned by line weight along the relevant dimension. In Figs. 8 and 9, the four codecs at one extreme of the relevant dimension are light and the four codecs at the other extreme are heavy. Since the transition from one extreme to the other is gradual for dimensions 1 and 2 and there is no clear division between two partitions, the two codecs in the middle are dashed. This is not the case for dimension 3; the codecs are positioned bimodally. Accordingly, the five codecs at one extreme in Fig. 10 are light and the five codecs at the other extreme are heavy.

Inspection of Figs. 8–10 reveals that we can make some weak statements about relationships between average spectrum and location on each of the three dimensions. Dimen-

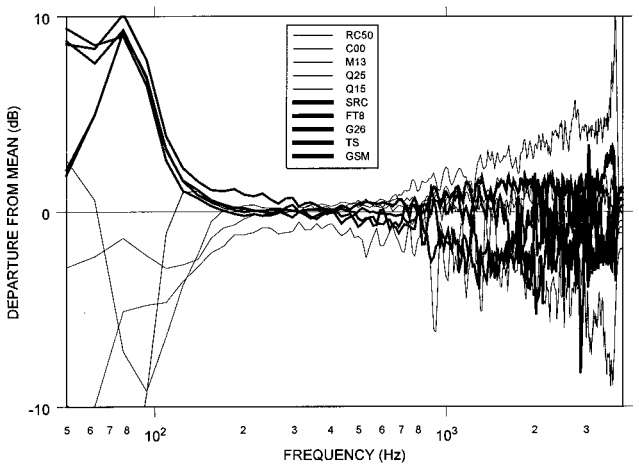

FIG. 10. Departure from average spectrum partitioned on dimension 3.

sion 1 is correlated with mean opinion score, and subjects tend to associate it with naturalness. Figure 8 shows that codecs that are at the ''unnatural'' end of dimension 1 (shown as thin lines) tend to have average spectra that deviate from the grand average spectrum at high frequencies, either above or below. Codecs that are at the ''natural'' end of dimension 1 (shown as heavy lines) tend to have average spectra that are close to the grand average spectrum.

Subjects tend to associate dimension 2 with noisiness. Figure 9 shows that codecs that are at the ''noisy'' end of dimension 2 (thick) tend to have average spectra that are above the grand average at high frequencies, and codecs that are at the opposite end (thin) tend to have average spectra that are below the grand average.

Subjects tend to associate dimension 3 with amount of low-frequency content. Figure 10 shows that codecs that are judged to have a greater amount of low-frequency content (thick) tend to have average spectra that are above the grand average at low frequencies, while codecs that are judged to have a lesser amount of low-frequency content (thin) tend to have average spectra that are below the grand average at low frequencies.

A similar analysis of spectra for the female talker leads to similar conclusions.

None of these relationships is particularly startling. We present them here as evidence that the dimensions provided by the multidimensional scaling program are meaningful both perceptually and physically, and therefore that the assumptions of the underlying model are valid.

V. A PROPOSED SPEECH QUALITY TEST

A. Introduction

We have established that, at least for the codecs used in this experiment, multidimensional scaling procedures can be used to establish a meaningful stimulus space for samples of coded speech. Different talkers generate similar stimulus spaces, the dimensions of this stimulus space appear to have meaningful physical and perceptual correlates, and the mean opinion score for a speech sample can be predicted accurately from its position in the stimulus space. These results are in themselves interesting and provide potentially useful insights into factors underlying the perception of coded speech. Beyond that, there is also a possibility that they can be implemented in an anchorable speech quality test that differs from conventional MOS testing in that it provides a quantitative description of the perceptual aspects of speech.

Consider what this test would look like from the user's point of view. The user is provided with (1) a source (uncoded) utterance, (2) a collection of several (perhaps 8 or 10) versions of this utterance processed by a variety of different codecs, (3) the stimulus space for the supplied utterances as determined by a listening test similar to the one described in this report, and (4) procedures for fitting a new utterance into the previously defined stimulus space. The user processes the source utterance through the new system to obtain a new coded utterance and carries out a listening test (we will refer to this test as the *field* listening test) to determine a distance vector between this new utterance and the 8 or 10 supplied utterances. Using this distance vector and supplied software, the user determines the location of the new utterance in the previously defined stimulus space. We suggest that this procedure will provide the user with a context-free anchorable measure by which each version of the system under development can be compared on an absolute basis with each other version. Furthermore, this quantitative description could perhaps provide diagnostic information useful for algorithm development or for development of objective speech-quality tests.

The provider of this test must first select coded utterances that span the anticipated stimulus space for the speech-processing systems under consideration. As was stated in the introduction, it is unclear exactly how this selection is to be made, and this is a subject for further investigation. Next, the provider carries out a large-scale listening test, similar to the one described in Sec. III of this report, to generate the stimulus space for these utterances. Several subjects make triadic comparisons among all n of the supplied utterances to generate $n \times n$ dissimilarity matrices, and weighted multidimensional scaling is applied to these dissimilarity matrices to obtain the stimulus space. As appropriate, the provider might also carry out listening tests to determine the relationship between position in the stimulus space and relevant perceptual properties of speech, such as MOS, or between position in the stimulus space and parameters of the speech-processing system under development. We stress that this test is *not* proposed as an alternative way of getting MOS scores. There are better ways to do this. However, for some applications it might be important for the user to know the mapping between position in the stimulus space and some properties of the speech or of the speech-processing system. Finally, the provider must supply to the user procedures for fitting a new unknown stimulus into the previously defined stimulus space.

Note that the field listening test carried out by the user would be much smaller than the listening test originally carried out to determine the sample space. With n supplied utterances, the original test would require judgments among $\binom{n+1}{3}$ triads (n supplied utterances plus the utterance under evaluation), but the field test would require judgments among only $\binom{n}{2}$ triads. Each triad would consist of the new

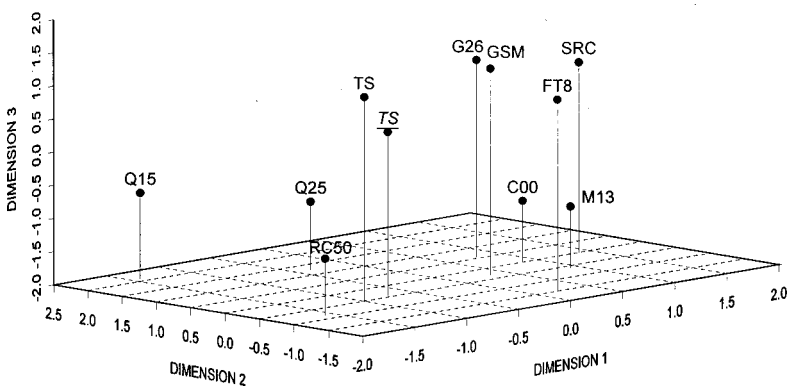

FIG. 11. Comparison of locations in stimulus space of coder TS as determined by weighted multidimensional scaling (''INDSCAL SOLUTION'' in Fig. 12, identical to Fig. 1, symbol TS) and by modified procedure (''RETROFIT SOLUTION'' in Fig. 12, symbol *TS*) for fitting new stimulus into established stimulus space.

unknown utterance and a pair of the supplied utterances, and there are $\binom{n}{2}$ such pairs. In general, the field test would be smaller than the original test by a factor of

$$\binom{n+1}{3} \Big/ \binom{n}{2} = \frac{n+2}{3}.$$

In Sec. V B, we present a procedure that we have developed for fitting a new utterance into an existing stimulus space, given a vector of distances between the new utterance and each of the utterances in the existing stimulus space. Using this procedure and subsets of our existing data, we have evaluated some aspects of the proposed speech quality test, including the ability of this test to predict the mean opinion score for a new utterance and the effect of reducing the number of listeners.

B. Procedure for fitting new utterance into existing stimulus space

In this section, we describe and assess a procedure for fitting a new utterance into an existing stimulus space. The procedure works as follows. First, carry out a listening test with several listeners to determine an n-dimensional vector of average dissimilarities between the new utterance and each of the n utterances in the existing space. Each listener makes triadic comparisons among the new utterance and each of the $\binom{n}{2}$ pairs of supplied utterances, and the resulting vectors from all listeners are averaged to obtain the average dissimilarity vector. Now, given this average dissimilarity vector, find the position of the new utterance in the existing stimulus space such that the rank ordering of distances between the new utterance and each of the provided utterances agrees as closely as possible with the rank ordering of dissimilarities in the average dissimilarity vector. We used the Nelder–Mead simplex algorithm as implemented in the PORT library function SMNSX to determine the position of the new utterance in the existing stimulus space that minimized the metric difference between the average dissimilarity vector and the vector of distances to other stimuli. Given this initial configuration, we then used an iterative procedure described in Chapter 5 of Davison (1983) to obtain the desired nonmetric result.

Note that, given the same experimental data, this modified procedure will not in general produce the same result as weighted multidimensional scaling applied to the complete set of $n+1$ stimuli. Weighted multidimensional scaling fits results for each individual subject by generating both a stimulus space and a subject space, which is a space describing the different weights given by each subject to the various dimensions of the stimulus space. The modified procedure does not consider the subjects individually but rather finds the location in an already-established stimulus space that provides the best nonmetric fit to a dissimilarity vector averaged over all subjects.

In order to determine whether this modified procedure would produce usable results, we compared results produced by weighted multidimensional scaling with results produced by the modified procedure using the same experimental data. For each of the 10 stimuli used in the listening experiment, we determined the average dissimilarity vector between this stimulus and each of the other nine stimuli. This is the average, over all subjects, of the appropriate row in the individual dissimilarity matrices. It can be obtained from the individual dissimilarity matrices or, equivalently, it can be obtained from the subset of $\binom{9}{2}=36$ triadic comparisons for each subject in the original experimental data in which one of the three stimuli was the stimulus under consideration. We then used the modified procedure to position the stimulus under consideration into the modified stimulus space obtained by excluding the stimulus under question from the stimulus space for all 10 utterances shown in Fig. 1. Note that this is a contrived test. The modified stimulus space is different from the stimulus space that weighted multidimensional scaling would generate given the dissimilarity matrices for the remaining nine stimuli, because of the normalization inherent in the multidimensional scaling process.

Figure 11 shows typical results, for codec TS. The point labeled ''TS'' shows the location of codec TS in the original stimulus space, and the point labeled ''*TS*'' (underlined, italics) is the location of codec TS obtained by the modified procedure. The location obtained by the modified procedure is close to the original location, but not identical. It is more positive on dimension 1, very slightly more positive on dimension 2, and more negative on dimension 3. The locations on the three dimensions are compared in Fig. 12.

Figures 11 and 12 serve to introduce Fig. 13, which compares the locations on the three dimensions of original and modified positions of all 10 codecs. The three points of Fig. 12 appear in Fig. 13, as well as the corresponding three points for each of the other nine codecs. It appears that the

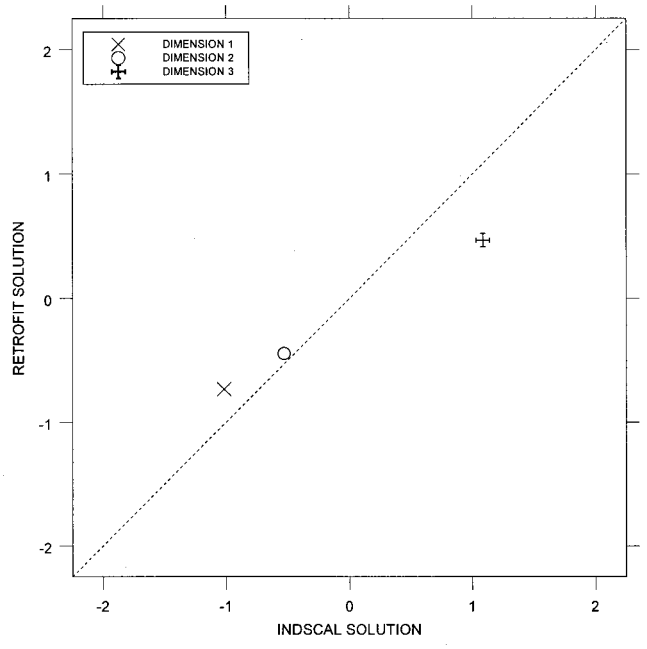

FIG. 12. Comparison of locations on three dimensions between original and modified position of coder TS.

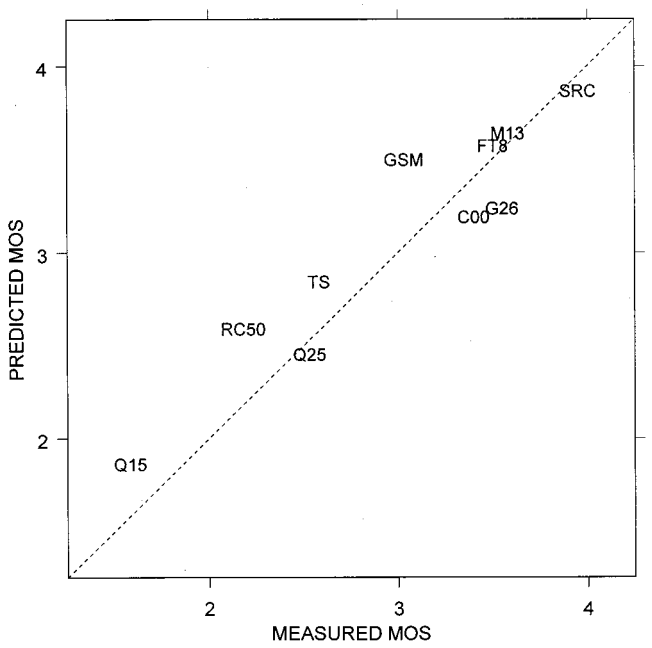

FIG. 14. MOS predicted from three-dimensional linear regression. This figure differs from Fig. 5 in that the prediction for each utterance is based on a stimulus space and linear regression computed from the other nine utterances.

procedure for fitting a new utterance into an existing stimulus space can provide usable results. The rms difference between the INDSCAL and the modified positions for the results shown in Fig. 13 is 0.31 units, and there do not appear to be any systematic biases.

C. Prediction of mean opinion score

We saw in Fig. 5 that there is a close mapping between position in stimulus space and MOS score. However, the results shown in Fig. 5 are biased because the ''predicted'' MOS score for each codec was based on three-dimensional linear regression of data that included that codec. Given enough degrees of freedom, we would expect perfect agreement between ''predicted'' and measured MOS scores. Now, however, we are in a position to use the procedure for fitting a new utterance into an already-established stimulus space to make actual predictions of mean opinion score. Again, we stress that prediction of MOS scores is only one example of an application of the multidimensional scaling procedure.

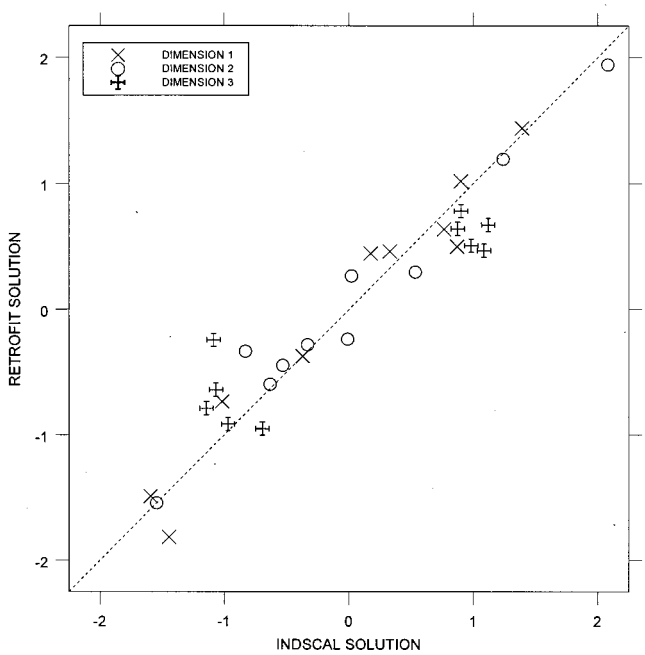

FIG. 13. Comparison of locations on three dimensions between original and modified position of all 10 coders.

The procedure for predicting MOS scores is as follows: Begin with the full body of $\binom{10}{3}=120$ triadic judgments from each of the sixteen subjects. Exclude the $\binom{9}{2}=36$ triads involving one of the codecs, and use weighted multidimensional scaling to generate a stimulus space from the remaining $\binom{9}{3}=84$ triads. Determine the three-dimensional linear regression of MOS on this stimulus space for the remaining nine codecs. Using the procedure described above, fit the excluded codec into the stimulus space. Using the just-determined linear regression, compute a predicted value for the mean opinion score for the excluded codec. Note that this is a true prediction of mean opinion score in the sense that the prediction is obtained from a stimulus space and from a linear regression that are not influenced by the codec being predicted. The procedure is closely analogous to the proposed speech quality test with the exception that judgments from the same group of subjects are used to generate the stimulus space and to fit the new utterance into this stimulus space.

We carried out this procedure for each of the 10 codecs. Figure 14 shows predicted vs measured MOS. This figure can be compared to Fig. 5, which shows predicted vs measured MOS using a stimulus space and linear regression based on all 10 codecs, including the one being predicted.

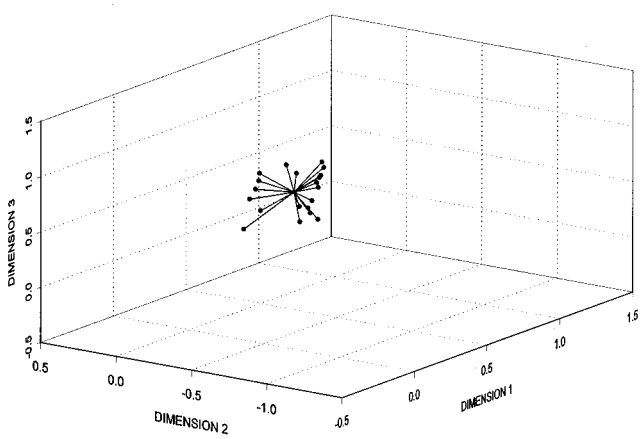

FIG. 15. Position estimates for coder GSM.

The rms difference between predicted and measured MOS is 0.27 units.

D. Selection of test stimuli

We stated in the introduction that the test stimuli should span the stimulus space under investigation. In this section we expand on and illustrate this requirement. We present results that demonstrate that a new stimulus can be fitted into an existing stimulus space more precisely if it falls near the middle of the existing space than if it falls near the periphery of the existing stimulus space.

We defined 20 groups of eight listeners, each group picked at random from the 16 listeners that took part in the listening experiment. For each of the 10 stimuli used in the listening experiment, we computed 20 average dissimilarity vectors, one for each group of eight listeners, between that stimulus and the other nine. Then, for each of the 20 dissimilarity vectors, we used the modified procedure described in Sec. V B above to position the stimulus under consideration into the previously defined stimulus space. The only difference between this procedure and the procedure described in Sec. V B above is that in Sec. V B the dissimilarity vector was obtained from all 16 subjects, while in this section each dissimilarity vector was obtained from a subgroup of eight subjects.

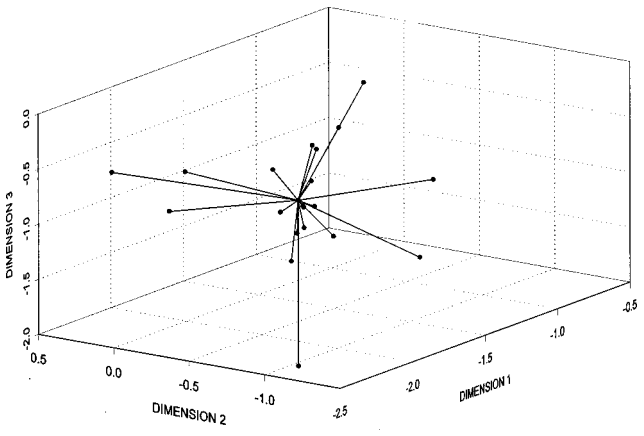

FIG. 16. Position estimates for coder RC50.

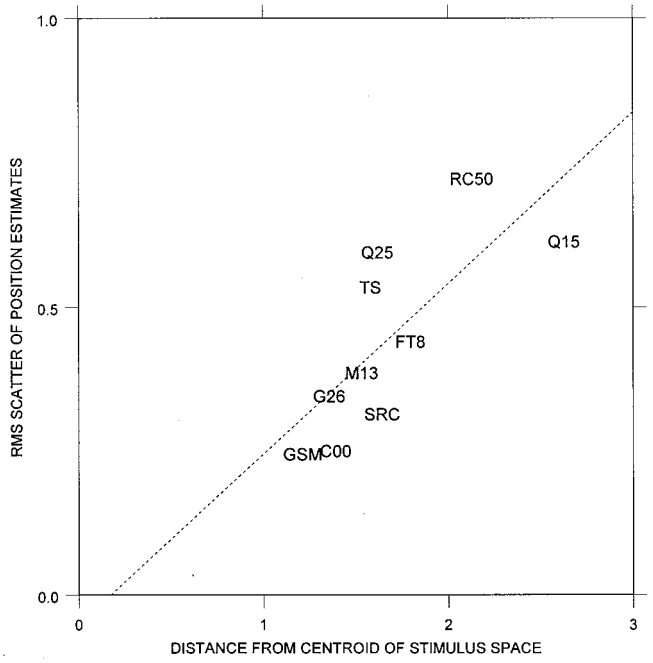

FIG. 17. rms distance between position estimates and mean of all position estimates, for each test utterance, plotted vs distance of test utterance in original stimulus space from centroid of stimulus space.

We thus obtained, for each of the 10 stimuli, 20 estimates of location in the stimulus space. These estimates are not independent, because there was overlap of listeners among the 20 groups, but they do serve to illustrate the point we want to make. The 20 estimates were more widely scattered for some stimuli than for others, and there is a systematic relationship between the amount of scatter and the average location of each stimulus in the stimulus space.

The rms distance between each position estimate and the mean of all 20 position estimates was smallest, 0.25 units, for codec GSM, and largest, 0.73 units, for codec RC50. Results for these two codecs are shown in Figs. 15 and 16. Each figure shows, in three-dimensional stimulus space, the location of each of the 20 estimates of stimulus position. The two figures are plotted to the same scale, and for ease of visualization a line is drawn between each point and the average of the 20 points.

Figure 17 shows the rms distance between each position estimate and the mean of all 20 position estimates for each of the 10 codecs, plotted vs the distance of each codec in the original stimulus space from the centroid of the original stimulus space. The two sets of numbers are positively correlated, with a correlation coefficient of 0.75. The conclusion to be drawn from Fig. 17 is that, as stated above, a stimulus can be more accurately fitted into an existing stimulus space if it falls near the center of the existing stimulus space than near an edge.

VI. CONCLUSION

We presented a brief review of multidimensional scaling techniques that describes how INDSCAL, weighted multidimensional scaling, can be applied to triadic dissimilarity

judgments to generate a stimulus space. Stimuli that sound similar are close together in this stimulus space and stimuli that sound dissimilar are far apart. Furthermore, the dimensions of this stimulus space are not arbitrary but rather can be identified with perceptual characteristics of the stimuli that subjects use in making the dissimilarity judgments.

We next presented results from a psychoacoustic listening experiment in which subjects made triadic dissimilarity judgments on samples of coded speech and the resulting dissimilarity matrices were processed by INDSCAL to generate stimulus and subject spaces. Samples of coded speech produced by two different talkers, one male and one female, generated similar but not identical stimulus spaces. This result is consistent with the accepted view that a codec can affect different voices differently and suggests that it may be possible to explore these differences quantitatively. For the stimuli used in this experiment, there was a close mapping between MOS and position in the stimulus space, even though the mean opinion scores were obtained in a separate experiment done 5 years ago with a different group of subjects, and the task in the study reported here did not involve making any judgment of speech quality. This is a remarkable result, and it illustrates the power of the multidimensional scaling procedure, but it should not obscure the fact that the true utility of the procedure is that it determines the appropriate dimensions for differentiating among the test stimuli and it determines the location of each stimulus on these dimensions.

In a second listening experiment, we were able to identify perceptual attributes and physical correlates of the three dimensions of the stimulus space. This result establishes that the underlying assumption of weighted multidimensional scaling, that different subjects use the same dimensions in determining perceptual dissimilarity but weight these dimensions differently, is justified. Subjects identify dimension 1 with naturalness. Codecs that are at the ''natural'' end of dimension 1 tend to have average spectra that are close to the grand average of average spectra of all codecs. Subjects identify dimension 2 with noisiness, and codecs that are at the ''noisy'' end of dimension 2 tend to have more high-frequency energy than the grand average. Subjects identify dimension 3 with amount of low-frequency content, and codecs that are judged to have a greater amount of low-frequency content have average spectra that are above the grand average at low frequencies.

Dimension 1, which has the least clearly defined physical correlate, is the one most highly correlated with MOS. Dimension 2, noisiness, is not highly correlated with MOS. This result is at first surprising, because we know that, other things being equal, MOS would be expected to decrease with increasing noisiness. Our explanation is that if the test stimuli differed only in amount of high-frequency noise, then INDSCAL would generate a stimulus space in which MOS and amount of high-frequency noise changed together along the same dimension. For the test stimuli used in the present experiment, noisiness was not the dominant factor. It appears that subjects preferred a natural-sounding sample to an unnatural-sounding one, even if the natural-sounding one was noisier.

Finally, we propose a new speech quality test based on multidimensional scaling techniques. The user is provided with a collection of speech stimuli and the stimulus space for these stimuli and fits the new stimulus under evaluation into the provided stimulus space. From the provider's point of view, the test is difficult. The provider must select stimuli that span the perceptual space of interest, and at this point it is not clear what the best way to do this is. Presumably the provided stimuli should show the same kinds of distortions as the new stimuli to be evaluated, and we present results that indicate that the new stimulus to be evaluated should fall near the center of the provided stimulus space. Furthermore, the provider must carry out large-scale listening tests to determine the stimulus space and the mapping between position in the stimulus space and perceptual attributes of the speech. However, from the user's point of view the test should be attractive. The field listening test that the user has to carry out is short, because the only comparisons that have to be made are between the new stimulus under evaluation and the provided stimuli. We have developed a procedure that takes as input the dissimilarity vector generated by the field listening test and uses the same nonmetric criteria as INDSCAL to position the new stimulus in the provided space.

This work is presented as a pilot study only. There remain a host of unanswered questions, and several areas of future research are suggested. At this point, we do not know how robust this proposed test is. If each new coding project requires the selection of a new set of stimuli and the generation of a new stimulus space, then the test is probably of theoretical interest only. If it is robust enough that a carefully chosen set of stimuli suffice for a variety of coding projects, then the anchorable property of the proposed test, combined with the ability of the proposed test to give much more information than a single MOS number, suggest that the test could be of practical value for some applications.

ACKNOWLEDGMENTS

I am indebted to Man Mohan Sondhi for providing valuable advice and suggestions, to Peter Kroon for making available the speech samples and MOS results used in this study and for providing advice about speech codecs, and to Joseph Kruskal for assistance with issues relating to multidimensional scaling and to three anonymous reviewers who made significant and useful comments on an earlier version of this report. Most of all, I am indebted to the subjects who made this study possible.

APPENDIX A: TYPICAL[2] INSTRUCTION SHEET FOR TRIADIC COMPARISONS LISTENING EXPERIMENT

Subjective distances experiment

This is an experiment to determine the subjective distances between speech samples processed by a variety of different speech coders. The headphone with the red connector goes on your right ear and the headphone with the black connector goes on your left ear. The speech will be presented to your right ear only.

To begin the first trial of the experiment, press and release the illuminated white button. The light will go off briefly and then light up when the speech is presented. The speech is a continuous loop of a male talker saying ''The rush for funds reached its peak Tuesday. The birch looks stark white and lonesome. The box is held by a bright red snapper.''

You can listen to three different versions of the speech by pushing the three white buttons. At any time, the button corresponding to the version you are listening to will be illuminated. You can switch from one version to another at any time; the speech continues without interruption.

Your task is to decide which two of the three versions sound *least* like each other and which two of the three versions sound *most* like each other. Listen to the three versions for as long as you want, and then push the green button between the two versions that sound the most *different*. The button will light up and stay lit until the end of the trial. Continue listening to the three versions for as long as you want, and then push the green button between the two versions that sound the most *similar*. The speech will stop, all the lights will go out, and after a short pause the next trial will begin with another three versions.

The display on the screen will remind you of which button to push and also keep you posted about how many trials you have completed and how many are left to do.

There are no ''right'' or ''wrong'' answers. All that matters is how the speech sounds to you. It is completely up to you to decide what makes two speech samples sound similar or different. We do ask that you listen to each of the three versions before making any judgments (the green buttons will not respond until you have listened to each of the three versions at least once), but do not spend an inordinately long time on any one trial. You may very well find some trials more difficult than others, and there is little to be gained by spending a very long time on these more difficult trials.

Do you have any questions?

APPENDIX B: COORDINATES OF SUBJECT AND STIMULUS SPACES FOR MALE TALKER

1. Stimulus space. Male talker, 10 speech samples

Coder	Dimension 1	Dimension 2	Dimension 3
SRC	1.3889	−0.0097	0.8734
C00	0.8684	0.0214	−1.0849
FT8	0.1746	−1.5423	0.8991
G26	0.7640	0.5345	0.9823
GSM	0.3283	−0.3313	1.1174
M13	0.8985	−0.6312	−1.0660
Q15	−1.4442	2.0806	−0.6931
Q25	−0.3713	1.2370	−0.9704
RC50	−1.5911	−0.8289	−1.1421
TS	−1.0161	−0.5301	1.0842

2. Subject space for 16 subjects. Male talker, 10 speech samples

Subject	Dimension 1	Dimension 2	Dimension 3
A	0.418	0.666	0.277
B	0.496	0.712	0.248
C	0.367	0.397	0.762
D	0.562	0.542	0.479
E	0.465	0.555	0.459
F	0.393	0.466	0.731
G	0.877	0.398	0.045
H	0.129	0.414	0.864
I	0.183	0.747	0.553
J	0.761	0.569	0.213
K	0.758	0.340	0.339
L	0.777	0.389	0.357
M	0.601	0.391	0.642
N	0.864	0.408	0.130
O	0.594	0.367	0.381
P	0.587	0.681	0.275

APPENDIX C: INSTRUCTION SHEET FOR IDENTIFICATION OF DIMENSIONS LISTENING EXPERIMENT

Subjective distances experiment II. Identification of perceptual dimensions

The results generated by you and the other people who took part in the first phase of this experiment indicate that the samples of coded speech that you listened to can be arranged in a three-dimensional space such that the distances between pairs of samples in this space correspond quite well to your perception of the subjective distances. The question we want to answer in this second phase of the experiment is, what are these three dimensions? That is, what perceptual attribute of the speech samples does each dimension represent?

We will work with one dimension at a time. You have a button box with eight buttons, numbered one to eight from left to right. The eight buttons produce speech samples ordered monotonically along the dimension being tested. Speech sample #1, produced by the leftmost button, is at one extreme of something, speech sample #8 is at the other extreme, and whatever this something is increases (or decreases, we don't know which) from left to right.

Listen to the eight speech samples for as long as you want, and try to decide what attribute increases (or decreases) monotonically from button #1 to button #8. For example, you might decide that the attribute that changes is loudness, naturalness, amount of noise, tinniness, boominess, or any one of a host of other attributes. These are examples only; you are not limited to the items on this list. Use your own words.

Bear in mind that while the attribute you are listening for changes monotonically from button #1 to button #8, the other attributes of the speech samples change in haphazard order. Your job is to try to isolate the attribute that changes monotonically.

Do you have any questions?

APPENDIX D: SUBJECTS' CHARACTERIZATIONS OF THE THREE DIMENSIONS

The first column in each table gives the subject, rank ordered by the importance of each dimension to each subject. Subject G, for example, gave a higher weight to dimension 1 than did any of the other subjects and so is listed first for dimension 1. The second and third columns give the subjects' responses (corrected for whether button #1 in Fig. 7 was the leftmost or the rightmost button).

1. Subjects' characterizations of dimension 1

Subject	Dimension 1 attribute	Direction
G	Distortion	decreases
N	General quality, let's say ''Clarity (Intelligibility).''	increases
L	High-frequency component	increases
J	Vowel naturalness	increases
K	Clarity	increases
M	Brightness, emphasis on mid and high frequencies	increases
O	Naturalness	increases
P	Naturalness	increases
	Spectral distortions	decreases
D	Naturalness	increases
B	No clue	
E	Fullness	increases
A	Naturalness	increases
F	Burbly speech like a vocoder	decreases
C	Bandwidth (becomes less muffled)	increases
I	Deepness, naturalness	increases
H	Distortion (noise)	decreases

2. Subjects' characterizations of dimension 2

Subject	Dimension 2 attribute	Direction
I	Amount of noise, maybe some kind of reverberation.	increases
	Clarity	decreases
B	No clue	
P	Loudness, particularly of noise at higher frequencies	increases
A	Harshness—noisiness	increases
J	Clarity and ''openness'' #1 muted, #8 open to the point of being buzzy	increases
E	Amount of bass (nonmonotonic)	decreases
D	Amount of speech-correlated noise	increases
F	High-frequency granular noise	increases
H	Raspy sound distortion	increases
N	Fullness/bandwidth	increases
	Noisy	increases
G	Distortion	increases
C	Can't tell what changes monotonically	
M	Amount of noise	increases
L	Background noise	increases
O	Amount of noise	increases
K	Roughness	increases

3. Subjects' characterizations of dimension 3

Subject	Dimension 3 attribute	Direction
H	Nonlinear distortion	decreases
	Bandwidth (HP)	increases
C	Noisiness (static)	decreases
F	Low-frequency content	increases
M	Could not find attribute that changes	
I	Increase of low-frequency sound	increases
D	Naturalness, amount of low frequencies	increases
E	Fullness (nonmonotonic)	increases
O	Loudness	increases
L	Loudness	increases
K	Naturalness	increases
A	No idea	
P	Spectral richness	increases
B	No clue	
J	Clarity of reverberant components?	increases
N	Could not see a trend	
G	Narrowness? (nonmonotonic)	

[1]The ITU-T recommendation for MOS treads a thin line in this respect. Recognizing that different voices can be affected differently, it states that results for male and female voices should be treated separately, but it goes on to state that ''... to reduce the danger that the results may depend heavily on peculiarities of the voices chosen, it is essential for more than one male and more than one female voice to be used in a balanced design'' (ITU-T, *op. cit.*, B.2.2). As was noted above in connection with the MOS score, a single composite number is appropriate for acceptance testing, but for some other applications the detailed information provided by the multidimensional scaling test may be useful.

[2]A similar instruction sheet, with the appropriate changes, was used for subjects who were presented with speech to the left ear.

Carroll, J. D. **(1972)**. ''Individual differences and multidimensional scaling,'' in *Multidimensional Scaling: Theory and Applications in the Behavioral Sciences Vol. 1*, edited by R. N. Shepard, A. K. Romney, and S. Nerlove (Seminar Press, New York).

Carroll, J. D., and Chang, J. J. (**1970**). ''Analysis of individual differences in multidimensional scaling via an *n*-way generalization of 'Eckart- Young' decomposition,'' Psychometrica **35**, 283–319.

Davison, M. L. **(1983)**. *Multidimensional Scaling* (Wiley, New York).

Huggins, A. W. F., Riswanathan, R., and Makhoul, J., (**1977**). ''Speech-quality testing of some variable-frame-rate (VFR) linear-predictive (LPC) vocoders,'' J. Acoust. Soc. Am. **62**, 430–434.

ITU-T P.800 **(1996)**. ''Methods for subjective determination of transmission quality,'' Telecommunication Standardization Sector of International Telecommunication Union, Series P: Telephone Transmission Quality.

Kroon, P. **(1994)**. Internal memorandum.

Kruskal, J. B., and Wish, M. **(1990)**. ''Multidimensional scaling,'' Sage University Paper series on Quantitative Applications in the Social Sciences, 07-011 (Sage Publications, Beverly Hills and London).

McDermott, B. J. (**1969**). ''Multidimensional analyses of circuit quality judgments,'' J. Acoust. Soc. Am. **45**, 774–781.

Precoda, K., and Meng, T. H. (**1997**). ''Listener differences in audio compression evaluations,'' J. Audio Eng. Soc. **45**, 708–715.

Quackenbush, S. R., Barnwell, T. P., and Clements, M. A. **(1988)**. *Objective Measures of Speech Quality* (Prentice-Hall, Englewood Cliffs, NJ).

Thorpe, L. A., and Yang, W. **(1999)**. ''Performance of current perceptual objective speech quality measures,'' Proceedings of 1999 IEEE Workshop on Speech Coding, pp. 144–146.
Thorpe, L. A. (**1999**). ''Subjective evaluation of speech compression codecsand other non-linear voice-path devices for telephony application,'' Int. J. Speech Technol. **2**, 273–288.
Voiers, W. D., Panzer, I. L., and Sharpley, A. D. **(1990)**. Validation of the diagnostic acceptability measure (DAM II-B). (Contract No. MD904-87-C-6026 for National Security Agency, Ft. Meade, MD), Dynastat, Inc., Austin, TX.
Voiers, W. D. **(2000)**. Private communication.
Young, F. W., and Harris, D. F. **(1997)**. ''Multidimensional scaling examples,'' Chapter 14 in SPSS *Professional Statistics™ 7.5*, Marija J. Norušis/SPSS Inc.

Effect of stimulus bandwidth on the perception of /s/ in normal- and hearing-impaired children and adults

Patricia G. Stelmachowicz, Andrea L. Pittman, Brenda M. Hoover, and Dawna E. Lewis
Boys Town National Research Hospital, 555 North 30th Street, Omaha, Nebraska 68131

(Received 19 January 2001; accepted for publication June 18, 2001)

Recent studies with adults have suggested that amplification at 4 kHz and above fails to improve speech recognition and may even degrade performance when high-frequency thresholds exceed 50–60 dB HL. This study examined the extent to which high frequencies can provide useful information for fricative perception for normal-hearing and hearing-impaired children and adults. Eighty subjects (20 per group) participated. Nonsense syllables containing the phonemes /s/, /f/, and /θ/, produced by a male, female, and child talker, were low-pass filtered at 2, 3, 4, 5, 6, and 9 kHz. Frequency shaping was provided for the hearing-impaired subjects only. Results revealed significant differences in recognition between the four groups of subjects. Specifically, both groups of children performed more poorly than their adult counterparts at similar bandwidths. Likewise, both hearing-impaired groups performed more poorly than their normal-hearing counterparts. In addition, significant talker effects for /s/ were observed. For the male talker, optimum performance was reached at a bandwidth of approximately 4–5 kHz, whereas optimum performance for the female and child talkers did not occur until a bandwidth of 9 kHz.
[DOI: 10.1121/1.1400757]

PACS numbers: 43.71.Ky, 43.71.Ft, 43.66.Ts [CWT]

I. INTRODUCTION

A number of studies have suggested that some listeners with sensorineural hearing loss may receive limited benefit from amplification in the high-frequency region. Specifically, it has been reported that systematic increases in high-frequency gain may not improve, and in some cases may degrade, speech recognition for listeners with steeply sloping high-frequency hearing losses (Skinner, 1980; Murray and Byrne, 1986; Rankovic, 1991; Ching, Dillon, and Byrne, 1998; Hogan and Turner, 1998; Turner and Cummings, 1999). The results of these studies have important implications for clinical practice. If amplifying speech to audible levels in the high frequencies does not improve speech recognition, then attempts to provide gain may not be necessary or desirable in certain cases. While the studies cited above appear to support the general notion that high-frequency amplification may not always be beneficial, the intersubject variability in most studies precludes a clearly defined rule that would distinguish listeners who are likely to benefit from high-frequency amplification from those who are not. Furthermore, differences in subject selection, filter conditions, and methodology across studies complicate the interpretation of results.

For example, Murray and Byrne (1986) assessed the effects of low-pass filtering at five frequencies (from 1.5–4.5 kHz) on judgments of intelligibility and pleasantness for continuous discourse. Subjects were normal-hearing (NH) and hearing-impaired (HI) adults with steeply sloping losses above 1 kHz. Although all of the NH subjects preferred the widest bandwidth, three of the five HI subjects preferred the 2.5- or 3.5-kHz bandwidth over the 4.5-kHz bandwidth. Because ''judged'' intelligibility was used in this study, the effects of low-pass filtering on objective measures of speech recognition were not described. Skinner (1980) used a high-frequency monosyllabic word list to assess the speech recognition ability of six adults with steeply sloping losses. Stimuli were filtered using five different frequency responses with increasing gain in the 1–8-kHz region. Results indicated that a frequency response with intermediate high-frequency gain was best for understanding speech at a conversational level. However, the two responses with the greatest high-frequency gain were best for understanding low-level speech. Ching *et al.* (1998) assessed recognition of filtered sentences in hearing-impaired adults and compared results to predictions based on variants of the Speech Intelligibility Index. Audible energy in the high-frequency region (2.8–5.6 kHz) contributed no information or actually decreased performance for listeners with thresholds $>$80 dB HL at 4 kHz. The majority of listeners with thresholds in the 50–80-dB HL range, however, benefited from audible signals in this high-frequency region.

Hogan and Turner (1998) also investigated the effects of stimulus bandwidth on phoneme recognition in listeners with steeply sloping hearing losses. Nonsense syllables were frequency shaped and low-pass filtered at 12 cutoff frequencies from 0.56 to 9 kHz. The benefit of providing additional high-frequency audibility was negligible or negative when the degree of loss at and above 4 kHz exceeded 55 dB HL. In some cases, performance decreased with increases in high-frequency audibility. In a similar study, Turner and Cummings (1999) investigated the benefit of high-frequency information in listeners with varying degrees and configurations of hearing loss. Recognition was evaluated as a function of increasing high-frequency information for nonsense syllables presented over a range of levels above and below threshold. Results confirmed the earlier findings that listeners with hearing loss $\geqslant$55 dB HL at and above 4 kHz did not benefit from high-frequency information. In contrast to some

of the previous studies, however, increased gain in the high-frequency region did not degrade performance.

In interpreting the results of these filtering experiments, it is important to consider the test stimuli. For example, Murray and Byrne (1986) and Ching *et al.* (1998) used sentences as the test materials. A study by Studebaker, Pavlovic, and Sherbecoe (1987) suggests that, when contextual information is available, the frequency region of maximum importance is between 0.4 and 5 kHz. Thus, high-frequency audibility may not be as critical to the perception of sentence materials as it would be for less linguistically complex speech materials. The stimuli used in the Hogan and Turner (1998) and Turner and Cummings (1999) studies contained a relatively large proportion of phonemes (e.g., /b,d,g,l,m,n,r,dʒ/) that can be perceived from mid- and low-frequency cues. Reduced performance for the small number of phonemes comprised primarily of high-frequency energy (e.g., /s,ʃ,z/) may not have influenced overall scores significantly. Although an error analysis was not reported for these two studies, a similar investigation by Sullivan *et al.* (1992) found large improvements in performance (30%–45%) for the phonemes /s,ʃ,ʒ,z/ as stimulus bandwidth was increased, despite nonsignificant differences in the overall scores for the different filter conditions.

Of these high-frequency fricatives, /s/ is known to be linguistically important. It is the third or fourth most frequently occurring phoneme in the English language and serves multiple linguistic functions, including plurality, tense, and possession (Tobias, 1959; Denes, 1963; Rudmin, 1983). Among both adults and children with hearing loss, /s/ is one of the most frequently misperceived phonemes (Owens, Benedict, and Schubert, 1972; Bilger and Wang, 1976; Owens, 1978; Dubno and Dirks, 1982; Danhauer *et al.*, 1986). In addition, Elfenbein, Hardin-Jones, and David (1994) have reported that the language samples of children with mild-to-moderate hearing loss often include increased errors in both noun and verb morphology (e.g., cat versus cats, keep versus keeps). It is likely that these findings are related to a reduction in audibility of the fricative noise and/or the vocalic transition in the presence of hearing loss. For adults with acquired hearing loss, there may be sufficient linguistic and redundant acoustic cues to compensate for this loss of audibility. When the hearing loss is congenital or acquired in early life, the reduction in audibility may be more problematic. Kortekaas and Stelmachowicz (2000) investigated the effects of low-pass filtering on the perception of /s/ in NH children (5-, 7-, and 10-year-olds) and adults. They found that the children required a wider signal bandwidth than did adults to perceive /s/ correctly when stimuli were presented in noise. To our knowledge, no studies have been conducted with HI children. If similar findings were observed in hearing-impaired children, restricting the bandwidth of speech may have a negative impact on speech and language development in young HI children.

The methodology used in the previous adult studies may not be ideal to address the effects of high-frequency amplification in young HI children. For example, subjective estimates of speech perception have poor test–retest reliability and do not correlate well with performance measures (Byrne, 1986; Gabrielsson, Schenkman, and Hagerman, 1988; Studebaker and Sherbecoe, 1988). Objective measures of performance using words and/or sentences also are problematic because the child's auditory experience and language competence may have an influence on test performance. Nonsense syllables circumvent these problems, but given that performance in the Sullivan *et al.* (1992) study differed across stimuli, it would seem reasonable to restrict the items to those that contain high-frequency information. It would also be most useful to focus on sounds that are important to speech and language development. The purpose of the present study was to determine the effect of stimulus bandwidth on the perception of /s/ in NH and HI children and adults. These four groups of subjects were included to separate the effects of hearing loss from general development.

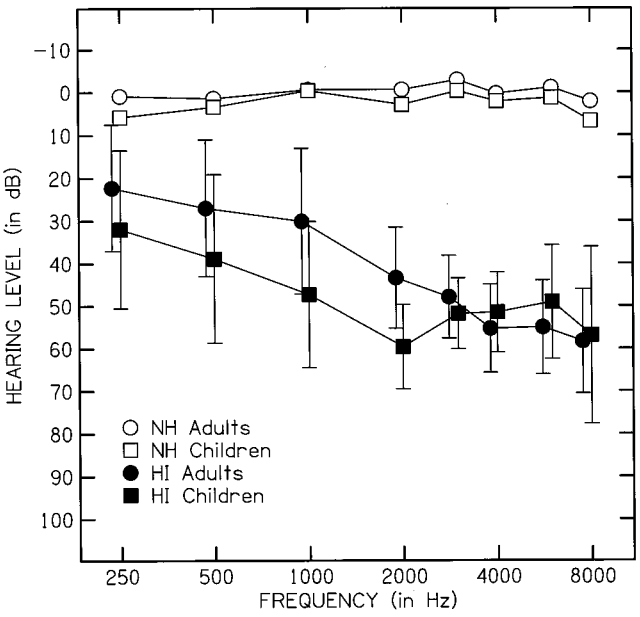

FIG. 1. Hearing thresholds as a function of frequency for the NH adults and children (open symbols) and the HI adults and children (filled symbols). Error bars (±1 standard deviation) are shown for the HI listeners only.

II. METHODS

A. Listeners

A total of 80 listeners participated in this study. The two NH groups were comprised of 20 adults (ages 19–43 years, $M=28$ years) and 20 children (5–8 years, $M=7$ years, 3 months). The two HI groups also consisted of 20 adults (26–65 years, $M=56$ years) and 20 children (5–8 years, $M=7$ years, 1 month). The NH listeners had pure-tone thresholds ≤15 dB HL for the octave frequencies from 0.25 to 8 kHz. The HI listeners had moderate to moderately severe sensorineural hearing losses that ranged between 40 and 70 dB HL at 2 and 4 kHz. Figure 1 shows the mean pure-tone thresholds for each group (±1 s.d. are shown for the HI listeners only). Based upon available audiological data and subjective history, all of the HI children had congenital losses and the HI adults had acquired their losses later in life. All listeners had normal middle-ear function at the time of testing.

B. Stimuli

Although the primary interest of this study was the perception of /s/, it was necessary to provide subjects with alternative stimuli that would be easily confused with /s/. A pilot study with NH adults indicated that filtered versions of /s/ were most likely perceived as either /f/ or /θ/. Thus, the test stimuli were consonant–vowel (CV) and vowel–consonant (VC) syllables comprised of the phonemes /s/, /f/, and /θ/ in an /i/ vowel context. The /i/ vowel was used to minimize the vocalic transition which might be used as a cue to distinguish the fricatives from one another. In addition, multiple repetitions of each sample were obtained from all three talkers, and samples with little or no transition were selected as stimuli for the study. The CV and VC syllables were produced by an adult male, an adult female, and a 6-year-old child (for a total of 18 stimuli). All speech samples were recorded in a sound-treated room at normal vocal levels using a microphone with a flat frequency response to 10 kHz (AKG Acoustics, C 535EB). The speech samples were amplified, filtered at 10 kHz, and digitized at a sampling rate of 20 kHz. The 18 syllables were edited to ensure equivalent rms levels (of the entire syllable) across all stimuli. The stimuli were analyzed in 17 1/3-octave bands (TOB) with a 20-ms Hanning window (50% overlap) after being transduced by the earphone (Sennheiser 25-1) and recorded in a flatplate coupler. Figure 2 shows the relative TOB spectra for the /s/, /f/, and /θ/ in the CV context for each talker. The spectrum for each phoneme in the final position showed a similar pattern. The spectral characteristics of /s/ varied markedly across talkers. Relative to the female talker, more mid-frequency energy was apparent for the male and child talkers. These spectral characteristics are consistent with previous data for this phoneme (Strevens, 1960; Heinz and Stevens, 1961; McGowan and Nittrouer, 1988; Nittrouer, Studdert-Kennedy, and McGowan, 1989; Boothroyd and Medwetsky, 1992; Boothroyd, Erickson, and Medwetsky, 1994; Jongman, Wayland, and Wong, 2000). The peak energy for both /f/ and /θ/ was lower in amplitude than for /s/ and talker differences were only observed for /f/ where the fricative amplitude for the child talker was approximately 10 dB higher than the other talkers. In the final consonant position, fricative amplitude for the child talker was higher only for /θ/.

To determine the influence of bandwidth on the perception of high-frequency voiceless fricatives, each syllable was low-pass filtered with a rejection rate of 50 dB/octave at six frequencies (2, 3, 4, 5, 6, and 9 kHz). Additional filtering for purposes of antialiasing was not necessary because the sampling rate of these syllables was greater than twice the widest bandwidth condition.

C. Procedure

All testing was conducted in a sound-treated room. The nonsense syllables were presented monaurally through the same earphone used to obtain hearing thresholds (Sennheiser, 25-1). Each listener was instructed to indicate which nonsense syllable was presented by touching the appropriate box on a touch-screen monitor or by selecting it with a mouse. The response boxes were labeled ''s,'' ''f,'' and ''th.'' Prior to testing, each child was asked to read or identify the orthographic form of the phonemes (/s/, /f/, and /θ/). The children were also shown pictures of words that contained these phonemes in the initial and final position and asked to identify them. Children who were unfamiliar with the orthographic forms of the phonemes, but could clearly produce them, were instructed to repeat the syllables so that the examiner could vote for the child. Those children who were unable to correctly produce the phonemes or identify their orthographic forms were excluded from the study.

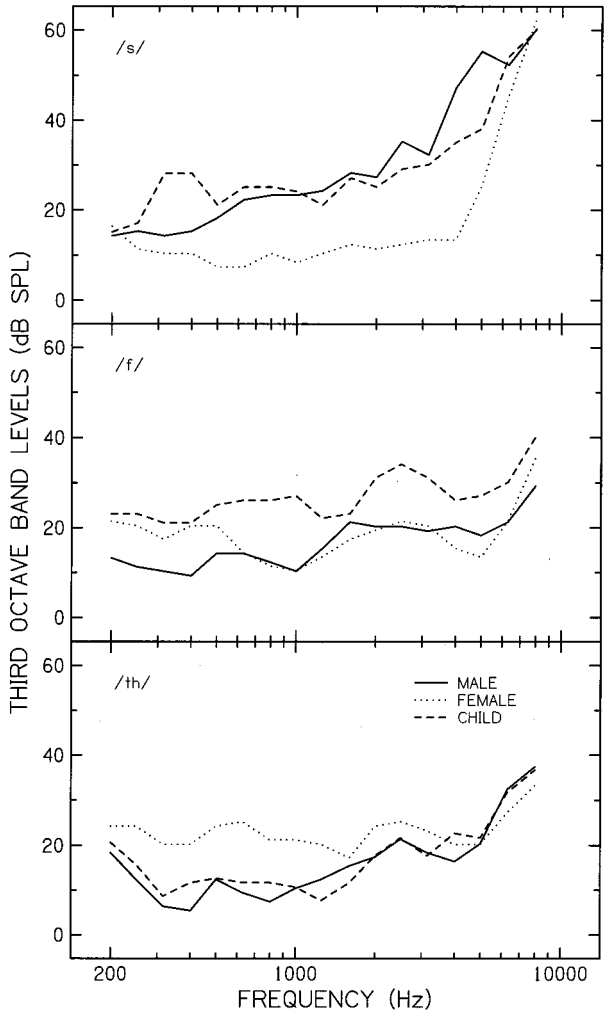

FIG. 2. Relative levels of the fricative noise in 1/3-octave bands for the utterances /si/, /fi/, and /θi/ as a function of frequency for the male, female, and child talkers.

The syllables were divided into CV and VC subtests. For each subtest, stimuli were presented 10 times for a total of 540 trials (6 filter conditions × 3 talkers × 3 fricatives × 10 repetitions). On any given trial, one of 540 stimuli could occur. This form of randomization was used to limit the loudness cues that might be present if each low-pass filter condition were tested separately. For example, at a 9-kHz band /s/ would be louder than either /f/ and /θ/. When randomized, /f/ and /θ/ filtered at 6 or 9 kHz could actually sound louder than an /s/ filtered at 2 kHz. Software was written in MATLAB (Mathworks) to randomly select the test

stimuli and filter condition. The program also was used to reinforce correct responses in a video game format. Both the children and adult listeners were tested with the same procedure. For the NH listeners, the syllables were presented at a level equivalent to soft speech (45 dB SPL). For the HI listeners, the stimuli were altered to provide frequency/gain characteristics as recommended by the desired sensation level procedure for soft speech (53 dB SPL) (Seewald *et al.*, 1997).

III. RESULTS AND DISCUSSION

Although data were collected for /s/, /f/, and /θ/, the primary interest of this study was the proportion of /s/ responses to the /s/ stimuli. Accordingly, results for /f/ and /θ/ are given only for comparison when necessary. To ensure that a stimulus bias toward /s/ did not occur, the data were screened to determine that the proportion of /s/ responses was appropriate. Collapsed across all filter conditions, the proportion of /s/ responses for all groups (28%–34%) was consistent with the fact that /s/ was presented in 33% of the trials. Given that no biases were observed, scores for /s/ were arcsine transformed to normalize the variance across performance levels and analyzed with a repeated-measures analysis of variance (ANOVA). Talker (male, female, and child), filter (2, 3, 4, 5, 6, and 9 kHz), and position (VC and CV) were the within-subjects factors and hearing (normal and hearing impaired) and age (child and adult) were the between-subjects factors. A Greenhouse–Geisser correction was used to adjust the degrees of freedom for those conditions that failed to meet the assumption of sphericity (Max and Onghena, 1999). Significant main effects were found for talker [$F(1.895,143.9)=444.99$; $p<0.01$] and filter [$F(5,380)=291.49$; $p<0.01$], but not for consonant position [$F(1,76)=0.80$; $p=0.37$]. In addition, the between-subjects factors revealed a significant effect of hearing [$F(1,76)=37.98$; $p<0.01$] and age [$F(1,76)=11.42$; $p<0.01$] with no hearing×age interaction [$F(1,76)=0.38$; $p=0.54$].

Since no significant differences in performance were found between the VC and CV conditions, data were collapsed across the two subtests. In Fig. 3, performance as a function of low-pass frequency is shown for the male, female, and child talkers with group as the parameter. In the top panel (male talker), performance for the NH children and adults exceeded 80% at a filter frequency of 4 kHz. In contrast, performance for the HI children and adults did not exceed 80% until a cutoff frequency of 5 kHz. For the female talker (middle panel), performance was near chance (33%) through 5 kHz for all groups, with an abrupt increase in performance at 6 kHz for the NH listeners and at 9 kHz for the HI listeners. All four groups reached optimum performance at 9 kHz, with the two NH groups and HI adults achieving >80% performance and the HI children achieving only 77%. This finding is not surprising given the narrow region of spectral energy for the female /s/. A different pattern was observed for the child talker (lower panel). As bandwidth increased, a more gradual improvement in performance was observed for all groups, with the NH groups and HI adults achieving ⩾80% performance at the 9-kHz cutoff frequency. The performance of the HI children, however, only reached 75% at the widest bandwidth. For all groups and all talkers, mean performance increased as a function of bandwidth with no evidence of a decrease in performance as bandwidth widened. Inspection of the 60 individual performance intensity functions (3 talkers×20 listeners) for the HI adults revealed no evidence of nonmonotonicity, whereas three of the 60 functions for the HI children showed a statistically significant decrease in performance at the widest bandwidth.

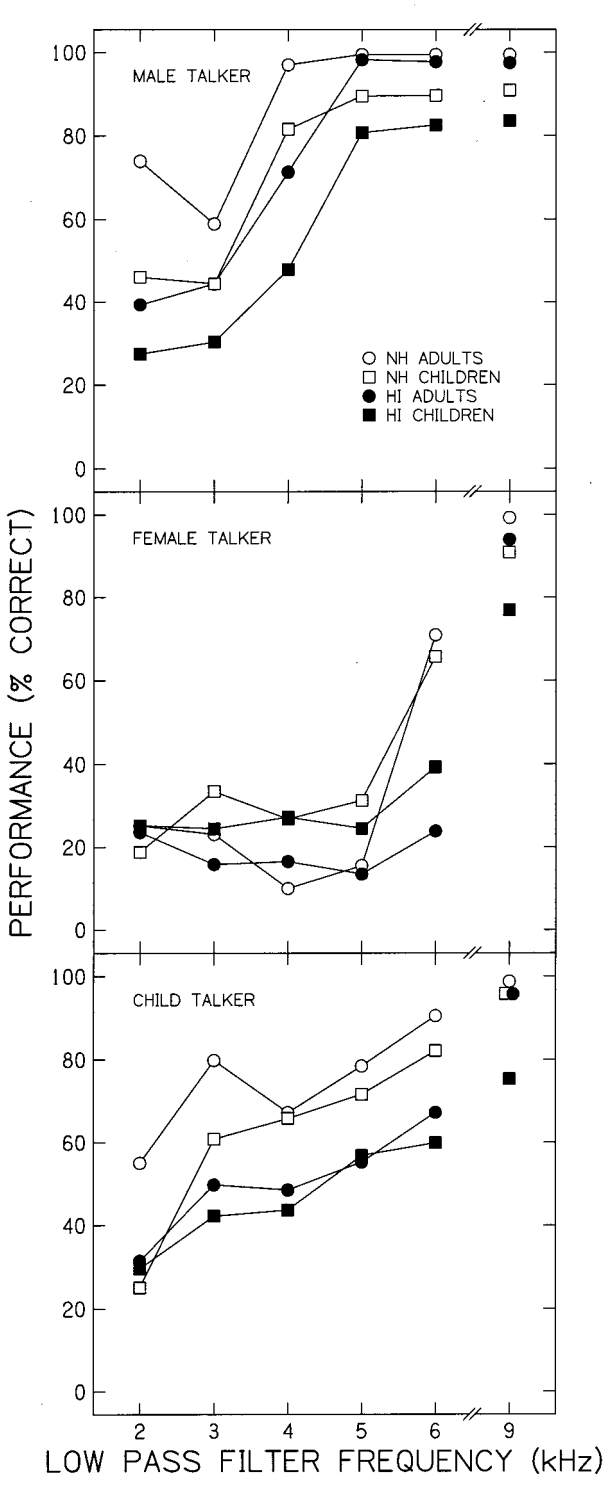

FIG. 3. Mean data illustrating percent correct as a function of low-pass filter frequency for the male (top panel), female (middle panel), and child (lower panel) talkers. The parameter in each panel is group.

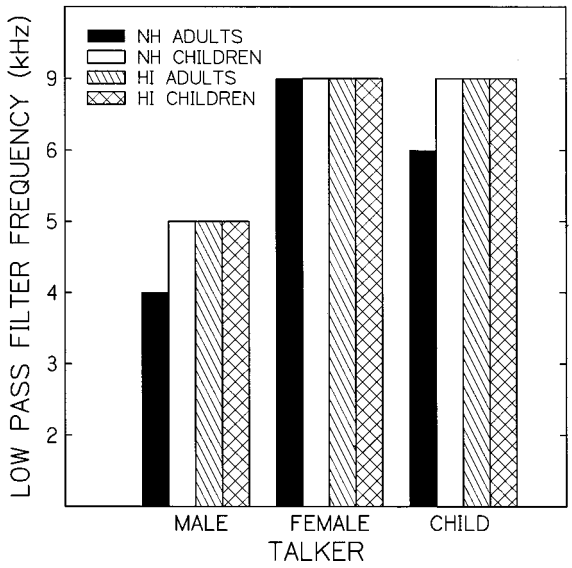

FIG. 4. Mean data showing the minimum low-pass filter frequency at which optimum performance was achieved by each group as a function of talker.

From a clinical perspective, it is of interest to determine the minimum bandwidth at which optimum performance was achieved for each group. Accordingly, the plateau portion of each function in Fig. 3 was defined as the range of bandwidths where data points were within ±5% of each other. The lowest frequency on the plateau was designated as the minimum bandwidth at which optimum performance occurred. The results for each group are shown as a function of talker in Fig. 4. For the male talker, optimum performance for the NH adults was achieved at a mean frequency of 4 kHz, whereas all other groups required a frequency of 5 kHz. For the female talker, performance continued to improve at a bandwidth of 9 kHz for all groups. For the child talker, the plateau occurred at 6 kHz for the NH adults and at 9 kHz for all other groups.

To compare performance across conditions in terms of stimulus sensation level, a measure of short-term audibility (STA) for the fricative portion of each utterance was calculated for all stimuli, filter conditions, and talkers using the following formula:

$$\mathrm{STA} = \frac{1}{15} \sum_{i=1}^{17} (\mathrm{TOB}_i - \theta_i) W,$$

where i is the center frequency of each 1/3-octave band, TOB is the 1% peak level of the fricative noise for each 1/3-octave band, θ is the hearing threshold in dB SPL for each TOB, and W is equal to 0.059, representing equal weights across the 17 bands (from 0.2–8 kHz). The sum of the weighted sensation levels was restricted to a 0- to 15-dB range by the multiplier 1/15. Previous studies have shown that the 30-dB range typically used for calculation of the Articulation Index is inappropriate for shorter segments of speech (Pittman and Stelmachowicz, 2000). Table I shows mean STA and performance for each group at the bandwidth where optimum performance was achieved. Because the audibility of /f/ and /θ/ may influence the performance for /s/, results for these stimuli are provided for comparison. For all phonemes, optimum performance was consistently lower for the two groups of children relative to their adult counterparts and optimum performance for the NH listeners exceeded that of their HI counterparts. For /s/, performance was well above chance (33%) for all groups and talkers. Consistent with the findings of Pittman *et al.* (2000), the HI adults achieved similar performance to the NH adults but at substantially lower STA levels. Unlike the results of Pittman *et al.*, however, the HI children were not able to correctly identify /s/ as well as their adult counterparts at low STA values. This may be due to the fact that the children in the current study were younger (5–8 years) than in the earlier study (8–11 years). For /f/ and /θ/, performance was well above chance in most cases even when STA values were low. The one exception is the HI children's chance performance for /θ/. This may be related to the fact that /θ/ has a low frequency of occurrence in the English language (Denes, 1963) and thus, young HI children may be less familiar with this phoneme.

TABLE I. Mean short-term audibility (STA) at optimum performance for all phonemes and talkers.

	Male		Female		Children	
	STA	%	STA	%	STA	%
/s/						
NH adults	0.42	100	0.26	99	0.53	98
NH children	0.50	91	0.22	91	0.46	91
HI adults	0.26	98	0.18	94	0.23	96
HI children	0.28	84	0.15	77	0.17	75
/f/						
NH adults	0.35	95	0.22	66	0.39	84
NH children	0.26	78	0.15	56	0.32	73
HI adults	0.12	87	0.08	59	0.25	72
HI children	0.08	60	0.05	55	0.19	51
/θ/						
NH adults	0.26	47	0.38	93	0.39	60
NH children	0.12	41	0.25	73	0.31	45
HI adults	0.08	46	0.11	59	0.20	51
HI children	0.06	32	0.07	35	0.13	30

It is also of interest to determine if the degree of hearing loss in these listeners influenced their ability to use high-frequency speech information. Recall that previous studies found high-frequency information to be of limited benefit for individuals with hearing loss ≥55 dB HL at and above 4 kHz (Hogan and Turner, 1998; Turner and Cummings, 1999). To determine if degree of hearing loss influenced the results in the present study, each of the two HI groups was subdivided into listeners with thresholds ≥55 dB HL and <55 dB HL at 4 kHz. Figure 5 shows mean performance as a function of low-pass frequency with degree of hearing loss as the parameter. Performance is similar for both categories of hearing loss and there is no evidence of decreased performance at the widest bandwidths. To ensure that this arbitrary grouping (at 55 dB HL) did not obscure trends associated with degree of hearing loss, the relation between performance and hearing level was inspected at each low-pass filter frequency. No systematic trends were observed for either HI group. It is worth mentioning, however, that the maximum hearing loss at 4 kHz did not exceed 70 dB HL in this study; inclusion of

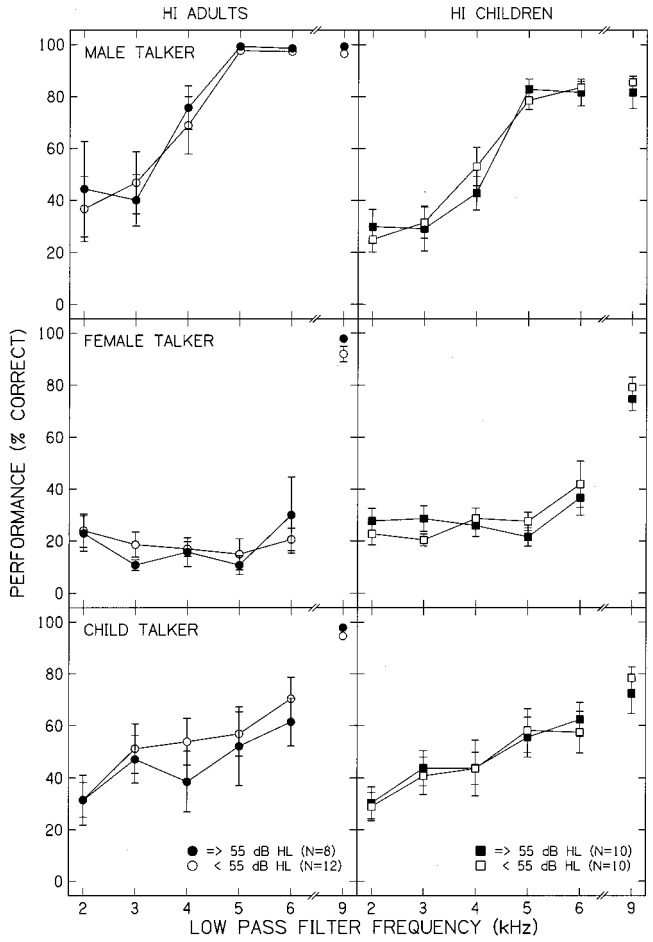

FIG. 5. Data for the HI listeners from Fig. 3 are replotted to illustrate the effects of degree of hearing loss. In each panel, results are shown for listeners with hearing loss at 4 kHz $\geqslant$55 dB HL (filled circles) or $<$55 dB HL (open circles). Error bars represent the variance about the mean.

individuals with more severe hearing losses may have yielded different results.

IV. GENERAL DISCUSSION

This study found significant differences in the perception of /s/ across the NH and HI adults and children. Optimum performance for the children was poorer than for the corresponding groups of adults. This finding is consistent with other studies in which the performance of adults and young children were compared. Specifically, developmental differences have been observed for a variety of auditory tasks including detection, masked thresholds, temporal processing, frequency discrimination, and speech recognition (Nozza and Wilson, 1984; Schneider *et al.*, 1989; Allen *et al.*, 1989; Wightman *et al.*, 1989; Veloso, Hall, and Grose, 1990; Nozza, Rossman, and Bond, 1991; Hnath-Chisolm *et al.*, 1998). In addition, the HI groups performed more poorly than their NH counterparts despite the frequency/gain shaping provided in accordance with the desired sensation level procedure (Seewald *et al.*, 1997). These results suggest that both age and hearing loss affect the perception of /s/ under filtered conditions, with young HI listeners at the greatest disadvantage.

The patterns of performance observed across the three talkers may have important implications for speech and language development in infants and children with hearing loss. Recall that for the male talker, the NH adults achieved optimum performance at a filter frequency of 4 kHz while the NH children and both groups of HI listeners required a somewhat wider bandwidth (5 kHz). For all subjects, mean performance for the female and child talkers continued to improve as the bandwidth increased to 9 kHz with no evidence of degradation. Until recently, most commercially available hearing aids have provided minimal amplification above 4 kHz. Even with advanced signal processing and feedback reduction schemes, very little gain is provided for frequencies above 5 kHz. Thus, it is likely that the peak energy of a female /s/ may not always be audible to hearing-aid users. Further, a young HI child may hear the plural form of certain words more often when spoken by a male. Since infants and preschool children tend to spend most of their waking hours with female caregivers and other children, they may experience inconsistent exposure to /s/ across different talkers, situations, and contexts. Because many of the linguistic functions of /s/ in the English language are rather subtle (e.g., ''Is that Beth?'' versus ''Is that Beth's?;'' ''She put it on'' versus ''She puts it on''), inconsistent audibility of /s/ during the early years of life may influence or delay the formation of linguistic rules.

Boothroyd and Medwetsky (1992) have suggested that hearing aids may require an upper limit of 10 kHz to ensure the audibility of /s/ for female talkers. Theoretically, with the selection of an appropriate receiver and an earmold carefully constructed to minimize feedback, the upper frequency limit could be extended to 7–8 kHz. Although manufacturers often report that the upper bandwidth of current hearing aids is $>$6 kHz, the upper- and lower-frequency range is defined as the 20-dB down point relative to the average gain at 1000, 1600, and 2000 Hz (ANSI, 1996). Thus, a hearing aid with an average use gain of 40 dB would only have 20 dB of gain at the upper frequency limit. In many cases, this may be inadequate to ensure the audibility of /s/. In addition, acoustic feedback will often limit usable gain due to factors such as intentional venting, imperfect seal of the earmold, leaks at tubing joints, and emission from tubing walls (Hellgren, Lunner, and Arlinger, 1999). Acoustic feedback is likely to pose a greater problem for children than for adults due to growth of the ear canal and the close proximity of the hearing-aid microphone to the potential sources of acoustic leakage.

Fortunately, there are multiple cues to the perception of /s/. For example, the production of /s/ is often visible on the lips. In addition, cues may be available in the noise energy at lower frequencies, such as in the transition from fricative noise to the vowel (Whalen, 1981; Nittrouer and Miller, 2000; Jongman *et al.*, 2000). Zeng and Turner (1990), however, reported that adults with hearing loss do not appear to use the vocalic transition, but rather rely on fricative noise for perception of /s/. Interestingly, Nittrouer, Crowther, and Miller (1998) reported that young NH children tend to rely more on the vocalic transition than the fricative noise. Un-

fortunately, similar studies have not been conducted in young HI children.

In addition to acoustic properties, linguistic cues also can be used to indicate the presence of /s/ for listeners with normal language skills (e.g., ''Give me a book'' versus ''Give me some books''). For NH children, it is likely that the development of these linguistic rules is contingent upon repeated exposure to multiple cues in a variety of contexts. It is not clear how well young HI children, who are still in the process of developing language, will be able to take advantage of linguistic cues when the audibility of /s/ is compromised.

It is important to emphasize that the focus of this study was HI children's perception of /s/ in quiet. As such, it is not possible to comment on the effects of high-frequency audibility on other phonemes or to rule out that an extended bandwidth may actually degrade performance for other speech sounds. Although studies using a wide range of speech sounds have been conducted with adults, additional studies are needed to address this issue for children. The current study represents a ''worst case'' scenario for the perception of /s/, because vocalic transitions and linguistic cues were not available to the listeners. Developmental studies using words and sentences are needed to refine our understanding of the importance of high-frequency audibility to the perception of /s/ and the formation of linguistic rules involving this phoneme. The current results also cannot be generalized to more difficult listening conditions, such as those in which noise and/or reverberation are present.

Since the spectra of talkers in the current study are consistent with earlier reports (Strevens, 1960; Heinz and Stevens, 1961; McGowan and Nittrouer, 1988; Nittrouer, Studdert-Kennedy, and McGowan, 1989; Boothroyd and Medwetsky, 1992; Boothroyd, Erickson, and Medwetsky, 1994; Jongman, Wayland, and Wong, 2000), these results suggest that, when fitting hearing aids to young children, audible energy through 5 kHz is needed to maximize perception of /s/ produced by a male talker and that a 9-kHz upper limit is needed for /s/ produced by a female. From a clinical perspective, it is important to distinguish between cases where performance *cannot be improved* by high-frequency amplification and cases where performance is actually *degraded*. In this study little or no evidence of degradation in the perception of /s/ was observed with increasing bandwidth. Previous studies with adults have produced mixed results with respect to this issue and, in all studies, the negative consequences of high-frequency amplification were evident in only some listeners. As such, when fitting hearing aids to young children, it would seem reasonable to provide as much of the prescribed high-frequency gain as possible. Exceptions would be those cases where it can be demonstrated that no usable hearing exists in the high-frequency region. In steeply sloping hearing losses, this can be determined by obtaining high-frequency thresholds in the presence of a low-pass masker (primarily to eliminate responses to amplifier noise). In addition, Moore *et al.* (2000) have developed a masking technique to identify ''dead regions'' within the cochlea (defined as areas where there is thought to be a complete loss of inner hair cells). If no usable hearing is present, then provision of amplification in that frequency region would be unwarranted. In all other instances, however, the potential benefit of high-frequency amplification should be determined on an individual basis.

ACKNOWLEDGMENTS

The authors wish to thank Michael Gorga, Donna Neff, Dawn Konrad-Martin, Arthur Boothroyd, and an anonymous reviewer for their helpful comments on an earlier version of this manuscript. This work was supported by NIH.

Allen, P., Wightman, F., Kistler, D., and Dolan, T. (**1989**). ''Frequency resolution in children,'' J. Speech Hear. Res. **32**, 317–322.

ANSI (**1996**). ANSI S3:22-1996, ''Specification of hearing aid characteristics'' (American National Standards Institute, New York).

Bilger, R. C., and Wang, M. D. (**1976**). ''Consonant confusions in patients with sensorineural hearing loss,'' J. Speech Hear. Res. **19**, 718–748.

Boothroyd, A., Erickson, F. N., and Medwetsky, L. (**1994**). ''The hearing aid input: A phonemic approach to assessing the spectral distribution of speech,'' Ear Hear. **15**, 432–442.

Boothroyd, A., and Medwetsky, L. (**1992**). ''Spectral distribution of /s/ and the frequency response of hearing aids,'' Ear Hear. **13**, 150–157.

Byrne, D. (**1986**). ''Effects of frequency response characteristics on speech discrimination and perceived intelligibility and pleasantness of speech for hearing-impaired listeners,'' J. Acoust. Soc. Am. **80**, 494–504.

Ching, T. Y., Dillon, H., and Byrne, D. (**1998**). ''Speech recognition of hearing-impaired listeners: Predictions from audibility and the limited role of high-frequency amplification,'' J. Acoust. Soc. Am. **103**, 1128–1140.

Danhauer, J. L., Abdala, C., Johnson, C., and Asp, C. (**1986**). ''Perceptual features from normal-hearing and hearing-impaired children's errors on the NST,'' Ear Hear. **7**, 318–322.

Denes, P. B. (**1963**). ''On the statistics of spoken English,'' J. Acoust. Soc. Am. **35**, 892–904.

Dubno, J. R., and Dirks, D. D. (**1982**). ''Evaluation of hearing-impaired listeners using a nonsense-syllable test. I. Test reliability,'' J. Speech Hear. Res. **25**, 135–141.

Elfenbein, J. L., Hardin-Jones, M. A., and Davis, J. M. (**1994**). ''Oral communication skills of children who are hard of hearing,'' J. Speech Hear. Res. **37**, 216–226.

Gabrielsson, A., Schenkman, B. N., and Hagerman, B. (**1988**). ''The effects of different frequency responses on sound quality judgments and speech intelligibility,'' J. Speech Hear. Res. **31**, 166–177.

Heinz, J. M., and Stevens, K. N. (**1961**). ''On the properties of voiceless fricatives consonants,'' J. Acoust. Soc. Am. **33**, 596.

Hellgen, J., Lunner, T., and Arlinger, S. (**1999**). ''System identification of feedback in hearing aids,'' J. Acoust. Soc. Am. **105**, 3481–3496.

Hnath-Chisolm, T. E., Laipply, E., and Boothroyd, A. (**1998**). ''Age-related changes on a children's test of sensory-level speech perception capacity,'' J. Speech Lang. Hear. Res. **41**, 94–106.

Hogan, C. A., and Turner, C. W. (**1998**). ''High-frequency audibility: Benefits for hearing-impaired listeners,'' J. Acoust. Soc. Am. **104**, 432–441.

Jongman, A., Wayland, R., and Wong, S. (**2000**). ''Acoustic characteristics of English fricatives,'' J. Acoust. Soc. Am. **108**, 1252–1263.

Kortekaas, R., and Stelmachowicz, P. (**2000**). ''Bandwidth effects on children's perception of the inflectional morpheme /s/: Acoustical measurements, auditory detection, and clarity rating,'' J. Speech Lang. Hear. Res. **43**, 645–660.

Max, L., and Onghena, P. (**1999**). ''Some issues in the statistical analysis of completely randomized and repeated measures designs for speech, language, and hearing research,'' J. Speech Lang. Hear. Res. **42**, 261–270.

McGowan, R. S., and Nittrouer, S. (**1988**). ''Differences in fricative production between children and adults: Evidence from an acoustic analysis of /sh/ and /s/,'' J. Acoust. Soc. Am. **83**, 229–236.

Moore, B. C., Huss, M., Vickers, D. A., Glasberg, B. R., and Alcantara, J. I. (**2000**). ''A test for the diagnosis of dead regions in the cochlea,'' Br. J. Audiol. **34**, 205–224.

Murray, N., and Byrne, D. (**1986**). ''Performance of hearing-impaired and normal hearing listeners with various high frequency cut-offs in hearing aids,'' Aust. J. Audiol. **8**, 21–28.

Nittrouer, S., Studdert-Kennedy, M., and McGowan, R. S. (**1989**). ''The emergence of phonetic segments: Evidence from the spectral structure of fricative-vowel syllables spoken by children and adults,'' J. Speech Hear. Res. **32**, 120–132.

Nittrouer, S., Crowther, C. S., and Miller, M. E. (**1998**). ''The relative weighting of acoustic properties in the perception of [s]+stop clusters by children and adults,'' Percept. Psychophys. **60**, 51–64.

Nittrouer, S., and Miller, M. E. (**2000**). ''The effect of segmental order on fricative labeling by children and adults,'' Percept. Psychophys. **62**, 266–284.

Nozza, R. J., Rossman, R. N., and Bond, L. C. (**1991**). ''Infant–adult differences in unmasked thresholds for the discrimination of consonant–vowel syllable pairs,'' Audiology **30**, 102–112.

Nozza, R. J., and Wilson, W. R. (**1984**). ''Masked and unmasked pure-tone thresholds of infants and adults: Development of auditory frequency selectivity and sensitivity,'' J. Speech Hear. Res. **27**, 613–622.

Owens, E. (**1978**). ''Consonant errors and remediation in sensorineural hearing loss,'' J. Speech Hear Disord. **43**, 331–347.

Owens, E., Benedict, M., and Schubert, E. D. (**1972**). ''Consonant phonemic errors associated with pure-tone configurations and certain kinds of hearing impairment,'' J. Speech Hear. Res. **15**, 308–322.

Pittman, A. L., and Stelmachowicz, P. G. (**2000**). ''Perception of voiceless fricatives by normal-hearing and hearing-impaired children and adults,'' J. Speech Hear. Res. **43**, 1389–1401.

Rankovic, C. M. (**1991**). ''An application of the articulation index to hearing aid fitting,'' J. Speech Hear. Res. **34**, 391–402.

Rudmin, F. (**1983**). ''The why and how of hearing /s/,'' The Volta Review **85**, 263–269.

Schneider, B. A., Trehub, S. E., Morrongiello, B. A., and Thorpe, L. A. (**1989**). ''Developmental changes in masked thresholds,'' J. Acoust. Soc. Am. **86**, 1733–1742.

Seewald, R. C., Cornelisse, L. E., Ramji, K. V., Sinclair, S. T., Moodie, K. S., and Jamieson, D. G. (**1997**). DSL V4.1 *for Windows: A Software Implementation of the Desired Sensation Level (DSL[i/o]) Method for Fitting Linear Gain and Wide-dynamic-range Compression Hearing Instruments* (University of Western Ontario, London, Ontario, Canada).

Skinner, M. W. (**1980**). ''Speech intelligibility in noise-induced hearing loss: Effects of high-frequency compensation,'' J. Acoust. Soc. Am. **67**, 306–317.

Strevens, P. (**1960**). ''Spectra of fricative noise in human speech,'' Lang. Speech **1**, 32–49.

Studebaker, G. A., Pavlovic, C. V., and Sherbecoe, R. L. (**1987**). ''A frequency importance function for continuous discourse,'' J. Acoust. Soc. Am. **81**, 1130–1138.

Studebaker, G. A., and Sherbecoe, R. L. (**1988**). ''Magnitude estimations of the intelligibility and quality of speech in noise,'' Ear Hear. **9**, 259–267.

Sullivan, J. A., Allsman, C. S., Nielsen, L. B., and Mobley, J. P. (**1992**). ''Amplification for listeners with steeply sloping, high-frequency hearing loss,'' Ear Hear. **13**, 35–45.

Tobias, J. V. (**1959**). ''Relative occurrence of phonemes in American English,'' J. Acoust. Soc. Am. **31**, 631.

Turner, C. W., and Cummings, K. J. (**1999**). ''Speech audibility for listeners with high-frequency hearing loss,'' Am. J. Audiol. **8**, 47–56.

Veloso, K., Hall III, J. W., and Grose, J. H. (**1990**). ''Frequency selectivity and comodulation masking release in adults and in 6-year-old children,'' J. Speech Hear. Res. **33**, 96–102.

Whalen, D. H. (**1981**). ''Effects of vocalic formant transitions and vowel quality on the English [s]–[ʃ] boundary,'' J. Acoust. Soc. Am. **69**, 275–282.

Wightman, F., Allen, P., Dolan, T., Kistler, D., and Jamieson, D. (**1989**). ''Temporal resolution in children,'' Child Dev. **60**, 611–624.

Zeng, F. G., and Turner, C. W. (**1990**). ''Recognition of voiceless fricatives by normal and hearing-impaired subjects,'' J. Speech Hear. Res. **33**, 440–449.

The harmonic-to-noise ratio applied to dog barks

Tobias Riede[a)]
Institut für Biologie, Humboldt-Universität zu Berlin, Invalidenstrasse 43, 10115 Berlin, Germany

Hanspeter Herzel
Innovationskolleg für Theoretische Biologie, Humboldt-Universität zu Berlin, Invalidenstrasse 43, 10115 Berlin, Germany

Kurt Hammerschmidt
Deutsches Primatenzentrum, Kellnerweg 4, 37077 Göttingen, Germany

Leo Brunnberg
Klinik und Poliklinik für Kleine Haustiere, Freie Universität Berlin, Oertzenweg 19b, 14163 Berlin, Germany

Günter Tembrock
Institut für Biologie, Humboldt-Universität zu Berlin, Invalidenstrasse 43, 10115 Berlin, Germany

(Received 14 December 2000; revised 25 June 2001; accepted 1 July 2001)

Dog barks are typically a mixture of regular components and irregular (noisy) components. The regular part of the signal is given by a series of harmonics and is most probably due to regular vibrations of the vocal folds, whereas noise refers to any nonharmonic (irregular) energy in the spectrum of the bark signal. The noise components might be due to chaotic vibrations of the vocal-fold tissue or due to turbulence of the air. The ratio of harmonic to nonharmonic energy in dog barks is quantified by applying the harmonics-to-noise ratio (HNR). Barks of a single dog breed were recorded in the same behavioral context. Two groups of dogs were considered: a group of ten healthy dogs (the normal sample), and a group of ten unhealthy dogs, i.e., dogs treated in a veterinary clinic (the clinic sample). Although the unhealthy dogs had no voice disease, differences in emotion or pain or impacts of surgery might have influenced their barks. The barks of the dogs were recorded for a period of 6 months. The HNR computation is based on the Fourier spectrum of a 50-ms section from the middle of the bark. A 10-point moving average curve of the spectrum on a logarithmic scale is considered as estimator of the noise level in the bark, and the maximum difference of the original spectrum and the moving average is defined as the HNR measure. It is shown that a reasonable ranking of the voices is achievable based on the measurement of the HNR. The HNR-based classification is found to be consistent with perceptual evaluation of the barks. In addition, a multiparametric approach confirms the classification based on the HNR. Hence, it may be concluded that the HNR might be useful as a novel parameter in bioacoustics for quantifying the noise within a signal. [DOI: 10.1121/1.1398052]

PACS numbers: 43.80.Ka, 43.80.Lb, 43.80.Nd [WA]

I. INTRODUCTION

In mammal bioacoustics the spectrographic structure of vocal utterances is typically considered as either tonal (referring to a harmonic spectrographic structure) or as atonal (referring to a noisy (or broadband) spectrographic structure). In this paper ''noise'' refers to any nonharmonic (irregular) energy within the bark signal.

There are two disadvantages of this classification of bioacoustic signals into ''tonal'' and ''atonal'' signals: (i) this classification is not sufficient to describe the spectrographic picture in many so-called atonal calls, and (ii) this classification does not take into account the fine graduation of the call type according to its communicative meaning. For instance, in canids a different communicative meaning is ascribed to the ratio of the harmonic and nonharmonic energy in bark vocalization (Tembrock, 1976; Feddersen-Petersen, 1996; Wilden, 1997).

In this study we investigate dog barks with the goal to quantify the amount of irregular energy. Dog barks contain harmonic and nonharmonic energy with varying amount. We compute the harmonic-to-noise-ratio (HNR) of dog barks. The HNR is defined as the ratio of the harmonic components to the noise (Yumoto *et al.*, 1982). The HNR can be related to the perceptual characteristics of an acoustic signal (Kojima *et al.*, 1980) as well as to the mechanism of its production. An acoustic signal with a low HNR sounds overwhelmingly noisy or hoarse, whereas a signal with a very high HNR sounds harmonic, clear, and metallic. The harmonic elements can be related to periodic tissue vibrations that interrupt the exhaled airstream. In mammals those periodic tissue vibrations are typically the vibrations of the vocal folds. Turbulent noise is generated at different constrictions within the vocal tract (including an incomplete closure of the glottis during the vocal fold's oscillation cycle). In addition,

a)Author to whom correspondence should be addressed; electronic mail: tobiasriede@web.de

noise can be caused by chaotic (irregular) oscillations of the vibrating tissue. The HNR has been extensively used in human phoniatrics as a diagnostic tool for the quantification of vocal changes (e.g., Yumoto *et al.*, 1982; Murphy, 1999). The HNR belongs to a group of parameters that is commonly called ''noise features'' (as suggested by Michaelis *et al.*, 1998). Two parameters designed to measure the relative noise component in the voice signal of humans belong to this group of noise features; (i) the harmonics-to-noise ratio (Yumoto *et al.*, 1982) and (ii) the normalized-noise energy (Kasuya *et al.*, 1986).

A second group are the so-called ''aperiodicity features,'' mainly ''jitter'' and ''shimmer,'' which quantify the variation of the fundamental frequency and the cycle-to-cycle peak-amplitude variation, respectively. (For an overview of the latter group see, for instance, Pinto and Titze, 1990).

Owren and Linker (1995) suggest the HNR as a useful tool in animal bioacoustics, and the study evaluation of the relative amounts of harmonic and noise energy in an animal's vocal utterance has been proposed several times (e.g., Seyfarth and Cheney, 1984; Owren and Bernacki, 1988). Seyfarth and Cheney (1984) and Owren and Bernacki (1988) consider the ''mixture of voicing and noise...'' in the signal of vervet monkey alarm calls by using cepstrum analysis of short segments, or by visually comparing narrow-band and broadband spectrograms. The scientific goal of both studies was to find out if there is any harmonic structure present in the studied utterances. Here, we extend that approach in the sense that we compare calls *quantitatively* according to different amounts of harmonic and noise energy and we apply the HNR measure systematically to animal acoustic signals.

For the calculation of the HNR we use a simple moving-average procedure, as already applied by Kitajima (1981), who studies the HNR of the human voice. In a preliminary experiment we test the procedure with artificial sounds with known HNRs, in order to ensure that the procedure can reliably extract all relevant information. The correlation between the expected and the measured HNRs is highly significant (Riede, 2000), suggesting that the procedure is able to mirror the HNR relationships within a group of given sound signals. In this study we present the application of the HNR measure to dog barks, and we present the results of a multiparametric approach (for a review on multiparametric analysis see Schrader and Hammerschmidt, 1997) using 60 parameters other than the HNR, which we apply to the same sample of calls. The rationale of the latter study was to investigate if the HNR results can be reproduced with a standard method established in animal bioacoustics.

II. MATERIAL AND METHODS

A. Subjects

We choose dogs of the breed ''dachshund,'' and we predispose the dachshunds for this study because they express a low bark release threshold. We take audio recordings from ten healthy dachshunds considered as the ''normal sample'' at the owner's property. The dogs ranged in age between 9 months and 11 years, and they ranged in weight between 6.8 and 10.0 kg. A general clinical investigation of these ten dogs confirmed no peculiarities in the state of health.

Studies in veterinary medicine have claimed that dogs with disorders express certain degrees of an ''audible dysphonia'' (see, for instance, Venker-van Haagen, 1992; Bagley *et al.*, 1993). For this reason we record barks from ten dachshunds in a veterinary clinic; some of them expressed several kinds of an audible dysphonia ('clinic sample'). We record the barks of those ten dachshunds in the Clinic for Small Animals at the Freie Universität Berlin. Dogs of this sample ranged in age between 3 and 8 years, and they ranged in weight between 7.9 and 10.7 kg. Both samples do not differ significantly in weight ($N_1=10$; $N_2=10$; F-test: $F=1.13$, $P=0.85$; unpaired t-test: $t=0.26$, $P=0.79$).

The ten dachshunds of the clinic sample were treated in the clinic for thoracolumbal intervertebral disc extrusion, a common disease of the 4-to-6-year-old dachshund (Grevel and Schwartau, 1997a,b). Intervertebral disc extrusion occurred in all ten dogs in the transition from the thoracic to the lumbal backbone. The extrusion results in a compression of the spinal cord, affecting the normal nerval supply behind (caudally) the affected point. Neurologic examination revealed paresis of the hind legs with intact spinal reflexes in all dogs. After detailed diagnostic examinations, the goal of the therapy was a decompression of the spinal cord. This was done by performing a surgery (hemilaminectomy) in six dogs and antiphlogistic therapy in the four other dogs.

B. Acoustic recordings

We take the audio recordings with a Marantz PMD 222 tape recorder and Sennheiser microphone (ME80 head with K3U power module) on ChromeSuper tapes (60 min.). The frequency response of the microphone is flat (40 Hz–20 kHz; ± 2.5 dB) within the frequency range of analysis. The tape recorder exhibits a flat frequency response (40 Hz–14 kHz, ± 3 dB), a distortion of 0.1%, and a signal-to-noise ratio of 57 dB. Distance between dog and microphone varied from 50 to 150 cm.

In all 20 dogs we release barking by staring into the dog's eyes (a mild threat to the animal). We include only those animals in which barking could be released in this way.

Barking is usually uttered in sequences of variable duration consisting of barks with interspersed pauses. We use the first 50 calls per session for acoustic analysis. We discard calls that are distorted by background signals (mostly other barking dogs) or calls that have an overloaded recording level (controlled by the Marantz built-in volume meter indicating the average recording level).

C. Acoustic analysis

We perform signal analysis on a PC using the signal-processing software HYPERSIGNAL-MACRO™. We digitize all recordings at a 16-bit quantization and a 44-kHz sampling rate using a DSP32C PC system board. We complete the spectrographic analysis by using a 512-point fast Fourier transformation, with 75% frame overlapping, a 30-kHz sampling frequency, and a Hanning window. To avoid aliasing effects we low-pass filter all barks at 14 kHz.

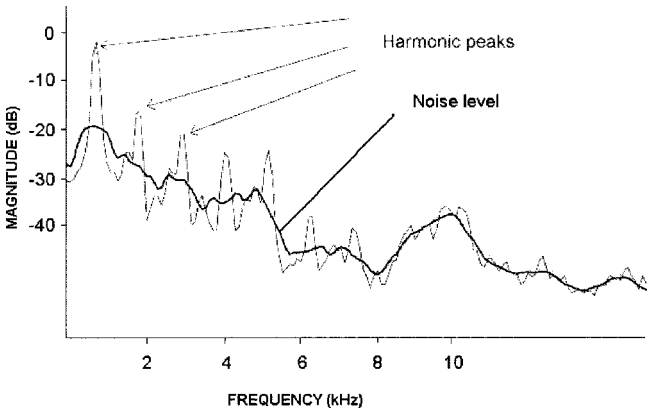

FIG. 1. Drawing of an original spectrum curve with harmonic peaks (thin line) and the 10-point moving-average curve of the same spectrum (thick line). The moving-average curve is used as estimator of the noise level within the bark. The largest distance between both curves is considered as HNR.

D. HNR calculation

As dog barks are amplitude- and frequency modulated, any harmonic peaks present in the spectrum are only visible in the short-time spectrum. Averaging over long time segments broadens these peaks, thereby ''smearing'' and hiding any harmonic structure. For the calculation of the HNR we choose a segment of 50 ms from the middle of the bark, from which we compute the power spectrum by averaging over all 512-point FFTs. We transform the logarithmic spectrum to an ASCII file and we estimate the noise level and determine the maximum difference between the harmonic peaks and the noise level by an EXCEL macro. We estimate the noise level by calculating the moving average of the logarithmic spectrum curve. We subtract the moving-average curve from the curve of the original spectrum, and we define the largest value of this difference as the HNR (Fig. 1). The fact that the difference of the logarithmic spectra corresponds to the ratio of the (nonlogarithmic) spectra justifies the term ''harmonic-to-noise ratio.''

We do not expect marked effects on the HNR due to the acoustics of the room, because the dog–microphone distance was only 0.5 to 1.5 m, resulting in a sufficient sound-pressure level of the bark above any room specific reflection. Two healthy dogs were recorded once in a clinic room (under the same conditions as for the clinic sample) and once outside. The HNR values differed only slightly under those two conditions (dog 1: 16.3 and 16.4; dog 2: 13.8 and 13.6).

E. Discriminant analysis

We measure 60 acoustic parameters of the spectrogram, the spectra, and time series of the same bark sample that we use for the HNR calculation. This multiparametric technique is established in animal bioacoustics (e.g., Schrader and Hammerschmidt, 1997). We test if the classification of individuals based on the HNR measure can be reproduced by the multiparametric approach.

We digitize 1000 barks using RTS 1.31 (Engineering Design, Belmont, MA) and transform the digitized calls into the frequency-time domain with SIGNAL 2.29 31 (Engineering Design, Belmont, MA), using an FFT size of 1024 points, a sampling frequency of 40 kHz, a frequency resolution of 39 Hz, and time resolution of 5 ms. We analyze the resulting frequency-time spectra with LMA 8.0, a software tool that can extract different sets of call parameters from complex acoustic signals (Schrader and Hammerschmidt, 1997). We use 60 parameters in the subsequent statistical analysis. These parameters describe the frequency structure, such as the fundamental frequency, and the distribution of the spectral energy, including the peak frequency and the frequency range.

We apply a technique called discriminant function analysis to test the affiliation of a dog's barks to a particular group. A data set must meet several assumptions before a discriminant function analysis can be applied. Field data sets rarely, if ever, meet assumptions precisely and there is evidence that certain of these assumptions can be violated moderately without large changes in correct classification results (for review see, for instance, McGarigal *et al.*, 2000). For instance the larger the sample sizes, the more robust the analysis is to violations. The key assumption is that group dispersions are homogeneous (Klecka, 1980), i.e., it requires that the variances of the discriminating variables be the same in the respective populations from which the groups of entities have been drawn. Moreover, it requires that the correlation between any two variables be the same in the respective populations from which the different groups have been sampled. To meet these assumptions approximately, the original 60 parameters were reduced to 16 ''principal components.'' Principal component analysis reduces the dimensionality of a multivariate data set by condensing a large number of original variables into a smaller set of new composite variables (principal components) with a minimum loss of information. The principal components share the property of having the same variance 1 and of being uncorrelated to each other, i.e., of having the same correlation coefficient 0.

We use the SPSSWIN 9.0 software package for both the discriminant function analysis and the principal component analysis.

The discriminant function analysis was used to measure the degree to which the HNR procedure had captured acoustic features of the barks that would allow them to be sorted into groups. Since discriminant function analysis relies on preassigning cases, dogs with similar HNR values were associated into groups. The mean HNR $\pm$ standard deviation of the normal sample ($N=10$) was 13.2 ± 3.4. We choose cutoffs at HNR$=10$ and HNR$=16$. Based on the HNR of the dog's voice signals we group them into three different groups: (i) a ''low-HNR'' group (mean HNR less than 9) consisting of 3 dogs; (ii) a ''medium-HNR'' group (mean HNR 10 to 16) consisting of 14 dogs, and (iii) a ''high-HNR'' group (mean HNR higher than 16) consisting of 3 dogs. The partitioning of the dogs in low, medium, and high HNR group was somewhat arbitrary. However, it allows the discriminant function analysis to be applicable. We then tested by means of discriminant function analysis how well the single calls could be assigned to those three groups.

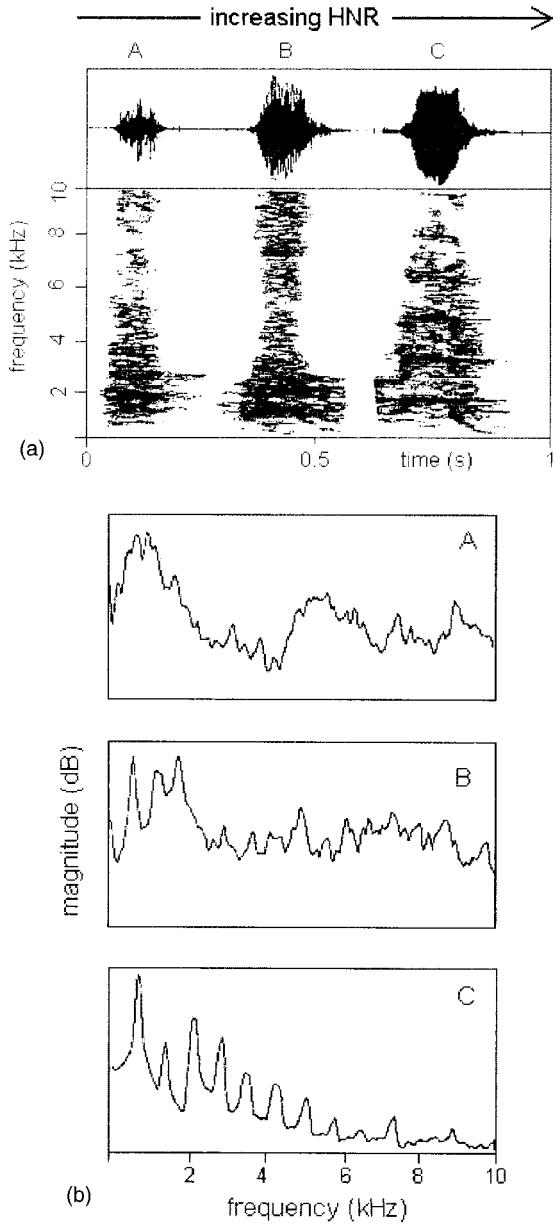

FIG. 2. (a) Spectrograms and time series, and (b) spectra of three barks with different HNR illustrating that in calls with high HNR values the harmonic peaks are stronger than in others. The HNR increases from call A to call C.

III. RESULTS

Figure 2 shows time series and spectrograms of barks from three dogs which we record in the same behavioral context. We find that a harmonic structure is clearly visible in the bark with the highest HNR, whereas almost no harmonic structure but only noise can be seen in the bark with the lowest HNR. We calculate all power spectra from 50-ms segments from the middle of the barks shown in the top row of Fig. 2. We can see strong harmonic peaks in the bark with a high HNR and only weak or no harmonic peaks in the bark with a low HNR.

A. The HNR of 20 dogs

Table I shows the HNR of all 20 dogs considered in this study. The mean HNR of the normal sample is 13.2 ± 3.4, and the mean of the clinic sample is 13.5 ± 4.2. The samples differ significantly in their variances (F-test: $F = 1.45$; $P < 0.001$) but not in their medians (Mann-Whitney test: $U = 0.000\,13$; $P1 = 0.19$; $P2 = 0.38$). The clinic and the normal sample are strongly overlapping. However, some individuals (12, 13, 14 on the one hand and 11, 17 on the other hand; see Table I) from the clinic sample represent the far ends of the HNR scale.

TABLE I. HNR values (mean and standard deviation) and weights of 20 individuals considered in this study.

Sex	HNR	Weight (kg)	HNR rank
	Normal sample		
m	15.5 ± 2.3	6.8	17
w	9.9 ± 2.3	10.0	3
w	13.8 ± 3.2	7.4	11
m	14.2 ± 3.1	8.4	13
m	14.9 ± 2.9	9.3	16
w	13.7 ± 2.0	8.9	10
m	11.8 ± 2.4	9.5	6
w	11.7 ± 2.2	9.4	5
w	14.3 ± 2.3	8.7	14
w	14.0 ± 2.2	9.1	12
	Clinic sample		
w	7.1 ± 1.4	7.9	1
w	17.8 ± 2.8	10.7	20
m	17.6 ± 3.3	10.1	19
w	16.3 ± 2.6	9.2	18
m	12.9 ± 2.9	8.7	7
w	13.2 ± 3.2	8.2	8
w	9.7 ± 2.8	9.3	2
m	14.4 ± 2.3	9.6	15
m	13.6 ± 2.7	8.4	9
m	10.6 ± 2.8	8.1	4

B. Discriminant analysis

We define three groups of dogs on the basis of the HNR scale, and we ask: ''How well does this classification apply to single barks?'' If there were a perfect classification of all calls we would expect that all 50 calls recorded from each individual would fall into the same class, as illustrated in Fig. 3(B). Figure 3(A) shows the distribution of calls into the three groups according their HNR values. For example, individuals 1 to 3 belong to the low-HNR group when considering their mean HNR. However, these individuals do not only produce calls with HNR values below 10. Some calls belong to the medium-HNR group, and some calls even belong to the high-HNR group. By comparing Fig. 3(A) to the ideal call distribution in Fig. 3(B) we find that on average 66.3% of the barks are assigned correctly to the three groups on the basis of their HNR.

Next, we perform a discriminant function analysis using the first 16 principal components as described above. The discriminant function analysis classification yields an average correct assignment of 83% to the three HNR groups, which is graphically shown in Fig. 3(C). This means 83% of the calls were assigned correctly to the three groups. Since these groups are defined on the basis of the mean HNR measure, the multiparametric analysis produces an 83% match to

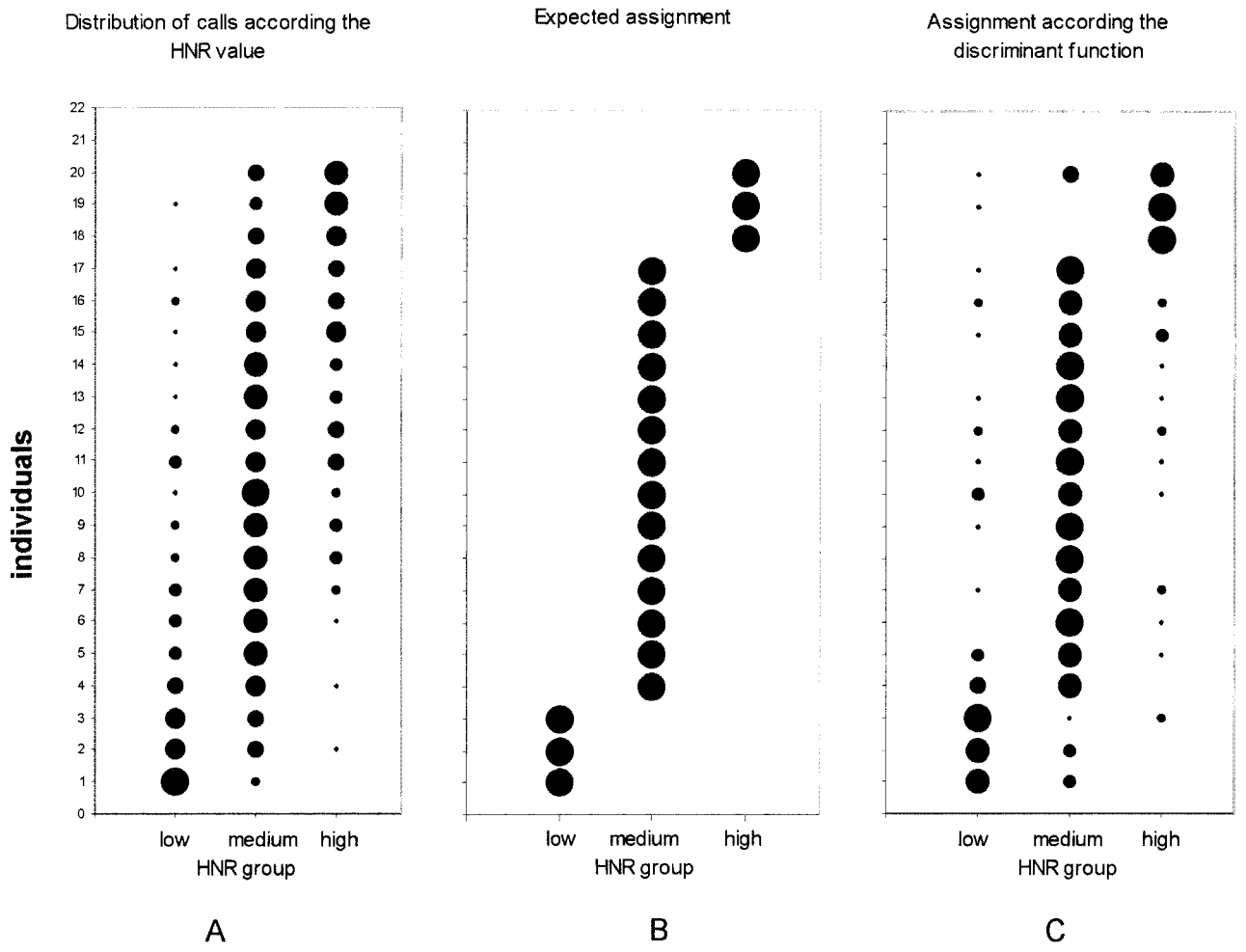

FIG. 3. Distribution of calls into three groups according to their HNR values (A), as expected in a 100% assignment of calls into one of the three groups (B), according to the assignment of the discriminant function (C).

HNR results. In order to test the robustness of the classification we perform two additional tasks. We first divide the sample of 50 calls into a training and a test set, and we repeat the classification experiment described above for both the training and the test. A classification with a 50%-random sample confirmed the previous results: the average correct assignment was 88% for the training set and 81% for the test set.

In a second classification experiment we remove single individuals from the sample and we use those individuals as a test set. The test with individuals from the medium-HNR group (HNR between 10 and 16) revealed correct assignment of above 85% in each of four tested individuals.

IV. DISCUSSION

We show that a reasonable ranking of the voices is achievable based on the measurement of the harmonics-to-noise ratio (HNR). The HNR of a normal sample of healthy dogs ranges from 10 to 16, whereas several unhealthy animals of the clinic sample exceeded those limits. Considering that low-HNR values produce the auditive impression of a hoarse voice and very high HNR values that of a pressed or metallic voice (in dogs ''yelping''), the observed deviations are consistent with those observed and verbally described by many veterinarians (e.g., Venker van Haagen, 1992; Bagley *et al.*, 1993).

We find that the HNR seems to be a useful numeric parameter to quantify vocal changes in disordered dogs. It would be interesting to further investigate if the HNR correlates to certain aspects of the state of health.

Earlier studies stating a varying communicative meaning of a variable amount of harmonic and noise energy (Tembrock, 1976; Morton, 1977; Feddersen-Petersen, 1996; Wilden, 1997) rely on spectrographic and auditive evaluation. In this study we could show that a simple numeric parameter, the HNR, to some degree reflects those complex spectrographic pictures and the auditive impression (Fig. 2).

A preliminary study (Riede, 2000) confirms that there is a correspondence between the HNR measure and the auditive impression. In that study the 20 dachshunds were paired, and from all 190 possible pairs of dachshunds 27 pairs were chosen. Fifteen successive barks from each of the dogs were considered for the playback experiment. Five persons were asked to judge the degree of hoarseness in both dogs by deciding which of those two utterances sounded ''more hoarse.'' The hypothesis to be tested was that in the dog judged ''hoarser'' the HNR should be lower than the HNR

value of the other dog. If the HNR measure relates to the subjects decision, we expect a more than 50% concordance between the subject's results and the HNR scale. The agreement between the HNR scale and the auditive impression in five persons was 70%, 75%, 77%, 78%, and 80%, i.e., 70% to 80% of the pairs were ordered as predicted by the HNR.

The ''auditive impression'' experiment and the correspondence between the spectrographic picture and the HNR suggests that the HNR could bear information about a varying communicative meaning of the signal. It would be interesting to study if the HNR can reflect some communicatively relevant information such as the motivational state.

The moving-average procedure for computing the HNR is used by Kitajima (1981) for the human voice. Like other perturbation measures this technique is judged to be a rough measure for human phoniatricians (Michaelis *et al.*, 1997), in the sense that fine graded changes in voice quality could not be quantified. We find that this roughness makes the technique robust against a number of handicaps in animal bioacoustics, like background noise or strong frequency modulation.

However, there are at least two problems of the moving-average technique. The first problem is the overestimation of the noise level. Frequency modulations result in a broadening of the harmonic peaks in an averaged spectrum. As the duration of the time segment and the number of harmonics increases, the broadening of the harmonics in the averaged spectrum increases. In order to circumvent this problem we propose to consider a time segment of only 50 ms for spectral analysis.

The second problem is related to the influence of the vocal tract on the spectrum envelope. The vocal tract acts as a filter that supports certain frequency areas (formants) and damps others. Fortunately, harmonic and noise components are affected similarly by this effect, and hence the difference is less dependent on vocal tract resonances. We tried to fix the problem by considering only dogs of the same breed assuming a comparable vocal tract length and shape. This limits the utility of the procedure presented in this paper, as the adjustment of the calculation parameters must be done for a specific breed. It will be interesting to investigate to which degree the calculation parameters will change from breed to breed and from species to species.

In order to evaluate the HNR results we apply a multiparametric analysis to the same sample of dog barks. The multiparametric analysis has been successfully used to analyze animal acoustic signals (Schrader and Hammerschmidt, 1997). In the multiparametric analysis 60 parameters are measured automatically from the time series, the spectrogram, and the spectrum. None of the 60 parameters can be considered equivalent to the HNR. We reduce the parameter set to the first 16 principal components. We find by discriminant function analysis that the call differentiation as suggested by the HNR parameter can be reproduced with an accuracy of 83%. The correct assignment suggests that the parameter set contains a large fraction of the HNR information.

Of course, there is information in the voice signals that is not captured by the HNR. As intuitively assumed after listening to the original signal (sound samples available from Riede, 2000) the amount of irregularity in the signals changes simultaneously with other parameters (such as, for instance, pitch). Those intercorrelating parameters are possibly considered by the multiparametric approach but not by the single-parameter HNR.

As the aim of this paper is the proposal of a new method of quantifying noise in animal signals, we address only briefly the occurrence of extreme HNR values in the clinic sample. The animal with the lowest HNR was housed in the clinic for 18 days, where it was treated only by anti-inflammatory therapy. During that time the animal was frequently barking. We assume that the observed low HNR was due to an exhaustion of the vocal folds, which corresponds to microlesions of the mucosal cover impacting the vocal-fold vibration behavior. This phenomenon is well known in humans (Wendler *et al.*, 1996) and it has been suggested to be the reason for a cat's dysphonia (Riede and Stolle-Malorny, 1999). *In vitro* studies have shown that hyperphonation can affect a dog's vocal-fold tissue (Gray *et al.*, 1987; Gray and Titze 1988). Similar effects, as described by Gray *et al.* (1987) and Gray and Titze, (1988) on the human vocal folds have massive impacts on the voice (e.g., Fex and Fex, 1986).

The three dogs with the highest HNR were treated surgically (hemilaminectomy). Laryngeal inspection by direct visualization prior and after the surgery (general anesthesia maintained via tracheal intubation) showed a normal situation. The high HNR was observed one day after the surgical decompression and was reversible toward normal sounding barks within three days. The HNR increase in those cases can be considered functional since the laryngoscopic image showed no obvious injuries or lesions. In humans, functional-hypertensive dysphonia is characterized by an increased harmonic-to-noise ratio (Baken and Daniloff, 1991). In this situation, voice generation is characterized by an increased tension of the vocal-fold muscle and optionally by increased subglottic pressure (Wendler *et al.*, 1996). We considered six other dogs with thoracolumbal intervertebral disc extrusion in this study. The barks of those dogs do not exhibit extreme HNR values. Three of them underwent surgical decompression of the spinal cord by hemilaminectomy, and three were treated with antiphlogistic therapy. Hence, we may speculate that extreme HNR values are not a regularly occurring symptom in this disease; they occur only in some cases after surgery.

One explanation of hypertension in the laryngeal configuration of the hemilaminectomized dogs is pain. However, we observed no disappearance of the hypertensive sound (i.e., high HNR values) under the regular pain-reducing butyrophenon (Temgesic®) therapy. A second plausible hypothesis for the observed hypertensive sound is peripheral nerve stimulation caused by the surgery, resulting in retrograde stimulus transport via central areas to the vagus nerve. Such a peripheral stimulation and the retrograde stimulus transport have been observed in the thermoregulatory system (Szolcsanyi, 1988; Szekely *et al.*, 1997), and further research is necessary to unveil the relationship between high HNR values and the course of this disease.

The presented spectrum-based measure might be

complemented by techniques from nonlinear dynamics. The widespread occurrence of nonlinear phenomena in animal vocalization has been shown by Wilden *et al.* (1998), Riede *et al.* (2000). In this study we do not distinguish turbulent noise from chaotic vibrations, but other techniques might distinguish these two sources of irregularities (Michaelis *et al.*, 1997; Herzel and Reuter, 2000).

ACKNOWLEDGMENT

We thank Michael Owren and Ivo Grosse for comments on an earlier version of the manuscript.

Bagley, R. S., Stefanacci, J. D., Hansen, B., and Kornegay, J. N. (**1993**). ''Dysphonia in two dogs with cranial cervical intervertebral disk extrusion,'' J. Am. Anim. Hosp. Assoc. **29**, 557–559.

Baken, R. J., and Daniloff, R. G. (**1991**). *Readings in Clinical Spectrography of Speech* (Singular, San Diego).

Feddersen-Petersen, D. U. (**1996**). Ist Bellen für Haushunde kommunikativ? KTBL-Schrift (Aktuelle Arbeiten zur artgemäßen Tierhaltung, Darmstadt) **376**, 59–71.

Fex, B., and Fex, S. (**1986**). ''Small vocal fold abnormalities and their influence on phonation,'' in *Vocal Fold Histopathology: A Symposium*, edited by J. A. Kirchner (College Hill, San Diego).

Gray, S. D., Titze, I., and Lusk, R. P. (**1987**). ''Electron microscopy of hyperphonated canine vocal cords,'' J. Voice **1**, 109–115.

Gray, S. D., and Titze, I. (**1988**). ''Histologic investigation of hyperphonated canine vocal cords,'' Ann. Otol. Rhinol. Laryngol. **97**, 381–388.

Grevel, V., and Schwartau, K. (**1997a**). ''Die Hemilaminectomie beim thorakolumbalen Bandscheibenvorfall des Hundes-1. Teil.'' Kleintierpraxis **42**, 5–20.

Grevel, V., and Schwartau, K. (**1997b**). ''Die Hemilaminectomie beim thorakolumbalen Bandscheibenvorfall des Hundes-2. Teil,'' Kleintierpraxis **42**, 173–196.

Herzel, H., and Reuter, R. (**2000**). ''Quantifying correlations in pitch and amplitude contours of sustained phonation,'' Acust. Acta Acust. **86**, 129–135.

Kasuya, H., Ogawa, S., Kikuchi, Y., and Ebihara, S. (**1986**). ''Normalized noise energy as an acoustic measure to evaluate pathologic voice,'' J. Acoust. Soc. Am. **80**, 1329–1334.

Kitajima, K. (**1981**). ''Quantitative evaluation of the noise level in pathologic voices,'' Folia Phoniatr. **33**, 115–124.

Klecka, W. R. (**1980**). ''Discriminant analysis,'' Sage University Paper Series. *Quantitative Applications in the Social Science*, Series No. 07-019 (Sage, Beverly Hills).

Kojima, H., Gould, W. J., Lambiase, A., and Isshiki, N. (**1980**). ''Computer analysis of hoarseness,'' Acta Oto-Laryngol. **89**, 547–557.

McGarigal, K., Cushman, S., and Stafford, S. (**2000**). *Multivariate Statistics for Wildlife and Ecology Research* (Springer, New York).

Michaelis, D., Fröhlich, M., and Strube, H. W. (**1998**). ''Selection and combination of acoustic features for the description of pathologic voices,'' J. Acoust. Soc. Am. **103**, 1628–1639.

Michaelis, D., Gramss, T., and Strube, H. W. (**1997**). ''Glottal to noise excitation ratio—A new measure for describing pathological voices,'' Acust. Acta Acust. **83**, 700–706.

Morton, E. S. (**1977**). ''On the occurrence and significance of motivation-structural rules,'' Am. Nat. **111**, 855–869.

Murphy, P. J. (**1999**). ''Perturbation-free measurement of the harmonics-to-noise ratio in voice signals using pitch synchronous harmonic analysis,'' J. Acoust. Soc. Am. **105**, 2866–2881.

Owren, M. J., and Bernacki, R. H. (**1988**). ''The acoustic features of vervet monkey alarm calls,'' J. Acoust. Soc. Am. **83**, 1927–1935.

Owren, M. J., and Linker, C. D. (**1995**). ''Some analysis methods that may be useful to acoustic primatologists,'' in *Current Topics in Primate Vocal Communication*, edited by E. Zimmermann, J. Newman, and U. Jürgens (Plenum, New York).

Pinto, N. B., and Titze, I. R. (**1990**). ''Unification of perturbation measures in speech signals,'' J. Acoust. Soc. Am. **87**, 1278–1289.

Riede, T., and Stolle-Malorny, A. (**1999**). ''The vocal change of a kitten with craniocerebellar trauma—A case study,'' Bioacoustics **10**, 131–141.

Riede, T. (**2000**). ''Vocal changes in animals during disorders,'' Ph.D. thesis, Humboldt-Universität zu Berlin (published at http://dochost.rz.hu-berlin.de/dissertationen/riede-tobias-2000-06-26/ together with sound samples).

Riede, T., Herzel, H., Mehwald, D., Seidner, W., Trumler, E., Tembrock, G., and Böhme, G. (**2000**). ''Nonlinear phenomena in the natural howling of a dog–wolf mix,'' J. Acoust. Soc. Am. **108**, 1435–1442.

Schrader, L., and Hammerschmidt, K. (**1997**). ''Computer-aided analysis of acoustic parameters in animal vocalizations: A multiparametric approach,'' Bioacoustics **7**, 247–265.

Seyfarth, R. M., and Cheney, D. L. (**1984**). ''The acoustic features of vervet monkey grunts,'' J. Acoust. Soc. Am. **75**, 1623–1628.

Szekely, M., Balasko, M., and Romanovsky, A. A. (**1997**). ''Peripheral neural input. Their role in fever development,'' Ann. N.Y. Acad. Sci. **549**, 427–434.

Szolcsanyi, J. (**1988**). ''Antidromic vasodilatation and neurogenic inflammation,'' Agents Actions **23**, 4–11.

Tembrock, G. (**1976**). ''Canid vocalizations,'' Behav. Processes **1**, 57–75.

Venker-van Haagen, A. J. (**1992**). ''Diseases of the larynx,'' Veterinary clinics of North America: Small animal practice **22**, 1155–1172.

Wendler, J., Seidner, W., Kittel, G., and Eysholdt, U. (**1996**). *Lehrbuch der Phoniatrie und Pädaudiologie. 3. Aufl* (Thieme, Stuttgart).

Wilden, I. (**1997**). Phonetische Variabilität in der Lautgebung Afrikanischer Wildhunde (*Lycaon pictus*) und deren frühe Ontogenese. Ph.D. thesis Humboldt University Berlin.

Wilden, I., Herzel, H., Peters, G., and Tembrock, G. (**1998**). ''Subharmonics, biphonation, and deterministic chaos in mammal vocalization,'' Bioacoustics **9**, 171–196.

Yumoto, E., Gould, W. J., and Baer, T. (**1982**). ''Harmonics-to-noise ratio as an index of the degree of hoarseness,'' J. Acoust. Soc. Am. **71**, 1544–1550.

Transforming echoes into pseudo-action potentials for classifying plants

Roman Kuc
Department of Electrical Engineering, Yale University, New Haven, Connecticut 06520-8284

(Received 1 March 2001; revised 10 July 2001; accepted 19 July 2001)

Animals perceive their environment by converting sensory stimuli into action potentials, or temporal point processes, that are interpreted by the brain. This paper investigates the information content of point processes extracted from echoes from *in situ* plants in an effort to understand how bats recognize landmarks in the field. A mobile sonar converts echoes into biologically similar temporal point processes, termed pseudo-action potentials (PAPs), whose inter-PAP interval relates to echo amplitude. The sonar forms a sector scan of an object to produce a spatial-temporal PAP field. Classifier neurons apply delays and coincidence detection to the PAP field to identify three distinct echo types, glints, blobs, and fuzz, which characterize plant features. Glints are large amplitude echoes exhibiting coherence over successive echoes in the sector scan, typically produced by favorably oriented isolated specular reflectors. Blobs are large echoes lacking coherence, typically bordering glints or formed by collections of interfering reflectors. Fuzz represents weak echoes, typically produced by collection of weak scatterers or by reflectors on the beam periphery. A small mirror reflector models a flat leaf surface and motivates the glint criteria. Classifiers are applied to experimental data from two types of tree trunks, a glint-producing sycamore (*Platanus occidenatalis*) and a glint-absent Norway maple (*Acer platanoides*) and two plants, a glint-producing rhododendron (*Rhododendron maximus*) and a glint-absent yew (*Taxus media*). We speculate that our narrow-band sonar models the activity of a single frequency bin in the frequency-modulated (FM) sweep emitted by bats, and that one function of the frequency bins in the FM sweep is to form a sector scan of the environment.
[DOI: 10.1121/1.1401741]

PACS numbers: 43.80.Ka, 43.64.Bt [WA]

I. INTRODUCTION

This paper investigates the information content of echoes from *in situ* plants in an effort to understand how bats recognize landmarks in the field. Attempts to classify objects from echoes typically employ synthetic emissions to probe small or simple objects.[1–3] Recent attempts to classify plants from echoes used analog-to-digital conversion to acquire echo waveforms observed by scanning potted plants in the laboratory along predetermined planes.[4,5] These studies employed wide bandwidth emissions to mimic the cochlear membrane and classify features using either neural networks[4] or statistical methods.[5] In contrast, our approach replaces expensive analog-to-digital conversion with simple nonlinear threshold detection to generate a point process and we model a single hair cell in the cochlear membrane, which responds to the frequency of the narrow-band excitation of our sonar. These data are generated by a mobile sonar operating in the field to scan plants *in situ* along scan planes that are favorable for plant classification, an ability we argue below bats have. All plants are in the Grove Street Cemetery in New Haven, CT.

Plants are interesting objects in that they have random shapes, change over time, and their classification as landmarks would benefit bat navigation.[5] The portability and real-time display capabilities of our sonar permit us to investigate objects that bats encounter in their natural setting. Controlling the sonar in a novel fashion converts echoes into multiple pulses, termed pseudo-action potentials (PAPs), which are analogous to action potentials observed at the biological auditory receptor.[6] The sonar forms a sector scan of the environment by rotating the transducer while emitting probing pulses and processing the echoes. The observed PAPs then form a PAP field that has both temporal (from one emission) and a spatial (from the sector scan) dimensions. Motivated by the classical neural delay line model suggested by Jeffress,[7] we process the PAP field using delays and coincidence detection to classify echoes into three categories for identifying features that could be employed as navigation landmarks.

To illustrate the range of echo information a plant provides, this paper examines plants exhibiting quite different acoustic properties, or those which can or cannot produce specular reflections. Specular plants, such as the rhododendron (*Rhododendron maximum*), have flat leaves that are large compared to the wavelength. These act as isolated specular reflectors that produce large echoes, or *glints*, when favorably oriented. As the sonar beam scans over a specular reflector, glints exhibit two exploitable features: a large amplitude and a coherence over successive echoes. Diffuse plants, such as the yew (*Taxus media*), have needles that are small with respect to the wavelength. These act as diffuse scatterers to produce many small echo components, which superimpose randomly at the detector. Strong echoes, termed *blobs*, can occur when the components constructively reinforce at the detector. Different from glints, blobs typically exhibit little or no coherence as the beam scans over the

 0001-4966/2001/110(4)/2198/9/$18.00

scatterer group. Multiple reflecting objects cause phase interference at the receiver which changes the amplitude of the component sum more rapidly with scan angle than an isolated specular reflector, thus disrupting coherence. This is well-known in radar cross-sections of simple and complex objects.[8]

Both plant types also produce weak echoes, which originate from small objects, from non-normal surfaces, or from scatterers near the beam edge. These produce sparse PAPs in time, which are classified as *fuzz*.

This paper describes the feature extraction and data reduction that results by applying PAP data to classifier neurons that produce outputs indicating the presence of glints, blobs, and fuzz, or features relevant to plant classification. The next section describes the sonar, methods for generating the PAP field, and experimental results motivating the criteria for the classifier neurons. Section III presents data observed from scanning plants. The procedure is discussed in Sec. IV, along with our speculations of its relevance to the bat echolation system.

II. METHODS

Our mobile sonar consists of the Polaroid 6500 ranging module,[9,10] an inexpensive and convenient system for acquiring *in situ* sonar data. The sonar connects to an IBM Thinkpad 380D laptop computer for real-time processing. All components mount on a modified wheelchair for universal access. The ranging module connects to a 3.6 cm diam Polaroid instrumentation grade ultrasound transducer to generate emissions and detect echoes. The emission contains 16 cycles at 49.4 kHz. This emission has a narrow bandwidth ($\approx$3 kHz) and exhibits a beam directivity pattern that approximates that of a vibrating circular piston in an infinite baffle, which has its first off-axis null at 14°.[11] The same transducer then detects echoes with a sensitivity pattern having the same shape. The computer sets the inter-emission period equal to 100 ms to allow echoes produced by the previous emission to decay below the threshold. The module includes a time-varying gain, which increases with time after emission to compensate for dispersion loss.

The processing performed by the ranging module is typical of most conventional detectors, while we control it in a novel way to produce multiple short pulses, as shown in Fig. 1. The module rectifies the detected echo waveform and applies the rectified signal to a lossy integrator. A digital output indicates when the integrator output first exceeds a threshold. This is its conventional mode of operation in metrology and mobile robot applications.[12] Our method samples the output every 2.5 μs to approximate the continuous-time auditory system and clears the indication when it occurs to form a pulse, a PAP. The module exhibits a refractory period, with the inter-PAP interval (IPI) varying inversely to the integrator output amplitude. This causes large isolated echoes, such as from a specular surface, to exhibit IPIs as short as 140 μs and produce as many as four PAPs before the integrator output decays below the threshold. Weak echoes produce as few as a single PAP. Echoes from range-distributed scatterers extend over time and produce additional PAPs whose IPIs relate to the instantaneous integrator output. Figures 1(e) and 1(f) show two sample PAP time sequences produced by echoes from a single emission observed from the rhododendron and yew, respectively, and analyzed below.

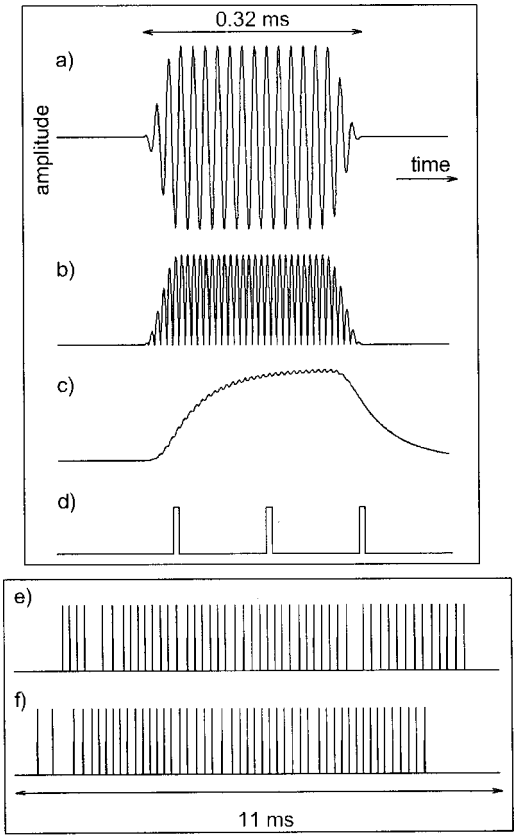

FIG. 1. Echo processing to produce pseudo-action potentials (PAPs). (a) Simulated echo waveform—acoustic stimulus. (b) Half-wave rectified waveform—transmitter substance release. (c) Signal appearing at the output of a lossy integrator—transmitter concentration at post-synaptic junction. Threshold level is shown as dashed line. (d) Module output showing a sequence of three PAPs. (e) PAP sequence observed for *Rhododendron maximum* (rf. Fig. 5). (f) PAP sequence observed for *Taxus media* (rf. Fig. 6).

This detector behavior can be easily mimicked with either analog electronics or computer programs operating on sampled data. The main advantage of the Polaroid module is that it offers an inexpensive and convenient portable device for acquiring *in situ* data, requiring only a laptop computer and a 6 V battery. The module is controlled through the printer port of the laptop computer (150 MHz Pentium) running a C language program under MS-DOS for real-time operation.

The module mounts at 1.5 m height on a motorized pan/tilt mechanism. Sector scans are formed by panning at 4.5° s^{-1} about an axis lying along the transducer aperture. An emission then occurs every 0.45°. A laser pointer directed along and mounted 5 cm above the transducer axis illuminates the object located near the beam center. This is useful for relating the observed data to the reflecting structures. The pan mechanism is mounted on a support that allows the scan plane to be tilted with respect to the horizontal plane. The scan plane can then be oriented to the normally incident to a leaf surface.

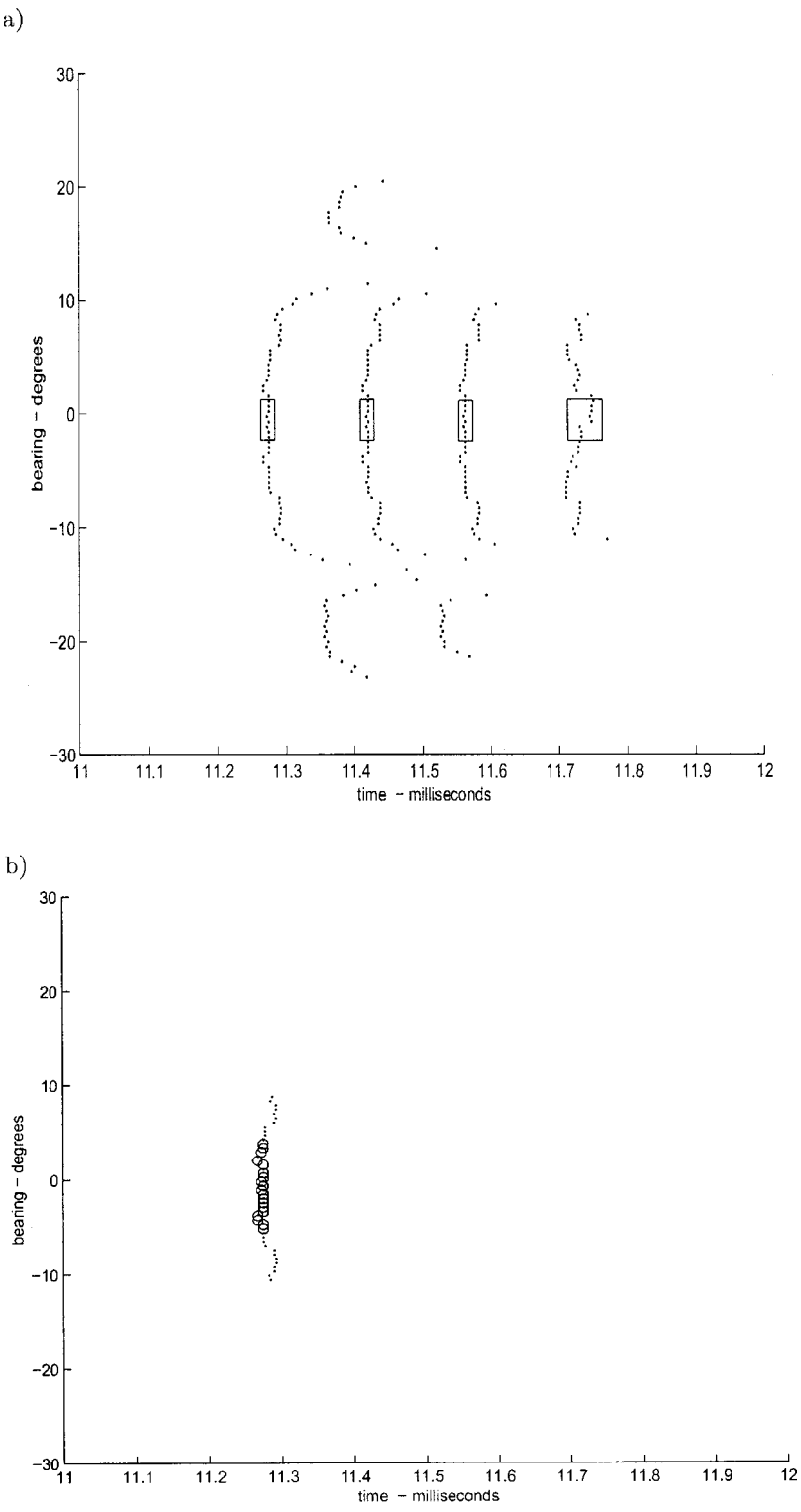

FIG. 2. Data observed when scanning across a 7 cm high by 5.7 cm wide mirror at 2 m range. (a) PAP field. Rectangles indicate the template satisfying glint criterion. (b) Classifier neuron outputs positioned at the occurrence times of PAPs satisfying the criterion: glints—circles, blobs—points.

Classifier neurons

A computer program implements three classifier neurons to process the PAP field formed by performing a sector scan across each object. The rules for classifying glints, blobs, and fuzz were motivated by neuronal delay and coincidence detection[7] and guided by observations from simple experiments. A small mirror mimics an isolated specular leaflike reflector. We suspended a 7 cm high by 5.7 cm wide mirror so the support generated no interfering echoes. We tilted the sonar scan plane with laser assistance to achieve normal incidence within $\pm 0.2°$ and positioned the mirror surface at 2 m range. At that range the beam main lobe diameter is 0.6 m, which is ten times larger than the mirror width. Figure 2(a) displays the PAP field when scanning across the mirror. Each PAP is represented by a point placed along the sonar orientation angle at the corresponding occurrence time. Echoes are detected and PAPs produced when the mirror is within the sonar beam, which extends over 40° in bearing. The largest echoes occur when the mirror surface normal is coincident with the transducer axis, defining zero bearing. These

large echoes exceed the threshold near the leading edge of the waveform and generate four PAPs. Four successive PAPs occur over most of the main lobe. The first three are spaced less than 150 μs apart, indicating the instantaneous echo waveform is much greater than the threshold, and the fourth PAP occurs within 175 μs, indicating that the echo energy is decreasing, and shows more temporal variation. First off-axis nulls appear at $\pm 14°$, and the first side lobes are also apparent. Echo amplitudes decrease as the bearing deviates from normal incidence and exceed the threshold later in the waveform, thus generating fewer and retarded PAPs compared to those produced at zero bearing. The smallest echoes generate only single PAPs. Small random variations in the PAP occurrence times in successive emissions in the sector scan are due to thermal and density fluctuations in the transmission medium.[13]

The first classifier neuron recognizes glints, which exhibit both temporal and spatial features evident in the mirror PAP field. Glints occur when the PAPs fall within the template shown as four rectangles in Fig. 2(a). In time, glints are composed of four successive PAPs, whose first three IPIs are each less than 150 μs (the minimum IPI is 140 μs) and whose fourth IPI is less than 175 μs. Four such successive-in-time PAPs are then examined for coherence over space. Each of these four PAPs must have eight neighbors, four on each side in bearing. The first three PAPs occur within ± 10 μs of the central PAP, and the fourth within ± 25 μs. The glint neuron then indicates the presence of a strong echo present over 3.6° in the scan.

The blob classifier neuron detects large echoes, which exhibit the PAP temporal behavior evident in glints, but lack the coherence over the scan angle. Blobs usually border glints, when neighboring PAPs fail to meet the coherence criterion, or are caused by echo components that interfere at the detector to disrupt the spatial coherence.

The fuzz classifier detects low-level echoes from a collection of range-distributed scatterers that generate sparse PAP sequences. This classifier detects a sequence of three widely spaced PAPs, which occur within 600 μs with neither IPI less than 175 μs.

Figure 2(b) displays the classifier neuron outputs for the mirror. A classifier output is placed at the location of the first PAP in the pattern satisfying the corresponding criterion. Glints are indicated by circles, blobs by points, and fuzz by asterisks. Only the glint and blob classifiers produced outputs for the mirror data since no PAPs satisfied the fuzz classifier criteria. The glints occur within $\pm 5°$ of normal incidence, thus improving the localization of the mirror compared to the raw PAP data. Blobs occur where the spatial coherence criterion is not satisfied, usually adjacent to glints. The classifiers have also reduced the complexity of the PAP field by eliminating PAPs not meeting their criteria. Additional classifiers could have been formed to detect PAP patterns other than glints, blobs, and fuzz, but only these three classifiers have been implemented in this paper because of their obvious physical interpretation.

Having implemented the classifiers, we acquired PAP field data from *in situ* plants, starting with simple forms and then progressing to more complex structures. These data were applied to the three classifiers with the results described below.

III. RESULTS

The first object was the 0.17 m diam trunk of a sycamore tree (*Platanus occidenatalis*) located at 2.3 m range and shown in Fig. 3(a). A 10 cm by 2 cm rectangle provides a size reference. Figure 3(b) displays the PAP field when scanning in a horizontal plane across trunk. Patches on the trunk surface were smooth on the scale of the wavelength (0.7 cm) and produced strong echoes. PAPs from the main lobe and side lobes are evident. Sequences of more than four successive PAPs are observed because the trunk is not planar and forms multiple strong reflectors distributed over range and the beam cross section. Figure 3(c) displays the classifier neuron field produced by the PAP field. Glints appear at three angles where the trunk surface approximates a specular reflector, modeled by the mirror. Multiple glints are produced by local specular patches. Glints that extend in range are due to strong reflectors that reinforce the large echo amplitude over a 9 cm range interval (0.5 ms). Blobs occur as the scan shifts between glints, which interfere to disrupt the coherence. Fuzz occurs on the trunk edges, where bark pieces act as weak reflectors.

Figure 4(a) shows 0.8 m wide trunk of an old Norway maple tree (*Acer platanoides*) located at 2.3 m range. Figure 4(b) displays the PAP field when scanning in a horizontal plane across the trunk. The trunk surface is rough on the wavelength scale and acts as a Lambertian surface. At initial inspection, the maple PAP field appears similar to the main lobe of the sycamore. The lack of side lobes indicates that there are no strong specular reflectors in the sample. More PAPs are observed from each interrogation pulse because the rough bark presents range-distributed scattering sites over the beam cross section. Figure 4(c) displays the classifier neuron field. Note that no glints are present. In this case, while the trunk is a strong reflector, each strong echo at the receiver is a superposition of many echo components, which fail to produce coherence over bearing necessary for a glint. The first-occurring PAPs exhibit greater variation than that of the sycamore. Blobs occur along the leading edge of the trunk and at more distant locations at which the bark scatterers produce reinforcing echo components at the receiver. Fuzz is apparent on the edges of the trunk and at the latest PAP produced by the maple. The edge PAPs are produced by scatterers located on the beam periphery when the sonar axis is off the trunk. When the beam axis falls near the tree center, the beam width is sufficiently broad to generate echoes from range-distributed scatterers lying on the trunk circumference. The resulting PAPs are placed along the sonar bearing value at their respective ranges and hence are retarded in time.

Figure 5(a) displays a 2 m diam rhododendron (*Rhododendron maximum*) located at 1.95 m range. Figure 5(b) displays the PAP field when the scan plane was tilted downward by 35° to orient the transducer axis to be normally incident to the leaves at closest range. We speculate that a bat would search for glints in a similar fashion. Ground echoes begin to appear at delays of 17 ms. Figure 5(c) displays the classifier

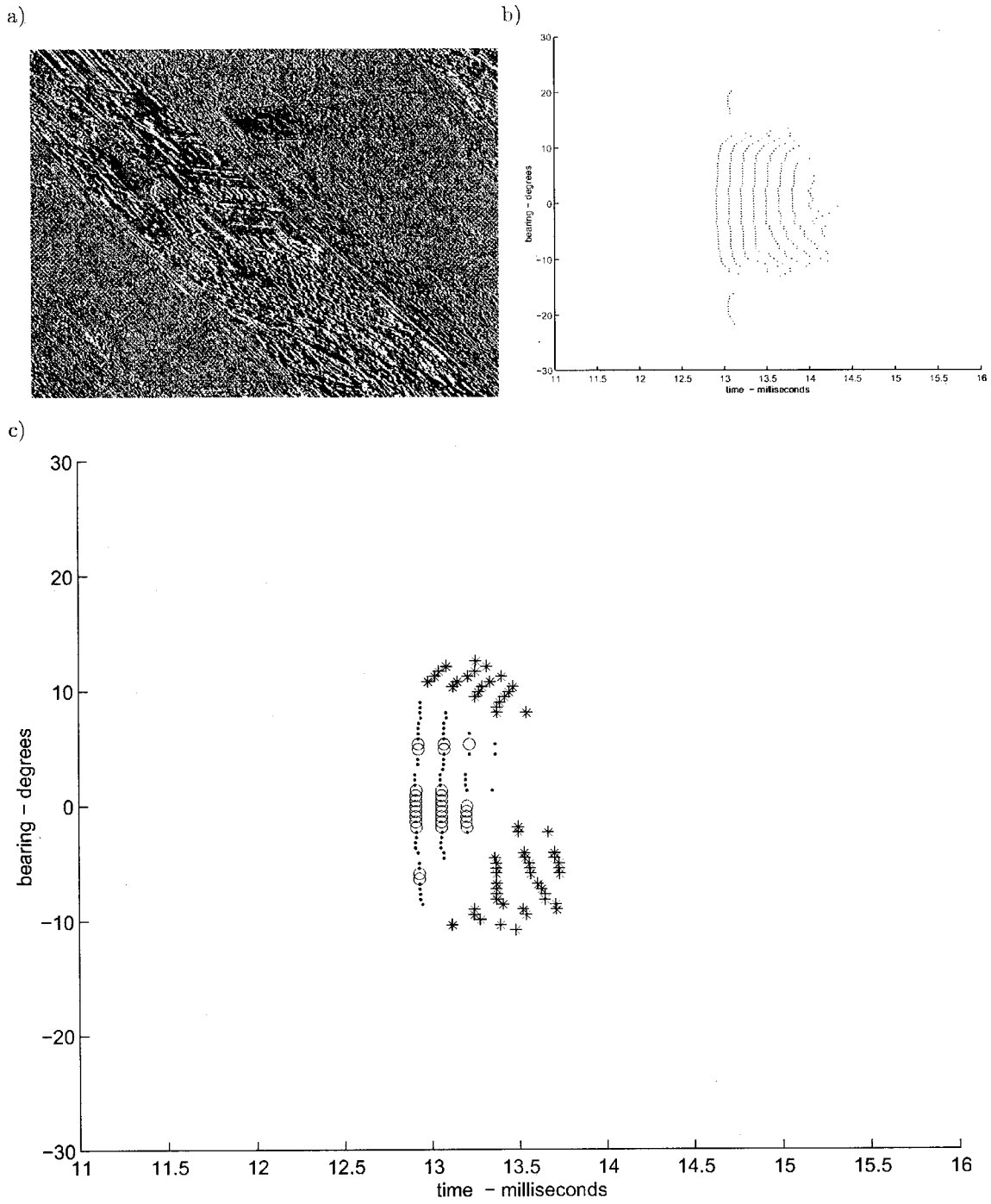

FIG. 3. Sycamore (*Platanus occidentalis*) located at 2.3 m range. (a) Picture at 0.17 m diam trunk with 10 cm by 2 cm marker. (b) PAP field produced by scan in horizontal plane. (c) Outputs of classifier neurons: glints—○; blobs—●; and fuzz—*.

neuron field. Glints occur at three positions on the rhododendron surface at locations of normally incident leaves. In addition the normally incident leaf that determined the scan plane, two other leaves within the beam pattern acted as strong specular reflectors. Additional scans of the rhododendron using different scan tilt angles produced glints when normally incident leaf surfaces are encountered. Blobs exhibit variations over bearing. Blob-producing structures on the plane periphery produce smooth trends, while those within the plant produce more random variations. Random blobs are produced by internal leaves and appear irregular due to wave front disruption experienced by forward scattering as the emitted pulse propagates into the plane. Echoes also experience forward scattering on the return path, serving to further disrupt their wave fronts at the detector. When echoes consist of a few strong components, wave front disruption typically varies smoothly with bearing. The chaos increases with the number of echo components having comparable intensities, as evidenced by the deeper blobs.

Figure 6(a) displays a 3 m diam untrimmed yew (*Taxus media*) starting at 1.8 m range. The yew has branches that extend randomly from the plant center, which are covered with cm-scale needles. The PAP field shown in Fig. 6(b) was produced when the sonar scan plane was tilted downward by

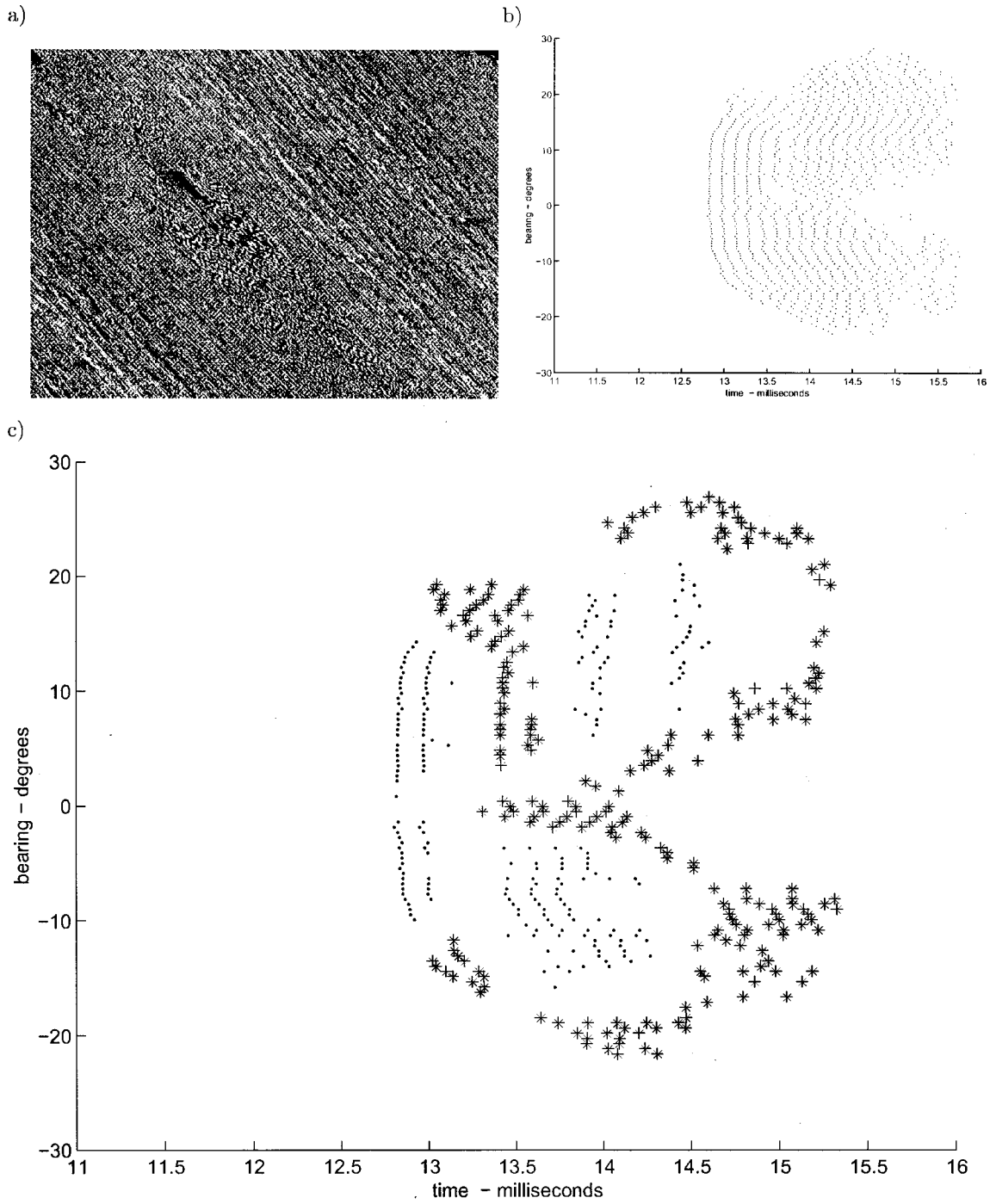

FIG. 4. Norway maple (*Acer platanoides*) located at 2.3 m range. (a) Picture of 0.8 m diam maple trunk. (b) PAP field produced by scan in horizontal plane. (b) Output of classifier neurons: glints—○; blobs—●; and fuzz—*.

10°. Additional scans of the yew at other scan angles indicated no qualitative differences in the PAP field or classifier outputs. The PAP field displays individual branches emanating out from the yew center. Figure 6(c) displays the classifier neuron field. The first PAPs were generated by the outreaching branches and are classified as fuzz. Blobs occur at internal locations where branches meet to form stronger reflectors. These blobs are random in appearance because the scatterer echo interaction varies quickly over bearing. Glints do not appear because no PAPs satisfy the glint criteria.

IV. DISCUSSION

These results indicate plant structural features can be extracted from the PAP field. To first order, leaf surfaces tend to lie tangentially along the plant periphery with surface normals pointed slightly upward toward the sun. Glints are detected at directions related to the leaf tilt angle, a feature helpful for classifying plants. Blobs border glints and indicate internal organized structures. Glints from internal reflectors are rare because forward scattering disrupts echo wave

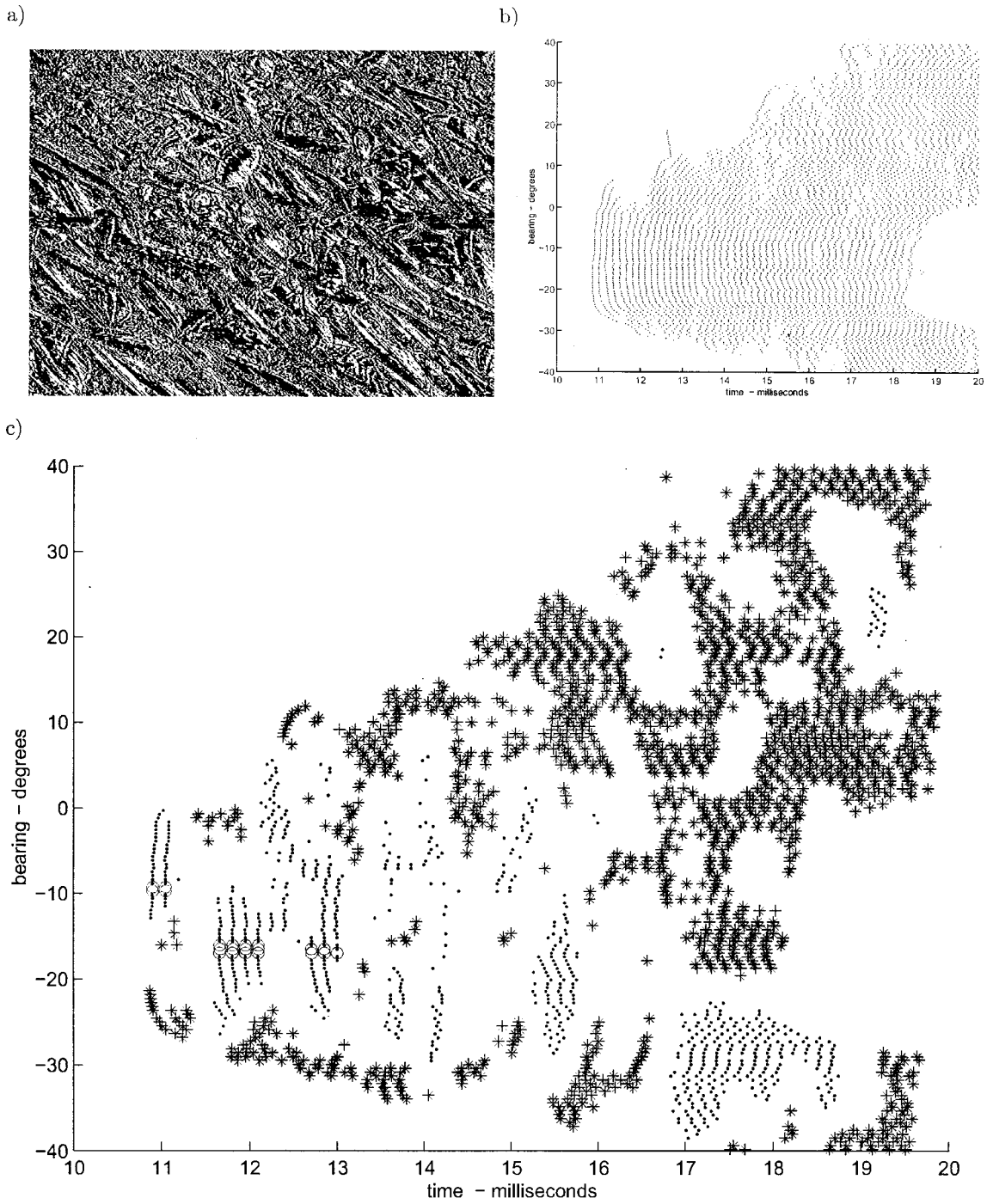

FIG. 5. Rhododendron (*Rhododendron maximum*) located at 1.95 m. (a) Picture of a 2 m diam rhododendron. (b) PAP field produced by scan plane tilted 35° downward from horizontal. (c) Outputs of classifier neurons: glints—○; blobs—●; and fuzz—*.

fronts at the detector. Diffuse plants typically produce only blobs and fuzz. Fuzz occurs on the edges of plants, providing a measure of their extent over angle.

Our sonar mimics the primary auditory receptor by producing a point process in response to echoes, with more intense stimuli producing a larger number of PAPs. Although PAPs occur too quickly to be generated by a single biological neuron, two or three neurons could conceivably generate the required PAPs for the coincidence detection described. The 10 μs coherence criterion in the glint and blob classifier is consistent with biological capabilities.[14]

Bats flying above specular plants and directing their emissions downward would observe glints at particular points in their trajectory. We speculate how the scanning process described here could be implemented by a bat. Our narrow-band emission can be viewed as a band-limited bin of the longer duration (10 ms) FM emissions used by bats to explore their environment. This idea is motivated by the bat auditory system, which is often modeled as a set of band-pass filters, which extract specific frequency components from echoes.[15] A glint is a reflection from a specular surface, which remains specular for all frequency bins in the sweep, as long as the surface has dimensions that are greater than roughly ten times the wavelength. Glints are classified by

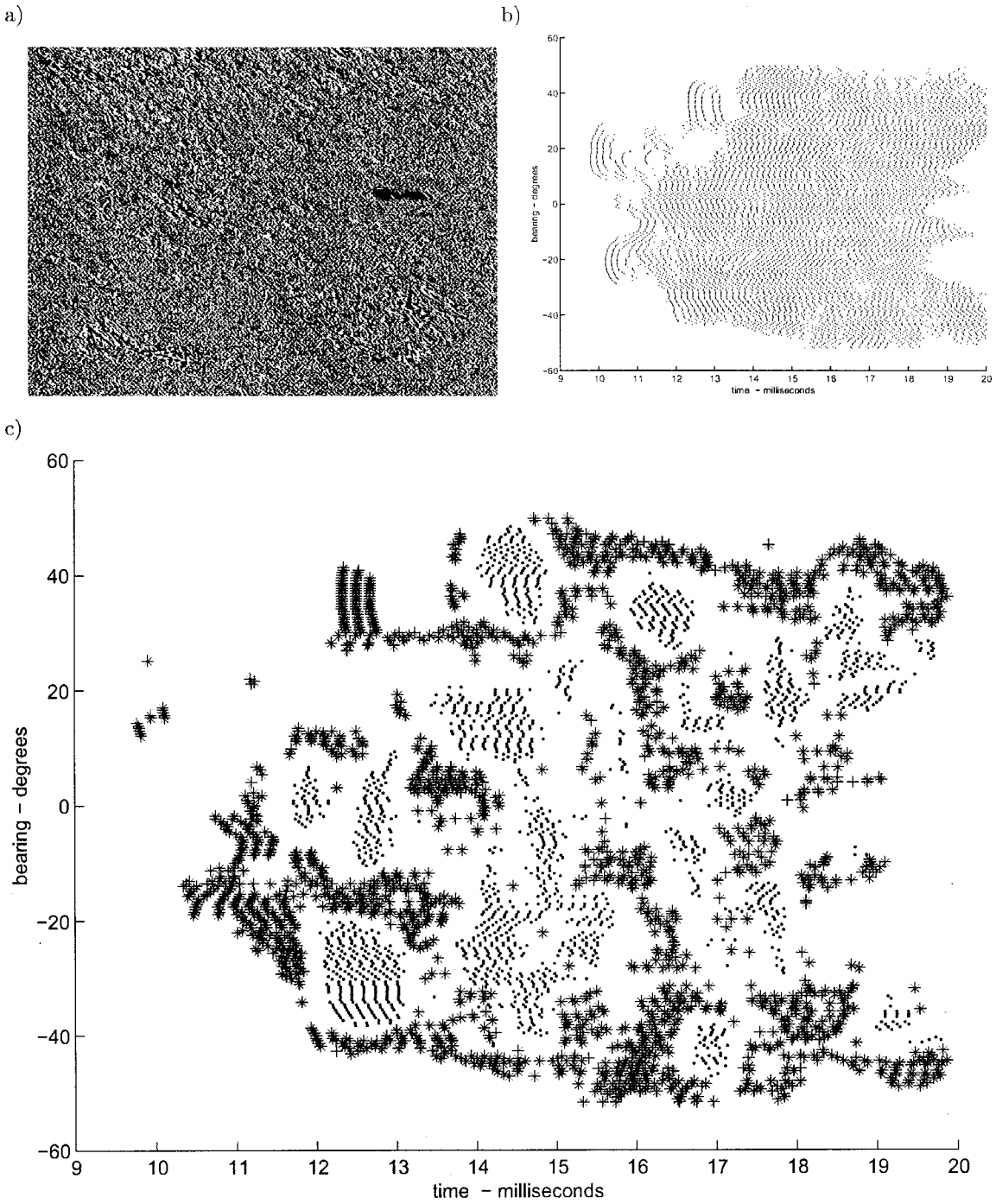

FIG. 6. Yew (*Taxus media*) located at 1.8 m range. (a) Picture of 3 m diam untrimmed yew. (b) PAP field produced by scan plane tilted 10° downward from horizontal. (c) Outputs of classifier neurons: glints—○; blobs—●; and fuzz—*.

considering a set of nine adjacent echoes, which occur in this paper during a 3.6° sector scan. Since bats usually fly when producing emissions, each bin examines a different part of the environment, thus naturally forming a scan. Scanning density can also be controlled by head rotation. A bat can accomplish the 0.45° scan increment employed in this paper by using 0.5 ms duration bins of a 50–25 kHz downward FM sweep lasting 10 ms by the head rotating at 900° s^{-1}, which is a quick nod. Performing this scan during a single FM sweep has two advantages over the method of data acquisition used in this paper. Each frequency bin would produce a single temporal PAP pattern, while adjacent bins would form adjacent scan lines. Generating the PAP field in a short time would reduce effects of dynamic changes in the transmission medium, which cause jitter in the PAP occurrence times when the emissions are 100 ms apart, as in our experiments. The second advantage is the reduction in the delays for glint coincident detection in adjacent scans from the 100 ms emission period to the 5 ms bin interval, which is physiologically more reasonable.

V. SUMMARY

This paper examined the information content of point processes extracted from echoes from *in situ* plants in an

attempt to understand how bats recognize landmarks in the field. A mobile sonar converted echoes into biologically similar pseudo-action potentials (PAPs), whose inter-PAP intervals relate to echo amplitude. We described a simple mechanism that converts an acoustic input into a point process, in which the temporal density increases with stimulus intensity. The sonar formed a sector scan to produce a spatial-temporal PAP field of an object. Classifier neurons applied delays and coincidence detection to the PAP field to identify three distinct echo types, termed glints, blobs, and fuzz, which characterize plant features. Glints are large amplitude echoes exhibiting coherence in successive echoes over bearing in the sector scan, typically produced by favorably oriented specular reflectors. Blobs are large echoes lacking coherence over bearing, typically formed by specular reflectors on the beam periphery or by collections of nonspecular reflectors. Fuzz represents weak echoes, typically produced by collections of weak scatterers, or objects on the beam periphery. A small mirror models a flat leaf surface to motivate the glint classifier criterion. Sycamore, Norway maple, rhododendron, and yew could be easily differentiated from the PAP classifier neuron field. We speculated that our sonar emission corresponds to a section of the FM emission produced by bats, and that one function of the FM sweep is to form a sector scan of the environment.

ACKNOWLEDGMENTS

Dr. R. Mueller clarified numerous issues in bat echolocation, neuroscience, and Linux. Plant identification and location assistance was provided by the caretakers of the Grove Street Cemetery in New Haven, CT, the oldest cemetery in the United States and the resting place of J. Willard Gibbs, Noah Webster, and Eli Whitney, among others. This research was supported by the National Science Foundation under Grant No. IRI-9504079.

[1] R. Kuc, ''Biomimetic sonar system recognizes objects using binaural information,'' J. Acoust. Soc. Am. **102**, 689–696 (1997).
[2] J. A. Simmons and L. Chen, ''The acoustic basis for target discrimination by fm echolocating bats,'' J. Acoust. Soc. Am. **86**, 1333–1350 (1989).
[3] H. L. Roitblat, P. W. B. Moore, R. H. Penner, and W. W. L. Au, ''Natural echolation with an artificial neural network,'' Int. J. Neural Networks **1**, 239–248 (1989).
[4] P. J. McKerrow and N. L. Harper, ''Recognizing leafy plants with in-air sonar,'' Sensor Rev. **19**, 202–206 (1999).
[5] R. Mueller and R. Kuc, ''Foliage echoes: A probe into the ecological acoustics of bat echolocation,'' J. Acoust. Soc. Am. **108**, 836–845 (2000).
[6] Ray Meddis, ''Simulation of mechanical to neural transduction in the auditory receptor,'' J. Acoust. Soc. Am. **79**, 702–711 (1986).
[7] L. A. Jeffress, ''A place theory of sound localization,'' J. Comp. Physiol. Psych. **41**, 35–39 (1948).
[8] Andrew Lewis Maffett, *Topics for a Statistical Description of Radar Cross Section* (Wiley, New York, 1989).
[9] C. Biber, S. Ellin, E. Sheck, and J. Stempeck, ''The Polaroid ultrasonic ranging system,'' in *Proceedings of the 67th Audio Engineering Society Convention*, 1990.
[10] Polaroid Corporation, Polaroid 6500 series ranging module, http://www.polaroid-oem.com/ultrason.htm, 2000.
[11] L. E. Kinsler, A. R. Frey, A. B. Coppens, and J. V. Sanders, *Fundamentals of Acoustics* (Wiley, New York, 1982).
[12] J. Borenstein, H. R. Everett, and L. Feng, *Navigating Mobile Robots* (A. K. Peters, Wellesley, MA, 1996).
[13] A. M. Sabatini, ''A stochastic model of the time-of-flight noise in airborne sonar ranging systems,'' IEEE Trans. Ultrason. Ferroelectr. Freq. Control **44**, 606–614 (1997).
[14] Catherine E. Carr, ''Processing of temporal information in the brain,'' Annu. Rev. Neurosci. **16**, 223–243 (1993).
[15] R. F. Lyon, ''A computational model of filtering detection and compression in the cochlea,'' in *Proceedings IEEE International Conference on Acoustics, Speech and Signal Processing* (1982).

Auditory scene analysis by echolocation in bats

Cynthia F. Moss[a)]
Department of Psychology, Program in Neuroscience and Cognitive Science, University of Maryland, College Park, Maryland 20742

Annemarie Surlykke[b)]
Center for Sound Communication, Institute of Biology, Odense University, SDU, DK-5230 Odense M., Denmark

(Received 30 October 2000; revised 27 June 2001; accepted 5 July 2001)

Echolocating bats transmit ultrasonic vocalizations and use information contained in the reflected sounds to analyze the auditory scene. Auditory scene analysis, a phenomenon that applies broadly to all hearing vertebrates, involves the grouping and segregation of sounds to perceptually organize information about auditory objects. The perceptual organization of sound is influenced by the spectral and temporal characteristics of acoustic signals. In the case of the echolocating bat, its active control over the timing, duration, intensity, and bandwidth of sonar transmissions directly impacts its perception of the auditory objects that comprise the scene. Here, data are presented from perceptual experiments, laboratory insect capture studies, and field recordings of sonar behavior of different bat species, to illustrate principles of importance to auditory scene analysis by echolocation in bats. In the perceptual experiments, FM bats (*Eptesicus fuscus*) learned to discriminate between systematic and random delay sequences in echo playback sets. The results of these experiments demonstrate that the FM bat can assemble information about echo delay changes over time, a requirement for the analysis of a dynamic auditory scene. Laboratory insect capture experiments examined the vocal production patterns of flying *E. fuscus* taking tethered insects in a large room. In each trial, the bats consistently produced echolocation signal groups with a relatively stable repetition rate (within 5%). Similar temporal patterning of sonar vocalizations was also observed in the field recordings from *E. fuscus*, thus suggesting the importance of temporal control of vocal production for perceptually guided behavior. It is hypothesized that a stable sonar signal production rate facilitates the perceptual organization of echoes arriving from objects at different directions and distances as the bat flies through a dynamic auditory scene. Field recordings of *E. fuscus*, *Noctilio albiventris*, *N. leporinus*, *Pippistrellus pippistrellus*, and *Cormura brevirostris* revealed that spectral adjustments in sonar signals may also be important to permit tracking of echoes in a complex auditory scene. [DOI: 10.1121/1.1398051]

PACS numbers: 43.80.Lb, 43.80.Ka, 43.66.Ba, 43.66.Lj, 43.66.Mk [WA]

I. INTRODUCTION

Auditory perception goes beyond the detection, discrimination, and localization of sound stimuli. It involves the organization of acoustic events that allows the listener to identify and track sound sources in the environment. For example, at a concert, individuals in the audience may be able to hear out separate instruments, or differentiate between music played from different sections of a symphony orchestra. At the same time, each listener may also follow a melody that is carried by many different sections of the orchestra together. In effect, the listener groups and segregates sounds according to similarity or differences in pitch, timbre, spatial location, and temporal patterning, to perceptually organize the acoustic information from the auditory scene. Auditory scene analysis thus allows the listener to make sense of dynamic acoustic events in a complex environment (Bregman, 1990).

Auditory scene analysis shares many perceptual phenomena with visual scene analysis, facilitating the application of Gestalt principles to its study. For example, both visual and auditory scene analyses involve the segregation and grouping of information to develop a coherent representation of the external sensory environment. The auditory and visual systems both perform operations such as object recognition, figure–ground segregation, and stimulus tracking.

The phenomenon of auditory stream segregation in humans appears to follow some fairly simple laws, namely the effect depends on the frequency similarity of groups of tones and the rate at which stimuli are presented. Similar laws also apply to apparent motion in vision, a phenomenon in which spatially separated lights that flash in sequence give rise to an observer's perception of a moving light. As with melodic motion in auditory streaming, visual apparent motion depends on the similarities among the lights that flash and the temporal separation of flashes (Körte, 1915).

Perceptual grouping and segregation of sounds plays an important role in auditory scene analysis. In human psychoacoustic studies, a subject listening to tones that alternate slowly between low and high frequencies (e.g., 300, 2000, 400, 2100, 500, 2200 Hz) reports hearing the individual tones in the sequence. However, when the stimulus presen-

a)Author to whom correspondence should be addressed; electronic mail: cmoss@psyc.umd.edu
b)Electronic mail: ams@dou.dk

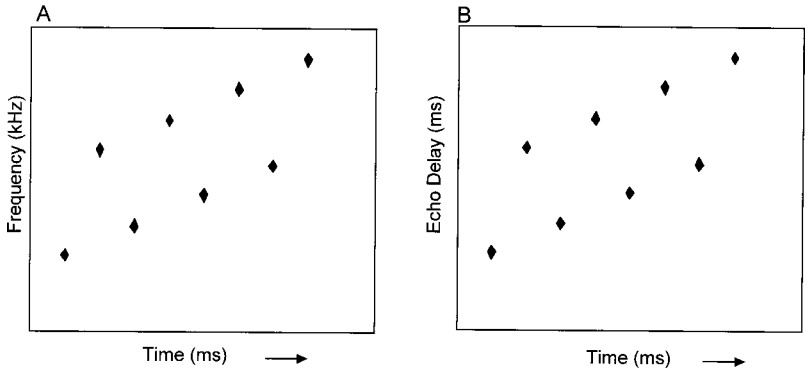

FIG. 1. (A) Schematic illustration of alternating tone frequencies over time that give rise to the perception of two pitch streams (after Bregman, 1990). (B) Schematic illustration of alternating echo delays over time that are hypothesized to give rise in the bat to the perception of two sonar target distance streams.

tation rate is increased, the listener hears out streams of tones, one containing the low-frequency signals (300, 400, 500 Hz) and the other containing the high frequency signals (2000, 2100, 2200 Hz). In some cases, the listener reports hearing these tone streams in alternation and in other cases reports two simultaneous auditory streams that differ in perceived amplitude (Bregman and Campbell, 1971). A schematic of these stimulus patterns is presented in Fig. 1(A).

Only recently have studies of animal perception examined the principles of auditory scene analysis in nonhuman species. Experiments with European starlings (Braaten and Hulse, 1993; Hulse *et al.*, 1997; Wisniewski and Hulse, 1997; MacDougall-Shackleton *et al.*, 1998) and goldfish (Fay, 1998, 2000) have demonstrated that spectral and temporal features of acoustic patterns influence the perceptual organization of sound in these animals. Using conditioning and generalization procedures, these researchers provide empirical evidence that both fish and birds can hear out complex acoustic patterns into auditory streams.

While the concept of auditory scene analysis applies broadly to all hearing animals, it is vividly illustrated in the echolocating bat, a mammal that probes the environment with sonar vocalizations and extracts spatial information about the world from the features of returning echoes. Each species of bat has a distinct repertoire of signals that it uses for echolocation, and the features of these sounds determine the echo information available to its sonar imaging system. The sonar sounds used by bats fall broadly into two categories, narrow-band, constant-frequency (CF) signals and broadband, frequency-modulated (FM) signals. Bats using CF signals for echolocation typically forage in dense foliage and are specialized to use Doppler shifts in returning echoes for the perception of target movement (e.g., Schnitzler *et al.*, 1983), aiding in the segregation of figure (insect target) and ground (vegetation). By contrast, many FM bats forage in the open or at the edge of forests, using shorter, broadband signals (Kalko and Schnitzler, 1998; Schnitzler and Kalko, 1998) that are well suited for target localization (e.g., Simmons, 1973, 1979; Moss and Schnitzler, 1989, 1995) and for separating figure and ground.

The acoustic parameters a bat uses to determine the features of an object is conveyed by the features of the echoes (Moss and Schnitzler, 1995). For example, a bat can discriminate the size of an object from the intensity of echoes (Simmons and Vernon, 1971), the velocity of a target from the Doppler shift of the echoes (Schnitzler, 1968), and the shape of an object from the spectrum of the echoes (Simmons *et al.*, 1974). Differences in arrival time, intensity and spectrum of echoes at the two ears encode the location of an object in azimuth (Blauert, 1997; Shimozowa *et al.*, 1974; Simmons *et al.*, 1983) and elevation (Batteau, 1967; Grinnell and Grinnell, 1965; Lawrence and Simmons, 1982; Wotton *et al.*, 1995). The third dimension, the distance between the bat and an object (target range), is determined from the time delay between the outgoing sound and the returning echo (Hartridge, 1945; Simmons, 1973). Together, these cues provide the bat with information to form a three-dimensional (3D) representation of a target and its position in space. While research over the last 30 years has elucidated the echo features that bats use to localize and discriminate sonar targets, we know little about how these acoustic features are perceptually organized in the representation of an auditory scene. Here, we present a conceptual framework to advance our understanding of the bat's perceptual organization of sound for the analysis of complex auditory scenes.

II. DETAILING THE PROBLEM: AUDITORY SCENE ANALYSIS BY ECHOLOCATION

The analogy between auditory scene analysis in bats and visual scene analysis in other animals is particularly strong, because sonar targets are auditory objects, and the echolocating bat uses spatial information carried by sonar echoes to identify and track these auditory objects. Many species of bat use echolocation to hunt small insect prey in the dark. This is a daunting perceptual task, given the acoustic environment in which the bat must operate. The bat produces sonar vocalizations and processes information in returning echoes to detect, track, and intercept insects that may be only a few millimeters in diameter. To accomplish this task, the bat must sort out its own sonar vocalizations from returning echoes. In addition, it may encounter echoes from multiple targets (several insects in a cluster, branches, walls, etc.), as well as signals produced by other bats in close proximity. To successfully intercept the insect and avoid obstacles, the bat must organize acoustic information collected from multiple

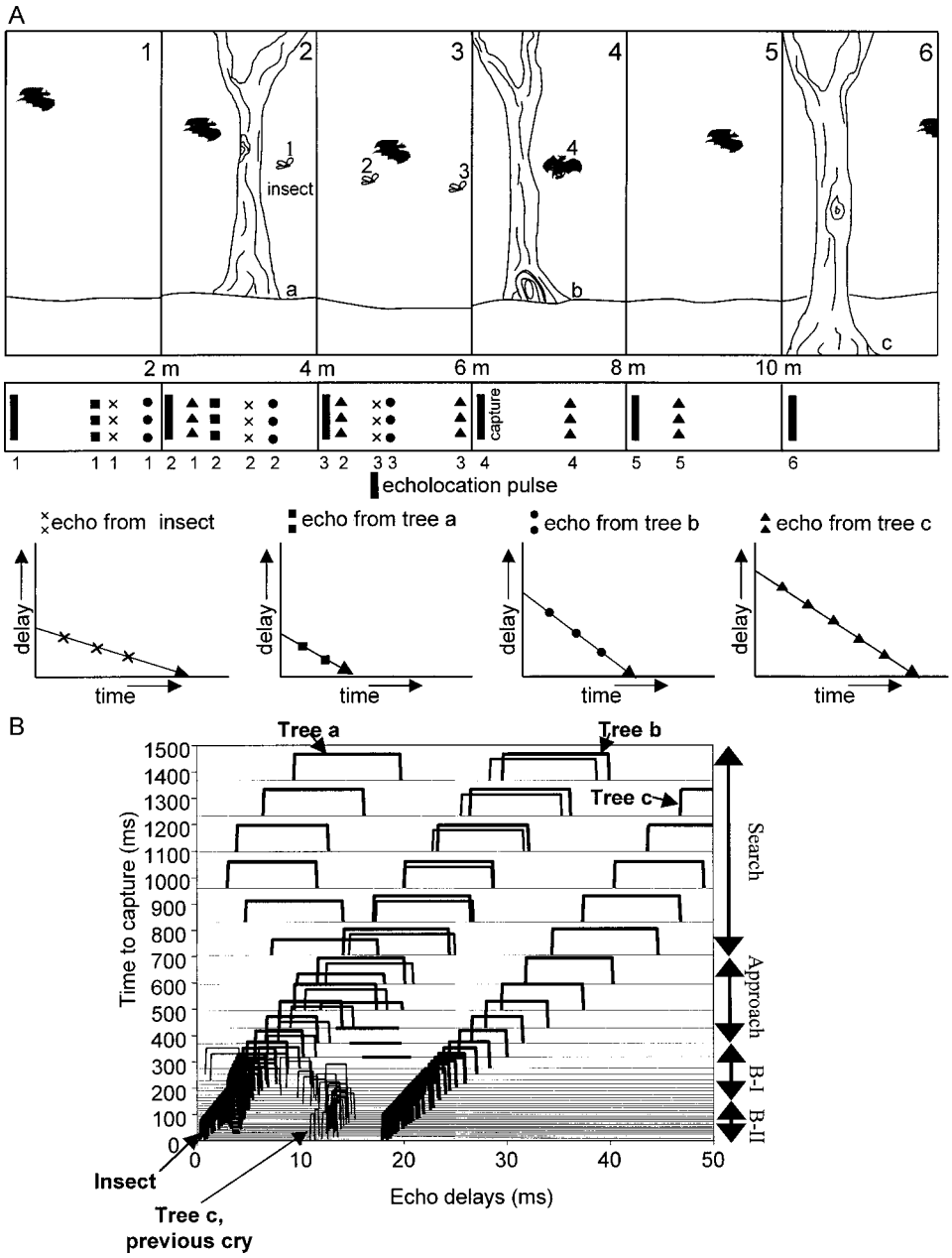

FIG. 2. (A) Illustration of a bat pursuing a prey item in the vicinity of trees. Each panel represents a new slice in time, each separated by a fixed interval. In each panel, the bat's position relative to the trees and insect changes, as the bat pursues its prey. Below the drawing is a schematic that displays the relative timing of sonar pulses (solid bars) and target echoes (individual trees and insect echoes are represented by filled triangles, circles, and x's). Bottom shows separate plots of the time delay between each sonar pulse and returning echo depends on the distance between the bat and the reflecting object, plotted separately for each of the objects. (B) A schematic that illustrates the changing echo delays for each of the reflecting objects. The right *y*-axis shows the stages of insect pursuit. B-I refers to buzz one and B-II refers to buzz two. As the bat flies closer to the trees and insect, the delays shorten. The echo amplitudes are arbitrarily set at fixed values that do not change with distance but durations and signal intervals were taken from a pursuit sequence recorded in the field. Only when the bat has passed an object does the amplitude decrease rapidly to reflect the low SPL radiated in the backward direction. The rate of delay changes over time for each of the reflecting objects as a distinct ridge with a particular slope. In this display, one can visually identify and track the returning echoes from the trees and insect over time.

sonar targets arriving from different directions and at different times. This problem is illustrated in Fig. 2(A).

Figure 2(A) (above) shows a bat pursuing an insect that is flying in the vicinity of trees. This figure contains six panels, each illustrating a slice in time, and the bat's position relative to the insect and trees changes over time. Below the illustrated panels is a schematic showing the timing of echolocation cries, one associated with each slice in time, and the corresponding echoes. Each of the bat's sonar vocalizations appears as a solid dark bar, and the echoes returning from the objects in the environment appear as stippled bars. Echoes from the insect and three trees are identified with distinct patterns. When displayed as a string of sounds, pulses, and echoes, it is difficult to identify patterns of delay change over time that the bat must sort out. In addition, echo returns from one sonar pulse may arrive after the production of a second pulse, as illustrated by the numbers below that identify the echoes associated with each pulse and the resulting echoes. The plots below separate out the delays of echoes for each of the objects in the bat's environment with a reduction in distance. In these plots, one can more readily see that the absolute delays and rates of delay changes over time are distinct for the insect and the three trees.

These data are presented in yet another format in Fig. 2(B), which displays an echo delay marker for each of the objects in the environment, stacked over time. This figure shows the reflecting objects as sloping ridges, whose placement along the axes and slopes depend on the bat's relative position and velocity with respect to the insect and trees. This figure also illustrates the change in sound repetition rate as the bat approaches a target [not conveyed in Fig. 2(A)], and the search, approach, and terminal buzz phases (I and II) of the insect capture sequence (Griffin *et al.*, 1960) are labeled on the right *y* axis. The duration of the signals is conveyed by the length of each marker. The amplitude of the echoes is arbitrarily set at a fixed level that does not change

with target distance, but the figure does illustrate how echo amplitude decreases rapidly after the bat flies past an object. It is important to note how the increase in sound repetition rate (and the decrease in signal duration) in the terminal phase defines and ''sharpens up'' the ridges corresponding to the insect and the three trees. Just as the layout of a graphic display can aid the identification of patterns in echo delay changes over time, we propose that the bat's auditory system perceptually organizes the signals arriving from multiple objects at different distances to create a readable display, which then permits tracking and capture of insects in a dynamic and complex acoustic environment.

Moreover, echolocation is an active system, i.e., the bat transmits the very sound energy it uses to probe the environment. As a bat flies toward a target, changes in the repetition rate, bandwidth, and duration of its sonar emissions occur, and these dynamic vocal production patterns are used to divide the bat's insect pursuit sequence into different phases: search, approach, and terminal buzz [Griffin *et al.*, 1960; Webster, 1963; see Fig. 2(B)]. Given that the perceptual organization of sound depends on the acoustic features of signals, changes in the bat's sonar vocalizations certainly impact its analysis of an auditory scene. While the active modulation of sonar vocalizations in response to changing echo information complicates our task of understanding scene analysis by echolocation, the bat's vocal production patterns also provide us with a window to the acoustic information the bat is actively controlling as it maneuvers through the environment.

How does the bat's sonar system operate to coordinate spatial acoustic information from a complex environment to avoid obstacles and intercept prey? Here, we describe some experimental data showing that the bat assembles acoustic information over time, a requirement for spatial tracking of moving targets and the analysis of auditory scenes. We also discuss sonar vocalization patterns of bats operating in a dynamic auditory scene. These vocalization patterns provide some insights to the bat's active control for scene analysis by echolocation.

III. CONCEPTUAL FRAMEWORK

As described above, humans listening to tone sequences may experience perceptual streaming of the acoustic patterns along the frequency axis. We propose here that echolocating bats, animals with well-developed three-dimensional (3D) spatial hearing, may stream acoustic patterns along the delay axis. Certainly a variety of acoustic parameters contributes to a bat's perceptual organization of sound, but we choose to focus here on the single parameter of echo delay. If the bat streams echo information along the delay axis, this could provide the perceptual foundation for sorting echoes arriving from different objects at different absolute delays and rates of delay change over time [see Fig. 1(B) and Fig. 2].

While the notion of the bat's acoustic scene has been considered in very general terms (e.g., Dear *et al.*, 1993a; Simmons *et al.*, 1995), a conceptual framework to identify and study the principles that operate in the perceptual organization of sound by an echolocating animal has not been previously formulated. In this paper, we take a small step towards unraveling the complicated problem of scene analysis in biosonar. Here, we articulate our working hypotheses and report on data that lay a foundation for understanding how the perceptual and vocal-motor systems may operate to support auditory scene by the echolocating bat. In this context, we wish to caution that our data only touch upon the many issues that bear on the problem of scene analysis through active sonar.

IV. STUDY 1. PSYCHOPHYSICAL EXPERIMENTS

FM bats, such as *Eptesicus fuscus*, receive brief acoustic flashes of a changing environment as they fly. In order for the FM bat to organize acoustic information from sonar targets in a dynamic scene, it must assemble echo information over time. *E. fuscus* must therefore use working- or short-term memory to track changing echo information about sonar targets.

Field and laboratory observations of the bat's increasing repetition rate during insect approach and capture might suggest that echolocating bats integrate acoustic information over time; however, these data have not been taken as the definitive demonstration of echo integration, because echo delay-dependent changes in vocal production patterns do not explicitly inform us about the animal's perception of echo sequences. To experimentally address this question, we have conducted some perceptual experiments, and the data demonstrate that *Eptesicus fuscus* can indeed assemble information about changing echo delay to discriminate sonar targets. These findings suggest that the bat's perceptual system meets the minimum requirements for analysis of a dynamic auditory scene.

A. Animals

Five FM bats of the species *E. fuscus* served as subjects in the different perceptual tasks. The animals were collected from private homes in Maryland during the summers of 1995 and 1996 and housed in a colony room at the University of Maryland, College Park. The temperature in the colony room was maintained at approximately 27 °C and the day/night cycle was reversed, with lights out between 7:00 a.m. and 7:00 p.m. Bats were given free access to water and maintained at about 85% of *ad lib* body weight. Food was available only as a reward during behavioral experiments, which were carried out 6–7 days/week over a period of 18 months.

B. Apparatus and target simulation

Behavioral experiments took place in a large ($5.6 \times 6.4 \times 2.5$ m) carpeted room, whose walls and ceiling were lined with acoustic foam (Sonex) that reduced the amplitude of ultrasonic reverberation by a minimum of 20–30 dB below what would be present if the room surfaces were hard and smooth.

Each bat was trained to rest at the base of an elevated Y-shaped platform (1.2 m above the floor) and to produce sonar sounds. The bat's sonar sounds were picked up by a vertically oriented 1/8 in. Bruel & Kjaer condenser microphone (model 4138) that was centered between the arms of the platform at a distance of 17 cm from the bat. The bat's

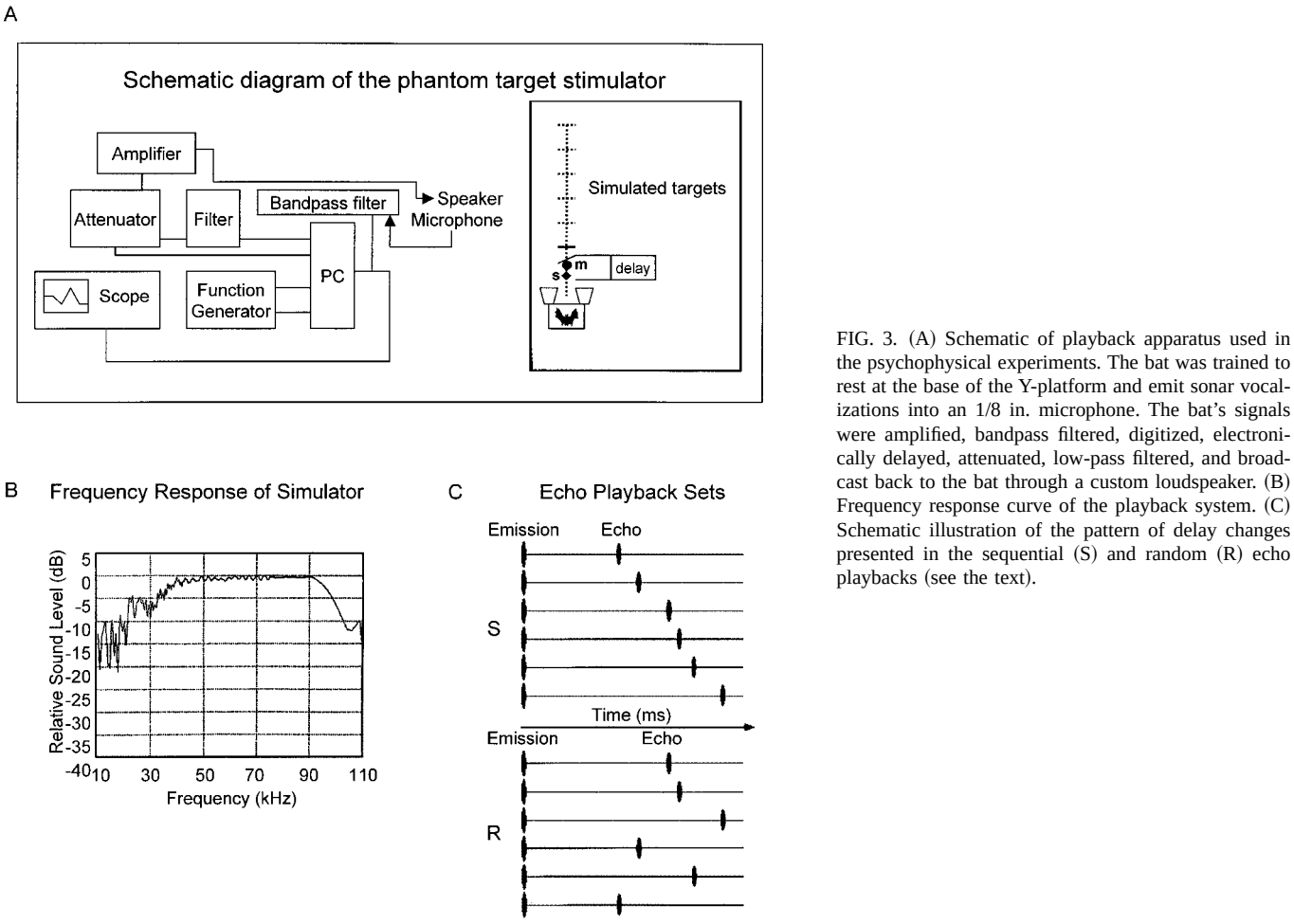

FIG. 3. (A) Schematic of playback apparatus used in the psychophysical experiments. The bat was trained to rest at the base of the Y-platform and emit sonar vocalizations into an 1/8 in. microphone. The bat's signals were amplified, bandpass filtered, digitized, electronically delayed, attenuated, low-pass filtered, and broadcast back to the bat through a custom loudspeaker. (B) Frequency response curve of the playback system. (C) Schematic illustration of the pattern of delay changes presented in the sequential (S) and random (R) echo playbacks (see the text).

echolocation sounds were amplified, bandpass filtered at 20–99 kHz (Stewart filter, model VBF7), digitized with 12-bit accuracy at a rate of 496 kHz (controlled externally by a Stanford Research Systems function generator), electronically delayed (custom DSP board, SPB2-Signal Data, installed in a 486 computer), attenuated (PA-4, Tucker-Davis Technologies), low-pass filtered (Krone-Hite), and broadcast back to the bat through a custom electrostatic loudspeaker (designed by Lee Miller, University of Odense, Denmark). The loudspeaker, positioned in front of the microphone (0.5 cm lower than the microphone grid) and 15 cm from the bat, was powered by a dc amplifier (Ultrasound Advice) and had a frequency response that was flat within 3 dB between 25 and 95 kHz [see Figs. 3(A),(B)]. Placement of the microphone behind the speaker eliminated feedback in the system, and the signals recorded were not distorted by the presence of the speaker (see Wadsworth and Moss, 2000).

The total gain of the system feeding into the DSP board was approximately 60 dB, to bring the peak–peak amplitude of most bat sonar sounds to a level just below the 12-bit limit of the processor for maximum signal-to-noise ratio (S:N). Digital attenuators (PA-4, Tucker Davis Technologies) permitted adjustment of the playback level of the sounds returning to the bat's ears, which was set at approximately 80 dB SPL (rms) for all experiments.

Each sound produced by the bat resulted in a single sonar signal playback that simulated an echo from a target positioned directly in front of the bat, whose distance was determined by an electronic delay controlled by the experimenter. The shortest echo delay used was 4.43 ms, corresponding to a target distance of 76 cm, and the longest echo delay was 4.93 ms, corresponding to a target distance of 85 cm.

Before each experiment, a calibration routine was run to test each of the components of the target simulator. The electrostatic loudspeaker broadcast a linear 1-ms 10–100-kHz frequency modulated sweep that was picked up by a condenser microphone (QMC) positioned on the test platform. The signal received by the microphone was amplified, filtered (Stewart VBF-7, 10–99 kHz), and delivered to the DSP board. The arrival time and power spectrum of the FM sound picked up by the microphone were measured and compared against standard values. Experimental data were collected only when the delay and power spectrum of the calibration signal matched the standard values, a 0.29-ms delay when the microphone was positioned 10 cm from the speaker (one-way travel delay, 2.9 ms/m) and a relatively flat spectrum [± 3 dB at 25–95 kHz; see Fig. 3(B)].

C. Behavioral task: Sequential versus random echo delay sequences

Each of the bats was trained in a two-alternative forced-choice experiment to discriminate between two stimulus sets

TABLE I. Summary of stimulus conditions in the sequential versus random echo delay discrimination task. Values refer to electronic echo delays in ms. Acoustic travel time from the bat to the microphone and from the loudpspeaker to the bat adds 0.93 ms to these values for the total echo playback delays presented in the sequential conditions.

		Condition 1			
Decreasing:					
4.00	3.90	3.80	3.70	3.60	3.50
		Condition 2			
Decreasing:					
4.00	3.95	3.90	3.85	3.80	3.75
		Condition 3			
Increasing:					
3.50	3.60	3.70	3.80	3.90	4.00
		Condition 4			
Increasing:					
3.75	3.80	3.85	3.90	3.95	4.00
		Condition 5			
Increasing:					
3.50 (unequal step sizes)	3.55	3.75	3.82	3.90	4.00

of echo delays. Each stimulus set contained the same set of six echo delays, and the bat received only one echo playback for each sonar emission. In one echo set, the delays systematically increased or decreased (stimulus ''S''), and in the other echo set, the sequence of delays was randomized (stimulus ''R''). The echo stimulus set repeated until the bat made its response (see below). The step size and direction of echo delay change was manipulated. The delay step size of echoes in stimulus set S was unequal in some experiments to ensure that the bat was discriminating the pattern of echo delay change, and not simply between variable and fixed delay steps in echo sets S and R. A schematic of these echo sets is illustrated in Fig. 3(C). Table I lists the different echo delay conditions tested in these experiments.

The bat learned to report whether it perceived a systematic increase or decrease in target distance by crawling down the left arm of the platform to indicate an ''S'' (sequential) response or if it perceived a random presentation of the same echo delays by crawling down the right arm of the platform to indicate an ''R'' (random) response. The presentation of the random and sequential echo sets followed a pseudorandom schedule (Gellerman, 1933), and the bat's response (S or R) was recorded. For each correct response, the bat received a food reward (a piece of mealworm), and for each incorrect response, the bat experienced a 10–30 s time-out. No correction trials were introduced. Each test day included 25–50 trials per bat.

D. Results

1. Behavioral performance

The data from two bats that successfully completed testing under all conditions are plotted in Fig. 4. (Three out of the five bats trained in the task fell ill during the experiment, and their data sets are incomplete.) The conditions are separated into different panels and identified by number 1–5 (see

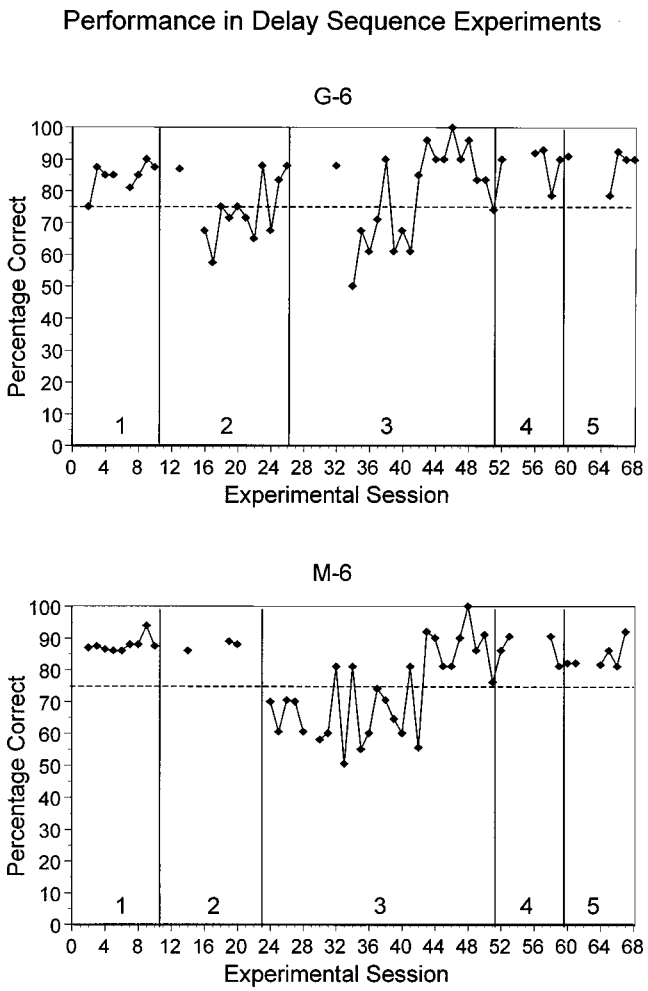

FIG. 4. Performance of two individual bats (M-6 and G-6) trained to discriminate between the sequential and random playbacks. Breaks between the data points appear when experimental trials were not run over consecutive days. Each block shows data that come from a single condition, indicated by numbers 1–5 above the *x*-axis (see Table I). Criterion for successful discrimination was 75%-correct performance over a minimum of 3 days.

Table I for stimulus details on each condition). Note that in some instances, the bat's discrimination of echo patterns in one condition transferred immediately to a new pattern, and performance remained at or above 75%-correct following the introduction of a new stimulus set. These data show that the bat can integrate echo sequences along the dimension of delay (Morris and Moss, 1995, 1996), and they lay the foundation for future studies that can directly probe the phenomenon of stream segregation along the delay axis in echolocating bats. Such experiments will determine whether the bat hears out delay streams from complex echo delay patterns.

V. STUDY 2: BEHAVIORAL STUDIES OF ECHOLOCATING BATS OPERATING IN A COMPLEX AUDITORY SCENE

A complete understanding of auditory scene analysis should specifically address the acoustic problems that must be solved by the species under study. The use of biologically relevant stimuli in the study of auditory scene analysis has not been widely applied, but this approach has been adopted

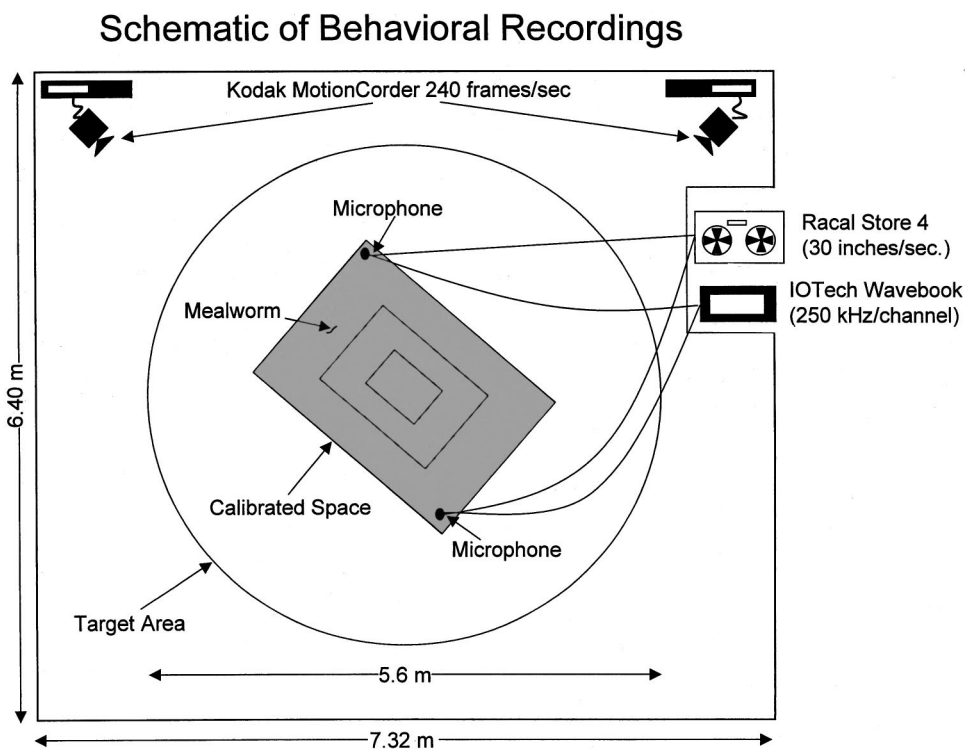

FIG. 5. Schematic of setup for video and sound recordings of tethered insect captures by echolocating bats. Two video cameras were mounted in the room to permit 3D reconstruction of the bat's flight path. Video recordings were synchronized with audio recordings taken with ultrasonic microphones delivering signals to either a digital acquisition system (IoTech Wavebook) or a reel-to-reel high-speed recorder (Racal).

by Hulse and colleagues working on the perceptual organization of sound in the European starling (Hulse *et al.*, 1997; Wisniewski and Hulse, 1997). They studied the European starling's perception of conspecific song and found evidence for stream segregation of biologically relevant acoustic signals by the starling. Similarly, in bats, one can study the phenomenon of scene analysis in the context of biologically relevant acoustic tasks. In particular, the bat's pursuit and capture of insect prey in a dynamic acoustic environment requires analysis of the auditory scene using echoes of its own sonar vocalizations. Thus, studies of vocal production patterns in echolocating bats can provide insights to the animal's perception and control of the auditory scene (Wadsworth and Moss, 2000). Indeed, the echolocating bat's perception of the world builds upon sonar returns of its vocalizations. Given that the repetition rate and frequency separation of sounds affect stream segregation in human listeners, the vocal production patterns of the bat would be expected to influence its perceptual organization of space using sonar echoes. Below, we describe high-speed video and sound recordings of the echolocating bat as it flies through a dynamic auditory scene to intercept insect prey tethered in open laboratory space and in the vicinity of echo clutter-producing leaves and branches.

A. Animals

Seven FM bats of the species *Eptesicus fuscus* served as subjects in the laboratory insect capture studies. Four of the animals were collected from private homes in Maryland during the summers of 1997–1999 and three from a cave in Ontario, Canada in the winter of 2000. Bats were housed in the University of Maryland bat colony room under conditions comparable to those of the bats in the psychophysical experiments. Food was available only as a reward during behavioral experiments, which were carried out 4–5 days/week over a period of 27 months.

B. Behavioral studies of echolocation behavior in free flight

Big brown bats (*Eptesicus fuscus*) were trained to capture tethered whole mealworms (*Tenebrio molitor*) in a large flight room (6.4 × 7.3 × 2.5 m) lined with acoustical foam (Sonex). Their vocalization behaviors were studied under open-space and clutter conditions. In the open-space condition, no obstacles were in the vicinity (within 1 m) of the insect target; however, the walls, ceiling, and floor of the flight room prevent us from creating a truly open space environment. In the clutter condition, the tethered mealworm was suspended 5–90 cm from leafy house plants placed in the calibrated space of the behavior room (see video processing methods below). The separation between target and clutter was manipulated between trials: close (5–15 cm), intermediate (20–30 cm), and far (>40 cm). A schematic of the setup for these experiments is presented in Fig. 5.

Experiments were carried out using only long-wavelength lighting (Plexiglas #2711; Reed Plastics and Bogen Filter #182) to eliminate the use of vision by the bat (Hope and Bhatnagar, 1979). Mealworms were suspended at a height of about 1.5 m above the floor by monofilament line (Trilene Ultra Thin, 0.1-mm diameter) within a 5.3-m target area in the center of the room. A mealworm was suspended at a randomly selected location within the target area, and then the bat was released in a random direction to orient to the target area and find the mealworm. So that the bat would not memorize the target area, the mealworm was suspended outside the target area 50% of the time, and those trials were

not recorded. Once each bat achieved a consistent capture rate of nearly 100% in open-space conditions (typically within 2 weeks of introduction to the task), audio and video recordings of its capture behavior began.

1. Video recordings

Two gen-locked (frame synchronized), high-speed video cameras (Kodak MotionCorder, 640×240 pixels, 240-Hz frame rate, and 1/240-s shutter speed) were positioned just below the ceiling in the corners of the flight room. A calibration frame (Peak Performance Technologies) was placed in the center of the room and filmed by both cameras prior to each recording session. The high-speed video cameras were used to record target position, bat flight path and capture behavior. The resulting images were used in calculation of the three-dimensional positions of the bat, target, and microphones.

The video buffer contained 1963 frames, allowing for recording of 8.18 s of data at 240 frames/s. Using an end-trigger on the video, we captured the behavior leading up to and just following successful and unsuccessful insect captures.

2. Audio recordings

Echolocation signals were recorded using two ultrasonic transducers (Ultrasound Advice) placed within the calibrated space. In some trials, the microphone output was amplified (Ultrasound Advice) and recorded on the direct channels of a high-speed tape recorder (Racal Store-4 at 30 in. per second). An FM channel of the tape recorder was used to record TTL synch pulses corresponding to the start of each video frame and gated to the end of video acquisition. In other trials, the microphone signals were amplified, bandpass filtered (10–99 kHz, 40-dB gain, Stewart, VBF-7) and recorded digitally on 2 channels of an IoTech Wavebook 512 at a sample rate of 240 kHz/channel. The Wavebook, controlled by a Dell Inspiron 7000 laptop computer, had 16 Mbytes of random access memory (RAM) and was set to record 8.18 s prior to the trigger; the trigger was set to simultaneously stop the audio and video acquisition. The experimenter triggered the system on each trial after the insect capture was attempted and/or accomplished. This approach allowed us to record 8.18 s of audio data that corresponded precisely to the video segment for a given trial.

C. Data analysis

1. Video processing methods

A commercial motion analysis system (Peak Performance Technologies, Motus) was used to digitize both camera views with a Miro DC-30 Plus interface. The Peak Motus system was also used to calculate the three-dimensional location of points marked in both camera views. Digitization was to 1/4-pixel resolution using magnification. The digitization procedure resulted in 2560×1920 lines of resolution. The video image spanned less than 6 m horizontally, so that 1/4-pixel resolution corresponded to approximately 0.4 mm. The accuracy of the system was within ±0.5% over a calibrated volume extending approximately 2.2×2.2 m across the room and 1.6 m vertically. The three-dimensional space calibration frame provided 25 control points for direct linear transformation (DLT) calibration. The calibration procedure produced a mean residual error of 1.0 cm in each coordinate for the 25 control points.

The video position data for the bat, the target, and clutter-producing plants (when present) were entered in a database for each trial. The bat's position with respect to the microphones was also measured, and a correction factor for the sound travel time from the bat to the microphone was used to accurately record the vocalization times.

2. Audio processing methods

Recordings of the bat's sonar vocalizations in the laboratory insect capture studies were processed following two distinct methods. The sounds recorded on the Racal Store 4 tape recorder were played back at 1/4th the recording speed (7.5 in. per s) and digitized using a National Instruments board AT-MIO-16-1 with a sampling rate of 60 kHz per channel, resulting in an effective sampling rate of 240 kHz per channel. Custom software (LABVIEW) trimmed the digitized audio data to begin with the first and end with the last frame of each trial's video segment, and output files were exported to a signal-processing program (SONA-PC©). Using SONA-PC, a fast Fourier transform (FFT) was performed over 256 points per time step, with 16–20 points being replaced in each time step, and the signals were displayed spectrographically. The onset time, duration, and start- and end frequencies of the first harmonic of the emissions were marked with a cursor on the display and entered in a database for further analysis. Data acquired digitally with the IoTech Wavebook were displayed as time waveforms and spectrograms (256-point FFT) using MATLAB. The onset time and duration of the signals were measured using the time waveforms, and frequency measurements were taken from the spectrograms. Audio and video data were merged in a single analysis file in order to associate vocal behavior with motor events. MATLAB animation permitted dynamic playback of the bat's position data and corresponding vocalizations, enabling detailed study of the bat's behavior under different task conditions (programming by Aaron Schurger). Examples can be found at http://batlab.umd.edu/insect_capture_trials.

D. Results

Three hundred and twenty trials were run in the open-space condition and 170 trials in the clutter condition. Bats successfully intercepted tethered insects at a rate of 95% in the open space and 80% in the presence of echo clutter-producing plants, when the target was 20–90 cm from the clutter. Detailed video and sound analyses were carried out for a subset of trials, 53 open-space trials and 107 clutter trials. Three-dimensional plots of the bats' flight paths in representative trials from selected open-space and clutter conditions are shown in Fig. 6. Each data point (open circle) along the bat's flight path indicates the occurrence of a sonar vocalization. The asterisks in the clutter trials denote the position of the branches. The final target position is shown with

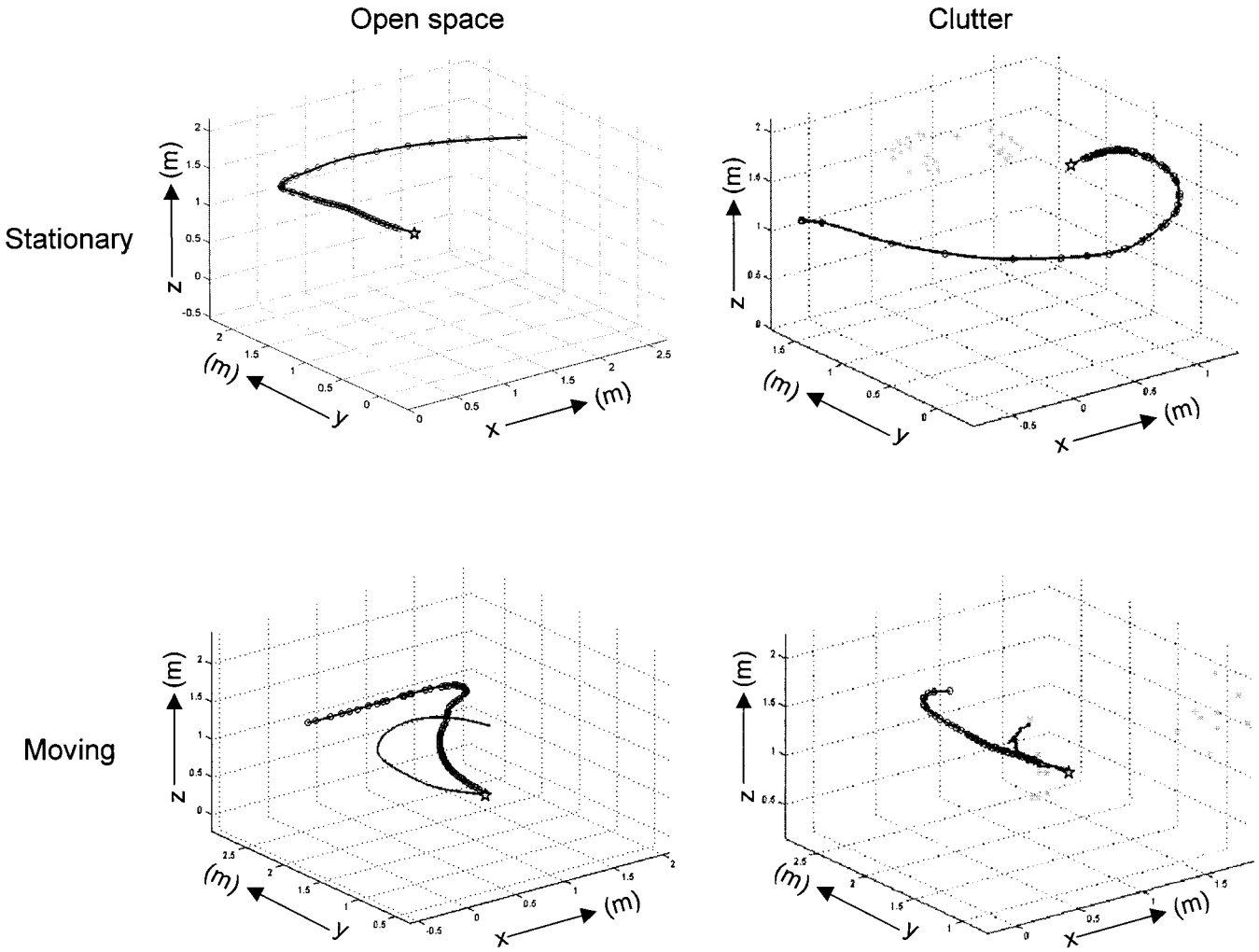

FIG. 6. Data from selected insect capture trials. Flight paths of bats pursuing tethered insects under open-space (left) and cluttered (right) conditions. Each point (open circle) along the flight path denotes the occurrence of a sonar vocalization. The star shows the end position of the target, which in the upper two examples was stationary and in the lower two examples was moving. In the moving target trials, the path of the insect is illustrated by a thin line. Note that the sonar vocalizations occur at a higher repetition rate as the bat approaches the target. For the clutter trials shown, asterisks denote the position of the branches. The bat successfully intercepted the target in all four trials shown.

a star, and in the case of moving target trials, the path of the insect is illustrated with a fine line. All trials presented in Fig. 6 resulted in successful target capture. Consistent with earlier reports (e.g., Griffin, 1953, 1958; Cahlander *et al.*, 1964; Webster, 1963), the interval between the bat's sonar vocalizations decreased as the bat approached the insect, but in general, the decrease was not continuous. In fact, most trials contained groups of sounds that occurred with relatively stable intervals, interrupted by a longer pause, and followed by another group of sounds, sometimes with the same stable interpulse interval (IPI). We will refer to the sound groups with stable intervals as sonar strobe groups.

Figure 7 shows the spectrograms of sounds produced by the bat as it approached and intercepted the tethered insect target under the same set of open-space (left panels) and clutter (right panels) trials presented in Fig. 6. Note in all of the trials that the bat's sonar sounds sometimes occurred in groups, interrupted by gaps. The groups of sounds contained signals with relatively stable intervals (less than 5% variance in the interval between sounds). This is displayed in Fig. 8, which plots the interpulse interval of successive sounds in the same four trials relative to the time of insect capture. In the example of the open-space moving target trial, the bat extends the production of these sound strobe groups with short IPIs over 1000 ms before contact, and the intervals remain just below 20 ms over several successive strobe groups. Processing these groups of sounds with relatively fixed repetition rate might facilitate the bat's analysis of sonar scenes and planning for target capture.

These sonar signal sequences, typical of those recorded in the lab (and under some conditions in the field; see below), include examples of several groups of sounds with stable intervals. Histograms summarizing the interpulse intervals and durations of these sonar sound groups in the open-space and cluttered conditions are presented in Fig. 9. Stable-space IPI groups with intervals smaller than 13 ms were excluded from this summary figure, as they comprise the terminal buzz (see Fig. 11). In both the open and cluttered environments, the strobe groups occurred most frequently with intervals characteristic of the late approach phase of insect pursuit: median = 16.5 ms under open space conditions and 17.4 ms under clutter conditions. The differ-

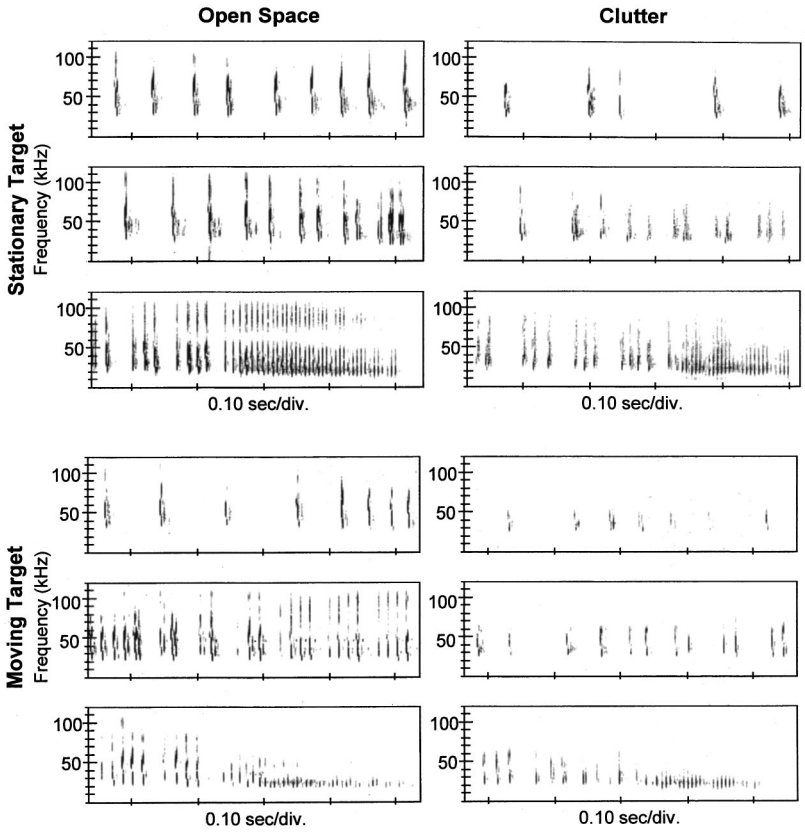

FIG. 7. Spectrograms of the sounds produced by the bats in the same trials as shown in Fig. 6. Each set of three panels comes from a single trial, with time wrapping from one panel to the next. Trials on the left come from open-space conditions and on the right from cluttered conditions. The upper panels display data taken when the target was stationary and the lower panels display data taken when the target was moving. Note that the sounds occur in stable IPI groups with a relatively consistent repetition rate, followed by a pause (e.g., clearly demonstrated in the middle panel of the open-space, moving target trial). Note that the panels show sonar sounds starting at approximately 1500 ms prior to target capture.

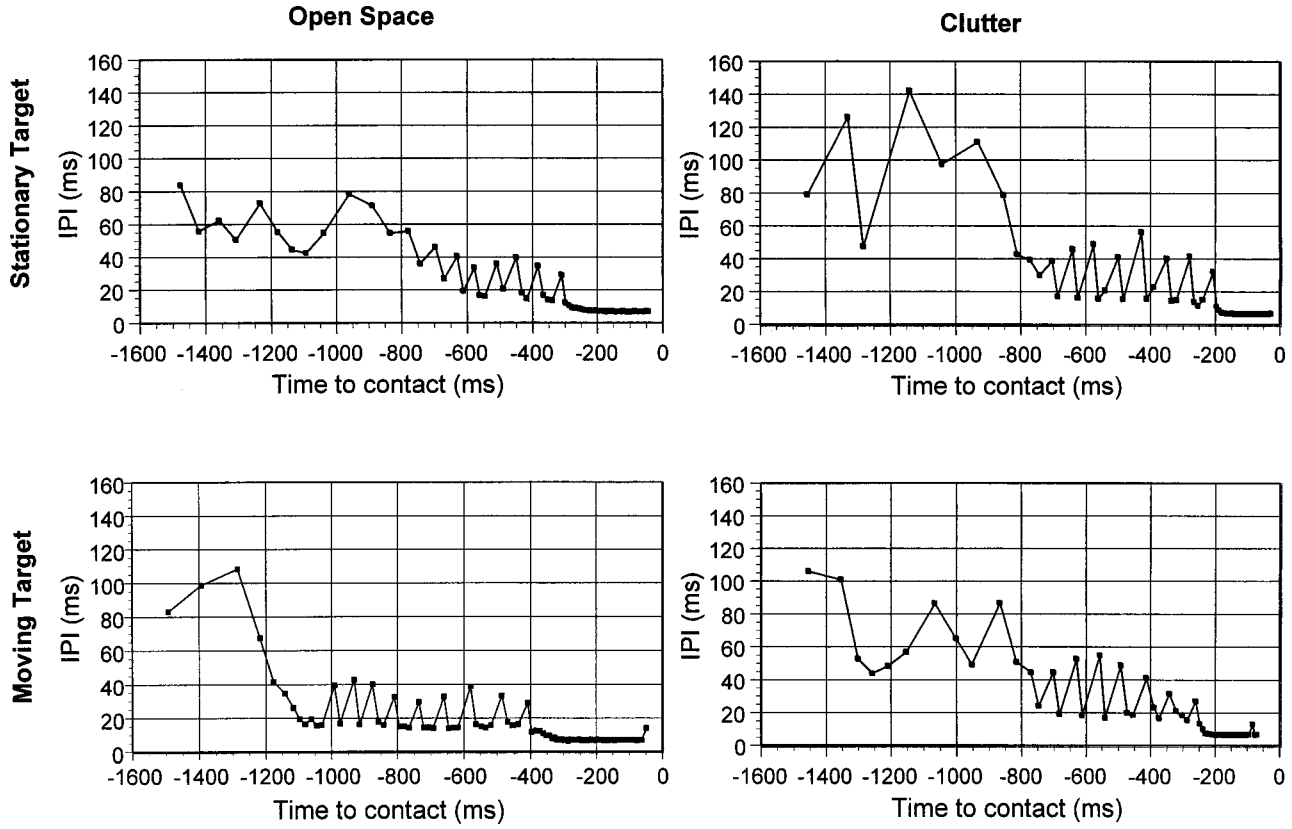

FIG. 8. Interpulse interval relative to target contact, plotted for the same four trials as shown in Figs. 6 and 7. The plots on the left show data from trials in open space and on the right from cluttered space. The upper plots show data from stationary target trials, and the lower plots show data from moving target trials. Note that the time scale on each panel shows sounds produced by the bat starting at 1500 ms prior to contact.

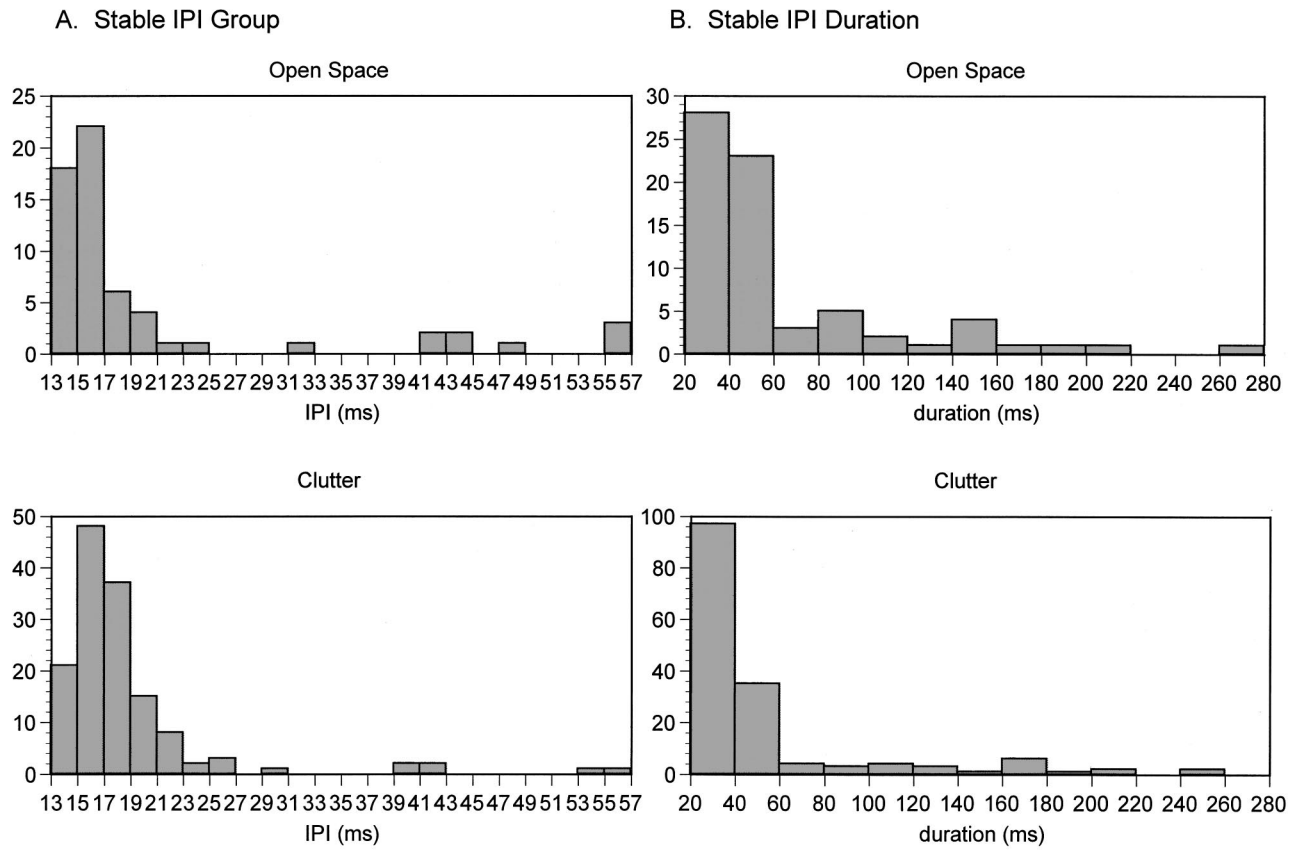

FIG. 9. (A) Distribution of the interpulse interval (IPI) of echolocation sounds produced in "stable IPI groups" under open-space (above) and cluttered (below) insect capture conditions. The median intervals for stable IPI groups were 17.4 ms for open space and 16.5 ms for cluttered trials. (B) Distribution of the duration over which the stable IPI groups occurred in open space (above) and cluttered (below) insect capture conditions. The median duration of stable IPI groups in the open space trials was 43.3 ms and in the cluttered trials was 37.6 ms.

ence in distribution of strobe group intervals between open space and clutter conditions was not statistically significant [Fig. 9(A)]. Across behavioral trials, stable IPI groups contained three, four, and sometimes more sounds. The median duration of the stable IPI groups (onset of the first sound to the onset of the last sound in the group) was 43.3 ms for the open space condition and 37.6 ms for the cluttered condition [Fig. 9(B)]. The difference between duration of strobe groups under open-space and cluttered condition was not statistically significant.

Figure 10 shows the incidence of sonar strobe groups for individual trials, displayed separately for open-space and clutter conditions. Individual trials analyzed are listed on the *y* axis (53 for open-space and 107 for clutter), and time relative to target contact on the *x* axis. Data points mark each sonar strobe group within a trial, and the position of each data point along the *x* axis indicates its time of occurrence relative to target contact (time zero). In both open-space and clutter trials, there is a clustering of strobe groups 250–750 ms before target contact. At earlier times relative to target contact, the incidence of sonar strobe groups is much lower in open space than in clutter. It is noteworthy that the incidence of strobe groups is much higher *after* target contact in the clutter condition than in the open space. In the clutter condition, the bat must negotiate the branches after contact, and this appears to influence the production of sonar strobe groups following insect capture in these trials.

As the bat gets closer to a target, it carefully adjusts its vocalizations to avoid overlap between sonar pulses and target echoes. In addition, the bat appears to adjust the interval between sounds to allow time for reception of relevant target echoes before producing the next sound. Just prior to capture, the bat produces sounds at a very high rate. This group of sounds, produced at a rate higher than about 80 sounds/second and reaching approximately 150/second just prior to capture, is called the terminal buzz [see Fig. 2(B)]. In some trials, the interval between the bat's sounds dropped abruptly from about 15–18 ms down to 6–8 ms, omitting the buzz I component from the terminal sequence. The terminal sequences recorded in the laboratory always contained a buzz II component (intervals less than 8 ms), and summary data on buzz II are presented in Fig. 11.

Figure 11(A) plots buzz onset and offset (relative to target contact) and total buzz II duration for insect capture sequences in open space (moving and stationary targets) and in the presence of clutter (far, intermediate, and close to the target). While moving insects were presented in both the open-space and clutter conditions, the data are excluded from the clutter summary in this plot, because physical limitations of our setup only allowed us to introduce moving targets at the intermediate and far target–clutter separations.

Buzz onset time differed across conditions ($F=5.37$; $p<0.001$), with the smooth motion open-space condition yielding significantly earlier onset time than stationary open

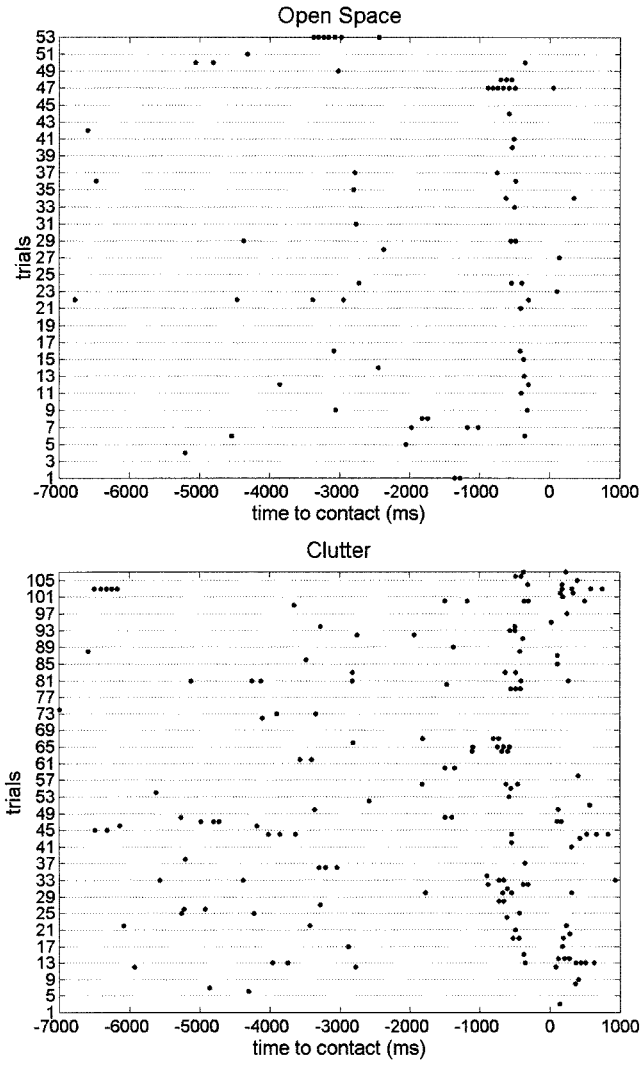

FIG. 10. Occurrence of sonar strobe groups relative to contact time, shown by •. Time of each strobe group is displayed across individual trials and relative to target contact time (0 on the *x* axis). Data from open-space trials are shown in the upper plot and from cluttered space in the lower plot.

space and clutter trials. The buzz onset time in the open-space moving target trials was earliest (mean=−265.3 ms, SEM 19.8 ms). The shortest target–clutter separation tested (5–15 cm) gave rise to the latest buzz onset time relative to contact (mean=−188.7 ms, SEM=12.2 ms). The intermediate target–clutter separation (20–30 cm) and the far target–clutter separation (>40 cm) yielded similar buzz onset times (intermediate mean=−202.85 ms, SEM=13.1 ms, and far mean=−195.8 ms, SEM=10 ms), which did not differ statistically from the open-space stationary buzz onset time (mean=−213.9 ms, SEM=4.7 ms).

The offset time of the buzz relative to target contact also differed significantly across conditions ($F=6.27$; $p<0.001$). It was earliest for the near-clutter condition (mean=−66.2 ms, SEM=3.8 ms), and decreased systematically from the intermediate (−53.7 ms, SEM=3.1 ms) to the far (−44.79 ms, SEM=3.9 ms) clutter conditions, and again slightly for the open-space stationary condition (−38.08 ms, SEM=2.9 ms). The mean open-space moving target trail buzz offset time relative to target contact was −54.6 ms (SEM=4.7 ms), similar to the mean for the intermediate target–clutter separation.

The mean duration of the buzz shortened systematically from the open-space moving target trials (mean=210.8 ms, SEM=17.2 ms) to the open-space stationary trials (mean=175.8 ms, SEM=4.8 ms) and across the far (151.06 ms, SEM=10.2 ms), intermediate (149.2 ms, SEM=13.5 ms), and near (122.5 ms, SEM=14.6 ms) clutter–target trials. This overall change in buzz duration was statistically significant ($F=6.23, p<0.001$). *Post hoc* analyses show that the significant contrasts were between open-space motion and all three target–clutter conditions (Tukey comparisons, $p<0.05$). By shortening the duration of the terminal buzz with target clutter, the bat shortened the time period when it was likely to experience a mixing of pulses and echoes from closely spaced sonar vocalizations.

Figure 11(B) shows that the target distance at which the bat initiated the terminal buzz was longer in open space than in clutter ($F=19.77, p<0.001$). In open space the mean distance was 61.55 cm (SEM=2.75 cm) and 64.69 cm (SEM=2.27 cm) for moving and stationary trials, respectively. As the target was placed closer to the clutter, the buzz onset distance became shorter, suggesting that the bat made its decision to intercept the target at closer range under these conditions. The mean target distances at buzz onset in cluttered space were 51.17 cm (SEM=2.57 cm), 42.92 cm (SEM=2.21 cm), and 33.77 cm (SEM=3.0 cm) for the far, medium, and near conditions, respectively. *Post hoc* comparisons across conditions show that the buzz onset distance differed significantly across all five conditions (Tukey test, $p<0.01$).

The difference in the bat's distance to the target when it terminated the buzz was not statistically significant across conditions ($F=2.36, p>0.05$); however, the distance traveled by the bat during the buzz was different across all conditions ($F=12.42, p<0.001$). Distances traveled over the course of the buzz were 86.64 cm (SEM=7.78 cm) in the open-space moving condition, 65.77 cm (SEM=3.94 cm) in the open-space stationary condition, 51.43 cm (SEM=3.3 cm) in the far-clutter condition, 49.93 cm (SEM=4.49 cm) in the medium-clutter condition, and 36.24 cm (SEM=5.73 cm) in the near-clutter condition.

VI. FIELD STUDIES OF ECHOLOCATION BEHAVIOR

The complex and dynamic acoustic environment of the echolocating bat requires perceptual organization of sound stimuli to segregate and track signals from different objects and other animals in the environment. Observations from field recordings suggest that the bat actively controls the information it extracts about the auditory scene by modulating the spectral and temporal characteristics of its sonar vocalizations. Here, we report on field recordings from several species of echolocating bat, with the goal of using sonar signal design and temporal patterning as a window to the bat's perceptual control of the spatial information sampled from the environment.

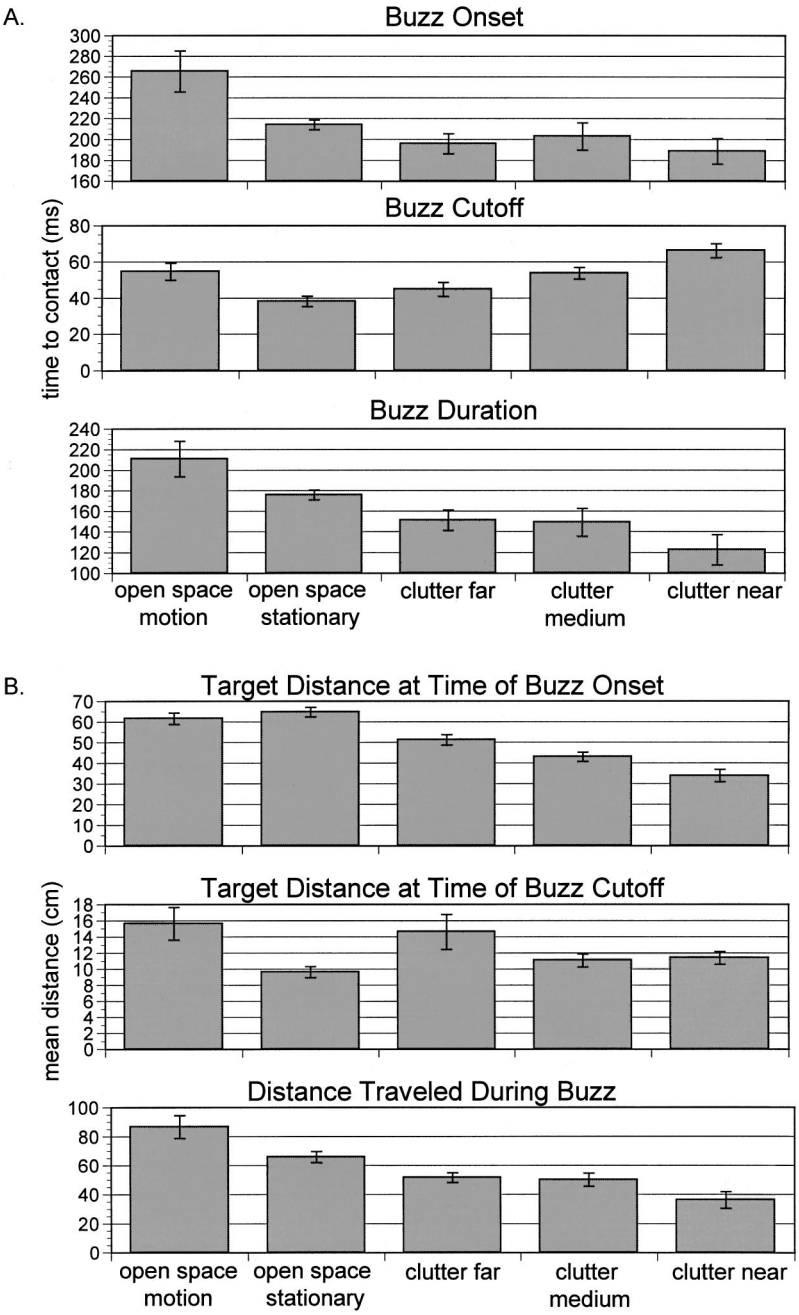

FIG. 11. (A) The onset and offset (relative to target contact) and duration of the terminal buzz II produced by bats just prior to insect capture under open space (moving and stationary) and stationary target in clutter trials (near, 5–15 cm; medium 20–30 cm, and far >40-cm target–clutter separations). (Error bars show one standard error of the mean.) (B) The bat's distance to the target at the time it initiated and ended the terminal buzz across the same five conditions. Also shown is the distance traveled by the bat while producing the terminal buzz sequence in the five insect capture conditions.

A. Field sites

Echolocating bats inhabit both temperate and tropical environments, and sound recordings of foraging bats were taken at several different sites around the world. *Noctilio albiventris* and *N. leporinus* (Noctilionidae) and *Cormura brevirostris* (Emballonuridae) were recorded on Barro Colorado Island in Panama in October, 1999 in collaboration with E. Kalko and M. E. Jensen. The *Noctilio* species flew low over a calm water surface in a small bay. They were using echolocation to capture fish swimming just below the water's surface and mealworms (set out by experimenters) floating on the water's surface. The *Commura brevirostris* was recorded while it hunted aerial insects in a small clearing in the tropical rain forest covering the island.

The vocalizations of *E. fuscus* were recorded in the summers of 1999 and 2000 as they foraged insect prey in Greenbelt, Maryland. At this field site, *E. fuscus* flew along the edge of a forest that abutted a meadow. Under moonlight, two bats were sited that flew 3–5 m above the ground and 2–6 m from the forest edge, and on two occasions we recorded several bats simultaneously at this location. The echolocation behavior of *Pipistrellus pipistrellus* [45-kHz phonic type (Barratt *et al.*, 1997)] was recorded in Montel (Midi-Pyrénées, southern France) in collaboration with Lee A. Miller *et al.* The area was under and close to a small bridge over a creek with brinks covered with shrubbery. Several pipistrelle bats hunted simultaneously in this area.

B. Recording methods

All recordings used microphones that operate in the ultrasonic range. In Panama, recordings were taken with a battery operated $\frac{1}{4}$-in. model 40BF G.R.A.S. microphone, am-

plified (40 dB) and high-pass filtered (13 kHz) through a G.R.A.S 12AA microphone power supply. This system is linear (±1 dB from 15–100 kHz). In Maryland, recordings were taken with a $\frac{1}{4}$-in. ACO Pacific microphone powered and amplified with a Larsen Davis battery-operated power supply. In all cases the microphone was mounted on the end of a 2-m thin rod. The microphone signals were continuously A/D converted on-line (12 bit, sampling rate 250 kHz) using a battery-operated IoTech Wavebook 512. The signals were stored in a ring buffer (FirstInFirstOut, FIFO). The Wavebook had 128 Mbytes of random access memory (RAM) and was set at 3–6 s pretriggering time and 1–2 s post-triggering time. The Wavebook was controlled by a laptop computer (AST Ascentia P series, IBM Thinkpad 600 or Dell Inspiron 7000). When we picked up strong signals on a bat detector (D240 Pettersson Electronics), we began signal acquisition with the Wavebook, storing the 3–6 s preceding and the 1–2 s following trigger. At all recordings sites, the data storage system was battery operated, resulting in a low noise floor.

In France the pipistrelle recordings were taken with a linear array of three Brüel & Kjaer $\frac{1}{4}$-in. microphones, each separated by 75 cm. The array was placed horizontally approximately 1.5 m above the ground with the microphones pointing forward and upward at an angle of 45 deg. The sounds were stored on a RACAL instrumentation tape recorder running at 30 ips (flat frequency response up to 150 kHz), and later digitized for analysis using the IoTech Wavebook (see above).

C. Results

The field recordings demonstrated that bats emit signals that, depending on species, allow them to exploit both time- and frequency cues to segregate their own signals and echoes from a complicated background of noise and emissions from other bats. In general, the bat diversity is much greater in the tropics, which is reflected in a broad representation of sonar signal characteristics from this part of the world. In temperate areas, there are not nearly as many bat species. However, acoustically, temperate species may face comparable sonar challenges, since several individuals of the same species may hunt in close proximity in areas with a high insect density. Naturally, the similarity of signals is greatest within the same species, and thus this situation may create confusion for the bat trying to discriminate between echoes from its own emissions and those of the neighbors.

The recordings of the two *Noctilio* species (*N. leporinus* and *N. albiventris*) illustrate just how complex the acoustic environment of the bat can be. Generally, the density of bats on Barro Colorado Island, Panama was very high. Up to 25 *Noctilio* bats, most of which were *N. leporinus*, might fly in the same area simultaneously. Thus, we recorded many overlapping sonar signals, and the silent breaks were few and short. *N. leporinus* emits signals with most energy around 55 kHz (Schnitzler *et al.*, 1994). Our recordings (Fig. 12) show peak energy around 58 kHz, whereas the dominant energy in the sonar signals of *N. albiventris* was around 74 kHz, close to the values (67–72 kHz) reported earlier (Kalko *et al.*, 1998). Figure 12 also illustrates that the *N. albiventris* recorded simultaneously emit slightly different frequencies, e.g., approximately 72 and 74 kHz.

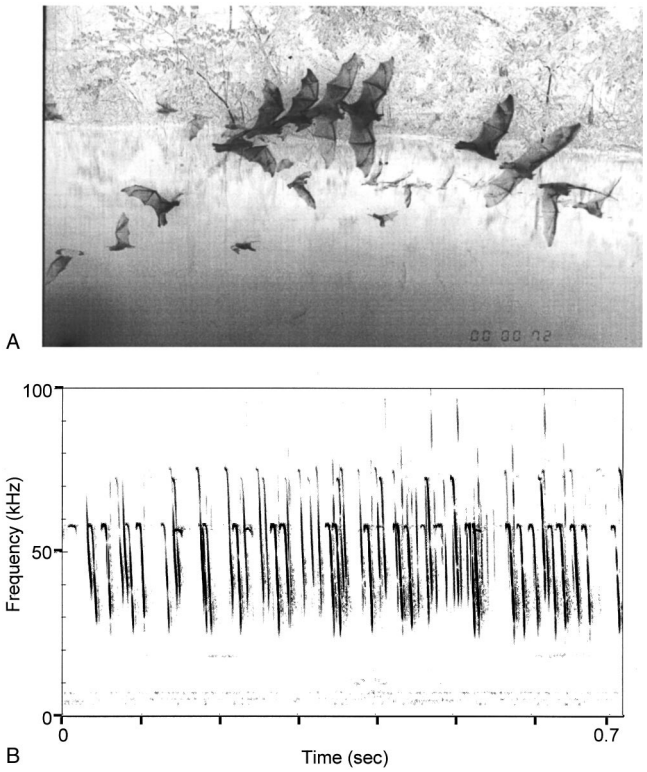

FIG. 12. Two *Noctilio* species (*N. leporinus* and *N. albiventris*) hunting over a calm water surface. (A) is a multiflash photo with 50 ms between flashes, except between 1 and 2 and 6 and 7. There are at least five different individuals in the photo. Photo by Elisabeth K. V. Kalko. (B) is a spectrogram of the sound recording corresponding to the multiflash photo in (A) illustrating how complex the acoustic scene can be in a dense group of bats. The spectrograms show that the main frequency of the *N. leporinus* is around 58 kHz, whereas the *N. albiventris* emissions fall in two groups, either around 72 or 74 kHz.

Similar to the insect capture recordings of *E. fuscus* in the laboratory (see Sec. V above and Figs. 6, 7, and 8), vocal sequences recorded in the field included stable IPI sequences. Groups of sonar signals produced at a stable repetition rate in the field again suggest active vocal control to facilitate analysis of the auditory scene. Illustration of sonar IPI sets produced by *E. fuscus* hunting along a forest edge is shown in Fig. 13. When *E. fuscus* is in cruising flight, the interpulse intervals are stereotyped (Surlykke and Moss, 2000). In contrast, a stable pulse repetition pattern, followed by short breaks and another group of signals at a stable, higher repetition pattern, clearly reveals active hunting, similar to the stable IPI groups described in our lab recordings of insect capture.

We took sound recordings of *E. fuscus* and *P. pipistrellus* hunting in close proximity of neighbors, and these sound sequences suggest active vocal control of the emitted dominant frequency to facilitate the identification and perceptual segregation of echoes from self-produced cries and those from neighbors. In the case of *E. fuscus*, a combination of the directionality of sonar emissions (Hartley and Suthers, 1989) and of the microphones indicates that bats recorded simultaneously were close in range. In the case of *P. pipistrellus*'s echolocation behavior, the linear array of micro-

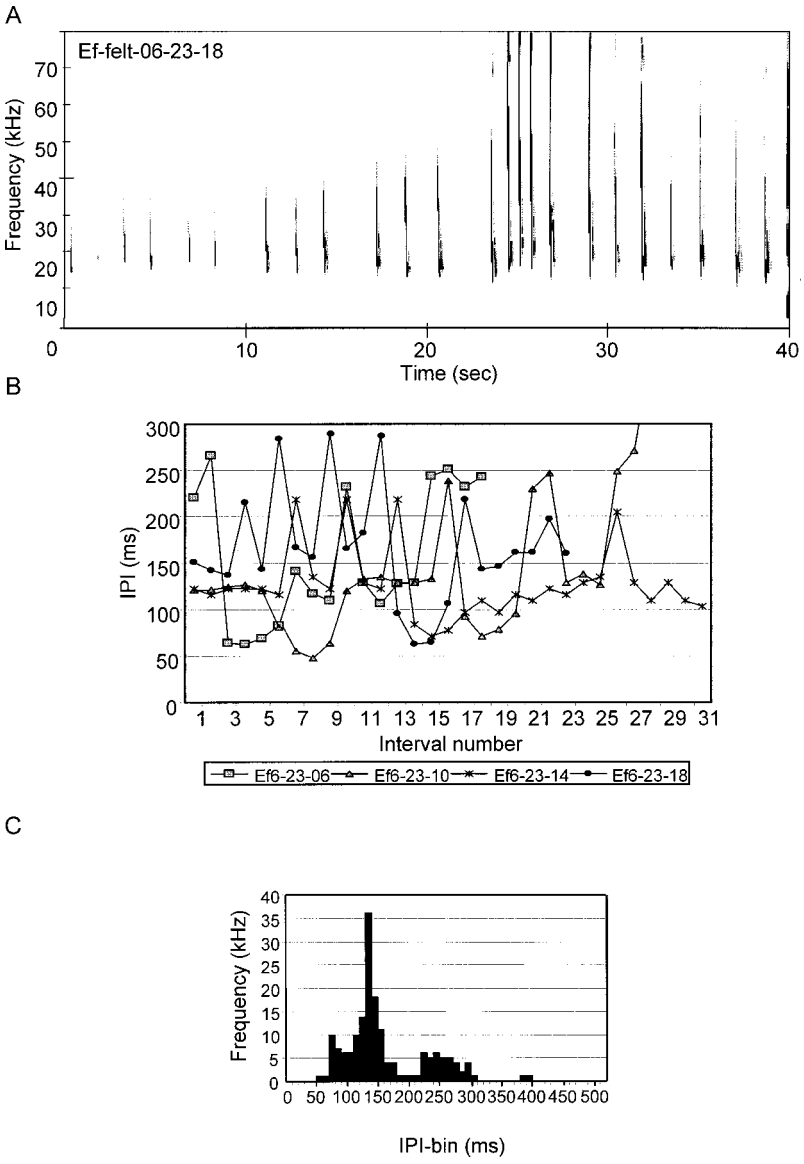

FIG. 13. The interpulse intervals (IPI) of four field recordings of *E. fuscus*. (A) shows spectrograms of one recording sequence. (B) shows IPI's of all four recordings illustrating the typical changes in the regular pattern of emission. One pattern is short breaks appearing as sharp peaks on the IPI curves. The other typical patterns are short bursts of higher but almost constant repetition rates (stable IPI groups) resulting in troughs in the curves, e.g., the five cries between interval 3 and 7 on the curve plotted with squares, or the five cries between interval 17 and 21 on the curve plotted with triangles. The histogram of cry intervals (C) (10-ms bin width) shows that besides the ''standard'' value of around 140 ms and approximately twice that value (see Surlykke and Moss, 2000), there is a lower peak around 70 ms corresponding to the stable IPI group present in the laboratory vocalization data.

phones allowed for determination of the distance to the bats, and the directionality of the microphones, combined with the voice notes on the tape, ensured that the recordings chosen for analysis were from bats in front of the array. Although flight angle and speed were not measured, Doppler shifts introduced by the bat's flight velocity would be less than 0.7 kHz at 25 kHz, assuming a flight velocity of 10 m/s. It is noteworthy that both species show evidence of frequency shifts of several kHz when two bats are flying close together. Thus, these frequency shifts are considerably larger than those that could be explained by Doppler shifts introduced by the bat's flight velocity (see Surlykke and Moss, 2000), and suggest a jamming avoidance response. Such frequency shifts could help segregate information relevant to different individuals (Fig. 14).

Finally, field recordings show that some bat species emit signals with systematic changes in frequency from emission to emission. Figure 15 shows a 500-ms recording of an Emballonurid bat, *Cormura brevirostris*, which emits triplets of multiharmonic sounds in the search phase. The dominant harmonic of the first signal is at 26 kHz, the second at 29 kHz, and the third at 33 kHz. This may be the bat's solution in the frequency domain to recognizing its own signals, and thus echoes, in areas with very high bat density and much acoustic activity in the same frequency range.

VII. DISCUSSION

Echolocating bats probe the environment with sonar vocalizations and use information contained in the returning echoes to maneuver through the environment and intercept small flying insect prey in the dark. These extraordinary behaviors lead one to speculate that the echolocating bat's representation of the environment obtained through sonar compares well with that of human spatial vision. Spatial vision does not arise from passive reception of retinal images but instead builds upon transformational rules that support interpretation of the visual scene (Hoffman, 1998). Similarly, auditory scene analysis utilizes organizational rules that permit the perceptual grouping and segregation of sound sources in the environment (Bregman, 1990). In the case of the echolocating bat, its vocal control over the acoustic environment

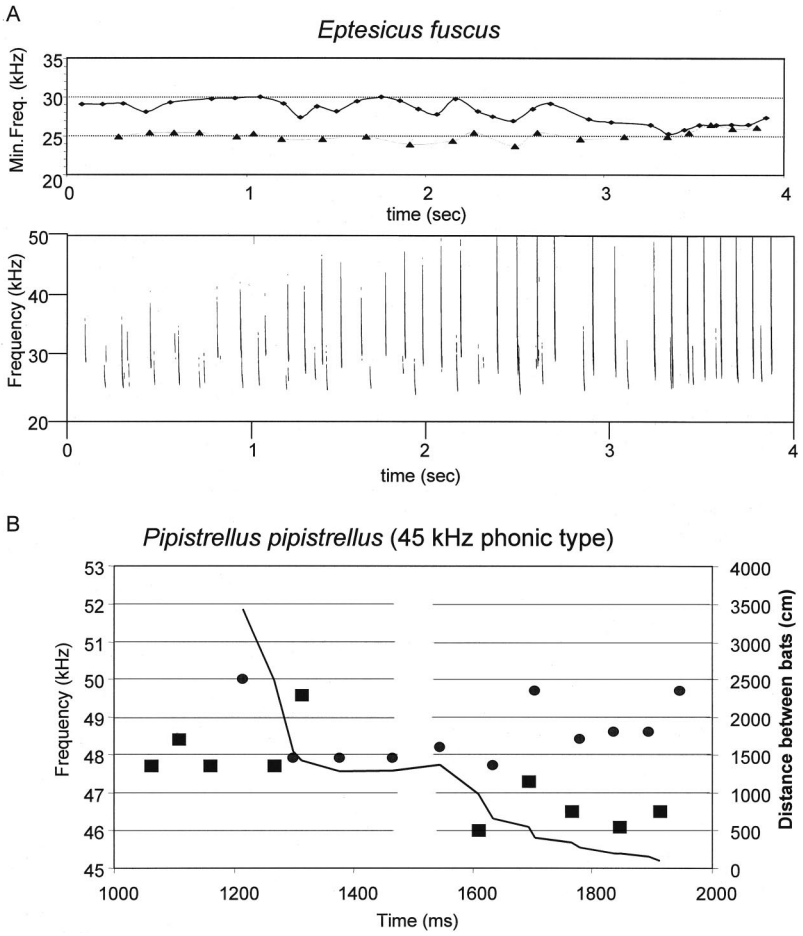

FIG. 14. (A) Signals from two *E. fuscus* recorded simultaneously. As long as both bats are recorded at high intensity while they are presumably close together (from 0 to around 2.5 s), they emit signals where the main frequency differs by 4–5 kHz. When one of the bats starts veering away and the other closes in on the microphone (as revealed by the reduced intensity of the low-frequency bat, and increased intensity of the high-frequency bat) both bats adjust the frequency of their emissions to approximately the same value, approximately 26 kHz. (B) Same pattern for *Pipistrellus pipistrellus*. In this case an array of three microphones allowed for discrimination between the emissions of the two bats (filled squares and filled circles, respectively) and for determinations of approximate distance between the bats (line curve). In this case the emitted frequencies of both bats are scattered around 48 and 50 kHz, but when the bats start closing in on one another (around 1600 ms) they adjust their frequencies to be separated by approximately 2.5 kHz.

allows the motor system to play directly into its analysis of the auditory scene. We hypothesize that active perceptual processes and active vocal control over echo information obtained from the environment operate in concert, permitting an elaborate representation of a dynamic auditory scene. Here, we have presented examples from perceptual and motor studies that illustrate the active processes that contribute to scene analysis by echolocation.

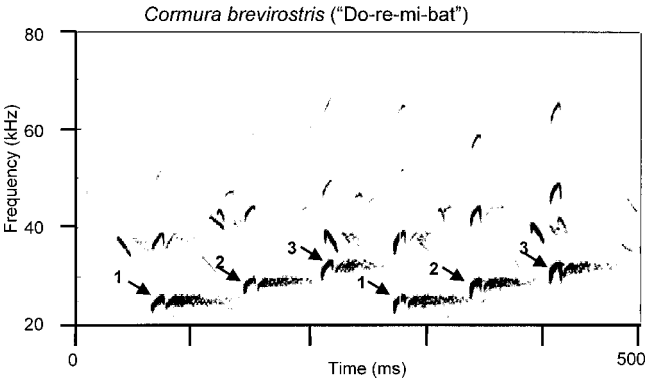

FIG. 15. In the search phase the tropical bat, *Cormura brevirostris* (Wagner's sacwinged bats, a.k.a. the ''do-re-mi-bat'') emits triplets of sonar sounds with main frequency increasing from 26 kHz to 29 kHz and ending at 33 kHz. This very distinct frequency pattern may help the bat to distinguish between its own emissions and those of the many other bats operating in the same frequency range. Background signals from other bats also appear in this figure. Single bat's signals are identified by the numbers 1, 2, 3. Another advantage of this frequency shift might be to reduce problems with overlap between emission and echo (see the text).

Over the past several decades, echolocation research has yielded valuable data on sonar performance and acoustic information processing by many different species of bats (see for example, Griffin, 1958; Busnel and Fish, 1980; Moss and Schnitzler, 1995); however, very little attention has been directed toward understanding how echo information may be interpreted by the bat's auditory system to build a perceptual representation of the auditory scene. The aims of this paper are to highlight the question of higher-level perception in sonar, to provide a conceptual framework for studying this problem, and to report on data that begin to address questions of scene analysis by echolocation in bats.

In this article, we have emphasized temporal processing of sonar signals for spatial analysis of the auditory scene. Certainly many distinct acoustic features contribute to the bat's perception of the world through sound (e.g., direction, spectrum, amplitude), but we have focused largely on the processing of echo delay for target distance estimation, because this signal parameter plays a central role in the bat's perceptually guided behavior through three-dimensional space. In particular, we have chosen to present data from echo discrimination experiments, laboratory insect capture studies, and field recordings, to illustrate the role of temporal patterning in perception and action for scene analysis by echolocation in bats. The contribution of spectral signal characteristics to the bat's perceptual organization of sound was discussed briefly in the context of sonar behavior in the field (Figs. 14 and 15). A more detailed analysis of a wide range

of acoustic parameters will be the focus of future work.

The perceptual experiments presented in this paper explicitly examined the fundamental issue of processing spatial information from a dynamic acoustic environment. Changes in the auditory scene, produced by movement of sonar targets and by the bat's own flight path, are sampled at a low duty cycle by species that use frequency-modulated (FM) echolocation cries, resulting in brief acoustic snapshots of the world. The bat's auditory system must assemble information over time to build a representation of the dynamic auditory scene. While others (e.g., Hartley and Suthers, 1992; Roverud, 1993, 1994; Roverud and Rabitoy, 1994) have shown that decreasing echo delay can evoke distance-appropriate increases in sonar signal production in trained echolocating bats, these earlier behavioral experiments did not directly study the bat's perceptual discrimination of echo delay patterns that increase or decrease over time. Here, we have presented psychophysical data demonstrating that the perceptual system of the big brown bat, *Eptesicus fuscus*, supports the integration of acoustic information over time, permitting the discrimination of increasing or decreasing echo delay patterns. Our future experiments will attempt to determine if the bat hears out streams of echoes from an echo-cluttered background that would allow it to segregate and track moving targets against background.

Here, we have also presented data on active vocal control by echolocating bats, operating both in the laboratory and in the field. Unlike the majority of hearing animals that perceive their surroundings by listening passively to acoustic signals generated in the environment, the echolocating bat actively transmits and controls the acoustic information it obtains about the auditory scene. The bat's active control over the acoustic information it receives from the environment prevents us from conducting the classical psychophysical experiments on auditory scene analysis with bats, like those employed with passively listening subjects. However, the active selection of sonar signal parameters under changing task conditions presents a valuable opportunity to attack the problem of scene analysis from the motor side.

We propose that the bat's vocal production patterns during insect capture are consistent with the notion that it uses information over successive echoes to build a representation of the world that ultimately guides its behavior. If the bat were to process each echo as a discrete event and modify its behavior based on the spatial information contained in single echoes, insect capture in a dynamic environment would surely fail. Assuming a behavioral response latency of 100–150 ms, the position of the target with respect to the bat would have changed by the time the bat localized and responded to it, and the bat's motor adjustments would lag behind the movement of the insect. Furthermore, if the bat were to process echo information from each sound before making appropriate motor adjustments, the intervals between sounds should be greater than the shortest behavioral response latency of approximately 100 ms. However, intervals between the bat's echolocation sounds are typically less than 100 ms, except during the early search phase of insect pursuit or during cruising (Griffin, 1958), suggesting that the bat emits and processes signals in groups with shorter interpulse intervals. In this context, it is noteworthy that the flight path data often show the bat predicting its point of interception with a moving target (example shown in Fig. 6).

Assuming that the general principles of auditory scene analysis apply to the echolocating bat, we hypothesize that the task of organizing acoustic information from a dynamic environment is simplified if the bat probes sonar targets with vocalizations occurring with a relatively stable interval, which we refer to as stable IPI sound groups. In human listening experiments, the interval between successive sounds influences the tendency to hear out auditory streams (Bregman, 1990), and in the bat, the interval between signals in a group may influence the acoustic streams it segregates from objects at different distances and directions.

What other benefits might the bat derive from the production of stable IPI sound groups? Information about target position may be encoded more reliably in the central nervous system under conditions in which the sonar production rate is stable. The echolocating bat's auditory system contains a population of neurons that shows facilitated and delay-tuned responses to pairs of sounds, simulating sonar emissions and echoes, a response property believed to be related to the encoding of target range (Suga and O'Neill, 1979). Echo-delay-tuned neurons, found in the auditory brainstem (Mittman and Wenstrup, 1995; Dear and Suga, 1995; Valentine and Moss, 1997), thalamus (Olson and Musil, 1992), and cortex (O'Neill and Suga, 1982; Sullivan, 1982; Wong and Shannon, 1988; Dear *et al.*, 1993b), show very weak responses to single FM sounds. However, these neurons respond vigorously to pairs of FM sounds (a simulated pulse and a weaker echo), separated by a delay. Typically, echo-delay-tuned neurons show facilitated responses to simulated pulse–echo pairs over a delay range of several milliseconds. The pulse-echo interval to which an echo-delay-tuned neuron shows the largest response is referred to as the best delay. For example, a neuron may respond maximally to a pulse–echo interval of 9 ms, which corresponds to a target range of 1.5 m. Pulse–echo pairs with intervals of 7 and 11 ms (simulating ranges between 1.1 and 1.9 m) may also evoke a response, but at a lower rate.

Delay-tuned neurons respond phasically to acoustic stimuli simulating FM sonar signals, and typically fire no more than one or two action potentials for each pulse–echo stimulus presentation. In addition, a population of echo-delay-tuned neurons exhibits shifts in the best delay with the stimulus presentation rate (O'Neill and Suga, 1982; Tanaka and Wong, 1993; Wong *et al.*, 1992). This shift in best delay may be several milliseconds, corresponding to a shift in best range of several centimeters. These two observations together, i.e., that the delay-tuned neurons fire one or two action potentials per stimulus presentation at the best delay, and that the best delay may change with stimulus repetition rate, suggest that sonar strobe groups may serve to stabilize the neural representation of the distance of objects in an auditory scene. For example, the repeated production of sounds with stable IPI for a sonar target at a given distance, e.g., 1.5 m from the bat, would consistently stimulate neurons responsive to the combination of a particular echo delay (e.g., 9 ms)

and repetition rate (e.g., 60 Hz) over several successive signals, which would then increase reliability of target distance estimation.

The stable IPI groups are interrupted by longer gaps, and thus the signals in each group occur in clusters, which may impact both perception and motor planning. With regard to perception, the grouping of signals would serve to increase the information carried by echoes in discrete blocks of time. It may be that the bat's sonar receiver can extract finer detail about the surroundings with the higher density of echoes that results from these groups. In this context, it is noteworthy that the bat increases its relative production of stable IPI groups shortly before target contact, and again just after capture, when a detailed assessment of the surroundings may be particularly important for planning the final attack and reorienting after tucking the head in the tail membrane to take the prey (Fig. 10). The stable IPI groups were also recorded from actively hunting bats but not from animals that were commuting from the roost to hunting grounds. All of this suggests to us that the stable IPI groups may be important for spatially segregating (streaming) the target (insect prey) and background. Moreover, we speculate that the spatial resolution of the auditory scene varies inversely with the interpulse intervals within stable IPI groups. Thus, shorter interpulse intervals, characteristic of the final stages of insect capture, may permit segregation of acoustic streams from closely spaced echo-producing auditory objects.

Naturally, the clustering of signals in groups, which results in greater echo density, also creates time periods when the echo density is reduced. We speculate that the bat may use the IPI gap time to update motor programs, using the acoustic information carried by echoes in the IPI groups. The median duration of the stable IPI groups was about 43 ms for the open-space condition and 38 ms for the cluttered condition, which might approximate the time over which information is assembled for motor program updates.

It is well established that the echolocating bat's respiration cycle is correlated with its wingbeat cycle, and the intervals between sonar vocalizations occur during inspiration. The coupling of wingbeat, respiration, and vocal production contributes to the temporal patterning of sonar signals (Schnitzler and Henson, 1980; Suthers *et al.*, 1972; Wong and Waters, 2001), and indeed this coupling can be used, in part, to explain the sonar signal groups we report here. However, some bat species do not produce sonar signal groups, but instead show a relatively regular and continuous decrease in interpulse intervals (see, e.g., Schnitzler and Henson, 1980). The fact that some species produce stable IPI groups and others do not suggests differences in the coordination of vocal production and respiration across bat species, even among those that use FM signals to hunt insects in temperate climates (e.g., compare *Eptesicus fuscus* and *Myotis lucifigus*, Schnitzler and Henson, 1980). Such differences in the temporal patterning of vocal production naturally results in differences in echo patterning received by the sonar systems of different species, since the vocal production pattern directly impacts the information available to the sonar receiver. We do not know why differences exist in the temporal patterning of sonar signals across species; however, we propose that the stable IPI groups produced by *Eptesicus fuscus* play into the analysis of the auditory scene in this species.

In our laboratory studies of insect capture behavior, a clear distinction in vocal production patterns across task conditions appeared in the duration of the terminal buzz. When the bats captured targets in the presence of clutter, they shortened the terminal buzz, as compared with the buzz produced under open uncluttered space conditions ($F=6.22, p<0.01$). This result is not surprising, when one considers that the bat typically waits to produce its next signal until it has received and processed echoes of interest. In other words, the bat avoids producing signals before all the relevant echoes have returned. In the terminal buzz the interval between signals is so short that there often is not time for all relevant echoes (from target and clutter) to return before the subsequent sound is produced. Thus, in the terminal buzz, the bat likely receives echoes from the clutter following one sonar signal after producing the next signal, and the bat reduces the time when it experiences the mixing of echoes from different vocalizations under clutter conditions by shortening the terminal buzz.

The onset of the buzz differed between stationary (open-space and clutter conditions) and moving target (open space) trials. When the bat pursued moving prey, it typically followed the insect from behind, in the direction of the target's motion. Thus, the insect was moving away from the bat during the final stage of capture, and the bat's approach direction presumably resulted in the extended buzz duration in the moving target trials. The buzz onset times relative to target capture were very similar in the open-space stationary and the three different clutter conditions. The consistency of buzz onset time in clutter relative to stationary prey capture suggests that it reflects a motor planning process for target interception, rather than serving as an indicator of target detection or localization. Measures of the distance between the bat and target when it initiated the buzz show that the bat was closer to the target when it entered the final capture sequence in clutter than in open space. Moreover, the closer the target was positioned relative to the clutter, the shorter was its distance to the prey when it began the terminal buzz. This is consistent with the observation that buzzes recorded in the field are shorter than in the lab (Surlykke and Moss, 2000), since natural prey is unpredictable, and motor planning must be delayed until the bat is closer to the point of capture.

Given the potential for mixing signals and echoes in the terminal buzz, one might then ask why the bat produces signals at such a high repetition rate. Furthermore, the bat has little time to react to any new information carried by echoes from the terminal buzz signals. However, the terminal buzz does allow the bat to sample information at a very high and stable repetition rate, providing details about the auditory scene that may be enhanced and sharpened, particularly if the information is assembled over time. This is conveyed in Fig. 2(B) by the clear ridges representing changing target distances during the buzz phase of insect pursuit. While the bat has little time to react to information about the target in the terminal buzz, it may use echoes from the terminal buzz to represent spatial information about the background that it still must negotiate following insect capture. The signal fre-

quencies in the terminal buzz drop well below 20 kHz (Surlykke and Moss, 2000), and this drop in sound frequency serves to reduce the directionality of the bat's sonar signals. Using lower-frequency, more omnidirectional signals may thus help the bat in sampling background information that could ultimately influence its flight path following target capture. Thus, if one thinks of the buzz as a sampling unit, rather than many closely spaced, discrete elements, one can begin to appreciate the rich information it may carry for the analysis of the auditory scene.

Field data from several different species highlight the perceptual requirements and vocal-motor strategies used by echolocating bats to analyze the auditory scene. In particular, we have presented sound recordings from *Noctilio* that illustrate the complicated acoustic environment the bat encounters, raising questions about how the bat sorts a cacophony of signals and echoes in an environment where many animals are hunting together. While hunting in less crowded conditions, *E. fuscus* and *P. pippistrellus* sometimes encounter conspecifics in close proximity, and we presented examples here of adjustments in the frequency of sonar emissions produced by these two species in response to the signals of neighbors. Such adjustments in signal spectrum and sweep rate may allow an individual bat to separate out echoes from its own signals from echoes of signals produced by conspecifics in close proximity. Finally, we presented the signals produced by a bat that samples the environment with multiharmonic signals with changing fundamental frequencies (*C. brevirostris*, dubbed the ''do-re-mi bat''). We have no data to speak directly to this species' perception of the world by sonar, but we note that vocal production patterns of *C. brevirostris* resemble frequency hopping used in wireless communication systems. Frequency hopping minimizes interference from other sources by carving the transmission band into separate frequency channels that are active for short intervals (about 100 milliseconds) before shifting to a neighboring frequency. This allows wireless communication more access points in the same area, and we speculate that *C. brevirostris* uses a similar strategy to minimize interference from neighboring echolocating bats.

In conclusion, we have introduced here a conceptual framework for the study of auditory scene analysis by echolocation in bats. We assert that the principles of auditory scene analysis, which have been identified in humans (Bregman, 1990), can be applied broadly to understand the perceptual organization of sound in other animals, including the echolocating bat. In particular, we postulate that the bat's perceptual system organizes acoustic information from a complex and dynamic environment into echo streams, allowing it to track spatially distributed auditory objects (sonar targets) as it flies. Our hypothesis emphasizes the importance of the echolocating bat's vocal production patterns to its analysis of the auditory scene, as motor behaviors and perception operate in concert in the bat's active sensing system. It is our goal that the conceptual framework presented here will stimulate new research avenues for unraveling the details of auditory scene analysis in animal systems.

ACKNOWLEDGMENTS

We gratefully acknowledge the following agencies, foundations, and institutions that have supported this work: NIMH (No. R01-MH56366), NSF (No. IBN-9258255), Whitehall Foundation (No. S97-20) and the Institute for Advanced Study, Berlin (to C.F.M.), Danish National Research Foundation and the Danish Natural Science Research Council (to A.S.). In addition, we thank the following individuals for their valued assistance: Kari Bohn for data collection, analysis, and figure preparation, Hannah Gilkenson, Aaron Schurger, and Willard Wilson for data collection, analysis, and processing of the laboratory insect capture experiments, Maryellen Morris for running the psychophysical experiments, and Amy Kryjak for data analysis and overseeing the complicated management of the many projects reported here. Carola Eschenbach and two anonymous reviewers provided critical comments on an earlier version of this manuscript. Discussions with Hans-Ulrich Schnitzler contributed to ideas presented here. We also thank Elisabeth Kalko and Marianne Jensen for their valued assistance in the field.

Barratt, E. M., Deaville, R., Burland, T. M., Bruford, M. W., Jones, G., Racey, P. A., and Wayne, R. K. (**1997**). ''DNA answers the call of pipistrelle bat species,'' Nature (London) **387**, 138–139.

Batteau, D. W. (**1967**). ''The role of the pinna in human localization,'' Proc. R. Soc. London **1011**, 158–180.

Blauert, J. (**1997**). *Spatial Hearing: The Psychophysics of Human Sound Localization* (MIT Press, Cambridge).

Braaten, R. F., and Hulse, S. H. (**1993**). ''Perceptual organization of temporal patterns in European starlings (*Sturnus vulgaris*),'' Percept. Psychophys. **54**, 567–578.

Bregman, A. S. (**1990**). *Auditory Scene Analysis* (MIT Press, Cambridge, MA).

Bregman, A. S., and Campbell, J. (**1971**). ''Primary auditory stream segregation and perception of order in rapid sequences of tones,'' J. Exp. Psychol. **89**, 244–249.

Busnel, R. G., and Fish, J. F. (**1980**). *Animal Sonar Systems* (Plenum, New York).

Cahlander, D. A., McCue, J. J. G., and Webster, F. A. (**1964**). ''The determination of distance by echolocation,'' Nature (London) **201**, 544–546.

Dear, S. P., Simmons, J. A., and Fritz, J. (**1993a**). ''A possible neuronal basis for representation of acoustic scenes in auditory cortex of the big brown bat,'' Nature (London) **364**, 620–622.

Dear, S. P., Fritz, J., Haresign, T., Ferragamo, M., and Simmons, J. A. (**1993b**). ''Tonotopic and functional organization in the auditory cortex of the big brown bat, *Eptesicus fuscus*,'' J. Neurophysiol. **70**, 1988–2009.

Dear, S. P., and Suga, N. (**1995**). ''Delay-tuned neurons in the midbrain of the big brown bat,'' J. Neurophysiol. **73**, 1084–1100.

Fay, R. R. (**1998**). ''Auditory stream segregation in goldfish (*Carassius auratus*),'' Hear. Res. **120**, 69–76.

Fay, R. R. (**2000**). ''Spectral contrasts underlying auditory stream segregation in goldfish (*Carassius auratus*),'' J. Assoc. for Res. in Otolaryngol., online publication.

Gellerman, L. W. (**1933**). ''Chance orders of alternating stimuli in visual discrimination experiments,'' J. Gen. Psychol. **42**, 206–208.

Griffin, D. R. (**1953**). ''Bat sounds under natural conditions, with evidence for echolocation of insect prey,'' J. Exp. Zool. **123**, 435–465.

Griffin, D. (**1958**). *Listening in the Dark* (Yale University Press, New Haven).

Griffin, D. R., Webster, F. A., and Michael, C. R. (**1960**). ''The echolocation of flying insects by bats,'' Anim. Behav. **8**, 141–154.

Grinnell, A. D., and Grinnell, V. S. (**1965**). ''Neural correlates of vertical localization by echolocating bats,'' J. Physiol. (London) **181**, 830–851.

Hartley, D. J. (**1992**). ''Stabilization of perceived echo amplitudes in echolocating bats. II. The acoustic behavior of the big brown bat, *Eptesicus fuscus*, when tracking moving prey,'' J. Acoust. Soc. Am. **91**, 1133–1149.

Hartley, D. J., and Suthers, R. A. (**1989**). ''The sound emission pattern of the echolocating bat, *Eptesicus fuscus*,'' J. Acoust. Soc. Am. **85**, 1348–1351.

Hartridge, H. (**1945**). ''Acoustic control in the flight of bats,'' Nature (London) **156**, 490–494.
Hoffman, D. D. (**1998**). *Visual Intelligence: How We Create What We See* (Norton, New York).
Hope, G. M., and Bhatnagar, K. P. (**1979**). ''Electrical response of bat retina to spectral stimulation: Comparison of four microchiropteran species,'' Experientia **35**, 1189–91.
Hulse, S. H., MacDougall-Shackleton, S. A., and Wisniewski, A. B. (**1997**). ''Auditory scene analysis by songbirds: Stream segregation of birdsong by European starlings (*Sturnus vulgaris*),'' J. Comp. Psychol. **111**(1), 3–13.
Julsz, B., and Hirsh, I. J. (**1972**). ''Visual and auditory perception—An essay of comparison,'' in *Human Communication: A Unified View,* edited by E. E. David, Jr. and P. B. Denes (McGraw-Hill, New York).
Kalko, E. K. V., Schnitzler, H.-U., Kaipf, I., and Grinnell, A. D. (**1988**). ''Echolocation and foraging behavior of the lesser bulldog bat, *Notilio albiventris*: Preadaption for piscivory?'' Behav. Ecol. Sociobiol. **42**, 305–319.
Kawasaki, M., Margoliash, D., and Suga, N. (**1988**). ''Delay-tuned combination-sensitive neurons in the auditory cortex of the vocalizing mustached bat,'' J. Neurophysiol. **59**, 623–635.
Körte, A. (**1915**). ''Kinomatoscopische Untersuchungen,'' Zeitschrift für Psychologie der Sinnesorgane **72**, 193–296.
Lawrence, B. D., and Simmons, J. A. (**1982**). ''Echolocation in bats: The external ear and perception of the vertical positions of targets,'' Science **218**, 481–483.
MacDougall-Shackleton, S. A., Hulse, S. H., Gentner, T. Q., and White, W. (1998). ''Auditory scene analysis by European starlings (*sturnus vulgaris*): Perceptual segregation of tone sequences,'' J. Acoust. Soc. Am. **103**, 3581–3587.
Mittmann, D. H., and Wenstrup, J. J. (**1995**). ''Combination-sensitive neurons in the inferior colliculus,'' Hear. Res. **90**(1–2), 185–191.
Morris, M. R., and Moss, C. F. (**1995**). ''Perception of complex stimuli in the echolocating FM bat, *Eptesicus fuscus*,'' Tenth International Bat Research Conference, Boston, MA.
Morris, M., and Moss, C. F. (**1996**). *Perceptual Organization of Sound for Spatially Guided Behavior in the Echolocating Bat* (Society for Neuroscience Abstracts, Washington, D.C.), Vol. 22, p. 404.
Moss, C. F., and Schnitzler, H.-U. (**1989**). ''Accuracy of target ranging in echolocating bats: Acoustic information processing,'' J. Comp. Physiol., A **165**, 383–393.
Moss, C. F., and Schnitzler, H.-U. (**1995**). ''Behavioral studies of auditory information processing,'' in *Springer Handbook of Auditory Research. Hearing by Bats*, edited by A. N. Popper and R. R. Fay (Springer, Berlin), pp. 87–145.
O'Neill, W. E., and Suga, N. (**1982**). ''Encoding of target range and its representation in the auditory cortex of the mustached bat,'' J. Neurosci. **2**(1), 17–31.
Olson, C. R., and Musil, S. Y. (**1992**). ''Topographic organization of cortical and subcortical projections to posterior cingulate cortex in the cat—Evidence for somatic, ocular, and complex subregions,'' J. Comp. Neurol. **324**(2), 237–260.
Roverud, R. C. (**1993**). ''Neural computations for sound pattern recognition: Evidence for summation of an array of frequency filters in an echolocating bat,'' J. Neurosci. **13**(6), 2306–2312.
Roverud, R. C. (**1994**). ''Complex sound analysis in the lesser bulldog bat: Evidence for a mechanism for processing frequency elements of frequency modulated signals over restricted time intervals,'' J. Comp. Physiol., A **174**, 559–565.
Roverud, R. C., and Rabitoy, E. R. (**1994**). ''Complex sound analysis in the FM bat *Eptesicus fuscus*, correlated with structural parameters of frequency modulated signals,'' J. Comp. Physiol., A **174**, 567–573.
Schnitzler, H.-U. (**1968**). ''Die Ultraschall-Ortungslaute der Hufeisen-Fledermaeuse (Chiroptera-rhinolophidae), in verschiedenen Orientierungssituationen,'' Zeitschrift vergl. Physiol. **57**, 376–408.
Schnitzler, H.-U., and Henson, W., Jr. (**1980**). ''Performance of airborne animal sonar systems. I. Microchiroptera,'' in *Animal Sonar Systems*, edited by R. G. Busnel and J. F. Fish (Plenum, New York), pp. 109–181.
Schnitzler, H.-U., and Kalko, E.K.V. (**1998**). ''How echolocating bats search and find food,'' in *Bats: Phylogeny, Morphology, Echolocation and Conservation Biology*, edited by T. H. Kunz and P. A. Racey (Smithsonian Inst. Press, Washington, D.C.), pp. 183–196.
Schnitzler, H.-U., Menne, D., Kober, R., and Heblich, K. (**1983**). ''The acoustical image of fluttering insects in echolocating bats,'' in *Neuroethology and Behavioral Physiology*, edited by F. Huber and H. Markel (Springer, Heidelberg), pp. 235–249.
Schnitzler, H.-U., Kalko, E. K. V., Keipf, I., and Grinnell, A. D. (**1994**). ''Fishing and echolocation behavior of the greater bulldog bat, *Noctilio leporinus*, in the field,'' Behav. Ecol. Sociobiol. **35**, 327–345.
Shimozowa, T., Suga, N., Hendler, P., and Schuetec, S. (**1974**). ''Directional sensitivity of echolocation system in bats producing frequency-modulated signals,'' J. Exp. Biol. **60**, 53–69.
Simmons, J. A. (**1973**). ''The resolution of target range by echolocating bats,'' J. Acoust. Soc. Am. **54**, 157–173.
Simmons, J. A. (**1979**). ''Perception of echo phase information in bat sonar,'' Science **204**, 1336–1338.
Simmons, J. A., Ferragamo, M. J., Saillant, P. A., Haresign, T., Wotton, J. M. Dear, S. P., and Lee, D.N. (**1995**). ''Auditory dimensions of acoustic images in echolocation,'' in *Springer Handbook of Auditory Research. Hearing by Bats*, edited by A. N. Popper and R. R. Fay (Springer, Berlin), pp. 146–190.
Simmons, J. A., Lavender, W. A., Lavender, B. A., Doroshow, D. A., Kiefer, S. W., Livingston, R., Scallet, A. C., and Crowley, D. E. (**1974**). ''Target structure and echo spectral discrimination by echolocating bats,'' Science **186**, 1130–1132.
Simmons, J. A., Kick, S. A., Lawrence, B. D., Hale, C., Bard, C., and Escudie, B. (**1983**). ''Acuity of horizontal angle discrimination by the echolocating bat, *Eptesicus fuscus*,'' J. Comp. Physiol., A **153**, 321–330.
Simmons, J. A., and Vernon, J. A. (**1971**). ''Echolocation: Discrimination of targets by the bat, *Eptesicus fuscus*,'' J. Exp. Zool. **176**, 315–328.
Suga, N., and O'Neill, W. E. (**1979**). ''Neural axis representing target range in the auditory cortex of the mustache bat,'' Science **206**, 351–353.
Sullivan, W. E. (**1982**). ''Neural representation of target distance in auditory cortex of the echolocating bat, *Myotis lucifugus*,'' J. Neurophysiol. **48**, 1011–1032.
Surlykke, A., and Moss, C. F. (**2000**). ''Echolocation behavior of the big brown bat, *Eptesicus fuscus*, in the field and the laboratory,'' J. Acoust. Soc. Am. **108**, 2419–2429.
Suthers, R. A., Thomas, S. P., and Suthers, B. J. (**1972**). ''Respiration, wingbeat and ultrasonic pulse emission in an echo-locating bat,'' J. Exp. Biol. **56**, 37–48.
Tanaka, H., and Wong, D. (**1993**). ''The influence of temporal pattern of stimulation on delay tuning of neurons in the auditory cortex of the FM bat, *Myotis lucifugus*,'' Hear. Res. **66**, 58–66.
Valentine, D. E. and Moss, C. F. (**1997**). ''Spatially-selective auditory responses in the superior colliculus of the echolocating bat,'' J. Neuroscience **17**, 1720–1753.
Wadsworth, J., and Moss, C. F. (**2000**). ''Vocal control of acoustic information for sonar discriminations by the echolocating bat, *Eptesicus fuscus*,'' J. Acoust. Soc. Am. **107**, 2265–2271.
Webster, F. A. (**1963**). ''Active energy radiating systems: The bat and ultrasonic principles in acoustical control of airborne interceptions by bats,'' Proc. International Congress on Technology and Blindness, Vol. I.
Wisniewski, A. B., and Hulse, S. H. (**1997**). ''Auditory scene analysis in European starlings (*Sturnus vulgaris*): Discrimination of song segments, their segregation from multiple and reversed conspecific songs, and evidence for conspecific song categorization,'' J. Comp. Psych. **111**, 337–350.
Wong, D., and Shannon, S. L. (**1988**). ''Functional zones in the auditory cortex of the echolocating bat, *Myotis lucifugus*,'' Brain Res. **453**, 349–352.
Wong, D., Maekawa, M., and Tanaka, H. (**1992**). ''The effect of pulse repetition rate on the delay sensitivity of neurons in the autory cortex of the FM bat, *Myotis lucifugus*,'' J. Comp. Physiol. **170**, 393–402.
Wong, J. G., and Waters, D. A. (**2001**). ''The synchronization of signal emission with wingbeat during the approach phase in soprano pipistrelles (*Pipistrellus pygmaeus)*,'' J. Exp. Biol. **204**, 575–583.
Wotton, J. M., Haresign, T., and Simmons, J. A. (**1995**). ''Spectral and temporal cues produced by the external ear of *Eptesicus fuscus* with respect to their relevance to sound localization,'' J. Acoust. Soc. Am. **98**, 1423–1445.

Auditory brainstem response recovery in the dolphin as revealed by double sound pulses of different frequencies

Vladimir V. Popov, Alexander Ya. Supin,[a] and Vladimir O. Klishin
Institute of Ecology and Evolution, Russian Academy of Sciences, 33 Leninsky Prospect, 117071 Moscow, Russia

(Received 2 January 2001; revised 23 July 2001; accepted 26 July 2001)

Recovery of auditory brainstem responses (ABR) in a bottlenose dolphin was studied in conditions of double-pip stimulation when two stimuli in a pair differed in frequency and intensity. When the conditioning and test stimuli were of equal frequencies, the test response was markedly suppressed at short interstimulus intervals; complete recovery appeared at intervals from about 2 ms (when two stimuli were of equal intensity) to 10–20 ms (when the conditioning stimulus exceeded the test by up to 40 dB). When the two stimuli were of different frequencies, the suppression diminished and was almost absent at a half-octave difference even if the conditioning stimulus exceeded the test one by 40 dB. Frequency-dependence curves (ABR amplitude dependence on frequency difference between the two stimuli) had equivalent rectangular bandwidth from ±0.2 oct at test stimuli of 20 dB above threshold to ±0.5 oct at test stimuli of 50 dB above threshold. © *2001 Acoustical Society of America.* [DOI: 10.1121/1.1404382]

PACS numbers: 43.80.Lb, 43.64.Ri, 43.64.Tk, 43.66.Gf [WA]

I. INTRODUCTION

Echolocating dolphins have to hear weak echo signals shortly after emitting intense echolocation sounds. Due to high sound velocity in water, the delay between the emitted and echo sounds may be very short, down to a few ms. To be able to distinguish the emitted and echo sounds, dolphins use rapid, short-duration pulses for echolocation (Au, 1993). On the other hand, their auditory system is capable of very high temporal resolution. Analysis of echolocation data has shown the integration time in the dolphin's auditory system to be as short as 200–300 μs (Au *et al.*, 1988; Au, 1990). Experiments with discrimination between pulse pairs have also suggested that pulses merge in an ''acoustic whole'' when separated no longer than 200–300 μs (Dubrovskiy, 1990). Backward masking in dolphins is also possible at intervals of up to 200–300 μs (Moore *et al.*, 1984; Dubrovskiy, 1990).

Double-click evoked-potential studies have shown directly that a test response can appear at a very short delay after the preceding (conditioning) response: it appears at delays from 0.2–0.3 ms to a few ms (depending on the intensity ratio between the two clicks), and complete recovery of the test response requires from a few ms to 10–20 ms (Supin and Popov, 1985, 1995a; Popov and Supin, 1990). Gap-in-noise detection experiments have shown a similarly short gap-detection limit (Popov and Supin, 1997). Correspondingly, evoked potential to rhythmic clicks or amplitude-modulated sounds appear at stimulation rates of up to 2000/s (Dolphin *et al.*, 1995; Supin and Popov, 1995b; Popov and Supin, 1998). The high temporal resolution of the dolphin's auditory system may play an important role in perception of echo signals shortly after the emitted ones.

However, all the data mentioned previously were obtained in experiments when both conditioning and test stimuli (e.g., conditioning and test clicks in the double-click paradigm; pregap and postgap noise; successive cycles of rhythmic-click or amplitude-modulated signals) were of equal frequency composition. This situation is not a precise simulation of real echolocation since the spectrum of an echo signal does not reproduce precisely the emitted pulse spectrum: it depends also on the target properties (Au, 1993). So detection of an echo signal should depend not only on temporal but also on frequency resolution in the auditory system.

Frequency tuning in dolphins is very acute in a wide frequency range: tone–tone masking and notch-noise masking experiments in conjunction with evoked-potential recordings resulted in equivalent-rectangular quality (the center frequency divided by the equivalent rectangular bandwidth, ERB) of 35–40 (Supin *et al.*, 1993; Popov *et al.*, 1995, 1997). However, these frequency-tuning data were obtained using threshold measurements and the simultaneous-masking paradigm; they did not show how response amplitude depended on frequency, intensity, and time interrelations between two short sound pulses, as it occurs in echolocation situation.

Therefore, the goal of the present study was as follows: Using double-pulse sound stimulation and evoked-potential recording, to investigate how the test evoked response depends on (i) the interstimulus interval; (ii) the relationship between conditioning and test stimulus intensity; and (iii) the relationship between conditioning and test stimulus frequency.

II. MATERIAL AND METHODS

A. Subject

The experimental animal was a bottlenose dolphin, *Tursiops truncatus*, male of 208 cm body length, with no apparent indication of any disease. The animal was captured two

[a]Author to whom correspondence should be addressed; electronic mail: 5837.g23@g23.relcom.ru

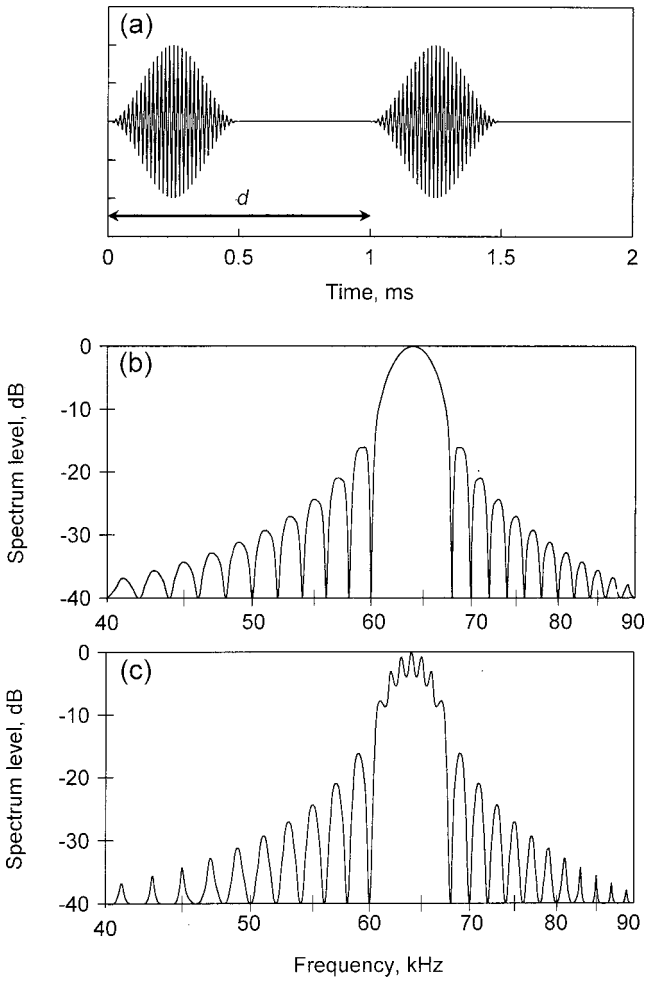

FIG. 1. Stimulus wave form and spectra. (a) A double-pip wave form: Both pips are of equal amplitudes and frequencies (64 kHz); interstimulus interval $d=1$ ms. (b) Frequency spectrum of the single pip. (c) Frequency spectrum of the pair of pips, phase difference between two pips is $\pi/4$.

month prior to the beginning of experimentation. The animal was kept at the Utrish Marine Station of the Russian Academy of Sciences (Black Sea coast) in a sea-water pool $9\times4\times1.5$ m in size. The care and use of the animal was performed under the guidelines established by the Russian Ministry of Higher Education on the use of animals in biomedical research.

B. Experimental conditions

Experiments were carried out during the 1999 summer season. During experimentation, the dolphin was placed in a bath ($4\times0.6\times0.6$ m) filled with sea water. The animal was supported by a stretcher so that the dorsal part of the body and blowhole were above the water surface. The animal was neither anaesthetized nor curarized. Daily experimental session lasted 2.5–3 h, after which the animal was returned to its home pool.

C. Stimuli

The stimuli were paired short tone pips [Fig. 1(a)]. The test pip carrier frequency was always 64 kHz; the conditioning pip carrier frequency varied within a range of 45–90 kHz. Pip envelope was always one 0.5-ms-long cosine cycle; thus pip duration at the half-level was 0.25 ms. Frequency spectrum of a pip of 64-kHz carrier frequency is shown in Fig. 1(b). Its bandwidth is 4 kHz at the −3-dB level and 6.5 kHz at the −10-dB level. Two pips—the conditioning and test ones—were produced by two independent carrier sine-wave generators modulated by a cosine envelope; thus, even when both pips had similar carrier frequencies, they were not coherent. This generation mode was used for the reason that two similar signals separated by a short delay τ result in a characteristic ''rippled'' pattern of the frequency spectrum of the combined signal with a ripple spacing of $1/\tau$. Therefore variation of interstimulus interval τ is accompanied by rippled spectrum variation, which could be a confounding effect. However, the ripple depth depends on the phase relationship between the two pips: At zero or π phase difference, ripples are maximal but of opposite peak-volley positions; at $\pi/2$ or $3\pi/2$ phase difference, ripples are absent; at other phase shifts, ripples have intermediate depths and positions. When two stimuli are not coherent, their phase relationships vary randomly during the series of stimuli, so ripple position and depth vary randomly as well, and the long-term spectrum of a series of stimulus pairs is free of ripples and thus independent of interstimulus interval.

Interstimulus intervals varied by steps as follows: 0.5, 0.7, 1, 1.4, 2, 3, 5, 7, and 10 ms (i.e., approximately $\sqrt{2}$-fold intervals). The shortest interval was limited by the pip duration of 0.5 ms; intervals longer than 10 ms were not used since in most cases test responses recovered almost completely at this interval.

The two pips (the conditioning and test ones) were independently amplified, attenuated, mixed, and played through a 8104-type B&K transducer. The transducer was immersed in water at a depth of 30 cm, 1 m in front of the animal's head. The walls, bottom, and water surface of the bath in front of the animal's head were covered by sound-absorbing material (rubber with air cavities) to minimize reflected sounds. Intensity and wave form of stimuli were monitored through a probe hydrophone with a passband of 150 kHz, located near the animal's head.

D. Evoked potential recording

Evoked potentials were recorded noninvasively using 1-cm disk electrodes secured at the body surface with adhesive electric-conductive gel. The active electrode was placed on the dorsal part of the head, 5–7 cm behind the blowhole, and the reference electrode near the dorsal fin, both above the water surface. This active electrode position is the best to record the auditory brainstem response (ABR). The recorded potentials were amplified, bandpass filtered between 200 and 5000 Hz, digitized using a 12-bit analog-to-digital converter, and averaged using a standard personal computer. Each evoked response was collected by averaging 500–1000 post-stimulus sweeps.

E. Data collection and analysis

Each evoked-potential collection cycle contained stimuli as follows (Fig. 2): the conditioning stimulus alone (S1), the

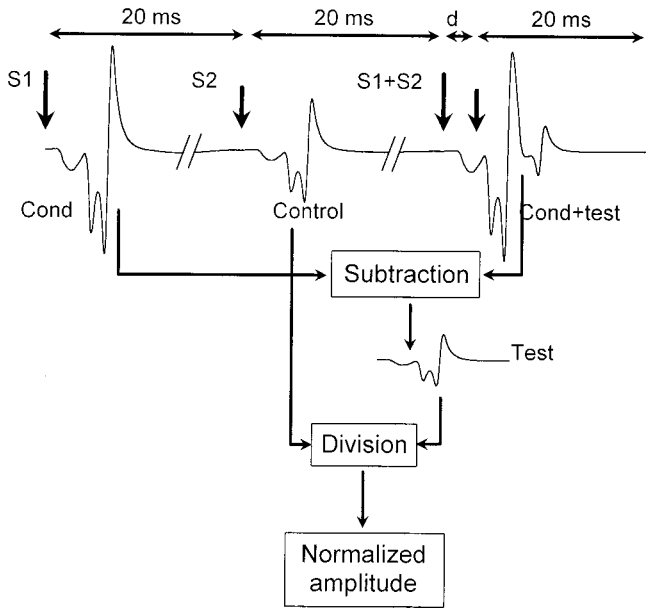

FIG. 2. Diagram of data acquisition and processing. One cycle of evoked-response collection is presented; down-headed arrows indicate stimuli instants: conditioning alone (S1), test alone (S2), and paired stimulus (S1 +S2); double-headed horizontal arrows indicate interstimulus intervals (*d*—variable interval in the pair). Rectangular arrows show which responses (conditioning, test, and conditioning + test) were used for the subtraction and for calculation of the normalized amplitude.

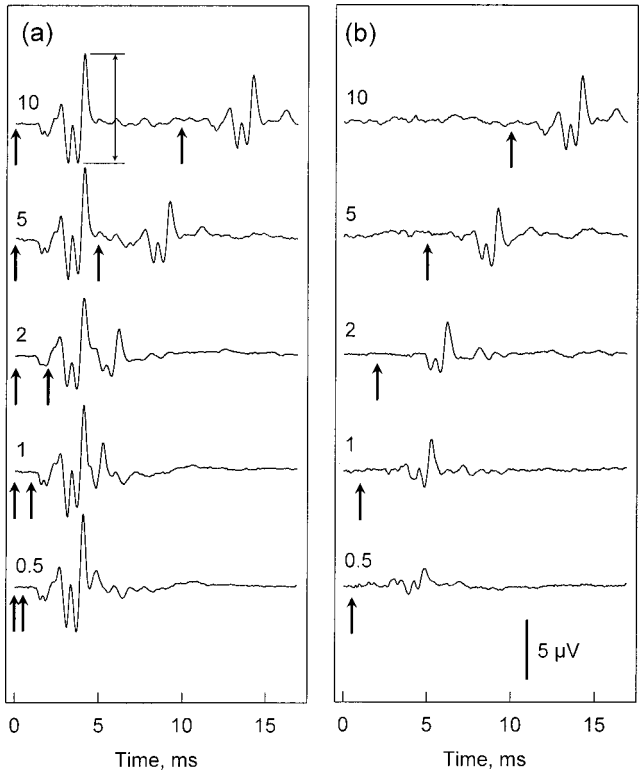

FIG. 3. (a) Examples of ABR to paired stimuli. (b) Responses to the test stimulus isolated using the subtraction procedure. Upward-headed arrows indicate instants of the stimuli: both conditioning and test stimuli in (a) and the second stimulus only in (b). Conditioning stimulus: 64 kHz, 50 dB above threshold; test stimulus: 64 kHz, 40 dB above threshold; interstimulus intervals are indicated in ms near records.

test stimulus alone (S2), and the pair of conditioning and test stimuli with a variable interval between them (S1+S2). Stimuli S1, S2, and S1+S2 were separated by 20-ms intervals. This stimulus succession was repeated 500–1000 times to collect one averaged ABR wave form. Thus, simultaneously with each response to the paired stimulus (''cond +test'' in Fig. 2), responses to the conditioning stimulus alone (''cond'') and test stimulus alone (''control'') were collected in an interleaving manner.

To extract the response to the test stimulus from that to the double stimulus, the response to S1 stimulus alone (''cond'' in Fig. 2) was point-by-point subtracted from that of the paired (S1+S2) stimulus (''cond+test'' in Fig. 2). The result was the response to the second stimulus of the pair (''test'' in Fig. 2). This test response was compared with the response to S2 stimulus alone (''control'' in Fig. 2) to present the test response amplitude in a normalized measure, i.e., as a percentage of the control one. Thus, in both subtraction and normalizing calculations, the conditioning and control response wave forms obtained in the same recording trial were used. This compensated possible long-term drifts of response amplitude due to small change of the animal position relative to the sound source and other causes.

At short interstimulus intervals, especially when the conditioning stimulus was of higher intensity than the test one, ABR amplitude was comparable with the background EEG noise. This made it difficult to extract a characteristic ABR wave form for measuring its amplitude with a satisfactory precision. Therefore, the following measurement procedure was used. A cross-correlation function was calculated between the measured record and a standard record containing ABR of high amplitude. The peak value of this function was taken as a measure of ABR wave form weight in the analyzed record.

III. RESULTS

ABR to double stimuli at the described stimulation conditions are shown in Fig. 3(a). For this example, pips of equal carrier frequency (64 kHz) and unequal intensity (conditioning and test stimuli of 50 and 40 dB above threshold. respectively) were arbitrarily chosen; only interstimulus intervals of 0.5, 1, 2, 5, and 10 ms are presented. The presented time window contains only responses to paired stimuli which corresponds to S1+S2 stimuli and ''cond+test'' response in Fig. 2. ABR wave form was fairly similar to that described in preceding studies in dolphins (Popov and Supin, 1990; Supin and Popov, 1995a). ABR to each of the paired stimulus consisted of a series of waves occurring mainly within the first 5–6 ms following a stimulus. At high stimulus intensities, response amplitude could reach values as large as 10–12 μV when measured between the highest positive and negative peaks, as the double-headed arrow in Fig. 3(a) shows.

At interstimulus intervals shorter than 2–3 ms, the conditioning and test responses were partially superimposed. Isolation of the test response by the subtraction procedure is demonstrated in Fig. 3(b). The figure shows effective elimination of the conditioning response even when its amplitude well exceeded that of the test response. The subtraction procedure made it possible to detect and measure test responses at interstimulus intervals as short as 0.5 ms. It can be noticed

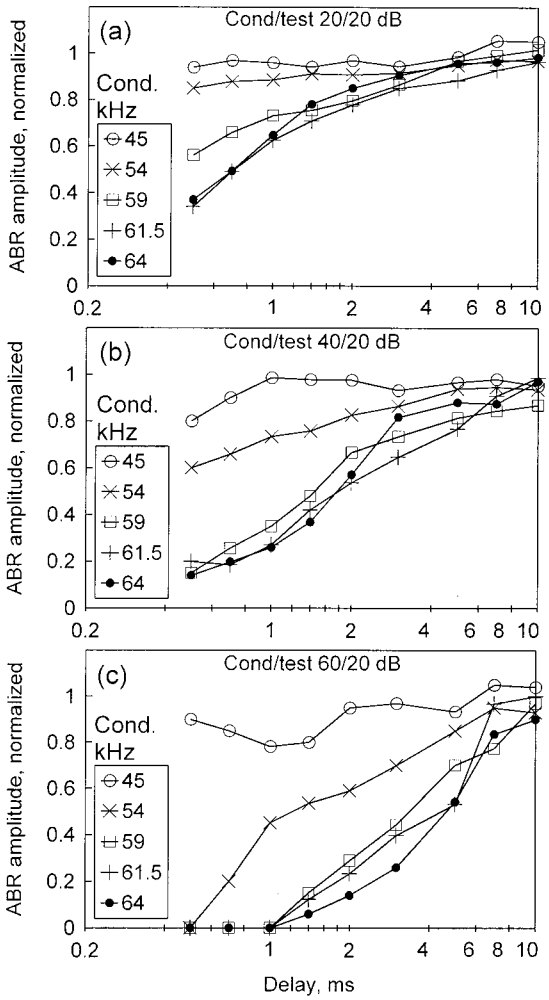

FIG. 4. ABR recovery functions at different relations between the conditioning and test stimuli. Test stimulus: 64 kHz, 20 dB above threshold; conditioning stimulus: from 45 to 64 kHz (as indicated in the legends), from 20 to 60 dB above threshold, as indicated in (a)–(c).

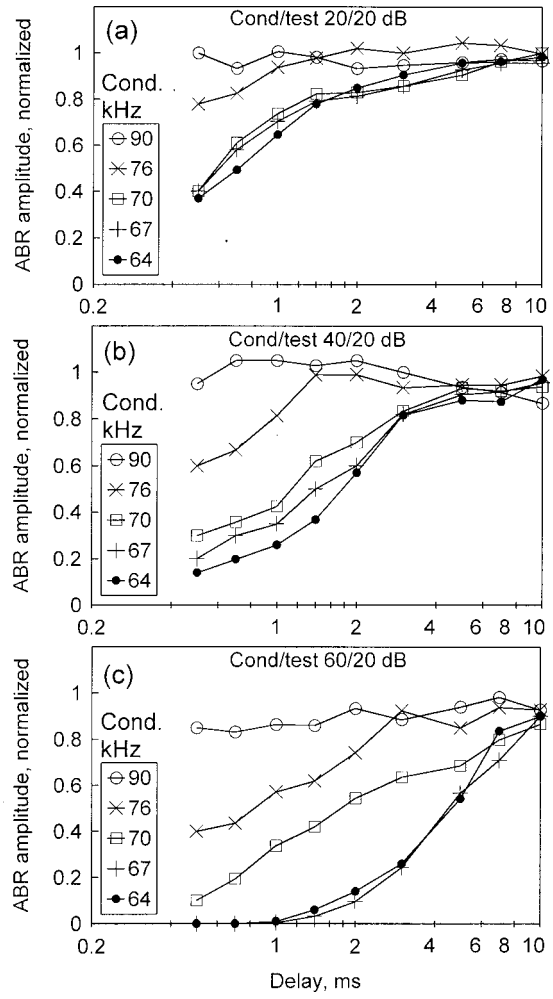

FIG. 5. The same as Fig. 4, at conditioning stimulus frequencies from 64 to 90 kHz.

that the response to the 0.5-ms delayed stimulus in Fig. 3(b) is really shifted by 0.5 ms relative to the conditioning response, so it is the isolated test response.

In the same manner as presented in Fig. 3, test response amplitude dependence on interstimulus interval was measured at a variety of stimulus parameters as follows: test stimulus frequency always of 64 kHz; conditioning stimulus frequency either equal to or above or below the test one by 1/16, 1/8, 1/4, or 1/2 oct; test stimulus levels of 20, 30, 40, 50, and 60 dB above the response threshold (the threshold was about 60 dB *re* 1 μPa); conditioning stimulus levels—the same values but not lower than the test stimulus level.

Some examples of recovery functions (ABR normalized amplitude as a function of interstimulus interval) are presented in Figs. 4 and 5. In these figures, only one test stimulus level (20 dB above threshold) and three conditioning stimulus levels (20, 40, and 60 dB, i.e., equal to, 20, and 40 dB higher than the test stimulus) are presented. To make the multiple plots better readable, they are separated into two figures: with conditioning stimulus frequencies below (Fig. 4: 64, 61.5, 59, 54, and 45 kHz) and above (Fig. 5: 64, 67, 70, 76, and 90 kHz) the test one. Both figures demonstrate regularities as follows.

(i) When conditioning and test stimulus frequencies were approximately equal, the test response suppression was rather weak and short at equal conditioning and test intensities (cond/test 20/20 dB in Figs. 4 and 5) and became deeper and longer with conditioning intensity increase above the test one (cond/test 40/20 and 60/20 dB in Figs. 4 and 5);

(ii) When conditioning and test stimulus frequencies were markedly different, the test response suppression became markedly weaker; in particular, at a frequency difference as large as ± 0.5 oct (conditioning frequencies of 45 kHz in Fig. 4 and 90 kHz in Fig. 5), the test response was not markedly suppressed even at the shortest interstimulus interval (0.5 ms) and the highest difference between conditioning and test stimulus intensities (60–20 dB).

Thus, ABR suppression by a preceding (conditioning) stimulus was obviously frequency selective. This frequency selectivity can be characterized quantitatively by frequency-dependence curves which present the normalized response amplitude as a function of conditioning-stimulus frequency at a certain interstimulus interval. Figures 6 and 7 present frequency-dependence curves at two representative interstimulus intervals, 1 and 5 ms, respectively, and at a variety of conditioning and test stimulus intensities. All the curves demonstrate that increasing the conditioning stimulus inten-

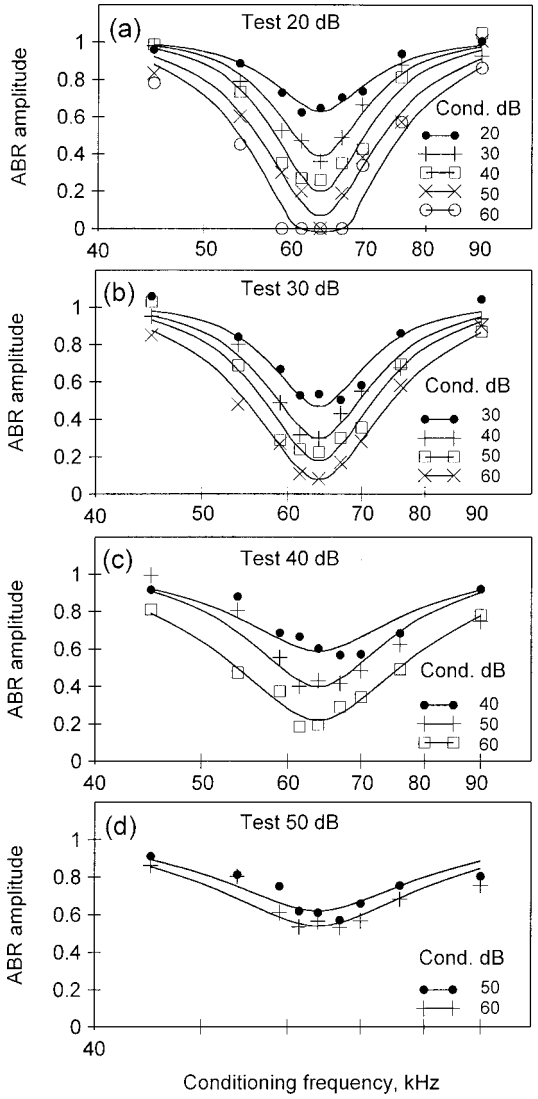

FIG. 6. Frequency-dependence curves (normalized ABR amplitude as a function of the conditioning stimulus frequency) at an interstimulus interval of 1 ms. Test stimulus: 64 kHz; from 20 to 50 dB above threshold, as indicated in (a)–(d). Conditioning stimulus levels are indicated in the legends. Pointing symbols—experimental data, smooth curves—approximation by roex functions.

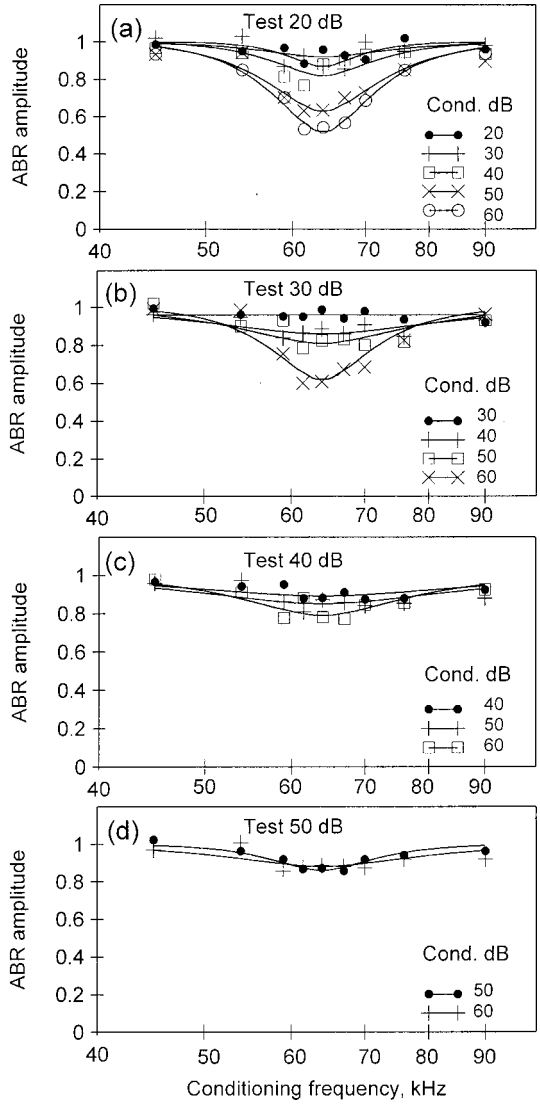

FIG. 7. The same as Fig. 6 at an interstimulus interval of 5 ms.

sity resulted in deeper suppression of the test response. The effect looks as increasing of the range between the base and tip of the curve. Quantitatively, this effect was more prominent at shorter interstimulus intervals (Fig. 6) rather than at longer ones (Fig. 7); however, qualitatively it was similar at all intervals.

To quantify the acuteness of frequency-dependence curves, we approximated experimental data by idealized curves. For this approximation, the inverted rounded-exponential (roex) function was arbitrary chosen, i.e., the function described as

$$A(g)=1-k(1+pg)\exp(-pg),$$

where A is the normalized test response amplitude, g is the deviation of the conditioning stimulus frequency from the test one (on the logarithmic scale), p is the parameter determining the acuteness of the curve (the higher p, the more narrow the curve), and k is the parameter determining the depth of suppression (the higher k, the deeper suppression). Thus, it was accepted by definition that suppression is maximal at equal frequencies of conditioning and test stimuli ($A=1-k$ at $g=0$ and $A>1-k$ at $g>0$) and disappears at large differences between these frequencies ($A\rightarrow 1$ at $g\rightarrow\infty$). For each curve, values of the parameters p and k were adjusted to minimize the mean-square deviation of the curve from the experimental data. Idealized curves obtained in such a way are exemplified in Figs. 6 and 7 for interstimulus intervals of 1 and 5 ms, respectively.

An adopted measure of acuteness of frequency-dependence curve is their equivalent rectangular bandwidth (ERB). For roex functions, ERB is equal to $4/p$. Figure 8 presents ERB of the frequency-dependence curves as a function of conditioning and test stimulus intensities; the data are presented for a variety of interstimulus intervals, from 0.5 to 5 ms. Although the base-tip range of the curves depended on interstimulus interval (compare Figs. 6 and 7), their ERB was rather similar at all intervals [compare Figs. 8(a) to 8(d)]. The general trend was that ERB depended little on the conditioning stimulus level but was much more dependent on the test stimulus level. At low-level test stimuli (20 and

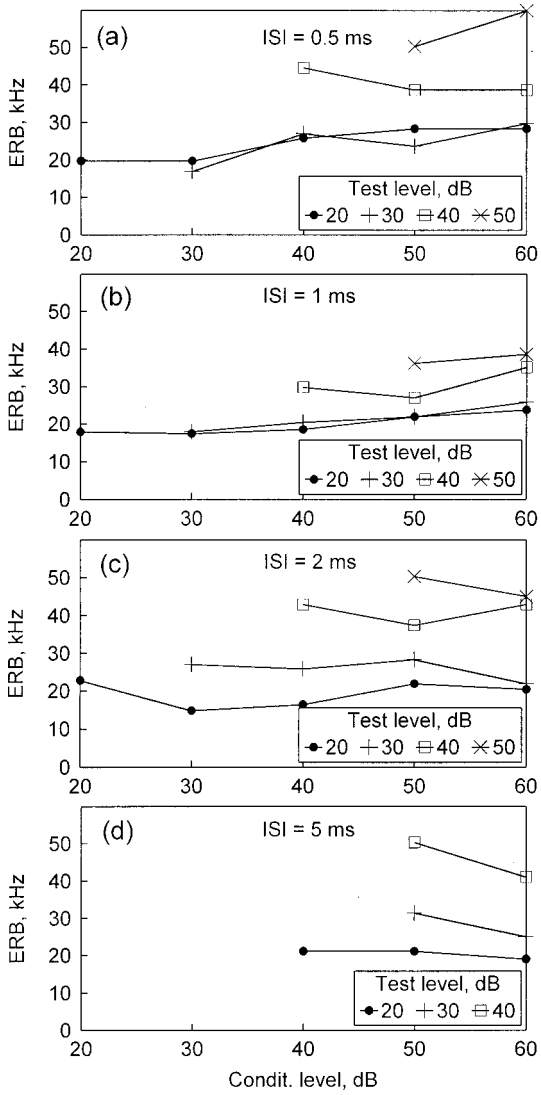

FIG. 8. ERB of frequency-dependence curves as a function of conditioning and test stimulus levels (the latter is indicated in the legend). The curves were obtained at interstimulus intervals (ISI) from 0.5 to 5 ms, as indicated in (a)–(d).

30 dB), ERB was 18–24 kHz, which corresponded to ±0.2 to ±0.26 oct. At higher-level test stimuli, the curves became wider, up to ±0.5 oct at 50 dB.

IV. DISCUSSION

The interaction between the conditioning and test stimuli can be considered as forward masking—a phenomenon which is widely used to study frequency selectivity of hearing. In dolphins, rather high frequency tuning of hearing (equivalent rectangular quality of 35–40) was demonstrated in various masking experiments with ABR recording (Supin *et al.*, 1993; Popov *et al.*, 1995, 1997). However, in those experiments, simultaneous instead of forward masking was used since very rapid recovery of ABR in dolphins made it difficult to achieve deep suppression of the test response in forward-masking conditions. This feature of the forward masking in dolphins manifested itself in the present study as well: At marked difference between the conditioning and test frequencies, the test response was suppressed very little even when the conditioning stimulus well exceeded the test one in intensity.

Therefore, the present study was not intended to obtain tuning curves which require deep (near-complete) masking of the test response. We believed that interrelations between stimuli of different frequencies may also be of interest when these interrelations are expressed in terms of response amplitude instead of thresholds. In particular, it may be of interest as a simulation of interactions between the emitted and echo pulses in echolocation. Being expressed in such a way, the data presented herein also demonstrated a prominent frequency selectivity: ERB of frequency-dependence curves as narrow as ±0.2 oct at low test levels. These ERB values are of an order of magnitude wider than those of dolphin's tuning curves presented in terms of masking thresholds: ERBs were as narrow as 1/30–1/35 of the central frequency; i.e., ±0.021 to ±0.025 oct (Popov and Supin, 1997). However, there is no contradiction between these data: Tuning curves presenting *stimulus power* and frequency-dependence curves presenting *response amplitude* as functions of masker frequency are basically different measures. Taking into account that several-times (i.e., a few dB) change of stimulus power results in a rather small change of response amplitude, the latter yields much wider frequency-dependence curves than the former at the same degree of frequency selectivity. The data presented herein show that this frequency tuning provides a significant magnitude of evoked response very soon after the conditioning stimulus which differs in frequency from the test one. Moreover, the frequency tuning might be underestimated in our experimental conditions because of inevitable spectrum splatter of short pips (see Fig. 1).

Extending these data to echolocation conditions, one can expect that if target features yield a noticeable difference between the emitted and echo spectra, the differing part of the echo spectrum should be the least masked by the emitted pulse, thus evoking the highest neuronal response. This may be helpful for extraction of proper spectral features of targets.

ACKNOWLEDGMENT

The study was supported by the Russian Foundation for Basic Research, Grant Nos. 00-15-97769, 00-04-48879.

Au, W. W. L. (**1990**). "Target detection in noise by echolocating dolphins," in *Sensory Abilities of Cetaceans: Laboratory and Field Evidence*, edited by J. A. Thomas and R. A. Kastelein (Plenum, New York), pp. 203–216.

Au, W. W. L. (**1993**). *The Sonar of Dolphins* (Springer, New York).

Au, W. W. L., Moore, P. W. B., and Pawloski, D. A., (**1988**). "Detection of complex echoes in noise by an echolocating dolphin," J. Acoust. Soc. Am. **83**, 662–668.

Dolphin, W. F., Au, W. W. L., and Nachtigall, P. (**1995**). "Modulation transfer function to low-frequency carriers in three species of cetaceans," J. Comp. Physiol., A **177**, 235–245.

Dubrovskiy, N. A. (**1990**). "On the two auditory systems in dolphins," in *Sensory Abilities of Cetaceans: Laboratory and Field Evidence*, edited by J. A. Thomas and R. A. Kastelein (Plenum, New York), pp. 233–254.

Moore, P. W. B., Hall, R. W., Friedl, W. A., and Nachtigall, P. E. (**1984**). "The critical interval in dolphin echolocation: What is it?," J. Acoust. Soc. Am. **76**, 314–317.

Popov, V. V., and Supin, A. Ya. (**1990**). "Auditory brain stem responses in characterization of dolphin hearing," J. Comp. Physiol., A **166**, 385–393.

Popov, V. V., and Supin, A. Ya. (**1997**). ''Detection of temporal gaps in noise in dolphins: Evoked-potential study,'' J. Acoust. Soc. Am. **102**, 1169–1176.

Popov, V. V., and Supin, A. Ya. (**1998**). ''Auditory evoked responses to rhythmic sound pulses in dolphins,'' J. Comp. Physiol., A **183**, 519–524.

Popov, V. V., Supin, A. Ya., and Klishin, V. O. (**1995**). ''Frequency tuning curves of the dolphin's hearing: Envelope-following response study,'' J. Comp. Physiol., A **178**, 571–578.

Popov, V. V., Supin, A. Ya., and Klishin, V. O. (**1997**). ''Frequency tuning of the dolphin's hearing as revealed by auditory brain-stem response with notch-noise masking,'' J. Acoust. Soc. Am. **102**, 3795–3801.

Supin, A. Ya., and Popov, V. V. (**1985**). ''Recovery cycles of the dolphin's brain stem responses to paired acoustic stimuli,'' (in Russ.), Dokl. Akad. Nauk SSSR **283**, 740–743.

Supin, A. Ya., and Popov, V. V. (**1995a**). ''Temporal resolution in the dolphin's auditory system revealed by double-click evoked potential study,'' J. Acoust. Soc. Am. **97**, 2586–2593.

Supin, A. Ya., and Popov, V. V. (**1995b**). ''Envelope-following response and modulation transfer function in the dolphin's auditory system,'' Hear. Res. **92**, 38–46.

Supin, A. Ya., Popov, V. V., and KLishin, V. O. (**1993**). ''ABR frequency tuning curves in dolphins,'' J. Comp. Physiol., A **173**, 649–656.